

DTIC FILE COPY

1

AD-A222 701

The Proceedings

Fifth

International
Conference on

Numerical
Ship Hydrodynamics

24-28 September 1989

Hiroshima International Conference Center
Hiroshima, Japan

DTIC

S

ELECTE

JUN 07 1990

CD D

D

DISTRIBUTION STATEMENT A

Approved for public release;
Distribution Unlimited

90 06 06 038

The
Proceedings

**Fifth
International
Conference on**

**Numerical
Ship Hydrodynamics**

Edited by
Kazu-hiro Mori

Sponsored by
Shipbuilding Research Association of Japan

David Taylor Research Center
Office of Naval Research

Naval Studies Board of the
National Research Council

24-28 September 1989
Hiroshima International Conference Center
Hiroshima, Japan

NATIONAL ACADEMY PRESS
Washington, D.C. 1990

NOTICE: The project that is the subject of this report was approved by the Governing Board of the National Research Council, whose members are drawn from the councils of the National Academy of Sciences, the National Academy of Engineering, and the Institute of Medicine. The members of the committee responsible for the report were chosen for their special competences and with regard for appropriate balance.

This report has been reviewed by a group other than the authors according to procedures approved by a Report Review Committee consisting of members of the National Academy of Sciences, the National Academy of Engineering, and the Institute of Medicine.

The National Academy of Sciences is a private, nonprofit, self-perpetuating society of distinguished scholars engaged in scientific and engineering research, dedicated to the furtherance of science and technology and to their use for the general welfare. Upon the authority of the charter granted to it by the Congress in 1863, the Academy has a mandate that requires it to advise the federal government on scientific and technical matters. Dr. Frank Press is president of the National Academy of Sciences.

The National Academy of Engineering was established in 1964, under the charter of the National Academy of Sciences, as a parallel organization of outstanding engineers. It is autonomous in its administration and in the selection of its members, sharing with the National Academy of Sciences the responsibility for advising the federal government. The National Academy of Engineering also sponsors engineering programs aimed at meeting national needs, encourages education and research, and recognizes the superior achievements of engineers. Dr. Robert M. White is president of the National Academy of Engineering.

The Institute of Medicine was established in 1970 by the National Academy of Sciences to secure the services of eminent members of appropriate professions in the examination of policy matters pertaining to the health of the public. The Institute acts under the responsibility given to the National Academy of Sciences by its congressional charter to be an adviser to the federal government and, upon its own initiative, to identify issues of medical care, research, and education. Dr. Samuel O. Thier is president of the Institute of Medicine.

The National Research Council was organized by the National Academy of Sciences in 1916 to associate the broad community of science and technology with the Academy's purposes of furthering knowledge and advising the federal government. Functioning in accordance with general policies determined by the Academy, the Council has become the principal operating agency of both the National Academy of Sciences and the National Academy of Engineering in providing services to the government, the public, and the scientific and engineering communities. The Council is administered jointly by both Academies and the Institute of Medicine. Dr. Frank Press and Dr. Robert M. White are chairman and vice chairman, respectively, of the National Research Council.

This work related to Department of Navy Contract N00014-87-C-0018 issued by the Office of Naval Research under contract authority NR 201-124. However, the content does not necessarily reflect the position or the policy of the Department of the Navy or the government, and no official endorsement should be inferred.

International Standard Book Number 0-309-04241-0
Library of Congress Catalog Number 90-60919

Copies available from:
Naval Studies Board
National Research Council
2101 Constitution Avenue
Washington, D.C. 20418

Printed in the United States of America

S129

AVAILABLE FREE OF CHARGE FROM NAVAL
STUDIES BOARD, NATIONAL RESEARCH COUNCIL
per Elizabeth Luchs, Naval Studies Board
2101 Constitution Ave., Wash, DC 20418
TELECON 6/7/90 VG

Accession For	
NTIS CRA&I	<input checked="" type="checkbox"/>
DTIC TAB	<input type="checkbox"/>
Unannounced	<input type="checkbox"/>
Justification	
By <i>per call</i>	
Distribution	
Availability	
Dist	SubCell
<i>A-1 21</i>	



PREFACE

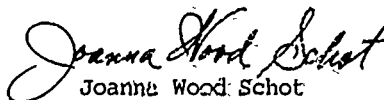
The Fifth International Conference on Numerical Ship Hydrodynamics (INC5) was held in Japan on 24-28 September 1989 at Hiroshima International Conference Center. The Conference was sponsored jointly by the Shipbuilding Research Association of Japan, and the following agencies in the Washington D.C. area: David Taylor Research Center, Office of Naval Research and Naval Studies Board of the National Research Council.

Over one hundred and ninety distinguished researchers from eighteen countries gathered for this conference and forty-six well-qualified papers were presented. Four keynote speakers were invited from outside the ship hydrodynamics community. Their presentations provided a good balance between the computational fluid dynamics and the experimental aspects of ship hydrodynamics. Because of the rapid progress in the computational fluid dynamics and the rather long time span of four years since the previous meeting, a large number of papers was submitted. For the first time in these conferences, several parallel sessions were held. Even so, many good papers had to be rejected. A special session for group discussions was arranged to allow extended interchange of ideas among the specialists and to deepen knowledge of ongoing research.

It was the paper committee's position that the validation of the computational fluid dynamics was of primary importance. Thus, the committee asked all the authors as a matter of policy to carry out an accuracy analysis with respect to grid sizes and/or time steps, convergence check or test computations for less complicated cases. This request influenced the content of the papers and resulted in more careful numerical analysis, including comparisons with other results. It was realized that this would entail additional expense and extra work for the authors, but the committee believed that the resulting papers would reflect a higher academic standard.

The committee enthusiastically supported the Workshop on Computational Fluid Dynamics Validation organized by the International Towing Tank Committee (ITTC) Validation Panel and Hiroshima University. This was a very well attended and highly productive workshop. The results should have an impact on the three components of CFD: analysis, computation, and experiment - the ACE of numerical ship hydrodynamics.

The success of the Conference was due to the collective efforts of a large number of individuals. The members of the Numerical Towing Tank Research Group in Japan (NTG) helped greatly in hosting the conference in Hiroshima. Grateful acknowledgements are also extended to the staff of Hiroshima University for their devoted assistance. Special thanks go to Ms. Chizuko Kodera for her invaluable organizing efforts. Without her skills the conference could not have been such a technical success and a very pleasant experience.


Joanna Wood Schot

Co-Chair

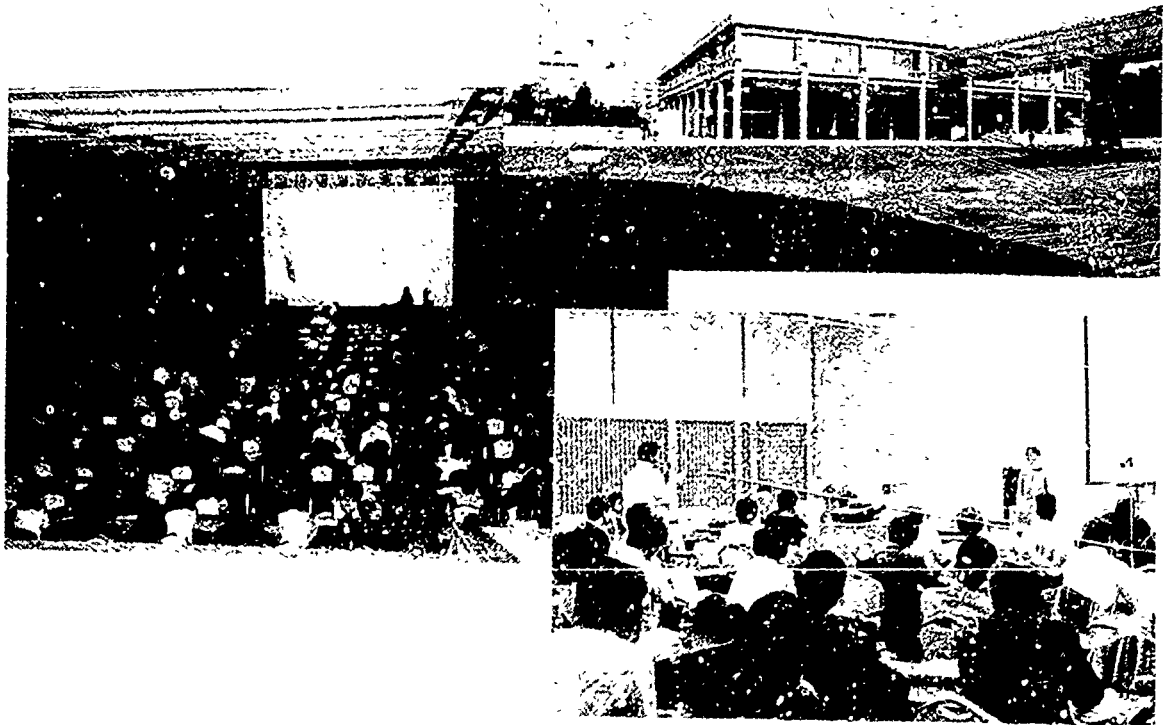
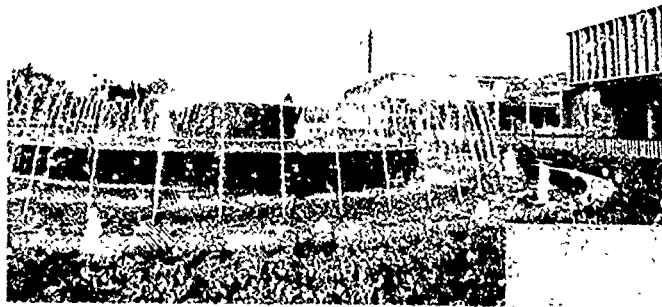
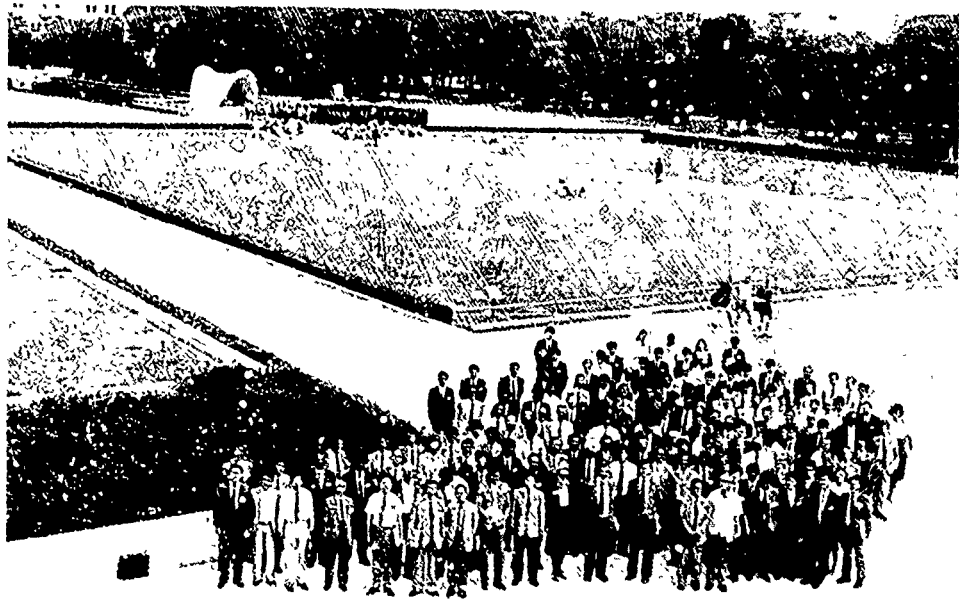
ORGANIZATION AND PAPERS COMMITTEE

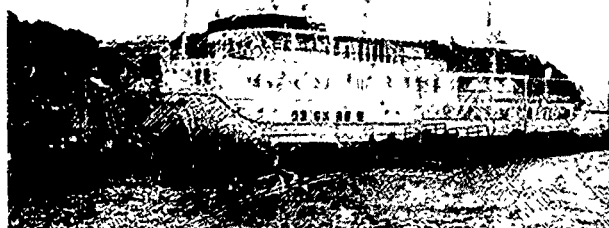
Co-Chairs

Hisashi Kajitani
Joanna Wood Schot

Members

Yasvaki Doi	Henry Haussling
Thomas Hwang	Yoshiaki Kodama
Hans J. Lugt	Hisaaki Maeda
Justin H. McCarthy	Hideaki Miyata
Kazu-hiro Móri	Tetsuro Nagamatsu
Kuniharu Nakatake	Francis Noblesse
Seiko Ogiwara	Makoto Ohkusu





Partial CONTENTS:

Preface	iii
Opening Session		
Welcoming Address, K. Horinokita	1
Opening Address, H. Kajitani	2
Keynote Lectures		
Chairmen: H. Kajitani, E. Rood, M. Ohkusu		
→ Developing an Accurate and Efficient Method for Viscous Compressible Flow Simulations - An Example of CFD in Aeronautics, - K. Fujii	5
→ Boundary-Layer Stability and Transition, W. S. Saric	23
→ RNG Modeling Techniques for Complex Turbulent Flows, S. A. Orszag	35
→ A Flood Control of Dam Reservoir by Conjugate Gradient and Finite Element Methods, M. Kawahara and T. Kawasaki	45
Session 1 : N-S solver		
Chairwoman: J. W. Schot, Co-chairman: T. Okuno		
→ Numerical Simulation of Three-Dimensional Viscous Flow around a Submersible Body, C-I Yang, P-M. Hartwich and P. Sundaram	59
Grid Generation and Flow Computation for Practical Ship Hull Forms and Propellers Using the Geometrical Method and the IAF Scheme Y. Kodama	71
Session 2A : Flow around ship		
Chairman: L. Larsson, Co-chairman: S. Ishikawa		
Recent Developments in a Ship Stern Flow Prediction Code, M. Hoekstra	87
6 Computation of a Free Surface Flow around an Advancing Ship by the Navier-Stokes Equations, T. Hino	103
→ Finite-Difference Simulation of a Viscous Flow about a Ship of Arbitrary Configuration; <i>→ next page</i> M. Zhu, H. Miyata and H. Kajitani	119
Session 2B : Green function & Neumann-Kelvin problem		
Chairman: K. Mori, Co-chairman: H. Kagemoto		
Numerical Evaluation of the Complete Wave-Resistance Green's Function Using Bessho's Approach H. T. Wang and J. C. W. Rogers	133

→ Numerical Evaluation of a Ship's Steady Wave Spectrum. F. Noblesse, W. M. Lin and R. Mellish	145
↳ Ship Wave Ray Tracing Including Surface Tension, D. B. Huang and K. Eggers	157

Session 3A : Flow around ship

Chairman: I. Tanaka, Co-chairman: M. Ito

↳ Numerical Calculations of the Viscous Flow over the Ship Stern by Fully Elliptic and Partially Parabolic Navier-Stokes Equations; K. J. Oh, S. H. Kang and T. Kobayashi	175
New Viscous and Inviscid CFD Techniques for Ship Flows L. Larsson, L. Broberg, K. J. Kim and D. H. Zhang	185
↳ Numerical Simulation of Viscous Flow around Practical Hull Form A. Masuko and S. Ogiwara	211

Session 3B : Free surface flows

Chairman: A. J. Hermans, Co-chairman: Y. Kyojuka

Calculation of Nonlinear Water Waves around a 2-Dimensional Body in Uniform Flow by Means of Boundary Element Method K. Suzuki	225
Nonlinear Simulation of Transient Free Surface Flows R. Cointe	239
Slamming of Flat-Bottomed Bodies Calculated with Exact Free Surface Boundary Conditions S. Falch	251

Session 4 : Turbulent flow simulation/Viscous flows

Chairman: Y. Himeno, Co-chairman: Y. Higo

↳ Pressure Transients in Transitional Boundary Layer over a Solid Surface; Sin-I-Gheng	269
↳ Large Eddy Simulation by Using Finite Difference Method Y. Doi	285
and Computation of the Flow past Shiplike Hulls, <i>Symposia Japan</i> J. Piquet and M. Visonneau	295

Session 5A : Viscous flows

Chairman: M. Ikeshata, Co-chairman: T. Eguchi

Simulations of Forces Acting on a Cylinder in Oscillatory Flow by Direct Calculation of the Navier-Stokes Equations T. Kinoshita, H. Hinatsu and S. Murashige	313
Numerical and Analytical Investigations of a Stationary Flow past a Self-Propelled Body N. P. Moshkin, V. V. Pukhnachov and V. L. Sennitskii	329

Session 5B : Motion of floating bodies among waves

Chairman: *C. M. Lee*, Co-chairman: *K. Takagi*

Time-Domain Calculation of the Nonlinear Hydrodynamics
of Wave-Body Interaction

C. Yang, Y. Z. Liu and N. Takagi 341

Two-Dimensional Numerical Modelling of Large Motions of
Floating Bodies in Waves

D. Sen, J. S. Pawlowski, J. Lever and M. J. Hinchey 351

Session 6 : Free-surface waves

Chairman: *J. H. Hwang*, Co-chairman: *K. Takagi*

The Effect of the Steady Perturbation Potential on the
Motions of a Ship Sailing in Random Seas

R. H. M. Huijsmans and A. J. Hermans 375

Numerical Prediction of Semi-Submersible Non-Linear
Motions in Irregular Waves

X. B. Chen and B. Molin 391

Numerical Computations for a Nonlinear Free Surface Flow
Problem

K. J. Bai, J. W. Kim and Y. H. Kim 403

Session 7 : Restricted waters

Chairman: *M. Ohkusu*, Co-chairman: *T. Fukasawa*

Numerical Grid Generation and Upstream Waves for Ships
Moving in Restricted Waters

R. C. Ertekin and Z. -M. Qian 421

Wave Resistance and Squat of a Slender Ship Moving near
the Critical Speed in Restricted Water

H. S. Choi and C. C. Mei 439

Session 8A : Surface tension/Free-surface viscous flows

Chairman: *E. Baba*, Co-chairman: *T. Fukasawa*

Some Numerical Computations about Free Surface Boundary
Layer and Surface Tension Effects on Nonlinear Waves

E. Campana, F. Lalli and U. Bulgarelli 455

A Boundary Integral Formulation for Free Surface Viscous
and Inviscid Flows about Submerged Bodies

C. M. Casciola and R. Piva 469

Session 8B : Image processing

Chairman: *H. Kato*, Co-chairman: *K. Kataoka*

Development of a New Velocity Measurement System by Using
Computerized Flow Visualization and Numerical Method

K. Mori and S. Ninomiya 481

Automatic Particle-Image Velocimetry Utilizing Laser-
Induced Fluorescent Particles

T. C. Fu, R. Bing, J. Katz and T. T. Huang 493

Session 9A : Radiation/Diffraction

Chairman: *M. Kan*, Co-chairman: *Y. Terao*

Side-Wall Effects on Hydrodynamic Forces Acting on a Ship with Forward and Oscillatory Motions <i>M. Kashiwagi and M. Ohkusu</i>	499
Interaction between Current, Waves and Marine Structures <i>R. Zhao and O. M. Faltinsen</i>	513
The Numerical Solution of the Motions of a Ship Advancing in Waves <i>G. X. Wu and R. E. Taylor</i>	529

Session 9B : Ship stern flows

Chairman: *J. McCarthy*, Co-chairman: *H. Tamashima*

On the Numerical Solution of the Turbulent Flow-Field past Double Ship Hulls at Low and High Reynolds Numbers <i>G. D. Tzabiras and T. A. Loukakis</i>	539
Computation of Viscous Flow around a Propeller-Shaft Configuration with Infinite-Pitch Rectangular Blades <i>F. Stern and H. T. Kim</i>	553
Computation of a Nonlinear Rotational Inviscid Flow through a Heavily-Loaded Actuator Disk with a Large Hub <i>B. Yim</i>	571

Session 10A : Rankine source method

Chairman: *K. Nakatake*, Co-chairman: *Y. Terao*

Computations of 3D Transom Stern Flows <i>B. H. Cheng</i>	581
Ship Wave-Resistance Computations <i>G. Jensen, V. Bertram and H. Söding</i>	593

Session 10B : Viscous flows/Vortex

Chairman: *G. van Oortmerssen*, Co-chairman: *M. Tamashima*

Numerical Solution of Viscous Flows about Submerged and Partly Submerged Bodies <i>P. G. Esposito, G. Graziani and P. Orlandi</i>	607
Simulation of Hydrodynamic Loading and Structural Response of a Marine Riser <i>A. Dercksen and F. van Walree</i>	617

Session 11A : Rankine source method

Chairman: *F. Noblesse*, Co-chairman: *Y. Kasahara*

Stability and Accuracy of a Non-Linear Model for the Wave Resistance Problem <i>A. J. Musker</i>	629
Calculation of Free-Surface Flow around a Ship in Shallow Water by Rankine Source Method <i>H. Yasukawa</i>	643

A Hybrid Model for Calculating Wave-Making Resistance V. Aaneslar	657
Session 11B : Cavitation	
Chairman: S. T. Don, Co-chairman: A. Masuko	
Finite Difference Analysis of Unsteady Cavitation on a Two-Dimensional Hydrofoil A. Kubota, H. Kato and H. Yamaguchi	667
Theoretical Prediction of Midchord and Face Unsteady Propeller Sheet Cavitation S. A. Kinnas and N. E. Fine	685
Propeller Inflow Corrections for Improved Unsteady Force and Cavitation Calculations T. S. Mautner	701
Closing session	
Concluding Remarks F. Noblesse	715
Group discussions	
Summary of the Group Discussion on Rankine Source Methods Chairman: A. J. Musker, Co-chairman: S. Ogiwara	719
Summary of the Group Discussion on Navier-Stokes Solvers Chairman: J. Piquet, Co-chairman: Y. Kodama	721
Summary of the Group Discussion on Boundary Integral Method for Radiation/Diffraction Problems Chairman: O. M. Faltinsen, Co-chairman: M. Takaki	725
List of participants	727

WELCOMING ADDRESS

Katsuro Horinokita,
Chief Executive, Shipbuilding Research Association of Japan

Ladies and gentlemen, on behalf of the Japanese sponsoring organization, it is of my great pleasure to welcome all of you to Japan and to the Fifth International Conference on Numerical Ship Hydrodynamics.

Four keynote lectures and forty six papers will be presented by international authorities during the four-day conference. More than 190 participants attend the conference from sixteen countries. This is actually an international conference. We are much delighted with such a positive reaction.

Behind such a positive reaction, I guess, there is a potential expectation for the computational fluid dynamics, CFD. As you may know, when we started to work out to host the conference in Japan, four years ago, the shipbuilding industries in Japan were suffering from a serious setback. Now they are expanding their activities into various fields and cultivating new frontier problems such as ocean engineering, environmental sciences, high speed marine vehicles with new concepts and so on. This may be the case internationally.

The computational dynamics or simulation is a promising tool for such unknown problems in new fields. CFD in marine hydrodynamics is expected not only to predict the flows around the marine vehicles or ocean structures but for more global aspects such as energy or environmental problems.

On the other hand the high speed computers are becoming much popular and easy to access. Their capability seems unbounded. CFD, with complementary use of the conventional tanks, will make us possible to make further steps into new frontier fields.

Thus much is expected for this conference. I believe the conference will be successful and fruitful. And I hope also that the conference may be a good occasion for international human channel.

Finally I would like to express our cordial gratitude to our co-sponsors. As you know, this conference has initiated and has been supported by David Taylor Research Center. Without their foresight and continuous efforts the conference has not existed. My gratitude should be extended to Office of Naval Research and Naval Studies Board National Research Council for their consistent supports.

Again I would like to say welcome to the Fifth International Conference on Numerical Ship Hydrodynamics. Thank you.

OPENING ADDRESS

Hisashi Kajitani
Professor, The University of Tokyo

The Fifth International Conference on Numerical Ship Hydrodynamics is now open at the newly built Hiroshima International Conference Center, gathering over one hundred and ninety distinguished researchers from eighteen countries. The Conference is sponsored by David Taylor Research Center, Office of Naval Research, Naval Studies Board of the National Research Council and the Shipbuilding Research Association of Japan. We appreciate heartily their continuous encouragement and financial support.

This is the fifth Conference. The first two were held in the United States in 1975 and 1977, the third in France in 1981 and the fourth again in the United States, Washington DC in 1985. With increasing the time, the remarkable progress was made in exchanging knowledge and new arts in the field of ship hydrodynamics and ocean engineering. It was about four years ago that a group of Japanese colleagues proposed first to invite this conference to Japan. Since then, Ms. Joanna Schot has endeavored on the US side greatly as a co-chairperson, and Prof. Kazu-hiro Mori of Hiroshima University worked hard as the main coordinator for the management of the Conference. It is hard to express our full acknowledgement for their contributions.

As you know through the program, four keynote lectures and high quality forty-six papers are presented. They deal with mainly 1) the flow simulation by Navier-Stokes solver, 2) simulation of free surface flow and forces by boundary element or boundary integral method including Rankine source method, 3) motion of ships or bodies among waves including waves of radiation and diffraction, and 4) several important topics about turbulent flow, ray theory, treatment of Green function for free surface flow, soliton, squat, free surface boundary layer with surface tension, image processing, cavitation, hull-appendage juncture flow and so on. Many papers were received for the proposed topics of the program. We endeavored to accept as many as possible by compressing the presentation time and setting up some parallel sessions. Even so, still some good papers could not be accepted. However, we earnestly expect hot and ample discussions by all the participants. For this purpose and to deepen our understanding, we decided to devote the final session, though optional, for group discussions. Participants may choose either of the three topics, i.e. Rankine source method, N-S solver and BIM for radiation and diffraction problems. I am expecting that a lot of free and dreamful discussions will be take place there.

Our interest to know the fluid dynamics phenomena is expanding widely and profoundly. We know that many new problems to be studied are arising and range from micro scale fluid flow for the resistance reduction to global scale flow as one of the importance in environmental science and technology.

Hiroshima, a cultural center of mid-west of Japan, is a reborn but historical city. A history around Hiroshima conveys a famous story of "three arrows" that has been transferred from a Samurai general M. Mohri of this district to his three sons of battle age about 450 years ago. The very old general Mohri said to his three sons; one arrow is easy to be broken down but three arrows are not if they are bounded together tightly. Thereby he asked his sons to cooperate each other for the best results. We admit that the development is great in numerical ship hydrodynamics. However, we recognize at the same time that the final target is to grasp the fundamental and fine knowledge about the fluid flow physics. For this end the cooperation and binding together of three arrows -- analysis, computation and experiment -- is essential.

I hope you'll enjoy the Conference as well as the scenery and the history of Hiroshima.

Keynote Lectures

Developing an Accurate and Efficient Method for Compressible Flow Simulations - An Example of CFD in Aeronautics -

K. Fujii

The Institute of Space and Astronautical Science
Sagamihara, Japan

Abstract

Capability of the current CFD technology in the aeronautical society is discussed with one of the representative Navier-Stokes codes in Japan, as an example. The code is named LANS3D and was developed for the numerical simulation of high-Reynolds number compressible flows. The algorithm used in this code is briefly described first and then the applications for aircraft simulation, vortical flow simulation and spaceplane simulation are presented. These examples show how the code has been improved to satisfy two important requirements of the computational fluid dynamics (CFD) codes; efficiency and accuracy. Importance of developing a supporting system on graphic workstations is finally discussed.

1. Introduction

Computational Fluid Dynamics (CFD) is beginning to play an important role in the aeronautical industry all over the world. People now realize that CFD can be a new and effective design tool with the aid of supercomputer. At the same time, CFD is becoming an important scientific tool for the fluid dynamics research. As high-speed supercomputers with large memory become popular, the research now is focused on the Navier-Stokes simulations for understanding fluid physics as well as for the future use as a design tool in engineering.

In the application of the CFD to the aeronautical problems, there are two important remarks to note. First, representative Reynolds number is large compared to many of the other CFD applications. Even though viscous equations are solved, contribution of viscous terms is small in most of the flow field. Thus, computational algorithms that have been developed for the Euler equations are mainly used. Physically, viscous effect is confined to the thin layers near the body surface and to evaluate viscous effect properly with the Navier-Stokes simulations, grid spacing near the body surface should be very small. For instance, typical Δy for the transonic flow simulation is $O(10^{-5}-10^{-6})$. Thus, explicit time integration is not appropriate and implicit time integration is indispensable.

At the same time, adding high-order artificial dissipation is required to keep the computation stable especially when the central difference is used for convective terms.

Second, accurate prediction of aerodynamic coefficients is required. A few percent of the drag reduction is important for aircraft design, and the effect of Reynolds number and other parameters should be accurately evaluated. Transition and turbulence modeling are also important. Simulation results for lower Reynolds-number flows can not be extrapolated to high Reynolds numbers. In some applications such as leading-edge separation flow field over a delta wing as shown later, strong separation vortices become key factor for the aerodynamic coefficients. Since the Reynolds number is high, flow field away from the body surface is considered to be rotational inviscid in such applications. However, as is the case of another applications, viscous effect near the body surface should be properly evaluated because that is the key factor to determine the location and the strength of the separation vortices.

The present author has been engaged in developing an efficient and accurate method for the simulation of complicated flows by solving the compressible Navier-Stokes equations. In the initial stage of the development, main effort was laid on improving the efficiency. With the progress of supercomputer capability, recent effort tends to be focused on the improvement of the accuracy. In the present paper, the method and the developed Navier-Stokes computer code named LANS3D ('LANS' stands for the LU-ADI Navier-Stokes code) is briefly described first. Some of the application examples are then presented. First example is the transonic flow over transport aircraft configuration. Second example is the simulation of vortex breakdown over a strake-delta wing conducted when the author was a research associate at NASA Ames Research Center. In this simulation, the importance of the grid resolution and the accuracy of the numerical algorithm was realized and the computer code was modified. Finally, recent application to the spaceplane configuration is presented. The spacecraft design is so critical that the simulation should be accurate for the

complicated flow field. These examples will show how the accuracy and efficiency of the code have been improved and what problems are left to be improved.

2. Governing Equations and Numerical Algorithm

Compressible Navier-Stokes Equations

The basic equations under consideration are the unsteady Navier-Stokes equations written for a body-fitted coordinate system (ξ, η, ζ) .

$$\partial_t \hat{Q} + \partial_\xi \hat{E} + \partial_\eta \hat{F} + \partial_\zeta \hat{G} = Re^{-1} \partial_\zeta \hat{S} \quad (1)$$

In Eq.(1), the thin-layer approximation has been introduced. The use of thin-layer Navier-Stokes equations is justified because the viscous effects are confined to a thin layer near the wall and are dominated by the viscous terms associated with the strain rates normal to the wall, and because the flow away from the body is essentially inviscid. It should be noted that all the viscous terms are not properly evaluated in the viscous layers even by the full Navier-Stokes equations because of the grid deficiency.

The pressure, density, and velocity components are related to the energy for an ideal gas by

$$p = (\gamma - 1) \left[e - \frac{1}{2} \rho (u^2 + v^2 + w^2) \right] \quad (2)$$

As will be mentioned later, thin-layer approximation is sometimes extended in two directions. In that case, additional terms appear in Eq.(1) although there is no essential change in the solution process.

Numerical Algorithm

The algorithm is called LU-ADI (or ADI-LU) factorization method proposed by Obayashi et al.[1] and the 3-D Navier-Stokes code based on this algorithm was developed by Fujii and Obayashi[2]. Note that this LU-ADI algorithm is different from the original algorithm presented in Refs. 3 and 4. Since the applications are focused on the Navier-Stokes simulations, LU-ADI algorithm uses the Euler implicit integration in time. With the aid of factorization, most of the implicit schemes avoid the memory problem of inverting huge matrices. They are usually classified into two categories based on how to factorize the implicit operator. One is the ADI factorization and the other is the LU factorization. In the ADI factorization method, the left-hand-side implicit operator is split into three components for each direction using approximate factorization. In the LU factorization, the operator is split into two components based on the positive and negative flux Jacobian matrices. The ADI factorization is efficient but has large factorization error and stability problem, and the LU factorization has more arithmetic operations and difficulty for the efficient-vectorization. LU-ADI algorithm tries

to decrease the arithmetic operations and can be considered as the compromise of the ADI and LU factorization algorithms as pointed out by Jameson[5]. In this algorithm, LU factorization is introduced in addition to the ADI factorization. Each ADI operator which is obtained by the so called Beam-Warming algorithm[6] is first diagonalized and then decomposed into two parts using the flux vector splitting idea[7]. To keep the diagonally dominance, approximate LDU decomposition is used instead of simple LU decomposition.

The Beam-Warming factorization applied to Eq. (1) is written as

$$\begin{aligned} & (I + h\delta_\xi \hat{A}^n - D_i|_\xi) (I + h\delta_\eta \hat{B}^n - D_i|_\eta) \times \\ & (I + h\delta_\zeta \hat{C}^n - hRe^{-1} \delta_\zeta J^{-1} \hat{M}^n J - D_i|_\zeta) \Delta \hat{Q}^n \\ & = -h (\delta_\xi \hat{E}^n + \delta_\eta \hat{F}^n + \delta_\zeta \hat{G}^n - Re^{-1} \delta_\zeta \hat{S}^n) \\ & \quad - (D_e|_\xi + D_e|_\eta + D_e|_\zeta) \hat{Q}^n \end{aligned} \quad (3)$$

where h is the time-step, and δ is a central finite-difference operator. The D_i and D_e terms are implicit and explicit artificial dissipation terms which should be added to the left-hand side and the right-hand side, respectively, to maintain stability. The basic algorithm is first-order accurate in time and second-order accurate in space.

In the LU-ADI algorithm, each ADI operator is diagonalized and then decomposed into two parts using the technique of flux vector splitting. For example, in the ξ -direction,

$$\begin{aligned} & I + h\delta_\xi \hat{A} \\ & \doteq T_\xi (I + h\delta_\xi^+ \hat{D}_A^+ + h\delta_\xi^- \hat{D}_A^-) T_\xi^{-1} \\ & \doteq T_\xi (I - \alpha h \hat{D}_A^- + h\delta_\xi^+ \hat{D}_A^+) (I + \alpha h |\hat{D}_A|)^{-1} \\ & \quad \times (I + \alpha h \hat{D}_A^+ + h\delta_\xi^- \hat{D}_A^-) T_\xi^{-1} \end{aligned} \quad (4)$$

where α is a coefficient appearing on the j -index for the upwind differencing. In other words, $\alpha = 1.0$ when first-order differencing is used for the ξ -derivative, and 1.5 when second-order differencing is used. Currently, α is set to be 1.0 to eliminate additional arithmetic operations. The decomposition in Eq. (4) can be called approximate LDU factorization, or diagonally dominant factorization. This decomposition is more stable than simple LU factorization because the diagonal element always has $|\hat{D}_A|$.

In the solution process, an inversion in one direction consists of one scalar forward sweep, and one scalar backward sweep. Thus, LU-ADI algorithm requires little additional memory and is easily vectorized. Note that an operator in each direction can be considered to be a single iteration of a symmetric Gauss Seidel relaxation in one dimension. The \hat{D}_A^\pm terms are modified to include an implicit artificial dis-

sipation term. Another modification is necessary in the ξ -direction to evaluate implicit viscous terms. Additional details of the derivation of the LU-ADI algorithm are given in Ref. 1. In the right-hand side, explicit artificial dissipation is necessary. the dissipation model was changed time to time, but currently, nonlinear second-order and fourth-order mixed dissipation model is implemented. The idea comes from the TVD scheme and the model is called simplified TVD-type dissipation. Again, the details are found in Ref. 1.

High-order upwind differencing has become popular in recently-developed Euler methods for compressible inviscid flow simulations. This feature has been extended in the straightforward manner for the evaluation of convective terms of Navier-Stokes computations. Lately, the matrix form of the dissipation terms implicitly introduced by upwind methods was studied[8,9] and, it was shown that such terms in the upwind schemes such as Roe's flux difference splitting became small in the viscous layers. Thus the use of the proper upwind could improve the accuracy in the viscous layer as well as make the discontinuities sharp.

Convective terms in the right-hand side of the code was recently modified and the code includes the option to choose either original central differencing with artificial dissipation or flux difference splitting with Roe's average[10]. Higher-order extension of flux difference splitting using the MUSCL approach is found in Ref. 3, but is briefly described again. When the convective terms are differenced with the flux-difference splitting of Roe, the spatial derivatives are written in the conservative form as a flux balance. For instance in the ξ -direction,

$$\left(\frac{\partial \tilde{E}}{\partial \xi}\right) = \frac{(\tilde{E}_{j+1/2} - \tilde{E}_{j-1/2})}{\Delta \xi} \quad (5)$$

The numerical flux $\tilde{E}_{j\pm 1/2}$ can be written as the solution to an approximate Riemann problem and the necessary metric terms are evaluated at the cell interfaces $j+1/2$.

$$\tilde{E}_{j+1/2} = \frac{1}{2}[\tilde{E}(Q_L) + \tilde{E}(Q_R) - |\tilde{A}|(Q_R - Q_L)]_{j+1/2} \quad (6)$$

where \tilde{E} is the flux vector and \tilde{A} is the corresponding Jacobian matrix computed using the Roe's average state $-$. Q_L and Q_R are the state variables to the left and right of the half-cell interface. These state variables are determined from the locally one-dimensional non-oscillatory interpolations called MUSCL approach. Primitive variables $q[\rho, u, v, w, p]^T$ are used for that purpose, and high-order accurate monotone differencing is given by a one-parameter κ .

$$\begin{aligned} (q_L)_{j+1/2} &= q_j + \frac{s}{4}[(1 - \kappa s)\Delta_- + (1 + \kappa s)\Delta_+]_j \\ (q_R)_{j+1/2} &= q_{j+1} - \frac{s}{4}[(1 - \kappa s)\Delta_+ + (1 + \kappa s)\Delta_-]_{j+1}, \end{aligned} \quad (7)$$

where

$$(\Delta_+)_j = q_{j+1} - q_j, \quad (\Delta_-)_j = q_j - q_{j-1}$$

and

$$s = \frac{2\Delta_+\Delta_- + \epsilon}{(\Delta_+)^2 + (\Delta_-)^2 + \epsilon}$$

s is the Van Albada's limiter and ϵ is a small constant to prevent zero division. For all the results here, third-order accuracy corresponding to $\kappa = 1/3$ is used. Near the boundary, the MUSCL interpolation goes back to the first-order.

The flux evaluation for the central difference method is written in the same form as Eq.(6) considering the artificial dissipation into account.

$$\begin{aligned} \tilde{E}_{j+1/2} &= \frac{1}{2}[E_j + E_{j+1} \\ &\quad - ((1 - \varphi)\epsilon_2 - \varphi\epsilon_4 \nabla_\xi \Delta_\xi)_{j+1/2}(Q_{j+1} - Q_j)] \end{aligned} \quad (8)$$

where φ is a kind of limiter function.

The first two terms E_j and E_{j+1} correspond to the second-order central difference and the last term corresponds to the dissipation model. The same is true for Eq.(6). The first two terms construct central difference and the last term is dissipative term implicitly added by upwinding. Without limiter functions, first two terms become second-order central difference for first-order upwind method, and become fourth-order central difference for third-order upwind method. The point here is the form of the dissipation terms. In the artificial dissipation model used with the central difference, magnitude of the coefficient is the same for all the equations. Suppose we decompose the Euler equations into a set of independent equations for the waves with the characteristic speed u , $u+c$, $u-c$, the magnitude of coefficient should be chosen to be large enough for any of the waves. In the flux evaluation of the Roe's flux difference splitting, this coefficient is in the form of matrix A . If you rewrite this dissipation term, it is recognized that dissipation depends on the strength of each wave and the magnitude is automatically determined for each wave by upwinding. Thus, artificial dissipation included in the high resolution upwind methods could be smaller than the dissipation used with the central difference methods. It should also be noted that Vatsa et al. demonstrated this dissipation terms become automatically small in the viscous layers near the body surface[8]. On the other hand, some kind of scaling to decrease the dissipation is necessary near the body surface for the central difference approach.

3. Application Examples

3.1 Aircraft Simulation

- Toward Efficient Code -

Following the several trial computations to evaluate the code capability[4], the developed 3-D Navier-Stokes code based on the LU-ADI algorithm was first used for the simulation of an isolated wing named W-14[2]. This wing geometry was developed as a wing for the transonic transport aircraft by Mitsubishi Heavy Industries. The purpose of this study was to compare the computed result with the experiment, and thus, several computations were carried out for the angles of attack varying from 0° to 7.5° . The Mach number was fixed to be the design Mach number 0.82. Total number of the grid points was 200,000. The angles of attack assigned for the computations were slightly modified from those of the experiment by MHI designers, and the computers: Fujii and Obayashi, were not informed of the experimental data in advance. The flow was assumed to be fully turbulent and the so-called Baldwin and Lomax turbulence model[11] was used. The comparison of the surface C_p distribution with the experiment for 2.46- deg. case is shown in Fig. 1. The computed result shows the same tendency as the experiment. The data agreement for both upper and lower surface is good at every station and, in addition the pressure at the trailing edge is well predicted, which is important for the design process of a new wing.

In early 1986, the code was modified for the simulation of wing-fuselage combination[12]. Again, the used geometry named W-18 was designed by the MHI and seven angle of attacks (from 0.0° to 6.0°) that were shifted a little from the experiment by the empirical way were suggested to the computers who were not informed of the experimental data. Figure 2 shows the grid for the upper half volume of the computational domain. Since not only the viscous layers over the wing but also the viscous layers over the fuselage should be considered, the thin-layer approximation is now adopted for two directions and thus, the basic equations (1) are modified. The turbulence model was also modified near the wing-fuselage junction. The computational grid was generated by Takanashi using his modified conformal mapping technique, and the number of the grid points was increased to about 800,000.

Figures 3a-3b show the surface pressure contour plots for the 6.0-deg case. There occurs a large shock-induced separation near the root section, and shock wave exists even at the fuselage surface. The shock wave has a strong spanwise curvature as in the case of isolated wing, but remarkable difference exists near the wing-fuselage junction. For an isolated wing, the shock

wave is always perpendicular to the center symmetry plane. On the other hand, the shock wave curves forward at the root section because of the large recirculating region induced by the wing-fuselage interaction. Computed off-body particle path traces are presented in Fig. 4. The strong spiral is created and moved outboard behind the shock wave over the wing. Near the wing-fuselage junction, there exists a large recirculating region, where the vortical flow resembles the coiled spring bent 90° . The vortex axis is perpendicular to both the wing and the fuselage surface. The C_p distributions over the wing and the fuselage surfaces for 4.0-deg case are compared with the experiment in Figs. 5a and 5b respectively. The overall agreement is fairly good, not only for the wing but also for the fuselage. Note that the discrepancy in the pressure level at the tip section can be explained by the elastic deformation of the test model in the experiment. It is possible that the tip section of the steel model was twisted by aerodynamic forces, since the aspect ratio of the wing is very high. The discrepancy in the inboard region may be due to the poor turbulence model. The details of the computations are found in Ref. 12.

In 1988, along with the parametric study for several wing-fuselage combinations, the flow simulation over an almost complete aircraft was tried by Takanashi et al[13]. In addition to the wing and fuselage, vertical and horizontal tails were added. The centerline symmetry plane was modified to include the viscous effect of the vertical tail. The horizontal tail wing were sandwiched between two chordwise grid lines and the effect of viscous layers over the tail surface was introduced there. Only the coarse grid simulation using about 600,000 grid points was carried out. The surface grid distribution and the computed surface pressure contours are plotted in Fig. 6 and 7, respectively. The Mach number is 0.6, the angle of attack is 0 deg and the Reynolds number is 3.5×10^6 for this case. Reference 13 shows the details of the computation.

All the computations above were carried out within the specified time frame, as they should be for the design purpose. The reliable solutions, thus, had to be obtained within reasonable computer time and the efficiency was the matter of concern. Initially, wing simulation required roughly two hours on Fujitsu VP supercomputer, and now requires 20 min. to 40 min. of computer time. Wing-fuselage simulation could be carried out within 2 to 3 hours. However, for the design purpose, twice as much should be considered for safety. Checking the effect of parameters such as grid spacing or artificial dissipation model is also necessary.

3.2 Vortex Breakdown Simulation

- Toward Accurate Code -

The flow over aircraft and missiles at moderate

to high angles of attack is characterized by the presence of large spiral vortices on the leeward side of the body. These separation vortices induce low pressure on the body upper surface, and this low pressure is the predominant factor of the resulting aerodynamic characteristic of the body. Research on such flow is of great importance practically as well as physically because understanding of the separated and vortical flow fields may lead to the control of vortex behavior and eventually to the enhancement of flight vehicle performance.

To understand vortical flow field structure over a strake-delta wing configuration, a series of computations was conducted when the author was a NRC research associate at NASA Ames Research Center[14]. Two types of vortex breakdown - bubble and spiral shaped - were successfully simulated and the difference of the flow structure of each breakdown was characterized. However, the result at the same time indicated still better grid resolution and reducing the artificial dissipation are critically important for an accurate simulation of vortical flow field. In all the aircraft simulations shown above, central difference was used for the convective terms. High-resolution upwind difference might have less dissipation as noted in the section 2, and was implemented as an option. Here, some of the results[15] are presented and compared with the result by central difference computation (note that central difference always requires some artificial dissipation model with it). The flow field is the subsonic flow over a strake-delta wing. The freestream Mach number is 0.3, and the Reynolds number based on the root chord is 1.3×10^6 in the following computations.

In the first example, the total number of grid points is about 850,000; 119 points in the chordwise direction, 101 point circumferentially and 71 points in the normal direction. Details of the grid generation and the grid distribution can be found in Ref. 14. Figure 8 shows the overall view of the spanwise total pressure contour plots at several chordwise stations at the angle of attack 12 degrees. The contours are plotted at 35% to 95 % chordwise stations with 10 % increase. At this angle of attack, there exist two vortices over the upper surface of the wing; one emanating from the strake leading edge and the other from the main-wing leading edge. These two vortices merge together over the main-wing surface because of the mutual interaction. Both results indicate the existence of two vortices over the wing surface and their interaction. It seems that the merging of the two vortices occurs more downstream in the upwind solution. The corresponding particle path traces showing the vortex trajectories are shown in Fig. 9 for the upwind result. The computed vortex trajectories are presented in Fig. 9. Also presented are the experiment and the result

by the central difference computation. It is clear that merging of two vortices occurs downstream in the upwind result, but still upstream than the experiment at the same Reynolds number.

The same computation was carried out using smaller number of grid points (about 120,000 in total). Compared to the previous grid, the number of the grid points are decreased in all the directions. Figures 10a and 10b represent the total pressure contour plots obtained by the upwind and central difference computations, respectively. The contours are again plotted at 35% to 95 % chordwise stations with 10 % increase. The upwind result shown in Fig. 10a indicates the existence of two vortices and their merging process although the inner vortex is not as distinct as the fine grid result. On the other hand, the central difference result in Fig. 10b shows only one flattened vortex instead of two vortices.

Final example is the result at 30 degrees. The previous study in Ref. 15 showed that vortex breakdown takes place near the trailing edge both in the experiment and in the computational results on the fine grid. Here medium grid (previously mentioned grid of about 120,000 points) computations are carried out both with the central differencing and the upwind differencing. The computed total pressure contour plots are presented in Figs. 11a and 11b. An abrupt increase of the vortex-core is observed near the trailing edge in the upwind result shown in Fig. 11a. This indicates that the vortex has undergone breakdown. In fact, the plot of the streamwise velocity (although not shown here) showed that there exists the reverse flow region near the trailing edge. The central difference result shown in Fig. 11b, on the other hand, does not show such a sudden change. Again, the resolution is enhanced by the use of the present upwind scheme at least on the grid used here (although a slight increase of the number of grid points may introduce breakdown phenomenon also in the central difference result).

It is recognized from these results that the present upwind scheme has better resolution than the conventional central difference scheme on the same grid although grid resolution itself is, of course, an important factor for an accurate flow simulation. Upwind scheme is more "vortex-preserving" than central differencing scheme (with added dissipation) since it has a lower level of dissipation. In the present upwind scheme where the dissipation terms are constructed in the matrix form, each characteristic wave has its own minimum dissipation. On the other hand, central difference scheme where dissipation terms are constructed in the scalar form, requires amount of dissipation which is large enough for all the waves.

Of course, solutions of both central and upwind difference schemes should converge to the solution of

the original partial differential equations as the computational grid is refined. The point here is that the accuracy estimation based on the idea of the Taylor expansion is important but not good enough for the system of nonlinear equations. What we need in numerical schemes is the better representation of the properties of original partial differential equations and, in that sense, upwind difference scheme shows better result than that of the central difference scheme for the grid distributions feasible under the memory restriction of the current supercomputers.

3.3 Spaceplane Simulation

- Accuracy and Efficiency Required -

Since February 1985, when U.S. President Reagan announced the NASP project, there occurred a strong acceleration on the research of orbiting or hypersonic flight vehicle. The CFD is one of the important areas necessary for the development, and the computations have been carried out for transonic to hypersonic flow regime for the spaceplane configuration proposed for the research at the NAL in Japan.

Following the comparison of the original central differencing and the new upwind differencing that is described above[15], a series of simulations were conducted. One of the result is presented in Fig. 12 where the computed surface density contours at the Mach number 1.5, the Reynolds number 4×10^6 , and the angle of attack 15° are plotted. The contours on the wing surface and the fuselage surface indicate the vortical flow generated above. The surface pressure distributions at one cross section is compared with the experiment in Fig. 13. The disagreement in the lower surface C_p at the final station is due to the model support, and otherwise pretty good agreement was obtained with the experiment. The details of the series of computations and the effect of each element such as tail fins will appear in Ref. 16.

3.4 Strategy for Complex Configurations

One of the important items to be solved in order to apply the CFD to practical problems is how to handle complex configurations. Although the sophisticated grid generation programs have been developed by many researchers, the application of the flow solution codes is still restricted to relatively simple configurations, and a method is needed to make the code applicable to the flow simulation over truly complex configurations (say, complete aircraft with nacelles, engines and so on). Another important item is the problem of the grid resolution. As is seen in the result shown above, even with the high-resolution upwind scheme, total number of grid points necessary for accurate flow simulations becomes enormous. As the number of the grid points becomes large, computer time also becomes large and, as a result, supercomput-

ers with much large memory and faster speed would be required.

Recent effort to solve these problems seems to be in two directions. One is the use of unstructured mesh. Using the unstructured mesh, handling complex geometry is easier and such grid system is combined with the finite element method or finite volume method for arbitrary cell shapes. So far as the Euler equations are concerned, such approach may be a good choice since explicit time integration can be used. However, for viscous flow simulations, implicit time integration may be necessary and the problem how to apply the implicit time integration and how to adopt turbulence models should be solved. The other approach is the zonal method. In this method, computational grid is constructed for each element of the geometry. For instance in aircraft simulation, each of the wing, fuselage and engine has its own grid distributions. Although modification of the existing finite difference codes to the zonal codes is relatively easy, accurate and robust interface method to transfer the data for each zonal region should be developed. In this approach, number of the grid points is also easily increased locally. One of the example[17] is shown in Fig. 14. The flow field and the solution algorithm are the same as Fig. 10b. Number of the grid points is globally decreased but is locally increase in the vortical flow region, and the result seems to be better than Fig. 10b although the total number of the grid points is almost the same. Currently the effort to develop the zonal interface algorithm such as Chimera method[18] is underway. With such method, the zonal code can handle complex body configuration, and the applicability of the code to the practical problems is to be improved.

4. Supporting System Development

With the increase of the data obtained by the CFD research, importance of visualization of the computed results began to be recognized. To help people to understand what happens in the flow field from the obtained data, we have to visualize the flow and the use of graphic workstations has an important role for that purpose. Compared to the circumstances several years ago, the level of the graphic software is improved, and visualizing complex flow field in realistic image now is not a difficult task. However, in most cases, such softwares are used only to create nice and beautiful pictures. That may be only important to advertise the CFD capability. What is really important is the development of the software to help understanding the result. Such softwares should be interactively used without requiring researcher's effort and can display the plots they want quickly. Displaying beautiful and real-image pictures does not have the first priority.

The computer programs that satisfy some of the

requirement mentioned above have been developed at NASA Ames Research Center. They are called 'PLOT3D', 'GAS' and 'RIP' and each of them has its own unique feature[19,20]. For instance in RIP, particle trajectories are computed on the CRAY-2 supercomputer and the result is displayed on the IRIS workstation. The graphic process is carried out interactively on the IRIS display.

Graphic workstations are also useful for grid generation. Sometimes, grid generation process requires more human time than flow computation itself. Interactive use of graphic workstation will reduce amount of effort for the grid generation process.

One of the super Graphic Workstation has been introduced at our laboratory lately and the preprocessor (grid generation) and postprocessor (flow visualization programs) for Navier-Stokes and other solvers having the features discussed in this paper are in the process of being built up on that machine[21]. Here some of the display examples for the post processor are presented. First, it has various function, not only contour plotters but also particle path tracer, shock wave detector and so on. Two or more flow functions can be displayed not only on the same window but also on the two or more windows respectively because displaying two or more functions at the same time would help understanding of the physical phenomenon. One of these examples are shown in Figure 15. It shows pressure contours of the flow field around a double delta wing (discussed above) on the left window and total pressure contours on the right window. The picture are obtained in the following simple manner. Firstly, the grid and flow data are read in. Then two windows are opened. The left window is selected to display the pressure contours and then the right window is selected to display the total pressure contours. The third window can be opened and on which another function can be displayed if necessary. Also the transformations, which are the translation, the rotation and the scaling, can interactively be done as will be described later.

Next is the other way of using the multi-windows. We use GWS because output list of enormous numbers obtained by the CFD computation is too difficult to understand. However, after displaying the computed results on the screen we frequently find that we want to extract the digital numbers from the result on the screen. One example is the three-dimensional positions such as the center of a vortex. Figure 16 shows an example of three-dimensional positioning using the multi-windows. The left window is the front view and the right window is the side view of the same objects. Hair cursors move corresponding to the movement of the mouse. If you want to know the position of the vortex center of the third cross section, for instance, it is achieved by setting the hair cursors crossed at the

center of vortex on the two windows as shown in Figure 16. Because the right window is perpendicular to the left one, the three-dimensional position is uniquely defined by the two set of the hair cursors.

The viewing of any windows can be modified by mouse input while the viewing has its own default values. Users do not need to know the exact definitions of viewing but move the mouse till the desired viewing is achieved.

5. Summary

The computer code named LANS3D, one of the representative Navier-Stokes codes in Japan, is taken as an example and the capability of the current CFD technology was discussed. This code was developed for the numerical simulation of high-Reynolds number compressible flows. The algorithm used in this code and how it has been improved so far explained two important aspects of the computational fluid dynamics (CFD) codes: efficiency and accuracy. Some of the application examples showed the capability of the code for engineering problems. The code and its modified versions have been extensively used by many researchers. Reference 22 reviews such applications. There are many problems (such as turbulence model, unsteady effect) to be solved before making the CFD codes an engineering tool, but imminent problem is the treatment of complex configurations. To use the best of the CFD, supporting system is important and the graphic software development for fluid dynamic research on the workstations should have attention.

Acknowledgement

The LANS3D code was mainly developed by the first author of this paper and Dr. Shigeru Obayashi (currently at NASA Ames Research Center) at the National Aerospace Laboratory, Japan and many people have helped improving the code capability and its applications. The authors express their special thanks to Dr. Susumu Takanashi and Mr. Masahiro Yoshida at the National Aerospace Laboratory and Ms. Kisa Matsushima at Fujitsu Limited.

References

1. Obayashi, S., Matsushima, K., Fujii, K. and Kuwahara, K., 'MIImprovements in Efficiency and Reliability for Navier-Stokes Computations Using the LU-ADI Factorization Algorithm, AIAA Paper 86-333', Jan., 1986.
2. Fujii, K. and Obayashi, S., "Navier-Stokes Simulations of Transonic Flows over a Practical Wing Configuration," AIAA J., Vol. 25, No. 3, March, 1987 pp. 369-370, also AIAA Paper 86-0513.
3. Obayashi, S. and Kuwahara, K., "An Approximate LU Factorization Method for the Com-

- pressible Navier-Stokes Equations, *Journal of Computational Physics*, Vol. 63, 1986, pp. 157-167.
4. Obayashi, S. and Fujii, K., "Computation of Three-Dimensional Viscous Transonic Flows with the LU Factored Scheme," AIAA Paper 85-1510, July, 1985.
 5. Jameson, A., "Successes and Challenges in Computational Aerodynamics," AIAA Paper 87-1184, June, 1987.
 6. Pulliam, T. H. and Steger, J. L., "Implicit Finite Difference Simulations of Three-Dimensional Compressible Flow," AIAA Journal, Vol. 18, No. 2, Feb. 1980, pp. 159-167.
 7. Steger, J. L. and Warming, R. F., "Flux Vector Splitting of the Inviscid Gas-Dynamic Equations with Application to Finite-Difference Methods," *Journal of Computational Physics*, Vol. 40, 1981, pp. 263-293.
 8. Vatsa, V. N., Thomas, J. L. and Wedan, B. W., "Navier-Stokes Computations of Prolate Spheroids at Angle of Attack," AIAA Paper 87-2627, August, 1987.
 9. Van Leer, B., Thomas, J. L., Roe, P. L. and Newsome, R. W., "A Comparison of Numerical Flux Formulas for the Euler and Navier-Stokes Equations," AIAA Paper 87-1104CP, June, 1987.
 10. Roe, P. L., "Finite-Volume Methods for the Compressible Navier-Stokes Equations, Proc. Int. Conf. Num. Methods for Laminar and Turbulent Flows," July, 1987.
 11. Baldwin, B. S. and Lomax, H., "Thin Layer Approximation and Algebraic Model for Separated Turbulent Flows," AIAA Paper 78-257, Jan., 1978.
 12. Fujii, K. and Obayashi, S., "Navier-Stokes Simulations of Transonic Flows over Wing-Fuselage Combination," AIAA J., Vol. 25, No. 12, Dec., 1987, pp. 1587-1596, also AIAA Paper 86-1831.
 13. Takanashi, S., Obayashi, S., Matsushima, K. and Fujii, K., "Numerical Simulation of Compressible Flows around Practical Aircraft Configurations," AIAA Paper 87-2410CP, August, 1987.
 14. Fujii, K. and Obayashi, S., "Use of High-Resolution Upwind Scheme for Vortical Flow Simulations," AIAA Paper 89-1955, June, 1989.
 15. Fujii, K. and Schiff, L. B., "Numerical Simulations of Vortical Flows over a Strake-delta Wing," AIAA Paper 87-1987, 1987, to appear as AIAA Journal in 1989.
 16. Matsushima, K., Takanashi, S. and Fujii, K., "Navier-Stokes Computations of the Supersonic Flows about a Space-plane," AIAA Paper 89-3402, August, 1989.
 17. Fujii, K., "A Method to Increase the Accuracy of Vortical Flow Simulations," AIAA Paper 88-2562CP, 1988.
 18. Buning, P. G., Chiu, I. T., Obayashi, S., Rizk, Y. M. and Steger, J. L., "Numerical Simulation of the Integrated Space Shuttle Vehicle in Ascent," AIAA Paper 88-4359, 1988.
 19. Lasinski, T., et. al., "Flow Visualization of CFD Using Graphics Workstations," AIAA Paper 87-1180, 1987.
 20. Watson, V., et. al., "Use of Computer Graphics for Visualization of Flow Fields," presented at AIAA Aerospace Engineering Conference and Show, February 17-19, 1987.
 21. Tamura Y. and Fujii, K., "Use of Graphic Workstations for Computational Fluid Dynamics," to be presented at the International Symposium on Computational Fluid Dynamics-Nagoya, to be held at Nagoya, Aug., 1989.
 22. Fujii, K., "Capability of Current Supercomputers for the Computational Fluid Dynamics," to be presented at the 1st International Conference on Applications of Supercomputers in Engineering, to be held at Southampton, U.K. Sept., 1989.

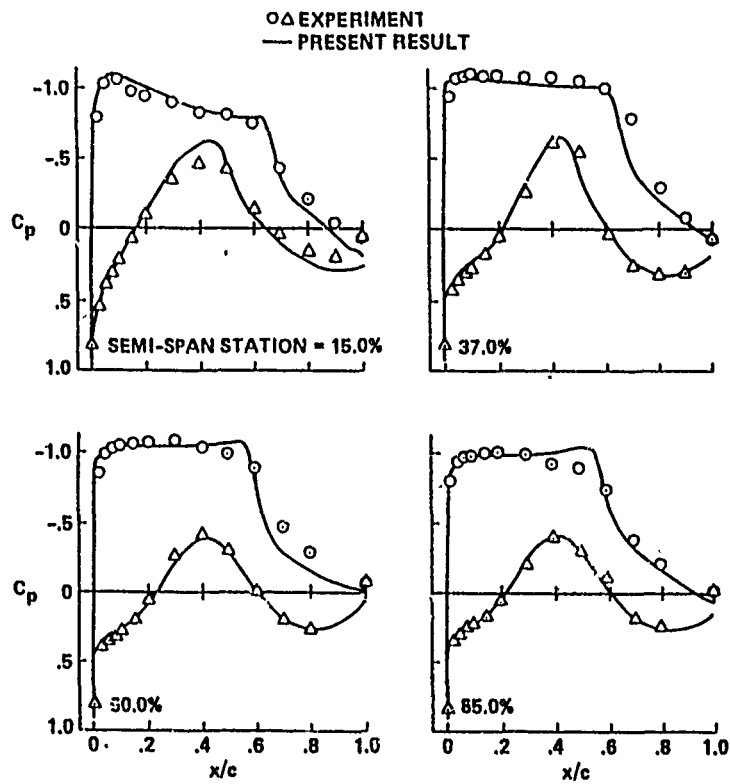


Fig. 1 Comparison of the computed C_p distributions with the experimental data at several spanwise stations
: $M_\infty = 0.82$, $\alpha = 2.46^\circ$, and $Re = 2.0 \times 10^6$.

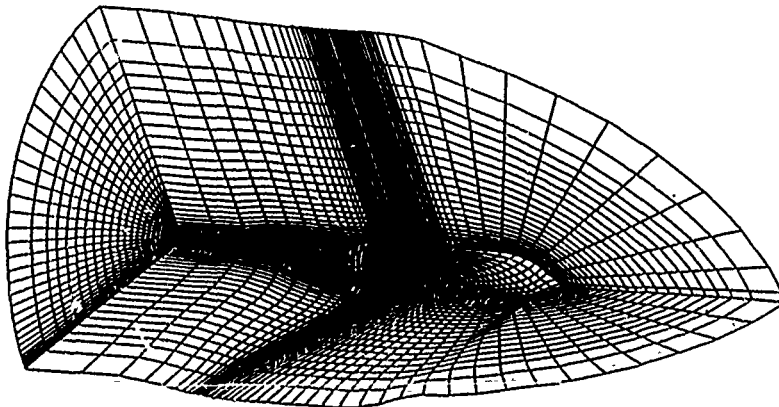
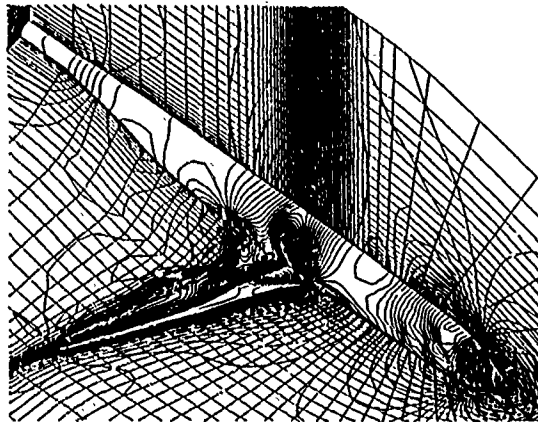


Fig. 2 Overall view of the discretized region of the grids (upper half of the computational volume).

a) overall view



b) close-up view

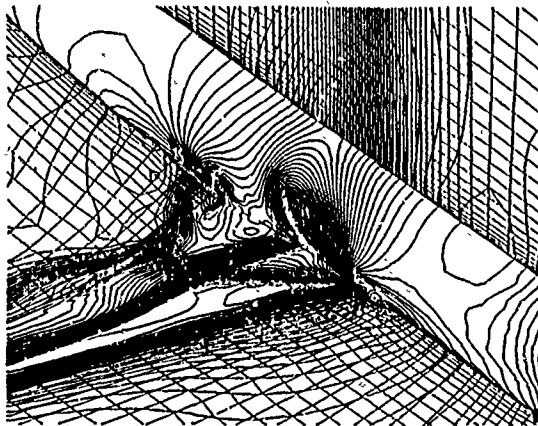


Fig. 3 Computed surface pressure contour plots
: $M_\infty = 0.82$, $\alpha = 6.00^\circ$, and $Re = 1.67 \times 10^6$.

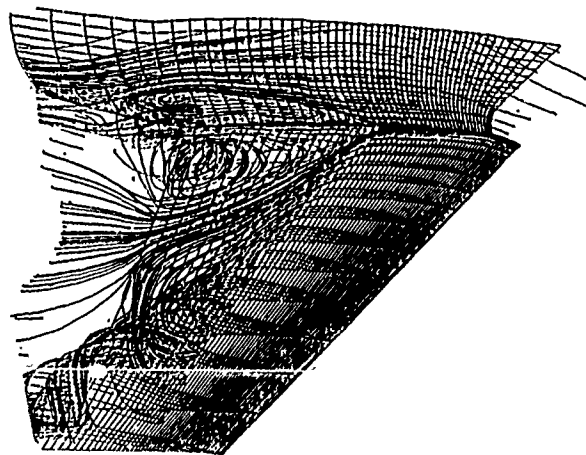


Fig. 4 Computed off-body particle path trace
: $M_\infty = 0.82$, $\alpha = 6.00^\circ$, and $Re = 1.67 \times 10^6$.

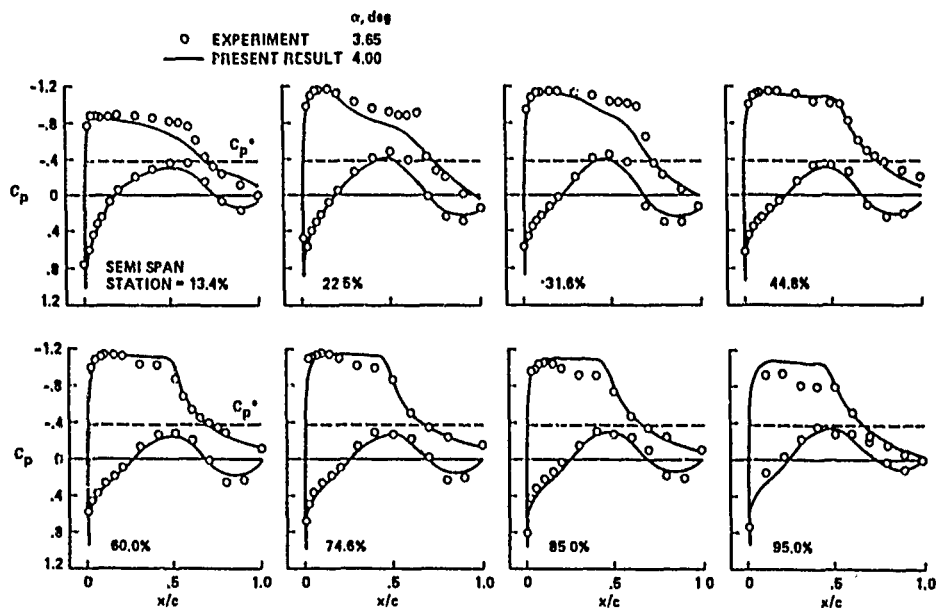


Fig. 5a Chordwise C_p distributions over a wing surface at several span-wise stations : $M_\infty = 0.82$, $\alpha = 4.00^\circ$, and $Re = 1.67 \times 10^6$.

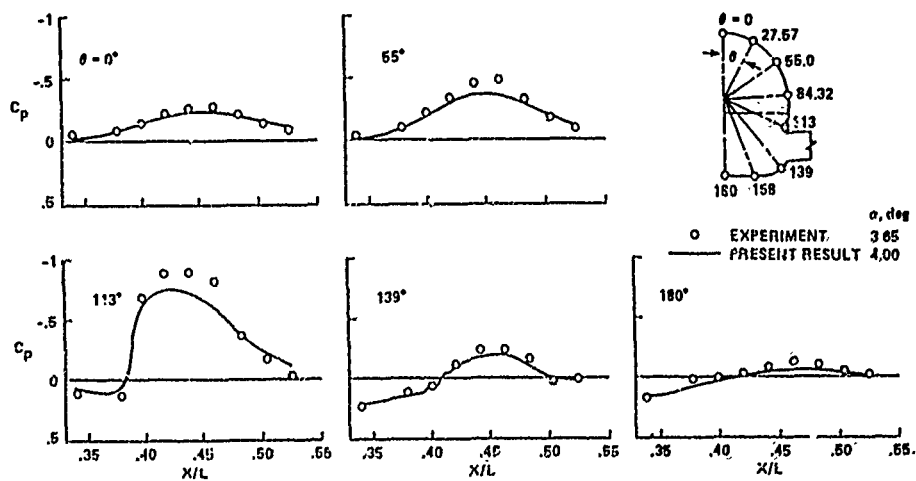


Fig. 5b Chordwise C_p distributions over a fuselage surface at several circumferential stations : $M_\infty = 0.82$, $\alpha = 4.00^\circ$, and $Re = 1.67 \times 10^6$.

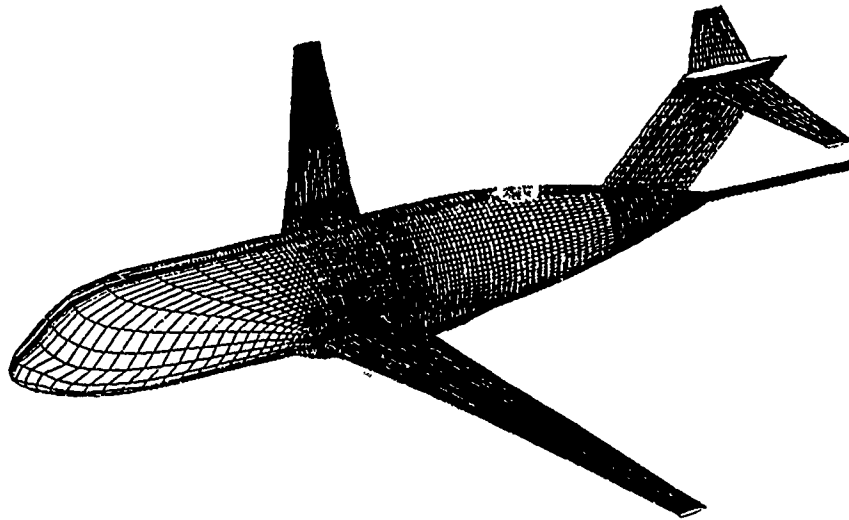


Fig. 6 Body geometry and the surface grid for the wing-fuselage-tail combination.

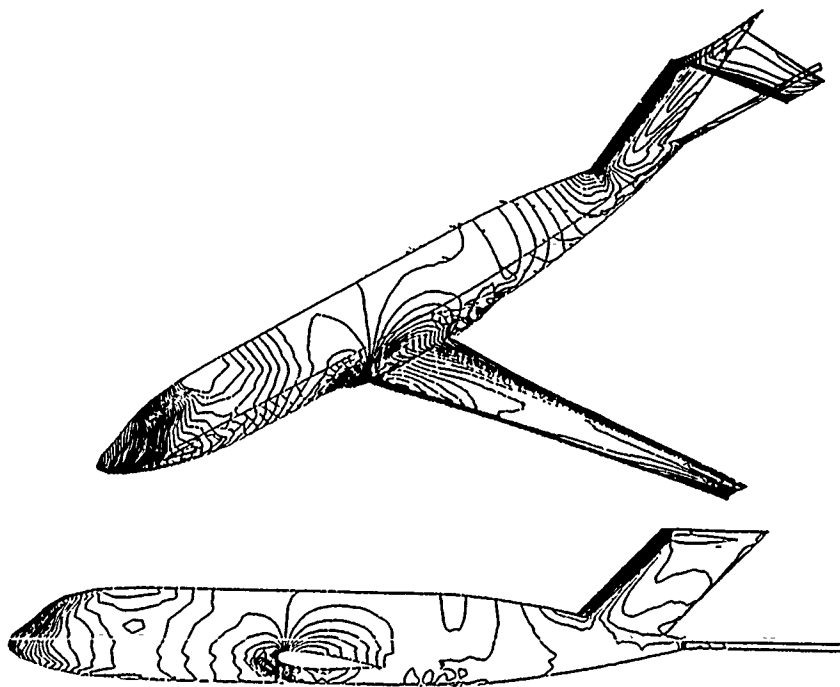


Fig. 7 Computed pressure contour plots for the wing-fuselage-tail combination
: $M_\infty = 0.60$, $\alpha = 0.0^\circ$, and $Re = 3.47 \times 10^6$.

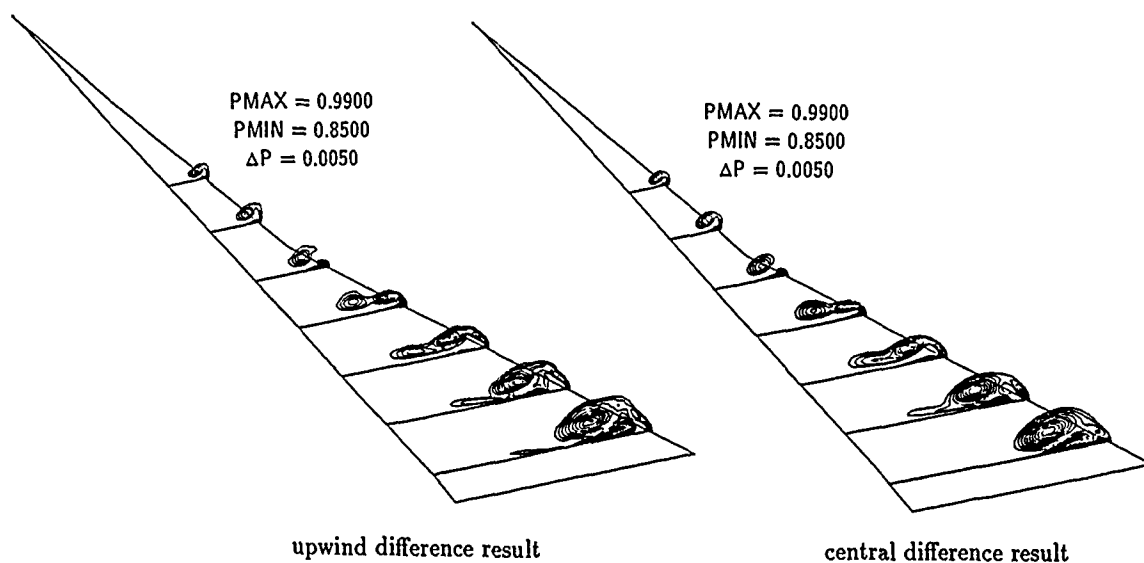


Fig. 8 Computed total pressure contour plots at several chordwise stations
: $M_\infty = 0.30$, $\alpha = 12.0^\circ$, and $Re = 1.3 \times 10^6$.

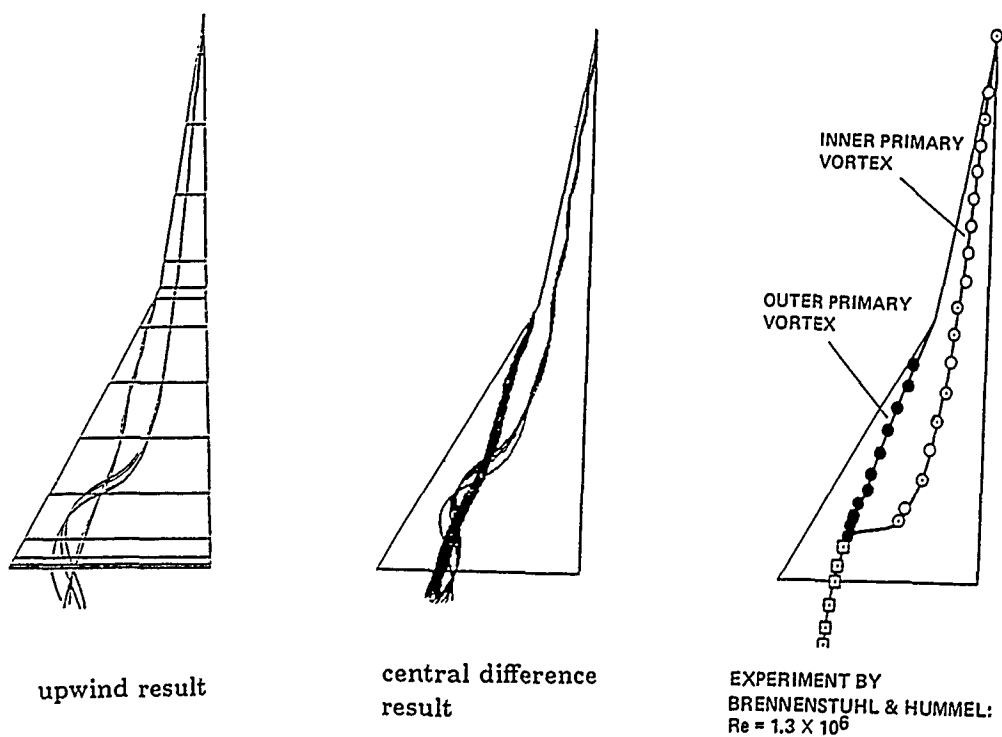


Fig. 9 Computed vortex position compared with experiment
: $M_\infty = 0.30$, $\alpha = 12.0^\circ$, and $Re = 1.3 \times 10^6$.

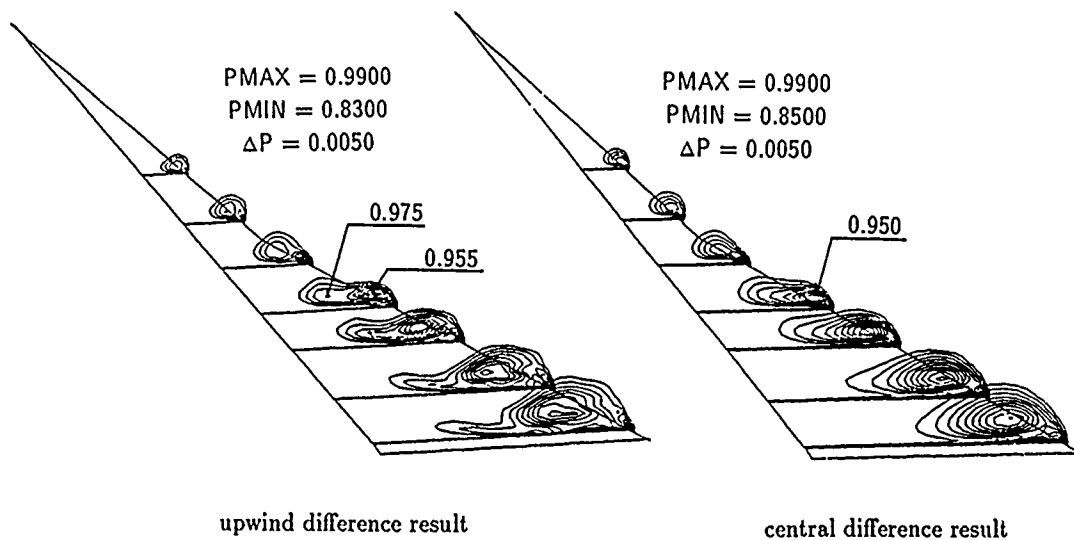


Fig. 10 Computed total pressure contour plots at several chordwise stations -medium grid-
: $M_\infty = 0.30$, $\alpha = 12.0^\circ$, and $Re = 1.3 \times 10^6$.

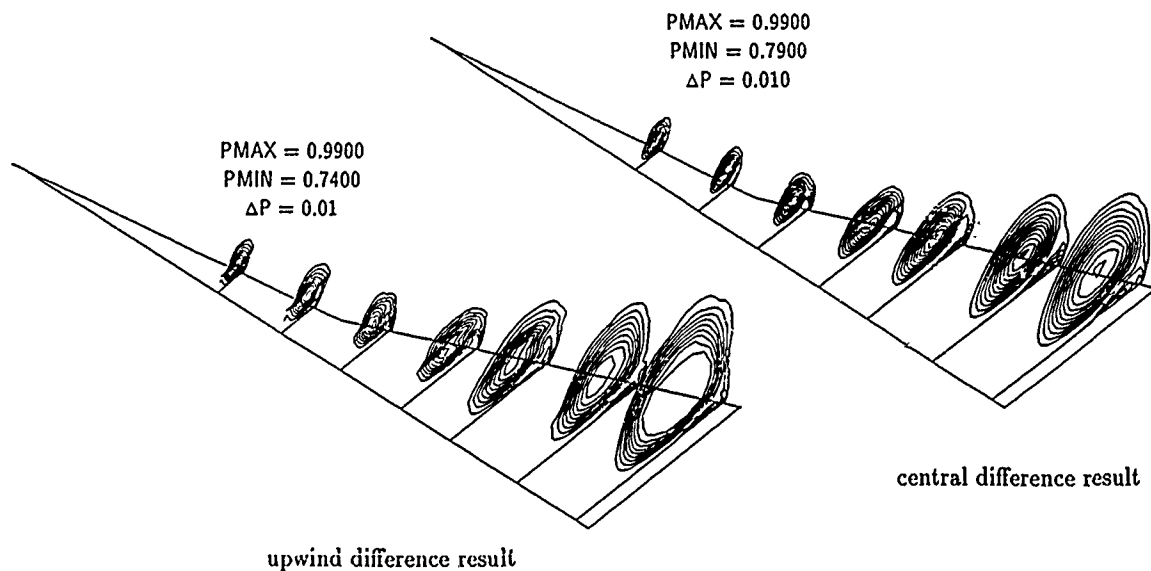


Fig. 11 Computed total pressure contour plots at several chordwise stations -medium grid-
: $M_\infty = 0.30$, $\alpha = 30.0^\circ$, and $Re = 1.3 \times 10^6$.

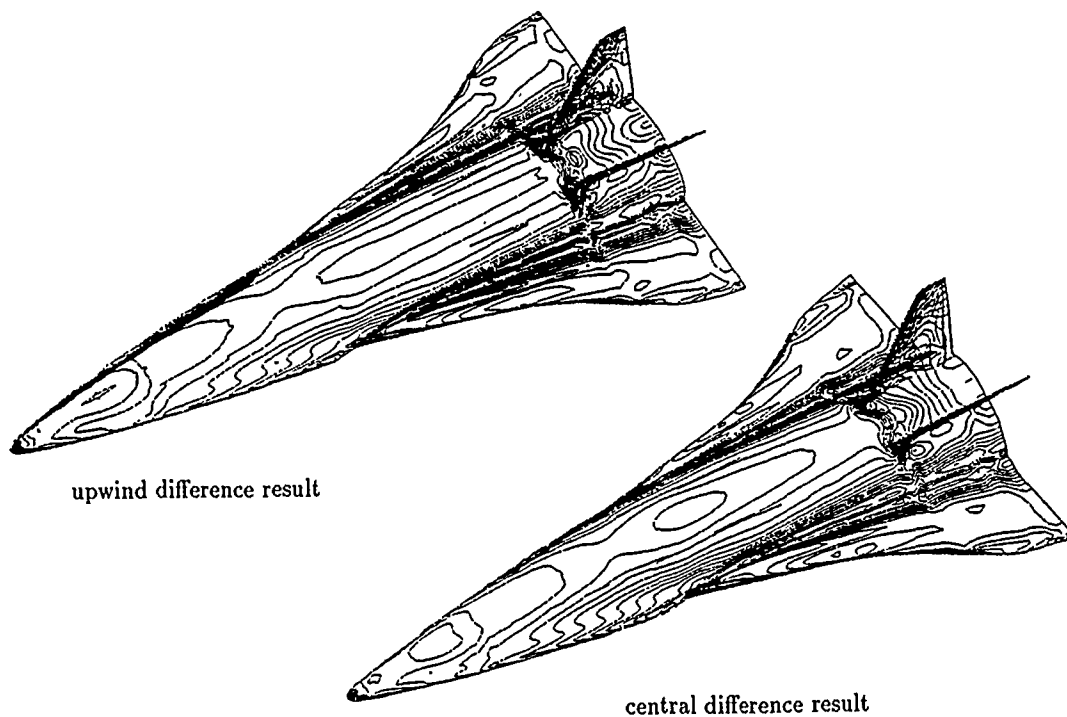


Fig. 12 Overall view of the computed surface density contour plots over a spaceplane
: $M_\infty=1.5$, $\alpha=15^\circ$, and $Re = 4.0 \times 10^6$.

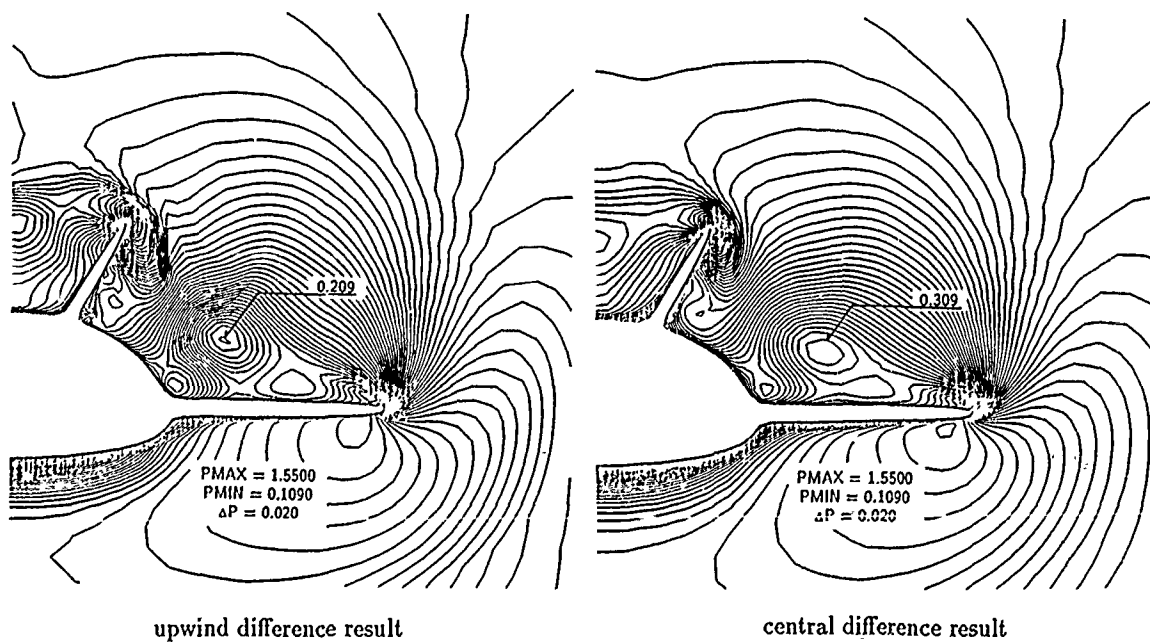


Fig. 13 Spanwise surface C_p plots ($x/c = 91\%$)
: $M_\infty=1.5$, $\alpha=15^\circ$, and $Re = 4.0 \times 10^6$.

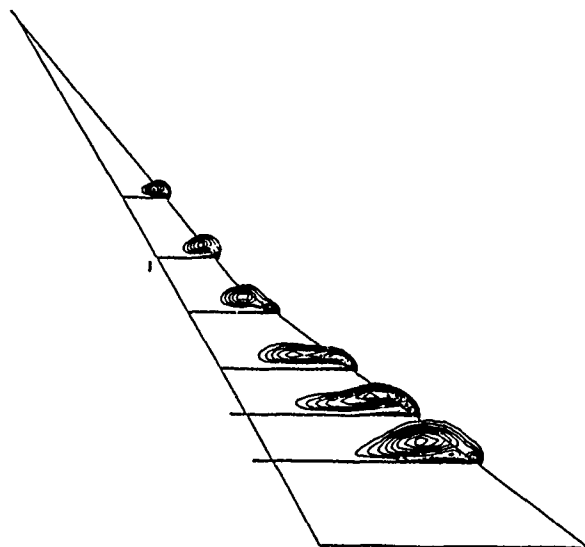


Fig. 14 Computed total pressure contour plots at several chordwise stations -zonal solution-
: $M_\infty = 0.30$, $\alpha = 12.0^\circ$, and $Re = 1.3 \times 10^6$.

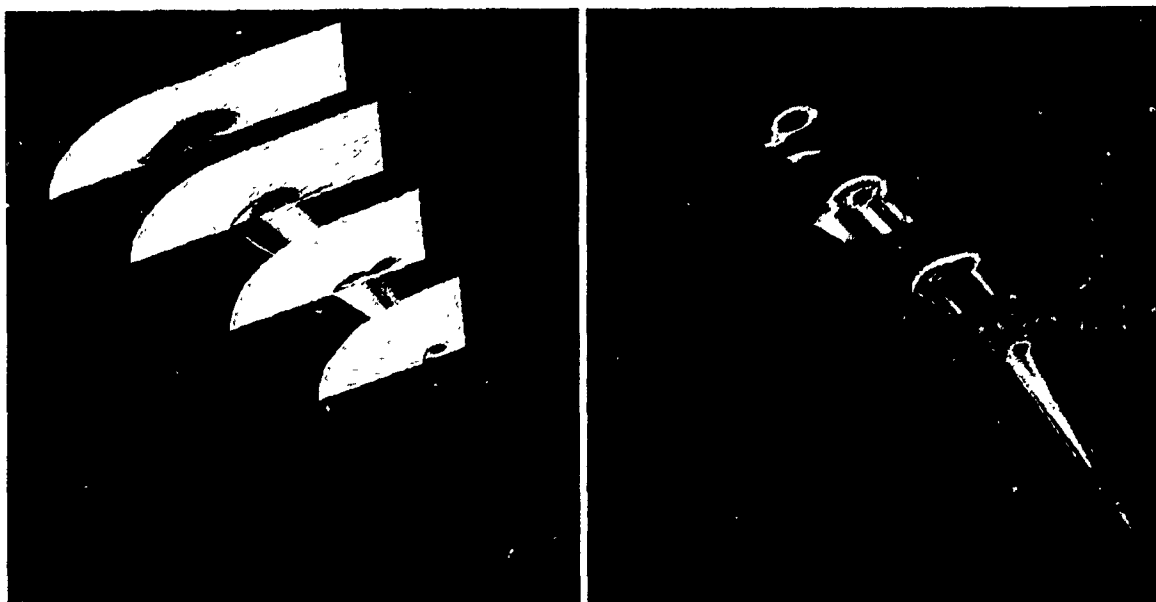


Fig. 15 Pressure and Total pressure contour plots over double delta wing

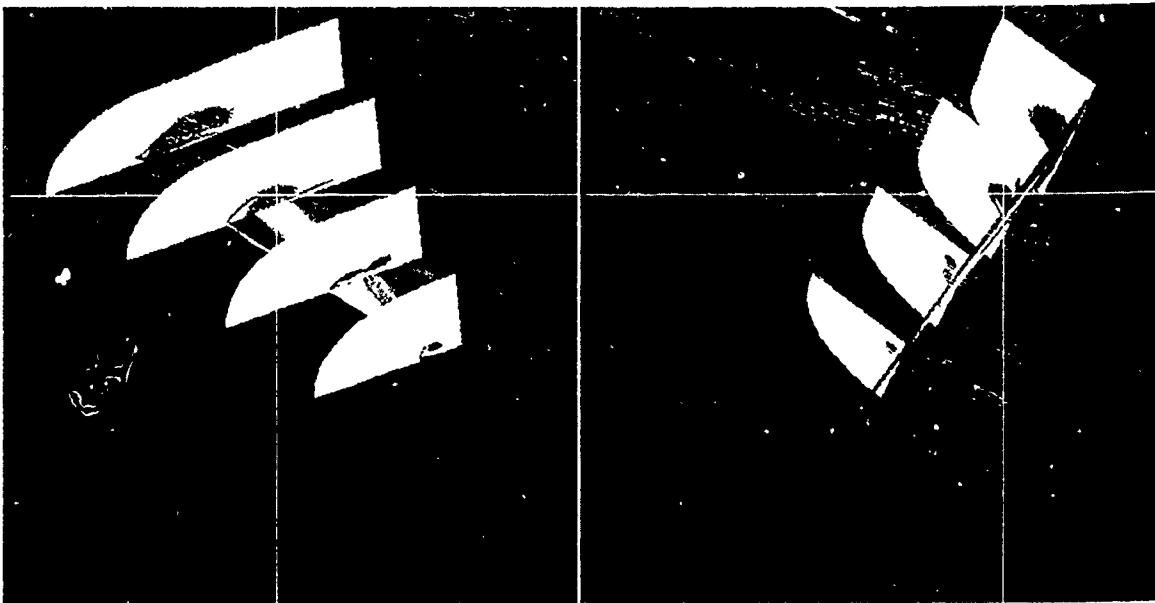


Fig. 16 Three dimensional positioning using multi-windows

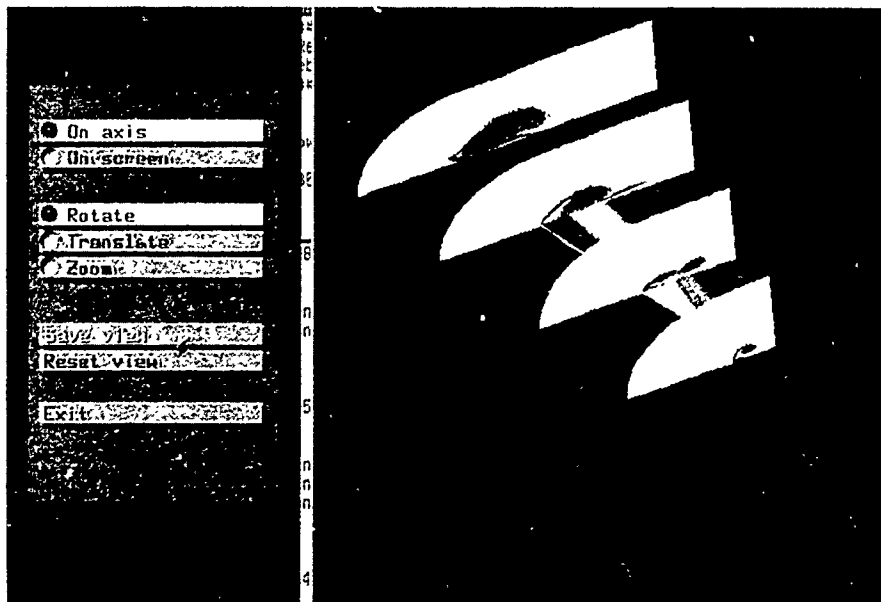


Fig. 17 Example of man-machine interface

DISCUSSION

by F. Stern

Most of the effort to improve the calculation results has been devoted to the discretization procedures (ie, upwind or central differencing) and grid resolution as opposed to the removal of the thin layer assumption; however, for the complex points considered in the paper, I do not believe that the thin layer approximation is appropriate. Please provide justification and evidence for its case. Also, what modifications were made to the Baldwin-Lomax turbulence model in junction regions?

Author's Reply

Your question is very important. Please read the paragraph after Eq.(1), P.2 in the manuscript. Computational grids usually used for high Reynolds number flow simulations have very small spacing from the body surface outward but have relatively large spacing along the body surface. In other words, cell aspect ratio is quite large. With such grid, we would never be able to resolve viscous terms associated with the strain rates along the body even though we included all the viscous terms in the program. This was checked by many research scientists at NASA Ames Research Center several years ago.

The same is true for the region away from the body surface. Since grid spacing is not as fine as that near the body surface, viscous terms are not properly evaluated even though the program computes viscous terms there. Thus, we can say that we are just simulating rotational inviscid flow in the region away from the body surface even when we are solving the Navier-Stokes equations. Again, I have checked how large the contribution by the viscous terms is compared to other terms, and the result said no contribution. However, because of the artificial dissipation, the solution tends to be dissipative there. For instance, strength of the vortex tends to decay easily even with the Euler computations. Thus before trying to evaluate viscous terms properly, we have to minimize the artificial dissipation effect and this can be realized by the use of high-resolution upwind method.

Inclusion of all the viscous terms is not a difficult task and probably would require only 10 to 20% more computational time. Number

of computational grid points is becoming larger and larger. With such background, I think it is the time to evaluate all the viscous terms to remove ambiguity. Thin-layer approximation is only a practical approximation and should be given up soon with the increase of the computational grid points.

Please refer [A1] about modification of turbulence model at juncture.

[A1] Hung, C.M. and Buning, P.G., "Simulation of Blunt-Fin Induced Shock Wave and Turbulent Boundary Layer Interaction", J. Fluid Mech., Vol.154, pp.163-185, 1985.

DISCUSSION

by Y. Kodama

You showed comparison of "coarse grid" case and "fine grid" case. But in some cases "fine grid" is not fine enough to resolve the flow field. When you compute a flow, on what principle do you determine the number of grid points?

Author's Reply

The best way to determine the number of the grid points is to compute the flow field until the solution does not change with further increase of the grid points. However, in practice, it is impossible to do so especially in the case of large scale computation. The fine grid I used in the computation was the maximum number of the grid points that fitted into the main memory of the super-computer used for that computation. We considered that the solution resolved at least the global feature of the flow by comparing it with the experiment. It is true that the solution I have shown lacks capturing small scales and thus, did not go into the quantitative comparison of the detail (See AIAA J. Sept., 1989 by Fujii and Schiff). Besides, there were many more assumptions such as flow symmetry (which never realize when breakdown takes place) and no turbulence model. We can still say that vortical flow requires fine grid resolution from the fact that the solution depended on the grid resolution. Further research in the near future using more grid points will show how reasonable the current solution is.

Boundary-Layer Stability and Transition

W. S. Saric
Arizona State University
Tempe, USA

Abstract

Within the last five years, increased emphasis on secondary instability analysis along with the experimental observations of subharmonic instabilities have changed the picture of the transition process for boundary layers in low-disturbance environments. Additional efforts with Navier-Stokes computations have formed an impressive triad of tools that are beginning to unravel the details of the early stages of transition. This paper reviews these recent efforts.

Symbols

α	chordwise complex wavenumber normalized by L
A	disturbance amplitude
A_0	amplitude at $R=R_0$, usually Branch I
C_p	pressure coefficient
F	$\omega/R = 6.28fv/U_0^2$: dimensionless frequency
f	dimensional frequency [hz]
L	$\sqrt{v_x^*/U_0}$: boundary-layer reference length.
N	$\ln(A/A_0)$: amplification factor
R	$\sqrt{R_x} = U_0 L/v$: boundary-layer Reynolds number
R_0	initial boundary-layer Reynolds number, usually Branch I
R_x	$U_0 x^*/v$: x-Reynolds number or chord Reynolds number
U	basic-state chordwise velocity normalized by U_0
U_0	freestream velocity, [m/s]
ν	kinematic viscosity [m ² /s]
ω	$2\pi fL/U_0$: dimensionless circular frequency
x^*	dimensional chordwise coordinate [m]
x	chordwise coordinate normalized with L

y normal-to-the-wall coordinate

z spanwise coordinate

1. Introduction

The problems of understanding the origins of turbulent flow and transition to turbulent flow are the most important unsolved problems of fluid mechanics and aerodynamics. There is no dearth of applications for information regarding transition location and the details of the subsequent turbulent flow. A few examples can be given here. (1) Nose cone and heat shield requirements on reentry vehicles and the "aerospace airplane" are critical functions of transition altitude. (2) Vehicle dynamics and "observables" are modulated by the occurrence of laminar-turbulent transition. (3) Should transition be delayed with Laminar Flow Control on the wings of large transport aircraft, a 25% savings in fuel will result. (4) Lack of a reliable transition prediction scheme hampers efforts to accurately predict airfoil surface heat transfer and to cool the blades and vanes in gas turbine engines. (5) The performance and detection of submarines and torpedoes are significantly influenced by turbulent boundary-layer flows and efforts directed toward drag reduction require the details of the turbulent processes. (6) Separation and stall on low-Reynolds-number airfoils and turbine blades strongly depend on whether the boundary layer is laminar, transitional, or turbulent.

The common thread connecting each of these applications is the fact that they all deal with *bounded shear flows* (boundary layers) in *open systems* (with different upstream or initial amplitude conditions). It is well known that the stability, transition, and turbulent characteristics of bounded shear layers are fundamentally different from those of free shear layers (Morkovin, 1969; Tani, 1969; Reshotko, 1976). Likewise, the stability, transition, and turbulent characteristics of open systems are fundamentally different from those of closed systems (Tatsumi, 1984). The distinctions are vital. Because of the influence of indigenous disturbances, surface geometry and roughness, sound, heat transfer, and ablation, it is not possible to develop general prediction schemes for transition location and the nature of turbulent structures in boundary-layer flows.

There have been a number of recent advances in the mathematical theory of chaos that have been applied to closed systems. Sreenivasan and Strykowski (1984), among others, discuss the extension of these ideas to open systems and conclude that the relationship is still uncertain. It appears from a recent workshop and panel discussion (Liepmann et al. 1986) that the direct application of chaos theory to open systems is still some distance away. However, the prospect of incorporating some of the mathematical ideas of chaos into open system problems and of encouraging the transfer of data to the mathematicians is good. Since there is still some uncertainty in the direct application of chaos theory to transition no further mention of this will be given here.

The purpose of this report is to bring into perspective certain advances to our understanding of laminar-turbulent transition that have occurred within the last five years. In particular, these advances have been made by simultaneous experimental, theoretical, and computational efforts.

1.1 Basic Ideas of Transition

With the increased interest in turbulent drag reduction and in large scale structures within the turbulent boundary layer, researchers in turbulence have been required to pay attention to the nature of laminar-turbulent transition processes. It is generally accepted that the transition from laminar to turbulent flow occurs because of an incipient instability of the basic flow field. This instability intimately depends on subtle, and sometimes obscure, details of the flow. The process of transition for boundary layers in external flows can be qualitatively described using the following (albeit, oversimplified) scenario.

Disturbances in the freestream, such as sound or vorticity, enter the boundary layer as steady and/or unsteady fluctuations of the basic state. This part of the process is called *receptivity* (Morkovin, 1969) and, although it is still not well understood, it provides the vital initial conditions of amplitude, frequency, and phase for the breakdown of laminar flow. Initially these disturbances may be too small to measure and they are observed only after the onset of an instability. The type of instability that occurs depends on Reynolds number, wall curvature, sweep, roughness, and initial conditions. The initial growth of these disturbances is described by *linear* stability theory. This growth is weak, occurs over a viscous length scale, and can be modulated by pressure gradients, mass flow, temperature gradients, etc. As the amplitude grows, three-dimensional and nonlinear interactions occur in the form of *secondary* instabilities. Disturbance growth is very rapid in this case (now over a convective length scale) and breakdown to turbulence occurs.

For many years, linear stability theory, with the Orr-Sommerfeld equation as its keystone, served as the basic tool for predictors and designers. Since the initial growth is linear and its behavior can be easily calculated, transition prediction schemes are usually based on linear theory. However, since the initial conditions (receptivity) are not generally known, only correlations are possible and, most importantly, these correlations must be between two systems with similar

environmental conditions. The impossibility of matching or fully understanding these environmental conditions has led to the failure of any absolute transition prediction scheme for even the simple Blasius flat-plate boundary layer.

The preceding does not always follow the observed behavior. At times, the initial instability can be so strong that the growth of linear disturbances is *bypassed* (Morkovin, 1969) in such a way that turbulent spots appear or secondary instabilities occur and the flow quickly becomes turbulent. This phenomenon is not well understood but has been documented in cases of roughness and high freestream turbulence (Reshotko, 1986). In this case, transition prediction schemes based on linear theory fail completely.

1.2 Review of the Literature

The literature review follows the outline of the process described above and begins with Reshotko (1984a, 1986) on receptivity (i.e. the means by which freestream disturbances enter the boundary layer). In these papers, Reshotko summarizes the recent work in this area and points out the difficulties in understanding the problem. Indeed, the receptivity question and the knowledge of the initial conditions are the key issues regarding a transition prediction scheme. Of particular concern to the transition problem are the quantitative details of the roles of freestream sound and turbulence. Aside from some general correlations, this is still an opaque area. However, in section 3.2 below, a demonstration of the role of initial conditions on the observed transition phenomenon is discussed.

The details of linear stability theory are given in Mack (1984b). This is actually a monograph on boundary-layer stability theory and should be considered required reading for those interested in all aspects of the subject. It covers 58 pages of text with 170 references. In particular, his report updates the three-dimensional (3-D) material in Mack (1969), covering in large part Mack's own contributions to the area.

The foundation paper with regard to nonlinear instabilities is Klebanoff et al. (1962). This seminal work spawned numerous experimental and theoretical works (not all successful) for the period of 20 years after its publication. It was not until the experimental observations of subharmonic instabilities by Kachanov et al. (1977), Kachanov and Levchenko (1984), and Saric and Thomas (1984), along with the work on secondary instabilities, that additional progress was made in this area. Recent papers of Herbert (1984a,b,c; 1985; 1986a,b) cover the problems of secondary instabilities and nonlinearities, i.e. those aspects of the breakdown process that succeed the growth of linear disturbances. It should be emphasized that two-dimensional waves do not completely represent the breakdown process since the transition process is *always* three-dimensional in bounded shear flows. Herbert describes the recent efforts in extending the stability analysis into regions of wave interactions that produce higher harmonics, three-dimensionality, subharmonics, and large growth rates--all harbingers of transition to turbulence. Recent 3-D Navier-Stokes computations by Fasel (1980,1986), Spalart (1984),

Spalart and Yang (1986), Kleiser and Laurien (1985, 1986) Reed and co-workers (Singer et al. 1986, 1987; Yang et al. 1987) have added additional understanding to the phenomena. More is said about this in section 3.2.

The paper by Arnal (1984) is an extensive description and review of transition prediction and correlation schemes for two-dimensional flows that covers 34 pages of text and over 100 citations. An analysis of the different mechanisms that cause transition such as Tollmien-Schlichting (T-S) waves, Görtler vortices, and turbulent spots is given. The effects that modulate the transition behavior are presented. These include the influence of freestream turbulence, sound, roughness, pressure gradient, suction, and unsteadiness. A good deal of the data comes from the work of the group at ONERA/CERT part of which has only been available in report form. The different transition criteria that have been developed over the years are also described which gives an overall historical perspective of transition prediction methods.

In a companion paper, Poll (1984b) extends the description of transition to 3-D flows. When the basic state is three-dimensional, not only are 3-D disturbances important, but completely different types of instabilities can occur. Poll concentrates on the problems of leading-edge contamination and crossflow vortices, both of which are characteristic of swept-wing flows. The history of these problems as well as the recent work on transition prediction and control schemes for 3-D flows are discussed by Reed and Saric (1989).

Reshotko (1984b, 1985, 1986) and Saric (1985b) review the application of stability and transition information to problems of drag reduction and in particular, laminar flow control. They discuss a variety of the laminar flow control and transition control issues which will not be covered here.

2. Review of T-S Waves

The disturbance state is restricted to two dimensions with a one-dimensional basic state. The 2-D instability to be considered is a viscous instability in that the boundary-layer velocity profile is stable in the inviscid limit and thus, an increase in viscosity (a decrease in Reynolds number) causes the instability to occur in the form of 2-D traveling waves called T-S waves. All of this is contained within the framework of the Orr-Sommerfeld equation, OSE. The historical development of this work is given in Mack (1984b) and a tutorial is given by Saric (1985a).

The OSE is linear and homogeneous and forms an eigenvalue problem which consists of determining the wavenumber, α , as a function of frequency, ω , Reynolds number, R , and the basic state, $U(y)$. The Reynolds number is usually defined as $R = U_\infty L/\nu = \sqrt{R_\tau}$ and is used to represent distance along the surface. In general, $L = \sqrt{vx^*}/U_\infty$ is the most straightforward reference length to use because of the simple form of R and because the Blasius variable is the same as y in the OSE. When comparing the solutions of the OSE with experiments, the

dimensionless frequency, F , is introduced as $F = \omega/R = 2\pi f\nu/U_\infty^2$ where f is the frequency in Hertz.

Usually, an experiment designed to observe T-S waves and to verify the 2-D theory is conducted in a low-turbulence wind tunnel (u'/U_∞ from 0.02% to 0.06%) on a flat plate with zero pressure gradient (determined from the shape factor = 2.59 and not from pressure measurements!) where the virtual-leading-edge effect is taken into account by carefully controlled boundary-layer measurements. Disturbances are introduced by means of a 2-D vibrating ribbon using single-frequency, multiple-frequency, step-function, or random inputs (Pupator and Saric, 1989) taking into account finite-span effects (Mack, 1984a). Hot wires measure the $U + u'$ component of velocity in the boundary layer and d-c coupling separates the mean from the fluctuating part. The frequency, F , for single-frequency waves remains a constant.

When the measurements are repeated along a series of chordwise stations, the maximum amplitude of the waves varies. At constant frequency, the disturbance amplitude initially decays until the Reynolds number at which the flow first becomes unstable is reached. This point is called the Branch I neutral stability point and is given by R_I . The amplitude grows exponentially until the Branch II neutral stability point is reached which is given by R_{II} . The locus of R_I and R_{II} points as a function of frequency gives the neutral stability curve. If the growth rate of the disturbances is defined as $\sigma = \sigma(R, F)$, Fig. 1 is the locus of $\sigma(R, F) = 0$. For $R > 600$ the theory and experiment agree very well for Blasius flow. For $R < 600$ the agreement is not as good because the theory is influenced by nonparallel effects and the experiment is influenced by low growth rates and nearness to the disturbance source. Virtually all problems of practical interest have $R > 1000$ in which case the parallel theory seems quite adequate (Gaster, 1974; Saric and Nayfeh, 1977).

By assuming that the growth rate, $\sigma = \sigma(R, F)$, to hold locally (within the quasi-parallel flow approximation), the disturbance equations are integrated along the surface with $R = R(x)$ to give:

$$A/A_0 = \exp(N)$$

where $dN/dR = \sigma$, A and A_0 are the disturbance amplitudes at R and R_I , respectively, and R_I is the Reynolds number at which the constant-frequency disturbance first becomes unstable (Branch I of the neutral stability curve).

The basic design tool is the correlation of N with transition Reynolds number, R_T , for a variety of observations. The correlation will produce a number for N (say 9) which is now used to predict R_T for cases in which experimental data are not available. This is the celebrated *e^N method* of Smith and von Ingen (e.g. Arnal, 1984; Mack, 1984b). The basic LFC technique changes the physical parameters and keeps N within reasonable limits in order to prevent transition. As long as laminar flow is maintained and the disturbances remain linear, this method contains all of the necessary physics to accurately predict disturbance behavior. As a transition prediction device, the *e^N method* is certainly the most popular technique used today. It works within

some error limits only if comparisons are made with experiments with identical disturbance environments. Since no account can be made of the initial disturbance amplitude this method will always be suspect to large errors and should be used with extreme care. When bypasses occur, this method does not work at all. Mack (1984b) and Arnal (1984) give examples of growth-rate and e^N calculations showing the effects of pressure gradients, Mach number, wall temperature, and three dimensionality for a wide variety of flows. These reports contain the most up-to-date stability information.

3. Secondary Instabilities and Transition

There are different possible scenarios for the transition process, but it is generally accepted that transition is the result of the uncontrolled growth of unstable three-dimensional waves. Secondary instabilities with T-S waves are reviewed in some detail by Herbert (1984b, 1985, 1986), Saric and Thomas (1984) and Saric et al. (1984). Therefore, only a brief outline is given in section 3.1 in order to give the reader some perspective of the different types of breakdown. Section 3.2 discusses the very recent results.

3.1 Secondary Instabilities

The occurrence of three-dimensional phenomena in an otherwise two-dimensional flow is a necessary prerequisite for transition (Tani, 1981). Such phenomena were observed in detail by Klebanoff et al. (1962) and were attributed to a spanwise differential amplification of T-S waves through corrugations of the boundary layer. The process leads rapidly to spanwise alternating "peaks" and "valleys", i.e., regions of enhanced and reduced wave amplitude, and an associated system of streamwise vortices. The peak-valley structure evolves at a rate much faster than the (viscous) amplification rates of T-S waves. The schematic of a smoke-streakline photograph (Saric et al. 1981) in Fig. 1 shows the sequence of events after the onset of "peak-valley splitting". This represents the path to transition under conditions similar to Klebanoff et al. (1962) and is called a *K-type* breakdown. The lambda-shaped (Hama and Nutant, 1963) spanwise corrugations of streaklines, which correspond to the peak-valley structure of amplitude variation, are a result of weak 3-D displacements of fluid particles across the critical layer and precede the appearance of Klebanoff's "hair-pin" vortices. This has been supported by hot-wire measurements and Lagrangian-type streakline prediction codes (Saric et al., 1981; Herbert and Bertolotti, 1985). Note that the lambda vortices are ordered in that peaks follow peaks and valleys follow valleys.

Since the pioneering work of Nishioka et al. (1975, 1980), it is accepted that the basic transition phenomena observed in plane channel flow are the same as those observed in boundary layers. Therefore, little distinction will be given here as to whether work was done in a channel or a boundary layer. From the theoretical and computational viewpoint, the plane channel is particularly convenient since the Reynolds number is constant, the mean flow is strictly parallel, certain symmetry conditions apply, and one is able to

do temporal theory. Thus progress has been first made with the channel flow problem.

Different types of three-dimensional transition phenomena recently observed (e.g. Kachanov et al. 1977; Kachanov and Levchenko, 1984; Saric and Thomas, 1984; Saric et al. 1984, Kozlov and Ramanosov, 1984) are characterized by staggered patterns of peaks and valleys (see Fig. 2) and by their occurrence at very low amplitudes of the fundamental T-S wave. This pattern also evolves rapidly into transition. These experiments showed that the subharmonic of the fundamental wave (a necessary feature of the staggered pattern) was excited in the boundary layer and produced either the resonant wave interaction predicted by Craik (1971) (called the *C-type*) or the secondary instability of Herbert (1983) (called the *H-type*). Spectral broadening to turbulence with self-excited subharmonics has been observed in acoustics, convection, and free shear layers and was not identified in boundary layers until the results of Kachanov et al. (1977). This paper reinitiated the interest in subharmonics and prompted the simultaneous verification of C-type resonance (Thomas and Saric, 1981; Kachanov and Levchenko, 1984). Subharmonics have also been confirmed for channel flows (Kozlov and Ramazanov, 1984) and by direct integration of the Navier-Stokes equations (Spalart, 1984). There is visual evidence of subharmonic breakdown before Kachanov et al. (1977) in the work of Hama (1959) and Knapp and Roache (1968) which was not recognized as such at the time of their publication. The recent work on subharmonics is found in Herbert (1985, 1986a,b), Saric, Kozlov and Levchenko (1984), and Thomas (1986).

The important issues that have come out of the subharmonic research is that the secondary instability depends not only on disturbance amplitude, but on phase and fetch as well. Fetch means here the distance over which the T-S wave grows in the presence of the 3-D background disturbances. If T-S waves are permitted to grow for long distances at low amplitudes, subharmonic secondary instabilities are initiated at disturbance amplitudes of less than $0.3\% U_\infty$. Whereas, if larger amplitudes are introduced, the breakdown occurs as K-type at amplitudes of $1\% U_\infty$. Thus, there no longer exists a "magic" amplitude criterion for breakdown.

A consequence of this requirement of a long enough fetch for the subharmonic to be entrained from the background disturbances is that the subharmonic interaction will occur at or to the right of the Branch II neutral stability point. Since this is in the stable region of the fundamental wave, it was not likely to be observed because the experimenters quite naturally concentrated their attention of measurements between Branch I and Branch II.

3.2 Recent Results

The surprise that results from the analytical model of Herbert (1986a,b) and the Navier-Stokes computations of Singer, Reed, and Ferziger (1986), is that under conditions of the experimentally observed K-Type breakdown, the subharmonic H-Type is still the dominant breakdown mechanism instead of the

fundamental mode. This is in contrast to Klebanoff's experiment, confirmed by Nishioka et al. (1975, 1980), Kachanov et al. (1977), Saric and Thomas (1984), Saric et al. (1984), and Kozlov and Ramazanov (1984) where only the breakdown of the fundamental into higher harmonics was observed. Only Kozlov and Ramazanov (1984) observed the H-type in their channel experiments and only when they artificially introduced the subharmonic.

This apparent contradiction was resolved by Singer, Reed, and Ferziger (1987). Here the full three-dimensional, time-dependent incompressible Navier-Stokes equations are solved with no-slip and impermeability conditions at the walls. Periodicity was assumed in both the streamwise and spanwise directions. The implementation of the method and its validation are described by Singer, Reed and Ferziger (1986). Initial conditions include a two-dimensional T-S wave, random noise, and streamwise vortices. No shape assumptions are necessary, the spectrum is larger, and random disturbances whether freestream or already in the boundary layer can be introduced and monitored for growth and interactions (Singer, Reed, and Ferziger, 1986). Other advantages realized by computations are 1) the inclusion of boundary-layer growth, neglected in linear theory but important to the growth of secondary instabilities, 2) the generation of ensemble averages, 3) the visualization of flow phenomena for comparison with experiments (advanced graphics capability), and 4) the calculation of vorticity and energy spectra, often unavailable from experiments.

The streamwise vortices can alter the relative importance of the subharmonic and fundamental modes. Streamwise vortices of approximately the strength of those that might be found in transition experiments can explain the difficulty in experimentally identifying the subharmonic route to turbulence (Herbert 1983).

The corresponding computational visualizations of Singer et al. (1987) are shown in Figs. 3 and 4; flow is from lower right to upper left. Figure 4 shows the vortex structures, commonly seen in the transition process, under the conditions of a forced 2-D T-S wave and random noise as initial conditions. The subharmonic mode is present as predicted by theory but not seen experimentally. Other views of the vortical structure are given by Herbert (1986a). However, when streamwise vorticity (as is present in the flow from the turbulence screens upstream of the nozzle) is also included, the subharmonic mode is overshadowed by the fundamental mode (as in the experiments!). The resulting pattern, ordered peak-valley structure, is seen in Fig. 4. Here is a case in which the computations have explained discrepancies between theory and experiments.

In the presence of streamwise vorticity, the fundamental mode is preferred over the subharmonic; this agrees with experimental observations, but not with theory (which does not account for this presence). Without streamwise vorticity, the subharmonic modes dominate, as predicted by theory and confirmed by computational simulations. In the presence of streamwise vorticity characteristic of wind-tunnel experiments, the K-type instability dominates and the numerical simulations predict the experimental results.

Direct numerical simulations are playing an increasingly important role in the investigation of transition; the literature is growing, especially recently. This trend is likely to continue as considerable progress is expected towards the development of new, extremely powerful supercomputers. In such simulations, the full Navier-Stokes equations are solved directly by employing numerical methods, such as finite-difference or spectral methods. The direct simulation approach is widely applicable since it avoids many of the restrictions that usually have to be imposed in theoretical models.

The Navier-Stokes solutions are taken hand-in-hand with the wind tunnel experiments in a complementary manner. The example of Singer, Reed, and Ferziger (1987) illustrates that these two techniques cannot be separated. The next step in the simulations will be to predict the growing body of detailed data being developed by Nishioka et al. (1980, 1981, 1984, 1985) on the latter stages of the breakdown process.

4. Transition Prediction and Control

When the recent work on subharmonics is added to the discussion at the end of section 3 on the limitations of the e^N method, one indeed has an uncertainty principle for transition (Morkovin, 1978). Transition prediction methods will remain conditional until the receptivity problem is adequately solved and the bypass mechanisms are well understood. In the mean time, extreme care must be exercised when using correlation methods to predict transition. Additional problems of transition prediction and laminar flow control are discussed by Reshotko (1985, 1986). The main principle of laminar flow control is to keep the disturbance levels low enough so that secondary instabilities and transition do not occur. Under these conditions, linear theory is quite adequate and e^N methods can be used to calculate the effectiveness of a particular LFC device.

The idea of transition control through active feedback systems is an area that has received considerable recent attention (Liepmann and Nosenchuck, 1982; Thomas, 1983; Kleiser and Laurien, 1984, 1985; Metcalfe et al., 1985). The technique consists of first sensing the amplitude and phase of an unstable disturbance and then introducing an appropriate out-of-phase disturbance that cancels the original disturbance. In spite of some early success, this method is no panacea for the transition problem. Besides the technical problems of the implementation of such a system on an aircraft, the issue of three-dimensional wave cancellation must be addressed. As Thomas (1983) showed, when the 2-D wave is canceled, all of the features of the 3-D disturbances remain to cause transition at yet another location. Some clear advantages over passive systems have yet to be demonstrated for this technique.

Acknowledgements

This work is supported by the Air Force Office of Scientific Research Contract AFOSR-85-NA-077.

References

- Arnal D., 1984. Description and prediction of transition in two-dimensional incompressible flow. *AGARD Report No. 709* (Special course on stability and transition of laminar flows) VKI, Brussels.
- Bacon, J.W. Jr., Pfenniger, W. and Moore, C.R., 1962. Influence of acoustical disturbances on the behavior of a swept laminar suction wing. Northrup Report NOR-62-124.
- Craik, A.D.D., 1971. Nonlinear resonant instability in boundary layers. *J. Fluid Mech.*, vol. 50, 393.
- Dagenhart, J.R., 1981. Amplified crossflow disturbances in the laminar boundary layer on swept wings with suction. *NASA TP-1902*.
- Fasel, H., 1980. Recent developments in the numerical solution of the Navier-Stokes equations and hydrodynamic stability problems. *Comp. Fluid Dyn.*, (Kollman, Wolfgang, ed.), Hemisphere.
- Fasel, H., 1986. Numerical simulation of laminar-turbulent transition. Invited Paper, U.S. National Congress of Applied Mechanics, ASME, June 1986.
- Floryan, J.M. and Saric, W.S., 1979. Stability of Görtler vortices in boundary layers. *AIAA Paper No. 79-1497 and AIAA J.*, vol. 20, 316.
- Floryan, J.M. and Saric, W.S., 1980. Wavelength selection and growth of Görtler vortices. *AIAA paper no. 80-1376 and AIAA J.*, vol. 22, 1529.
- Gaster, M., 1974. On the effects of boundary-layer growth on flow stability. *J. Fluid Mech.*, vol. 66, 465.
- Gregory, N., Stuart, J.T. and Walker, W.S., 1955. On the stability of three-dimensional boundary layers with applications to the flow due to a rotating disk. *Phil. Trans. Roy. Soc. Lon.*, vol. A248, 155.
- Hall, P., 1983. The linear development of Görtler vortices in growing boundary layers. *J. Fluid Mech.*, vol. 130, 41.
- Hama, F.R., 1959. Some transition patterns in axisymmetric boundary layers. *Phys. Fluids*, vol. 2, 664.
- Hama, F.R. and Nutant, J., 1963. Detailed flow-field observations in the transition process in a thick boundary layer. *Proc. 1963 Heat Trans. Fluid Mech. Inst.*, 77.
- Herbert, T., 1983. Subharmonic three-dimensional disturbances in unstable plane shear flows. *AIAA Paper No. 83-1759*.
- Herbert, T., 1984a. Analysis of the Subharmonic Route to Transition in Boundary Layers. *AIAA Paper No. 84-0009*.
- Herbert, T., 1984b. Secondary instability of shear flows. *AGARD Report No. 709* (Special course on stability and transition of laminar flows) VKI, Brussels.
- Herbert, T., 1984c. Nonlinear effects in boundary-layer stability. *AGARD Report No. 709* (Special course on stability and transition of laminar flows) VKI, Brussels.
- Herbert, T., 1985. Three-dimensional phenomena in the transitional flat-plate boundary layer. *AIAA Paper No. 85-0489*.
- Herbert, T., 1986a. Vortical Mechanisms in Shear Flow Transition. *Euromech 199 Colloquium, Direct and Large Eddy Simulation*, Vieweg Verlag.
- Herbert, T., 1986b. Analysis of secondary instabilities in boundary layers. Invited Paper, U.S. National Congress of Applied Mechanics, ASME, June 1986.
- Herbert, T. and Bertolotti, F.P., 1985. Effect of pressure gradients on the growth of subharmonic disturbances in boundary layers. In *Proc. Conf. on Low Reynolds Number Airfoil Aerodynamics*, ed. T.J. Mueller, Univ. of Notre Dame.
- Herbert, T., Bertolotti, F.P. and Santos, G.R., 1985. Floquet analysis of secondary instability in shear flows. *ICASE/NASA Workshop on Stability of Time-Dependent and Spatially Varying Flows*, August 19-20, Hampton, VA.
- Herbert, T. and Morkovin, M. V., 1980. Dialogue on bridging some gaps in stability and transition research. *Laminar-Turbulent Transition*, ed: R. Eppler and H. Fasel, Springer.
- Kobayashi, R. and Kohama, Y., 1985. Spiral vortices in boundary layer transition on a rotating cone. *Proc. 2nd IUTAM Symp. on Laminar-Turbulent Transition*, Novosibirsk.
- Kachanov, Yu.S., Kozlov, V.V. and Levchenko, V.Ya., 1977. Nonlinear development of a wave in a boundary layer (in Russian). *Mekhanika Zhidkosti i Gaza*, no. 3, 49.
- Kachanov, Yu.S. and Levchenko, V.Ya., 1984. Resonant interactions of disturbances in transition to turbulence in a boundary layer. *J. Fluid Mech.*, vol. 138, 209. (in Russian in 1982).
- Kaups, K. and Cebeci, T., 1977. Compressible laminar boundary layers with suction on swept and tapered wings. *J. Aircraft*, vol. 14, 661.

- Klebanoff, P.S., Tidstrom, K.D. and Sargent, L.M., 1962. The three-dimensional nature of boundary-layer instability. *J. Fluid Mech.*, vol. 12, 1.
- Kleiser, L. and Laurien, E., 1984. Three-dimensional numerical simulation of laminar-turbulent transition and its control by periodic disturbances. *Proc. 2nd IUTAM Symp. Laminar-Turbulent Transition*, Novosibirsk, USSR.
- Kleiser, L. and Laurien, E., 1985. Numerical investigation of interactive transition control. *AIAA Paper No. 85-0566*.
- Knapp, C.F. and Roache, P.J., 1968. A combined visual and hot-wire anemometer investigation of boundary-layer transition. *AIAA J.*, vol. 6, 29.
- Kohama, Y. and Kobayashi, R., 1983. Boundary layer transition and the behavior of spiral vortices on rotating spheres. *J. Fluid Mech.* 137, pp 153-164.
- Kozlov, V.V. and Ramazanov, M.P., 1984. Development of finite amplitude disturbances in a Poiseuille flow. *J. Fluid Mech.*, vol. 147, 149.
- Liepmann, H.W. and Nosenchuck, D.M., 1982. Active control of laminar-turbulent transition. *J. Fluid Mech.*, vol. 118, 201.
- Liepmann, H., Ghil, M., Newell, A., Roshko, A., and Saric, W. 1986. "Is chaos relevant to shear flows?" Chaotic Motion in Open Flows, UC Institute for Nonlinear Studies Workshop, Lake Arrowhead, California, Feb. 7-9, 1986.
- Mack, L.M., 1969. Boundary-layer stability theory. Jet Propulsion Lab. Rpt. 900-277, Rev. A.
- Mack, L.M., 1984a. Line sources of instability waves in a Blasius boundary layer. *AIAA Paper 84-0168*.
- Mack, L.M., 1984b. Boundary-layer linear stability theory. *AGARD Report No. 709* (Special course on stability and transition of laminar flows) VKI, Brussels.
- Malik, M.R., 1986. Wave interactions in three-dimensional boundary layers. *AIAA Paper No. 86-1129*.
- Malik, M.R. and Poll, D.I.A., 1984. Effect of curvature on three-dimensional boundary layer stability. *AIAA Paper No. 84-1672*.
- Malik, M.R., Wilkinson, S.P. and Orszag, S.A., 1981. Instability and transition in rotating disk flow. *AIAA J.*, vol. 19, 1131.
- Metcalf, R.W., Rutland, C., Duncan, J.H. and Riley, J.J., 1985. Numerical simulations of active stabilization of laminar boundary layers. *AIAA Paper No. 85-0567*.
- Michel, R., Arnal, D. and Coustols, E., 1984. Stability calculations and transition criteria in two- or three-dimensional flows. *Proc. 2nd IUTAM Symp. on Laminar-Turbulent Transition*, Novosibirsk.
- Michel, R., Arnal, D., Coustols, E. and Juillen, J.C., 1984. Experimental and theoretical studies of boundary layer transition on a swept infinite wing. *Proc. 2nd IUTAM Symp. on Laminar-Turbulent Transition*, Novosibirsk.
- Morkovin, M.V., 1969. On the many faces of transition. *Viscous Drag Reduction* ed: C.S. Wells, Plenum.
- Morkovin, M.V., 1978. Instability, transition to turbulence and predictability. *AGARDograph No. 236*.
- Morkovin, M.V., 1983. Understanding transition to turbulence in shear layers - 1983. AFOSR Final Report, Contract F49620-77-C-0013.
- Nayfeh, A.H., 1980. Three-dimensional stability of growing boundary layers. *Laminar-Turbulent Transition*, ed: R. Eppler and H. Fasel, Springer.
- Nayfeh, A.H., 1981. Effect of streamwise vortices on Tollmien-Schlichting waves. *J. Fluid Mech.*, vol. 107, 441.
- Nishioka, M., Iida, S., and Ichikawa, Y., 1975. An experimental investigation of the stability of plane Poiseuille flow. *J. Fluid Mech.*, 72, pp. 731-751.
- Nishioka, M., Asai, M. and Iida, S., 1980. An experimental investigation of secondary instability. *Laminar-Turbulent Transition*, ed: R. Eppler and H. Fasel, Springer.
- Nishioka, M., Asai, M. and Iida, S., 1981. Wall phenomena in the final stages of transition to turbulence. *Transition and Turbulence*, ed. R.E. Meyer, Academic Press.
- Nishioka, M. and Asai, M., 1984. Evolution of Tollmien-Schlichting waves into wall turbulence. *Turbulence and Chaotic Phenomena in Fluids*, ed: T. Tatsumi, North-Holland.
- Nishioka, M. and Asai, M., 1985. 3-D wave disturbances in plane Poiseuille flow. *Laminar-Turbulent Transition*, Vol 2. ed. V. Kozlov, Springer.
- Poll, D.I.A., 1979. Transition in the infinite swept attachment line boundary layer. *Aeronautical Quart.*, vol. XXX, 607.
- Poll, D.I.A., 1984a. Some observations of the transition process on the windward face of a yawed cylinder. *Cranfield College of Aeronautics Report 8407*.

- Poll, D.I.A., 1984b. Transition description and prediction in three-dimensional flows. *AGARD Report No. 709* (Special course on stability and transition of laminar flows) VKI, Brussels.
- Pupator, P.T. and Saric, W.S., 1986. Control of Random Disturbances in a Boundary Layer. *AIAA Paper No. 89-1007*.
- Reed, H.L., 1984. Wave interactions in swept-wing flows. *AIAA Paper No. 84-1678*.
- Reed, H.L., 1985. Disturbance-wave interactions in flows with crossflow. *AIAA Paper No. 85-0494*.
- Reed, H.L. and Saric, W.S., 1989. Stability and transition of three-dimensional flows. *Ann. Rev. Fluid Mech.* 21, 235-284
- Reshotko, E., 1975. Boundary-layer stability and transition. *Ann. Rev. Fluid Mech.* 8, 311.
- Reshotko, E., 1984a. Environment and receptivity. *AGARD Report No. 709* (Special course on stability and transition of laminar flows) VKI, Brussels.
- Reshotko, E., 1984b. Laminar flow control - Viscous simulation. *AGARD Report No. 709* (Special course on stability and transition of laminar flows) VKI, Brussels.
- Reshotko, E., 1985. Control of boundary-layer transition. *AIAA Paper No. 85-0562*.
- Reshotko, E., 1986. Stability and Transition, how much do we know? Invited Paper, U.S. National Congress of Applied Mechanics, ASME, June 1986.
- Saric, W.S., 1985a. Boundary-layer transition: T-S waves and crossflow mechanisms. *Proc. AGARD Special Course on Aircraft Drag Prediction and Reduction*, VKI, Belgium, May 1985.
- Saric, W.S., 1985b. Laminar flow control with suction: theory and experiment. *Proc. AGARD Special Course on Aircraft Drag Prediction and Reduction*, VKI, Belgium, May 1985.
- Saric, W.S., Carter, J.D. and Reynolds, G.A., 1981. Computation and visualization of unstable-wave streaklines in a boundary layer. *Bull. Amer. Phys. Soc.*, vol. 26, 1252.
- Saric, W.S., Kozlov, V.V. and Levchenko, V.YA., 1984. Forced and unforced subharmonic resonance in boundary-layer transition. *AIAA Paper No. 84-0007*.
- Saric, W.S. and Nayfeh, A.H., 1977. Nonparallel stability of boundary layers with pressure gradients and suction. *AGARD C-P No. 224*, 6.
- Saric, W.S. and Thomas, A.S.W., 1984. Experiments on the subharmonic route to transition. *Turbulence and Chaotic Phenomena in Fluids*, ed: T. Tatsumi, North-Holland.
- Saric, W.S. and Yeates, L.G., 1985. Experiments on the stability of crossflow vortices in swept-wing flows. *AIAA Paper No. 85-0493*.
- Singer, B.A., Reed, H.L. and Ferziger, J.H., 1986. Investigation of the effects of initial disturbances on plane channel transition. *AIAA Paper No. 86-0433*.
- Singer, B.A., Reed, H.L., and Ferziger, J.H., 1987. Effect of streamwise vortices on transition in plane channel flow. *AIAA Paper No. 87-0048*.
- Spalart, P. and Yang, K.S., 1986. Numerical simulation of boundary layers. Part 2. Ribbon-induced transition in Blasius flow. Accepted *Journal of Fluid Mechanics*.
- Spalart, P.R., 1984. Numerical simulation of boundary-layer transition. *NASA TM-85984*.
- Sreenivasan, K.R. and Strykowski, P.J., 1984. On analogies between turbulence in open flows and chaotic dynamical systems. *Turbulence and Chaotic Phenomena in Fluids* (Tatsumi, T., ed.), IUTAM Proc., Kyoto, Japan, Sept. 5-10, 1983.
- Tani, I., 1969. Boundary layer transition. *Ann. Rev. Fluid Mech.* 1, 169-196.
- Tani, I., 1981. Three-dimensional aspects of boundary-layer transition. *Proc. Indian Acad. Sci.*, vol. 4, 219.
- Tatsumi, T. (ed.), 1984. *Turbulence and Chaotic Phenomena in Fluids*. Proc. IUTAM Symp., Kyoto, Japan, Sept. 5-10, 1983.
- Thomas, A.S.W., 1983. The control of boundary-layer transition using a wave superposition principle. *J. Fluid Mech.*, vol. 137, 233.
- Thomas, A.S.W., 1986. Experiments on secondary instabilities in boundary layers. Invited Paper, U.S. National Congress of Applied Mechanics, ASME, June 1986.
- Thomas, A.S.W. and Saric, W.S., 1981. Harmonic and subharmonic waves during boundary-layer transition. *Bull. Amer. Phys. Soc.*, vol. 26, 1252.
- Yang, K.S., Spalart, P.S., Reed, H.L., and Ferziger, J.H., 1987. Navier-Stokes computations of pressure-gradient effects on transition in a boundary layer. *IUTAM Symposium on Turbulence Management and Relaminarization*, Bangalore, India, 19-23 January.

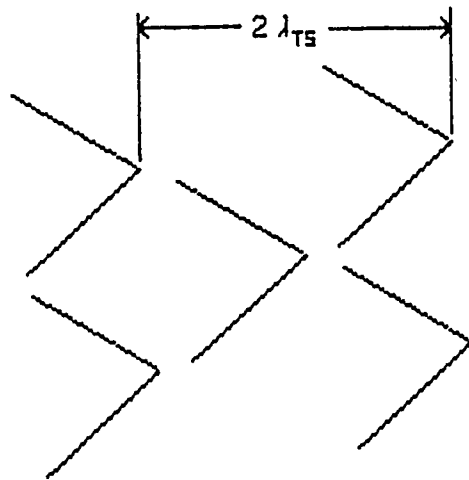


Figure 1. Staggered peak-valley structure (H-type mode).

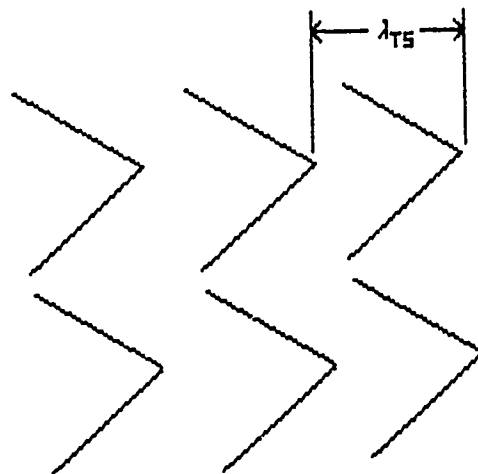


Figure 2. Peak-valley splitting structure (K-type mode).

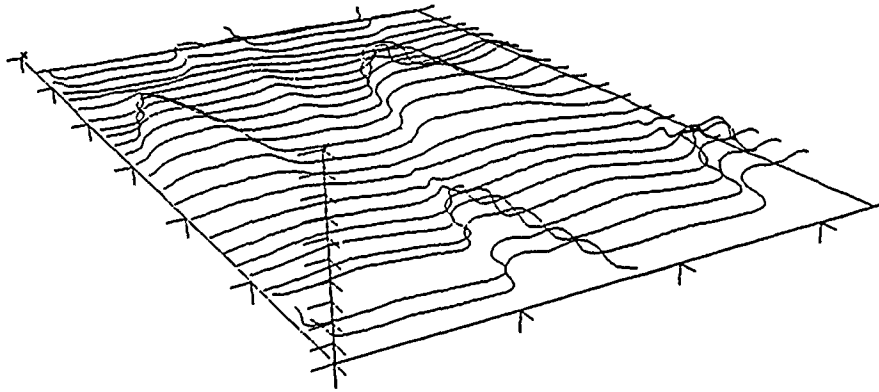


Figure 3. Vortex lines with $A = 2.0\%$, $t = 177$. The flow goes from lower right to upper left.

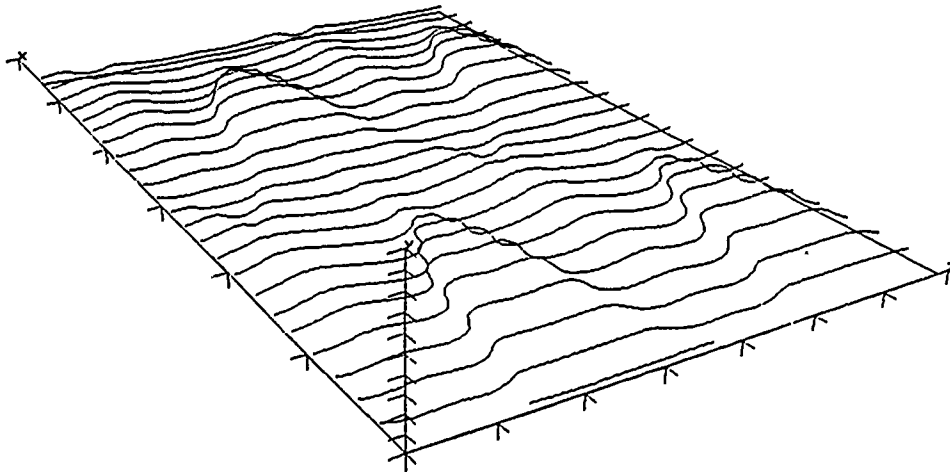


Figure 4. Vortex lines with $A = 2.0\%$, $t = 132$. The flow goes from lower right to upper left. Elliptical streamwise vortices with maximum u perturbation of 1.8% are included.

DISCUSSION

by F. Stern

Please comment on the influence of the type of breakdown on the state of the resulting turbulent boundary layer, which is quite important both in experiments and calculations. Also, are there any similarities between the processes you have classified for transition and those associated with relaminarization?

Author's Reply

The first part of this question hits to the heart of the motivation for doing work on the latter stages of transition.

The type of transition is important because of its influence on the large-scale

structure in "low" Reynolds number turbulent boundary layers. The control of turbulent boundary layers then rests on the type of large scale structure that may be present. For "high" Reynolds number turbulent boundary layers, the situation is not so clear i.e. it is hard to imagine that the details of the transition process influence the structure of fully developed turbulence.

It is unlikely that any of the structure of the transition process is recovered during relaminarization of a turbulent flow. I believe relaminarization to be highly dissipative due to large changes in the basic state which cause a loss in the turbulence production mechanisms. Unfortunately, there is a dearth of detailed experiments in this area.

RNG Modeling Techniques for Complex Turbulent Flows

S. A. Orszag and G. E. Karniadakis
Princeton University, Princeton, USA

A. Yakhot¹
Ben-Gurion University of the Negev, Beesheva, Israel
V. Yakhot
Princeton University, Princeton, USA

¹ Permanent address: Ben-Gurion University of the Negev
Beesheva, Israel

Abstract

In this paper, we combine RNG modeling techniques with spectral element discretization procedures to formulate an algorithm appropriate for simulating high Reynolds number turbulent flows in complex geometries. Three different approaches of modeling are followed based on RNG algebraic, differential $k - \epsilon$, and subgrid-scale models for the turbulent viscosity. Results obtained for the fully developed channel flow, and for the separated flow in a cavity and over a backwards-facing step suggest that all three formulations are suitable for turbulent flow simulations. The implementation of RNG models within the framework of a high-order discretization scheme (i.e. spectral element methods) is essential, as it results in resolution of fine turbulence structures even with the simple differential $k - \epsilon$ model at relatively small number of degrees of freedom.

1. RENORMALIZATION GROUP FORMULATION

Renormalization Group Theory (RNG) has proven to be a very useful tool in theoretical physics and statistical mechanics to study systems with a very large number of degrees of freedom. The most prominent use of this approach was in developing the theory of phase transitions of the second kind. Although RNG theory has found its way into fluid mechanics relatively recently, particularly in developing turbulence theory [1], it has already proved to be a valuable research tool, and it has provided a series of interesting theoretical and numerical results. A milestone for RNG theory in fluid mechanics was the establishment of the so-called correspondence principle, stating that in the inertial range the behavior of the small-scale Navier-Stokes turbulence is statistically equivalent to the modeled Navier-

Stokes equation with the addition of a random noise term. This principle makes it possible to use all the formalism of classical RNG theory.

Recently, renormalization group methods have been developed [1], [2] to analyse a variety of turbulent flow problems. For homogeneous turbulent flows, such important quantities as the Kolmogorov constant, Batchelor constant, turbulent Prandtl number, rate of decay to isotropy, skewness factor, etc. have been obtained directly from this theory in good agreement with available data. Efforts in developing RNG methods for sub-grid (large-eddy simulation) model constants have also been notably successful [3].

RNG methods involve systematic approximations to the full Navier-Stokes equations that are obtained by using perturbation theory to eliminate or decimate infinitesimal bands of small scale modes, iterating the perturbation procedure to eliminate finite bands of modes by constructing recursion relations for the renormalized transport coefficients, and evaluating the parameters at a fixed point in the lowest order of a dimensional expansion around a certain critical dimension. The decimation procedure, when applied successively to the entire wavenumber spectrum leads to the RNG equivalent of full closure of the Reynolds averaged Navier-Stokes equations. The resulting RNG transport coefficients are differential in character as opposed to ad hoc algebraic coefficients of conventional closure methods. All constants and functions appearing in the RNG closures are fully determined by the RNG analysis.

In essence, the RNG method provides an analytical method to eliminate small scales from the Navier-Stokes equations, thus leading to a dynamically consistent description of the large-scales. The formal process of successive elimination of small scales together with re-scaling of the resulting equations results in a calculus for the derivation of transport approximations in turbulent flows.

The renormalization group method has been used to derive three different types of models: an algebraic eddy viscosity model, a differential $k-\epsilon$, and a subgrid scale turbulence model for large eddy simulations[1]. The governing equations for the flow motion are the Navier-Stokes equations:

$$\frac{\partial v_i}{\partial t} + v_j \frac{\partial v_i}{\partial x_j} = -\frac{\partial p}{\partial x_i} + \frac{\partial}{\partial x_j} \left(\nu \frac{\partial v_i}{\partial x_j} \right) \quad (1)$$

along with the incompressibility constraint

$$\frac{\partial v_i}{\partial x_i} = 0 \quad (2)$$

Here ν is the total viscosity defined as $\nu = \nu_0 + \nu_T$ (the sum of the molecular and turbulent viscosity, respectively).

RNG Algebraic Model

This model is the simplest of all, however it is not very general as it requires the *a priori* postulation of the characteristic integral length scale, and thus an assumption needs to be made based on physical considerations. The eddy viscosity ν is obtained from the following relation:

$$\nu = \nu_0 \left[1 + H \left(\frac{a\epsilon}{(2\pi)^4 \nu_0^3} \Delta^4 - C \right) \right]^{1/3} \quad (3)$$

where $H(x)$ is the Heaviside function defined by $H(x) = x$ for $x \geq 0$ and $H(x) = 0$ otherwise, and Δ is an integral length scale of the turbulence in the inertial range. The constants $a = 0.120$ and $C = 100$ are derived in [1]. The mean dissipation rate ϵ can be expressed entirely through the resolvable field as

$$\epsilon = \frac{\nu}{2} \left(\frac{\partial v_i}{\partial x_j} + \frac{\partial v_j}{\partial x_i} \right)^2 \quad (4)$$

The total viscosity is then obtained by solving an algebraic cubic equation at every node of the computational domain at each time step.

RNG $k-\epsilon$ Model

This is a differential model based on differential recursion relations discussed in [1]. It is free of adjustable parameters, however two additional equations are derived for the turbulent kinetic energy k , and the rate of dissipation ϵ .

$$\frac{Dk}{Dt} = P - \epsilon + \frac{\partial}{\partial x_i} \left(\alpha \nu \frac{\partial k}{\partial x_i} \right) \quad (5)$$

$$\frac{D\epsilon}{Dt} = \bar{P} - Y + \frac{\partial}{\partial x_i} \left(\alpha \nu \frac{\partial \epsilon}{\partial x_i} \right) \quad (6)$$

Here we define the production term P based on the turbulent viscosity

$$P = \frac{\nu_T}{2} \left(\frac{\partial v_i}{\partial x_j} + \frac{\partial v_j}{\partial x_i} \right)^2 \quad (7a)$$

and the terms \bar{P} , Y are defined subsequently from:

$$\bar{P} = 0.656 \epsilon^{1/2} Y_c P \quad (7b)$$

$$Y = \epsilon^{2/2} Y_c \quad (7c)$$

The RNG procedure provides the additional two differential equations for Y_c and $\frac{k}{\epsilon^{1/2}}$, which can be integrated as follows

$$Y_c \nu_0^{1/2} = \alpha_Y - \gamma_Y \int_1^{\frac{k}{\epsilon^{1/2}}} \frac{dt}{(t^3 - 1 + C)^{1/2}} \quad (8a)$$

$$\frac{k}{\nu_0^{1/2}} = \alpha_k + \gamma_k \int_1^{\frac{k}{\epsilon^{1/2}}} \frac{tdt}{(t^3 - 1 + C)^{1/2}} \quad (8b)$$

Here the coefficients (α_Y, γ_Y) and (α_k, γ_k) are known constants derived from the asymptotic behavior of the model, while the parameter α involved in equations (5-6) is the inverse total Prandtl number defined from the RNG algebraic relation (α_0 refers to molecular properties)

$$\left| \frac{\alpha - 1.3929}{\alpha_0 - 1.3929} \right|^{0.6321} \left| \frac{\alpha + 2.3929}{\alpha_0 + 2.3929} \right|^{0.3679} = \frac{\nu_0}{\nu} \quad (9)$$

The total viscosity ν is implicitly defined from equations (8) at each node of the computational domain. In the high Reynolds number region where $\nu \gg \nu_0$, we obtain

$$\nu = 0.0845 \frac{k^2}{\epsilon} \quad (10)$$

This high Reynolds number approximation is similar to that commonly used in algebraic models. Thus, the algebraic models contain terms like $\frac{\epsilon^2}{k}$, which diverge when $k \rightarrow 0$ (i.e., near wall regions or separation zones) thus creating immense difficulties computationally. The differential relations obtained via RNG techniques, however, do not contain such singular behavior and thus have great potential for success with separating flows. The differential relations provide definitive interpolation formulae to connect low and high Reynolds regions of the flow.

RNG subgrid-scale Model

In large eddy simulations (LES) the velocity field v_i is decomposed into large scales \bar{v}_i and subgrid components v'_i . It is the modeling of terms involved these latter components that is crucial for accurate computations as previous attempts using various subgrid models [4] have indicated. The RNG subgrid model is derived by elimination of modes from the interval Λ_0 to Λ , where $\Lambda = \gamma \left(\frac{\epsilon}{\nu_0^3} \right)^{1/4}$ ($\gamma = 0.20$) is a dissipation cut-off limit, and the wavevector $\Lambda_0 = \Lambda e^{-r}$ can be expressed through the computational mesh size $\bar{\Delta}$. The general RNG derived viscosity given by

$$\nu_r = \nu_0 \left(1 + \frac{a\epsilon}{\nu_0^3 \Lambda^4} (e^{4r} - 1) \right)^{1/3} \quad (11)$$

can then be expressed in terms of a length scale Δ , which in LES represents the width of a suitably chosen Gaussian filter. Thus, equation (11) reduces to an identical equation as in (3), where Δ is given by the integral

$$\Delta^4 = \int^{\Lambda_1} \int^{\Lambda_2} \int^{\Lambda_3} \frac{dk dp dq}{(k^2 + p^2 + q^2)^{7/2}} \quad (12)$$

Here $\Lambda_i = \pi/\Delta_i$ (for $i = 1, 2, 3$) and $\Delta_i = 2\tilde{\Delta}_i$. The above integral can be readily evaluated by breaking it up to three asymptotic integrals and a finite triple integral that can be computed numerically. In cases of simple geometries (i.e. plane channels) the integral can be evaluated through algebraic relations [3].

2. SPECTRAL ELEMENT METHODOLOGY

Let us denote by Ω the three-dimensional computational domain, and by $\partial\Omega$ the computational boundary-surface; we can then rewrite the governing equations (1) in the form,

$$\frac{\partial v_i}{\partial t} = -\frac{\partial p_i}{\partial x_i} + \frac{\partial}{\partial x_j} \left(\nu \frac{\partial v_i}{\partial x_j} \right) + H_i \quad \text{in } \Omega \quad (13)$$

where H_i includes all nonlinear and forcing terms (e.g. the random force to be included in LES). The separation of linear and nonlinear terms in the above equation leads naturally to a mixed (explicit-implicit) time advancement scheme. The temporal discretization proceeds by employing the splitting scheme; accuracy and relative advantages of the scheme in the current applications are discussed in [5]. The resulting system of equations is a system of separately solvable elliptic equations for pressure and velocity. The discretization of these equations in space is obtained through the spectral element method. For simplicity we only present the two-dimensional equations, however our implementation is general for truly three-dimensional geometry and flow. Here we follow a 'layered' approach, according to which the discretizations and solvers are constructed on the basis of a hierarchy of nested operators proceeding from the highest to the lowest derivatives. This approach is motivated by the fact that the highest derivatives in an equation govern the continuity requirements, conditioning, and stability of the system. Given the brevity of the current paper we shall limit our description of spectral element methods to the innermost layer, the elliptic 'kernel', which represents both the pressure equation and the viscous corrections in equation (13).

A typical elliptic equation for a field variable ϕ can be put in a standard Helmholtz equation form with variable coefficients as follows

$$\frac{\partial}{\partial x_j} \left(\nu \frac{\partial \phi}{\partial x_j} \right) - \lambda^2 \phi = f \quad \text{in } \Omega \quad \text{for } j = 1, 2 \quad (14)$$

In addition, let us assume homogeneous boundary conditions $\phi = 0$ on $\partial\Omega$. Equation (14) can then be further discretized using planar spectral elements in plane $x-y$. If we define H_0^1 the standard Sobolev space that contains functions which satisfy homogeneous boundary conditions, and introduce testfunctions $\psi \in H_0^1$, we can then write the equivalent variational statement of (14) as,

$$\int_{\Omega} \nu \frac{\partial \psi}{\partial x_j} \frac{\partial \phi}{\partial x_j} ds + \lambda^2 \int_{\Omega} \psi \phi ds = - \int_{\Omega} \psi f ds. \quad (15)$$

The spectral element discretization corresponds to numerical quadrature of the variational form (15) restricted to the space $X_h \subset H_0^1$. The discrete space X_h is defined in terms of the spectral element discretization parameters (K, N_1, N_2) , where K is the number of "spectral elements", and N_1, N_2 are the degrees of piecewise high-order polynomials in the two directions respectively that fill the space X_h . By selecting appropriate Gauss-Lobatto points ξ_{pq}^k and corresponding weights $\rho_{pq} = \rho_p \rho_q$, equation (15) can be replaced by,

$$\sum_{k=1}^K \sum_{p=0}^{N_1} \sum_{q=0}^{N_2} \rho_{pq} J_{pq}^k \left[\nu \frac{\partial \psi}{\partial x_j} \frac{\partial \phi}{\partial x_j} \right]_{\xi_{pq}^k} + \lambda^2 \sum_{k=1}^K \sum_{p=0}^{N_1} \sum_{q=0}^{N_2} \rho_{pq} J_{pq}^k [\psi \phi]_{\xi_{pq}^k} = - \sum_{k=1}^K \sum_{p=0}^{N_1} \sum_{q=0}^{N_2} \rho_{pq} J_{pq}^k [\psi f]_{\xi_{pq}^k} \quad (16)$$

Here J_{pq}^k is the Jacobian of the transformation from global to local coordinates $(x, y) \Rightarrow (r, s)$, for the two-dimensional element k . The Jacobian is easily calculated from the partial derivatives of the geometry transformation r_x, r_y, s_x, s_y . The next step in implementing (16) is the selection of a basis which reflects the structure of the piecewise smooth space X_h . We choose an interpolant basis with components defined in terms of Legendre-Lagrangian interpolants, $h_i(r_j) = \delta_{ij}$. Here, r_j represents local coordinate and δ_{ij} is the Kronecker-delta symbol. It was shown in [6], [7] that such a spectral element implementation converges spectrally fast to the exact solution for a fixed number of elements K and $N \rightarrow \infty$, for smooth data and solution, even in non-rectilinear geometries.

Having selected the basis we can proceed in writing the local to the element k spectral element approximations for ϕ^k (or ψ^k) as follows,

$$\phi^k = \phi_{mn}^k h_m(r) h_n(s) \quad \forall m, n \in (0, \dots, N_1), (0, \dots, N_2), \quad (17a)$$

where ϕ_{mn}^k is the local nodal value of ϕ . The geometry is also represented via similar type tensorial products with same-order polynomial degree, i.e.

$$(x, y)^k = (x_{mn}^k, y_{mn}^k) h_m(r) h_n(s) \quad \forall m, n \in (0, \dots, N_1), (0, \dots, N_2), \quad (17b)$$

Here x_{mn}^k, y_{mn}^k are the global physical coordinates of the node mn in the k element. This isoparametric mapping leads to a compatible pressure formulation without the presence of spurious modes [5].

We now insert (17) into (16) and choose test functions ψ_{mn} , which are non-vanishing at only one global node to arrive at the discrete matrix system. This procedure is straightforward and here we cite the final matrix system,

$$\sum_{k=1}^K \sum_{m=0}^{N_1} \sum_{n=0}^{N_2} (H_{ijmn}^{x,k} + H_{ijmn}^{y,k} + \lambda^2 J_{ij}^k B_{im}^k B_{jn}^k) \phi_{mn}^k$$

$$= - \sum_{k=1}^K \sum_{m=0}^{N_1} \sum_{n=0}^{N_2} J_{ij}^k B_{im}^k B_{jn}^k f_{mn}^k, \quad (18a)$$

where ℓ denotes direct stiffness summation for the global system to insure that the ensemble is performed in space H^1 . The x-component, for example, of the Helmholtz operator is defined as follows,

$$H_{mn}^{x,k} = \rho_{pq} J_{pq}^k \nu_{pq}^k \{ (r_x)^2 D_{pq}^2 D_{pm}^2 \delta_{nq} + (s_x)^2 D_{pq}^2 D_{qn}^2 \delta_{mp} \\ + (r_x s_x) D_{pq}^2 D_{pm}^2 \delta_{qn} + (r_x s_x) D_{pq}^2 D_{qn}^2 \delta_{mp} \} \quad (18b)$$

Here $\nu_{pq} = \nu(\xi_{pq}^k)$, and $D_{ij} = \frac{dh_i}{dx}(\xi_j)$; all other parameters have been defined previously. The mass matrix B_{ij}^k is diagonal and is defined as $B_{ij}^k = \rho_i \delta_{ij}$. The y-component of the Helmholtz operator is defined similarly.

The natural choice of solution algorithm for a time- and space-dependent viscosity $\nu(x, y, t)$ is an iterative procedure; to date both conjugate gradient techniques and multigrid methods have been implemented for elliptic equations [6],[8]. The advantage of the formulation proposed here as compared to the formulation in [6] is that the splitting scheme results in separate, elliptic equations for the pressure and velocity that can be very efficiently solved using those iterative techniques. We have found that, for spectral element discretizations involving elements of low aspect ratio, multigrid methods converge much faster than conjugate gradient methods; their convergence rate, however, is greatly deteriorated for large aspect ratio or very deformed spectral elements. A more quantitative analysis of the computational complexity as well as of the convergence properties of the aforementioned iterative methods in spectral element approximations, and in particular in the context of parallel implementation, is given in [8].

3. NUMERICAL RESULTS

In this section we first present results for the flow in a lid-driven cavity obtained using the algebraic model and two-dimensional spectral element simulations. We then validate the RNG methodology by simulating two different flows for which detailed experimental data and results from direct numerical simulations are available: the fully developed turbulent channel flow, and the flow over a backwards-facing step. These results are obtained using the $k-\epsilon$ and the subgrid-scale RNG models.

Turbulent Flow in a Lid-Driven Cavity

Here we consider a square two-dimensional cavity in $x-y$ with mean flow being two-dimensional also. The exact geometry and the corresponding spectral element mesh is

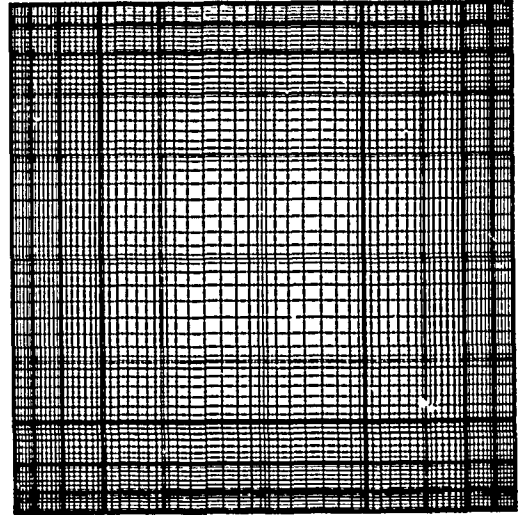


Fig. 1 Spectral Element Mesh employed for the simulation of flow in a lid-driven cavity

shown in figure 1. Flow is generated by driving the lid of the cavity in the x-direction at a constant velocity $U = 1$. To avoid the spurious effects due to the step changes of the velocity at the two upper corners a sufficiently smooth velocity profile that asymptotes to U in the immediate vicinity of the corners was imposed. Experimental evidence suggests that the flow in the cavity becomes turbulent at a Reynolds number slightly above $R = 5,000$ with the initiation point of transition being at the downstream lower corner [9].

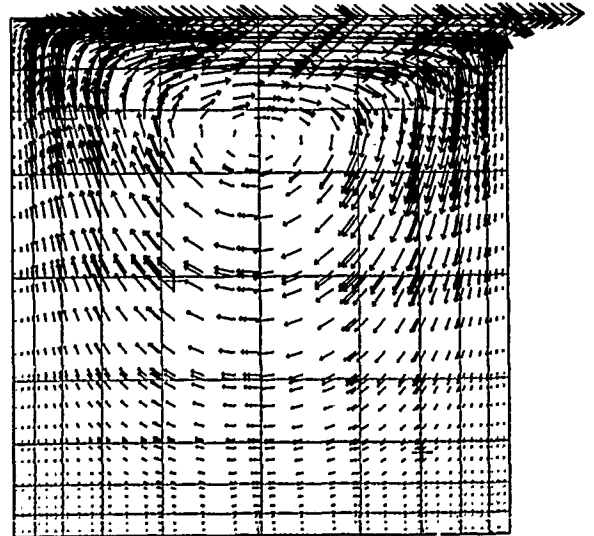


Fig. 2 Velocity vectors of mean turbulent flow at Reynolds number $R = 50,000$

We simulate the lid-driven cavity flow at Reynolds number $R = 50,000$ with the algebraic model (equation (3)) employed in the computation. As a characteristic length Δ needed for the model at each nodal point we consider the distance from the point to the nearest wall which is proportional to the characteristic size of the largest eddies of turbulence in this flow. In figure 2 we plot the velocity vectors of the mean turbulent flow and in figure 3 several x -velocity profiles in the neighborhood of the right lower corner of the cavity. It is seen that the flow undergoes separation as we move from the center of the cavity to the corner, as expected. However, the size of the recirculation zone as well as the strength of the reverse flow is weak due to the effects of the increased apparent viscosity. Indeed, direct numerical simulations on the same mesh at Reynolds number $R = 10,000$ shows regions of multiple small and large size instantaneous eddies (figure 4); the time-averaged flow however exhibits only very small recirculation zones similar to the ones shown in figures 2-3.

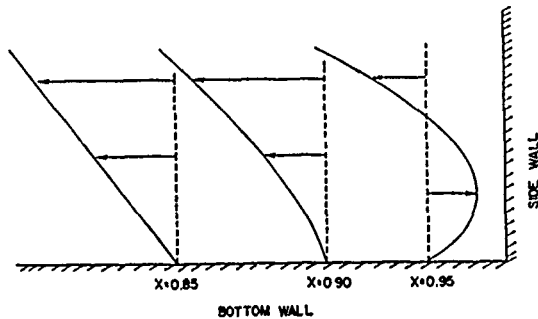


Fig. 3 Velocity (x -component) profiles at station $x = 0.85$ (a); 0.90 (b); 0.95 (c) in the neighborhood of the downstream secondary eddy

To examine the spatial variation of the eddy-viscosity after a stationary state is reached we plot in figure 5a the total viscosity at a vertical station through the center of the cavity. We see that the distribution is smooth and peaks at the lid where there is enhanced mixing, while it achieves a minimum at the wall (molecular viscosity) and in the region close to the center of the cavity where the fluid is almost stagnant. Thus, the total viscosity increases by almost three orders of magnitude from its molecular to its maximum value at the moving wall. In figure 5b we plot the total viscosity at the same position as in figure 5a but at Reynolds number $R = 25,000$. We see in this case that the region close to the bottom wall where the fluid motion is weaker the region of molecular viscosity is broader, whereas the outside distribution is similar to the one in figure 5a.

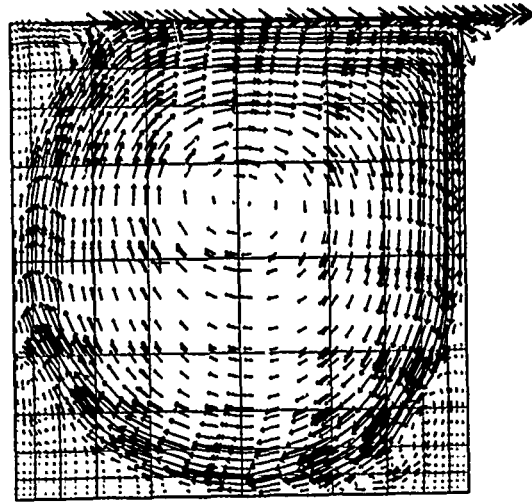


Fig. 4 Instantaneous velocity vectors at $R = 10,000$: The flow is computed via direct spectral element simulation

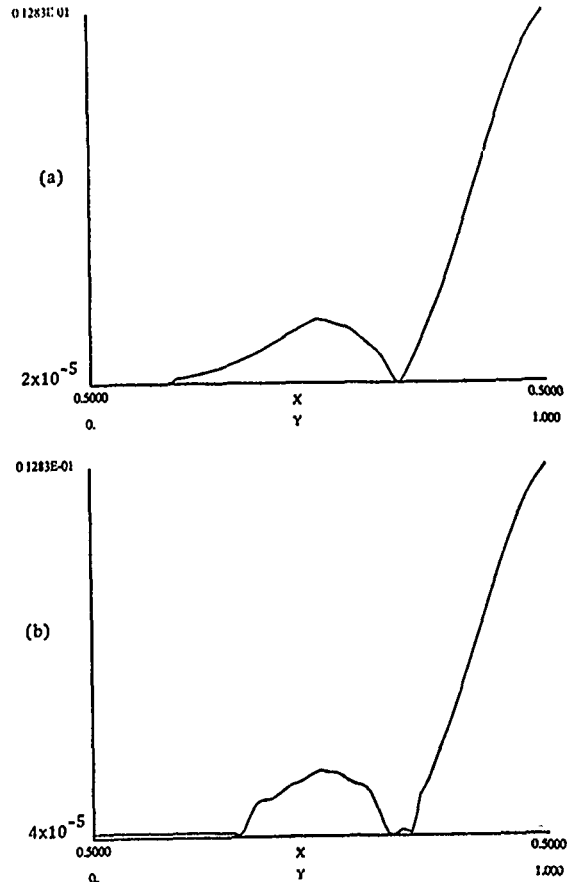


Fig. 5 Total viscosity variation at a vertical station through the cavity center
(a) $R = 50,000$
(b) $R = 25,000$

$k - \epsilon$ Modeling of Turbulent Channel Flow

We simulate first flow in a plane channel at Reynolds number $R_* = 1000$. Here the Reynolds number is based on the wall-shear velocity U_* and the channel half width. The computational domain extends from $y_+ = 8.5$ to $y_+ = 1991.5$, so that the constant shear regions next to the walls are excluded from the simulation. Two-dimensional spectral elements are employed for the discretization, ($K = 12$), of order $N = 9$, so that there are 97 collocation points across the channel. The boundary conditions are prescribed u , k and ϵ at the y -sides of the domain, while periodicity conditions in the streamwise direction (x) ensure one-dimensionality of the mean flow. The simulation starts from an equilibrium state and integration proceeds for a long time. Results of the mean quantities are presented in figures 6 and 7. As a next test we simulated the same flow but with the computational domain extended to walls. The boundary conditions at the walls are now no-slip for velocity, zero for kinetic energy, and Neumann

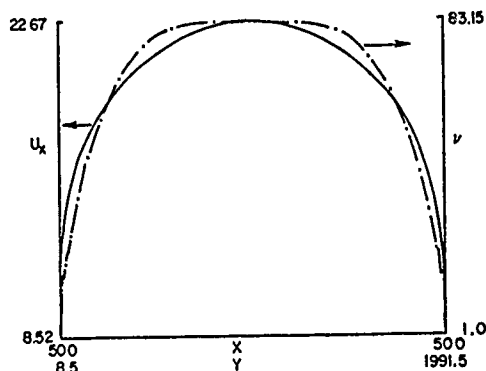


Fig. 6 Mean velocity and eddy-viscosity profiles at $R_* = 1000$ for the turbulent flow in a channel

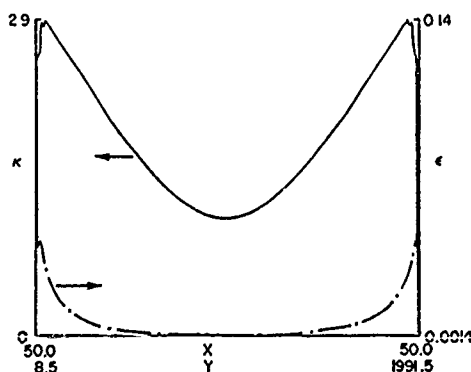


Fig. 7 Turbulent kinetic energy (k) and dissipation rate (ϵ) profiles at $R_* = 1000$ for the turbulent flow in a channel

condition for the dissipation rate. In order to minimize discretization errors and ensure accurate imposition of the zero flux condition on ϵ we increased the resolution to order $N = 15$ per element. The results of this simulation were identical to results displayed in figures 6 and 7, which suggests that the zero flux condition on ϵ is a meaningful one.

$k - \epsilon$ Modeling of Turbulent Flow Over a Backward-Facing Step

The geometry for this flow and the corresponding spectral element mesh are shown in figure 8; this geometry is identical with the geometry used in experiments of Kim et al [10] and in the computations of Avva et al [11]. The outflow length is taken to be twenty times the step height H . A total of $K = 92$ elements of order $N = 9$ were employed in the discretization. The Reynolds number $R_* = \frac{U_* H}{\nu_0}$ is 1870 (or $R_c = 45,000$). In this simulation the computational domain includes the walls, where we impose the zero flux condition for the dissipation rate ϵ ; at the outflow Neumann conditions are specified for all field variables. The inflow conditions match the measured profiles in the experiment of Kim et al [10] and employed in the computations of Avva et al [11]. Finally, the initial data are based on the results reported in [11] and some initial perturbation.

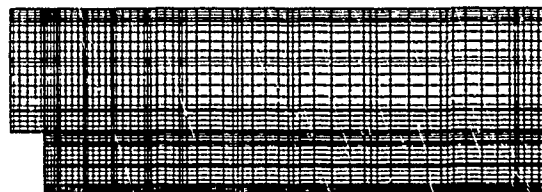


Fig. 8 Spectral Element Mesh employed for the simulation of flow over a backward-facing step

In figure 9 we first present the results of this simulation in the form of streamlines. In addition to the large recirculation zone shown in this plot eddies of smaller size of opposite rotation appear at the step test section floor juncture consistent with the experimental findings [12]. To the best of our knowledge no other simulation has resolved such fine structures previously using a single or a zonal modeling approach. Furthermore, the length of the recirculation zone (figure 9-10) is computed to be $L = 7.3H$ in close agreement with the experimental value [10]. Most studies to date fall short of predicting the correct value due to errors both in numerics and turbulence models. In figure 10 and 11 we plot all mean variables at a station very close to the reattachment point. The eddy viscosity distribution attains its maximum close to that point where the turbulence intensity exhibits its extremum.

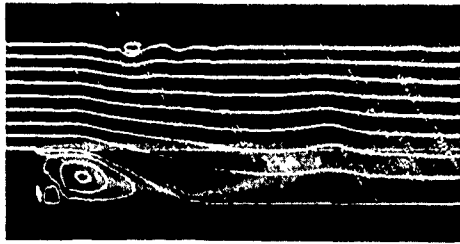


Fig. 9 Spectral Element-RNG/ k - ϵ Simulation of flow over a step at $R_* = 1870$. The curves are mean flow streamlines while color represents turbulent kinetic energy (red=max, blue=min). In this calculation, no *ad hoc* fitted parameters or experimental input is used. The recirculation zone length is 7.3 step heights in agreement with the experiments of Kim, et al (1979). The small vortices in the step corner are observed experimentally too.

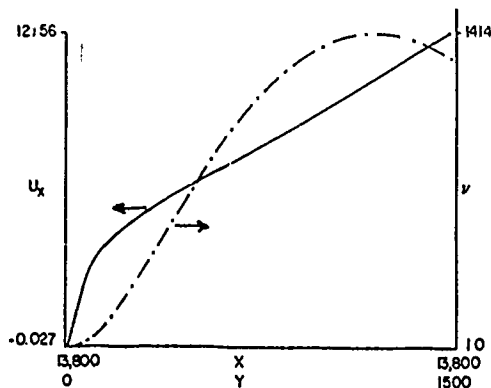


Fig. 10 Mean velocity and eddy-viscosity profiles at $R_* = 1870$ for the flow described in Figure 9

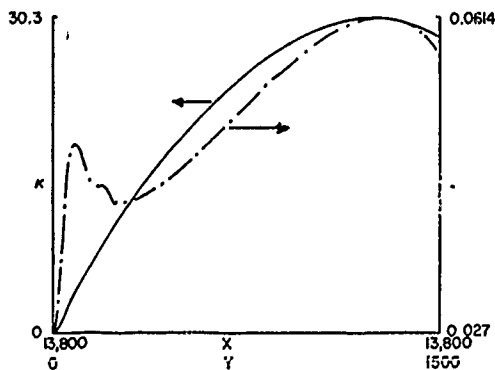


Fig. 11 Turbulent kinetic energy (k) and dissipation rate (ϵ) profiles at the reattachment point ($R_* = 1870$) (flow as in Figure 9)

Large-Eddy Simulations of Turbulent Channel Flow

In the last example we employ the RNG subgrid-scale model to simulate the turbulent channel flow at $R_* = 185$. This simulation corresponds to identical conditions as the direct simulation recently reported by Kim, Moin and Moser (1987) [13]. In our simulation we have used however 60 times fewer grid points. In particular, for this case we employ a global spectral discretization based on Fourier expansion in streamwise and spanwise directions, and Chebyshev expansion in the inhomogeneous direction ($16 \times 64 \times 64$). The initial conditions are based on three-dimensional Tollmien-Schlichting waves. The results of our simulation are essentially identical with the results of the direct simulation as shown in figures 12 and 13, and in close agreement with the experiments [14]. The agreement extends also to higher order statistics as well as to flow structure and the streak spacing; the results of our simulations are plotted in figure 14 as color contour plots of the fluctuating velocity component at a plane close to the wall (here red indicates low velocity; blue high velocity). The mean separation between streaks is $\lambda_s \approx 90$ [3] in close agreement with the experimentally observed spacing; all previous LES have failed to predict the correct value of streak separation [15].

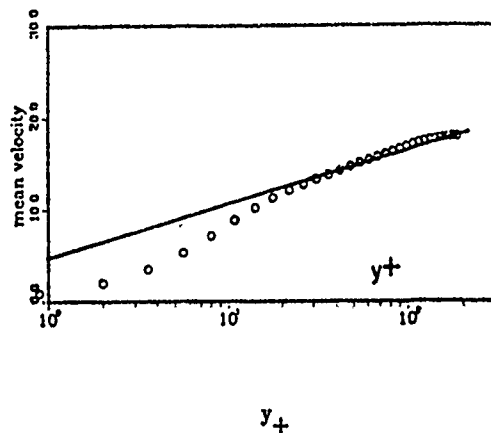


Fig. 12 Mean Velocity Profile at $R_* = 185$ of the turbulent channel flow computed via RNG-large eddy simulations $-\cdot- 5.0 + 2.5 \ln y_+$

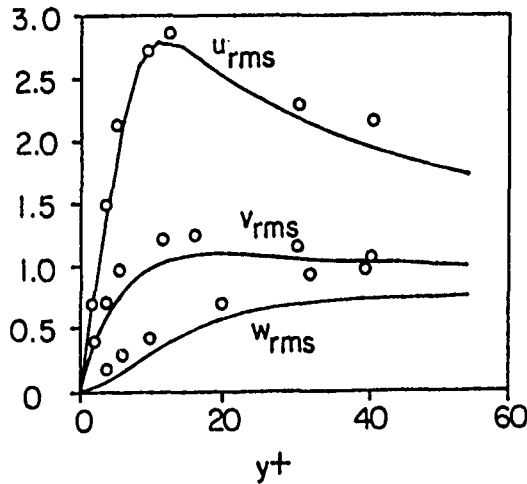


Fig. 13 Turbulent intensities for the flow described in Figure 12. Also shown are experimental results of Kreplin and Eckelman (1979)



Fig. 14 Contours (low velocity: red; high velocity: blue) of near-wall fluctuations x-velocity in a turbulent channel flow large eddy simulation using the renormalization group-based subgrid scale eddy viscosity at $R_\tau = 185$. Observe the alignment of the flow in the streamwise direction and the formation of low-speed streamwise streaks.

4. CONCLUSIONS

Turbulent flows are difficult to compute because they require order R^3 work and order $R^{9/4}$ storage to resolve dynamically significant velocity fluctuations at large Reynolds number R . These requirements become more severe in complex geometry flows where a broader spectrum of significant scales is present. Direct numerical simulation although can provide a very faithful description of the flow is limited severely at the present time and in the next few years by the

aforementioned computational requirements to flow simulations at a Reynolds number of a few thousands. Progress in simulating realistic flows of engineering importance can be made if reliable and well validated modeling techniques are combined with highly-accurate numerical methods. In the current work, we demonstrated how RNG methodology can be used to represent all scales of turbulent flow using for example a differential $k - \epsilon$ model, or to represent only the small-scale dynamics using a subgrid-scale model. This methodology is very robust and can be applied to a variety of flows as a totally prognostic tool of analysis, since it requires no *a priori* known parameters or any experimental input, which is typically the case with the currently used turbulence modeling techniques. A computationally efficient implementation of the RNG methodology is obtained if it is combined with spectral or spectral element discretization methods, which are used today primarily in direct computations of transitional and turbulent flows. We are currently working in further validating our RNG/spectral element methodology in unsteady turbulent flows (e.g. vortex streets) in complex geometries.

5. ACKNOWLEDGEMENTS

This work was supported by AFOSR under Contract F49620-87-C-0036, by ONR under Contract N00014-82-C-0451, and by DARPA under contract N00014-86-K-0759. Most of the computations were performed on the CRAY-X/MP48 at the Pittsburgh Supercomputing Center.

References

- [1] Yakhot V. and Orszag S.A. Renormalization Group analysis of turbulence.I. Basic theory. *J. Sc. Comp.*, 1:3, 1986.
- [2] Yakhot V. and Orszag S.A. Relation between Kolmogorov and Batchelor constants. *Phys. Fluids*, 30:3, 1987.
- [3] Yakhot A., Orszag S.A., and Yakhot V. Renormalization Group formulation of large-eddy simulations. *J. Sc. Comp.*, to appear, 1989.
- [4] Piomelli U., Ferziger J., and Moin P. *Models for Large Eddy Simulations of Turbulent channel flows including transpiration*. Technical Report Report TF-32, Thermosciences Division, Dept. Mech. Engineering, Stanford University, California, 94305, 1987.
- [5] Karniadakis G.E. Spectral element simulations of laminar and turbulent flows in complex geometries. *Appl. Num. Math.*, to appear, 1989.

- [6] Rønquist E.M. *Optimal spectral element methods for the unsteady three-dimensional incompressible Navier-Stokes equations*. PhD thesis, Massachusetts Institute of Technology, 1988.
- [7] Patera A.T. A spectral element method for Fluid Dynamics; Laminar flow in a channel expansion. *J. Comput. Phys.*, 54:468, 1984.
- [8] Fischer P., Ho L.W., Karniadakis G.E., Rønquist E., and Patera A.T. Recent advances in parallel spectral element simulation of unsteady incompressible flows. *Computers and Structures*, 30:217, 1988.
- [9] Prasad A.K. and Koseff J.R. Reynolds number and end-wall effects on a lid-driven cavity flow. *Phys. of Fluids A*, 1:208, 1989.
- [10] Kim J., Kline S.J., and Johnston J.P. *Investigation of separation and reattachment of a turbulent shear layer: flow over a backward-facing step*. Technical Report Report MD-37, Dept. Mech. Engineering, Stanford University, California, 94305, 1978.
- [11] Avva R.K., Kline S.J., and Ferziger J.H. Computation of turbulent flow over a backward-facing step-zonal approach. In *AIAA-88-0611*, 1989.
- [12] Abbott D.E. and Kline S.J. Experimental investigation of subsonic turbulent flow over single and double backward facing steps. *J. Basic Engineering*, 84, 1962.
- [13] Kim J., Moin P., and Moser R. Turbulence statistics in fully developed channel flow at low Reynolds number. *J. Fluid Mech.*, 177:133, 1987.
- [14] Kreplin H. and Eckelman H. Behavior of the three fluctuating velocity components in the wall region of a turbulent channel flow. *Phys. Fluids*, 22:1233, 1979.
- [15] Moin P. and Kim J. Numerical investigation of turbulent channel flow. *J. Fluid Mech.*, 118:341, 1982.

DISCUSSION

by E.P. Rood

For some applications a requirement is free surface flows near their intersection to predict with boundary layers or in the turbulent wake of a ship. What experimental or other physical information is needed to develop an adequate turbulence model for such free surface flows?

Author's Reply

In the renormalization group approach, full turbulence closure is obtained without a priori experimental input. This is true for both free surface and other flows. However, in developing turbulence models for free surface flows, it may be best to "tune" the model using experimental observations of free surface turbulence. It is hoped that many of these questions can be answered in the near future with detailed application of the renormalization group models.

A Flood Control of Dam Reservoir by Conjugate Gradient and Finite Element Methods

M. Kawahara and T. Kawasaki
Chuo University
Tokyo, Japan

Abstract

A flood control of dam reservoir by the combined method of conjugate gradient and finite element methods is presented. For the numerical integration procedure, the two step explicit scheme originally presented by the authors' group was effectively used. Using the numerical computation based on the imaginary river basin and estimated hydrograph, it is seen that the water elevation can be controlled by the discharge of the dam gate to obtain almost the flat water surface. It is detected out that the flow rate of the dam gate should discharge in advance before the peak value of the flood arrives to control the wave propagation caused by the sudden close of the dam gate. This paper presents the strategy how to operate the dam gate knowing the flood configuration beforehand.

1. Introduction

It is necessary to construct a large dam to protect the human property from a flood caused by heavy rain fall on the mountains. Normally, a reservoir is set up by the dam. The flood propagates through the reservoir from upstream to downstream. To protect the downstream area, the gate equipped to the dam will be closed. The bore would be generated sometimes in case that the capacity of the reservoir is not satisfactory enough if the dam gate would have been shut suddenly. There

are several practical examples that the human property at the upstream area was destroyed by the reflected bore which seems to be caused by the dam gate operation. Thus, it is strictly necessary and practically important that the dam gate should be controlled to secure the operation that the water elevation of the reservoir would be as small as possible. Is it possible to obtain almost the flat water elevation of the reservoir during the flood by way of controlling the dam gate? The answer in this paper is affirmative.

The flood propagation through the reservoir can be expressed by the shallow water equation. One dimensional linear equation with the hydrograph as the upstream boundary condition is used. This is because the present paper aims mainly at presenting the numerical controlled method. It is simple to extend the present method to the two dimensional case. The optimal control system can be established introducing the water elevation of reservoir as the state function and the discharge of the dam gate as the control function. The quadratic functional of the water elevation and the control discharge is chosen as the performance function. Because the hydrograph of the flood is given at the upstream of the reservoir as the time function over the interval to be analyzed, the problem is resulted to the so called quadratic tracking control problem. Conventionally, the shallow water equation is described by the finite difference method or method of characteristics^{[1]-[5]}. The

discretization of the shallow water equation is carried out by the finite element method^{[6], [7]} in this paper. For the computation of the optimal control, the conjugate gradient method is effectively employed^{[8]-[10]}. The Lagrangian function is introduced to express the constraints of the state equation. To solve the time dependent equation for the Lagrange function, the backward integration should be introduced. To do this, a two step scheme has been originated similar to the forward two step scheme which was presented by the authors' group in the previous paper^{[6], [7]}. To determine the amplitude of the direction vector, the line search method is used. To show the adaptability of the control method presented in this paper, several numerical examples are carried out. Comparing with the results obtained by the dynamic programming technique, it is found that the present method is more suitable for the practical computation because the computer core storage in the present method is much smaller than that in the dynamic programming. This paper detected out a possibility that the control of the dam gate can be performed in the manner that almost the flat water elevation of the reservoir at the flood can be obtained on the condition that the hydrograph of the flood flowing to the reservoir is known in advance.

2. Basic Equations

The flood propagation behavior in a dam reservoir can be expressed by the linearized shallow water equation. Consider one dimensional channel with x coordinate and time t . Denoting mean discharge and water elevation as q and ζ , one dimensional equations of motion and continuity can be written in the following forms:

$$\frac{\partial q}{\partial t} + gh \frac{\partial \zeta}{\partial x} = 0 \quad (1)$$

$$\frac{\partial \zeta}{\partial t} + \frac{\partial q}{\partial x} = 0 \quad (2)$$

where g , h are gravity acceleration

and water depth respectively.

The flood is given as the upstream boundary conditions of mean discharge:

$$q = \hat{q} \quad \text{on } S_1 \quad (3)$$

where superscripted $\hat{}$ represents a function given on the boundary. The flood control in a dam reservoir is assumed to be carried out by the discharge decided by the optimal control of the operation of the water gate equipped on the dam. Thus, it is expressed that

$$\bar{q} = q \quad \text{on } S_c \quad (4)$$

where superscripted $\bar{}$ denotes a function determined by the optimal control analysis. The initial condition are given as:

$$\begin{aligned} \zeta &= \hat{\zeta}_0 \\ q &= \hat{q}_0 \end{aligned} \quad \text{at } t=t_0 \quad (5)$$

The governing equations (1) and (2) discretized by the finite element method about a piece of one dimensional element shown in Figure 1 can be described as follows.

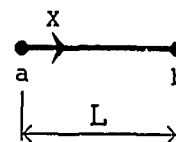


Figure 1

$$\begin{bmatrix} \frac{L}{3} & \frac{L}{6} \\ \frac{L}{6} & \frac{L}{3} \end{bmatrix} \begin{bmatrix} \dot{q}_a \\ \dot{q}_b \end{bmatrix} + \begin{bmatrix} -\frac{gh}{2} & \frac{gh}{2} \\ -\frac{gh}{2} & \frac{gh}{2} \end{bmatrix} \begin{bmatrix} \zeta_a \\ \zeta_b \end{bmatrix} = \begin{bmatrix} 0 \\ 0 \end{bmatrix} \quad (6)$$

$$\begin{bmatrix} \frac{L}{3} & \frac{L}{6} \\ \frac{L}{6} & \frac{L}{3} \end{bmatrix} \begin{bmatrix} \dot{\zeta}_a \\ \dot{\zeta}_b \end{bmatrix} + \begin{bmatrix} -\frac{1}{2} & \frac{1}{2} \\ -\frac{1}{2} & \frac{1}{2} \end{bmatrix} \begin{bmatrix} q_a \\ q_b \end{bmatrix} = \begin{bmatrix} 0 \\ 0 \end{bmatrix} \quad (7)$$

The usual superposition procedure leads to the finite element equation as:

$$[M]\{\dot{X}(t)\} + [H]\{X(t)\} + [A]\{F(t)\} + [B]\{U(t)\} = \{0\} \quad (8)$$

where

$$\{X(t)\} = \begin{Bmatrix} q(t) \\ \zeta(t) \end{Bmatrix} \quad (9)$$

in which $q(t)$ and $\zeta(t)$ mean discharge and water elevation at all nodal points of the flow domain to be analyzed. The boundary condition (3) is transformed to the term $[A]\{F(t)\}$,

$$\{F(t)\} = \begin{Bmatrix} \hat{q}(t) \\ 0 \end{Bmatrix} \quad (10)$$

where $\hat{q}(t)$ denotes the discharge of flood at the upstream point. The control term $[B]\{U(t)\}$ is derived from equation (4), and

$$\{U(t)\} = \begin{Bmatrix} \bar{q}(t) \\ 0 \end{Bmatrix} \quad (11)$$

where $\bar{q}(t)$ represents control discharge applied at the point corresponding to the dam. The initial condition can be described as follows:

$$\{X(t_0)\} = \begin{Bmatrix} \hat{q}_0(t) \\ \hat{f}_0(t) \end{Bmatrix} \quad (12)$$

3. Optimal Control Theory

The optimal control theory employed in this paper is the quadratic control theory. The problem can be converted to determine an optimal function $\{U(t)\}$ that minimizes the performance function:

$$J = \frac{1}{2} \int_{t_0}^{t_f} (\{f(t)\}^T [S] \{f(t)\} + \{U(t)\}^T [R] \{U(t)\}) dt \quad (13)$$

under the state equation:

$$\begin{aligned} \dot{\{X(t)\}} = & -[M]^{-1}[H]\{X(t)\} \\ & -[M]^{-1}[A]\{F(t)\} \\ & -[M]^{-1}[B]\{U(t)\} \end{aligned} \quad (14)$$

with the initial condition $\{X(t_0)\}$, where $[S], [R]$ are weighting matrices and t_0, t_f are starting and final times respectively.

To obtain the optimum control, the conjugate gradient method has been used. To apply the conjugate gradient method, the Hamiltonian is introduced as:

$$\begin{aligned} H = & -\frac{1}{2} (\{f(t)\}^T [S] \{f(t)\} \\ & + \{U(t)\}^T [R] \{U(t)\}) \\ & + \{P(t)\}^T (-[M]^{-1}[H]\{X(t)\} \\ & -[M]^{-1}[A]\{F(t)\} \\ & -[M]^{-1}[B]\{U(t)\}) \end{aligned} \quad (15)$$

where $\{P(t)\}$ denotes Lagrange multiplier. Euler equation and transversality condition lead to the

following equations.

$$\begin{aligned} \dot{\{P(t)\}} = & -\frac{\partial H}{\partial \{X\}} \\ = & ([M]^{-1}[H])^T \{P(t)\} + [K]\{X(t)\} \end{aligned} \quad (16)$$

$$\{P(t_f)\} = \{0\} \quad (17)$$

The gradient of the performance function $\{J_u(t)\}$ is given as:

$$\begin{aligned} \{J_u(t)\} = & -\frac{\partial H}{\partial \{U\}} \\ = & [R]\{U(t)\} + ([M]^{-1}[B])^T \{P(t)\} \end{aligned} \quad (18)$$

The gradient of the performance function is used to determine that the convergence is obtained. If the gradient comes to almost zero, the optimal control $\{U(t)\}$ can be obtained.

To obtain the optimal control solution, differential equation (14) with (12) and equation (16) with (17) must be solved. Moreover, equation (16) must be solved from t_f to t_0 because the initial condition (17) is given at the final time t_f . To solve these equations, the time marching numerical integration scheme is introduced. The total time interval to be analyzed is divided into short time interval Δt by a plenty of time points n . For equation (14), the forward two step explicit method can be applied as follows^{[6], [7]}:

For the first step:

$$\begin{aligned} \{X(t)^{n+1/2}\} = & [\bar{M}]^{-1}[\bar{M}]\{X(t)^n\} \\ & - \frac{\Delta t}{2} [\bar{M}]^{-1}[H]\{X(t)^n\} \end{aligned} \quad (19)$$

and for the second step:

$$\begin{aligned} \{X(t)^{n+1}\} = & [\bar{M}]^{-1}[\bar{M}]\{X(t)^n\} \\ & - \Delta t [\bar{M}]^{-1}[H]\{X(t)^{n+1/2}\} \end{aligned} \quad (20)$$

starting from the initial condition equation (12). For equation (16), the backward two step explicit method is used:

For the first step:

$$\begin{aligned} \{P(t)^{n+1/2}\} = & ([\bar{M}]^{-1}[\bar{M}])^T \{P(t)^n\} \\ & + \frac{\Delta t}{2} (([\bar{M}]^{-1}[H])^T \{P(t)^n\} \\ & + [K]\{X(t)^n\}) \end{aligned} \quad (21)$$

and for the second step:

$$\{P(t)^{n+1}\} = ([\tilde{M}]^{-1}[\tilde{M}])^T \{P(t)^n\} + \Delta t ([\tilde{M}]^{-1}[H])^T \{P(t)^{n+1/2}\} + [K]\{X(t)^{n+1/2}\} \quad (22)$$

starting from the initial condition equation (17). In equations (19)-(22), the lumped coefficient matrix $[\tilde{M}]$ is introduced to obtain the full explicit scheme. The mixed coefficient matrix $[\tilde{M}]$ is also used as:

$$[\tilde{M}] = e[\bar{M}] + (1-e)[M] \quad (23)$$

where e is referred to as the lumping parameter.

4. Computational Algorithm

The conjugate gradient method is successfully applied for the computational algorithm. To express the procedure of equations (19) and (20) with equation (12), the abbreviated form is introduced as:

$$\{X_i\} = \{X(t; U_i(t))\} \quad (24)$$

where subscripted i means the function is the value in the i th iteration cycle and $U_i(t)$ means the optimal control function assumed at the i th iteration. Thus, equation (24) represents to solve equation (14) with (12) by the procedure of equations (19) and (20) assuming the control function as $U_i(t)$. Similarly, the abbreviated form:

$$\{P_i\} = \{P(t; U_i(t))\} \quad (25)$$

is introduced to express the procedure to solve equations (16) with (17) by equations (21) and (22) assuming the control function as $U_i(t)$. Using those notations, the computational algorithm can be described as follows.

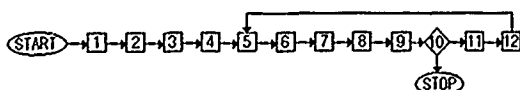


Figure 2

- 1) Assume initial control function $U_0(t)$, $t \in [t_0, t_f]$
- 2) Solve $\{X_0(t)\} = \{X(t; U_0(t))\}$
- 3) Solve $\{P_0(t)\} = \{P(t; U_0(t))\}$
- 4) Compute $\{S_0(t)\} = -\{J_{U_0(t)}\} = -([R]\{U_0(t)\} + ([M]^{-1}[B])^T \{P_0(t)\})$
- 5) Determine amplitude α_1 by minimizing $J[U_1(t) + \alpha_1 S_1(t)]$.
- 6) Compute $\{U_{1+1}(t)\} = \{U_1(t)\} + \alpha_1 \{S_1(t)\}$
- 7) Solve $\{X_{1+1}(t)\} = \{X(t; U_{1+1}(t))\}$
- 8) Solve $\{P_{1+1}(t)\} = \{P(t; U_{1+1}(t))\}$
- 9) Compute $\{J_{U_{1+1}}(t)\} = [R]\{U_{1+1}(t)\} + ([M]^{-1}[B])^T \{P_{1+1}(t)\}$
- 10) If $J_{U_{1+1}}(t) < \epsilon$ then stop else $i = i + 1$
- 11) Compute
$$\beta_1 = \frac{\{J_{U_1}(t)\}^T \{J_{U_{1+1}}(t)\}}{\{J_{U_{1-1}}(t)\}^T \{J_{U_{1-1}}(t)\}} \quad (26)$$
- 12) Compute $\{S_1(t)\} = -\{J_{U_1}(t)\} + \beta_1 \{S_{1-1}(t)\}$

Go to 5)

The parameter ϵ is a small number which expresses the convergence allowance. The flow chart of the computation is shown in Figure 2.

5. Line Search Method

The amplitude α can be determined by minimizing $J[U_1(t) + \alpha_1 S_1(t)]$ where present position U and the search direction S are both given. Determine the amplitude α that minimizes $J(U)$ by means of $U + \alpha S$ on a quadratic line. Put $g(\alpha) = J(U + \alpha S)$, then it is converted to the problem of searching the minimum point of function $g(\alpha)$. This algorithm is called as the line search algorithm.

Three points $U_{(1)}$, $U_{(2)}$, $U_{(3)}$ in Figure 3 are called as the U-shape three points where $U_{(1)} < U_{(2)} < U_{(3)}$, $J(U_{(1)}) > J(U_{(2)}) < J(U_{(3)})$. If the U-shape three points are found, the minimum point of $J(U)$ can get in between section $[U_{(1)}, U_{(3)}]$.

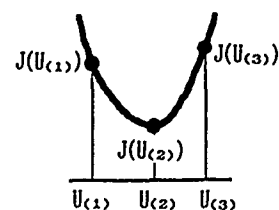


Figure 3

The value $J(U_{(0)})$ is computed by the initial point $U_{(0)}$. The value $J(U_{(1)})$ is computed by

$U_{(1)} = U_{(0)} + \alpha S$. If $J(U_{(0)}) > J(U_{(1)})$, the direction is right. And the amplitude α doubles the step size, then $J(U_{(2)})$ is computed by $U_{(2)} = U_{(1)} + 2\alpha S$. If $J(U_{(1)}) > J(U_{(2)})$, the amplitude α doubles the step size again and determine $U_{(3)}$, then continue the same procedure. If $J(U_{(1)}) < J(U_{(2)})$, the U-shape three points are found. If the U-shape three points are found, $U_{(n+1)}$ divides the section $[U_{(n+2)}, U_{(n)}]$ into 2:1 (or 1:2). $J(U)$ is solved by the middle point between $U_{(n+2)}$ and $U_{(n+1)}$. Comparing both sides, the even intervals of U-shape three points are obtained. If the iteration of the three points approach is complete, $J(U)$ can be obtained by the parabolic interpolation of the three points. The minimum point of the parabola through three points is given as follows;

$$U_{(4)} = \frac{1}{2} \frac{(U_{(1)}^2 - U_{(2)}^2)J(U_{(3)}) + (U_{(2)}^2 - U_{(3)}^2)J(U_{(1)}) + (U_{(3)}^2 - U_{(1)}^2)J(U_{(2)})}{(U_{(1)} - U_{(2)})J(U_{(3)}) + (U_{(2)} - U_{(3)})J(U_{(1)}) + (U_{(3)} - U_{(1)})J(U_{(2)})} \quad (27)$$

Giving this point as the initial point, next iteration can be carried out. The amplitude α gives $\alpha/10$. And the U-shape three points are found again. If the amplitude α is obtained as small enough as less than preassigned given value, the amplitude α is obtained.

6. Test Examples

To show the validity and adaptability of the control method presented in this paper, two test examples are carried out. One of them is the control of solitary flood propagating through a simple reservoir, the other is the comparison with the results obtained by the dynamic programming. For the computational model, the simple one dimensional reservoir as shown in Figures 4 and 8 are used. The boundary S_1 is called as the inflow point, at which the discharge of the flood flow is specified. On the boundary S_0 which is referred to as the control point, the discharge of the flow is controlled. At the middle of the reservoir, the observation

point is set for reference. The total length and subdivisions are represented in each computational example. For the weighting matrix, S was chosen as unit matrix because the same weight was given to the water elevation of all finite elements in reservoir.

1) Test example No.1

For the computation, the reservoir shown in Figure 4 is used. The total length $L=40m$ and water depth $10m$ in the model is used for the test example No.1. Numbers of total nodal points and elements are 151 and 150 respectively. Total time intervals 12sec. was divided into short time intervals 0.004sec. For the weighting coefficient $R=1.0 \times 10^{-4}$ was used. For the lumping parameter $e=0.9$ is employed.

Specify the flow discharge at the inflow point as the time dependent function

$$q = \hat{q}(t) \quad \text{on } S_1$$

where $\hat{q}(t)$ is shown in Figure 5. The optimal control discharge can be computed at the control point as

$$q = \bar{q}(t) \quad \text{on } S_0$$

where $\bar{q}(t)$ is shown in Figure 6.

For information, the water elevations at each point are also represented in Figure 7. Looking at these figures, it is clearly understood that the inflow and the control flow are completely coincident except the phase lag. This fact shows that the control discharge can be obtained completely in the same form as that of inflow. Namely, the optimal control can be obtained by leaving the gate of dam full open. This simple result corresponds to the fact that there is no need to control the gate in case of this type of simple flood propagation. The fact that the computation was successful for this simple phenomenon suggests that this computational method is also

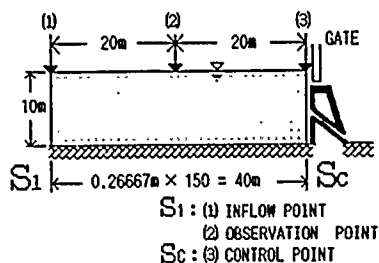


Figure 4 Reservoir model-1

(1) INFLOW POINT (40M)

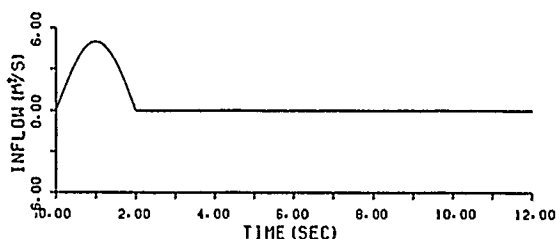


Figure 5 Hydrograph of inflow(model-1)

(3) CONTROL POINT (0M)

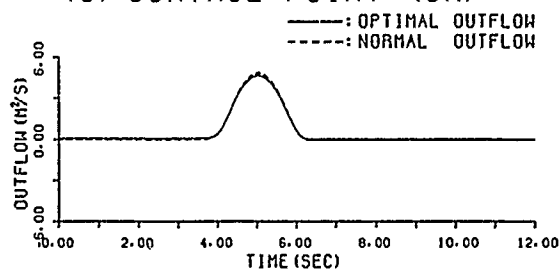
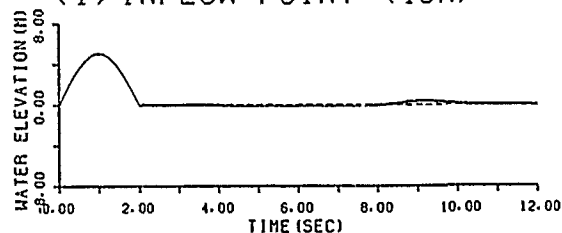
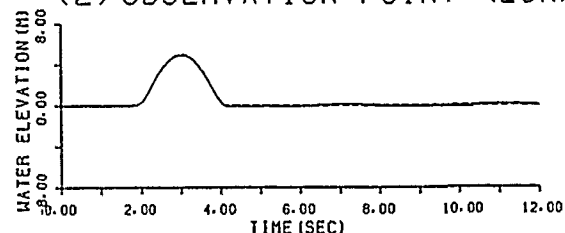


Figure 6 Control discharge at the control point(model-1)

(1) INFLOW POINT (40M)



(2) OBSERVATION POINT (20M)



(3) CONTROL POINT (0M)

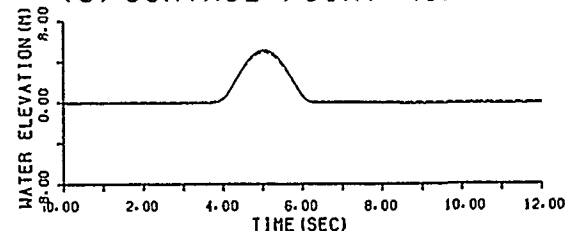


Figure 7 Water elevations at each point (model-1)

available for the more complicated control problem.

2) Test example No.2

The control results computed by the conjugate gradient method is compared with the ones by the dynamic programming which was originally used for the structural control by one of the authors^[12]. For the computation, the reservoir shown in Figure 8 is employed. Total length L is 3km and water depth is 60m. Total numbers of nodal points and elements are 31 and 30 respectively. Total time 10min. is

divided into short time interval 1.0sec. For the lumping parameter $e=0.9$ is used.

The computation has been carried out specifying the discharge at the inflow point as a function shown in Figure 9. The resulted control obtained at the control point is represented in Figure 10. The dotted line shows the outflow at the control point without control. The solid line is the optimal control discharge computed. The computed water elevations at inflow, observation and control points are illustrated in Figure 11. The water elevation at

every point is computed smaller than that without control, which is expressed by the dotted line. The same problem has been computed by the method of the dynamic programming. The resulted control and water elevations are represented in Figures 12 and 13. All results are completely coincident with the results obtained by the conjugate gradient method.

In case of the method of dynamic programming, 2.5 times as long intervals as that of the conjugate gradient method can be employed. However, all of the intermediate values of the computation must be stored in this type of tracking problems. Thus, a large amount of core storage capacity must be required. Considering this, the method of the dynamic programming is not suitable for the large scale problem.

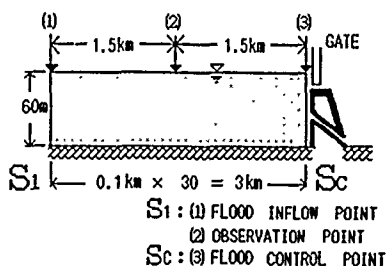


Figure 8 Reservoir model-2

(1) FLOOD INFLOW POINT (3KM)

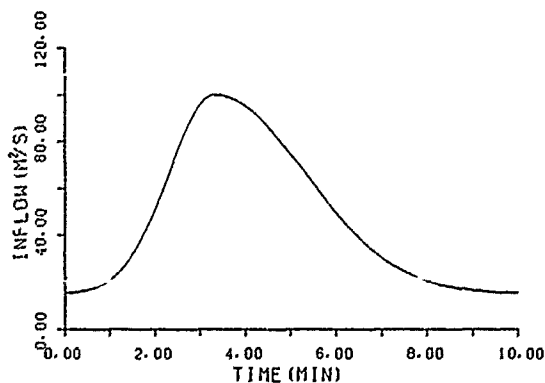


Figure 9 Hydrograph of inflow(model-2)

(3) FLOOD CONTROL POINT (0KM)

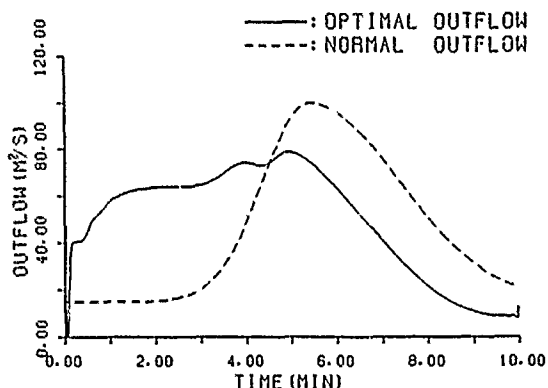
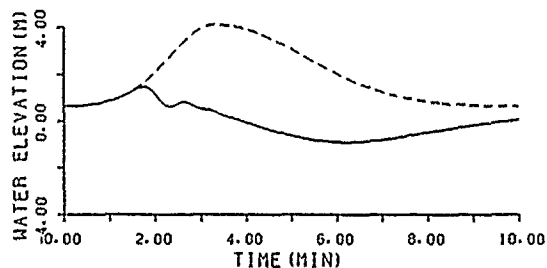
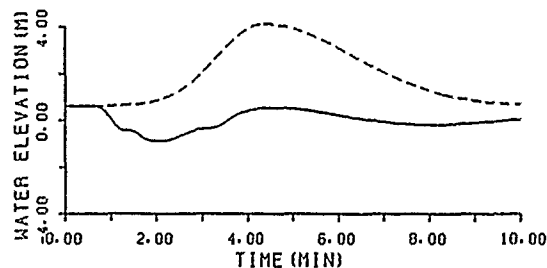


Figure 10 Control discharge by conjugate gradient method(model-2-1)

(1) FLOOD INFLOW POINT (3KM)



(2) OBSERVATION POINT (1.5KM)



(3) FLOOD CONTROL POINT (0KM)

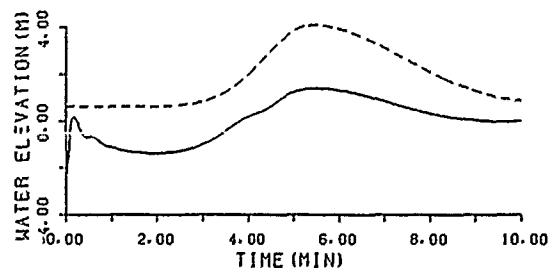


Figure 11 Water elevations at each reference point(model-2-1)

(3) FLOOD CONTROL POINT (0KM)

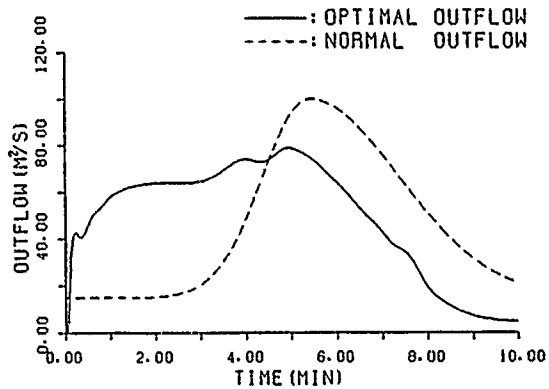
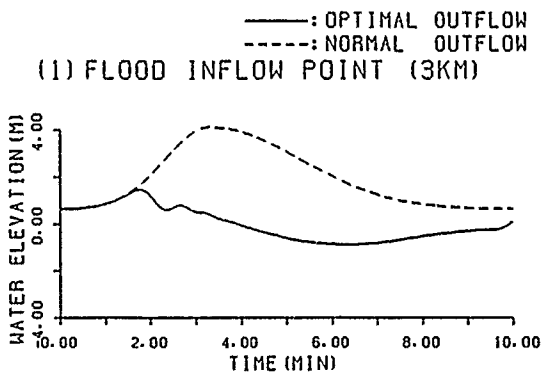
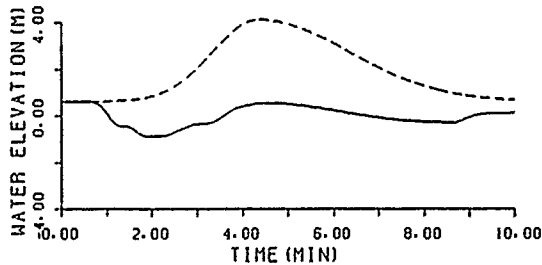


Figure 12 Control discharge by the dynamic programming(model-2-<2>)

(1) FLOOD INFLOW POINT (3KM)



(2) OBSERVATION POINT (1.5KM)



(3) FLOOD CONTROL POINT (0KM)

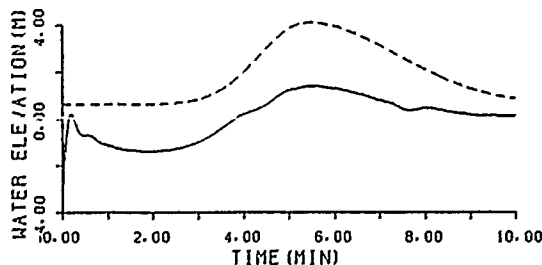


Figure 13 Water elevations at each reference point(model-2-<2>)

7. Flood Control

The flood control problem by a dam based on the imaginal river basin and estimated hydrograph using the observed data is carried out as a practical example to show the practicability of the present method. The river basin used is shown in Figure 14 by water depth and width. The total length of the model is 30km long. The maximum width of the reservoir is 1350m and the upstream river is 50m wide. On the most upstream side of the model the flood inflow discharge is specified and it is referred to as the flood inflow discharge point. The flood control point is set on the most downstream side where the dam is assumed to be equipped. The water elevation computed is expressed on the reference point at the center of the model which is called as the observation point.

Total numbers of nodal points and elements are 61 and 60 respectively. Total time interval used is 48 hours, which is divided into short time intervals 13.824sec. The steady state computation has been carried out to get the steady state water elevation $\{\zeta_s(t)\}$. In the practical computation, it is more suitable to modify the performance function as:

$$J = \frac{1}{2} \int_{t_0}^{t_f} \{ (\zeta(t) - \zeta_s(t))^T [S] (\zeta(t) - \zeta_s(t)) + [U(t)]^T [R] [U(t)] \} dt \quad (28)$$

where the weighting matrix $[S]$ is set unit matrix and the weighting coefficient for $[R]$ matrix is $R = 1.0 \times 10^{-7}$. The lumping parameter is chosen as $e = 0.9$.

Specifying the flow discharge at the inflow point as the time dependent function:

$$q = \hat{q}(t) \quad \text{on } S_1$$

where $\hat{q}(t)$ is shown in Figure 15, the optimum control discharge at the control point can be computed as

$$q = \bar{q}(t) \quad \text{on } S_c$$

where $\bar{q}(t)$ is expressed in Figure 16.

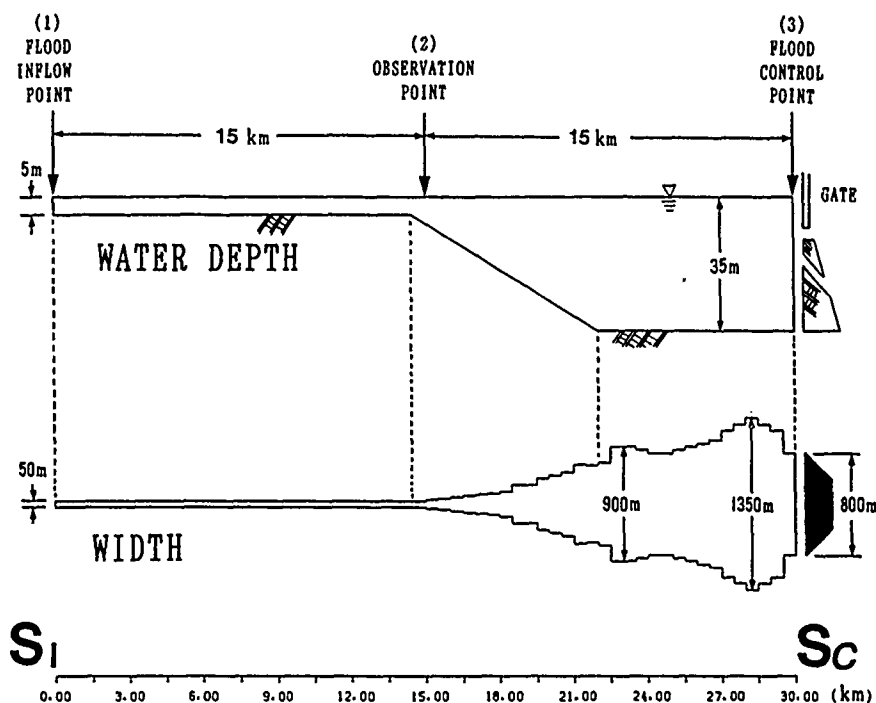


Figure 14 Reservoir model-3

(1) FLOOD INFLOW POINT (30KM)

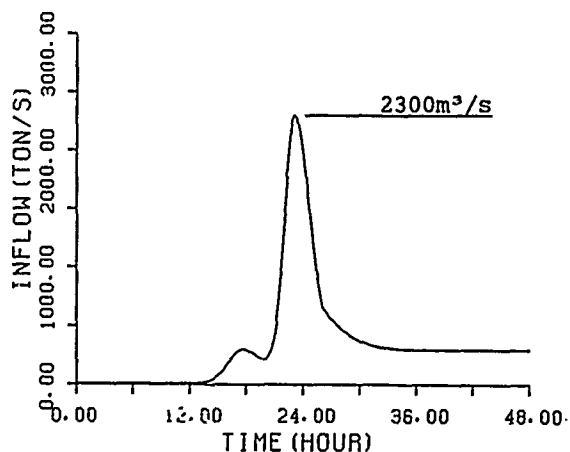


Figure 15 Hydrograph of inflow (model-3)

In this figure, the outflow discharge at the control point without control is also expressed by the dotted line. An outlook of the uncontrolled discharge is almost coincident with that of the inflow discharge shown in Figure 15 until the maximum peak value arrives. The duration to arrive the peak value of the outflow corresponds to that of inflow.

However, the uncertain oscillation of the discharge can be found after the peak value of the flood, which is caused by the reflection of the wave by the dam. By the optimum control of the discharge, the maximum peak value can be reduced. Moreover, the oscillation of the discharge after the peak value can be eliminated. It is important to note that the control of discharge must start before the peak value of the flood will arrive to the dam.

The computed water elevations at the inflow, observation and control points are illustrated in Figure 17. The dotted lines show the computed water elevations without control. At the inflow point, which represents the upstream area, oscillation of the water elevation can be found in case of the flow without control. It is detected out that there is a possibility that the oscillation of the water elevation can cause severe damages to the human properties around upstream area. For the water elevation controlled at the dam, the upstream oscillation has completely been eliminated. The variation of the water elevation controlled is smaller than that of uncontrolled. The water

(3) FLOOD CONTROL POINT (0KM)

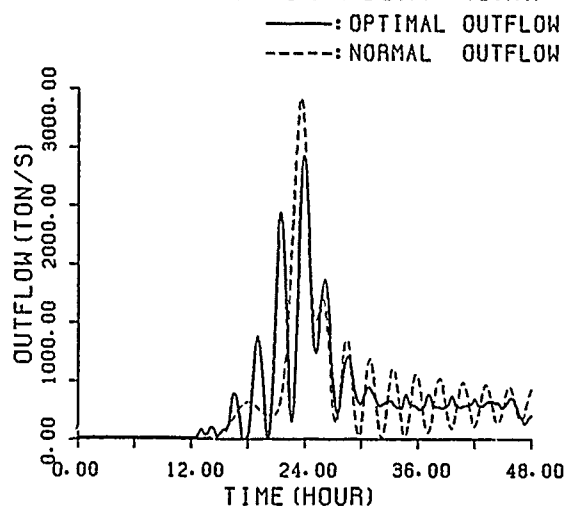


Figure 16 Control discharge
at the control point
(model-3-<1>)

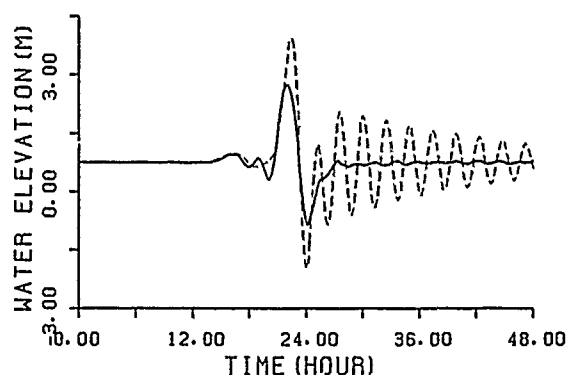
elevations computed at every reference point show almost flat water elevation excluding the duration after the peak value of the flood.

In the practical problem, it is usually seen that the maximum ability of the flow rate of the dam gate is limited. In Figures 18 and 19, control example of which maximum flow rate is limited as $1000\text{m}^3/\text{s}$ is illustrated. In Figures 20 and 21, control example of which maximum flow rate is limited as $1500\text{m}^3/\text{s}$ is illustrated. Figures 18 and 20 show the control discharge at the control point. Figures 19 and 21 are the computed water elevations at each reference point compared with the water elevations without control. In these examples, it is also detected out that the water elevations can be controlled by the discharge of the dam gate. It is also seen that the secondary oscillation of the water elevation at the upstream has been eliminated.

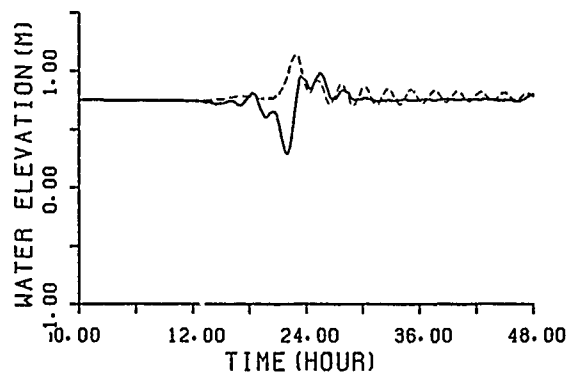
8. Conclusion

This paper has presented the optimum control method for the wave propagation caused by the flood

(1) FLOOD INFLOW POINT (30KM)



(2) OBSERVATION POINT (15KM)



(3) FLOOD CONTROL POINT (0KM)

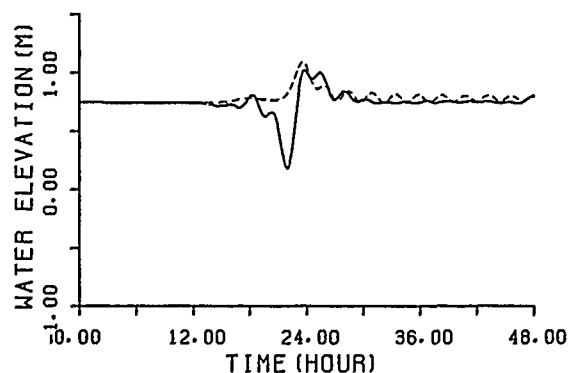


Figure 17 Water elevations
at each reference point
(model-3-<1>)

(3) FLOOD CONTROL POINT (OKM)

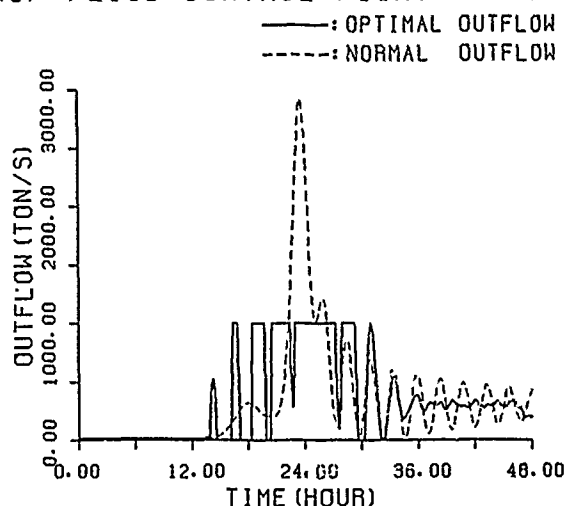
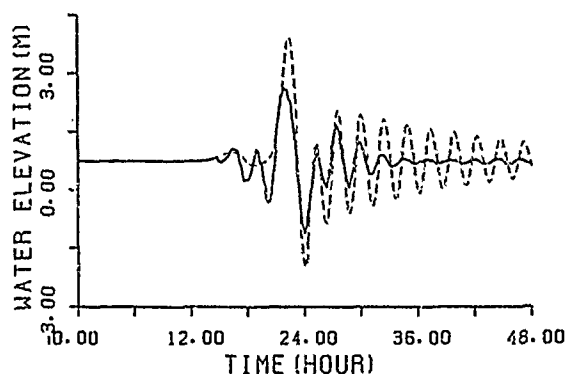


Figure 18 Control discharge
at the control point
(model-3-<2>)
[outflow $\leq 1000 \text{ m}^3/\text{s}$]

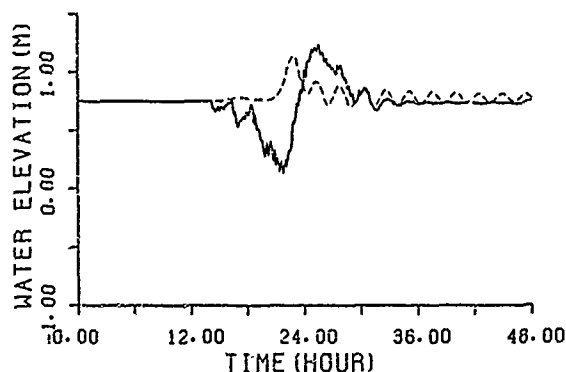
through the reservoir set up by a dam. It is detected out that the control of the dam can be effectively performed by the conjugate gradient method combined with the finite element method. Comparing with the dynamic programming, the computer core storage of this method can be extraordinary reduced. For the forward and backward numerical integrations in time, the two step scheme can be effectively introduced. For the determination of the magnitude of the gradient vector, the line search method is shown to be one of the most efficient method of the analysis.

Using the numerical computation based on the practical basin and estimated hydrograph, it has been cleared that the water elevation can be controlled by the discharge of the dam to reduce the peak value and to eliminate the secondary wave propagation toward the upstream of the dam reservoir. To control the wave propagation generated by the reflection of the sudden close of dam gate, it is necessary to discharge through the dam gate in advance before the peak value of the flood arrives. The strategy how to open and shut the dam gate can be determined by the present method knowing the flood configuration beforehand.

(1) FLOOD INFLOW POINT (30KM)



(2) OBSERVATION POINT (15KM)



(3) FLOOD CONTROL POINT (OKM)



Figure 19 Water elevations
at each reference point
(model-3-<2>)

(3) FLOOD CONTROL POINT (OKM)

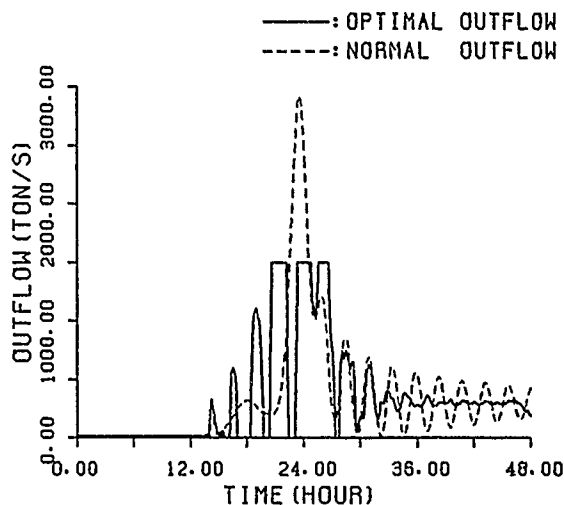
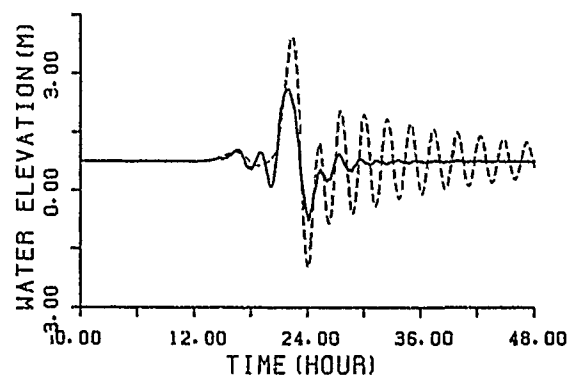


Figure 20 Control discharge
at the control point
(model-3-<3>)
[outflow $\leq 1500\text{m}^3/\text{s}$]

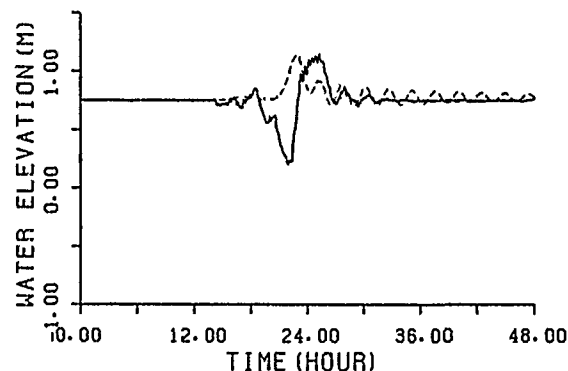
References

- [1] D.A.Hughes and H.C.Murrell: "Non-linear runoff routing-A comparison of solution methods", Jour.Hydro., Vol.85, pp339-347, 1986
- [2] B.Hunt: "A symptotic solution for dam break on sloping channel", Proc.ASCE, Vol.109, No.HY12, pp1698-1706, 1983
- [3] V.M.Ponce and A.J.Tsivoglou: "Modeling gradual dam breaches", Proc.ASCE, Vol.107, No.HY7, pp829-838, 1981
- [4] A.O.Akan and B.C.Yen: "Diffusion-wave flood routing in channel networks", Proc.ASCE, Vol.107, No.HY6, pp719-732, 1981
- [5] V.M.Ponce: "Linear reservoirs and numerical diffusion", Proc.ASCE, Vol.106, No.HY5, pp691-699, 1980
- [6] M.Kawahara and T.Umetsu: "Finite element method for moving boundary problems in river flow", Int.J.Num.Meth.Fluid, Vol.6, pp365-386, 1986
- [7] M.Kawahara, H.Hirano, K.Tsubota and K.Inagaki: "Selective lumping finite element method for shallow water flow", Int.J.Num.Meth.Fluid, Vol.2, pp89-112, 1982
- [8] H.Kanoh: "Theory and Computational Methods in Optimization", Corona Publishing Co., 1987
- [9] A.E.Bryson and Y.C.Ho: "Applied optimal control", Hemisphere Publishing Corporation, 1975
- [10] R.F.Stengel: "Stochastic optimal control", John Wiley & Sons, 1986
- [11] M.Kawahara and T.kawasaki: "A flood control of dam reservoir by conjugate gradient method and finite element method", Proc.7th Int.Conf FEM in Flow Problems, pp629-634, 1989
- [12] M.Kawahara and K.Fukazawa: "Optimal control of structures subjected to earthquake loads using dynamic programming", J. Structural Engineering, Vol.34A, J.S.C.E. 1988

(1) FLOOD INFLOW POINT (30KM)



(2) OBSERVATION POINT (15KM)



(3) FLOOD CONTROL POINT (OKM)

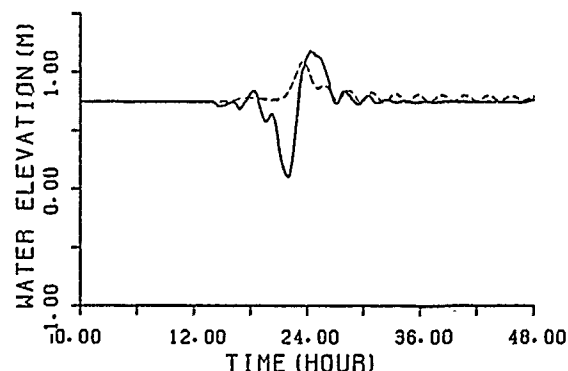


Figure 21 Water elevations
at each reference point
(model-3-<3>)

General Sessions

Numerical Simulation of Three-Dimensional Viscous Flow around a Submersible Body

C-I Yang

David Taylor Research Center
Bethesda, USA

P-M. Hartwich and P. Sundaram
NASA Langley Research Center
Hampton, USA

Abstract

A second-order accurate, implicit, high resolution upwind scheme has been used to solve the three-dimensional incompressible Navier-Stokes equations in general curvilinear coordinates for the steady-state computation of the flow field around axisymmetric hull geometries at high Reynolds numbers. A hybrid algorithm with relaxation in the streamwise direction and approximate factorization in the cross-flow plane is used to reduce the temporal splitting error. Three axisymmetric bodies with different stern shapes have been chosen for the present investigation to highlight the boundary layer development and to pinpoint flow separation in the stern regions of the hull geometries. Three-dimensional viscous grids of C-O topology have been generated around each body using a transfinite interpolation technique. Turbulence is simulated using algebraic eddy viscosity model of Baldwin-Lomax. The computed results are compared with the available experimental data for on-body pressure distribution and radial and axial velocity profiles in the afterbody boundary layers with and without propeller in operation. The computed results show close agreement with the measurements in most cases.

I. Introduction

The flow in the stern region of a submersible is characterized by the presence of a thick and possibly separated turbulent boundary layer. There is an increase in the stern pressure drag and skin friction drag, called thrust deduction, due to the upstream suction produced by the propeller when operating. Accurate numerical prediction of the flow in the stern region of the hull both with and without the propeller operating is important to evaluate the afterbody thrust deduction, thus limiting the expensive resistance and self propulsion model experiments in a towing tank. Although several numerical algorithms have been so far developed for computing the two and three dimensional incompressible Navier-Stokes equations, most of them are prohibitively expensive for very high Reynolds number flows typical in marine hydrodynamics.

Several panel methods such as VSAERO (1) are used in aircraft design and analysis practices. However, their true application in marine flows, particularly for computing the flow field in the stern region, is limited because of the presence of fairly thick boundary layers in the stern

region. A viscous-inviscid interaction procedure might be once again inadequate because of the possible presence of flow separation in this region. Hence, an accurate computational method for this problem should attempt to solve the incompressible Navier-Stokes equations.

Aziz and Hellums (2) proposed a vector potential vorticity formulation to solve the three-dimensional incompressible Navier-Stokes equations. Because of its large storage requirements and the necessity to solve three Poisson equations at each time level, the method is not very popular. The direct extension of time-dependent methods, both explicit and implicit, developed for the compressible Navier-Stokes equations to incompressible flows is not possible because of the 'stiffness' of the physical problem associated with low speed viscous flow. To circumvent this problem, Chorin (3) proposed the use of artificial compressibility when solving the equation of continuity, thus introducing an unsteady term to make the system hyperbolic as in the case of compressible flows.

In this paper, we compute complex flow fields around various axisymmetric bodies by obtaining numerical solutions of the incompressible Navier-Stokes equations in primitive variable formulation. A hybrid second-order accurate implicit high resolution upwind scheme is used to solve the system of conservation laws in general curvilinear coordinates. Three axisymmetric bodies with different stern shapes to highlight specific flow details in that region have been chosen for the present study, primarily because of the availability of well documented experimental results for these bodies (4,5,6,7). Body fitted three-dimensional grid systems of C-O topology have been generated around these bodies using an algebraic grid generator based on transfinite interpolation procedure. The computed on-body pressures together with axial and radial velocity profiles are compared with the experimental data. In addition, the flow around the stern region of one of the bodies with a propeller in operation is computed. The propeller is simulated by imbedding body forces in a disk located at propeller plane as suggested by Stern et al(8). Finally, in order to illustrate the ability of this scheme to simulate a separated flow, the results of a low speed vortical flow about a 3.5 caliber tangent-ogive cylinder at an angle of attack are presented.

II. Governing Equations

Using Chorin's (3) artificial compressibility formulation, the incompressible Navier-Stokes equation are written in conservation law form for three-dimensional flow as

$$\mathbf{Q}_t + (\mathbf{E}^* - \mathbf{E}_v^*)_x + (\mathbf{F}^* - \mathbf{F}_v^*)_y + (\mathbf{G}^* - \mathbf{G}_v^*)_z = 0 \quad (1)$$

In Equation (1) the dependent variable vector \mathbf{Q} is defined as

$$\mathbf{Q} = (p, u, v, w)^T$$

and the inviscid flux vectors $\mathbf{E}^*, \mathbf{F}^*, \mathbf{G}^*$ and the viscous shear flux vectors $\mathbf{E}_v^*, \mathbf{F}_v^*, \mathbf{G}_v^*$ are given by

$$\begin{aligned} \mathbf{E}^* &= (\beta u, u^2 + p, uv, uw)^T \\ \mathbf{F}^* &= (\beta v, uv, v^2 + p, vw)^T \\ \mathbf{G}^* &= (\beta w, uw, vw, w^2 + p)^T \\ \mathbf{E}_v^* &= Re^{-1}(0, \tau_{xx}, \tau_{xy}, \tau_{xz})^T \\ \mathbf{F}_v^* &= Re^{-1}(0, \tau_{yx}, \tau_{yy}, \tau_{yz})^T \\ \mathbf{G}_v^* &= Re^{-1}(0, \tau_{zx}, \tau_{zy}, \tau_{zz})^T \end{aligned} \quad (2)$$

The coordinates x, y, z are scaled with an appropriate characteristic length scale L . In Eq. (2), the Cartesian velocity components u, v, w are nondimensionalized with respect to the free stream velocity V_∞ , while the normalized pressure is defined as $p = (P - P_\infty)/\rho V_\infty^2$. The kinematic viscosity ν is assumed to be constant, and the Reynolds number is defined as $Re = \frac{V_\infty L}{\nu}$. The artificial compressibility parameter β monitors the error associated with the addition of the unsteady pressure term $\frac{\partial p}{\partial t}$ in the continuity equation which is needed for coupling the mass and momentum equations in order to make the system hyperbolic.

For large values of β or when the solution of Eq. (1) has approached asymptotically a steady state, the continuity equation is accurately satisfied. However, the choice of β is also dictated by the important constraint of the stiffness of the partial differential equation as discussed in Ref. 9. Hence, $\beta = 1$ has been chosen uniformly in the present computations.

To develop the equations in a general curvilinear coordinate system, a coordinate transformation of the form

$$\zeta = \zeta(x, y, z), \quad \xi = \xi(x, y, z) \quad \text{and} \quad \eta = \eta(x, y, z)$$

has been considered. Eq. (1) is rewritten in strong conservation law form as

$$(\mathbf{Q}/J)_t + (\mathbf{E} - \mathbf{E}_v)_\zeta + (\mathbf{F} - \mathbf{F}_v)_\xi + (\mathbf{G} - \mathbf{G}_v)_\eta = 0 \quad (3)$$

with

$$(\mathbf{E}, \mathbf{F}, \mathbf{G})^T = [\mathbf{T}] (\mathbf{E}^*, \mathbf{F}^*, \mathbf{G}^*)^T$$

and

$$(\mathbf{E}_v, \mathbf{F}_v, \mathbf{G}_v)^T = [\mathbf{T}] (\mathbf{E}_v^*, \mathbf{F}_v^*, \mathbf{G}_v^*)^T$$

where

$$[\mathbf{T}] = \begin{bmatrix} \zeta_x & \zeta_y & \zeta_z \\ \xi_x & \xi_y & \xi_z \\ \eta_x & \eta_y & \eta_z \end{bmatrix}$$

and the Jacobian of the coordinate transformation is given by

$$J^{-1} = \det \begin{bmatrix} x_\zeta & y_\zeta & z_\zeta \\ x_\xi & y_\xi & z_\xi \\ x_\eta & y_\eta & z_\eta \end{bmatrix}$$

The Cartesian derivatives of the shear fluxes are obtained by expanding them using chain rule expansions in the ζ, ξ, η directions.

The Jacobians of the inviscid fluxes \mathbf{E}, \mathbf{F} and \mathbf{G} are needed for the flux-difference splitting and for the implicit algorithm. The Jacobian matrices in the different coordinate directions are obtained as the linear combination of the Cartesian Jacobian matrices as

$$\mathbf{D} = a_1 \mathbf{A}^* + a_2 \mathbf{B}^* + a_3 \mathbf{C}^*$$

where $\mathbf{D} = \mathbf{A}, \mathbf{B}$, or \mathbf{C} with $\mathbf{A} = \frac{\partial \mathbf{E}}{\partial \mathbf{Q}}, \mathbf{B} = \frac{\partial \mathbf{F}}{\partial \mathbf{Q}}, \mathbf{C} = \frac{\partial \mathbf{G}}{\partial \mathbf{Q}}$, and (a_1, a_2, a_3) are the row vectors of the \mathbf{T} matrix. For the Jacobian matrix \mathbf{A} , $a_1 = \zeta_x/J$, $a_2 = \zeta_y/J$, $a_3 = \zeta_z/J$, and so on. The Jacobians in the Cartesian coordinates themselves are

$$\begin{aligned} \mathbf{A}^* &= \frac{\partial \mathbf{E}^*}{\partial \mathbf{Q}} = \begin{bmatrix} 0 & \beta & 0 & 0 \\ 1 & 2u & 0 & 0 \\ 0 & v & u & 0 \\ 0 & w & 0 & u \end{bmatrix} \\ \mathbf{B}^* &= \frac{\partial \mathbf{F}^*}{\partial \mathbf{Q}} = \begin{bmatrix} 0 & 0 & \beta & u \\ 0 & v & u & 0 \\ 1 & 0 & 2v & 0 \\ 0 & 0 & w & u \end{bmatrix} \\ \mathbf{C}^* &= \frac{\partial \mathbf{G}^*}{\partial \mathbf{Q}} = \begin{bmatrix} 0 & 0 & 0 & \beta \\ 0 & w & 0 & u \\ 0 & 0 & w & v \\ 1 & 0 & 0 & 2w \end{bmatrix} \end{aligned}$$

The eigenvalues of \mathbf{D} are

$$\Lambda = \text{diag}(\lambda_1, \lambda_2, \lambda_3, \lambda_4) = \text{diag}(U - S, U + S, U, U)$$

where U is the contravariant velocity component in the corresponding coordinate direction given by

$$U = a_1 u + a_2 v + a_3 w$$

and

$$S = [U^2 + \beta(a_1^2 + a_2^2 + a_3^2)]^{1/2} = S(u, v, w, a_1, a_2, a_3)$$

The Jacobian matrices in different directions are diagonalized using a similarity transformation $\mathbf{D} = \mathbf{R} \mathbf{\Lambda} \mathbf{R}^{-1}$ to obtain the eigenvalues of \mathbf{D} . The rows of \mathbf{R}^{-1} and the columns of \mathbf{R} are computed such that they give an orthonormal set of left and right eigenvectors. The generalized similarity matrices \mathbf{R} and \mathbf{R}^{-1} are given by (Ref. 6)

$$\mathbf{R} = \begin{bmatrix} -\beta \hat{S} & \beta \hat{S} & 0 & 0 \\ \hat{a}_1 \beta + u \hat{\lambda}_1 & \hat{a}_1 \beta + u \hat{\lambda}_2 & -\hat{a}_2 & -\hat{a}_3 \\ \hat{a}_2 \beta + v \hat{\lambda}_1 & \hat{a}_2 \beta + v \hat{\lambda}_2 & \hat{a}_1 + \hat{a}_3 & -\hat{a}_3 \\ \hat{a}_3 \beta + w \hat{\lambda}_1 & \hat{a}_3 \beta + w \hat{\lambda}_2 & -\hat{a}_2 & \hat{a}_1 + \hat{a}_2 \end{bmatrix}$$

and

$$\mathbf{R}^{-1} = \frac{1}{2\hat{S}^2} \begin{bmatrix} -\hat{\lambda}_2/\beta & \hat{a}_1 & \hat{a}_2 & \hat{a}_3 \\ -\hat{\lambda}_1/\beta & \hat{a}_1 & \hat{a}_2 & \hat{a}_3 \\ (\hat{\lambda}_2 d_1 + \hat{\lambda}_1 d_2)/\beta & -2\hat{S}^2/k - \hat{a}_1 d_5 & -2\hat{S}^2/k - \hat{a}_2 d_5 & -\hat{a}_3 d_5 \\ (\hat{\lambda}_2 d_3 + \hat{\lambda}_1 d_4)/\beta & -2\hat{S}^2/k - \hat{a}_1 d_6 & -\hat{a}_2 d_6 & -2\hat{S}^2/k - \hat{a}_3 d_6 \end{bmatrix}$$

where $k = \hat{a}_1 + \hat{a}_2 + \hat{a}_3$, $\hat{a}_1 = \frac{a_1}{\sqrt{a_1^2 + a_2^2 + a_3^2}}$ etc. and

$$d_1 = (r_{31} - r_{21})/k, \quad d_2 = (r_{32} - r_{22})/k, \quad d_3 = (r_{41} - r_{21})/k,$$

$$d_4 = (r_{42} - r_{22})/k, \quad d_5 = d_1 + d_2, \quad \text{and} \quad d_6 = d_3 + d_4$$

Quantities such as r_{ij} represent the i th row and j th column of the \mathbf{R} matrix and $\hat{S} = S(u, v, w, \hat{a}_1, \hat{a}_2, \hat{a}_3)$.

In high Reynolds number flows, it is appropriate to make use of the thin-layer approximation. The justification for such a simplification can be found in Pulliam and Steger (10). Consequently, all viscous derivatives in the η and ξ direction (along the body) are neglected. The viscous shear flux \mathbf{G}_v (normal to the body) and its Jacobian can be derived after Steger (11). That produces the coefficient matrices

$$\mathbf{G}_v = (\mathbf{Re} \cdot \mathbf{J})^{-1} \begin{bmatrix} 0 \\ \psi_1 u_\eta + \psi_2 \eta_x \\ \psi_1 v_\eta + \psi_2 \eta_y \\ \psi_1 w_\eta + \psi_2 \eta_z \end{bmatrix}$$

and

$$\mathbf{Z} = \frac{\partial \mathbf{G}_v}{\partial \mathbf{Q}} = (\mathbf{Re} \cdot \mathbf{J})^{-1} \begin{bmatrix} 0 & 0 & 0 & 0 \\ 0 & Z_{22} & Z_{32} & Z_{42} \\ 0 & Z_{32} & Z_{33} & Z_{43} \\ 0 & Z_{42} & Z_{43} & Z_{44} \end{bmatrix}.$$

with

$$\begin{aligned} \psi_1 &= \eta_x^2 + \eta_y^2 + \eta_z^2 & \psi_2 &= \frac{1}{3}(\eta_x u_\eta + \eta_y v_\eta + \eta_z w_\eta) \\ Z_{22} &= \frac{4}{3}\eta_x^2 + \eta_y^2 + \eta_z^2 & Z_{32} &= \frac{1}{3}\eta_x \eta_y \\ Z_{42} &= \frac{1}{3}\eta_x \eta_z & Z_{33} &= \eta_x^2 + \frac{4}{3}\eta_y^2 + \eta_z^2 \\ Z_{43} &= \frac{1}{3}\eta_y \eta_z & Z_{44} &= \eta_x^2 + \eta_y^2 + \frac{4}{3}\eta_z^2 \end{aligned}$$

The inviscid fluxes, the viscous shear fluxes and their Jacobians just obtained in this section are ready for discretization later.

III. Numerical Flux Differencing

It is well known that upwind schemes possess an inherent solution-adaptive dissipation that eliminates the addition and fine tuning of artificial dissipation terms for numerical stability and accuracy required in schemes based on central differencing. In the present approach the inviscid fluxes are discretized by using Roe's flux-differencing splitting concept (12) and the viscous fluxes are discretized by the central differencing technique. We shall discuss the numerical discretization scheme in one dimension and assemble them together for three-dimensions.

Discretization of the Inviscid Fluxes

Consider a system of quasi one-dimensional, hyperbolic partial differential equations

$$(\mathbf{Q}/J)_t + \mathbf{H}_\theta = 0 \quad (4)$$

where $\theta = \zeta, \xi, \text{ or } \eta$. Defining computational cells with their centroids at $l = \frac{\theta}{\Delta\theta}$ and their cell interfaces at $l \pm 1/2$, a discrete approximation to (4) is written as,

$$\left(\frac{1}{\Delta t J}\right) \Delta \mathbf{Q}^n + \Delta_l \mathbf{H} = 0 \quad (5)$$

where Δt is the time step, $\Delta \mathbf{Q}^n = \mathbf{Q}^{n+1} - \mathbf{Q}^n$ and $\Delta_l(\cdot) = [(\cdot)_{l+1/2} - (\cdot)_{l-1/2}]/\Delta\theta$. Superscript denotes the time level at which the variables are evaluated.

To construct an approximate Riemann solver for the initial value problem in Eq. (5), each variable is regarded as an averaged state in each cell so that the flux difference is preserved in each cell and Eq. (5) can be regarded as an integral rather than a differential law. According to Roe's scheme (12), the flux at interface $l \pm 1/2$ can be expressed in terms of the left and right travelling waves,

$$\mathbf{H}_{l\pm 1/2} = \mathbf{H}_l \pm (\Delta \mathbf{H}_{l\pm 1/2}^\mp) \quad (6)$$

Using (6) we can write (5) as

$$\left(\frac{1}{\Delta t J}\right) \Delta \mathbf{Q}^n + \Delta \mathbf{H}_{l+1/2}^- + \Delta \mathbf{H}_{l-1/2}^+ = 0 \quad (7)$$

Equation (7) relates the development of \mathbf{Q} at the centroid to the waves at the interfaces according to their propagation directions. Defining a mean value matrix according to Roe (12)

$$\mathbf{D}_{l+1/2} = \mathbf{D}(\mathbf{Q}_l, \mathbf{Q}_{l+1})$$

so that

$$\mathbf{D}_{l\pm 1/2} \Delta_{l\pm 1/2} \mathbf{Q} = \Delta \mathbf{H}_{l\pm 1/2},$$

Using the above we can write (7) in delta form as

$$\begin{aligned} & \left[\left(\frac{1}{\Delta t J}\right) - (\mathbf{D}_{l+1/2}^-)^n \Delta_{l+1/2} + (\mathbf{D}_{l-1/2}^+)^n \Delta_{l-1/2} \right] \Delta \mathbf{Q}^n \\ &= (\mathbf{D}_{l+1/2}^-)^n \Delta_{l+1/2} \mathbf{Q}^n - (\mathbf{D}_{l-1/2}^+)^n \Delta_{l-1/2} \mathbf{Q}^n \end{aligned} \quad (8)$$

where

$$\mathbf{D}_{l\pm 1/2}^n = (\mathbf{R} \mathbf{A} \mathbf{R}^{-1})_{l\pm 1/2} = [\mathbf{R}(\mathbf{A}^+ - \mathbf{A}^-) \mathbf{R}^{-1}]_{l\pm 1/2}^n,$$

and

$$(\mathbf{D}_{l+1/2}^-)^n = (\mathbf{R} \mathbf{A}^- \mathbf{R}^{-1})_{l+1/2}$$

$$(\mathbf{D}_{l-1/2}^+)^n = (\mathbf{R} \mathbf{A}^+ \mathbf{R}^{-1})_{l-1/2}$$

with

$$\mathbf{A}^\pm = (|\mathbf{A}| \pm \mathbf{A})/2.$$

The construction of $D_{i\pm 1/2}^n$ is accomplished in two steps. First, the analytic Jacobian $D = \partial H / \partial Q$ is formed. D is found to be a function of metric coefficients, of the parameter β , and of the state vector Q

$$D = D(a, b, c, \beta, Q)$$

where a, b, c are the metric quantities $\xi_x/J, \xi_y/J, \xi_z/J$, etc. Second, the local values $a_{i\pm 1/2}, b_{i\pm 1/2}, c_{i\pm 1/2}$, and $Q_{i\pm 1/2}^n$ are computed at interfaces and fed into D to form $D_{i\pm 1/2}^n$. In addition, in order to ensure that the flux differences taken over the six bounding surfaces, $(i \pm 1/2, j, k)$, $(i, j \pm 1/2, k)$ and $(i, j, k \pm 1/2)$ of a three-dimensional cell at (i, j, k) cancel out completely so that the present finite difference formulation essentially becomes a finite volume method, a special weighted averaging procedure has been adopted (9), for example,

$$(\zeta_x/J)_{ijk} = [(\sigma_k \delta_j y)(\sigma_j \delta_k z) - (\sigma_j \delta_k y)(\sigma_k \delta_j z)]_i$$

where

$$\sigma_k \delta_j y = [(\delta_j y)_{k+1} + (\delta_j y)_{k-1}]/2$$

with

$$\delta_j(\cdot) = [(\cdot)_{j+1} - (\cdot)_{j-1}]/2$$

The advantage of the delta form formulation is that the steady-state solution is independent of the time step size Δt . The justification for the accuracy of Eq. (8) as the approximate Riemann solver for the present problem is given in Ref. 9.

In order to ensure that the present scheme has a high resolution capability, which is equivalent to preserving Total Variation Diminishing (TVD) property for a nonlinear equation, it is necessary to construct a quantity subject to TV requirement. For a linear problem such as the one described above, the TV of the characteristic variable $W = R^{-1}Q$ can be forced to diminish in time. Assuming R, R^{-1} and Λ to be constant and using the definition for the characteristic variables, the scheme given in Eq. (8) can be rewritten as

$$\left[\left(\frac{1}{\Delta t J} \right) \pm \lambda_m^\pm \Delta t_{i\mp 1/2} \right] \Delta W_m^n = \mp \lambda_m^\pm \Delta t_{i\mp 1/2} W_m^n \quad (9)$$

($m = 1, 2, 3, 4$)

The above equation comprises four scalar linear equations. To enhance the accuracy up to third order, the characteristic variables W_m^n at the cell interfaces are reconstructed by using piecewise linear distributions as described in Ref. 9. We then obtain a family of implicit TVD schemes

$$\begin{aligned} & \left[\left(\frac{1}{\Delta t J} \right) \pm \lambda_m^\pm \Delta t_{i\mp 1/2} \right] \Delta W_m^n = \\ & [\lambda_m^- - \{(1 - \omega)\lambda_m^- + (1 + \omega)\lambda_m^+\} \\ & \times (\phi_{m,i+1}^- - \phi_{m,i}^+)/4] \Delta t_{i+1/2} W_m^n \\ & - [\lambda_m^+ + \{(1 - \omega)\lambda_m^+ + (1 + \omega)\lambda_m^-\} \\ & \times (\phi_{m,i}^+ - \phi_{m,i-1}^-)/4] \Delta t_{i-1/2} W_m^n \end{aligned} \quad (10)$$

where

$$\phi_{m,i}^\pm = \phi(r_{m,i}^\pm)$$

and

$$r_{m,i}^\pm = \begin{cases} (\Delta t_{i-1/2} W_m^n / \Delta t_{i+1/2} W_m^n)^\pm, & \text{for } \Delta t_{i\pm 1/2} W_m^n \neq 0 \\ 0, & \text{for } \Delta t_{i\pm 1/2} W_m^n = 0 \end{cases}$$

Extending this TVD scheme to non-linear hyperbolic conservation laws, we obtain

$$\begin{aligned} & \left[\left(\frac{1}{\Delta t J} \right) - (\lambda_{m,i+1/2}^- \Delta t_{i+1/2} - \lambda_{m,i-1/2}^+ \Delta t_{i-1/2})^n \right] \Delta W_m^n = \\ & \{ \lambda_{m,i+1/2}^- - [(1 - \omega)\lambda_{m,i+1/2}^- + (1 + \omega)\lambda_{m,i+1/2}^+] \\ & \times (\phi_{m,i+1}^- - \phi_{m,i}^+)/4 \}^n \Delta t_{i+1/2} W_m^n - \\ & \{ \lambda_{m,i+1/2}^+ + [(1 - \omega)\lambda_{m,i+1/2}^+ + (1 + \omega)\lambda_{m,i-1/2}^-] \\ & \times (\phi_{m,i}^+ - \phi_{m,i-1}^-)/4 \}^n \Delta t_{i-1/2} W_m^n \end{aligned} \quad (11)$$

The extension of Eq. (11) to a nonlinear system of conservative laws is obtained in two steps. First, the nonlinear equivalent of Eq. (11) is formed. then it is multiplied R throughout from the left to get

$$\begin{aligned} & \left[\left(\frac{1}{\Delta t J} \right) - (D_{i+1/2}^- \Delta t_{i+1/2} - D_{i-1/2}^+ \Delta t_{i-1/2}) \right] \Delta Q^n = \\ & (RK^- R^{-1})_{i+1/2} \Delta t_{i+1/2} Q^n - \\ & (RK^+ R^{-1})_{i-1/2} \Delta t_{i-1/2} Q^n \end{aligned} \quad (12)$$

where

$$K_{i\pm 1/2}^\mp = \pm \{ \Lambda_{i\pm 1/2}^\mp - [(1 - \omega)\Lambda_{i\pm 1/2}^\mp + (1 + \omega)\Lambda_{i\pm 1/2}^\pm] \times \left(\frac{\Phi_{i\pm 1}^\mp - \Phi_i^\pm}{4} \right)^n \}$$

and

$$\Phi_i^\pm = \text{diag}(\phi_1^\pm, \phi_2^\pm, \phi_3^\pm, \phi_4^\pm)_i$$

Discretization of the Viscous Fluxes

To discretize the viscous fluxes, the derivatives at the cell interfaces are approximated like

$$(u_\xi)_{j+1/2} = \Delta_{j+1/2} u, \text{ etc.}$$

wherever possible. Otherwise, they are computed from the central differences at the two nearest neighboring points, such as

$$(u_\xi)_{i+1/2} = 0.25 [(u_{j+1} - u_{j-1})_{i+1} + (u_{j+1} - u_{j-1})_i]$$

The above one dimensional discretization scheme can be used to estimate the interface-flux function in multidimensional problem. The discussions of the extension of the fluxes differencing and TVD schemes from one-dimensional to multi-dimensional application can be found in Roe (13) and Yee (14). Our present strategy is to sum up all independent discretizations of the flux derivatives in each coordinate direction to form a three-dimensional formulation.

Time Differencing and the Implicit Scheme

The backward Euler time differencing of the three-dimensional conservation equations with the thin-layer approximation is

$$\frac{\Delta Q^n}{\Delta t} = -[\Delta_\zeta(E^{n+1}) + \Delta_\xi(F^{n+1}) + \Delta_\eta(G^{n+1} - G_v^{n+1})] \quad (13)$$

Linearizing it about time level n , we obtain

$$\begin{aligned} \left[\frac{1}{\Delta t J} + \left(\frac{\partial E^n}{\partial Q} \right) \Delta_\zeta + \left(\frac{\partial F^n}{\partial Q} \right) \Delta_\xi + \left(\frac{\partial G^n}{\partial Q} - \frac{\partial G_v^n}{\partial Q} \right) \Delta_\eta \right] \Delta Q^n \\ = -[\Delta_\zeta(E^n) + \Delta_\xi(F^n) + \Delta_\eta(G^n - G_v^n)] \end{aligned} \quad (14)$$

The left hand side is the implicit part and the right hand side is the explicit part of the formulation. The explicit part is the spatial derivatives in Eq. 3 evaluated at the known time level n ; its value diminishes as the steady state solution is approached. Hence, it is also called the residual. The L_2 norm of the residual is often used as a measure of convergence of a solution. Discretize the inviscid and viscous fluxes according to upwind differencing scheme and central differencing scheme respectively in ζ , ξ and η coordinate direction independently according to Eq. (8) and then assemble them together. Eq. (14) becomes

$$\begin{aligned} \left[\left(\frac{1}{\Delta t J} \right) - A_{i+1/2}^- \Delta_{i+1/2} + A_{i-1/2}^+ \Delta_{i-1/2} \right. \\ \left. - B_{j+1/2}^- \Delta_{j+1/2} + B_{j-1/2}^+ \Delta_{j-1/2} \right. \\ \left. - (C^- + Z)_{k+1/2} \Delta_{k+1/2} + (C^+ + Z)_{k-1/2} \Delta_{k-1/2} \right] \Delta Q^n \\ = -Res(Q^n) \end{aligned} \quad (15)$$

where i, j , and k are spatial indices associate with the ξ, η and ζ coordinate direction. A^\pm, B^\pm, C^\pm , and Z are 4×4 block matrices (flux Jacobians) associated with implicit spatial differencing in the coordinate directions by evaluating the metric terms at cell interfaces in each direction. Eq.(15) is solved by an implicit hybrid algorithm, where a symmetric planar Gauss-Seidel relaxation is used in the streamwise direction ζ in combination with approximate factorization in the remaining two coordinate directions ξ and η . It is used to avoid the Δt^3 spatial splitting error incurred in fully three-dimensional approximate factorization methods. The hybrid scheme is unconditionally stable for linear systems and offers the advantage of being completely vectorizable like a conventional three-dimensional approximate factorization algorithm. As a result, Eq. (15) becomes

$$\begin{aligned} [M - (B^-)_{j+1/2} \Delta_{j+1/2} + (B^+)_{j-1/2} \Delta_{j-1/2}] \Delta \hat{Q} \\ = -Res(Q^n, Q^{n+1}) \\ [M - (C^- + Z)_{k+1/2} \Delta_{k+1/2} + (C^+ + Z)_{k-1/2} \Delta_{k-1/2}] \Delta \hat{Q} \\ = M \Delta \hat{Q} \end{aligned} \quad (16)$$

$$Q^{n+1} = Q^n + \Delta Q^n$$

with

$$M = \left[\frac{1}{\Delta t J} + (A^-)_{i+1/2} + (A^+)_{i-1/2} \right]$$

and the residual on the RHS indicates the nonlinear updating of the residual by using Q^{n+1} whenever it becomes available while sweeping in the ζ direction back and forth through the computational domain.

Turbulence Modeling

For laminar flow computations the coefficient of molecular viscosity $\mu = \mu_l$ is obtained from Sutherland's law. Turbulence is simulated using the Baldwin-Lomax algebraic turbulence model. For turbulent flow computations the laminar flow coefficients are replaced by,

$$\mu = \mu_l + \mu_t$$

The turbulent viscosity coefficient μ_t is computed by using the isotropic, two-layer Cebeci type algebraic eddy-viscosity model as reported by Baldwin-Lomax. In this formulation μ_t is given by

$$\mu_t = \begin{cases} (\mu_t)_{inner} & y \leq y_c \\ (\mu_t)_{outer} & y > y_c \end{cases}$$

where y is the local distance measured normal to the body surface and y_c is the smallest value of y at which the values from the inner and outer region viscosities are equal. Within the inner region, the Prandtl-Van Driest formulation is used

$$(\mu_t)_{inner} = l^2 |\omega|$$

where $l = ky[1 - e^{-(y^+/A^+)}]$ and $|\omega|$ is the magnitude of vorticity given by

$$|\omega| = \sqrt{\left(\frac{\partial u}{\partial y} - \frac{\partial v}{\partial x} \right)^2 + \left(\frac{\partial v}{\partial z} - \frac{\partial w}{\partial y} \right)^2 + \left(\frac{\partial w}{\partial x} - \frac{\partial u}{\partial z} \right)^2}$$

and $y^+ = (\tau_w / \mu_w) y$.

In the outer region, for attached and separated boundary layers, the turbulent viscosity coefficient is given by

$$\begin{aligned} (\mu_t)_{outer} &= K C_{ep} F_{wake} F_{Kleb}(y) \\ F_{wake} &= \min(y_{max} F_{max}, C_{wk} y_{max} U_{dif}^2 / F_{max}) \\ F_{Kleb}(y) &= [1 + 5.5(C_{Kleb} / y_{max})^6]^{-1} \end{aligned}$$

In the above equation k and C_{ep} are constants and

$$F_{max} = \max[|\omega| y (1 - e^{-(y^+/A^+)})]$$

and y_{max} is the value of y at which F_{max} occurs. The quantity U_{dif} is the difference between maximum and minimum total velocity in the profile

$$U_{dif} = \sqrt{(u^2 + v^2 + w^2)_{max}} - \sqrt{(u^2 + v^2 + w^2)_{min}}$$

The various constants in the model are given in Ref. 15 as

$$A^+ = 26, \quad k = 0.4, \quad K = 0.0168,$$

and

$$C_{ep} = 1.6, \quad C_{wk} = 0.25, \quad C_{Kleb} = 0.3.$$

IV. Grid Generation

An algebraic grid generation procedure based on transfinite interpolation technique has been used to generate the viscous grid around the hull geometry. The three-dimensional grid generated around the body is of C-O type. The C-O grid is particularly needed to adequately resolve the wake region. Details of the theoretical aspects of the transfinite interpolation method and the various mapping functions and their behavior in grid control is highlighted in Ref. 16. The method is fundamentally a two body grid generation procedure. The stern shape could be either open or closed. A modified osculating interpolation function has been used in the present program.

V. Results and Discussion

The hydrodynamic characteristic of the boundary layer flow around the stern of a ship is quite different with and without a propeller in operation. The action of a propeller produces suction that accelerates the flow upstream. As a result, the pressure and the skin friction drag around the stern increase and the thickness of the boundary layer decreases. The knowledge of the effective flow profile near the propeller plane and the amount of the added drag is essential for designing an efficient propulsor. In the past, extensive efforts have been made to study the interaction between a propeller and a thick boundary layer experimentally and computationally (4,5,6,7,8,17,18). For the reason of simplicity, in most cases, axisymmetric bodies were chosen. At present, we perform the numerical simulations of flow over DTRC Afterbodies 1, 2 and 5 without a propeller. In addition the flow over afterbody 1 with a propeller in operation is analyzed. The results are then compared with available experimental data. The purpose of the simulations is to develop and validate a numerical scheme for analyzing the complex interaction between boundary and propeller. The details of the afterbodies are shown in Fig. 1, where r_{max} is the maximum radius of the body, r is the radial distance measured from the body axis, x is the axial distance from the nose and L is the total body length. The afterbody length to maximum diameter ratios of all three afterbodies are different; they are 4.308, 2.247 and 2.018 for Afterbodies 1, 2 and 5, respectively. Here, the afterbody length is defined as the distance between the end of the parallel middle body and the after perpendicular. Furthermore, Afterbody 5 has an inflected stern. The hubs of all three afterbodies are identical at the position where the propeller can be mounted. The different stern shapes generate a large data base variation of stern flow suitable for the purpose of validation of the computational scheme.

Flow over Axisymmetric Bodies

Flow variables such as pressure and velocity components of an axisymmetric flow are independent of circumferential variation. They can be obtained through a set of de-generated equations based only on two spatial dimensions. However, in order to validate the three dimensional formulation we have just presented, full three dimensional computations over three different segments of a body are performed. The sizes of the segments are 45° , 90° and 180° .

A viscous grid with C-O topology around the body is generated by a transfinite interpolation method. Grid domain extends to three body lengths both upstream and downstream of the body. Figure 2 shows a partial view of a C-O grid around a generic body. The grid size used for presented simulations is $91 \times 25 \times 49$ in ζ (streamwise), η (circumferential) and ξ (normal) direction. In the ξ direction, the grid is clustered near the body with the smallest grid spacing 5×10^{-4} of the body length. In the η direction, the grid is clustered near the bow and the stern. Grid sizes used for all three segments (45° , 90° and 180°) are identical. Consequently, we can perform computations based on three different grid densities in the η direction. The differences among the solutions are negligibly small, therefore, only the results based on the 90° segment will be presented here. In all our axisymmetric flow computations, the mixing length of the turbulence model has been modified according to Huang et al (5).

A detailed analysis of the measurement accuracies is not available. However, the standard deviations of measured data were estimated from repeat runs. The standard deviation of the measured static wall pressure was less than 5 percent of their mean values and the deviation of the measured velocities was less than 2 percent of the free-stream velocity (19).

The experiments of flow over Afterbodies 1, 2 and 5 were carried out at Reynolds numbers of 6.60×10^6 , 6.80×10^6 and 9.30×10^6 , respectively (based on total body length). Figures 3, 4 and 5 show the comparisons of the computed and the measured pressure distributions over the surfaces for Afterbodies 1, 2 and 5, respectively. The body profiles are included in the figures in order to show the relationship between the pressure gradients and the stern shapes. At the region near the end of the body where the stern and the hub meet, the computed pressure shows a sharp decrease followed by a equally sharp increase. Based on some different numerical schemes, this peculiar feature has also been encountered by Chen and Patel (18) and Lee et al (20) in their computations. Chen and Patel attributed such phenomenon to the rapid change of geometry near the hull-hub juncture as well as the upstream influence of the complex pressure interactions in the tail region. A solution we obtained with a panel method exhibited the same feature, as long as enough panel resolution around the hull-hub juncture region was provided. Unfortunately, the experimental data lack the resolution needed to verify this feature.

Figures 6, 7 and 8 show the comparisons between the computed and the measured velocity components at several streamwise locations for afterbodies 1, 2 and 5, respectively, where r_0 denotes the radius of body surface. For Afterbody 1, the agreement is very good. The computation predicted the development of the boundary layer very well. For Afterbodies 2 and 5, the agreement in general is good, except the radial velocity profiles which are less satisfactory. The agreement deteriorates as the measurement location moves further downstream. The radial velocity component is relatively small and is more difficult to measure accurately. For both Afterbodies 2 and 5, the maximum difference between computed and measured values is about 4 percent of free-stream velocity. The error bound of

the measurement is 2 percent. The measured axial velocities for Afterbodies 2 and 5 are progressively slower than the computed velocities as the end of stern is approached, although the difference is small. Near the end of the stern, the measured axial velocities for both Afterbodies 2 and 5 show an inflection point which is not captured by the computations. The pressure gradient of the stern boundary layer is directly affected by the fullness of the stern shape. The stern of Afterbody 1 is the least full among all three bodies studied here. It caused only a mild adverse pressure gradient in the boundary layer surrounding the stern region. This may explain the reason why the simulation for Afterbody 1 is the most successful.

In each computation presented above, 220 iteration steps were taken. The L_2 norm of the residual dropped two orders of magnitude from 10^{-3} to 10^{-5} . 220 iteration steps were chosen since further iterations produced only insignificant variations. Each computation requires 17 CPU minutes on a CRAY-YMP machine.

Flow over an Axisymmetric Body with a Propeller

Flow experiment for an axisymmetric body with a propeller were conducted at DTRC by Huang et al (4,6,7). A propeller was mounted on Afterbody 1 at $x/L = 0.983$. The geometrical and hydrodynamic characteristics of the propeller are given in Huang et al (4) and Huang and Groves (7). The experiment was performed at a Reynolds number of 6.6×10^6 (based on body length).

Numerically, the propeller effect is simulated by imbedding body forces in a disk of finite thickness located in the propeller region. The details of this type of formulation can be found in Stern et al (8). Distribution of body forces depends on the propeller's characteristics such as, thrust coefficient C_T , torque coefficient K_Q , advance coefficient J and radial circulation distribution $G(r)$. The axial and circumferential body force per unit volume are obtained from the following equations:

$$fb_x = \frac{C_T R_p^2 G(r)}{4\Delta X \int_{R_h}^{R_p} G(r) r dr}$$

$$fb_\theta = \frac{4K_Q R_p^3 G(r)}{\pi r J^2 \Delta X \int_{R_h}^{R_p} G(r) r dr}$$

where fb_x and fb_θ are the body forces per unit volume in the axial and circumferential directions, respectively, R_h and R_p are the radii of propeller hub and blade, respectively, and ΔX is the thickness of the disk. The following propeller data were used in our computation:

$$J = 0.370, K_T = 0.227, K_Q = 0.0453, C_T = 0.370$$

The computed body forces are then incorporated into the right hand side of Eq. 16 and forms a part of the residual. Based on the identical grid size and grid distribution used previously, a computation was carried out for 220 iteration steps. The L_2 norm of the residual dropped two orders of magnitude from 10^{-3} to 10^{-5} without suffering from any numerical instability.

From the results of the computation, the influence of propeller action can be detected up to about two propeller diameters upstream. The differences between axial velocity components $\Delta u_x/V_\infty$ with and without the propeller

in operation at two streamwise locations are shown in Fig. 9. The measurement locations are at $x/L = 0.954$ and $x/L = 0.977$. The agreement between the computed and the measured values is very good. The differences in pressure distribution on the afterbody surface upstream of the propeller plane are shown in Fig. 10. The results of the computation are to the same degree of accuracy as those reported by Huang and Groves (7). The swirl velocity was also computed but due to lack of experimental data to compare with, it is not presented here.

Flow over Tangent-Ogive Forebody

With the same numerical scheme discussed above and a modified turbulent model the flow over a 3.5 caliber tangent-ogive forebody was studied (21) at angles of attack of 20° and 30° and at Reynolds numbers in the range $0.2 - 3.0 \times 10^6$. The purpose of the study was to investigate the Reynolds number effect on low speed vortical flow and to validate the numerical scheme. A $C-O$ type grid was generated for the purpose of computations. The grid size was $97 \times 40 \times 91$ in ζ (streamwise), ξ (normal) and η (circumferential) direction. Fig. 11 shows a comparison of the computed and the measured surface flow patterns at a Reynolds number of 0.8×10^6 (based on diameter) and an angle of attack of 20° . The lines indicate that the primary separations are in good agreement. Top views show two distinct regimes in which the surface streamlines appear to collocate. Figure 12 shows a comparison of the computed and the measured circumferential surface pressure distributions. The Reynolds numbers are 0.8×10^6 and 0.3×10^6 and the angle of attack is 30° . The Reynolds number effect is more pronounced on the leeward side, near the nose. The agreement is good.

VI. Conclusion

The 3-D incompressible Navier-Stokes equations was discretized by the flux-difference splitting and the implicit high resolution schemes. A discretized system of equations was solved by an implicit hybrid algorithm, where a symmetric planar Gauss-Seidel relaxation was used in the streamwise direction in combination with approximation factorization in the two remaining directions. The algorithm is highly vectorizable and suitable for computation on a modern supercomputer.

For the simulation of afterbody boundary layer flows, this method is proven to be effective. Inclusion of the body force propeller model poses no additional problem. To obtain a converged solution with the propeller model included, it does not require more iteration steps in comparison with the case without including a propeller model. The method was also shown to simulate low speed vortical flow with good results.

Acknowledgement

This study was supported by The Office of Naval Technology. The computing time of CRAY-YMP was provided generously by NASA Ames Numerical Aerodynamic Simulation (NAS) Program.

References

- Maskew, B.M., "Prediction of Subsonic Aerodynamic Characteristics - A Case for Low Order Panel Methods", AIAA J. of Aircraft, Vol 19 (2), Feb. 1982, pp157-163
- Aziz, K., Hellums, J. D., "Numerical Solution of the Three-Dimensional Equations of Motion for Rectangular Natural Laminar Convection", Physics of Fluids, Vol. 8, Dec. 1965, pp 2182-2189.
- Chorin, A. J., "A Numerical Method for Solving Incompressible Viscous Flow Problems", Journal of Computational Physics, Vol. 2, No. 1, Aug. 1967, pp 12-26.
- Huang, T. T., Wang, H. T., Santelli, N., Groves, N. C., "Propeller/Stern/Boundary Layer interaction on Axisymmetric Bodies, Theory and Experiment", DTRC Report 76-0113, 1976.
- Huang, T. T., Santelli, N., Belt, G., "Stern Boundary layer Flow on Axisymmetric Bodies", Proceedings, 12th Office of Naval Research Symposium on Naval Hydrodynamics, Washington D.C., 1978, pp 127-157.
- Huang, T. Y., Groves, N.C., Belt, G., "Boundary Layer Flow on an Axisymmetric Body with an Inflected Stern", DTRC Report 80/064, Aug. 1980.
- Huang, T.T., Groves, N.C., "Effective Wake: Theory and Experiment", Proceedings, 13th Office of Naval Research Symposium on Naval Hydrodynamics, Tokyo, 1980, pp 651-673.
- Stern, F., Kim, H.T., Patel, V.C., Chen, H.C., "A Viscous Flow Approach to the Computation of Propeller-Hull Interaction", Journal of Ship Research, Vol.32, No. 4, Dec. 1988, pp 246-262.
- Hartwich, P.-M., Hsu, C. H., "High Resolution Upwind Schemes for the Three-Dimensional, Incompressible Navier-Stokes Equations", AIAA Journal, Vol. 26, No. 11, Nov. 1988, pp 1321-1328.
- Pulliam, T. H., Steger, J. L., "An implicit Finite Difference Solution of Three-Dimensional Flow", AIAA Paper 78-10, Jan. 1978.
- Stager, J.L., "Implicit Finite Difference Simulation of Flow about Arbitrary Two-Dimensional Geometries", AIAA Journal, Vol. 16, No. 7, Jul. 1978, pp 679-686.
- Roe, P.L., "Approximate Riemann Solvers, Parameter Vectors, and Difference Schemes", Journal of Computational Physics, Vol. 43, No. 2, Oct. 1981, pp 357-372.
- Roe, P.L., "Characteristic-Based Schemes for the Euler Equations", Ann. Rev. Fluid Mech., Vol. 18, 1986, pp 337-365.
- Yee, H.C., "Construction of Explicit Symmetric TVD Schemes and Their Applications", Journal of Computational Physics, Vol. 68, 1987, pp 151-179.
- Baldwin, B.S., Lomax, H., "Thin Layer Approximation and Algebraic Model for Separated Turbulent Flows", AIAA Paper 78-257 Jan. 1978.
- Eriksson, L.-E., Rizzi, A., "Practical Three Dimensional Mesh Generation Using Transfinite Interpolation", VKI Lecture Series 1983-04 Vol. 1, Mar. 1983.
- Zhou, L.-D., Yuan, J.-L., "Calculation of the Turbulent Flow around the Stern and the Wake of a Body of Revolution", Proceedings, 15th Office of Naval Research Symposium on Naval Hydrodynamics, Hamburg, Germany, Sep. 1984 pp 279-290.
- Chen, H.C., Patel, V.C., "Calculation of Stern Flow by a Time-Marching Solution of the Partially-Parabolic Equations", Proceedings, 15th Office of Naval Research Symposium on Naval Hydrodynamics, Hamburg, Germany, Sep. 1984 pp 505-522.
- Huang, T.T., Cox, B.D., "Interaction of Afterbody Boundary Layer and Propeller", Symposium on 'Hydrodynamics of Ship and Offshore Propulsion System', Hovik Outside Oslo, Mar. 20-25 1977.
- Lee, Y.T., Huang, T.T., Sung, C.-H., "Flow Prediction about an Appended Body of Revolution", 6th International Conference on Numerical Methods in Laminar and Turbulent Flow", Jul. 1989, Swansea, U.K.
- Hartwich, P.-M., Hall R.M., "Navier-Stokes Solutions for Vortical Flows over a Tangent-Ogive Cylinder", AIAA Paper No. 89-0337, Jan. 1989

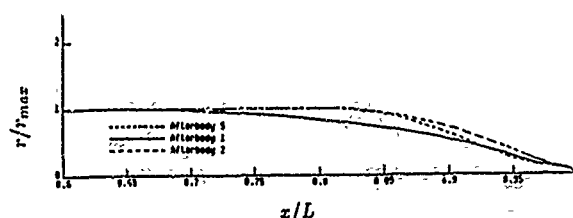


Fig. 1 Axisymmetric afterbodies

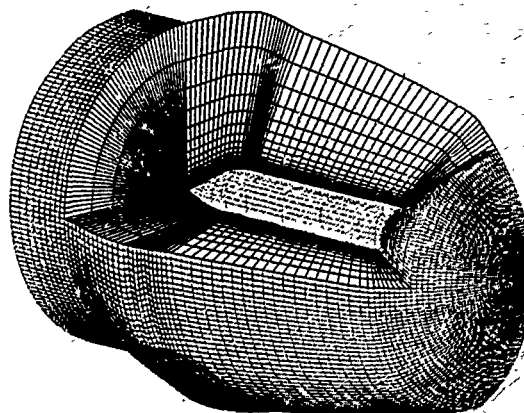


Fig. 2 Partial View of a C - O Grid around a Body

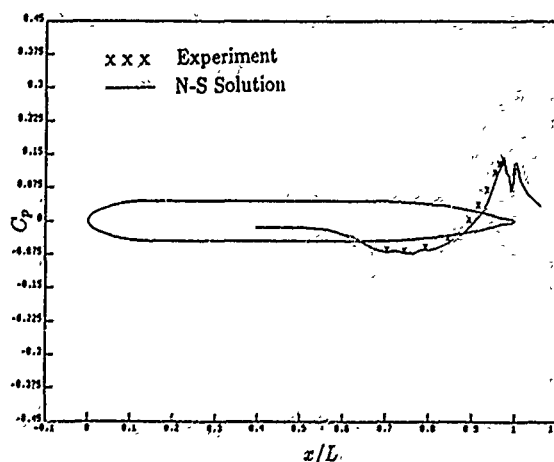


Fig. 3 Pressure Distribution on Afterbody 1

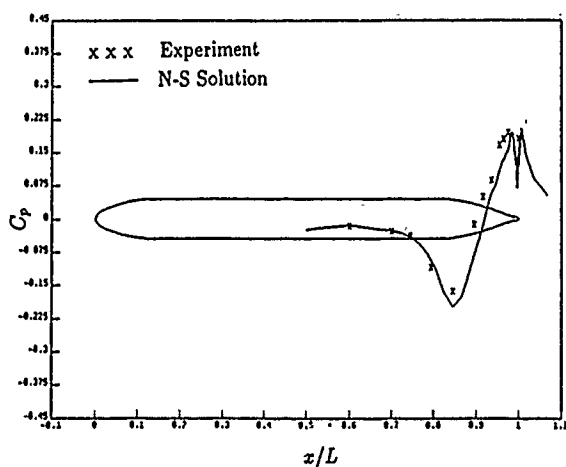


Fig. 4 Pressure Distribution on Afterbody 2

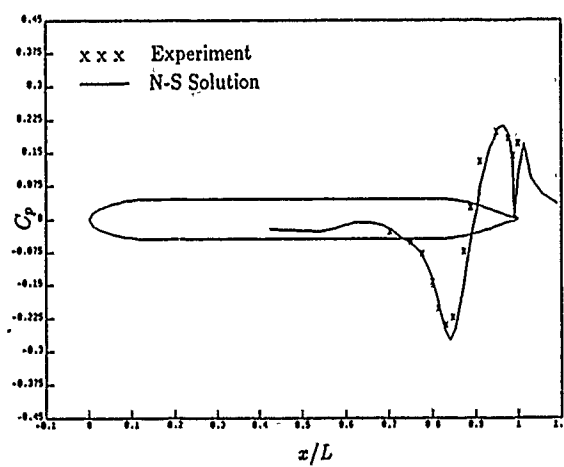


Fig. 5 Pressure Distribution on Afterbody 5

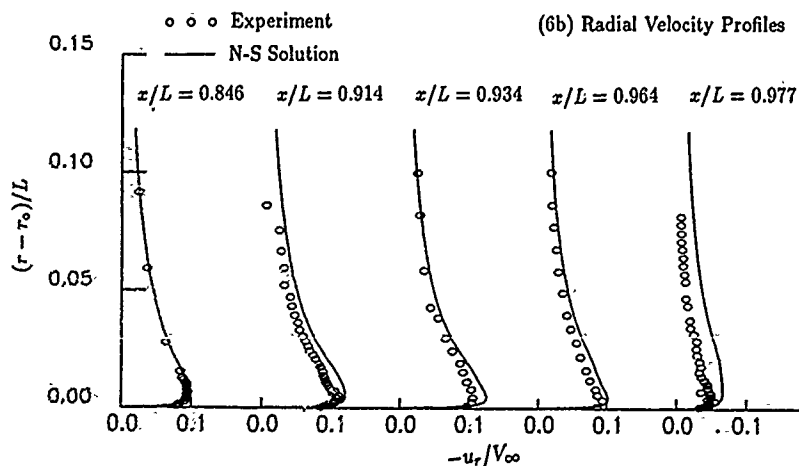
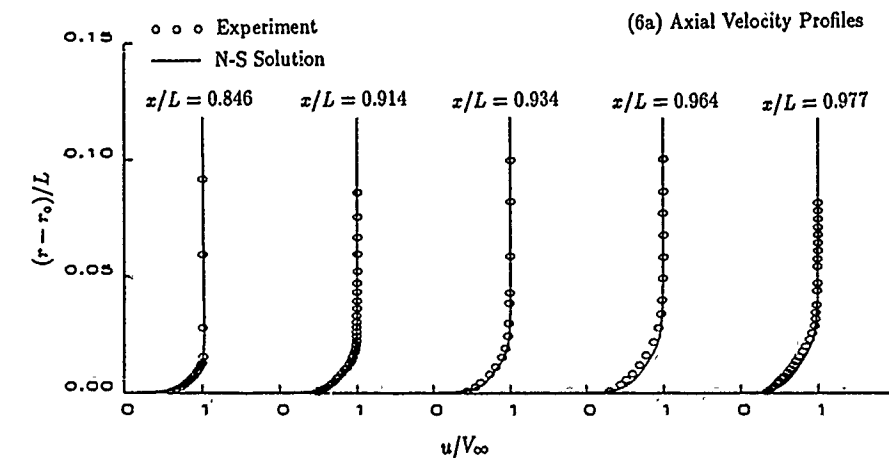


Fig. 6 Velocity Profiles on Afterbody 1

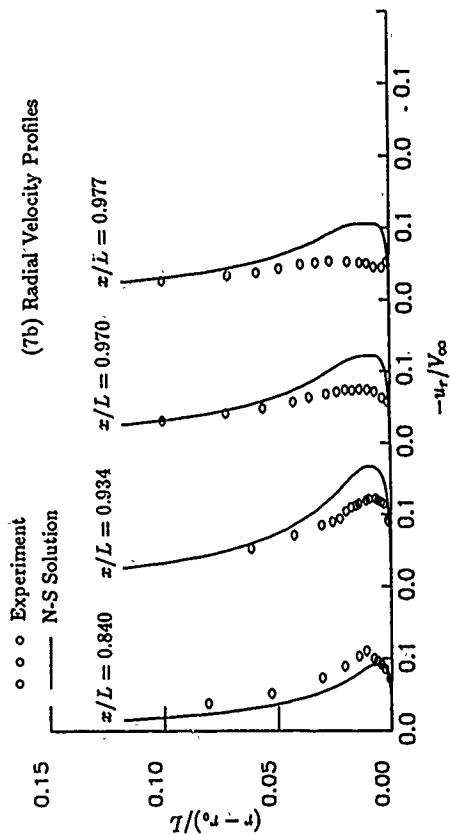
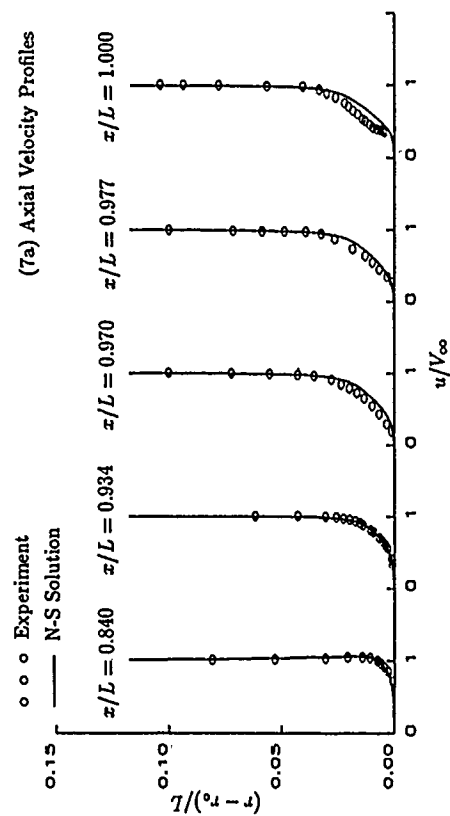


Fig. 7 Velocity Profiles on Afterbody 2

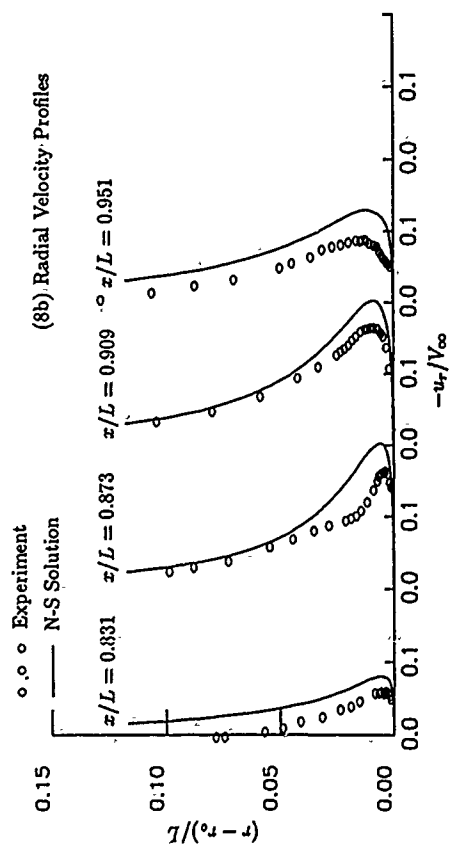
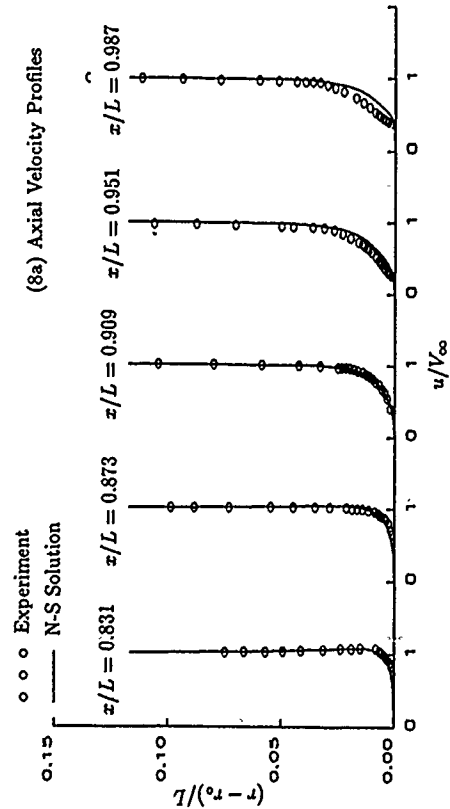


Fig. 8 Velocity Profiles on Afterbody 5

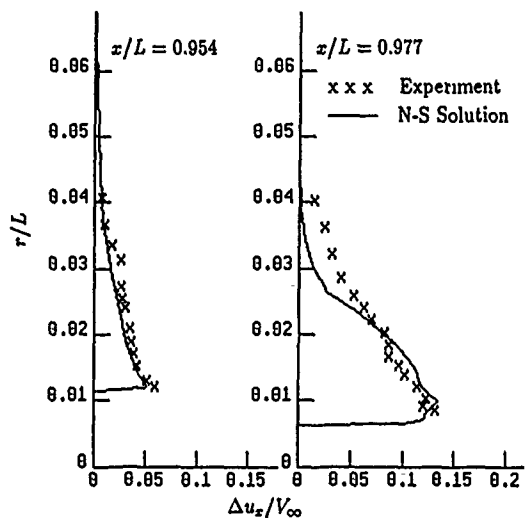


Fig. 9 Measured and Computed Axial Velocity Increase on Afterbody 1 Due to Propeller Suction

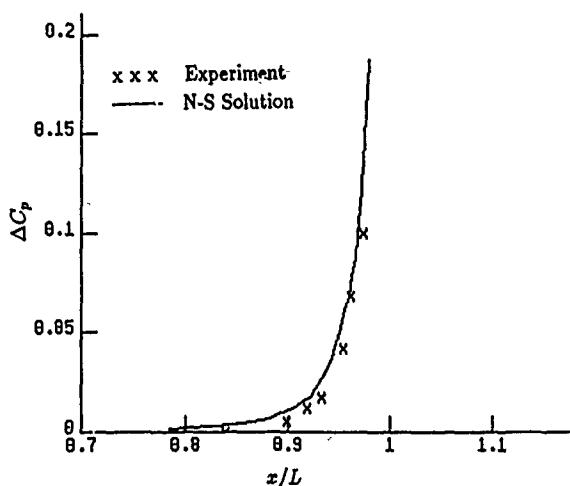


Fig. 10 Measure and Computed Surface Pressure Decrease on Afterbody 1 Due to Propeller Suction

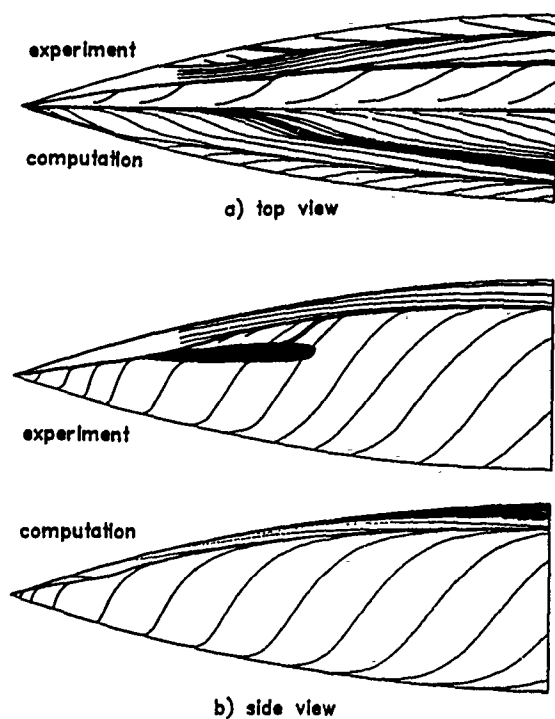


Fig. 11 Surface Flow Patterns

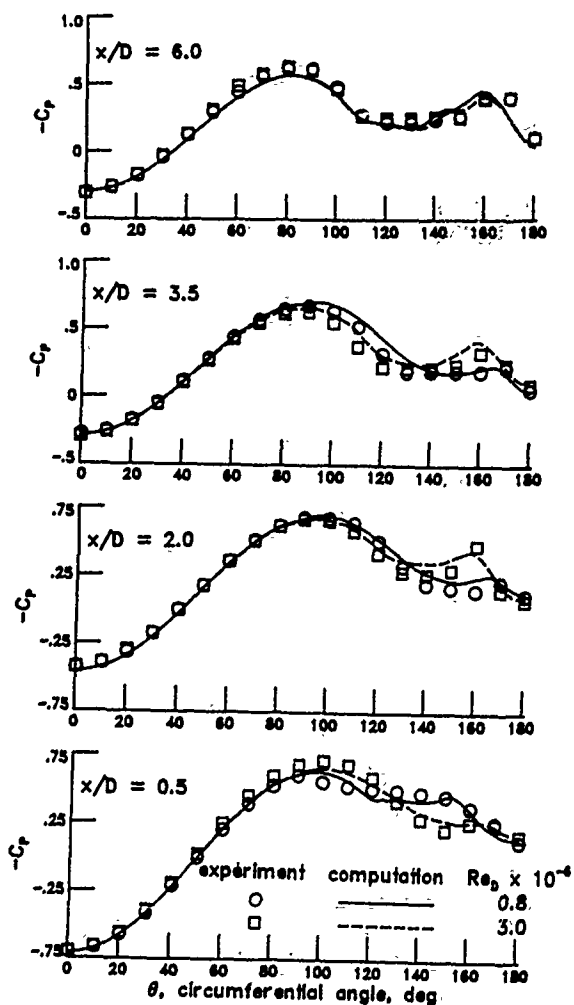


Fig. 12. Measured and Computed Circumferential Pressure Distributions

Grid Generation and Flow Computation for Practical Ship Hull Forms and Propellers Using the Geometrical Method and the IAF Scheme

Y. Kodama
Ship Research Institute
Tokyo, Japan

Abstract

Grid generation for ship hulls and a propeller blade was made using the geometrical method, where an initial grid is modified iteratively under several geometrical requirements such as orthogonality, smoothness, and clustering.

Using the generated grid, the computation of the incompressible Navier-Stokes equations was made for flows past a flat plate and four different ship hull forms using the IAF scheme and the Baldwin-Lomax zero-equation turbulence model. The hull forms chosen are a Wigley hull and Series 60 ($C_b=0.6, 0.7, 0.8$) hulls. Prior to the ship flow computation, the flow around a flat plate was computed, where the agreement of the computed result with experiment was very good in terms of the wall shear stress, displacement thickness, shape factor, and velocity distribution. The computed flow past a Wigley hull, which is not very different from the flat plate result because of its fine hull form, showed good agreement with experiments. The computed flows past Series 60 ($C_b=0.6, 0.7$, and 0.8) hull forms showed systematic change with the C_b block coefficient values. The computed $C_b=0.6$ result showed reasonable agreement with experiments. However, the agreement became poorer with increase in the C_b values ($=0.7, 0.8$).

1. Introduction

Prediction of flow past a ship hull has been an important subject in ship hydrodynamics because of its practical importance. If one succeeds in accurate prediction of the flow, one can get a resistance value to be used in powering, and the wake field at the propeller plane to be used in propeller performance estimation.

A classical approach to the above problem is the boundary-layer method [1]. But recently, aided by the rapid development of computer hardware, methods called NS solvers, in which the governing equations of

the flow are discretized and computed, are becoming increasingly popular [2],[3],[4]. The author previously computed the flow past a Wigley hull using the non-conservation form of the NS solver [5]. The present work is an extension of the previous work. The major change is in the use of the conservation form. The scheme is called the IAF scheme [6], which is widely used for computing compressible flows. Pseudo-compressibility is introduced in the continuity equation of the incompressible flow, in order to make the system of equations hyperbolic. A conservative 2nd-order central differencing is used for convection and diffusion terms, and the 4-th order numerical dissipation terms are explicitly added to the equations to damp out high frequency wiggles.

The degree of accuracy of computed results of NS solvers is affected by the quality of the grid used. Therefore, it is important to be able to generate grids of high quality, in order to obtain good computed results. In the present paper, a grid generation method called the geometrical method is used. It is an extension of the method used by the author previously [7]. Using the method, the grid on a propeller blade and the grids around ship hulls are generated.

Although the use of NS solvers greatly reduces the need for experimental informations, a turbulence model is still needed for computing high Reynolds number flows such as those past ship hulls. The turbulence models widely used today in engineering applications are the Cebeci-Smith (CS) zero-equation turbulence model [8], and the $k-\epsilon$ two-equation model [9]. In the present paper the Baldwin-Lomax (BL) zero-equation turbulence model, derived by making a modification to the CS model, is used. There, in contrast to the original CS model, the necessity for finding the edge of the boundary-layer is avoided. The model is widely used for computing compressible flows in the field of aerodynamics, and is said to be accurate for unseparated flows,

but poor for separated flows. One of the objectives of the present work is to test the validity of the turbulence model for incompressible flows past ship hulls, and to find the range of applicability of the model by computing flows past ship hulls with various degree of fullness. Although further modification to the BL model was published recently [10], the original BL model is used here.

In Chapter 2, the NS solver is described, with discussions on the conservation property, boundary conditions, and the turbulence model. In Chapter 3, the geometrical grid generation method is described, where the use of bi-cubic splines for representing a body surface geometry is explained. In Chapter 4, computed results of flows past a flat plate, a Wigley hull, and Series 60 Cb=0.6, 0.7, and 0.8 hulls are shown. In Chapter 5, conclusions are drawn. The flow past a propeller, which was originally planned, is not included in the present paper.

2. NS Solver

2.1 Governing Equations

The governing equations are the combination of the incompressible Navier-Stokes equations and the continuity equation. They are, in conservation form,

$$q_t + F_x + G_y + H_z = 0 \quad (2.1a)$$

where

$$q = \begin{bmatrix} u \\ v \\ w \\ p \end{bmatrix}, F = \begin{bmatrix} u^2 + p - \tau_{xx} \\ uv - \tau_{xy} \\ uw - \tau_{xz} \\ \beta u \end{bmatrix}, G = \begin{bmatrix} uv - \tau_{xy} \\ v^2 + p - \tau_{yy} \\ vw - \tau_{yz} \\ \beta v \end{bmatrix}, H = \begin{bmatrix} uw - \tau_{xz} \\ vw - \tau_{yz} \\ w^2 + p - \tau_{zz} \\ \beta w \end{bmatrix} \quad (2.1b)$$

where all the subscripts except those with τ denote partial derivatives. The 1st, 2nd, and 3rd components are x-, y-, and z- momentum equations. In the 4th component, which is the continuity equation, $\partial p / \partial t$ is artificially added to give pseudo-compressibility, thus making the system of equations hyperbolic. β in the equation is a positive constant. The shear-stress terms τ are expressed as follows.

$$\begin{aligned} \tau_{xx} &= \left(\frac{1}{Re} + \nu_t\right) 2u_x, & \tau_{xy} &= \left(\frac{1}{Re} + \nu_t\right) (u_y + v_x) \\ \tau_{yy} &= \left(\frac{1}{Re} + \nu_t\right) 2v_y, & \tau_{xz} &= \left(\frac{1}{Re} + \nu_t\right) (w_x + u_z) \\ \tau_{zz} &= \left(\frac{1}{Re} + \nu_t\right) 2w_z, & \tau_{yz} &= \left(\frac{1}{Re} + \nu_t\right) (v_z + w_y) \end{aligned} \quad (2.2)$$

where ν_t is the kinematic eddy viscosity.

Coordinate transformation from the (x,y,z) Cartesian coordinate system to the body-fitted (ξ, η, ζ) coordinate system is made to the governing equation eq.(2.1). The transformation is assumed time-independent. The resulting equation is, again in conservation form

$$\frac{\partial}{\partial t} \left(\frac{q}{J} \right) + \hat{F}_\xi + \hat{G}_\eta + \hat{H}_\zeta = 0 \quad (2.3a)$$

where

$$\begin{cases} \hat{F} = \frac{\xi_x}{J} F + \frac{\xi_y}{J} G + \frac{\xi_z}{J} H \\ \hat{G} = \frac{\eta_x}{J} F + \frac{\eta_y}{J} G + \frac{\eta_z}{J} H \\ \hat{H} = \frac{\zeta_x}{J} F + \frac{\zeta_y}{J} G + \frac{\zeta_z}{J} H \end{cases} \quad (2.3b)$$

J is the Jacobian, and all the x, y, and z derivatives of ξ, η , and ζ are expanded using the chain rule.

Numerical dissipation terms are added to the above equation to enhance numerical stability.

$$\frac{\partial}{\partial t} \left(\frac{q}{J} \right) + \hat{F}_\xi + \hat{G}_\eta + \hat{H}_\zeta + \omega (q_{\xi\xi\xi\xi} + q_{\eta\eta\eta\eta} + q_{\zeta\zeta\zeta\zeta}) = 0 \quad (2.4)$$

where ω is a positive constant. In order that computed results obtained by solving eq.(2.4) satisfy the original equation with accuracy, these added terms must be small.

2.2 Discretization

First, the time derivative is replaced by the time differencing. The Padé time differencing form is used here.

$$\frac{\partial q}{\partial t} = \frac{1}{\Delta t} \frac{\Delta}{1 + \theta \Delta} q^n \quad \text{where } \Delta q^n \equiv q^{n+1} - q^n \quad (2.5)$$

where q^n denotes q at timestep n. θ is a constant which takes the value of either 0 (Euler explicit), 0.5 (Trapezoidal), or 1.0 (Euler implicit). Here $\theta=1.0$ is adopted. The nonlinear flux terms $\Delta \hat{F}$, $\Delta \hat{G}$, $\Delta \hat{H}$ are locally linearized into the form, for example,

$$\Delta \hat{F} = \hat{A} \Delta q + \hat{A}^\xi \Delta q_\xi + \hat{A}^\eta \Delta q_\eta + \hat{A}^\zeta \Delta q_\zeta \quad (2.6a)$$

$$\text{where } \hat{A} = \frac{\partial \hat{F}}{\partial q}, \hat{A}^\xi = \frac{\partial \hat{F}}{\partial q_\xi}, \hat{A}^\eta = \frac{\partial \hat{F}}{\partial q_\eta}, \hat{A}^\zeta = \frac{\partial \hat{F}}{\partial q_\zeta} \quad (2.6b)$$

Then the governing equation becomes

$$\begin{aligned} & \Delta q^n + \theta \Delta t \left[J \frac{\partial}{\partial \xi} (\hat{A} \Delta q + \hat{A}^\xi \Delta q_\xi + \hat{A}^\eta \Delta q_\eta + \hat{A}^\zeta \Delta q_\zeta) \right. \\ & + J \frac{\partial}{\partial \eta} (\hat{B} \Delta q + \hat{B}^\xi \Delta q_\xi + \hat{B}^\eta \Delta q_\eta + \hat{B}^\zeta \Delta q_\zeta) \\ & + J \frac{\partial}{\partial \zeta} (\hat{C} \Delta q + \hat{C}^\xi \Delta q_\xi + \hat{C}^\eta \Delta q_\eta + \hat{C}^\zeta \Delta q_\zeta) \\ & \left. + \omega (\Delta q_{\xi\xi\xi\xi} + \Delta q_{\eta\eta\eta\eta} + \Delta q_{\zeta\zeta\zeta\zeta}) \right] \\ & = -\Delta t [J (\hat{F}_\xi + \hat{G}_\eta + \hat{H}_\zeta) + \omega (q_{\xi\xi\xi\xi} + q_{\eta\eta\eta\eta} + q_{\zeta\zeta\zeta\zeta})]^n \quad (2.7) \end{aligned}$$

The mixed derivative terms such as $\partial(\hat{A}^n \Delta q_\eta)/\partial \xi$ are lagged to the timestep (n-1) and evaluated time-explicitly. Then the above equation can be approximately factored into ξ -, η -, and ζ -sweeps.

ξ -sweep

$$\begin{aligned} & \{I + \theta \Delta t [J \frac{\partial}{\partial \xi} (\hat{A} + \hat{A}^t \frac{\partial}{\partial \xi}) + \omega \frac{\partial^4}{\partial \xi^4}]^n\} \Delta q^* \\ &= -\Delta t [J(\hat{F}_\xi + \hat{G}_\eta + \hat{H}_\zeta) + \omega(q_{\xi\xi\xi\xi} + q_{\eta\eta\eta\eta} + q_{\zeta\zeta\zeta\zeta})]^n \\ & - \theta \Delta t J[(\hat{A}^n \Delta q_\eta + \hat{A}^t \Delta q_\zeta)_\xi + (\hat{B}^t \Delta q_\xi + \hat{B}^t \Delta q_\zeta)_\eta \\ & \quad + (\hat{C}^t \Delta q_\xi + \hat{C}^n \Delta q_\eta)_\zeta]^{n-1} \end{aligned} \quad (2.8)$$

η -sweep

$$\{I + \theta \Delta t [J \frac{\partial}{\partial \eta} (\hat{B} + \hat{B}^n \frac{\partial}{\partial \eta}) + \omega \frac{\partial^4}{\partial \eta^4}]^n\} \Delta q^{**} = \Delta q^* \quad (2.9)$$

ζ -sweep

$$\{I + \theta \Delta t [J \frac{\partial}{\partial \zeta} (\hat{C} + \hat{C}^t \frac{\partial}{\partial \zeta}) + \omega \frac{\partial^4}{\partial \zeta^4}]^n\} \Delta q^n = \Delta q^{**} \quad (2.10)$$

Δq^* and Δq^{**} are intermediate variables defined as the above two equations. I is a (4x4) unit matrix. After the above three equations are solved, the variable q^n is updated using eq.(2.5). That is

$$q^{n+1} = q^n + \Delta q^n \quad (2.11)$$

In order to solve eqs. (2.8) to (2.10), spatial differencing has to be approximated by spatial differencing. Here the following 2nd-order central differencings are used.

$$\begin{cases} \frac{\partial}{\partial \xi} = -E_\xi^{-1/2} + E_\xi^{+1/2} \\ \frac{\partial^4}{\partial \xi^4} = E_\xi^{-2} - 4E_\xi^{-1} + 6E_\xi^0 - 4E_\xi^{+1} + E_\xi^{+2} \end{cases} \quad (2.12)$$

E_ξ^{+m} is a shift operator in ξ -direction defined as

$$E_\xi^{+m} q_{i,j,k} \equiv q_{i+m,j,k} \quad (2.13)$$

where (i,j,k) are the numberings in ξ -, η -, and ζ - directions respectively. Similar central differencing operators are used in η and ζ directions. The non-staggered grid system is used, i.e. velocity, pressure, and eddy viscosity values are stored at the grid points. Substituting the differencing operators into eq.(2.8) results in

$$\begin{aligned} & K \Delta q^*_{i-2} + L \Delta q^*_{i-1} + M \Delta q^*_i + N \Delta q^*_{i+1} + O \Delta q^*_{i+2} \\ &= [\text{RHS of (2.8)}] \end{aligned} \quad (2.14a)$$

$$K = \theta \Delta t \omega I$$

$$L = \theta \Delta t [J(-\frac{1}{2} \hat{A}_{i-1/2} + \hat{A}_{i-1/2}^t) - 4\omega I]$$

$$\begin{aligned} M &= I + \theta \Delta t [J(-\frac{1}{2} \hat{A}_{i-1/2} + \frac{1}{2} \hat{A}_{i+1/2} + \hat{A}_{i-1/2}^t + \hat{A}_{i+1/2}^t) \\ & \quad + 6\omega I] \end{aligned} \quad (2.14b)$$

$$N = \theta \Delta t [J(\frac{1}{2} \hat{A}_{i+1/2} + \hat{A}_{i+1/2}^t) - 4\omega I]$$

$$O = \theta \Delta t \omega I$$

The above set of equations form a system with block pentadiagonal coefficient matrices, and can be efficiently solved. The coefficient matrices K , L , M , N , and O for η - or ζ -sweep are obtained by replacing (i, \hat{A} , \hat{A}^t) with (j, \hat{B} , \hat{B}^n) or (k, \hat{C} , \hat{C}^t) in the above equation.

As a consequence of the approximate factorization, each line of block pentadiagonal system in any of the three sweeps is decoupled completely from others, and therefore highly vectorized coding is possible.

The use of the differencing forms shown in eq.(2.12) results in the global conservation of momentum and mass in the discretized form. As shown in Fig. 2-1, where the area covered by a discretized governing equation at a grid point is shown hatched, all the numerical flux terms are evaluated at halfway between the grid points, and therefore cancel out when they are summed up, thus the global conservation holds. The added numerical dissipation terms, having constant coefficients, cancel out when they are summed up, and therefore do not affect the conservation property. However, there is exception in this conservation property. In the zone between the boundary point and the halfway point next to it, the conservation property does not hold unless the boundary condition is made consistent with the conservation property of the governing equation. In the present computation, this consistency is not satisfied, and therefore the conservation property holds not all the way down to the boundary point but to the halfway point next to the boundary. The same is true to the numerical dissipation terms, since they cannot find their counterparts to cancel out near the boundary.

2.3 Boundary Conditions

Fig. 2-2 (a),(b),(c) shows the grid topology and the location of the boundaries. The x-axis is in the streamwise direction, with $x=0.0$ at F.P. and $x=1.0$ at A.P.. The z-axis is in upward direction, and the y-axis is in the lateral direction, forming a right-handed system. The grid system is in the negative y and negative z quarter. The grid topology is H-O. The ξ -, η -, and ζ - axes are approximately in streamwise, girthwise, and normal-to-surface directions respectively. The star marks in Figs. (a) and (c) are the point of mapping singularity. At Upstream boundary, the uniform flow condition is used. That is, $q=(1,0,0)^T$ and $\Delta q=0$. At Downstream boundary, zero extrapolation in ξ -direction is used. They are $q_\xi=0$ and $\Delta q_\xi=0$. At (x-z) and (x-y) symmetry plane boundaries, zero-derivative condition is used, instead of an exact symmetry condition. That is, $q_\eta=0$ and $\Delta q_\eta=0$. At Inner boundary, the solid wall boundary condition is used. They are $u=v=w=0$ and an approximate boundary condition for pressure, which is $p_\zeta=0$ and $\Delta p_\zeta=0$. Finally, at Outer boundary, the uniform flow condition is used.

2.4 Turbulence Model

The turbulence model used is the Baldwin-Lomax (BL) zero-equation algebraic model, whose original form is the Cebeci-Smith (CS) model. The kinematic eddy viscosity ν_t is evaluated in the inner and outer layers separately.

In the inner region, the kinematic eddy viscosity ν_t has the same form with the CS model.

$$\nu_t = l^2 |\omega| \quad (2.15)$$

with

$$l = kn[1 - \exp(-n^+/A^+)] \quad (2.16)$$

$$n^+ = nR_c\sqrt{\tau_w} \quad (2.17)$$

where ω is the vorticity and n is the normal distance from the wall. In the present computation, as shown in Fig. 2-3, the normal distance n is determined by projecting a vector connecting the point in concern with the root point on the same ζ -direction line, onto the normal vector defined at the root point.

In the outer region, the necessity of finding the edge of the boundary-layer, which existed in the CS model, is removed in the BL model. The eddy viscosity ν_{to} has the following form.

$$\nu_{to} = KC \cdot F_{kleb} n_{max} F_{max} \quad (2.18)$$

or

$$\nu_{to} = KC_{cp} F_{kleb} C_{wk} U_{diff}^2 \frac{n_{max}}{F_{max}} \quad (2.19)$$

with $K=0.0168$, $C_{cp}=1.6$, and $C_{wk}=0.25$. The smaller value of the above two equations is taken. The quantities F_{max} and n_{max} are determined from the function

$$F = n |\omega| [1 - \exp(-n^+/A^+)] \quad (2.20)$$

The quantity F_{max} is the maximum value of F that occurs in a velocity profile, and n_{max} is the value of n at that point. U_{diff} is the difference between maximum and minimum velocity in the profile.

$$U_{diff} = U_{max} - U_{min} \quad (2.21)$$

where U_{min} is taken to be zero except in wakes. The intermittency factor F_{kleb} is given by

$$F_{kleb} = \frac{1}{1 + 5.5(C_{kleb} n/n_{max})^6} \quad (2.22)$$

with $C_{kleb} = 0.3$.

3. Grid Generation

The grid generation method used is the geometrical method. Since the method is described in detail in [11], descriptions are limited here on the modifications made thereafter.

3.1 Body Surface Grid

In the grid generation method, first the surface grids at inner and outer boundaries are generated. The inner boundary usually corresponds to a body surface. The body surface geometry is represented using parametric bi-cubic splines. Then the grid points on the surface can be shifted along the surface according to four geometrical requirements, i.e., orthogonality, smoothing, clustering, and minimum spacing. Fig. 3-1 shows a spline surface on a Series 60 ($C_b=0.6$) hull, which has been determined from given offset points. Fig. 3-2 shows a surface grid on the same hull. Clustering has been imposed toward bow and stern edges, as well as toward bottom and waterline edges. Orthogonality has been imposed at all the four edges.

The same method has been applied to the surface grid on a propeller blade. Fig. 3-3 (a),(b) show surface grids on a propeller blade before and after modification. Clustering is made toward leading, trailing, and tip edges, with various degree of clustering. Here all the points on the surface are allowed to move except for those at the four corners, and therefore highly flexible grid generation is possible.

3.2 Total Grid

After the surface grid is generated, intermediate grid points, which are the points between the inner and outer boundaries, are generated, by simply connecting the corresponding points on the inner and outer boundaries with a straight line, and distributing points on it. Then the initial grid is modified iteratively under the same geometrical requirements as those used in the surface grid modification. The grid points on the boundaries are kept fixed.

The most important change since ref.[11] is in the combination of the grid point modifications. In the original method, grid points were shifted separately due to each modification requirement, whereas in the present method the grid points are shifted only once in each iteration as a result of the combined shifts. The combination is made with weights which change locally according to the local grid geometry. The parameter used to represent local grid geometry is the aspect ratio of a grid cell. The value of the parameter varies greatly depending on the location, since the grid is highly clustered near the solid wall surface. The minimum spacing requirement has been modified. In the old version, if a spacing between two neighboring points in a certain direction is smaller than a given value, that spacing is made larger to the given value in that direction by re-distributing points along that direction with the total length kept unchanged. This requirement was found to be too "active" in some cases, especially near the solid wall boundary where the grid is highly clustered in the normal direction. There the re-distribution in the along-the-wall direction sometimes results in kinks in the other direction. Therefore in the present version

the requirement has been changed to a "passive" one, where, if a grid spacing is found to be smaller than a given value, the modification which makes the spacing even smaller is made zero.

After the grid is modified according to the four requirements, the final grid for high Reynolds number flow computation is obtained by re-clustering. Re-clustering is the process in which the grid is re-distributed, in a single sweep, in the normal-to-wall direction according to a given minimum spacing adjacent to the solid wall and a new given number of grid points in that direction, making the information inherent in the original grid point distribution reflected in the new distribution. This process makes possible to use smaller number of grid points and much larger minimum spacing near the solid wall in the iterative modification stage, thus making the grid generation much faster and easier. No change has been made to the re-clustering process. Fig. 3-4 (a),(b),(c) shows the generated grid around a Series 60 ($C_b=0.6$) hull. The $i=38$ section shown in (b) is approximately at midship, and the $i=60$ section is at the stern edge (see Table 4-1).

4. Computed Results

4.1 Tested Cases and Parameters

Computations were made for seven cases with five different bodies. The bodies vary in the degree of fullness, from a flat plate to a Series 60 ($C_b=0.8$) hull. Table 4-1 shows the cases and the parameters. There im , jm , and km are the number of grid points in ξ (streamwise), η (girthwise) and ζ (normal-to-wall) directions. The experiments with Froude number values (Fn) were made in circulating water channels with free surface, and all the others were made using double models in wind tunnels. Followings are the parameters common to all the computational cases:

$$\begin{aligned} ifp=16 \quad iap=60 \quad x_{upstream\ end} = -0.5 \\ x_{fp} = 0.0 \quad x_{ap} = 1.0 \quad x_{downstream\ end} = 2.0 \\ \text{Outer boundary radius} = 1.0 \quad \beta = 0.1 \end{aligned}$$

where ifp and iap are the numberings in i at bow and stern (or leading and trailing for a flat plate) edges. As shown in Fig. 4-1, the minimum spacing of grid points adjacent to the inner boundary (solid wall or symmetry plane) Δ_{min} is determined as

$$\begin{aligned} \Delta_{min} &= \Delta_{min1} \sqrt{0.1} & (x \leq 0.1) \\ &= \Delta_{min1} \sqrt{x} & (0.1 \leq x \leq 1.0) \\ &= \Delta_{min1} & (1.0 \leq x) \\ \Delta_{min1} &= \frac{0.05}{\sqrt{R_e}} & (4.1) \end{aligned}$$

Computations were made using the Stellar GS-1000 graphic workstation with a vector processor unit and 32 MB main memory. The NS solver took approximately 40 secs (Cases 5,6,7). CPU time per timestep,

using a highly vectorized code. Δt varied from 0.005 NTU (Nondimensional Time Unit) for the Wigley hull case, to 0.001 NTU for the Series 60 $C_b=0.8$ case. It took approximately 4 to 5 NTU to reach the steady state. It corresponds to a day or two in the real time. The grid generation and post-processing were made using interactive graphics on the Sun-4/260 engineering workstation with 32 MB main memory.

4.1 Flat Plate

Fig. 4-2 shows the flat plate grid. The grid was generated based on the Wigley grid at the (x - z) symmetry plane, with y values made zero on the hull surface. The coordinates are nondimensionalized using the length of the flat plate. Transition switch in the turbulence model has been suppressed, i.e. the flow is assumed turbulent starting from the leading edge.

Fig. 4-3, 4-4, and 4-5 show respectively the wall shear stress τ_w , the displacement thickness δ_1 , and the shape factor H . The solid lines are empirical curves [12]

$$\tau_w = \frac{1}{2} C_f' = \frac{1}{2} (2 \log_{10} R_x - 0.65)^{-2.3} \quad (4.1)$$

$$\delta_1 = \frac{0.01738}{R_e} R_x^{0.861} \quad (4.2)$$

$$H = 1.3 \quad (4.3)$$

where C_f' is the local skin friction coefficient. They are in good agreement.

Figs. 4-6 (a),(b), and (c) show logarithmic plot of velocity at three streamwise locations. The empirical curves are

$$\begin{aligned} u^+ &\equiv \frac{u}{u_w} = n^+ \quad \text{in sublayer} \\ &= 2.54 \ln(n^+) + 5.56 \quad \text{in log region} \end{aligned} \quad (4.4)$$

where u_w is the friction velocity. They are in good agreement, both in the sublayer and the logarithmic regions.

Fig. 4-7 shows the kinematic eddy viscosity ν_t distributions. They are nondimensionalized using u_w and the momentum thickness δ_2 . They fall on a single curve. The straight line stemming from the origin has slope value of $\kappa=0.41$ [13]. The horizontal line has the value of 0.828, derived by combining an empirical velocity distribution with $\nu_t/u_w \delta=0.065$, where δ is the boundary-layer thickness. The disagreement with the computed values seems to come from the ambiguity in determining the boundary layer edge.

4.2 Wigley Hull

The results shown in this section are mostly for Case 2 (see Table 4-1), the standard case for the computation of flow past a Wigley hull. Experimental results shown for comparison in this section are all taken from ref.[14]. The flow is assumed laminar up to $x=0.05$, and

turbulent thereafter, to be consistent with the experiment, where the studs were placed at the same location. This applies to all the cases with ship hulls.

Fig. 4-8 shows pressure contours on the hull surface, (x-z) symmetry plane, and (x-y) symmetry plane. The flow is from left to right. The contour lines are wiggle-free. In the previous computation [5], where the non-conservation form was used, there were wiggles at fore and aft ends of the hull.

Fig. 4-9 (a),(b),(c),(d) show wake contours at $x=\text{constant}$ sections, from midship ($x=0.5$) to downstream ($x=1.5$). The contours at an $x=\text{constant}$ section is obtained by interpolating the values at grid point locations using parametric tri-cubic splines, which is an extension of bi-cubic splines to three-dimensions. The computed values show good agreement with the measured values. Fig. 4-10 shows the kinematic eddy viscosity ν_t contours at $i=53$ section ($x \approx 0.95$). The step-wise change of ν_t in the girthwise direction occurs because the location of F_{max} in ζ -direction is determined at either of the grid points, which are widely spaced in the outer region.

Fig. 4-11 (a),(b) show the effect of changing parameters on the wake contour at $x=1.0$. The figure (a) shows the result with $\omega = 5.0$ (Case 3). The difference from the $\omega = 1.0$ result is small, which implies that the value $\omega = 1.0$ in Case 2 is small enough such that the added numerical dissipation terms do not affect the computed result. The figure (b) shows the result where the number of grid points in ζ -direction is doubled. The difference is again small, which implies that the number of grid points used in Case 2 is large enough.

Fig. 4-12 (a),(b),(c) show the wall shear stress τ_w distributions at $z/D = 0.2, 0.5$, and 0.8 sections, where D is the depth of the hull. The empirical curves are the same as those in the flat plate case. The agreement with the measured values are generally good. The τ_w values agree well with the flat plate values in most of the regions.

Fig. 4-13 (a),(b),(c) show the displacement thickness δ_1 distributions at $z/D = 0.2, 0.5$, and 0.8 sections. The agreement is again generally good. The δ_1 values deviate considerably from the empirical flat plate values shown as solid lines in the figures.

Fig. 4-14 shows the shape factor H at $z/D = 0.2, 0.5$, and 0.8 sections. They show tendencies similar to those of flat plate results, except near the stern.

Fig. 4-15 (a),(b),(c) show logarithmic plot of velocity at three $i=\text{constant}$ sections, i.e. $i=25$ ($x \approx 0.07$), $i=38$ ($x=0.5$), and $i=53$ ($x \approx 0.95$). It can be seen that logarithmic law holds in every case. Fig. 4-16 (a),(b),(c) shows the distribution of the kinematic eddy viscosity ν_t , the locations of which correspond to those in Fig. 4-15. The tendency is similar to that of the flat plate.

4.3 Series 60 ($C_b=0.6, 0.7, 0.8$) Hulls

In this section, the measured data shown are taken

from [15] ($C_b=0.6$), [16] ($C_b=0.7$), and [17] ($C_b=0.8$). Fig. 4-17 (a),(b),(c) shows computed pressure contours for Series 60 $C_b=0.6, 0.7$, and 0.8 hulls. They are plotted at the same pressure values as those for the Wigley case (Fig. 4-8). There are slight pressure oscillations just below the points of mapping singularity in the wake.

Fig. 4-18 shows comparison of the computed pressure distribution near the stern region on the $C_b=0.6$ hull with the measurement [15]. The agreement is good, though there is systematic deviation which increases toward midship, and the adverse pressure gradient is greater in the computed result.

Fig. 4-19 (a) to (h) show the wake contours. The agreement with the measurements are good in general, except in the wake. There the downward movement of the low speed region near the (x-z) symmetry plane is not captured in the computation. There are two possible reasons for this failure. One is that the intensity of the downwash due to the pair of longitudinal vortices is insufficient. The other is in the way the eddy viscosity is determined. In the wake, the normal distance n^+ is taken from the (x-z) symmetry plane. However, when the flow near the stern is highly three-dimensional, the (x-z) symmetry plane is not necessarily suitable for this purpose, in contrast to the situation with the Wigley hull. There the longitudinal vortices are not strong, and the flow in the wake remains similar to that of a flat plate.

Figs. 4-20, 4-21, 4-22 show the wall shear stress τ_w , the displacement thickness δ_1 , and the shape factor H at three $z=\text{constant}$ locations. There at $z/D=0.8$, the separation occurs near the stern.

Fig. 4-23 (a),(b),(c) show the logarithmic plot of velocity at three streamwise locations. It is seen that all the points adjacent to the solid wall are well within the viscous sublayer as the turbulence model used demands, and that all the velocity profiles follow the logarithmic distribution law in the inner layer. They suggest that the Baldwin-Lomax turbulence model, a simple zero-equation model, can be used for this type of flow. Fig. 4-24 (a),(b),(c) show the kinematic eddy viscosity ν_t distributions at the same three streamwise locations as in the logarithmic velocity plot. The distributions are similar to those in the Wigley hull case shown in Fig. 4-16.

Finally, Fig. 4-25 (a),(b) show the wake contours for the $C_b=0.7$ case (Case 6 in Table 4-1), and Fig. 4-26 shows the wake contours for the $C_b=0.8$ case (Case 7). In the $C_b=0.7$ case, the computed wakes still show reasonable agreement with the measurements in those streamwise locations. However, in the $C_b=0.8$ case, the agreement becomes poor. By looking at the three computed wake contours, i.e. the cases $C_b=0.6, C_b=0.7$, and $C_b=0.8$, a systematic trend is observed. In the stern region, the wake near the bottom becomes thinner than the measured one, and the wake in the mid-depth region becomes very thick, as the fullness of the

ship hull (Cb) becomes greater. Clearly the turbulence model needs modification there (see Supplement).

5. Conclusions

Flows past ship hulls were computed and compared with measurements. The NS solver used is the IAF scheme, where the pseudo-compressibility is introduced in the continuity equation, in order to make the system of equations hyperbolic. The accuracy and convergence of the computed results were tested by computing flows using different number of grid points, or using different amount of the added numerical dissipation terms.

The Baldwin-Lomax zero-equation turbulence model was used. The validity and limitation of the turbulence model was tested by computing flows past five different bodies. They are a flat plate, a Wigley hull, Series 60 Cb=0.6, 0.7, and 0.8 hulls. They vary in the degree of fullness, from complete flatness of the flat plate to high fullness of the Series 60 C=0.8 hull. By comparing the computed results with measurements, the turbulence model was found to be useful for fine hull forms, such as a flat plate, a Wigley hull, and a Series 60 Cb=0.6 hull. However, the agreement between the computed and measured data was not satisfactory for the Series 60 Cb=0.7 or 0.8 hulls. This suggests that the turbulence model needs modification for such flows where strong adverse pressure gradient exists and three-dimensionality becomes important.

The grid generation method called the geometrical method was used to generate grid around those ship hulls mentioned above. The method was also applied to generate a surface grid on a propeller blade. The body surface was represented using parametric bi-cubic splines, and the grid points on the body surface were allowed to move along the surface, in order to meet the requirements imposed, i.e. orthogonality, clustering, smoothing, and minimum spacing.

Acknowledgements

The author would like to thank Profs. I. Tanaka and T. Suzuki of Osaka University, Prof. T. Okuno of University of Osaka Prefecture, and Prof. V.C. Patel of University of Iowa for providing references and material on the measured data used in the present work. The author also thanks the members of the CFD group at the Ship Research Institute for many valuable discussions.

References

- [1] Himeno, Y."Calculation Method of the Two-Dimensional Turbulent Boundary-Layers", Proceedings of the Symposium on Viscous Resistance, SNAJ, pp.59-93 (1973) (In Japanese).
- [2] Chen, H.C. and Patel, V.C."Calculation of Trailing-Edge, Stern and Wake Flows by a Time-Marching Solution of the Partially-Parabolic Equations", IIHR Report No. 285, IIHR, University of Iowa (1985).
- [3] Sato, T. et al."Finite-Difference Simulation Method for Wave and Viscous Flows about a Ship", J. of SNAJ vol. 160, (Dec. 1986).
- [4] Masuko, A. et al."Numerical Simulation of Viscous Flow around a Series of Mathematical Ship Models", J. of SNAJ vol. 162, pp.1-10 (Dec. 1987).
- [5] Kodama, Y."Computation of High Reynolds Number Flows Past a Ship Hull Using the IAF Scheme", J. of SNAJ vol. 161, pp.25-34 (1987).
- [6] Beam, R.M. and Warming, R.F."An Implicit Factored Scheme for the Compressible Navier-Stokes Equations", AIAA Journal, Vol.16, No.4, (April 1978).
- [7] Kodama, Y."Three-Dimensional Grid Generation around a Ship Hull Using the Geometrical Method", J. of SNAJ vol. 164, pp.9-16 (1988).
- [8] Cebeci, T. and Smith, A.M.O."A Finite-Difference Method for Calculating Compressible Laminar and Turbulent Boundary Layers", J. of Basic Engineering, Trans. of the ASME, pp.523-535 (Sept. 1970).
- [9] Rodi, W."Turbulence Models and Their Application in Hydraulics", IAHR (1980).
- [10] Stock, H.W. and Haase, W."Determination of Length Scales in Algebraic Turbulence Models for Navier-Stokes Methods", AIAA Journal, Vol.27, No.1, (January 1989).
- [11] Kodama, Y."Three-Dimensional Grid Generation around a Ship Hull Using the Geometrical Method", J. of SNAJ vol. 164, pp.9-16 (Dec. 1988).
- [12] Schlichting, H."Boundary-Layer Theory", 6th Edition, McGrawHill (1968).
- [13] Cebeci, T. and Bradshaw, P."Momentum Transfer in Boundary Layers", Hemisphere Publishing, p.168 (1977).
- [14] Sarda, O.P."Turbulent Flow Past Ship Hulls - An Experimental and Computational Study", Ph.D. Thesis, Univ. of Iowa (Aug. 1986).
- [15] Toda, Y. et al."Mean-Flow Measurements in the Boundary Layer and Wake of a Series 60 Cb=0.6 Model Ship With and without Propeller", IIHR Report No.326, Iowa Institute of Hydraulic Research, Univ. of Iowa (Nov. 1988).
- [16] Okuno, T."Study on Three-dimensional Boundary-Layers on Ship Hulls", Ph.D. Thesis, Univ. of Osaka Prefecture (In Japanese). (Nov. 1980).
- [17] Fukuda, K. and Fujii, A."Turbulence Measurements in Three Dimensional Boundary Layer and Wake around a Ship Model", J. of SNAJ, Vol.150 pp.85-98 (In Japanese) (Dec. 1981).

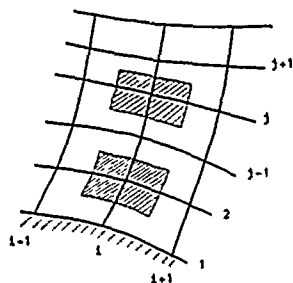


Fig. 2-1 Area covered by the discretized governing equations.

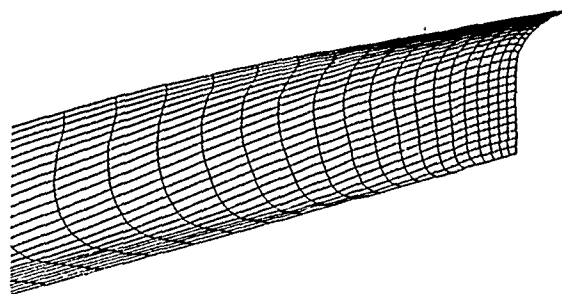
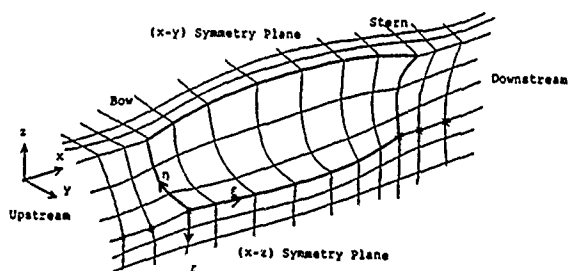
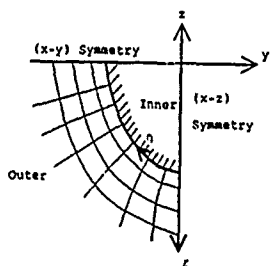


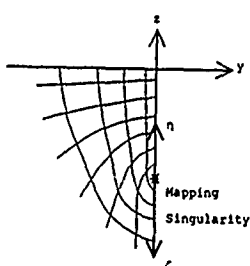
Fig. 3-2 Surface grid on a Series 60 ($C_b=0.6$) hull



(a) Perspective view



(b) Body section



(c) Wake region

Fig. 2-2 Grid topology and boundaries

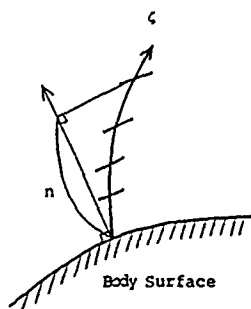


Fig. 2-3 Normal distance from body surface

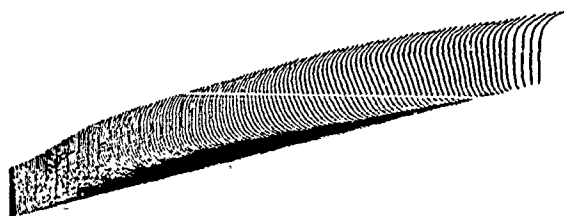
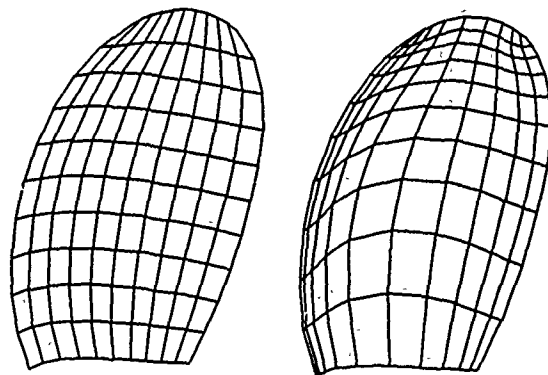


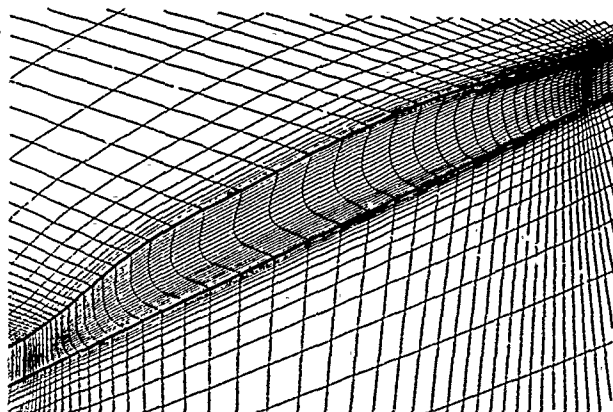
Fig. 3-1 Spline surface on a Series 60 ($C_b=0.6$) hull



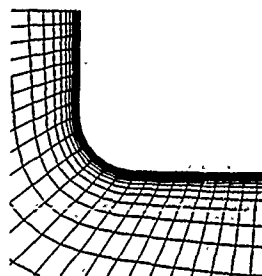
(a) Initial grid

(b) Modified grid

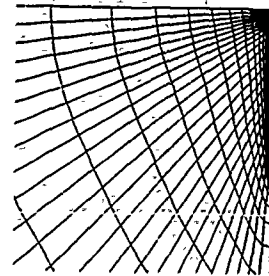
Fig. 3-3 Surface grid on a propeller blade



(a) Perspective view



(b) $i=38$ section (midship)



(c) $i=60$ section (stern)

Fig. 3-4 Grid around a Series 60 ($C_b=0.6$) hull

Table 4-1 Computation parameters

Case	Body	im	jm	km	ω	Re	Experiment	Ref.
1	flat plate	81	5	31	1.	4.0×10^6	Re= 1.7×10^6 to 18×10^6	[12]
2	Wigley	81	15	31	1.	4.0×10^6	Re= 4.5×10^6	[14]
3	Wigley	81	15	31	5.	4.0×10^6	Re= 4.5×10^6	[14]
4	Wigley	81	15	61	1.	4.0×10^6	Re= 4.5×10^6	[14]
5	S. 60 Cb=0.6	81	25	31	1.	4.0×10^6	Re= 3.94×10^6 , Fn=0.16	[15]
6	S. 60 Cb=0.7	81	25	31	1.	1.7×10^6	Re= 1.7×10^6 , Fn=0.21	[16]
7	S. 60 Cb=0.8	81	25	31	1.	2.1×10^6	Re= 2.1×10^6	[17]

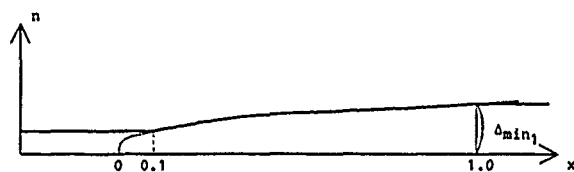


Fig. 4-1 Minimum spacing



L.E. T.E.

Fig. 4-2 Flat plate grid

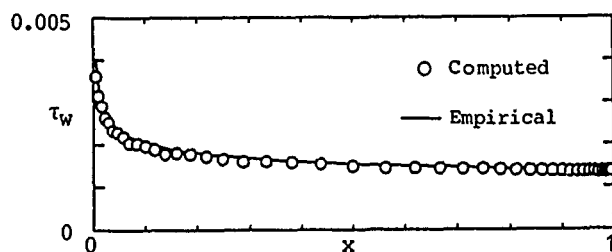


Fig. 4-3 Wall shear stress τ_w on a flat plate

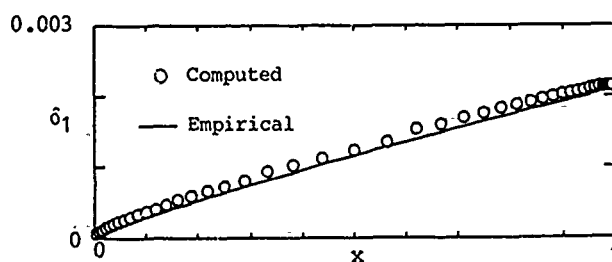


Fig. 4-4 Displacement thickness δ_1 on a flat plate

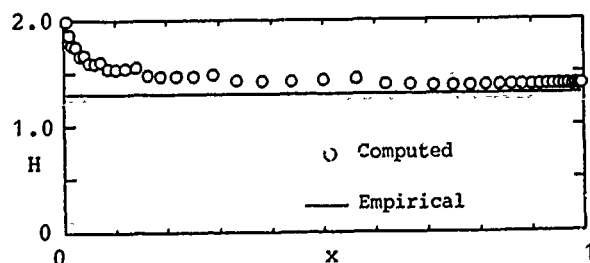
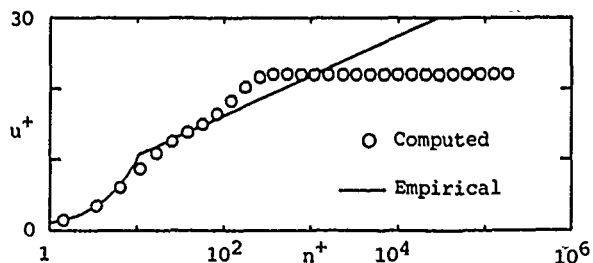
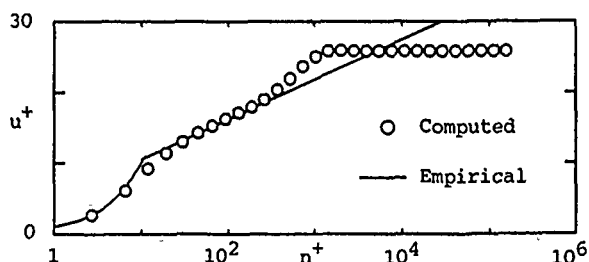


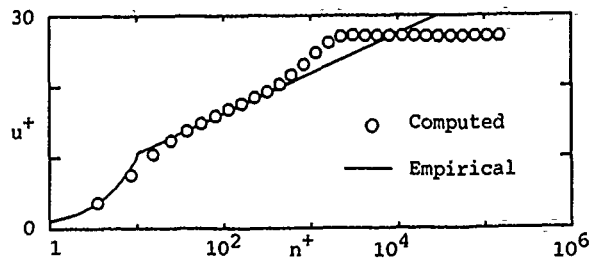
Fig. 4-5 Shape factor H on a flat plate



(a) $x=0.07$



(b) $x=0.5$



(c) $x=0.953$

Fig. 4-6 Log plot of velocity on a flat plate

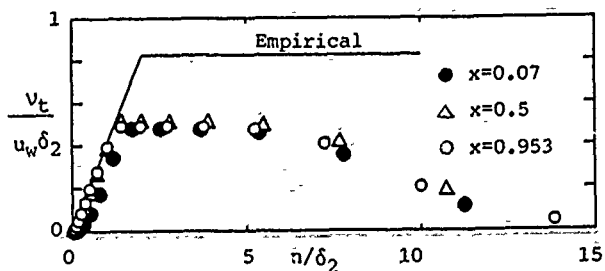


Fig. 4-7 Kinematic eddy viscosity ν_t on a flat plate

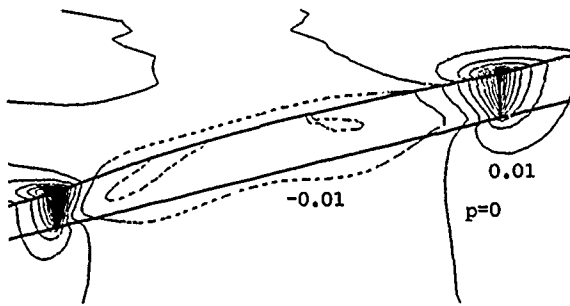


Fig. 4-8 Pressure contours of a Wigley hull

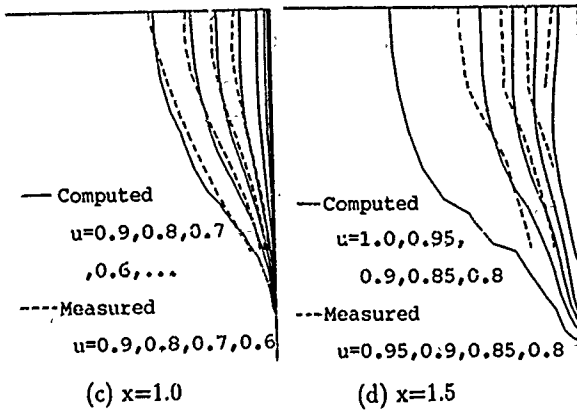
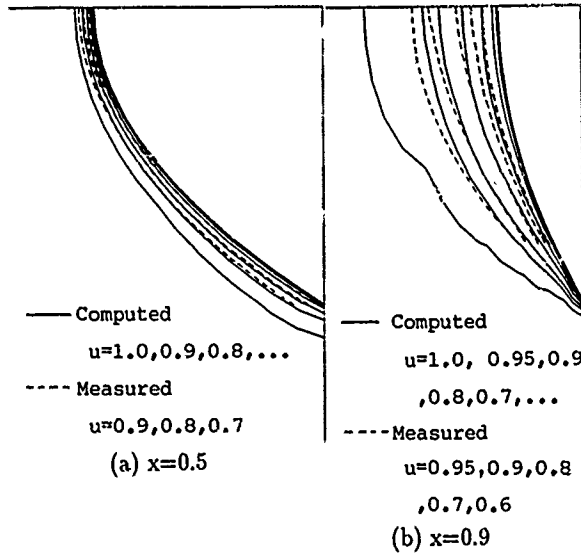


Fig. 4-9 Wake contours of a Wigley hull

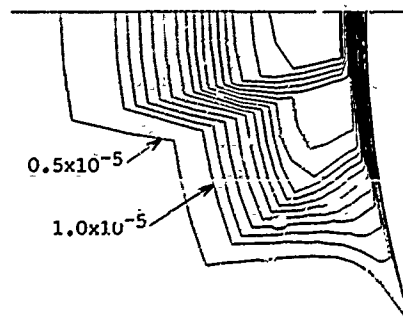


Fig. 4-10 Kinematic eddy viscosity ν_t of a Wigley hull at $i=53$ ($x \sim 0.95$)

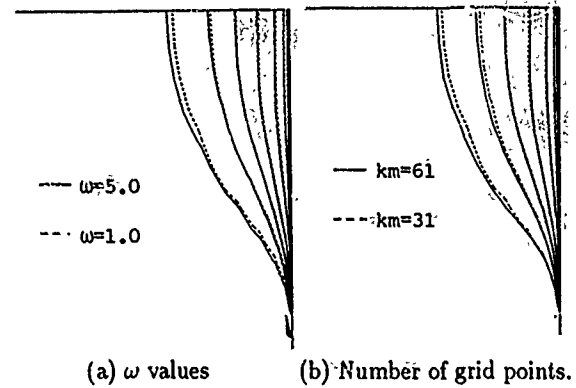


Fig. 4-11 Effect of changing parameters on wake at $x=1.0$

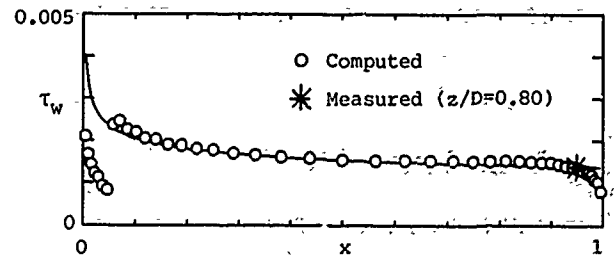
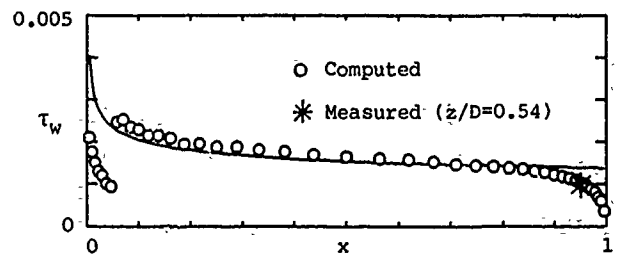
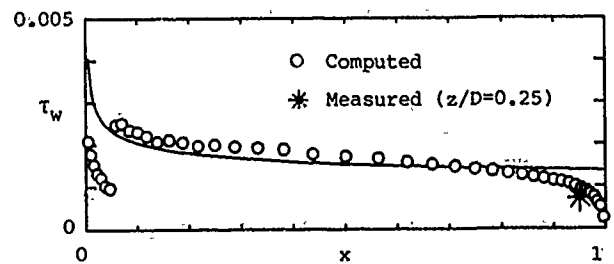
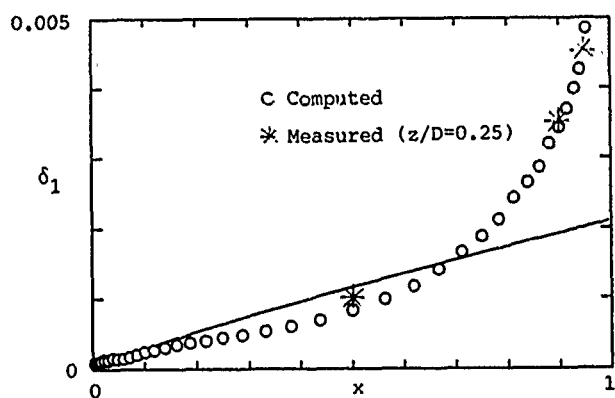
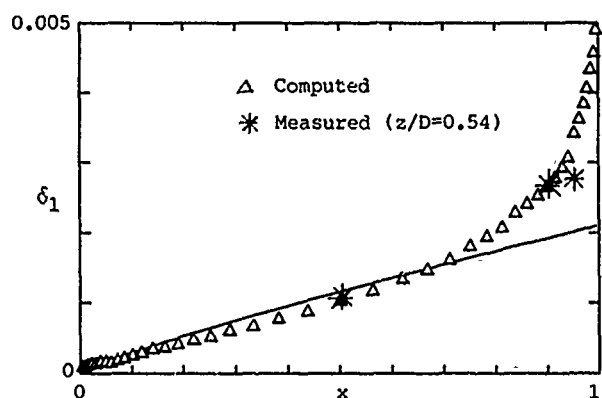


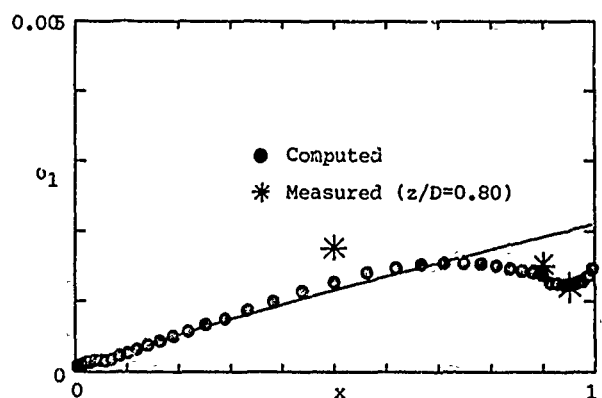
Fig. 4-12 Wall shear stress τ_w on a Wigley hull



(a) $z/D = 0.2$



(b) $z/D = 0.5$



(c) $z/i = 0.8$

Fig. 4-13 Displacement thickness δ_1 on a Wigley hull

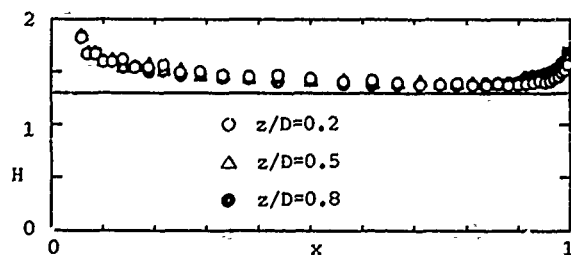
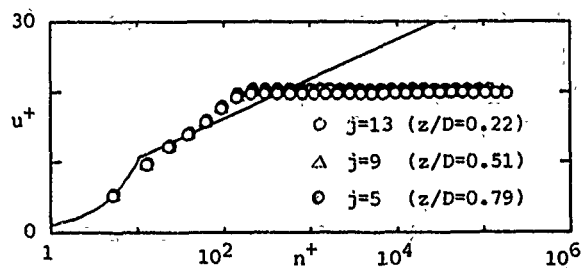
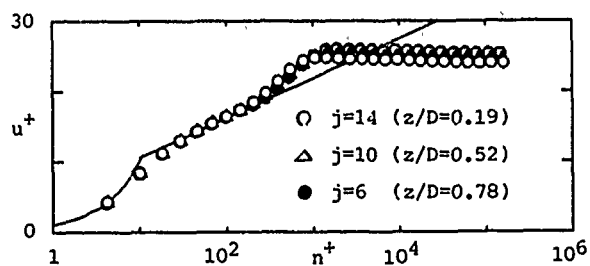


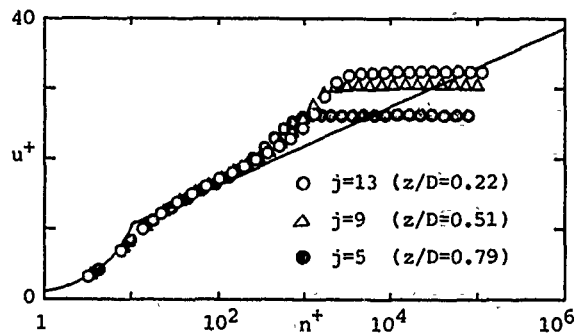
Fig. 4-14 Shape factor H on a Wigley hull



(a) $i = 25$ ($x \approx 0.07$)

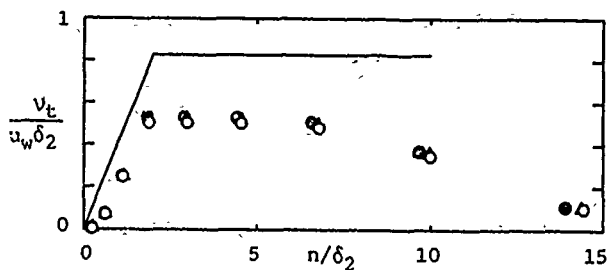


(b) $i = 38$ ($x \approx 0.5$)

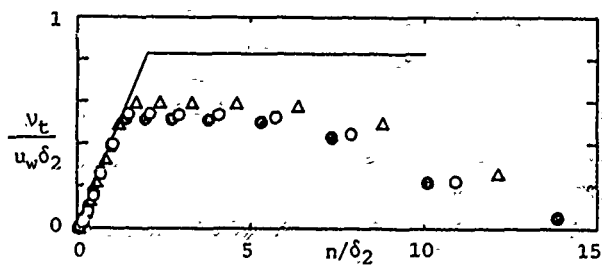


(c) $i = 53$ ($x \approx 0.95$)

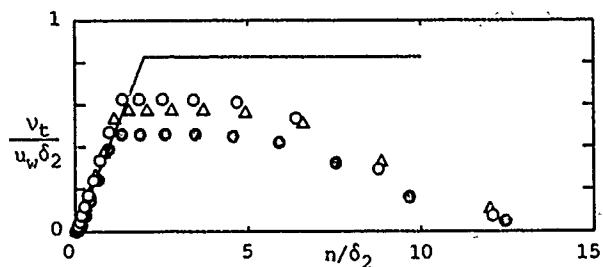
Fig. 4-15 Log plot of velocity on a Wigley hull



(a) $i = 25$ ($x \approx 0.07$)



(b) $i = 38$ ($x \approx 0.5$)



(c) $i = 53$ ($x \approx 0.95$)

Fig. 4-16 Kinematic eddy viscosity ν_t on a Wigley hull

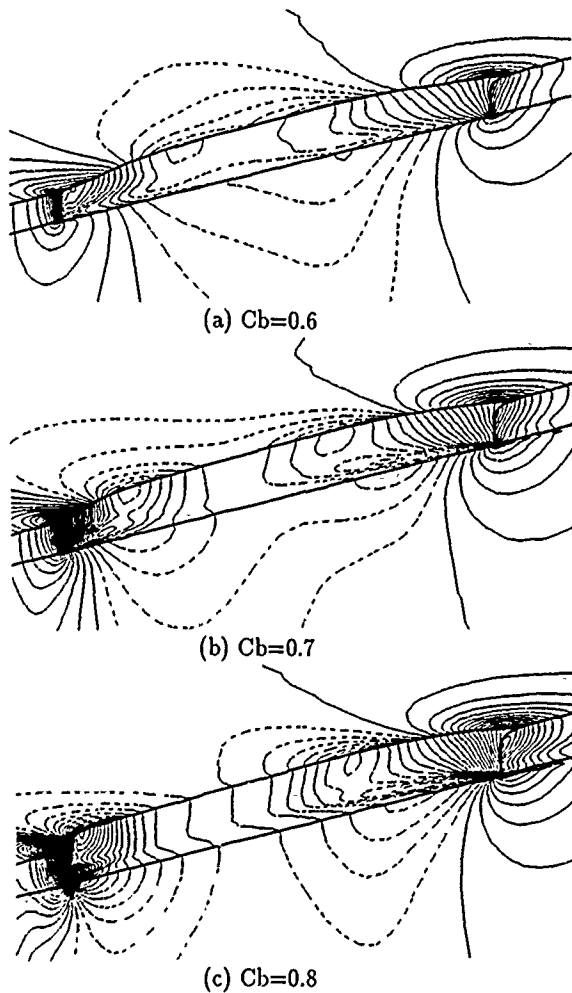


Fig. 4-17 Pressure contours on Series 60 hulls

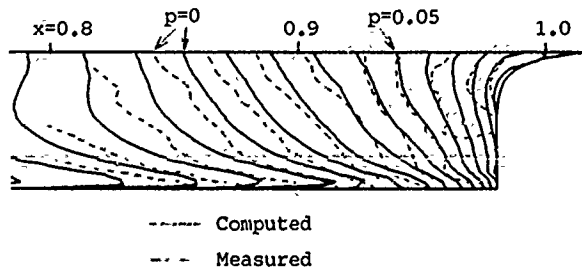


Fig. 4-18 Pressure contours at the stern of a Series 60 ($C_b=0.6$) hull

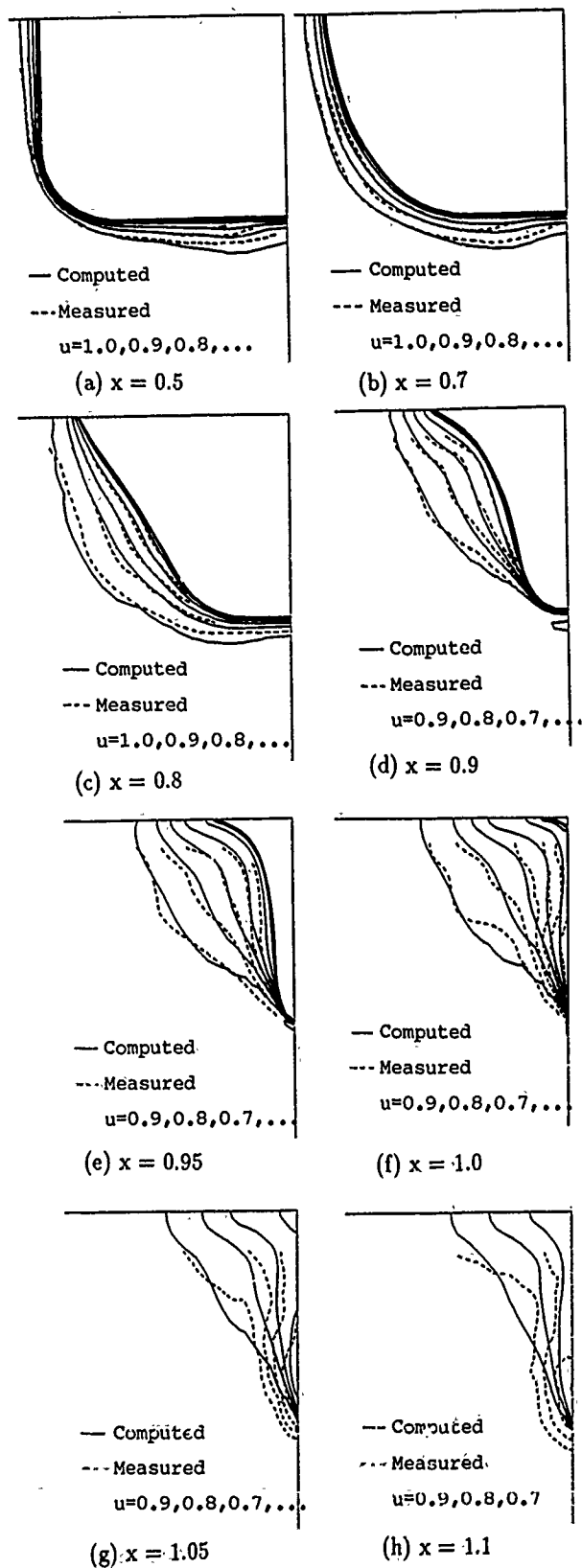


Fig. 4-19 Wake contours on a Series 60 ($C_b=0.6$) hull

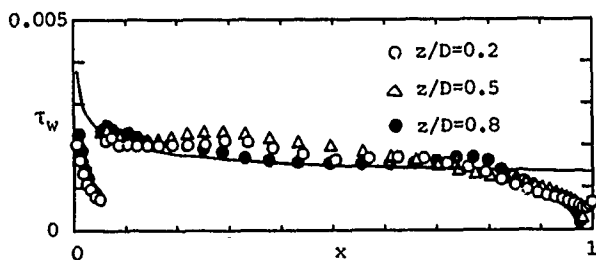


Fig. 4-20 Wall shear stress τ_w on a Series 60 ($C_b=0.6$) hull

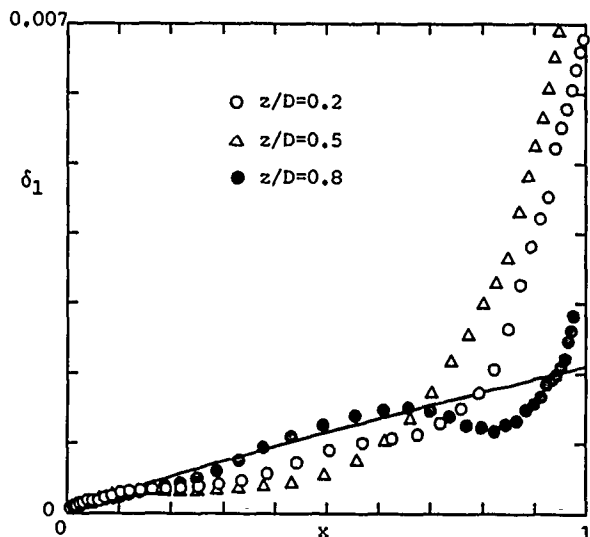


Fig. 4-21 Displacement thickness δ_1 on a Series 60 ($C_b=0.6$) hull

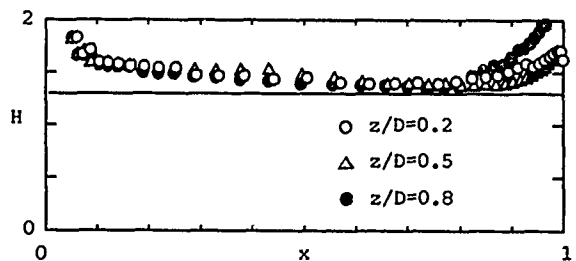
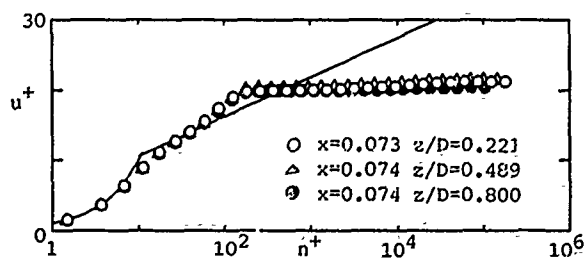
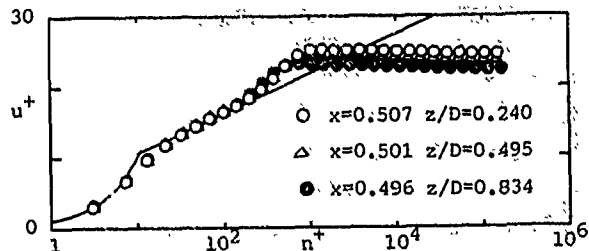


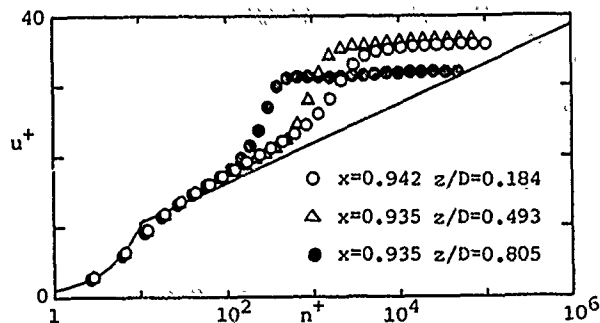
Fig. 4-22 Shape factor H on a Series 60 ($C_b=0.6$) hull



(a) $i = 25$

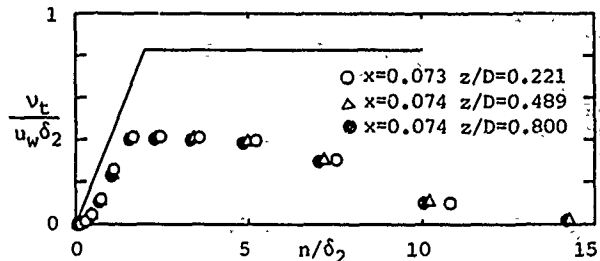


(b) $i = 38$

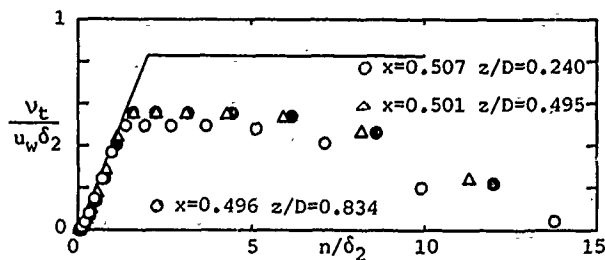


(c) $i = 53$

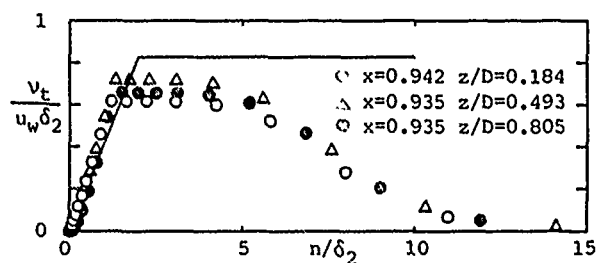
Fig. 4-23 Log plot of velocity on a Series 60 ($C_b=0.6$) hull



(a) $i = 25$



(b) $i = 38$



(c) $i = 53$

Fig. 4-24 Kinematic eddy viscosity ν_t on a Series 60 ($C_b=0.6$) hull

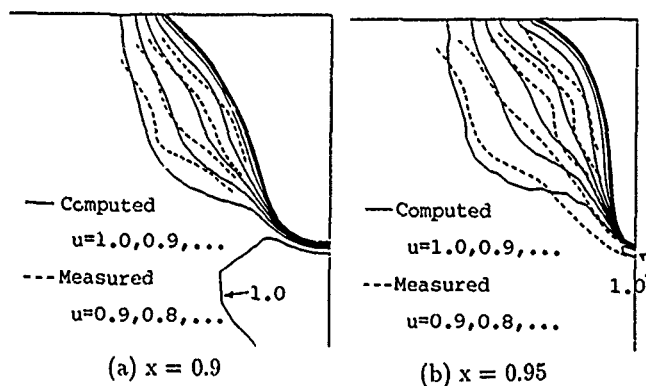


Fig. 4-25 Wake contours on a Series 60 ($C_b=0.7$) hull

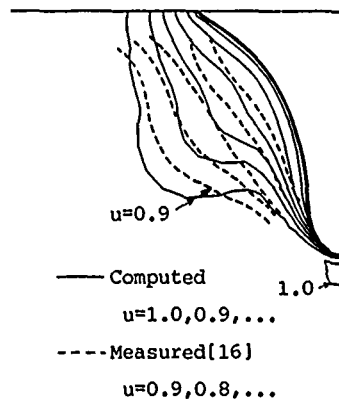


Fig. A-1 Wake contours on a Series 60 ($C_b=0.8$) hull. $x=0.95$

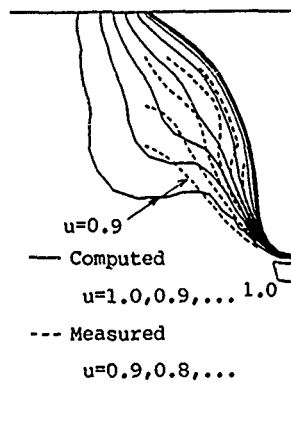


Fig. 4-26 Wake contours on a Series 60 ($C_b=0.8$) hull. $x = 0.95$

Supplement

After the present paper was submitted for the presentation at the Conference, the following disagreement between the two measured results [16],[17] on the wake contours of the Series 60 ($C_b=0.8$) model has been found out. In Fig. A-1 the computed wake is compared

with the measurement obtained by Okuno [16], while in Fig. 4-26 it is compared with the the measured result obtained by Fukuda and Fujii [17]. The computed wake in Fig. A-1 shows reasonable agreement with the Okuno's measurement, whereas it shows significant discrepancy from the Fukuda's measurement in Fig. 4-26. This clearly shows that measurements must be carefully validated before they are used in the validation of computations.

DISCUSSION

by C.M. Lee

I know that a few people in the past have shown the NS-Solver results for the DTRC body forms. I am wondering if further progresses in computational techniques for a fully appended submerged body with propeller have been made.

From the paper of Dr. Fujii this morning, the CDF people in aeronautics seem to have progressed to the stage that they can compute the flow about a fully appended airplane. Have you tried to include the sail and stern control surfaces in your computations?

Author's Reply

I have tried to compute a ship-stern flow with propeller effect, using the body force method. Though I got a converged result, there was pressure oscillation, which is due to the use of central differencing. I have not yet tried to compute flows with appendages. In order to do that, I think a multi-block approach should be used.

Recent Developments in a Ship Stern Flow Prediction Code

M. Hoekstra
Maritime Research Institute Netherlands
Wageningen, The Netherlands

Abstract

This paper is concerned with developments in a numerical method for the prediction of the steady incompressible flow around the stern of a ship. The method is based on a finite-difference discretisation of the Reynolds-averaged Navier-Stokes equations on a boundary-fitted curvilinear grid. The attention will be focused on three aspects, viz. the choice of the velocity variables, the boundary conditions and the global (outer) iteration process for the pressure field. Various illustrations will be given of the improved performance of the method.

1. Introduction

It is in the first place owing to computer hardware developments that a computational simulation of the ship stern flow field has become feasible. Indeed, the availability of adequate computer facilities may be considered as a prerequisite for an accurate calculation to be carried out. It is not a sufficient condition, however. For some years already, the numerical simulation of the steady viscous flow around a ship's stern - usually under neglect of free surface effects - has been a prominent research topic. Yet, something like a *communis opinio* on how a reliable, efficient and robust code is to be constructed has not been attained. It indicates that developing a suitable algorithm for the solution of the Reynolds-averaged Navier-Stokes equations for incompressible flows around complex body shapes is not plain sailing.

At the author's institute, work in the field of stern flow computation was initiated around 1980 and has continued steadily since. It has resulted in a computational procedure that has been applied with some success to a number of ship forms and axisymmetric bodies. The main features of the method have been outlined previously [1,2,3] and a brief recollection of

these features (Section 2) will suffice here as a framework for the subsequent discussion of some aspects of the method.

Where the title of this paper promises the presentation of recent developments, 'recent' is to be interpreted in relation to the time of appearance of the above references. The length limitations to which this paper is subjected do not allow a presentation of all changes that have taken place in the code since 1985. Therefore three major items have been selected for discussion here. They are: the choice of the velocity variables in relation to regular solution behaviour near grid singularities in the wake (Section 3); boundary conditions and their numerical implementation (Section 4) and a new global pressure relaxation scheme (Section 5). Moreover, results of a representative application will be shown as an illustration of the progress that has been made (Section 6).

2. Outline of computational procedure

We are interested in a numerical simulation of the behaviour of the flow around the stern of a ship, being towed steadily through still water. The free surface disturbances created by the ship are assumed to be of little significance so that it is allowed to replace the undisturbed free surface by a symmetry plane. Thus, taking a reference frame moving with the ship, we consider actually the double model of the submerged part of a ship, held fixed in a uniform flow directed from bow to stern. The flow domain is now assumed to be unbounded and the fluid to be incompressible. Three subdomains are distinguished as shown in Fig. 1, viz. the external flow zone where the flow behaves as being inviscid and irrotational, the boundary-layer zone, covering the forward part of the hull surface, where first-order boundary-layer theory is supposed to provide an adequate description of the flow; the stern-flow-and-wake zone which is of

primary concern in this paper. In the latter zone we solve effectively the Reynolds-averaged Navier-Stokes equations but we shall assume that a predominant flow direction exists. Among other things, it allows us to drop all diffusion terms associated with that primary flow direction. The equations are supplemented by an algebraic turbulence model. The boundary conditions will be described in Section 4.

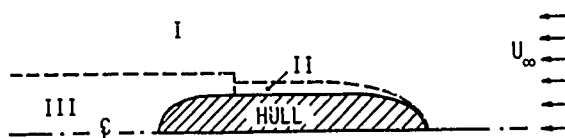


Fig. 1. Division of flow field into three zones

The flow-governing equations are written in terms of general curvilinear coordinates. The contravariant formulation of the momentum equations is adopted, which gives three relations expressing momentum conservation along each of the three coordinate lines. The velocity components and the pressure are the dependent variables but a particular choice for the velocity variables is made as described in Section 3. The continuity equation is solved in its original form and is not replaced by a Poisson equation for the pressure as in Marker-and-Cell type methods.

The equations are discretised on a boundary-fitted curvilinear grid. It is a single-block regular grid of $N_X * N_Y * N_Z$ nodes. The grid is partly non-orthogonal but conceptually simple. All variables are defined on the grid nodes, in other words we do not apply grid staggering of one kind or another. That is convenient in many respects but it poses certain demands on the discretisation of the pressure gradients and the continuity equation which we are careful to fulfill to avoid 'checkerboarding' [4]. The discretisation is second or third order accurate with the exception of the main stream pressure gradient which is of first order accuracy. All derivatives with respect to the coordinate associated with the main stream direction are modelled by upstream difference formulae except the pressure gradient. Newton linearization is applied to the convective terms.

The solution is obtained iteratively where the iteration sequence may be characterized as a multiple-sweep space-matching process which takes maximum benefit of the existence of a predominant flow direction. In fact, two iteration cycles can be distinguished: the local (or inner) and the global (or outer) iteration process.

The local process refers to the solution of a subset of difference equations applying to all grid nodes having the same value of the main-stream coordinate. It is based on the Coupled Strongly Implicit Procedure (CSIP) [5], an incomplete factorization scheme, and yields a simultaneous solution of all variables in a cross-section of the computation domain. Iteration is required both by the non-linearity of the differential equations and by the incompleteness of the factorization. The CSIP has been selected because we think that a high degree of implicitness is desirable if not necessary for an efficient solution algorithm and because it retains the coupling between the momentum and the continuity equations in the numerical solution.

The global iteration process involves the evaluation of the solution in repeated sweeps from the upstream to the downstream boundary of the computation domain. This process allows the influence of downstream occurrences to be felt by the upstream flow, an inherent property of the mathematical model used. To improve its convergence rate, each downstream sweep is followed by an update of the solution of the pressure field in a reversed sweep as will be explained in Section 5. A further enhancement of the computational efficiency is obtained by grid sequencing, with which we mean that the grid used is initially very coarse in the mainstream direction and is subsequently refined in two or three stages.

3. Grid singularities

Fig. 2 gives a sketch of the computation domain as it looks after the symmetry properties of the flow have been taken into account. In addition to the Cartesian reference frame x, y, z a curvilinear boundary-fitted coordinate system ξ, η, ζ is introduced. A transformed space can be imagined in which ξ, η, ζ forms a rectangular coordinate system and in which the hull surface is plane. The appearance of the ξ, η, ζ system in physical space depends on the transformation relations between ξ, η, ζ and x, y, z .

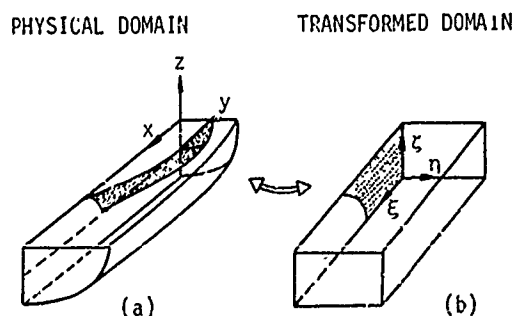


Fig. 2. Computation domain

To simplify the grid generation procedure we have chosen $\xi = x$ so that transverse sections in the physical space remain so in the transformed space. An orthogonal mesh is then constructed in selected transverse sections by a procedure which relies on conformal mapping although the final mesh is not conformal due to subsequent stretching [6]. By connecting these grids, the 3-D mesh is completed. It leads inevitably to non-orthogonality of the ξ, η and ξ, ζ lines in a part of the computation domain.

However, before this task can be carried out it must be decided where the four corners of the transverse section in the transformed space are to appear in the physical space. A glance at Fig. 2 will help to recognize that the choice is obvious in the upstream part of the domain but less so behind the stern. Referring to Fig. 3, the location of point A corresponding with A' can be taken somewhere between B and D or even coinciding with either of these points. In practice the final choice is primarily governed by the requirement that the ξ -lines must roughly be aligned with the main flow. The points A are therefore usually located on a straight line extending from the keel (cf. Fig. 2).

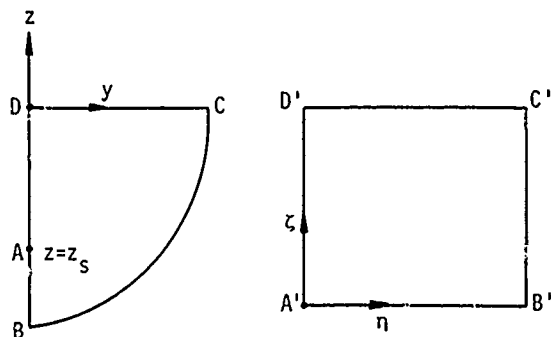


Fig. 3. Cross-section of physical (left) and transformed (right) computation domain behind hull

The coordinate transformation is singular in such points: the Jacobian of the transformation vanishes. Singularities may also appear elsewhere on the boundaries of the domain - e.g. along the waterline when the frame line of the hull does not meet the symmetry plane (undisturbed free surface) at a right angle - but the mapping technique used excludes their occurrence in the interior of the domain.

Grid singularities may deteriorate the accuracy of the calculations or destabilize the iterative solution process [7]. This is particularly true when there is a finite velocity in the singularity as is the case behind the hull. Suppose for example that coordinate-

oriented physical velocity variables are used, so that v and w are the η and ζ component of the physical velocity. Then we must have $v=0, w=\text{finite}$ along AD (Fig. 3), while $w=0, v=\text{finite}$ along AB. It leads to a conflict at A because v and w cannot both be zero in A. Although this problem can be circumvented by e.g. grid staggering, the accuracy of finite-difference approximations is likely to be low in the vicinity of the singularity due to the sudden changes of some of the variables.

We alleviate the difficulty by a special choice of the velocity variables, which may be explained as follows. The coordinate transformation near the grid singularity in the wake tends to

$$y + i(z - z_s) = -i\alpha(R\eta + i\zeta)^2 \quad (1)$$

where $i = \sqrt{-1}$, $R = \sqrt{g_{22}/g_{33}}$ is the grid cell aspect ratio, α is a proportionality constant while the singularity is located at the point $y = 0, z = z_s$. Because of the relation (1) the singularity is called parabolic. Formula (1) is a well-known type of transformation in potential flow theory. It can be used to transform a parallel flow to a corner flow. If the parallel flow is supposed to occur in the physical space and is described by a velocity potential

$$\Phi = V_T(z - z_s), \quad (V_T \text{ is constant}),$$

we find with the aid of (1)

$$\Phi = V_T\alpha(\zeta^2 - R^2\eta^2).$$

Thus

$$V_2 = \frac{\partial \Phi}{\partial \eta} = -2\alpha R^2 V_T \eta;$$

$$V_3 = \frac{\partial \Phi}{\partial \zeta} = 2\alpha V_T \zeta.$$

We see that the velocity components V_2, V_3 behave nicely in the transformed space. They vanish at the corner and increase linearly away from it so that accurate discretisation is possible.

It is important now to recognize that V_2, V_3 are covariant quantities since Φ is a scalar. Apparently, covariant velocity components behave regularly near a parabolic singularity in contrast to physical or contravariant components as can readily be verified. For example the contravariant velocity component V^2 is in an orthogonal grid (as we have behind the hull) given by

$$V^2 = g^{22}V_2 = V_2/g_{22} = -2\alpha R V_T \eta / \sqrt{g}$$

and tends to infinity for $\eta \rightarrow 0$.

Formerly, we employed the contravariant velocity components directly as dependent variables in the mathematical formulation. Denoting them by V^i ($i = 1, 2, 3$), we define now the three velocity variables as

$$u = V^1; v = g_{22}V^2; w = \sqrt{g}V^3$$

instead. Notice that v and w are not strictly covariant velocity components. But the multiplication factors for both V^2 and V^3 involve the Jacobian \sqrt{g} ($g_{22} = R\sqrt{g}$), which is sufficient to obtain regular behaviour near the singularity.

If the y, z velocity components in the physical space must be determined from these variables, difficulties are encountered at the singularity. There is no trouble, however, in evaluating them in neighbouring grid points whereupon the required values at the singular point can be derived by interpolation.

4. Boundary conditions

The stern-flow-and-wake zone has eight boundaries (Fig. 2): the hull surface, an inlet and an outlet boundary and the external boundary, the remaining boundary surfaces being located in symmetry planes. The terminology is intentional: the velocity component u is assumed to be positive on both the in and outlet boundaries. On the other hand the flow may enter or leave through the external boundary.

Like the Navier-Stokes equations themselves, the Reynolds-averaged Navier-Stokes equations for incompressible flow require three boundary conditions on all boundaries [e.g. 8]. However, if diffusion along the coordinate associated with the predominant flow direction is neglected, the equations exhibit Euler character in that direction with a consequent change in the boundary condition requirements. Three conditions are still required at the inflow boundary, but only one condition must be imposed at the outflow boundary [9].

It is obvious what conditions should be applied on the natural boundaries of the computation domain, viz. the hull surface and the symmetry planes. On the hull surface the no-slip and the impermeability condition give us three Dirichlet conditions for the velocity components. On a symmetry plane there is one Dirichlet condition for the normal velocity component and a Neumann condition for each of the two other components.

It is perhaps worth mentioning here that we impose the hull boundary conditions directly by calculating the flow down to the hull and not indirectly via the use of wall functions as an approximate description of the near-wall flow behaviour.

The remaining boundaries are artificial boundaries and it is not immediately clear what are suitable conditions. On the outlet boundary only one condition must be prescribed, either for the pressure or for the normal velocity (i.e. u) [9]. In view of our discretisation it is natural to choose a condition for the pressure. A Neumann type condition is to be preferred because it is less restrictive and allows some pressure variation over the outlet plane which may be important in view of the frequent occurrence of longitudinal vortices in a ship's wake; the existence of such vortices demand the pressure to be somewhat lower in the vortex core than in its surroundings.

Mostly we use a vanishing longitudinal pressure gradient at the outlet plane, but sometimes a non-zero value, derived from potential flow calculations, is preferred.

A remark should be made here about the numerical implementation of the pressure boundary condition. In a space-marching scheme the discretisation of the streamwise pressure gradient involves a pressure value of the current as well as one of the preceding global iteration, in our discretisation.

$$(p_{i+1}^{n-1} - p_i^n)/\Delta x_i$$

where n counts the global iterations and i is the x -station index. When the solution on the outlet plane at station x_{NX} is to be determined, a value for p_{NX+1}^{n-1} must be derived from the boundary condition, $p_x = pgrad$ say. One might feel tempted to simply replace the pressure gradient as discretised above by the given boundary condition on the outlet plane:

$$(p_{NX+1}^{n-1} - p_{NX}^n)/\Delta x_{NX} = pgrad.$$

It leads to unquiet solution behaviour near the outlet plane which eventually may deteriorate the global convergence. The correct procedure is to apply the Neumann condition for the pressure for each iteration level separately. Thus

$$(p_{NX+1}^n - p_{NX}^n)/\Delta x_{NX} = pgrad \text{ for all } n$$

which implies that the pressure gradient term in the ξ -momentum equation must be modelled on the outlet boundary as :

$$pgrad + (p_{NX+1}^{n-1} - p_{NX}^n)/\Delta x_{NX},$$

i.e. the discretisation must include the pressure change with respect to the previous sweep.

The three conditions to be specified on the inlet boundary must, again in view of the discretisation, apply to the velocity components. Dirichlet condi-

tions may be chosen but since inlet conditions are obtained either from usually incomplete experimental data or from thin-boundary-layer calculations carried out in an approximate grid geometry, they are often imperfect, leading to a non-smooth solution near the inlet plane. This is the reason why we mostly replace the Dirichlet condition for v by a Neumann condition.

Let us next turn to the boundary conditions on the external boundary. The old practice was to specify the pressure and the two tangential velocity components. They were obtained from a potential flow calculation for the bare hull, neglecting the displacement effect of the boundary layer on the external flow. Such conditions are good enough if the external boundary is chosen far (several boundary-layer thicknesses) from the hull. But that is an unattractive option if one aims at computational economy because the mathematical model is then unnecessarily complicated in a considerable part of the domain. On the other hand, the conditions are evidently not exact when the extent of the computation domain is reduced. It may result in the formation of a weak non-physical boundary layer on the external boundary [9]. After a close inspection we have indeed found ample evidence of its occurrence in our calculations in which we have always tried to use relatively small domains.

A remedy is of course to correct the boundary conditions for viscous-inviscid interaction in the course of the solution process. Stern *et al.* [10] have compared a procedure of that type with a large domain approach and found it to be effective for two relatively simple test cases. Surprisingly, they applied the displacement body concept to update the external flow; surprisingly because of the ambiguity in the definition of the displacement thickness and the approximate nature of the displacement body concept in viscous-inviscid interaction studies. A more accurate and unambiguous procedure is to use the normal velocity on the external boundary resulting from the viscous flow calculations as a boundary condition for repeated potential flow calculations for the exterior of hull plus stern-flow-and-wake zone. A practical implementation might be as follows.

The potential flow around the bare hull may be obtained by, say, a discrete source distribution on the hull surface, the source strengths are found by imposing the impermeability condition and they are denoted here by σ_1 . Their induction yields as it were a first guess of the flow, being inviscid and irrotational in all three zones of Fig. 1. Moreover, it gives a certain velocity on the boundaries between zones I and II and zones I and III, respectively, which may

be decomposed into a normal ($v_{n,pot}$) and a tangential ($v_{t,pot}$) component. Keep in mind now that the part of this basis flow covered by region I of Fig. 1 might be reproduced by a source distribution σ_2 on the boundary of the union of hull, zone II and zone III, if the normal velocity ($v_{n,pot}$) would be used as a boundary condition.

The viscous flow calculations in zones II and III, with ($v_{t,pot}$) as a boundary condition, will yield a different normal velocity ($v_{n,visc}$) on the boundaries between the zones because of boundary-layer displacement effects. The related adjustment of the external flow might be calculated by using ($v_{n,visc}$) as a new boundary condition to yield a new source distribution σ_3 defined on the same boundary as σ_2 . However, as will become clear in a moment, it is better to operate with $\Delta\sigma_2 = \sigma_3 - \sigma_2$, the correction of σ_2 due to viscous-inviscid interaction. So we suggest to calculate $\Delta\sigma_2$, associated with a correction potential ϕ_{cor} , under the condition

$$\frac{\partial \phi_{cor}}{\partial n} = v_{n,visc} - v_{n,pot},$$

to evaluate the tangential velocity induced by them and to add it to ($v_{t,pot}$). The pressure follows from Bernoulli's law which completes the set of new boundary conditions for the next viscous flow calculation. The process can be repeated until the solutions in the three zones match well enough.

The advantage of operating with $\Delta\sigma_2$ appears as soon as further approximations are introduced. In first-order boundary-layer theory the displacement effects caused by boundary-layer formation in zone II has a negligible effect on the external flow. One may therefore simplify the procedure by assuming that $\Delta\sigma_2$ is non-zero on the external boundary of zone III only. The number of source panels required in a practical calculation is thereby drastically reduced.

Although we think the above method to be practicable, we propose here an alternative that may lead to a more elegant procedure because it does not involve new potential flow calculations. Instead of prescribing fixed values for pressure and tangential velocity components, we set the two tangential vorticity components to zero and we let the pressure satisfy the Bernoulli equation on the external boundary in the viscous flow computations. It implies that two of the three Dirichlet conditions are replaced by conditions of Neumann type. These conditions are exact on any external boundary, provided it is chosen in the effectively inviscid part of the flow. Viscous-inviscid interaction should automatically be taken care of with these boundary conditions. As far as the author is

aware, the use of vorticity boundary conditions in primitive variable formulations has not been applied earlier although it has been suggested by Roe [11].

One might wonder whether such conditions guarantee a unique solution. After all, the conditions are valid for any external potential flow while no information on the velocity at infinity is conveyed by them. How is the correct solution selected from the many possible ones?

Although a rigorous analysis is difficult and has not been completed yet, we think that the new boundary conditions give the solution appropriate for unbounded flow conditions. It is clear that an outside influence, disturbing the external flow, such as a nearby wall, would not be felt, except via the conditions specified on the inlet boundary. But in the absence of outside disturbances, the establishment of a certain external flow is fully governed by what happens inside the stern-flow-and-wake zone (displacement effects of boundary layer and wake); there is no need for a communication of particulars of the external flow to the stern-flow-and-wake zone other than that it is an irrotational flow. The conditions on the inlet boundary make sure that we obtain the flow at the correct Reynolds number.

At this moment, we have a limited experience with the application of vorticity boundary conditions. The test results seem to confirm that the correct solution is obtained but unfortunately they have all shown so far a reduced convergence rate. After a while the global convergence is fully governed by the changes on the external boundary which decrease very slowly. An example is given in Fig. 4, showing global convergence results for the Wigley hull. As a measure for the rate of convergence we use the rate of decay of the maximum pressure change between successive iterations anywhere in the computation domain. Besides two lines representing the results for the old and the new boundary conditions, respectively, a dashed line is shown indicating the maximum pressure change on the external boundary. It is obvious from the figure that a grid refinement has been applied between iteration numbers 3 & 4 and 6 & 7; the new boundary conditions were imposed on the finest grid only.

We may note that the slower convergence is not the result of a slow drift of the pressure level; the pressure adjustments continue to be partly positive and partly negative.

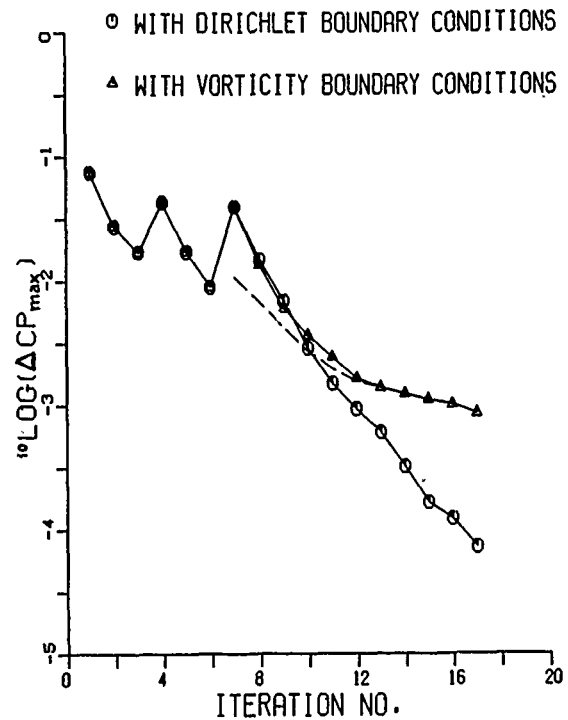


Fig. 4. Influence of boundary conditions on the global convergence for the flow around the Wigley hull

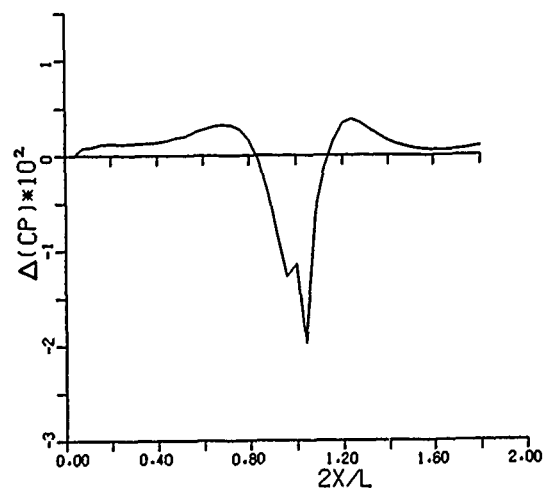


Fig. 5. Calculated pressure change due to viscous-inviscid interaction

To illustrate that viscous-inviscid interaction is automatically taken into account with the new boundary conditions, we show a result of the calculated change of the pressure on the external boundary with respect to the data obtained from the potential flow calculation around the bare hull. In Fig. 5 the pressure changes on the intersection of the external boundary and the horizontal symmetry plane (undisturbed free surface) for the flow around the Wigley hull are presented. The figure shows the typical effect of viscous-inviscid interaction, viz. a pressure drop in a region in the vicinity of the stern bordered on both the upstream and the downstream side by a region of pressure rise. The slight increase of the pressure change towards the outlet station has been verified in an axisymmetric flow case to be a consequence of the inexactness of the boundary condition $p_x = 0$; it disappears when a slightly negative pressure gradient is imposed as a boundary condition.

We may conclude that the application of vorticity boundary conditions is worth to be investigated further. The only deficiency that we have observed is the reduced convergence rate caused by it. Attempts to remove this deficiency have not yet been made, however. As an aside we note that it is questionable whether with the alternative technique of repeated potential flow calculations the matching accuracy can ever be as good as $\Delta C_p = 10^{-3}$ - achieved in Fig. 4 after 17 iterations - in view of the use of two totally different discretisation methods for, respectively, the viscous and inviscid part of the flow.

5. Global relaxation

After discretisation and linearization, the difference equations for all grid nodes can be put together in a matrix/vector equation

$$A\phi = b$$

where A is a sparse square matrix, ϕ is the vector of unknowns and b is a known vector (but containing previous iterates of the velocity components due to the non-linear convection terms). Let the entries of A be grouped in blocks so that all entries associated with the unknown variables in a certain transverse plane form a block. If such a block is represented by one element of a new matrix B and a corresponding grouping is carried through for the vectors ϕ and b , we get

$$B\psi = c \quad (2)$$

where B is a $NX * NX$ square matrix with (in our discretisation) four non-zero diagonals and ψ and c are vectors of size NX . The iterative solution of this system has been called in Section 2 the global or outer

iteration process, to be distinguished from the local or inner iteration process needed to solve the block of equations associated with a certain transverse section.

What will be called in this paper the 'basic method' to solve (2) is a Gauss-Seidel type iteration process: B is split into a sum of a lower (L) and an upper (U) triangular part where the elements of L are identical with the corresponding entries of B while U contains the upper diagonal of B only; the solution is updated via

$$L\psi^n = c - U\psi^{n-1}.$$

To enhance the convergence rate of this process we have used earlier a source term in the ξ -momentum equation, as originally proposed by Israeli and Lin [12] and described for our application in [1]. It has in many cases proved to be a useful artifice, but our experience tells that it may have undesirable side-effects, particularly when used in combination with an algebraic turbulence model. Notably in the initial phase of the calculations the source term may assume appreciable values, generating a significant overshoot in the velocity profiles or provoking flow separation. In the first case the turbulence model may show pathological behaviour in the determination of the outer length scale, which deteriorates the global convergence. In the second case the required change of the discretisation formulae will have an influence to the same effect.

We have now abandoned the source term scheme in favour of an alternative convergence accelerator with a superior performance. It is described below.

When an iterative process is used to solve a time-independent problem, it is often preferable to operate with a transient form of the mathematical model and to try to find the steady state solution [13]. Following this suggestion, we add a quasi-time derivative of the pressure to the ξ -momentum equation. If for the sake of compact notation we consider the equations valid in a Cartesian coordinate system, the momentum equation for the dominant flow direction becomes

$$\mathcal{L}(u, v, w) + p_x = p_t \quad (3)$$

where \mathcal{L} is a differential operator incorporating the convection and diffusion terms but no 'time' derivatives.

In the above Gauss-Seidel process the discretised x -momentum equation is

$$\mathcal{L}_\Delta(u, v, w)_i^n + (p_{i+1}^{n-1} - p_i^{n-1})/\Delta x_i - (p_i^n - p_i^{n-1})/\Delta t = RHS_i \quad (4)$$

where \mathcal{L}_Δ is a finite-difference analogue of \mathcal{L} , RHS_i is a known right-hand side which does not contain variables at iteration level n and Δt is taken equal to Δx . Next, one may conceive a complementary discretisation of (3):

$$\mathcal{L}_\Delta(u, v, w)_i^n + \frac{(p_{i+1}^{n+1} - p_i^{n+1})/\Delta x_i - (p_i^{n+1} - p_i^n)/\Delta t}{\Delta t} = RHS_i \quad (5)$$

such that half of the sum of (4) and (5) yields a discretisation of all terms of (3) at time (or iteration) level n , provided that

$$\bar{p}^n = \frac{1}{2}(p^{n+1} + p^{n-1}) \quad (6)$$

is considered as a new value for p^n .

From the combination of the formulae (4),(5),(6) above, a predictor-corrector scheme for the pressure is readily constructed. The predictor step is the basic method, the Gauss-Seidel scheme:

$$\mathcal{L}_\Delta(u, v, w)_i^n + (p_{i+1}^{n-1} - p_i^*)/\Delta x_i = RHS_i,$$

giving new values u^n, v^n, w^n for the velocity components and a first approximation p^* to a new value of the pressure. The difference of (4) and (5) yields a simple algebraic relation to determine a fictitious p^{n+1} . The improved guess for p^n is then obtained from the mean of this p^{n+1} and the old pressure p^{n-1} . The latter operations may be combined in the corrector step

$$p_i^n = \frac{1}{2}(p_i^{n-1} + p_i^*) + \frac{1}{2}(p_{i+1}^n - p_{i+1}^{n-1}). \quad (7)$$

Because of the appearance of p_{i+1}^n in the right-hand side, p_i^n must be evaluated in an upstream marching sequence. Thus the basic process of a sweep from inlet to outlet station is followed by reversed sweep in which an improved value for the pressure is obtained via the simple algebraic relation (7). As a start for this reversed sweep we have

$$p_{NX}^n = p_{NX}^*$$

as immediately follows from the above formulae when the mainstream pressure gradient is zero on the outlet boundary.

It is easily verified by repeated substitution of (7) that a pressure change at station x_i can be expressed as

$$\Delta p_i^n = \frac{1}{2} \left[\sum_{k=i}^{NX} \left(\frac{1}{2}\right)^{k-i} \Delta p_k^* + \left(\frac{1}{2}\right)^{NX-i} \Delta p_{NX}^* \right]$$

where

$$\Delta p_i^n = p_i^n - p_i^{n-1}, \quad \Delta p_i^* = p_i^* - p_i^{n-1}.$$

It implies that Δp_i^n is determined by a fraction (diminishing with distance) of downstream pressure changes resulting from the basic method. Thus we have incorporated the desirable feature of an infinite propagation speed of pressure influences in upstream direction (a property of the continuum equations) in the numerical scheme. In both the basic method and the Israeli/Lin source term scheme the propagation speed is only Δx_i per iteration.

Readers familiar with the recent literature on solution methods for the Reynolds-averaged Navier-Stokes equations in flows characterized by a dominant flow direction will have observed that the predictor-corrector scheme introduced here has some similarity with a procedure suggested by Davis *et al.* in [14]. The differences are essential, however. In [14] the two discretisations (4) and (5) appear also but the solution process is continued with p^{n+1} . That would be all-right if the x -momentum equation stood on its own but when it is coupled with other equations in which the pressure appears as well it is a completely unsatisfactory approach. For $\Delta t = \Delta x$ an essentially unstable scheme results. Also for smaller values of Δt we have not been able to produce acceptable results with their method.

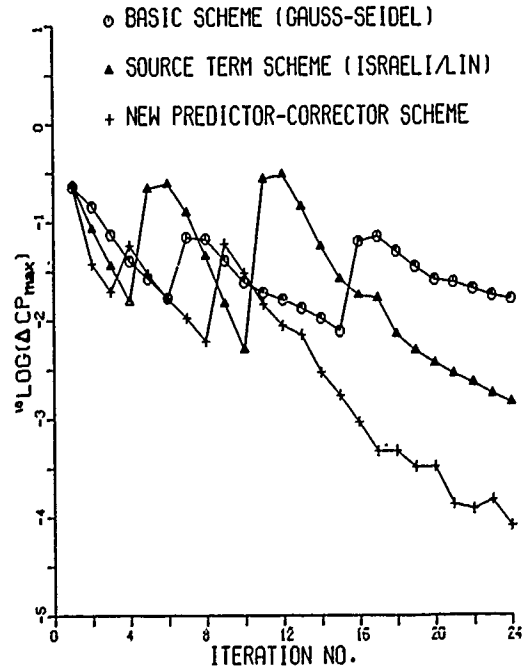


Fig. 6. Maximum pressure change between successive sweeps in global iteration process for three methods

As an illustration of the excellent performance of our proposal we give global convergence results for the flow around an axisymmetric body as obtained by the basic scheme, the source term scheme and our new scheme in Fig. 6. In all three convergence curves two jumps appear which correspond each to a grid refinement, being executed when $\Delta C_{p_{max}} \leq 0.02$ and ≤ 0.01 respectively. Most striking is the gain in convergence rate with respect to the basic method which differs from the new method by the correction step (7) only. The more so because the correction step is extremely simple, requiring a completely insignificant amount of computation time. Similar results have been obtained for other cases.

6. Application

Since the appearance of our earlier publications [1,2,3], the number of applications of our method has considerably increased. Some of these applications were repeated calculations for 'old' test cases (e.g. Wigley hull, SSPA 720), others concerned new explorations. Among them were computations including a representation of a propeller and/or a duct by a specified external force field. Instead of giving results of some of those exercises or improved results for the test cases that appeared in previous publications, we have selected for presentation some data obtained for a rather demanding test case: the HSVA tanker.

What makes this hull form to a difficult case for flow computations is in the first place the fullness of the hull (block coefficient = 0.85), implying a high viscous pressure resistance and presumably complex flow with a risk of boundary-layer separation.

The body plan of the hull is given in Fig. 7. A 2.74 m model of it has been subjected to detailed measurements in a slotted-wall wind tunnel by Wieghardt and Kux [15] and a data tape with a part of their results has been kindly made available to us. On the basis of the geometry information provided on the data tape, a reconstruction of the hull shape was carried out with our hull fairing system. Intermediate frame lines were obtained by spline interpolation.

Calculations were made at the Reynolds number of the measurements: $Rn = 5 \cdot 10^6$. Neither the wind tunnel wall nor the rod extending from the back of the wind tunnel model were included in the simulation. The lengthwise extension of the stern-flow-and-wake zone was chosen as $0.5 \leq 2x/L \leq 1.65$, where L is the length between perpendiculars and $x = 0$ midships. The results to be presented were obtained on a $45 \cdot 29$ grid.

Potential flow and boundary-layer calculations provided us with the non-trivial part of the boundary conditions. On the external boundary, conventional conditions (prescription of tangential velocity components and pressure from the potential flow) were applied, while a zero pressure gradient condition was imposed on the outlet boundary. The initial guess for the pressure field was obtained by assuming $p_\eta = 0$.

One of the aims of the calculation of the stern flow field is to acquire information on the velocity distribution near the location where the propeller is to be mounted. Let us therefore first have a look at some contour plots of the axial velocity field near the stern. Fig. 8 shows the comparison of measurements and predictions in six transverse sections. In the measurements, the flow disturbance caused by a support wire in the wind tunnel is clearly visible. When that anomaly is taken into consideration there is generally good agreement between both sets of data in the outer part of the boundary layer or wake. Near the hull, on the other hand, in the region just below the concave part of the frame lines, the measurements indicate a much stronger retardation of the flow. S-shaped iso-velocity contours show up which do not clearly appear in the computed results.

Usually the formation of that kind of wake distribution is connected with the development of a longitudinal vortex. How well that phenomenon is reproduced by the calculations may be judged from Fig. 9. It shows vector plots of the transverse velocity components at various stations. From the measurements as well as the calculations only a part of the available information has been plotted but such that the vector lengths are directly comparable.

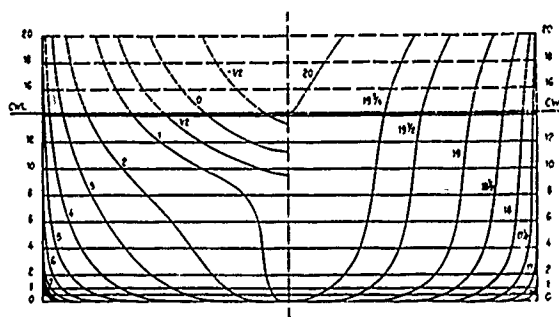


Fig. 7. Body plan HSVA tanker

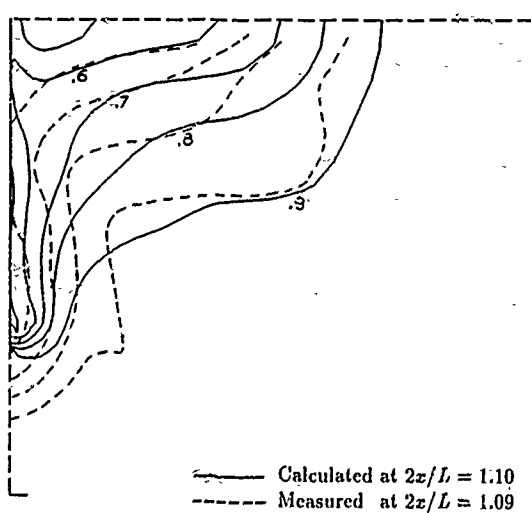
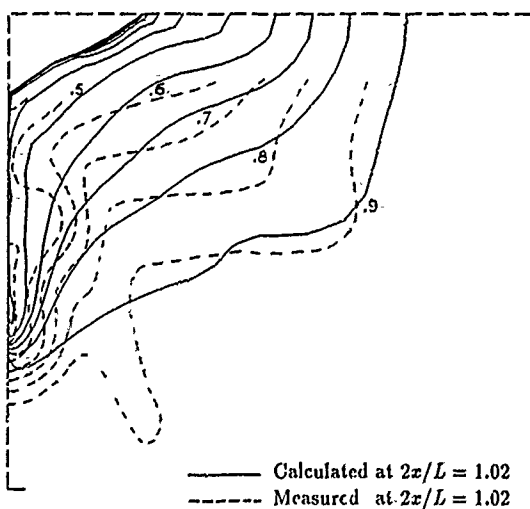
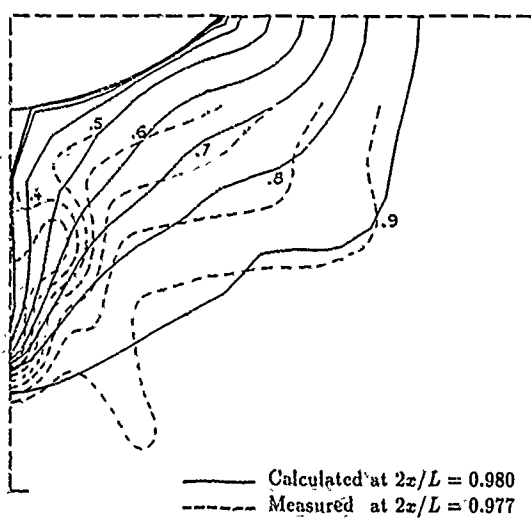
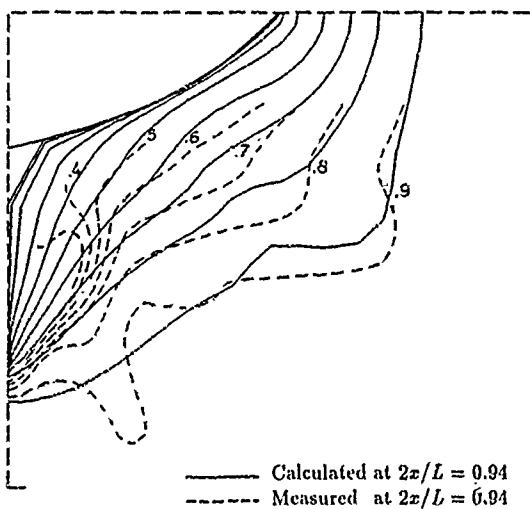
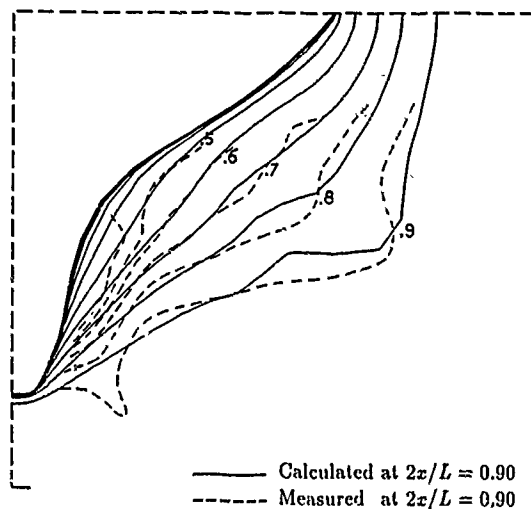
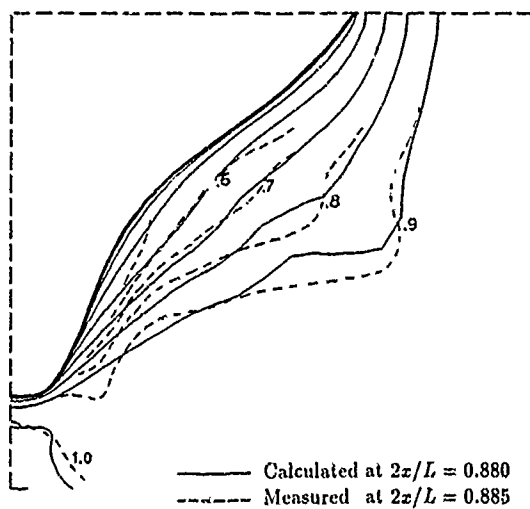


Fig. 8. Contour plots of axial velocity distributions

There is no clear evidence that the vortex formation is predicted to start at a wrong position but the vortex core seems to stay closer to the vertical symmetry plane than in the measurements, especially when it is taken into account that the measurements are not truly symmetric with respect to the geometric symmetry plane. This is in accordance with the stronger deceleration of the axial flow.

The question remains what is the cause of the discrepancy in the axial velocity distribution. We may observe that there is little reason to suppose that a gross misprediction of the pressure is responsible.

Fig. 10 shows the girthwise pressure distribution on the hull at station $2x/L = 0.88$ with an excellent agreement between measurements and calculations while the potential flow results deviate considerably.

A preliminary exercise with vorticity boundary conditions on the external boundary indicated that the inclusion of viscous-inviscid interaction does not bring about either a change in the near-hull flow to the extent required for a reconciliation of measurements and predictions. Still to be investigated are the effects of grid refinement and of a variation in the turbulence model.

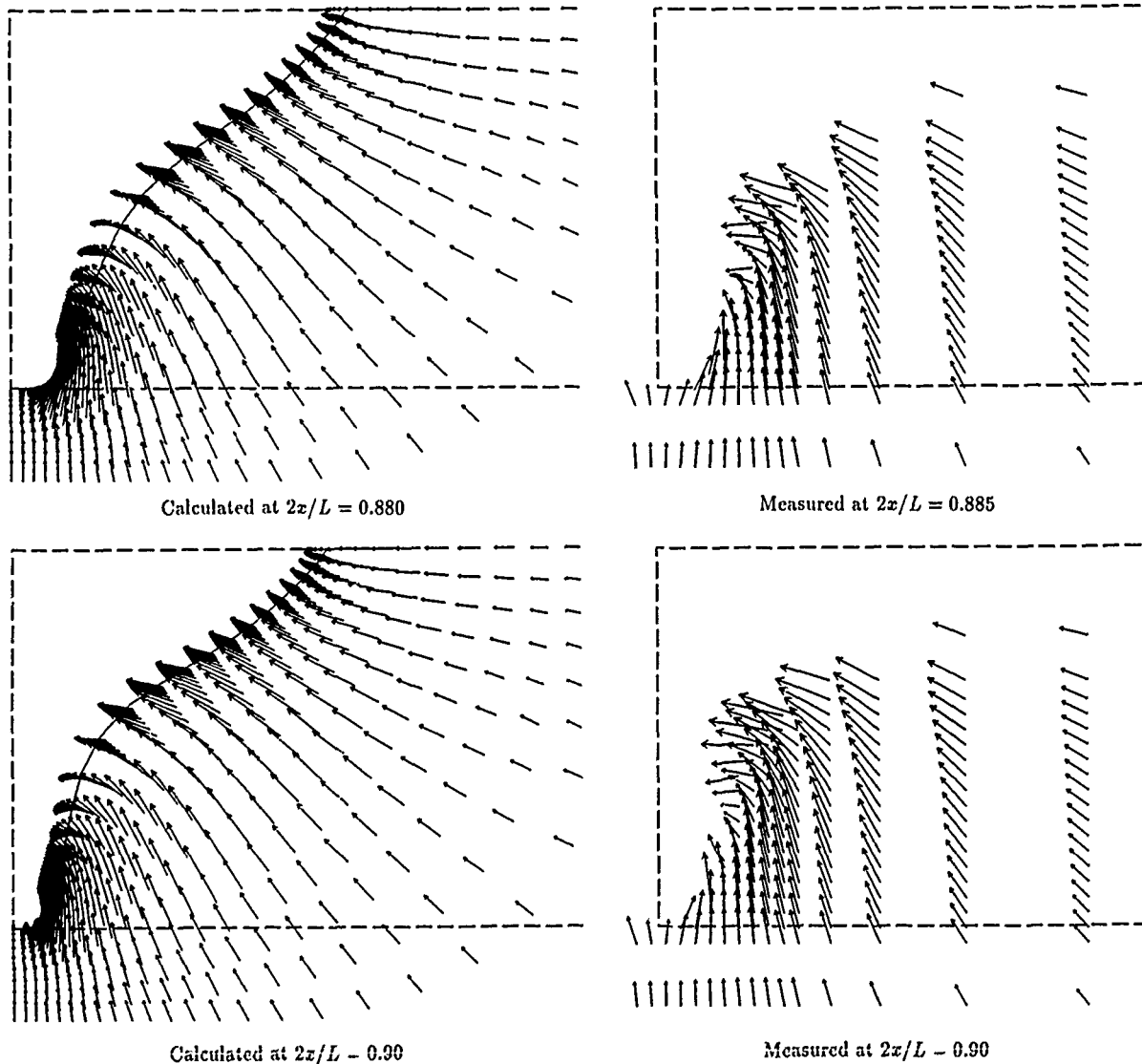
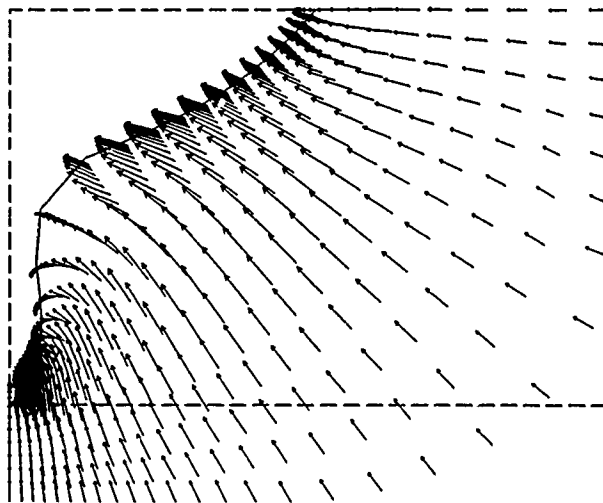
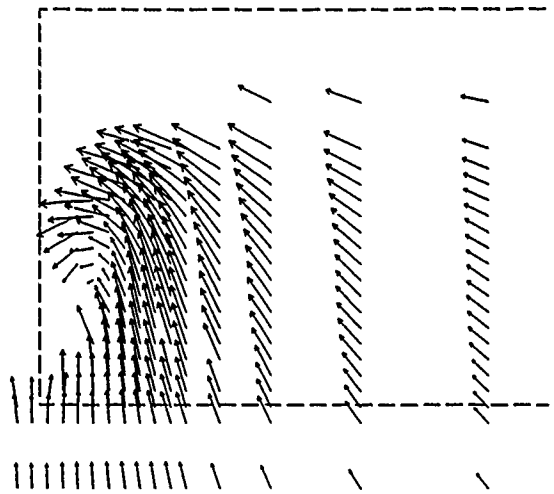


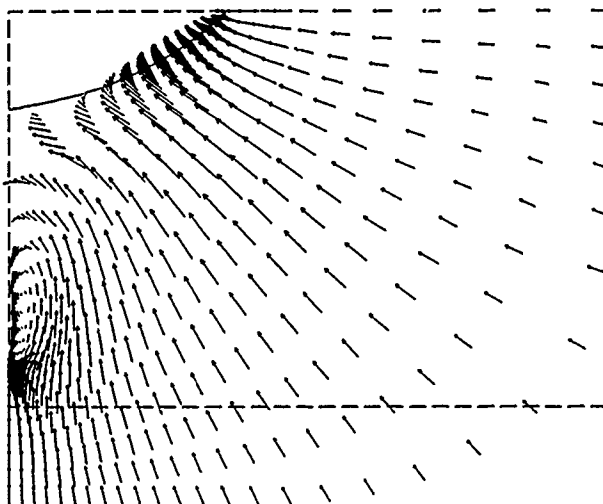
Fig. 9. Vector plots of transverse velocity components



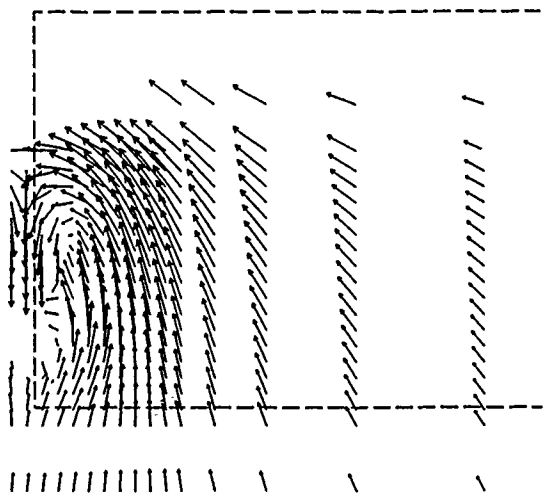
Calculated at $2x/L = 0.920$



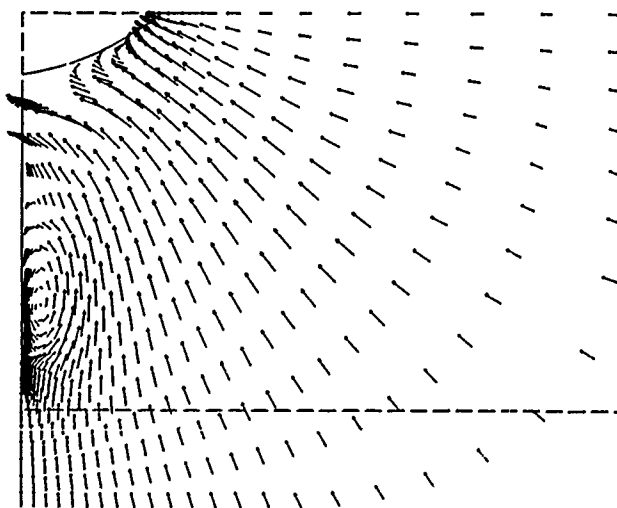
Measured at $2x/L = 0.926$



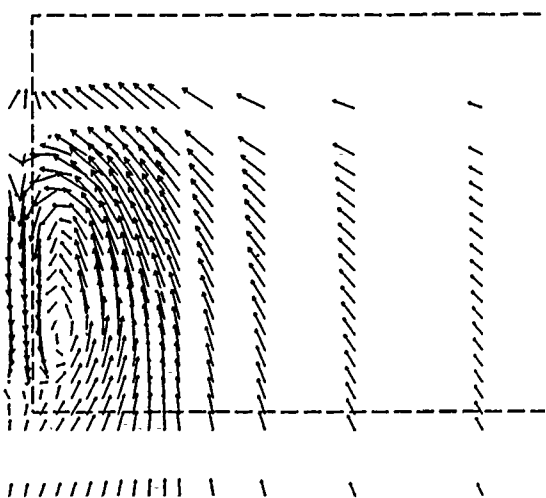
Calculated at $2x/L = 0.980$



Measured at $2x/L = 0.977$



Calculated at $2x/L = 1.020$



Measured at $2x/L = 1.015$

Fig. 9 (continued)

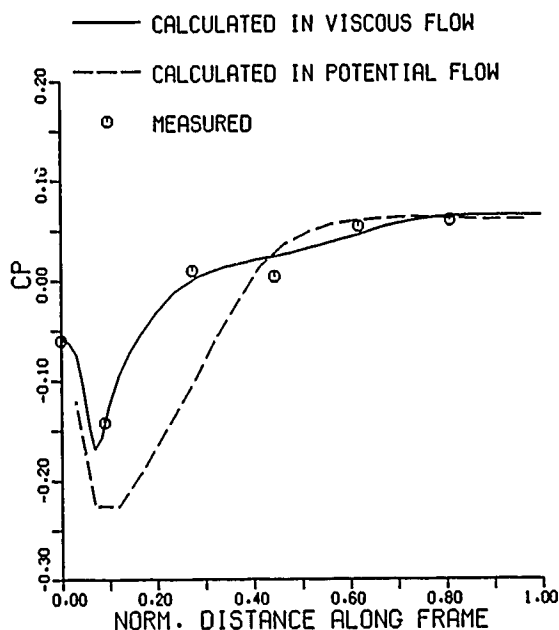


Fig. 10. Girthwise pressure distributions at station $2x/L = 0.88$

It is not apparent from Fig. 8, but our results indicate boundary-layer separation at two locations: in a small region just above the level of the imaginary propeller axis, starting from about station $2x/L = 0.9$, and near the waterline (horizontal symmetry plane) aft of station $2x/L = 0.97$. In both cases the thickness of the separation bubble is very small. Only an oil flow experiment for the visualization of the limiting streamlines could shed some light on the faithfulness of that prediction. However, the girthwise skin friction distribution at station $2x/L = 0.88$, just ahead of one of the separation regions, is in fair agreement with the experimental data [16], as Fig. 11 shows.

It may be concluded that many features of the experimental data are satisfactorily reproduced. Indeed, the present results are perhaps the most realistic ones among the few that have been reported so far for this test case. Yet, they can hardly be considered good enough, if the available set of measurements is considered to satisfy high quality standards. Where our method has been set up with the idea that it should give ultimately reliable results for a case like the HSVA tanker, further improvements are needed. They are to be found in a fine-tuning of the turbulence model and the use of finer grids rather than in the numerical scheme.

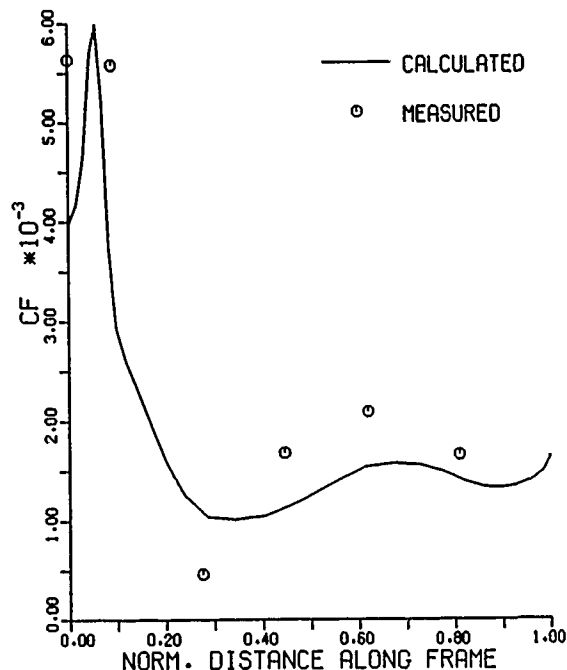


Fig. 11. Girthwise skin-friction distributions at station $2x/L = 0.88$

7. Concluding remarks

In this paper we have given a detailed description of new developments in certain aspects of a computer code for the prediction of the stern flow field of a ship:

- We have explained how coordinate-oriented velocity variables may be chosen so as to maintain a high numerical accuracy near the grid singularity in the wake;
- We have presented some results of our first application of a new set of boundary conditions on the external boundary of the computation domain, which allow this boundary to be chosen close to the edge of the boundary layer and wake;
- We have shown how the convergence rate of the global relaxation of the solution may be improved by an easy algebraic update of the pressure field after every iteration cycle.

Moreover results have been given of the application of the code to a difficult test case which indicate that the numerical scheme can cope with the complex flow around a full tanker, although the correlation with the available experimental data should be further improved.

References

1. Hoekstra, M. and Raven, H.C., "Ship boundary layer and wake calculation with a parabolised Navier-Stokes solution system", 4th International Conference on Numerical Ship Hydrodynamics, Washington D.C. (1985).
2. Hoekstra, M. and Raven, H.C., "Application of a parabolised Navier-Stokes solution system to ship stern flow computation", Osaka International Colloquium on Ship Viscous Flow, Osaka (1985).
3. Hoekstra, M., "Computation of steady viscous flow near a ship's stern", in *Notes on Numerical Fluid Mechanics*, Vol. 17 (ed. Wesseling) (Vieweg) (1986).
4. Bube, K.P. and Strikwerda, J.C., "Interior regularity estimates for elliptic systems of difference equations", *SIAM Journal of Numerical Analysis*, Vol. 20, No. 4 (1983).
5. Rubin, S.G., "Incompressible Navier-Stokes and parabolised Navier-Stokes formulations and computational techniques", in *Computational Methods in Viscous Flows*, Vol. 3 in the series Recent Advances in Numerical Methods in Fluids (ed. Habashi) (Pineridge Press) (1984).
6. Hoekstra, M., "Coordinate generation in symmetrical interior, exterior and annular 2-D domains using a generalised Schwarz-Christoffel transformation", in *Numerical Grid Generation in Computational Fluid Dynamics*, (ed. Häuser & Taylor) (Pineridge Press) (1986).
7. Eriksson, L-E., "A study of mesh singularities and their effects on numerical errors", FFA TN 1984-10 (1984).
8. Strikwerda, J.C., "Finite difference methods for the Stokes and Navier-Stokes equations", *SIAM Journal of Scientific and Statistical Computations*, Vol. 5, No. 1, pp. 56-68 (1984).
9. Olinger, J. and Sundström, A., "Theoretical and practical aspects of some initial boundary value problems in fluid dynamics", *SIAM Journal of Applied Mechanics*, Vol. 35, No. 3, pp. 419-446 (1978).
10. Stern, F., Yoo, S.Y. and Patel, V.C., "Interactive and large-domain solutions of higher-order viscous-flow equations", *AIAA Journal*, Vol. 26, No. 9 (1988).
11. Roe, P.L., "Remote boundary conditions for unsteady multidimensional aerodynamic computations", *Computers & Fluids*, Vol. 17, No. 1, pp. 221-231 (1989).
12. Israeli, M. and Lin, A., "Numerical solution and boundary conditions for boundary-layer like flows", 8th International Conference on Numerical Methods in Fluid Dynamics, Aachen (1982).
13. Roache, P.J., "Computational Fluid Dynamics", Hermosa Publishers, Albuquerque, N.M. 87108 (1972).
14. Davis, R.T., Barnett, M. and Rakich, J.V., "The calculation of supersonic viscous flows using the parabolised Navier-Stokes equations", *Computers & Fluids*, Vol. 14, No. 3, pp. 197-224 (1986).
15. Wieghardt, K. and Kux, J., "Nomineller nachstrom auf Grund von Windkanalversuchen", *Jahrbuch STG* 74, pp. 303-318 (1980).
16. Hoffmann, H.P., "Untersuchung der 3-dimensionalen, turbulenten Grenzschicht an einem Schiffsdoppelmodell im Windkanal", IFS Bericht No. 343 (1976).

DISCUSSION

by Y. Kodama

You assumed a predominant flow direction and omitted a few terms. I'd like to hear your opinion about the effect of those neglected terms.

Author's Reply

The effect of those neglected terms on the final solution is of no practical significance in ship stern flows. They do however influence the boundary condition requirements on the outlet boundary.

Computation of a Free Surface Flow around an Advancing Ship by the Navier-Stokes Equations

T. Hino
Ship Research Institute
Tokyo, Japan

Abstract

The finite-difference solution method for the Navier-Stokes equations with nonlinear free surface condition is applied to the simulation of flow field with a free surface around an advancing ship. The body-fitted coordinates system is used in order to cope with a ship of an arbitrary hull form. The coordinates system does not fit to the free surface geometry which must be determined as the part of solution in the time marching procedure. The nonlinear free surface condition is implemented in the numerical scheme. The algebraic turbulence model is used together with the wall function on the body boundary condition to simulate high Reynolds number flow. The numerical results are compared with the experimental data.

1. Introduction

A viscous flow field around a ship is strongly nonlinear even when the free surface effects are neglected. When a free surface deformation is taken into account, the geometry of free surface boundary should be determined as a part of solution by the nonlinear free surface condition and flow field becomes more complicated in both physical and numerical aspects. A number of efforts have been made to solve this nonlinear problem. Among them, the finite-difference solution methods for the Navier-Stokes equations with free surface effects [1,2] seem to be most promising because of their generality. However, even the Navier-Stokes solvers for double-model flow around a ship [3,4] have not been established well in the case of turbulent flow simulation because of various problems. There are much more difficulties to be overcome in the development of free surface flow solvers, such as the treatment of free surface boundary condition, grid generation strategy and turbulence model.

In the present paper, the finite-difference method for the Navier-Stokes equations with nonlinear free surface condition developed in Reference [1] is extended to high Reynolds number flow simulation around an advancing ship. Nonlinear free surface condition is implemented in the scheme. The algebraic turbulence model

is used together with the wall function method for the body boundary condition.

The outline of numerical scheme is described in Section 2. The numerical results for Wigley's parabolic hull and Todd's Series 60, $C_b=0.6$ are shown and compared with measured data in Section 3 and 4, respectively. The concluding remarks is given in Section 5.

2. Numerical Scheme

2.1 Governing Equations

The governing equations are the Reynolds averaged Navier-Stokes equations and the continuity equation for mean velocity of unsteady three-dimensional incompressible fluid. They are written in dimensionless form as follows;

$$u_t + uu_x + vu_y + wu_z = -p_x + (1/Re + \nu t)(u_{xx} + u_{yy} + u_{zz}) \quad (1a)$$

$$v_t + uv_x + vv_y + wv_z = -p_y + (1/Re + \nu t)(v_{xx} + v_{yy} + v_{zz}) \quad (1b)$$

$$w_t + uw_x + vw_y + ww_z = -p_z + (1/Re + \nu t)(w_{xx} + w_{yy} + w_{zz}) - 1/Fn^2 \quad (1c)$$

$$u_x + v_y + w_z = 0 \quad (2)$$

(x, y, z) are Cartesian coordinates normalized by ship length L where x is the free stream direction and y is the lateral direction and z , the vertical direction, upward positive. (u, v, w) are mean velocity components normalized by uniform flow U_0 in (x, y, z) directions, respectively. t is time normalized by L/U_0 and p is pressure normalized by ρU_0^2 , where ρ is the density of water. Re is the Reynolds number, $U_0 L / \nu$ and Fn is the Froude number, U_0 / \sqrt{gL} , where ν is the kinematic viscosity of water and g is the gravitational acceleration constant. νt is the dimensionless eddy viscosity.

In Eqs. (1)–(4), subscripts, x, y, z and t mean the partial differential.

The body-fitted curvilinear coordinates system (ξ, η, ζ) is introduced to cope with the body boundary of an arbitrary form, where ξ is the direction from fore to aft, η the direction from a ship or a center plane to the side outer boundary and ζ , the girth direction from keel to deck. As same as the previous method [1], the computational coordinates do not fit to the free surface shape, so they are not time-dependent. The coordinates transformation is given as follows;

$$\xi = \xi(x, y, z), \eta = \eta(x, y, z), \zeta = \zeta(x, y, z), t = t \quad (3)$$

The momentum equations (1) and the continuity equation (2) are transformed through Eqs. (3) as

$$u_t + Uu_\xi + Vu_\eta + Wu_\zeta = -(\xi_x\phi_\xi + \eta_x\phi_\eta + \zeta_x\phi_\zeta) + (1/Re + \nu t)(\nabla^2 u) \quad (4a)$$

$$v_t + Uv_\xi + Vv_\eta + Wv_\zeta = -(\xi_y\phi_\xi + \eta_y\phi_\eta + \zeta_y\phi_\zeta) + (1/Re + \nu t)(\nabla^2 v) \quad (4b)$$

$$w_t + Uw_\xi + Vw_\eta + Ww_\zeta = -(\xi_z\phi_\xi + \eta_z\phi_\eta + \zeta_z\phi_\zeta) + (1/Re + \nu t)(\nabla^2 w) \quad (4c)$$

$$\xi_x u_\xi + \eta_x u_\eta + \zeta_x u_\zeta + \xi_y v_\xi + \eta_y v_\eta + \zeta_y v_\zeta + \xi_z w_\xi + \eta_z w_\eta + \zeta_z w_\zeta = 0 \quad (5)$$

where (U, V, W) are the unscaled contravariant velocity components and defined

$$U = \xi_x u + \xi_y v + \xi_z w \quad (6a)$$

$$V = \eta_x u + \eta_y v + \eta_z w \quad (6b)$$

$$W = \zeta_x u + \zeta_y v + \zeta_z w \quad (6c)$$

ϕ is pressure from which hydrostatic component is extracted;

$$\phi = p + z/Fn^2 \quad (7)$$

∇^2 is the transformed Laplacian operator and defined as

$$\begin{aligned} \nabla^2 q = & (\xi_x^2 + \xi_y^2 + \xi_z^2)q_{\xi\xi} + (\eta_x^2 + \eta_y^2 + \eta_z^2)q_{\eta\eta} \\ & + (\zeta_x^2 + \zeta_y^2 + \zeta_z^2)q_{\zeta\zeta} \\ & + 2(\xi_x\eta_x + \xi_y\eta_y + \xi_z\eta_z)q_{\xi\eta} \\ & + 2(\eta_x\zeta_x + \eta_y\zeta_y + \eta_z\zeta_z)q_{\eta\zeta} \\ & + 2(\xi_x\zeta_x + \xi_y\zeta_y + \xi_z\zeta_z)q_{\xi\zeta} \\ & + (\xi_{xx} + \xi_{yy} + \xi_{zz})q_\xi + (\eta_{xx} + \eta_{yy} + \eta_{zz})q_\eta \\ & + (\zeta_{xx} + \zeta_{yy} + \zeta_{zz})q_\zeta \end{aligned} \quad (8)$$

where q is arbitrary scalar quantity. ξ_x, ξ_y and so on appeared in Eqs. (4)–(8) are the metrics of the grid.

2.2 Basic Algorithm

The basic algorithm is same as that of the MAC method [5]. The discretization is made in the non-staggered grid, that is, all variables are defined in the intersections of grid lines. The present method is based on the time marching procedure and is divided into two stages.

On the first stage, velocity is updated by the momentum equations (6). The forward difference is used in time. The spatial differences are the third-order upstream difference by Kawamura and Kuwahara [6] for the convection terms, the second-order central difference for the pressure gradient terms and for the diffusion terms and the fourth-order central difference for the grid metrics terms.

On the second stage, pressure on the next time step is computed so that the velocity field on the next time step may satisfy the continuity condition. By taking divergence of the momentum equations (6), the following Poisson equation for pressure is derived.

$$\begin{aligned} \nabla^2 \phi = & -\xi_x K_\xi - \eta_x K_\eta - \zeta_x K_\zeta \\ & -\xi_y L_\xi - \eta_y L_\eta - \zeta_y L_\zeta \\ & -\xi_z M_\xi - \eta_z M_\eta - \zeta_z M_\zeta \\ & -D_t \end{aligned} \quad (9)$$

where

$$\begin{aligned} K &= Uu_\xi + Vu_\eta + Wu_\zeta - (1/Re + \nu t)(\nabla^2 u) \\ L &= Uv_\xi + Vv_\eta + Wv_\zeta - (1/Re + \nu t)(\nabla^2 v) \\ M &= Uw_\xi + Vw_\eta + Ww_\zeta - (1/Re + \nu t)(\nabla^2 w) \end{aligned}$$

and

$$D = \xi_x u_\xi + \eta_x u_\eta + \zeta_x u_\zeta + \xi_y v_\xi + \eta_y v_\eta + \zeta_y v_\zeta + \xi_z w_\xi + \eta_z w_\eta + \zeta_z w_\zeta$$

The right-hand-side of Eq.(9) is evaluated by the values at the present time step. The spatial differences for K, L and M are same as that for Eqs.(6). The time differential appeared in the last term is expressed by the forward difference. Then D , divergence of velocity, on the next time step is set zero from the continuity condition, while D on the present time step which is not necessarily zero is evaluated by the second-order central difference to avoid accumulation of numerical error[5]. The left-hand-side of Eq.(9) is evaluated by the second-order central difference and solved iteratively by the Jacobi method.

The initial condition is still state, that is, velocity and wave elevation are zero and pressure is hydrostatic in the whole domain of computation. The constant acceleration is made by adding the inertia force to the momentum equation in x -direction. Eq.(4a), until the inflow velocity becomes unity.

2.3 Free Surface Conditions

When the effects of viscosity and free surface tension are neglected, the free surface conditions consist of the following two conditions. One is the pressure condition that means that pressure on the free surface is equal to atmospheric one. The other is the kinematic condition that tells the fluid particles on the free surface keep staying on it.

Because the grid points are not on the free surface in the present grid system, it is not easy to satisfy the free surface conditions on the exact location of the free surface. The pressure condition is implemented in the solution process of the Poisson equation for pressure. To give the boundary condition at the intermediate point between grid points, the 'irregular stars method' used in the SUMMAC method [7] is extended to the curvilinear coordinates system.

The kinematic condition is used to determine the free surface shape in the time marching process. The wave elevation is defined in the computational coordinates as

$$\zeta = h(\xi, \eta, t) \quad (10)$$

The kinematic condition is written as

$$h_t + Uh_\xi + Vh_\eta - W = 0 \quad \text{on} \quad \zeta = h \quad (11)$$

Eq.(11) is transformed into the finite-difference form in the same manner as that for the momentum equations (6). Velocity (U, V, W) on the free surface is extrapolated equally from the value at the lower grid points.

2.4 Body Surface Conditions

For the body surface condition, the wall function approach is used to reduce the computation time. With the no-slip condition, the minimum grid spacing in the direction normal to the body surface should be small enough to resolve the viscous sublayer of the boundary layer on the body. Because the explicit scheme in time is used, the time increment is limited by the CFL condition and should be also small in proportion to the grid spacing. The total computational time to convergence would be too large for the present computer power.

The wall function used here is the general logarithmic law, that is,

$$q/u_\tau = 1/\kappa \ln y^+ + B \quad (12)$$

where q is velocity magnitude, u_τ the friction velocity and y^+ the normal distance from the wall normalized by ν/u_τ . The constants κ and B are set 0.4 and 5.5, respectively.

Following Chen and Patel [8], the two velocity points ($j = 2$ and 3, where $j = 1$ is the wall) are

assumed to be located in the logarithmic region. From q and the normal distance from the wall at $j = 3$, u_τ is determined from Eq. (12). Then q at $j = 2$ can be calculated from u_τ and the normal distance of the point. Velocity at $j = 2$ is treated as the boundary value in the velocity updating process. The direction of velocity at $j = 2$ is assumed parallel to the wall. In the accelerating period, the no-slip condition is imposed for velocity on the body. Pressure and wave elevation on the wall ($j = 1$) is set equal to those at $j = 2$.

By the use of the wall function, the minimum grid spacing can be more than ten times as large as that in the case of the no-slip condition. In the present computations, typical value of y^+ at $j = 3$ is taken about from 20 to 100. The computing time is reduced drastically by this procedure.

2.5 Other Boundary Conditions

On the inflow boundary, velocity is uniform flow in x -direction after the acceleration and pressure is hydrostatic with zero wave elevation. On the outflow and side boundaries, pressure, velocity and wave elevation are extrapolated with zero gradient from the inside.

2.6 Turbulence Model

Turbulence model used is the two-layer algebraic model by Baldwin and Lomax [9]. It is widely used in the aerodynamic computations and also in the incompressible flow computation around a ship by Kodama [3]. In the present study, flow is enforced to be turbulent from the fore end of a ship. The free surface effect on turbulence is not included in the model. There has not been any turbulence model that can be applied to the boundary layer and wake of a surface-piercing body like a ship. Further investigation in both computation and experiment is required to establish a turbulence model under the free surface effects.

3. Computation for Wigley's Hull

3.1 Computational Condition

The first computational results are for Wigley's parabolic hull. The waterlines and the frame lines of the hull geometry are defined by the parabolic lines. The computations are made with two, coarse and fine, grids. The grid generation scheme based on the geometrical method is used.

The coarse grid is shown in Fig.1a. The number of grid points is 51, 20 and 18 in the (ξ, η, ζ) directions, respectively. The H-O grid topology is adopted. The grid points are clustered near the body and near the still water surface. The computational domain in the dimensionless coordinates (where $x = 0$ is the midship, $y = 0$ the center plane and $z = 0$ the still water level) is

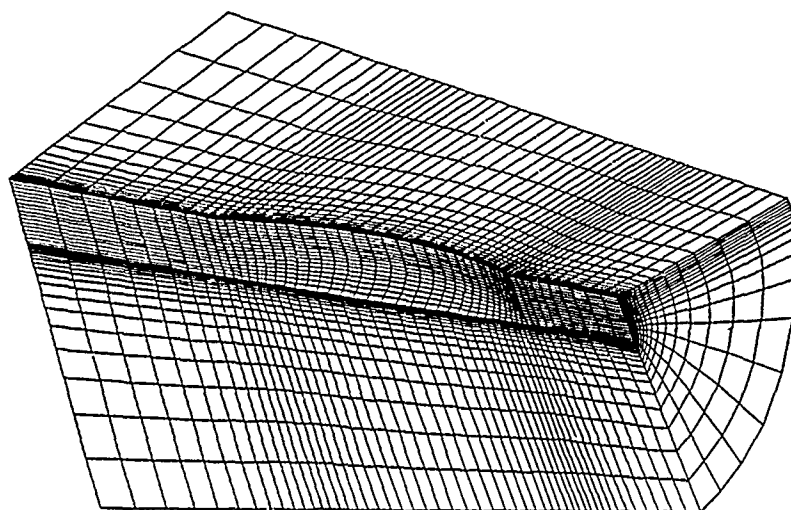


Fig. 1a Coarse computational grid for Wigley's hull.

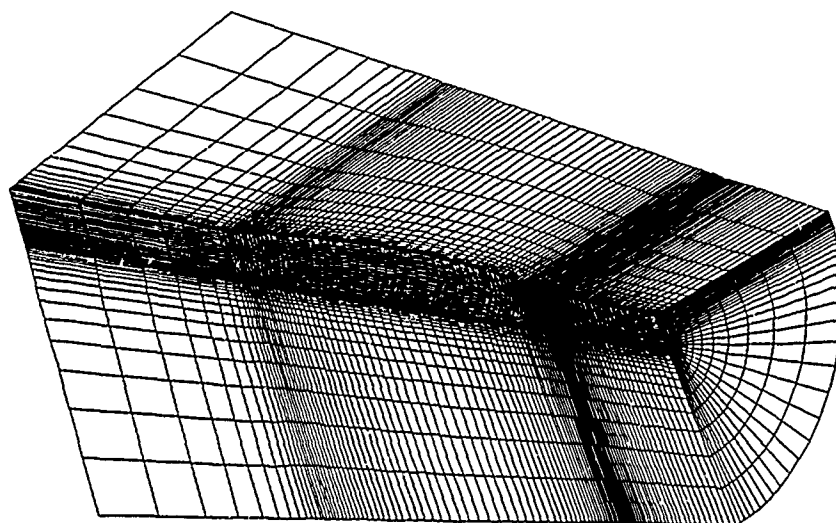


Fig. 1b Fine computational grid for Wigley's hull.

$$-1 \leq x \leq 1, 0 \leq y \leq 0.5, -0.5 \leq z \leq 0.0555$$

It should be noted that the domain includes the region above the undisturbed free surface, that is, $z > 0$. The grid points below the still water surface is $51 \times 20 \times 10$. The number of grid points inside the fluid varies as the wave field develops. The minimum grid spacing in η -direction is 0.001.

The fine grid shown in Fig. 1b has $100 \times 20 \times 38$ grid points in (ξ, η, ζ) directions, respectively. The computational domain is same as that for the coarse grid, except that $-0.5 \leq z \leq 0.036$. The grid points under the free surface is $100 \times 20 \times 30$ and the minimum grid spacing in η -direction is 0.0008 in this case.

The Froude number is 0.25 and the Reynolds num-

ber is 10^6 in both computations. The acceleration is made in the first 500 time steps. The dimensionless time increment is 0.0005 for the coarse grid computation. In the fine grid case, the dimensionless time increment is 0.0005 from 1 to 2000-th time step and 0.0003 from 2001-th time step for stabilization of computation.

3.2 Accuracy Analysis

The time derivatives in the momentum equations (6) and in the free surface kinematic condition (11) are replaced by the forward one-sided difference, that means accuracy in time of the present method is the first-order. For the spatial differences, the pressure gradient terms and the diffusion terms have the second-order accuracy. The third-order difference is used for the convection terms, in which the leading error is the fourth-derivative term and does not affect the diffusion

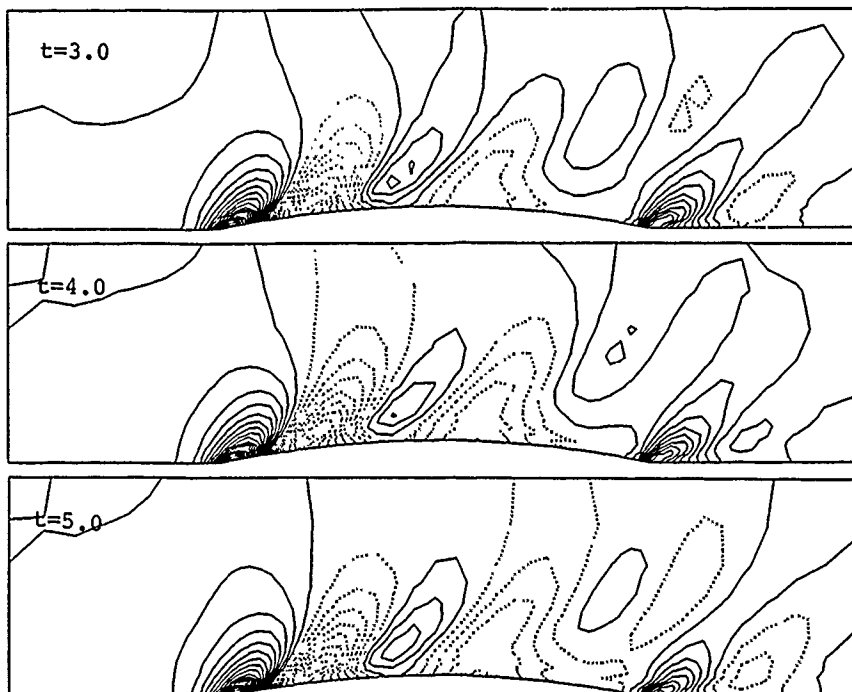


Fig. 2a Time evolution of computed wave pattern around Wigley's hull with the coarse grid. Contour interval is $0.02 \times 2gh/U_0^2$. Dotted lines show negative values. Top; 6000-th step ($t = 3.0$), middle; 8000-th step ($t = 4.0$) and bottom; 10000-th step ($t = 5.0$).

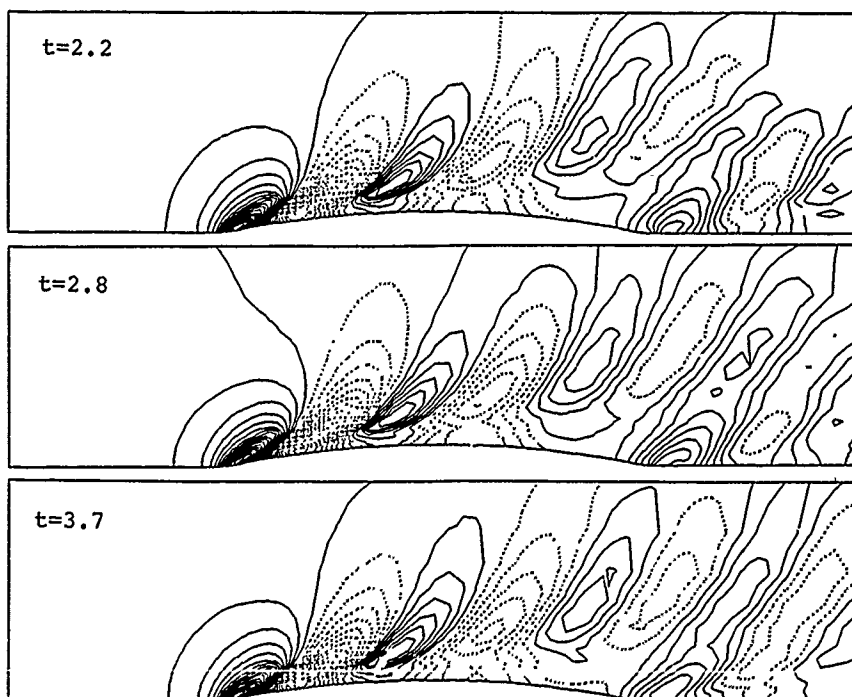


Fig. 2b Time evolution of computed wave pattern around Wigley's hull with the fine grid. Contour interval is $0.02 \times 2gh/U_0^2$. Dotted lines show negative values. Top; 6000-th step ($t = 2.2$), middle; 8000-th step ($t = 2.8$) and bottom; 11000-th step ($t = 3.7$).

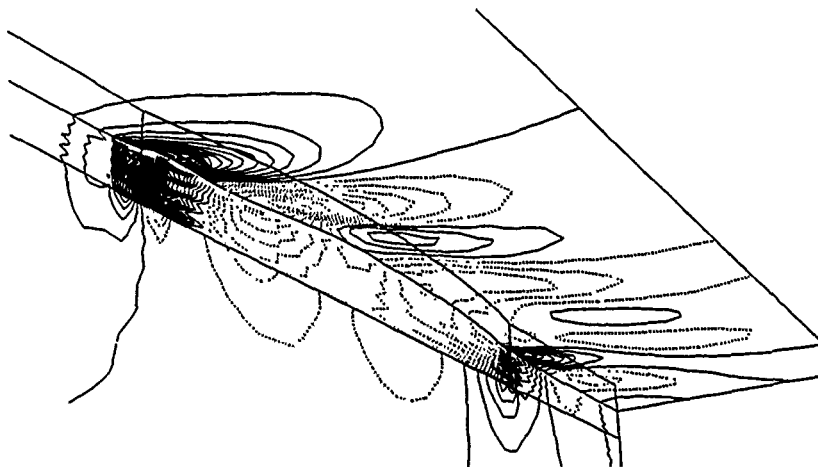


Fig. 3a Pressure distribution on hull surface, center plane and free surface around Wigley's hull computed with the coarse grid. Contour interval is $0.02C_p$. Dotted lines show negative values.

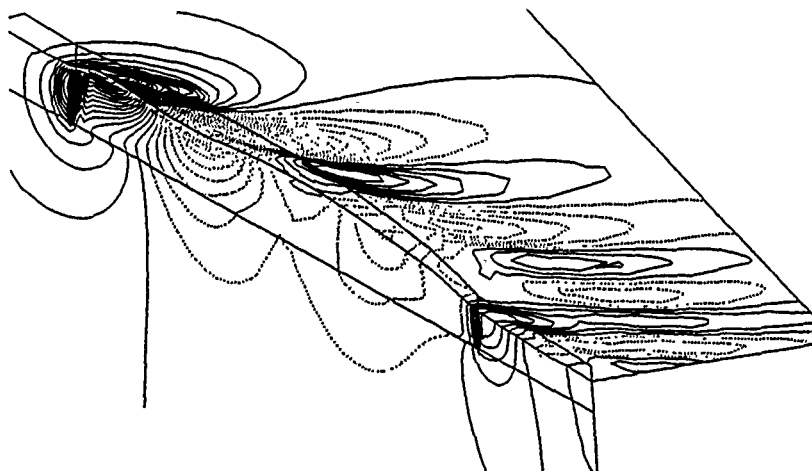


Fig. 3b Pressure distribution on hull surface, center plane and free surface around Wigley's hull computed with the fine grid. Contour interval is $0.02C_p$. Dotted lines show negative values.

terms of the momentum equations. The grid metrics are evaluated by the fourth-order difference. Numerical errors due to these finite differencing are the function of the time increment and the grid spacing.

Other factor that determines accuracy is convergence. As for convergence of the Poisson solution for pressure, the residual is typically $O(10^{-4})$ after 20 iterations. In the time integration process of the present method, the quantity that converges most slowly is the wave elevation. Therefore, convergence of the solution is examined by steadiness of the wave patterns

The comparison of the numerical results with the fine and coarse grids provides information concerning grid density effect. Fig. 2a shows the time sequence of the wave patterns around Wigley's hull computed with the coarse grid. The wave pattern has not reached the steady state at 10000-th time step when the dimensionless time is 5.0. The grid resolution seems to be not sufficient to get convergence. In the case of the fine grid shown in Fig. 2b, on the other hand, the wave pattern has become almost steady at 11000-th time step (the dimensionless time is 3.49). The waves far from the body in the coarse grid case are less steep than those in the fine grid case. The numerical dissipation due to the finite differencing error decreases the wave amplitude when the grid spacing is large.

Fig. 3a and 3b show the pressure distribution on body surface, center plane and free surface in the coarse and fine grid cases, respectively. Pressure value on the free surface is identical to the wave elevation, because hydrostatic component is extracted from static pressure. Strong wiggles of pressure can be seen on the body surface in the coarse grid case. That may be one reason why the solution has not converged. In the fine grid

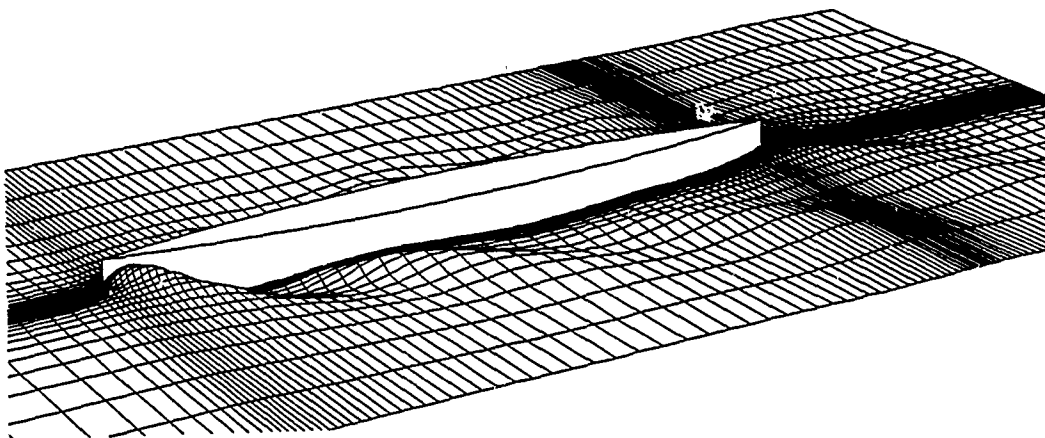


Fig. 4 Perspective view of computed waves around Wigley's hull. Wave height is three times magnified.

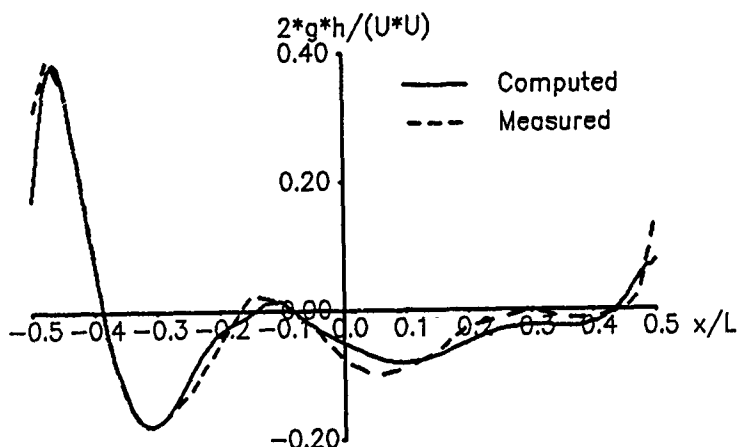


Fig. 5 Comparison of computed and measured wave profiles on ship surface of Wigley's hull. $Fn = 0.25$, $Re = 10^6$ in computation and $Re = 5 \times 10^6$ in measurement.

case, however, the wiggles are limited in the restricted regions such as near the fore end and the aft end or near the free surface and their magnitude is small.

3.3 Results

Hereafter, only the fine grid results are shown. Fig.4 shows the perspective view of the free surface configuration, where the wave amplitude is magnified by three times. Waves far from the ship hull cannot be seen clearly. The grid spacing is still too large, particularly far from the ship hull, to diminish the numerical dissipation effects. Fig.5 is the comparison of the computed and the measured [10] wave profiles on the body surface. Agreement is very well in wave amplitude and in wave length. The origin of wave making, apart from the propagation of waves which is affected by the numerical dissipation, is simulated properly.

In Figs.3b and 5, stern wave generation which is not clear in the previous computation for the low Reynolds number laminar flow [1] is simulated in the present results. Stern waves are related to pressure recovery at the stern region and this becomes higher as the Reynolds number increases.

Computed pressure distribution on body surface is shown in Fig.6 together with the measured one [10]. Pressure patterns are in good accordance with each other, except for the region of wiggles described above. These wiggles seem to come from inappropriate treatment of the boundary condition. Pressure recovery at the stern in the high Reynolds number flow described above is simulated well.

Figs.7 show the wake (u velocity) contours and the cross flow vectors (v and w velocity) at various stations. The vertical velocity component appears beneath the

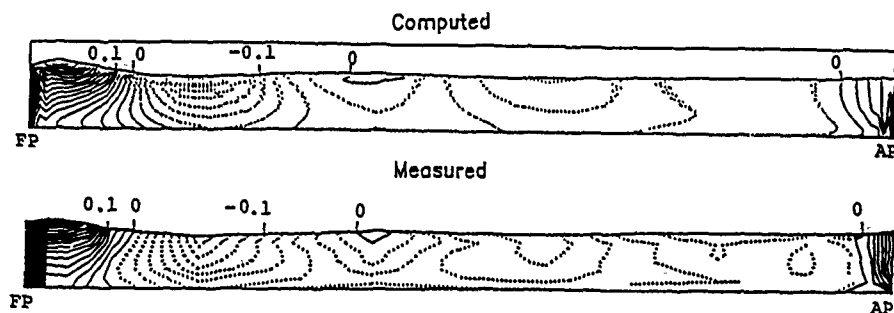


Fig. 6 Comparison of computed and measured pressure distribution on ship surface of Wigley's hull. Contour interval is $0.02C_p$. Dotted lines show negative values. $Fn = 0.25$, $Re = 10^6$ in computation and $Re = 3.4 \times 10^6$ in measurement.

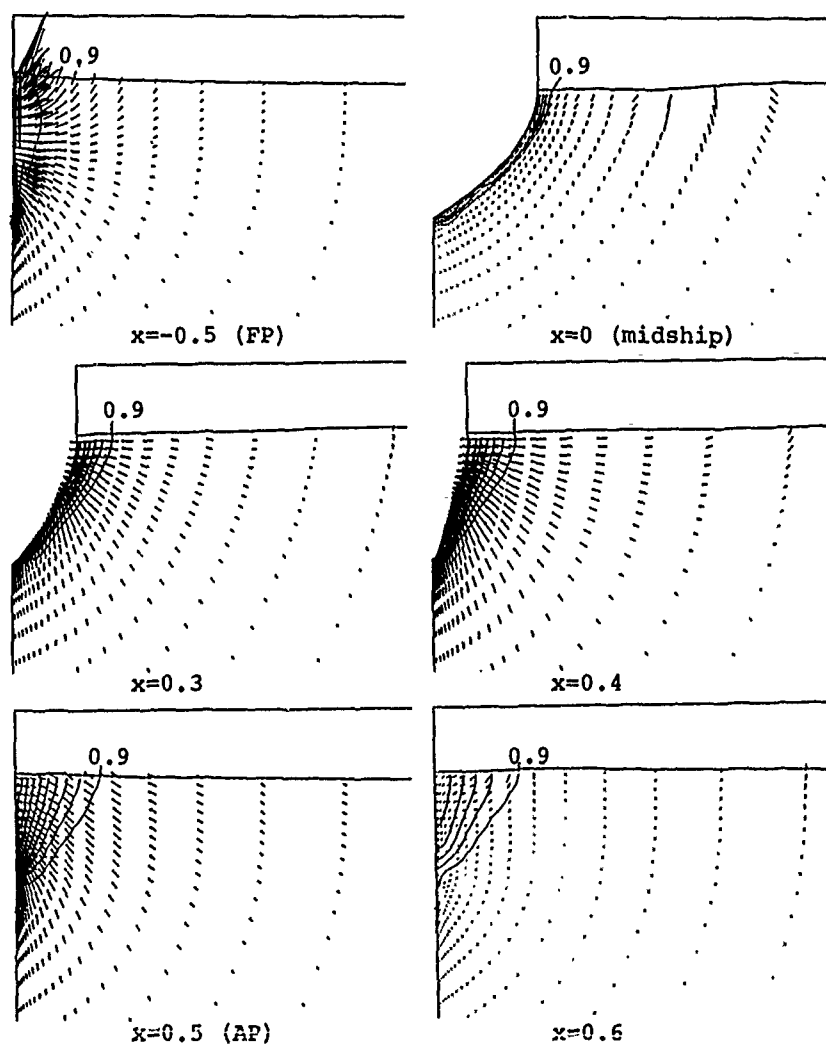


Fig. 7 Computed wake contours and cross flow vectors at various stations of Wigley's hull. Contour interval is $0.1 \times u$. Top left; $x = -0.5$ (F.P.), top right; $x = 0$ (midship), middle left; $x = 0.3$, middle right; $x = 0.4$, bottom left; $x = 0.5$ (A.P.), bottom right $x = 0.6$.

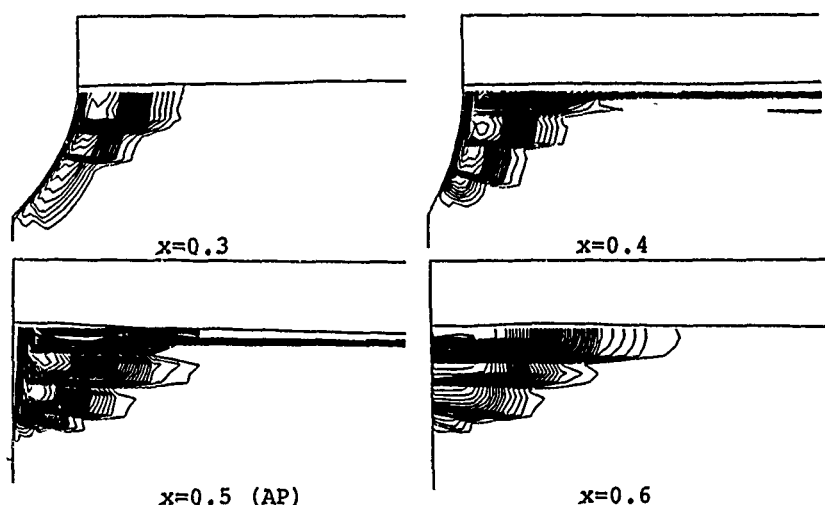


Fig. 8 Computed eddy viscosity distribution at various stations of Wigley's hull. Contour interval is $4.0 \times 10^{-6} \nu t$. Top left; $x = 0.3$, Top right; $x = 0.4$, bottom left; $x = 0.5$ (A.P.), bottom right $x = 0.6$.

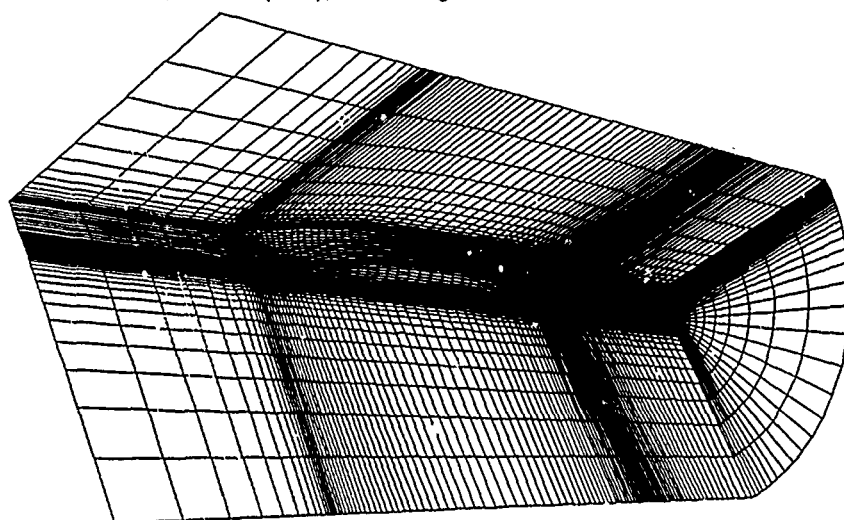


Fig. 9 Computational Grid for Series 60, $C_b=0.60$

free surface. In particular, large upward velocity is seen at F.P. station, which corresponds with the generation of bow waves. The wake contours at A.P. station seems to be too thick though the corresponding measured data is not presented. The improvement of the turbulence model and/or the wall function approach is required.

In Figs.8, the eddy viscosity distributions at various stations are presented. The discontinuity in the distribution comes from the fact that the eddy viscosity is determined line by line. The strong eddy viscosity regions spread widely near the free surface at $x = 0.4$ and 0.5 stations. This may be because the turbulence model is affected by the free surface motion and it does not have physical meaning.

4. Computation for Series 60, $C_b=0.6$

4.1 Computational Condition

The second result is for the practical ship hull form, Series 60, $C_b=0.6$. The computational domain is

$$-1 \leq x \leq 1, 0 \leq y \leq 0.5, -0.5 \leq z \leq 0.0384$$

and the number of grid points is $100 \times 20 \times 38$ which is same as the fine grid case for Wigley's hull. The computational grid is shown in Fig. 9. The minimum grid spacing in η -direction is 0.0008. The Froude number is 0.22 and the Reynolds number is 10^5 in this case. The acceleration is made in the first 500 time steps. The dimensionless time increment is made smaller gradually as the time step increases, otherwise the computation cannot be stable. From 1st to 1200-th time step, the time increment is set 0.0005, then 0.0003 from 1201-th to 2000-th time step, 0.00025 from 2001-th to 3000-th time step and 0.0002 after that.

4.2 Results

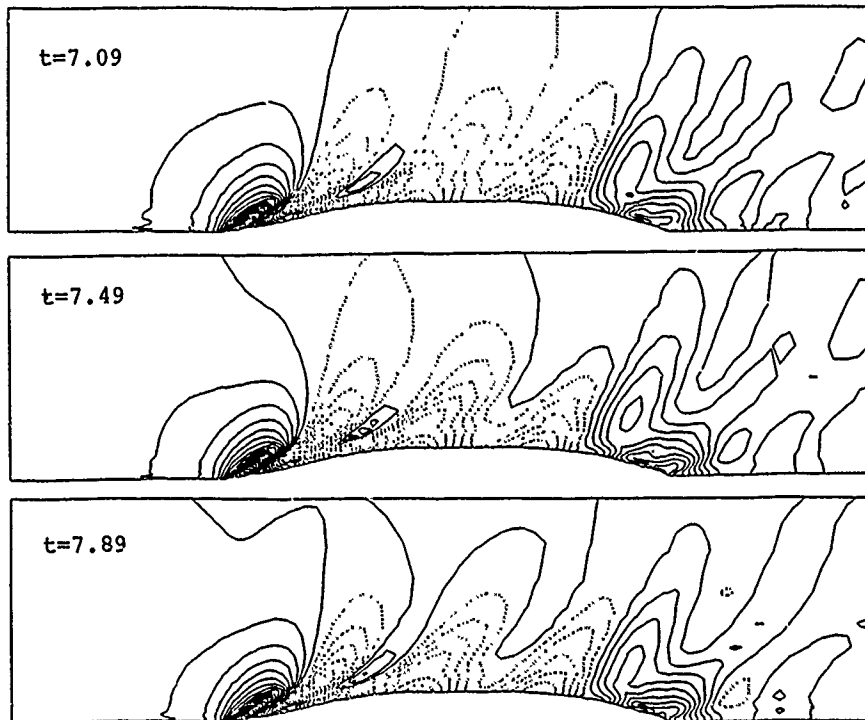


Fig. 10 Time evolution of computed wave pattern around Series 60. Contour interval is $0.02 \times 2gh/U_0^2$. Dotted lines show negative values. Top; 31000-th step ($t = 7.09$), middle; 33000-th step ($t = 7.49$) and bottom; 35000-th step ($t = 7.89$).

The time evolution of wave patterns are shown in Figs.10. The wave field has not reached the steady state at 35000-th time step (the dimensionless time is 7.89). It takes very large time to get converged solution for free surface problems by the time marching procedure, though the use of the wall function approach contributes to time saving to some extent. Improvement of the numerical scheme is required to get faster convergence. One reason why it takes longer to get convergence in the case of Series 60 than in the case of Wigley's hull may be the difference of flow complexity. The hull geometry of a practical ship, such as Series 60, is more complicated than that of Wigley's hull and flow around the complicated geometry does not become steady in a short time.

Hereafter, the numerical results at 35000-th time step are shown, because the flow field near the ship can be considered as almost steady.

Fig.11 shows the pressure distribution on body surface, center plane and free surface. Wiggles of pressure can be seen on the body surface near the fore and aft ends and near the free surface. Wiggles beneath the free surface is partly due to the discontinuity of grid spacings near the free surface which comes from the constraint of the grid generation scheme.

Fig.12 shows the perspective view of the free surface configuration, where wave amplitude is magnified

by three times. Fig.13 is the comparison of the computed and measured wave profiles [11] on the body surface. The slight unphysical oscillation of wave elevation is found in the aft part. The hull geometry of Series 60 is more complicated, particularly in the stern part, than that of Wigley's hull and the grid lines around the stern are more distorted. Numerical error due to the distorted grid causes the oscillation of waves. Except that, the computed result agrees well with measured data in wave amplitude and in wave length.

In Fig.14, the computed pressure distribution on body surface is compared with the measured one [12]. Pressure patterns are in good accordance with each other except for the slight wiggles of computed results. Free surface effects on pressure distribution beneath the free surface, that is, the low pressure zone below the wave trough and the high pressure zone below the wave crest, can be seen in both computation and measurements.

Figs.15 show the wake (u velocity) contours and the cross flow vectors (v and w velocity) at various stations together with the measured data [12]. At the F.P. station, large upward velocity appears as well as in the case of Wigley's hull. The wake contours at the midship station becomes thin around the bilge circle in the measurement and this is well simulated in the computation. At the A.P. station, longitudinal vortices can be seen

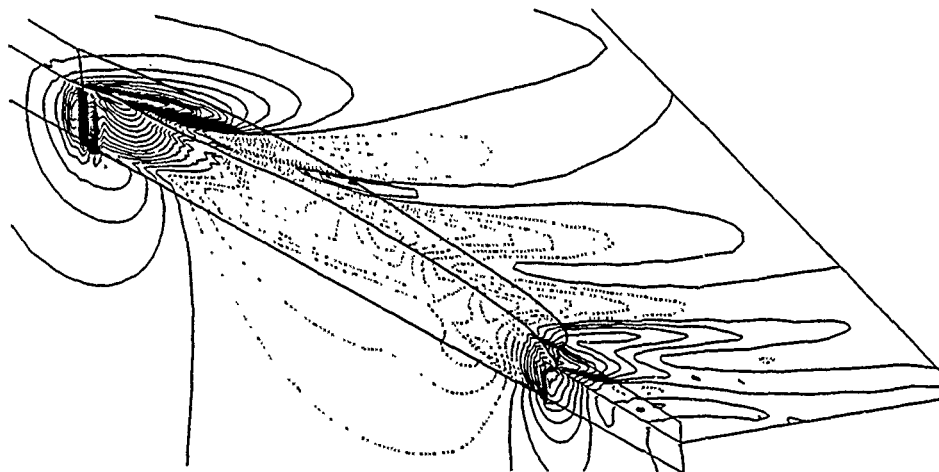


Fig. 11 Pressure distribution on hull surface, center plane and free surface around Series 60. Contour interval is $0.02C_p$. Dotted lines show negative values.

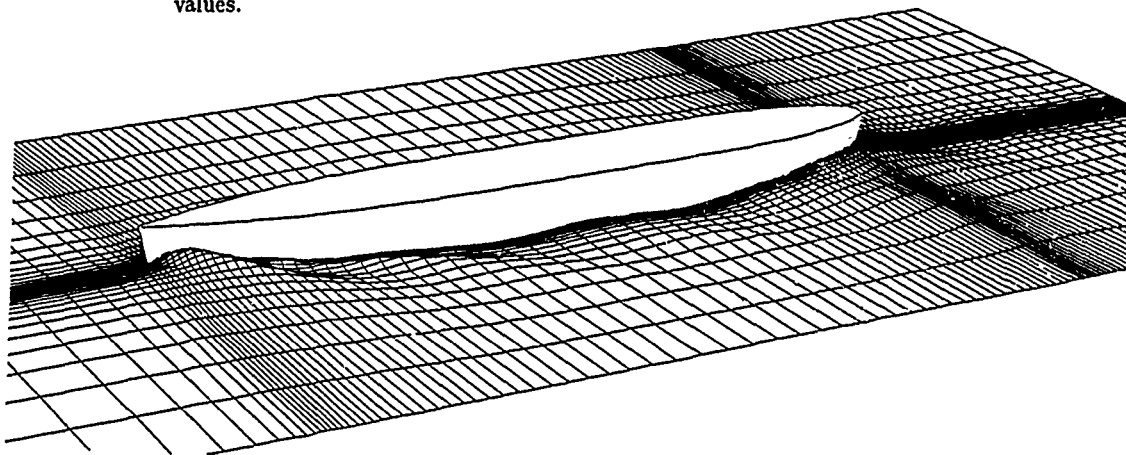


Fig. 12 Perspective view of computed waves around Series 60. Wave height is three times magnified.

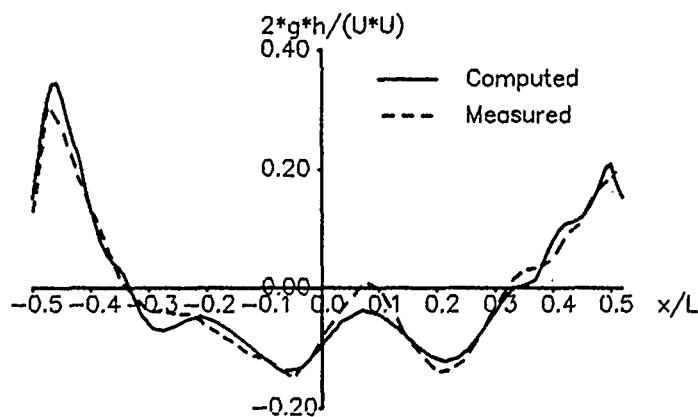


Fig. 13 Comparison of computed and measured wave profiles on ship surface of Series 60. $Fn = 0.22$, $Re = 10^6$ in computation and $Re = 1.39 \times 10^7$ in measurement.

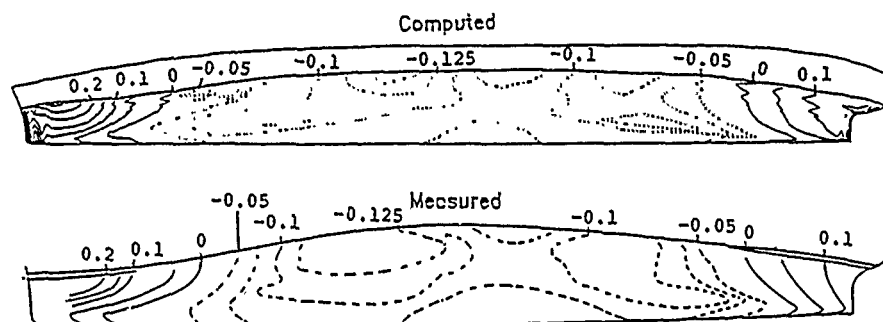


Fig. 14 Comparison of computed and measured pressure distribution on ship surface of Series 60. Contour interval is shown in figure. Dotted lines show negative values. $Fn = 0.22$, $Re = 10^6$ in computation and $Re = 7.7 \times 10^6$ in measurement.

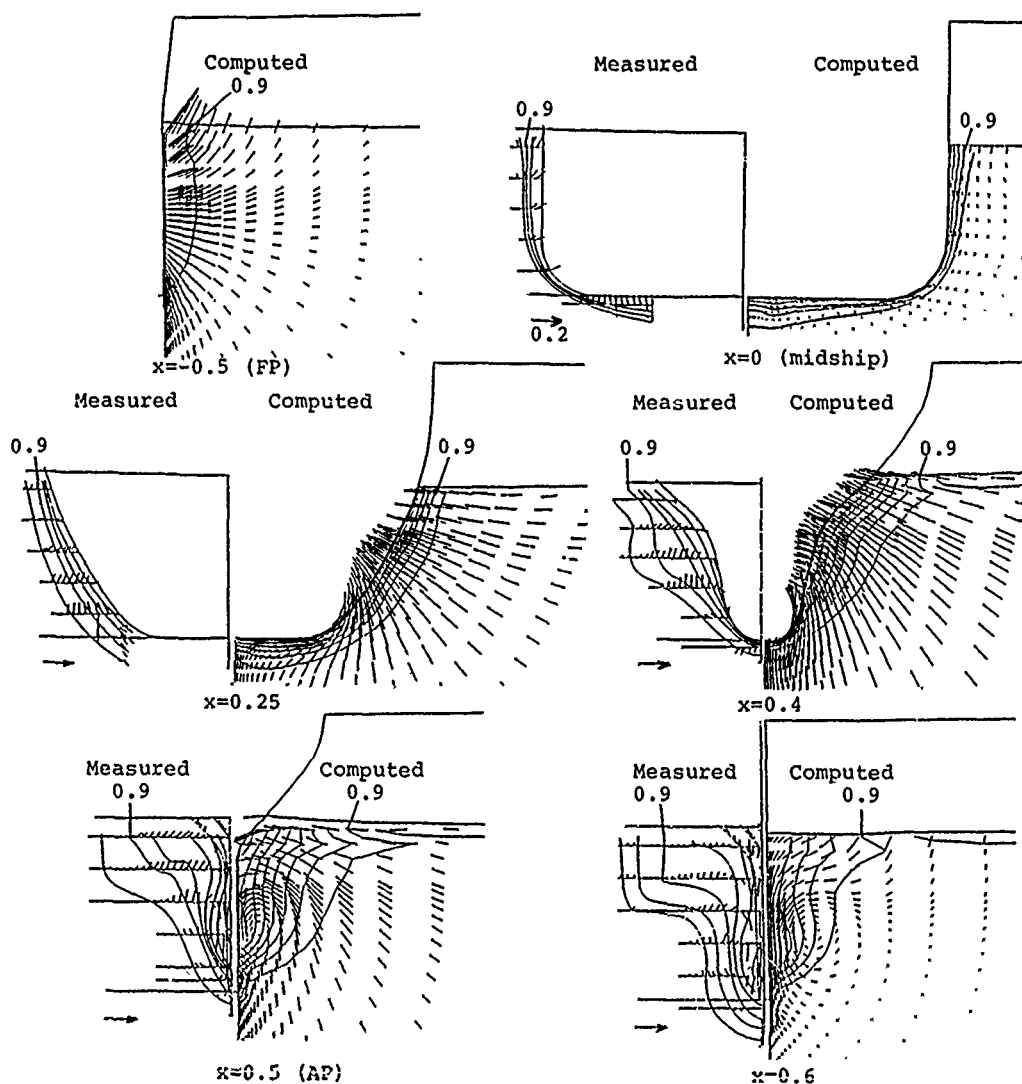


Fig. 15 Computed and measured wake contours and cross flow vectors at various stations of Series 60. Contour interval is $0.1 \times u$. $Fn = 0.22$, $Re = 10^6$ in computation and $Re = 7.7 \times 10^6$ in measurement. Top left; $x = -0.5$ (F.P.), top right; $x = 0$ (midship), middle left; $x = 0.25$, middle right; $x = 0.4$, bottom left; $x = 0.5$ (A.P.), bottom right $x = 0.6$.

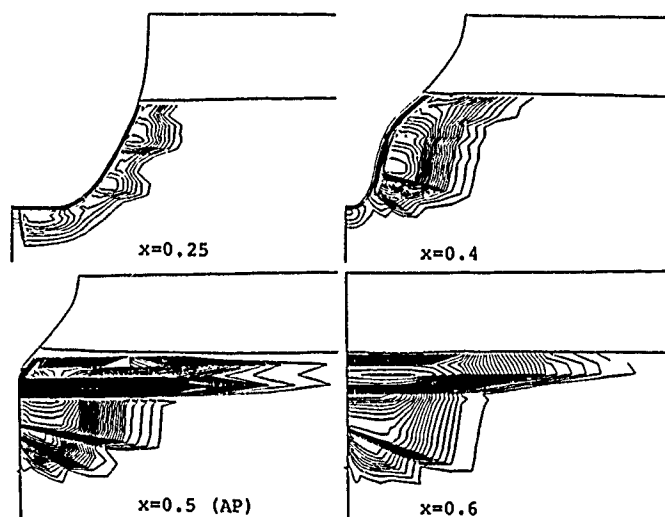


Fig. 16 Computed eddy viscosity distribution at various stations of Series 60. Contour interval is $4.0 \times 10^{-6} \nu t$. Top left; $x = 0.25$, top right; $x = 0.4$, bottom left; $x = 0.5$ (A.P.), bottom right $x = 0.6$.

in both measurement and computation at the almost same position. However, the computed wake contour is thicker than measured one. At the section of $x=0.6$, the positions of the longitudinal vortices are different from each other.

Figs.16 show the eddy viscosity contours at various stations. Non-physical eddy viscosity beneath the free surface appeared in the case of Wigley's hull cannot be seen in this case.

5. Concluding Remarks

The finite-difference solution method for the Reynolds averaged Navier-Stokes equations is applied to the simulation of high Reynolds number flow with a free surface around an advancing ship. The numerical results for Wigley's hull and Series 60, $C_b=0.6$ show good agreement with the experimental data in wave profiles and pressure distributions on the hull surface. The further efforts are required in the turbulence modeling under the free surface effect to obtain quantitative agreement for the wake distribution. The improvement of the numerical scheme is also needed to get converged solution faster.

Acknowledgment

The author would like to express his sincere gratitude to the members of the CFD group at Ship Research Institute for their valuable discussions. In particular, he is grateful to Dr. Yoshiaki Kodama, Ship Research Institute, for his suggestions and for providing the author with the graphic output code.

The computations were carried out by ACOS 910 with Scientific Attached Processor at the Computer Center, Ship Research Institute. The CPU time was

about two hours per 1000 time steps in the fine grid case.

References

- [1] T. Hino, "Numerical Simulation of a Viscous Flow with a Free Surface around a Ship Model", *Journal of The Society of Naval Architects of Japan*, Vol.161, (1987).
- [2] T. Sato, H. Miyata, N. Baba and H. Kajitani, "Finite-Difference Simulation Method for Waves and Viscous Flows about a Ship", *Journal of The Society of Naval Architects of Japan*, Vol.160, (1986).
- [3] Y. Kodama, "Computation of High Reynolds Number Flows Past a Ship Hull Using the IAF Scheme", *Journal of The Society of Naval Architects of Japan*, Vol.161, (1987).
- [4] A. Masuko, Y. Shirose, Y. Ando and M. Kawai, "Numerical Simulation of Viscous Flow around a Series of Mathematical Ship Models", *Journal of The Society of Naval Architects of Japan*, Vol.162, (1987).
- [5] F.H. Harlow and J.E. Welch, "Numerical Calculation of Time-Dependent Viscous Flow of Fluid with Free Surface", *The Physics of Fluids*, Vol.8, (1965).
- [6] T. Kawamura and K. Kuwahara, "Computation of High Reynolds Number Flow around a Circular Cylinder with Surface Roughness", *AIAA paper*, 84-0340, (1984).

- [7] R.K.C. Chan and R.L. Street, "A Computer Study of Finite-Amplitude Water Waves", *Journal of Computational Physics*, Vol.6, (1970).
- [8] H.C.Chen and V.C. Patel, "Calculation of Trailing-Edge, Stern and Wake Flows by a Time-Marching Solution of the Partially-Parabolic Equations", *IIHR Report*, No.285, (1985).
- [9] B. Baldwin and H. Lomax, "Thin-Layer Approximation and Algebraic Model for Separated Turbulent Flows", *AIAA paper*, 78-257, (1978).
- [10] "Cooperative Experiments on Wigley Parabolic Models in Japan", *17th ITTC Resistance Committee Report*, (1983).
- [11] H. Takeshi, T.Hino, M. Hinatsu, Y. Tsukada and J. Fujisawa, "ITTC Cooperative Experiments on a Series 60 Model at Ship Research Institute", *Papers of Ship Research Institute*, Supplement No.9, (1987).
- [12] F. Mewis and H.J. Heinke, " Untersuchungen der Umströmung eines Modells der Serie 60 mit $C_b=0,60$ ", *Schiffbau Forschung*, Vol.23, No.3, (1984).

DISCUSSION

by S. Ju

1. In the wall function approach, y^+ values of third grid points from the body between 20 and 100 look too small, since y^+ values of 2nd grid points from the body will be less than 10 and in the region of laminar sublayer.

2. How the transition from the laminar to turbulent flow is treated?

Author's Reply

1. Yes. The grid spacing near the wall in this calculation is a little too small. This should be improved in the future calculation.

2. Though the original Baldwin-Lomax turbulence model can cope with the transition, flow is assumed to be turbulent from the fore-end of a ship in this computation.

DISCUSSION

by R.C. Ertekin

I would like to ask two questions.

1) Because you are solving a symmetric problem, and therefore, using the symmetry condition on the center plane, the normal vector at the point where the center plane meets the bow or stern is double valued or it has discontinuous first derivatives. As a result, the Jacobian of the transformation matrix vanishes there. How did you cope with this problem? Where were the stagnation points on the bow and stern? Have you had any difficulty with the no-slip boundary condition at these points?

2) I am surprised not to see any comparisons with the care in which the linear free surface boundary condition is supposed. Why can you solve the nonlinear problem but not the linear one? I don't also understand why you can not calculate the resistance experienced by the hull. After all, shouldn't the objective of such calculations be the determination of power requirements? By the way when I say the linear problem I mean the linear (viscous) governing equations and boundary conditions!

Author's Reply

1. Along the line of mapping singularity, flow quantities, are not computed but set the average of values of the adjacent grid points. The present scheme does not use the no-slip boundary condition but use the wall-function approach. Anyway, I don't have any difficulty on the bow or stern.

2. The implementation of the linearized free surface condition in the present scheme is not impossible, but apparently the solution becomes less accurate. We cannot compute the wave-making resistance separately from the numerical results but, of course, we can compute total resistance. Please see the reply to Dr. Musker.

DISCUSSION

by A.J. Musker

I should be interested to know whether you have made any efforts to calculate total resistance. The pressure contours appear to be well predicted and you presumably also have calculated data on wall shear stress. Perhaps you could comment.

Author's Reply

Pressure resistance and friction resistance are computed by the integration of numerical results as follows.

Ship	F_n	Re	r_p	r_F	r_T
Wigley	0.25	10^6	1.44×10^{-3}	3.73×10^{-3}	5.17×10^{-3}
Series 60	0.22	10^6	0.41×10^{-3}	4.13×10^{-3}	4.54×10^{-3}

where $r_p = (\text{Pressure Resist.}) / \frac{1}{2} \rho U^2 S$

$r_F = (\text{Friction Resist.}) / \frac{1}{2} \rho U^2 S$

$r_T = r_p + r_F$

Finite-Difference Simulation of a Viscous Flow about a Ship of Arbitrary Configuration

M. Zhu, H. Miyata and H. Kajitani
University of Tokyo
Tokyo, Japan

Abstract

The improved version of the WISDAM-II method, a finite-difference solution method for a three-dimensional viscous flow about a ship of arbitrary configuration, is described. A zonal method is used for the boundary-fitted coordinate system so that the boundary layer is sufficiently resolved with proper boundary conditions on the body surface. The robustness and the accuracy are improved by the introduction of a new difference scheme. Computations are performed for a flow about a Wigley hull at $Re=10^6$ and the appropriateness of the zero-equation and the SGS turbulence models are examined.

1. Introduction

A great deal of efforts have been focused for the development of theoretical or numerical methods of solving the whole features of the flow about a ship advancing steadily in the deep water [5] [6] [8]. Since the difficulties arise from the high Reynolds number viscous flow, its separation, its interaction with the free-surface waves and so forth, we are still far away from the completion of the method.

However, methods so far developed have already turned out to be useful for the partial explanation of the flow about a ship. One example is the TUMMAC-IV method by Miyata et al., which is currently used for the design of the fore-part of the hull, see Miyata et al [1] [2] [3] [4]. The success of this method is mostly due to the fact that the wave length of the ship waves is sufficiently long and can be resolved by the available grid system.

For the numerical solution of a viscous flow about a ship, many research activities are known. Larsson and his coworkers are developing a method of designing hull forms by use of the integral method for the boundary layer, see Kim and Larsson [5]. Chen and Patel have developed a partial-parabolic and a fully-elliptic method for the viscous flow about the after-body of a ship [7] [8]. However, it is still difficult to have satisfactory solution of the separated flow, the streamwise vortices and the viscous flow

under the influence of the free-surface.

For the elucidation of the details of a turbulent flow a numerical approach by so-called large eddy simulation (LES) technique is often employed, see Moin and Kim, et al [11] [12] [13]. Since a turbulent flow at high Reynolds number is composed of vortical motions of wide-ranged spectrum and small-scaled motions may also play an important role, the resolution of viscous motions of high frequency is very important. They must be directly solved or appropriately approximated in the numerical solution method.

With the aim of developing a LES-like technique for a flow about a body of complex geometry with free-surface, a new finite-difference method called WISDAM-II is developed, see Miyata et al [6]. A boundary-fitted coordinate system, which moves at each time step owing to the deformation of the free-surface caused by waves, is employed and the subgrid-scale (SGS) turbulence model is incorporated following Deardorff [11]. This method seems to be very promising since it is very close to the direct solution of the Navier-Stokes equation, and both the viscous motion and free-surface motion are simultaneously solved. However, the improvement of the robustness and the accuracy is postponed to the future study.

The objective of this paper is twofold, one is to show the improved version of the WISDAM-II method and the other is to examine the appropriateness of the turbulence models. In order to obtain sufficiently fine spacing in the boundary layer a zonal method is employed. To attain sufficient robustness as well as accuracy the fourth-order accurate differencing scheme combined with the artificial dissipation of the fourth-derivative term is used. Both the zero-equation model and the SGS model are used and compared. The movement of the free-surface is not considered in this paper.

2. Grid system for a zonal method

Elliptic partial differential grid generation system proposed by Thompson et al. [9] is adopted to construct a boundary-

fitted curvilinear coordinate system similar to the previous study [6] both in topology and in numerical process. The three-dimensional grid system has a H-H type topology. Figure 2.1 illustrates the transformation from the physical region D (x^1, x^2, x^3) to the imaginary transformed region R (ξ^1, ξ^2, ξ^3), where the streamwise direction is approximately parallel to the ξ^1 direction, the lateral grid lines are approximately perpendicular to the ship hull surface are in the ξ^2 direction, and the grid lines parallel to the girth line of ship hull is the ξ^3 direction. The grid generation is conducted in a well-documented grid generation procedure [6] by solving the transformed Poisson equation with Richardson relaxation method, that is

$$g^{ij} \frac{\partial^2 r}{\partial \xi^i \partial \xi^j} + p^k \frac{\partial r}{\partial \xi^k} = 0$$

where for convenience, the notation of the geometric coefficients is defined as

$$g_{ij} = T_i^k T_j^l \delta_{kl}$$

$$g = \det(g_{ij})$$

$$g^{ij} = \frac{1}{g} g^{-1} e^{imn} e^{lpq} g_{mp} g_{nq}$$

where T_i^j is the transformation matrix, g_{ij} the covariant metric tensor, and g^{ij} the contravariant metric tensor. δ is the Kronecker delta and e the Eddington permutation symbol.

Since the elliptic grid generation system used in the present study works for smoothing the grid distribution rather than for clustering grid lines in the regions of interest, a great number of grid points are required when a single grid system is employed for a high Reynolds number flow. In the present study, a grid system, which is generated in the elliptic method with more than 250,000 ($170 \times 30 \times 50$) grid points, provides satisfactory resolution for the viscous flow only at the Reynolds number 10^5 .

In order to alleviate the grid-refinement problems in the vicinity of the ship hull, a zonal method is adopted in this study so that sufficient grid resolution is achieved in the turbulent boundary layer of ship at the Reynolds number 10^6 . The zonal method is applied only in the ξ^2 direction. Therefore, the inner zone with finer spacing is located in the vicinity of the hull surface and centerplane. In this study, the original grid system generated by the elliptic grid generation procedure is called "coarse grid", while a finer grid system in the vicinity of

the hull surface is called "fine grid". In the fine grid system about 12 grid points of the coarse grid system are subdivided into 40 grid points overlapping a region with the thickness about $2y/B=0.4$ from the ship hull. The locations of the fine grid points is set so that they may accord with the grid points of the coarse grid system. Therefore, at the boundary of two zonal regions called "zonal-boundary" only metric discontinuity exists. Figure 2.2 illustrates the methodology of the grid-refinement along the ξ^2 -grid lines and shows that the coarse grid points are at the same locations with the correspondent fine grid points. Figure 2.3 shows a pair of the coarse grid system and the fine grid system of a cross section of the ship. The flux conservation across the zonal-boundary is on the satisfactory degree. The details of the boundary condition at the zonal-boundary will be described in the subsequent section.

3. Computational procedure and algorithm

Time-dependent Navier-Stokes equations in rotational form and the continuity equation are the governing equations. [6] [10]

$$\frac{\partial u}{\partial t} = -grad(P + \frac{1}{2} u \cdot u) + u \times \omega - \nu rot(\omega) + R$$

$$div(u) = 0$$

where u is the velocity vector, t is the time, P is the pressure divided by the density, ν is the kinematic viscosity, and R is the net contribution of the turbulent fluxes described in the following section. All of the physical values are defined in the regular grid system of the general curvilinear coordinates. Since the vectors are expressed with contravariant components, the governing equations are written by using the notation of metric tensors as follows.

$$\frac{\partial u^i}{\partial t} = -g^{ij} \frac{\partial}{\partial \xi^j} (P + \frac{1}{2} g_{kl} u^k u^l) + g^{ij} e_{jkl} u^k \omega^l - \nu e^{ijk} \frac{\partial}{\partial \xi^j} (g_{kl} \omega^l) + R^i_j$$

$$g^{-1/2} \frac{\partial}{\partial \xi^i} (g^{1/2} u^i) = 0,$$

where ω^i is the contravariant component of vorticity vector,

$$\omega^i \equiv e^{ijk} \frac{\partial}{\partial \xi^j} (g_{kl} u^l)$$

and e^{ijk} is a permutation third-order tensor defined as

$$e^{ijk} = g^{-1/2} e^{ijk}$$

The well-known MAC method is employed as the computational procedure. The time derivative term of Navier-Stokes equations is approximated explicitly by the forward difference. From the mass conservation condition, a Poisson equation is derived for the Bernoulli-like scalar field [6]. After solving the Poisson equation iteratively by the Richardson relaxation method, a correspondent Bernoulli-like field is given. The details of the computational procedure is described in [6].

Since the zonal method is used in the present study, the time increment for the fine grid system is set at one fifth of that of the coarse grid system for the safety of the computational stability. Therefore after one step of time-marching is conducted in the coarse grid system, five steps of time-marching are conducted in the fine grid system. The zonal-boundary conditions seem to be of crucial importance in this algorithm and will be discussed in the subsequent section.

The calculation is started with the flow field of uniform velocity and constant pressure.

4. Differencing scheme

The accuracy of the differencing scheme is very important in the finite-difference method, especially in the calculation of a turbulent flow at a high Reynolds number. Since the dominant equations are written in the form with conjugate components of the transformed coordinates, it is possible to adopt various high-order differencing schemes so far known for the Cartesian coordinates. The authors have employed the third-order upwind difference scheme for variable mesh system and suggested that one may change the factor of the fourth-order velocity differential derivative depending on the mesh size and the Reynolds number to compromise the accuracy with the stability since the third-order upwind scheme is composed of the fourth-order centered scheme and the artificial dissipation of the fourth-order derivative of velocity [21] [22].

In this study, the above scheme is used in the transformed coordinates. Although the convection term is in the rotational form, the dissipation term is derived from the convection term in the gradient form. In the curvilinear coordinates, the covariant derivative of the contravariant velocity component is written by using Christoffel symbol as

$$u^i_{,j} = \frac{\partial u^i}{\partial \xi^j} + \Gamma^i_{jk} u^k$$

and the convection term in the gradient form becomes

$$u^j u^i_{,j} = u^j \frac{\partial u^i}{\partial \xi^j} + \Gamma^i_{jk} u^j u^k$$

then using the differencing scheme recommended by Baba and Miyata [23], the dissipation term is obtained as follows

$$\alpha |u^j| \frac{\partial^4 u^i}{\partial \xi^{j4}}$$

where α is the factor for the artificial dissipation term. Further details of the derivation are referred to Miyata, Zhu et al. [21] [22] and Baba and Miyata [23]. The derivatives of the convection term at and near the boundaries where sufficient grid points are not available are approximated by one-sided upwind differencing scheme and second-order centered differencing scheme with the artificial diffusion term.

The other derivatives are approximated by the second-order centered differencing scheme. The time derivative term is approximated by the forward differencing scheme.

5. Turbulence models

In the numerical simulation it is considered that because of the machine ability of the temporary computer it is impossible to calculate the turbulent flow of high Reynolds number without turbulence model except few cases of direct simulation of a flow with very simple geometry. The choice of the turbulence model as well as the computational procedure depends on the purpose of the simulation. Although the turbulent flow is substantially unsteady, only averaged steady flow field is required in some of the engineering problems. However, for scientific purposes and in some engineering problems the detailed unsteady flow should be simulated. Many simulations of turbulent flow around ship hull conducted so far use Reynolds-averaged Navier-Stokes equations and turbulence models such as algebraic turbulence model, K equation, K- ϵ model or their combination [8] [14] [15]. It is a general approach in this area that when the solution of simulation converges, the results are compared with the experimental ones which are the averaged data of the real physical values. Some simulations have shown excellent agreement with the averaged experimental results. But nobody so far answered several fundamental questions how the flow of the boundary layer is deformed to develop into wake and how is the transition from laminar to turbulent flow on the surface of the forepart of a hull.

In order to investigate into the fundamental physical features of the turbulent flow around a ship, the authors employ a zonal method near the ship hull surface, and on the other hand adopt a computational procedure with SGS turbulence model, the latter of which is similar to large eddy simulation and is called LES-like procedure by the authors. Contrary to the methods for an averaged flow this method is

supposed to resolve unsteady turbulent fluid motions of smaller scale and it will provide useful information for the understanding of the fundamental features of the turbulence structure of the ship boundary layer. The present study from above-mentioned standpoint will hopefully to throw a light to the research of this area.

In this study two turbulence models are used, one is the algebraic turbulence model and the other is subgrid-scale turbulence model. In order to examine the possibility of applying the SGS turbulence model to the turbulent flow around ship by comparing the computational results of the two turbulence models with the experimental data. Then the details of the physical features from the computation are discussed. The formulation of the subgrid-scale turbulence model is essentially same with the previous study by Deadroff-type [11] and is based on the eddy viscosity concept, that is to say, the subgrid-scale stresses used in this study are isotropic ones. The SGS eddy viscosity is defined as

$$\nu_s = (C_0 \Delta)^2 (2\bar{v}_{ij} \bar{e}^{ij})^{1/2}.$$

and the SGS stresses R^{ij} are written as

$$R^{ij} \equiv \overline{u^i u^j} = \frac{1}{2} g^{ij} \overline{u^m u^m} g_{lm} - 2\nu_s \bar{e}^{ij}.$$

However, using this formulation of SGS turbulence model without any special treatment near the ship hull surface, the turbulent production may be insufficient and be diffused out in the vicinity region inside the laminar viscous sublayer [12] [13]. This is because the essential turbulence generation near the hull surface is due to the inhomogeneous wall turbulence, which is characterized by a mixing length of the scale of sublayer thickness and of boundary layer thickness. The effects of the curvature of a wall as well as the pressure gradient should also be considered in the turbulence models. However, they are postponed to the future study.

In order to take into account the inhomogeneous effect of the wall turbulence in the subgrid-scale turbulence model, the Prandtl-van Driest formulation is introduced for the reduction of the turbulence scale near the hull surface by multiplying the subgrid-scale in the Smagorinsky eddy viscosity by the exponential damping function, that is,

$$\Delta = \Delta [1 - e^{-y^+/\Lambda}]$$

where Λ is set constant at 26.0. The details of the formulation of subgrid-scale turbulence model are described in [6].

The algebraic turbulence model used in this study is a modified Cebeci-Smith type [17] [18]. For the inner region of the boundary layer the Prandtl-van Driest formulation is used as

$$\epsilon = l^2 \left| \frac{\partial U}{\partial y} \right|$$

$$l = ky[1 - e^{-y^+/\Lambda}]$$

and for the outer region the Clauser's formulation together with Klebanoff's intermittency function is applied as follows.

$$\epsilon = \alpha U \delta^* F_{Kleb}$$

$$F_{Kleb} = \frac{1}{[1 + 5.5(y/\delta)^6]}$$

The correspondent boundary layer displacement thickness δ^* and boundary layer thickness δ in the case of zero-pressure gradient are determined by y_{max} of the maximum point of the root of the shear stress where the velocity is defined from the law of the wall of the Coles formulation [19]

$$F = y \left| \frac{\partial U}{\partial y} \right| [1 - e^{-y^+/\Lambda}]$$

and the boundary layer thickness δ^* and the displacement thickness δ are obtained as

$$\delta = 1.936 y_{max}$$

$$\delta^* = \delta \frac{\sigma}{K} [11 + 1]$$

Also both the accelerated and the decelerated flows including separated flows are considered in this formulation of the modified Cebeci-Smith model, see Stock and Hasse [17].

6. Boundary Condition

No-slip velocity condition is implemented at the ship hull surface. In this study the first grid point in the fluid region is set inside the viscous sublayer, and the velocity at this point is interpolated by the velocity profile of van Driest [18] given as

$$l^{+2} \left(\frac{\partial u^{+}}{\partial y^{+}} \right)^2 + \frac{\partial u^{+}}{\partial y^{+}} = 1$$

$$l^{+} = \kappa y^{+} [1 - e^{-y^{+}/\kappa}]$$

where $u^{+} = u/u_{\tau}$ and $y^{+} = y^{*} u_{\tau}/\nu$. As shown in Figure 6.1, point A is the nearest point and point B is the second point. At each time-step the friction velocity on the ship hull surface is calculated so that the velocity at point B satisfies the above equation. And then the velocity at point A is interpolated by the following equation.

$$\frac{u_A^1}{u_B^1} = \frac{u_A^3}{u_B^3} = \frac{q_A}{q_B}$$

where u^1 is the component of velocity along ξ^1 grid line and u^3 is along ξ^3 grid line, both of the lines are parallel to the ship hull surface. And q is the velocity magnitude at the grid point, which is calculated by the ordinary procedure at point B and by the equation of van Driest's velocity profile at point A.

At the other boundaries, the uniform stream velocity is set at the inflow boundary and zero normal-gradient condition is set at the side and outflow boundaries.

The pressure is fixed at the bottom boundary and zero normal-gradient condition of pressure are set at the other boundaries.

The zonal-boundary that connects two zones described in the previous section is placed along the ξ^2 grid line. As shown in figure 6.2, the velocities and momentum terms of the Navier-Stokes equation in the overlapping region of the coarse grid system are set at the same values with those of the fine grid system for the mass and momentum conservation. The algorithm of the calculation with the zonal-boundary is as follows.

1. Calculation in the coarse grid (zone 2):

a. Calculate the momentum terms of the Navier-Stokes equation while they are interpolated from zone 1 in the overlapping region by using the updated velocity in zone 2.

b. Calculate the source term of the Poisson equation in zone 2 and iterate the pressure solution loop under the zonal-boundary condition, which the pressure at the point A' (figure 6.2) is set at the same values with the pressure at point A of the fine grid (zone 2).

c. Update the velocity in the coarse grid (zone 2).

2. Calculation in the fine grid (zone 1):

a. Calculate the momentum terms of the Navier-Stokes equation by using the velocity of the fine grid (zone 1).

b. Compose the Poisson equation for the fine grid (zone 1) and solve it under the zonal-boundary condition that the pressure at point B (figure 6.2) is set at the same value with that at point B' in the coarse grid (zone 1).

c. Update the velocity at the fine grid (zone 1) and update the velocities in the overlapping region of the coarse grid system.

7. Computed results

Computations are performed for a flow about a Wigley hull at the Reynolds number (Re) 10^6 with the algebraic turbulence model (modified Cebeci-Smith model) (Case 1) or the subgrid-scale model (Case 2). It is noted that in the computed results the viscous flow about a hull is not wholly developed but it is on the transition stage, since the computations are continued only for $T=1.2$ (dimensionless time, $T=tU_0/L$, U_0 is uniform flow velocity and L is ship length) in the Case 1 and for $T=0.8$ in the Case 2.

The grid system shown in Fig.2.3 is used and the number of grid points is 255,000 for the coarse grid system and 340,000 for the fine grid system. The smallest grid spacing in the ξ^2 direction about 0.005% of the ship length. The time increment Δt is 0.00005 for the coarse grid system and 0.00001 for the fine grid system, respectively. The factor of the artificial dissipation term α is set at 6.0. The computations are conducted on HITAC S820/80 supercomputer with almost 20 hours of CPU time. The vectorization ratio of CPU time is 98% for both cases.

The pressure distribution on the ship hull surface ($x^3=0.0$) computed with the algebraic turbulence model is compared in Fig.7.1. The agreement with the measured results by Sarda [20] is not very satisfactory since the flow is not fully developed and furthermore in the algebraic turbulence model used in this study the displacement thickness of the boundary layer is determined by the well-known Coles velocity profiles for the zero-pressure gradient [17] while the decelerated flow near the after end of ship is involves large pressure gradient. However it is noted the overall flow field is approximately realistic.

In order to examine the detailed flow field comparison is made of the flow variables at two longitudinal location $x^1/L=0.8012$ ($\xi^1=110$) and $x^1/L=0.9218$ ($\xi^1=120$), where the viscous flow along the hull surface may gradually develops and three-dimensional motions may become important. The data are illustrated in Fig.7.3 and 7.4 for Case 1, and in Fig.7.5 and 7.6 for Case 2. All variables are made dimensionless following the equations described in the previous sections. The distribution of velocity components,

vorticity components, eddy viscosity coefficient and Reynolds shear stresses along the lateral ξ^2 grid line are presented at two vertical location $x^3 = -0.0463$ ($\xi^3 = 30$) and $x^3 = -0.0341$ ($\xi^3 = 35$) while the water plane is at $x^3 = 0.0$ and the keel is at $x^3 = -0.0625$.

The contour maps of u^1 and ω^1 indicate that the boundary layer is still developing and the streamwise vortex is going to be formed in it. The thickness of boundary layer in Case 1 is much thinner than Case 2. This is mostly due to the small magnitude of the eddy viscosity, which may deteriorate the diffusive effect of turbulent flow. It is approximately one seventh of the case of the subgrid-scale model. At the bottom of Fig.7.3 to 6 the computed Reynolds shear stresses are shown. Since their magnitude reaches the maximum value of 10^3 according to the measured results [20], the turbulent flow is not wholly developed in the computations. However it is shown that two components of the shear stresses which are not considered in Case 1 are important in this flow field and hence the use of the algebraic zero-equation model is questionable.

The relation between the location of the maximum shear and the boundary layer thickness is shown in Fig.7.2. According to Stock and Haase [17], the relation should be given by the linear equation $\delta = 1.936Y_{...}$. This indicates that the boundary layer is excessively enlarged by the subgrid-scale model and on the contrary it is suppressed by the zero-equation model. This tendency is amplified at $\xi^1 = 120$ more than at $\xi^1 = 110$. It is supposed that the subgrid-scale turbulence model overestimates the turbulence stresses and the zero equation model underestimates in this region.

The figures for vorticity components indicates that all three components play some important roles and their interactions may be significant. Notwithstanding the difference in the thickness of the boundary layer it is common to Case 1 and 2 that the inflection of vorticity profile appears at $\xi^1 = 120$.

8. Concluding remarks

The improved version of the WISDAM-II method is still under development and comprehensive comparison with the measured results or interesting elucidation of the complicated turbulent motions are beyond the scope of the paper. Since the present method avoid approximation as far as possible, the accuracy seems to be on a high level but it is often accompanied by the extremely long CPU time even by the supercomputer.

The purpose of the present method is to solve both wave and viscous motions simultaneously. It is already demonstrated that this is achieved by use of the moving grid system. [6] However the difference of wave length between free-surface waves and viscous turbulent motions is tremendous. The use of zonal method described here will be one

of the promising approach.

For the numerical simulation of the detailed viscous flows on the hull surface we must be very careful as suggested by the present test computations. The zero-equation model ignores some of the Reynolds stresses which may not be sufficiently small in the real flow. The two-equation model is said to be insufficient for the separated flow. The subgrid-scale model may give excessive turbulence stresses when it is used in the grid system of which spacing is not sufficiently small. The subgrid-scale model will be useful not only for the large eddy simulation but also for the flow simulation of engineering purposes. However, the coefficients and scales for the model must be carefully chosen.

This research is supported partly by the Grant-in-Aid for Cooperative Research of the Ministry of Education, Science, and Culture and partly by the LINEC group of shipbuilders in Japan.

References

1. Miyata, H., Nishimura, S. and Masuko, A., "Finite difference simulation of nonlinear waves generated by ships of arbitrary three-dimensional configuration", J. Computational Phys., Vol.60, No.3 pp.391-436 (1985a)
2. Miyata, H. and Nishimura, S., "Finite-difference simulation of nonlinear waves", J. Fluid Mech., Vol.157, pp.327-357 (1985b).
3. Miyata, H., Nishimura, S. and Kajitani, H., "Finite-Difference simulation of non-breaking 3-D bow waves and breaking 2-D bow waves", Proceedings of Fourth International Conference on Numerical Ship Hydrodynamics, Washington D.C., pp.259-291 (1985c).
4. Maekawa, Y., Kawasumi, K. and Miyata, H., "A method of optimizing hull-forms by use of the finite-difference technique TUMMAC-IV", Proceedings of International Symposium on Ship Resistance and Powering Performance, Shanghai, pp.70-77 (1989)
5. Kim, J. and Larsson, L., "Comparison between first and higher order methods for computing the boundary layer and viscous resistance of arbitrary ship hulls", Proceedings of International Symposium on Ship Resistance and Powering Performance, Shanghai, pp.17-24 (1989).
6. Miyata, H., Sato, T. and Baba, N., "Difference solution of a viscous flow with free-surface wave about an advancing ship", J. Computational Phys., Vol.72, No.2, pp.393-421 (1987).
7. Chen, H. and Patel, V. C., "Calculation of trailing-edge, stern and wake flows by a time-marching solution of the partially-parabolic equations", IIHR Report No.285 (1985).

8. Chen, H. and Patel, V. C., "Practical near-wall turbulence models for complex flows including separation", AIAA paper 87-1300 (1987).
9. Thompson, J. F. et al., "Boundary-fitted coordinated systems for numerical solution of partial differential equation - A review", J. Computational Phys., Vol.47, pp.1-108 (1982).
10. Warsi, Z. U. A., "Conservation form of the Navier-Stokes equations in general nonsteady coordinates", AIAA J., Vol.19, No.2, pp.240-242 (1980).
11. Deardorff, J. W., "A numerical study of three-dimensional turbulent channel flow at large Reynolds numbers", J. Fluid Mech., Vol.41, pp.453-480 (1970).
12. Moin, P. and Kim, J., "Numerical investigation of turbulent channel flow", J. Fluid Mech., Vol.118, pp.341-377 (1982).
13. Shumann, U., "Subgrid scale model for finite difference simulations of turbulent flows in plane channels and annuli", J. Computational Phys., Vol.18, pp.376-404 (1975).
14. Kodama, Y., "Computation of high Reynolds number flows past a ship hull using the IAF scheme", J. the Society of Naval Architects of Japan, Vol.161, pp.22-33 (1987).
15. Masuko, A. et al., "Numerical simulation of viscous flow around a series of mathematical ship models" (in Japanese), J. the Society of Naval Architects of Japan, Vol.162, pp.1-10 (1987).
16. Rai, M. M., "A conservative treatment of zonal boundaries for Euler equation calculations", J. Computational Phys., Vol.62, pp.472-503 (1986).
17. Stock, H. W. and Haase, W., "Determination of length scales in algebraic turbulence models for Navier-Stokes methods", AIAA J., Vol.27, pp.5-14 (1989).
18. Cebeci, T. and Smith, A. M. O., *Analysis of Turbulent Boundary Layer*, Academic Press, New York (1974).
19. Baldwin, B. S. and Lomax, H., "Thin layer approximation and algebraic models for separated turbulent flows", AIAA -78-257 (1978).
20. Sarda, O. P., "Turbulent flow past ship hulls - an experimental and computational study", Ph.D thesis of Univ. of Iowa (1986).
21. Miyata, H., Kajitani, H., Zhu, M. and Kawano, T., "Nonlinear forces caused by breaking waves", Proceedings of 16th Symposium on Naval Hydrodynamics, Berkeley, pp.514-536 (1986).
22. Miyata, H., Kajitani, H., Zhu, M., Kawano, T. and Takai, M., "Numerical study of some wave-breaking problems by a finite-difference method", J. Kansai Soc. N.A., Japan, No.207, pp.11-23 (1987).
23. Baba, N. and Miyata, H., "Effect of the form of Navier-Stokes equation on a separated flow simulation", J. Computational Phys. (1989) (submitted).

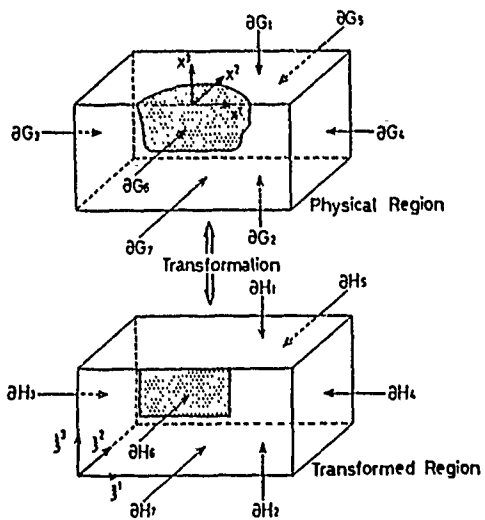


Fig.2.1 Coordinate transformation.

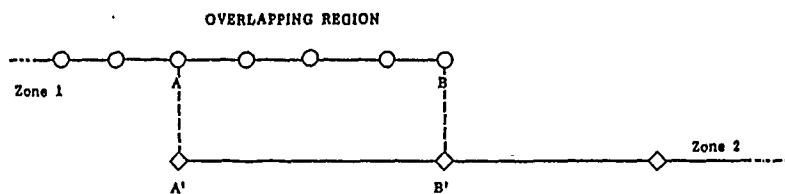


Fig.2.2 Definition sketch for the interfacing region.

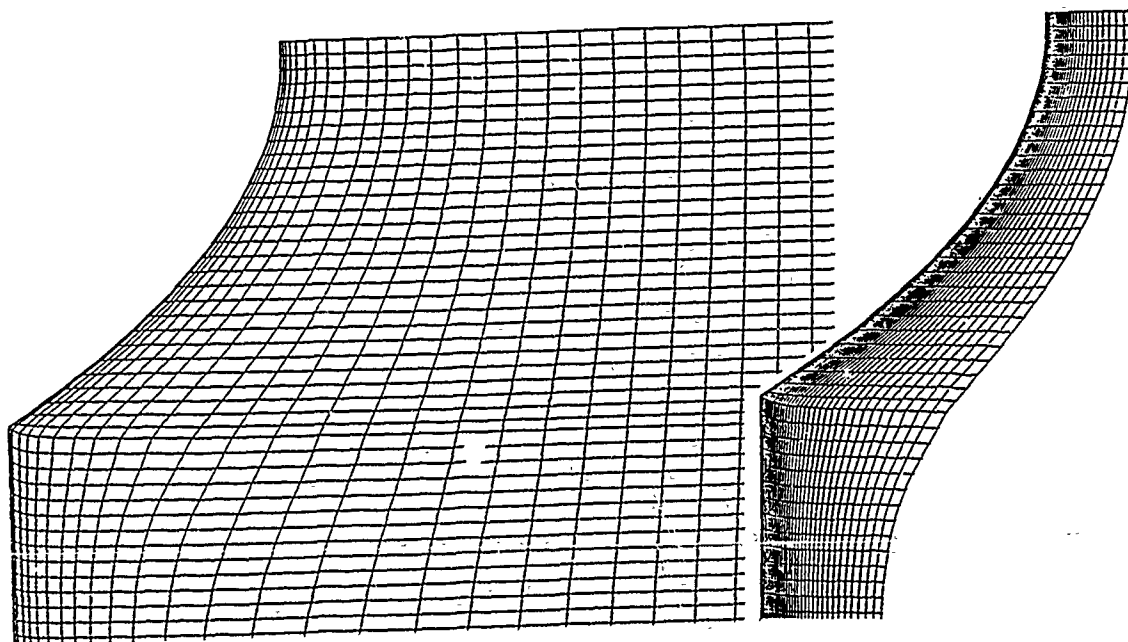


Fig.2.3 Grid system for the zonal method (transverse section), coarse (left) and fine (right) grids.

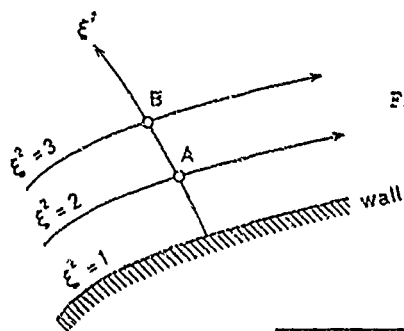


Fig.6.1 Definition sketch for the treatments on the wall.

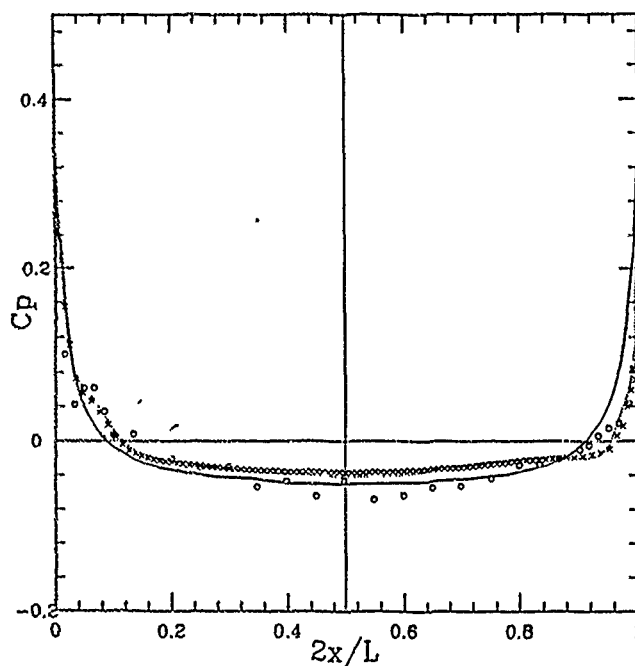


Fig.7.1 Longitudinal distribution of pressure on the hull surface, —; potential theory, \circ ; experiment by Sarda [20] at $Re=4.5 \times 10^6$, ---- ; present computation with zero-equation model at $T=0.6$, \cdot ; do at $T=1.2$.

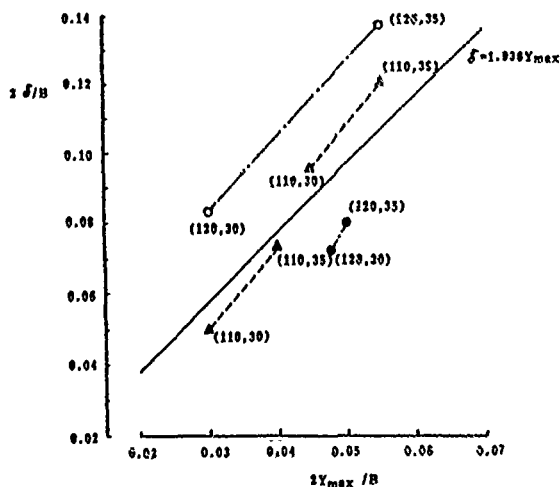


Fig.7.2 Relation between the boundary layer thickness (δ) and the location of maximum Reynolds stress (Y_{max}), blank and black marks are for the SGS and the zero-equation model, respectively, and numbers in parentheses indicate location.

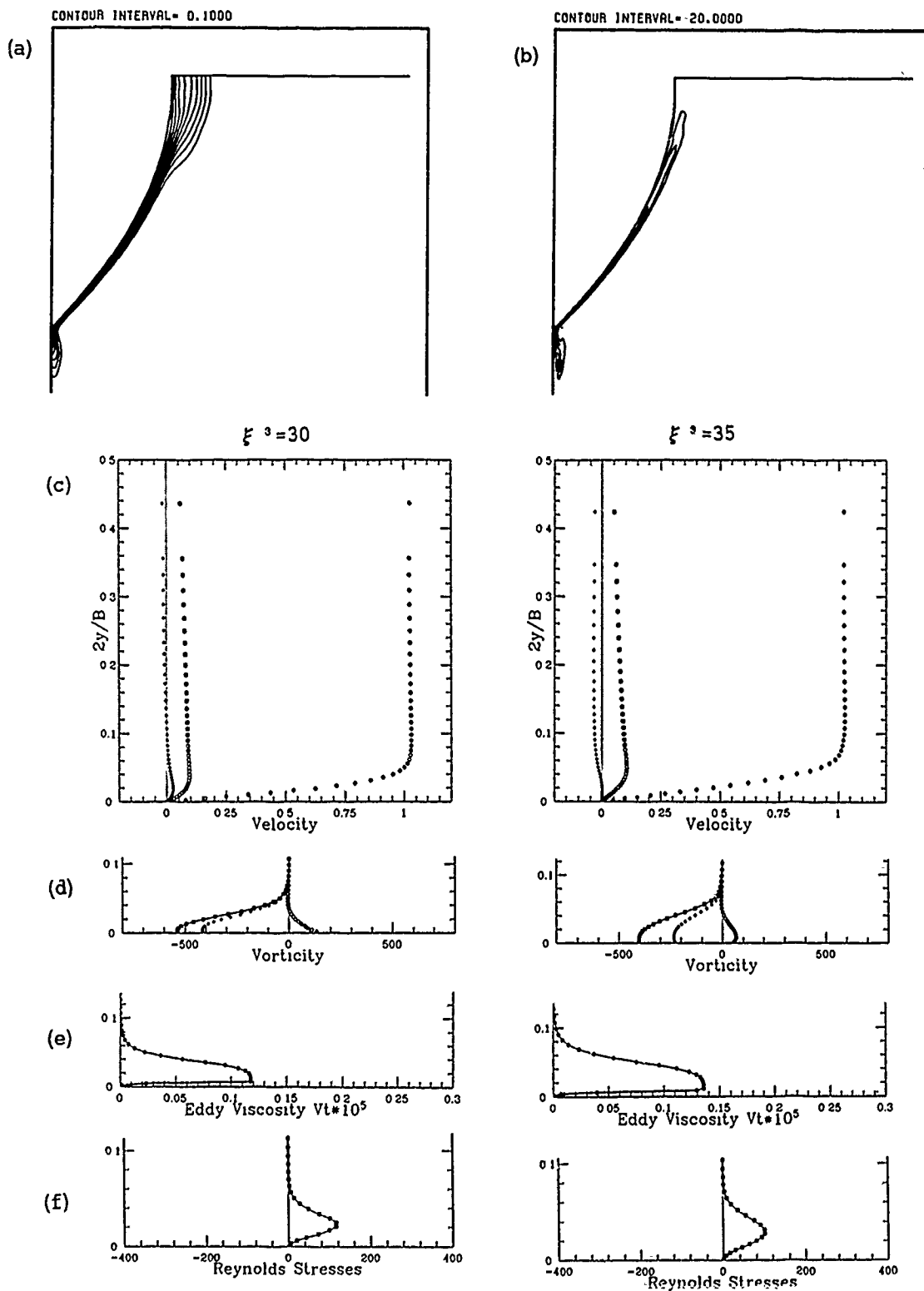


Fig.7.3 Computed results with the zero-equation model at $\xi^{-1} = 110$, $T = 1.2$.
 (a) contour map of u_1 , (b) contour map of u_1 , (c) velocity profiles, $\circ; u_1$, $\diamond; u_2$, $\square; u_3$ (left; $\xi^{-1} = 30$, right; $\xi^{-1} = 35$), (d) vorticity profiles, $\circ; \omega_1$, $\diamond; \omega_2$, $\square; \omega_3$ (do),
 (e) turbulent eddy viscosity, (f) Reynolds shear stress $-R_{12}/u_{\tau}^2$

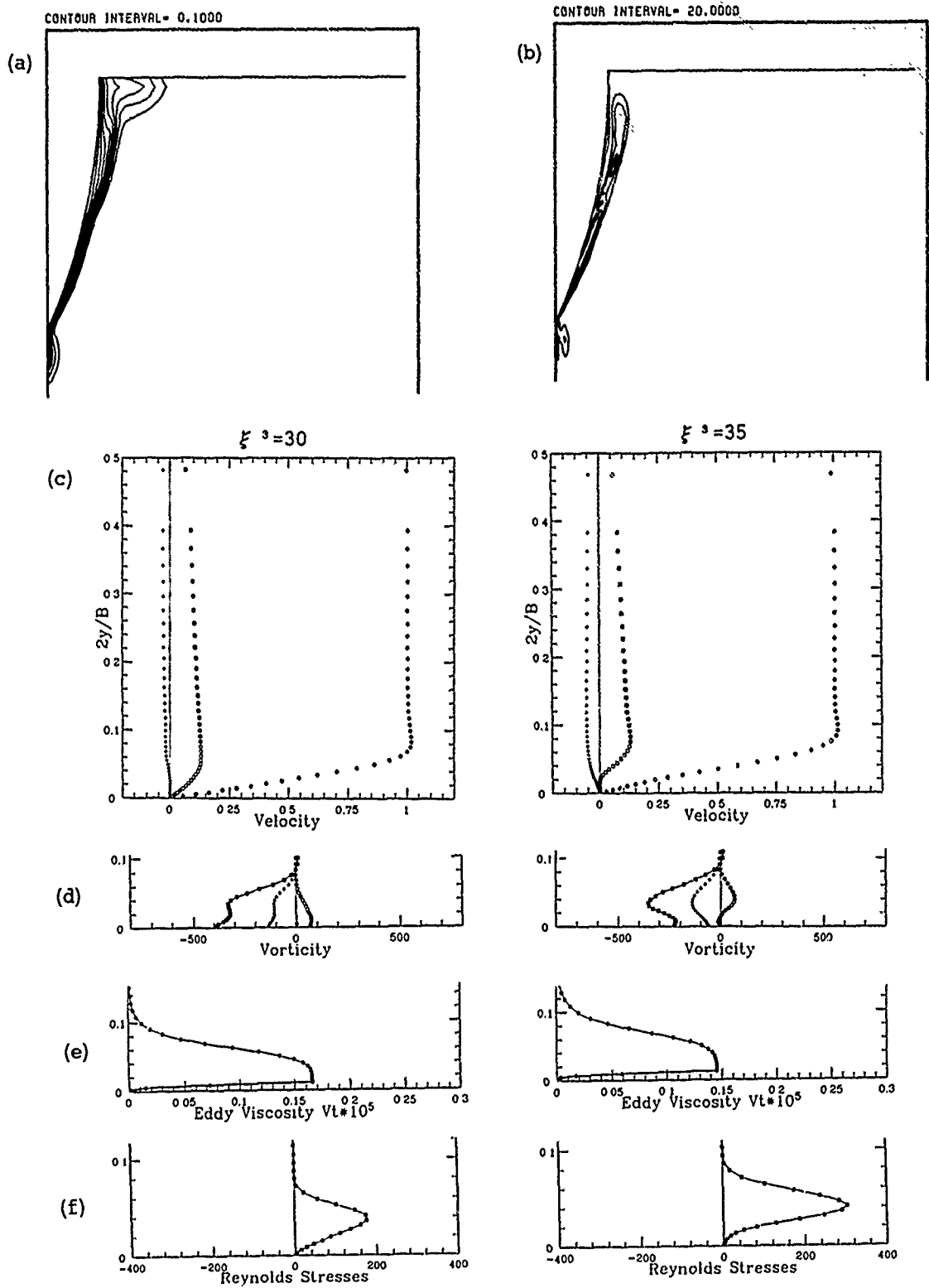


Fig.7.4 same as Fig.7.3 at $\xi^1 = 120$, $T = 1.2$.

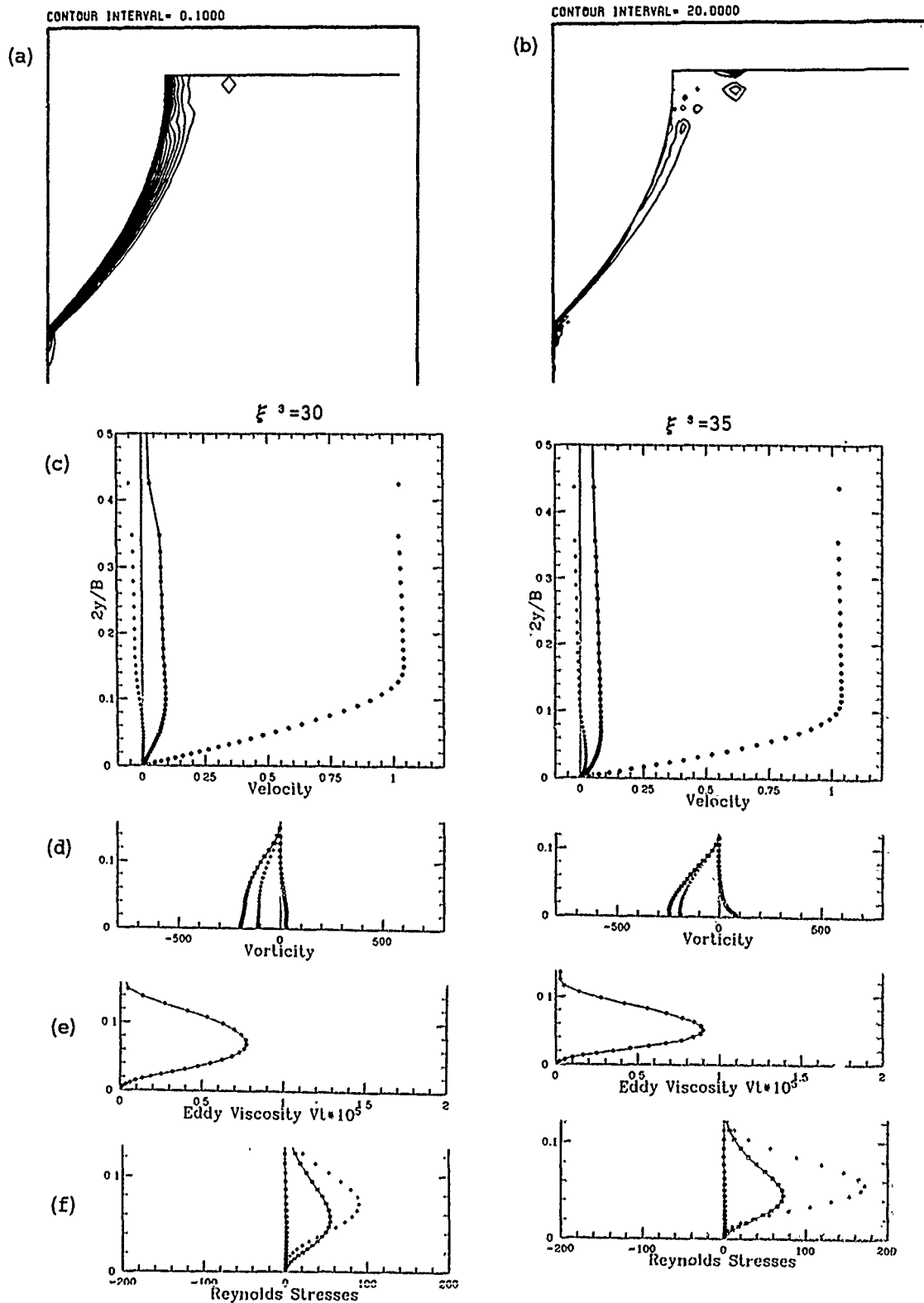


Fig.7.5 Computed results with the SGS model at $\xi^1=110$, $T=0.8$.
 (a) contour map of u_1 , (b) contour map of u_1 , (c) velocity profiles, $\diamond; u_1$, $\diamond; u_2$, $\square; u_3$ (left; $\xi^3=30$, right; $\xi^3=35$), (d) vorticity profiles, $\diamond; \omega_1$, $\diamond; \omega_2$, $\square; \omega_3$ (do),
 (e) turbulent eddy viscosity, (f) Reynolds shear stresses, $\diamond; -R^{12}/\rho u_3^2$, $\diamond; -R^{13}/\rho u_3^2$, $\square; -R^{23}/\rho u_3^2$

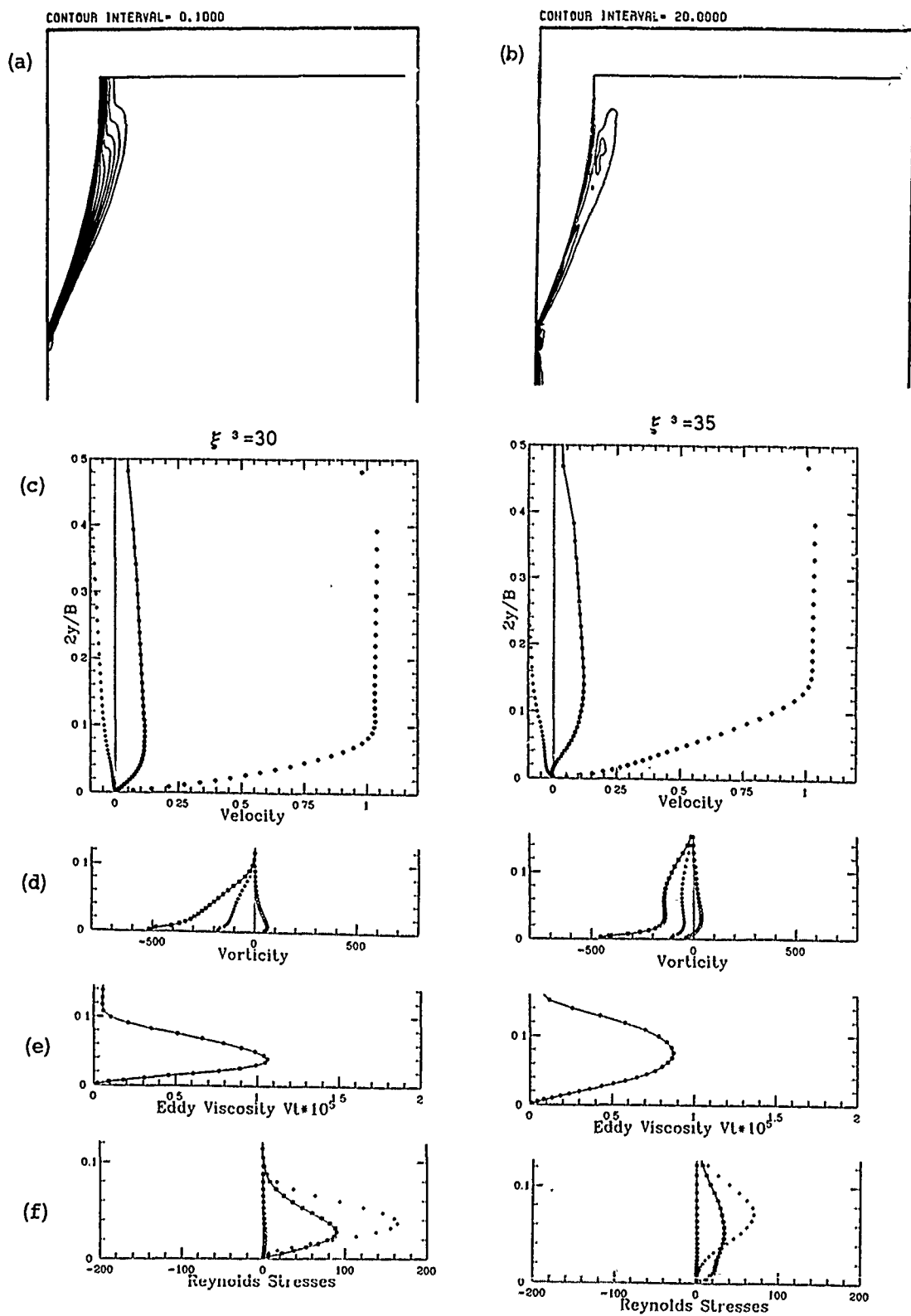


Fig.7.6 same as Fig.7.5 at $\xi^1 = 120$, $T = 0.8$.

Numerical Evaluation of the Complete Wave-Resistance Green's Function Using Bessho's Approach

H. T. Wang
Naval Research Laboratory
Washington, USA
J. C. W. Rogers
Polytechnic Institute of New York
New York, USA

Abstract

This paper presents a numerical method for calculating the total Green's function for the wave resistance case of a source in steady translation below the free surface. Starting with a representation of this function in the complex plane given by Bessho a series of transformations of variables are used to reduce it to three real single integrals. The integrands are regular and are entirely in terms of elementary functions. Two of the integrals are even in the direction of flow while the remaining integral is odd. The even and odd integrals may also be conveniently expressed in terms of the near and far field components. While the method is applicable nearly everywhere (except for the well known difficulties at the limiting cases when the source is located near the free surface or the field point is close to the source), computer time varies in the computation domain.

A computer code has been written to implement the above method. Sample calculated results are given in several forms to show the accuracy and computer time requirements of the code. A series of line and contour plots are given to show typical shapes of the integrands at different locations in the computation domain as well as to exhibit the relative behavior of the various component integrals.

1. Introduction

For a number of decades, interest in the important Green's function for a submerged nonoscillating source moving at constant forward speed in fluid of infinite depth has largely centered on its far field characteristics. This was both due to the greater simplicity of the far field evaluation as well as its direct applicability to finding the hull resistance component due to wavemaking. The far field wave pattern required only the evaluation of a single integral with a regular integrand over a one-dimensional wavenumber space while the complete Green's function involves the additional calculation of a double integral with a singular integrand over a two-dimensional wavenumber space. The applicability of using only the far field analysis to obtain the wave resistance was aided by the pioneering work of Michell [1] who showed that reasonable estimates of the source strengths modeling the hull surface for the case of thin ships could be obtained directly from ship geometry,

without need to ascertain the near field mutual influence of the sources. The landmark paper by Eggers, Sharma, and Ward [2] presents a comprehensive survey of different methods of using the single-integral far field Green's function to obtain the wave resistance.

In recent years, with the availability of ever larger and faster computers, interest has been enlarged to include the near field terms of the Green's function as well as a more accurate calculation of its far field behavior. An evaluation of the near field terms would give a more accurate determination of the source strengths for hull forms which do not conform to thin ship theory as well as a more detailed definition of the flow field and pressure forces on or near the hull. In the far field case, the use of modern day remote sensing technology makes it of interest to assess the ship wake for wavelengths which are significantly shorter than those applicable to the wave resistance problem.

Efforts at rendering the initial double integral representation of the Green's function amenable to numerical calculation usually involve expressing it as a series of single integrals. Noblesse [3] gives several alternate single integral representations. A popular form is to express the Green's function as two single integrals consisting of a near field part N which is even in the flow direction x , and a wave disturbance part W which is defined only downstream of the source. The near field part N has an integrand which is in terms of the higher order derived exponential integral function. Noblesse [4] and Euvrard [5] have conducted detailed studies of the behavior of N and W , especially at limiting regions of the computation domain.

In terms of actual numerical implementation, Newman [6] has developed a procedure for calculating N in terms of extensive sets of tabulated coefficients of Chebyshev or ordinary polynomials. The coefficients take on four different sets of values, depending on the radial distance R from the source. In the case of the wave disturbance part W , Noblesse [7] and Newman [8] have developed procedures for the specialized case of the vertical xz centerplane while Baar and Price [9] implement a more general calculation for the entire domain with the exception of the region near the free surface. In these studies, the computation region is again divided into several regions depending on the values of x/z or $x/\sqrt{y^2 + z^2}$. In many cases, the solution is in terms of

a series of functions, and there is often a delicate balance between the regions of convergence of near field and asymptotic expansions.

Our paper presents a numerical implementation of a representation of the Green's function developed by Bessho [10]. By means of a series of ingenious transformations, he succeeds in reducing the entire Green's function to a single integral along a curved path in the complex plane. The integrand is regular and is entirely in terms of elementary functions. This remarkable representation has been noted by previous investigators [4,6] and has prompted Ursell [11] to give a more complete derivation, including the justification of an important intermediate step. Our work differs from previous numerical implementations in several aspects. Our work is entirely in terms of integrals as opposed to the use of expansions in series. Our implementation is for nearly the entire computation domain and for the complete Green's function as opposed to specialized domains or particular parts of the Green's function.

The paper starts with a concise statement of the critical points of Bessho's contribution. Then, a more complete description of the derivation, as given by Ursell, is given in outline form. One reason for giving this derivation is to point out the starting point for our numerical work, which occurs before the final single integral representation is reached. A detailed description is then given of the transformations required to convert the original complex integrals to three real integrals, two of which are even in x (G_e) and one is odd in x (G_o). The simple relationship between G_e and G_o and the commonly used N and W is pointed out. Peculiar features of each of the three integrands are discussed, and the procedures used for their integration are pointed out. A special limiting process is used to obtain G_e and G_o on the axis directly downstream of a source at the free surface. The variation of computer time requirements and accuracy of the calculated results in the computation domain are discussed. Numerical results are presented to check on the accuracy of our procedure and to illustrate in graphical form the behavior of the integrands and their integrated values. The paper concludes with a summary of the principal findings.

2. Derivation of Bessho's Single Integral Representation

2.1 Initial Representation in Double Integral Form

In this work, we will consistently follow the notation used by Ursell [11]. Figure 1 shows the coordinate system used in our work, where x corresponds to the direction of the current flow U , y is the horizontal direction perpendicular to x , and z is the vertical direction positive downwards. For a stationary nonoscillating source located at (X, Y, Z) the Green's function $G(x, y, z; X, Y, Z)$ at field point (x, y, z) is given by

$$G(x, y, z) = \frac{1}{R^1} - \frac{1}{R} + G_0 \quad (1)$$

where $R^1 = [(x-X)^2 + (y-Y)^2 + (z-Z)^2]^{1/2}$

$$R = [(x-X)^2 + (y-Y)^2 + (z+Z)^2]^{1/2}$$

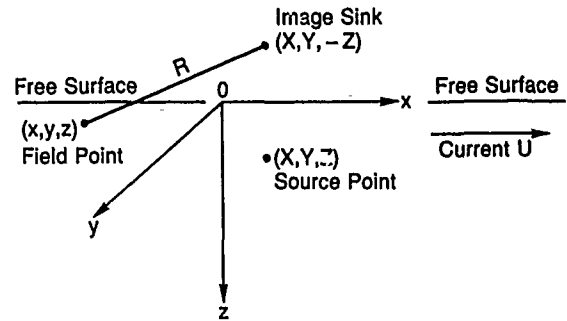


Figure 1. Definition of Coordinate System and Flow Configuration

$$G_0 = \frac{-1}{\pi} \lim_{\epsilon \rightarrow 0} \int_{-\pi}^{\pi} d\theta \int_0^{\infty} dk$$

$$\frac{\exp[-k(z+Z) + ik(x-X)\cos\theta + ik(y-Y)\sin\theta]}{k \cos^2\theta - 1 - i\epsilon \cos\theta} \quad (2)$$

In the above equation, all length variables have been made dimensionless by multiplication by the factor g/U^2 where g is the gravity constant. G_0 represents an inverse double Fourier transform over the two-dimensional $k-\theta$ wavenumber space. The parameter $\epsilon(>0)$ is added to ensure that the radiation condition is satisfied at infinity. Also, following Ursell, the terms $(x-X)$, $(y-Y)$, and $(z+Z)$ appearing in Eq. (2) are simply replaced by x, y , and z for the sake of convenience.

2.2 Concise Statement of Bessho's Approach

The usual way of simplifying the double integral expression for G_0 is to perform an initial integration over k or θ , thus reducing the double integral to a single integral. The integrand, however, is not entirely in terms of elementary functions but contains the higher order derived exponential integral function $E_1(u)$ defined by

$$E_1(u) = -\int_u^{\infty} \frac{e^{-\lambda}}{\lambda} d\lambda \quad (3)$$

In Bessho's approach, the initial integration to reduce the double integral to a single integral is not performed at the outset. Instead, after a series of transformations of the double integral, including changes of variables, deformation of the paths of integration in the complex plane, expressing G_0 as derivatives of more convergent integrals, and interchanging order of integration, the double integral is finally converted to single integral form by means of the following crucial equality

$$\int_{-\infty}^{\infty} \frac{\exp(imP)}{m-Q} dm \quad (4)$$

$$\begin{aligned} & 2\pi i \exp(iPQ) \quad (P > 0, \text{Im } Q > 0) \\ & = -2\pi i \exp(iPQ) \quad (P < 0, \text{Im } Q < 0) \\ & 0 \quad (P \cdot \text{Im } Q < 0) \end{aligned}$$

where F is real and Q is complex. Thus, the order of integration is reduced entirely in terms of elementary functions. The following section gives a summary of Ursell's detailed derivation and justification of Bessho's approach.

2.3 Summary of Ursell's Derivation

Using the equality

$$\int_{\pi/2}^{\pi} \cos \theta d\theta = \int_0^{\pi/2} -\cos \theta d\theta \quad (5)$$

rewrite G_0 in Eq. (2) as the following sum of A and B

$$G_0(x, y, z) = A(x, y, z) + B(x, y, z) \quad (6)$$

where A and B are now integrated from $-\pi/2$ to $+\pi/2$ over θ .

By introducing the following two sets of new variables

$$m = k \cos \theta, \quad \tanh v \doteq \sin \theta \quad (7)$$

$$y = \rho \sin \alpha, \quad z = \rho \cos \alpha, \quad x = \rho \sinh \beta, \quad R = \rho \cosh \beta \quad (8)$$

and writing A and B as

$$A = A_0 + i \frac{\partial}{\partial x} A_1, \quad B = B_0 + i \frac{\partial}{\partial x} B_1 \quad (9)$$

the following expressions are obtained for A_0 , B_0 , A_1 , and B_1 ,

$$A_0 = \frac{1}{\pi} \int_0^{\infty} dm \int_{-\infty}^{\infty} dv \exp[-m\rho \cosh(v-i\alpha) + imx] \quad (10a)$$

$$B_0 = \frac{1}{\pi} \int_0^{\infty} dm \int_{-\infty}^{\infty} dv \exp[-m\rho \cosh(v-i\alpha) - imx] \quad (10b)$$

$$A_1 = \frac{1}{\pi} \lim_{\epsilon \rightarrow 0} \int_0^{\infty} dm \int_{-\infty}^{\infty} dv \frac{\exp[-m\rho \cosh(v-i\alpha) + imx]}{m - \cosh v - i\epsilon} \quad (10c)$$

$$B_1 = \frac{-1}{\pi} \lim_{\epsilon \rightarrow 0} \int_0^{\infty} dm \int_{-\infty}^{\infty} dv \frac{\exp[-m\rho \cosh(v-i\alpha) - imx]}{m - \cosh v + i\epsilon} \quad (10d)$$

The reason for introducing the new integrals A_1 and B_1 is that they are more strongly convergent than the original integrals A and B .

The double integrals A_0 and B_0 are simplified by Ursell by making the change of variables $v - i\alpha \rightarrow v$, and using equality (9.6.24) of Ref. [12] to convert the integrand in terms of the Bessel function K_0

$$\begin{aligned} A_0 + B_0 &= \frac{4}{\pi} \int_0^{\infty} dm K_0(m\rho) \cos mx \\ &= \frac{2}{\sqrt{\rho^2 + x^2}} = \frac{2}{R} \end{aligned} \quad (11)$$

Actually, the integral $A_0 + B_0$ can be more directly simplified (without the need to use Bessel functions) by noting that the order of integration can be interchanged since it is absolutely convergent, carrying out the simple integral with respect to m , and making the change of variables $w = e^v$ in the resulting single integral to arrive at the same result given above.

By making similar shifts in the paths of integration of A_1 ($v = i\alpha + \frac{1}{2}\pi i + w$, w real) and B_1 ($v = i\alpha - \frac{1}{2}\pi i + w$, w real), the sum $A_1 + B_1$ takes the form

$$A_1 + B_1 = \frac{1}{\pi} \lim_{\epsilon \rightarrow 0} \int_{-\infty}^{\infty} dm \int_{-\infty}^{\infty} dw$$

$$\frac{\exp(-im\rho \sinh w + im\rho \sinh \beta)}{m - i \sinh(w + i\alpha) - i\epsilon} + (\text{single integrals}$$

due to residues at poles crossed by the shifts) (12)

By interchanging the order of integration, Bessho notes that the integral with respect to m is of the form given in Eq. (4) and thus the double integral is converted to a single integral entirely in terms of elementary functions.

Ursell points out that the double integral in Eq. (12) does not satisfy the sufficient (but not necessary) condition of absolute convergence in order to justify the interchange of order of integration. His proof of the validity of the interchange basically consists of extending Bessho's idea of generating derivative functions, shown in Eq. (9), to generate the following still more strongly convergent integrals A_2 and B_2

$$A_2 = \frac{1}{\pi} \lim_{\epsilon \rightarrow 0} \int_0^{\infty} dm \int_{-\infty}^{\infty} dv \frac{\exp[-m\rho \cosh(v-i\alpha) + imx]}{(1-i)(m - \cosh v - i\epsilon)} \quad (13a)$$

$$B_2 = \frac{-1}{\pi} \lim_{\epsilon \rightarrow 0} \int_0^{\infty} dm \int_{-\infty}^{\infty} dv \frac{\exp[-m\rho \cosh(v-i\alpha) - imx]}{(1+im)(m - \cosh v + i\epsilon)} \quad (13b)$$

which are related to A_1 and B_1 as follows

$$A_1 = (1 - \frac{\partial}{\partial x}) A_2, \quad B_1 = (1 - \frac{\partial}{\partial x}) B_2 \quad (14)$$

Ursell proceeds to operate on A_2 and B_2 in a manner similar to Bessho's transformations of A_1 and B_1 . That is, once again the paths of integration are shifted for A_2 ($v = i\alpha + \frac{1}{2}\pi i + w$, w real) and B_2 ($v = i\alpha - \frac{1}{2}\pi i + w$, w real), and the resultant residue evaluated at the pole of the integrand crossed by this shift (for some but not all m) where the pole V is defined by

$$\cosh V(m) = \begin{matrix} m + i\epsilon & \text{for } B_2 \\ m - i\epsilon & \text{for } A_2 \end{matrix} \quad (15)$$

By making the further change of variables from m to V , as given in Eq. (15), in the single integral resulting from the residue evaluation, the following expressions are obtained for A_2 and B_2 , where each is given in terms of a single integral and a double integral

$$A_2 = \frac{1}{\pi} \lim_{\epsilon \rightarrow 0} \int_0^\infty \frac{dm}{1 - im} \int_{-\infty}^\infty dw \frac{\exp(-im\rho \sinh w + im\rho \sinh \beta)}{m - i \sinh(w + i\alpha) - i\epsilon} \quad (16a)$$

$$- 2i \int_{\frac{1}{2}\pi i}^{-\infty} dV \frac{\exp(-\rho \cosh V \cosh(V - i\alpha) + ix \cosh V)}{1 - i \cosh V} \quad (16b)$$

$$B_2 = \frac{-1}{\pi} \lim_{\epsilon \rightarrow 0} \int_0^\infty \frac{dm}{1 + im} \int_{-\infty}^\infty dw \frac{\exp(im\rho \sinh w - im\rho \sinh \beta)}{m + i \sinh(w + i\alpha) + i\epsilon} \quad (16c)$$

$$- 2i \int_{i(\alpha - \frac{\pi}{2})}^{-\infty} dV \frac{\exp(-\rho \cosh V \cosh(V - i\alpha) - ix \cosh V)}{1 + i \cosh V} \quad (16d)$$

where α is taken to be ≥ 0 in Eqs. (16b) and (16d).

Ursell shows that the double integrals (16a) and (16c) are absolutely convergent, and thus it is permissible to interchange the order of integration. By writing $-m$ for m in Eq. (16c) the two double integrals can be combined into a single form, with order of integration interchanged

$$\begin{aligned} & \frac{1}{\pi} \int_{-\infty}^\infty dw \int_{-\infty}^\infty dm \frac{\exp(-im\rho \sinh w + im\rho \sinh \beta)}{(1 - im)[m - i \sinh(w + i\alpha)]} \\ &= \frac{1}{\pi} \int_{-\infty}^\infty dw I(w, \beta) \end{aligned} \quad (17a)$$

The presence of the extra factor $(1 - im)$ in the denominator makes the equalities given by Eq. (4) not directly applicable for evaluating $I(w, \beta)$. Instead, Ursell evaluates it by means of an elaborate contour integration, accounting for the residues due to the poles which are enclosed for $0 < w < \beta$ and $\beta < w < \infty$. Actually, Eq. (17a) can be put in a form to which Eq. (4) is applicable, by rewriting the denominator, as follows

$$\begin{aligned} & \frac{1}{(1 - im)[m - i \sinh(w + i\alpha)]} \\ &= \frac{1}{\sinh(w + i\alpha) + 1} \left[\frac{1}{m - i \sinh(w + i\alpha) - \frac{1}{m + i}} \right] \end{aligned} \quad (17b)$$

In either case, Eq. (17a) is expressed as the following sum of two single integrals

$$\begin{aligned} & \frac{1}{\pi} \int_{-\infty}^\infty I(w, \beta) dw \\ &= 2i \int_0^\beta \frac{\exp[-\rho(\sinh \beta - \sinh w) \sinh(w + i\alpha)]}{1 + \sinh(w + i\alpha)} dw \quad (18a) \\ &+ 2i \int_\beta^\infty \frac{\exp[\rho(\sinh \beta - \sinh w)]}{1 + \sinh(w + i\alpha)} dw \quad (18b) \end{aligned}$$

The component single integrals (16b), (16d), (18a), and (18b) which together define $A_2 + B_2$ form the starting point for our numerical analysis and implementation. Ursell proceeds to essentially sum these component integrals and perform the derivatives indicated in Eqs. (14) and (9) to obtain Bessho's representation of $G_0 = A + B$ as a single integral in the complex plane.

To begin the compacting process, these four integrals are all expressed in terms of the variable u by letting $V = u + \frac{1}{2}\pi i$ in Eq. (16b), $V = u - \frac{1}{2}\pi i$ in Eq. (16d), and $w = u - i\alpha$ in Eqs. (18a) and (18b), resulting in

$$\begin{aligned} A_2 + B_2 &= 2i \left[\int_{-\infty + \frac{1}{2}\pi i}^{\beta + i\alpha} + \int_{-\infty - \frac{1}{2}\pi i}^0 \right] \\ & \frac{du}{1 + \sinh u} \exp[(\rho \sinh(u - i\alpha) - x) \sinh u] \\ &+ 2i \int_{\beta + i\alpha}^{\infty + i\alpha} \frac{du}{1 + \sinh u} \exp[-(\rho \sinh(u - i\alpha) - x)] \end{aligned} \quad (19)$$

In carrying out the differentiations $\partial/\partial x$ indicated in Eqs. (14) and (9) it is important to recognize that the limits of integration involve the variables α and β . From the transformation Eq. (8), it is seen that

$$\frac{\partial \alpha}{\partial x} = 0, \quad 1 = \rho \cosh \beta \frac{\partial \beta}{\partial x} - \frac{\partial \beta}{\partial x} = \frac{1}{R} \quad (20)$$

Performing first the operations indicated in Eq. (14) on $A_2 + B_2$ to obtain $A_1 + B_1$ and then the transformations indicated by Eq. (9), using the result given in Eq. (11), the following complex single integral representation for G_0 is obtained

$$\begin{aligned} G_0 = A + B &= \frac{2}{R} + i \frac{\partial}{\partial x} (A_1 + B_1) = 2 \left[\int_{-\infty - \frac{1}{2}\pi i}^{\beta + i\alpha} \right. \\ & \left. + \int_{-\infty + \frac{1}{2}\pi i}^0 \right] \sinh u \exp[(\rho \sinh(u - i\alpha) - x) \sinh u] du \end{aligned} \quad (21)$$

The above integration paths are not the same as those used by Bessho, shown in Fig. 2. In order to obtain the integrals in the Bessho form, make the substitutions $x = -X$, $X = \rho \sinh b$, $u = -v$, and note that $G_0(\alpha) = G_0(-\alpha)$, resulting in

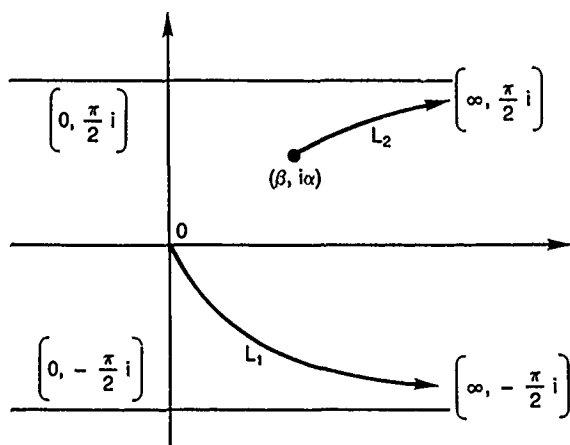


Figure 2. Bessho's Integration Paths

$$G_0(-X, y, z) = -2 \left[\int_0^{\infty - \frac{1}{2}\pi i} + \int_{b+i\alpha}^{\infty + \frac{1}{2}\pi i} \right] \sinh v \exp [(\rho \sinh(v - i\alpha) - X) \sinh v] dv \quad (22)$$

3. Computational Implementation of Bessho's Method

In this chapter we will present our computational implementation of Bessho's method. As mentioned previously, our analysis starts from the four component complex single integrals given in Eqs. (16b), (16d), (18a), and (18b). Through a series of transformations, we simplify and condense these complex integrals to three real integrals, two of which are even in x and the other is odd in x . Taken together, these integrals represent the entire Green's function. Reference [13] describes the FORTRAN 77 computer program which evaluates these integrals.

3.1 Simplification of Complex Integrals

We start by making the change of variables $\zeta = iV$ for part of the integration of Eqs. (16b) and (16d) and then rewrite each integral as two integrals with real limits of integration, resulting in the following expression for $A_2 + B_2$

$$A_2 + B_2 = \text{Eq. (18a)} + \text{Eq. (18b)}$$

$$-2 \int_0^{\frac{1}{2}\pi} \frac{\exp[-\rho \cos \zeta \cos(\zeta - \alpha) + ix \cos \zeta]}{1 - i \cos \zeta} d\zeta \quad (16b.1)$$

$$+ 2i \int_0^{\infty} \frac{\exp[-\rho \cosh V \cosh(V - i\alpha) + ix \cosh V]}{1 - i \cosh V} dV \quad (16b.2)$$

$$+ 2 \int_0^{\frac{\pi}{2} - \alpha} \frac{\exp[-\rho \cos \zeta \cos(\zeta + \alpha) - ix \cos \zeta]}{1 + i \cos \zeta} d\zeta \quad (16d.1)$$

$$+ 2i \int_{-\infty}^0 \frac{\exp[-\rho \cosh V \cosh(V - i\alpha) - ix \cosh V]}{1 + i \cosh V} dV \quad (16d.2)$$

In the above, use has been made of the identity $\cosh(iV) = \cos V$ relating trigonometric and hyperbolic cosines.

Carrying out the differentiations indicated in Eq. (14), the following integrals are obtained for $A_1 + B_1$

$$A_1 + B_1 = (1 - \frac{\partial}{\partial x})(A_2 + B_2)$$

$$= 2i \int_0^{\frac{1}{2}\pi} \exp[-\rho(\sinh \beta - \sinh w) \sinh(w + i\alpha)] dw \quad (23a)$$

$$- 2 \int_0^{\frac{1}{2}\pi} \exp[-\rho \cos \zeta \cos(\zeta - \alpha) + ix \cos \zeta] d\zeta \quad (23b)$$

$$+ 2i \int_{-\infty}^0 \exp[-\rho \cosh V \cosh(V - i\alpha) + ix \cosh V] dV \quad (23c)$$

$$+ 2 \int_0^{\frac{\pi}{2} - \alpha} \exp[-\rho \cos \zeta \cos(\zeta + \alpha) - ix \cos \zeta] d\zeta \quad (23d)$$

$$+ 2i \int_{-\infty}^0 \exp[-\rho \cosh V \cosh(V - i\alpha) - ix \cosh V] dV \quad (23e)$$

The above equation is a result of the following considerations. Recalling from Eq. (20) that $\partial \beta / \partial x = 1/R$, the derivatives $\partial / \partial x$ of the variable limits of integration appearing in Eqs. (18a) and (18b) cancel each other. Recalling from Eq. (8) that $x = \rho \sinh \beta$ the operation $(1 - \partial / \partial x)$ applied to the integrands results in Eq. (18b) going to zero and a removal of the denominator in the other five integrals.

Proceeding similarly, using Eqs. (9) and (11), we obtain G_0 in the form

$$G_0 = \frac{2}{R} + i \frac{\partial}{\partial x} (A_1 + B_1) = G_1 + G_2 + G_3 + G_4$$

$$= 2 \int_0^{\frac{1}{2}\pi} \sinh(w + i\alpha)$$

$$\exp[-\rho(\sinh \beta - \sinh w) \sinh(w + i\alpha)] dw \quad (24a)$$

$$+ 2 \int_0^{\frac{1}{2}\pi} \cos \zeta \exp[-\rho \cos \zeta \cos(\zeta - \alpha) + ix \cos \zeta] d\zeta \quad (24b)$$

$$+ 2 \int_0^{\frac{\pi}{2} - \alpha} \cos \zeta \exp[-\rho \cos \zeta \cos(\zeta + \alpha) - ix \cos \zeta] d\zeta \quad (24c)$$

$$+ 4 \int_{-\infty}^0 \cosh V \sin(x \cosh V)$$

$$\exp[-\rho \cosh V \cosh(V - i\alpha)] dV \quad (24d)$$

In the above equation, the two integrals in terms of the variable V have been combined into a single integral by using the well known identity $e^{ix \cosh V} - e^{-ix \cosh V} = 2i \sin(x \cosh V)$.

In the following, we express the above complex integrals as the sum of real and imaginary parts, and consider only the real part. By means of a series of transformations, we reduce the resulting integrals to compact form.

3.2 Conversion to Real Integrals

Consider first G_1 given by Eq. (24a). By first expanding $\sinh(w + i\alpha)$ and then making the change of variables $\cosh w dw = dw'$, G_1 becomes the following

$$G_1 = 2 \int_0^{\sinh \beta = x/\rho} \left[\cos \alpha \frac{w}{\sqrt{w^2 + 1}} \cos(x \sin \alpha \sqrt{w^2 + 1}) - yw \sqrt{w^2 + 1} + \sin \alpha \sin(x \sin \alpha \sqrt{w^2 + 1}) - yw \sqrt{w^2 + 1} \right] e^{-x \cos \alpha w + zw^2} dw \quad (25)$$

Let us now consider G_2 and G_3 given by Eqs. (24b) and (24c). By using the well known relationship $e^{\pm i x \cos \zeta} = \cos(x \cos \zeta) \pm i \sin(x \cos \zeta)$, the real part of these two integrals can be conveniently written out. By making the change of variables $\zeta = -\zeta'$ in G_3 , $G_2 + G_3$ can be written as the following single integral

$$G_2 + G_3 = 2 \int_{-\frac{\pi}{2} + \alpha}^{\frac{\pi}{2}} \cos \zeta \cos(x \cos \zeta) e^{-\rho \cos \zeta \cos(\zeta - \alpha)} d\zeta \quad (26)$$

By making the change of variables $\zeta = \zeta' + \alpha/2$, using various trigonometric identities for the cosine terms, keeping only the even functions of ζ (since the odd functions give a zero integral), and (very similar to the final transformation indicated for Eq. (25)) making the change of variables $\cos \zeta d\zeta = dw$, the integrand of $G_2 + G_3$ takes on a form resembling that of G_1 given in Eq. (25)

$$G_2 + G_3 = 4 \int_0^{\cos \frac{\alpha}{2}} \left[\cos \frac{\alpha}{2} \cos(x \cos \frac{\alpha}{2} \sqrt{1 - w^2}) \cos(x \sin \frac{\alpha}{2} w) - w \frac{\sin \frac{\alpha}{2}}{\sqrt{1 - w^2}} \sin(x \cos \frac{\alpha}{2} \sqrt{1 - w^2}) \sin(x \sin \frac{\alpha}{2} w) \right] e^{-\frac{\rho}{2}(\cos \alpha + 1 - 2w^2)} dw \quad (27)$$

Finally, let us consider G_4 given by Eq. (24d). By making use of the identity $\cosh(V - i\alpha) = \cosh V \cos \alpha - i \sinh V \sin \alpha$ the real part of G_4 is written as

$$G_4 = 4 \int_0^\infty \cosh V \sin(x \cosh V) \cos(\rho \cosh V \sinh V \sin \alpha) e^{-\rho \cosh^2 V \cos \alpha} dV \quad (28)$$

By making the change of variables $\cosh V dV = dw$ and recalling Eq. (8), G_4 becomes

$$G_4 = 4 \int_0^\infty \sin(x \sqrt{w^2 + 1}) \cos(yw \sqrt{w^2 + 1}) e^{-z(w^2 + 1)} dw \quad (29)$$

By making the further change of variables $dw = \sec^2 \theta d\theta$, we can transform G_4 to the single integral form given in Eq. (13.3b) of Wehausen and Laitone [14]

$$G_4 = 4 \int_0^{\pi/2} \sin(x \sec^2 \theta \cos \theta) \cos(y \sec^2 \theta \sin \theta) e^{-z \sec^2 \theta} \sec^2 \theta d\theta \quad (30)$$

In our numerical computations we find it somewhat more convenient to make the change of variables $\sec^2 \theta \sin \theta = u$ and use the following alternate form proposed in [2]

$$G_4 = 4 \int_0^\infty \sin(xs) \cos(yu) e^{-s^2 z} \frac{s}{2s^2 - 1} du \quad (31)$$

$$\text{where } s(u) = \left[\frac{1 + \sqrt{1 + 4u^2}}{2} \right]^{1/2} = \sec \theta.$$

Adding the component integrals given by Eqs. (25), (27), and (31), the resulting form for G_0 in real form is given by

$$G_0 = G_x + G_c + G_o = G_e + G_o$$

$$= 2 \int_0^{x/\rho} \left[\cos \alpha \frac{w}{\sqrt{w^2 + 1}} \cos(x \sin \alpha \sqrt{w^2 + 1}) - yw \sqrt{w^2 + 1} + \sin \alpha \sin(x \sin \alpha \sqrt{w^2 + 1}) - yw \sqrt{w^2 + 1} \right] e^{-x \cos \alpha w + \rho \cos \alpha w^2} dw \quad (32a)$$

$$+ 4 \int_0^{\cos \frac{\alpha}{2}} \left[\cos \frac{\alpha}{2} \cos(x \cos \frac{\alpha}{2} \sqrt{1 - w^2}) \cos(x \sin \frac{\alpha}{2} w) - w \frac{\sin \frac{\alpha}{2}}{\sqrt{1 - w^2}} \sin(x \cos \frac{\alpha}{2} \sqrt{1 - w^2}) \sin(x \sin \frac{\alpha}{2} w) \right] e^{-\frac{\rho}{2}(\cos \alpha + 1 - 2w^2)} dw \quad (32b)$$

$$+ 4 \int_0^\infty \sin(xs) \cos(yu) e^{-s^2 z} \frac{s}{2s^2 - 1} du \quad (32c)$$

where $s(u)$ is defined in Eq. (31), and ρ and α in Eq. (8). Since G_o given by Eq. (32c) corresponds to the single integral part of the total Green's function given in [14], G_e , the sum of G_x and G_c given respectively by Eqs. (32a) and (32b), corresponds to the double integral part. Equation (32c) shows that G_o is odd about $x = 0$ and has an infinite upper limit of integration while Eqs. (32a) and (32b) show that the G_e is even about $x = 0$ and has upper limits of integration which depend on the field point.

The integrals G_o and G_e are also simply related to the commonly used near field and wave disturbance components N and W [4,6,9]. Comparison of the expressions for G_o and W shows that

$$W(x, y, z) = G_o(x, y, z) + G_o(|x|, y, z) \quad (33)$$

Since $W + N = G_o + G_e$, N is related to G_e and G_o as follows

$$N(x, y, z) = G_e(x, y, z) - G_o(|x|, y, z) \quad (34)$$

3.3 Behavior of the Integrands

It is of interest to investigate the behavior of the three integrands in different regions of the x, y, z computation domain in order to derive effective integration schemes. While the behavior of the integrand for the odd integral G_o is relatively well known, we do not believe that the integrands of the even integrals G_x and G_e have been previously considered.

Figures 3 to 5 respectively show the integrands for G_x , G_e , and G_o at various (x, y, z) locations. In these figures, the horizontal and vertical coordinates have been normalized so that the independent variable lies between 0 and 1, and the integrand lies between -1 and 1.

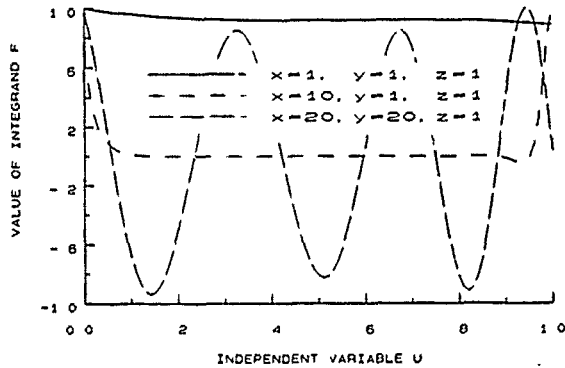


Figure 3. Integrands for G_x

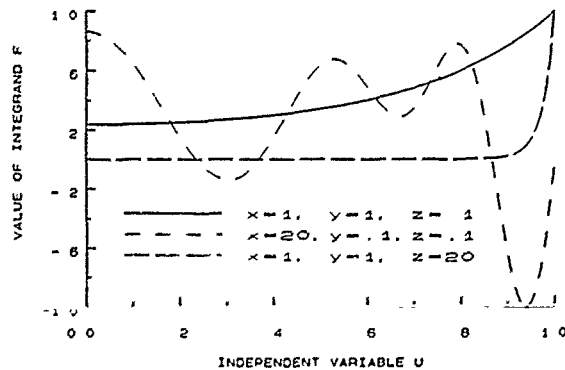


Figure 4. Integrands for G_e

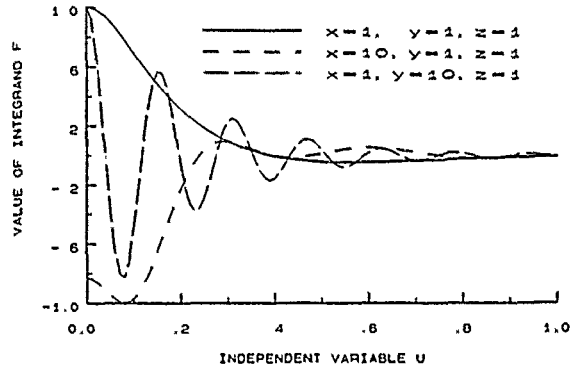


Figure 5. Integrands for G_o

These figures show that the behavior of the integrands varies greatly, depending on (x, y, z) . Thus, it is not likely that any single integration approach will be optimum throughout the entire computation domain for a given integral. It is this great divergence in behavior which has led previous investigators to consider only specialized components of G_o and to divide the computation domain into several regions [4-9]. Our principal effort has been to determine minimum integration domains for the two integrals which have theoretically infinite upper limits of integration: G_o and (as $x/\rho \rightarrow \infty$) G_x .

Figure 3 shows that G_x has a smooth integrand for small or moderate values of x/ρ , but at larger values, the integrand seems to concentrate at thin strips at the left and right ends of the domain of integration. This is due to the fact that the argument of the exponential function in Eq. (32a), $f(w) = -x \cos \alpha w + \rho \cos \alpha w^2$ is zero at the ends of the integration interval, $w = 0$ and $w = x/\rho$, and takes on negative values in between. Noting that $f(w)$ is symmetric about the midpoint of the interval, $w = x/2\rho$, the following integration scheme is adopted for G_x . First, the limits of integration lying on either side of $x/2\rho$ are determined by setting $f(w) = -A$, where A may be chosen to be suitably large, say, 20 (i.e., $e^{-A} = 2 \times 10^{-9}$), resulting in

$$\frac{x}{2\rho} \pm \Delta w = \pm \frac{x}{2\rho} \pm \sqrt{(x/2\rho)^2 - 4A/(\rho \cos \alpha)} \quad (35)$$

For cases where the term under the square root sign is negative, $\Delta w \equiv 0$. Integration for G_x is thus confined to the two strips Δw as follows

$$G_x = \int_0^{x/2\rho - \Delta w} g(w) e^{f(w)} dw + \int_{x/2\rho + \Delta w}^{x/\rho} g(w) e^{f(w)} dw$$

$$= \int_0^{x/2\rho - \Delta w} [g(w) + g(-w + x/\rho)] e^{f(w)} dw \quad (36)$$

where $g(w)$ are the trigonometric functions multiplying $e^{f(w)}$ in Eq. (32a) and the last equality results from the symmetry of $f(w)$ about $x/2\rho$.

The error incurred by using a finite upper limit u_M in the integral for G_o , Eq. (32c), may be estimated as follows. By neglecting the trigonometric factors, which have magnitudes less or equal to 1, and changing the variable of integration from u to s , defined in Eq. (31), the error ϵ is bounded by

$$\epsilon \leq 4 \int_{s_M}^{\infty} e^{-s^2 z} \frac{s^2}{u} ds \quad (37)$$

where $s_M^2 = \frac{1}{2} + \sqrt{\frac{1}{4} + u_M^2}$. By making the change of variables $t = s^2$, the above may be integrated by parts to give

$$\epsilon \leq \frac{2 e^{-s_M^2 z}}{z u_M} + \frac{2}{z} \int_{s_M}^{\infty} e^{-s^2 z} \frac{d}{ds} \left(\frac{s}{u} \right) ds \quad (38)$$

where $\frac{d}{ds} \left(\frac{s}{u} \right) = \frac{d}{ds} (s^2 - 1)^{-1/2} \leq 0$. Therefore, it is necessary to consider only the first term in deriving estimates of the maximum error incurred by using finite values of u_M . By considering ϵ and z to be given parameters, Eq. (38) may be solved iteratively for the required upper limit u_M . Table 1 gives the calculated values of u_M for $\epsilon = (10^{-3}, 10^{-4}, 10^{-6})$ and $z = (10., 1., 0.1, 0.01)$. Table 1 shows the manner in which u_M increases with decreasing values of ϵ and z .

Table 1 — Variation of the Upper Limit of Integration u_M in G_o with Error Criterion ϵ and Source Submergence z

ϵ	$z = 10.$	$z = 1.0$	$z = 0.1$	$z = 0.01$
10^{-3}	0.01	6.2	77.	880.
10^{-4}	0.085	8.4	99.	1100.
10^{-6}	0.60	13.0	140.	1500.

3.4 Limiting Behavior as $\rho \rightarrow 0$

Use of the above error estimate appears to indicate that $u_M \rightarrow \infty$ as $z \rightarrow 0$. Yet it is well known [4,8] that $G_o(x, y = 0, z = 0)$ is given by

$$G_o(x, 0, 0) = \frac{1}{2} W(x) = -2\pi Y_1(x), \quad x > 0 \quad (39)$$

where Y_1 is the Bessel function of the second kind of order one [12]. The existence of the limit shows that a higher order error analysis, accounting for the oscillatory trigonometric functions in Eq. (32c), would lead to a more efficient procedure for the integration of G_o .

In order to obtain the complete function G_o for $(x, 0, 0)$ it is necessary to calculate G_x and G_c defined in Eqs. (32a) and (32b) as $y \rightarrow 0$ and $z \rightarrow 0$. Since G_o exhibits singular behavior in the neighborhood of this axis, it is necessary to use care in taking this limit. By starting with Eq. (29) for G_o , and neglecting terms which are well behaved near the axis $\rho = 0$ and which are of the order of

$1/|x|$ as $|x| \rightarrow \infty$, we have derived in [13] the following expression giving the first order far field behavior in the neighborhood of the axis $(x, 0, 0)$

$$G_o(x, y, z) \sim \text{sgn}(x) 2 \sqrt{\frac{\pi}{\rho}} e^{-x^2 z / 4(y^2 + z^2)} \sin\left(-\frac{x^2 y}{4(y^2 + z^2)}\right) + \frac{y}{2} + \frac{\alpha}{2} + 2 \sqrt{\frac{\pi}{|x|}} (\sin x + \text{sgn}(x) \cos x) e^{-x^2} \quad (40)$$

This equation generalizes, for the case of large x , the expression given in [5] for the wave disturbance W for the specialized case $z = 0$. The above equation confirms the findings in [5] that the limit $z = 0, y \rightarrow 0$ is singular, and that (provided $z \neq 0$) the limit $y = az, z \rightarrow 0$ is independent of a . Since the near field component N is well behaved, Eq. (34) shows that G_c must show a similar behavior.

We find it convenient to compute the values of G_x and G_c for $y = 0, z \rightarrow 0$. In this case, $\alpha = \tan^{-1}(y/z) = 0$. The integral G_c may be calculated in a straightforward manner by setting $z = 0$ and then evaluating the well behaved integrand between the finite limits 0 and 1. In the case of G_x , the limiting process must be applied with some care. In particular, taking care to preserve the previously noted symmetry of the exponential factor about the midpoint of the integration interval $x/2z$, the integral G_x has the following limit

$$\begin{aligned} \lim_{z \rightarrow 0} G_x(x, 0, z) &= \lim_{z \rightarrow 0} 2 \int_0^{x/z} \frac{w}{\sqrt{w^2 + 1}} e^{-xw + zw^2} dw \\ &= \lim_{z \rightarrow 0} 2 \int_0^{x/2z} \left[\frac{w}{\sqrt{w^2 + 1}} + \frac{x/z - w}{\sqrt{(x/z - w)^2 + 1}} \right] e^{-xw} dw \\ &= 2 \int_0^{\infty} \frac{w}{\sqrt{w^2 + 1}} e^{-xw} dw + \frac{2}{x} \end{aligned} \quad (41)$$

Thus, G_o may be conveniently calculated on the axis $(x, 0, 0)$ by adding G_o , G_c , and G_x .

3.5 Computer Time Requirements

Computer time depends on various factors, of which the values of x, y , and z , the error criterion ϵ , the type of integral, and the integration rule are the most important. The simple trapezoidal rule and the higher order Simpson's rule were used to integrate each of the three integrals over a range of x, y, z , and ϵ . The integration starts with an initial partition of the given range into two intervals, and then successively doubling the number of intervals until the integrated values from two successive iterations agree to within the specified error ϵ .

We have found that on average, the use of Simpson's rule for $G_c (= G_x + G_c)$ results in a computer time which is 0.3 of the time using the trapezoidal rule, while the corresponding ratio for G_o is 1.5 [13]. These trends may be due to the fact that the (usually) smoother integrands of G_c benefit from the parabolic fit through the points used in Simpson's rule, while the (often) oscillatory integrands of

G_0 seem to be better approximated by the straight line fit of the trapezoidal rule. We realize that, based on the diverse behavior of the integrands shown in Figures 3 to 5, the use of different integration rules (for the same integral) based on x , y , and z would result in even greater savings of computer time. We have not, however, pursued such detailed refinements.

Figure 6 shows the average CPU time per field point for G_x , G_c , and G_0 , respectively, using the Hewlett Packard (HP) 9000, Model 550 minicomputer for $\epsilon = 10^{-4}$ for various intervals in the region $0.1 \leq x, y, z \leq 40$. It is well known that for values of x, y, z near the origin (0, 0, 0) and the axis $(x, 0, 0)$ the behavior of G_0 is singular. For a given x -interval, the figure shows two sets of numbers. The upper set gives the average CPU time for a fixed value of y (indicated on the vertical axis) and a uniform xz grid of field points over the interval indicated on the horizontal axis. The lower set of numbers gives corresponding results for a fixed value of z and a uniform xy grid. Several runs were repeated using $\epsilon = 10^{-6}$ and these suggest that average CPU time is approximately tripled compared to the $\epsilon = 10^{-4}$ results. Also, some runs have been made on the Cray XMP/24 mainframe computer and the corresponding CPU times are typically 60 times smaller.

	x		
	0.1 y: (.02, .05; -)	1.0 (.05, .30; -)	10 (.20, 1.3; -) 40
0.1	z: (.02, .02; 1.0)	(.10, .10; 1.5)	(.65, .20; 2.3)
1.0	(.01, .05; -)	(.05, .25; -)	(.20, 1.0; -)
	(.01, .10; .10)	(.10, .10; .15)	(.35, .20; .20)
10	(.02, .10; -)	(.02, .20; -)	(.20, .40; -)
	(.01, .25; .02)	(.02, .25; .02)	(.20, .45; .02)
40	(.01, .25; -)	(.02, .20; -)	(.10, .20; -)
	(.01, .25; .01)	(.01, .30; .01)	(.10, .45; .01)

Figure 6. Approximate Computer Times per Field Point for $\epsilon = 10^{-4}$

Most of the computer time trends can be directly inferred from the expressions contained in Eq. (32) or shown in Figs. 3-5. One trend is that the overall sum of the CPU times for all three integrals tends to be a minimum around (1,1,1), which may be inferred from the smooth behavior of all the integrands at this point. Another trend is the increase in CPU time with increasing x since this leads to increasing oscillatory behavior of the integrand. With increasing z , computer times decrease for G_0 (larger effect of the exponential decay factor) and G_x (smaller values of

x/ρ) but tend to increase somewhat for G_c (more confinement of the exponential factor to a narrow region near $w = \cos(\alpha/2)$). It may be noted that in the analysis given in [9] for W , which is closely related to G_0 , the calculation is limited to values of y/z less than $\tan(86.4^\circ) = 15.9$.

4. Numerical Results

We first present various checks which have been made on the accuracy of our formulation. We then present contour plots of the various integrals to show their overall behavior. Finally, we give line plots of these integrals to show the finer details of their individual and relative behavior.

4.1 Numerical Checks

Newman [6] gives accurately calculated benchmark values of $N(x, y, z)$ for the field points $(R, 0, 0)$, $(0, R, 0)$, and $(0, 0, R)$ where $R = 1, 4, 10$. The last two sets are most convenient for us to calculate and we shall discuss these first. For both of these cases $x = 0$, where $G_0 = 0$, and Eq. (34) then shows that $N = G_c$. In addition, since $x = 0$, then $x/\rho = 0$, the integral $G_x = 0$, reducing the calculation to $N = G_c$. For an $\epsilon = 0.0001$, our calculated values [13] agree with those given in [6] to at least four decimal places.

The set $(R, 0, 0)$ provides a more thorough check on the accuracy of our formulation since all three of the integrals G_x , G_c , and G_0 would be involved. Unfortunately, our upper limit of integration for $G_0 \rightarrow \infty$ as $z \rightarrow 0$. We perform this check in two ways. One way is for us to calculate the three integrals and form N according to Eq. (34) for small values of z . For an $\epsilon = 0.001$ and $z = 0.01$, we obtain agreement to at least two decimal places with the benchmark results [13]. While this method is computationally expensive and inefficient, it does show the stability of our formulation as $z \rightarrow 0$. The second and more convenient method is to calculate $N(x, 0, 0)$ with the aid of Eqs. (39) and (41) for $G_0(x, 0, 0)$ and $G_x(x, 0, 0)$, respectively. Using this approach, our results agree with those in [6] to six decimal places for $\epsilon = 10^{-6}$.

4.2 Contour Plots

Figures 7a to d respectively show contour plots for the component integrals G_x , G_c , G_0 , and N for the case of $z = 0.1$ over a 101×41 rectangular grid with $0 \leq x \leq 50$, and $0 \leq y \leq 20$. To illustrate the effect of z , Figures 8a and b respectively show G_c for $z = 0.1$, and 1.0 for the same rectangular grid.

Figure 7a shows that the largest waves of G_x are confined in a triangular region which does not extend to the x axis. Figure 7b shows that the wave pattern for G_c is relatively simple, consisting of waves whose crests are nearly parallel to the y axis. Figure 7c shows the familiar far field wave patterns confined to the Kelvin sector. Figure 7d shows that the near field integral N has contour lines which are nearly circular and asymptotically decay as $2/R$.

Figures 8a and b show the well known disappearance of the clutter corresponding to the short waves as z increases.

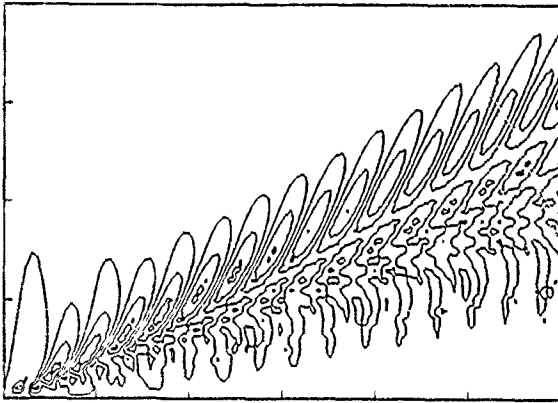


Figure 7a. Contour Plot of G_z , $z = 0.1$

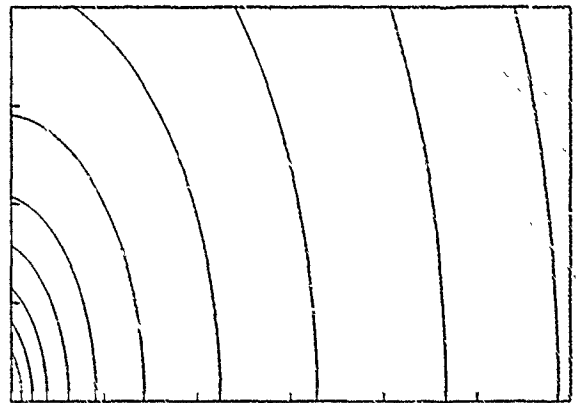


Figure 7d. Contour Plot of N , $z = 0.1$

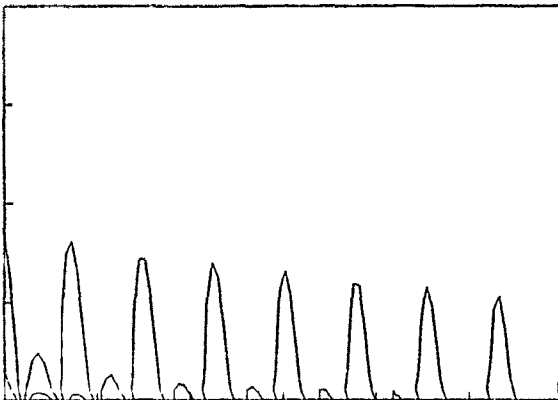


Figure 7b. Contour Plot of G_c , $z = 0.1$

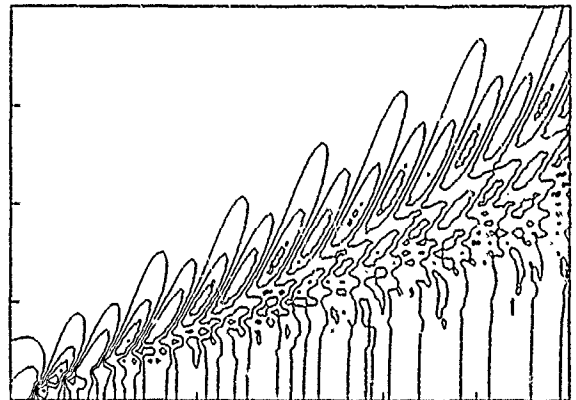


Figure 8a. Contour Plot of G_c , $z = 0.1$

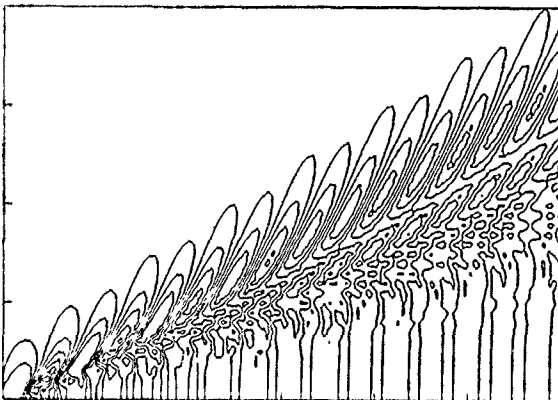


Figure 7c. Contour Plot of G_o , $z = 0.1$

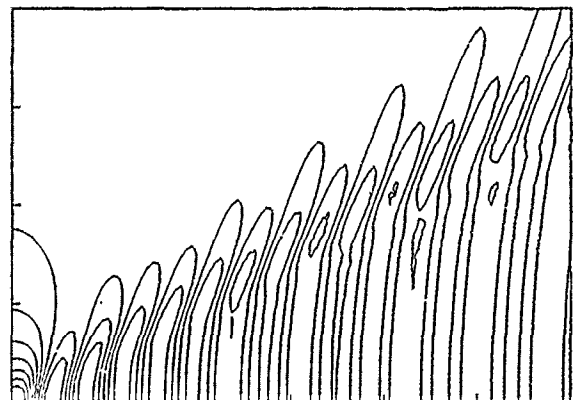


Figure 8b. Contour Plot of G_c , $z = 1.0$

4.3 Detailed Line Plots

Figures 9a and b respectively show line plots of the component integrals G_x , G_c , and G_o at $y = 0$ and 4 for $z = 0.1$ and $0 \leq x \leq 20$. To obtain a view of the behavior of the integrals over a wider range of x , including upstream values, Figures 10a and b respectively show plots of G_0 at $y = 0$ and 20 for $z = 0.1$ and $-100 \leq x \leq 100$.

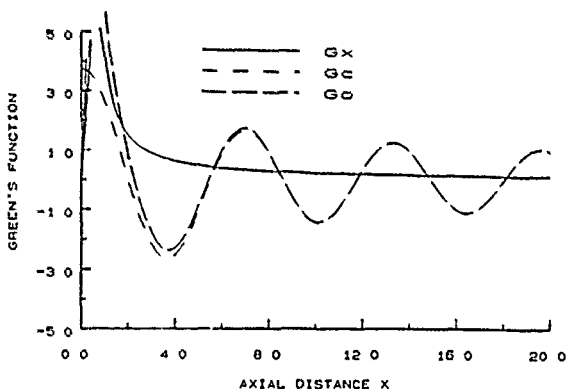


Figure 9a. Line Plots of G_x , G_c , G_o ; $y = 0$

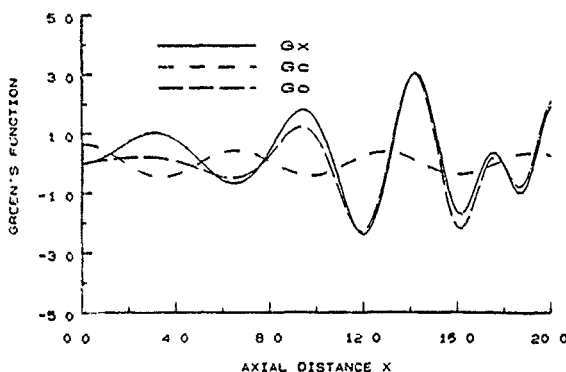


Figure 9b. Line Plots of G_x , G_c , G_o ; $y = 4$

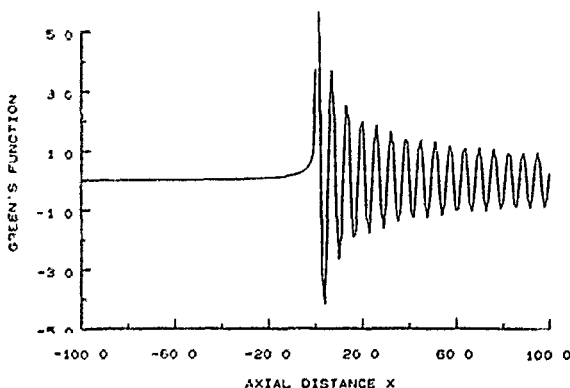


Figure 10a. Upstream and Downstream Line Plots of G_0 , $y = 0$

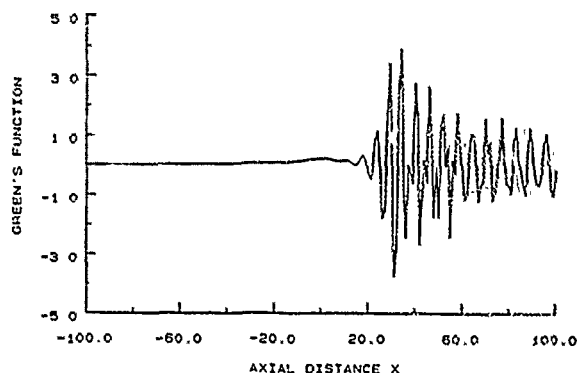


Figure 10b. Upstream and Downstream Line Plots of G_0 , $y = 20$

Figure 9 shows that the relative behavior between the component integrals varies with the location y . Figure 9a shows that on the x axis, $y = 0$, the even integral component G_c resembles the odd integral G_o , while the component G_x serves as a correction factor indicating the differences between G_c and G_o . At the off axis location $y = 4$, Figure 9b shows that the reverse is true, i.e., now G_x resemble G_o , while G_c tends to serve as the correction factor.

Figure 10 shows the expected trend that $G_0 \rightarrow 0$ far upstream of the source. This is a verification of our approach in that the separate calculations of G_c and G_o do combine to give the required annulment far upstream. This figure shows that the local disturbance is nonoscillatory, decays rapidly near $x = 0$, and then shows a slow but perceptible decay far upstream.

5. Conclusions

A numerical procedure has been developed to calculate the complete wave resistance Green's function G_0 for the case of a nonoscillating source translating below the free surface. The numerical implementation is based on the unique work of Bessho, who succeeds in representing G_0 as a single integral in the complex plane. We have recast this integral as three real single integrals G_x , G_c , and G_o , where $G_x + G_c$ corresponds to the double or even integral G_e and the third integral to the single or odd integral in the usual representation of G_0 . By simple rearrangement, we can also express our results in terms of the more physical near field and wavelike components N and W . Computer time depends on a number of factors, principally the submergence of the source z , the required accuracy ϵ , and the horizontal distances x and y from the source.

A number of checks have been performed on the accuracy of our numerical analysis and computer code development. For field points located on each of the three coordinate axes, our calculated values for N agree well with accurately calculated benchmark values. Our comparison for the points on the x axis is facilitated by using specialized limit expressions for $y = 0$, $z \rightarrow 0$ for two of our three integrals.

Also, the calculated results show the required mutual annulment of G_e and G_o far upstream. A number of line plots are given to show the often dramatic differences in the behavior of the integrands in different regions of the computation domain. Contour and line plots show the relative and detailed behavior of the various integrals.

6. Acknowledgments

This work was conducted as part of a research program in free surface and marine hydrodynamics supported by the Naval Research Laboratory and by Code 12 of the Office of Naval Research. The second author performed this work under the sponsorship of the U.S. Navy-ASEE Summer Faculty Research Program.

7. References

1. Michell, J.H., "The Wave Resistance of a Ship," *Philosophical Magazine*, Vol. 45, No. 272, pp. 106-123, January 1878.
2. Eggers, K.W.H., Sharma, S.D., and Ward, L.W., "An Assessment of Some Experimental Methods for Determining the Wavemaking Characteristics of a Ship Form," *Transactions of the Society of Naval Architects and Marine Engineers*, Vol. 75, pp. 112-157, November 1967.
3. Noblesse, F., "Alternative integral representations for the Green function of the theory of ship wave resistance," *Journal of Engineering Mathematics*, Vol. 15, No. 4, pp. 241-265, October 1981.
4. Noblesse, F., "The Fundamental Solution in the Theory of Steady Motion of a Ship," *Journal of Ship Research*, Vol. 21, No. 2, pp. 82-88, June 1977.
5. Euvrard, D., "Les mille et une facettes de la fonction de Green du problème de la résistance de vagues," *Ecole Nationale Supérieure de Techniques Avancées Report 144*, June 1983.
6. Newman, J.N., "Evaluation of the Wave-Resistance Green Function: Part 1 — The Double Integral," *Journal of Ship Research*, Vol. 31, No. 2, pp. 79-90, June 1987.
7. Noblesse, F., "The Steady Wave Potential of a Unit Source, at the Centerplane," *Journal of Ship Research*, Vol. 22, No. 2, pp. 80-88, June 1978.
8. Newman, J.N., "Evaluation of the Wave-Resistance Green Function: Part 2 — The Single Integral on the Centerplane," *Journal of Ship Research*, Vol. 31, No. 3, pp. 145-150, September 1987.
9. Baar, J.J.M. and Price, W.G., "Evaluation of the Wavelike Disturbance in the Kelvin Wave Source Potential," *Journal of Ship Research*, Vol. 32, No. 1, pp. 44-53, March 1988.
10. Bessho, M., "On the Fundamental Function in the Theory of the Wave-Making Resistance of Ships," *Memoirs of the Defense Academy, Japan*, Vol. IV, No. 2, pp. 99-119, 1964.
11. Ursell, F., "Mathematical Note on the Fundamental Solution (Kelvin Source) in Ship Hydrodynamics," *IMA Journal of Applied Mathematics*, Vol. 32, pp. 335-351, 1984.
12. Abramowitz, M. and Stegun, I.A., *Handbook of Mathematical Functions with Formulas, Graphs, and Mathematical Tables*, U.S. Government Printing Office, Washington, D.C., June 1964.
13. Wang, H.T. and Rogers, J.C.W., "Calculation of the Odd and Even Integral Components of the Wave Resistance Green's Function," *Naval Research Laboratory Report 6411* (in press).
14. Wehausen, J.V. and Laitone, E.V., "Surface Waves," *Encyclopedia of Physics*, Vol. 9, Springer-Verlag, Berlin, pp. 446-778, 1960.

Numerical Evaluation of a Ship's Steady Wave Spectrum

F. Noblesse

David Taylor Research Center, Bethesda, USA

W. M. Lin

Science Applications International, Annapolis, USA

R. Mellish

David Taylor Research Center, Bethesda, USA

ABSTRACT

The study presents a modified mathematical expression for the wave-spectrum function in the Fourier representation of the wave pattern of a ship advancing at constant speed in calm water. This new expression is obtained from the well-known usual expression via several applications of Stokes' theorem resulting in the combining of the integrals along the waterline and over the hull surface of the ship. The modified expression for the wave-spectrum function is considerably better suited than the usual expression for accurate numerical evaluation because the significant numerical cancellations which occur between the waterline and hull integrals in the usual expression are automatically and exactly accounted for in the modified expression, as is demonstrated mathematically and confirmed numerically.

INTRODUCTION

Near-field potential-flow calculations about ships advancing at constant speeds in calm water are routinely required for evaluating their hydrodynamic characteristics, both in calm water and in waves, and for determining the required propulsion and control devices. Calculations of far-field ship wave patterns are also important in connection with wave-resistance predictions and remote sensing of ship wakes. In particular, the latter practical application requires the capability to determine the short divergent waves in the wave spectrum having wavelengths between 5 cm and 40 cm associated with Bragg scattering of the electromagnetic waves in typical SAR systems used in remote sensing of ship wakes. No meaningful predictions of such short waves can be obtained on the basis of currently available numerical methods. More generally, numerical predictions of the steady wave pattern at large and moderate distances behind a ship are notoriously difficult and unreliable, as was recently made clear at the Workshop on Kelvin Wake Computations [1]. Ship wave-resistance calculations are also known to be unreliable.

Several alternative numerical methods have been developed for evaluating near-field flow about a ship, that is, flow at the hull surface and in its vicinity. These include finite-difference methods, e.g. Coleman [2] and Miyata and Nishimura [3], and the more widely used boundary-integral-equation methods, also known as panel methods. The latter methods can be divided into two main groups, according to the Green function that is used. These two groups of methods are the Rankine-source method and the Neumann-Kelvin method, which are based on the simple Rankine (free-space) fundamental solution and the more complex Green function satisfying the linearized free-surface boundary condition, respectively.

The Rankine-source method was initiated by Gadd [4], Dawson [5] and Daube [6], and has since been adopted by many authors. The Neumann-Kelvin approach has a long history. A survey of recent numerical predictions obtained by a number of authors on the basis of the Neumann-Kelvin method may be found in Baar [7]. This study and that by Andrew, Baar and Price [8] also contain extensive comparisons of the authors' own Neumann-Kelvin numerical predictions with experimental data. An approximate solution, defined explicitly in terms of the value of the Froude number and the hull shape, to the Neumann-Kelvin problem was proposed in Noblesse [9]. This slender-ship approximation was recently used by Scragg et al. [10] and compared to both Neumann-Kelvin predictions and experimental data in [7] and [8] and to experimental data in [1] and [11].

The aforementioned alternative numerical methods for predicting flow in the vicinity of a ship are not all directly suitable for predicting the far-field wave pattern of a ship. More precisely, the finite-difference method and the Rankine-source panel method require truncating the flow domain at some relatively-small distance away from the ship and therefore can only be used for near-field flow calculations. (However, these near-field flow predictions can be used as input to the far-field Neumann-Kelvin flow representation considered in this study.) On the other hand,

the Neumann-Kelvin theoretical framework is equally suitable for near-field and far-field flow predictions. Indeed, the far-field Neumann-Kelvin flow representation is a simplified particular case of the corresponding near-field representation.

The problem considered in this study is that of evaluating the steady wave spectrum and the wave pattern of a ship at moderate and large distances behind it in terms of the near-field flow on the hull surface. The near-field flow thus is assumed known for the purpose of the present study, which is concerned with the prediction of the steady wave spectrum and the wave potential behind a ship stern within the Neumann-Kelvin theoretical framework as was just noted.

This theory expresses the wave potential in terms of a Fourier representation, as is well known and is specifically indicated by Eq. (3) in this study. The wave-spectrum (or wave-amplitude) function in this Fourier representation is defined by the sum of an integral along the mean waterline and an integral over the mean wetted-hull surface. This expression for the wave-spectrum function is ill suited for accurate numerical evaluation because the waterline integral and the hull integral largely cancel out, as is shown further on in this study. Errors which inevitably occur in the numerical evaluation of the waterline and hull integrals cause imperfect numerical cancellations between these integrals and corresponding large errors in their sum. This fundamental difficulty was recognized in [9] and in [12], where attempts to remedy it were presented. However, these ad hoc approximate numerical remedies, based upon combining the waterline integral with the contribution to the hull integral stemming from the upper part of the hull surface are not satisfactory.

A conceptually simpler and numerically more effective remedy is presented in this study, in which a modified mathematical expression for the wave-spectrum function is obtained via several applications of Stokes' theorem resulting in the combining of the waterline integral and the hull integral. This new expression for the wave-spectrum function is considerably better suited than the usual expression for accurate numerical evaluation because the significant numerical cancellations which occur between the waterline and hull integrals in the usual expression are automatically and exactly accounted for, via a mathematical transformation, in the modified expression obtained in this study. The fundamental advantage of the new expression over the usual one may readily be appreciated from Fig. 4.

Another interesting feature of the modified expression for the wave-spectrum function is that it only requires the tangential velocity at the hull, not the potential, whereas the usual expression requires the values of both the velocity potential and its gradient at the hull. The modified expression thus defines the wave-spectrum function

in terms of the speed and the size of the ship, the shape of the mean wetted-hull surface and the tangential velocity at the mean hull surface. This expression is suitable for use in conjunction with any near-field flow-calculation method, including boundary-integral-equation methods based on source distributions and other numerical methods in which the velocity vector is determined directly on the mean hull surface rather than derived from the potential. It provides a practical and reliable method for coupling a far-field Neumann-Kelvin flow representation with any near-field flow-calculation method, including methods based on the use of Rankine sources or finite differences.

NEUMANN-KELVIN REPRESENTATION FOR THE WAVE POTENTIAL

As already noted, this study considers steady potential flow about a ship advancing at constant speed in calm water of infinite depth and lateral extent. Nondimensional coordinates and flow variables are defined in terms of the length L and the speed U of the ship and the water density ρ . The undisturbed sea surface is chosen as the plane $z = 0$, with the z -axis pointing upwards, and the x -axis is taken in the ship centerplane (port- and starboard-symmetry is assumed) and pointing toward the bow, as is depicted in Fig. 1. The Froude number and its inverse are denoted by F and ν , respectively, and are given by

$$F = U/(\rho L)^{1/2} = 1/\nu, \quad (1)$$

where g is the acceleration of gravity.

Within the so-called Neumann-Kelvin theoretical framework, the velocity potential $\phi(\xi)$ at any point $\xi = (\xi, \eta, \zeta \leq 0)$ strictly outside the ship hull surface is defined in terms of an integral representation [9, 13] involving integrals along the mean waterline and over the mean wetted-hull surface of the ship. The integrands of these integrals involve the values of the potential ϕ and of its gradient at the mean hull surface as well as the Green function and its gradient. The Green function may be expressed as the sum of three terms [14] corresponding to a Rankine source/sink pair, a nonoscillatory near-field flow disturbance and the wave pattern behind the singular point in the Green function. Likewise, the potential $\phi(\xi)$ may then be expressed as the sum of three terms, as follows:

$$\phi(\xi) = \phi_S(\xi) + \phi_N(\xi) + \phi_W(\xi), \quad (2)$$

where ϕ_S , ϕ_N and ϕ_W correspond to the singular source/sink term, the nonoscillatory near-field term and the wave term, respectively, in the expression for the Green function. This study is restricted to the numerical evaluation of the wave potential ϕ_W , which is the most complex of the three components in Eq. (2) and is dominant at some distance behind the ship.

More precisely, the problem considered in this study is that of evaluating the wave potential $\phi_W(\xi)$ at any point $(\xi, \eta, \zeta \leq 0)$ behind the ship stern. It is shown in [9] and [13] that the wave potential may be defined in terms of the following Fourier integral representation:

$$\phi_W(\xi) = (2/\pi) \int_0^\infty \exp(v^2 \zeta p^2) \cos(v^2 \eta p t) \operatorname{Im} \exp(i v^2 \xi p) K(t) dt, \quad (3)$$

where p is defined in terms of the Fourier variable t by the relation

$$p = (1 + t^2)^{1/2}, \quad (4)$$

and $K(t)$ represents the wave-spectrum function defined further on in this study. The wave potential $\phi_W(\xi)$ in Eq. (3) is expressed in terms of a familiar Fourier superposition of elementary plane waves propagating at angles θ from the ship track given by

$$\tan \theta = t. \quad (5)$$

The amplitudes of these elementary plane-wave components are essentially given by the function $K(t)$, which may thus be referred to as the far-field wave-amplitude function or as the free-wave spectrum function. The wave-spectrum function $K(t)$ contains essential information directly relevant to a ship's wave resistance and wave pattern. In particular, the wave resistance, R say, experienced by the ship is defined in terms of the wave-spectrum function by means of the well-known Havelock formula

$$\pi R / (\rho U^2 L^2) = \int_0^\infty [K(t)]^2 p dt. \quad (6)$$

The wave-spectrum function $K(t)$ in Eqs. (3) and (6) may be expressed as the sum of two terms [9], as follows:

$$K(t) = K_0(t) + K_\phi(t), \quad (7)$$

where K_0 represents the (zeroth-order) slender-ship approximation and K_ϕ the Neumann-Kelvin correction term in the Neumann-Kelvin approximation $K_0 + K_\phi$. More precisely, the function $K_0 + K_\phi$ corresponds to the usual linearized Neumann-Kelvin approximation, in which the nonlinear terms in the free-surface boundary condition are neglected. These nonlinear terms yield an additional term in the expression for the spectrum function K , defined by an integral over the mean free surface [9,13], which is ignored here. The slender-ship approximation K_0 is defined explicitly in terms of the value of the Froude number and the hull shape, whereas the Neumann-Kelvin correction K_ϕ also depends on the value of the potential ϕ at the mean hull surface. The functions K_0 and K_ϕ are considered in turn, beginning with the slender-ship approximation K_0 .

THE SLENDER-SHIP APPROXIMATION

The slender-ship approximation $K_0(t)$ to the wave-spectrum function $K(t)$ is defined in [9] as the sum of a line integral $K_w(t)$ along the ship's mean waterline w and a surface integral $K_h(t)$ over the ship's mean wetted-hull surface h , as follows:

$$K_0(t) = K_w(t) + K_h(t), \quad (8)$$

where the waterline and hull integrals are given by

$$K_w = \int_w (E_+ + E_-) n_x^2 t_y d\ell, \quad (9a)$$

$$K_h = v^2 \int_h \exp(v^2 p^2 z) (E_+ + E_-) n_x da. \quad (9b)$$

In these expressions, E_\pm represent the trigonometric functions defined as

$$E_\pm = \exp[-i v^2 p^2 (u x \pm v y)], \quad (10)$$

where u and v are given by

$$u = 1/p \quad \text{and} \quad v = t/p; \quad (11a,b)$$

it may then be seen from Eq. (4) that we have

$$1 \geq u \geq 0 \quad \text{and} \quad 0 \leq v \leq 1 \quad (12a,b)$$

for $0 \leq t \leq \infty$, with

$$u^2 + v^2 = 1. \quad (13)$$

Furthermore, w and h represent the positive halves of the mean waterline and of the mean wetted-hull surface, respectively, as is depicted in Fig. 1 where $h = s + b$ with s = hull side and b = hull bottom. Also, $d\ell$ is the differential element of arc length of w and da the differential element of area of h . Finally, $n = (n_x, n_y, n_z)$ is the unit vector normal to h and pointing outside the ship, and $t = (t_x, t_y, t_z = 0)$ is the unit vector tangent to w and pointing toward the bow, as is shown in Fig. 1.

The hull bottom of a typical ship is a nearly horizontal surface, so that we have $n_x \approx 0$ on b , but n_x is usually significant on the hull side in the bow and stern regions. However, the hull side of a typical ship is a nearly vertical surface, i.e. we have $n_z \approx 0$ on s . It is therefore convenient to express the hull integral as the sum of integrals over the hull side and the hull bottom, and to modify the hull-side integral into a form involving the source density n_z instead of n_x by using Stokes' theorem in the manner shown in [13]. The slender-ship approximation $K_0(t)$ may then be expressed in the form

$$K_0(t) = K_w^*(t) + K_{w'}(t) + K_h^*(t), \quad (14)$$

where the functions $K_w^*(t)$, $K_{w'}(t)$ and $K_h^*(t)$ are defined as

$$K_w^* = \int_w (E_+ + E_-) (n_x^2 - u^2) t_y d\ell, \quad (15a)$$

$$K_w = u^2 \int_w \exp(v^2 p^2 z) (E_+ + E_-) t_y \, dl, \quad (15b)$$

$$K_h^* = -iv^2 u \int_s \exp(v^2 p^2 z) (E_+ + E_-) n_z \, da + v^2 \int_b \exp(v^2 p^2 z) (E_+ + E_-) n_x \, da. \quad (15c)$$

In the foregoing modified expression for the slender-ship approximation $K_0(t)$, the function $K_w^*(t)$ represents a modified waterline integral, with source density $(n_x^2 - u^2)t_y$ instead of $n_x^2 t_y$ in Eq. (9a). Furthermore, the function $K_w^*(t)$ corresponds to a line integral along the waterline-like curve w' separating the hull side s and the hull bottom b , as is shown in Fig. 1; the unit tangent vector $t = (t_x, t_y, t_z)$ to the "lower waterline" w' points toward the bow. Finally, $K_h^*(t)$ represents a modified hull integral consisting of the sum of an integral over the hull bottom b and the hull side s , with source densities given by n_x and $-iun_z$, respectively. The latter source density is null for a wall-sided ship and, more generally, vanishes in the limit $t \rightarrow \infty$, as may be seen from Eqs. (4) and (11a). The hull-side integral therefore is generally less important in the modified expression (14) than in the original expression (8). In particular, the hull-side and hull-bottom integrals in Eq. (15c) are null for a wall-sided ship with a flat horizontal bottom (i.e., a strut-like form), for which Eq. (14) thus expresses the slender-ship approximation $K_0(t)$ as the sum of two line integrals. For large values of $v^2 p^2 = (\sec^2 \theta)/F^2$, the trigonometric functions E_{\pm} defined by Eq. (10) oscillate rapidly. The dominant contribution to the modified waterline integral K_w^* in Eq. (14) therefore stems from the points, if any, where the phases $v^2 p^2 (ux \pm vy)$ of the trigonometric functions E_{\pm} are stationary. These points of stationary phase are defined by the conditions $u dx \pm v dy = 0$, which yield the relations

$$u t_x \pm v t_y = 0, \quad t_x = v, \quad t_y = \mp u; \quad (16a, b, c)$$

the latter two relations can be obtained from Eq. (16a) by using Eq. (13) and the identity $t_x^2 + t_y^2 = 1$.

The term u^2 in the integrand of the modified waterline integral K_w^* defined by Eq. (15a) stems from the integral on the hull side in Eq. (8), as may be seen by comparing the alternative expressions for the function K_0 given by Eqs. (8), (9a, b) and Eqs. (14), (15a, b, c). We have $n_x = -t_y$ along the top waterline of a wall-sided ship; Eq. (16c) therefore shows that the term $n_x^2 - u^2$ in the integrand of the modified waterline integral K_w^* vanishes at a point of stationary phase for a wall-sided ship. This result indicates that the waterline integral and the hull-side integral in Eq. (8) cancel out in a first approximation (specifically, within the stationary-phase approximation) for a wall-sided ship. The major contributions to these two integrals thus are combined into the modified waterline integral K_w^* in the modi-

fied expression (14), and the modified hull-side integral in Eq. (14) is less important than the original hull-side integral in Eq. (8) as was already noted.

The modified expression for the slender-ship approximation $K_0(t)$ defined by Eqs. (14) and (15a, b, c) thus is better suited for accurate numerical evaluation than the usual expression defined by Eqs. (8) and (9a, b) for large values of $v^2 p^2$, that is for small values of the Froude number and/or large values of $t = \tan \theta$. However, significant cancellations may be expected to occur between the line integrals K_w^* and K_h^* in Eq. (14) for relatively large values of the Froude number and small values of $\tan \theta$. More precisely, the term $-u^2(E_+ + E_-)t_y$ in the integrand of the top-waterline integral K_w^* defined by Eq. (15a) and the integrand $u^2 \exp(v^2 p^2 z)(E_+ + E_-)t_y$ of the lower-waterline integral K_w^* defined by Eq. (15b) may nearly cancel out if $\exp(v^2 p^2 z) \approx 1$, that is for small values of $v^2 p^2 d$ where d is the ship draft.

It therefore is useful to express Eq. (14) in the following form:

$$K_0(t) = K_*(t) + K'(t), \quad (17)$$

where the functions $K_*(t)$ and $K'(t)$ are defined as

$$K_* = \int_w (E_+ + E_-) [n_x^2 - u^2 + u^2 \exp(v^2 p^2 z)] t_y \, dl, \quad (18a)$$

$$K' = u^2 \int_w \exp(v^2 p^2 z) (E_+ + E_-) t_y \, dl - u^2 \int_w \exp(v^2 p^2 z) (E_+ + E_-) t_y \, dl - iv^2 u \int_s \exp(v^2 p^2 z) (E_+ + E_-) n_z \, da + v^2 \int_b \exp(v^2 p^2 z) (E_+ + E_-) n_x \, da. \quad (18b)$$

In the integrals along the top waterline w in Eqs. (18a, b), z is to be taken equal (or, more generally, approximately equal) to the vertical coordinate of the point (x, y, z) on the lower waterline w' , in such a way that the integrals along the lower waterline w' and the top waterline w in Eq. (18b) nearly cancel out.

In the simple case of a strut-like hull form we have $n_x = 0$ on the hull bottom b and $n_z = 0$ on the hull side s . Furthermore, the lower waterline w' is identical to the top waterline w except for a vertical translation equal to the ship draft d , and z in the integrals along the lower and top waterlines w' and w in Eq. (18b) is equal to $-d$. For such a simple strut-like hull we then have $K'(t) = 0$ and Eq. (17) yields $K_0(t) = K_*(t)$. The modified waterline integral K_* defined by Eq. (18a) thus provides an exact expression for the slender-ship approximation K_0 in the special case of a strut-like hull form.

For a simple hull in the shape of a strut the alternative expressions for the slender-ship approximation K_0 defined by Eqs. (8) and (17) become

$$K_0(t) = K_w(t) + K_s(t) = K_*(t), \quad (19)$$

where the hull integral K_h in Eq. (8) was replaced by the hull-side integral K_s since we have $n_x = 0$ on the horizontal bottom of a strut. The real and imaginary parts of the functions $K_w(t)$, $K_s(t)$ and $K_0(t) \equiv K_*(t)$ are depicted in Fig. 2 for $0 \leq t = \tan \theta \leq 5$ (corresponding to $0 \leq \theta < 79^\circ$) for a specific strut-like hull form at three values of the Froude number, namely 0.1 (top row), 0.2 (center row) and 0.3 (bottom row). The strut considered for the calculations presented in Fig. 2 has beam/length and draft/length ratios equal to 0.16 and 0.07, respectively, and consists of a pointed bow region $0.2 \leq x \leq 0.5$ with parabolic waterlines, a straight middle-body region $-0.3 \leq x \leq 0.2$ and a rounded stern region $-0.5 \leq x \leq -0.3$ with elliptic waterlines.

The top row of Fig. 2, corresponding to the small value of the Froude number F equal to 0.1, shows that the function K_0 is significantly smaller than the waterline and hull-side integrals K_w and K_s in Eqs. (19) and (8). This numerical result is in accordance with the previously-established theoretical result that the major contributions to the integrals K_w and K_s cancel out for small values of the Froude number. The function K_0 , especially its real part represented by a solid line, is also appreciably smaller than the functions K_w and K_s in the center row of Fig. 2 corresponding to $F = 0.2$ and, to a reduced degree, in the bottom row corresponding to the fairly large value 0.3 of F .

The integral $K_w'(t)$ along the lower waterline w' in Eqs. (14), (15b) and (18b) is also depicted in Fig. 2. The top row of this figure, corresponding to $F = 0.1$, shows that the lower-waterline integral $K_w'(t)$ is negligible in comparison with the function $K_0(t) \equiv K_*(t)$ for all values of t due to the exponential function $\exp(v^2 p^2 z)$ in the integrand of the lower-waterline integral K_w' . However, this integral is significant for small and moderate values of $t = \tan \theta$ in the center and bottom rows of Fig. 2 corresponding to $F = 0.2$ and 0.3, respectively.

For typical hull forms Eq. (17) expresses the slender-ship approximation $K_0(t)$ as the sum of the modified waterline integral $K_*(t)$ defined by Eq. (18a) and the remainder $K'(t)$ defined by Eq. (18b). The remainder $K'(t)$ may generally be expected to provide a relatively small correction to the dominant waterline integral $K_*(t)$. In particular, the integrals along the lower and top waterlines w' and w and the hull-bottom integral in Eq. (18b) decay exponentially due to the exponential function $\exp(v^2 p^2 z)$ in their integrands. These three integrals thus are negligible for sufficiently large values of $v^2 p^2$, for which the major contribution to the remainder K' stems from the upper part of the hull side in the hull-side integral in Eq. (18b).

It may thus be useful to divide the hull side into an upper part $-\delta \leq z \leq 0$ and a lower part $z \leq -\delta$, where δ is some fraction

of the depth of the hull side s . The upper hull side can be approximately defined by the parametric equations $x = a(\ell) + z \alpha(\ell)$ and $y = b(\ell) + z \beta(\ell)$ for $-\delta(\ell) \leq z \leq 0$, where ℓ represents the arc length along the top waterline w defined by $x = a(\ell)$ and $y = b(\ell)$, and $\alpha = \partial x / \partial z$ and $\beta = \partial y / \partial z$ are the slopes of the hull surface at the waterline. The contribution of the upper part of the hull side to the hull-side integral in Eq. (18b) can then be expressed as an integral along the top waterline w , which can be grouped with the top-waterline integral K_* defined by Eq. (18a). In this manner the dominant waterline integral K_* is modified by including the contribution of the upper part of the hull side to the hull-side integral in Eq. (18b), whereas the remainder K' is modified by restricting the integration in the hull-side integral to the lower part of the hull side.

This modified remainder K' thus is exponentially small for large values of $v^2 p^2 = (\sec^2 \theta) / F^2$ and can only be significant for small and moderate values of $v^2 p^2$. The hull bottom b , the lower part of the hull side s and the lower and top waterlines w' and w in expression (18b) for the remainder K' may then be approximated by using a relatively coarse discretization, whereas a finer discretization may be used for representing the top waterline w in expression (18a) for the dominant waterline integral K_* . The modified form of the top-waterline integral (18a) including the contribution of the upper hull side to the hull-side integral in Eq. (18b) can easily be derived from Eq. (18b).

THE NEUMANN-KELVIN APPROXIMATION

The correction term K_ϕ in Eq. (7) for the Neumann-Kelvin approximation $K_0 + K_\phi$ to the wave-spectrum function K is defined by the sum of a waterline integral and a hull-surface integral [9,13]:

$$K_\phi(t) = K_w(t) + K_w'(t) + K_H'(t), \quad (20)$$

where $K_w(t)$ and $K_w'(t)$ are the waterline integrals and $K_H'(t)$ the hull-surface integral defined as

$$K_w = \int_w (E_+ + E_-) (t_x \phi_t + s_x \phi_s) t_y \, d\ell, \quad (21a)$$

$$K_w' = i v^2 p \int_w (E_+ + E_-) \phi_t t_y \, d\ell, \quad (21b)$$

$$K_H' = (v^2 p)^2 \int_h \exp(v^2 p^2 z) (E_+ n_+ + E_- n_-) \phi \, da. \quad (21c)$$

In the foregoing equations E_\pm are the trigonometric functions defined by Eq. (10). The functions n_\pm in Eq. (21c) are defined as

$$n_\pm = -n_z + i(un_x \pm vn_y). \quad (22)$$

In Eqs. (21a-c) and (22), $t = (t_x, t_y, 0)$ is the unit vector tangent to the waterline w and pointing toward the bow, as was already defined, $s = (s_x, s_y, s_z)$ is a unit vector

tangent to the hull surface h and pointing downwards and $n = (n_x, n_y, n_z)$ is the unit vector normal to h and pointing outside the ship, as is shown in Fig. 1. Finally, ϕ_t and ϕ_s in Eq. (21a) represent the components of the velocity vector $\nabla\phi$ in the directions of the unit tangent vectors t and s to h , respectively.

Numerical evaluation of the waterline and hull integrals in Eq. (20) is a seemingly simple task, given the value of the potential ϕ on the mean hull surface $h + w$; in particular, the integrands of the integrals defined by Eqs. (21a-c) are continuous functions. Nevertheless, accurate and efficient numerical evaluation of these integrals requires careful analysis because the trigonometric functions E_{\pm} defined by Eq. (10) oscillate rapidly for large values of $v^2 p^2$, as is the case for typical values of the Froude number $F = 1/v$ and of the Fourier variable $p^2 = 1 + t^2 = \sec^2\theta$, and because the potential ϕ in the integrands of the waterline and hull integrals K_W' and K_H' in Eqs. (21b,c) is multiplied by the large numbers $v^2 p$ and $(v^2 p)^2$, respectively. More precisely, we have $10^2 < v^4 < 10^4$ for $0.1 < F < 0.32$ and $p^2 > 10$ for $\theta > 72^\circ$; values of $(v^2 p)^2$ as large as 10^5 thus are possible. The waterline and hull integrals K_W' and K_H' in Eq. (20) may then be expected to be dominant and to largely cancel out, as is shown in Fig. 3.

More precisely, Fig. 3 depicts the functions K_ϕ , $K_W + K_W'$ and K_H' for $0 \leq t \leq 10$ (corresponding to $0 \leq \theta < 85^\circ$) for the simple hull form considered previously in Fig. 2 with an assumed simple mathematical expression for the value of the velocity potential ϕ at the hull surface. Specifically, the potential in Eqs. (21a-c) is taken as $\phi = F^2 \exp(v^2 z) \cos[v^2(x-1/2)-3\pi/8]$, which corresponds to an elementary plane progressive wave. This simple hull form and assumed simple expression for the potential at the hull surface are used for the calculations presented in Fig. 3 because they permit accurate numerical calculations (the required integrations can be partially performed analytically) and they are adequate for the purpose of numerically illustrating the essential properties of the several alternative mathematical expressions for the Neumann-Kelvin correction K_ϕ examined in this study. Figure 3 corresponds to a value of the Froude number equal to 0.15. It may be seen from Fig. 3 that the function K_ϕ is considerably smaller than the waterline and hull integrals $K_W + K_W'$ and K_H' . In particular, the waterline and hull integrals $K_W + K_W'$ and K_H' do not appear to vanish in the limit $t \rightarrow \infty$ ($\theta \rightarrow 90^\circ$). Significant cancellations therefore occur between the waterline and hull integrals in Eq. (20). These significant cancellations occur for all values of ∂ but are especially notable for large values of θ , corresponding to the short divergent waves in the spectrum.

The errors which inevitably occur in the numerical evaluation of the integrals $K_W +$

K_W' and K_H' cause imperfect numerical cancellations between these components and corresponding large errors in their sum. Numerical errors in the sum K_ϕ can be especially difficult to control because the errors associated with the numerical evaluation of the hull integral K_H' and the waterline integral $K_W + K_W'$ are not necessarily comparable (due to differences in the errors associated with numerical integration over hull panels and waterline segments). The usual expression (20) for the Neumann-Kelvin correction K_ϕ in Eq. (7) thus is ill suited for accurate numerical evaluation. A modified mathematical expression in which the cancellations between the waterline and hull integrals $K_W + K_W'$ and K_H' depicted in Fig. 3 are automatically and exactly accounted for, via a mathematical transformation, is presented below.

By using Stokes' theorem in the manner explained in [13] we can combine the waterline and hull integrals K_W' and K_H' defined by Eqs. (21b,c) into a modified hull integral K_H , as follows:

$$K_H(t) = K_W'(t) + K_H'(t), \quad (23)$$

where the modified hull integral K_H is given by

$$K_H = iv^2 p \int_h \exp(v^2 p^2 z) (E_+ a_+ + E_- a_-) da \quad (24)$$

with

$$a_{\pm} = n_z \partial\phi/\partial x - n_x \partial\phi/\partial z \pm iv(n_x \partial\phi/\partial y - n_y \partial\phi/\partial x). \quad (25)$$

By substituting Eq. (23) into Eq. (20) we may then obtain the following modified expression for the Neumann-Kelvin correction $K_\phi(t)$:

$$K_\phi(t) = K_W(t) + K_H(t). \quad (26)$$

The functions K_W' , K_H' and K_H are depicted in Fig. 3. This figure shows that the waterline and hull integrals K_W' and K_H' are considerably larger than the modified hull integral K_H . Although the latter integral is identical to the sum of the integrals K_W' and K_H' , it clearly is preferable to evaluate K_H directly by means of Eqs. (24) and (25) rather than as the sum of the integrals K_W' and K_H' defined by Eqs. (21b,c). The modified expression for the Neumann-Kelvin correction $K_\phi(t)$ given by Eqs. (26), (21a), (24) and (25) therefore represents a significant improvement in comparison with the usual expression given by Eqs. (20) and (21a-c). It is shown in [13] that the cancellations between the waterline integral K_W' and the hull integral K_H' depicted in Fig. 3 can be explained mathematically for a wall-sided ship form by performing an asymptotic analysis in the limit $v^2 p^2 \rightarrow \infty$ similar to that presented previously in this study for the slender-ship approximation K_0 .

The functions K_W , K_H and K_ϕ in the modified expression (26) for the Neumann-Kelvin

correction are depicted in Fig. 3. It may be seen that the waterline integral K_W and the modified hull integral K_H are appreciably larger than their sum K_ϕ , especially for large values of t . Significant cancellations therefore still occur between the waterline and hull integrals in Eq. (26). Further modifications of the expression for the function K_ϕ defined by Eqs. (26), (21a), (24) and (25) are then desirable for numerical calculations. These modifications are now presented.

By making use of Stokes' theorem and a classical formula in vector analysis we can obtain [13] the following alternative expression for the Neumann-Kelvin correction K_ϕ :

$$K_\phi(t) = K_W(t;C) + K_H(t;C), \quad (27)$$

where $K_W(t;C)$ and $K_H(t;C)$ are the modified waterline and hull integrals defined as

$$K_W = \int_W (E_{+a} + E_{-a}) dl, \quad (28a)$$

$$K_H = i\nu^2 \int_h \exp(\nu^2 p^2 z) (E_{+A} - E_{-A}) da. \quad (28b)$$

The amplitude functions a_\pm and A_\pm in Eqs. (28a,b) are given by

$$a_\pm = (t_x \phi_t + s_x \phi_s) t_y \pm u(v - Cu) \partial \phi / \partial t, \quad (29a)$$

$$A_\pm = (Cu - v)(n_y \partial \phi / \partial z - n_z \partial \phi / \partial y) \pm (Cv + u)(n_z \partial \phi / \partial x - n_x \partial \phi / \partial z) + iC(n_x \partial \phi / \partial y - n_y \partial \phi / \partial x). \quad (29b)$$

In the foregoing expressions, C is an arbitrary complex function of t which may be selected at will. Equations (27), (28a,b) and (29a,b) thus define a one-parameter family of alternative mathematically-equivalent expressions for the Neumann-Kelvin correction K_ϕ in Eq. (7).

The velocity components $\partial \phi / \partial x$, $\partial \phi / \partial y$ and $\partial \phi / \partial z$ in Eq. (29b) defining the amplitude functions A_\pm in Eq. (28b) can be expressed in terms of the components ϕ_t and ϕ_s of the velocity vector $\nabla \phi$ along two unit vectors

$$t = (t_x, t_y, t_z) \quad \& \quad s = (s_x, s_y, s_z) \quad (30a,b)$$

tangent to the hull surface. More precisely, we have $\nabla \phi = n \partial \phi / \partial n + t \phi_t + s \phi_s$, which yields

$$\partial \phi / \partial x = n_x \partial \phi / \partial n + t_x \phi_t + s_x \phi_s, \quad (31a)$$

$$\partial \phi / \partial y = n_y \partial \phi / \partial n + t_y \phi_t + s_y \phi_s, \quad (31b)$$

$$\partial \phi / \partial z = n_z \partial \phi / \partial n + t_z \phi_t + s_z \phi_s, \quad (31c)$$

where $\partial \phi / \partial n$ is the velocity component along the unit outward normal vector n to the hull surface defined as

$$n = (t \times s) / |t \times s|. \quad (32)$$

The vectors t and s to the ship hull surface

are tangent to curves which approximately correspond to waterlines and framelines and they point toward the bow and the keel, respectively. The vectors t and s thus are roughly (but not necessarily exactly) orthogonal. At the mean free surface, the vector t is tangent to the top waterline (and we thus have $t_z = 0$) in agreement with our previous definition.

Equations (31a-c) yield

$$n_y \partial \phi / \partial z - n_z \partial \phi / \partial y = (n_y t_z - n_z t_y) \phi_t + (n_y s_z - n_z s_y) \phi_s, \quad (33a)$$

$$n_z \partial \phi / \partial x - n_x \partial \phi / \partial z = (n_z t_x - n_x t_z) \phi_t + (n_z s_x - n_x s_z) \phi_s, \quad (33b)$$

$$n_x \partial \phi / \partial y - n_y \partial \phi / \partial x = (n_x t_y - n_y t_x) \phi_t + (n_x s_y - n_y s_x) \phi_s. \quad (33c)$$

By using Eqs. (33a-c) in Eq. (29b) we may express the amplitude functions A_\pm in the form

$$|t \times s| A_\pm = [(v - Cu)t_x \mp (u + Cv)t_y - iCt_z] \partial \phi / \partial s - [(v - Cu)s_x \mp (u + Cv)s_y - iCs_z] \partial \phi / \partial t. \quad (34)$$

The components ϕ_s and ϕ_t of $\nabla \phi$ along the unit tangent vectors s and t and the velocities $\partial \phi / \partial s = \nabla \phi \cdot s$ and $\partial \phi / \partial t = \nabla \phi \cdot t$ are related as follows

$$\partial \phi / \partial s = \phi_s + \epsilon \phi_t, \quad (35a)$$

$$\partial \phi / \partial t = \phi_t + \epsilon \phi_s, \quad (35b)$$

$$\phi_s = (\partial \phi / \partial s - \epsilon \partial \phi / \partial t) / (1 - \epsilon^2), \quad (35c)$$

$$\phi_t = (\partial \phi / \partial t - \epsilon \partial \phi / \partial s) / (1 - \epsilon^2), \quad (35d)$$

where ϵ is defined as

$$\epsilon = t \cdot s. \quad (36)$$

An asymptotic analysis [13] indicates that the modified waterline and hull integrals $K_W(t;C)$ and $K_H(t;C)$ in Eq. (27) vanish more rapidly than the corresponding integrals $K_W(t)$ and $K_H(t)$ in Eq. (26) if the function $C(t)$ vanishes in the limit $t \rightarrow \infty$, that is if we have

$$C(t) \rightarrow 0 \quad \text{as } t \rightarrow \infty. \quad (37)$$

An obvious choice for the arbitrary function $C(t)$ that satisfies this condition is

$$C(t) = 0. \quad (38)$$

The corresponding expression for the Neumann-Kelvin correction K_ϕ may be written in the form

$$K_{\phi}(t) = K_W''(t) + K_H''(t), \quad (39)$$

where the waterline and hull integrals K_W'' and K_H'' are defined by Eqs. (28a,b), (29a), (34) and (38).

The functions K_W and K_H in Eq. (26) and the functions K_W'' and K_H'' in Eq. (39) are depicted in Fig. 3. It may be seen that the functions K_W'' and K_H'' vanish more rapidly than the functions K_W and K_H for increasing values of t , in accordance with condition (37). The cancellations occurring between the waterline and hull integrals K_W and K_H for large values of t thus are significantly reduced in the alternative expression (39), which is therefore preferable to expression (26) for large values of t . However, the functions K_W'' and K_H'' are appreciably larger than the functions K_W and K_H for small values of t , and significant cancellations thus occur between the waterline and hull integrals K_W'' and K_H'' for small values of t . Expression (26) therefore is preferable to expression (39) for small values of t , whereas the reverse holds for large values of t .

The amplitude functions in the integrands of the waterline and hull integrals in Eqs. (26) and (27) can be shown [13] to be nearly identical for small values of t if the arbitrary function $C(t)$ satisfy the condition

$$v - u C(t) \ll 1 \quad \text{as } t \rightarrow 0. \quad (40)$$

This condition ensures that the waterline and hull integrals in Eq. (27) are nearly identical to the corresponding integrals in Eq. (26) in the limit $t \rightarrow 0$. The large- t and small- t conditions (37) and (40) are satisfied if the function $C(t)$ is selected in the form

$$C(t) = u v \lambda(t). \quad (41)$$

Condition (40) then becomes $v(1-u^2\lambda) \ll 1$ as $t \rightarrow 0$. Equation (13) shows that we have $v(1-u^2\lambda) \sim v^3$ as $t \rightarrow 0$ if the arbitrary function $\lambda(t)$ satisfies the condition

$$\lambda(t) \rightarrow 1 \quad \text{as } t \rightarrow 0. \quad (42)$$

An obvious choice for the function $\lambda(t)$ satisfying condition (42) is

$$\lambda(t) = 1. \quad (43)$$

The corresponding expression for the Neumann-Kelvin correction K_{ϕ} may be written in the form

$$K_{\phi}(t) = K_W^*(t) + K_H^*(t), \quad (44)$$

where the waterline and hull integrals K_W^* and K_H^* are defined by Eqs. (28a,b), (29a) and (34) in which C is replaced by uv , that is

$$C(t) = u v = t / (1 + t^2). \quad (45)$$

The functions K_W and K_H in Eq. (26) and

the functions K_W^* and K_H^* in Eq. (44) are depicted in Fig. 3. It may be seen that the functions K_W^* and K_H^* vanish more rapidly than the functions K_W and K_H for increasing values of t . In this respect, the functions K_W^* and K_H^* are comparable to the functions K_W'' and K_H'' also depicted in Fig. 3. However, the functions K_W^* and K_H^* and the functions K_W'' and K_H'' are significantly different for small and moderate values of t . More precisely, the functions K_W'' and K_H'' are appreciably larger than the functions K_W and K_H , as was already noted, whereas the functions K_W^* and K_H^* are comparable to, indeed somewhat smaller than, the functions K_W and K_H for small and moderate values of t . Figure 3 shows that the cancellations which occur between the waterline and hull integrals K_W and K_H in Eq. (26) are reduced significantly for the modified waterline and hull integrals K_W^* and K_H^* in Eq. (44). The latter expression for the Neumann-Kelvin correction K_{ϕ} therefore is preferable to the former one for accurate numerical calculations.

In summary, the waterline and hull integrals $K_W + K_W'$ and K_H' in the original expression (20) for the Neumann-Kelvin correction K_{ϕ} and the modified waterline and hull integrals K_W^* and K_H^* in the alternative expression (44) are depicted in Fig. 4 for the simple case considered previously in Fig. 3 and for three values of the Froude number, namely $F = 0.1$ (top row), 0.2 (center row) and 0.3 (bottom row). The function K_{ϕ} is also represented in Fig. 4. This figure shows that the spectrum function K_{ϕ} is significantly smaller and vanishes much more rapidly with increasing values of t than its components $K_W + K_W'$ and K_H' in the usual expression (20), as was already observed in Fig. 3. Large cancellations therefore occur among these components and Eq. (20) is ill suited for accurate numerical calculations, notably for evaluating the short divergent waves in the wave spectrum corresponding to large values of t . However, Fig. 4 also shows that the modified waterline and hull integrals K_W^* and K_H^* in Eq. (44) are appreciably smaller than the original waterline and hull integrals $K_W + K_W'$ and K_H' , and are in fact comparable to the function K_{ϕ} . Although the alternative expressions (20) and (44) are mathematically equivalent, the modified expression (44) clearly is considerably better suited than the usual expression (20) for accurate numerical calculations.

CONCLUSION

In expression (2) for the velocity potential of steady flow about a ship, the wave potential $\phi_W(\xi)$ at any point $\xi = (\xi, \eta, \zeta \leq 0)$ behind the stern of the ship is defined by Eq. (3), where v and p are given by Eqs. (1) and (4), respectively, and $K(t)$ represents the wave-spectrum function. The latter function is defined by Eq. (7) as the sum of the slender-ship approximation K_0 , which is defined explicitly in terms of the Froude

number and the shape of the hull, and the Neumann-Kelvin correction term K_ϕ , which also involves the potential at the hull. The wave resistance of the ship is defined in terms of the wave-spectrum function by means of the Havelock formula (b). The Fourier variable t in Eqs. (3) and (6) is related to the angle θ of propagation of the free waves in the ship wave pattern by the relation $t = \tan\theta$, as is given by Eq. (5).

The slender-ship approximation K_0 in Eq. (7) is defined by the usual expression given by Eqs. (8) and (9a,b), or by the alternative modified expression defined by Eqs. (17) and (18a,b). The latter expression defines the spectrum function K_0 as the sum of a modified integral K_* along the ship waterline w and a remainder K' . In the special case of a strut-like hull form, the remainder K' is null and the modified waterline integral K_* provides an exact expression for the slender-ship approximation K_0 .

The Neumann-Kelvin correction K_ϕ in Eq. (7) is defined by the usual expression given by Eqs. (20) and (21a-c) or by the alternative modified expression given by Eqs. (27), (28a,b), (29a) and (34). This alternative expression involves an arbitrary complex function $C(t)$, and thus defines a one-parameter family of mathematically-equivalent expressions for the Neumann-Kelvin correction K_ϕ in Eq. (7). In particular, the first modified expression, defined by Eqs. (26), (21a), (24) and (25), obtained in this study is a special case of the general expression given by Eqs. (27), (28a,b), (29a) and (34) corresponding to the choice $C(t) = t$. Analytical and numerical considerations led to the particular expression given by Eq. (44), which corresponds to the choice $C(t) = uv$ defined by Eq. (45) where u and v are given by Eqs. (11a,b). Figure 4 shows that the mathematical expression corresponding to Eq. (44) is considerably better suited than the usual expression (20) for accurate numerical evaluation because the large cancellations which occur between the waterline integral $K_W + K_W'$ and the hull integral K_H' in the usual expression (20) are automatically and exactly accounted for, via a mathematical transformation, in the new expression (44) involving the modified waterline and hull integrals K_W^* and K_H^* .

Another interesting feature of the new expression for the Neumann-Kelvin correction K_ϕ given by Eqs. (27), (28a,b), (29a) and (34) is that it only requires the tangential velocity at the hull, not the potential. whereas the usual expression given by Eqs. (20) and (21a-c) requires the values of both the velocity potential and its gradient at the hull. The new expression for K_ϕ obtained in this study thus defines the wave-spectrum function $K_0 + K_\phi$ in terms of the speed and the size of the ship, the shape of the mean wetted-hull surface and the tangential velocity at the mean hull surface. This expression is suitable for use in conjunction with any near-field flow-calculation method, including

boundary-integral-equation methods based on source distributions and other numerical methods in which the velocity vector is determined directly rather than derived from the potential. It provides a practical and robust method for coupling a far-field Neumann-Kelvin flow representation with any near-field flow-calculation method, including methods based on the use of Rankine sources or finite differences.

For large values of $t = \tan\theta$, the major contributions to the integrals over the ship hull surface in Eqs. (18b) and (28b) stem from the upper part of the hull surface in the vicinity of the mean waterline w due to the exponential function $\exp(v^2 p^2 z)$. These hull integrals, and consequently the spectrum functions K_0 and K_ϕ , may then be approximated by waterline integrals for large values of $\tan\theta$, as has indeed been shown in this study for the special case of a wall-sided hull. This asymptotic approximation can be extended to ship forms having flare, and refined by retaining the first few terms in the asymptotic approximation. A detailed short-wave asymptotic analysis has been performed and will be reported elsewhere as it is important for evaluating the short divergent waves of interest for applications to remote-sensing of ship wakes. Simplified approximate expressions for the wave spectrum functions K_0 and K_ϕ defined in terms of single (one fold) integrals along the ship axis (or waterline) can also be obtained in the long-wave limit by expanding the exponential function $\exp(v^2 p^2 z)$ and the trigonometric function $\exp(iv^2 p t y)$ in Taylor series. These long-wave approximations will also be reported elsewhere. The short-wave and long-wave asymptotic analyses mentioned above may also suggest alternative choices for the arbitrary function $C(t)$ in Eqs. (27), (29a) and (34) to that defined by Eq. (45).

ACKNOWLEDGMENTS

This study was funded by the Office of Naval Research under the Applied Hydrodynamics Research program at the David Taylor Research Center.

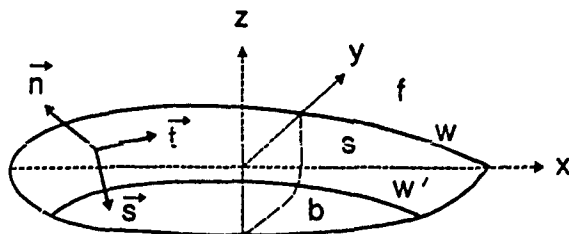


Fig. 1 - Definition Sketch

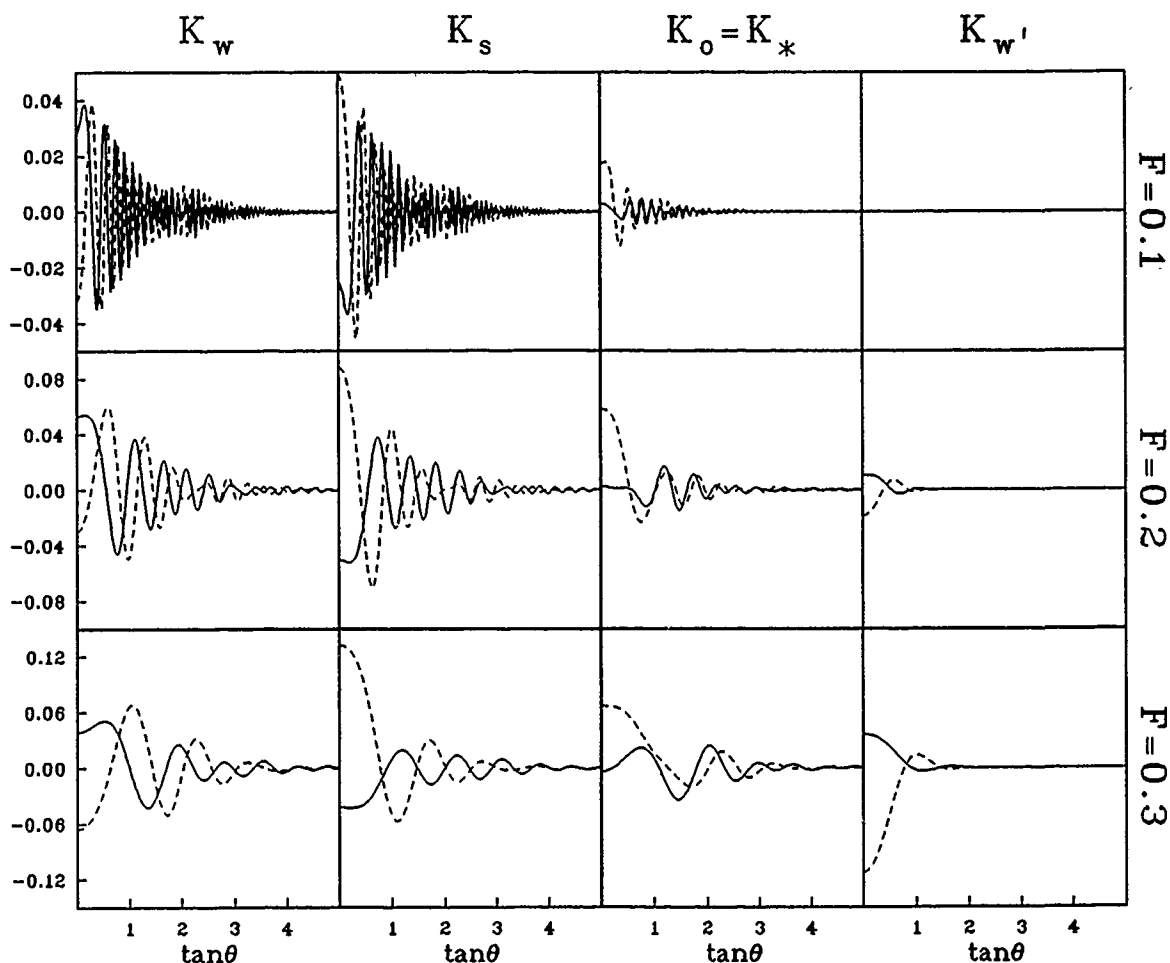


Fig. 2 - Comparison of the usual expression $K_0 = K_w + K_s$ and the alternative modified expression $K_0 = K_*$ for the slender-ship approximation K_0 to the wave-spectrum function $K(t)$ in the special case of a simple strut-like hull form. The real (solid line) and imaginary (dashed line) parts of the functions K_w (first column on left), K_s (second column) and $K_0 = K_*$ (third column) are depicted for $0 \leq \tan \theta \leq 5$, corresponding to $0 \leq \theta < 79^\circ$, and for three values of the Froude number F , namely 0.1 (top row), 0.2 (center row) and 0.3 (bottom row). The integral K_w' along the lower waterline w' in Eqs. (14) and (18b) is also depicted in the column on the right.

REFERENCES

1. Lindenmuth, W.T., T.J. Ratcliffe and A.M. Reed, "Comparative Accuracy of Numerical Kelvin Wake Code Predictions - Wake Off," David Taylor Research Center Report DTRC/SHD-1260-01 (1988).
2. Coleman, Roderick M., "Nonlinear Flow About a Three-Dimensional Transom Stern," Proceedings of the Fourth International Conference on Numerical Ship Hydrodynamics, Washington, DC, pp. 234-244 (1985).
3. Miyata, Hideaki and Shinichi Nishimura, "Finite-Difference Simulation of Nonlinear Ship Waves," Journal of Fluid Mechanics, Vol. 157, pp. 327-357 (1985).
4. Gadd, G.E., "A Method of Computing the Flow and Surface Wave Pattern Around Hull Forms," Transactions of the Royal Institute of Naval Architects, Vol. 118, pp. 207-215 (1976).
5. Dawson, C.W., "A Practical Computer Method for Solving Ship-Wave Problems," Proceedings of the Second International Conference on Numerical Ship Hydrodynamics, Berkeley, CA, pp. 30-38 (1977).
6. Daube, Olivier, "Calcul non linéaire de la résistance de vagues d'un navire," Comptes Rendus de l'Académie des Sciences, Paris, France, Vol. 290, pp. 235-238 (1980).
7. Baar, Job J.M., "A Three-Dimensional Linear Analysis of Steady Ship Motion in Deep Water," Ph.D. thesis, Brunel University, U.K., 182 pp. (1986).
8. Andrew, R.N., J.J.M. Baar and W.G. Price, "Prediction of Ship Wavemaking Resistance and Other Steady Flow Parameters Using Neumann-Kelvin Theory," Transactions of the Royal Institution of Naval Architects, Vol. 130, pp. 119-129 (1988).
9. Noblesse, Francis, "A Slender-Ship Theory of Wave Resistance," Journal of Ship Research, Vol. 27, pp. 13-33 (1983).

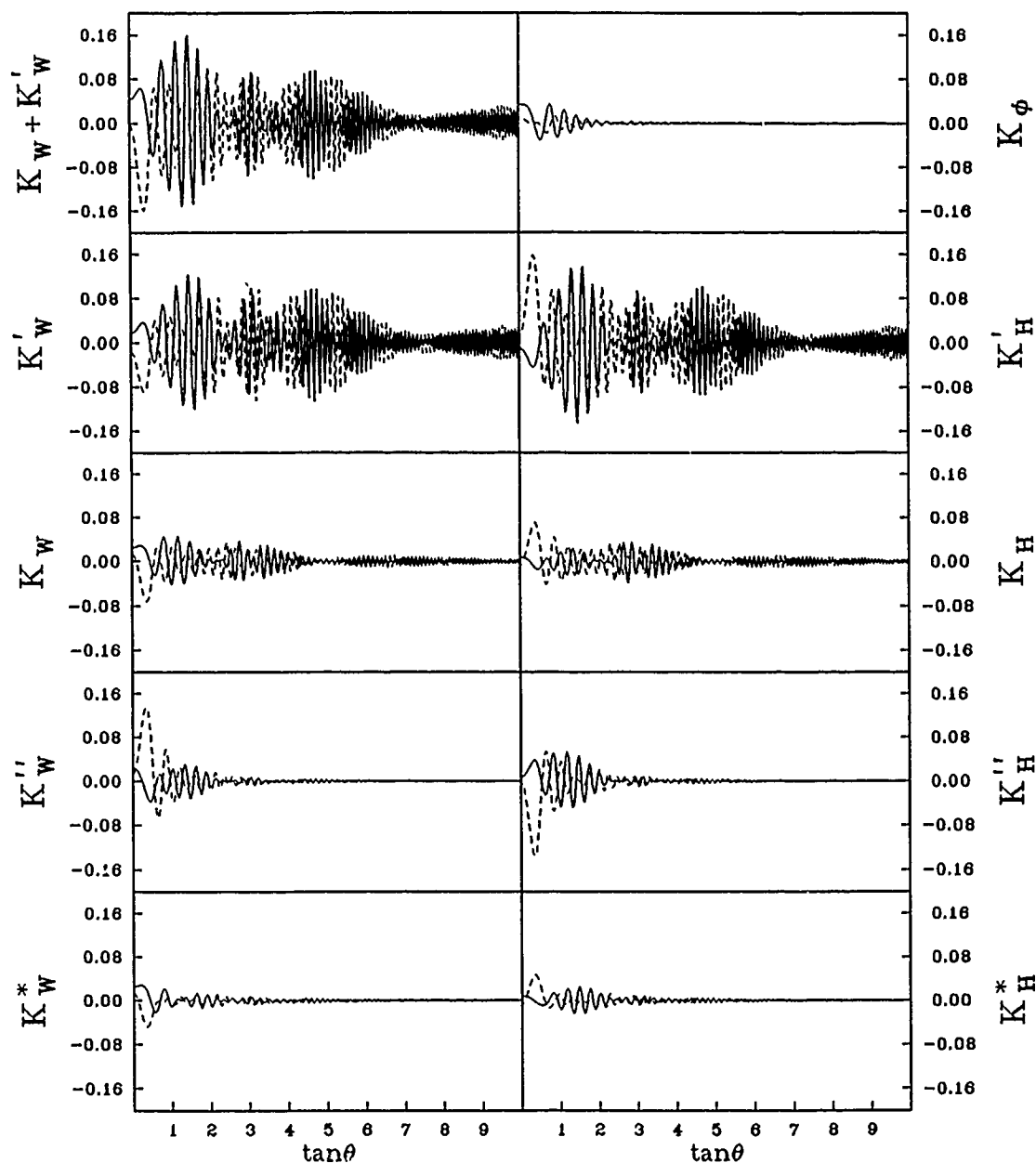


Fig. 3 - Comparison of the usual expression $K_\phi = K_W + K_W' + K_H'$ and the three alternative modified expressions $K_\phi = K_W + K_H$, $K_\phi = K_W'' + K_H''$ and $K_\phi = K_W^* + K_H^*$ for the Neumann-Kelvin correction term K_ϕ in the expression for the wave spectrum function $K(t)$ for a simple strut-like hull form and an assumed simple expression for the potential at the hull surface. The real and imaginary parts of the ten functions K_ϕ , $K_W + K_W'$, K_W' , K_H' , K_W , K_H , K_W'' , K_H'' , K_W^* and K_H^* are depicted for $0 \leq \tan\theta \leq 10$, corresponding to $0 \leq \theta < 85^\circ$, and for a value of the Froude number equal to 0.15.

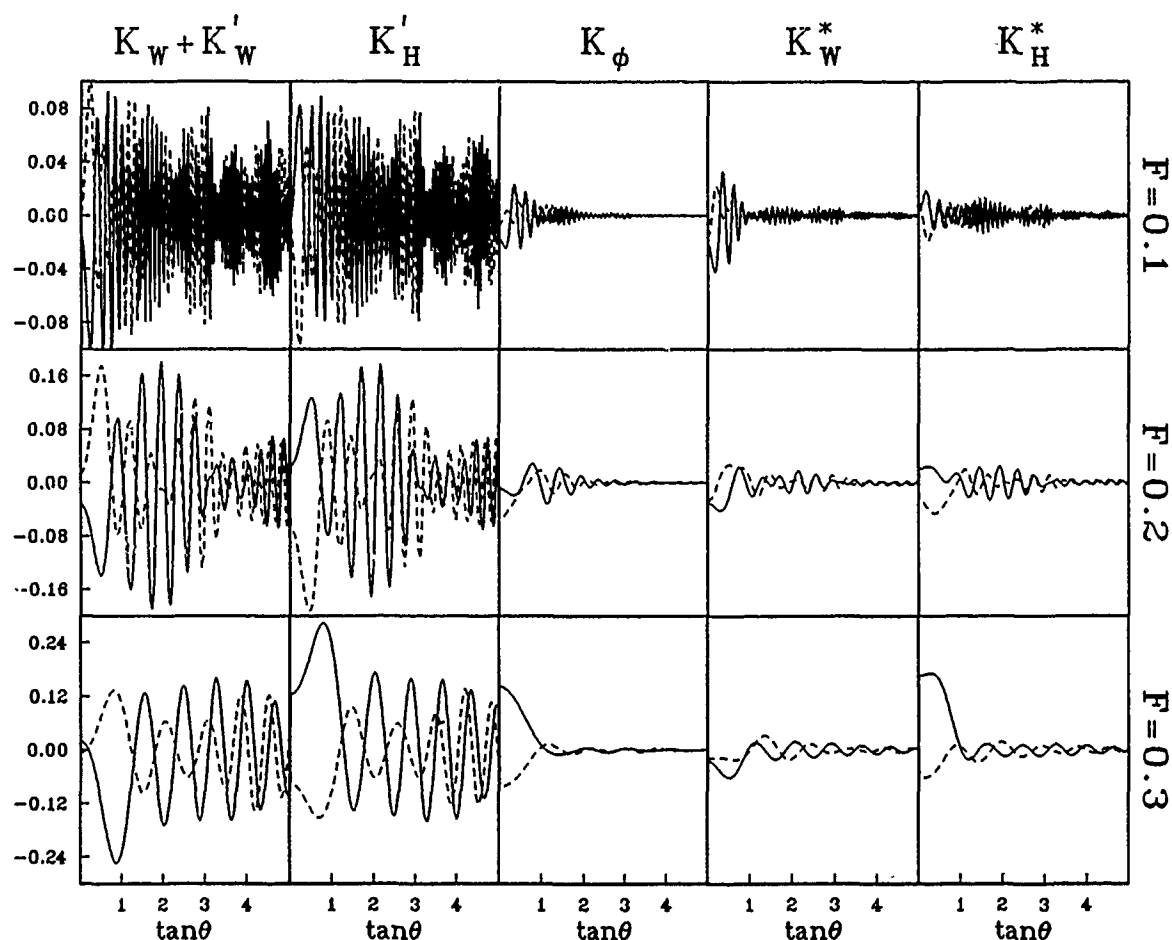


Fig. 4 - Comparison of the usual expression $K_\phi = K_W + K'_W + K'_H$ and the alternative modified expression $K_\phi = K_W^* + K_H^*$ for the Neumann-Kelvin correction term K_ϕ in the expression for the wave-spectrum function $K(t)$ for a simple strut-like hull form and an assumed simple expression for the potential at the hull surface. The real and imaginary parts of the five functions $K_W + K'_W$ (first column on left), K'_H (second column on left), K_ϕ (center column), K_W^* (second column on right) and K_H^* (first column on right) are depicted for $0 \leq \tan \theta \leq 5$, corresponding to $0 \leq \theta < 79^\circ$, and for three values of the Froude number F , namely 0.1 (top row), 0.2 (center row) and 0.3 (bottom row). Large cancellations occur between the waterline integral $K_W + K'_W$ and the hull integral K'_H in the usual expression for K_ϕ which is then ill suited for accurate numerical calculations, notably for evaluating the short waves in the spectrum corresponding to large values of $\tan \theta$. The modified waterline integral K_W^* and hull integral K_H^* in the alternative new expression for K_ϕ are significantly smaller than the usual waterline and hull integrals, and are comparable to the function K_ϕ . Although the alternative expressions $K_\phi = K_W + K'_W + K'_H$ and $K_\phi = K_W^* + K_H^*$ are mathematically equivalent, the latter expression is considerably better suited than the former one for accurate numerical evaluation.

REFERENCES

10. Scragg, Carl A., Britton Chance Jr., John C. Talcott and Donald C. Wyatt, "Analysis of Wave Resistance in the Design of the 12-Meter Yacht Stars and Stripes," *Marine Technology*, Vol. 24, pp. 286-295 (1987).
11. Noblesse, F., D. Hendrix and A. Barnell, "The Slender-Ship Approximation: Comparison Between Experimental Data and Numerical Predictions," *Proceedings of the Deuxièmes Journées de l'Hydrodynamique, Ecole Nationale Supérieure de Mécanique, Nantes, France*, pp. 175-187 (1989).
12. Barnell, A. and F. Noblesse, "Numerical Evaluation of the Near- and Far-Field Wave Pattern and Wave Resistance of Arbitrary Ship Forms," *Proceedings of the Fourth Conference on Numerical Ship Hydrodynamics*, Washington, DC, pp. 324-341 (1985).
13. Noblesse, F., and W.M. Lin, "A Modified Expression for Evaluating the Steady Wave Pattern of a Ship," *David Taylor Research Center Report No. 88/041* (1988).
14. Noblesse, F., "Alternative Integral Representations for the Green Function of the Theory of Ship Wave Resistance," *Journal of Engineering Mathematics*, Vol. 15, pp. 241-265 (1981).

Ship Wave Ray Tracing Including Surface Tension

D. B. Huang

Harbin Shipbuilding Engineering Institute
Harbin, China

K. Eggers

University of Hamburg
Hamburg, Germany

Abstract

The aim of this work is to clarify the validity of ship wave ray theories at and near the ship's surface. As previous numerical investigations have led to ambiguities due to a breakdown of the ray analysis near the bow and stern stagnation points, we shall take care for the surface tension effect in order to milder such deficiencies; then the wave length never surpasses a positive minimum length which is attained at the boundary of a finite waveless zone around a stagnation point. It is found, however, that the ray equations degenerate at these boundaries, and that rays can be traced into the far field only if their starting point is selected outside a finite belt surrounding the waveless zone.

For a class of bi-circular prismatic struts of infinite downward extent we investigate two alternative formulations of the free surface condition and their implications for the ray geometry. For low speeds we find in both cases an increase of the Kelvin wave cusp angle due to capillarity. We extended the ray tracing to capillary waves ahead of a blunt bow.

Introduction

The wave field at a point far away from a ship in stationary motion is well represented through Kelvin's pattern, found in a wedge-shaped region, with only a finite number of wave components, given through wave length, wave front angle and complex amplitude. The first two are constant along straight lines (characteristics) through a hypothetical origin, conceived as the locus of a point disturbance.

Observations suggest that under local modifications such a wave model may be adequate even *near* a ship; Ursell [1] hence generalised this approach for waves due to a point disturbance in a slightly non-uniform flow. From a set of physical assumptions, he replaced the intensity and direction of the uniform flow by the local components to obtain an analogous spatially varying "dispersion relation" between wave angle and wave number; from a partial differential equation he obtained "rays" along the resultant of the local flow with a group

velocity vector. To simplify the problem, Ursell considered only rays passing *through* the disturbance, though he admitted that his assumptions are questionable there. Inui and Kajitani [2] used this approach for waves near a ship's bow, with the "double body flow" as the basic non-uniform flow.

Keller [3] derived Ursell's results from a more formal approach, tacitly assuming pertinence and uniform validity of his ray theory up to the ship's water line; he even concluded for certain ships that rays *must* originate from the double body flow stagnation points *only*. Yim [4] evaluated this approach numerically, but due to zero wave length at these points he had to start ray tracing using values at some distance. For certain rays carrying transverse waves he observed that they re-entered the hull; to avoid this, he introduced some mechanism of reflection.

Brandsma [5] investigated a class of bi-circular forms with varying entrance angle. Even with "backshooting" from downstream, he failed to find rays due to transverse waves originating at the stagnation points; he therefore concluded that *no* transverse waves can emanate from the bow. We shall demonstrate analytically that the rate of change of the wave front angle along the ray together with the change of ray direction has a factor as inverse distance from the stagnation points. Thus it demands more detailed analysis to clarify the validity of Keller's ray theory near the stagnation points.

Through our present investigation we want to clarify whether the inclusion of surface tension effects can improve the situation at least to the point that ray theory can give some qualitative information about the wave pattern geometry in accord with experimental observations for not so slender ships. We selected the class of bi-circular struts and thus have even the case of a blunt bow included.

¹Otherwise rays could be extended to the domain far ahead through backward tracing, at least in case of a submerged disturbance.

The underlying analysis was presented by Eggers [6], where two alternative approaches were considered: $(A)'$ based on the conventional surface condition (A) of slow ship theory, supplemented for surface tension following Maruo [7] and $(A^+)'$ based on a modified free surface condition, derived by Eggers [8] from certain invariance requirements for wave resistance, again supplemented for capillarity effects. In both cases we obtain zones around the stagnation points where no steady waves can exist; at their boundaries, only waves of minimum wave speed, with wave front orthogonal to the double body flow, can occur. If we start rays from these boundaries rather than from the stagnation points, we apparently have a well defined initial value problem, even for blunt bow forms.

In our computational investigations, we could confirm Maruo's experimental finding that capillarity effects can be significant even if the model speed exceeds the minimum wave speed considerably.

However, we found ourselves confronted with some instability phenomenon. Due to the strong rate of change of the wave angle along the ray near its origin, the wave length re-approached its minimum value after a short time and the analysis broke down. To find rays which can be continued into the far field, we had to select the starting point outside some "belt of short-livety" surrounding the waveless zone.

Derivation Of Dispersion Relation And Ray Equations From Free Surface Conditions.

For simplicity, we shall restrict ourselves to a 2-D flow around prismatic struts of infinite vertical extension. Let us consider a velocity potential of the form $U\phi_r + U\phi$, where U stands for the far field uniform flow in the $+x$ direction, $U\phi_r$ represents the "double body flow" (unbounded in the upward z -direction) and $U\phi$ is the lowest order wavy potential. With $u \doteq U\phi_{rx}$, $v \doteq U\phi_{ry}$, with $\zeta_r \doteq (U^2 - u^2 - v^2)/2g$ and $D_r(x, y) \doteq (u\zeta_r)_x + (v\zeta_r)_y$, φ for $z = 0$ has to satisfy

$$u^2\varphi_{xx} + 2uv\varphi_{xy} + v^2\varphi_{yy} + g(\varphi_x + \zeta_r\varphi_{zz}) = 2g(\zeta_{rx}\varphi_x + \zeta_{ry}\varphi_y) + D_r(x, y) \quad (1)$$

(see Eggers [10]); for inclusion of surface tension, a term $\kappa\varphi_{zzz}$ has to be added on the l.h.s. (see Maruo [7]).

Seeking for wave-type solutions, we concentrate on the homogenous part of above d.e.; we further disregard the (amplitude modulating)³ terms with φ_x and φ_y . Hence we consider the "modified approach" $(A^+)'$

$$u^2\varphi_{xx} + 2uv\varphi_{xy} + v^2\varphi_{yy} - g\zeta_r(\varphi_{xx} + \varphi_{yy}) = -\kappa\varphi_{zzz} - g\varphi_z \quad (2)$$

³Quite recently, this approach has been justified under new arguments by van Gemert [9].

⁴See Longuet-Iliggins and Stewart [11] and [8].

The neglect of $g\zeta_r\varphi_{zz}$ (the second term of a formally divergent Taylor expansion) leads to the approach $(A)'$ investigated by Maruo, which was developed from the "conventional" approach (A) underlying the ray analyses of Keller, Yim and Brandsma. Let us now consider u and v as slowly-varying (i.e. locally constant) quantities and let us disregard effects of phase and of amplitude, as they are of no concern for investigations on ray geometry. A potential of the form

$$\Phi \propto e^{(kx - iS)} \quad \text{with} \quad S = S(x, y) \quad (3)$$

represents a wave with wave number vector

$$\vec{k} \doteq \nabla S \doteq \{k_1, k_2\} \doteq \{k \cos \theta, k \sin \theta\} \quad (4)$$

if k_1 and k_2 are also slowly varying. Here θ is the angle of \vec{k} against the x -direction. Let us define the speed ratio q and the flow angle β through $u \doteq Uq \cos \beta$ and $v \doteq Uq \sin \beta$. Then $\gamma \doteq \theta - \beta$ is the angle of \vec{k} against the flow direction. In accord with Brandsma and Yim, we have selected the orientation of \vec{k} such that $\cos \gamma$ is non-negative, i.e. \vec{k} is "opposite" to the propagation of a wave stationary to the ship.

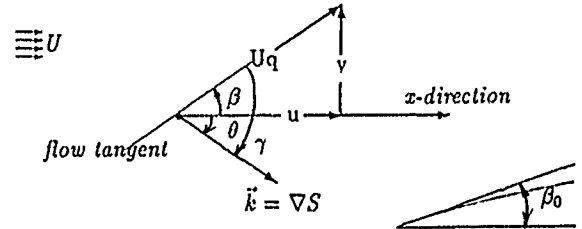


Fig.1 Sketch for flow angle β and wave angles θ and γ (both shown with negative values, typical for the starboard side of the bow).

Inserting (3) into (2) leads to

$$(ku \cos \theta + kv \sin \theta)^2 = gk + g\zeta_r k^2 + \kappa k^3 \quad (5)$$

Denote c as the phase velocity with direction $\{-\cos \theta, -\sin \theta\}$. If we consider stationary waves only, c must balance with the projection of the basic flow $\{u, v\}$ in the direction of c , i.e. $c = u \cos \theta + v \sin \theta = Uq \cos \gamma$. Equation (5) thus leads to the "dispersion relation"

$$c = \sqrt{g/k + g\zeta_r + \kappa k} \quad (6)$$

Equation (5) may equivalently be expressed as

$$F(x, y, k_1, k_2) \doteq 1 - (k_1^2 + k_2^2)c^2 / (uk_1 + vk_2)^2 = 0 \quad (7)$$

Noting that $k_1 = \frac{\partial S}{\partial x}$, $k_2 = \frac{\partial S}{\partial y}$, we may consider this as a partial d.e. for the function $S(x, y)$ for which

⁴Note that the term $g\zeta_r$ appears only under $(A^+)'$, not under $(A)'$; it may remind us of $c = \sqrt{gh}$ for waves on shallow water of depth h .

"characteristic stripes" (i.e. characteristic curves in the $\{x, y, k_1, k_2\}$ -space) can be found from the equations

$$\frac{dx}{d\tau} = \frac{\partial F}{\partial k_1}; \frac{dy}{d\tau} = \frac{\partial F}{\partial k_2}; \frac{dk_1}{d\tau} = -F_x; \frac{dk_2}{d\tau} = -F_y \quad (8)$$

which define a curve parameter τ . Under multiple use of above relations, considering that

$$\frac{\partial(uk_1 + vk_2)}{\partial k_1} = u; \frac{\partial(uk_1 + vk_2)}{\partial k_2} = v \quad (9)$$

$$\frac{\partial(ck)}{\partial k_1} = c_g \cos \theta; \frac{\partial(ck)}{\partial k_2} = c_g \sin \theta \quad (10)$$

(where $c_g \doteq d(ck)/dk$ is in accord with the concept of group velocity related to $Uq \cos \gamma$ as phase velocity), we find

$$\begin{aligned} c_g &= \frac{d}{dk}(ck) = \frac{d}{dk} \sqrt{kg + k^2 g \zeta_r + k^3 \kappa} \\ &= \frac{1}{2kc} (g + 2g\zeta_r + 3k^2 \kappa) = \frac{c}{2} \left(1 + \frac{g\zeta_r + 2k\kappa}{c^2}\right) \end{aligned} \quad (11)$$

We obtain

$$\begin{aligned} \frac{dx}{d\tau} &= \frac{\partial F}{\partial k_1} = 2 \cdot \frac{-kc}{uk_1 + vk_2} \cdot \frac{\partial}{\partial k_1} \frac{kc}{uk_1 + vk_2} \\ &= -\frac{2}{ck} \cdot \frac{\partial}{\partial k_1} (kc - uk_1) = \frac{2}{kc} (u - c_g \cos \theta) \end{aligned} \quad (12)$$

In a similar way

$$\frac{dy}{d\tau} = \frac{2}{kc} (v - c_g \sin \theta) \quad (13)$$

From (6) we find

$$\frac{\partial(ck)}{\partial x} = \frac{k}{2c} \frac{\partial}{\partial x} g \zeta_r \quad (14)$$

and thus

$$\begin{aligned} F_x &= -\frac{dk_1}{d\tau} = -2 \frac{kc}{uk_1 + vk_2} \cdot \frac{\partial}{\partial x} \frac{kc}{uk_1 + vk_2} \\ &= -2 \frac{\partial}{\partial x} (kc - uk_1 - vk_2) \\ &= -\frac{2}{kc} \cdot \frac{\partial}{\partial x} \left(\frac{k}{c} g \zeta_r - uk_1 - vk_2\right) \\ &= \frac{2}{c^2} ((u u_x + v v_x)/2 + c(u_x \cos \theta + v_x \sin \theta)) \end{aligned} \quad (15)$$

$$F_y = \frac{2}{c^2} ((u u_y + v v_y)/2 + c(u_y \cos \theta + v_y \sin \theta)) \quad (16)$$

Then we find the rate of change of the wave angle θ from

$$\begin{aligned} \frac{kc^2}{2} \frac{d\theta}{d\tau} &= \frac{kc^2}{2} \frac{d}{d\tau} \arctan \frac{k_2}{k_1} \\ &= \frac{c^2}{2k} \left(k_1 \frac{dk_2}{d\tau} - k_2 \frac{dk_1}{d\tau}\right) \end{aligned} \quad (17)$$

$$\begin{aligned} &= -c^2 (F_y \cos \theta - F_x \sin \theta)/2 \\ &= ((g \zeta_r)_y \cos \theta - (g \zeta_r)_x \sin \theta)/2 \\ &+ cu_x \sin 2\theta - cv_x \cos 2\theta \end{aligned} \quad (18)$$

where we have used $u_x = -v_y$, $u_y = v_x$ for our 2-D basic flow. In a similar way we obtain⁵

$$\begin{aligned} \frac{c^2}{2} \cdot \frac{dk}{d\tau} &= \frac{c^2}{2k} \cdot \left(k_1 \frac{dk_1}{d\tau} + k_2 \frac{dk_2}{d\tau}\right) \\ &= ((g \zeta_r)_x \cos \theta + (g \zeta_r)_y \sin \theta)/2 \\ &- cu_x \cos 2\theta - cv_x \sin 2\theta \end{aligned} \quad (19)$$

From equs. (12) and (13) we can easily confirm the general result

$$\tan(\beta + \alpha) \doteq \frac{dy}{dx} = \frac{v - c_g \sin \theta}{u - c_g \cos \theta} \quad (20)$$

(with α defined as the ray angle against the double body flow) which contains the choice of approach only through the explicit expression for c_g . We may thus recall Ursell's observation that the ray direction is along the resultant of the basic flow and the "group velocity" taken along the wave normal vector $-\vec{k}$, and that this does not require asymptotic analysis such as the principle of stationary phase (see discussion to [8])⁶

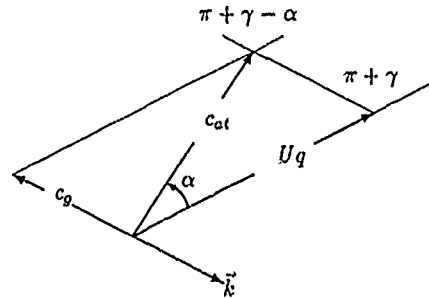


Fig.2 Ray direction as resultant of basic flow and c_g along direction of $-\vec{k}$ (with angle α against flow direction).

Restrictions For The Wave Parameters.

From the dispersion relation (6) we have

$$c^2 = g/k + g \zeta_r + \kappa k \quad (21)$$

⁵The terms with $g \zeta_r$ (missing under approach (A)') reflect the statement of Longuet-Higgins and Stewart [11] that short waves superposed a long wave shorten when climbing, increasing their length again when descending.

⁶For later use, we have introduced in Fig.2 an "action transport velocity" c_{at} along the tangent to the ray direction.

A minimum of c is found at $k = \sqrt{g/\kappa}$ giving

$$c = c_m \sqrt{1 + \frac{1}{2}(1 - q^2)/p^2} = U \sqrt{(1 - q^2 + 2p^2)/2} \quad (22)$$

where $c_m = \sqrt{4\kappa g}$ is the minimum velocity of capillary-gravity waves and $p \doteq c_m/U$ is a dimensionless parameter of surface tension. We introduce a dimensionless wave length $\Lambda \doteq g/(kU^2)$; then (5) is equivalent to

$$q^2 \cos^2 \gamma = \Lambda + (1 - q^2)/2 + p^4/4\Lambda \quad (23)$$

In a plane of the variables q^2 and Λ , for p constant, (22) represents a family of hyperbolas between the asymptotes $\Lambda = 0$ and $\Lambda = \Lambda_\gamma \doteq (1 + 2\cos^2 \gamma)q^2 - 1/2$.

We are interested in the branch with $\Lambda > 0$; (otherwise, we would have an increase of the wave flow downwards, see(3)). Solving for Λ , we obtain

$$\Lambda = \frac{(1 + 2\cos^2 \gamma)q^2 - 1}{2} \cdot \frac{1 \pm Sq}{2} \quad (24)$$

$$Sq \doteq \sqrt{1 - (2p^2/(2\cos^2 \gamma + 1)q^2 - 1))^2} \quad (25)$$

Sq is real only for $q^2 \geq (1 + 2p^2)/(2\cos^2 \gamma + 1) \geq (1 + 2p^2)/3$; this implies that in the zones around the stagnation points where $q^2 \leq (1 + 2p^2)/3$ no steady waves can exist.

The upper sign of the root corresponds to gravity dominated waves ($\Lambda = \Lambda_g$); the capillarity dominated waves ($\Lambda = \Lambda_c$, lower sign) are better described by⁷

$$\Lambda = \frac{p^4}{4} \cdot \frac{2}{(1 + 2\cos^2 \gamma)q^2 - 1} \cdot \frac{2}{1 + Sq} \quad (26)$$

For any γ , confluence of the two roots occurs for $\Lambda = p^2/2$ corresponding to the minimum of c found earlier (21). For the range $(1 + 2p^2)/3 \leq q^2 \leq 1 + 2p^2$ the angle γ is restricted through

$$|\gamma| \leq \frac{1}{2} \arccos \left(\frac{1 + 2p^2}{q^2} - 2 \right) \quad (27)$$

(under approach (A)), $|\gamma| \leq \arccos p$, independent from q^2). Beyond this range, for $q^2 > 1 + 2p^2$, the minimum of Λ_g is no longer $p^2/2$ but the value corresponding to $\gamma = \pi/2$. Then we have

$$\Lambda_g \geq \frac{q^2 - 1}{2} \cdot \frac{1 + \sqrt{1 - (2p^2/(q^2 - 1))^2}}{2} \approx \frac{q^2}{2} - \frac{1}{2} \quad (28)$$

If we accept the argument that stationary waves cannot propagate into areas where c_g/c is negative, the domain of admitted Λ values is further restricted (see(11)) through

$$\frac{2cc_g}{U^2} = \Lambda + 1 - q^2 + \frac{3p^4}{4\Lambda} \geq 0 \quad (29)$$

⁷The relevant analysis has been established and profoundly discussed by Crapper [13] for the non-modified approach (A)

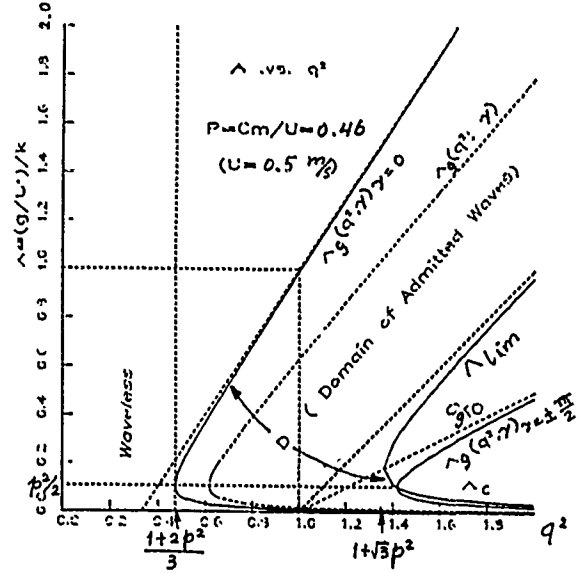


Fig.3 Domain D of Admitted Waves for $p = 0.46$ (i. e. $U = 0.5$ m/s)

For gravity waves with $q^2 > 1 + \sqrt{3}p^2$ this implies

$$\Lambda > \Lambda_{lim} \doteq (q^2 - 1) \left(1 + \sqrt{1 - 3p^4/(1 - q^2)^2} \right) / 2 \quad (30)$$

One may observe that this limitation is automatically met if $|\gamma| \leq \pi/4$ with $d\Lambda/dq^2 \geq 1/2 + \cos^2 \gamma \geq 1$ then (see Fig.3). One may note that for any γ we find from (22), (25) and (5)

$$(c/U)^2 = \Lambda_g + \Lambda_c + (1 - q^2)/2 \quad (31)$$

All the above restrictions can be visualized through a display of the dependence between the wave front angle γ and the ray direction angle α with p and q held constant. From a geometrical interpretation of (19), invoking the sine theorem of elementary trigonometry (see Fig2.), we find

$$\frac{\sin \alpha}{c_g} = -\frac{\sin(\gamma - \alpha)}{Uq} = -\frac{\sin \gamma}{c_{at}} \quad (32)$$

and hence

$$\tan \alpha = \frac{\sin \gamma}{\cos \gamma - Uq/c_g} = \frac{\sin 2\gamma}{1 + \cos 2\gamma - 2c/c_g} \quad (33)$$

Setting $p = 0$, $q \neq 1$, we have $c_g/c = 1/2$ in accord with Kelvin's results; we find that $|\alpha|$ will increase with $|\gamma|$ up to some maximum $\alpha_k = \arctan(1/\sqrt{8})$ and then fall off to zero with $\gamma = \pi/2$. We may observe that for non-zero p , unless $q^2 \geq 1$, α approaches zero only together with γ , as $\cos \gamma$ will remain positive. Thus an outgoing ray ($\alpha > 0$) can turn inward again only if the wave front normal changes from inward ($\gamma < 0$) to outward at the "caustic" (in the terminology of Yim [17]) under a maximum of the wave length due to $\gamma = 0$.

One may consider the range of negative α in order to have γ positive. If we exclude here those parts of curves where α turns positive due to $c_g \leq 0$ (only for $q^2 > 1$ under $(A^+)'$), we may observe that α as an odd function will in general have opposite sign to γ .

Let us refer to the range for which $|\alpha|$ is increasing from zero with $|\gamma|$ as to that of *transverse waves* and define the maximum value attained for α in this range as the *modified Kelvin angle* α_k . Then we find that for $q^2 \leq 1 + 2p^2$ each curve for gravity dominated waves turns under horizontal tangent (with $\alpha = \pi/2 + \gamma$) into one for capillarity dominated waves, so that after $\tan \alpha$ changed sign due to increase of $c_g/c > 1$ for such waves, γ falls off to zero again with the ray finally normal to the wave crest again, but opposite now to the flow direction.

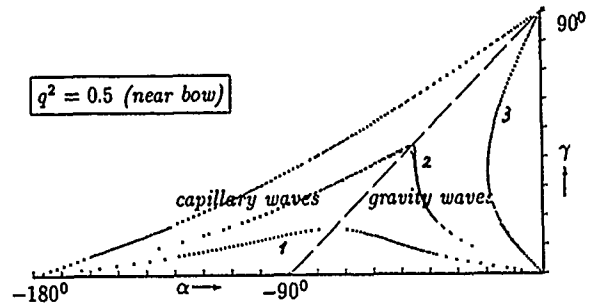
Note that our formulations and considerations throughout this paper are referred to the domain around the starboard side of the bow, where α is positive, hence γ negative in general. To deal with the other ship side, statements remain valid if β and θ , γ and α are counted *clockwise* against the x-axis and flow direction there. Note that, observing $4k\kappa/c^2 = p^4/(\Lambda q^2 \cos^2 \gamma)$ in (11), we have the deviation of c_g/c from 1/2 depending on p^2 and on q^2 even under approach $(A)'$, where the term $(1 - q^2)/2$ is disregarded. c_g/c and hence $|\alpha|$ increases with decreasing speed U (i.e. increasing p) and with decreasing distance from the stagnation point (i.e. decreasing q) for γ held constant. This implies an increase of the modified Kelvin angle (which is measured against the flow direction!) especially near the bow, in particular under approach $(A^+)'$. This is well in accord with the experimental observations of Miyata[14] with wedge-shaped models with $U = 0.5m/s$, ($p \approx 0.462$) and $U = 1m/s$, ($p \approx 0.231$).

Away from the bow, where $q^2 \approx 1$, thus $\zeta_r \approx 0$, there is little difference between $(A^+)'$ and $(A)'$. But again we observe an increase of α_k with decreasing U in accord with Miyata's experiments with a rudder model (see Inui [15]) for the speeds $U = 1.15m/s$, $1.72m/s$ and $U = 2.3m/s$ corresponding to $p = 0.3$, 0.14 and 0.1 .

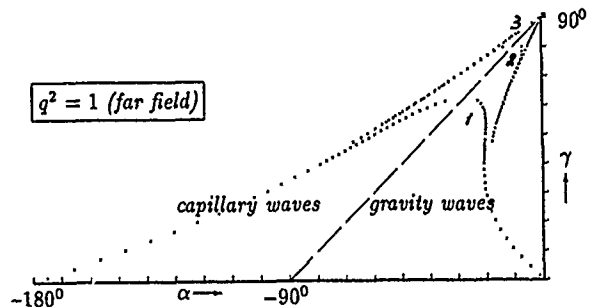
In the domain where $q^2 > 1$ aside of the ship, a *reduction* of α_k is predicted under $(A^+)'$ including a termination of rays with short gravity waves with c_g approaching negative values. We may mention that for a vertical circular cylinder, q^2 increases up to 4.0, whereas for conventional forms q^2 will not exceed 1.2.

It is only for not too small q and for not too large p that α is really stationary for $\alpha = \alpha_k$ and thus marks a transition from transverse to divergent waves, so that with $d\alpha/d\gamma = 0$ we may expect a wave cusp effect. Let us search for the most forward point along the water line of a ship where stationarity occurs (i.e. immedi-

ately near the stagnation point for pointed bows) and trace a curve from there with $dy/dx = \tan(\beta + \alpha_k)$; this should define some cusp line.

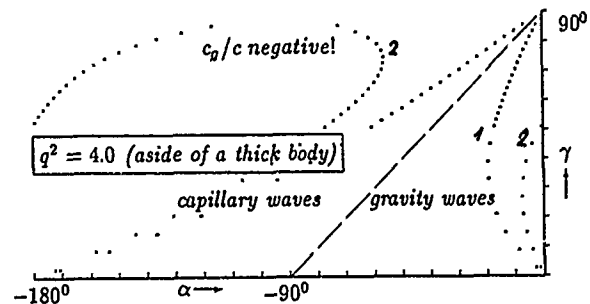


$$^1 U = 0.5m/s, ^2 U = 2.5m/s \text{ (both } (A^+)'), ^3 \cdot (A)'$$



$$^1 U = 0.5m/s, ^2 U = 1.5m/s, ^3 U = 2.5m/s$$

For $q^2 = 1$ there is no difference between $(A)'$ and $(A^+)'$.



$$^1 (A)', ^2 (A^+)'$$

(only negligible dependence on p)

Fig.4 Wave front angle γ versus ray angle α

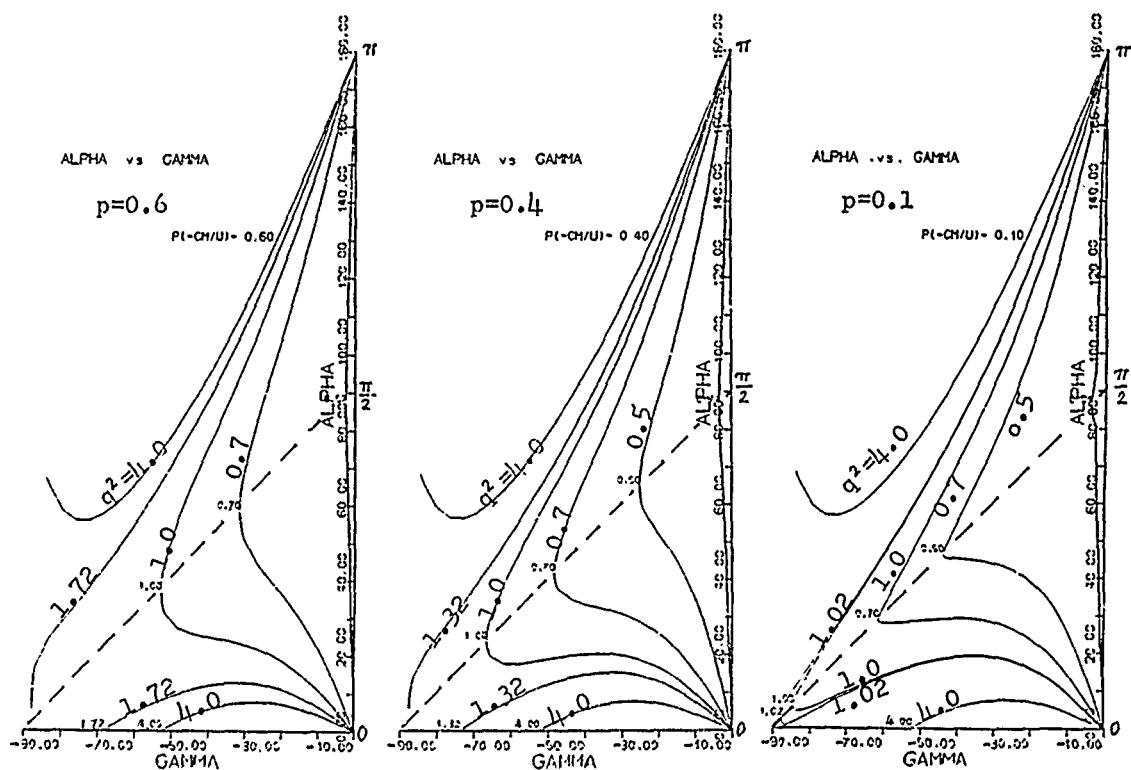


Fig.4 (a) α vs. γ (for (A^+))
 curves over the dotted line; for capillary waves; curves
 under the dotted line; for gravity waves.

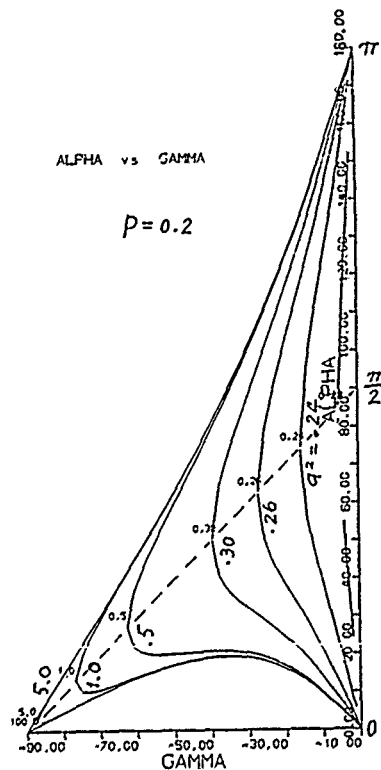


Fig.4 (b) α vs. γ (for (A^-))

The Situation Of Ray Tracing Near A Corner And The Short Life Of Rays Near The Waveless Zone.

Let us again consider 2-D potential flow as the basic flow, so that complex analysis can be used. We introduce

$$Z \doteq x + iy = r \cdot e^{i\theta} \bar{V} \doteq u - iv = Uq \cdot e^{-i\theta}, \quad (34)$$

$$K \doteq k_1 - ik_2 = k \cdot e^{-i\theta} \quad (35)$$

and

$$P \doteq (g\zeta_r)_x - i(g\zeta_r)_y = -(dV/dZ)\bar{V} \quad (36)$$

The P stands for some gradient of the double body flow pressure⁸ We can write the first ray equations (12) and (13) as

$$\frac{d\bar{Z}}{d\tau} = \frac{2}{kc} (V - \frac{c_g}{k} K) = \frac{2}{kc} c_{at} \cdot e^{-i(\alpha+\beta)} \quad (37)$$

With ds as differential of the arclength along the ray, this implies that $d\tau/ds = 1/|dZ/d\tau| = kc/2c_{at}$, so that we can write (19) and (18) as

$$\begin{aligned} \frac{1}{K} \frac{dK}{ds} &= \left(\frac{1}{k} \frac{dk}{d\tau} - i \frac{d\theta}{d\tau} \right) \cdot \frac{d\tau}{ds} \\ &= -\frac{e^{i\theta}}{c_{at}} \cdot \frac{dV}{dZ} \left(\diamond \frac{\bar{V}}{2c} + e^{i\theta} \right) \end{aligned} \quad (38)$$

Here \diamond means 1 for (A^+) and $(A^+)'$, it means 0 for (A) and $(A)'$. The flow in the vicinity of a stagnation point due to a corner is basically the flow near a corner between infinite planes as described by Milne-Thomson [12], we have

$$V \approx Q \cdot e^{i\pi\beta_0/(\pi-\beta_0)} \cdot Z^{\beta_0/(\pi-\beta_0)} \quad (39)$$

where Q is a real constant; this means that the range $\beta_0 \leq \delta \leq \pi$ for the polar angle δ is mapped on the range $\beta_0 \geq \beta(\delta) = \beta_0(\pi - \delta)/(\pi - \beta_0) \geq 0$ for the flow angle. In the special case of a bi-circular strut of opening angle $2\beta_0$ and length L , under parallel flow of strength U , we have

$$Q = U \frac{\pi}{\pi - \beta_0} \cdot L^{-\beta_0/(\pi-\beta_0)} \quad (40)$$

so that $q = q(r) = \pi/(\pi - \beta_0) \cdot (r/L)^{\beta_0/(\pi-\beta_0)}$ and hence

$$\frac{dV}{dZ} = \frac{\beta_0}{\pi - \beta_0} \cdot \frac{V}{Z} \quad (41)$$

$$P = -\frac{\beta_0}{\pi - \beta_0} \cdot \frac{1}{Z} V \cdot \bar{V} \quad (42)$$

⁸Tulin [16] considered a quantity related to $|F|$ as a disturbance parameter and came to the vexing conclusion that ray theory does not apply for bow entrance angles $\beta_0 \leq \pi/3$ as otherwise P is not bounded; on the other hand, Maruo [7] disclaimed the validity of ray theory for $\beta_0 \geq \pi/3$ due to divergence of an integral representing the phase.

Then the rate of change of θ, β , and k along the ray is found from

$$\frac{1}{K} \frac{dK}{ds} = -\frac{e^{i\theta}}{c_{at}} \cdot \frac{\beta_0}{\pi - \beta_0} \cdot \frac{V}{Z} \left(\diamond \frac{\bar{V}}{2c} + e^{i\theta} \right) \quad (43)$$

Observing (34) and (5), separating real and imaginary part in (43), we find

$$\frac{d\theta}{ds} = +\frac{1}{r} \frac{Uq}{c_{at}} \cdot \frac{\beta_0}{\pi - \beta_0} \left(\diamond \frac{\sin(\theta - \delta)}{2 \cos \gamma} + \sin(\gamma + \theta - \delta) \right) \quad (44)$$

$$\begin{aligned} \frac{d\beta}{ds} &= -Im \frac{dV}{dZ} \frac{1}{V} \frac{dZ}{ds} = -Im \frac{\beta_0}{\pi - \beta_0} \frac{1}{Z} \cdot e^{i(\alpha+\beta)} \\ &= -\frac{1}{r} \cdot \frac{\beta_0}{\pi - \beta_0} \cdot \sin(\alpha + \beta - \delta) \end{aligned} \quad (45)$$

and thus

$$\frac{d\gamma}{ds} = \frac{d(\theta - \beta)}{ds} = \frac{1}{r} \cdot \frac{\beta_0}{\pi - \beta_0} \times \dots \quad (46)$$

$$\left(\sin(\alpha + \beta - \delta) + \frac{Uq}{c_{at}} \left(\diamond \frac{\sin(\gamma + \beta - \delta)}{2 \cos \gamma} + \sin(2\gamma + \beta - \delta) \right) \right)$$

Due to the presence of the factor $1/r$, which tends to infinity at the stagnation point, that might cause trouble when doing ray tracing near the bow. This may explain the dilemma of Brandsma (taking $\diamond = 0$)

In order that a ray should travel along the ship's water line (or more generally just coincide with a streamline), we must have $\alpha \equiv 0$ i.e. $\gamma \equiv 0$ hence $d\alpha/ds$ i.e. $d\gamma/ds \equiv 0$. It is not clear why this should be possible for general hull geometries, as for $\alpha = \gamma = 0$, hence $\theta = \beta$, we find with $c_{at} = c - c_g$

$$\frac{d\gamma}{ds} = Im \left[\frac{dV}{dZ} \left(\frac{1}{c} - \frac{\diamond/2 + 1}{c - c_g} \right) e^{2i\beta} \right] \quad (47)$$

valid even away from stagnation points.

For the rate of change of the wave number k we find

$$\frac{1}{k} \frac{dk}{ds} = -\frac{1}{r} \frac{Uq}{c_{at}} \frac{\beta_0}{\pi - \beta_0} \left(\diamond \frac{\cos(\gamma + \beta - \delta)}{2 \cos \gamma} + \cos(2\gamma + \beta - \delta) \right) \quad (48)$$

If the value of Λ along a ray should equal the critical value $p^2/2$, this would correspond to the minimum for gravity waves; hence k then must decrease along the ray. However, due to the rapid increase of γ near a stagnation point, the sum of cosine terms may change sign, so that k increases (in particular for $(A)'$ where the first cosine term is deleted) and Λ approaches $p^2/2$ again. Here the ray must terminate, as for $\Lambda = p^2/2$, even off the waveless zone boundary, the partial derivatives of Λ both regarding q^2 and γ vanish simultaneously in conflict with the ray equations, q^2 can not be varied independent from γ . This explains the previously mentioned occurrence of short life rays. Thus the choice of initial points for rays is moot, quite apart from the ambiguity of assigning initial values there for amplitude and phase.

Further Considerations About The Ray Approach

A "ray" in the sense of our analysis is defined as a characteristic to a partial differential equation $F(x, y, S_x, S_y) = 0$ for a function $S(x, y)$, see(3).

But we should ascertain that the essential features of the complex 3-D flow near the ship, including sensitive variations, can really be modeled adequately through functions $S(x, y)$ with slowly varying gradient and associated complex amplitude functions $A(x, y)$. Note that until Yin's [17] recent investigations, no effects of the Froude number on ray curvature could be modeled, and the variation of wave resistance only resulted from interference effects in the far field computed through integration along the rays.

Nevertheless, our investigation showed that certain *global* characteristics the wave pattern, such as the variation of α_k , and hence of the tangential direction of the wave domain boundary (visible in the rich stock of Miyata's experimental results) can be predicted even near the bow with approach (A^+) .

An evaluation of merits for the competitive approaches $(A)^+$ and (A^+) may be attempted. But

it does not seem pertinent to discriminate between a "correct" and a "less consistent" approach, although it is obvious that with inclusion of surface tension effects the rule of "automatic order change through differentiation", essential for (A) , can not be maintained.

Actually, the omission of terms with $g\zeta_r$ (and hence with $1-q^2$) under $(A)^+$ has no fundamental consequences for our analysis in general. Certainly, the extent of zones without steady waves ahead of a blunt bow is considerably larger under (A^+) , well in accord with data from experiments with a vertical circular cylinder, for which we have evaluated both approaches. However, the numerous recent investigations on the flow ahead of a blunt bow (see the survey by Mori [18]) make clear that between the bow and the stationary capillary wave zone we have to expect a finite domain with either a stationary plateau, a turbulent free surface or instationary waves propagating forward (Osawa [19]), and the flow visualisation experiments of Kayo et al [20] display a system of instationary "necklace vortices" in this domain. And the decay of capillary waves through viscosity, as investigated by Messick and Wu [21] should be considered.

Numerical Calculations.

Our calculations have been performed both for approach (A^+) and approach $(A)^+$. We considered the class of bi-circular cylinders which had already been investigated by Brandsma with conventional ray theory. The analytical expression for the velocity potential W is given in complex notation [12] in terms of bicircular coordinates ξ and η through

$$Z = x + iy = L/2 \cdot \cot(\zeta/2) \quad (49)$$

$$W = \varphi + i\psi = UL \cdot i/n \cot(\zeta/n) \quad (50)$$

with $\zeta = \xi + i\eta$, $\xi = \delta_1 - \delta_2$, $\eta = \ln(r_1/r_2)$, $n = \frac{2(\pi - \beta_0)}{\pi}$, where β_0 stands for half the entrance angle and L for the half of the strut. The symbols $r_1, \delta_1, r_2, \delta_2$ stand for polar coordinates regarding the strut end points. For economical reasons, we deduced explicit expressions in real mode for u, v and their derivatives. We evaluated the ray equations by the Runge-Kutta method.

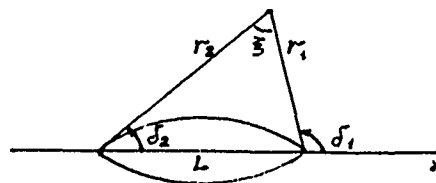


Fig.5 Bi-circular coordinate system around a bi-circular strut.

The aforementioned boundary of the short-life zone was determined numerically, assuming $q^2 = \text{const}$ there. It did not require much accuracy, we found that rays emanating outside such a border line were not sensitive to the choice of their origin. We selected $\gamma = 0$ as initial value, securing a maximum for the wave length and its rate of increase, hence minimum probability that it may become stationary and decrease again along the ray. Thus it is obviously adequate rather to operate with a continuous distribution of disturbances than with a concentration in the stagnation points.

Due to inclusion of surface tension, steady components of bow capillary waves could be investigated as well. We traced rays with capillary waves from that part of the outer boundary of the short-life belt where the basic flow is incoming, and rays with gravity waves from the part with outgoing flow; the two domains have no common boundary, save the point where the basic flow is tangent to the belt.

The rays of gravity- and capillarity- waves in the cases of different body advance speeds and entrance angles are shown in Fig.6, 8, 9, and Fig.14.

To show the difference between ours and the conventional ray theory and test part of our program, forward- (downstream) and backward- (upstream from the far field) tracing based on conventional ray theory are also performed. For the latter, considering the uncertainty due to the stagnation point, rays are backtraced from the far field towards the bow, iterately, by changing initial conditions, the results in the far field by usual (forward tracing) method being used as the first set of which, till ray reaches a given-sized neighborhood of bow stagnation point, and wave angle converges at the same time, the results are shown in Fig.12.

In all the figures of rays presented, the pairs of members attached to each ray give θ_i and θ_f the initial and final values of θ (in degree). The short segments on the rays show the local wave fronts.

To get better accuracy, step widths in ray tracing with Runge-Kutta method were carefully chosen, and the reliability was checked by halving the step widths.

Conclusions

In the course of an assesment of the ray approach with regard to representing essential features of the wave pattern, we have incorporated capillarity effects in our analysis to overcome obvious shortcomings near the bow stagnation point.

Our formulation $(A^+)'$ (eq. (2)) generalizes approach $(A)'$, where certain terms related to the double-body flow pressure are disregarded. Although within our work we could neither provide a rational model for ray generation nor even a justification for extending the ray approach the hull surface vicinity, the following facts have been discovered or confirmed.

Our numerical investigations have displayed several global effects on the wave pattern geometry resulting from the inclusion of capillarity to our analytical model; they gain practical relevance for small speeds, say for $U=2$ m/s (if we consider a minimum capillary wave speed of 0.23 m/s.) :

- (1) Both the far-field Kelvin angle and the "modified Kelvin angle" near the bow (i.e. the angle between tangents to the wave region boundary and to the hull water line) are found to increase with decreasing U .
- (2) With increasing bow entrance angle, both the zones of no steady waves and the surrounding short-life belt, from which no rays proceeding into the far field can be found, grow in size.

- (3) The outward extent of this belt is decreasing with increasing U , i.e. the stronger the capillarity the larger the short life belt.

The above findings are in qualitative accord with some tendencies one may observe from experimental visualizations of flow and wave pattern as presented by Inui[15] (his Fig.2-2 is reproduced in our Fig.7), of Miyata[14], of Maruo[7] and of Osawa[19] (see Fig.11). It is true that we can not expect our analytical model to cover all features of the complex phenomena observed, effects of viscosity and finite wave elevation in particular, though the latter may be assumed to be less significant considering the low speeds of the models. Thus it seems that in this regard ray theory displays a certain value for predicting ship wave phenomena, although the re-entrance of rays or their reflection at the water line must be considered an open problem, among others. In any case, the authors would like to emphasize the need to take account of surface tension at low speeds, well in accord with Maruo[7]. We hope that our work reported here can add some further weight on this aspect

Acknowledgements

The authors express appreciation and gratitude to the Deutsche Forschungs- und Versuchsanstalt für Luft- und Raumfahrt for sponsoring the first author's one year research fellowship at IfS Hamburg. Our thanks go to faculty and staff of IfS for all their kind assistance.

The authors would like to dedicate this paper to Prof. T.Y. Wu to the occasion of his sixty fifth birthday.

References

- 1 Ursell, F.: "Steady wave patterns on non uniform fluid flow." J. Fluid Mech. Vol. 9 pp 337-364 (1960)
- 2 Inui T. and Kajitani, H.: "A study on local non-linear free surface effects in ship waves and wave resistance." Schiffstechnik Vol.24 pp.178-213 (1979)
- 3 Keller, J.B.: "The ray theory of ship waves and the class of streamlined ships." J. Fluid Mech. Vol.91 pp.465-487 (1979)
- 4 Yim, B.: "A ray theory for non-linear ship waves and wave resistance." Proc. Third Intern. Conf. on Num. Ship Hydrodynamics Paris pp.55-70 (1981)
- 5 Brandsma, F.J.: "Low Froude number expansions for the wave pattern and the wave resistance of general ship forms." Thesis T.U. Delft 111pp. (1987)
- 6 Eggers, K.: "On stationary waves superposed to the flow around a body in a uniform stream." IUTAM Sympos. on nonlinear water waves, Tokyo. ed. by K. Horikawa and H. Maruo. Springer Verlag pp.313-323 (1987)
- 7 Maruo, H.: and Ikehata, M.: "Some discussion on the free surface flow around the bow." Proc. 16th. Symp. on Naval Hydrodynamics Berkeley pp 65-77 (1986)
- 8 Eggers, K.: "Non-Kelvin dispersive waves around non-slender ships." Schiffstechnik Vol.28 pp.223-252 (1981)
- 9 van Gemert, P.H.: "A linearized surface condition on low speed hydrodynamics." Delft T.U. 26pp (1988)
- 10 Eggers, K.: "A comment on free surface conditions for slow ship theory and ray tracing." Schiffstechnik 32 pp.42-47 (1985)
- 11 Longuet-Higgins M.S. and Stewart R.W.: "Changes in the form of short gravity waves on long waves and tidal currents" J. Fluid Mech. 8 pp.566-588 (1960)
- 12 Milne Thomson: "Theoretical Hydrodynamics" MacMillan
- 13 Crapper, G.D.: "Surface waves generated by a travelling pressure point." Proc. Roy. Soc. A 282 pp.547-558 (1964)
- 14 Miyata, H.: "Characteristics of nonlinear waves in the near field of ships and their effect on resistance." Proc. 13th Symp. on Naval Hydrodynamics Tokyo pp.335-353 (1980)
- 15 Inui, T.: "From bulbous bow to free surface shock waves- Trends of 20 year's research at the Tokyo University." The Third Georg Weinblum Memorial Lecture. Journ. Ship Res, 25 147-180 (1981)
- 16 Tulin, M.P.: "Surface waves from the ray point of view." The Seventh Georg Weinblum Memorial Lecture. Proc. 14th. Symp. on Naval Hydrodynamics Hamburg pp.9-29 (1984)
- 17 Yim, B.: "Some recent developments in nonlinear ship wave theory." Proc. Int. Symp. on ship resistance and power performance, Shanghai. pp.82-88 (1989)
- 18 Mori, K.: "Necklace vortex and bow wave around blunt bodies." Proc. 15th Symp. on Naval Hydrodynamics Hamburg pp.303-317 (1985)
- 19 Osawa, K.: "Aufmessung des Geschwindigkeitsfeldes a und unter der freien Wasseroberfläche in der Bugumströmung eines stumpfen Körpers Bericht Nr.476 Institut für Schiffbau der Universität Hamburg, 125pp (1987)
- 20 Kayo, Y., Takekuma, K., Eggers, K. and Sharma S.D.: "Observation of free surface shear flow and its relation to bow wave-breaking on full forms." Bericht Nr.420 Institut für Schiffbau der Universität Hamburg, 33pp (1982)
- 21 Wu, T.Y. and Messick, R.E.: "Viscous effects on surface waves generated by steady disturbances. Rep. 85-8 Engg. Div. Cal. Inst. Techn. 31pp (1958)

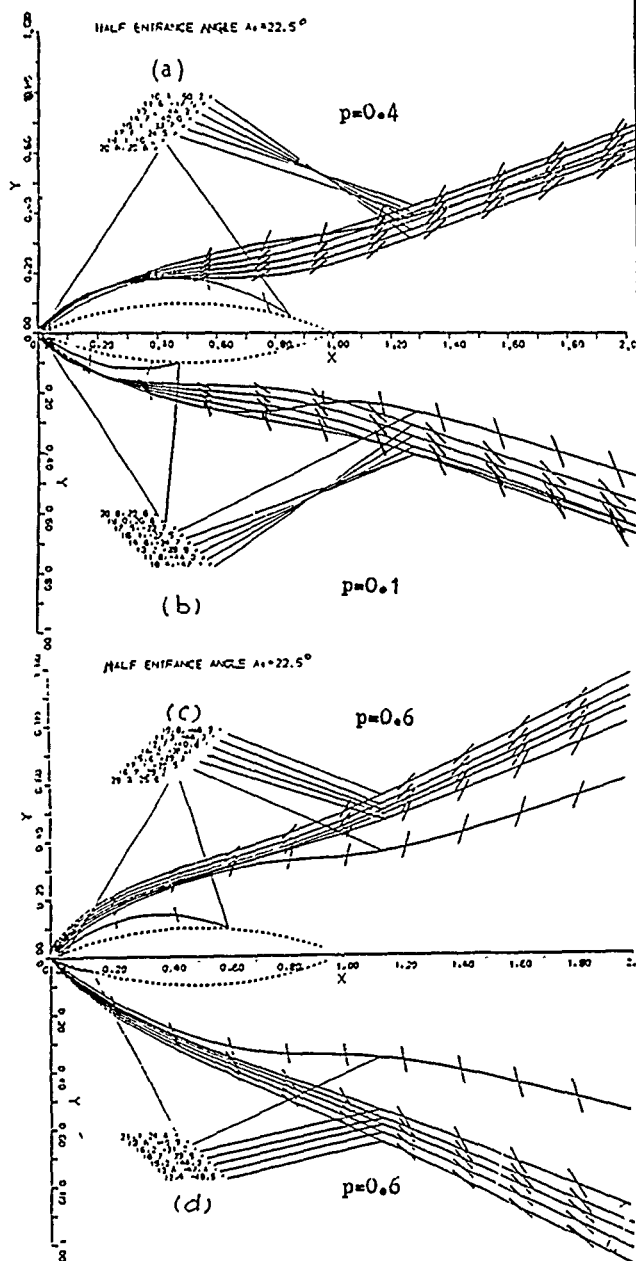


Fig.6 Rays of gravity waves for a bicircular cylinder with half entrance angle $A_e = 22.5^\circ$, in cases $p = 0.6, 0.4$ and 0.1 , corresponding to $U = 0.39, 0.58$ and 2.31 m/s respectively, for $C_m = 0.231 \text{ m/s}$.

(a), (b), and (c) are based upon $(\Lambda^+)^i$;

(d) is based upon $(\Lambda)^i$.

(tracing is stopped if the ray enters the body)

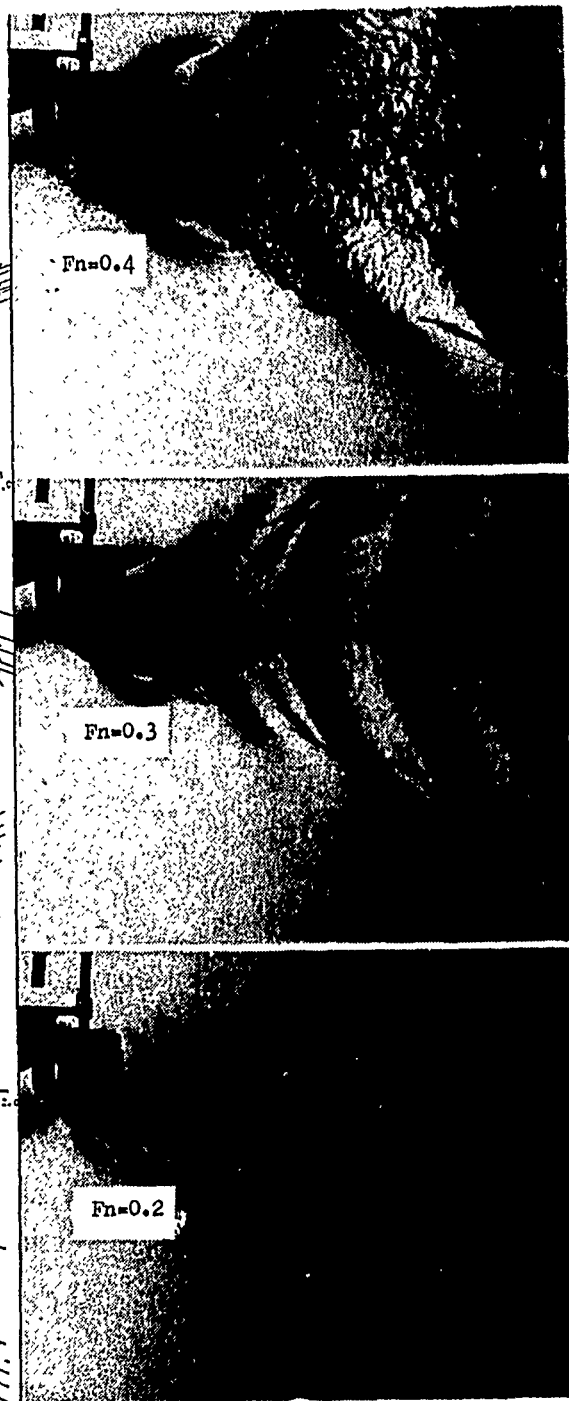


Fig.7 Wave pattern of a rudder model of length 0.3 m with $U = 0.65, 0.5$ and 0.34 m/s (by courtesy of Prof. T.Inui from [15]).

(For this rudder, $Fn=0.4, p=0.33$;

$Fn=0.3, p=0.45$;

$Fn=0.2, p=0.68$)

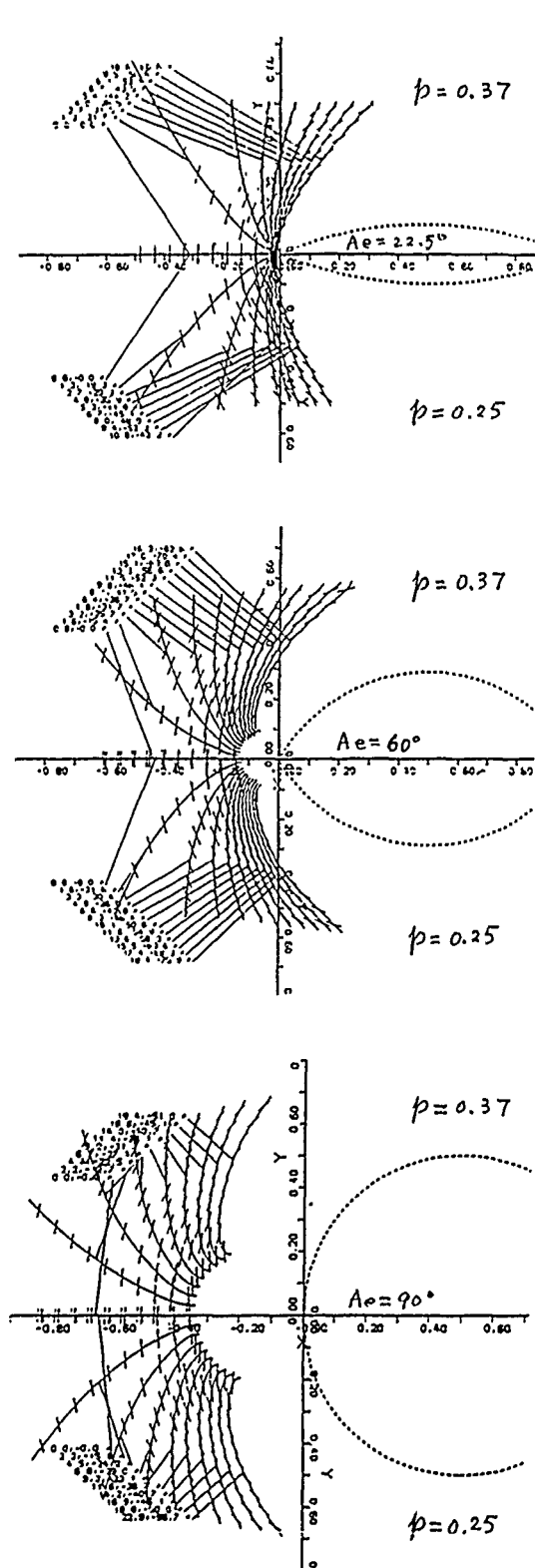


Fig.8 Rays of bow capillary waves for different entrance angles and body speeds. (based upon $(A^+)'$)
($U = 0.62$ and 0.92 m/s)

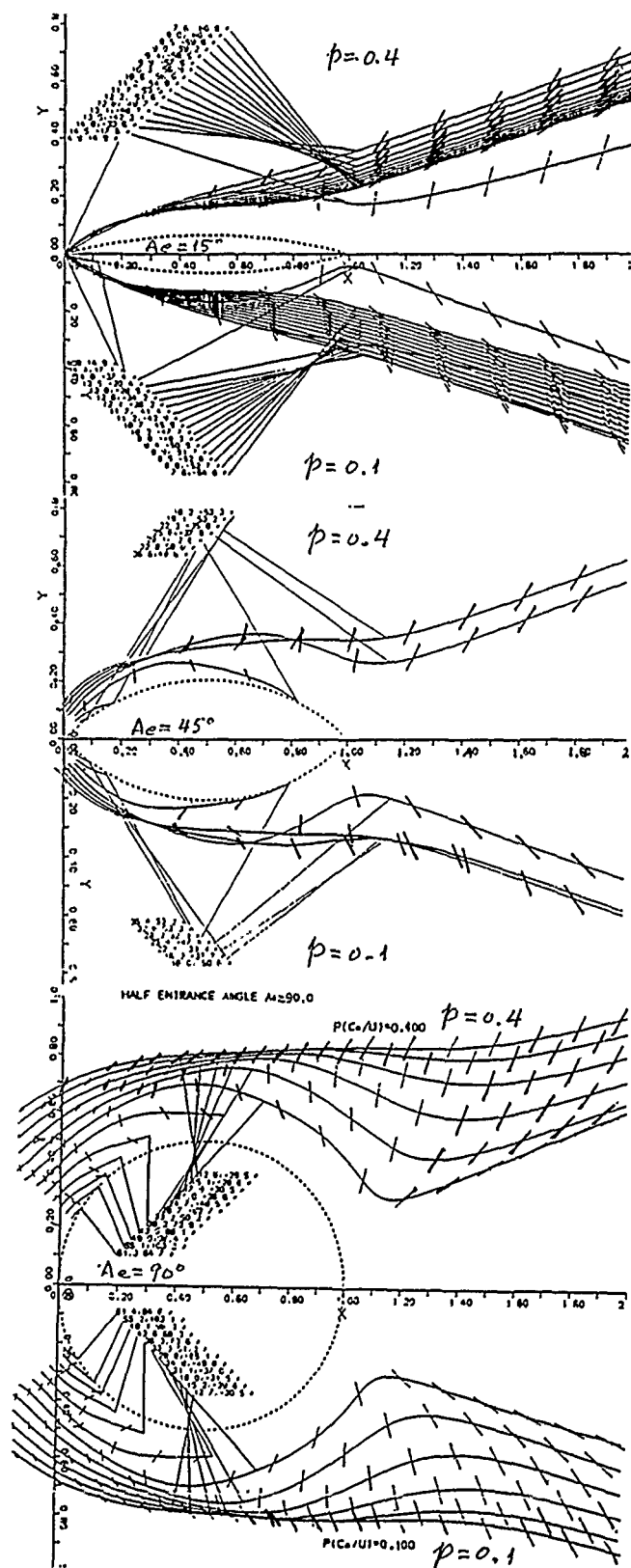


Fig.9 Rays of gravity waves for different entrance angles and body speeds. (based upon $(A^+)'$)
($U = 0.58$ and 2.31 m/s)

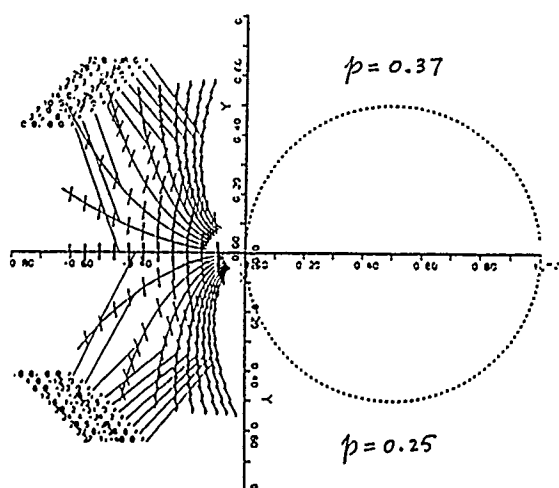


Fig.10 Rays of bow capillary waves in front of a circular cylinder (moving to the left) under approach (A)' for $U = 0.6\text{m/s}$ ($p=0.37$) and $U=0.7\text{m/s}$ ($p=0.25$).

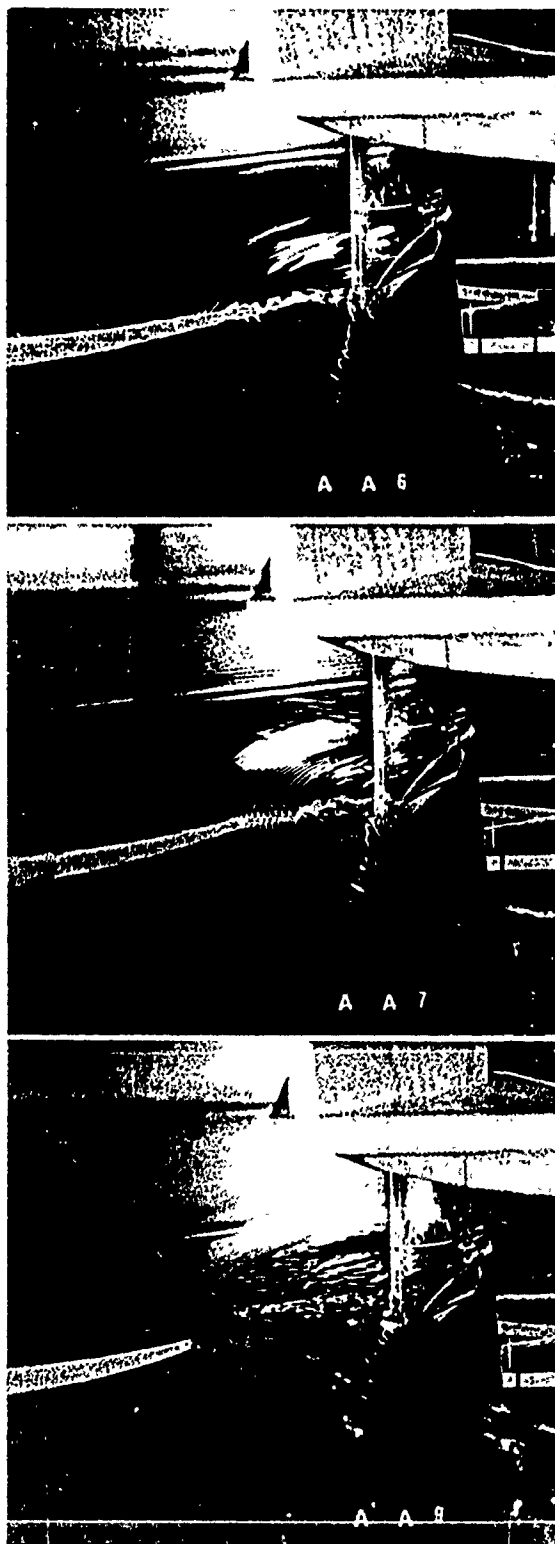


Fig.11 Bow waves in front of an advancing cylinder with diameter $D= 0.46\text{ m}$, moving to the left, at the speeds of $U=0.6, 0.7$ and 0.9 m/s (From K. Osawa [19])

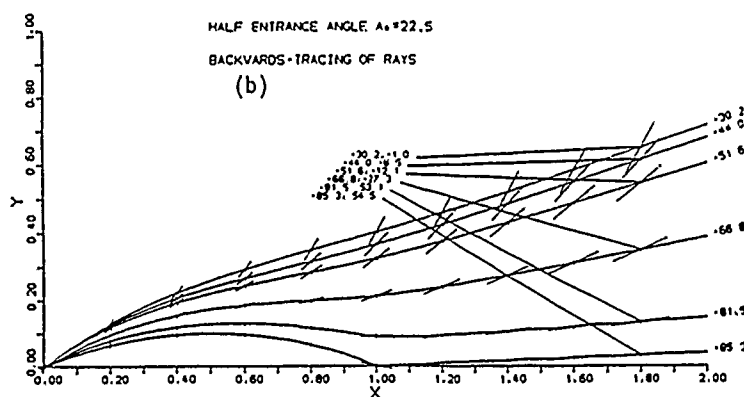
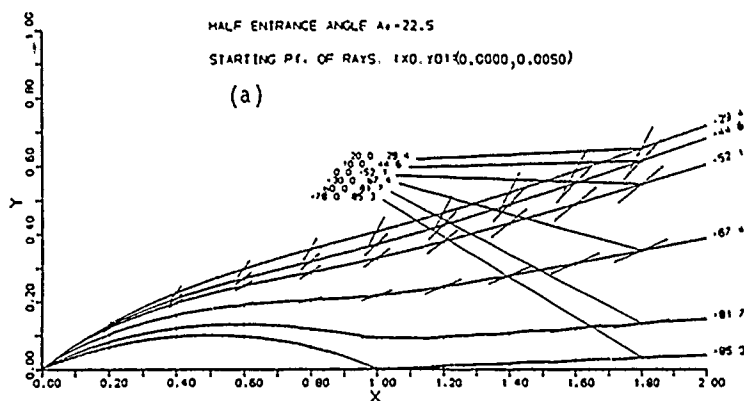


Fig.12 Rays traced with ap-

proaches based upon conven-
tional ray theory:

(a) Forward (downstream) tra-
cing;

(b) Backward (upstream)
tracing from far field.

(Rays that enter the body
have been removed)

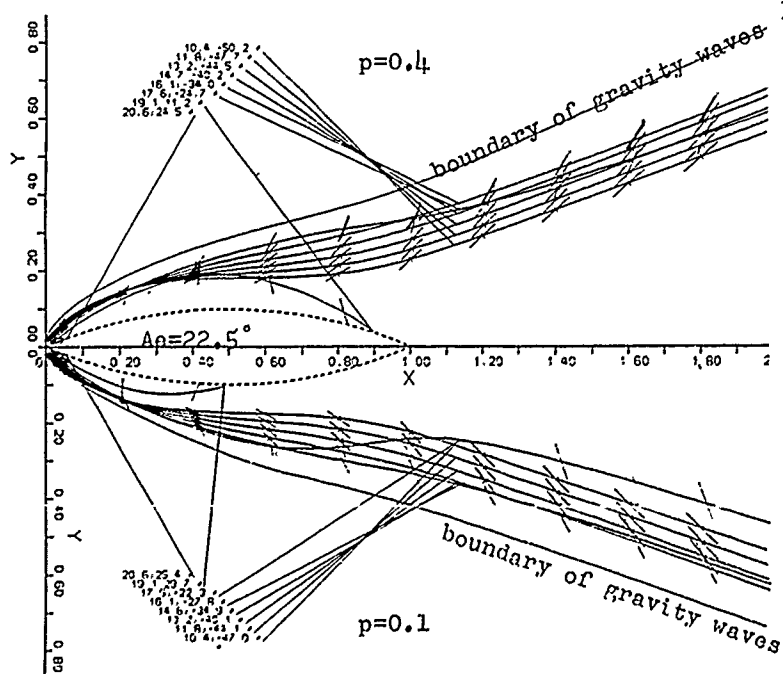


Fig.13. outer boundary of rays

of gravity waves, traced
with $dy/dx = \tan(\alpha'_h + \beta)$, based
upon (A^+) .

N.B. it might not be the at-
tainable boundary of rays
of gravity waves; and, it
is not a boundary between
ray families of gravity-
and capillary- waves.

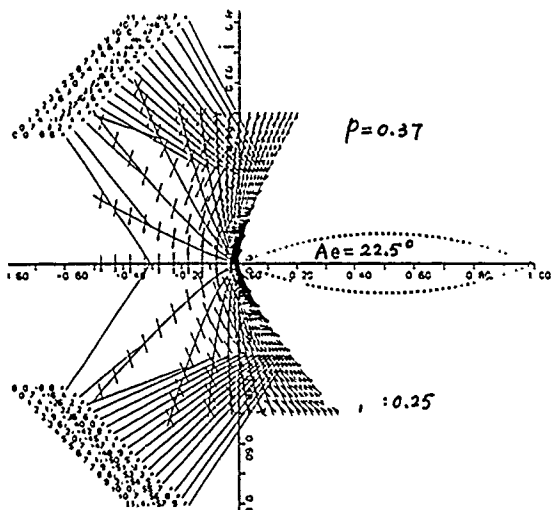


Fig.15 Rays of bow capillary waves
(based upon (A)')

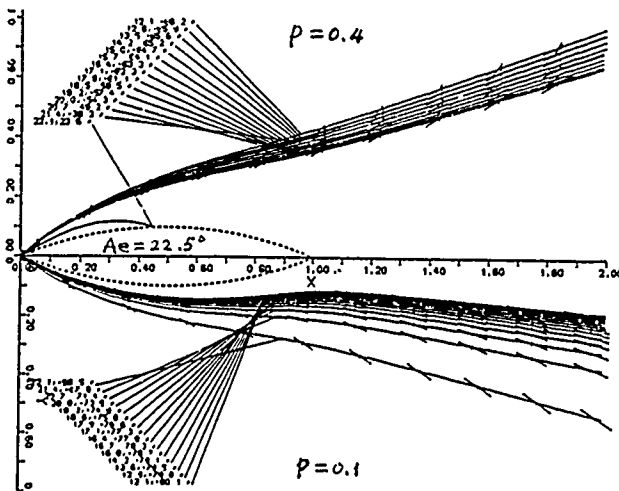


Fig.16 Rays of gravity waves
(based upon (A)')

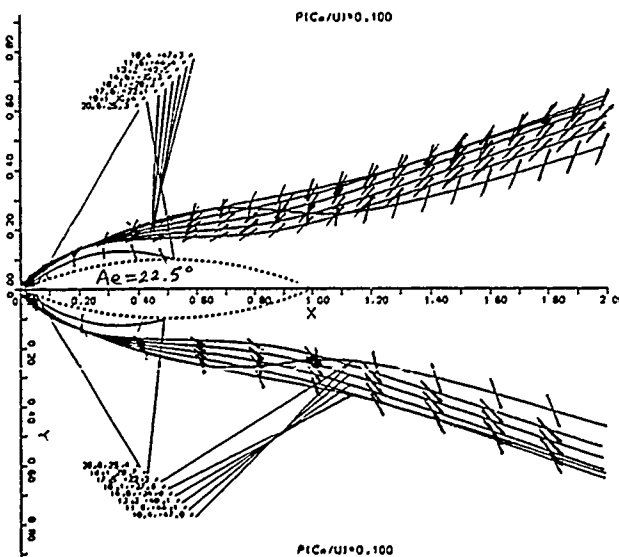


Fig.17 Precision check for the tracing technique, the upper curves are obtained by halving the step width used for the lower curves, the difference is shown negligible.

DISCUSSION

by H. Kajitani

1) I suppose the ray tracing is a kind of low speed theory. I'm not sure that a pretty high Fn applied in Fig.7 is available or not.

2) Could you comment on what difference can be observed on the traced characteristic lines between with and without surface tension effects?

3) The wave length of capillary waves in front of a ship bow changes with its distance. Have you computed the capillary wave phase?

Author's Reply

Prof. Kajitani's worrying about applying ray theory for high Fn is certainly natural. We use Fig. 7, the highest Fn is 0.4 there, (from Inui and Miyata) to show the qualitative confirmation with the test results. We don't think that ray theories (at present) can predict strong non linear effect. Keller[3] claimed that ray theory may be useful for $Fn \leq 0.7$. We are more conservative in this regard. As to the differences between those with and without surface tension, they could be listed in Table A1.

We have not yet calculated the capillary wave phase. It could be carried out through integration.

DISCUSSION

by H.S. Choi

First of all, I would like to congratulate the authors that the surface-tension effect

Table A1

Conventional ray theory (no surface tension)	Present ray theory (include surface theory)
1 Point disturbance, all rays are from stagnation point; Stationary waves exist even near the stagnation point.	1 Region disturbance, rays that can reach far field are from the boundary of that region; No stationary waves can exist inside of it.**
2 Ray and wave patterns are independent of body speed U .	2 Patterns are dependent on U . Change tendencies of size of short life belt, local and far field Kelvin Angles etc. are in accordance with experiments.

*) In Fig.7, the rudder being small, $Fn=0.4$ corresponds to a "slow" speed in the scale of minimum phase velocity C_m (in uniform flow)

**) Observing carefully the region right in front of slowly advancing body of blunt bow, say a circular cylinder as shown in Fig.11, one could find (in some region of body speed) in stationary waves between the stationary capillary region and a turbulent region close to the bow. What we considered was only the stationary waves.

has been successfully included in the ray theory to clarify the wave pattern around the bow more clearly. It may be more usefully applied to a small-scale models. If it is the case it is possible that the local phase velocity reaches to the minimum celerity of capillary gravity waves (≈ 25 cm/sec) and the capillary wave breaks. It implies that a new source of singularity has been invited to your method. I would be happy if you comment on it.

Author's Reply

Thank you for your comment. If the wave length of a gravity wave is decreasing when progressing, the wave might break before the local phase speed c reaches the local minimum phase speed c_m . In our approach, we start rays of gravity waves from the short-life-belt boundary, where exist the shortest omitted gravity waves. The waves seem to become longer when propagating (cf. (48), which shows that near the bow, $1/k \cdot dk/ds < 0$, that means increasing wave length along rays). If $c < c_m$ does happen somewhere, our program will treat the corresponding ray as short life ray, terminate the tracing and enlarge the short life belt. We thus have not that kind of new source of singularity. You may be right to consider these new singularities. But I wonder if they would cause only secondary effect.

DISCUSSION

by A. Hermans

I congratulate the authors with their interesting extension of ray theory. I agree with them that in the region of very short waves (near the stagnation points) surface tension is dominant and that its influence on the ray pattern is seen in the whole field. It

makes the mode for the ray pattern more accurate than the one described by Brandsma and myself. It is a pity that the authors do not say one word on the influence of the wave excitation coefficients and the corresponding wave amplitude. It is my philosophy that one must try to balance all components of the building. To my opinion one approach has such a balance at its own level. Do the authors expect that our approach to the amplitude problem is applicable in this case? If so, do they expect that the influence of surface tension is noticeable there just as well.

Author's Reply

Thank you for your congratulations and comments. The aim of this paper is to find out if surface tension is taken into consideration, the ambiguity and difficulties of the conventional Ray theory, as found by many others, can be overcome. We would not blame an

existing theory for not being perfect. On the contrary, we appreciate every effort made by previous authors who developed ray theory and made it possible to apply it in practice. In view of that some important features of the real world can not be predicted with conventional ray theory, we think that some improvements may be necessary.

We have not yet calculated amplitude. Our concern in this paper is on ray pattern. Our results show that surface tension may not be disregarded for slow ship problems, at least in small scale cases. Even if it turns out to have no significant effect on the final results in some cases, it can still be used as a way to circumvent the difficulties in ray theory. From the viewpoint of validation, the assumption of infinitesimal wave length at the stagnation point is always an unpleasant thing. We tried to get rid of it.

makes the mode for the ray pattern more accurate than the one described by Brandsma and myself. It is a pity that the authors do not say one word on the influence of the wave excitation coefficients and the corresponding wave amplitude. It is my philosophy that one must try to balance all components of the building. To my opinion one approach has such a balance at its own level. Do the authors expect that our approach to the amplitude problem is applicable in this case? If so, do they expect that the influence of surface tension is noticeable there just as well.

Author's Reply

Thank you for your congratulations and comments. The aim of this paper is to find out if surface tension is taken into consideration, the ambiguity and difficulties of the conventional Ray theory, as found by many others, can be overcome. We would not blame an

existing theory for not being perfect. On the contrary, we appreciate every effort made by previous authors who developed ray theory and made it possible to apply it in practice. In view of that some important features of the real world can not be predicted with conventional ray theory, we think that some improvements may be necessary.

We have not yet calculated amplitude. Our concern in this paper is on ray pattern. Our results show that surface tension may not be disregarded for slow ship problems, at least in small scale cases. Even if it turns out to have no significant effect on the final results in some cases, it can still be used as a way to circumvent the difficulties in ray theory. From the viewpoint of validation, the assumption of infinitesimal wave length at the stagnation point is always an unpleasant thing. We tried to get rid of it.

Numerical Calculations of the Viscous Flow over the Ship Stern by Fully Elliptic and Partially Parabolic Navier-Stokes Equations

K. J. Oh and S. H. Kang
Seoul National University
Seoul, Korea
T. Kobayashi
University of Tokyo
Tokyo, Japan

Abstract

Two computer codes have been developed to solve the Reynolds averaged Navier-Stokes equations; namely the fully elliptic method and the partially parabolic method. These are applied to simulate flows over the stern of the SSPA model as a bench mark as well as a multi-purpose ship with a barge type stern. The numerically generated body-fitted coordinate system is used to manage the complex geometry of the ship-hull. A standard form of the $k-\epsilon$ turbulence model is adopted for modelling of the Reynolds stresses.

Simulated results by both methods are nearly identical when the longitudinal flow reversal does not appear. The partially parabolic method requires only half of the memory storage and cuts CPU time by 20% in comparison with the fully elliptic method. The capability of programs developed in the present study are confirmed by successfully simulating pressures, skin frictions and mean velocities over sterns of the two models. The growth of the viscous layer over the stern is well-simulated and the secondary motion is also captured, which is usually observed in the experiments. Nevertheless the standard form of the $k-\epsilon$ model is not adequate for predicting the turbulent kinetic energy over the stern. Simulated nominal wake fractions show good accordance with wake measurements. However, values of the outpart of the wake are over-estimated, while the trends of the circumferential variations are consistent with wake measurements. Coefficients of the viscous resistance predicted by present methods are under-estimated by 10 percent. If further developments on the turbulence model and numerics are accomplished, this method of numerical simulations of the viscous flow over the stern would be promising for the hull form design.

1. Introduction

The importance of the viscous flow simulations around the ship hull has received wide acknowledgement in the light of the hull-form design. Predictions of the viscous resistance are useful in the stage of the bare hull-form design. Ship forms of good resistance and propulsion performance cannot be developed without considering the propulsion efficiency as well as the form factor. Such design and development can be effectively attained, only if numerical method can estimate form factors, nominal and effective wakes on the propeller plane, and thrust deduction factors. These design parameters can not be reasonably obtained without complex three-dimensional turbulent flow simulations over the ship stern and in the wake.

Viscous flows over the ship hull have been calculated by the three-dimensional boundary layer theory. If free surface effects are excluded, experiments and calculations indicate that the first-order boundary layer equations adequately describe the flow over a large part of a ship hull. But it begins to break down gradually over the stern, which is around 10-20 percent of the ship length[1,2]. Experimental information pertaining to the evolution of the flow over the stern as well as in the near wake has been reviewed by Patel[2]. Much research has been done for thick boundary layers over the stern in the past, but they have failed to provide a designer with valuable information.

The partially parabolic, or the semi-elliptic type, of the Navier-Stokes equations have been recently employed to simulate the complex viscous flow over the stern instead of the full elliptic Navier-Stokes(NS) equations in consideration of physical phenomena that there is usually no region of flow reversal in the direction of ship motion. These equations can be used to describe flows between the thin boundary layer upstream and the wake far downstream from the ship. The partially parabolic Navier-Stokes(PPNS) equations have been first employed to calculate flows and heat transfer in the straight square duct by Pratap and Spalding[3]. Abdelmeguid et al.[4] was the first to have applied to ship hulls. Markatos et al.[5], Muraoka[6,7] etc. have presented further researches and several papers[8,9,10] appear in the 2nd Symposium on Ship Viscous Resistance in 1985. Chen and Patel[11] have adopted the finite analytic numerical scheme and produced reasonably accurate results for flows external to an axisymmetric body of revolution and three-dimensional mathematical models. A computer program STERN/PPNS has been developed based on the partially parabolic method and applied to several models to demonstrate its performance by Kang and Oh[12,13,14]. The program proved to be reasonably accurate in describing the pressure distributions on the hull and the velocity contours.

When there appears flow reversal over the hull, the NS equations should be solved. A computer code STERN/NS has been developed in the present study and its performance has been investigated by cross checking each of their respective simulated results of flows over the stern. The SSPA 720 model is selected as an bench-mark model and a multi-purpose ship with a barge type stern for the present study. The possibility for the program to be used for design purposes is investigated in the present paper by estimating the viscous resistance and nominal wakes on the propeller plane of a barge type ship form. Estimated results are compared with measured data in the towing tank. Before going further, basic equations and calculation method are briefly summarized.

2. Governing Equations and Boundary Conditions

2.1 Governing Equation

Geometry of the ship hull is described in the cylindrical coordinate system (x, r, θ) as shown in Fig.1. Governing equations for the incompressible, steady, and turbulent flow are given by the continuity and Reynolds averaged Navier-Stokes equations. Reynolds stresses are modelled by using the eddy viscosity. In the $k-\epsilon$ turbulence model adopted in the present study, the eddy viscosity is given by turbulence kinetic energy k and dissipation rate ϵ which are obtained from their transport equations. In the cylindrical coordinate, above governing equations can be written in the general form as follows;

$$\begin{aligned} \frac{\partial}{\partial x}(U\phi) + \frac{1}{r} \frac{\partial}{\partial r}(rV\phi) + \frac{1}{r} \frac{\partial}{\partial \theta}(W\phi) = \frac{\partial}{\partial x}(\Gamma_\phi \frac{\partial \phi}{\partial x}) + \\ + \frac{1}{r} \frac{\partial}{\partial r}(r\Gamma_\phi \frac{\partial \phi}{\partial r}) + \frac{1}{r} \frac{\partial}{\partial \theta}(\Gamma_\phi \frac{\partial \phi}{\partial \theta}) + S_\phi \end{aligned} \quad (1)$$

where ϕ , Γ_ϕ , S_ϕ stand for the flow variables, diffusion coefficient and source terms for each variables. These are summarized in Table 1.

2.2 Boundary-Fitted Coordinate System

The calculation domain is bounded by the hull surface S , the center-plane C , the water surface W , the upstream section A , the downstream section B , and the outer boundary Σ far from the hull surface as shown Fig.1. A boundary fitted coordinate is adopted to transform the physical domain in the cylindrical coordinate into a rectangular computational domain in Fig.2. The numerical grid generation is widely used for such a transformation. With the values of the coordinates specified on the boundaries of the physical domain (x, r, θ) , it then remains to generate the values of these coordinates in the interior of the domain (ξ, η, ζ) . This can be obtained from the solutions of the following elliptic partial differential equations[11];

$$\nabla^2 x = 0, \quad \nabla^2 r = \frac{1}{r}, \quad \nabla^2 \theta = 0 \quad (2)$$

where

$$\begin{aligned} \nabla^2 = g^{11} \frac{\partial^2}{\partial \xi^2} + g^{22} \frac{\partial^2}{\partial \eta^2} + g^{33} \frac{\partial^2}{\partial \zeta^2} + 2g^{12} \frac{\partial^2}{\partial \xi \partial \eta} \\ + 2g^{13} \frac{\partial^2}{\partial \xi \partial \zeta} + 2g^{23} \frac{\partial^2}{\partial \eta \partial \zeta} + f^1 \frac{\partial}{\partial \xi} + f^2 \frac{\partial}{\partial \eta} + f^3 \frac{\partial}{\partial \zeta} \end{aligned}$$

A : upstream
B : downstream
S : hull and wake axis
 Σ : outer boundary
C : center plane
W : water surface

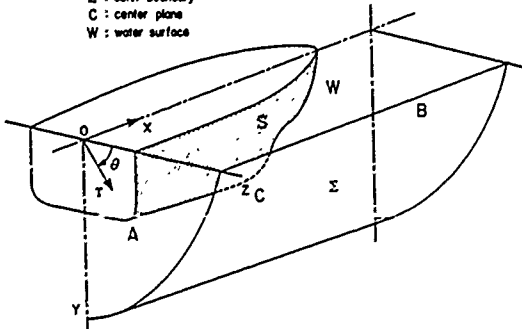


Fig.1 Physical domain and coordinate system.

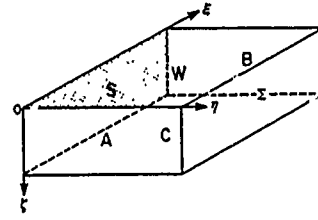


Fig.2. Computational domain.

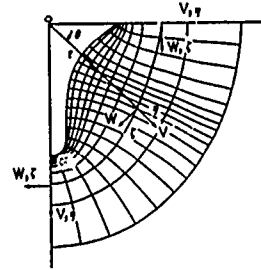


Fig.3 Body-fitted coordinate system and velocity components.

g^{ij} denote metric tensors, and f^i are control functions for alignment of grid points in the domain.

Design parameters and experimental data are usually presented at each stations of the ship hull. Therefore it is convenient if constant ξ planes are chosen to be coincided with constant x planes. If we put $\xi = \xi(x)$, then following equations are obtained.

$$\begin{aligned} g^{11} r_{,\xi\xi} + g^{22} r_{,\eta\eta} + g^{33} r_{,\zeta\zeta} + 2g^{12} r_{,\xi\eta} + 2g^{13} r_{,\xi\zeta} \\ + 2g^{23} r_{,\eta\zeta} + f^1 r_{,\xi} + f^2 r_{,\eta} + f^3 r_{,\zeta} = \frac{1}{r} \end{aligned} \quad (3)$$

$$\begin{aligned} g^{11} \theta_{,\xi\xi} + g^{22} \theta_{,\eta\eta} + g^{33} \theta_{,\zeta\zeta} + 2g^{12} \theta_{,\xi\eta} + 2g^{13} \theta_{,\xi\zeta} \\ + 2g^{23} \theta_{,\eta\zeta} + f^1 \theta_{,\xi} + f^2 \theta_{,\eta} + f^3 \theta_{,\zeta} = 0 \end{aligned} \quad (4)$$

Grid control function f^1 is calculated from the distribution of the x planes. In the radial direction, grid control function f^2 is determined by grid distributions on the inlet and exit plane for grid lines to be smoothly generated. Grid control function f^3 is prescribed with the grid distribution on the outer boundary.

$$f^1(\xi, \eta, \zeta) = -g^{11} \frac{x_{,\xi\xi}}{x_{,\xi}} \quad (5)$$

$$f^2(\xi, \eta, \zeta) = \frac{1}{rr_{,\eta}} + F^2 \quad (6)$$

$$f^3(\xi, \eta, \zeta) = -g^{33} \left[\frac{\theta_{,\zeta\zeta}}{\theta_{,\zeta}} \right]_{\xi=\xi_1, \eta=\eta_2} \quad (7)$$

where

$$F^2(\xi, \eta, \zeta) = \frac{[(\xi_2 - \xi)F_1 + (\xi - \xi_1)F_2]}{(\xi_2 - \xi_1)},$$

$$F_1(\xi, \eta, \zeta) = -g^{22} \left[\frac{r_{,\eta\eta}}{r_{,\eta}} \right]_{\xi=\xi_1},$$

$$F_2(\xi, \eta, \zeta) = -g^{22} \left[\frac{r\eta\eta}{r_\eta} \right]_{\xi=\xi_2}$$

ξ_1, ξ_2 denote values of ξ corresponding to upstream and downstream sections respectively and η_2 denote the value at the outer boundary. Symmetric Neumann boundary conditions are used at the water plane ($\theta=0^\circ$) and the center plane ($\theta=90^\circ$). Dirichlet boundary condition is used at other boundaries.

2.3 Transformed Governing Equations

Transformation of independent variables (x, r, θ) in governing equations are considered, leaving velocity components (U, V, W) in the original (x, r, θ) coordinate in Fig.3. Then governing equations are generally represented as the following form[12].

$$\begin{aligned} & \frac{1}{J} \left[\frac{\partial}{\partial \xi} (b_1^1 U \phi + b_2^1 V \phi + b_3^1 W \phi) \right. \\ & + \frac{\partial}{\partial \eta} (b_1^2 U \phi + b_2^2 V \phi + b_3^2 W \phi) \\ & + \left. \frac{\partial}{\partial \zeta} (b_1^3 U \phi + b_2^3 V \phi + b_3^3 W \phi) \right] \\ & = \frac{1}{J} \left[\frac{\partial}{\partial \xi} (\Gamma_\phi J g^{11} \frac{\partial \phi}{\partial \xi}) + \frac{\partial}{\partial \eta} (\Gamma_\phi J g^{22} \frac{\partial \phi}{\partial \eta}) \right. \\ & + \left. \frac{\partial}{\partial \zeta} (\Gamma_\phi J g^{33} \frac{\partial \phi}{\partial \zeta}) \right] + S_\phi \end{aligned} \quad (8)$$

The above equations are still the exact equations in so far as no approximations have been made beyond those inherent in the turbulence model. The equation (8) can be rendered partially parabolic by neglecting the first term which involves the second order derivative term with respect to ξ . Physically this is not the same as neglecting ϕ_{xx} nor does it imply that diffusion in either x or ξ direction is neglected[11].

2.4 Boundary Conditions

Boundary conditions at each boundaries of the solution domain are summarized as below.

(1) Upstream A; The position is extended to the upstream as far as thin boundary layer equations and the potential flow theory are valid. Then distributions of (U, V, W, k, ϵ) can be prescribed from boundary layer calculation. If it is placed over the mid-ship, then distributions may be assumed by using integral parameters without exerting significant influences on downstream calculation. The streamwise velocity profile in the boundary layer is specified by 1/7th law,

$$\frac{U}{U_e} = \left(\frac{y}{\delta} \right)^{1/7} \quad (9)$$

and the velocity in the inviscid region is given as the free stream velocity. The turbulent kinetic energy k and the dissipation rate ϵ are also given by the flat plate correlations with the boundary layer thickness and skin-friction coefficient.

(2) Downstream B; At one ship length downstream from the stern, zero gradient condition is assumed for the all variables. In partially parabolic calculation, only the zero pressure gradient condition is required.

(3) Hull surface S; The wall function is adopted in the present study. The grid points next to the wall are located in

the fully turbulent layer, and it is assumed that the law of the wall is satisfied and the velocity vectors in this region are collateral. The boundary values at the first grid point are obtained by assuming the local equilibrium between turbulent kinetic energy production and dissipation. They are given as follows.

$$\frac{\tau_w}{\rho} = \kappa V_\tau C_\mu^{1/4} \frac{k^{1/2}}{\ln(E n_p^+)} \quad (10)$$

$$k = \frac{\tau_w}{\rho C_\mu^{1/2}} \quad (11)$$

$$\epsilon = \frac{C_\mu^{3/4} k^{3/2}}{\kappa n} \quad (12)$$

The magnitude of the velocity at the first grid point n_p near the wall is given as V_τ and n is normal distance from the wall.

(4) External boundary Σ ; It is placed sufficiently far from the hull surface so that uniform flows and no turbulence condition can be assumed there.

$$U = U_o, W = k = \epsilon = 0, \frac{dV}{d\eta} = 0, p = p_o \quad (13)$$

(5) Center plane C and water plane W; Symmetric condition are imposed.

$$W = 0, \frac{dU}{d\zeta} = \frac{dV}{d\zeta} = \frac{dk}{d\zeta} = \frac{d\epsilon}{d\zeta} = 0 \quad (14)$$

(6) Wake center line C; Following conditions are enforced.

$$V = W = 0, \frac{dU}{d\eta} = \frac{dk}{d\eta} = \frac{d\epsilon}{d\eta} = 0 \quad (15)$$

3. Numerical Scheme

Uniform grid spacings are taken in the calculation domain ($\Delta\xi=\Delta\eta=\Delta\zeta=1$) and grid control functions are determined by specified values on the boundaries. The grid construction is obtained by solving equation (3), (4) by the finite difference method.

The Finite Volume Method is applied for discretizing the governing equations and the hybrid scheme is employed in the evaluation of the convection terms. The finite difference equations are obtained by integrating the governing equations over individual control volumes formed by the staggered grids system[15]. The scalar variables p, k, ϵ are located at the grid nodes themselves, while velocity components are positioned between the scalar nodes. Such a staggered grid has benefit of having the velocities at the boundaries of the scalar cells where they are needed in integrating convective terms. Furthermore the pressure nodes are located on either side of the velocity node and it is easy to calculate the pressure gradient terms in the momentum equations.

Then the final form of the discretized governing equations are obtained.

$$\begin{aligned} a_P \phi_P &= a_N \phi_N + a_S \phi_S + a_E \phi_E + a_W \phi_W \\ &+ a_U \phi_U + a_D \phi_D + S_\phi \end{aligned} \quad (16)$$

The subscript P refer to the grid node to be considered and the subscript U, D correspond to the upstream and downstream grid respectively. The other neighbouring grids in the sections are given by the subscript N, S, E, W . The $\phi_U, \phi, \phi_N, \phi_S$ etc. represent the convection and diffusion at each corresponding control surface[16].

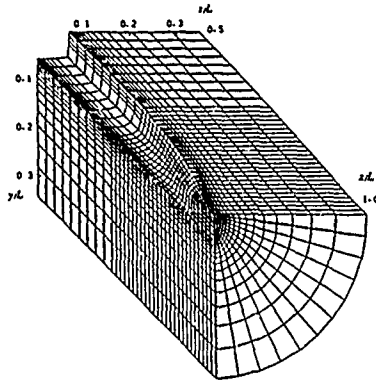


Fig.4 Over-view of generated grids of the SSPA model.

When the partially parabolic form of equation (8) is solved, the discretized equations are obtained by the similar way.

$$a_P \phi_P = a_N \phi_N + a_S \phi_S + a_E \phi_E + a_W \phi_W + C_u \phi_U + \bar{S}_\phi \quad (17)$$

Since the diffusion term in the ξ direction is removed from the equation (8), only the convection term C_u is included in the ξ direction. The unknown variables (U, V, W, k, ϵ) can be obtained by solving the equation (16) or (17) under the assumed or estimated pressures.

The estimated pressures are indirectly corrected for the continuity equation to be satisfied. If SIMPLE(Semi-Implicit Pressure Linked Equation) algorithm is adopted[15], the discretized equation for the pressure-correction is obtained. This equations can be represented by the same form with the equation (16), which has fully elliptic characteristics.

In the fully elliptic calculation, the flow variables are iteratively solved and the converged solutions are obtained. The procedures are summarized as:

- (1) Construct the coordinate system, and calculate the metric tensors and Jacobian.
- (2) Specify initial conditions at the inlet plane.
- (3) Solve the velocities with assumed or previously calculated pressures.
- (4) Solve the pressure-correction equations
- (5) Correct pressure distributions and velocities.
- (6) Calculate the k, ϵ .
- (7) Return to step(3) and repeat step(3)-(7) until the residues are reduced by 0.1% of the reference values.

To solve the partially parabolic equation, the marching procedure along the ξ -direction is employed. (U, V, W, k, ϵ) at each sections are calculated with upstream values of each variables and previously calculated pressure. Pressure-corrections are achieved on each section without any correction of the upstream and the downstream pressures during the marching procedure. Pressure of the whole domain should be stored in the partially parabolic method and several sweeps in the ξ -direction are required to obtain the converged solutions. The procedure are summarized as:

- (1) Construct the coordinate system, and calculate the metric tensors and Jacobian.
- (2) Specify initial conditions at the upstream boundary.
- (3) Calculate velocities at the downstream with the previously calculated pressures.

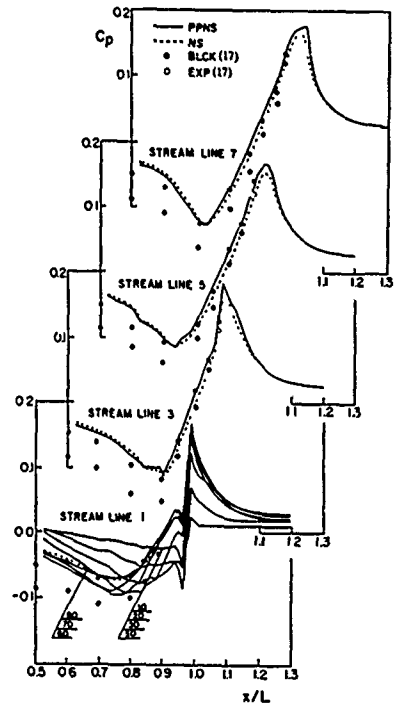


Fig.5 Pressure distributions over several streamlines on the SSPA model.

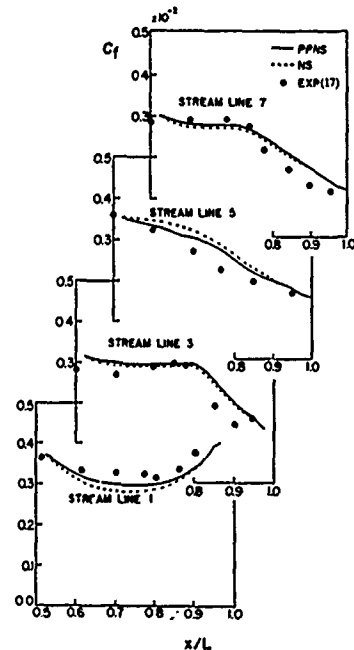


Fig.6 Skin friction coefficients over several streamlines on the SSPA model.

- (4) Correct the pressure distributions and velocities.
- (5) Calculate k, ϵ at the downstream
- (6) Marching to the downstream boundary.
- (7) Return to step(3) and repeat step(3)-(6) until the mass residue are reduced by 0.1% of the reference value.

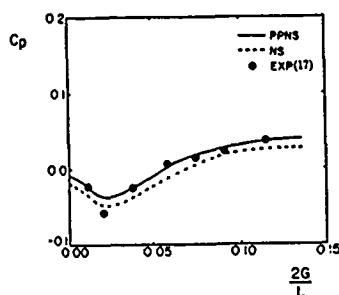


Fig.7 Girth-wise variation of pressure coefficient at $x/L=0.9$ of the SSPA model.

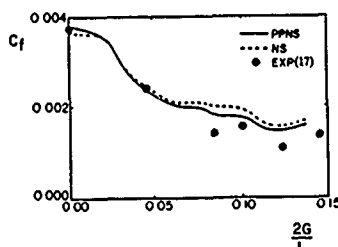


Fig.8 Girth-wise variation of skin-friction coefficients at $x/L=0.9$ of the SSPA model.

4. Calculations and Discussion

A computer code, STERN/PPNS based on PPNS equations has been developed by the method described above and is applied to flows over several mathematical models. Calculated results by STERN/PPNS have been discussed by Kang et al.[12,13,14]. Simulated flow fields and pressure distributions are generally in good agreement with tested data. But calculations have a marked trend to over-estimate turbulent kinetic energies near the stern. Such a trend has also been pointed out by Chen and Patel[11].

Another code STERN/NS based on NS equations has been developed in the present study. General performances of the code have been checked by simulating flows over several mathematical models by Oh[16]. Performance characteristics of two programs have been intensively investigated and compared in the present study by simulating flows over the SSPA 720 model and a multi purpose barge type ship. The first one was a container ship model, which was tested in the wind-tunnel by Larsson[17] and used as one of standard models of ITTC-SSPA Workshop[2]. The latter model has a barge type stern, which was chosen to investigate the possibility of the numerical simulation of viscous flows to be used for design purposes.

4.1 SSPA 720 model

Part of the numerically generated grid system is presented in Fig.4. Numbers of meshes in the (ξ, η, ζ) -directions are (58, 25, 14) respectively. They cover the calculation domain of $0.5 < x/L < 2.0$, $r/L < 0.8$. Circumferential grids are distributed to coincide with external stream lines along which measurements have been taken. Meshes in the radial direction are progressively closely spaced near the hull. Calculation is performed at Reynolds number 5.0×10^6 , where the model was tested in the wind tunnel. Converged solutions are obtained after 90 sweeps by STERN/PPNS and 190 iterations by STERN/NS. PPNS procedure save CPU time by 20 percent as well as considerable memory storage in comparison with the full elliptic procedure.

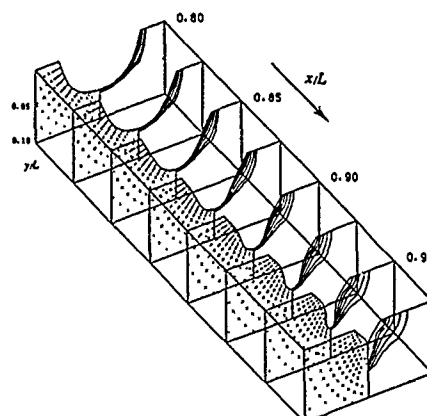


Fig.9 Simulated viscous layer over the stern of the SSPA model by STERN/NS.

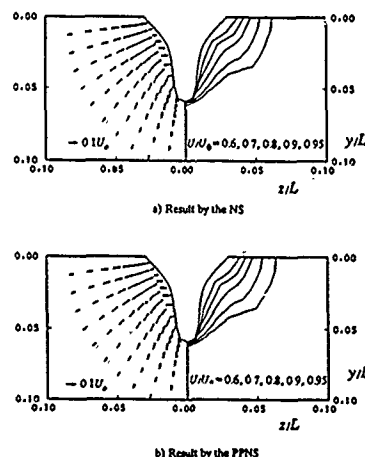


Fig.10 Comparison of calculated velocity contours and cross velocity vectors at $x/L=0.95$ of the SSPA model.

Estimated pressure coefficients along each streamlines are shown in Fig.5. Both calculations are in very good agreement with blockage corrected data. The present programs can take into account the blockage effect by considering the existence of the outer wall. Even though STERN/NS shows slightly lower estimations than STERN/PPNS, differences are negligible in this case of flow without separation. However, some attenuations appear in the estimated pressures just over the stern by using fully elliptic calculations. Such attenuations might be originated from neglected longitudinal diffusion terms in the partially parabolic method. The capability of the both programs is confirmed to simulate the interaction between the thick boundary layer and the external flow by successful prediction of hull pressures. On the other hand, predicted skin friction coefficients are qualitatively in good accordance with measurements as shown in Fig.6. Considerable uncertainty should be taken into account as far as skin friction measurements are concerned. It is also true that enough number of grids could not be allocated near the surface. It is seen that coefficients of skin friction reduces over the stern, where the shear layer grows thick according to the strong adverse pressure gradient and the stream line convergence except along the keel line. Girthwise

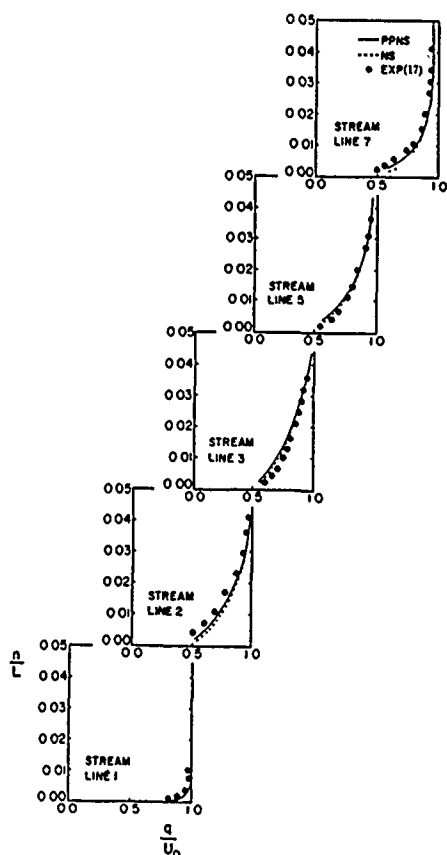


Fig.11 Profiles of resultant velocity at $x/L=0.95$ of the SSPA model.

distribution of pressure coefficients and skin friction coefficients calculated in the present study are compared with measured values in Fig.7 and Fig.8. Secondary flow is directed away from the keel and the water plane according to the girth-wise pressure gradient, and the shear layer rapidly grows thick at the mid-girth. Skin friction coefficients at the keel show their largest values and decreases along the girth to the water plane.

The feature of shear layer formation over the stern by STERN/NS program is shown in Fig.9. The contours of the axial velocity component and the pattern of the transverse motion at $x/L=0.95$ are shown in Fig.10. The boundary layer remains thin along the keel line according to the divergence of streamlines. The thickness of the viscous layer over the mid-girth is almost as large as the draft of the model. The axial velocity contour is well-simulated in comparison with the measured contour. The bilge vortex, which is a general feature of the stern-flow, is also observed in the simulation. Distributions of the total velocity at several points where each streamlines intersect with the $x/L=0.95$ section are compared with measured data in Fig.11. Here it should be noted that measurements are obtained normal to the hull and calculations are computed on transverse sections. There are good agreements between calculations and measurements, although some error might be involved due to such differences in the location. Turbulent kinetic energy distributions are compared in Fig.12, where typical characters of turbulence in the stern flow appear. Turbulence kinetic energy shows considerable reduction in the magnitude near the hull over streamlines 3, 5, and 7, which is quite a unusual

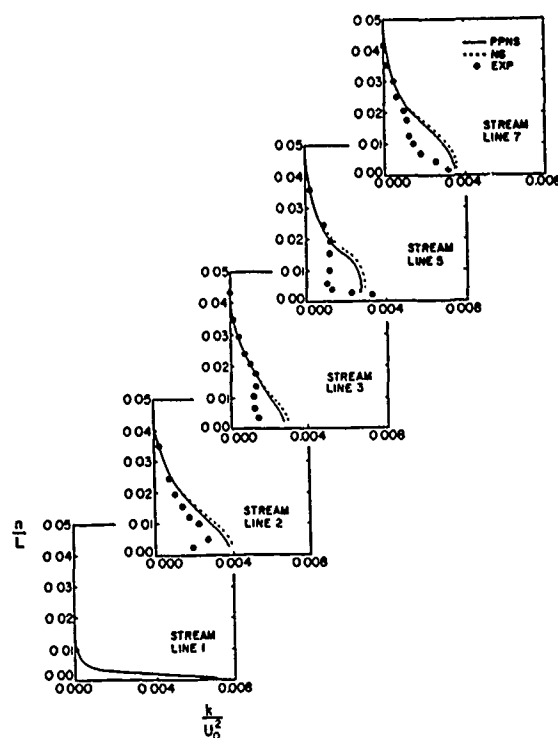


Fig.12 Profiles of turbulent kinetic energy at $x/L=0.95$ of the SSPA model.

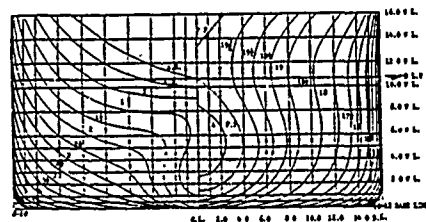


Fig.13 Body plan of 37K PROBOCON.

feature in the thin boundary layer. It is explained that such reduction is due to strong flow convergence without enough generation in the turbulence kinetic energy over the stern. The $k-\epsilon$ model in the present study fails to capture such a phenomena taking place over the stern. An algebraic stress model may well be a future choice for successful simulations.

4.2 Barge Type Ship

An object of the present study is to investigate the potentiality of programs to be used for design purposes. The selected model, 37K PROBOCON, was originally designed by KSEC(Korea Shipbuilding and Engineering Co.) and developed by SSPA through several series tests in the towing tank. The body plan is shown in Fig.13. Considerable reductions in the viscous resistance as well as increases in the propulsion efficiency have been reported in comparison with conventional stern shapes. Components of the resistance coefficient and measured nominal wake distributions in the towing tank are available[18]. Furthermore pressure

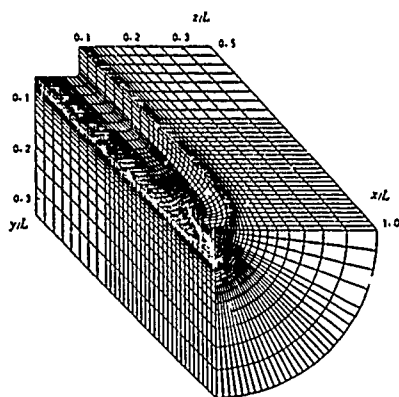


Fig.14 Over-view of generated grids of 37K PROBOCON.

distributions on the corresponding double body have been measured in the wind-tunnel[19].

Numerically generated grids are shown in Fig.14. Numbers of mesh points in the (ξ, η, ζ) -directions are (54, 25, 32) respectively. Calculation is performed in the domain of $0.5 < x/L < 2.0$, $r/L < 0.963$, and at Reynolds number 8.5×10^6 , where the model was tested in the towing tank. Converged solutions are obtained after 90 sweeps with STERN/PPNS and 200 iterations with STERN/NS.

Pressure distributions at several stations over the stern by the present calculations, by the inviscid calculations with Hess and Smith program, and by the wind-tunnel experiment are compared in Fig.15. The experiment has been carried out at $Re_r = 2.0 \times 10^6$ and the measured data includes a small amount of blockage effects. The present methods generally show good performance of the pressure estimation on the hull. The fully elliptic procedure gives somewhat lower predictions of pressure. The potential flow theory does not properly simulate pressures, especially near $\theta = 30^\circ - 40^\circ$ where the boundary layers have been grown thick according to the streamline convergence.

Overall feature of axial velocity contours and velocity vectors on transverse sections to the downstream are shown in Fig.16. As observed in the experiment[19], streamlines are uniformly distributed over the stern, and consequently the gradual girth-wise variation of the boundary layer thickness is obtained. Bilge vortex is usually generated over the stern due to the girth-wise pressure distribution. Such vortex is simulated as an open type separation over the afterbody as shown in Fig.17. The region of vortex extends and the strength at the core decreases downstream as shown in Fig.18.

Although the physical propeller plane is not divided into fine enough grids to expect reasonable results, estimations of the nominal wakes are tried. It is not found how to allocate grids effectively not only for the whole flow domain but also for the local region near the propeller by adjusting grid control functions. Wake fractions have been measured at four radial positions (0.4R, 0.64R, 0.88R, 1.12R) in the towing tank. R denotes the radius of the propeller. Predicted results in Fig.19 are generally acceptable at 0.64R and 0.88R, except between the stern bulb and the ship bottom, where only a few mesh points can afford to be allocated. However, wake fractions are over-estimated at the outer part of the propeller and under-estimated near the hub. The trends are qualitatively consistent with measurements. As far as grids generations are concerned, it should be stressed that enough meshes are to be allocated locally over the propeller plane, as well as globally over each ship sections. It is also noted that free surface effects are included in wake measurements.

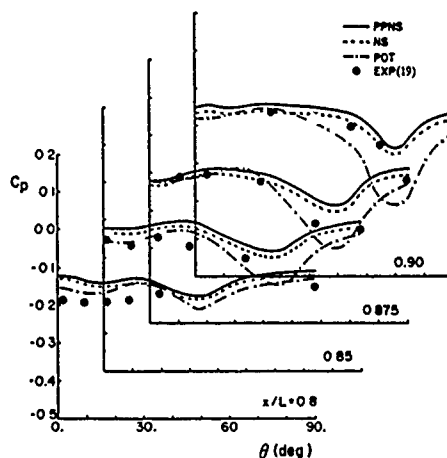


Fig.15 Girth-wise variations of pressures at several stations of 37K PROBOCON.

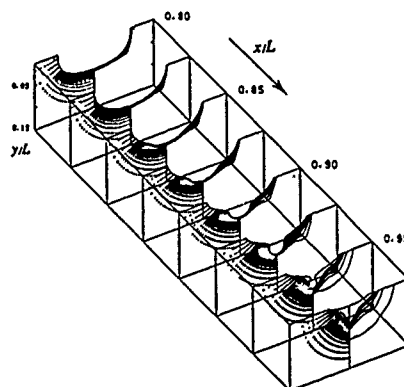


Fig.16 Simulated viscous layer over the stern of 37K PROBOCON by STERN/NS.

Finally the capability of codes to estimate the viscous resistance is investigated. It may be obtained by integrating the pressures and the skin frictions over the hull surface of the double model while free surface effects are neglected. But considerable numerical errors are expected during the integration. A wake survey method to estimate the viscous resistance component in the towing test[20] is adopted.

$$C_v = \frac{\rho g \int_w [(H_o - H) - \frac{1}{2\epsilon} (U_o - (U_o^2 - 2g(H_o - H))^{1/2})^2] dS}{1/2 \rho U_o^2 S_w} \quad (18)$$

where $H_o = p_o + \rho U_o^2/2$, $H = p + \rho U^2/2$ and S is the wetted surface area of the hull. The integration position of the wake w is half the ship-length downstream from the stern. Estimated coefficients of the viscous resistance by the partially parabolic method and by the fully elliptic method are 3.57×10^{-3} and 3.52×10^{-3} respectively. On the other hand, the measured value was 3.9×10^{-3} and the form factor was 0.23. All the simulation errors, i.e. pressures and velocities, are summed up to show 10% under-estimation. It should be noted that wave effects on the viscous resistance can not be taken into account at all during the resistance test. If we take into account such uncertainties, the present predictions give us acceptable values. If changes in the viscous resistance with any modification of the hull form is reasonably estimated, the computer codes will be very useful as far as the bare hull design is concerned.

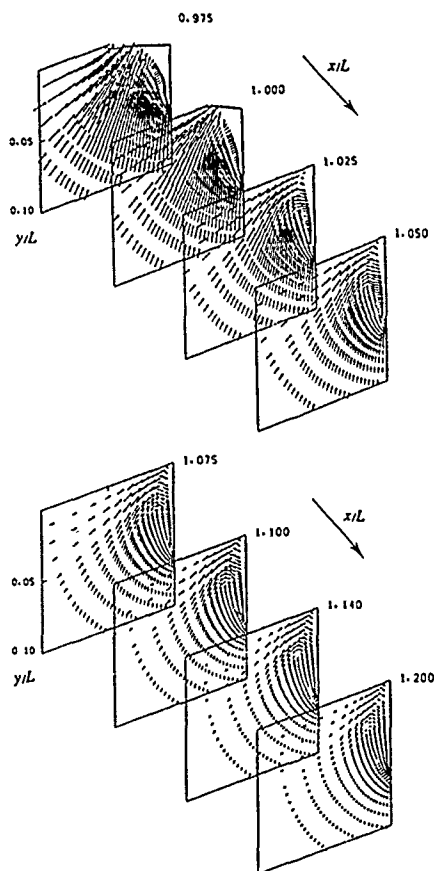


Fig.17 Simulation of bilge vortex over the stern of 37K PROBOCON by STERN/NS.

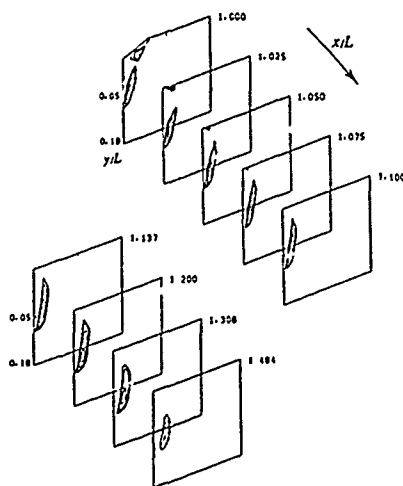


Fig.18 Variation of longitudinal component of vorticity in the wake of 37K PROBOCON.

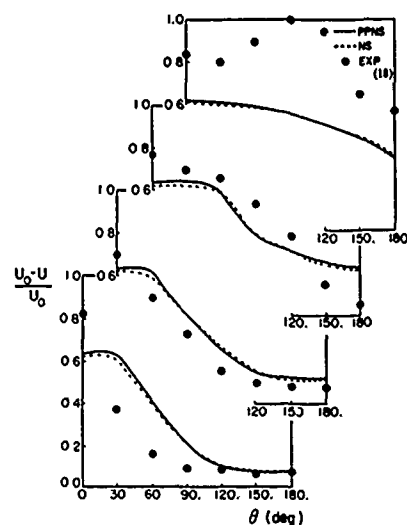


Fig.19 Variation of nominal wake of 37K PROBOCON ($x/L=0.975$).

5. Conclusion

(1) Two computer programs have been developed in the present study. STERN/PPNS simulates flows over the stern by the partially parabolic method, and the STERN/NS by the fully elliptic method. Simulated results are shown to be nearly identical. This indicates that the effects of stream-wise diffusion terms are negligible when the flow reversal does not appear over the stern. They also cross check each others' numerical scheme. The partially parabolic method requires only half of the memory storage and reduces CPU time by 20% in comparison with the fully elliptic method.

(2) The capability of programs developed in the present study is confirmed by successfully simulating pressures, skin frictions and mean velocities over the stern of the both models. The growth of the viscous layer over the stern is well-simulated and the secondary motion is also captured, which is usually observed in the experiments.

(3) There appears to be some deficiency of the $k-\epsilon$ model enough to simulate the turbulence fields over the stern. The standard form of the model usually over-predicts the turbulent kinetic energy. It is also investigated that the model cannot properly account for the reduction of the turbulent kinetic energy near the wall when the viscous layer becomes thick over the stern.

(4) The streamlines over the stern of the barge type ship form show uniform distributions, consequently the gradual girth-wise variations of the boundary layer thickness and the pressure distribution are noted.

Table 1. ϕ , Γ_ϕ and S_ϕ for the governing equation.

ϕ	Γ_ϕ	S_ϕ
1	0	0
U	ν_e	$-\frac{1}{\rho} \frac{\partial p}{\partial x}$ $+\frac{\partial}{\partial x}(v_i \frac{\partial U}{\partial x}) + \frac{1}{r} \frac{\partial}{\partial r}(r v_i \frac{\partial V}{\partial r}) + \frac{1}{r} \frac{\partial}{\partial \theta}(v_i \frac{\partial W}{\partial \theta})$
V	ν_e	$-\frac{1}{\rho} \frac{\partial p}{\partial r}$ $+\frac{\partial}{\partial x}(v_i \frac{\partial U}{\partial r}) + \frac{1}{r} \frac{\partial}{\partial r}(r v_i \frac{\partial V}{\partial r}) + \frac{1}{r} \frac{\partial}{\partial \theta}(v_i \frac{\partial W}{\partial r}) + \frac{W^2}{r}$ $-\frac{1}{r^2} \frac{\partial}{\partial \theta}(v_i W) - \frac{2v_e}{r^2} \frac{\partial W}{\partial \theta} - v_e \frac{V}{r^2} - v_i \frac{V}{r^2}$
W	ν_e	$-\frac{1}{\rho r} \frac{\partial p}{\partial \theta}$ $+\frac{\partial}{\partial x}(\frac{v_i}{r} \frac{\partial U}{\partial \theta}) + \frac{1}{r} \frac{\partial}{\partial r}(v_i \frac{\partial V}{\partial \theta}) + \frac{1}{r} \frac{\partial}{\partial \theta}(\frac{v_i}{r} \frac{\partial W}{\partial \theta})$ $-\frac{1}{r} \frac{\partial}{\partial r}(v_i W) + \frac{2}{r} \frac{\partial}{\partial \theta}(\frac{v_i}{r} V) - v_e \frac{W}{r^2} - \frac{VW}{r^2}$ $+\frac{v_i}{r} \frac{\partial W}{\partial r} + \frac{v_e}{r^2} \frac{\partial V}{\partial \theta} + \frac{v}{r^2} \frac{\partial V}{\partial \theta}$
k	$\frac{\nu_e}{\sigma_k}$	$G - C_D \epsilon$
ϵ	$\frac{\nu_e}{\sigma_\epsilon}$	$\frac{\epsilon}{k} (C_1 G - C_2 \epsilon)$

note; $G = v_i \{ 2[(\frac{\partial U}{\partial x})^2 + (\frac{\partial V}{\partial r})^2 + (\frac{1}{r} \frac{\partial W}{\partial \theta} + \frac{V}{r})^2]$
 $+(\frac{\partial U}{\partial r} + \frac{\partial V}{\partial x})^2 + (\frac{1}{r} \frac{\partial U}{\partial \theta} + \frac{\partial W}{\partial x})^2 + (\frac{1}{r} \frac{\partial V}{\partial \theta} + \frac{\partial W}{\partial r} - \frac{W}{r})^2 \}$
 $\nu_e = \nu + \nu_t, \quad \nu_t = C_\mu k^2 / \epsilon$
 $C_\mu = 0.09, C_D = 1.0, C_1 = 1.44, C_2 = 1.92, \sigma_k = 1.0, \sigma_\epsilon = 1.3$

(5) Simulated nominal wake fractions show good accordance with wake measurements. But values of the outpart of the wake are over-predicted, while the trends of the circumferential variation are consistent with wake measurements. Setting aside the question of the validity of the turbulence model, it should be studied further how to allocate enough meshes locally over the propeller plane, as well as globally over each ship sections.

(6) The capability of the codes to estimate the viscous resistance is investigated. A coefficients of the viscous resistance predicted by the present method are shown to be under-estimated by 10 percent. If further developments on the turbulence model and numerics are accomplished, the numerical simulation of the viscous flow over the stern will be promising for the hull form design.

References

1. L.Larsson, SSPA-ITTC Workshop on Boundary Layers-Proceedings, SSPA-Publication No. 90., (1981).

2. V.C.Patel, "Some Aspects of Thick Three-Dimensional Boundary Layers," Proc. 14th ONR Symp., (1982).
3. V.S.Fratap, D.B.Spalding, "Fluid Flow and Heat Transfer in Three-Dimensional Duct Flows," Int. Journal of Heat and Mass Transfer, Vol.19, (1979).
4. A.M.Abdelmeguid, N.C.Markatos, K.Muraoka, D.B.Spalding, "A Comparison Between the Parabolic and Partially Parabolic Solution Procedures for Three-Dimensional Turbulent Flows around Ship's Hull," Appl. Math. Modelling, Vol.3, (1979).
5. N.C.Markatos, M.R.Malin, D.G.Tatcheel, "Computer Analysis of Three-Dimensional Turbulent Flows around Ship's Hulls," Proc. Inst. Engrs., London, Vol.194, (1980).
6. K.Muraoka, "Calculation of Thick Boundary Layer and Wake of Ships by a Partially Parabolic Method," Proc. 13th ONR Symp., Tokyo, (1980).
7. K.Muraoka, "Calculation of Viscous Flow around Ships with Parabolic and Partially Parabolic Solution Procedures," Trans. West Japan Soc. Naval Arch., Vol.63, (1982).
8. C.E.Janson, L.Larsson, "Ship Flow Calculations Using the PHOENICS Computer Code," Proc. 2nd Int. Symp. on Ship Viscous Resistance, SSPA, (1985).
9. H.C.Raven, M.Hoekstra, "A Parabolized Navier-Stokes Solution Method for Ship Stern Flow Calculations," 2nd Int. Symp. on Ship Viscous Resistance, SSPA, (1985).
10. G.D.Tzabiras, "On the Calculation of the 3-D Reynolds Stress Tensor by Two Algorithm," 2nd Int. Symp. on Ship Viscous Resistance, SSPA, (1985).
11. H.C.Chen, V.C.Patel, "Calculation of Stern Flows by a Time Marching Solution of the Partially-Parabolic Equations," Proc. 16th ONR Symp., (1986).
12. S.H.Kang, K.J.Oh, S.B.Lee, "Study on the Stern Design by Using Viscous Flow Simulations," RIIS Rept.87-092, Coellege of Eng., Seoul N. University, (1987).
13. S.H.Kang and K.J.Oh, "Numerical Calculations of Three-Dimensional Viscous Stern-Flows by Semi-Elliptic Equations," 26(1), (1989).
14. S.H.Kang, K.J.Oh, "Numerical Calculation of Three-Dimensional Using Viscous Flow over a Barge Type Stern by Semi-Elliptic Equations," Seminar on Ship Hyrodynamics, Seoul, (1988).
15. S.V.Pantankar, Numerical Heat Transfer and Fluid Flow, McGraw-Hill, (1980).
16. K.J.Oh, "Numerical Study on the Viscous Flows over the Ship Stern," Ph.D. Thesis, Seoul N. University, (1989).
17. L.Larsson, "Boundary Layers of Ships. Part 3: An Experimental Investigation of the Turbulent Boundary Layer on a Ship Model," SSPA Rept.46, Goteborg, Sweden, (1974).
18. SSPA, 37K PROBOCON Wake Measurements, Rept.3202-12, (1987).
19. S.H.Kang, J.Y.Yoo, B.Y.Shon, S.B.Lee, and S.J.Baik, "Experimental Study on Viscous Flows around Ship Sterns by Using the Hot-Wire Anemometer in the Wind-Tunnel," JSNAK, 11(5), (1987).
20. S.H.Kang and B.S.Hyun, "A Simple Estimation of the Viscous Resistance of Ships by Wake Survey," JSNAK, Vol.19, No.2, (1982).

New Viscous and Inviscid CFD Techniques for Ship Flows

L. Larsson¹ and L. Broberg
FLOWTECH International AB⁴, Sweden

K. J. Kim²
Daewoo Shipbuilding & Heavy Machinery LTD, Korea

D. H. Zhang³
Wuhan University of Water Transportation, China

ABSTRACT

The research on CFD for ship flows carried out at SSPA and Chalmers University of Technology in recent years is summarized. Methods for potential flow calculations including first and higher order theories with linear or non-linear free surface boundary conditions are presented. The importance of higher order effects and non-linearity is discussed. A viscous flow method based on the Reynolds-averaged Navier-Stokes equations is also introduced. The method may be run either in the partially parabolic mode or fully elliptically. A comparison is made between results of the two modes. Grid dependence studies and validation against experiments are presented for all methods.

1. INTRODUCTION

Computational Fluid Dynamics (CFD) has been a major research area at SSPA for a number of years. During the seventies several computer programs for calculating laminar and turbulent boundary layers were developed. These methods turned out to be very useful for thin boundary layers but failed completely near the ship stern [1]. During the eighties a strong effort has therefore been made to develop more

accurate methods, such as the higher order boundary layer integral method [2], [3], the ADI method in body-fitted coordinates [4] and the streamline curvature method [5]. All of these produced improved results near the stern, but none of them could accurately predict the near wake and the viscous/inviscid interaction. A more accurate approach to these problems was obviously required.

The situation was anticipated around 1980, when the development of a Navier-Stokes method was started. After testing and analysing various routes to find the best possible coordinate system and solution procedure a method was developed in 1985-1988. Several different programs were written based on somewhat different approximations of the Navier-Stokes equations [6], [7], [8] and [9]. Introduction of the propeller effect has been made recently [10].

In the early eighties interest was also directed towards the free surface potential flow, and the first methods, based on Dawson's theory, were developed during 1983-1986 [11], [12], [13]. The call for more accurate solutions in certain cases prompted the development of methods with a more exact free surface boundary condition and better numerical accuracy. These methods are presented in detail in [14], [15], [16], [17], [18] and [19]. The purpose of the present paper is to introduce the new development, to give some examples of the application of the programs and to compare the results from different levels of approximation, in the potential flow as well as in the viscous flow.

¹ Also Chalmers University of Technology

² Presently at FLOWTECH International AB

³ Presently at SSPA Maritime Consulting AB

⁴ FLOWTECH International AB is a SSPA subsidiary specialized in CFD for external flows.

2. POTENTIAL FLOW METHODS

2.1 Governing equations

In this class of methods, the flow is considered steady, inviscid, irrotational and incompressible. A right-handed coordinate system $Oxyz$ is employed with the origin on the mean free surface, x positive in the direction of the uniform flow, and z positive upwards. A ship, piercing the free surface, is assumed to be in a uniform onset flow of velocity U_∞ . (See Fig 1.) The flow field around the ship may be described by a velocity potential ϕ , which is generated by a distribution of sources on a surface S and by the uniform onset flow in the x -direction.

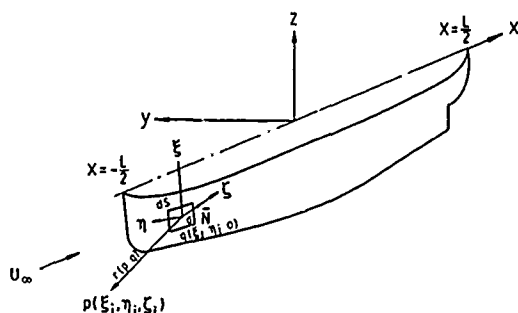


Fig 1 Coordinate systems in potential flow methods

$$\phi(x, y, z) = \int_S \sigma(q) / r(p, q) dS + U_\infty x \quad (1)$$

where $\sigma(q)$ is the source density on the surface element dS and $r(p, q)$ is the distance from the point q to the field point $p(x, y, z)$ where the potential is being evaluated.

The potential ϕ given in Eq (1) is governed by the Laplace equation.

$$\nabla^2 \phi = 0 \quad (2)$$

in the fluid domain and satisfies the regularity condition at infinity

$$\nabla \phi = O(1/r) \text{ as } r \rightarrow \infty \quad (3)$$

The source density σ is to be determined from the boundary conditions on the hull and free surface. On the wetted hull surface the solid boundary condition is

$$\phi_n = 0 \quad (4)$$

where n denotes the outward normal.

At the free surface, two boundary conditions must be imposed, i.e. the flow must be tangent to the surface

$$\phi_x h_x + \phi_y h_y - \phi_z = 0 \quad (5)$$

and the pressure constant

$$gh + \frac{1}{2} (\nabla \phi \cdot \nabla \phi - U_\infty^2) = 0 \quad (6)$$

Further, no upstream waves must be generated.

The exact problem formulated above is nonlinear, since the equations (5) and (6) are nonlinear and are to be satisfied on the wavy surface $z=h(x, y)$, which is unknown. In the present work an iteration procedure is applied and the free surface boundary condition in each iteration is linearized about the previous solution. When the process converges the exact solution is approached.

Unknown sources σ on the hull and wavy surface $z=h(x, y)$ will induce a potential ϕ and a wave elevation h , which satisfy the boundary conditions (5) and (6).

$$\begin{aligned} D_1(\sigma, h) &= \phi_x h_x + \phi_y h_y - \phi_z = 0 \\ D_2(\sigma, h) &= h - \frac{1}{2g} [U_\infty^2 - (\phi_x^2 + \phi_y^2 + \phi_z^2)] = 0 \end{aligned} \quad (7)$$

Small perturbations $\delta\sigma$ and δh of the previous solution are introduced, and the equations expanded to first order in a Taylor series.

$$\begin{aligned} D_1(\sigma, h) &\approx D_1(\sigma^0, h^0) + \Delta D_1(\sigma, h^0) \\ &+ \Delta D_1(\sigma^0, h) \\ &\approx D_1(\sigma^0, h^0) + \frac{\partial}{\partial \sigma} D_1(\sigma, h^0) \delta\sigma \\ &+ \frac{\partial}{\partial h} D_1(\sigma^0, h) \delta h \approx 0 \end{aligned} \quad (8)$$

$$\begin{aligned} D_2(\sigma, h) &\approx D_2(\sigma^0, h^0) + \Delta D_2(\sigma, h^0) \\ &+ \Delta D_2(\sigma^0, h) \\ &\approx D_2(\sigma^0, h^0) + \frac{\partial}{\partial \sigma} D_2(\sigma, h^0) \delta\sigma \\ &+ \frac{\partial}{\partial h} D_2(\sigma^0, h) \delta h \approx 0 \end{aligned}$$

Here the superscript, $^{\circ}$, corresponds to the previous solution, which is assumed to be known. Thus,

$$D_1(\sigma^{\circ}, h^{\circ}) = \phi_x h_x^{\circ} + \phi_y h_y^{\circ} - \phi_z \quad (9)$$

$$D_2(\sigma^{\circ}, h^{\circ}) = h^{\circ} - \frac{1}{2g} [U_{\infty}^2 - (\phi_x^2 + \phi_y^2 + \phi_z^2)]$$

where ϕ is the potential induced by σ° on the free surface $z = h^{\circ}(x, y)$. Introducing the perturbation $\delta\phi$, the partial increments of D_1 and D_2 may be written

$$\Delta D_1(\sigma, h^{\circ}) = \delta\phi_x h_x^{\circ} + \delta\phi_y h_y^{\circ} - \delta\phi_z \quad (10)$$

$$\Delta D_1(\sigma^{\circ}, h) = \phi_x \delta h_x + \phi_y \delta h_y + (\phi_{xz} h_x^{\circ} + \phi_{yz} h_y^{\circ} - \phi_{zz}) \delta h$$

$$\Delta D_2(\sigma, h^{\circ}) = \frac{1}{g} (\phi_x \delta\phi_x + \phi_y \delta\phi_y + \phi_z \delta\phi_z) \quad (11)$$

$$\Delta D_2(\sigma^{\circ}, h) = \delta h + \frac{1}{g} (\phi_x \phi_{xz} + \phi_y \phi_{yz} + \phi_z \phi_{zz}) \delta h$$

Therefore the linearized free surface boundary conditions are

$$\phi_x h_x^{\circ} + \phi_y h_y^{\circ} - \phi_z + \phi_x \delta h_x + \phi_y \delta h_y + (\phi_{xz} h_x^{\circ} + \phi_{yz} h_y^{\circ} - \phi_{zz}) \delta h = 0 \quad (12)$$

$$\left\{ 1 + \frac{1}{g} (\phi_x \phi_{xz} + \phi_y \phi_{yz} + \phi_z \phi_{zz}) \right\} \delta h = \frac{1}{2g} [U_{\infty}^2 - \phi_x^2 - \phi_y^2 - \phi_z^2 - (\phi_x \delta\phi_x + \phi_y \delta\phi_y + \phi_z \delta\phi_z)] - h^{\circ} \quad (13)$$

(12) and (13) are to be applied on $z = h^{\circ}(x, y)$

To start the iteration process the double model case is first computed. This yields ϕ and h° , and a linear solution ϕ , h may be obtained from (12) and (13). However, for this particular case ϕ_z , as well as z -derivatives of ϕ_x and ϕ_y are equal to zero, for symmetry reasons, so (12) and (13) are simplified to

$$\phi_x h_x^{\circ} + \phi_y h_y^{\circ} - \phi_z + \phi_x \delta h_x + \phi_y \delta h_y = 0 \quad (14)$$

$$\delta h = \{U_{\infty}^2 + \phi_x^2 + \phi_y^2 - 2(\phi_x \phi_{xz} + \phi_y \phi_{yz})\} / 2g - h^{\circ} \quad (15)$$

These are the equations solved in the linear methods. They may be applied either on $z=0$ [11], [19] or on $z=h^{\circ}(x, y)$ [15], the so called Bernoulli wave.

To obtain a solution satisfying the exact boundary conditions (non-linear in ϕ and h) the iterations continue from the linear solution using (12) and (13). After 5-10 iterations δh and $\delta\phi$ are usually sufficiently small, and the process may be considered converged.

2.2 Numerical Solution

2.2.1 Free Surface Grid

In the numerical implementation the first step is to discretize the integral domain S in (1) into a large number of small panels. The domain consists of the hull surface and part of the free surface. In principle the free surface panel distribution should be extended over the entire region where there are significant waves, but for practical reasons the region of free surface panels has to be limited to the area near the hull. The influence of the truncation will be discussed later.

To generate the free surface grid, two different principles have been used. Following Dawson [26], Xia [11] generated a grid based on the streamlines of the double model flow. This approach has the advantage that a somewhat simpler form of the boundary conditions (14) and (15) may be used in the linear case. Dawson showed that the equations can be rewritten as ordinary differential equations in l , when l is the arc length along a streamline. Using a streamline grid thus enables simple numerical differentiation (Dawson's derivation was not quite correct, but the error is small). There is, however, one serious disadvantage of the streamline grid, as noted by Xia & Larsson [12]: the grid gets very coarse at the ends of the hull, where a fine grid is required. Therefore another approach has been chosen in the more recent methods [12]-[19]. The longitudinal lines are now generated numerically by interpolation between the edge of the panelled region and the hull. The transverse lines can be

either hyperbolas [11]-[17] or straight lines [18], [19]. A typical grid is shown in Fig.2. For non-linear calculations the free surface panels are moved to the wavy surface in each iteration.

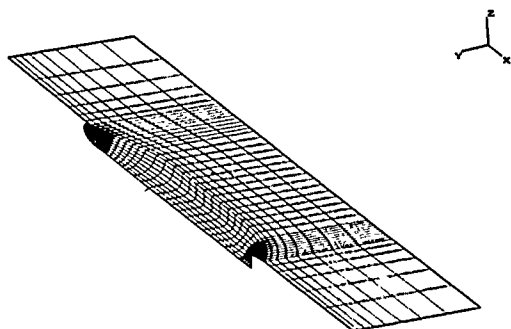


Fig 2 Panel distribution. SSPA Ro-Ro ship, medium bulb

To obtain derivatives of a function g in the x and y directions, derivatives along the L (longitudinal) and T (transverse) directions are obtained from

$$g_x = ax_1 g_T - ax_2 g_L \quad (16)$$

$$g_y = g_T$$

where

$$ax_1 = f_L^i$$

$$ax_2 = - \sqrt{1 + f_L^2}$$

and $y = f_L(x)$ is the equation for a longitudinal line.

Derivatives with respect to L and T are obtained either from three point or four point finite difference operators

$$\begin{aligned} g_{Li} &= CA_i g_i + CB_i g_{i-NL} + CC_i g_{i-2NL} \\ g_{Ti} &= GA_i g_i + GB_i g_{i+1} + GC_i g_{i+2} \end{aligned} \quad (17)$$

or

$$\begin{aligned} g_{Li} &= CA_i g_i + CB_i g_{i-NL} + CC_i g_{i-2NL} \\ &\quad + CD_i g_{i-3NL} \\ g_{Ti} &= GA_i g_i + GB_i g_{i+1} + GC_i g_{i+2} \\ &\quad + GD_i g_{i+3} \end{aligned}$$

where NL is the number of longitudinal strips on the free surface.

The coefficients of the upstream operator (CA , CB , CC and CD) and the downstream operator (GA , GB , GC , GD)

are calculated from the distance between successive control points on the free surface panels, see [11].

Dawson conjectured that the use of upstream differences along the streamlines should prevent upstream waves. This has been true of all cases computed by the present methods even though the streamlines have been replaced by the body-fitted longitudinal lines.

During the iteration process in the nonlinear procedure the calculation domain is changed in each iteration. The free surface sources are moved to the previous wavy surface in every step and the boundary condition is applied there. This means that the hull surface has to change as well, so a special panelization procedure has been introduced in the program. A typical panel distribution is shown in Fig. 3.

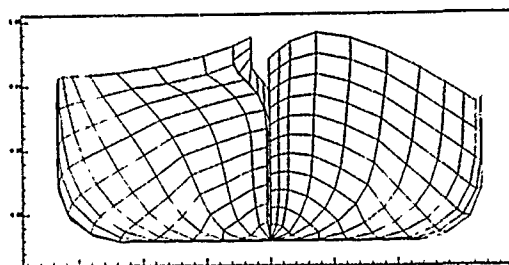


Fig 3 Hull panel distribution in the non-linear method. Series 60, $C_B = 0.60$, $F_n = 0.32$

2.2.2. Higher Order Effects

Xia's methods [11]-[14] were of first order i.e. the panels on the hull and free surface were flat and with a constant source strength. To obtain a more accurate solution without increasing the number of panels N_i [15]-[18] introduced a higher order technique in which the panels are parabolic and the source distribution linear. The technique, which is similar to the one proposed by Hess [20], has been further improved by Kim [19].

A parabolic panel is defined in following form

$$\begin{aligned} \zeta' &= z_0 + A_0 \xi' + B_0 \eta' \\ &\quad + P_0 \xi'^2 + 2Q_0 \xi' \eta' + R_0 \eta'^2 \end{aligned} \quad (18)$$

where a panel element co-ordinate system (ξ', η', ζ') is constructed using the four corner points. Thus, the

origin is defined as the average of the corner points, while the ξ' -direction is normal to the two diagonal vectors. The six parameters (Z_0, A_0, B_0, P_0, Q_0 and R_0) are determined by: (a) requiring the panel to pass through the corner points of the panel (four conditions), and (b) requiring the panel to pass as closely as possible, in a least squares sense, to the eight additional input points for the adjacent panels (two additional conditions).

In the present method the control point is the point on the curved panel closest to the average point of the four input points. This control point is characterized by the condition that the vector from the origin is parallel to the local normal vector

$$[\xi' \hat{e}_1 + \eta' \hat{e}_j + \zeta' (\xi', \eta') \hat{e}_k] \times [-\zeta' \hat{e}_1 - \zeta' \hat{e}_j + \hat{e}_k] = 0 \quad (19)$$

Eq (19) is equivalent to the two scalar equations

$$G(\xi', \eta') = \xi' + \zeta' (\xi', \eta') \zeta'_\xi (\xi', \eta') = 0 \quad (20)$$

$$H(\xi', \eta') = \eta' + \zeta' (\xi', \eta') \zeta'_\eta (\xi', \eta') = 0$$

These nonlinear equations are solved by Newton-Raphson iteration.

Once the control point is determined, the panel co-ordinate system (ξ', η', ζ') is transformed to a new projected flat panel which is tangent to the parabolic panel and the tangent point is both the control point and the origin of new panel co-ordinate system (ξ, η, ζ) see Fig 1. The equation of the panel may be written

$$F(\xi, \eta, \zeta) = \zeta - [P\xi^2 + 2Q\xi\eta + R\eta^2] = 0 \quad (21)$$

The source density distribution is assumed to be linear on each panel.

$$\sigma(\xi, \eta) = \sigma_0 + \sigma_\xi \xi + \sigma_\eta \eta \quad (22)$$

This is fitted in the least squares

sense to the values of source density at the control points of the M adjacent panels. Thus the source derivatives on the panel in question may be expressed in terms of the unknown values of the source density on the adjacent panels in the form

$$\sigma_\xi = \sum_{k=0}^M C_k^{(\xi)} \sigma_k \quad (23)$$

$$\sigma_\eta = \sum_{k=0}^M C_k^{(\eta)} \sigma_k$$

The desired source density coefficients $C_k^{(\xi)}$ and $C_k^{(\eta)}$ are obtained by minimizing the error function ϵ

$$\text{Min } \epsilon = \text{Min}_{C_k^{(\xi)}, C_k^{(\eta)}} \sum_{k=0}^M [\sigma_k - (\sigma_0 + \sigma_\xi \xi_k + \sigma_\eta \eta_k)]^2 \quad (24)$$

According to Eq (1) the perturbation potential ϕ_{ij} at the i -th field point (ξ_i, η_i, ζ_i) induced by the j -th panel on which the source density σ is distributed is

$$\phi_{ij} = \int_{A_j} (\sigma/r) dS \quad (25)$$

Since in the higher order method the integration is to be carried out over a curved surface, expressions for $1/r$ and dS are different from the corresponding first order ones. The expression for ϕ_{ij} is further complicated by the variation of σ on each panel. In [18] the following expression for ϕ_{ij} is derived

$$\begin{aligned} \phi_{ij} &= \phi_{ij}^{(0)} \sigma_j + \{ P \phi_{ij}^{(P)} + 2Q \phi_{ij}^{(Q)} \\ &\quad + R \phi_{ij}^{(R)} \} \sigma_j + \phi_{ij}^{(1\xi)} \sigma_\xi + \phi_{ij}^{(1\eta)} \sigma_\eta \\ &= \phi_{ij}^* \sigma_j + \sum_{k=1}^{M-1} \{ C_k^{(\xi)} \phi_{ij}^{(1\xi)} \\ &\quad + C_k^{(\eta)} \phi_{ij}^{(1\eta)} \} \sigma_k \end{aligned} \quad (26)$$

Here M is the number of adjacent panels.

All the ϕ terms in (26) can be calculated numerically and they may be interpreted as follows: $\phi_{ij}^{(0)}$ corresponds to a flat panel with a constant source density, $\phi_{ij}^{(P)}$, $\phi_{ij}^{(Q)}$ and $\phi_{ij}^{(R)}$ are caused by the parabolic panel shape, $\phi_{ij}^{(1\xi)}$ and $\phi_{ij}^{(1\eta)}$ come from the linear variation of the source density. All these terms depend only on the geometry of the j -th panel, but the curvature terms P , Q , R and the source derivative coefficients $C_k^{(\xi)}$ and $C_k^{(\eta)}$ depend on the surrounding panels.

The individual ϕ 's in Eq (26) are

$$\begin{aligned}\phi_{ij}^{(0)} &= \int_{A_j} \frac{1}{r_f} d\xi d\eta \\ \phi_{ij}^{(P)} &= \int_{A_j} \zeta_i \xi_j^2 / r_f^3 d\xi d\eta \\ \phi_{ij}^{(Q)} &= \int_{A_j} \zeta_i \xi_j \eta_j / r_f^3 d\xi d\eta \\ \phi_{ij}^{(R)} &= \int_{A_j} \zeta_i \eta_j^2 / r_f^3 d\xi d\eta \\ \phi_{ij}^{(1\xi)} &= \int_{A_j} \xi_j / r_f d\xi d\eta \\ \phi_{ij}^{(1\eta)} &= \int_{A_j} \eta_j / r_f d\xi d\eta\end{aligned}\quad (27)$$

where r_f is the distance between (ξ_i, η_i, ζ_i) and the j -th control point $(\xi_j, \eta_j, 0)$ on the flat panel (see Fig 1). Then the velocity induced by the panel is obtained by taking the gradient of the corresponding potential.

$$\begin{aligned}\phi_{\xi} &= \phi_{\xi}^* \sigma_j + \sum_{k=1}^{M-1} \{C_k^{(\xi)} \phi_{\xi}^{(1\xi)} + C_k^{(\eta)} \phi_{\xi}^{(1\eta)}\} \sigma_k \\ \phi_{\eta} &= \phi_{\eta}^* \sigma_j + \sum_{k=1}^{M-1} \{C_k^{(\xi)} \phi_{\eta}^{(1\xi)} + C_k^{(\eta)} \phi_{\eta}^{(1\eta)}\} \sigma_k \\ \phi_{\zeta} &= \phi_{\zeta}^* \sigma_j + \sum_{k=1}^{M-1} \{C_k^{(\xi)} \phi_{\zeta}^{(1\xi)} + C_k^{(\eta)} \phi_{\zeta}^{(1\eta)}\} \sigma_k\end{aligned}\quad (28)$$

The subscript ij is omitted in the equation for simplicity, and new velocity terms (ϕ_{ξ}^* , ϕ_{η}^* , ϕ_{ζ}^*) are introduced. They are velocity components induced at the i -th control point by a unit source density on the j -th panel. All the induced velocities in (28) can be obtained analytically.

The velocities the reference coordinate can be calculated from the coordinate transformation

$$\begin{Bmatrix} \phi_x \\ \phi_y \\ \phi_z \end{Bmatrix} = \begin{bmatrix} a_{11} & a_{21} & a_{31} \\ a_{12} & a_{22} & a_{32} \\ a_{13} & a_{23} & a_{33} \end{bmatrix} \begin{Bmatrix} \phi_{\xi} \\ \phi_{\eta} \\ \phi_{\zeta} \end{Bmatrix} \quad (29)$$

These velocities may also be written as

$$\begin{aligned}\phi_{xi} &= \sum_{j=1}^{NE} X_{ij} \sigma_j + U_{\infty} \\ \phi_{yi} &= \sum_{j=1}^{NE} Y_{ij} \sigma_j \\ \phi_{zi} &= \sum_{j=1}^{NE} Z_{ij} \sigma_j\end{aligned}\quad (30)$$

Here the velocity influence coefficients X_{ij} , Y_{ij} and Z_{ij} are the velocity components in the reference coordinate system (x, y, z) at the i -th control point, induced by a source density which is unity at the control point of the j -th panel. In the first order method the velocity induced by a panel depends only on the panel itself. The essentially new feature of the higher order method is that the velocity induced by a panel depends on the values of source density also at the control points of adjacent elements. Thus the influence coefficients for a panel depend not only on the geometry of that panel but also on the geometry of adjacent panels.

The second order derivatives of ϕ_{ij} required in (12) and (13) are more complicated than the first order ones. In the present work, the magnitude of the second derivative terms related to the curvature and linear variation of source density are assumed to be small and vanish rapidly during the iteration. Therefore the second order derivative terms are calculated from a source velocity which corresponds to the flat panel with constant source density.

$$\begin{Bmatrix} \phi_{xz} \\ \phi_{yz} \\ \phi_{zz} \end{Bmatrix}_i = \sum_{j=1}^{NE} \begin{bmatrix} a_{13} \\ a_{23} \\ a_{33} \end{bmatrix}_j^T$$

$$\begin{bmatrix} a_{11} & a_{21} & a_{31} \\ a_{12} & a_{22} & a_{32} \\ a_{13} & a_{23} & a_{33} \end{bmatrix} \cdot \begin{bmatrix} \phi_{\xi\xi} & \phi_{\xi\eta} & \phi_{\xi\zeta} \\ \phi_{\eta\xi} & \phi_{\eta\eta} & \phi_{\eta\zeta} \\ \phi_{\zeta\xi} & \phi_{\zeta\eta} & \phi_{\zeta\zeta} \end{bmatrix}_{ij} \quad (31)$$

NE is here again the total number of panels.

2.2.3 Solution Procedure

The boundary conditions (4) and (12), (13) or (14), (15) may be transformed into a set of linear equations in σ using the relations above for the first and second derivations of ϕ .

$$[A] \{ \sigma \} = \{ B \} \quad (32)$$

where $[A]$ is a $NE \times NE$ matrix and $\{B\}$ is the right-hand side array.

The upper part of the A-matrix and B-vector, corresponding to the hull boundary condition, is obtained in a straightforward way, while the lower part, corresponding to the free surface, is considerably more complex. The equations are given in [18] and [19]. Unfortunately, the lower part of the matrix is not diagonally dominant, so iterative methods cannot be used in the solution. This is therefore found by a Gaussian elimination procedure.

2.2.4 Wave Resistance

Having obtained the source strengths, velocities may be computed from (30) and the pressures from the Bernoulli equation. To obtain the resistance, two principally different methods have been employed. Either the force is found by pressure integration over the hull or by integration of the sources over the free surface. In the former case, different formulas are used depending on whether or not the higher order technique is employed, i.e.

$$C_W = \sum_i^{NB} C_{pi} N_{xi} \Delta S_i / \sum_i^{NB} \Delta S_i \quad (33)$$

where NB is the number of panels and N_x and ΔS_i are the x-component of the normal and the area respectively of a panel, or

$$C_W = \sum_i^{NB} \int_{E_i} (C_{p0} + C_{p\xi} \xi + C_{p\eta} \eta) (a_{11} N_{\xi}^E + a_{21} N_{\eta}^E + a_{31} N_r^E) (1+2\psi_2) d\xi d\eta \quad (34)$$

The latter formula is derived assuming that the pressure varies linearly over the panel in a similar way as the source strength. $C_{p\xi}$ and $C_{p\eta}$ are the slopes of the pressure

variation, a_{11} , a_{21} and a_{31} are the first column of the transformation matrix between the panel and reference coordinate systems, N_{ξ}^E , N_{η}^E and N_r^E are the components of the normal vector in the panel coordinate system and ψ_2 is a term which takes into account the change in panel area due to curvature.

The formula for obtaining the resistance from the free surface sources is derived from the momentum theorem applied to a control volume outside the hull, under the undisturbed free surface and extending to infinity sideways, downwards and longitudinally. The detailed derivation is given in [18]. It yields

$$C_W = (4\pi \sum_i^{NF} u_{B1} \sigma_i \Delta S_i) / (U_{\infty}^2 \sum_i^{NB} \Delta S_i) \quad (35)$$

It should be noted that this formula is valid only for the linear case.

2.3 Validation

The methods presented have been validated in a number of ways. A grid dependence study was first carried out for the linear first order method to investigate the sensitivity of the solution to the panelization on the free surface. Most likely the results from this study are valid also for the other methods. The improvement in accuracy when introducing the higher order method was then tested against two analytical results without a free surface.

Comparison with measurements have been made for a number of cases such as the Wigley hull, the Series 60, $C_B=0.60$ hull, the HSVA-tanker, the high speed ship ATHENA, a Ro-Ro ship designed at SSPA and two sailing yachts. All these comparisons are described in detail in [11]-[19]. As an example only the calculations for the Ro-Ro ship will be presented here. This case is particularly interesting since a study of several bulb alternatives was made. It is also the only case for which calculations have been carried out using the first and higher order linear, as well as the higher order non-linear method. Interesting comparisons between all three methods may thus be made.

2.3.1 Grid Dependence Study

Since one of the most important questions in connection with the present methods is the dependence of the solution on the panel distribution, particularly on the free surface, a systematic variation was carried out.

The test case was the Wigley hull. Employing the coordinate system defined in Fig 1, the equation for the hull surface reads

$$y = \frac{1}{10} (1 - x^2) (1 - \frac{z^2}{64}) \quad (36)$$

In table 1 (last page) the number of panels on the hull and on the surface, the extent of the panelled part of the free surface in the x- and y-directions, the Froude number and the wave resistance coefficient are given.

In run No 1, only approximately 1/4 of the half ship length, 1, was used for the free surface extent in the y-direction. The calculation gave an unreasonably high wave resistance at $F_n = 0.266$ and broke down at $F_n = 0.45$. In runs of No 2, 3 and 4, the free surface region was enlarged and divided into 5, 10, and 15 strips respectively. At $F_n = 0.266$, the resistance changed significantly from run to run, but at $F_n = 0.45$ there was no change between the last two runs.

The free surface extent in the x-direction was tested in runs No 3, 5, 6, 7 and 8. From No 3 to No 5 the free surface region was extended by 1/4 l. The wave resistance did not change very much, but as the free surface region was enlarged by 1/2 from run No 6 to No 7, the wave resistance changed, particularly for the highest Froude numbers. From run No 7 to run No 8, part of the free surface region was moved from the bow to the stern. The wave resistance did not change at $F_n = 0.266$, whereas it was increased by 10% at $F_n = 0.45$.

There were no systematic changes in the panel distribution on the hull, but two slightly different hull panel distributions were used in the successive tests. This should not cause large changes in the final results. The considerable difference in the wave resistance between runs No 3 and No 6 is likely to have been caused by the change of the panels on the free surface. More even panels were placed on the free surface for run No 6 than those for case No 3.

The results obtained imply that the choice of the panels depends on the Froude number to be evaluated. Smaller panels should be used for low Froude numbers, while a larger free surface portion is required for high Froude numbers. It is wise to vary the panel arrangement for different Froude numbers.

A panel distribution similar to case No 9 of Table 1 has been used in most work afterwards.

2.3.2 Analytical Test Cases

To investigate the improvement in accuracy when introducing the higher order technique the flow around a sphere was calculated. In Fig 4 the velocity distribution along a generator through the stagnation point is shown. Two grids were tested, one with a distribution similar to a typical ship case, i.e. with 22 longitudinal and 40 transverse strips on one quarter of the sphere and one with 5x10 strips. It is seen that both higher order solutions are extremely accurate, while there is some error also for the 880 panel first order case. Small as this error may seem, it may have a significant influence on the drag. Integrating the pressure on one half of the sphere yields the following results for the drag coefficient C_x

	First order	Higher order	Exact
C_x	0.0550	0.0622	0.0625
Error	12%	0.5%	-

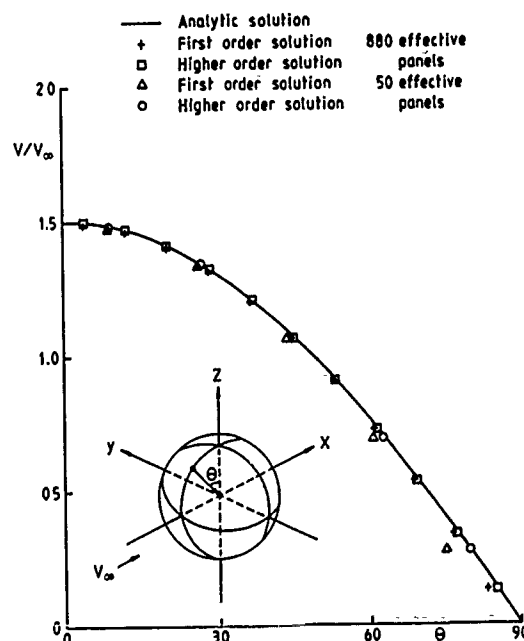


Fig 4 Velocity distribution on a sphere

The higher order calculation is thus considerably more accurate. It should be noted that the computer time for a given number of panels increases by about 10% for a case of this size.

2.3.4 The SSPA Ro-Ro Ship

The body plan of the SSPA Ro-Ro ship is shown in Fig 5 with a small, a medium and a large bulb. A comparison between the measured residuary resistance and the computed wave resistance (pressure integration) using two linear (first and higher order) versions and one non-linear (higher order) version of the same program [19] is made for the medium bulb in Fig 6. The panel distribution is shown in Fig 2.

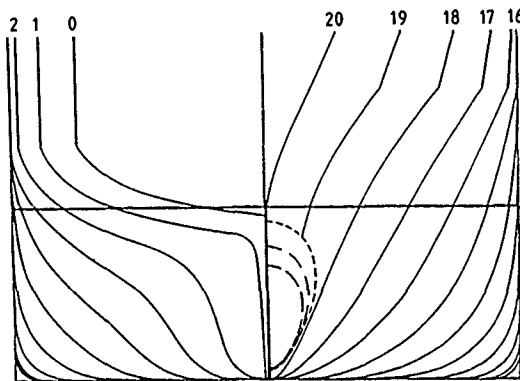


Fig 5 Body plan, SSPA Ro-Ro ship with different bulbs

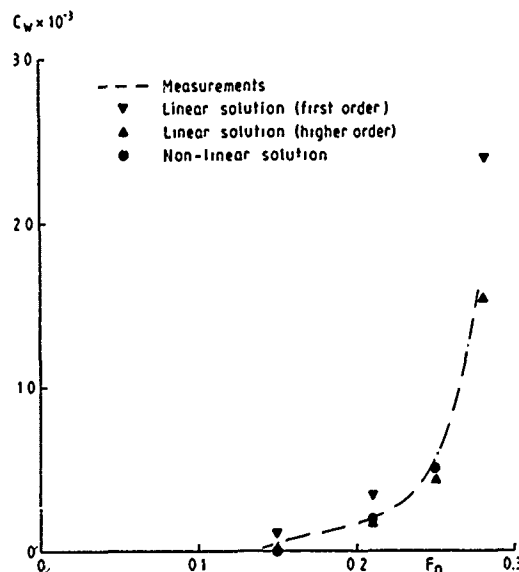


Fig 6 Predicted wave resistance compared with measured residual resistance. SSPA Ro-Ro ship, medium bulb

A common problem in most evaluations of wave resistance calculations is that the wave pattern resistance is seldom measured. In the present case the form factor has been determined using a Prohaska plot, and the viscous resistance based on the ITTC-57 correlation and the form factor has been subtracted from the total resistance to get the residuary resistance.

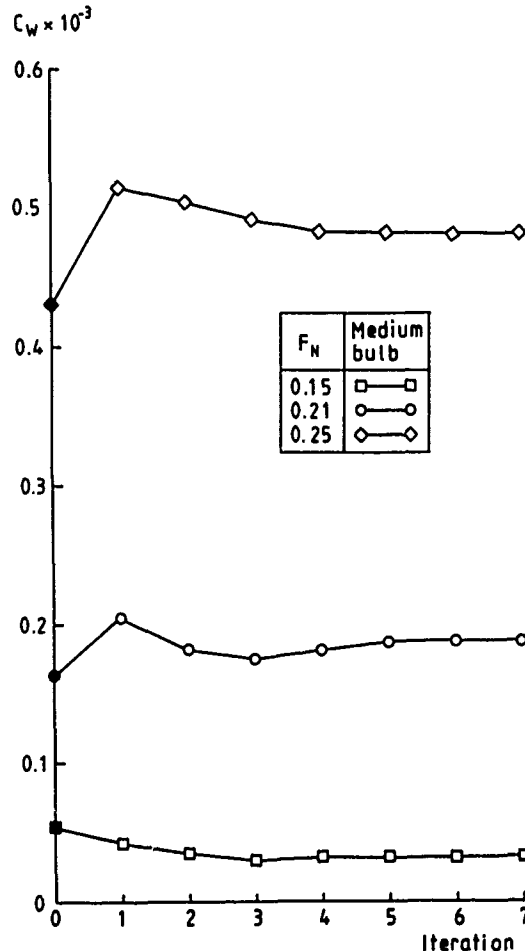


Fig 7 Convergence history. Wave resistance of SSPA Ro-Ro ship, medium bulb

As appears from Fig 6 the difference between the linear and non-linear higher order methods is quite small for this case. This is also apparent from Fig 7 where the convergence history of the wave resistance is shown. The final converged value after 7 iterations is not very much different from the first value, corresponding to the linear solution. Larger differences have been noted for bluffer ships [16] and non-linearity should be extremely important for hulls with large overhangs such as sailing yachts.

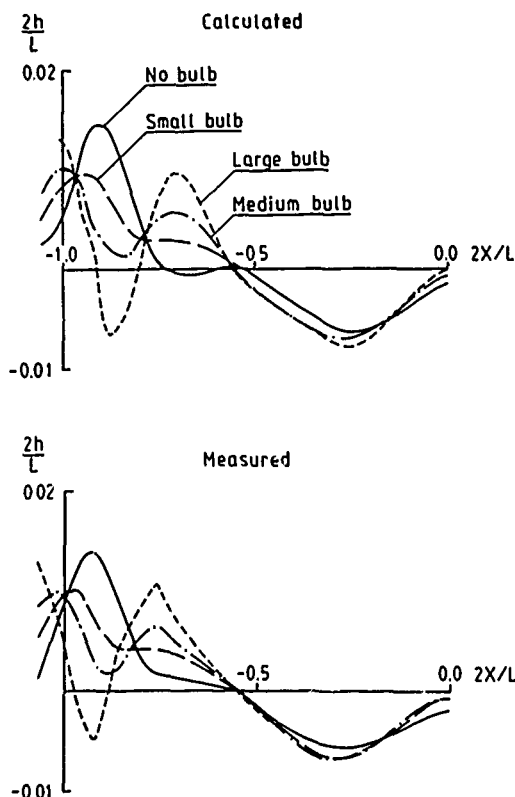


Fig 8 Wave profiles at $F_n = 0.21$.
SSPA Ro-Ro ship

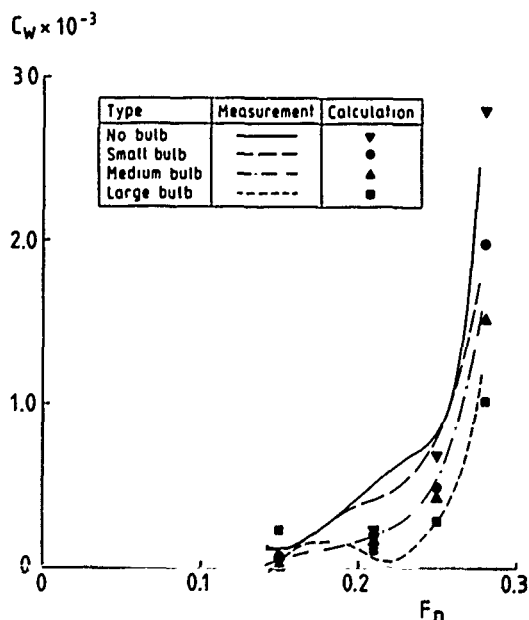


Fig 9 Wave resistance. SSPA Ro-Ro ship

The first order solution of Fig 6 is not as accurate as the higher order solutions, but even the first order results are not grossly in error.

Interesting comparisons between results for the three bulbs and the case without a bulb can be made in Fig 8 and 9 based on higher order linear solutions. The measured wave profiles of the four cases are very much different as appears from Fig 8, and the differences are quite well predicted. The absolute values of the wave resistance, Fig 9, are not as accurate in all cases, but the method is able to rank the cases in the right order.

3 VISCOUS FLOW METHODS

Although, as indicated in the Introduction, a number of different methods for computing the viscous flow (boundary layer/wake) around ships have been developed at SSPA/CTH, only the Navier-Stokes methods will be presented in the present review.

3.1 Coordinate systems and grid

In the SSPA Navier-Stokes methods the coordinate systems of Fig 10 are employed. These systems, which differ from the ones of the potential flow methods, are more convenient for tensor notation which is required for the fully transformed Navier-Stokes equations in curvilinear nonorthogonal coordinates. ξ^i are the global Cartesian reference coordinates, while x^i are the grid oriented ones, as appears from Fig 10. The relation between the two systems is of the form

$$\nabla^2 x^i = f^i \quad (i = 1, 2, 3) \quad (37)$$

where ∇^2 is the Laplacian operator in orthogonal coordinates (ξ^i) and f^i are control functions which may be assigned appropriate values to yield the desired stretching of coordinate surfaces. The equations are inverted by exchanging the dependent and independent variables

$$g^{ij} \partial_i \partial_j \xi^1 + f^k \partial_k \xi^1 = \nabla^2 \xi^1 \quad (38)$$

The Laplacian operator may be written

$$\nabla^2 = \frac{1}{h_1 h_2 h_3} \sum_{j=1}^3 \frac{\partial}{\partial \xi^j} \left(\frac{h_1 h_2 h_3}{h^2_j} \frac{\partial}{\partial \xi^j} \right) \quad (39)$$

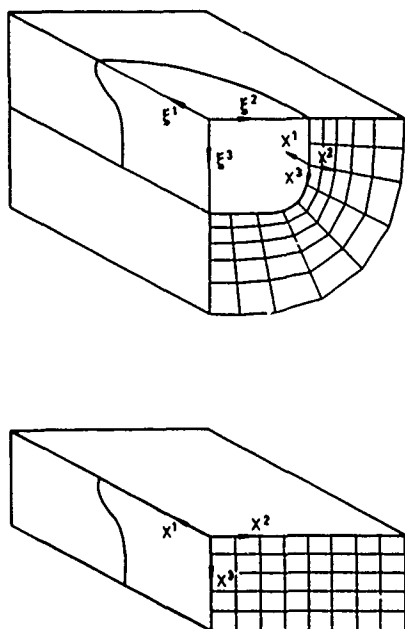


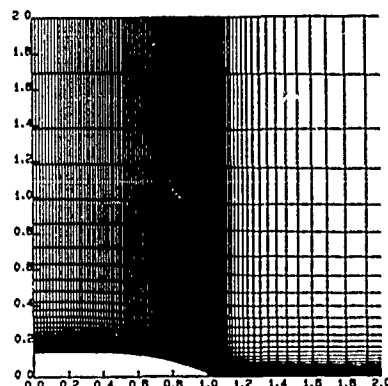
Fig 10 Coordinate systems in Navier-Stokes methods

here h_1, h_2, h_3 are metric coefficients in the frame ξ^1 . After selecting $\xi^1(x^1)$ and assigning proper values for the control functions f^1 , equations are solved numerically. A more detailed description of the grid generation is given in [9]. Fig 11 shows the coordinate system for the SSPA 720 Model.

3.2 Governing equations

The governing equations solved are the Reynolds equations obtained from the Navier-Stokes equations by averaging over the largest, turbulent time scale. In this way the unsteadiness due to turbulence is removed at the expense of having to introduce a turbulence model for the Reynolds stresses. In the coordinate system above the incompressible momentum equations may be written (see [6] for a derivation).

$$\begin{aligned} \partial_t u^i + h_{(k)}^{-1} u^k u_{,k}^i &= - h_{(i)} g^{ik} \partial_k p + \\ (g^{jk} u_{,j}^i + h_{(i)} h_{(k)}^{-1} g^{ji} u_{,j}^k) \partial_k v_E &+ \\ v_E \{ g^{jk} \partial_k \partial_j u^i + g^{jk} \partial_k (u^l Q_{jl}^i) + g^{jk} Q_{kl}^i u_{,j}^l - \\ g^{jk} \Gamma_{kj}^l u_{,l}^i \} \end{aligned} \quad (40)$$



View of the water plane

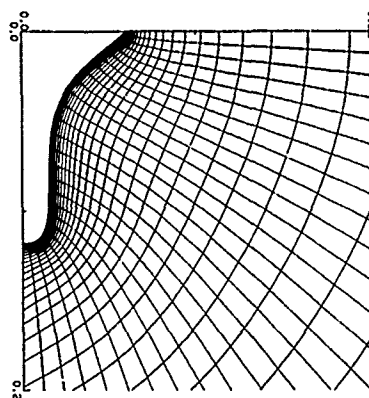


Fig 11 Longitudinal and transverse views of the grid. SSPA 720 Model

The incompressible continuity equation may be written

$$J^{-1} \partial_k (J h_{(k)}^{-1} u^k) = 0 \quad (41)$$

where J is the Jacobian

u^i are the physical components of the velocity vector, i.e. the components based on unit vectors parallel to the covariant base vectors g_i , whose magnitude $|g_i|$ is denoted $h_{(i)}$. g^{ij} is the contravariant metric tensor and Γ_{ij}^l is a Christoffel symbol of the second kind. ∂_i is to be interpreted as a partial derivative with respect to x^i and $u_{,j}^i$ is defined from the relation

$$u^i_{,j} = \partial_j u^i + Q^i_{j1} u^1 \quad (42)$$

where

$$Q^i_{j1} = h_{(j)} \bar{Q}^i_{j1} \quad (43)$$

and

$$\bar{Q}^i_{j1} = h_{(j)}^{-1} h_{(1)}^{-1} h_{(i)} r^i_{j1} - \delta^i_1 h_{(i)}^{-1} \partial_j h_{(i)} \quad (44)$$

where δ^i_1 is the Kronecher delta and

$$k = h_{(k)} \partial_k$$

An index written within a bracket means that it is not considered in the summation rule. The quantity ν_E , finally, is the effective viscosity

$$\nu_E = \frac{1}{R_n} + \nu_t \quad (46)$$

where R_n is the Reynolds number and ν_t is the eddy viscosity which is obtained from

$$\nu_t = C_\mu \frac{k^2}{\epsilon} \quad (47)$$

The following standard values are used for the constants: $C_\mu = 0.09$, $C_{\epsilon 1} = 1.44$, $C_{\epsilon 2} = 1.92$, $\sigma_k = 1.0$ and $\sigma_\epsilon = 1.3$

Two turbulence models are being used. If no wall functions are employed the turbulence model is of the two-layer type. Thus, in the inner region an equation for the turbulent kinetic energy k is solved together with a prescribed length scale. In the outer part the length scale is replaced by an equation for the rate of dissipation of kinetic energy, ϵ . If wall functions are used as the inner boundary condition for the flow, the k - ϵ model is used throughout. The transport equations for k and ϵ are as follows

$$\begin{aligned} \partial_t k + h_{(i)}^{-1} u^i \partial_i k = \\ \frac{\nu_E}{\sigma_k} [g^{ij} \partial_i \partial_j k - g^{ij} r^1_{ij} \partial_1 k] \\ + \frac{1}{\sigma_k} g^{ij} \partial_j \nu_E \partial_i k + G - \epsilon \end{aligned} \quad (48)$$

$$\begin{aligned} \partial_t \epsilon + h_{(i)}^{-1} u^i \partial_i \epsilon = \frac{\nu_E}{\sigma_\epsilon} [g^{ij} \partial_i \partial_j \epsilon - g^{ij} r^1_{ij} \partial_1 \epsilon] + \\ \frac{1}{\sigma_\epsilon} g^{ij} \partial_j \nu_E \partial_i \epsilon + \end{aligned} \quad (49)$$

$$C_{\epsilon 1} \frac{\epsilon}{k} G - C_{\epsilon 2} \frac{\epsilon^2}{k}$$

The generation term can be written

$$\begin{aligned} G = \nu_t (h_{(m)}^{-1} h_{(i)}^{-1} u^m_{,i} u^i_{,m} + \\ g^{ni} g_{mj} h_{(m)}^{-1} h_{(j)}^{-1} u^m_{,i} u^j_{,n}) \end{aligned} \quad (50)$$

If no wall functions are used the rate of dissipation and the eddy viscosity are obtained from

$$\begin{aligned} \epsilon = \frac{k^{3/2}}{l_\epsilon} \\ \nu_t = C_\mu \sqrt{k} l_\mu \end{aligned} \quad (51)$$

respectively. The following length scales are used

$$\begin{aligned} l_\epsilon = C_1 y (1 - e^{-R_y/A_\epsilon}) \\ l_\mu = C_1 y (1 - e^{-R_y/A_\mu}) \end{aligned} \quad (52)$$

where $R_y = R_n / k y$, y is the distance in the normal direction to the surface. The following constants are used:

$$\begin{aligned} C_1 = \kappa C_\mu^{-3/4}, \quad A_\epsilon = 2C_1, \quad A_\mu = 70 \\ \kappa = 0.418, \quad \text{as reported in Chen and Patel [23]} \end{aligned}$$

The velocity components u^i , the turbulent quantities k and ϵ , the time t and the pressure p are made dimensionless in the usual way by the free-stream velocity U_0 , the reference length L and the density ρ .

3.3 Numerical solution

The Reynolds equations and the transport equations for k and ϵ can be rearranged into the following general form

$$g^{11}\partial_1\partial_1\phi + g^{22}\partial_2\partial_2\phi + g^{33}\partial_3\partial_3\phi = \\ 2A\phi\partial_3\phi + 2B\phi\partial_2\phi + D\phi\partial_1\phi + E\phi\partial_t\phi + S\phi \\ \text{where} \quad (53)$$

$$2A\phi = R_{eff}(a\phi u^3/h(3) - g^{1j}\partial_j v_E)$$

$$2B\phi = R_{eff}(a\phi u^2/h(2) - g^{2j}\partial_j v_E)$$

$$D\phi = R_{eff}(a\phi u^1/h(1) - g^{1j}\partial_j v_E)$$

$$E\phi = a\phi R_{eff}$$

$$S\phi = s\phi - 2(g^{12}\partial_1\partial_2\phi + \\ g^{13}\partial_1\partial_3\phi + g^{23}\partial_2\partial_3\phi)$$

$$a\phi = 1 \text{ for } \phi = u^1, u^2, u^3 \text{ and}$$

$$a_k = \sigma_k \quad a_\epsilon = \sigma_\epsilon$$

R_{eff} is the effective Reynolds number and is defined as

$$R_{eff} = 1/v_E$$

Finally, the source terms $s\phi$ are

$$s_{u^i} = R_{eff}[(h_{(m)}^{-1} u^m - g^{mj}\partial_j v_E)Q_{m1}^i u^1 \\ + h_{(i)}g^{ij}\partial_j (p + \frac{2}{3}k)] - \\ (54)$$

$$-h_{(i)}h_{(m)}^{-1}g^{ji}u^m_{,j}\partial_m v_E] - g^{jm}\partial_m Q_{j1}^i u^1 -$$

$$2g^{jm}Q_{m1}^i u^1_{,j} + g^{jm}Q_{j1}^i Q_{nm}^1 u^n + g^{jm}\Gamma_{jm}^1 u^1_{,1}$$

$$s_k = g^{jm}\Gamma_{jm}^1 \partial_1 k - R_{eff}(G - \epsilon)$$

$$s_\epsilon = g^{jm}\Gamma_{jm}^1 \partial_1 \epsilon - R_{eff}(c_{\epsilon 1} \frac{\epsilon}{k} G - c_{\epsilon 2} \frac{\epsilon^2}{k})$$

In most ship flows there is a predominant flow direction usually approximately aligned with the x^1 direction of the grid. Under these circumstances the term $\partial_1\partial_1\phi$ may be neglected and the elliptic equations (53) become parabolic. The advantage of this approximation is that a marching technique may be used in the solution. On the other hand, the fully elliptic equations are more accurate for complex flows, particularly if recirculation of the flow occurs. At SSPA two different programs have been developed: NASELL for the fully elliptic equations and NASPAR for the parabolized equations.

The discretization scheme by Chen & Patel [21] has been adopted with some minor modifications due to the presence

of the term $g^{11}\partial_1\partial_1\phi$. Within each cell the coefficients are treated as constant. The finite-analytical scheme is used in the cross-plane and a second-order central and first-order upwind difference approximation is used for the second and first-order derivative in the x^1 -direction, respectively. In NASELL, this results in an eleven-point discretization formula that takes the following form using compass notations:

$$\phi_P = \sum_{NB} A_{NB} \phi_{NB} + A_t \phi_P^{n-1} - R_\phi \quad (55)$$

$$NB = D, U, N, S, E, W, NE, NW, SE, SW$$

$$A_{NB} = C_{NB}/\beta, \quad A_t = C_P E_\phi / (\beta \Delta t), \quad R_\phi = C_P S_\phi / \beta$$

$$\beta = 1 + C_P(|D_\phi| + 2g^{11} + E_\phi/\epsilon \Delta t)$$

$$C_D = (-D_\phi, 0)_{\max} + g^{11}$$

$$C_U = (D_\phi, 0)_{\max} + g^{11}$$

$$C_S = P_A/g(Bk), \quad C_N = P_A - C_S$$

$$C_W = P_B/g(Ah), \quad C_E = P_B - C_W$$

$$C_{SW} = (1 - P_A - P_B)/g(Ah)/g(Bk)$$

$$C_{SE} = e^{-2Ah} C_{SW}, \quad C_{NW} = e^{-2Bk} C_{SW}$$

$$C_{NE} = e^{-2Ah} C_{NW}$$

$$C_P = h^2(1 - P_A)/f(Ah)/2 =$$

$$k^2(1 - P_B)/f(Bk)/2$$

$$P_A = E_2 e^{Ah+Bk} g(Ah)g(Bk)f(Ah)$$

$$P_B = 1 + (h/k)^2(P_A - 1)f(Bk)/f(Ah)$$

$$E_2 = \sum_{m=1}^{\infty} \frac{-(-1)^m (\lambda_m h)}{[(A_n)^2 + (\lambda_m h)^2]^2 \cos \sqrt{(A^2 + B^2 + \lambda_m^2 k)}}$$

$$\lambda_m h = (m - \frac{1}{2})\pi$$

$$g(x) = 1 + e^{-2x}, f(x) = xg(x)/(1 - e^{-2x})$$

$$h = 1/\sqrt{g_P^{33}}, k = 1/\sqrt{g_P^{22}}, A = h(A_\phi)_P$$

$$B = k(B_\phi)_P \quad (56)$$

In NASPAR, downstream points, index D, are excluded, so the discretization formula contains ten points.

The compass notation and the location of points are described further in Fig 12. The superscript n-1 denotes the previous time level, while the superscript n for the present time level has been left out. The time step is denoted dt. Asymptotic expressions for P_A and P_B are used for large cell Reynolds numbers, following Chen & Patel [21].

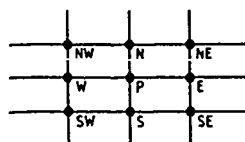
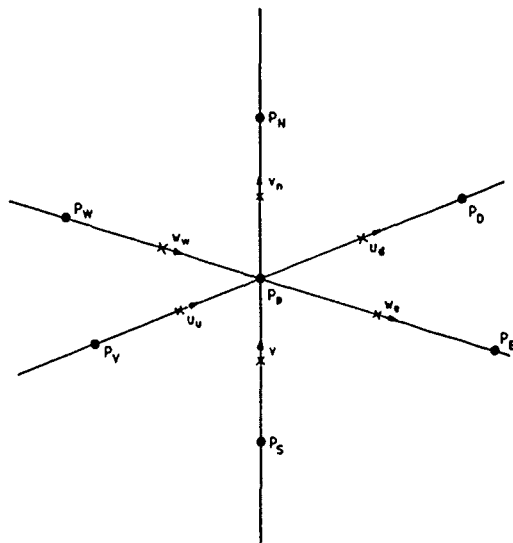


Fig 12 Staggered grid and compass notations

The scheme is not symmetric with respect to the coordinate directions, but treats the x^1 -direction in a simpler way. Therefore special care has to be taken with solutions produced in regions where the velocity vector is at large angles to the x^1 -coordinate line. In the present application to ship stern flows this problem is rarely encountered. Longitudinal vortices occur, but without any larger deviation between the velocity and coordinate-line directions. In very few cases small local separations with reverse flow may occur in the stern-most part. The flow in the transverse plane is very essential for stern flows, since it controls phenomena such as the transverse distribution of fluid and the curvature of the streamlines, which determines the pressure. The more accurate finite-analytical scheme is therefore applied in this plane.

The pressure-velocity coupling is treated with the SIMPLER-algorithm, Patankar [22]. Details from a derivation of the equations for the particular coordinate system and velocity components are given in [6]. The resulting equations are

$$u_d^1 = u_d^{1*} - B_d^1(p_D' - p_P')$$

$$u_n^2 = u_n^{2*} - B_n^2(p_N' - p_P') \quad (57)$$

$$u_e^3 = u_e^{3*} - B_e^3(p_E' - p_P')$$

where the u^{i*} is the solution of the momentum equations using the pressure from the previous time level and B^i is the coefficient for the orthogonal part of the pressure gradient in the i -th momentum equation.

$$B^i = R_{eff} h_{(i)} g^{ii} C_P / \beta \quad (\text{no summation})$$

The compass notation for the location of the velocity components in the staggered grid are shown in Fig 12. The pressure correction p is determined from the equation

$$a_p p_p' = \sum_{NB} a_{NB} p_{NB}' - D^* \quad (58)$$

where

$$a_{NB} = (JB)_{nb}, \quad a_p = \sum_{NB} a_{NB}$$

$$NB = D, U, N, S, E, W$$

$$D^* = [u^{1*} J/h_{(1)}]_u^d + [u^{2*} J/h_{(2)}]_s^n + [u^{3*} J/h_{(3)}]_w^e \quad (59)$$

The pressure, finally, is calculated from the pressure equation:

$$a_p p_p = \sum_{NB} a_{NB} p_{NB} - \hat{D} \quad (60)$$

where

$$\hat{D} = [\hat{u}^1 J/h_{(1)}]_u^d + [\hat{u}^2 J/h_{(2)}]_s^n + [\hat{u}^3 J/h_{(3)}]_w^e \quad (61)$$

The pseudo-velocities \hat{u}^i equal the sum of the terms on the right-hand side of the corresponding momentum equation (55), except for the source term, which is modified in such a way that the orthogonal part of the pressure gradient is taken out:

$$\hat{u}^i = \sum A_{nb} u_{nb}^i + A_t (u^i)_p^{n-1} - \bar{R}_i \quad (62)$$

$nb = u, d, n, s, e, w, ne, nw, se, sw$
and $\bar{R}_i = R_i + B^i \partial_i p$ (no summation)

In NASPAR the pressure correction equation has to be parabolic so the downstream values are taken from a previous time step. This may be expected to slow down convergence, but does not influence the final result.

The methods can handle unsteady flows, but only steady flows have been considered so far. The time history is therefore merely a route to the steady state. Time accuracy is irrelevant and the largest possible time step should be used. The different steps in NASPAR, involved in the calculation of velocities, turbulence quantities and pressure at a time level can be described as follows:

- The momentum, pressure correction and turbulence equations are parabolic and can therefore be solved in one x^1 -constant plane at a time from inlet to outlet plane. This is done as follows:

o The momentum equations (55) are solved using pressure and coefficients based on velocities from previous time level. The algebraic equation systems are solved using a fixed number of line by line sweeps with a tri-diagonal matrix algorithm. Lagging and zero pressure field are used in the first time level.

o The coefficients for the parabolized pressure-correction equation (58) are calculated and the algebraic equations are solved using a fixed number of line by line sweeps with a tri-diagonal matrix algorithm. The velocities are corrected using (57).

o The divergence of the pseudovelocities \hat{u}^i (61) and the coefficients of the pressure equation are stored.

o The transport equations for the turbulent kinetic energy and the rate of turbulent energy dissipation (54) are solved using a fixed number of line by line sweeps with a tri-diagonal matrix algorithm.

- When the marching procedure is completed, i.e. the last x^1 -constant plane is reached, the elliptic pressure equation (60) is solved. Two techniques have been used to solve the resulting algebraic equations. One in which the pressure has been updated in one plane at a time, sweeping upstream from the outlet to the inlet plane. A line by line sweep technique is then used in each plane. The other solution technique is complete line by line sweep with a tri-diagonal matrix algorithm.

- The calculation continues at the next time level and all the above steps are repeated.

In the elliptic program NASELL the marching technique cannot be employed. The steps are then as follows

- Velocities, pressures and turbulence quantities in the solution domain are estimated, usually from a NASPAR solution.

- The momentum equations (55) are solved based on the known pressure using a line by line iteration technique.

- The velocity field is corrected to become divergence free using (57) and (58) Stones strongly implicit algorithm is used.

- The pressure is computed from (60) using the same algorithm.

- The transport equations for k and ϵ are solved using the line by line technique.

- The same steps are repeated at the next time level.

In both methods the solution is assumed converged when the global divergence is below a critical value.

3.4 Boundary Conditions

The calculation domain is shown in Fig 11.

(1) Upstream and initial condition

The profiles of the velocity components u^1 and the turbulent quantities k and ϵ are required at the inflow section. Only standard boundary layer profiles for u^1 , k and ϵ ($u^2 = u^3 = 0$) have been used in the calculations so far. No condition for the pressure is required.

Lagging has been used during the first time step for the velocity and the turbulent quantities and the pressure field is assumed to be constant and equal to zero.

(2) Outflow condition

In the present calculations the outflow section is located in the far wake and a zero pressure gradient condition $\partial_1 p = 0$ is used.

(3) Outer edge

The outer plane may be located far from the body, where the flow is nearly undisturbed and thus

$$p = 0, u^1 = 1, u^3 = 0, \partial_2 k = \partial_2 \epsilon = 0$$

and the normal velocity component u^2 is calculated from the local continuity.

Alternatively, p , u^1 and u^3 may be taken from a potential flow solution.

(4) Symmetry planes

The undisturbed water surface and the centerline plane are treated as symmetry planes, i.e.

$$u^3 = 0, \partial_3 u^1 = \partial_3 u^2 = \partial_3 k = \partial_3 \epsilon = 0$$

(5) Wake center plane

The following conditions have been applied at wake center planes that are degenerated to a single line

$$u^2 = u^3 = 0, \partial_2 u^1 = \partial_2 k = \partial_2 \epsilon = 0$$

otherwise

$$u^2 = 0, \partial_2 u^1 = \partial_2 u^3 = \partial_2 k = \partial_2 \epsilon = 0$$

For the body boundary condition there are two alternatives: either the computational domain may be extended into the viscous sublayer and the no-slip condition applied (this requires a two-layer turbulence model) or the wall law may be used. In the former case the conditions are simply

$$u^1 = u^2 = u^3 = k = 0$$

If wall functions are used a procedure similar to the one of Chen & Patel [21] has been employed. The procedure requires that the two points closest to the wall are located in the logarithmic layer. It is assumed that the velocity at the innermost point is parallel to the wall which yields $u^2 = 0$ at $x^2 = 2$ and that the velocity vector does not rotate between the first and second point in the plane parallel to the wall. The last assumption yields

$$\begin{aligned} \left(\frac{u^1}{q}\right)_{x^2=2} &= \left(\frac{u^1}{q}\right)_{x^2=3} \\ \left(\frac{u^3}{q}\right)_{x^2=2} &= \left(\frac{u^3}{q}\right)_{x^2=3} \end{aligned} \quad (63)$$

where q is the magnitude of the velocity.

The procedure is iterative and starts by calculating the magnitude of the velocity q_2 at $x^2 = 2$ with an assumed skin friction velocity u_τ from the wall law

$$q_2 = \kappa^{-1} \ln y^+_2 + B$$

where $\kappa = 0.42$, $B = 5.45$ and $y^+ = \text{Re } u_\tau y$.

The velocity components at $x^2 = 2$ can then be calculated from equation (63). The components serve as boundary conditions for the momentum equations. q_3 can be calculated from the solution and an updated u_τ can be calculated from the wall law applied at point $x^2 = 3$. The procedure is repeated until convergence.

The boundary conditions at $x^2 = 2$ for the k - and ϵ -equations are

$$k_2 = \frac{u_\tau^2}{\sqrt{c_\mu}}$$

$$\epsilon_2 = \frac{u_\tau^3}{\kappa y_2}$$

3.5 Validation

3.5.1 Grid dependence study

A study was carried out to investigate how the solutions depend on the grid and what the proper number of clusters is in each coordinate direction for ship stern flow calculations. Due to computer limitations the study had to be rather restricted, however.

The systematic variations were made using four different grids to investigate the grid dependence in the three coordinate directions. For all four grids the calculation domain was the same, that is the inlet plane was placed at the midship, $2x/L = 0.0$; the outlet plane at $2x/L = 10$ in the far wake; the outer edge boundary on a circular cylinder located one ship length from the centre line; and the two innermost grid points were located within the logarithmic layer.

In case 1 the grid has a number of clusters equal to $LL \times MM \times NN = 60 \times 19 \times 9$, where LL , MM and NN are the number of clusters in the x^1 , x^2 and x^3 directions respectively.

The number of clusters in the transverse direction x^3 in case 1 might be too small to capture the variation of the cross flow and the rapid pressure change near the region of the keel. Thus in case 2, NN was increased to 15. The grid in case 2 has the number of clusters equal to $LL \times MM \times NN = 60 \times 21 \times 15$.

In case 3, the grid was designed to test the grid dependence in the predominant flow direction x^1 , LL was decreased to 30. The grid had the number of clusters equal to $LL \times MM \times NN = 30 \times 21 \times 15$.

The velocity profiles and the profiles of other physical quantities in the normal direction might be quite influenced by the number of clusters in the normal direction x^2 . Based on the grid of case 3, we increased the number of clusters in the normal direction to $MM = 41$, getting the grid case 4: $LL \times MM \times NN = 30 \times 41 \times 15$.

A summary of the four cases is given in Table 2.

Case	LL	MM	NN	Total number of clusters
1	60	19	9	10 260
2	60	21	15	18 900
3	30	21	15	9 450
4	30	41	15	18 450

Table 2. The four grid variation cases

The calculations for the four cases were carried out using standard boundary layer profiles for u^1 , k and ϵ ($u^2 = u^3 = 0$) as the inlet profiles.

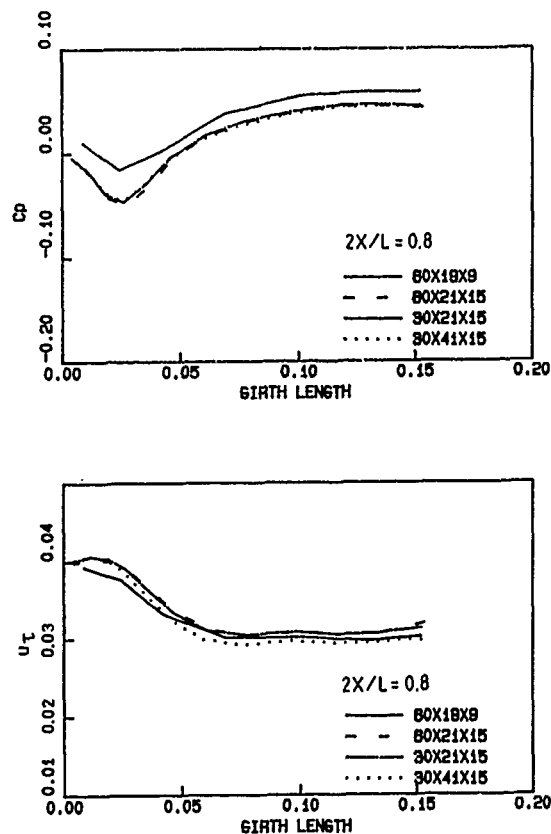


Fig 13 Grid dependence. Distribution of C_p and u_t at $2x/L = 0.8$

The girthwise pressure and friction velocity variations at $2x/L = 0.8$ for the four grids are shown in Fig 13. The influence of the cluster numbers in the transverse direction can clearly be seen from the figure. Comparing the grid case 1, $60 \times 19 \times 9$, with other grids it is obvious that nine clusters are too few to resolve the problem in the transverse direction. The C_p variation is almost the same for the other three grids, since the same number of clusters was used in the transverse direction. Owing to the

limitation of the computer size we did not increase the number of clusters in the transverse direction to more than 15. So it is difficult to say whether or not the solution would be improved if more than 15 clusters were used. This number seems to be the minimum required, however.

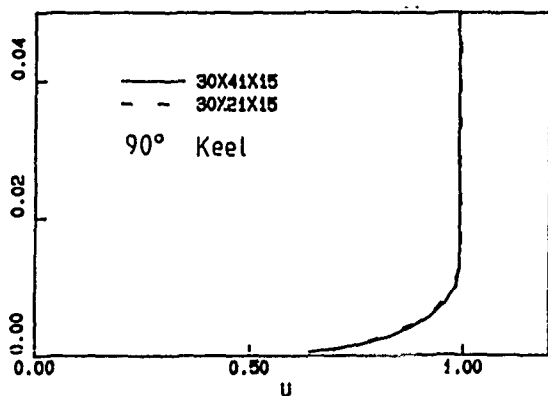
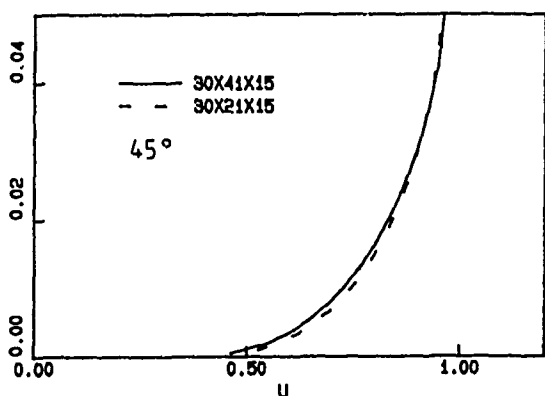
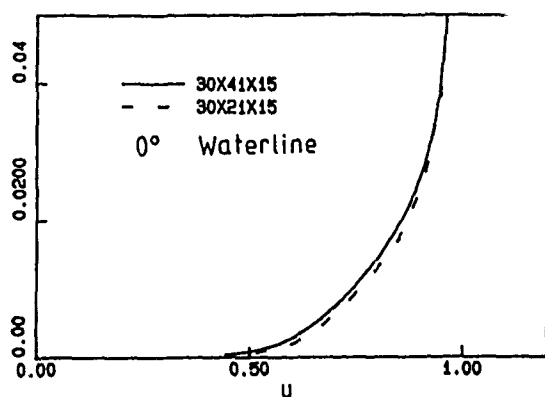
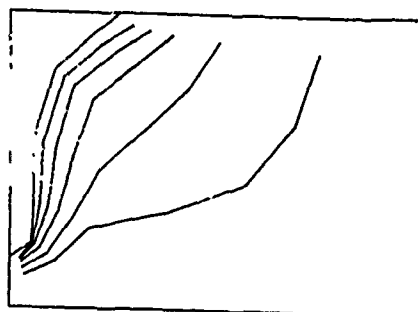
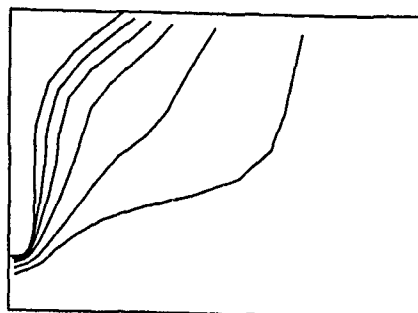


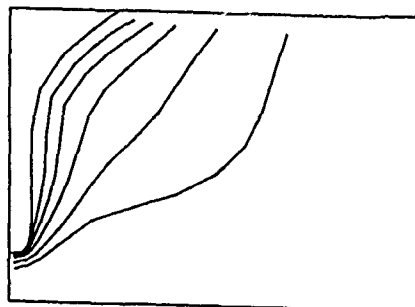
Fig 14 Grid dependence. Velocity profiles at $2x/L = 0.8$ Waterline, mid-girth and keel



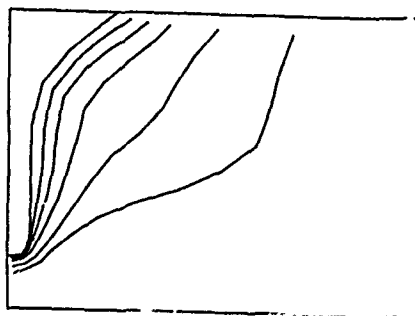
Grid 60 x 19 x 9



Grid 60 x 21 x 15



Grid 31 x 41 x 15



Grid 31 x 21 x 15

Fig 15 Grid dependence. Iso-wakes at $2x/L = 0.9$

The influence of the number of clusters in the normal direction can be tested by comparing the results of grid 3 and grid 4. The total velocity profiles at $2x/L = 0.8$ along the waterline, keel and at the bilge are shown in Fig 14. There are small discrepancies between the results for the two grids. Also in Fig 13 the girthwise u_T variation of the grid $30 \times 41 \times 15$ is only slightly different than the others. This means that there is a very small grid sensitivity in the normal direction. If we look at the isowakes from the results of the four grids at $2x/L \approx 0.91$ shown in Fig 15, they correspond quite well with each other.

The pressure and friction velocity variations along the water line and the keel from the results of grid 2 and 3 are shown in Fig 16. Grids 1 and 4 are not shown in this figure, since their (x^1, x^2) -planes are slightly different.

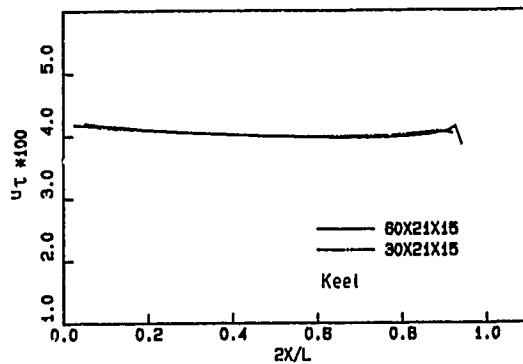
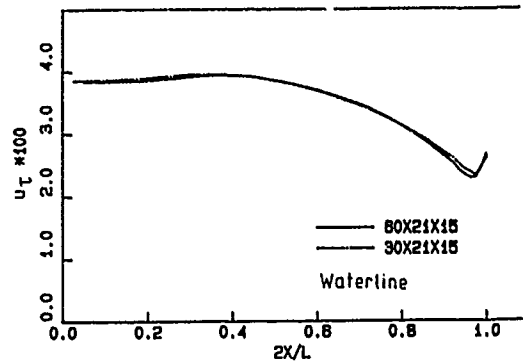
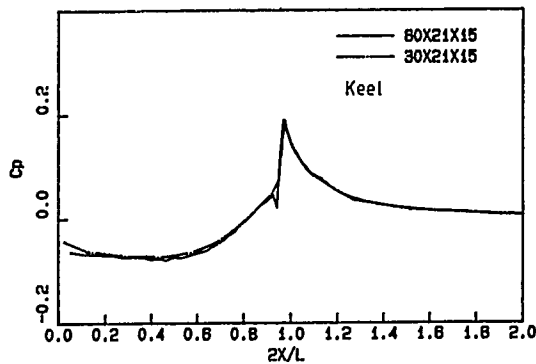
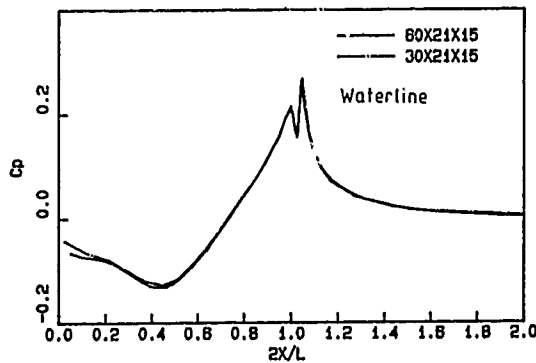


Fig 16 Grid dependence. C_p and u_T along the waterline and keel

The influence of the number of clusters in the x^1 -direction is tested from this comparison. The results are almost the same in the whole region. Increasing the number of clusters from 30 to 60 gives only very small changes. It is therefore concluded that 30 clusters is enough in this direction.

These limited systematic studies of grid-dependence indicate that there is some grid sensitivity in the cross section, but not in the longitudinal direction. Special attention must be paid to regions of abrupt change in geometry, such as the stern region and near the keel. Concentration of clusters to these regions may be an adequate alternative to fine grids. Considering this possibility a grid of $30 \times 20 \times 15$ would be proper for practical use.

3.5.2 Location of the outer edge of the computational domain

As indicated above, the outer edge of the computational domain can be located so far from the body that free stream conditions may be specified. Another alternative is to obtain velocities (except for the normal component) and pressure from a potential flow solution. However, outside the boundary-layer there is a region in which the viscous and inviscid flow interact. To apply the boundary condition here an iterative procedure between the potential and viscous solutions must be introduced. To investigate the location of the region of viscous-inviscid interaction for the SSPA Model a series of calculations was carried out using different locations of the outer edge. The largest distance to the edge measured from the keel is 1.08 (dimensionless by $L/2$) for a grid with $60 \times 19 \times 15$ clusters. The distance was varied by dropping clusters in the normal direction so that the distance was reduced to 0.51, 0.24, 0.11 and 0.05 respectively. The last grid consists of $60 \times 11 \times 15$ clusters. For each calculation the boundary conditions at the outer edge and at the inflow (outside the boundary layer) were calculated from the potential flow solution. The resulting pressure-fields are normalized at a point by subtracting a constant in the following comparisons. Fig 17 shows pressure profiles at four different x-stations, distinguished by symbols. The symbols are placed at the corresponding outer edge. The line types distinguish different calculations, i.e. different locations of the outer edge. The profiles shown in Fig 17 ($N = 14$) are from the region close to the keel where the boundary layer is very thin, and the profiles shown in Fig 17 ($N = 7$) are from bilge region, where the boundary layer is thick. Both figures show that the profiles from the calculation with the outer edge located at 0.05 are different from the others, indicating that the boundary conditions have been applied in the interaction region. Thus, the interaction region extends out to a surface which is located between the outer edges of the calculation domain 0.11 and 0.05.

A calculation of the potential flow and the laminar and thin turbulent boundary-layer normally precedes the stern-flow calculation. The cost for using the potentialflow condition is therefore low. The gain would be a reduction of clusters in the normal direction and a convenient way to handle blockage-effects in tunnel simulations.

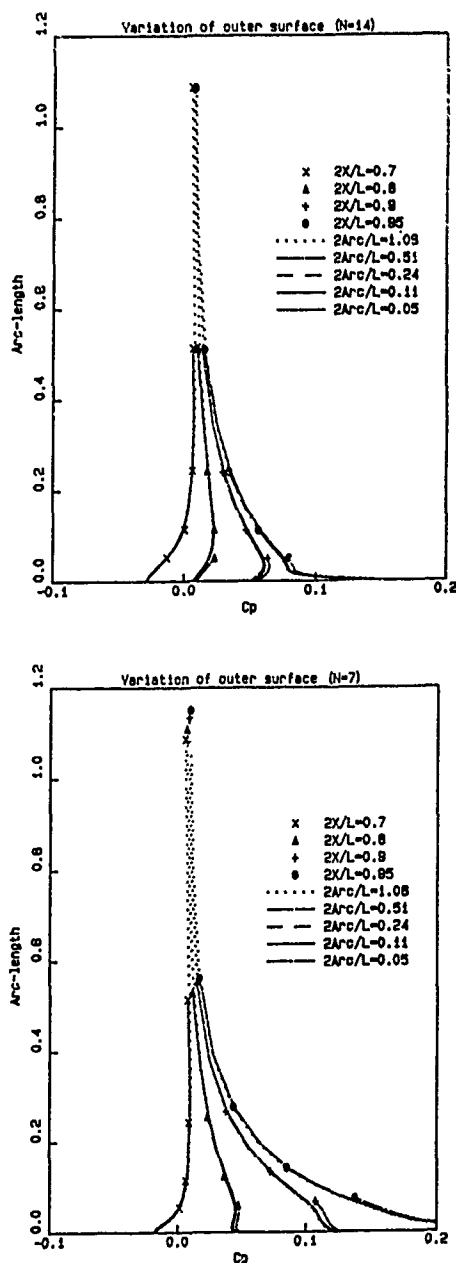


Fig 17 Variation in outer edge location. C_p distribution in the x^2 direction

3.5.3 Comparison between parabolized and elliptic solution

The comparison between the parabolized and elliptic methods was carried out for the SSPA 720 Model with a grid consisting of $60 \times 19 \times 15$ clusters. The inlet profiles were standard boundary-layer profiles, normal and transverse velocity

components were zero and a constant velocity $u^1 =$ was outside the boundary-layer. The solution after one sweep from the partially-parabolic method was used as input for the fully-elliptic algorithm.

The pressure and friction velocity variation in the girthwise direction at $2x/L = 0.8$ are shown in Fig 18. The partially-parabolic and fully-elliptic algorithms give almost the same results. No noticeable difference between the solutions can be seen.

This is not surprising since the only simplification made in the parabolized algorithm, as mentioned before, is that the second derivative ($\partial_1 \partial_1 \phi$) in the predominant direction is neglected. This higher order term is of significant importance only for bluff stern flow with separation, but not for slender sterns, like the one of the SSPA model. Thus the two algorithms should give the same results.

The CPU time for the partially-parabolic algorithm is about 70% of that of the fully elliptic one.

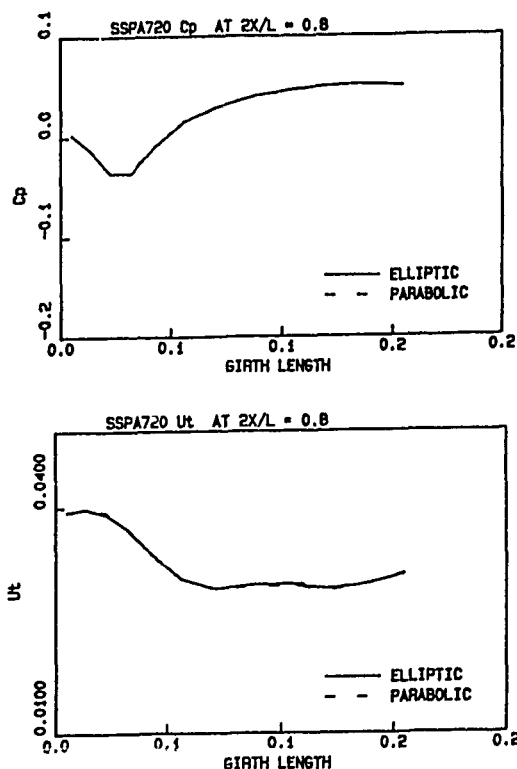


Fig 18 Comparison between results of elliptical parabolized methods

3.5.4 Comparison with experimental data

The grid $60 \times 21 \times 15$ was used to make the final calculations. The inlet profile at midship ($2x/L = 0.0$) for the longitudinal velocity component U within the boundary layer was determined from the wall law using the measured boundary layer thickness and friction velocity from Larsson. The normal component V and the transverse component W were assumed to be zero. Outside the boundary layer the distribution of U was calculated using Hess & Smith's potential flow calculation method. The k and ϵ within the boundary layer were calculated according to Klebanoff & Bradshaw as presented in [24] and set to zero outside.

The calculated results for the Reynolds number $Re = U_\infty L / \nu = 5.0 \times 10^6$, were compared with the experimental data of Larsson [25]. Owing to the different coordinate systems used in the calculations and the experiments it is difficult to make direct comparisons of all quantities of interest. Therefore only limited comparisons are presented here.

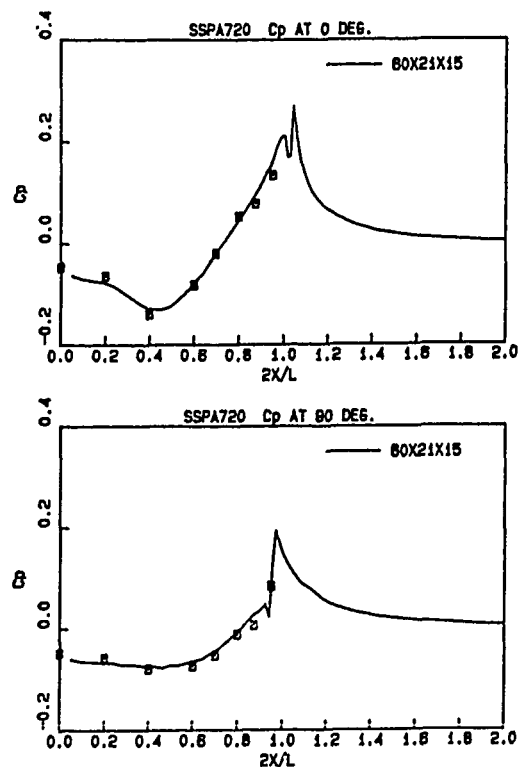


Fig 19 Comparison with experiments. C_p distribution along waterline and keel

The pressure distribution on the hull surface along the water line and the wake centerline as well as along the keel are presented in Fig 19 along with the measurements. The original experimental data of Larsson[25] are subject to windtunnel blockage effects. Corrections have been introduced in the figures using the formula given by Larsson[25], which was formulated after carrying out potential-flow calculations with and without tunnel constraints. Fig 20 shows the girthwise pressure distributions at three stations. It is clear from these figures that the agreement between calculations and measurements is quite good.

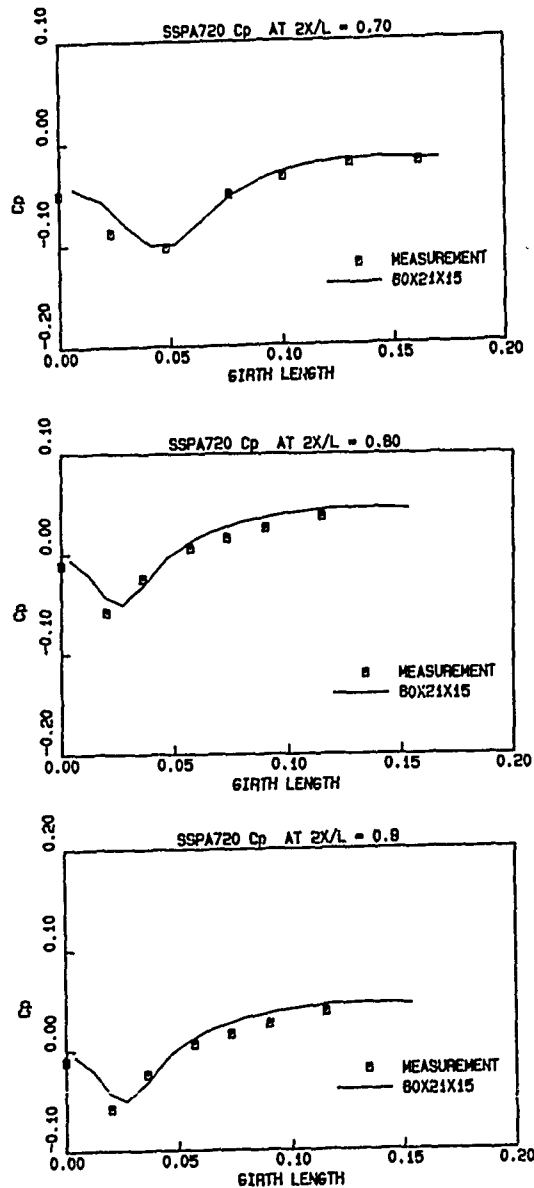


Fig 20 C_p distribution at three stations

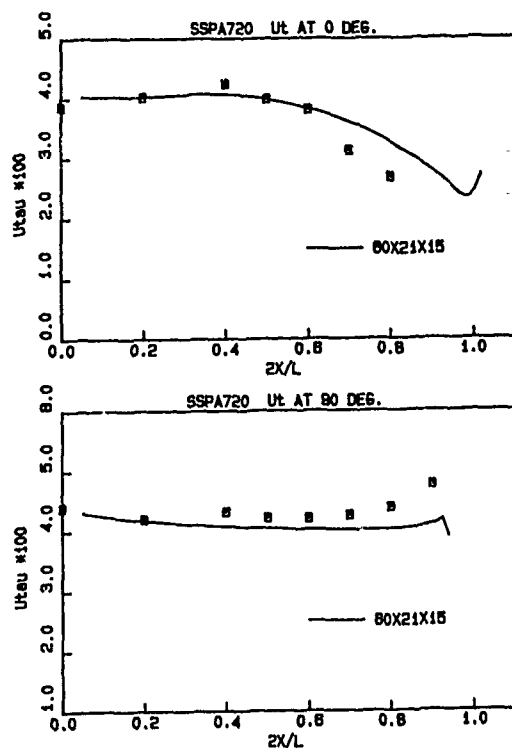
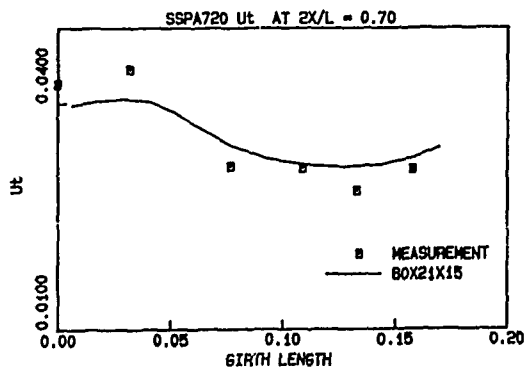


Fig 21 u_{τ} distribution along waterline and keel

Fig 21 shows the calculated wall shear velocity distributions along water line and keel and in Fig 22 the girthwise distributions at three transverse cross sections are given along with the measurements. It can be seen from the figures that in the stern region the calculations overpredict the wall shear velocity along the water line, but underpredict it along the keel. This indicates that the calculated velocity profiles in these regions might differ somewhat from the measured profiles. It is difficult to make comparisons of velocity profiles, owing to the different coordinate systems used in calculations and experiments, as mentioned above.



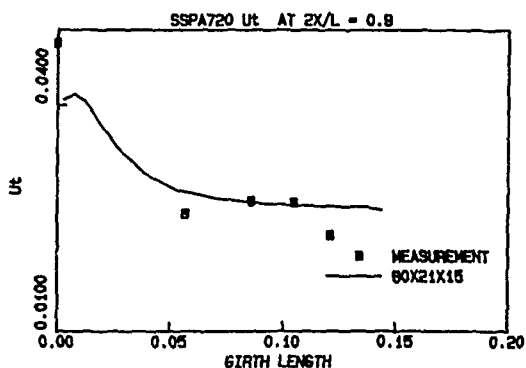
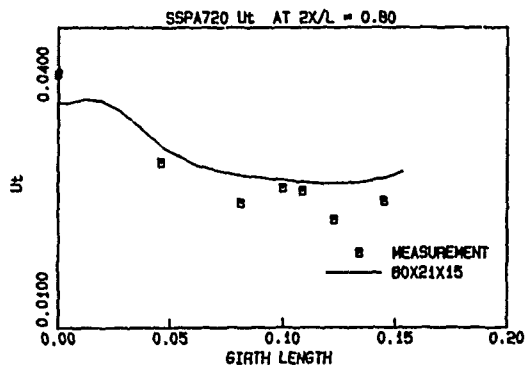


Fig 22 u_t distribution at three stations

Wake contours are given for two stations in Fig 23. A reasonable correspondence with measurements is noted at $2x/L = 0.8$, while at 0.9 the outermost iso-wake is displaced outwards. Close to the keel the boundary layer thickness is over-predicted at both stations. The results were obtained with the wall law as the inner boundary condition. Preliminary results from the latest version of NASPAR, where the wall law is removed, indicate that the prediction of the flow near the keel can be much improved in this way.

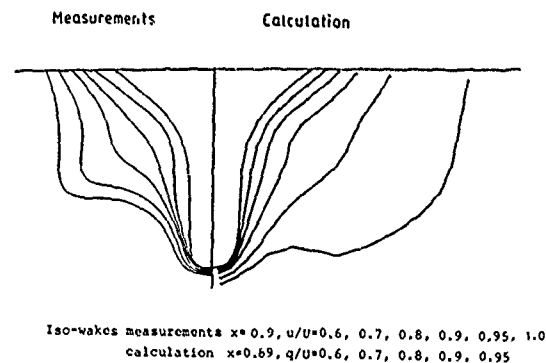
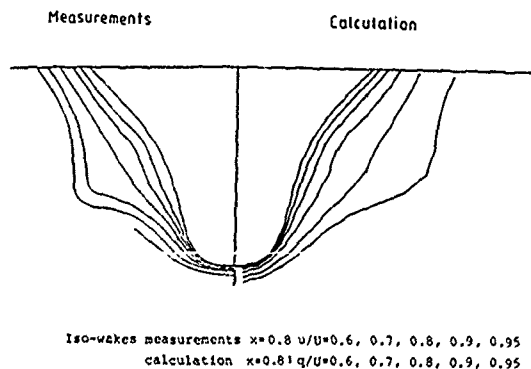


Fig 23 Iso-wakes at two stations

4 FINAL COMMENTS

Methods for computing free surface potential flows as well as complex viscous flows have been presented. The development has taken place over a long period of time and includes five PhD projects. Several computer programs have been written, but they are now combined into one program for the potential flow and one for the Navier-Stokes flow. These flow programs, together with a boundary layer code (for laminar and turbulent flows as well as transition) represent a powerful tool, named SHIPFLOW, for investigating the flow and resistance properties of ships. The SHIPFLOW system is also equipped with state-of-the-art pre- and postprocessors, which makes it easy to use. For preliminary project investigations the system represents an alternative to tank testing, i.e. it could be used as a numerical towing tank. It should be noted that there are several features of the programs which have not been presented in this survey.

Such features are the transom stern option and the sinkage and trim calculation in the potential flow as well as the propeller effect in the Navier-Stokes code. Quite interesting is also the most recent development, in which a mathematical optimization scheme is linked to the flow programs, enabling optimization of hull forms from a resistance point of view to be carried out automatically. Owing to space limitations these features have had to be left out, but they are explained in the references [10], [11] and [19].

Table 1. Grid dependence study.
Wigley hull.

run no	panel arrangement (half range)		extent of the free surface (in half ship length)		F_n	C_w $\times 10^3$
	hull	free surface	x-direction	y-direction		
1	24 x 6	34 x 5	-1.50 to 1.50	0.28	0.266 0.450	1.204 —
2	24 x 6	34 x 5	-1.50 to 1.50	0.775	0.266 0.313	0.598 1.437
3	24 x 6	34 x 10	-1.50 to 1.50	0.775	0.266 0.313 0.350 0.400 0.450	0.785 1.495 1.212 1.849 3.054
4	24 x 6	34 x 15	-1.50 to 1.50	0.775	0.266 0.450	0.847 3.054
5	24 x 6	36 x 10	-1.75 to 1.75	0.775	0.220 0.310 0.350 0.450	0.603 1.551 1.199 3.046
6	22 x 6	36 x 10	-1.50 to 1.50	0.775	0.266 0.450	0.859 2.788
7	22 x 6	32 x 10	-2.00 to 2.00	0.775	0.266 0.450	0.931 3.317
8	22 x 6	40 x 10	-1.50 to 2.50	0.775	0.266 0.450	0.931 3.662
9	22 x 6	40 x 10	-2.00 to 2.00	0.775	0.266 0.450	0.913 (0.966) 3.168 (3.235)

References

1. Larsson, L. (editor), "The SSPA-ITTC Workshop on Ship Boundary Layers 1980", SSPA Publication No. 90 (1981).
2. Larsson, L., & Chang, M.-S., "Numerical Viscous and Wave Resistance Calculations Including Interaction", 13th Symposium on Naval Hydrodynamics, Tokyo (1980).
3. Kim, K.-J. & Larsson, L., "Comparison Between First and Higher Order Methods for Computing the Boundary Layer and Viscous Resistance of Arbitrary Ship Hulls", International Symposium on Resistance and Powering Performance, Shanghai (1989).
4. Broberg, L. & Larsson, L., "A Calculation Method for Ship Stern Flows Using and Analytic Body-Fitted Coordinate System", 15th Symposium on Naval Hydrodynamics, Hamburg (1984).
5. Larsson, L. & Johansson, L.-E., "A Streamline Curvature Method for Computing the Flow near Ship Sterns", 14th Symposium on Naval Hydrodynamics, Ann Arbor (1982).
6. Broberg, L., "Calculations of Partially Parabolic Stern Flows", SSPA Report 2801-2 (1988).
7. Broberg, L., "Numerical Solution of the Time Averaged Navier-Stokes Equations for Ship Stern Flow", SSPA Report No. 2803-1 (1988).

8. Broberg, L., "Numerical Calculation of Ship Stern Flow", Ph.D. Thesis, Chalmers University of Technology (1988).
9. Zhang, D.H., Broberg, L. & Larsson, L., "A Numerical Method for Generating Smooth Body-Fitted Coordinate Systems Suitable for Ship Stern Flow Calculations", International Symposium on Resistance and Powering Performance, Shanghai (1989).
10. Zhang, D.H., "Numerical Prediction of Propeller-Hull Interaction in Viscous Flow", SSPA Report No. 2963-1 (1989).
11. Xia, F., "Calculation of Potential Flow with a Free Surface", SSPA Report No. 2912-1 (1984). See also Report No. 65, Dept of Marine Hydrodynamics, Chalmers University of Technology, Gothenburg, Sweden (1984).
12. Xia, F. & Larsson, L., "A Calculation Method for the Lifting Potential Flow around Yawed, Surface-Piercing 3-D Bodies", 16th Symposium on Naval Hydrodynamics, Berkeley (1986).
13. Xia, F., "Numerical Calculation of Ship Flows with Special Emphasis on the Free Surface Potential Flow", Ph.D. Thesis, Chalmers University of Technology (1986).
14. Xia, F., "A Study on the Numerical Solution of Fully Non-Linear Ship Wave Problems", SSPA Report No. 2912-3 (1986).
15. Ni, S.Y., "A Higher Order Panel Method for Double Model Linearized Free Surface Potential Flows", SSPA Report No. 2912-5 (1987).
16. Ni, S.Y., "A Method for Calculating Non-Linear Free Surface Potential Flows Using Higher Order Panels", SSPA Report No. 2912-6 (1987).
17. Ni, S.Y., "Higher Order Panel Methods for Potential Flows with Linear or Non-Linear Free Surface Boundary Conditions", Ph.D. Thesis, Chalmers University of Technology (1987).
18. Ni, S.Y., Kim, K.-J., Xia, F. & Larsson, L., "A Higher Order Panel Method for Calculating Free Surface Potential Flows with Linear Surface Boundary Conditions", International Symposium on Resistance and Powering Performance, Shanghai (1989).
19. Kim, K.-J., "Ship Flow Calculations and Resistance Minimization", Ph.D. Thesis, Chalmers University of Technology (1989).
20. Hess, J.L., "A Higher Order Panel Method for Three-Dimensional Potential Flow", Douglas Report N 62269-77-C-0437 (1979).
21. Chen, H.C. & Patel, V.C., "Calculation of Trailing Edge, Stern and Wake Flows by a Time-Marching Solution of the Partially Parabolic Equations", Iowa Inst. of Hydraulic Research, Report No. 285 (1985).
22. Patankar, S.V., "Numerical Heat Transfer and Fluid Flows", McGraw Hill (1980).
23. Chen, H.C. & Patel, V.C., "Practical Turbulence Models for Complex Flows Including Separation", AIAA 19th Fluid Dynamics, Plasma Dynamics and Lasers Conference, Honolulu (1987).
24. Markatos, N.C., "The computation of Thick Axisymmetric Boundary Layers and Wakes around Bodies of Revolution", Proc. Inst. Mech. Engineers, Vol 198C (1984).
25. Larsson, L., "Boundary Layer of Ships. Part III: An Experimental Investigation of the Turbulent Boundary Layer on a Ship Model", SSPA, Göteborg, Report No. 46 (1974).
26. Dawson, C.W.: "A Practical Computer Method for Solving Ship-Wave Problems", Proceedings of the Second International Conference on Numerical Ship Hydrodynamics, Berkeley (1977).

DISCUSSION

by C.M. Lee

This is one of the rare papers which cover both inviscid and viscous flows about ships. I believe that a rational approach to ship flow problems should be based on an intelligent combination of potential and viscous flow solutions. This paper apparently shows the efforts in that direction. The authors deserve congratulation for their efforts. Bulbous bows certainly can be cited as one of the useful inventions achieved by the ship hydrodynamic research community. However, we are still uncertain of its effects on flow around ship bows, particularly on the viscous flows. Does a bulbous bow really contribute to reducing the total resistance of a fat ship like a super tanker at low speeds? I think it is about the right time to examine the bow flow for ships with bulbous bow in detail to find the stagnation point on the bow as a function of ship speed in order to develop a correct model for computing ship flows more scientifically.

Author's Reply

We agree with Prof. Lee that a thorough investigation of the flow around the bulb of a fat hull would be a most interesting exercise. Ideally, such an investigation should include an experimental and a numerical part. The experiments should include detailed velocity measurement, such as the ones by Fry and Kim, presented at the 15th Symposium on Naval Hydrodynamics using an LDV, and flow visualization to find the stagnation point. The numerical part should include free surface as well as viscous flow calculations. For this detailed investigation the best approach would be to use a free surface Navier-Stokes method, like the one developed by Prof. Miyata and his co-workers. In such a case the wave breaking, which is likely to be important in this case, could also be considered.

DISCUSSION

by S. Ogiwara

There are several ways in prediction of wave resistance by the panel method, namely, the pressure integral over a hull surface, computation of momentum change and so on. If you have experiences to compare the results between them, especially for the case of the series models with protruding bulb, would you comment about that?

Author's Reply

We have compared the two ways of computing the resistance for several hulls. Results are presented in reference [19] of the paper. For the thin Wigley hull the differences between the two methods are very small, while for the Series 60, $C_B=0.60$ hull, differences of about 10% were noted. The momentum approach yielded smaller values than the higher order pressure integrations. The Series 60 results are in our experience typical for ships of moderate thickness. However, for the very full HSVA tanker we experienced the opposite trend with the momentum results higher than the ones from the pressure integration. The differences were again around 10%.

DISCUSSION

by F. Stern

Fig.17 of your paper is very surprising and contradictory to our work on viscous-inviscid interaction, ie, our work indicates a much greater extent of the interaction. Is the inviscid-flow calculation for the bare or displacement body? If for the former, please comment on the lack of dependency in your solution to the location of the outer boundary even for outer-boundary locations near the boundary-layer edge.

Author's Reply

It should be noted that the distance to the outer edge of the grid is measured from the keel, where the boundary layer is very thin. Fig.A1 may be helpful. We claim in the paper that there is an interaction at $2x/L \approx 0.05$ but not at $2x/L = 0.11$. As appears from Fig.A1, the latter edge is about three times the maximum boundary layer thickness away from the hull. When reading the paper one might get the impression that the $2x/L = 0.11$ grid extends only to the boundary layer edge, in which case the results would have been most questionable.

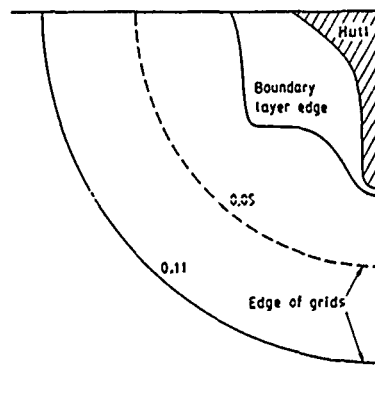


Fig.A1

Numerical Simulation of Viscous Flow around Practical Hull Form

A. Masuko and S. Ogiwara
Ishikawajima-Harima Heavy Industries Co.
Yokohama, Japan

Abstract

This paper deals with numerical simulations of viscous flow around ships having practical hull form under propeller operating condition. The Reynolds-averaged Navier-Stokes equations for three-dimensional flow are discretized by finite-difference approximation and solved with SIMPLE algorithm. The $k-\epsilon$ turbulence model and the standard wall-function are adopted. A propeller is simulated by giving pressure jump at its position.

In order to eliminate skew grid around practical hull form, which violates the computational result, adjustment of grid angle is applied to the grid generated by solving the elliptic partial differential equation. Computational examples for the cargo ship Series-60 model and the practical tanker models under propeller operating condition are presented and compared with experiments.

1. Introduction

In the ship building industries, computational fluid dynamics (CFD) technique is being introduced to design and develop the ship hull form under the concept of "numerical tank". Although quantitative accuracy of the prediction is not sufficient at the present stage, qualitative prediction of flow field can be applied to evaluate the propulsive performance and to design a new hull form. It is considered to become a useful design tool from the point of efficiency and cost for the development.

The authors have been developing the numerical code for calculation of viscous flow¹ around ship hull aiming at the practical use in ship design. The preliminary studies using mathematical ship models² showed that the method has a sufficient robustness of convergence for iteration number and the variation of computational grid. The comparisons between calculation and experiment demonstrated that the method is effective to predict the wake distribution, viscous pressure drag and propeller effects on them, although some discrepancies, for instance in strength of bilge vortices, are found in

detail.

In this paper, this method is applied to simulation of the flow around the practical hull form with complicated shape. Computational grid becomes often extremely skew for such form and calculation by the author's method diverges due to skew grid. In order to stabilize the calculation, the computational grid generated by solving the partial differential equation³ is modified to eliminate the skew grid. The above flow calculation method is applied to the cargo ship Series-60 model and two types of tanker model, one is the ordinary type and the other has the IHI B.O. (Bulbous Open) stern⁴. The calculated wake and pressure are compared with the experiments and propeller/hull interaction is numerically investigated.

2. Calculation method

2.1 Basic equation

The governing time-averaged equations for three-dimensional turbulent flows in Cartesian coordinates are:

$$\frac{\partial}{\partial x_j}(\rho u_j) = 0 \quad (1)$$

$$\frac{\partial}{\partial x_j}(\rho u_i u_j) = -\frac{\partial p}{\partial x_i} + \frac{\partial}{\partial x_j}[\mu_e \left(\frac{\partial u_i}{\partial x_j} + \frac{\partial u_j}{\partial x_i} \right)] \quad (2)$$

where u_i is the velocity component, ρ is the fluid density and p is the pressure. μ_e is the effective turbulent viscosity and given by:

$$\mu_e = \mu + \mu_t = \mu + \frac{C_\mu \rho k^2}{\epsilon} \quad (3)$$

where μ is the laminar viscosity, μ_t is the turbulent viscosity, C_μ is the constant, k is the turbulent kinetic energy and ϵ is the dissipation rate of k .

In the $k-\epsilon$ model of turbulence⁵, k and ϵ are governed by the following equations:

$$\frac{\partial}{\partial x_j}(\rho u_j k) = \frac{\partial}{\partial x_j} \left(\frac{\mu_e}{\sigma_k} \frac{\partial k}{\partial x_j} \right) + P_k - \rho \epsilon \quad (4)$$

$$\frac{\partial}{\partial x_j}(\rho u_j \epsilon) = \frac{\partial}{\partial x_j} \left(\frac{\mu_e}{\sigma_\epsilon} \frac{\partial \epsilon}{\partial x_j} \right) + C_1 P_k \frac{\epsilon}{k} - C_2 \rho \frac{\epsilon^2}{k} \quad (5)$$

where P_k is the production rate of k and given by :

$$P_k = \mu_k \frac{\partial u_i}{\partial x_j} \left(\frac{\partial u_i}{\partial x_j} + \frac{\partial u_j}{\partial x_i} \right) \quad (6)$$

Standard values for the constants in Eqs.(4) and (5) are as follows⁶ :

$$\begin{aligned} C_D &= 0.09 & C_1 &= 1.44 & C_2 &= 1.92 \\ \sigma_k &= 1.0 & \sigma_\epsilon &= 1.3 \end{aligned} \quad (7)$$

Eqs.(1), (2), (4) and (5) are represented in the following general form :

$$\frac{\partial}{\partial x_j} (\rho u_i \phi) = \frac{\partial}{\partial x_j} \left(\Gamma_i \frac{\partial \phi}{\partial x_j} \right) + S_i \quad (8)$$

where ϕ is a general dependent variable, $\phi=(1, u_i, k, \epsilon)$. When a general curvilinear coordinate system $(\xi_1, \xi_2, \xi_3)=(\xi, \eta, \zeta)$ is introduced, Eq.(8) is transformed to the following equation :

$$\begin{aligned} \frac{\partial}{\partial \xi_j} (\rho G_i \phi) &= \frac{\partial}{\partial \xi_j} \left(\Gamma_i \frac{A_{ij}}{J} \frac{\partial \phi}{\partial \xi_j} \right) + S_i' \\ &= \frac{\partial}{\partial \xi_j} \left(\Gamma_i \frac{A_{ij}}{J} \frac{\partial \phi}{\partial \xi_j} \right) + S_i' \end{aligned} \quad (9)$$

where J is the Jacobian of transformation, S_i' is the transformed source term corresponding to Eq.(8), and S_i'' is the modified source term including S_i' and the cross derivatives in the diffusion terms. G_i is the contravariant velocity components without the metric normalization, and defined as follows :

$$G_i = a_{ij} u_j \quad (10)$$

A_{ij} and a_{ij} are the metric coefficients for transformation :

$$a_{ij} = \frac{\partial \xi_i}{\partial x_j} J \quad (11)$$

$$A_{ij} = a_{ik} a_{jk} \quad (12)$$

Production term P_k in general curvilinear coordinate is given by :

$$P_k = \mu_k \frac{a_{ij}}{J} \frac{\partial u_i}{\partial \xi_j} \left(\frac{a_{ij}}{J} \frac{\partial u_i}{\partial \xi_j} + \frac{a_{ji}}{J} \frac{\partial u_j}{\partial \xi_i} \right) \quad (13)$$

Table 1 shows ϕ , Γ_i and S_i' in Eq.(9).

2.2 Finite difference equation

Variables u_i and p are set at staggered location to avoid spurious error⁷. Integrating Eq.(9) over a control volume (Fig.1), the finite difference equations are given as follows :

$$\begin{aligned} &[\rho G_1 \phi]_{\nu} \Delta \xi_2 \Delta \xi_3 + [\rho G_2 \phi]_{s'} \Delta \xi_1 \Delta \xi_3 \\ &+ [\rho G_3 \phi]_{b'} \Delta \xi_1 \Delta \xi_2 \\ &= [\Gamma_i \frac{A_{ij}}{J} \frac{\partial \phi}{\partial \xi_j}]_{\nu} \Delta \xi_2 \Delta \xi_3 + [\Gamma_i \frac{A_{ij}}{J} \frac{\partial \phi}{\partial \xi_j}]_{s'} \Delta \xi_1 \Delta \xi_3 \\ &+ [\Gamma_i \frac{A_{ij}}{J} \frac{\partial \phi}{\partial \xi_j}]_{b'} \Delta \xi_1 \Delta \xi_2 + S_i' J \Delta \xi_1 \Delta \xi_2 \Delta \xi_3 \end{aligned} \quad (14)$$

Further discretization by the Hybrid scheme⁷ leads to the following algebraic equation :

$$\begin{aligned} A_P \phi_P &= A_E \phi_E + A_W \phi_W + A_N \phi_N + A_S \phi_S + A_T \phi_T + A_B \phi_B \\ &+ S_u (\phi_E, \dots, \phi_N, \dots, \text{etc.}) \end{aligned} \quad (15)$$

where S_u denotes a source term which involves the diagonal terms (ϕ_E , etc.) and off-diagonal terms (ϕ_N , etc.). Coefficients $A_E \sim A_P$ are as follows :

$$\begin{aligned} A_E &= [0, D_{1e} - 0.5C_{1e}, -C_{1e}] \\ A_W &= [0, D_{1w} + 0.5C_{1w}, C_{1w}] \\ A_N &= [0, D_{2n} - 0.5C_{2n}, -C_{2n}] \\ A_S &= [0, D_{2s} + 0.5C_{2s}, C_{2s}] \\ A_T &= [0, D_{3t} - 0.5C_{3t}, -C_{3t}] \\ A_B &= [0, D_{3b} + 0.5C_{3b}, C_{3b}] \\ A_P &= A_E + A_W + A_N + A_S + A_T + A_B - S_p \end{aligned} \quad (16)$$

and

$$\begin{aligned} D_1 &= \Gamma_i \frac{A_{1j} \Delta \xi_2 \Delta \xi_3}{J \Delta \xi_1} & C_1 &= \rho G_1 \Delta \xi_2 \Delta \xi_3 \\ D_2 &= \Gamma_i \frac{A_{2j} \Delta \xi_1 \Delta \xi_3}{J \Delta \xi_2} & C_2 &= \rho G_2 \Delta \xi_1 \Delta \xi_3 \\ D_3 &= \Gamma_i \frac{A_{3j} \Delta \xi_1 \Delta \xi_2}{J \Delta \xi_3} & C_3 &= \rho G_3 \Delta \xi_1 \Delta \xi_2 \end{aligned} \quad (17)$$

A sign [, ,] in Eq.(16) means the maximum value in []. S_u and S_p are given by the following equation :

$$S_u + S_p \phi_P = JS_i' \Delta \xi_1 \Delta \xi_2 \Delta \xi_3 \quad (18)$$

The SIMPLE algorithm⁷ links the pressure to the velocity through the pressure-correction equation. When pressure p is supposed to be summation of previous value p' and correction p'' , the pressure-correction equation is obtained from the continuity equation and momentum equations. The discretized pressure-correction equation has the same form of Eq.(15). In the present calculation, off-diagonal terms in S_u of pressure-correction equation are assumed to be small compared with diagonal terms and neglected for saving computing time.

In consequence, the sequence of solving the governing equations is as follows :

- (1) Solve the momentum equations with the initial or previous pressure field to obtain the intermediate velocity components u_i' .
- (2) Calculate the intermediate contravariant velocity components G_i' with u_i' .
- (3) Solve the pressure-correction equation using G_i' .
- (4) Obtain the new values of G_i and u_i which satisfy the continuity equation using pressure

correction.

(5) Correct the pressure by the pressure correction.

(6) Solve the governing equations for k and ϵ .

(7) Iterate steps (1) to (6) until the solution converges.

As a solving algorithm of algebraic equation, a "checker-board" method with SUR (Successive Under Relaxation method)^{1,8} is employed to vectorize the calculation on a supercomputer.

2.3 Computational domain

In this paper, a body fixed Cartesian coordinates are adopted whose origin is settled at the bow on the still waterplane, x -axis in positive direction of uniform flow and z -axis downwards. In the body fitted coordinate system (ξ, η, ζ), constant- ξ planes are chosen as correspond to constant- x planes, η -axis in radial direction from hull surface and ζ -axis in girth direction.

Calculation is carried out in the domain surrounded by the following boundaries (see Fig.2):

Hull Surface	: $x = 0.0 \sim L$ $y = y_0$ $z = 0.0 \sim d$
Center plane	: $y = 0.0$
Water plane	: $z = 0.0$
Upstream boundary	: $x = -0.5L$
Downstream boundary	: $x = 2.0L$
Outer boundary	: $r = 0.5L$

where L , d and y_0 denote ship length, draft and half breadth of a ship respectively.

2.4 Boundary conditions

As for flow field around a fixed model in the uniform flow U , the boundary conditions are given as follows under neglect of free surface disturbance :

On hull surface :

$$u, v, w, k, \epsilon = 0$$

On center plane :

$$v = 0, \frac{\partial u}{\partial n}, \frac{\partial w}{\partial n}, \frac{\partial k}{\partial n}, \frac{\partial \epsilon}{\partial n} = 0$$

(19)

On water plane :

$$w = 0, \frac{\partial u}{\partial n}, \frac{\partial v}{\partial n}, \frac{\partial k}{\partial n}, \frac{\partial \epsilon}{\partial n} = 0$$

At infinity :

$$u = U, v, w, p, k, \epsilon = 0$$

where $\partial/\partial n$ is normal derivative to the boundary surface.

When the finite difference equation is solved in the computational domain shown in Fig.2, the boundary values subscribed with p are determined by the following manners

considering the boundary conditions.

On the hull surface :

$$u_p = 0, v_p = 0, w_p = 0, \\ k_p = 0, \epsilon_p = 0$$

On the center plane :

$$u_p = u_n, v_p = 0, w_p = w_n, \\ k_p = k_n, \epsilon_p = \epsilon_n$$

On the water plane :

$$u_p = u_t, v_p = v_t, w_p = 0, \\ k_p = k_t, \epsilon_p = \epsilon_n$$

(20)

On the upstream boundary :

$$u_p = U, v_p = 0, w_p = 0, \\ p_p = 0, k_p = 0, \epsilon_p = 0$$

On the downstream boundary :

$$u_p = u_d, v_p = v_d, w_p = w_d, \\ p_p = p_d, k_p = k_d, \epsilon_p = \epsilon_d$$

On the outer boundary :

$$u_p = U, v_p = 0, w_p = 0, \\ p_p = 0, k_p = 0, \epsilon_p = 0$$

Since the standard k - ϵ model cannot be applied in the viscous sublayer and transition layer around the hull, the standard wall-functions⁹ are adopted. In the present calculation, the effective exchange coefficient Γ_* is modified at the wall boundary so as to make the velocity profile fit to that from the log-law. Therefore the grid spaces in η -direction adjacent to the hull surface have to be set to satisfy the following criterion.

$$20 < y^+ = \Delta\eta_{in} \rho u^+ / \mu < 100 \quad (21)$$

where $\Delta\eta_{in}$ denotes the minimum spacing of η direction (distance from the hull surface to the nearest grid point) and u^+ means the frictional velocity.

2.5 Propeller model

In order to simulate the propeller effect, the pressure jump model is employed in which a propeller is replaced by a accelerating disc¹. The pressure jump is assumed uniform in the disc and its value is derived from the measured thrust of the self-propulsion test. Fig.3 shows the grid configuration at the section of the propeller. The grid is not fitted to the propeller disc and the uniform pressure jump is applied at the grid points indicated by circles.

Fig.4 shows the pressure distribution calculated by this method for a propeller which is operating in open water. The calculated pressure connects smoothly with the given pressure jump at the propeller position. The velocity at the propeller position and far behind the propeller coincide with the values given by the momentum theory.

3. Computational grid for practical hull form

In the present calculation, the computational grids are generated by solving the elliptic partial differential equations, however these grids do not always suitable for practical hull form. In general, computational grid for viscous flow calculation requires some characteristics such as orthogonality, smoothness, adequate concentration, configuration like streamlines and so on. Above method does not guarantee orthogonality condition of the grid and often provides the extremely skew grid.

The present flow calculation method has a characteristic to be sensitive to the skew of the grid and the convergence of the calculation is violated by highly skew grid. Fig.5 shows an example of the grid configuration including skew grids and the results of flow calculation which is violated by skew grid. The grid in Fig.5 is generated by Kodama's method⁹, which satisfy the above characteristics necessary for computational grid by geometrical manner. This is one of the sophisticated method to generate the grid for arbitrary hull form and the flow calculation method proposed by Kodama gives satisfactory results using these grids. However there are some skew grids near stern region because the grid line is chosen to correspond to the end profile and when these grids are applied to the flow calculation by the present method, the solution diverges. The computational results shown in Fig.5 is the velocity vector near hull surface just before calculation breaks down. It is found that the calculation is getting to be violated around the skew grid. The reason why this breakdown occurs is considered that the all off-diagonal terms are treated as the source term and they are ignored in the pressure-correction equation. Although it is possible to treat these terms more precisely, it brings enormous increase of computational time. Therefore, from the practical point of view, it is much convenient to generate the computational grids which restrain the breakdown of calculation.

In order to restrain this breakdown, computational grid generated by Thompson's method is modified so as to improve the shape of the grid in the transverse plane. For convenience of expression of computational results, constant- ξ stations are chosen to correspond to the transverse section.

3.1 Grid points on the hull surface

The coordinates of grid points on the hull surface are given by interpolation technique from the offset data. The method of a circular arc approximation¹⁰ is adopted for the interpolation. The procedure of the interpolation is as follows (see Fig.6).

First, an angle of tangent of each data point (P_i) is determined as follows. Using four data points near the point P_i , make three circular arcs (arc $P_{i-2}P_{i-1}P_i$, arc $P_{i-1}P_iP_{i+1}$ and arc $P_iP_{i+1}P_{i+2}$). Each arc has an angle

of tangent at point P_i ($(\beta_i)_1$, $(\beta_i)_2$ and $(\beta_i)_3$), and then a mean of these three angles is taken for an angle of tangent of point P_i .

Next make a triangle $P_iP_{i-1}P'$ using a segment P_iP_{i-1} , and tangents at P_i and P_{i-1} , where P' is a cross point of two tangents. An interpolated point Q is taken at a inner center of this triangle.

By treating an interpolated point as a new data point, these process are repeated until a length of the segment becomes sufficiently short. These process are carried out along the waterlines and frame lines. The coordinates of grid points on the hull surface are determined by choosing a point from these sequential points.

3.2 Generation of grid

The coordinates of grid points in the computational domain are generated by Thompson's method. They are solutions of the following Poisson equation :

$$\frac{\partial^2 \xi_i}{\partial x_i^2} = P_i \quad (22)$$

Exchanging the independent variables and the dependent variables in Eq.(22), following partial differential equation is obtained :

$$A_i \frac{\partial^2 x_i}{\partial \xi_i \partial \xi_i} + J^2 P_i \frac{\partial x_i}{\partial \xi_i} = 0 \quad (23)$$

It is not necessary to solve the equation for x_i in Eq.(23), because the constant- ξ stations are chosen to correspond to the transverse sections.

This method has some problems when generating grid for arbitrary hull form. Since this method does not guarantee the orthogonality of the grid, extremely skew grid is often generated depending on the hull form. When sufficient number of grid points cannot be taken for the limitation of computer storage, grid lines often break into the ship hull. Fig.7(a) shows a typical example of such case. This is the grid at the section of bulbous bow which has extremely convex configuration. At the side of bulb, highly skew grids are found and some grid lines break into the bulb.

Since the stability of the solution by the present flow calculation method is very sensitive to the skew of the grid, a method of grid modification which adjusts the angle between grid lines is adopted. Fig.8 shows the way of this adjustment. The two segments on constant- ξ lines which close to the hull surface are adjusted normal to the constant- η lines. For the other segments on constant- ξ lines, the direction is adjusted to the angle between 45 deg. and 135 deg. When this adjustment is carried out directory, the change of the grid direction is too large and the computational grid breaks down. So the above adjustment is carried out iteratively using relaxation method. After obtaining constant- η coordinates, smoothing of constant- η line is carried out by Lagrange

interpolation.

At the same time, the minimum spacing of the grid $\Delta\eta_{n,n}$ is set constant and determined using C_f of the Prandtl-Schlichting's formula at the aft end of equivalent flat plate as follows :

$$\Delta\eta_{n,n} = \frac{30\mu}{\rho u^*} = \frac{30\mu}{\sqrt{\tau_w} \rho} \quad (24)$$

$$\begin{aligned} \tau_w &= \frac{1}{2} \rho u^2 C_f \\ &= \frac{1}{2} \rho u^2 0.455 (\log R_N)^{-2.58} \left(1 - \frac{1.12}{\log R_N}\right) \end{aligned} \quad (25)$$

Fig.7(b) shows the modified result of Fig.7(a) by this method. Fig.9 and Fig.10 show the computational grids for tanker forms with normal stern and IHI B.O. stern respectively. In every case, orthogonality condition is almost satisfied.

4. Convergence property

Convergence histories of pressure at three monitoring points, midship, after perpendicular (A.P.) and in the wake, close to the keel line, are shown in Fig.11 in the case of Series-60 model ($C_b=0.6$) at the Reynolds number based on ship length $R_N=9.22 \times 10^6$. The number of grid points is $94 \times 25 \times 21$ and the iterative calculation is repeated 300 times. The calculation seems to converge at about 100 times.

Fig.12 shows the convergence histories of variables u , w , p , k and ϵ near the keel line at A.P. The values are non-dimensionalized by the differences between maximum and minimum values of each variable. Convergence of variables excepting pressure is considerably slow. This may be attributed to the lack of grid smoothness.

Fig.13 shows the variation of mass-imbalance with the number of iteration. SSUM means a sum of mass-imbalance for all the grid points normalized by inlet mass flow rate. SSUM decreases rapidly with the number of iteration and this verifies that the equation of continuity is satisfied.

From the above results, 200 iteration steps is chosen for practical use. It takes about 20 minutes of CPU time to calculate 200 steps using the supercomputer FACOM VP-50. In the following calculations, the iteration is stopped at 200 steps in every case.

5. Computational results and discussions

5.1 Wigley model

The Wigley hull is defined by the following parabolic equation :

$$y_0 = \frac{B}{2} \left[1 - \left(\frac{2x}{L} - 1 \right)^2 \right] \left[1 - \left(\frac{z}{d} \right)^2 \right] \quad (26)$$

where B is the ship breadth.

Calculations are carried out using $93 \times 25 \times 19$ grid with $L=6.0\text{m}$, $B=0.6\text{m}$, $d=0.375\text{m}$, $U=0.85\text{m/s}$ and $R_N=4.5 \times 10^6$, and compared with two kinds of

experimental data. One is obtained in the towing tank of Ishikawajima-Harima Heavy Industries Co., Ltd. (IHI) with 6m length model, where resistance and hull surface pressure are measured at $R_N=4.2 \times 10^6$, and the other data is from the wind tunnel test by Sarda¹¹ using a double model at $R_N=4.5 \times 10^6$.

Fig.14 shows the iso-wake contours at the aft end station compared with Sarda's results. The calculated result shows qualitative agreement with the experimental results, however, it is a little diffusive due to the numerical diffusion of the Hybrid scheme.

Fig.15 shows the comparison of hull surface pressure distributions, and reveals good agreement between the calculation and experiment. In this figure, inviscid results obtained by Hess-Smith method are also shown. The results of the present method agree with the inviscid results in the fore part and the displacement effect of boundary layer is simulated near the aft end.

Fig.16 shows the comparison of the local skin-friction coefficient C_f . Calculated skin-friction is given by the following equation :

$$\begin{aligned} C_f &= \frac{\tau_w}{\rho U^2 / 2} \\ &= \frac{1}{U^2 / 2} \frac{\kappa q C_D^{1/4} k^{1/2}}{\ln(E \rho C_D^{1/4} k^{1/2} \Delta\eta_{n,n} / \mu)} \end{aligned} \quad (27)$$

where κ is Karman constant and E is constant. The figure shows good agreement between the calculation and experiment except slight discrepancy at the station $x=5.9\text{m}$ close to the aft end.

Agreement of the turbulent kinetic energy between calculation and experiment is poor as shown in Fig.17. Calculation does not simulate the sharp peak of the turbulent kinetic energy in the region close to the hull near the after end. As the same tendency appears in Sarda's calculation which also adopts $k-\epsilon$ model, this seems to be due to the defect of the turbulence model.

The pressure resistance and the frictional resistance are calculated by integrating the hull surface pressure and local skin-friction respectively on the hull surface. The calculated results are as follows compared with the experimental values given by three dimensional analysis of the resistance tests.

Calculation		Experiment	
Total resist. (r_T)	12.6×10^{-3}	Total resist. (r_T)	13.2×10^{-3}
Fric. resist. (r_F)	10.8×10^{-3}	Fric. resist. (r_{FA})	12.7×10^{-3} (Schoenherr)
Press. resist. (r_P)	1.8×10^{-3}	Residual resist. (r_R)	0.5×10^{-3}

($R_N=4.2 \times 10^6$ $F_N=0.1043$)

where $r=R/\rho U^2 \nabla^{2/3}$, R is the resistance and ∇ is the displacement of the model. Calculated value of the pressure resistance is larger than residual resistance which does not include wave resistance because of very low Froude number. This may result from the fact that the calculated pressure of after part is a little lower than measured one as shown in Fig.15 observing in detail. However the order of the total resistance comparatively agrees with experiment.

5.2 Series-60 model ($C_b=0.6$)

The first application to a practical hull form is made for prediction of flow field around Series-60 model ($C_b=0.6$) under propeller operation. The calculation is carried out with $L=7.0m$ and $U=1.5m/s$, corresponding Reynolds number is $R_N=9.22 \times 10^6$. In the calculation of propeller operating condition, pressure jump $\Delta p=412.47N/m^2$ which is equivalent to the measured thrust $T=22.119N$ (propeller diameter is .2613 m) is set on the propeller disc. Total number of grid points is $94 \times 25 \times 21$.

Fig.18 shows the hull surface pressure distribution, where measured data is from VEB towing tank using 5m model at $U=1.54m/s$ ($R_N=7.7 \times 10^6$)¹². Calculated and measured patterns of pressure contour without propeller resemble each other. In the propeller operating condition, suction effect of propeller is appeared in the stern region.

Fig.19 shows a comparison of wake patterns at three different transverse sections. Experimental data is obtained in IHI towing tank using 7m model. The unit of calculated vector is twice of the measured one in order to make clear the direction of the flow. The calculated contour of $w_x=0.1$ is a little diffusive compared with the measured one, however, the pattern of the iso-wake contour is well simulated as a whole.

Fig.20 shows the effect of propeller on the iso-wake contours. It can be seen that the effect of propeller is restricted in the propeller disc. The measured iso-wake contours with propeller at A.P. section (just abaft the propeller) show the asymmetrical feature about center line due to the rotating flow (Fig.21). As the present method does not deal with the rotating flow, calculated results are compared with the measured contour taking the mean of the contours in starboard and port side. It is found that the present method can simulate well the propeller effect on the contour.

5.3 Practical tanker form

The second example of the application to practical hull form is the simulation of the flow around two kinds of tanker form shown in Fig.10 and Fig.11.

Fig.22 shows the comparison of iso-wake contour of ordinary tanker form (Fig.10) at propeller position in towing condition at $R_N=7.8 \times 10^6$. The vortical motion can be simulated, however, it is smaller than that

of experiment and an island-like contour of vortical motion is not found in the computed results.

The flow around tanker form with IHI B.O. stern (Fig.11) is calculated at $R_N=4.94 \times 10^6$. IHI B.O. stern is developed aiming at both merits of wake gain by bulbous stern and low thrust deduction by open stern. The configuration of B.O. stern is so complicated that the flow calculation does not succeed by the ordinary method of grid generation. However the present method of grid modification makes the flow calculation possible.

Fig.23 and Fig.24 are the comparison of hull surface pressure distribution and wake pattern in towing condition respectively. Calculated pressure distribution agrees well with the experiment except near the stern end where calculation gives lower pressure. B.O. stern gives uniform wake in propeller disc compared with ordinary stern shape. Present calculation simulates this feature of wake pattern, however the correspondence with measured results is not good because the bilge vortex is not simulated well. In order to improve the accuracy of the prediction, further examinations are necessary for finite-difference scheme, grid generation, adoption of wall-function, turbulence model and so forth.

Fig.25 shows the velocity vectors near the hull surface for both cases of with and without propeller. In the propeller operating condition, the pressure jump of $691.67N/m^2$ which corresponds to measured thrust of 17.6N is set on the propeller disc of diameter 0.18m. Applying this propeller model, the accelerated flow afore and abaft the propeller can be simulated as well as decelerated flow just above the propeller. The present method predicts the boundary layer flow into the propeller around such a complicated stern form.

6. Conclusions

Present studies are summarized as follows :

(1) In the present flow calculation method, the off-diagonal terms in source term in pressure-correction equation are ignored as small quantities in order to save the computational time. It is found, however, that this leads to the breakdown of computational results when there are skew grids in computational domain around practical hull form.

(2) In order to stabilize the calculation for practical hull form without increase of computational time, improvement of the grid shape generated by solving the elliptic partial differential equation is carried out by adjustment of grid angle.

(3) Using this grid, the calculations of viscous flow around practical hull form (Series-60 and tanker forms) under propeller operating condition are carried out and the

results are compared with experimental results. This method is applicable for hull form examination at the initial design stage. In order to improve the accuracy of the prediction, further examinations are necessary for finite-difference scheme, grid generation, turbulence model, adoption of wall-function and so forth.

The final goal of the present study is to build a design code which can evaluate self propulsion factor of a ship taking account rudder effect.

Acknowledgements

The authors are indebted to Dr.Y.Kodama of Ship Research Institute for providing us the computational grid of Series-60 generated by his own method. They also express their thanks to Dr.Y.Ando, Mr.M.Kawai, Dr.T.Tsutsumi, Dr.R.Sato and Mr.Y.Shirose of Ishikawajima-Harima Heavy Industries Co.,Ltd. for their support and advice, and all the staff of IHI towing tank for their help with the experiments.

References

1. Ando,Y., Kawai,M., Sato,Y. and Toh,H., "Prediction of three-dimensional turbulent flows in a dump diffuser", AIAA 26th Aerospace Sciences Meeting, Reno, Nevada, (1988).
2. Masuko,A., Shirose,Y. and Ishida,S., "Numerical simulations of the viscous flow around ships including bilge vortices", Proceedings of the 17th ONR Symposium on Naval Hydrodynamics, The Hague, (1988).
3. Thompson,J.F., Warsi,Z.U.A. and Mastin,C.W., "Numerical grid generation, foundation and applications", North-Holland, New York, Amsterdam and Oxford, (1985).
4. Koshiya,Y. and Mori,M., "How to design the stern form"(in Japanese), Ishikawajima-Harima Engineering Review, Vol.27, No.5, pp288-pp293, (1987).
5. Launder,B.E. and Spalding,D.B., "Mathematical models of turbulence", Academic Press, London and New York, (1972).
6. Launder,B.E. and Spalding,D.B., "The numerical computation of turbulent flow", Computer Method in Applied Mechanics and Engineering, Vol.3, (1974).
7. Patanker,S.V., "Numerical heat transfer and fluid flow", Hemisphere Publishing, (1980).
8. Orli,S. and Haraguchi,M., "Efficient Implementation of a fluid simulation algorithm on the FACOM-VP 100/200"(in Japanese), The 28th National Convention of ISPJ, Information Processing Society of Japan, (1984).

9. Kodama,Y., "Three-dimensional grid generation around a ship hull using the geometrical method", Journal of the Society of Naval Architects of Japan, Vol.164, pp.9-16, (1988).

10. Oki,Y., Ochi,M. and Ohgane,E., "Ship lines design system"(in Japanese), Ishikawajima-Harima Engineering Review, Vol.21, No.5, pp.422-427, (1981).

11. Sarda,O.P., "Turbulent flow past ship hulls -- An experimental and computational study --", Ph.D. Thesis, the University of Iowa, (1986).

12. "Flow examination on a model of Series 60 with $C_b=0.60$ Model No.675", VEB Report, (1983, Applied to the ITTC Cooperated Experimental Program).

Table 1 Effective exchange coefficients and source terms of equation (9)

ϕ	Γ_ϕ	S_ϕ
$\frac{1}{t}$	0	0
u_i	μ_0	$-\frac{a_i}{J\partial\xi_j} \frac{\partial p}{\partial\xi_j} + \frac{a_i}{J\partial\xi_j} \frac{\partial \mu_0}{\partial\xi_j} \frac{a_j}{J\partial\xi_i} \frac{\partial u_k}{\partial\xi_k}$ $+ \sum_k \frac{\partial}{\partial\xi_j} \frac{\mu_0 A_{jk}}{J\partial\xi_k} \frac{\partial u_i}{\partial\xi_k}$
k	$\frac{\mu_0}{\sigma_k}$	$P_k - \rho \epsilon + \sum_k \frac{\partial}{\partial\xi_j} \frac{\mu_0 A_{jk}}{\sigma_k J\partial\xi_k} \frac{\partial k}{\partial\xi_j}$
ϵ	$\frac{\mu_0}{\sigma_\epsilon}$	$C_1 P_k \frac{\epsilon}{k} - C_2 \rho \frac{\epsilon^2}{k}$ $+ \sum_k \frac{\partial}{\partial\xi_j} \frac{\mu_0 A_{jk}}{\sigma_\epsilon J\partial\xi_k} \frac{\partial \epsilon}{\partial\xi_j}$

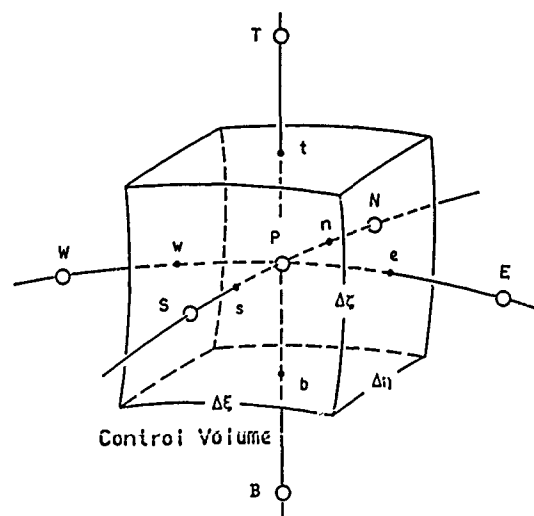


Fig.1 Grid points and a control volume

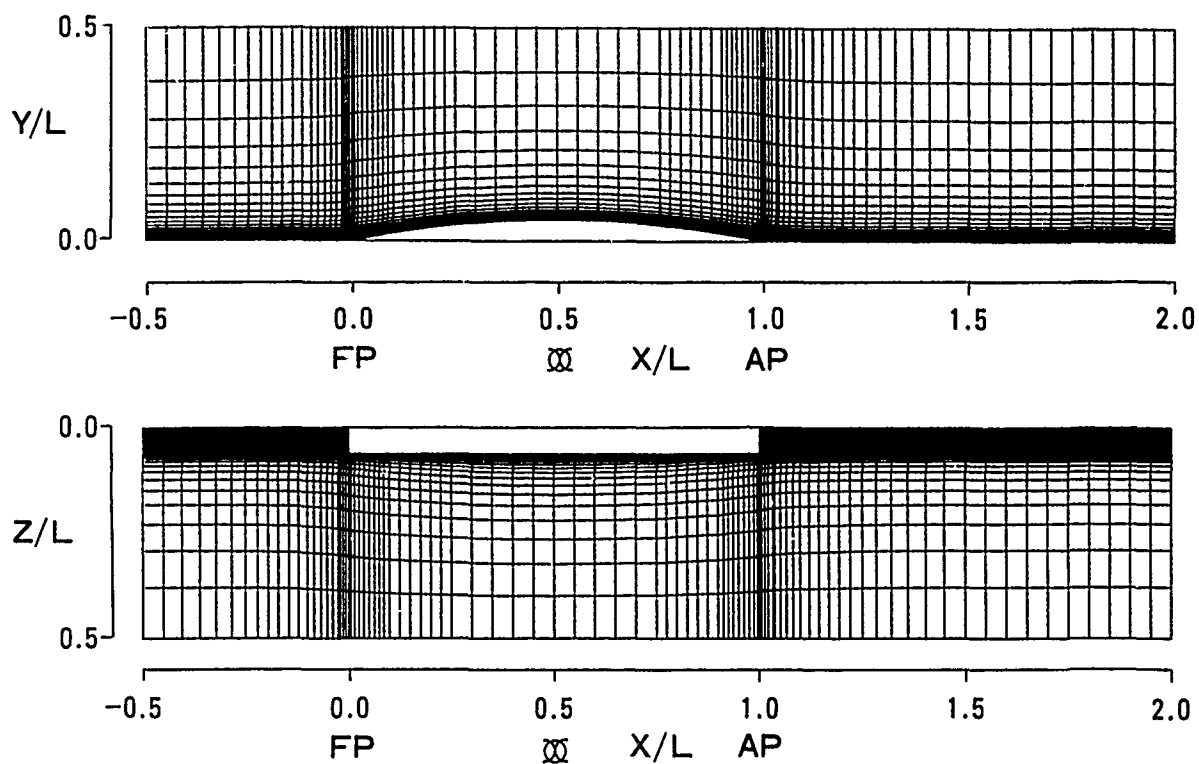
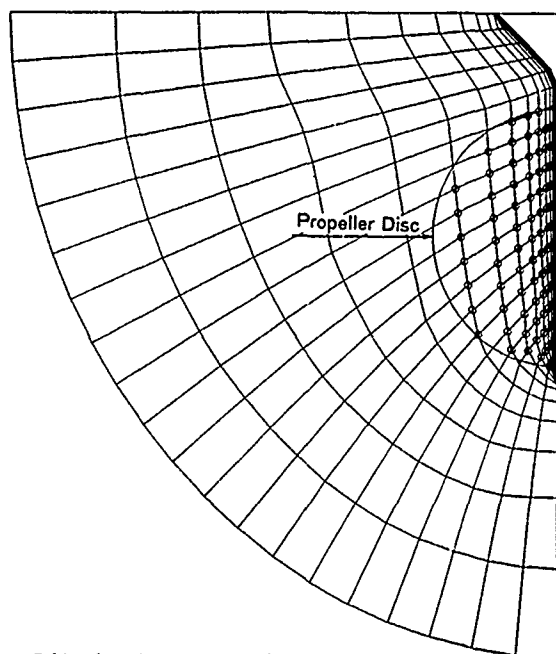


Fig.2 Computational domain and grid configuration



○ Grid point where pressure jump is imposed

Fig.3 Grid configuration at the propeller position

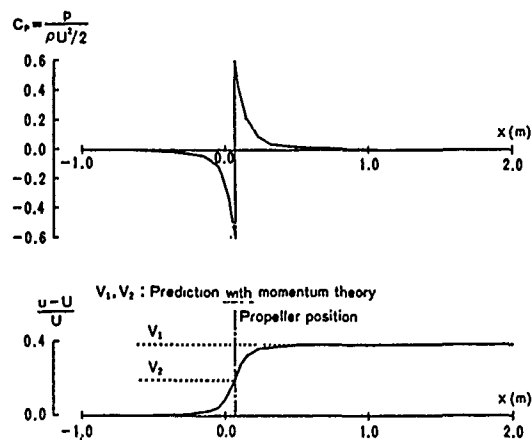


Fig.4 Computational examination of pressure jump model

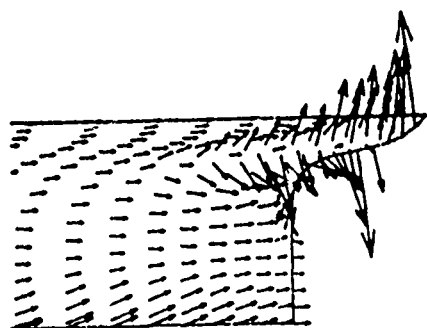
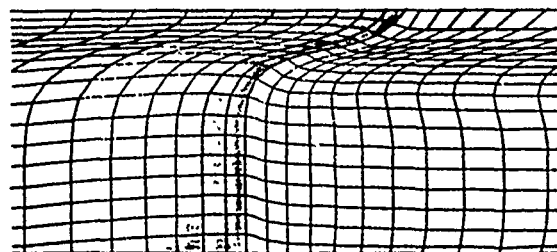
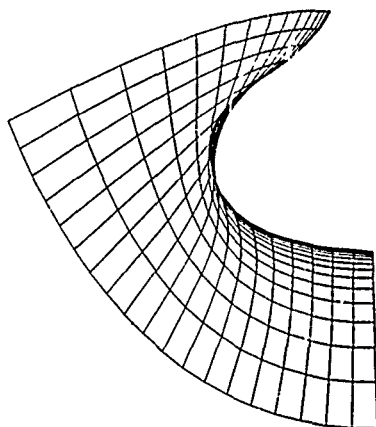
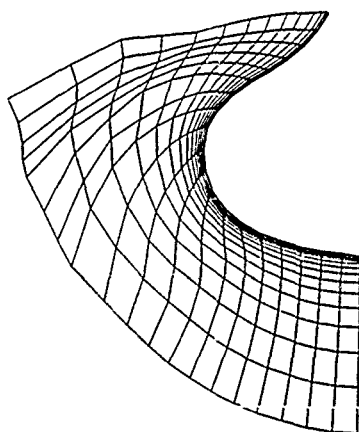


Fig.5 Influence of skew grid



(a) Before modification



(b) After modification

Fig.7 Modification of the grid

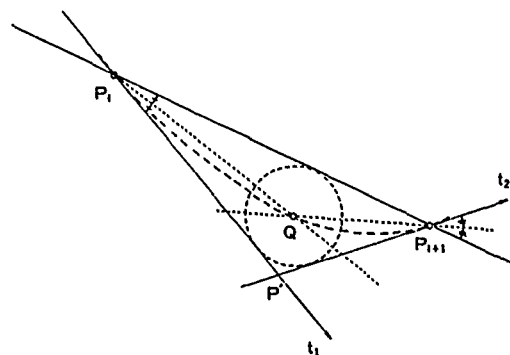
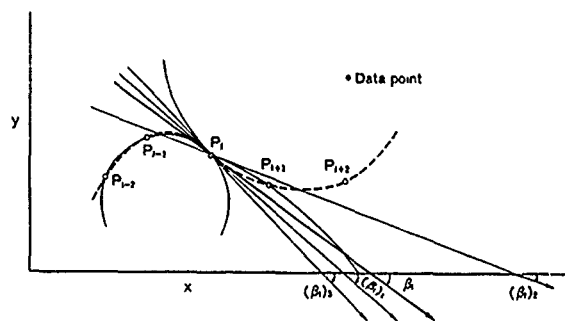
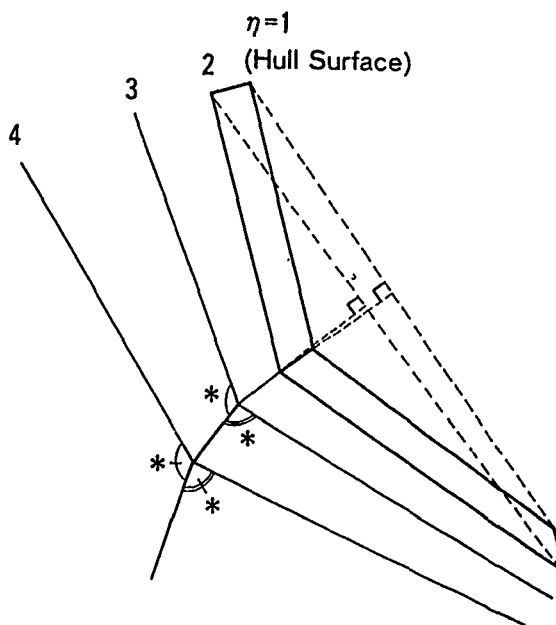
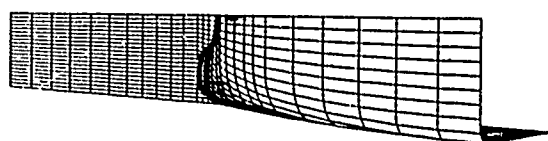


Fig.6 Generation of interpolated point

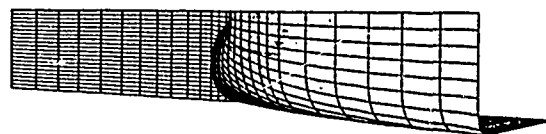


* : Angle adjusted to be between $45^\circ \sim 135^\circ$

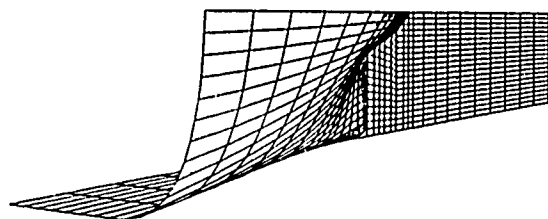
Fig.8 Adjustment of grid angle



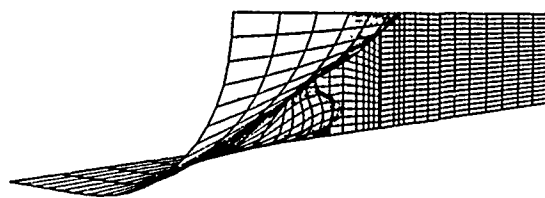
Bow Part



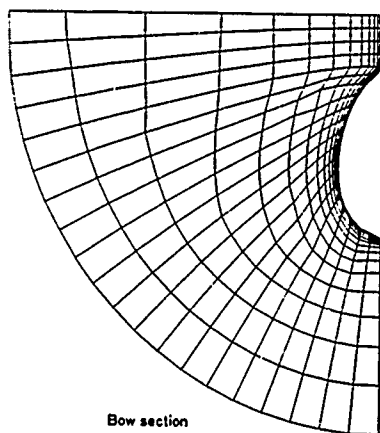
Bow Part



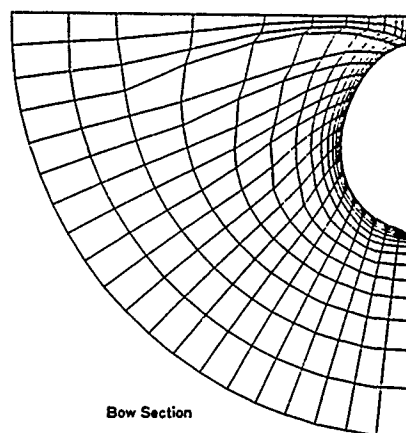
Stern Part



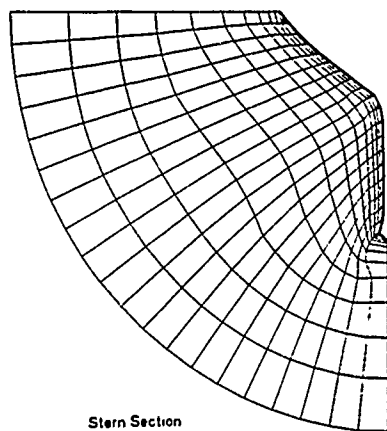
Stern Part



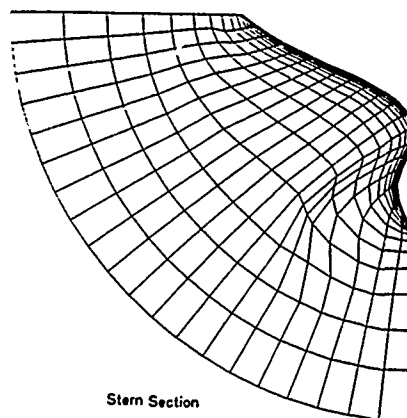
Bow section



Bow Section



Stern Section



Stern Section

Fig.9 Generated computational grid
(Tanker form with normal stern)

Fig.10 Generated computational grid
(Tanker form with IHI B.O. Stern)

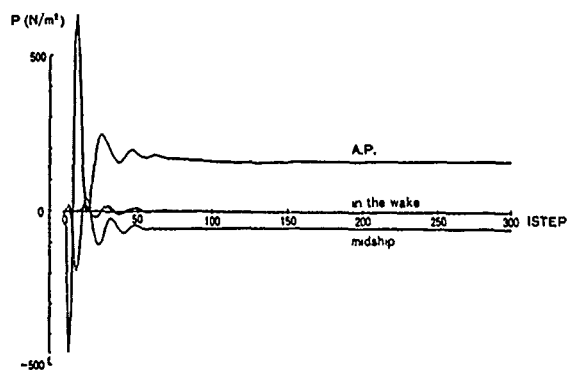


Fig.11 Convergence history of pressure

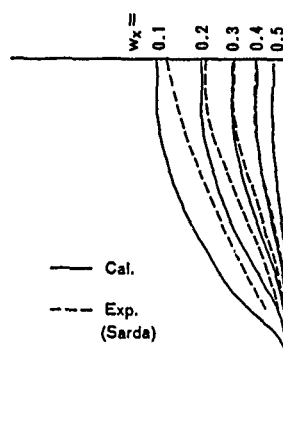


Fig.14 Calculated and measured wake pattern
(Wigley model, $R_N=4.5 \times 10^6$)

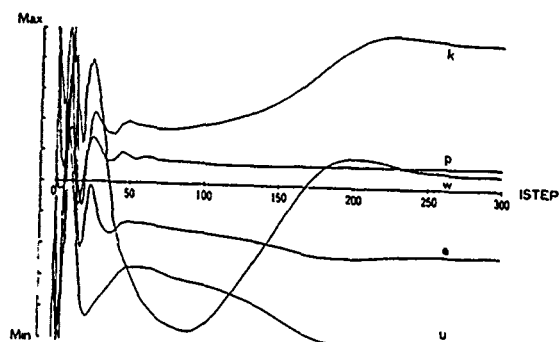


Fig.12 Convergence history of u, w, p, k, ϵ (at A.P.)

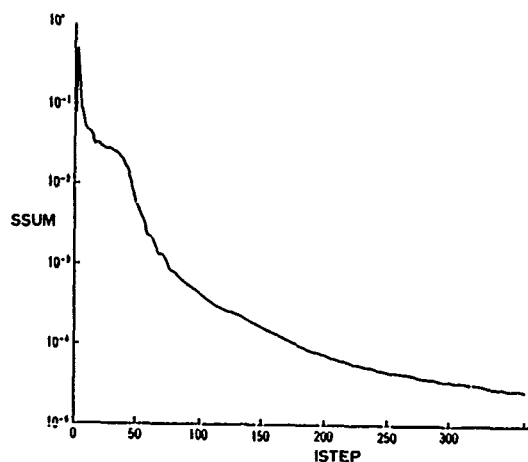


Fig.13 Convergence history of mass-imbalance

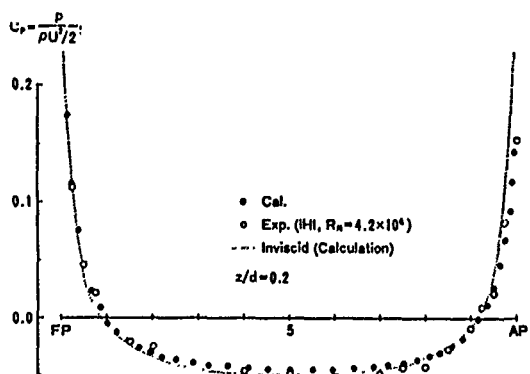


Fig.15 Hull surface pressure distribution
(Wigley model, $R_N=4.5 \times 10^6$)

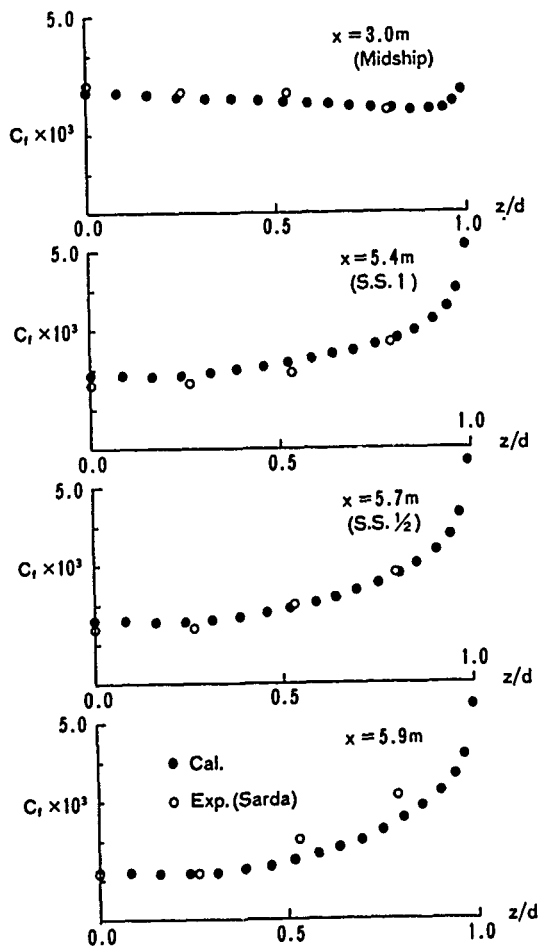
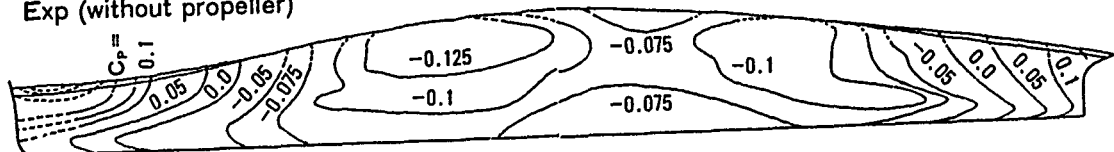
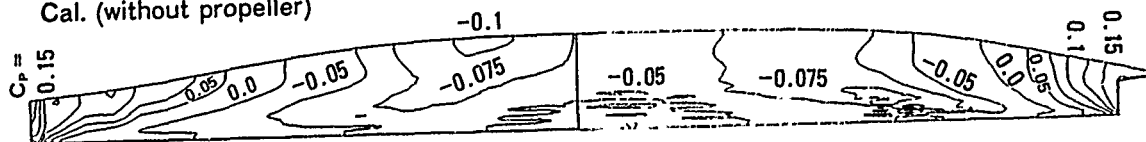


Fig.16 Comparison of local skin-friction coefficient
(Wigley model, $R_N=4.5 \times 10^6$)

Exp (without propeller)



Cal. (without propeller)



Cal. (with propeller)

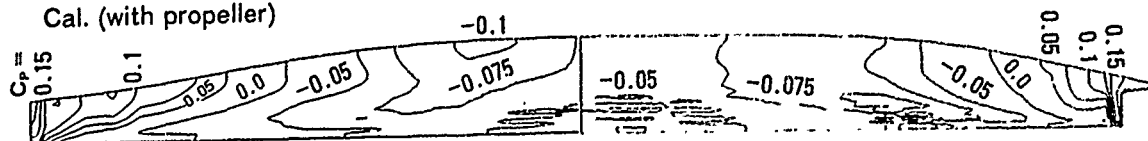


Fig.18 Hull surface pressure distribution (Series-60 $C_b=0.6$)

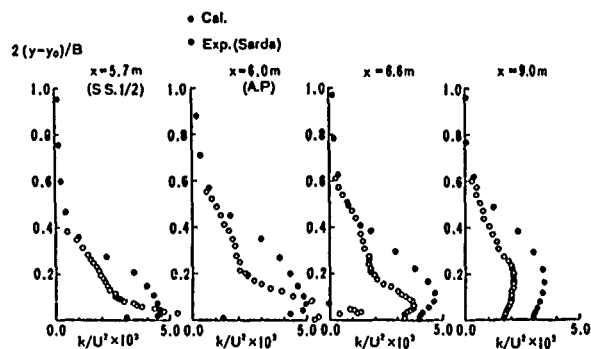


Fig.17 Comparison of turbulent kinetic energy
profiles
(Wigley model, $R_N=4.5 \times 10^6$, $z/d=0.0$)

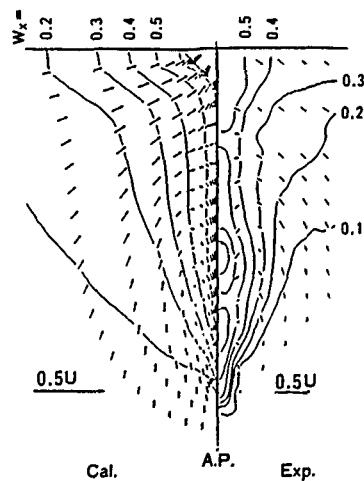
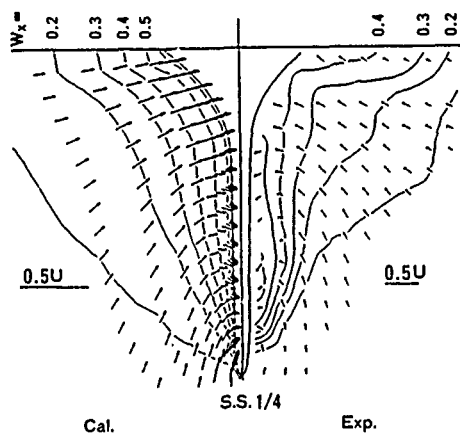
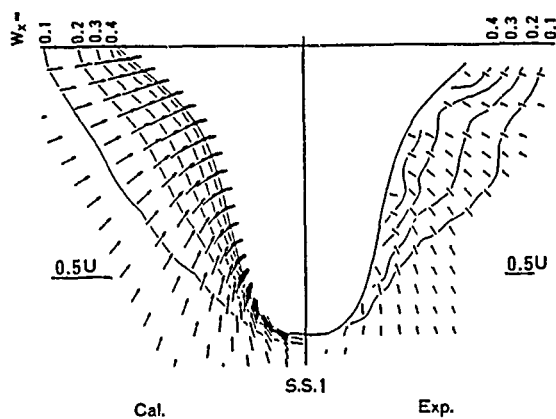


Fig.19 Calculated and measured wake patterns
(Series-60 $C_b=0.6$, $R_N=9.22 \times 10^6$)

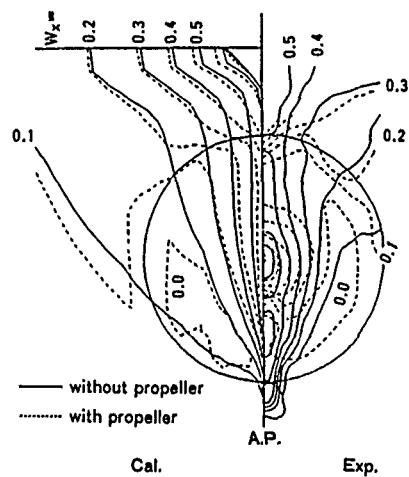
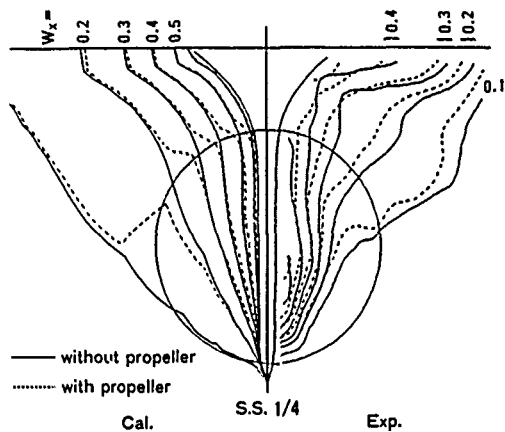


Fig.20 The effect of propeller on the
calculated and measured wake patterns
(Series-60 $C_b=0.6$, $R_N=9.22 \times 10^6$)

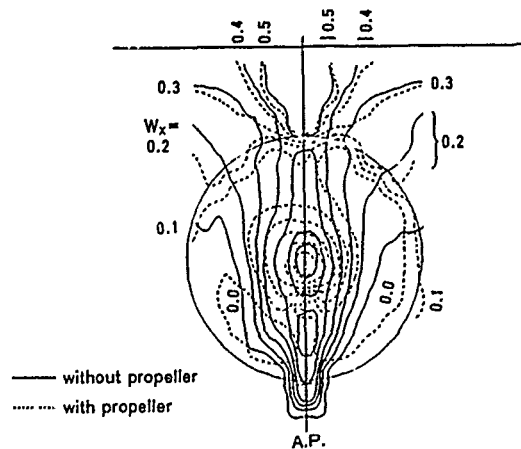


Fig.21 The effect of propeller on the
measured wake pattern
(Series-60 $C_b=0.6$, $R_N=9.22 \times 10^6$)

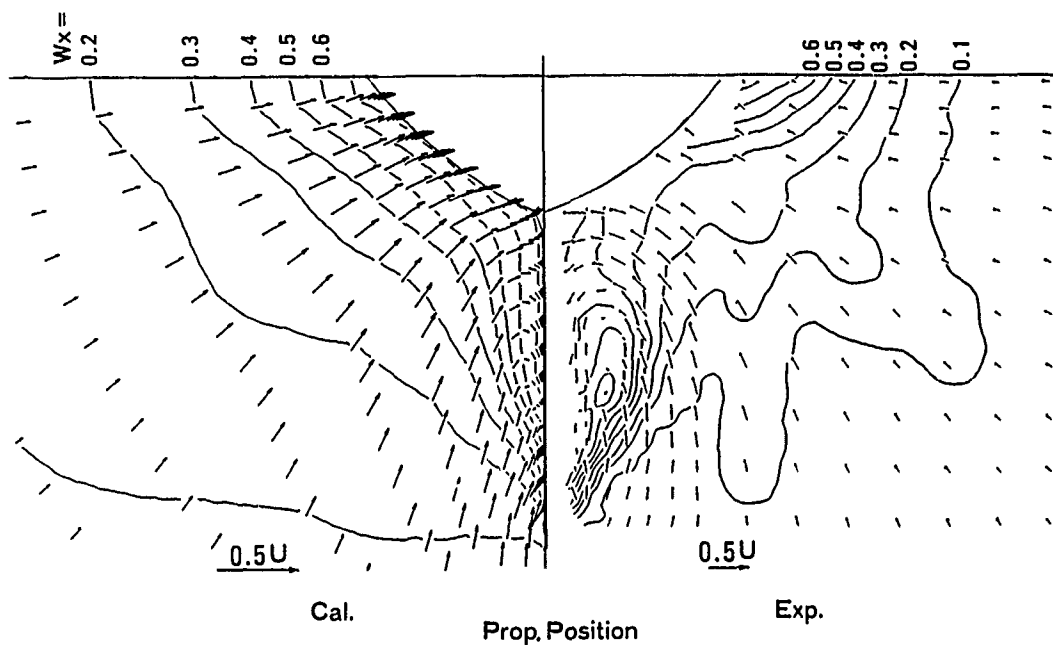


Fig.22 Calculated and measured wake patterns (Tanker form with normal stern, $R_n=7.8 \times 10^6$)

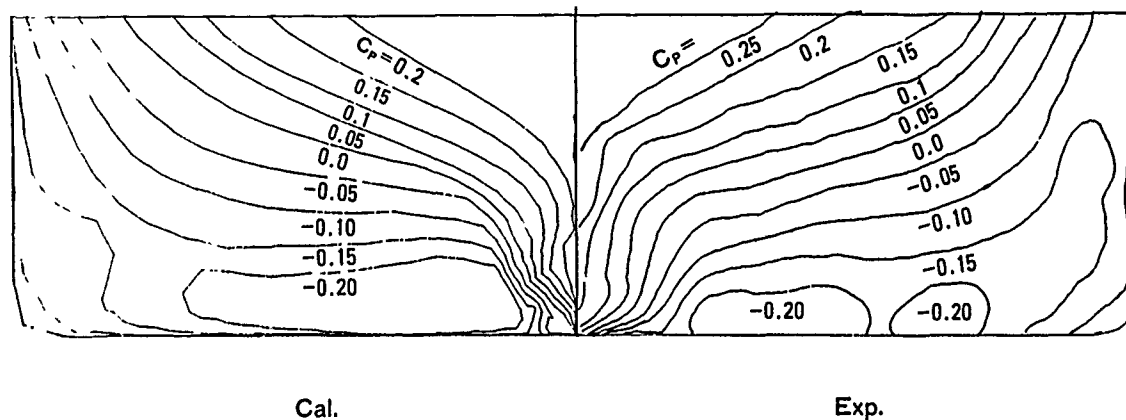


Fig.23 Hull surface pressure distribution (Tanker form with IHI B.O. Stern, $R_n=4.94 \times 10^6$)

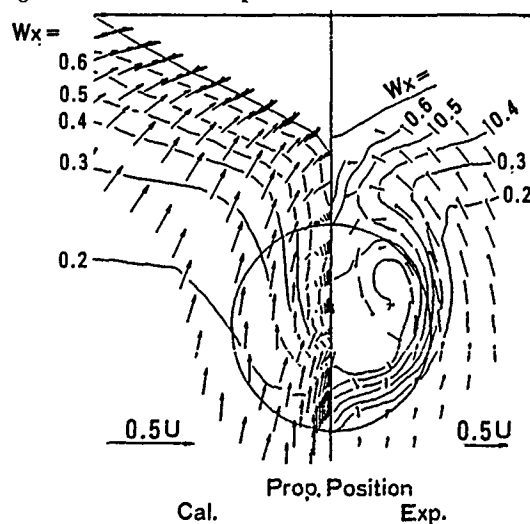


Fig.24 Calculated and measured wake pattern

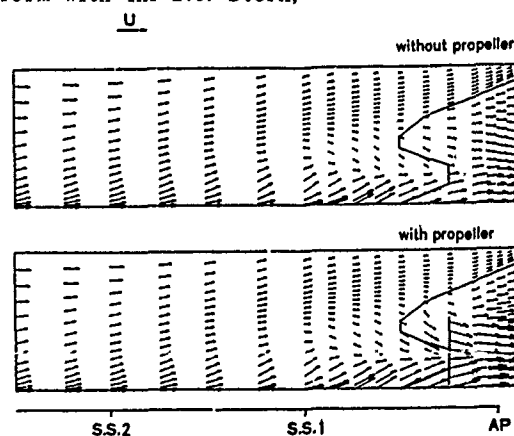


Fig.25 The effect of propeller on the velocity vector near hull surface

Calculation of Nonlinear Water Waves around a 2-Dimensional Body in Uniform Flow by Means of Boundary Element Method

K. Suzuki
Yokohama National University
Yokohama, Japan

Abstract

In this paper, nonlinear wave making phenomena around a two dimensional body is studied. The analysis uses the boundary element method based on Cauchy's integral theorem and the wave profile is calculated by time marching integration based on the semi-Lagrangian approach. Steepening or Breaking waves can be simulated by this scheme.

Two problems are discussed; a semi-circular mound in shallow water, and a floating body with semi-infinite length. In cases including a uniform flow component, numerical treatments have some difficulties. In the semi-circular mound problem, nodal points on the free surface move out of the calculation region, and in the floating body problem, nodal points concentrate in front of the bow. In the present work, numerical difficulties caused by these problems are settled and numerical examples are given for several cases.

1. Introduction

Many numerical schemes have been presented for the purpose of the analysis of free surface flow in recent years. Some of the schemes, however, need high performance computers with very large memory storage. In those cases, some difficulties remain in practical applications. In the problems of nonlinear water waves with steepening or breaking, many complicated numerical procedures and considerable CPU time are needed. If we neglect viscosity and assume irrotational motion, a numerical scheme based on the less complex boundary integral equation can be employed, which does not need high performance computers.

For the problem of two dimensional free surface flow, Longuet-Higgins and Cokelet [1] introduced the boundary element method (abbreviated as BEM) based on Green's integral theorem, in which they used the mixed Eulerian-Lagrangian method in order to follow nodal points on the free surface by means of time marching integration. This scheme was modified by Vinje and Greenhow [2], who employed BEM based on Cauchy's integral theorem and highly accurate scheme of time marching integra-

tion. Similar schemes were developed in last decade and investigations of two dimensional nonlinear water wave including steepening or breaking have been carried out [3][4][5][6]. In most cases, however, wave-making phenomena around a body in uniform flow [7] have not been tried. The main difficulty is that nodal points on the free surface can move according to the uniform flow component.

In the present study, two problems are described; a semi-circular mound in shallow water, and a rectangular floating body with semi-infinite length. In the former problem, nodal points on the free surface will pass through the downstream boundary, and in the latter problem, nodal points will concentrate at the stagnation region in front of the bow, if the suitable way cannot be found. In this paper, numerical treatments for these problems and related ones are discussed, and several numerical examples are given. Some checks about the validity of the present numerical method are also given by comparing the results to the other theories and experiments, and by varying the number of nodal points, the size of calculation region and the time interval.

2. Basic Equations

Two examples of nonlinear wave making phenomena around a two dimensional body in uniform flow are discussed in this paper.

- 1) Semi-circular mound in shallow water as in Fig. 1.
- 2) Rectangular floating body with semi-infinite length as in Fig. 2.

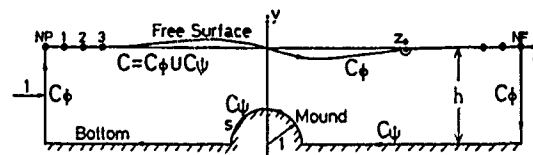


Fig. 1 Semi-circular mound in shallow water.

The downstream boundary is open in the first problem, and a stagnation region exists in front of the bow in the second problem. When using the numerical method explained below, various numerical difficulties are arisen because of these features of the problem. Numerical treatments for each of these problems are explained in later sections.

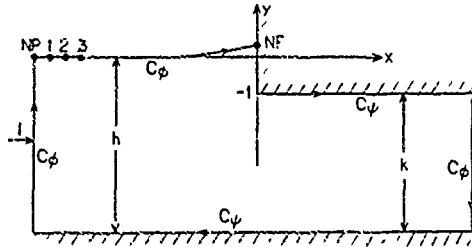


Fig. 2 Rectangular floating body with semi-infinite length.

The coordinate system is taken as shown in Fig. 1 or Fig. 2. For the sake of convenience, all equations in this paper are normalized by a characteristic length l , and a uniform flow U . For example, the normalised time t is expressed as $U/l \times \text{real time}$. In the first problem, the radius a of semi-circular mound can be chosen as the characteristic length, and in the second problem, the draught d can be chosen as the characteristic length. If we neglect the fluid viscosity and also assume irrotational motion, the governing equation of the flow field is Laplace's equation. The complex velocity potential can be introduced as follows,

$$w(z; t) = \phi(x, y; t) + i\psi(x, y; t) \quad (1)$$

$$z = x + iy \quad (2)$$

where ϕ is the velocity potential and ψ is the stream function. If the contour C of clockwise direction is chosen and the singular point z_0 is considered on C as shown in Fig. 1 or Fig. 2, the following equation can be introduced by Cauchy's integral theorem,

$$i\alpha w(z_0; t) + \int_C \frac{w(z; t)}{z - z_0} dz = 0 \quad (3)$$

where $\alpha = \pi$, if the contour is smooth at z_0 . If ϕ is given at z_0 (C_ϕ part of C), the real part of eq. (3) can be taken. On the contrary, if ψ is given at z_0 (C_ψ part of C), the imaginary part of eq. (3) can be taken. Taking the real and imaginary parts of eq.(3), following equations are obtained.

$$-\alpha\psi(z_0; t) + \text{Re} \int_C \frac{w(z; t)}{z - z_0} dz = 0 \quad \text{on } C_\phi \quad (4)$$

$$\alpha\phi(z_0; t) + \text{Im} \int_C \frac{w(z; t)}{z - z_0} dz = 0 \quad \text{on } C_\psi \quad (5)$$

These formulae are integral equations of Fredholm type of the second kind, in which ψ is unknown on C_ϕ (eq.(4)) and ϕ is unknown on C_ψ (eq.(5)) respectively. To solve these

integral equations, nodal points are distributed along the contour C as shown in Fig. 1 or Fig. 2. We have NF nodal points on the free surface which are movable and a total of NP nodal points on the contour C . On each boundary element divided by these nodal points, it is assumed that the complex velocity potential w varies linearly in z . Using the well known procedures by means of these linear boundary elements, the following discrete expressions are obtained with respect to eq. (4) and (5),

$$\text{Re} \left[\sum_{n=1}^{NP} \Gamma_{k,n} w_n \right] = 0 \quad \text{on } C_\phi \quad (6)$$

$$\text{Im} \left[\sum_{n=1}^{NP} \Gamma_{k,n} w_n \right] = 0 \quad \text{on } C_\psi \quad (7)$$

where

$$\Gamma_{k,n} = \frac{z_k - z_{n-1}}{z_n - z_{n-1}} \ln \frac{z_n - z_k}{z_{n-1} - z_k} + \frac{z_k - z_{n+1}}{z_n - z_{n+1}} \ln \frac{z_{n+1} - z_k}{z_n - z_k} \quad (8)$$

$$\Gamma_{k,k-1} = \frac{z_k - z_{k-2}}{z_{k-1} - z_{k-2}} \ln \frac{z_{k-1} - z_k}{z_{k-2} - z_k} \quad (9)$$

$$\Gamma_{k,k} = \ln \frac{z_{k+1} - z_k}{z_{k-1} - z_k} \quad (10)$$

$$\Gamma_{k,k+1} = \frac{z_k - z_{k+2}}{z_{k+1} - z_{k+2}} \ln \frac{z_{k+2} - z_k}{z_{k+1} - z_k} \quad (11)$$

Since terms including known ϕ and ψ remain in left hand side of eq. (6) and (7), these terms must be transposed to the right hand side. A set of simultaneous equations is thus obtained. Since the coefficient matrix of this equation system has a property of diagonal superiority, Gauss-Seidel iterative method can be used to solve the simultaneous equation.

In order to follow nodal points and velocity potential values on the free surface, the mixed Eulerian-Lagrangian formulation is employed. Namely the dynamical free surface boundary condition is expressed as follows by using the material derivative

$$\frac{d\phi}{dt} = \frac{1}{2} \left\{ \left(\frac{\partial \phi}{\partial x} \right)^2 + \left(\frac{\partial \phi}{\partial y} \right)^2 \right\} - \gamma_0 y + \frac{1}{2}, \quad (12)$$

where $\gamma_0 = gl/U^2$. In eq. (12), a uniform flow component is taken into consideration. The kinematical free surface boundary conditions are also expressed as follows.

$$\frac{dx}{dt} = \frac{\partial \phi}{\partial x} = \text{Re} \frac{dw}{dz} \quad (13)$$

$$\frac{dy}{dt} = \frac{\partial \phi}{\partial y} = -\text{Im} \frac{dw}{dz} \quad (14)$$

Integrating the ordinary differential equations (12)~(14) numerically with time increment, the wave profile can be obtained at each time step. Hamming's predictor-corrector method is used as the time marching integration technique. This method needs the values at the first three time steps, which are calculated by means of Runge-Kutta method.

Wave making drag acting on the mound or the rectangular floating body can be estimated in each time step. Since the pressure coefficient is expressed as

$$C_p = \frac{p - p_0}{\frac{1}{2}\rho U^2} = 1 - \left(\frac{\partial\phi}{\partial x}\right)^2 - \left(\frac{\partial\phi}{\partial y}\right)^2 - 2\gamma_0 y - 2\frac{\partial\phi}{\partial t} \quad (15)$$

by Bernoulli's theorem, the coefficient of wave making drag is obtained by the following pressure integral,

$$C_w = \frac{R_w}{\rho l U^2} = -\frac{1}{2} \int_s C_p n_x ds, \quad (16)$$

where s is the girth of the mound or the wetted bow part of the floating body, and n_x is the direction cosine of outward normal on s to x -axis.

3. Semi-circular Mound in Shallow Water

3.1 Treatments for Numerical Computations

General descriptions of the numerical method used in this work are given in the preceding section. In practical free surface computations, however, some difficulties caused by the uniform flow component must be settled.

First the initial condition must be given. In general, the initial condition is given by $U = 0$ at $t = 0$ and the flow is increased gradually to uniform to maintain the stability of the numerical computations. In the present study, however, the uniform flow is given at $t = 0$ as

$$\phi = x \text{ on } C_\psi, \quad \psi = 0 \text{ on } C_\phi, \quad (17)$$

in order to eliminate the acceleration effect on the flow. This initial condition gives no influence on the stability of the numerical computations. This procedure is effective also for saving CPU time.

Since the nodal point NF shown in Fig. 1 can move according to the uniform flow component, the treatment of the downstream boundary is more difficult. If this boundary is fixed, nodal points on the downstream free surface will move out of the calculation region. In order to avoid this difficulty, a new nodal point is introduced on the upstream surface, and a nodal point which passed through the downstream boundary is deleted. The detailed numerical process can be described as follows:

1) As shown in Fig. 3, a fixed upstream boundary and an initial downstream boundary are given. On the free surface, NF nodal points which are movable with time marching are given.

2) The downstream boundary can move corresponding to the nodal point NF . Unless the nodal point $NF - 1$ pass through the initial downstream boundary, the computation is continued without changing numerical procedures as shown in Fig. 3 (1).

3) If the nodal point $NF - 1$ passed through the initial boundary, the downstream boundary is changed to new position of the nodal point $NF - 1$ at next time step. At the same time, as in Fig. 3, the nodal point NF is deleted, the nodal point numbers are replaced, and the new nodal point 1 is added between nodal point NP and 2.

The position and the velocity potential of the new nodal point 1 is given simply like

$$x_1 = \frac{1}{2}(x_{NP} + x_2), \quad y_1 = \frac{1}{2}(y_{NP} + y_2), \quad \phi_1 = \frac{1}{2}(\phi_{NP} + \phi_2). \quad (18)$$

This replacement technique is convenient, because the calculation region can be kept almost the same size.

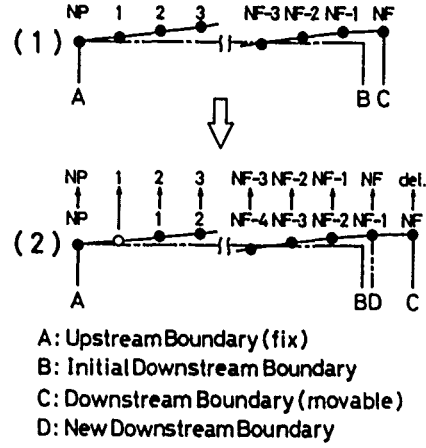


Fig. 3 Treatment of nodal points on the free surface.

For the movable downstream boundary, the condition for ϕ must be given, because this boundary is C_ϕ as in Fig.

1. In the finite difference method, the zero-extrapolation technique is ordinarily used for an open boundary of this kind. In this analysis, however, BEM is employed, and another way must be found. When the disturbance velocity potential φ is introduced as

$$\phi = x + \varphi, \quad \phi_{NF} = x_{NF} + \varphi_{NF}, \quad (19)$$

the downstream conditions for φ are given below, which utilize the solution form based on the linearized free surface condition.

1) If $y_{NF} > 0$,

for $y > 0$,

$$\varphi = \varphi_{NF} \frac{ky \sinh kh + \cosh kh}{ky_{NF} \sinh kh + \cosh kh} \quad (20)$$

for $y \leq 0$,

$$\varphi = \varphi_{NF} \frac{\cosh k(y+h)}{ky_{NF} \sinh kh + \cosh kh} \quad (21)$$

2) and if $y_{NF} \leq 0$,

$$\varphi = \varphi_{NF} \frac{\cosh k(y+h)}{\cosh k(y_{NF}+h)} \quad (22)$$

where

$$k - \gamma_0 \tanh kh = 0. \quad (23)$$

These equations satisfy the condition of $\phi = \phi_{NF}$ at $y = y_{NF}$ and the continuity condition, and eq. (20) is the linear extrapolation of eq. (21).

As described in the previous section, in order to follow the wave profile in each time step, the numerical integrations of differential equations (13), (14) are needed. For

this purpose, dw/dz on the free surface must be evaluated. Several methods are known, however, the following two simplest methods for approximations of dw/dz were used for the present problem.

1) Upstream difference

$$\frac{dw}{dz} = \frac{w_n - w_{n-1}}{z_n - z_{n-1}} \quad (24)$$

2) Downstream difference

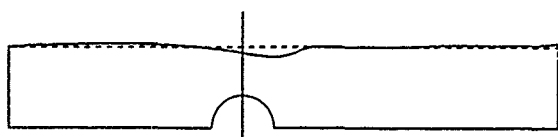
$$\frac{dw}{dz} = \frac{w_n - w_{n+1}}{z_n - z_{n+1}} \quad (25)$$

3.2 Numerical Examples

Numerical examples are shown for the semi-circular mound of radius $a = 0.1m$ in the uniform flow of $U = 0.5m/sec$ and the water depth $h(= depth/a) = 0.25$. Some examples are also given for the other speeds of uniform flow or the other water depths.

As the first example, the schemes for dw/dz on the free surface have to be examined numerically. The computed wave profiles based on the schemes of upstream difference and downstream difference are shown in Fig. 4. In this example, numerical conditions are chosen as; the position of downstream boundary $x_{min} = -7.5$, the position of upstream boundary $x_{max} = 10.0$, the number of nodal points on the free surface $NF = 100$ (length of all elements are equivalent), and the time interval $\Delta t = 0.05$. Fig. 5 shows the wave drag coefficients for the same cases. In Fig. 4 and 5, the scheme of downstream difference seems to be a suitable one for this problem. However, if extending the wave height to vertical direction as in Fig. 6, the reflected wave from the downstream boundary can be observed. For this reason, the upstream difference which can simulate the steep wave as in Fig. 4 is employed as the scheme for dw/dz .

$t=3.50$ (0.70 sec) DOWN-STREAM DIFFERENCE



$t=2.55$ (0.51 sec) UP-STREAM DIFFERENCE

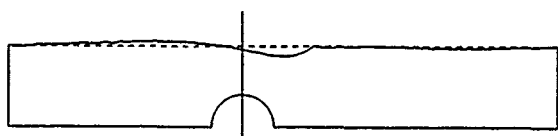


Fig. 4 Wave profiles based on the scheme of upstream difference and downstream difference.

According to the numerical conditions, some examples are computed. Fig. 7 shows the computed wave profiles for $U = 0.3, 0.4, 0.5m/sec$ where $h = 2.5$ at real time =

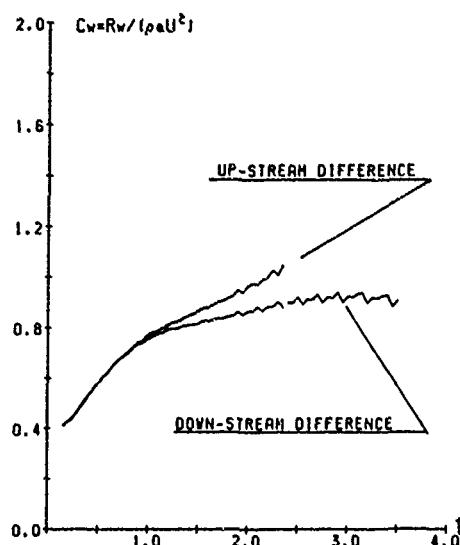


Fig. 5 Wave drag coefficients based on the schemes of upstream difference and downstream difference.

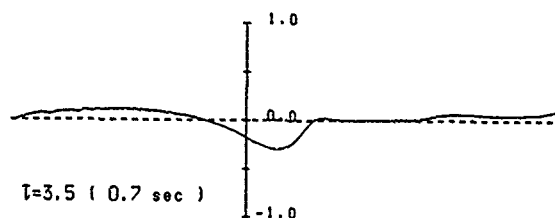


Fig. 6 Wave profile based on the scheme of downstream difference.

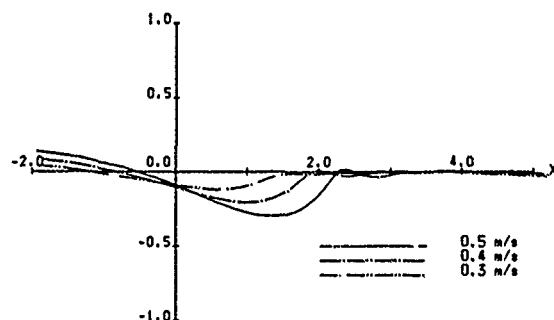


Fig. 7 Wave profiles for $U = 0.3, 0.4, 0.5m/sec$. ($h = 2.5$, real time = 0.51 sec)

0.51 sec in all cases. The difference of wave steepening points can be simulated well in this example. Fig. 8 shows the computed wave profiles for $h = 1.25, 2.5, 5.0$, where $U = 0.5m/sec$ and $t = 0.5$. Fig. 9 shows the wave drag coefficients for the same cases. The case of $h = 1.25$ is the limit of what can be computed by the present technique. As shown in Fig. 9, wave breaking occurs immediately after the wave profile in Fig. 8. As is well known, numerical techniques based on BEM cannot simulate the wave after breaking.

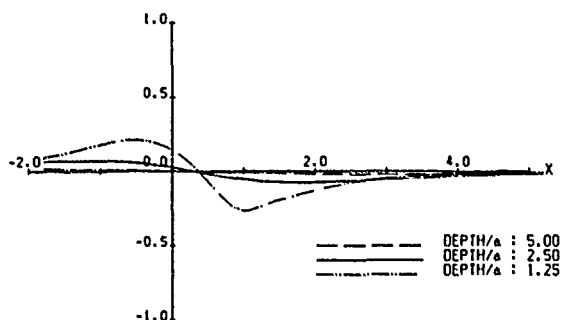


Fig. 8 Wave profiles for $h = 1.25, 2.5, 5.0$.
($U = 0.5 \text{ m/sec}, t = 0.5$)

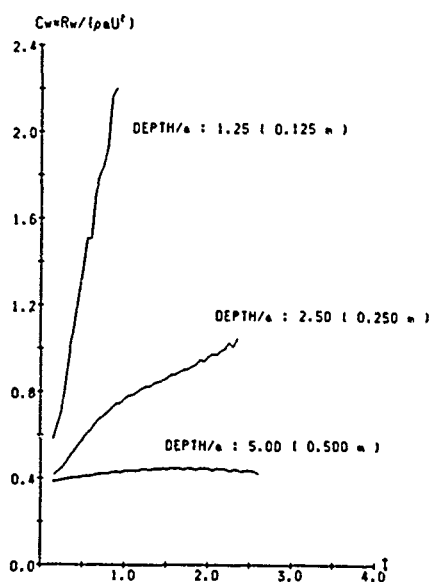


Fig. 9 Wave drag coefficients for $h = 1.25, 2.5, 5.0$.
($U = 0.5 \text{ m/sec}$)

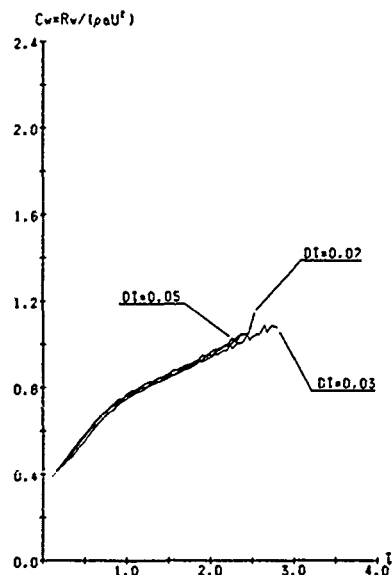


Fig. 10 Wave drag coefficients for the cases of
 $\Delta t = 0.03, 0.05, 0.07$.

37th step $t = 2.59$ (0.518 sec) $\Delta t = 0.07$

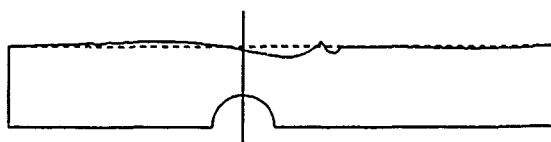


Fig. 11 Wave profile for the case of $\Delta t = 0.07$.

For the first example, effects of the time interval are exemplified. The wave drag coefficients for the cases of $\Delta t = 0.03, 0.05, 0.07$ do not show serious differences caused by the time interval (Fig. 10). In Fig. 11, however, the wave breaks unusual in case of $\Delta t = 0.07$. Since the wave profiles for $\Delta t = 0.03$ and 0.05 are almost same in this problem, $\Delta t = 0.07$ is considered as a rough time step for the present problem.

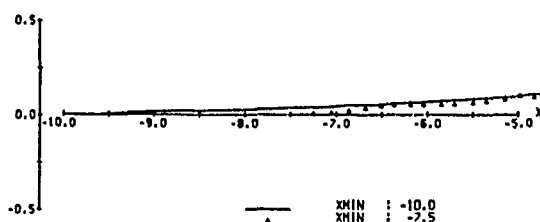


Fig. 12 Upstream free surfaces for the cases of
 $x_{\min} = -7.5$ and -10.0 .

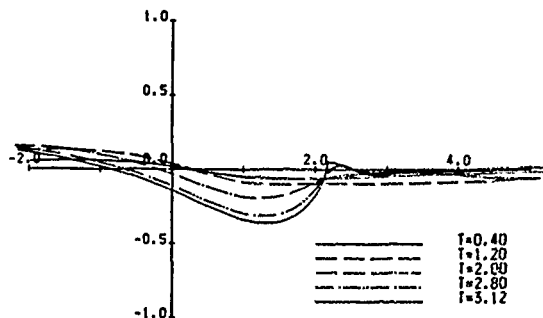


Fig. 13 Time history of wave profile. ($U = 0.5 \text{ m/sec}$,
 $x_{\min} = -10.0, NF = 157, \Delta t = 0.04$)

In some of the examples, small undesirable oscillations can be seen on the upstream surface. When the numerical conditions are changed to $x_{\min} = -10.0$ and $NF = 115$, those undesirable oscillations are suppressed (Fig. 12). In the final three examples, $x_{\min} = -10.0$, $NF = 157$, and $\Delta t = 0.04$ are used (Fig. 13, 14 and 15). The computed time history of the wave evolution is given as in Fig. 13. At the final time step, the wave becomes very steep. In Fig. 14, this steep wave profile just before breaking is compared with the result based on the finite difference method by Miyata et. al.[8][9]. Both results show a fairly good agreement. The wave profile before steepness predicted by the present method is also compared with the experimental result by Miyata et.al.[8][9] in Fig. 15. Since the experimental wave profile is replotted from the published photograph, small errors are probably included, and

the time step is not equivalent in both cases, because initial conditions are different with each other. Though clear conclusions cannot be described for the above reasons, the present method can be regarded as one of the powerful simulation tools for real phenomena of steep wave.

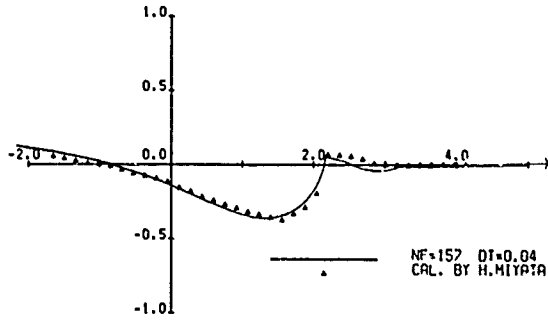


Fig. 14 Wave profiles by the present method and the finite difference method. ($U = 0.5 \text{ m/sec}$)

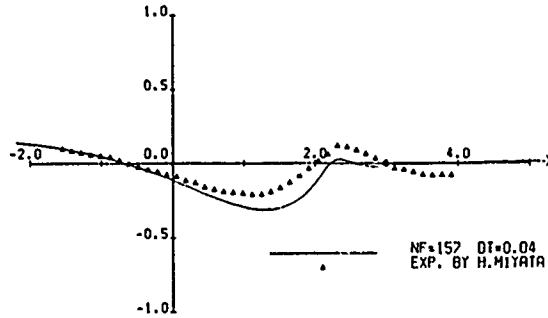


Fig. 15 Wave profiles by the present method and the experiment. ($U = 0.5 \text{ m/sec}$)

4. Rectangular Floating Body with Semi-infinite Length

4.1 Treatment for Numerical Computations

As described in section 3.1, the means of solving some numerical difficulties have to be given also for this problem. If the deep water depth is assumed, the boundary conditions of upstream and downstream are simply written as

$$\phi = z \text{ on the upstream boundary,} \quad (26)$$

$$\phi = \frac{h}{k} z \text{ on the downstream boundary} \quad (27)$$

respectively, because there is no free surface at the downstream boundary in this case. However the condition (27) is not applied to the top and bottom nodal point at the downstream boundary, which are regarded as points of C_ϕ on the body and the bottom in the present calculation. If the water depth become shallower, the problem becomes more complicated and other considerations will be needed for both boundary conditions.

In order to start the computation, an initial condition is needed. Though the uniform flow condition is employed on all C_ϕ region as in eq. (17), it is not able to be applied to the present problem, because of existence of stagna-

tion point on the bow. For this type of the flow field, the numerical solution of the double model flow can be introduced as the initial condition. The double model solution can be obtained by the boundary conditions of

$$\psi = 0 \text{ on the body and the free surface at rest,} \quad (28)$$

$$\psi = -h \text{ on the bottom} \quad (29)$$

with eq. (26) and (27). The obtained values of ϕ on the free surface are employed as the initial condition with the other boundary conditions.

The most serious problem is caused by the existence of the stagnation region. Because of the uniform flow component, the nodal points will concentrate in front of the bow and the distance between nodal points NP and 1 will become larger and larger. This causes unusual wave profile around the nodal point 1, which is shown in the subsequent section by a numerical example. In this case, the replacement technique of nodal points as explained in section 3.1 cannot be introduced, because the vertical boundary with the nodal point NF is not movable and nodal points in front of the bow cannot be deleted in order to simulate the wave breaking. To counter this difficulty, long elements are introduced on $y = 0$ before the nodal point 1 as shown in Fig. 15. Following boundary conditions are imposed on nodal points on these long elements.

$$\phi = z \text{ on the long element region} \quad (30)$$

These long elements act as wave suppression plates.

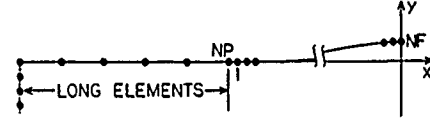


Fig. 16 Long elements on the upstream surface.

In order to evaluate dw/dz on the free surface, the following three methods are used.

- 1) Upstream difference (same as eq. (24))
- 2) Downstream difference (same as eq. (25))
- 3) Centered difference

$$\frac{dw}{dz} = \frac{\frac{w_n - w_{n-1}}{z_n - z_{n-1}} |z_n - z_{n-1}| + \frac{w_n - w_{n+1}}{z_n - z_{n+1}} |z_n - z_{n+1}|}{|z_n - z_{n-1}| + |z_n - z_{n+1}|} \quad (31)$$

Eq. (31) corresponds to the weighted mean of the upstream difference and the downstream difference. Nodal points on the free surface can be followed by the above numerical procedures. For the nodal point NF , however, the horizontal velocity component $\text{Re}(dw/dz)$ is neglected, because this nodal point must be restricted to move along the bow.

4.2 Numerical Examples

Before showing several numerical examples, the numerical accuracy of the double model solution must be

studied, because it is employed as the initial condition for the present problem. Two numerical solutions of $x_{max} = 20.0$ and 80.0 , where $x_{min} = -10.0$, are compared with the analytical solution based on Schwarz-Christoffel transformation [10] in Fig. 17. The results are slightly different, though the same tendency of ϕ is obtained. The extension of the upstream boundary does not improve the numerical solution. Since the numerical solution is employed as the initial condition, it cannot be avoided that ϕ includes small errors initially. However, initial flow velocities on the free surface are accurate, because the velocities are obtained from derivatives of ϕ .

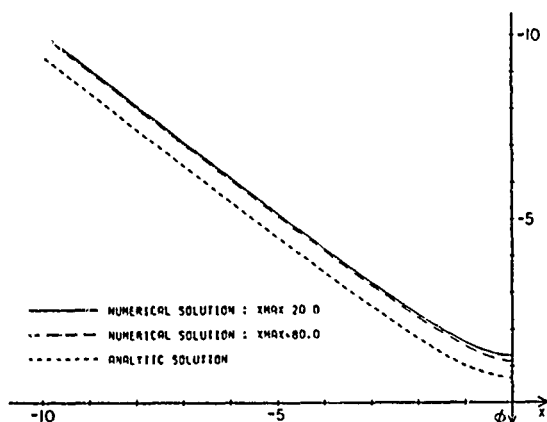


Fig. 17 Double model solutions.

As discussed in section 3.2, several numerical treatments and conditions are studied. These are carried out as $d = 0.1m$ and $U = 1.0m/sec$ (Fig. 18 ~ Fig. 24). First, the effectiveness of long elements on the upstream free surface is verified. Long elements are arranged before $x = -10.0$, $x = -10.0 \sim -8.0$ is divided by 10 normal el-

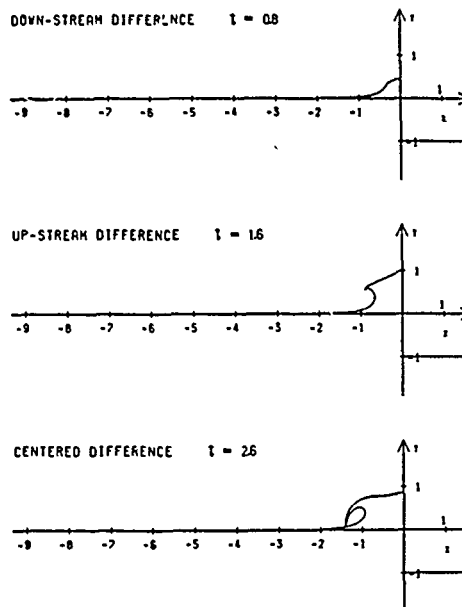


Fig. 19 Wave profiles based on the schemes of upstream, downstream and centered difference.

ements, and $x = -8.0 \sim 0.0$ is divided also by 120 normal elements. By employment of these long elements, unnatural waves induced on the upstream surface, shown in the upper example of Fig. 18, are suppressed as in the lower example. In this example, the centered difference scheme is used to calculate dw/dz on the free surface. The predicted wave profiles at final time step by three schemes of downstream difference, upstream difference and centered difference are shown in Fig. 19. For the present problem, both the downstream difference and the upstream difference are not suitable, because computations failed

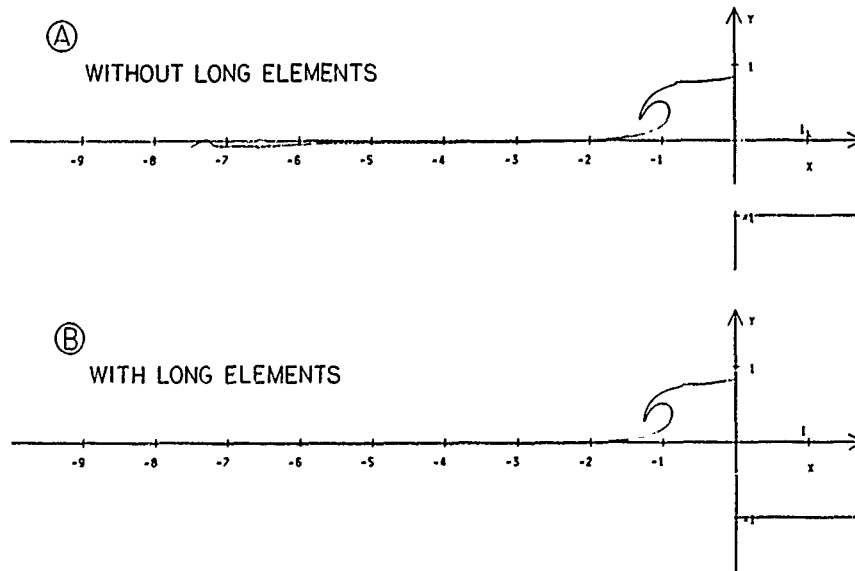


Fig. 18 Wave profiles for the cases without and with long elements on the upstream surface. ($t = 2.4$, $\Delta t = 0.04$)

without sufficient wave overturning. In the case of the centered difference, however, the plunging breaker can be simulated. The centered difference includes both information from upstream and downstream. In order to express the flow field in the stagnation region, both are needed. Differences in the wave drag coefficient are also observed with respect to the upstream difference and the centered difference as in Fig. 20. In all following examples, the scheme of centered difference is employed.

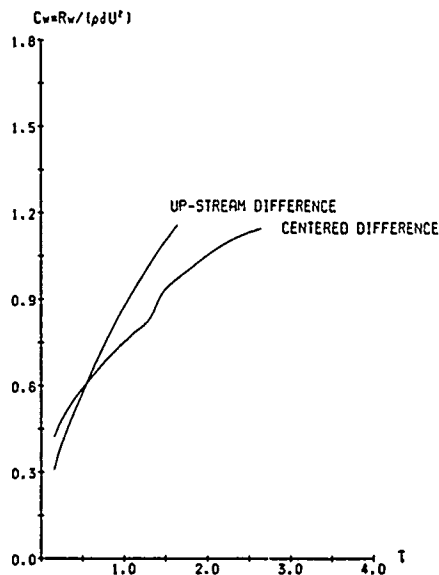


Fig. 20 Wave drag coefficients based on the schemes of upstream and centered difference.

Effects of the size of calculation region and the time interval are examined. Fig. 21 shows the wave profiles at $t = 2.4$ for the cases of $x_{max} = 10, 20, 30$, and Fig. 22 shows the wave drag coefficients for the same cases. The wave overturning point is closer to the bow of floating

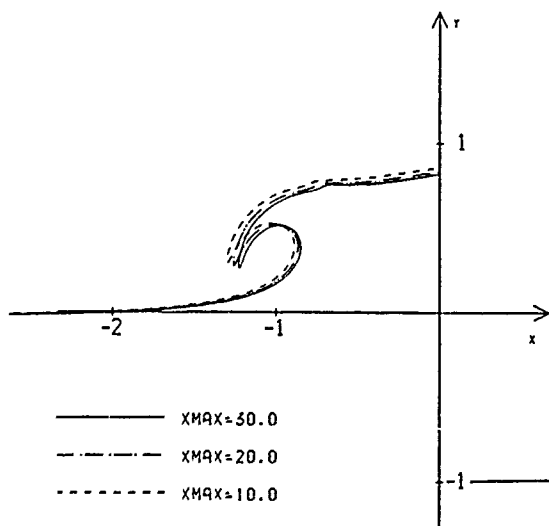


Fig. 21 Wave profiles for the cases of $x_{max} = 10, 20, 30$. ($NF = 130, t = 2.4, \Delta t = 0.04$)

body as x_{max} increases. On the contrary, the extension of the upstream boundary has no effect for the numerical solution.

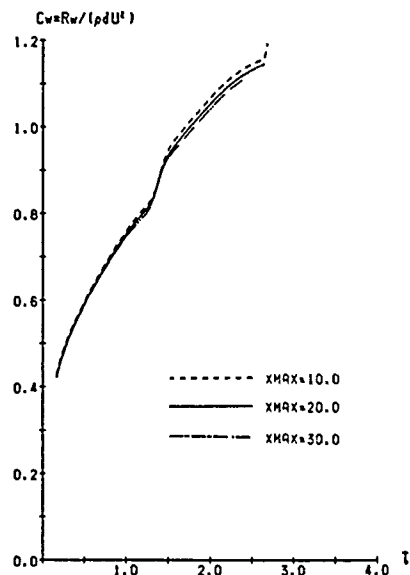


Fig. 22 Wave drag coefficients for the cases of $x_{max} = 10, 20, 30$.

Fig. 23 shows the wave drag coefficients for the cases of $\Delta t = 0.02, 0.04, 0.08$, and 0.12 , where $x_{max} = 20$. At $\Delta t = 0.02$ and 0.04 , almost the same results are obtained. As in Fig. 24, the detailed simulation of wave breaking is shown, where $t = 0 \sim 2.6$ and $\Delta t = 0.02$.

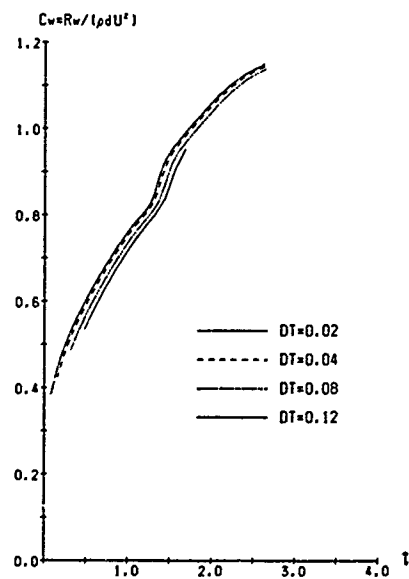


Fig. 23 Wave drag coefficients for the cases of $\Delta t = 0.02, 0.04, 0.08, 0.12$.

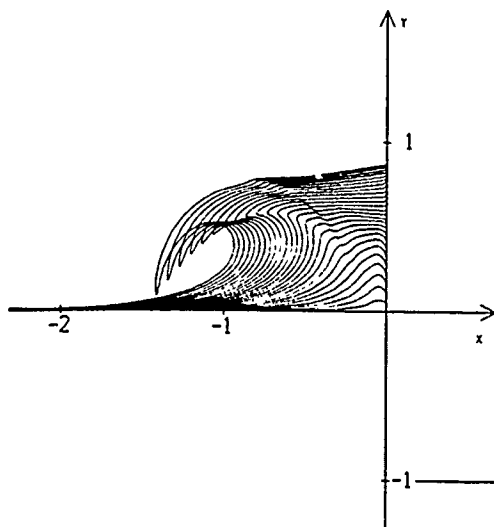


Fig. 24 Wave breaking simulation.
($U = 1.0 \text{ m/sec}$, $x_{\text{max}} = 20$, $t = 0 \sim 2.6$, $\Delta t = 0.02$)

According to the above studies about numerical treatments and conditions, simulations of wave making phenomena are carried out for $F_d = U/\sqrt{gd} = 0.5$, 0.8 and 1.0 as in Fig. 25, 26 and 27 respectively. In the case of $F_d = 0.5$ a spilling breaker is obtained, though the other cases show plunging breakers. Since reliable experimental data is not available, these solutions cannot be compared with experiments. However, under the numerical treatment that the numerical solution of double model flow is employed as the initial condition, these solutions must be considered as accurate ones, if the above mentioned studies are acceptable.

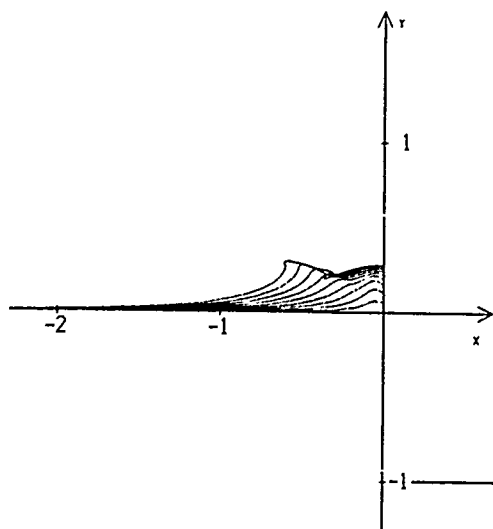


Fig. 25 Wave breaking simulation for $F_d = 0.5$.
($t = 0 \sim 0.9$, $\Delta t = 0.02$)

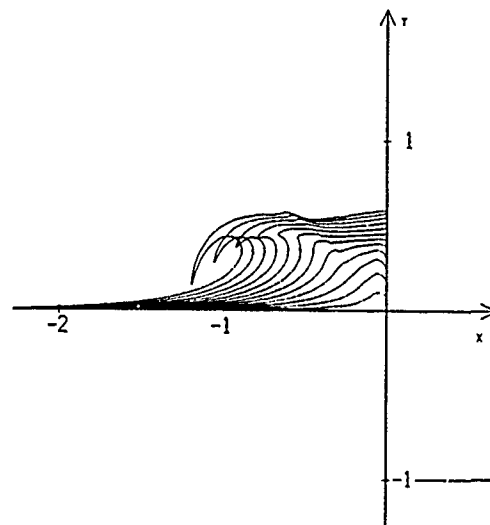


Fig. 26 Wave breaking simulation for $F_d = 0.8$.
($t = 0 \sim 1.92$, $\Delta t = 0.032$)

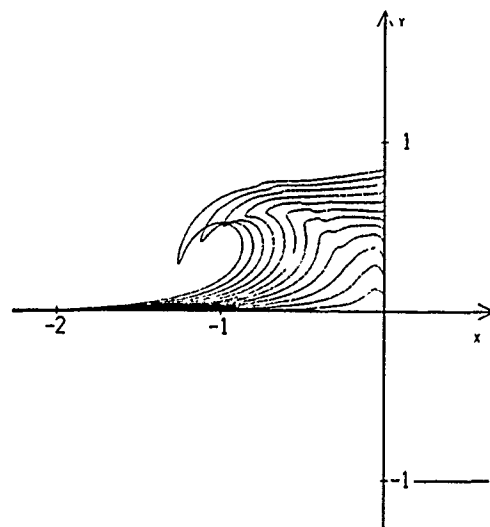


Fig. 27 Wave breaking simulation for $F_d = 1.0$.
($t = 0 \sim 2.4$, $\Delta t = 0.04$)

The present results are compared with the other theoretical and numerical results. Dagan and Tulin [11] obtained the wave profile in front of the rectangular body by a perturbation method based on small Froude number expansion. In Fig. 28, wave height at the bow η based on the present method is plotted for F_d with their result. The present result is not equivalent to $\eta = 0.5 F_d^2$ by Dagan and Tulin. Wave steepening is related to their second order solution, but wave breaking phenomena cannot be explained by their analytical approaches. Finally as shown in Fig. 29, wave profile for $F_d = 1.0$ is compared with the result based on the similar method by Grosenbaugh and Yeung [7]. Fairly good agreement is observed except the sharpness of overturning waves.

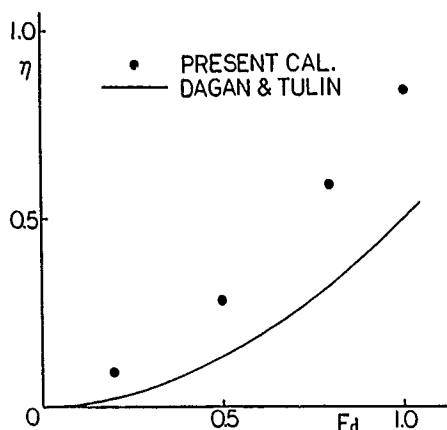


Fig. 28 Wave height at the bow by the present method and by Dagan and Tulin.

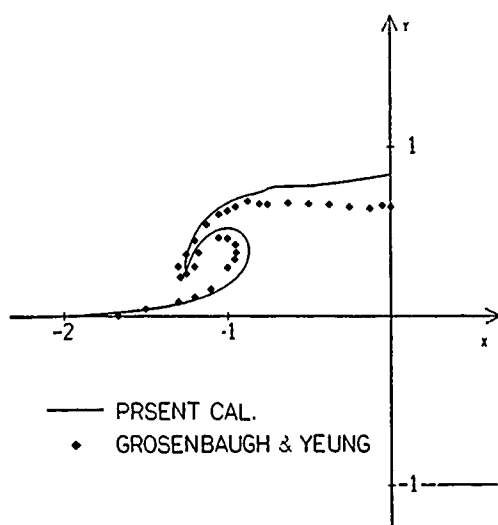


Fig. 29 Wave profiles for $F_d = 1.0$ by the present method and by Grosenbaugh and Yeung.

5. Conclusion

In the present study, the simulation method of two dimensional nonlinear water waves based on BEM and the mixed Eulerian-Lagrangian approach is applied to two wave making problems around a body in uniform flow; the semi-circular mound in shallow water and the rectangular floating body with semi-infinite length.

For numerical difficulties caused by respective problems, some treatments are given and those effectiveness are confirmed numerically by several examples. The present method can simulate the nonlinear wave making phenomena including steepening or breaking, but cannot simulate the wave after breaking. In the case of the floating body problem, overturning waves (plunging breaker) in front of the bow can be simulated. Numerical validations

of the present method are shown by examples for several cases with numbers of nodal points, sizes of calculation region, and time intervals. For the detailed experimental verifications, reliable data is needed. The present method, however, can be regarded as one of the powerful simulation tools for the nonlinear wave making phenomena. The present method can be extended to general problems of two dimensional wave making phenomena.

Acknowledgement

The author wishes to express his deep appreciation to Prof. M. Ikehata and Emeritus Prof. H. Maruo of Yokohama National University for their useful suggestions and encouragements. This paper was written while at the University of British Columbia under the financial support of the Government of Canada Award. The author would also like to express his deep gratitude to Prof. S.M. Calisal of U.B.C. and the World University Service of Canada. He thanks also Mr. D. McGreer and Dr. J.L.K. Chan of U.B.C., and Mr. D. Jimbo, Mr. N. Nakajima, Mr. S. Masuda and Mr. K. Furusawa of Y.N.U. for their kind cooperations.

References

- [1] Longuet-Higgins, M.S. and Cokelet, E.D. : "The deformation of Steep Surface Waves on Water, I. A Numerical Method of Computation", *Proc. R. Soc. (A)*, 350 (1976).
- [2] Vinje, T. and Brevig, P. : "Nonlinear Ship Motions", *Proc. 3rd Int. Conf. Numerical Ship Hydrodynamics* (1981).
- [3] Greenhow, M. and Vinje, T. : " Extreme Wave Forces on Submerged Wave Energy Devices", *Applied Ocean Res.*, Vol. 4, No. 4 (1982).
- [4] Lin, W.-N., Newman, J.N. and Yue, D.K. : "Nonlinear Forced Motions of Floating Bodies", 15th Symp. on Naval Hydrodynamics (1984).
- [5] Takagi, K., Naito, S. and Nakamura, S. : "Computation of Nonlinear Hydrodynamic Forces on Two-Dimensional Body by Boundary Element Method", *Journal of Kansai Soc. of Naval Architects of Japan*, Vol. 197 (1985). (in Japanese)
- [6] Schultz, W.W., Ramberg, S.E. and Griffin, O.M. : "Steep and Breaking Deep Water Waves", 16th Symp. on Naval Hydrodynamics (1986).
- [7] Grosenbough, M.A. and Yeung, R.W. : "Nonlinear Bow Flows - An Experimental and Theoretical Investigation", 17th Symp. on Naval Hydrodynamics (1988).
- [8] Miyata, M., Matsukawa, C. and Kajitani, H. : "A Separating Flow near the Free Surface", *Osaka Int. Colloquium on Ship Viscous Flow* (1985).

- [9] Miyata, M., Matsukawa, C. and Kajitani, H. :
"Shallow Water Flow with Separation and Breaking
Wave", Journal of Soc. of Naval Architects of Japan,
Vol. 158 (1985).
6th Ed., p287.
- [10] Milne-Thomson : "Theoretical Hydrodynamics",
[11] Dagan, G. and Tulin, M.P. : "Nonlinear Free-Surface
Effects in the Vicinity of Blunt Ship Bows", 8th
Symp. on Naval Hydrodynamics (1970).
-

DISCUSSION

by R.C. Ertekin

I think your paper lacks quite important references on the upstream waves that can be seen in your figures. It is well known by now (see the three papers by Bai et al.; Choi and Mei; and Ertekin & Qian) that when a disturbance moves in finite depth, then upstream waves (solitons) will be generated if the blockage coefficient is significantly high (like yours) and the depth Froude number is not very small (>0.2). So the upstream waves that you obtain are not necessarily "undesirable oscillations" but a gift of nature. By the way, you are solving Laplace's equation and there is no difference between the body moving (steady) in an otherwise calm water and the fixed body placed in an uniform oncoming flow.

With regard to the "open-boundary" conditions you can very well calculate the phase speed at these boundaries and use Orlanski's scheme coupled with the Sommerfeld's radiation condition. Your results show that your "open-boundary" conditions are reflective.

Author's Reply

In the case of solitons, the waves propagate from the body to the upstream. In my case, however, the upstream waves appear around the nodal point 1 and propagate to the downstream direction. It is caused by the numerical technique of the addition of new nodal point 1 and can be avoided by the extension of the calculation region. In the present case, the wave breaking occurs before the generation of solitons. In near future, I would like to simulate the soliton by the present technique.

Exactly speaking, your opinion about the radiation condition is right. For the practical use, however, we usually need the simple and numerical radiation condition. For example, in the research field of Rankine source method, several numerical radiation conditions are employed. In the present method, the combined technique of the upstream difference approximation of dw/dz , the replacement of nodal points on the free surface and the employment of the linear solution form at the downstream boundary can be expected as the numerical radiation condition.

DISCUSSION

by C.G. Kang

Usually there is singular behavior at the intersection point between the body and the free surface. Even if the potential and the stream function are not singular at the point, the velocity is singular when the intersection angle is not 90 degrees. Could you show us how to remove the singular behavior? Greenhow showed that the solution using fine grids is poorer than that using coarse grids. Did you check the convergence of the velocity at the intersection point?

Author's Reply

As described in my paper, the intersection point NF is treated as the free surface nodal point, and its horizontal velocity component calculated by $Re(dw/dz)$ is ignored. Along the bow, only this intersection point is movable, that is, the other nodal points on the bow under the free surface are fixed. In this approximation, the velocity at the intersection can be obtained without difficulty.

DISCUSSION

by J.H. Hwang

I congratulate on your fine presentation. Your calculation is seemed to be basically based on Vinje-Brevig method. Could you give some comments on major advantages of your calculation in the numerical scheme including the treatment of the intersection point between the free surface and the body.

Author's Reply

As described in my paper, the intersection point NF is treated as the free surface nodal point, and its horizontal velocity component calculated by $Re(dw/dz)$ is ignored. Along the bow, only this intersection point is movable, that is, the other nodal points on the bow under the free surface are fixed. In this approximation, the velocity at the intersection can be obtained without difficulty.

Discussion

by J.W. Kim

We would like to comment on your treatment of the downstream condition and your finite difference schemes.

The downstream condition given in Eqs.(20)-(22) is based on the steady linear solution. But your calculation is made on an unsteady problem. In a transient stage many components of waves with different wave lengths are evolved and eventually hit the downstream boundary. The wave components which do not satisfy the dispersion relation in (23) will be reflected back to the computational domain. Even for the wave components satisfying the equation (23), this equation cannot distinguish incoming or out-going waves with respect to the computation domain.

You have tried various difference schemes in your paper and the final choice was made from computational results. We do not understand how one can choose a specific finite difference scheme if we don't know the correct result in advance. We strongly believe that one should decide a certain numerical scheme for a given problem based on rational mathematical analysis, not after comparing with the known result.

Author's Reply

Strictly speaking, your comments are true. For numerical treatments in my paper, however, it is not suitable to discuss separately the downstream condition and the finite difference schemes of dw/dz . These treatments connect with each other through eqs.(12)-(14), that is, ϕ_{NF} in eqs.(20)-(22), which is time dependent variable, is determined from eqs.(12) and (19). In this treatment, the position of downstream boundary is not fixed. If we find a suitable way to estimate the wave number as a time dependent variable, these numerical treatments will be improved more precisely. We should not pursue an ideal, but find more convenient way.

Nonlinear Simulation of Transient Free Surface Flows

R. Cointe
Institut Français du Pétrole
Rueil-Malmaison, France

1 Abstract

The application of the Mixed Eulerian-Lagrangian method to the simulation of transient free surface flows in the vicinity of a free surface piercing structure is considered. A particular attention is given to the validation of the numerical procedure.

Several applications are studied. Comparisons between the results of the numerical scheme and those of approximate theories and/or experiments are shown. They demonstrate the accuracy and versatility of the simulation that can be used as a "standard" to check the applicability of approximate theories.

The main limitation of the method is that it cannot account for viscous effects, in particular in the vicinity of the free surface. Approximate ways to simulate dissipative phenomena associated to breaking would be most useful.

2 Introduction

The direct numerical simulation of unsteady two-dimensional potential free surface flows using a Mixed Eulerian-Lagrangian method (MEL) has received considerable attention since the pioneering work of Longuet-Higgins and Cokelet [22]. If many codes exist now that use this method, their suitability for the study of nonlinear fluid-structure interaction problems has only been demonstrated for some particular applications (e.g., water impact [15], simulation of breaking in a tank [12], forced heaving of a cylinder [18], etc...).

Compared to the initial application of the MEL to the study of steep periodic waves (e.g., [22]), several new difficulties appear when a structure is present, especially if it pierces the free surface. The first one is related to the proper description of the flow in the vicinity of intersection points between the body and the free surface. A second difficulty is to be able to control the incident wave train that interacts with the body.

The main difficulty, however, is probably that the accuracy of the simulation is difficult to establish for transient flows in the vicinity of free surface piercing bodies, because of a lack of reference cases. Checking such requirements as conservation of fluid or energy might not be sufficient. Surprisingly enough, the linear solution is not always computed and quantitative validations of the numerical procedure are almost inexistant, even for weakly nonlinear flows.

These considerations have partly motivated the present work which associates numerical and analytical studies. A code based on the MEL — Sindbad — has been developed that has for purpose the simulation of a two-dimensional wave tank using potential flow theory. A particular attention is given to the proper validation of the numerical scheme by comparison of its results to those of experiments and of asymptotic studies. To make this comparison easier, an option of the code allows the linear problem to be solved. Such an approach appeared necessary in order to gain confidence in the code and eventually extend its range of applicability.

A direct simulation of experiments that can be carried out in a wave tank is performed. For this purpose, waves are generated in a rectangular tank by use of a piston-type wavemaker. These waves can then interact with submerged or free surface piercing cylinders in forced or free motion. Reflection from the wall opposite to the wavemaker is avoided by the use of a damping zone — see figure 1

The results of the classical first- and second-order diffraction radiation theories can be recovered using the simulation. A good agreement with experimental results is obtained in cases where these classical theories fail.

The main limitation of the method is that viscous and turbulent effects cannot be accounted for. This problem is crucial when viscous effects occur in the near vicinity of the free surface, in particular during breaking.

This work has been reported elsewhere while in progress ([5], [6], [8], [9]). If we focus here on the results of the simulation, a more detailed description of the numerics and of some of the approximate theories referred to here can be found in [7].

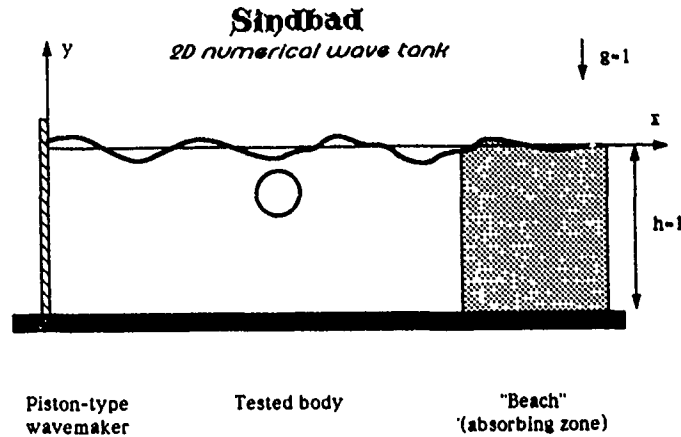


Figure 1: Sindbad — geometric definitions

3 Numerical Scheme

3.1 Outline of the Method

Since there exists now quite a large number of codes based on the MEL, the numerical method used will only be briefly outlined. The attention will focus in the next sections on the main difficulties that have been encountered and on the methods used to overcome them.

The main idea of the numerical procedure is to choose markers initially at the free surface and to follow them in their motion.

We use a coordinate system (x, y) . The x -axis coincides with the reference position of the free surface and the y -axis is upward vertical — see figure 1 for geometric definitions. The fluid is assumed to be incompressible and the flow irrotational so that the velocity field \vec{v} is given by:

$$\vec{v} = \vec{\nabla} \phi, \quad (1)$$

with:

$$\Delta \phi = 0. \quad (2)$$

The computation is performed in a bounded domain. Along rigid boundaries ($\vec{x} \in \Gamma_n(t)$), the normal velocity in the fluid is equal to the normal velocity of the boundary. We have, therefore, a Neumann boundary condition.

Along the free surface, we use Bernoulli equation and the fact that the free surface is a material surface. The corresponding equations are written for a marker \vec{x} on the free surface ($\vec{x} \in \Gamma_d(t)$) and the associated value of the potential, $\phi(\vec{x})$. This yields¹:

$$\frac{D\phi}{Dt} = -y - \left(\frac{1}{2} - \zeta\right) \phi_s^2 + \frac{1}{2} \phi_n^2 - p + c(t) \quad (3)$$

$$\frac{D\vec{x}}{Dt} = \zeta \phi_s \vec{s} + \phi_n \vec{n}, \quad (4)$$

where D is used to indicate a material derivative, \vec{s} and \vec{n} are vectors tangent and normal to the free surface, respectively, and ζ is an arbitrary constant.

¹ For the sake of simplicity, we use units such that the acceleration of gravity, g , the specific mass of water, ρ , and the depth of the tank, h , are equal to 1.

This constant specifies the tangential motion of the markers: $\zeta = 1$ identifies markers and particles while $\zeta = 0$ yields a zero tangential motion of the markers. This last choice allows a current to be simulated in the tank. For the applications discussed here, we will however always take $\zeta = 1$.

We will assume that the pressure is constant along the free surface. It can therefore be included in the function of time $c(t)$. With an appropriate choice of the velocity potential, this function can be taken equal to zero.

At a given instant t , if ϕ and ϕ_n are known along the free surface $\Gamma_d(t)$, then the right-hand sides of (3)-(4) can be evaluated. The fact that ϕ is harmonic in the fluid domain allows the value of ϕ_n along $\Gamma_d(t)$ to be computed from the values of ϕ along $\Gamma_d(t)$ and of ϕ_n along $\Gamma_n(t)$. The kinematical constraint $\Delta \phi = 0$, associated with the boundary condition on Γ_n , permits therefore to express the free surface boundary conditions (3)-(4) as an evolution equation for (ϕ, \vec{x}) . This evolution equation can be solved numerically using standard time-stepping procedures, such as a fourth-order Runge-Kutta algorithm.

The main numerical difficulty is to be able, at each time-step, to solve for the harmonic function ϕ knowing ϕ along $\Gamma_d(t)$ and ϕ_n along $\Gamma_n(t)$. We use the integral equation:

$$\begin{aligned} & -\theta(P) \phi(P) + \int_{\Gamma_d + \Gamma_n} \phi(Q) G_n(P, Q) ds_Q \\ & = \int_{\Gamma_d + \Gamma_n} \phi_n(Q) G(P, Q) ds_Q, \end{aligned} \quad (5)$$

where P is a point on the boundary, G is the Green function, $\theta(P)$ the angle between two tangents of the boundary at P (equal to π for a smooth curve) and s a curvilinear abscissa along Γ . Equation (5) is discretized using a standard collocation method. The boundary of the domain is approximated by segments and ϕ and ϕ_n are assumed to vary linearly along each segment. This allows an analytical integration of the Green function, its normal derivative and their products by the curvilinear abscissa so that the calculation of the matrix elements is rather simple (and vectorizes well).

3.2 Numerical Treatment at the Intersections

At each time-step, we have to solve a Neumann [along $\Gamma_n(t)$] – Dirichlet [along $\Gamma_d(t)$] boundary value problem. It is well known that the solution of such a “mixed” problem is singular at the intersection points, i.e., at points belonging both to $\Gamma_n(t)$ and $\Gamma_d(t)$ — e.g., [16].

Let us consider, as an example, the wavemaker problem. For a piston type wavemaker and an horizontal free surface (90° intersection angle), the complex potential $\Psi = \phi + i\psi$ solution of such a problem behaves like $z \log z$ near an intersection located at $z = 0$. This gives the expected behavior of the problem discretized in time.

Discretizing in time is similar to performing a small time expansion, i.e., to write:

$$\phi(\vec{x}, t) = \phi_0(\vec{x}) + t \phi_1(\vec{x}) + \dots \quad (6)$$

Not surprisingly, performing such an expansion also leads to a $z \log z$ behavior for ϕ_1 (e.g., [27], [21]). Does this, however, necessarily imply that this singular behavior has to be expected for the solution of the transient problem?

The answer is no, just because the small time expansion is not regular near the intersection point. It is, therefore, improper for a local analysis.

A regular expansion can be found in the *weakly nonlinear regime*, i.e. here, for a small acceleration of the wavemaker (relative to that of gravity) — see [9]. It appears that in this case the first approximation (in an asymptotic sense) is provided by the classical linear solution. The boundary condition for this solution is not a Dirichlet boundary condition; it is given by:

$$\phi_{tt} + \phi_y = 0. \quad (7)$$

If regularity in time is assumed, the local behavior of the complex potential for this solution can be shown to be in $z^2 \log z$. Not surprisingly, this singularity is the same as that appearing for the harmonic problem (for which $\phi = \varphi \exp(i\omega t)$) which was studied by Kravtchenko [20] as early as 1954. It is much weaker than that of the problem discretized in time.

The singularity can also be studied in a similar fashion for an arbitrary angle of intersection θ . Assuming that the complex potential is bounded near the intersection, the leading behavior of the complex potential can be shown to be in $z^{\pi/\theta}$ or $z^{\pi/\theta} \log z$ if π/θ is an integer².

A consequence is that, for an intersection angle smaller than π , ϕ is continuous along the boundary Γ while ϕ_s and ϕ_n are piecewise continuous but experience a finite jump at the intersections.

The numerical treatment at the intersection has been devised to accommodate such a behavior, referred to as *weakly singular*. More details on the numerical implementation can be found in [5] [7].

These results only apply in the weakly nonlinear regime, i.e., when the classical linear solution yields a first reasonable approximation to the problem. Obviously, it would be interesting to study other regimes.

The impulsive regime (very large acceleration of the wavemaker) has been studied by several authors. As ex-

pected, the local behavior of the classical linear solution cannot yield any information for the nonlinear problem in this case (e.g., [28]). It seems that Peregrine's solution [27] corresponds to an outer solution to which an inner solution should be matched. Of course, only this inner solution is relevant to the study of the local behavior. If work has been carried out to find an inner solution (e.g., [21] and [8]), it leads to serious difficulties and, to our knowledge, no definitive answer has been provided. It is only for the related — but different — water entry problem that there exists some results concerning the local behavior of the nonlinear solution (e.g., [7]).

3.3 Wave Absorption

In order to make proper comparisons with experiments and classical theories, it is often necessary to compute a steady state response.

When the linear solution is computed, one prescribes an incident wave and write a “radiation” condition that transmitted and radiated waves have to satisfy. Writing a proper radiation condition for the second-order problem has long been a matter of controversy. For the fully nonlinear problem, such an approach does not seem possible.

In the absence of any mathematically satisfying answer, we have chosen a pragmatic solution similar to that used for an experiment in a tank. This approach does not involve any hypothesis concerning the steepness of the outgoing waves.

Waves are generated by a wavemaker, either piston-type or flap-type. A “beach” is used for the absorption of the waves that are generated in the tank — see figure 1. It is in fact a damping zone, similar to that used in [1]. In this zone, the free surface boundary conditions are modified by adding a damping term. We therefore, write :

$$\frac{D\phi}{Dt} = -y - \left(\frac{1}{2} - \zeta\right) \phi_s^2 + \frac{1}{2} \phi_n^2 - \nu(x) (\phi - \phi_e) \quad (8)$$

$$\frac{D\vec{x}}{Dt} = \zeta \phi_s \vec{s} + \phi_n \vec{n} - \nu(x) (\vec{x} - \vec{x}_e), \quad (9)$$

where the subscript e corresponds to the reference configuration for the fluid. The function $\nu(x)$ is homogenous to a frequency.

The principle of this damping zone is to absorb the incident wave energy before it can reach the wall. It may be intuited that if the absorption is too weak, part of the incident wave energy will reach the wall and be reflected. Inversely, if the absorption is too strong, part of the energy will be reflected by the damping zone itself.

In practice, the damping coefficient $\nu(x)$ is equal to zero except in the damping zone ($x > x_0$), is chosen continuous and continuously differentiable, and is “tuned” to a characteristic wave frequency ω and to a characteristic wave number k :

$$\nu(x) = \alpha \omega \left\{ \frac{k}{2\pi} x - \beta \right\}^2, \quad x \geq x_0 = \frac{2\pi \beta}{k}. \quad (10)$$

If the proper scales have been chosen, values of α and β of order 1 should be appropriate for the absorption of a wave train of wave frequency ω and wave number k .

²The same singularity occurs at corners of rigid boundaries.

3.4 Validation

As indicated previously, the proper validation of the numerical simulation has been one of our main objectives. Solving the fully nonlinear problem can only be interesting if the accuracy of the numerical scheme is well established.

Several strategies exist for this validation.

Consistency checks should of course be performed. For that purpose, the volume and the rate of change of energy are computed. When no damping zone is present, this last quantity is compared to the power input from exterior loads. The pressure exerted by the fluid on rigid boundaries is computed by two different methods. Both of them use Bernoulli's equation, but they differ by the evaluation of the ϕ_t term. In one case, this term is evaluated by finite differences in time. In the other case, it is obtained by solving the boundary integral equation for ϕ_t .

In our opinion, consistency checks are not sufficient and comparisons with results from approximate methods are also needed. In the weakly nonlinear regime, the reference solution is the classical linear solution. However, a direct comparison with this linear solution is difficult, for two main reasons:

- * comparing the nonlinear simulation to a linear result can be confusing since discrepancies might be due to nonlinear phenomena. For that reason, a linear version of the code has been derived that only differs from the nonlinear version by the boundary conditions that are satisfied;

- * usually linear results are for the steady-state response while the simulation is transient. Discrepancies might be due to long-lasting transient phenomena, to the wave generation or absorption mechanism used, etc... A first step has therefore been to make proper comparisons with linear results for the transient problem in a tank of finite length.

The main interest of the method being to be able to account for nonlinear phenomena, a proper validation of the nonlinear response should be made. For that purpose, a comparison is performed with approximate nonlinear theories, such as second-order theory or shallow water theory.

A final test is provided by comparisons with experiments. In our opinion, however, these comparisons should only be made last if it is the accuracy of the numerical

scheme that has to be evaluated. In any event, a comparison with a linear result appears necessary in order to be sure that nonlinear phenomena are important. It should also be kept in mind that viscous effects can play an important role and are not accounted for in the simulation so that discrepancies might not be due to the inaccuracy of the numerical scheme but to an improper physical modeling.

4 Numerical Results

The purpose of this section is to show some numerical results that can appropriately be compared to other theories or to experiments. Numerical instabilities — encountered by many similar methods — may appear for waves of large steepness. In this case, a 5 points smoothing algorithm similar to that used in [22] is employed.

4.1 Sloshing in a Tank

The study of sloshing provides a first simple test for the accuracy of the simulation. We consider a rectangular tank and the free motion of a fluid initially out of equilibrium.

One of the main advantages of this configuration is that it allows quasi-analytical solutions of the transient problem to be derived at first- and second-order [9]. The efficiency of the numerical scheme for the solution of the linear and nonlinear problems can therefore be directly evaluated.

We consider the case of a constant initial slope of the free surface, i.e., an initial elevation given by:

$$y = \zeta d \left(\frac{x}{d} - 0.5 \right), \quad (11)$$

where d is the length of the tank. We show on figure 2 the free surface profiles for $d = 1$ (i.e., a depth equal to the length) and $\zeta = 0.35$. With such an initial amplitude, breaking occurs in the tank.

In order to evaluate the accuracy of the simulation, we compare on figure 3 the perturbation elevation,

$$y_p = \frac{y - y_{\text{linear}}}{(\zeta d)^2} \quad (12)$$

to the second-order wave elevation that has been computed quasi-analytically [9]. For $\zeta = 0.1$, a good agreement is

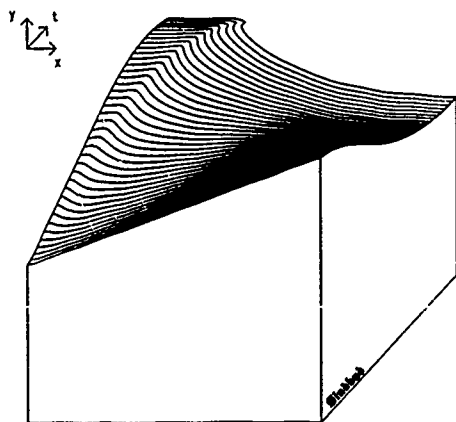


Figure 2: Sloshing — free surface profiles

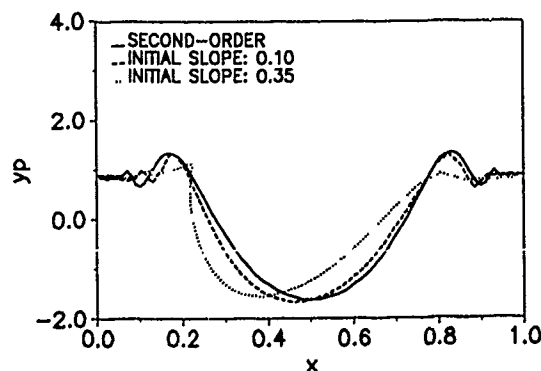


Figure 3: Sloshing — perturbation elevation

achieved, indicating that both the linear and second-order component of the wave elevation are accurately computed. For $\zeta = 0.35$, breaking occurs and the agreement deteriorates, suggesting that higher order effects become important. More results on this topic can be found in [9].

4.2 Harmonic Motion of a Piston-Type Wavemaker

The wavemaker problem is interesting because it provides a simple configuration to study most of the difficulties associated with the simulation. In particular, it involves a moving free surface piercing body (the wavemaker itself) that is absent in the sloshing problem.

In this section, the wavemaker motion is given by:

$$\ell(t) = 0 \quad t \leq 0 \quad (13)$$

$$\ell(t) = -\frac{a_\ell}{2} \cos(\omega t) \quad t \geq 0. \quad (14)$$

The length of the tank is d . Note that even though the motion is harmonic for $t \geq 0$, transient phenomena are expected.

4.2.1 Linear Solution in a Tank of Finite Length

For a tank of finite length, it is possible to derive a quasi-analytic solution for the linear transient problem that can be evaluated quite easily. This solution can be found in [12]; an alternative solution that seems to have better convergence properties has also been derived [9].

Since this problem involves a moving rigid boundary that pierces the free surface, it allows the numerical treatment of the intersection point to be evaluated. Here, we compare the result of the linear simulation and the quasi-analytic result. This ensures that discrepancies are only due to numerical errors.

As an example, we consider a wavemaker motion at the frequency $\omega = \pi/2$. The corresponding wave period and wave length are 4 and 2.5, respectively. The accuracy of the simulation has been evaluated at $t = 5$ in a tank of length 5. We show on table 1 the root mean square of the error (the reference 100 is taken as the error for the coarsest grid used, equal to $0.0903 a_\ell$) as a function of the number of nodes per wave length, NX , and the number of time steps per wave period, NT^3 .

$NT \downarrow / NX \rightarrow$	5	10	20	40	80	160
4	100	∞	∞	∞	∞	∞
8	61.3	26.2	10.6	∞	∞	∞
16	63.7	29.3	11.5	4.2	1.8	∞
32	64.0	29.9	13.7	5.3	2.3	1.3
64	64.0	29.9	14.4	5.4	2.5	1.4
128	64.0	29.9	14.4	5.4	2.5	1.4
256	64.0	29.9	14.4	5.4	2.5	1.4

Table 1: Convergence table

³A uniform grid is used and, thanks to the symmetry, the bottom is not discretized. No smoothing is applied. However, using the 5 points smoothing procedure introduced in [22], even a each time-step, does not significantly alter the accuracy of the method.

From this table, it appears that:

* a sufficiently small time-step has to be used in order for the numerical scheme not to blow up. The influence of the time-step is otherwise rather small;

* for a given spatial discretization, results converge as the time-step goes to zero. Note, however, that the numerical results do not converge to the exact solution;

* as the spatial discretization increases, results seem to converge to the exact solution. However, the convergence rate is not second-order in the grid size. This is very likely due to the numerical treatment at the intersection that is not second-order⁴.

4.2.2 Linear Solution in a Tank of Infinite Length

In order to test the efficiency of the damping zone, we consider now a tank of infinite length. For a piston type wavemaker, the solution far from the wavemaker and for large times is a progressive wave of amplitude:

$$a = a_\ell \frac{\sinh^2 k}{k + \sinh k \cosh k}. \quad (15)$$

where k is the wavenumber associated to ω ($\omega^2 = k \tanh k$). Note that in deep water ($k \rightarrow \infty$), $a \simeq a_\ell$.

We perform the simulation for the same wavemaker motion as in 4.2.1 but in a tank of length 10 equipped at its end of an absorbing zone. We compare on figure 4 the steady state linear solution and the result of the linear simulation with and without an absorbing zone for the wave elevation at the middle of the tank (distance 5 from the wavemaker). The damping coefficient is given by (10) with $\alpha = 1$ and $\beta = 1$. It appears clearly that the damping zone provides a simple and efficient way to avoid any reflection.

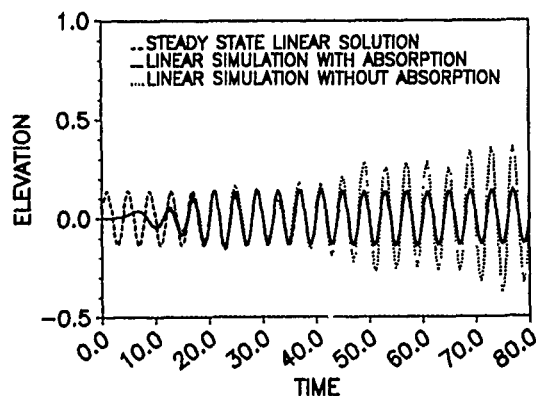


Figure 4: Wave elevation with and without damping zone

⁴This indicates that numerical errors are mainly due to the numerical treatment at the intersection. A convergence test for the problem with periodic boundary conditions is therefore not relevant to assess the accuracy of the simulation applied to the wavemaker problem.

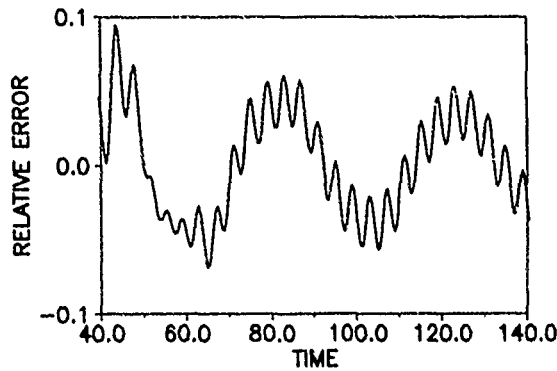


Figure 5: Damping zone — relative error vs. time

In order to evaluate more precisely the efficiency of the damping zone, we show on figure 5 the difference between the steady state linear solution and the result of the linear simulation for the relative wave elevation (wave elevation divided by the wave amplitude $\approx a_t$) at the same point. If long-lasting low frequency oscillations appear, the relative error is only of a few percents and the absorption mechanism appears to be quite satisfactory.

4.2.3 Nonlinear Solution in Shallow Water

In order to estimate the accuracy of the method for the nonlinear computation, we first consider the case of a shallow water swell.

Mei and Unliata [24] have explained how such a swell can experience very drastic nonlinear deformations when it propagates. Very recently, Chapalain [2] has performed experiments at the Institut de Mécanique de Grenoble that neatly confirm this bi-harmonic resonant behavior. It appeared therefore interesting to try and reproduce them with the simulation.

The only data for the numerical simulation are the geometry of the tank, the law of motion of the wavemaker and the friction coefficient f_w used to model dissipation⁵. The experiment was performed in a 40 cm deep tank with a piston-type wavemaker the motion of which was given by (14) with $a_t = 15.9$ cm and $\omega = 2.5$ rad/s. The total length of the tank, 36 m, is simulated using 300 nodes on the free surface. The simulation on 30 s took approximately 7 minutes on a CRAY-XMP.

⁵In order to model dissipative effects in a way similar to that used by Chapalain for Boussinesq equations we substitute to Bernoulli equation:

$$\phi_t + \frac{1}{2} \nabla \phi \cdot \nabla \phi + y + \nu \phi = 0$$

with

$$\nu = \frac{4}{3\pi} f_w \frac{a_t \omega}{2}.$$

We took the value of f_w used by Chapalain, $f_w = 0.1$. Note that this modeling of dissipative effects, already used in [14] for the study of sloshing, is similar to the modeling of the damping zone.

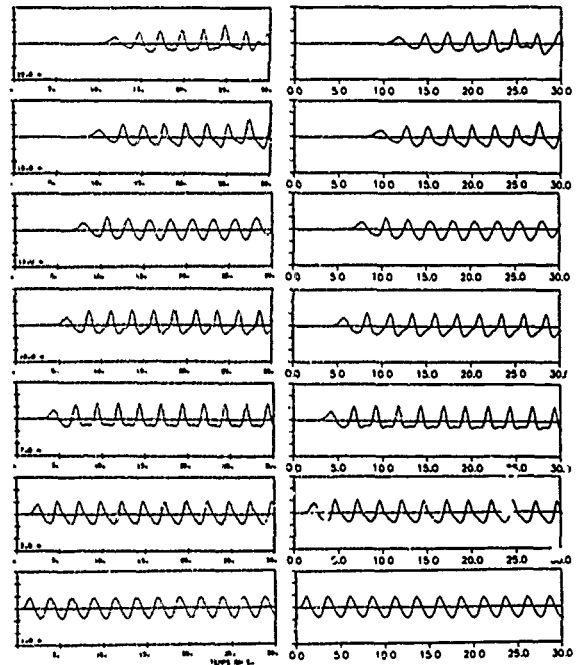


Figure 6: Shallow water swell — measured (left) vs. computed (right) wave elevations at several points in the tank

We compare on figure 6 the measured and computed wave elevations at several points in the tank. An excellent agreement is achieved. This agreement is confirmed by a Fourier analysis performed once a steady state is reached. The amplitude of the first three harmonics is plotted as a function of the distance along the tank on figure 7. It appears that the simulation is very efficient to model shallow water waves and their generation by a wavemaker.

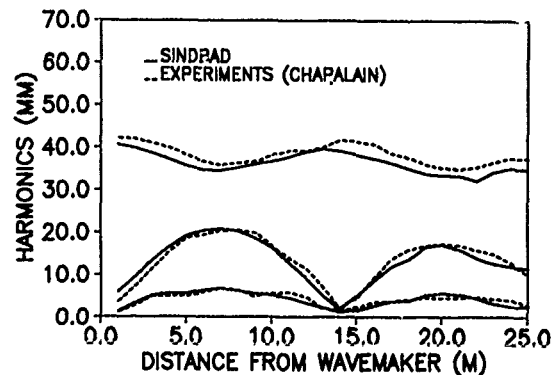


Figure 7: Shallow water swell — measured vs. computed Fourier components

4.3 Arbitrary Motion of a Piston-Type Wavemaker

In deep water, nonlinear phenomena in the propagation of a regular swell are rather long to develop. Numerical methods with periodic boundary conditions, such as [10], are probably more suited to the study of this problem than the direct simulation of a wave tank.

An appropriate choice for the motion of the wavemaker can however lead to wave focusing that results in breaking. Experiments based on this principle were performed at MIT and a comparison with a numerical simulation similar to ours made — see [12] where the law of motion of the wavemaker is given. The main drawback of this test case is that it involves a large amount of computer time. We have run Sindbad on the same case, but using an absorbing zone and a somehow coarse grid in order to minimize computational effort. The calculation has been performed on a CRAY-XMP and demanded "only" 30 minutes with 250 nodes on the free surface (compared to 30 hours with 500 nodes on a CRAY 1 for the simulation performed at MIT).

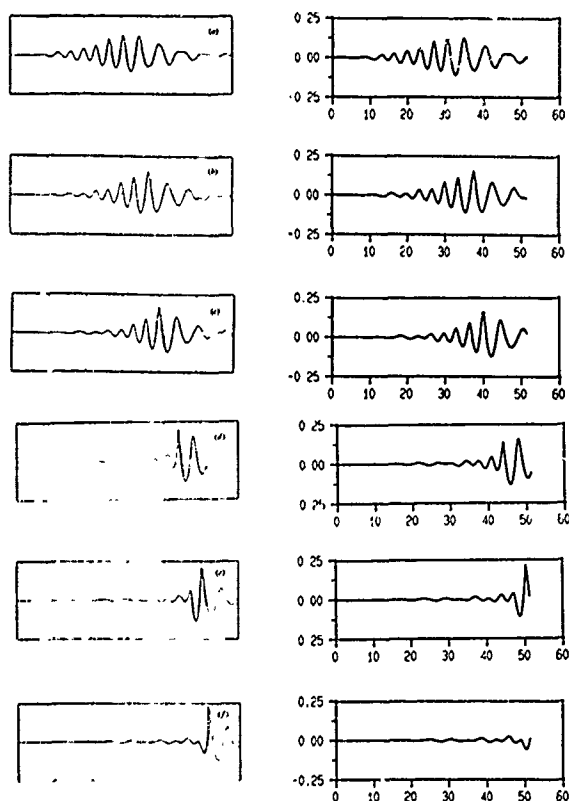


Figure 8: Steep deep water waves — measured (left, dashed line) vs. computed (solid line, left: MIT, right: Sindbad) wave elevations at several points in the tank

⁶Our own experience tends to suggest that "numerical" overturning is very sensitive to the discretization used and more particularly to the node distribution along the free surface. Here again the validity of the simulation is difficult to establish. Our interest has been mainly to perform the simulation up to the point where breaking occurs.

The results of our simulation are in good agreement with both experimental and numerical results obtained at MIT up to breaking — see figure 8. If overturning develops at the same time, our computation fails sooner than their (before the closing of the tube)⁶.

This confirms that the numerical simulation can reproduce accurately nonlinear phenomena observed experimentally.

4.4 Wave Diffraction on a Submerged Cylinder

The case of the wave diffraction on a submerged cylinder allows a first study of wave-structure interaction. This problem has been studied extensively in the past. In particular, Ursell [31] used linear theory and showed that, for a circular cylinder, there is no reflection. Ogilvie [25] extended Ursell's results and computed the second-order vertical drift force. Very recently, Vada [32] computed the second-order potential and calculated the diffraction loads and the diffracted waves to second-order.

Chaplin [3] measured diffraction loads in the laboratory while Grue and Granlund [17] measured the diffracted waves. These experiments have partly confirmed the results of first- and second-order theories. They have also exhibited some important nonlinear phenomena not accounted for by these theories. Such nonlinear phenomena can either be due to nonlinear free surface effects (of third-order or higher) or to viscous effects.

Consequently, the present study has two main objectives:

- ★ to recover the results of first- and second-order theories in order to assess the numerical accuracy of the method;
- ★ to compare with experimental results in order to determine the relative importance of viscous and free surface effects for the nonlinear phenomena observed.

Fully nonlinear simulations similar to ours have been performed by several authors (e.g., [29], [11]). In general, periodic boundary conditions were used. To our knowledge, however, comparisons with second-order theory were not achieved.

4.4.1 Diffraction Loads

We consider a circular cylinder of radius $r = 0.06$. The coordinates of its center are $x_c = 3.5$ and $y_c = -0.12$. Waves are generated by a piston-type wavemaker moving at the frequency $\omega = 1.85$. The simulation is made in a tank of length 10 with 200 markers at the free surface and 60 time-steps per period.

The forces acting on the cylinder are computed by direct integration of the pressure.

In order to compare the results with those of experiments or of first- and second-order theory, we use a Fourier series expansion of the transient signal (once a steady-state is reached). This yields :

$$\frac{F_x}{r^3\omega^2} = F_x^{(0)} + \sum_{n \geq 1} F_x^{(n)} \cos(n\omega t + \theta^{(n)}) \quad (16)$$

$$\frac{F_y}{r^3\omega^2} = F_y^{(0)} + \sum_{n \geq 1} F_y^{(n)} \cos(n\omega t + \theta^{(n)}), \quad (17)$$

where the subscript x and y denote the horizontal and vertical components of the force, respectively.

ka	K_c	$F_x^{(0)}$	$F_y^{(0)}$	$F_x^{(1)}$	$F_y^{(1)}$	$F_x^{(2)}$	$F_y^{(2)}$
0.05	0.50	0.00	0.04	1.07	1.07	0.07	0.07
0.07	0.75	0.00	0.10	1.58	1.58	0.15	0.15
0.10	1.00	-0.01	0.16	2.07	2.06	0.24	0.25
0.12	1.25	-0.02	0.24	2.52	2.51	0.33	0.34
0.14	1.47	-0.03	0.30	2.88	2.87	0.41	0.41

Table 2: Diffraction loads — Sindbad

As in [3] we introduce the Keulegan-Carpenter number, K_c . For a linear deep-water wave, K_c is given by:

$$K_c = \frac{\pi a}{r} \exp(ky_c). \quad (18)$$

Table 2 gives the values of $F_x^{(n)}$ and $F_y^{(n)}$ for $n = 0, 1, 2$ vs. K_c in the case just described (that corresponds to Chaplin case E [3]).

Following Chaplin, we write :

$$F_x^{(n)} = \sum_{m \geq 1} C_{xnm} K_c^m, \quad (19)$$

$$F_y^{(n)} = \sum_{m \geq 1} C_{ynm} K_c^m. \quad (20)$$

The classical inertia coefficients are equal to C_{x11} et C_{y11} . According to linear theory, these are the only non-zero coefficients and they are equal. Ogilvie [25] calculated them; they go to 2 as the immersion depth goes to infinity.

We give on figure 9 the horizontal and vertical inertia coefficients vs. K_c . For a small value of the Keulegan-Carpenter number, both experimental and numerical results go the value predicted by linear theory, 2.25. As K_c increases, however, the sharp decrease of the inertia coefficient observed experimentally is not predicted by the simulation. As argued by Chaplin, this is very likely due to viscous effects (creation of a circulation around the cylinder).

Figures 10 and 11 give the second-order vertical drift force and the force at the double frequency, respectively. Here, a good agreement appears between experiments, second-order theory and the present simulation. It should be stressed that recovering the results from second-order steady theory with the simulation is by no means obvious: it demands a good accuracy and a proper control of the wave generation and absorption mechanism. It can be argued that the results of the simulation are better than those of second-order theory for large values of K_c .

4.4.2 Diffracted Waves

Grue and Granlund [17] performed experiments related to incoming deepwater Stokes waves passing over a restrained submerged circular cylinder. For a small cylinder submergence, a strong local nonlinearity is introduced at the free surface above the cylinder and free higher order harmonic waves are generated.

We remind of the observations of Grue and Granlund

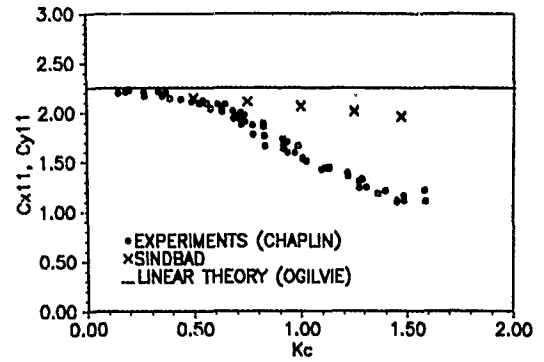


Figure 9: Diffraction loads — inertia coefficients

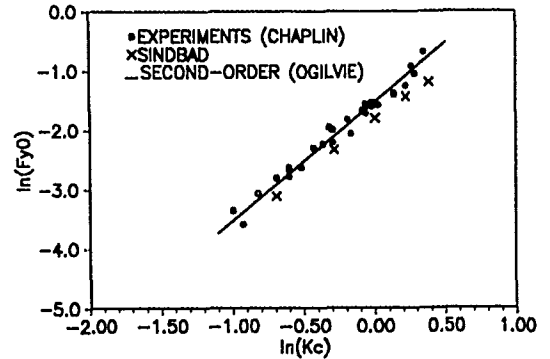


Figure 10: Diffraction loads — vertical drift force

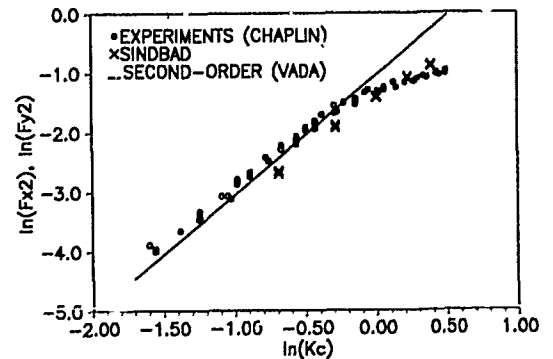


Figure 11: Diffraction loads — response at double frequency

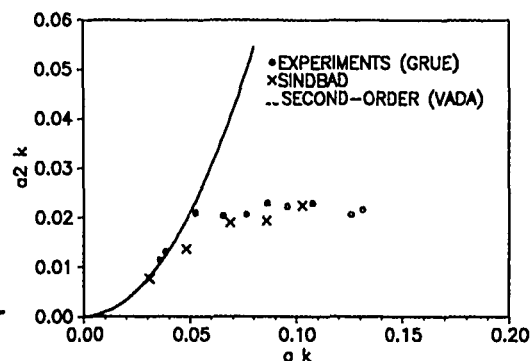


Figure 12: Diffracted waves — amplitude of second-order free wave

concerning the wavefield far away from the cylinder:

★ upstream of the cylinder: an incoming Stokes wave-train. No reflected waves, even to higher order;

★ downstream of the cylinder: shorter free second harmonic waves of considerable amplitude are riding on the transmitted Stokes wave.

If these trends are well predicted by second-order theory [32], the quantitative agreement with experiments is rather disappointing. The amplitude of the second harmonic free wave, a_2 , only increases as the square of the amplitude of the incoming wave, a , for very small values of a . A “saturation” rapidly appears; thereafter a_2 remains almost constant — see figure 12.

These findings suggest that the range of validity of second-order theory is quite narrow in this case. Observing that this theory predicts amplitudes of the second-order free wave as large as that of the incoming wave, this should not appear as totally unexpected. In order to see if nonlinear free surface effects — and not viscous effect — are, indeed, responsible for this deficiency, it appeared interesting to run Sindbad on this case.

In order to compare our results with those of Grue and Granlund, we write (once a steady state is reached):

★ for the incident wave:

$$\eta_i = a \cos(kx - \omega t + \theta) + a^2 \cos 2(kx - \omega t + \theta) + \dots, \quad (21)$$

where a^2 is the amplitude of the second-order locked wave;

★ for the diffracted wave:

$$\eta_d = a_1 \cos(kx - \omega t + \theta_1) + a_2^L \cos 2(kx - \omega t + \theta_1) + a_2 \cos(4kx - 2\omega t + \theta_2) + \dots, \quad (22)$$

where a_2^L and a_2 are the amplitudes of the second-order locked and free wave, respectively.

In order to exhibit the second-order free wave, it is necessary to take a rather fine grid. The wavenumber of this free wave is, indeed, four times larger than the wavenumber of the incoming wave. The wavenumber of the incoming wave is chosen equal to $k = 3.42$ (so that we are in deep

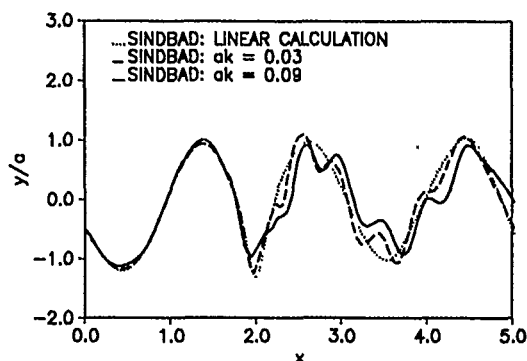


Figure 13: Diffracted waves — free surface profiles

water). With these choices, the results shown by Grue and Granlund correspond to a cylinder radius $r = 0.117$ and a depth of immersion of the center of the cylinder $y_c = -0.1755$.

The simulation was performed in a tank of length 8, with a damping zone of length 3. The cylinder center was located at a distance $x_c = 2$ from the wavemaker. 340 nodes were distributed on the free surface and 60 time steps used per period of the incoming wave.

On figure 13, free surface profiles after 7 periods are shown for several amplitudes of the incident wave. The apparition of a perturbation of wavenumber $4k$ is obvious. However, its amplitude does not increase as the square of the incident wave amplitude.

A Fourier analysis of the diffracted wave confirms this trend. We show on figure 12 the comparison between Grue and Granlund's experiments, Vada's second-order theory and the present calculation. The agreement between the numerical simulation and the experiments is very good, indicating that the “saturation” is, indeed, a nonlinear free surface phenomenon not accounted for by second-order theory.

Grue and Granlund observed breaking for $ak \approx 0.085$, while we were able to perform the numerical simulation up to $ak = 0.12$. It is rather interesting to note that this does not seem to affect the amplitude of the second-order free wave.

A little more surprising is the reason for which the numerical computation fails for $ak = 0.12$ after 3.2 periods. The computation does not blow up because of the overturning of the crest, as would have been expected, but because of a concentration of particles just aft the cylinder. Physically, it seems that particles flow very rapidly over the cylinder and are then decelerated. Here again, the validity of the simulation is difficult to establish.

It is rather interesting to note that for waves passing over a submerged cylinder, nonlinear free surface effects are important for the diffracted waves but do not seem to affect very much the forces.

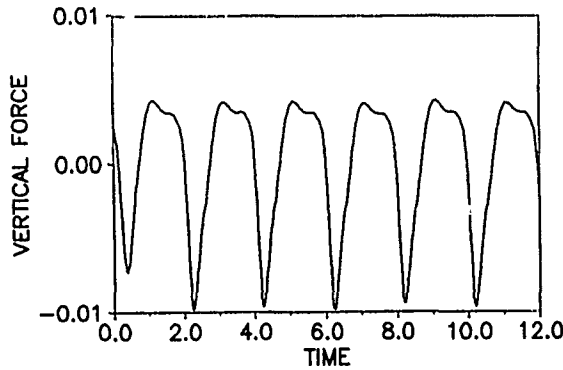


Figure 14: Forced heaving — transient force

4.5 Wave Radiation by a Free Surface Piercing Cylinder

As a last example, we consider the case of a free surface piercing body in forced or free motion.

4.5.1 Forced Motion

Forced motions of a free surface piercing circular cylinder have been studied quite extensively using linear and second-order theory (e.g., [26], [19]). Fully nonlinear calculations have also been attempted for forced heaving of a circular cylinder by a few authors. Initially ([13], [33]) only the starting phase was considered. Recently, Hwang et al. [18] calculated the steady state response and made comparisons with first- and second-order theories and with experiments.

As an example, we consider the case of a half-immersed circular cylinder with $kr = 1$. The simulation is performed in a tank of length 4 with a forcing frequency $\omega = 3.16$ (so that $k = 10$). The cylinder center has for elevation:

$$y_c = 0 \quad t \leq 0 \quad (23)$$

$$y_c = a_c \sin(\omega t) \quad t \geq 0. \quad (24)$$

Because there is no wavemaker in this case, absorbing beaches (with $\alpha = \beta = 1$) are located at each end of the tank. We used 200 nodes on the free surface. In order to avoid too small or too large segment sizes near the intersection, a regridding procedure similar to that introduced in [11] was used when a node came too close or too far from the intersection.

We show on figure 14 the transient vertical force on the cylinder as a function of time for $a_c = 0.5 r$. If a steady state is rapidly reached, the signal is obviously not monochromatic and harmonics are present.

The free surface profiles corresponding to this case are shown on figure 15.

Once a steady state is reached, we write the force as:

$$\begin{aligned} \frac{F_y + 2r y_c}{0.5\pi r^2 a_c \omega^2} &= F_y^{(0)} + F_y^{(1a)} \sin(\omega t) - F_y^{(1v)} \cos(\omega t) \\ &+ \sum_{n=2}^{\infty} F_y^{(n)} \sin(n\omega t + \theta^{(n)}). \end{aligned} \quad (25)$$

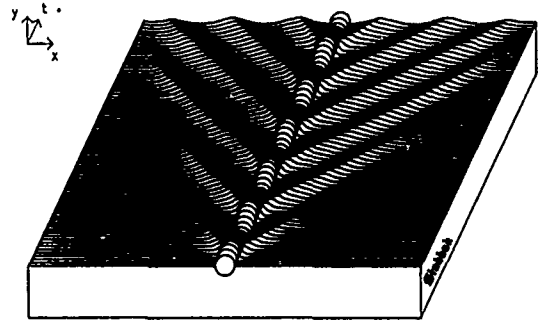


Figure 15: Forced heaving — free surface profiles

The second term on the left-hand side is the *linear* hydrostatic contribution. The acceleration-phase and velocity-phase components of the force at the forcing frequency would correspond to the added mass and damping coefficients for the linear problem⁷.

ϵ	$F_y^{(0)}$	$F_y^{(1a)}$	$F_y^{(1b)}$	$F_y^{(2)}$	$F_y^{(3)}$	$F_y^{(4)}$
0.1	-0.02	0.61	0.39	0.06		
0.2	-0.03	0.62	0.38	0.12	0.02	
0.3	-0.05	0.63	0.36	0.18	0.04	0.02
0.4	-0.07	0.65	0.35	0.23	0.08	0.05
0.5	-0.10	0.66	0.33	0.30	0.14	0.09

Table 3: Radiation loads — Sindbad

We give on table 3 the amplitude of the different harmonics as a function of $\epsilon = a_c/r$. The Fourier analysis is performed on the four last periods of the signal. For small values of ϵ , the results from linear and second-order theory are recovered (e.g., [26], [19]). As the amplitude of the motion increase, the added mass increases while the damping coefficient decreases. This behavior is in agreement with available experimental observations [19] and other numerical results [18].

The importance of relatively high-order harmonics is quite remarkable. For $\epsilon = 0.5$, the ratio of the amplitude of the fourth harmonic to that of the first is almost equal to 15%. This behavior, that obviously cannot be accounted for using second-order theory, is quite different from that observed for the diffraction over a submerged cylinder. It shows the interest of a fully nonlinear simulation, in particular in order to assess the range of validity of approximate theories. If these results for forced motions are very promising, more experimental data would be needed to make proper comparisons.

Note that for $\epsilon = 0.6$ the numerical computation breaks down before a steady state is reached, apparently because the cylinder goes out of the water.

⁷Note that for the nonlinear problem the distinction between added-mass and hydrostatic components is somehow arbitrary.

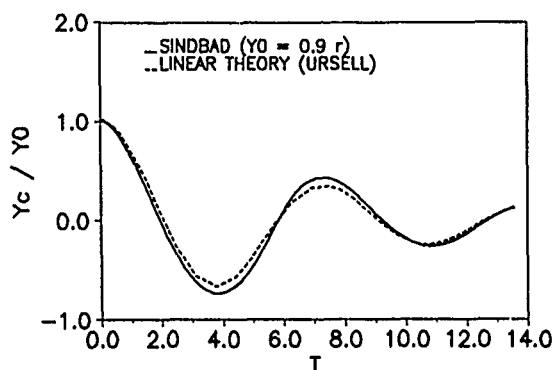


Figure 16: Free heaving — vertical displacement

4.5.2 Free Motion

The free motion of a surface piercing circular cylinder was calculated using linear theory in [23]. A fully nonlinear computation was performed in [33] using periodic boundary conditions. A good agreement between these two theories was achieved.

Here, we performed again the same calculation. The body motion is calculated in a way similar to that used in [33] (see [7] for details on the numerical implementation). At $t = 0$, the fluid is at rest and the cylinder, which is half-immersed at equilibrium, has an elevation:

$$y_c(0) = y_0. \quad (26)$$

We show on figure 16 the subsequent vertical displacement of the cylinder, y_c , for $y_0 = 0.9 r$. The simulation is performed exactly in the same conditions as in the preceding section. The absence of any nonlinear behavior for the cylinder elevation is rather striking and contrasts with the forced motion case.

5 Conclusions

The MEL has been applied to the numerical simulation of a wave tank equipped at one end with a wave maker and at the other end with a damping zone. This configuration allows two-dimensional wave-structure interaction problems to be studied.

Results have been presented that include a wide range of applications, such as wave generation and absorption, wave diffraction and wave radiation by submerged or surface piercing bodies in forced or free motion. Results from approximate theories (linear, second-order or shallow water theory) can be recovered, not only for short transient evolutions but also for steady state responses. Some nonlinear phenomena observed experimentally and that have not been otherwise explained are also accounted for. This seems to indicate that the simulation can be used as a "standard" that allows the validity of approximate theories to be assessed. Applications of the method in that direction suggest themselves. In particular, the roll motion of barges is being presently studied.

If the MEL provides an efficient and versatile way to study two-dimensional free surface problems, it cannot account for viscous effects (except in a very crude way for instance for the modeling of bottom friction). This is particularly a problem for viscous effects occurring in the near vicinity of the free surface, i.e., viscous effects associated to breaking. Breaking is a major limitation for the simulation because the calculation has to stop whenever a local breaking event occurs.

It would therefore be most useful to be able to simulate breaking and associated dissipative effects, even in a crude way. Some hope exists (e.g., [30], [4]) for spilling breakers, but there is an obvious need for more theoretical and experimental work on the subject.

6 Acknowledgements

This work is a result of research sponsored in part by the "Ministère de la Défense", DRET, under convention number 88/073. This support is gratefully acknowledged.

References

- [1] BAKER, G.R., MEIRON, D.I., and ORSZAG, A., 1981, "Applications of a generalized vortex method to nonlinear free-surface flows," Third International Conference on Numerical Ship Hydrodynamics, Paris, pp. 179-191.
- [2] CHAPALAIN, G., 1988, "Etude hydrodynamique et sédimentaire des environnements littoraux dominés par la houle," Thèse de Doctorat de l'Université Joseph Fourier, Grenoble (in French).
- [3] CHAPLIN, J.R., 1984, "Nonlinear forces on a horizontal cylinder beneath waves," *J. Fluid Mech.*, Vol. 147, pp. 449-464.
- [4] COINTE, R., 1987, "A theory of breakers and breaking waves," Ph. D. Dissertation, University of California, Santa Barbara.
- [5] COINTE, R., 1988, "Remarks on the numerical treatment of the intersection point between a rigid body and a free surface," Third International Workshop on Water Waves and Floating Bodies, Woods Hole, Mass.
- [6] COINTE, R., 1989, "Calcul des efforts hydrodynamiques sur un cylindre horizontal en théorie potentielle non-linéaire", Deuxièmes Journées de l'Hydrodynamique, Nantes, pp. 89-104 (in French).
- [7] COINTE, R., 1989, "Quelques aspects de la simulation numérique d'un canal à houle", Thèse de Doctorat de l'Ecole Nationale des Ponts et Chaussées, Paris (in French).
- [8] COINTE, R., JAMI, A., and MOLIN, B., 1987, "Nonlinear impulsive problems," Second International Workshop on Water Waves and Floating Bodies, Bristol.
- [9] COINTE, R., MOLIN, B., and NAYS, P., 1988, "Nonlinear and second-order transient waves in a rectangular tank," BOSS'88, Trondheim.

- [10] DOLD, J.W., and PEREGRINE, D.H., 1986, "Water-wave modulation," Bristol University, Report AM-86-03.
- [11] DOMMERMUTH, D.G., 1987, "Numerical methods for solving nonlinear water-wave problems in the time domain," Ph.D. Dissertation, MIT.
- [12] DOMMERMUTH, D.G., YUE, D.K.P., RAPP, R.J., CHAN, E.S., and MELVILLE, W.K., 1988, "Deep-water plunging breakers: a comparison between potential theory and experiments," *J. Fluid Mech.*, Vol. 189, pp. 423-442.
- [13] FALTINSEN, O.M., 1977, "Numerical solutions of transient nonlinear free surface motion outside or inside moving bodies," 2nd International Conference on Numerical Ship Hydrodynamics, Berkeley, pp. 347-357.
- [14] FALTINSEN, O.M., 1978, "A numerical method of sloshing in tanks with two-dimensional flow," *Journal of Ship Research*, Vol. 22, pp. 193-202.
- [15] GREENHOW, M., 1987, "Wedge entry into initially calm water," *Applied Ocean Research*, Vol. 9, pp. 214-223.
- [16] GRISVARD, P., 1984, "Problèmes aux limites dans les polygones — mode d'emploi", Prépublication du laboratoire de mathématiques de l'Université de Nice (in French).
- [17] GRUE, J., and GRANLUND, K., 1988, "Impact of nonlinearity upon waves traveling over a submerged cylinder," Third International Workshop on Water Waves and Floating Bodies (Woods Hole).
- [18] HWANG, J.H., KIM, Y.J., and KIM, S.Y., 1988, "Nonlinear Hydrodynamic Forces Due to Two-dimensional Forced Oscillation," Proceedings, IUTAM Symposium on Nonlinear Water Waves (Tokyo), Springer-Verlag, pp. 231-238.
- [19] KYOZUKA, Y., 1982, "Experimental study of second-order forces acting on a cylindrical body in waves," Proceedings, 14th Symposium Naval Hydrodynamics, Ann Arbor.
- [20] KRAVTCHENKO, J., 1954, "Remarques sur le Calcul des Amplitudes de la Houle Linéaire Engendrée par un Batteur", 5th Conf. Coastal Eng., Grenoble, France, pp. 50-61 (in French).
- [21] LIN, W.M., 1984, "Nonlinear motion of the free surface near a moving body," Ph. D. Dissertation, MIT, Cambridge, Mass.
- [22] LONGUET-HIGGINS, M.S., and COKELET, E.D., 1976, "The deformation of steep surface waves on water. 1. A numerical method of computation," *Proc. R. Soc. London*, Vol. A 364, pp.1-26.
- [23] MASKELL, S.J., and URSELL, F., 1970, "The transient motion of a floating body," *J. Fluid Mech.*, Vol. 44, pp. 303-313.
- [24] MEI, C.C., and UNLUATA, U., 1972, Harmonic generation in shallow water waves," *Waves on beaches*, R.E. Meyer, Ed., Academic Press, pp. 181-202.
- [25] OGILVIE, T.F., 1963, "First- and second-order forces on a cylinder submerged under a free surface," *J. Fluid Mech.*, Vol. 16, pp. 451-472.
- [26] PAPANIKOLAOU, A., and NOWACKI, H., 1980, "Second-order theory of oscillating cylinders in a regular steep wave," Proceedings, 13th Symposium Naval Hydrodynamics, Tokyo.
- [27] PEREGRINE, D.H., 1972, Unpublished note.
- [28] ROBERTS, A.J., 1987, "Transient Free Surface Flows Generated by a Moving Vertical Plate," *Q. J. Mech. Appl. Math.*, Vol. 40, Pt. 1.
- [29] STANSBY, P.K., and SLAOUTI, A., 1984, "On nonlinear wave interaction with cylindrical bodies: a vortex sheet approach," *Appl. Ocean Res.*, Vol. 6, pp. 108-115.
- [30] TULIN, M.P., and COINTE, R., 1987, "Steady and unsteady spilling breakers: theory," Proceedings, IUTAM Symposium on Nonlinear Water Waves, Tokyo, pp. 159-165.
- [31] URSELL, F., 1950, "Surface waves in the presence of a submerged circular cylinder, I and II," *Proc. Camb. Phil. Soc.*, Vol. 46, pp. 141-158.
- [32] VADA, T., 1987, "A numerical solution of the second-order wave-diffraction problem for a submerged cylinder of arbitrary shape," *J. Fluid Mech.*, Vol. 174, pp. 23-37.
- [33] VINJE, T., and BREVIG, P., 1981, "Nonlinear, two-dimensional ship motions," Norwegian Institute of Technology, Rapport R-112.81.

Slamming of Flat-Bottomed Bodies Calculated with Exact Free Surface Boundary Conditions

S. Falch
Norwegian Marine Technology Research Institute
Trondheim, Norway

ABSTRACT

The impact of a flat-bottomed two-dimensional body which falls vertically towards initially calm water is studied theoretically and numerically. The flow in the compressible air layer between the body and the water surface is calculated by assuming that the air is inviscid and the flow is one-dimensional. The calculation of the flow in the water is based on potential theory, and a boundary-integral-equation technique with exact nonlinear boundary conditions are used. The effect of various deadriseangles has been studied, and the pressure acting on the bottom of the body is calculated until the body makes contact with the deformed water surface.

List of symbols

b	Half width of body
c	Velocity of sound in air.
c_0	Velocity of sound in air at atmospheric pressure.
c_w	Velocity of sound in water.
C_D	Constant in nondimensional momentum equation.
C_*, C_*	Family of characteristic curves.
g	Acceleration of gravity.
h	Distance between body and water surface.
H	Elevation of the bottom of the body at centerline.
H_0	Value of H at start of the numerical calculation.
H_A	Amplitude of forced heave oscillation
K	Number of elements on body.
M	Two-dimensional mass of body.
N	Number of elements in air calculation.
N_A	Number of surface elements between $x = 0$ and $x = b$.
N_F	Total number of boundary elements.
n_2	y-component of the unit normal vector.
p	Pressure in the air
p_0	Atmospheric pressure.
r	Radius of cylinder.
S	Surface of body.
S_1	Cylindrical surface of small radius.
S_B	Horizontal control surface far down.
S_c	The free surface of water.
S_∞	Vertical control surface far away.
t	Time.
u	Velocity of air in x-direction.
v	Velocity of body.
v_0	Velocity of body at start of the numerical calculation.

x	Horizontal space coordinate.
x_F	x-coordinate of fluidparticle.
y	Vertical space coordinate.
γ	Exponent in the relationship between p and ρ .
ζ	Elevation of the water surface.
θ	Deadrise angle.
ρ	Density of air.
ρ_0	Density of air at atmospheric pressure.
ρ_w	Density of water.
ϕ	Velocity potential.
ψ	Streamfunction.
ω	Circular frequency of heave oscillation.
Δx	Width of element along the x-axis.
Δt	Timeperiod between two timesteps.

CHAPTER 1. INTRODUCTION

Section 1.1 General

The aim of this work is to calculate the pressure on a flat-bottomed body which is falling through air towards initially calm water and subsequently penetrates into the water. The effect of the entrapped air between the body and the water surface is specially studied.

This is a particular case of the general slamming problem where an arbitrary shaped body hits the arbitrary shaped free surface of the water, or it may be the water that hits the body. The pressure and the force acting on the body due to this, will in several applications be of significant interest to marine designers.

The classic example occurs when a ship is travelling at high speed or in heavy sea, and the bow moves out of and reenters the water. Severe damage on shipbows has been reported as a consequence [8].

Considerable impact forces may also occur when large waves hit cross members or deckstructures of offshore oilrigs.

Finally the situation must be mentioned where different kind of equipment such as a mini-submarine is lowered or lifted through the splash-zone. Specially if the equipment is operated by a crane situated on some kind of floating platform, the relative motion between the water surface and the equipment may in rough weather be considerable causing significant impact loads.

The calculation of impact loads in these situations is needed in order to determine the required strength of the structures involved.

For the case of slamming of a ship bow or lowering of equipment through the splash zone, knowledge of the impact loads is also required in order to determine in what kind of weather condition certain operations may be carried out.

A better understanding of the whole phenomena of slamming will also give information on how to design the shape of the structures in order to minimize the impact loads.

To calculate the impact loads in the cases mentioned here, is very difficult. The problem has to be simplified. The purpose of such simplifications may partly be to find approximate solutions to the real problems, and partly to be a step on the road to more sophisticated methods. For this purpose it seems reasonable that one way of making the simplifications is to divide the problem into sub-problems. Special phenomena can then be studied separately. The most obvious simplification will be to start to study two-dimensional problems. Another simplification which seems reasonable, is to assume that the real problem may be approximated by the entry of a body into calm water with velocity equal to the relative velocity between the body and the moving free surface. Such an approximation is expected to be good if the dimensions of the body is small compared to the wavelength. With the above approximations are made by several other authors. The bodies involved may have various different forms. Some of them lead to certain phenomena which needs to be studied specially. In this work it has been chosen to study flat-bottomed bodies.

This discussion leads to the conclusion that it is interesting to study the following particular case, and which may be characterized by

- The calculations will be two-dimensional. That means that the results will be approximately valid for a slender horizontal body.
- The body will be symmetrical.
- The water is initially calm.
- The body is falling vertically under influence of gravity and the pressure force on the bottom. (The body may also have prescribed motion.)
- The body is completely rigid.
- The body is almost flat-bottomed. That means it may have a small deadrise angle.

For this particular case, the aim is to calculate the pressure distribution on the surface of the body and the flow in the water and the air as a function of time, both before and after the moment when the body makes contact with the water surface.

The calculation will include both the effect of entrapped air and the possibility of large water surface elevation. This is a theoretical and numerical study. No experiments have been carried out, but the results of this work have been compared with other works, both theoretical and experimental.

In the effort to achieve this aim, several simplifications, especially on the properties of water and air, will be made. The introduction, and the discussion of the justification, of these simplifications will be done in the following chapter, but they will all be of such a kind that they will have more or less negligible influence on the results of the calculation.

Section 1.2 Background

Until the beginning of the nineteensixties, the theories of von Karman [1] and Wagner [2] was used to predict hydrodynamic impact forces. These theories neglected the influence from the air, and in the case of a flat-bottomed body, von Karman suggested that the maximum impact pressure was the acoustic pressure of water.

Then several experimental and theoretical works was done, which showed that for the case of a flat-bottomed body the effect of the air between the body and the water surface has to be taken into account in order to predict the impact pressure more correctly.

They found that the cushioning effect of the trapped air in the layer between the falling body and the water surface reduced the impact pressure to approximately one-tenth of the acoustic pressure.

The most significant of these works was experiments made by Chuang [3, 4] and Lewison and Maclean [5] and a theoretical and experimental study made by Verhagen [6].

In 1977 Koehler and Kettleborough [7] presented a theoretical study which shows in detail the calculated pressure in the airgap and the surface elevation for one of the cases used in the experimental study of Lewison and Maclean.

Verhagen describes that pictures taken during his experiments shows that the water elevation is at first noticeable at the edges of the body just before the plate touches the water surface. Next, the air layer breaks up into bubbles beginning at the edges and extending to the center of the body with a speed in the order of magnitude equal to the velocity of sound in air. With increasing time the bubbles drift relatively slowly outwards.

Chuang [4] present some interesting sketches of the situation after impact based on photographs taken during experiments. These sketches are given in Fig. 1.1.

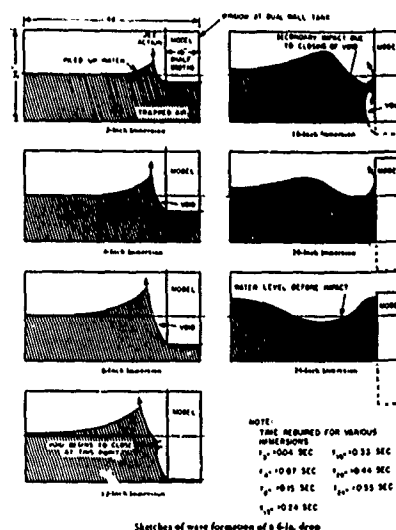


Fig. 1.1

In the theoretical work of both Verhagen and Koehler and Kettleborough a two-dimensional problem was studied. They assumed that a compressible inviscid air layer exists between the body and the water surface. As the body falls, the air in the layer flows one-dimensionally outwards from the centre of the body. The water is assumed to be incompressible and Verhagen states that this is a good approximation if the velocity of the body do not exceed a few meters per second.

In both works the calculation of the flow in the water is based on linear free surface condition. The pressure distribution is calculated until the edge of the body makes contact with the elevated water surface, and Koehler and Kettleborough assumes that the maximum impact pressure is reached at this time-instant. Verhagen also calculates the pressure in the trapped air bubble after this time by a simplified method assuming that the pressure in the bubble and the downward velocity of the water surface within the bubble is only a function of time. Koehler and Kettleborough makes the calculation with different deadriseangles. The intention is to predict the uncertainty in experiments due to the fact that in an experimental set up it is not possible to be sure that the bottom of the body is exactly parallel to the undisturbed water surface.

Some of the results presented in the papers mentioned above will be used for comparison in the present work and will then be discussed in more detail.

As mentioned in section 1.1 it was the intention in the present work to calculate impact pressure both before and after the moment when

contact occurs. It is then clear from Fig. 1.1 that the method used for calculating the flow in the water must necessarily be based on exactly non-linear boundary condition. Such a method has therefore been used, and this is the main deviation from earlier works. It has however not been possible within the limit of the present research project to fully develop a method which calculates the pressure on the body during all phases of the impact. The computer programme which has been made, calculates the flow in the air and the water prior to the moment when contact is made between the body and the water surface.

CHAPTER 2. OVERALL DESCRIPTION OF THE PROBLEM AND THE SOLUTION

The problem to be solved is the one described in section 1.1. Fig. 2.1 shows the situation at time $t = 0$ which is the starting point of the numerical calculation.

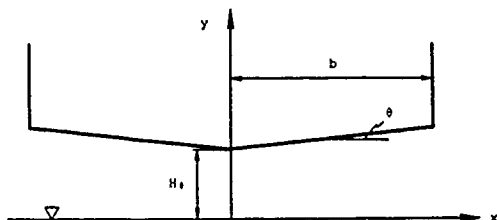


Fig. 2.1

A right-handed, earth-fixed coordinate system is used with the x-axis horizontally, the y-axis vertically and positive upwards, and the origin at the intersection between the undisturbed water surface and the centerline of the body. b is the halfwidth of the body and θ is the deadrise angle. The elevation of the keelpoint (that is the intersection point between the centerline and the bottom of the body) is designated $H(t)$, and the velocity of the body $V(t)$. V is defined to be positive upwards.

The numerical calculation starts ($t = 0$) when the body has reached the position $H = H_0$, and the velocity is $V = V_0$.

Because the effect of the viscosity in the water is confined to thin boundary layers, the water may be regarded as inviscid. This means that the flow in the water will be irrotational and it may be characterized by a velocity potential $\phi(x, y, t)$.

After the moment when the bottom of the body has passed the water surface and continue to move downwards through the water, it is possible that vorticity will be shed from the edge of the body. This effect, however, will not be studied in this work. It will probably have negligible influence on the pressure on the bottom of the body. On the other hand, if a study of the effect of a secondary impact as shown in Fig. 1.1, as well as an exact calculation of the pressure along the sidewall of the body are to be carried out, it may be necessary to take this vortex shedding into account.

Whether the water might be regarded as incompressible or not depends on whether the duration of the impact is large compared to the time it takes for a pressure shock wave in the water to travel a distance equal to the half width of the body. If the width of the impact pressure-time history curve is called Δt , the half-width of the body is b and the velocity of sound in water is c_w , then the condition for the water to be regarded as incompressible becomes:

$$\Delta t \gg \frac{b}{c_w}$$

Experiments and earlier works have shown that this condition holds for the range of velocity which has been studied, so the water will be treated as an incompressible fluid.

Finally, it is assumed that the effect of surface tension can be neglected.

For the same reason as for the water, it is assumed that the air may be treated as inviscid.

However the compressibility of the air will not be neglected. This is necessary because the calculation shows that the flow in the air becomes supersonic.

Verhagen [6] assumes the flow in the air to be isentropic (=reversible adiabatic) which means that:

$$\frac{p}{\rho} = \left(\frac{p_0}{\rho_0}\right)^\gamma, \quad \gamma = 1.4$$

On the other hand Koehler and Kettleborough [7] assumes that γ is closer to 1.0, which is the value for an isothermal process, and he argues that the temperature will be kept constant because of all the waterspray in the gap between the body and the water surface.

In this work both values are used. For the idealized case which is studied here, and also for the experiments used to compare with, the heat-transfer from the air in the gap to the surroundings will be negligible during the very short time of the pressure build up, which means that the flow in the air will be isentropic. This assumption will be used through the paper if not otherwise stated. On the other hand in a more realistic slamming situation where the water is not initially calm, and there is wind and waves, the situation will be different. Because of the spray in the air, the contact-surface between the air and the water will be very large, which means that the heat transfer will be much faster. It is possible that this causes the flow in the air to be isothermal.

When the body approaches the water surface, the pressure in the air between the body and the water starts to build up at the same time as the air starts to flow outwards from the centerline towards the edges of the body. The pressure rise causes the water surface to deform, and this situation is illustrated in Fig. 2.2.

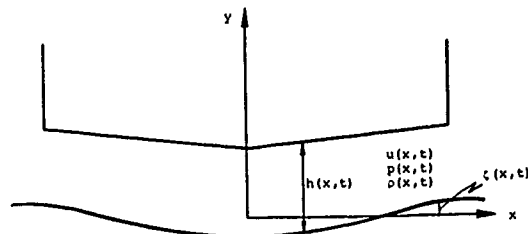


Fig. 2.2

From experiments it is known that the pressure will not exceed the atmospheric pressure significantly until $H \ll b$. This means that the flow in the air may be regarded as one-dimensional, that is the flow is parallel to the x-axis and all quantities are a function of x and t only. This assumption has also been made by other authors [6], [7]. The elevation of the water surface is designated $\zeta(x, t)$, and the distance between the body and the water surface is $h(x, t)$. The relationship between these two is

$$h(x, t) = H(t) + \theta x - \zeta(x, t) \quad (2.2)$$

The one-dimensional flow in the air is characterized by the horizontal velocity $u(x, t)$, the pressure $p(x, t)$ and the density $\rho(x, t)$.

As mentioned above the pressure build up in the gap under the body causes the water surface to deform. Or in other words, before the body makes contact the flow in the water and particularly the free surface elevation depends on the pressure in the air above the water surface. On the other hand the calculation of the pressure in the air

depends on the width of the gap $h(x,t)$ which partly depends on the elevation of the water surface $\zeta(x,t)$. This may be illustrated like this

$$h(x,t) = p(x,t) - \zeta(x,t) - h(x,t) \quad (2.3)$$

The first arrow will be treated in chapter 3 and the second arrow in chapter 4. The third arrow is given by eq. (2.2), and the arrow from p to h indicates that h depends on the pressure through the motion and the force on the body.

Of course, to get a solution to our problem, all calculations have to be made simultaneously, which in the numerical procedures means that all the calculations will be carried out in each timestep. How this is done, is described in chapter 5.

CHAPTER 3. THE AIR REGION

The assumptions and simplifications made in chapter 1 and 2 which regards the air region, may be summarised as:

The body is two-dimensional, symmetrical, rigid and flat-bottomed. It falls vertically under influence of gravity and pressure or has a prescribed vertical motion. The flow in the air is one-dimensional, inviscid, compressible and isentropic. The situation is shown in Fig. 3.1 where the coordinate system and the symbols are the same as introduced in chapter 2.

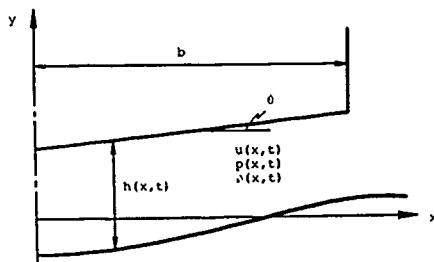


Fig. 3.1

For this flow the equation of motion becomes

$$\frac{\partial u}{\partial t} + u \frac{\partial u}{\partial x} = -\frac{1}{\rho} \frac{\partial p}{\partial x} \quad (3.1)$$

The equation of continuity

$$\frac{\partial}{\partial x}(\rho u h) + \frac{\partial}{\partial t}(\rho h) = 0 \quad (3.2)$$

The relationship between pressure and density is.

$$\frac{p}{p_0} = \left(\frac{\rho}{\rho_0}\right)^\gamma \quad (3.3)$$

In this chapter $h(x,t)$ is assumed to be known, which means that there are three equations for the three unknowns u , p , ρ . By the use of equation (3.3) p may be eliminated from eq. (3.1), which means that eq. (3.1) and (3.2) contains only the two unknowns $u(x,t)$ and $\rho(x,t)$. These unknowns are to be determined in the region $x \in [-b, b]$, $t \in [0, t_k]$, where t_k is the time where the body has reached a point where this calculation is no longer valid. The equation system is hyperbolic, and in order to solve the problem, initial-conditions at $t = 0$ is needed for both the unknowns. As long as the flow is subsonic, a boundary condition along $x = \pm b$ for one of the unknowns is also needed.

At the edge of the body the air will flow as a free jet (see [6] and [7]), which means that the following boundary condition should be used

$$p = p_0 \text{ at } x = \pm b \quad (3.4)$$

However this boundary condition can only be used as long as the flow is subsonic. After the flow has become supersonic, the problem will be completely determined in the region we are interested in without any boundary condition at $x = \pm b$.

The initial condition will be determined in the same way as in [6] and [7]. The initial height, H_0 , of the falling body is assumed to be sufficiently above the free surface so that the air is not behaving compressible and the pressure distribution within the air layer is essentially atmospheric so that no initial effect will be felt by the water. At this height the water free surface will be undisturbed and for the case $\theta = 0$, $h(x,0)$ will be a constant. Since $p(x,0)$ also is assumed to be constant, an initial velocity distribution may be derived from the continuity equation (3.2). Since the problem is symmetrical, u will be zero at the centerline ($x = 0$), and the result is:

$$u(x,0) = -\frac{x}{h} \frac{\partial h}{\partial t} \bigg|_{t=0} = -\frac{V_0}{H_0} x \quad (3.5)$$

and hence if the velocity is assumed constant:

$$\frac{\partial u}{\partial t}(x,0) = \frac{1}{h^2} \frac{\partial h}{\partial t} \times \frac{\partial h}{\partial t} \bigg|_{t=0} = \frac{V_0^2}{H_0^2} x$$

Using this initial velocity distribution and holding $p(x,0)$ constant = p_0 , an initial air pressure distribution can be obtained from the equation of motion (3.1). With the boundary condition $p = p_0$ at $x = b$, the result is:

$$p(x,0) = p_0 + \rho_0 \frac{V_0^2}{H_0^2} (b^2 - x^2) \quad (3.6a)$$

and hence from eq. (3.3)

$$\rho(x,0) = \rho_0 \left(\frac{p(x,0)}{p_0}\right)^{1/\gamma} \quad (3.6b)$$

The derivation of the initial condition was based on the assumption that the pressure distribution is essentially atmospheric. This means that

$$\rho_0 \frac{V_0^2}{H_0^2} b^2 \ll p_0$$

which gives the following restriction on the choice of H_0 :

$$\frac{H_0}{b} \gg \frac{V_0}{\sqrt{p_0/\rho_0}}$$

This must hold at the same time as

$$\frac{H_0}{b} \ll 1$$

which earlier has been introduced as a restriction which is necessary in order to use a one-dimensional model.

Initial-condition for the case $\theta \neq 0$ may be derived in a similar way and it can be shown that the deviation from the above results is small if

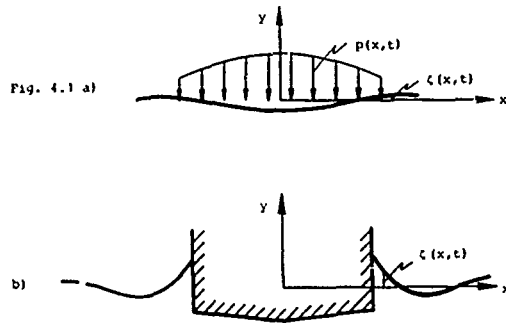
$$\theta \ll \frac{H_0}{b}$$

The problem described here has been solved using the method of characteristics with specified time intervals, similar to the method used by Verhagen [6]. The method together with a numerical scheme called CHAR-S is described in ref. [17].

Section 4.1 Introduction

The assumptions and simplifications made in chapter 1 and 2 which regards the water region, may be summarized as:

The problem is two-dimensional and symmetrical and the water is initially at rest. The water is assumed to be inviscid and incompressible which means that the flow may be represented by a velocity potential. The surface tension is neglected. Two typical situations which will be treated, are illustrated in Fig. 4.1.



The coordinate system and the notation is the same as introduced in chapter 2. In this chapter it is assumed that the pressure distribution over the water surface and/or the motion of the body is known, and the flow in the water is examined. There are several methods which may be applied to obtain this flow. No detailed evaluation of these methods has been made in this work. It was however a demand that the method should not have any other restrictions than those mentioned in chapter 1 and 2.

The method chosen is a boundary-integral-equation technique with exact nonlinear boundary condition based on Faltinsen [13]. This method is described in section 4.2. Running of a computer program derived from the method, shows that problems may occur in some situations. The problems are connected to the intersection point between the body and the free surface. This will be explained in more detail in section 4.4.

Some effort has been made to overcome this problems. A modified version of the method used in section 4.2 has been developed. This is described in section 4.3. The modifications have however not been very successful in solving the intersection-point problem. In section 4.4 some numerical examples are presented and compared by the work of other authors.

Section 4.2 A boundary-integral-equation technique

Let the water be infinite in extent and be of infinite depth. Since we have assumed irrotational flow in an incompressible fluid, there will exist a velocity potential ϕ which satisfies the Laplace equation in the fluid:

$$\frac{\partial^2 \phi}{\partial x^2} + \frac{\partial^2 \phi}{\partial y^2} = 0 \quad (4.1)$$

The pressure p in the air over the water surface may differ from the atmospheric pressure p_0 , and since the surface tension is neglected the dynamic free surface condition can be written as:

$$\frac{\partial \phi}{\partial t} + \frac{1}{2} \left(\frac{\partial \phi}{\partial x} \right)^2 + \left(\frac{\partial \phi}{\partial y} \right)^2 + g \zeta - \frac{p - p_0}{\rho} = 0 \quad (4.2)$$

on $y = \zeta(x,t)$

where g is the acceleration of gravity.

The kinematic free surface condition is:

$$\frac{\partial \zeta}{\partial t} - \frac{\partial \phi}{\partial y} + \frac{\partial \phi}{\partial x} \frac{\partial \zeta}{\partial x} = 0 \quad (4.3)$$

$$\text{on } y = \zeta(x,t)$$

If there is a body penetrating the water surface, the boundary condition on the wetted body surface will be:

$$\frac{\partial \phi}{\partial n} = V(t) \cdot \eta_2 \quad (4.4)$$

where V as before is the vertical velocity of the body, η_2 is the y -component of the unit normal vector to the body, which is assumed to be positive into the fluid, and $\frac{\partial}{\partial n}$ is the derivative along this normal vector.

The initial condition are set to be:

$$\phi = 0 \text{ on the free surface } \zeta = 0 \quad (4.5)$$

The boundary value problem defined by eq. (4.1-4) has to be solved for each timestep. This will be done by applying Green's second identity to the velocity potential ϕ and the function ψ defined by:

$$\psi(x,y) = \ln \sqrt{(x-x_1)^2 + (y-y_1)^2}$$

where (x_1, y_1) is a point in the fluid-domain. We can then write:

$$\int_{S'} \left(\phi \frac{\partial \psi}{\partial n} - \psi \frac{\partial \phi}{\partial n} \right) ds = 0 \quad (4.6)$$

where $S' = S + S_v + S_B + S_F + S_1$

which are illustrated in Fig. 4.3.

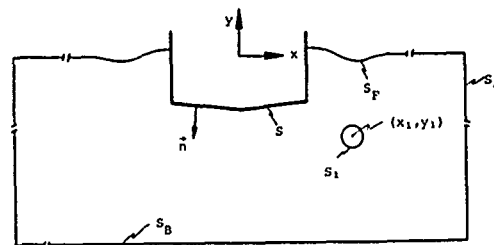


Fig. 4.3

S is the wetted body surface, S_v is a vertical control surface at $x = \pm \infty$, S_B is a horizontal control surface far down in the fluid, S_F is the free surface and S_1 is a cylindrical surface of small radius and with axis through (x_1, y_1) perpendicular to the x - y plane.

Since the problem is transient with the fluid initially at rest, the contribution to (4.6) from S_v and S_B are both zero.

This means that eq. (4.6) can be written as

$$-2\pi\phi(x_1, y_1) = \int_{S+S_F} \left\{ \phi(x,y) \frac{\partial \psi(x,y;x_1,y_1)}{\partial n(x,y)} - \psi(x,y;x_1,y_1) \frac{\partial \phi(x,y)}{\partial n(x,y)} \right\} ds(x,y) \quad (4.7)$$

For $x \gg b_F(t)$, where b_F is large compared to the half width of the body b , we can, since the problem is symmetrical, approximate ϕ to the velocity potential of a dipole with singularity in origin and axis along the y -axis:

$$\phi(x,y) = \frac{Ay}{x^2+y^2} \quad (4.8)$$

where A at this stage is unknown.

$b_F(t)$ is assumed to be so large that no wave has reached the points $x = \pm b_F(t)$, which means that the free surface outside those points

will coincide with the x-axis. Hence the contribution to (4.7) from the part of S_F with $x > b_F$ is:

$$\int_{b_F}^{\infty} \left\{ \phi(x, y) \frac{\partial \phi(x, y, x_1, y_1)}{\partial n(x, y)} - \phi(x, y, x_1, y_1) \frac{\partial \phi(x, y)}{\partial n(x, y)} \right\} dx \Big|_{y=0} = AI(x_1, y_1) \quad (4.9)$$

and the contribution from the part of S_F with $x < -b_F$ is:

$$\int_{-\infty}^{-b_F} \left\{ \phi(x, y) \frac{\partial \phi(x, y, x_1, y_1)}{\partial n(x, y)} - \phi(x, y, x_1, y_1) \frac{\partial \phi(x, y)}{\partial n(x, y)} \right\} dx \Big|_{y=0} = AJ(x_1, y_1) \quad (4.10)$$

An analytical expression for $I(x_1, y_1)$ and $J(x_1, y_1)$ are given in ref. [13].

When solving the integral equation (4.7) at each timestep, $\frac{\partial \phi}{\partial n}$ will be known on the body by the use of the boundary condition on the body (4.4), and ϕ will be known on the free surface. At the first timestep ϕ will be known on the free surface from the initial condition (4.5), which also determines the position of the free surface at this time. When the problem has been solved for one timestep, the free surface conditions are used to find ϕ on the free surface and the position of the free surface for the next timestep. This is done by the following timestepping procedure. If we follow a fluid particle on the free surface, we can write:

$$\frac{D\phi}{Dt} = \frac{\partial \phi}{\partial t} + \frac{\partial \phi}{\partial x} \frac{dx}{dt} + \frac{\partial \phi}{\partial y} \frac{dy}{dt}$$

Using the dynamic free surface condition (4.2) this becomes:

$$\frac{D\phi}{Dt} = -g\zeta + \frac{1}{2} \left[\left(\frac{\partial \phi}{\partial x} \right)^2 + \left(\frac{\partial \phi}{\partial y} \right)^2 \right] - \frac{p-p_0}{\rho_w} \quad (4.11)$$

By the use of the kinematic free surface condition (4.3) we can further write:

$$\frac{D\zeta}{Dt} = \frac{\partial \phi}{\partial y} \quad (4.12)$$

and

$$\frac{Dx_F}{Dt} = \frac{\partial \phi}{\partial x} \quad (4.13)$$

where x_F is the x-coordinate of the fluid particle. A fourth order Runge-Kutta method is used to perform the timestepping. No investigations have been done in this work to find out whether any other methods would have been useful.

When solving the integral equation (4.7), the wetted body surface and that part of the free surface lying between $x = -b_F$ and $x = b_F$ are divided into straight-line elements (see Fig. 4.4).

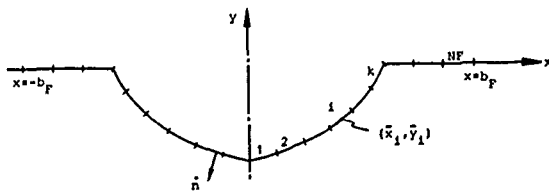


Fig. 4.4

The elements are symmetrically arranged. The total number of elements are $2NF$, while the number of elements on the body is $2K$. (For the situation illustrated in Fig. 4.1a, K will be equal to zero.)

The midpoint of element number i are denoted (\bar{x}_i, \bar{y}_i) , and the surface of this element will be called S_i . It is assumed that both ϕ and $\frac{\partial \phi}{\partial n}$ are constant over each element. For element no. i these constants will be denoted $\phi_i = \phi(\bar{x}_i, \bar{y}_i)$ and $\frac{\partial \phi}{\partial n_i}$ respectively. Due to the symmetry of the problem it is clear that $\phi_i = \phi_{-i}$ and $\frac{\partial \phi}{\partial n_i} = -\frac{\partial \phi}{\partial n_{-i}}$. If we now apply the integral eq. (4.7) NF times, putting (x_1, y_1) equal to (\bar{x}_i, \bar{y}_i) , $i = 1, 2, \dots, NF$, the result is:

$$\begin{aligned} -2\pi\phi(\bar{x}_i, \bar{y}_i) &= \sum_{j=1}^{NF} \left\{ \phi_j \int_{S_j+S_{-j}} \frac{\partial}{\partial n} \ln \sqrt{(x-\bar{x}_i)^2 + (y-\bar{y}_i)^2} ds(x, y) \right. \\ &\quad \left. - \frac{\partial \phi_j}{\partial n_j} \int_{S_j+S_{-j}} \ln \sqrt{(x-\bar{x}_i)^2 + (y-\bar{y}_i)^2} ds(x, y) \right. \\ &\quad \left. + A I(\bar{x}_i, \bar{y}_i) + A J(\bar{x}_i, \bar{y}_i) \right\} \quad (4.14) \end{aligned}$$

For $|x| > b_F$, ϕ is assumed to be given by eq. (4.8). We now assume that $\frac{\partial \phi}{\partial n}$ is determined by this expression also on the element NF :

$$\frac{\partial \phi}{\partial n_{NF}} = -\frac{A}{x_{NF}^2}$$

Hence:

$$A = -x_{NF}^2 \frac{\partial \phi}{\partial n_{NF}} \quad (4.15)$$

If this is inserted into eq. (4.14), and all the known parts are gathered on the right-hand side of the equation, we will have for $i = 1, 2, \dots, K$:

$$\begin{aligned} 2\pi\phi_i &+ \sum_{j=1}^K \phi_j \int_{S_j+S_{-j}} \frac{\partial}{\partial n} \ln \sqrt{(x-\bar{x}_i)^2 + (y-\bar{y}_i)^2} ds \\ &+ \sum_{j=K+1}^{NF} \frac{\partial \phi_j}{\partial n_j} \int_{S_j+S_{-j}} \ln \sqrt{(x-\bar{x}_i)^2 + (y-\bar{y}_i)^2} ds \\ &- [I(\bar{x}_i, \bar{y}_i) + J(\bar{x}_i, \bar{y}_i)] x_{NF}^2 \frac{\partial \phi}{\partial n_{NF}} \\ &= \sum_{j=K+1}^{NF} \phi_j \int_{S_j+S_{-j}} \frac{\partial}{\partial n} \ln \sqrt{(x-\bar{x}_i)^2 + (y-\bar{y}_i)^2} ds \\ &+ \sum_{j=1}^K \frac{\partial \phi_j}{\partial n_j} \int_{S_j+S_{-j}} \ln \sqrt{(x-\bar{x}_i)^2 + (y-\bar{y}_i)^2} ds \quad (4.16) \end{aligned}$$

For $i = K+1, K+2, \dots, NF$, we will have similar equations but with $2\pi\phi_i$ on the other side of the equal sign.

These equations may be written in matrix form as

$$A \cdot x = b \quad (4.17)$$

where the unknowns are:

$$x = (\phi_1, \phi_2, \dots, \phi_K, \frac{\partial \phi}{\partial n_{K+1}}, \dots, \frac{\partial \phi}{\partial n_{NF}}) \quad (4.18)$$

A is an $NF \times NF$ matrix with elements:

$$\begin{aligned} A_{ij} &= 2\pi\delta_{ij} + \int_{S_j+S_{-j}} \frac{\partial}{\partial n(x, y)} \ln \sqrt{(x-\bar{x}_i)^2 + (y-\bar{y}_i)^2} ds(x, y) \\ i &= 1, \dots, NF \\ j &= 1, \dots, K \quad (4.19) \\ A_{ij} &= - \int_{S_j+S_{-j}} \ln \sqrt{(x-\bar{x}_i)^2 + (y-\bar{y}_i)^2} ds(x, y) - \delta_{jNF} [I(\bar{x}_i, \bar{y}_i) + J(\bar{x}_i, \bar{y}_i)] x_{NF}^2 \\ i &= 1, \dots, NF \\ j &= K+1, \dots, NF \end{aligned}$$

$$\begin{aligned} B_i &= \sum_{j=1}^K \frac{\partial \phi_j}{\partial n_j} \int_{S_j+S_{-j}} \ln \sqrt{(x-\bar{x}_i)^2 + (y-\bar{y}_i)^2} ds(x, y) \\ i &= 1, \dots, NF \quad (4.20) \end{aligned}$$

$$+ \sum_{j=K+1}^{NF} \phi_j \left[- \int_{S_j+S_{-j}} \frac{\partial}{\partial n(x, y)} \ln \sqrt{(x-\bar{x}_i)^2 + (y-\bar{y}_i)^2} ds(x, y) - 2\pi\delta_{ij} \right]$$

where δ_{ij} is defined by:

$$\delta_{ij} = \begin{cases} 1 & \text{if } i = j \\ 0 & \text{if } i \neq j \end{cases}$$

When the algebraic equation system (4.17) has been solved, the flow in the fluid will be determined for the actual time instant we are dealing with. In order to step the solution forward, the substantive derivatives given by eq. (4.11-13) will be applied to the fluid particle at the midpoint of each element on the free surface. We then need to know $\frac{\partial \phi}{\partial x}$ and $\frac{\partial \phi}{\partial y}$ for the midpoints, which can be calculated when the equation system (4.17) has been solved. The timestepping will give new values for the velocity potential ϕ on the free surface, and new positions of the fluid particles where these ϕ -values are valid. Knowing these new positions for the fluid particles, new elements have to be arranged. The midpoints of these new elements will not always coincide with the positions of the fluid particles, and in that case the value of ϕ at the new midpoints will be determined by interpolation.

How the new elements are arranged and how the interpolation are carried out, are explained in more detail in Appendix A.

After the fluid motion has been determined, the Bernoulli equation may be used to obtain the force on the wetted surface of the body. However, another procedure is used. This is derived by Faltinsen [13] and he finds that the force on the wetted surface of the body is:

$$F = \rho_w \frac{d}{dt} \int_{S_F} \phi n ds + \int_{S_F} \rho_w g y n ds \quad (4.21)$$

Section 4.3 A Modified Method

As mentioned in section 4.1, some problems may occur at the intersection between the body surface and the water free surface. In an attempt to overcome the problems some modifications to the previously described method has been developed. The modifications have been based on the following considerations: In the method in section 4.2 new position of the free surface and new values of ϕ on the free surface are calculated by timestepping of fluid particles at the midpoints of the old elements. It is then necessary to create new free surface elements and calculate the value of ϕ at the midpoints of these. One way of doing this is described in Appendix A. However if the curvature of the free surface is large, the position of the new elements are strongly dependent on the details of this new-element-creation-procedure. To avoid this it would have been better to use the endpoints of the elements as fluid particles which shall be given new position and new ϕ -value by the timestepping procedure. This would have determined the new free-surface elements directly.

Another consideration which has been made, was inspired by Lin et al. [14]. They used the Vinje and Brevig [15] approach based on Cauchy's theorem and made one modification to this method at the intersection point. In these methods the velocity potential ϕ and the stream function ψ varies linearly over each boundary element. ψ is known on the body by the use of the body boundary condition, and ϕ is known on the water free surface in the same way as in section 4.2. Vinje and Brevig chooses ϕ to be the known function at the intersection point between the body and the free surface. The modification made by Lin et al. [14] was that they assumed that both ϕ and ψ was known at the intersection point, and reduced the algebraic equation system with one equation. Lin et al. [14] found that this modifications improved the method and that the problems at the intersection point was reduced. If a similar modification could be made to the method in section 4.2, it would be worth trying.

The above considerations has lead to the following modifications in the method in section 4.2. The wetted surface of the body and that part of the free surface which lies between $x = -b_f$ and $x = b_f$ are divided into $2NF$ elements as before. Now the endpoints of element no. i will be (x_i, y_i) and (x_{i+1}, y_{i+1}) . The velocity potential ϕ varies linearly over each element. The value of ϕ at the endpoint is now denoted $\phi_i = \phi(x_i, y_i)$. However $\frac{\partial \phi}{\partial n}$ is still assumed to be a

constant over each element. This corresponds to ϕ varying linearly over the elements. $\frac{\partial \phi}{\partial n_i}$ is this constant value i = element no. i . We now need to introduce for each element two functions $w_1(x, y)$ and $w_2(x, y)$. They are defined to vary linearly over the elements, w_1 decreasing from 1 to 0, and w_2 increasing from 0 to 1 when moving along the element from the symmetryline and outwards. If we apply the integral equation (4.7), putting (x_i, y_i) equal to (x_i, y_i) the result will now become:

$$\begin{aligned} -2\pi\phi(x_i, y_i) = & \sum_{j=1}^{NF} \left\{ \phi_j \int_{S_j+S_{-j}} w_1 \frac{\partial}{\partial n} \ln \sqrt{(x-x_i)^2 + (y-y_i)^2} ds(x, y) \right. \\ & + \phi_{j+1} \int_{S_j+S_{-j}} w_2 \frac{\partial}{\partial n} \ln \sqrt{(x-x_i)^2 + (y-y_i)^2} ds(x, y) \\ & - \frac{\partial \phi}{\partial n_j} \int_{S_j+S_{-j}} \ln \sqrt{(x-x_i)^2 + (y-y_i)^2} ds(x, y) \left. \right\} \\ & + A[i(x_i, y_i) + J(x_i, y_i)] \quad (4.22) \end{aligned}$$

By applying the same expression for A as before (4.15) and by gathering the known terms on the right hand side, (4.22) may for $i=1, 2, \dots, K$ be rewritten as:

$$\begin{aligned} 2\pi\phi_i + \phi_i \int_{S_i+S_{-i}} w_1 \frac{\partial}{\partial n} \ln \sqrt{(x-x_i)^2 + (y-y_i)^2} ds \\ + \sum_{j=2}^K \left\{ \phi_j \int_{S_j+S_{-j}} w_1 \frac{\partial}{\partial n} \ln \sqrt{(x-x_i)^2 + (y-y_i)^2} ds \right. \\ + \int_{S_{j-1}+S_{-(j-1)}} w_2 \frac{\partial}{\partial n} \ln \sqrt{(x-x_i)^2 + (y-y_i)^2} ds \left. \right\} \\ + \sum_{j=K+1}^{NF} \left\{ \frac{\partial \phi}{\partial n_j} \int_{S_j+S_{-j}} - \ln \sqrt{(x-x_i)^2 + (y-y_i)^2} ds \right. \\ - [i(x_i, y_i) + J(x_i, y_i)] \frac{\partial \phi}{\partial n_{NF}} \left. \right\} \\ + \sum_{j=K+1}^{NF} \left\{ \phi_j \int_{S_j+S_{-j}} - w_1 \frac{\partial}{\partial n} \ln \sqrt{(x-x_i)^2 + (y-y_i)^2} ds \right. \\ + \int_{S_{j-1}+S_{-(j-1)}} - w_2 \frac{\partial}{\partial n} \ln \sqrt{(x-x_i)^2 + (y-y_i)^2} ds \left. \right\} \\ + \phi_{NF+1} \int_{S_{NF}+S_{-NF}} - w_2 \frac{\partial}{\partial n} \ln \sqrt{(x-x_i)^2 + (y-y_i)^2} ds \\ + \sum_{j=1}^K \left\{ \frac{\partial \phi}{\partial n_j} \int_{S_j+S_{-j}} \ln \sqrt{(x-x_i)^2 + (y-y_i)^2} ds \right. \quad (4.23) \end{aligned}$$

For $i = K+1, \dots, NF$, the term $2\pi\phi_i$ will be on the other side. These equations may be written in matrix form:

$$Ax = b \quad (4.24)$$

with unknowns

$$x = (\phi_1, \phi_2, \dots, \phi_K, \frac{\partial \phi}{\partial n_{K+1}}, \dots, \frac{\partial \phi}{\partial n_{NF}})$$

and the elements of the coefficient matrix A will now be:

$$A_{1j} = 2\pi\delta_{1j} + \int_{S_j} w_1 \frac{\partial}{\partial n} \ln \sqrt{(x-x_1)^2 + (y-y_1)^2} dS(x,y) \\ i=1, \dots, NF \\ j=1$$

$$A_{1j} = 2\pi\delta_{1j} + \int_{S_j} w_1 \frac{\partial}{\partial n} \ln \sqrt{(x-x_1)^2 + (y-y_1)^2} dS \\ i=1, 2, \dots, NF \\ j=2, 3, \dots, k \\ + \int_{S_{j-1} \cup S_{-(j-1)}} w_2 \frac{\partial}{\partial n} \ln \sqrt{(x-x_1)^2 + (y-y_1)^2} dS \quad (4.25)$$

$$A_{1j} = - \int_{S_j \cup S_{-(j-1)}} \ln \sqrt{(x-x_1)^2 + (y-y_1)^2} dS \\ i=1, \dots, NF \\ j=k+1, \dots, NF$$

$$- \delta_{jNF} [i(x_1, y_1) + j(x_1, y_1)] x_{NF}^2$$

The elements of the vector b is:

$$B_i = \sum_{j=k+1}^{NF} \phi_j \left[- \int_{S_j} w_1 \frac{\partial}{\partial n} \ln \sqrt{(x-x_1)^2 + (y-y_1)^2} dS \right. \\ i=1, \dots, NF \\ \left. - \int_{S_{j-1} \cup S_{-(j-1)}} w_2 \frac{\partial}{\partial n} \ln \sqrt{(x-x_1)^2 + (y-y_1)^2} dS - 2\pi\delta_{1j} \right] \quad (4.26)$$

$$- \phi_{NF+1} \int_{S_{NF} \cup S_{-NF}} w_2 \frac{\partial}{\partial n} \ln \sqrt{(x-x_1)^2 + (y-y_1)^2} dS$$

$$+ \sum_{j=1}^k \frac{\partial \phi}{\partial n_j} \int_{S_j} \ln \sqrt{(x-x_1)^2 + (y-y_1)^2} dS$$

For the case $k=0$

$$B_i = \phi_{NF+1} \int_{S_1 \cup S_{-1}} w_1 \frac{\partial}{\partial n} \ln \sqrt{(x-x_1)^2 + (y-y_1)^2} dS - 2\pi\delta_{11} \\ i=1, \dots, NF$$

$$+ \sum_{j=2}^{NF} \phi_j \left[- \int_{S_j} w_1 \frac{\partial}{\partial n} \ln \sqrt{(x-x_1)^2 + (y-y_1)^2} dS \right.$$

$$\left. - \int_{S_{j-1} \cup S_{-(j-1)}} w_2 \frac{\partial}{\partial n} \ln \sqrt{(x-x_1)^2 + (y-y_1)^2} dS - 2\pi\delta_{1j} \right]$$

$$- \phi_{NF+1} \int_{S_{NF} \cup S_{-NF}} w_2 \frac{\partial}{\partial n} \ln \sqrt{(x-x_1)^2 + (y-y_1)^2} dS$$

$$+ \sum_{j=1}^k \frac{\partial \phi}{\partial n_j} \int_{S_j} \ln \sqrt{(x-x_1)^2 + (y-y_1)^2} dS \quad (4.27)$$

In order to step the solution forward, the substantive derivatives given by eq. (4.11-13) will now be applied to the fluid particles at the endpoint for each element on the free surface. To carry out this, $\frac{\partial \phi}{\partial x}$ and $\frac{\partial \phi}{\partial y}$ have to be known at the endpoints. However with the model used here, $\frac{\partial \phi}{\partial x}$ and $\frac{\partial \phi}{\partial y}$ will generally be singular at the endpoints. This means that $\frac{\partial \phi}{\partial x}$ and $\frac{\partial \phi}{\partial y}$ have to be calculated at the midpoints of each element, and then the value at the endpoints are found by interpolation.

Another modification to the method in section 4.2 is also made. Since the fluid is incompressible, we will have that:

$$\int_{S \cup S_F \cup S_B} \frac{\partial \phi}{\partial n} dS = 0 \quad (4.28)$$

If the dipole approximation, eq. (4.8), are used far away from the body, it turns out that the contribution from S_B and S_{∞} is zero. The contribution from S_F outside $x = \pm b_F$ may also be calculated by the use of the dipole approximation in this area. Still assuming that $\frac{\partial \phi}{\partial n}$ is constant over each element eq. (4.28) becomes:

$$\sum_{j=1}^{NF} \frac{\partial \phi}{\partial n_j} \Delta S_j - \frac{A}{b_F} = 0 \quad (4.29)$$

where ΔS_j is the length of element no. j .

Using the same expression for A as before (see eq. (4.15)), this can be rewritten as:

$$\sum_{j=k+1}^{NF+1} \frac{\partial \phi}{\partial n_j} \Delta S_j + \frac{\partial \phi}{\partial n_{NF}} (\Delta S_{NF} + \frac{x_{NF}^2}{b_F}) = - \sum_{j=1}^k \frac{\partial \phi}{\partial n_j} \Delta S_j \quad (4.30)$$

with the unknown terms on the left side.

This equation may be used instead of one of the equations in the equation system (4.24). If equation no. i is interchanged, the new coefficients are:

$$A_{1j} = 0$$

$$j=1, \dots, k$$

$$A_{1j} = \Delta S_j + \delta_{jNF} \frac{x_{NF}^2}{b_F}$$

$$j=k+1, \dots, NF$$

$$B_i = - \sum_{j=1}^k \frac{\partial \phi}{\partial n_j} \Delta S_j \quad (4.31)$$

The introduction of the eq. (4.30) corresponds to the use of ψ as known at the intersection point in the Vinje-Brevig-method. This may be explained as follows. If we look at that part of the free surface S_F having $x > 0$, it is true that:

$$\int_{S_F} \frac{\partial \phi}{\partial n} dS = \int_{S_F} \frac{\partial \phi}{\partial s} ds = \psi_{\infty} - \psi_1 \quad (4.32)$$

which means that $\int_{S_F} \frac{\partial \phi}{\partial n} dS$ will be known if ψ_1 , which is ψ at the intersection point, is given.

The method described in this section is used in a computer program. This has been run for the case of a cylinder oscillating vertically in the free surface. The method has been tried with and without interchanging one of the equation in the equation system (4.24) with the equation (4.30). The only way to avoid instability in the solution is to interchange equation (4.30) with equation number $k+1$. This means that the equation formed by setting (x_1, y_1) equal to the intersection point (x_{k+1}, y_{k+1}) in the integral equation (4.7), is not used. In this form the modified method in this section has been compared with the method in section 4.2 and with the numerical results obtained by other authors. This is presented in section 4.4.

The numerical results shows that the modified method do not handle the intersection point problem any better than the method in section 4.2. If the modified method is used in the case $k=0$, which means that there is no body penetrating the free surface, it is not possible to avoid instability in the solution whether the equation (4.30) is used or not.

Instability here means that $\frac{\partial \phi}{\partial n}$ on the free surface shows large oscillations for each element when moving along the surface, see Fig. 4.5. This is not unexpected since in this case the eq. (4.7) will be a Fredholm integral equation of 1. kind over the entire boundary.

Section 4.4 Numerical results and discussion

The computer programmes developed from the two methods described in section 4.2 and 4.3 are compared with the work of other authors. For brevity the two programmes are called SLN and SLN-Mod, respectively.

Two different cases are calculated.

In the first case both programmes are used to calculate the force on a

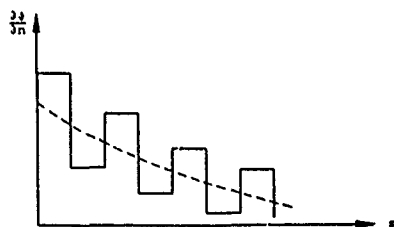


Fig. 4.5

cylinder with forced vertical oscillation (position of center: $y(t) = H_0 \sin \omega t$). The results are compared with results obtained by Faltinsen using a programme based on the same method described in section 4.2 and presented in [13], and also with results presented by Vinje and Brevig [15]. Fig. 4.6 shows the results for the three values of the amplitude: $H_0/r = 0.1, 0.3$ and 0.6 (r is radius of the cylinder), $\omega r/g = 1.0$.

The good conformity between the results for $H_0/r = 0.1$ indicates that there are no bugs in the programmes, but the deviation in the results for $H_0/r = 0.3$ and 0.6 is difficult to explain.

The reason why the case $H_0/r = 0.6$ is not calculated for higher time values, is that the calculation breaks down shortly after because of problems with the element lying closest to the intersection point. In Fig. 4.7 the elements on the cylinder and the free surface are shown for the two last timesteps before the programme SLM breaks down.

As seen from the force curve in Fig. 4.6 the programme SLM-Mod. tends to break down even before.

The second case which are used to test the programmes, is one which are presented by Doctors [16]. He uses a triangular pressure-element acting on the free surface of the water. The pressure-element as a function of position x and time t is defined by Fig. 4.8. The free surface elevation which is the result of the pressure-element, is calculated by a method which is based on potential theory and with linear free surface condition.

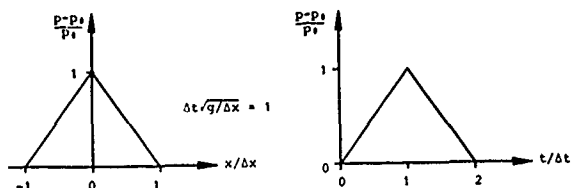


Fig. 4.8

In Fig. 4.9 results presented in [16] are compared with results obtained by the programme SLM. Because SLM is based on exactly free surface conditions, the value of the parameter Δx has to be chosen. Since the intention is to compare with the linear case, the parameter Δx has to be chosen in such a way that the slope of the free surface is small. From the figure it is seen that the maximum value of $\rho_0 g \Delta x / P_0$ is approximately equal to one. So the choice has been made: $\rho_0 g \Delta x / P_0 \approx 100$ or $\Delta x = 1000$ m.

The agreement in the results are good, and since this case are very similar to the slamming case for the time-period before the body makes contact with the water, the programme SLM seems to be well suited for calculating flat-bottomed slamming.

As mentioned before the programme SLM-Mod. is not able to calculate this case properly because $\frac{\partial \eta}{\partial n}$ on the free surface oscillates when moving along the surface.

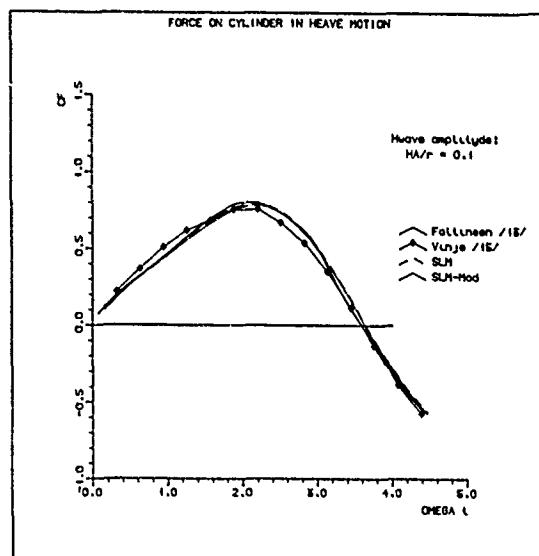


Fig. 4.6 a

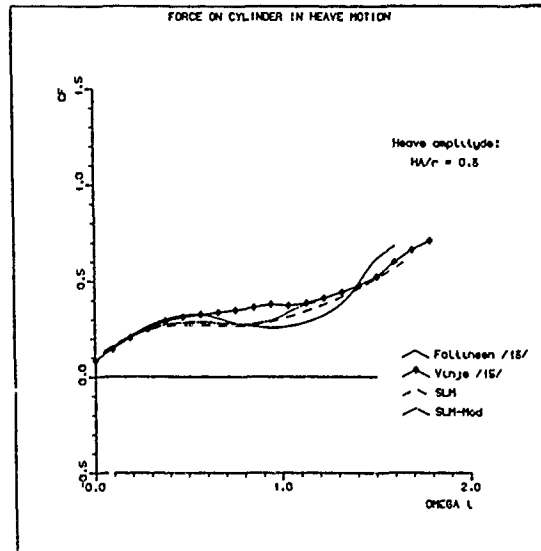


Fig. 4.6 b

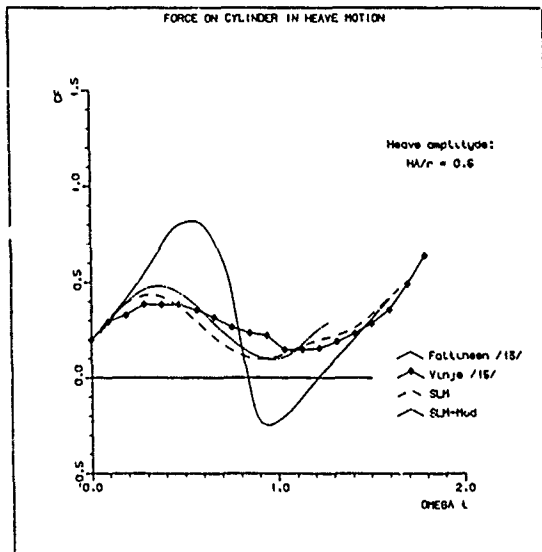


Fig. 4.6 c

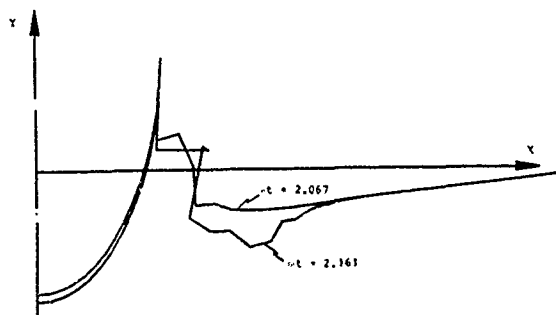


Fig. 4.7 Boundary elements for circular cylinder in forced heave motion: $y(t) = H_a \sin(\omega t)$, $H_a/r = 0.6$, $\omega r/a = 1.0$

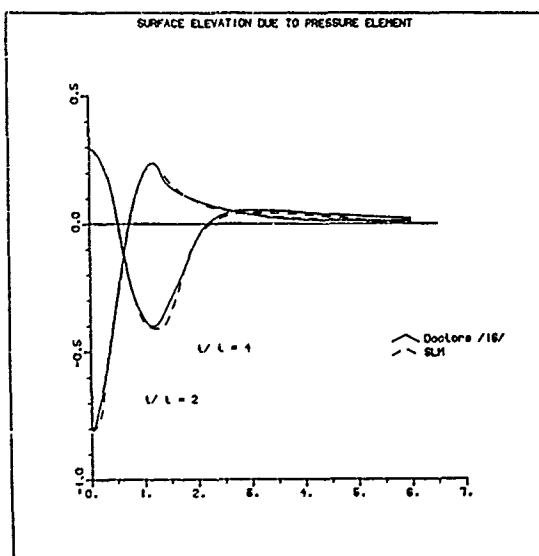


Fig. 4.9

CHAPTER 5. CALCULATION OF FLAT-BOTTOMED SLAMMING

Section 5.1. General

As mentioned at the end of chapter 3 and 4 the programme CHAR-S which was based on the method described in ref. [17] and the programme SLM which was developed from section 4.2, will be used as subprogrammes in the overall calculation of the flat-bottomed slamming problem.

For each timestep CHAR-S is used to calculate the pressure acting on the water surface between $x = -b$ and $x = b$. Outside these points the pressure is set equal to the atmospheric pressure. The value of the pressure at the midpoint of each free surface element are then used in equation (4.11) in order to step the solution in the fluid forward.

In the programme CHAR-S it is necessary to use much smaller timesteps than will be used in the overall programme. When the solution in the water region has been obtained at time t_j , then the pressure in the airgap at t_j will be calculated. In this calculation $h(x, t)$ will be needed, and it is found by the use of linear interpolation between $h(x, t_{j-1})$ and $h(x, t_j)$.

The calculated pressure distribution in the airgap and the above statement that the pressure outside the gap is set equal to the atmospheric pressure together results in a pressure distribution acting on the water surface which is not smooth at the edge of the body.

The pressure distribution before and after the flow in the air has reached supersonic speed are illustrated in fig. 5.1.

In a real case however the pressure distribution will probably be smoothed out over a distance in the order of magnitude equal to the width of the airgap at the edge (see [6]). In the present numerical calculation, only the value of the pressure at the midpoint of each free surface element is used as input to the calculation of the flow in the fluid. This means that the pressure distribution are smoothed out over a distance equal to the size of the surface elements.

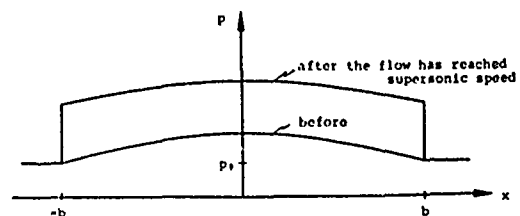


Fig. 5.1

Section 5.2. Dimensional analysis

The pressure, p , under the body and the surface elevation, ζ , will be calculated as a function of x and t . The parameters involved in the problem are:

Halfwidth of the body	b	[m]
Deadrise angle	θ	[°]
Mass of body	M	[kg/m]
Position of the body when the numerical calculation starts	u_0	[m]
Velocity at this point	V_0	[m/s]
Density of water	ρ_w	[kg/m³]
Atmospheric pressure	p_0	[Pa]
Density of air at atmospheric pressure	ρ_0	[kg/m³]
Adiabatic constant	γ	[°]
Acceleration of gravity	g	[m/s²]

One possible choice is then to write that p/p_0 and z/b are a function of:

$$\frac{x}{b}, \frac{tV_0}{b}, \frac{V_0}{\sqrt{p_0/\rho_0}}, \frac{V_0}{\sqrt{b/g}}, \frac{M}{\rho_0 b^2}, \frac{H_0}{b}, \frac{p_0}{\rho_0}, \theta, \gamma$$

Here $V_0/\sqrt{p_0/\rho_0}$ is again the Mach number, and $V_0/\sqrt{b/g}$ has the same form as a Froude number. Instead of $M/\rho_0 b^2$ it would have been possible to use $Mg/p_0 b$, but since the motion of the body will be dominated by its mass and the pressure force on the body rather than the gravity force, the former will be used.

In addition to these parameters which describes the physical problem, the computer programme also contains parameters which defines how the free surface initially is divided into elements, as well as the interval $\Delta t(t)$ between the timesteps.

In the calculations which have been made with the programme, free surface elements of equal length have been used. The number of elements between $x = 0$ and $x = b$ is called NA, and NF is as before the total number of elements along the positive x-axis. This means that the end of the last element is at the position:

$$x = b_F = NF \frac{b}{NA}$$

In the CHAR-S subprogramme, which calculates the pressure in the air, the number of elements along the x-axis between $x = 0$ and $x/b = 1.0$ is $N = 2 NA$.

Section 5.3 Numerical results and discussion

Three cases which has been investigated in the literature will be used for comparison. The first one is one of the cases which was measured experimentally by Lewison and Maclean [5]. The same case was also calculated numerically by Koehler and Kettleborough [7]. The model used by Lewison and Maclean was completely flat-bottomed, but Koehler and Kettleborough made calculations for the same body but with three different deadrise angles ($\theta = 0$, $\theta = 0.25$ and $\theta = 0.5$ deg.). The two next cases was investigated both experimentally and numerically by Verhagen [6]. The model is the same for both cases but two different drop heights are studied.

Data for all the three cases are given in table 5.1.

Case	b [m]	M [kg/m]	Dropheight [m]	Reference
A	1.5	4014.0	1.52	[5], [7]
B	0.2	20.0	0.04	[6]
C	0.2	20.0	0.40	[6]

Table 5.1

In the present work the starting point of the numerical calculation is selected so that $H_0/b = 0.2$ in case A and C, and $H_0/b = 0.1$ in case C, and then V_0 is calculated by assuming that only gravity forces are acting prior to this moment. For case A H_0 was selected to be the same as used by Koehler and Kettleborough. The values of H_0 and V_0 for the three cases are given in table 5.2.

Case	H_0 [m]	V_0 [m/s]
A	0.3	-4.88
B	0.02	-0.626
C	0.04	2.66

Table 5.2

In order to compare with the results presented by Koehler and Kettleborough [7], case A in table 5.1 has been calculated with three different deadrise angles. In [7] $\gamma = 1.0$ was used, but there is no specific information about the number of elements. However the figures in [7] indicates that $NA = 5$. These values together with $NF = 20$ has therefore been used in this comparison.

The results are presented in Fig. 5.2-8.

Fig. 5.2 compares the pressure-time history at the centerline. The curves from [7] are translated along the t-axis so that the body has the position $H = 0.0$ at the same time as in the present calculation.

In order to see the effect of the choice of γ , case A with $\theta = 0.0$, $NA = 5$, $NF = 20$ has been calculated also with $\gamma = 1.4$. In Fig. 5.10 the pressure at the centerline is compared for the two values of the adiabatic constant.

In section 5.1 it was mentioned that the discontinuous pressure at the edge of the body will, in the present numerical model, be smoothed out over a distance equal to the size of the surface elements. To see the effect of this, case A with $\theta = 0.0$, $\gamma = 1.4$ has also been calculated with $NA = 20$, $NF = 80$. The results are given in Fig. 5.11-12. The influence on the pressure and the surface elevation at the centerline is small, but the shape of the free surface and the pressure close to the edge of the body is very different.

$NA = 5$ is probably far too less to handle the steep pressure-curvature at the edge of the body, and this value of NA has only been used in the present work to make the comparison with the results presented by Koehler and Kettleborough [7].

It may even be that $NA = 20$ is too small but further investigation of this has not been done.

As mentioned before, case A has also been investigated experimentally. In [5] time-history curves at $x/b = 0.0, 0.5$ and 1.0 are presented. If those curves shall be compared with the present calculation, it is not clear where the t-axis shall start since the position of the body is not given. The same problem also occurs when pressure-time history for case B and C are to be compared with the curves presented in [6]. Koehler and Kettleborough assumes that the maximum impact pressure is reached at the moment of contact between the body and the water surface. This would of course solve the problem of locating the t-axis since the time of maximum pressure is given in the curves presented in [5] and [6]. However the maximum pressure will probably not be reached at the moment of contact. The argument for this is that at the time instant when contact is made, results from the present numerical method shows that the downward velocity of the water surface has not reached the same magnitude as the velocity of the body. Which means that after the time of contact the airbubble under the body, will be compressed for some period of time. Verhagen [6] uses a simplified method to calculate the pressure in the airbubble after contact, but it is not indicated on the curves at what time the contact is made.

Because of this problems, any direct comparison between the pressure-time history curves presented in [5] and [6] and those calculated by the present method has not been plotted. The results of the present calculation of case B and C are instead given in Fig. 5.13-16.

The pressure on the centerline at the moment of contact as presented in Fig. 5.12, 14, 16 is significantly smaller than the maximum pressure found in [5] and [6].

Koehler and Kettleborough explains this deviation for case A by assuming that the larger maximum pressure obtained in experiments occurs because the flat bottom of the body may not be completely parallel to the water surface. This explanation may well be true, and the very large influence of small variations in the deadrise-angle, which has been calculated both by Koehler and Kettleborough [7] and in the present work, support this.

However the deviation between the pressure calculated at contact by the present method and the maximum pressure obtained in experiments

may also be partly explained by assuming that the maximum pressure will not be reached until a short time-period after the calculated contact. The argument for this was stated above.

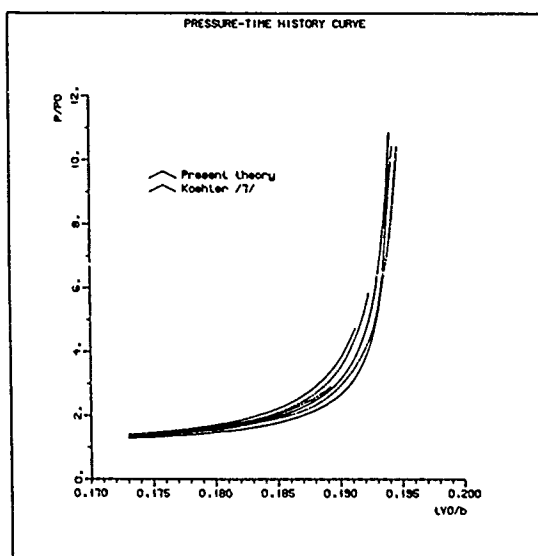


Fig. 5.2 Case A, $\nu=1.0$, $NA=5$

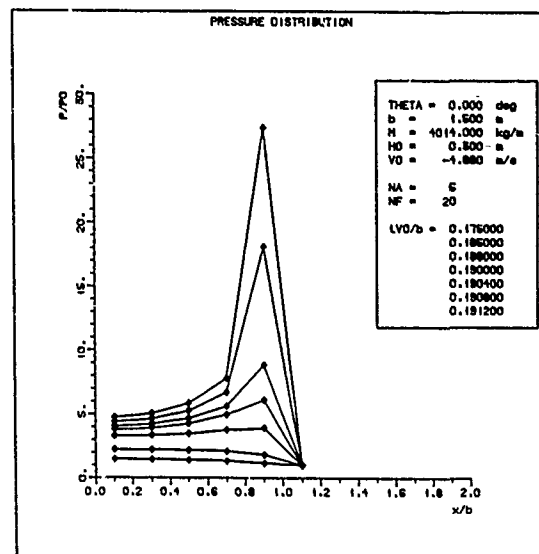


Fig. 5.4 Case A, $\nu=1.0$

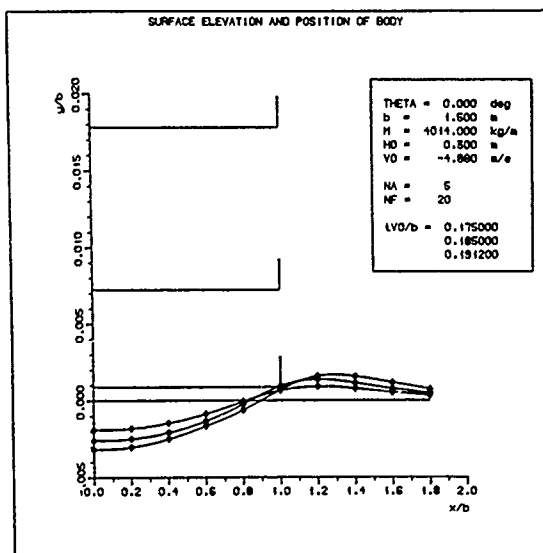


Fig. 5.3 Case A, $\nu=1.0$

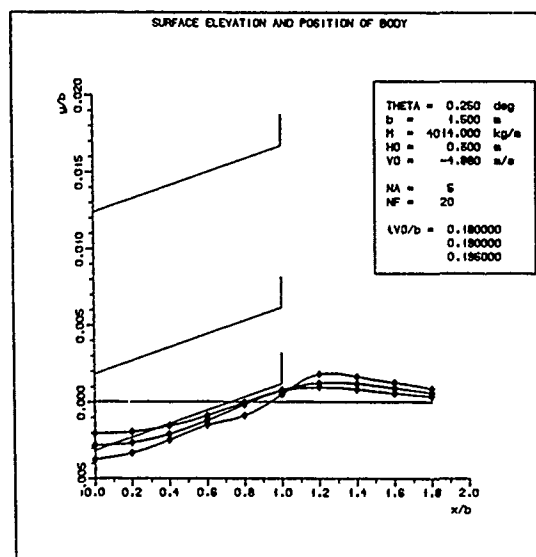


Fig. 5.5 Case A, $\nu=1.0$

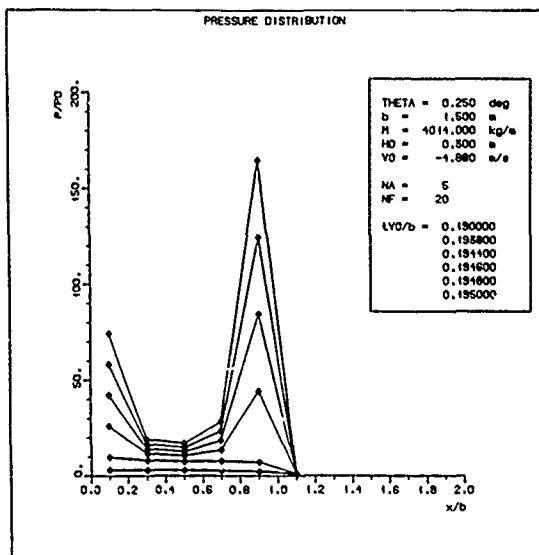


Fig. 5.6 Case A, $\gamma=1.0$

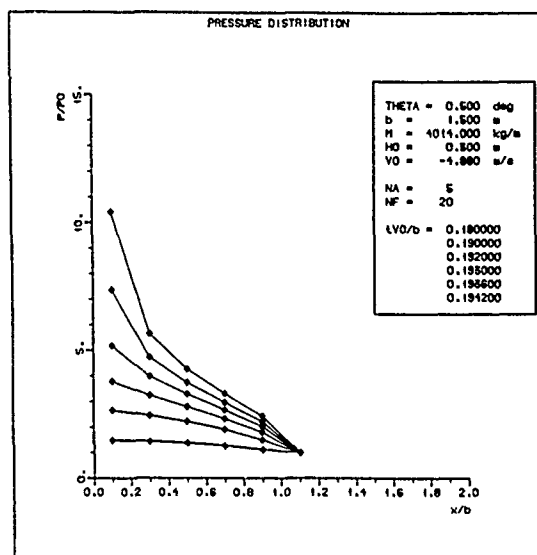


Fig. 5.8 Case A, $\gamma=1.0$

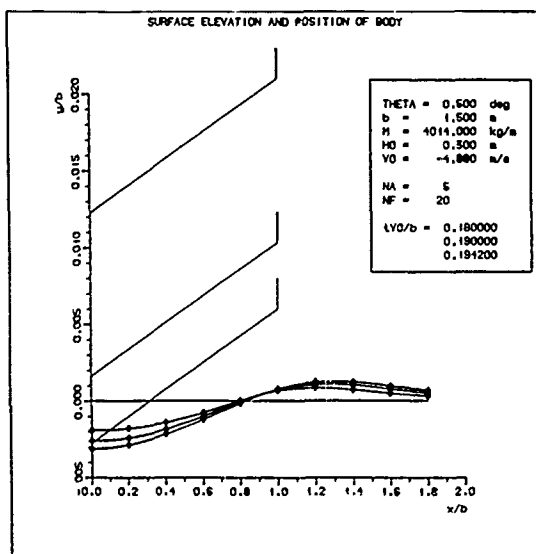


Fig. 5.7 Case A, $\gamma=1.0$

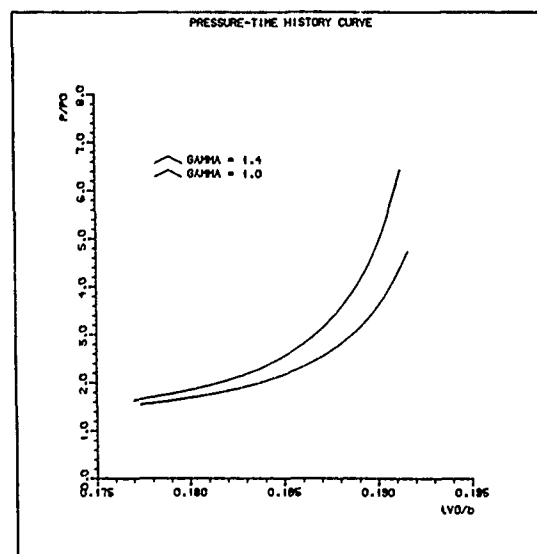


Fig. 5.10 Case A, $NA=5$

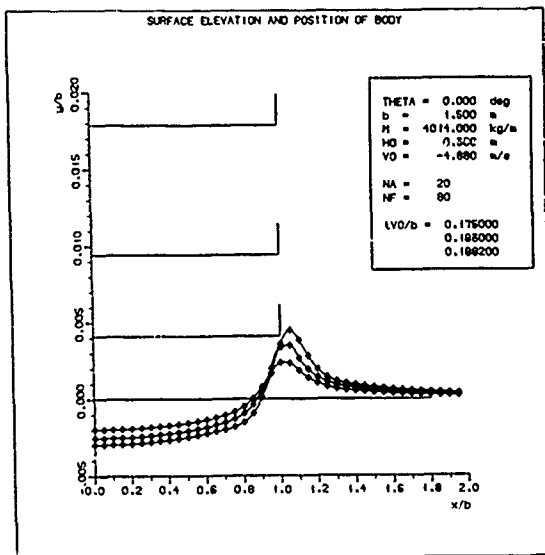


Fig. 5.11 Case A, $\gamma=1.4$

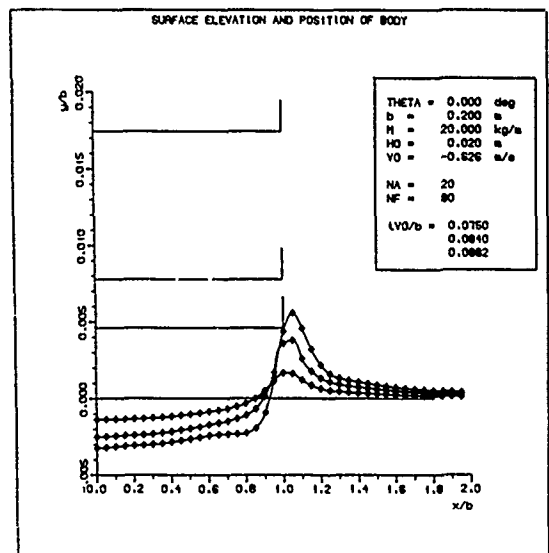


Fig. 5.13 Case B, $\gamma=1.4$

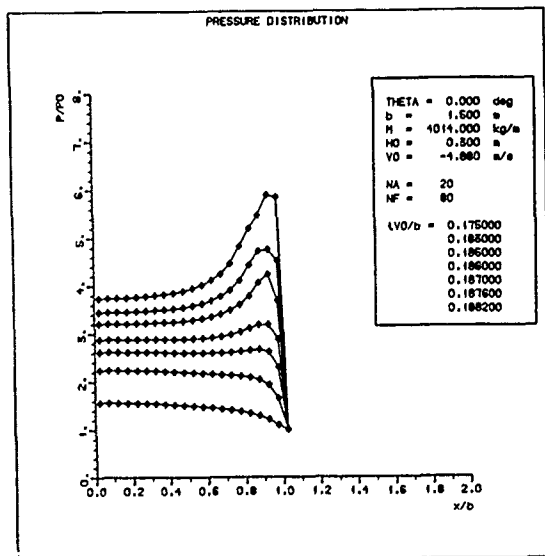


Fig. 5.12 Case A, $\gamma=1.4$

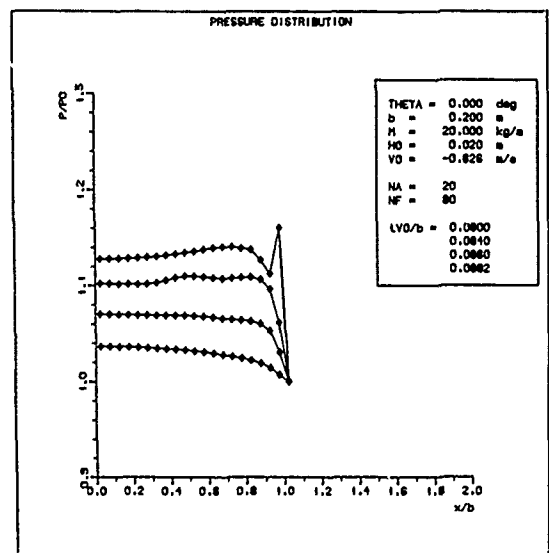


Fig. 5.14 Case B, $\gamma=1.4$

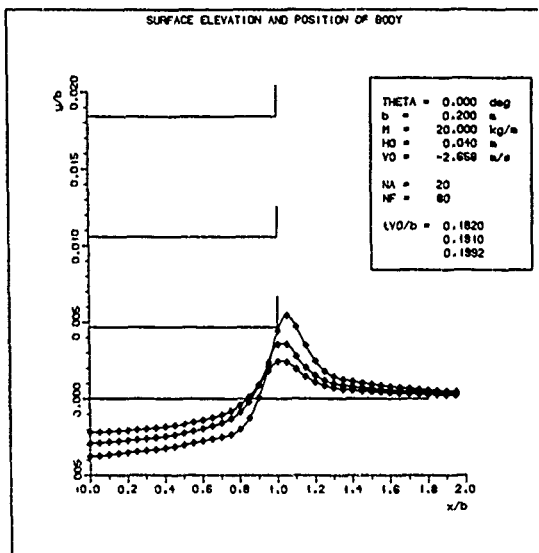


Fig. 5.15 Case C, $\gamma=1.4$

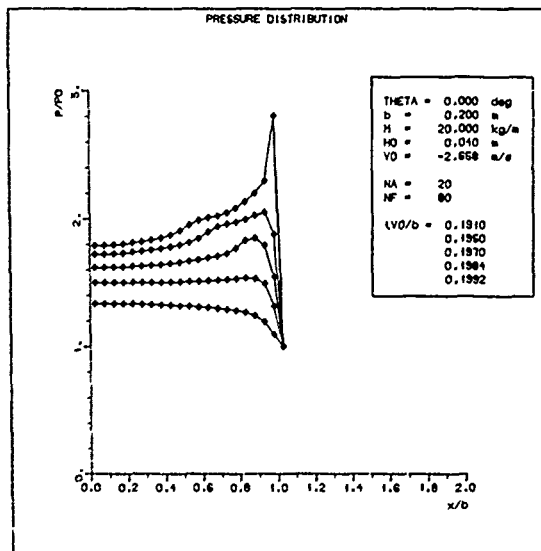


Fig. 5.16 Case C, $\gamma=1.4$

CHAPTER 6. CONCLUSIONS

The discussion at the end of the previous chapter shows that it is necessary to calculate the pressure on the bottom of the body also after the time of contact between the body and the elevated water surface. Without such information it is not possible to compare the pressure build-up calculated in the time-period before contact by the present numerical method with experimental results.

As regarding the calculation of the flow in the water, this work has shown that the method described in section 4.2 may be used in the present situation without instability problems, despite the fact that the integral equation which is used is a Fredholm integral equation of 1. kind along the entire boundary. The comparison with Doctors which was made in section 4.4 also indicates that the surface elevation due to a pressure distribution acting on the water surface is calculated quite correctly.

For the purpose of calculating the flow in the air, three methods have been used. They support each other, but no independent comparison with other results has been made.

The results of the present work shows that the influence of a small deadriseangle is very large.

The present work also shows that the smoothening of the calculated discontinuous pressure distribution has a large effect on the shape of the water surface and the pressure close to the edge of the body.

REFERENCES

- [1] von Karman, T.H., "The impact on Seaplane Floats during Landing", NACA TN 321, 1929.
- [2] Wagner, H., "Über Stoss und Gleitvorgänge an der Oberfläche von Flüssigkeiten", Zeitschr. f. Angewandte Mathematik und Mechanik, Band 12, Heft 4, 1932, pp. 193-215.
- [3] Chuang, S.L., "Experimental Investigation of Rigid Flat-Bottom Body Slamming", DTNSRDC Report 2041, 1965.
- [4] Chuang, S.L., "Experiments on Flat-Bottom Slamming", Journal of Ship Research, Vol. 10, No. 1, 1966, pp. 10-17.
- [5] Lewison, G. and Maclean, W.M., "On the Cushioning of Water Impact by Entrapped Air", Journal of Ship Research, Vol. 12, No. 2, 1968, pp. 116-130.
- [6] Verhagen, J.H.G., "The Impact of a Flat Plate on a Water Surface", Journal of Ship Research, Vol. 11, No. 4, 1967, pp. 211-223.
- [7] Koehler, B.R. and Kettleborough, C.F., "Hydrodynamic Impact of a Falling Body upon a Viscous Incompressible Fluid", Journal of ship Research, Vol. 21, No. 3, 1977, pp. 165-181.
- [8] Yamamoto, Y., Iida, K., Fukasawa, T., Murakami, T., Arai, M. and Ando, A., "Structural Damage Analysis of a Fast Ship Due to Bow Flare Slamming", Int. Shipbuilding Progress, Vol. 32, No. 369, 1985, pp. 124-136.
- [9] Abbot, M.B., "An Introduction to The Method of Characteristics", American Elsevier, New York, 1966.
- [10] Ames, W.F., "Numerical Methods for Partial Differential Equations", 2. edition, Academic Press, 1977.

DISCUSSION

by J. Matusiak

My question concerns the importance of air cushioning loads.

It is obvious that in a case of flat plate inspecting water surface it has a very pronounced effect. However an increase of deadrise angle might significantly increase an "escape of air" and thus decrease its influence on slamming loads. Did you conduct a numerical experiment in which you calculated loads (both pressures and total forces) for the air cushioning being included and disregarded. If so what is practical limit value of deadrise angle for which air does not cushion the slamming loads?

Author's Reply

This is of course a most interesting and important question.

First of all, since I only carry on the calculation until the moment when the body makes contact with the water-surface, I do not find the maximum pressure. Secondly, I did not make any comparison with slamming loads calculated without the effect of air cushion, so I don't know the limit value of the deadrise angle. But if you look at Figs 5.5-5.8 in the paper, you can see that a change in the deadrise angle of half a degree gives a dramatic change in the result. So my guess is that the effect of air cushion will be small for a deadrise angle in the order of one, two or three degrees.

Pressure Transients in Transitional Boundary Layer over a Solid Surface

Sin-I Cheng
Princeton University
Princeton, USA

I. INTRODUCTION

The Navier-Stokes system of equations of an incompressible fluid, upon neglecting the gravity and other extraneous forces, stands as:

$$\text{Continuity: } \Delta = \frac{\partial u_i}{\partial x_i} = 0 \quad (1)$$

$$\text{Momentum: } \frac{\partial u_i}{\partial t} + u_j \frac{\partial u_i}{\partial x_j} = -\frac{1}{\rho} \frac{\partial p}{\partial x_i} + \nu \frac{\partial^2 u_i}{\partial x_j \partial x_j} \quad (2)$$

The continuity equation (1) is a limiting form of

$$\frac{\partial u_i}{\partial x_i} = -\frac{1}{\rho} \frac{d\rho}{dt} = -\frac{1}{\rho} \left(\frac{\partial}{\partial t} + u_j \frac{\partial}{\partial x_j} \right) \rho \quad (3)$$

for a compressible fluid, when $d\rho/dt$ vanishes.

For a compressible fluid with a barotropic relation $\rho(p)$, equation (3) stands as

$$\left(\frac{\partial}{\partial t} + u_j \frac{\partial}{\partial x_j} \right) p = \rho c^2 \left(\frac{\partial u_i}{\partial x_i} \right) \quad (3a)$$

where $c^2 = dp/d\rho$ is the square of the speed of sound in the medium for the specified barotropic thermodynamic process, which speed of sound becomes infinitely large for incompressible fluids. Equations (2) and (3a) define an initial value problem with the specific choice of $\rho(p)$ and the initial data for the solution of the four scalar unknowns p and u_i , $i = 1, 2, 3$. Equations (1) and (2) is a singular limit of (3) and (3a) when $d/dt \rho$ vanishes in the incompressibility limit. There is no explicit means to advance pressure in time.

In classical hydrodynamics⁽¹⁾, a velocity potential ϕ with $u_i = \nabla \phi = \partial \phi / \partial x_i$ is introduced for an irrotational ($\omega = \nabla \times u = 0$) flow, the continuity equation is reduced to $\nabla^2 \phi = 0$ which can be solved without any reference to pressure under suitable boundary formulation. For steady state potential flows, the Bernoulli's relation $p + \rho u^2/2 = B$ as an integral of the momentum equation enables us to find p where B can be evaluated from the boundary data. For time dependent flows, $B \sim \partial \phi / \partial t$ depends on both the initial and the boundary data so that pressure transients are not so easily determined from the Bernoulli's integral even for potential flows. The pressure $p(t, x)$ and the velocity $u(t, x)$ should be solved simultaneously from equations (1) and (2).

In the absence of a $\partial p / \partial t$, (1) serves as a subsidiary condition that the correct $p(t, x)$ must evolve simultaneously with $u(t, x)$ so as to keep the velocity field solenoidal at all times and everywhere. In the computational solution of some discrete form of (1) and (2), we can only solve them iteratively. We hope that the successive iterations would yield better approximations to the pressure and the solenoidal velocity fields and that the sequence might eventually "converge" to the true solution. Given a solenoidal initial data $u_i(0)$ at $t = t_0$ and the corresponding initial pressure field $p(0)$. We wish to find $u_i^{(1)}(t_0 + \delta t)$ that is solenoidal at $t_0 + \delta t$ and its corresponding $p^{(1)}(t_0 + \delta t)$. We do not know the evolving pressure to advance u_i from (2) throughout the interval δt . Hence we take it to be the known $p(0) = p(t_0, x)$ or some otherwise conceived pressure field $p(0, 1)$ for evaluating the gradient $\partial p / \partial x_i$ throughout x and during the interval δt . Equations (2) then give the estimate $u_i(0, 1)$ of $u_i(1)$. This estimate of $u_i(0, 1)$ will possess some residual divergence $\Delta(0, 1)$ over the field. We wish to devise some format to estimate the correction to $p(0, 1)$ such that $p(0, 2) = p(0, 1) + \delta p(0, 1)$ that will generate a new estimate of $u_i(0, 2)$ with a smaller residual divergence $\Delta(0, 2)$; and its repeated application yielding $\Delta(0, n) \rightarrow 0$ almost everywhere at some sufficiently large n .

By taking the divergence of equation (2), we obtain

$$\left(\frac{\partial}{\partial t} + u_j \frac{\partial}{\partial x_j} - \nu \frac{\partial^2}{\partial x_j \partial x_j} \right) \Delta + \frac{\partial u_j}{\partial x_i} \frac{\partial u_i}{\partial x_j} - \frac{1}{\rho} \frac{\partial^2}{\partial x_j \partial x_j} \quad (4)$$

which should stand as the evolution equation for the divergence Δ of the velocity field. Equation (4) is, however, often interpreted as the Poisson equation defining the pressure $p(t, x_i)$. In particular, for an incompressible fluid with $\Delta = \partial u_i / \partial x_i = 0$, we have

$$\nabla^2 p = -\rho \frac{\partial u_i}{\partial x_j} \frac{\partial u_j}{\partial x_i} - \frac{1}{4} = \rho (e_{ij} e_{ij} - \omega_{ij} \omega_{ij}) \quad (4a)$$

so that the pressure field $p(t, x)$ can be determined from the solenoidal velocity field $u_i(t, x)$ at any time t . It is often that $p(0, 2)$ is taken as some discrete solution of (4a) as a Poisson Equation with the source terms estimated from the perturbed velocity field $u_i(0, 1)$ or some weighted averages of $u_i(0, 0)$ and $u_i(0, 1)$. Alternatively, $p(0, 2)$ may be taken as some weighted average of the solution of this Poisson equation with $p(0, 1)$ for further iteration. There are numerous such alternatives. They give rise to a pressure iterate $p(0, 2)$ with significant spurious oscillations that quickly become chaotic and apparently diverging with repeated applications. The use of smaller δt fails to help. The spurious oscillatory field has to be filtered and smoothed to keep the results bounded. (2) Filtering and smoothing has been very popular and built into many robust computational codes. The nature of such filtering functions is obscure and its desirable form highly problem-dependent.

Clearly, with $\Delta(0, 1) = \partial / \partial x_i u_i(0, 1) \neq 0$, equation (4) should be used instead of (4a). To solve (4) as a Poisson equation, we need the estimate of $\partial / \partial t \Delta$ which may be directly estimated from $\Delta(0, 1)$ in a variety of ways, such as $+\Delta(0, 1) / \delta t$, zero or $-\Delta(0, 1) / \delta t$ depending on how (4) is supposed to achieve physically in the iterative procedure. (2) Such iterative solutions of p from the Poisson Equation (4) also failed to converge to some meaningful $u_i(1)$ and $p(1)$ at $t_0 + \delta t$, but led to chaos. Such chaotic fields are numerical turbulence generated by the iterative procedure for solving the nonlinear system. They can hardly be suppressed or damped by any reasonable amount of artificial viscosity that might be introduced into the computational algorithm.

Such computational difficulty of securing detailed mass balance by varying pressure prompts the development of computational methods that avoid the determination of pressure. Since the curl of the momentum equations (2) eliminates the pressure explicitly to give the vorticity transport equations:

$$\frac{\partial}{\partial t} \omega = \nabla \times (u \times \omega) + \nu \nabla^2 \omega \quad (5)$$

$$\text{where } \omega = \nabla \times u \quad (6)$$

and

$$\nabla^2 u = \frac{\partial^2}{\partial x_j \partial x_j} u_i = -\nabla \times \omega \quad (7)$$

the vorticity ω may be advanced by (5) and the velocity u solved from (6) or (7), apparently without any explicit reference to pressure. This approach has been quite successful for flows in two space dimensions where the continuity relation can always be satisfied with a stream function, and the vorticity vector with only one nonzero component $\nabla^2 \psi$ is always solenoidal. The vector equation (5) is simplified to a scalar equation of vorticity transport. This stream function ψ , and hence the velocity-vorticity field, can be solved computationally. Presumably the pressure $p(t, x)$ can be obtained by integrating the momentum equation spatially. The pressure so evaluated at a given point turns out to depend on different paths of integration even if $\psi(t, x)$ has converged to some well defined steady

state. (3) Thus the pressure transients cannot be determined with such stream function vorticity formulation even for flows in two space dimensions.

For flows in three space dimensions, the flow field evolution is generally visualized according to equation (5) as the processes of convection $u \cdot \nabla \omega$, interaction $\omega \cdot \nabla u$ and dissipation $\nu \Delta^2 \omega$. The effect of vorticity interaction is often evaluated through the Biot-Savart Law as a consequence of equation (7). Such numerical solutions have often been referred to as the solution of the Navier-Stokes system (4). Without ingenious smoothing and filtering, such computational solutions quickly lead, however, to chaotic oscillations even at Reynolds numbers significantly below the critical Reynolds numbers of laminar flow instability. Such chaotic oscillations are clearly of numerical origin (or numerical turbulence). The question of associated pressure field is rarely mentioned. Why should the computational solution through vorticity formulations for the three-dimensional flows be so much more difficult than that of the two-dimensional flows?

It is simple to verify that a planar field will rapidly become three-dimensional and nonsolenoidal under its own convective motion and their mutual vorticity interaction as is evaluated by the Biot-Savart Law. A nonsolenoidal vorticity field is mathematically incompatible with its definition equation (6). A nonsolenoidal velocity field violates the continuity relation (1). The derivation of equations (5) from (2) implies solenoidal vorticity and the derivation of equations (7) from (6) implies solenoidal velocity. The popular approach of considering vorticity transport and interaction in discrete form without due attention of retaining solenoidal velocity and vorticity fields is fundamentally questionable. It is often tolerated in the construction of approximate solutions if the residual divergences could be controlled to remain small, and the global mass conservation can be monitored and likewise maintained. Thus, many forms of Mark and Cell (MAC) and the Particle in Cell (PIC)

methods were developed as early as 1950's for integrating (1) and (2) by introducing Lagrangian particles to track the mass balance of many sub-ensembles represented by such particles. Alternatively, the Navier-Stokes equations may be integrated in some mixed Lagrangian-Eulerian formulations. The calculated flow field can appear quite reasonable and even be made to reproduce selected details of global experimental data; but adequate pressure field is yet to be recovered from the computed velocity field that is not quite solenoidal.

For flows in three space dimensions the velocity vector can be represented as $u = \nabla\phi + \nabla \times A$ where the scalar potential ϕ is defined through $\nabla^2\phi = 0$ and the vector potential A is related to vorticity as $\omega = \nabla \times \nabla \times A$. The pressure and the velocity transients are clearly not solely determined by the evolution of vorticity ω alone. For the solution of ϕ and ω (or $\nabla \times A$), the nonslip condition $u = 0$ is split into normal and tangential components and applied separately. There is no guarantee that the sum of $\nabla\phi$ and $\nabla \times A$ will satisfy either. It is not surprising that computational solutions of such stream function-vorticity formulation can hardly be kept bounded without constant and repeated "smoothing" and "filtering". While it is possible to devise ingenious "filtering" schemes to reproduce some preconceived solution, we hardly understand their physical basis. Therefore we attempt to analyze the situation and then develop a computational algorithm free from such uncertainties.

II. Analysis of Artificial Compressibility Approaches

The solution of (5) and (7) with nontrivial boundary is not really independent of pressure. On a solid boundary at rest, for example, the nonslip conditions require

$$\nu \nabla \times \omega = \frac{1}{\rho} \nabla p \quad (8)$$

under the solenoidal velocity and vorticity fields. Any approximate formulation of the vorticity boundary data in the solution of

(5), such as $\nu \nabla \times \omega = \partial^2 / \partial x_j \partial x_j u_i$ evaluated with the previous iterate, is actually some approximation to the spatial gradient of the pressure field on the solid surface. With the appropriate pressure boundary data on the solid surface and those at infinity (or other closure surface), equation (4) or (4a) will define the corresponding approximate pressure fields. The iterative solution of the vorticity transport equation (5) with successive approximate boundary formulations on the nonslip surface is equivalent to an iterative process with the corresponding sequence of approximate pressure field. Accordingly, the iterative solution of (5) and (7) through the intermediate variable vorticity is simply an alternative form of the pressure iterative solution of (1) and (2) in terms of the primitive variables p and u_i . It suffices, therefore, to study the iterative processes for the solution of (1) and (2) in primitive variables, $u_i(t, x_j)$ and $p(t, x_j)$, to identify some property conducive to a converging iterative process.

We shall show that the iterative processes described in the previous sections attempting to reduce the residual divergences cannot converge for nontrivial initial boundary value problems in three space dimensions over a drag body (or surface). For convenience, we shall refer to these methods as "Artificial Compressibility" in view of equation (3) that any residual divergence $\Delta = \partial u_i / \partial x_i$ represents the "condensation" or the rate of fractional variation of fluid density, i.e., "compressibility." The sequence of iterants may be interpreted as describing the succession of "compressible states" which, in the limit of small residual divergence and compressibility, was hoped to converge to the limit of incompressible flow.⁽⁵⁾⁽⁶⁾

We describe the succession of such artificial compressible flows by the discrete equivalent of the following set of partial differential equations:

$$\epsilon \frac{\partial p}{\partial t} = -\Delta = -\frac{\partial u_i}{\partial x_i} \quad (9)$$

$$\frac{\partial u_i}{\partial t} + u_j \frac{\partial u_i}{\partial x_j} - \frac{1}{\rho} \left(\frac{\partial p}{\partial x_i} + F_i \right) + \nu \frac{\partial^2}{\partial x_j \partial x_j} u_i \quad (10)$$

Here, ϵ is the function that describes how $\delta p^{(0,1)} = p^{(0,2)} - p^{(0,1)}$ is evaluated from $\Delta^{(0,1)}$ in the iterative correction scheme to achieve $\Delta^{(0,n)} \rightarrow 0$ for the time step δt . It clearly depends also on the details of the scheme of discretizing (9) and (10) for computational solution.

For a physical medium with $\delta p / \delta \rho \sim \rho c^2 > 0$ and $\Delta = \rho^{-1} \delta \rho / \delta t$, ϵ is always positive and vanishes as $\Delta \rightarrow 0$ in a physical limit process of approaching an "incompressible" state through successive "artificial compressible states" of decreasing compressibility. A residual divergence Δ in an incompressible fluid is a volumetric source of the flow or the mass source divided by fluid density. This mass source will carry with it some momentum which should be represented by some external force F_i in the momentum equation (10). Our attempt to construct a converging computational algorithm for the solution of (1) and (2) is thus recast into finding the four scalar functions ϵ and F_i such that a converging solution of (9) and (10) through some discrete equivalent system would exist (and hopefully unique as a well posed problem) in the limit of $\Delta \rightarrow 0$ at all times. It is therefore necessary that:

$$\begin{aligned} \lim_{\Delta \rightarrow 0} \epsilon(\Delta) &= 0 \\ \lim_{\Delta \rightarrow 0} F_i(\Delta) &= 0 \end{aligned} \quad (11)$$

so that (9) and (10) will reduce to (1) and (2) respectively. The four functions ϵ , F_i are otherwise completely arbitrary, and may be distinct for different discretization details through finite difference, finite element, spectral, or any other method. We attempt to identify first the properties of ϵ and F_i that would facilitate, if not secure, convergence.

By multiplying p into (9) and ρu_i into (10) and integrating their sum over the volume V of computation, the following temporal variation of an energy integral E , is obtained where the Stokes theorem has been used to convert some volume integrals into surface integrals over the bounding surface S of V .

$$\begin{aligned} \frac{\partial E}{\partial t} &= \frac{\partial}{\partial t} \int_V \left(\frac{\rho}{2} u^2 + \frac{\epsilon}{2} p^2 \right) dv \\ &= -\mu \int_V \left(\frac{\partial u_i}{\partial x_j} \frac{\partial u_i}{\partial x_j} \right) dv \\ &+ \int_V u_i \left[\frac{\rho}{2} u_i \Delta - F_i \right] dv \\ &+ \mu \int_S \frac{\partial}{\partial x_i} \left(\frac{\rho u^2}{2} \right) ds_i + \int_S - \left(p + \frac{\rho u^2}{2} \right) \end{aligned} \quad (12)$$

With ϵ non-negative the quantity $E = \rho u^2/2 + \epsilon p^2/2$ can serve as the measure or the magnitude of the set of computed results, converging (or diverging) if $\partial E / \partial t \leq 0$ (or > 0) at all later times.

The first volume integral on the right hand side of (12) represents viscous dissipation which is always negative and stabilizing. The last two surface integrals depend exclusively on the formulation of the computational boundary. Then for a given boundary formulation:

(i) The convergence behavior of an iterative scheme depends only on the choices of $F_i(t, x_j)$, i.e. the momenta carried by the mass associated with the residual divergence Δ , not the details ϵ how the pressure correction δp is evaluated from Δ . In other words, it is futile to devise different iterative algorithms ϵ of advancing pressure from residual divergence as is described in the previous section, to promote convergence $\Delta \rightarrow 0$.

(ii) The boundary formulation that determines the surface integrals on the left hand side of (12) is important. Computational methods highly successful for periodic boundary value problems need not be as successful for nontrivial problems as will be explained below.

For periodic boundary values problems, both the two surface integrals in (12) vanish. The first volume integral is proportional to viscosity and always negative. Therefore, if we choose $F_i = \rho u_i \Delta / 2$ everywhere at every iterative steps to render the second volume integral zero, the iterative scheme will always converge regardless of how the pressure δp is evaluated from Δ . The convergence rate, in terms of the weighted L_2 or RMS norm expressed as $\partial E / \partial t$ globally, is proportional to the fluid viscosity (or the dissipation). The standard L_2 norm convergence rate of pressure corresponding to a converging velocity field will, however, vary as $\epsilon^{-1/2}$, which can be troublesome as $\epsilon \rightarrow 0$.

Actual computational solutions of simple periodic boundary value problems of (9) and (10) with some preassigned small values of ϵ and $F_i = \rho u_i \Delta / 2$ for different simple test problems have rendered highly successful approximations to the corresponding incompressible flow velocity fields (5,6) although without as satisfactory pressure results. The schemes of discretization and various other details apparently do not matter. Such solutions of periodic, boundary value problems can be much improved with smaller ϵ and through Richardson's Extrapolation etc. The evaluation of the pressure field is, however, more difficult as $\epsilon \rightarrow 0$ as is suggested by the theoretical result given above. Computational methods, have often been developed with periodic boundary value and applied to nontrivial boundary value problems. The results have

been mixed. Various filtering and smoothing schemes can be built into robust codes for computing the velocity fields. They are not solenoidal and cannot provide meaningful solutions of the pressure field.

In the presence of a drag (or lift) body (or surface) in the flow field, the boundary formulation cannot be periodic. The last surface integral in equation (12) representing the net outflux of the stagnation pressure $p + \rho u^2/2$ over the external boundary, will remain positive and non-zero even in the limit of $\Delta \rightarrow 0$. With both viscous contributions small at sufficiently large Reynolds numbers and with $\lim_{\Delta \rightarrow 0} F_1(\Delta) = 0$, equation, (12) shows that

$\partial E/\partial t$ will eventually be dominated by the drag contribution, (i.e. the positive surface

$$\text{integral } E_d = \int_S \left(p + \frac{\rho u^2}{2} \right) u_1 \, ds_1$$

and remain positive as $\Delta \rightarrow 0$. Thus $\partial E/\partial t$ will remain positive at sufficiently small Δ and E will eventually diverge as $\Delta \rightarrow 0$. Then these iterative scheme of reducing the residual divergence cannot converge.

It is of course possible to choose F_1 sufficiently large all the times so as to have $\partial E/\partial t < 0$, and hence, an apparently converging iterative process. This converged solution is, however, not that of (1) and (2) since (10) remains different from (2) with large $F_1 \neq 0$. We do not know how such a converged solution might render a satisfactory approximation to our problem. In any case we never compute till $\Delta \rightarrow 0$ and have to stop at some finite Δ or ϵ . We could presume that F_1 would, from there on decrease toward the set of values $\rho u_1 \Delta/2$ or the like such that the E would decrease to some E_{\min} before diverging under the influence of E_d . Such an E_{\min} could suggest some asymptotic approximation to the solution of our problem.

There can be a variety of choices of F_1 including those ingenuous forms of smoothing and filtering. Such choices may render good approximations to the velocity field especially if we have some preconceived ideas. For such an approximate velocity field, the asymptotic errors are concentrated in the pressure field. In terms of the standard L_2 norm, the r.m.s. error of the pressure field will grow as $\epsilon^{-1/2}$ which can be very large if the velocity field should be nearly solenoidal ($\epsilon \ll 1$). Thus the pressure solution has to be postponed. This is reminiscent of the situation of the computational solutions described in section II. Our interest in the pressure transients, however, are not well served by such methods of artificial compressibility including those with suitable filter(s).

A reasonable iterative solution for the pressure transients should be constructed from velocity iterants that are solenoidal everywhere and at all times at least after some fixed time t_0 , i.e. iterations in solenoidal subspace. The pressure field associated with each solenoidal velocity iterate can be consistently determined from (4a) unique up to a constant. The evolving solenoidal velocity field and its associated pressure field will have to satisfy (2) or its equivalent discrete set.

III. An Iterative Solution Method in Solenoidal Subspace

The evolution of a solenoidal velocity field $u_1^{(0)}(t_0)$ under some prescribed smooth pressure field $p^{(0)}(t_0)$ according to equation (2) will not necessarily produce a solenoidal velocity field. Indeed the $\Delta = \partial u_1/\partial x_1$ will evolve according to equation (4). There is no reason to expect the prescribed pressure field $p^{(0)}(t_0)$ and $u_1^{(0)}$ to satisfy 4(a) so as to warrant the natural evolution into a solenoidal velocity field. In any case, the flow system could be subjected to arbitrary disturbance of pressure and/or velocity that violates (4a) and generate residual divergence in the course of time. Therefore we have to face the question what is the physical meaning of such a residual divergence although not physically admissible to an incompressible fluid.

H. Lamb⁽¹⁾ introduced the notion that a residual divergence in an incompressible fluid is "equivalent" to a set of associated "impulsive forces". In otherwords, an equal and opposite set of associated impulsive forces would annihilate the local residual divergence to leave a solenoidal velocity field, being disturbed by the set of associated impulsive forces. This concept has been little developed; but gives equations (9) and (10) a physical meaning different from the artificial compressibility extension of the equations system (1) and (2) for an incompressible fluid. The residual divergence Δ is accompanied by an equal but opposite pair of impulsive forces $-F_1$ and F_1 introduced or developed at any point and any time. The $-F_1$ will remove the residual divergence Δ to restore a solenoidal flow field. The F_1 remains as the "equivalent" set of impulsive forces acting on the solenoidal flow. Thus (9) can be replaced by (1) with $\Delta = 0$; and (10) by (10) with F_1 disturbances equivalent to the nonsolenoidal velocity disturbance Δ . For a given residual divergence Δ , this set of equivalent impulsive forces F_1 is not unique and not in "dynamic equilibrium". An impulsive force is a point source of "discontinuous" wave, propagating into the flow field and modifying the local velocity and pressure as it passes. The wave will reflect from boundaries and interact with

waves from other sources to relax the disturbed flow field to establish a new "smooth" solenoidal velocity field with an equilibrated smooth pressure field consistent with (4a) and the physical boundary data. This relaxation process is very fast in an incompressible fluid where the wave speed (or the speed of "sound") is "infinitely" large. The dissipative forces of friction and heat transfer have no time to act, so that this relaxation process is essentially "potential". This relaxed solenoidal disturbance velocity field can be represented uniquely by the gradient of a velocity potential ϕ as $\nabla\phi$

$$u^{(1)}(t_0 + \delta t) = \tilde{u}^{(1)}(t_0 + \delta t) + \nabla\phi \quad (13)$$

This potential function ϕ is given by

$$\nabla^2\phi = -\text{div } \tilde{u}^{(1)} = -\Delta \quad (14)$$

and can be solved with the appropriate Dirichlet and/or Neumann type boundary formulation over the field without altering the physical boundary conditions of $u^{(1)}$. In terms of the relaxed solenoidal velocity $u^{(1)}$ from (13), we can solve for the associated pressure field $p^{(1)}(t_0 + \delta t)$ from (4a). This $p^{(1)}(t_0 + \delta t)$ and $u^{(1)}(t_0 + \delta t)$ is the first physical iterate at the first time step $t_0 + \delta t$. It need not be consistent with the discrete form of (2) in stepping from t_0 to $t_0 + \delta t$. As such, they have to be iteratively corrected. We designate this first iterate for the first time step $p^{(1,1)}$ and $\tilde{u}^{(1,1)}$ etc. (i) If there is an external non-solenoidal velocity disturbance, take the non-solenoidal

disturbed velocity field as $u^{(1,1)}$. If there is no external disturbance, advance the initial solenoidal velocity $u^{(0)}$ to $\tilde{u}^{(1,1)}$ by evaluating $\partial p/\partial x$ from the initial data $p^{(0)}$ over the time step δt .

(ii) Obtain $\phi^{(1,1)}$ according to (14) and $u^{(1,1)}$ from (13)
(iii) Obtain $p^{(1,1)}$ according to (4a) and then choose some average pressure $\bar{p}^{(1,1)} = p^{(1,1)}/2 + p^{(0)}/2$ or the like, for the improved evaluation of the spatial pressure gradient in (2).
(iv) Repeat (i) with the chosen average pressure $\bar{p}^{(1,1)}$ and some averaged convecting velocity $u^{(1,1)}$ to obtain a new estimate of $\tilde{u}^{(1,2)}$, then $\phi^{(1,2)}$, $u^{(1,2)}$ and $p^{(1,2)}$.
(v) Repeat the above until $u^{(1,n)}$, $p^{(1,n)}$ remain essentially "unchanged" according to some specified error norm. Take these converged values as $u(t_0 + \delta t)$ and $p(t_0 + \delta t)$. They will serve as the initial data for advancing the solution to the next time step $t_0 + 2\delta t$, etc.. As a standard initial value problem without subsidiary conditions iterative convergence can be expected with many standard difference schemes (both temporarily and spatially) for some finite time interval T.

We can solve (5)-(7) iteratively in the vorticity formulation in a similar manner. A residual divergence of vorticity is equivalent to an impulsive couple (i.e equal and opposite

pair of impulsive forces). The relaxation of such impulsive couples will likewise be "potential" and the equilibrated vortical field can be represented as

$$\omega^{(1)}(t_0 + \delta t) = \tilde{\omega}^{(1)}(t_0 + \delta t) + \nabla\psi \quad (15)$$

with the potential function ψ governed by

$$\nabla^2\psi = -\text{div } \tilde{\omega}^{(1)} \quad (16)$$

to be solved with the appropriate mixed boundary formulation for nontrivial problems.

If there is an external nonsolenoidal vorticity disturbance, take it to be the $\omega^{(1,1)}$. If there is no external disturbance, advance the initial solenoidal vorticity $\omega^{(0)}$ to $\omega^{(1,1)}$ with the vorticity transport equation (5) under some approximate boundary formulation. Then obtain $\psi^{(1,1)}$ from (16)

and $\omega^{(1,1)}$ from (15) for future iterative corrections to obtain the converged value of $\omega^{(1,1)}$. We find it much more convenient to obtain the disturbed velocity field u as solution of (7) rather than as the induced velocity evaluated from Biot & Savart Law. $u^{(1,1)}$ is then rendered solenoidal by $\nabla\phi$ according to (13) and (14). If the updating of the boundary data for the solution of (5) involves pressure, we would solve (4a) to obtain $p^{(1)}$. Otherwise, we can go direct to equation (5) for up-dating $\omega^{(1,1)}$ to $\omega^{(1,2)}$ etc with some average values of u and p until, $\omega^{(1,n)}$, $u^{(1,n)}$ and $p^{(1,n)}$ converge before proceeding to construct solution at $t_0 + 2\delta t$.

In our earlier computations at rather coarse meshes, we used the vorticity formulation which avoids the differentiation of the numerical velocity data to obtain vorticity. In flow visualization experiments, the flow fields are generally described in terms of vorticity. We know of no experimentally measured pressure transients for checking or comparing with the presently computed results. The most time consuming part of the solution in vorticity formulation is to solve the 6 Poisson equations (3 in u-p formulation). The solution of Poisson equation is tedious and prone to numerical instability. We tried many "Fast Poisson solvers" extended to 3 space; but adopted the classical method with experimentally determined relaxation parameter which we found to be flexible, reliable and actually considerably faster than most. We adopted also the simplest difference scheme of forward time and centered space for discretization. Many discrete treatments of the outer boundary in integrating (5) or (2) have been tried to minimize the propagation of boundary errors that limits the number of time steps of computation before the flow field development in the center of the computational region is clearly affected. We tried many but adopted the format of simple extrapolation normal to the boundary.

We studied computationally the development of disturbances in a uniform shear flow field between two parallel plates with the top plate moving in its own plane with a

unit velocity relative to the stationary plate. The flow Reynolds number based on the separation distance between the two plates is 3000, a typical value in the transition range. Some computations were performed at $Re \sim 300$ to verify the stabilizing effect of the lower flow Reynolds numbers. Artificial disturbances were introduced at a cluster of six mesh points mostly next to the stationary plate. We began our study with the coarse meshes $(15-45) \times 15 \times 15$ and $\Delta t = 0.02$ on the IBM 3081 at Princeton University based on vorticity formulation. We introduced different types of artificial impulsive disturbances of velocity and/or vorticity components of wide range of magnitudes. They are artificial or nonphysical since the disturbed velocity (and/or vorticity) field is not solenoidal and hence not physical. Each such artificial disturbance field $u^{(1,1)}$ and/or $\omega^{(1,1)}$, is accordingly equilibrated to a solenoidal velocity disturbance field $u^{(1)}$ and/or $\omega^{(1)}$ and its associated pressure disturbance $p^{(1)}$ to serve as a physically valid initial disturbance. Both the equilibrated $u^{(1)}$ and $p^{(1)}$ are highly oscillatory over the entire field of computation, with large peaks and valleys next to where the impulses are applied. Away from such peaks, the wide spread oscillations are an order(s) of magnitude smaller. They are highly variable in details. For convenience, we shall refer to each case as the evolution of the impulsive velocity (or vorticity etc.) rather than the natural evolution of the complicated pair of the physical initial data in $u^{(1)}$, $\omega^{(1)}$ and $p^{(1)}$.

For unit impulses of velocity and/or vorticity components clustered in different localities, the resulting pressure disturbances vary considerably in peak magnitudes. The magnitudes of their solenoidal velocity disturbances remain $O(1)$ while those of their peak pressures vary from $O(10^{-2})$ to $O(10^{-4})$. We computed the evolution of dozens of such disturbances. The behavior of their evolution falls into three categories, each of which turns out to be characterized by the initial peak magnitude of the numerically small equilibrated pressure disturbances.

(i) A small peak pressure disturbances of $O(10^{-4})$ rapidly decays to restore uniform shear flow within numerical noises, commensurate with the available resolution.

(ii) An intermediate peak pressure disturbance of $< 10^{-3}$ spreads rapidly to form some locally "turbulent" region but rapidly decays to restore some disturbed laminar flow.

(iii) A large peak pressure disturbance of $O(10^{-2})$ rapidly evolves into some asymptotic pattern of an expanding local "turbulent" region. The pattern propagates and evolves slowly in details, reminiscent of the circumstances revealed in many flow visualization studies of "turbulent spots" in transitional flows⁽⁷⁾⁽⁸⁾⁽⁹⁾. The asymptotic stage of evolution of such large disturbances is well formed at ~ 50 time steps in our computations of $45 \times 15 \times 15$ resolution in IBM3081, well before the boundary errors appear to distort appreciably the flow field evolution in the center of the computational field.

These qualitative features are confirmed by finer mesh computations on CRAY 1 at NCAR Colorado, with $(31-45) \times 20 \times 45$ meshes and $\Delta t = 0.01$. We were able to observe some flow field details of the evolution in these finer mesh results. Further mesh refinements to $(45-61 \times 20 \times 45)$ have been carried out on CRAY 2 at Minnesota and CRAY XMP at Illinois for more detailed studies of the evolution of selected cases. We recomputed some cases with the primitive variables, i.e. u-p formulation and evaluated the vorticity field by numerical differentiation of the computed velocity field. These results of vorticity agree to at least two significant figures everywhere and at all times with those computed directly from the vorticity formulation. Thus most of our recent computations at fine meshes on CRAY 2 and XMP use the u-p formulation to half the memory requirement and the computing time. The results reported in the next section have been computed with both formulations, which our graphics can not distinguish.

The peak pressure magnitude of a given initial cluster of impulsive disturbances decreases rapidly as the cluster recedes from the plate surface. Thus most of our computed cases are for clusters in the proximity of the stationary plate. For such clusters next to the plate, unit impulses of all vorticity components turn out to be "small" while unit impulses of transverse velocity components are "intermediate" disturbances. Unit impulses of streamwise velocity component is the only "large disturbance". Thus, the magnitude of the artificial impulse appears irrelevant as a measure of disturbance "strength". The peak magnitudes of the equilibrated pressure disturbances correlate well with the eventual course of evolution as is described above despite that they are much less than those of the associated solenoidal velocity disturbances. This is physically understandable from Newtonian Mechanics, that the evolution of the velocity field $d/dt u_i$ (or $\partial/\partial t u_i$) is primarily driven by the unbalanced pressure forces, (at least at large Reynolds numbers). We are therefore much interested in the evolution equation of pressure in an incompressible fluid.

By inverting approximately the Poisson operator in (4a), we have

$$\frac{\partial}{\partial t} p + \alpha \left(u_1 - \frac{1}{Re} \nabla^2 u_1 \right) \frac{\partial}{\partial x_1} p - \epsilon_{ij} \frac{\partial^2}{\partial x_1 \partial x_j} p + \beta_{ijk} \frac{\partial^3}{\partial x_1 \partial x_j \partial x_k} p + \dots \quad (17)$$

Here ϵ_{ij} and β_{ijk} are the diffusivity and dispersion tensors of the field, both as complicated functions of the instantaneous velocity field and the flow field boundary and α is a constant depending on the boundary geometry only. If one dimensional model could be any guide, the pressure evolution according to (17) would be dissipative and heat like if $|| \epsilon_{ij} || / || \beta_{ijk} || > 1$, and dispersive and wavelike if $|| \epsilon_{ij} || / || \beta_{ijk} || < 1$ in support of the three different courses of evolution as depicted by our computed results.

We are reasonably confident in the eventual convergence of our algorithm in the limit of zero mesh sizes without smoothing and filtering; but not so confident in the quantitative aspects of our results of such coarse mesh computations. Neither are quantitative experimental results available to check and guide our computations. The global features of flow field evolution described above are common to our results at different mesh resolutions, and appear to be in agreement with experimental observations. In the next section, we report some flow field details as have been observed in our finer mesh results.

IV. Evolution of Large Disturbances in a Uniform Shear Flow over a Wall

We focus our attention on the evolution of unit impulses of streamwise velocity components in the immediate vicinity of the plate ($j=1$) applied at a cluster of 6 mesh points (I.J.K.) = (20, 2, 14-16). The equilibrated pressure field over section J-2 is illustrated in Fig. 1 with two distinct peaks of magnitudes $\sim 3 \times 10^2$. The pressure over the transverse section I-20 inbetween the two peaks is shown in Fig. 2 and that over section K-14 (off from peaks in K-15) is given as Fig. 3. The point (20, 2, 15) appears to be a "Saddle" inbetween the two peaks. There are two valleys in the transverse section. The two distinct high pressure regions over the plate surface appear to be two neighbouring isolated globules or half domes encased in a low pressure valley in the shape of some semi-spherical caps in three space. This is typical of "large" initial disturbances that promptly evolve into propagating local turbulent regions. When the magnitude of the initial artificial u_1 impulses is reduced to 10^{-1} , it becomes marginally an "intermediate" disturbance that fails to reach the asymptotic state of development. Likewise a set of unit impulses of u_2 normal to and directed away

from the plate is "intermediate" or marginally large. Unit u_2 impulses directed toward the plate or u_3 impulses are "intermediate" and marginally "small." All unit vorticity impulses are "small" disturbances that decay

monotonically. The detailed profiles of all these disturbances, vary considerably but without significant implications on the course of development of such disturbances.

We take the evolution of the set of unit streamwise velocity impulses u_1 as the test case for detailed study. The evolution history of the peak pressure over section J-2 is illustrated in Fig. 4. The precipitous drop of peak pressure in the first few time steps is accompanied by a broadening of the high pressure region and significant changes in the shape of the profile, including the "disappearance" of one of the initial peaks with the creation of many others around it. An asymptotic shape begins to form at about $20\Delta t$, followed by some rise and fall in the peak magnitude with significant broadening of fluid volume under high pressure. The peak pressure magnitude rises and falls but manages to stay at $\sim 10^{-3}$ up to $200\Delta t$, the longest we have computed so far. Each time step (0.01 H/U) at $Re = 3000$ corresponds to a physical time $\sim 10^{-5}$ sec. Our computation has thus far covered only a couple of milli-second in physical time during much of this period the pressure transient in Section J-2 has been developing in some complicated "asymptotic" or "quasi-steady" form.

The pressure elevation in Section J-2 at time step $20\Delta t$ is given as Fig. 5. The downstream initial pressure peak has all but disappeared while the upstream initial pressure peak at I-19 of magnitude 0.39×10^{-1} has become the only dominant peak at I-20, K-15 of magnitude 0.96×10^{-2} . There are now four lower peaks surrounding the main peak and many smaller ones further out forming almost a ring of emerging peaks. The pattern is evolving slowly, convecting downstream and spreading out with additional "rings". Fig. 6 displays the pressure distribution at $20\Delta t$ over a vertical section perpendicular to the stationary plate at K-14, i.e. one Δz off from the peak in the J-2 plane to illustrate the three dimensional nature of the many peaks and valleys.

The pressure elevations over Section J-2 at the successive time steps, 40, 80, 120, 160 and $200 \Delta t$ are given as Fig. 7-11. The primary peaks rise and fall as they propagate outwards so that the location of the largest pressure peak can suddenly shift in the plane J-2. The secondary pressure peaks proliferate and also vary in magnitudes extensively especially at later times. Their general pattern as an expanding entity of high pressure regions remains unchanged despite the great variations in details and the rapid increase of the number of secondary and/or emerging pressure peaks. The pressure

transient has apparently reached some asymptotic stage of dynamic development. The proliferation and the conspicuous variations of the outer emerging peaks clearly suggest actual wave dynamics (rather than numerical and/or graphical uncertainties). The pressure elevations over Section K-14 remain little changed through out the evolution in so far as the variation in J are concerned. The dynamic development of the pressure field appears to lie largely in the streamwise direction. Therefore, the dissipative K.D.V. equation

$$\frac{\partial p}{\partial t} + p \frac{\partial p}{\partial x} = \epsilon \frac{\partial^2 p}{\partial x^2} + \beta \frac{\partial^3 p}{\partial x^3} \quad (18)$$

with its well known asymptotic behavior⁽¹⁰⁾, at least in the nondissipative limit, may serve as a useful model of (17) for studying the global qualitative aspects of the pressure evolution in a transitional flow field as mentioned in the previous section.

To better appreciate the three dimensional aspects of the pressure transients next to the plate surface we give in Fig. 12 the colored 3D elevations of the pressure field in J=2 from different view angles. The color illustrates the magnitude corresponding to the scale in the figure. We note that the valleys appear as deep as the hill's height. The streamwise pair of the peaks are always accompanied by a crossstream pair of valleys to form a "quadruple" and the number of such "quadruples" increases at later times. The pressure elevations at planar sections with somewhat larger values of J are similar although with different magnitudes and distributions. Thus the dynamics of pressure transients appears to be describable by the evolution of such "quadruples" across localized half dome of high pressure region encased in a shell of valley in three space. As such it might be possible that the dynamics of each quadruple may be governed by some equation like the dissipative K.D.V. equation (18).

The evolution of the vector velocity and the vector vorticity field appears much more complex and extended much further out than that of pressure. It is difficult to describe with a few planar sections. We are unsure that the movie in preparation can describe fully the complexities of the evolution of the contorted fields of u and ω . The local variations of velocity with time are chaotic, similar to those "measured" hot wire responses. There appears, however, some "Order" out of the "Chaos" when viewed globally. Such a global order is likely associated with the quadruple structure of the pressure disturbances. We describe first the initial velocity impulse in Fig. 13 over the transverse section I-20 inbetween the two distinct pressure peaks at I-19 and 21 respectively (Fig. 1). The curved lines in Fig. 13 are formed by the projections of the

local instantaneous velocity vector at a point in the Section I-20 onto the section. It is designated as "Streamlines" in the figure for convenience, which describes the perturbation velocity in the section over the uniform shear flow u-y perpendicular to the plane. Note that the initial artificial U_1 impulses are applied at j=2, while the equilibrated solenoidal disturbed velocity field appears to "converge" to a much higher point at $j \sim 7$ to 8. This "node" might be interpreted as a "sink" in the transversal surface and a "source" for the longitudinal (streamwise) flow. It is also apparent in Fig. 13 that the flow next to the surface below this node is too complex for our computation to resolve. A similar projection of the velocity vector for surface J-2 (Fig. 14) suggests the presence of counter rotating spiral fluid motion at this "node".

This node in the transversal plane I-20 shifts toward the surface and reaches halfway at $8\Delta t$. By $14\Delta t$ the transversal flow appears to collapse toward the surface as is illustrated in Fig. 15. This collapse is strengthened and widened at $20\Delta t$ suggesting the formation of a counter-rotating vortex pair next to the wall (Fig. 16) that becomes conspicuous at $120\Delta t$ (Fig. 17). This vortical pair disappeared from the surface at $140\Delta t$ (Fig. 18). It is apparently lifted from the wall, displaced outward and replaced by a jet of fluid toward the surface as in Fig. 15. Such a transverse flow pattern is evident in Fig. 19 at $160\Delta t$ and Fig. 20 at $200\Delta t$, with the emergence of a new set of rapidly expanding counter-rotating vortices of opposite sign midstream. A strong transversal flow away from the surface (i.e. the "ejection") is accompanied by the fluid flow down toward the plate surface, displacing the existing complex flow pattern next to the surface outwards. The successive events appear to result from the arrival of a local high pressure globule with its associated vortex pattern in the transversal section I-20. Under the "convective" motion, such high pressure "domes" or "quadruples" carry with them the spiral flow pattern generated by the large local pressure gradients. The successive patterns at I-20 reflect the simultaneous flow patterns over the various neighbouring transverse sections as a high pressure "dome" or "quadruples" passes by according to the dispersion dynamics of pressure described by equation (17).

Fluid elements, "collapsing" or "converging" toward a high pressure "dome" are deflected sideways to fall into a pressure valley on the side, temporarily trapped in the valley. They may escape and then trapped again further downstream into the next spiral of a neighbouring oncoming pressure dome. Or they may escape collectively as a vigorous jet away from the plate in the absence of an immediate oncoming high pressure dome, i.e.

"Ejection". Different fluid elements will undergo "spiral" motions of different dimensions and intensities from "Collapse" to "Ejection". Such an event will generate intense chaotic fluid motions further out.

There results then a turbulent or chaotic flow region centered around an expanding array of spiral vortices with repeated collapses and ejections next to the solid surface. The phenomena of "collapse" and "ejection" and the formation of counter rotating axial vortex pairs have been widely observed in flow visualization experiments^(7,8,9). We are much encouraged to have reproduced all these without numerical artifices. It appears that the "Burst" into local flow turbulence at a point is associated with the passage of a high pressure dome or quadruples over this observation point.

The motion of the pattern of dispersive pressure waves described by equation 17 is much different from the local instantaneous velocity u_1 . Where the local pressure gradient is large with sufficiently large $\nabla^2 u_1$ or $\nabla \times \omega$, the motion of the high pressure region can differ much from the local fluid velocity u_1 . Thus fluids are "drawn" toward the pressure quadruples, "stirred up" through the spirals and "ejected" into neighbouring flow region as chaotically moving fluids. The quadruple nature of the pressure field transients appears to be crucial in driving the laminar to turbulent transition. The substantial velocity differential of the fluid and the quadruple motion is responsible for the spread of the "chaos" or "turbulence" beyond the confine of the propagating pressure quadruples.

When the water (or other liquid) saturated with dissolved air (or other gases) is swept over by such pressure quadruples, the rapid decompression accompanying the arrival of a pressure quadruple will lead to the formation of "air bubbles". Such air bottles moving with the fluid will escape the quadruples and remain in the fluid after the passage of the quadruple. Accordingly the proliferation of such quadruples in a propagating local turbulent region becomes a powerful source of "Cavitation". The pressure elevation on the solid surface ($j=1$) around a pressure quadruple is well represented in Fig. 12. Air bubbles are generated in the pressure valleys; they need not "collapse" there. The cavitating bubbles

can escape into the surrounding turbulent region, be drawn together (Fig. 14, 15) by some oncoming quadruples, and "coalesce" into large bubbles before their eventual "collapse". The collapse of a reasonably sized bubble can be a "large" pressure disturbance of magnitudes comparable to $10^{-2} - 10^{-3} \rho U^2$ i.e the local Froude Number based on the bubble diameter $U^2/gD < 10^2$ or 10^3 . Such a collapse generates a new local turbulent region to perpetuate the propagation of

chaotic flow as flow transition and turbulence. With the magnitudes of the pressure peaks and valleys generally some fraction ($> 10^{-3}$) of the dynamic head (ρU^2) of the relative motion of the solid surface with the "outer free stream", pitting would naturally be more serious nearer to the tip of a propellor or for propellers of higher speeds.

A pressure quadruple in the proximity of the plate surface around a given point gives rise to a surface pressure pattern like Fig. 12. This surface pressure pattern will set the plate into vibration in some characteristic manner. The multiple of such convecting pressure quadruples in a local turbulent region is thus a powerful "acoustic" source, with identifiable characteristics, directionally, spectrally and/or in selected correlation functions to distinguish itself from the prevailing noisy environment. Better understanding of the quadruple structure of the propagating local turbulent region in a transitional flow field could have far reaching implications. The absolute magnitudes of the "large" disturbances that will generate propagating pressure quadruples $\sim 10^{-3} \rho U^2$ at $Re \sim 3000$ are of the order of 10^{-1} Kg/m^2 (or $2 \times 10^{-1} \text{ lbs/ft}^2$). They are comparable to the pressure differentials produced by a rather small or even insignificant free surface waves in open sea. Thus at $Re > 3000$, turbulent flow conditions will likely prevail over a submerged solid surface. A 100db noise in air will generate such quadruples at $Re \sim 3000$ to cause flow transition.

IV. Concluding Remarks

We developed an algorithm to compute the evolution of the pressure and the velocity disturbances in a flow field of an incompressible fluid with the Navier-Stokes equations system through iteration in solenoidal subspace(s). The discrete equivalent of the initial value problem can be obtained through any simple, consistent and stable schemes with Δt satisfying the condition of zone of dependence without any numerical artifices of smoothing, filtering and/or damping. We computed the evolution of many artificial impulsive disturbances of different types and magnitudes in a uniform shear flow between two parallel plates at $Re = 3000$. Computations have been repeated at successive mesh refinements and both in terms of the primitive variables (u, p) and with the help of the derived variable vorticity ω .

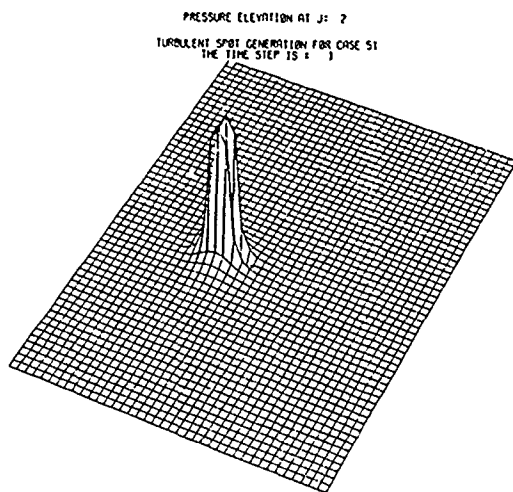
The eventual course of evolution depends primarily on the peak magnitude of the equilibrated pressure disturbance, not so much on the profile details, nor on the nature of the artificial disturbances generating it. Small disturbances are dissipative and stable.

Intermediate disturbances are diffusive, spreading out and decay rapidly. Sufficiently large disturbances will propagate and proliferate to become asymptotically a multitude of propagating local high pressure regions each surrounded by valleys. Over the planar section next to the stationary plate they appear as quadruples with spiral vortices attached to the sides and fluid ejection and collapse fore and aft. These convecting quadruples generate "chaotic" motions of the surrounding fluids. The flow is in transition from the "Laminar" to the "Turbulent" state. Such asymptotic "Order" persists, nevertheless, within the apparent "Chaos".

The evolution of the pressure field can be described by a three dimensional analog of the dissipative KDV equation possessing the different limiting properties described above. As such the propagating large pressure disturbances are likely dispersive waves whose "convective" velocity can be much different

from the local instantaneous velocity of the fluid. If the "Soliton" like character of the solution of KDV equation should prevail, "Turbulent" flows would retain such "orderly" transitional structure, even if not as the strict superposition of such "quadruples". Such convecting quadruples of pressure are powerful acoustic sources that may possess distinct characteristics for recognition or identification. For water "saturated" with air, a pressure quadruple is a source of cavitating bubbles to help spreading turbulence through the collapse of coalesced bubbles.

The author wishes to acknowledge the support of the National Science Foundation under grant MAE 80-10876 and MSM 83-12094, and to thank Dr. Sylvian Roy and Ms. Min Chen and Mr. Jerry Syms in carrying out the computations and data analysis reported in their theses.



MAXIMUM PRESSURE = 0.3912E-01

Fig. 1

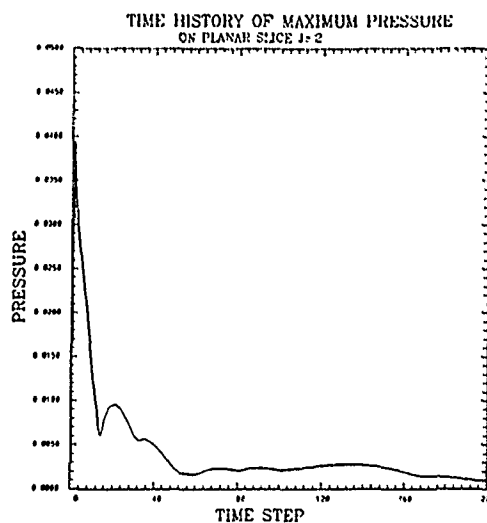
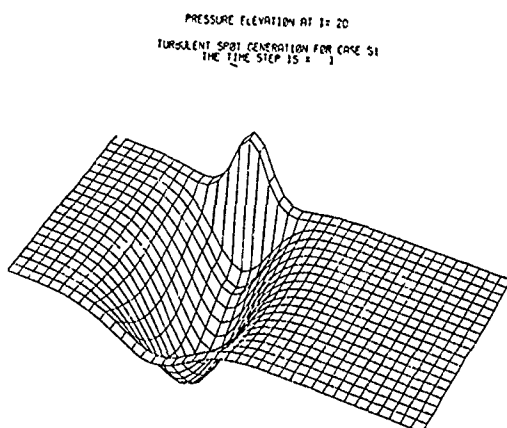
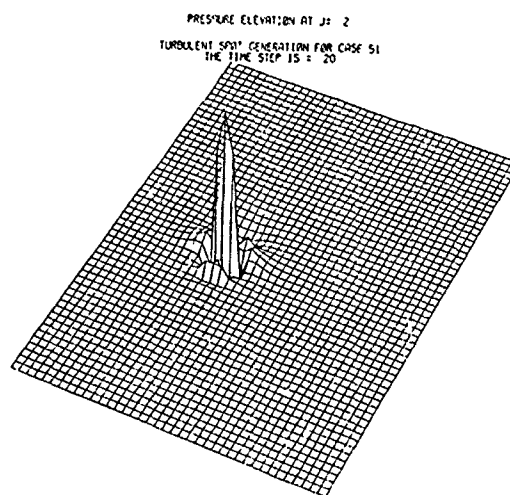


Fig. 4



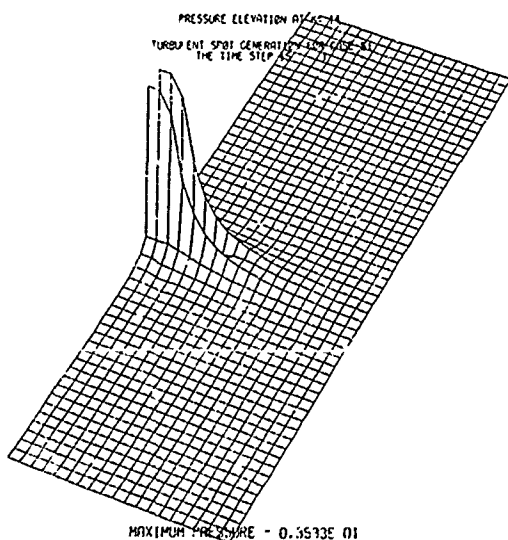
MAXIMUM PRESSURE = 0.2174E-05

Fig. 2



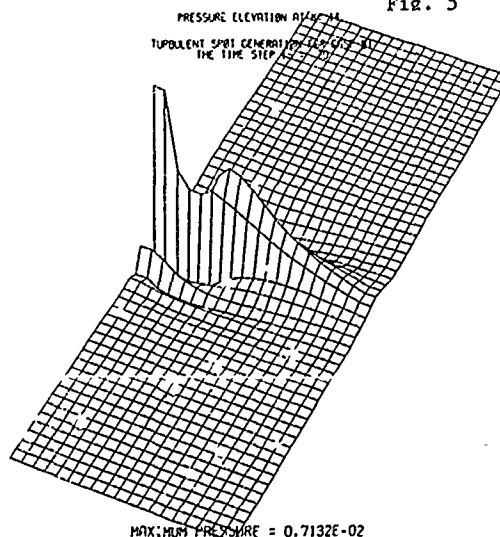
MAXIMUM PRESSURE = 0.9655E-02

Fig. 5



MAXIMUM PRESSURE = 0.3513E-01

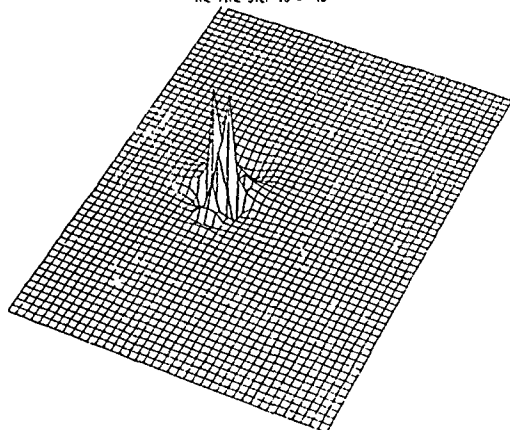
Fig. 3



MAXIMUM PRESSURE = 0.7132E-02

Fig. 6

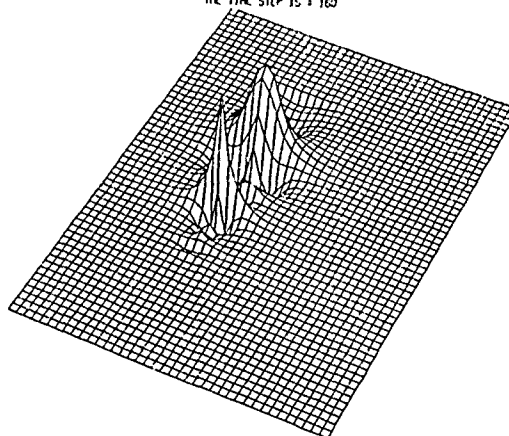
PRESSURE ELEVATION AT J: 2
TURBULENT SPOT GENERATION FOR CASE 51
THE TIME STEP IS = 10



MAXIMUM PRESSURE = 0.5016E-07

Fig. 7

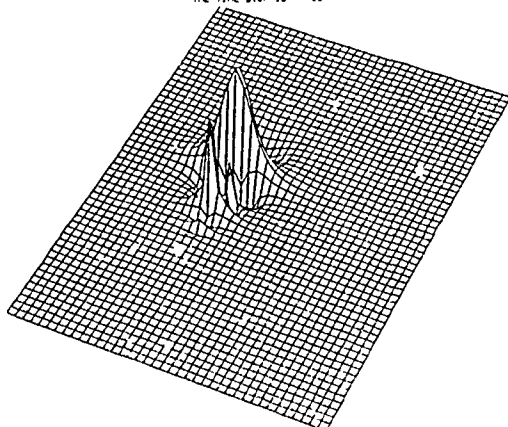
PRESSURE ELEVATION AT J: 2
TURBULENT SPOT GENERATION FOR CASE 51
THE TIME STEP IS = 160



MAXIMUM PRESSURE = 0.1927E-02

Fig. 10

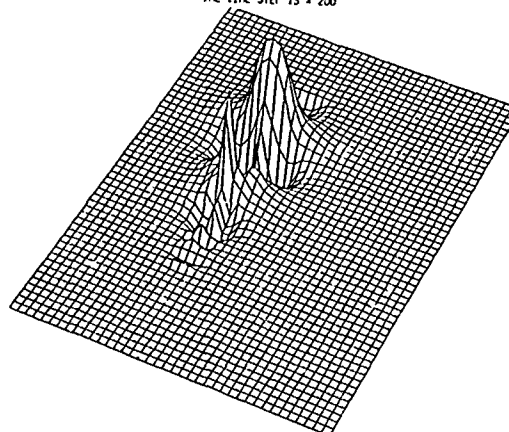
PRESSURE ELEVATION AT J: 2
TURBULENT SPOT GENERATION FOR CASE 51
THE TIME STEP IS = 180



MAXIMUM PRESSURE = 0.2053E-02

Fig. 8

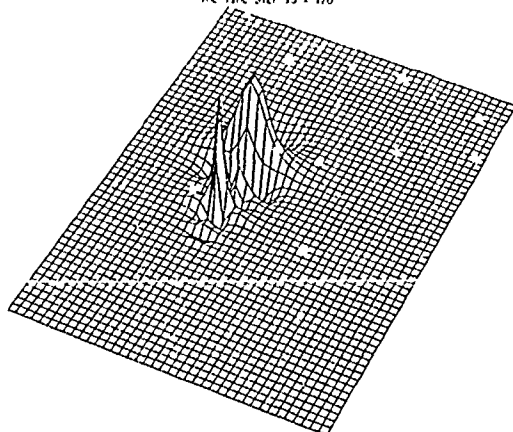
PRESSURE ELEVATION AT J: 2
TURBULENT SPOT GENERATION FOR CASE 51
THE TIME STEP IS = 200



MAXIMUM PRESSURE = 0.9070E-03

Fig. 11

PRESSURE ELEVATION AT J: 2
TURBULENT SPOT GENERATION FOR CASE 51
THE TIME STEP IS = 170



MAXIMUM PRESSURE = 0.2613E-02

Fig. 9

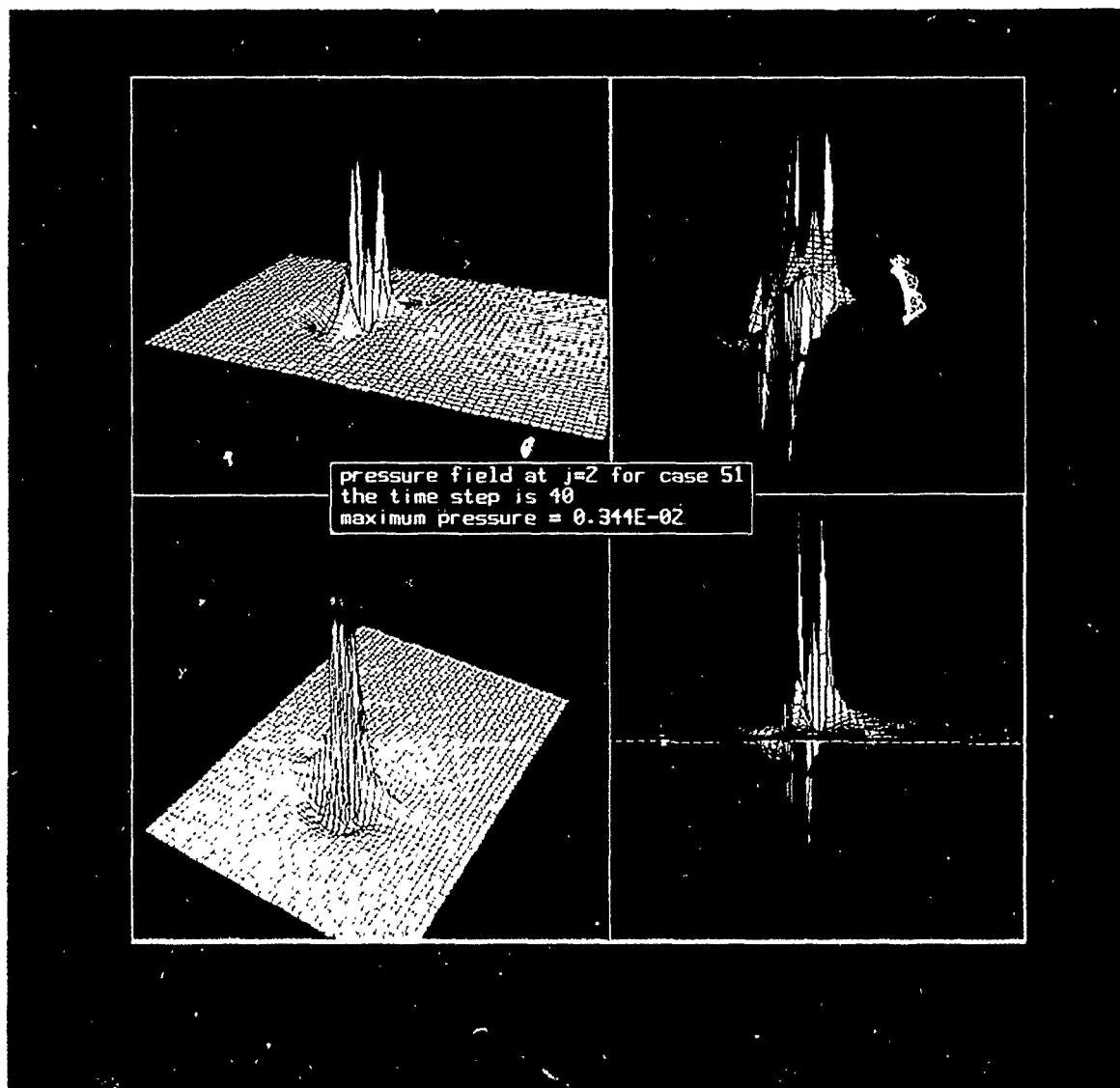


Fig. 12

STREAMLINES AT $t = 20$
THE TIME STEP IS = 1
TURBULENT SPOT GENERATION FOR CASE 51

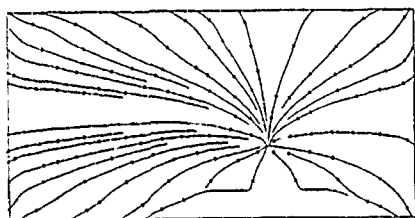


Fig. 13

STREAMLINES AT $t = 20$
THE TIME STEP IS = 20
TURBULENT SPOT GENERATION FOR CASE 51

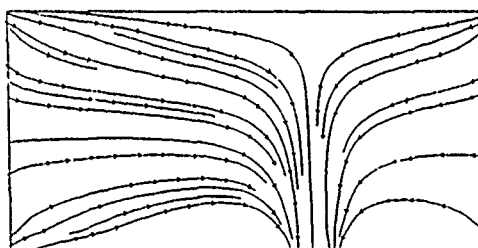


Fig. 16

STREAMLINES AT $t = 2$
THE TIME STEP IS = 1
TURBULENT SPOT GENERATION FOR CASE 51

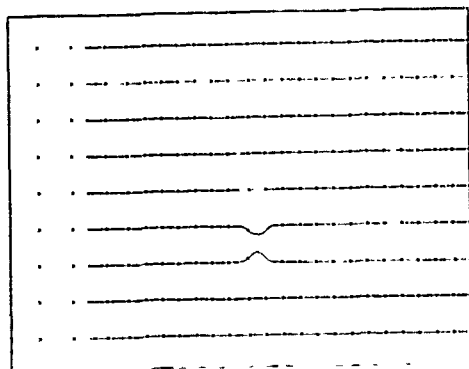


Fig. 14

STREAMLINES AT $t = 20$
THE TIME STEP IS = 120
TURBULENT SPOT GENERATION FOR CASE 51

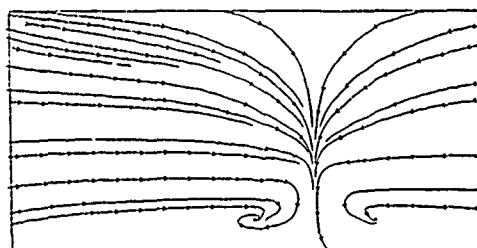


Fig. 17

STREAMLINES AT $t = 20$
THE TIME STEP IS = 14
TURBULENT SPOT GENERATION FOR CASE 51

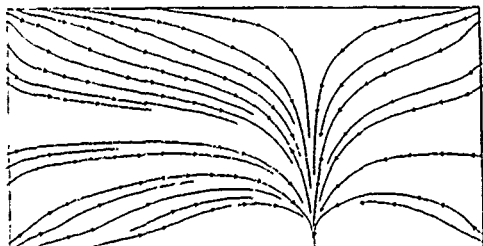


Fig. 15

STREAMLINES AT $t = 20$
THE TIME STEP IS = 140
TURBULENT SPOT GENERATION FOR CASE 51

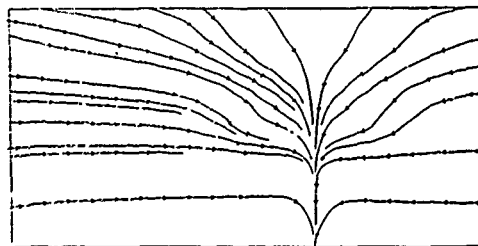


Fig. 18

STREAMLINES AT $t = 20$
 THE TIME STEP IS = 160
 TURBULENT SPOT GENERATION FOR CASE 5*



Fig. 19

STREAMLINES AT $t = 20$
 THE TIME STEP IS = 200
 TURBULENT SPOT GENERATION FOR CASE 51

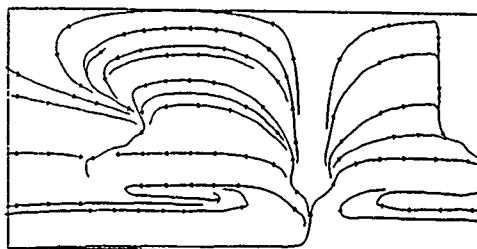


Fig. 20

REFERENCES

1. Lamb, Hydrodynamics, 6th Edition, Dover Publication. A general reference and specifically Art .1, p. 10. Art. 19. pp. 161-2 and Art. 152, pp. 214-216 (1932).
2. Nichols, B. & Hirt. C., "Calculation of 3D Free Surface Flows in the vicinity of submerged and exposed structures". Jour. of Comp. Phy. Vol. 12, no. 173, pp. 234-246.
3. Rimon Y. & Cheng, S. I., "Numerical Solution of a Uniform Flow over a Sphere at Intermediate Reynolds Numbers", The Physics of Fluid, Vol. 12, No. 5 (1969).
4. Leonard, A., "Vortex Stimulation of 3D Spotlike Disturbances in a Laminar Boundary Layer", Second Symposium of Turbulent Shear Flows", London (1979) or NASA TM 78579.
5. Temam, R., "Navier Stokes Equation", North Holland Elseviers, (1978).
6. Chorin, A. J., "Numerical Solutions of the Navier Stokes Equations", Math. Comp. pp. 745-762, (1968).
7. Hinze, J. O., "Turbulence", McGraw Hill, Second Edition (1975). A general reference on Turbulence and specifically on Transition and Turbulence Structure, pp. 605-614, Fig. 7.7, p. 611, pp. 639-641, p. 647, p. 659-666 and p. 724-742.
8. Cantwell, B. J., "Organized Motion in Turbulent Flow" Section in Ann. Review Fluid Mech. 13, pp. 457-515, (1981), Annual Reviews Inc.
9. Kline, S. J., Reynolds, W. C., Schraub, F. A., Runstadler, P. W., "The Structure of Turbulent Boundary Layers", J. Fluid Mechanics, 30, pp. 741-773, (1967).
10. Lax, P. & Levermore, C. D., "The Small Dispersion Limit of the Korteweg-deVries Equation I", Comm. on Pure and Applied Math., Vol. XXXVI, pp. 253-290 (1983).

Large Eddy Simulation by Using Finite-Difference Method

Y. Doi
Hiroshima University
Hiroshima, Japan

Abstract

Turbulent channel flow is studied numerically by using Large eddy simulation (LES). Finite difference method is employed in the LES. The simulation is stably executed by using the 3rd order upwind difference scheme which dissipate numerical errors. First, a computing test is performed for a laminar flow past a circular cylinder. After that, several pilot tests are performed with respect to a turbulent channel flow, in order to investigate the effect of the numerical dissipation terms on the turbulent flow structures. Turbulent flow structures in turbulent channel flows can be well simulated by using the 3rd order upwind difference scheme.

1. Introduction

Large eddy simulation is a relatively new approach to the calculation of turbulent flows. Since the first application of LES was made by Deardorff[1], many attempts on LES have been made. However the typical LES calculations are limited to the flows in the simple configurations in order to resolve the precise structure of the turbulent flows and to calculate the turbulent flows stably. For the practical engineering applications, the application for the flows in or around the more complicated configurations is necessary. For the convenience to simulate the flow around an arbitrary configuration for general purposes, boundary fitted coordinate systems and regular grid systems are usually introduced, although they cause numerical errors which diverge the calculations. So that there needs some numerical damping.

Some attempts to calculate LES have been done for the flows around the complicated configurations by use of the finite difference method([2],[3]). In these methods, the 4th derivative numerical dissipation terms are

introduced artificially in order to damp numerical disturbances with short wave length. The numerical dissipation, which damps numerical disturbances caused by numerical truncations, must be distinguished from SGS model which expresses the sub-grid scale effects.

In this paper, several numerical experiments are performed in order to investigate the effect of numerical dissipation on turbulent flows. First, computing test is performed for a laminar flow past a circular cylinder. After that, several pilot tests are performed for a turbulent parallel channel flow.

2. Formulation

2.1 Governing Equations for the Large Scale Field

We consider an incompressible flow whose time evolution is given by the Navier-Stokes and continuity equations for the velocity components u_i ($i=1,2,3$) and pressure p ,

$$\frac{\partial u_i}{\partial t} = - \frac{\partial (u_i u_j)}{\partial x_j} - \frac{\partial p}{\partial x_i} + (1/Re^*) \frac{\partial^2 u_i}{\partial x_k \partial x_k} \quad (1)$$

$$\partial u_k / \partial x_k = 0 \quad (2)$$

where $i(j)=1,2,3$ correspond to x_1, x_2, x_3 respectively, where $0-x_1x_2x_3$ is the Cartesian coordinate (x_1 is in the downstream direction, x_2 is the direction normal to boundary, x_3 is the lateral direction, see Fig.1). Subscripts denote the partial differentiation with respect to the referred variables. All variables and coordinates have been made dimensionless by means of the length scale D , distance of parallel channel, and the friction

velocity of the parallel channel(u^*).

2.2 Filtered Momentum and Continuity Equations

In LES, each flow variable "f" is decomposed as follows,

$$f = \bar{f} + f' \quad (3)$$

where \bar{f} is the resolvable grid scale(GS) component and f' is the residual sub-grid scale(SGS) component. We denote the grid scale field as,

$$\bar{f}(x_1, x_2, x_3) = \iiint G(x_1 - x_1', x_2 - x_2', x_3 - x_3') \cdot f(x_1', x_2', x_3') dx_1' dx_2' dx_3' \quad (4)$$

In the present study, Top-Hat filter is used as G,

$$G(x_1, x_2, x_3) = 1/\Delta^3 \quad ; \quad |x_1 - x_1'| \leq \Delta x_1/2 \\ (\Delta^3 = \Delta x_1 \Delta x_2 \Delta x_3) \\ = 0 \quad ; \quad \text{other} \quad (5)$$

After applying the filtering operator to the momentum equations and the continuity equation, we get the following equations for the filtered field.

$$\frac{\partial \bar{u}_i}{\partial t} = - \frac{\partial (\bar{u}_i \bar{u}_j)}{\partial x_j} + \frac{\partial \bar{p}}{\partial x_i} \\ + (1/Re^*) \frac{\partial^2 \bar{u}_i}{\partial x_k \partial x_k} \quad (6)$$

In the present study, following assumption is applied.

$$\overline{u_i u_j} = \bar{u}_i \bar{u}_j + R_{ij} + L_{ij} + C_{ij} \quad (7)$$

$$R_{ij} = \overline{u_i' u_j'} \\ L_{ij} = \overline{u_i \bar{u}_j} - \bar{u}_i \bar{u}_j \\ C_{ij} = \overline{u_i u_j'} + \bar{u}_i' \bar{u}_j \quad (8)$$

The terms R_{ij} , L_{ij} and C_{ij} are SGS Reynolds Stress term, Leonard term and Cross term which must be modeled in terms of grid scale components to proceed the calculation.

2.3 Representation of SGS Reynolds Stresses, Leonard Term and Cross Term

SGS Reynolds stresses are modeled as follows introducing SGS eddy viscosity K.

$$\overline{u_i' u_j'} = \delta_{ij} \overline{u_k' u_k'} / 3 \\ = -K (\partial \bar{u}_i / \partial x_j + \partial \bar{u}_j / \partial x_i) \quad (9)$$

where δ_{ij} is Kronecker's delta. K is SGS eddy coefficient, which is modeled by Smagorinsky et al.[4] as follows,

$$K = (c \Delta)^2 \{ \partial \bar{u}_i / \partial x_j (\partial \bar{u}_i / \partial x_j + \partial \bar{u}_j / \partial x_i) \}^{1/2} \quad (10)$$

c is Smagorinsky's constant, which is statistically analysed by Yoshizawa[5]. Here c is taken as 0.1, which is a standard value used for a parallel channel flow.

Leonard term and Cross term are approximated as follows by use of Taylor series expansion,

$$L_{ij} = \frac{\Delta^2}{24} \left(\frac{\partial^2 (\bar{u}_i \bar{u}_j)}{\partial x_k \partial x_k} \right) \quad (11)$$

$$C_{ij} = - \frac{\Delta^2}{24} \left(\bar{u}_i \frac{\partial^2 \bar{u}_j}{\partial x_k \partial x_k} + \bar{u}_j \frac{\partial^2 \bar{u}_i}{\partial x_k \partial x_k} \right) \quad (12)$$

$$L_{ij} + C_{ij} = \frac{\Delta^2}{12} \frac{\partial \bar{u}_i \partial \bar{u}_j}{\partial x_k \partial x_k} \quad (13)$$

Substituting eqs.(7),(8) to eq.(6), we get the following momentum equations.

$$\frac{\partial \bar{u}_i}{\partial t} = - \frac{\partial [\bar{u}_i \bar{u}_j - K (\partial \bar{u}_i / \partial x_j + \partial \bar{u}_j / \partial x_i)]}{\partial x_j} \\ - \frac{\partial [\Delta^2 / 12 \cdot \partial \bar{u}_i / \partial x_k \cdot \partial \bar{u}_j / \partial x_k]}{\partial x_j} \\ - \frac{\partial (\bar{p} - 2x_1)}{\partial x_i} + (1/Re^*) \frac{\partial^2 \bar{u}_i}{\partial x_k \partial x_k} \quad (14)$$

$$\bar{p} = \bar{p} + \overline{u_k' u_k'} / 3 + 2x_1 \quad (15)$$

Here the quantity $\partial (2x_1) / \partial x_i$ in eq.(14) is the dimensionless gross downstream pressure gradient in case of parallel channel flows. The term $\overline{u_k' u_k'} / 3$ is subtracted from the Reynolds stress terms and added to the pressure term.

2.4 Wall Damping Function

Near the walls, Smagorinsky model is not appropriate because of the inhomogeneous effect of the wall turbulence. Therefore the filter length Δ is multiplied by the Van Driest exponential damping function f_D after Moin-Kim[6] as follows,

$$f_D = (1 - \exp(-y^+ / A^*)) \quad (16) \\ y^+ = x_2 Re^* \quad 0 \leq x_2 \leq 0.5$$

$$y^* = (1-x_2)Re^* \quad 0.5 \leq x_2 \leq 1.0$$

where $A^+ = 25$ and y^+ is the distance to the wall in the wall unit.

2.5 Boundary-fitted Curvilinear Coordinate System

The basic idea of transformation of the Cartesian coordinate to the boundary-fitted curvilinear coordinate is to carry out finite-difference computations in a regular rectangle mesh system without extensive interpolation, though transformed partial differential equations become more complicated.

The physical region (x_1, x_2, x_3) is transformed to the imaginary computational region (x^1, x^2, x^3) . The basic equations (14) in the transformed region are as follows,

$$\frac{\partial \bar{q}}{\partial t} = \bar{C} - \frac{\partial (\bar{P} - 2x_1)}{\partial x^1} \bar{g}^1 + \bar{A} \quad (17)$$

$$\begin{aligned} \bar{C} = & -(\bar{g}^1 \cdot \bar{q}) \frac{\partial \bar{q}}{\partial x^1} + (\bar{g}^1 \cdot \bar{g}^j) \frac{\partial K}{\partial x^j} \\ & + \frac{\partial \bar{q}}{\partial x^1} + \frac{\partial K}{\partial x^j} \bar{g}^j (\bar{g}^1 \cdot \frac{\partial \bar{q}}{\partial x^1}) \end{aligned} \quad (18)$$

$$\bar{A} = (K+1/Re^*) \left(\frac{\partial}{\partial x^1} \left(\frac{\partial \bar{u}_1}{\partial x^k} \bar{g}^k \cdot \bar{g}^j \right) \cdot \bar{I}_1 \right) \quad (19)$$

$$\bar{g}^1 = \text{grad}(x^1) \quad (20)$$

$$\bar{q} = \bar{u}_1 \bar{I}_1 + \bar{u}_2 \bar{I}_2 + \bar{u}_3 \bar{I}_3 \quad (21)$$

where \bar{g}^1 is the covariant base vector and \bar{I}_1 is the unit vector directed to x_1 axis.

3. Numerical Scheme

3.1 Finite Difference Forms

Regular grid system is employed in the present study. The derivatives in the momentum equations are discretized by 4th order centered difference approximations except for the convective terms. For the convective terms, following 3rd order upwind difference approximation is used in order to stabilize the computation,

$$\begin{aligned} U \partial f / \partial x &= U_1 (-f_{1,2} + 8f_{1,1} - 8f_{1,-1} + f_{1,-2}) / 12 \Delta x \\ &+ \alpha |U_1| (f_{1,2} - 4f_{1,1} + 6f_{1,-1} - 4f_{1,-2}) / 4 \Delta x \\ &\sim U \partial f / \partial x + \alpha |U| (\Delta x)^3 / 4 \cdot \partial^4 f / \partial x^4 \end{aligned} \quad (22)$$

The first term of eq.(22) is 4th order centered difference approximation and the second term is 4th derivative artificial dissipation. α is the dissipation coefficient. It must be noted that the artificial dissipation terms depend on the velocity with respect to the reference frame. Therefore the momentum equations fail to be "Galilean invariant" and the dissipation is larger where the velocity is larger. In the present study the effect of the artificial dissipation term on the calculated result is investigated.

Fractional Step method is employed for the time derivative. The term \bar{C} is approximated by Adams-Bashforth method and the term \bar{A} is approximated by Euler explicit method.

$$\bar{V} = \bar{q}^n + \Delta t \{ (1+a) \bar{C}^n - a \bar{C}^{n-1} \} + \bar{A}^n \quad (23)$$

$$\bar{q}^{n+1} = \bar{V} - \Delta t \frac{\partial (\bar{P} - 2x_1)}{\partial x^1} \bar{g}^1 \quad (24)$$

$$\frac{\partial}{\partial x^j} \left(\frac{\partial \bar{P}}{\partial x^i} \bar{g}^i \right) \bar{g}^j = \frac{\partial \bar{V}}{\partial x^i} \bar{g}^i / \Delta t \quad (25)$$

When $a=1/2$, the time derivative is called Adams-Bashforth method. The time derivative becomes Euler explicit method for $a=0$. The pressure equation (25) is given by taking divergence of eq.(24), requiring the divergence of the velocity at t^{n+1} must be zero. So that if the pressure p^{n+1} satisfies eq.(25), the velocity field satisfies continuity at t^{n+1} . It is important to note that the difference operation of the Poisson equation (25) can not be chosen independently of the operator used in the momentum and continuity equations. However, 2nd order centered difference operator is used for the divergence of the pressure gradient which is expressed by 4th order centered difference operator in order to avoid the wiggles in numerical solutions.

3.2 Initial and Boundary Conditions

The initial conditions are given as the superposition of a random function to the mean velocity profile \bar{u}_1 and \bar{u}_2 . The mean velocity profile of \bar{u}_1 is given as the following law of the wall and the log law,

$$\begin{aligned} \bar{u}_1 &= (\log y^*) / 0.41 + 5.0 & y^* \geq 10.80 \\ \bar{u}_1 &= y^* & 0 \leq y^* \leq 10.80 \\ y^* &= x_2 \cdot Re^* & 0 \leq x_2 \leq 0.5 \\ y^* &= (1-x_2) \cdot Re^* & 0.5 \leq x_2 \leq 1.0 \end{aligned} \quad (26)$$

The velocity component \bar{u}_3 is determined to satisfy the continuity equation. The magnitude of the random function is 5% of the mean

velocity.

Cyclic boundary conditions are imposed for velocity and pressure, in downstream and spanwise directions. No-slip boundary conditions are imposed at walls. Zero gradient of the pressure normal to the wall is imposed.

4. Computed Results

4.1 Computing Test for Laminar Flow

Before the LES calculation, computing test is performed for a laminar flow past a circular cylinder. Although the flow for this case is 2 dimensional one, the computation is performed by 3 dimensional code in order to check the code. In this case, all variables have been made dimensionless by means of the cylinder diameter(D) and the uniform flow velocity(U). The number of grid points are 80 in circumferential direction, 40 in radial and 5 in axial of the cylinder. The diameter of the computational domain is about 28 times of that of the circular cylinder. The minimum spacings in the radial direction, in the circumferential direction and in the axial direction are 0.01D, 0.008D and 2.0D, respectively. In this calculation, Euler explicit method is employed for the time derivative. The flow around the circular cylinder is accelerated from U=0 to the steady speed(U). The acceleration is set to be $1.0U^2/d$. The time increment is set to be $0.001U/D$ when the flow is accelerated, and after the acceleration the time increment is set to be $0.0015U/D$.

No-slip boundary condition is imposed on walls. Zero gradient of the pressure normal to the wall is imposed. On the outer boundary, the pressure is fixed to zero. With respect to the velocity on the outer boundary, a linear extrapolation is given except a upstream point at which the velocity is given by the inviscid flow solution. Cyclic boundary conditions are imposed for the velocity and pressure in the axial direction.

In this case, the flow is laminar so that the Smagorinsky's constant 'c' is set to be zero. The artificial dissipation factor α is set to be 1.0. The convergence condition of the Poisson eq.(25) is set as the divergence of the velocity is less than 10^{-3} .

The calculated pressure distribution on the circular cylinder is shown in Fig.2 together with the experimental data[7] and the calculated result by Kodama[8]. Reynolds number(Re) based on the cylinder diameter and the uniform flow velocity is 40. The computed result shows good agreement with the experimental data. In Fig.3 drag coefficient is compared with the Tritton's experimental curve[9] and Kodama's calculated results. The

calculated result agrees well with them.

In Kodama's calculation, 4-th order artificial dissipation terms were also added to the momentum equations in order to stabilize the calculation. Kodama analyzed the truncation errors and indicated that the artificial dissipation terms were so small that the accuracy of the solution was not degraded by them.

Without the 4-th order artificial dissipation terms, the calculation diverges always. Although the 2-nd order artificial dissipation terms distort the calculated solutions, the distortion of the 4-th order artificial dissipation terms is not so large.

4.2 Computed Results for a Channel Flow

Simulations are performed for a parallel channel flow. Reynolds number(Re^*) based on the channel breadth(D) and the friction velocity(u^*) is 500. The calculated region has a downstream length of 3D and a lateral width of 0.75D. The downstream length and the lateral width are subdivided into 30 equal grid intervals. Therefore, the intervals in a downstream direction(x_1) and lateral direction(x_3) are as follows,

$$\Delta x_1 = 0.1 \quad \Delta x_3 = 0.025.$$

Non-uniform grid systems are used in the normal direction. The minimum and maximum intervals in the normal direction are as follows,

$$\Delta x_{2min} = 0.0033 \quad \Delta x_{2max} = 0.0728.$$

In this calculation, Adams-Bashforth and Euler explicit methods are employed for the time derivative. Smagorinsky's constant 'c' is set to be 0.1. The convergence condition of the Poisson eq.(25) is set as the divergence of the velocity is less than 10^{-2} .

Dependency of the artificial dissipation factor α on the calculated results is shown in Figs.4,5. Figs.4-a,-b show the turbulence intensities normalized by the friction velocity. From top to bottom, they are $\langle (u_1')^2 \rangle^{1/2}$, $\langle (\bar{u}_2')^2 \rangle^{1/2}$, $\langle (\bar{u}_3')^2 \rangle^{1/2}$, respectively. The angular brackets $\langle \rangle$ denotes the x_1 - x_3 plane average of a quantity and the double prime " denotes the deviation of a quantity from the x_1 - x_3 plane average. They are compared with the experimental data by Clark[10] and Hussain-Reynolds[11] and with the calculated result by Moin-Kim[6]. The calculation diverges when α is less than 0.03. Therefore artificial dissipation is required for the stable calculation. However, the serious effect of the artificial dissipation on the turbulence intensities is

shown in case of $\alpha = 0.06$.

The profile of the mean velocity non-dimensionalized by the friction velocity is shown in Figs.5-a,-b. The solid line represents the law of the wall and the Coles' log law. The experimental data by Hussain-Reynolds[11]($Re^+ = 1280$) is also plotted in Fig.5. The calculated velocity in the log law region is higher than the experimental one. This discrepancy partially depends on the difference of Reynolds number. A noticeable discrepancy does not exist between such a change of artificial dissipation factor $\alpha = 0.03$ and 0.06 . However, if we take a large artificial dissipation factor, for instance $\alpha = 1.0$ so called Kawamura's scheme[12], the velocity profile is seriously deformed[13].

The order of magnitude of each term in the stream-wise momentum equation is compared in Figs.6,7. The contour lines shown in Figs.6,7 are the convection terms, artificial dissipation terms, the SGS model terms (Leonard, Cross and SGS Reynolds terms) and the viscous terms on x_1 - x_3 plane. The convection terms are dominant in the middle of channel, whereas the convection and the viscous terms are dominant near the wall. The SGS model terms are too small compared with the convection terms or the viscous terms. In order to implement the LES calculation, the artificial dissipation terms must be smaller than the SGS model terms. In case of $\alpha = 0.06$, the artificial dissipation terms are greater than or the same order as the SGS model terms in places on $y^+ = 22.2$ plane. Because of this artificial dissipation terms, the turbulence intensities are excessively damped in the middle of the channel. As a result each term is damped as shown in Fig.7-b.

Even for the case of $\alpha = 0.03$, the artificial dissipation terms are the same order as the SGS model terms in the middle of the channel. So that, there still remains room to improve the present computing scheme.

When we use Euler explicit method instead of the Adams-Bashforth method, the scheme of the time derivative is only first order accuracy. To proceed the stable calculation, the artificial dissipation factor must be greater than 0.15 for Euler explicit method, which is 5 times as large as the factor required for Adams-Bashforth method.

The contour lines of each term calculated by Euler explicit method are shown in Fig.8. The artificial dissipation terms are greater than the SGS model terms and also greater than the results calculated by Adams-Bashforth method. This is caused by the large dissipation factor.

Fig.9 shows the turbulence intensities calculated by Euler explicit method. Although

the artificial dissipation terms are greater than the SGS model terms, the calculated turbulence intensities are not so much damped but agree with the experiments. In Fig.10, the profile of the mean velocity is shown. The velocity profile calculated by Euler method is almost same with that of Adams-Bashforth method except the middle of channel. When we take a larger dissipation factor, the turbulence intensities are damped in the middle of channel as shown in Fig.11. This tendency is the same with the case of Adams-Bashforth method (Fig.4-b). Figs.12-a,b,c show the instantaneous velocity vectors on x_2 - x_3 plane. Although the velocity fluctuation is attenuated in the middle of the channel for $\alpha = 0.06$ (Adams-Bashforth), the velocity fluctuation is not so much attenuated for $\alpha = 0.15$ (Euler). When we chose a dissipation factor suitable for the calculating method, even for Euler method, the global feature of the turbulence flow can be obtained.

Conclusions

Turbulent channel flow is studied numerically by using finite difference method. The simulation is stably executed by using the 3rd order upwind difference scheme. The numerical dissipation terms attenuate the turbulence intensities. When we chose a dissipation factor suitable for the calculating method, turbulent flow structures in a turbulent channel flow can be well simulated. However a problem still remains how to determine the dissipation factor.

The present study is partially undertaken as a student project at Hiroshima University. Author is indebted to Mr. K. Murakami who discussed and helped the author in the course of this study.

The computations were executed by Apollo DN10000 and HITAC M-680H at Hiroshima University.

References

- [1] Deardorff, J.W.; A Numerical Study of Three Dimensional Turbulent Channel Flow at Large Reynolds Numbers, J. Fluid Mech. vol.41, (1970), p.453.
- [2] Miyata, H., Kajitani, H., Zhu, M., Kawano, T., Takaki, M.: Numerical Study of Some Wave-Breaking Problems by a Finite-Difference Method, J. of the Kansai Soc. of Naval Architects, (1987), pp.11-24

- [3] Sato, T., Miyata, H., Baba, N., Kajitani, H.: Finite-Difference Simulation Method for Waves and Viscous Flows about a Ship, J. of the Soc. of Naval Architects of Japan, (1986), pp.14-20
- [4] Smagorinsky, J., Manabe, S. & Holloway, J.L.; Numerical Results from a Nine-Level General Circulation Model of the Atmosphere, Mon. Weath. Rev. vol.93, (1965), p.727.
- [5] Yoshizawa, A.; A Statistically-Derived Subgrid Model for the Large-Eddy Simulation of Turbulence, Phys. of Fluids. 25(9), (1982), p.1532.
- [6] Moin, P., Kim, J.; Numerical Investigation of Turbulent Channel Flow, J. Fluid Mech. vol.118, (1982), p.341.
- [7] Grove, A.S., Shair, E.S., Petersen, E.E. and Acrivos, A.: An experimental investigation of the steady separated flow past a circular cylinder, JFM vol.19, (1964), pp.60-80.
- [8] Kodama Y.: Computation of the Two-Dimensional Incompressible Navier-Stokes Equations for Flow Past a Circular Cylinder Using an Implicit Factored Method, Papers of Ship Research Institute, Vol.22, No.4, July (1985), pp.335-377.
- [9] Tritton, D.J.: Experiments on the flow past a circular cylinder at low Reynolds numbers, JFM vol.6, (1959), pp.547-567.
- [10] Clark, J.A.; A Study of Incompressible Turbulent Boundary Layers in Channel Flow, Trans. ASME, J. Basic Eng. vol.90, (1968), p.455.
- [11] Hussain, A.K.M.F., Reynolds, W.C.; Measurement in Fully Developed Turbulent Channel Flow, Trans. ASME, J. Fluid Eng. vol.97, (1975), p.568.
- [12] Kawamura, T. et al.: Computation of High Reynolds Number Flow around a Circular Cylinder with Surface Roughness, AIAA paper, 84-0340 (1984)
- [13] Doi, Y., Kimura, T.: Large-Eddy Simulation of Turbulent Channel Flow, J. of the Soc. of Naval Architects of Japan, (1988), pp.23-30

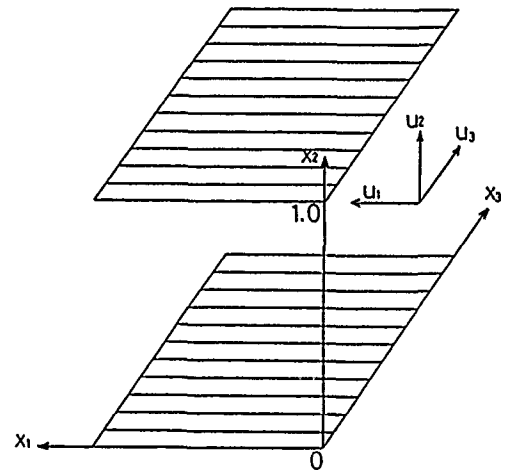


Fig.1 Coordinate system

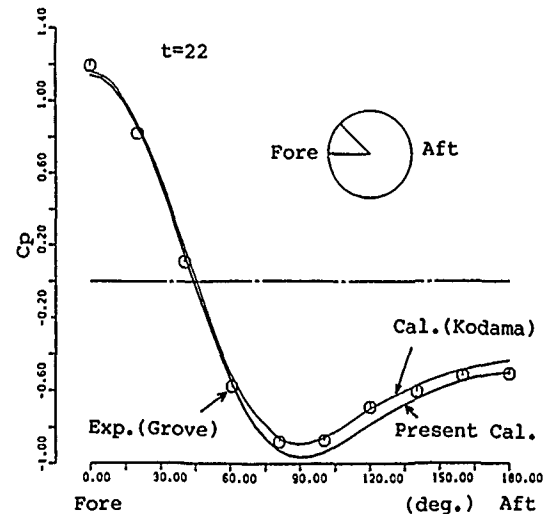


Fig.2 Pressure distribution on a circular cylinder at $Re=40$

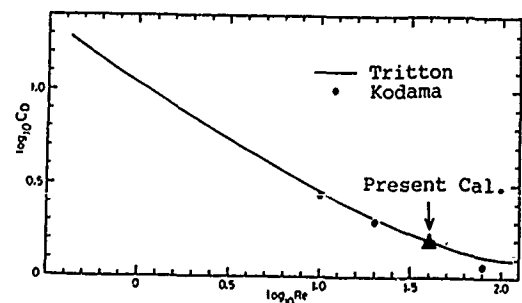


Fig.3 Drag coefficient

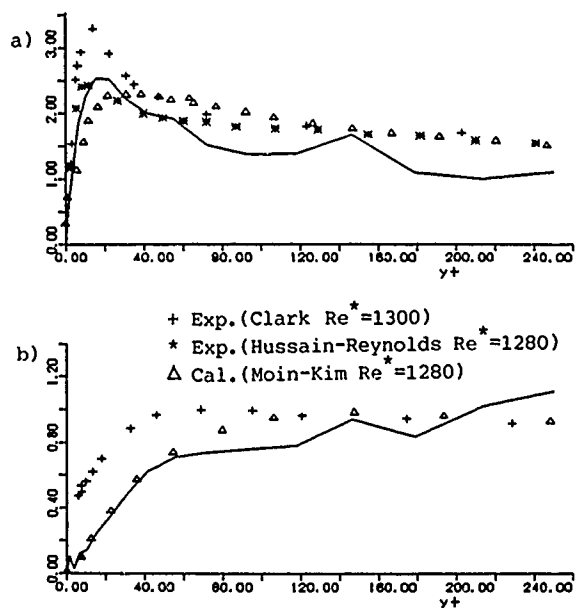


Fig.4-a Turbulence intensities $\alpha = 0.03$
 $t = 10.5$, $Re^* = 500$
 a: $\langle (u_1'')^2 \rangle^{1/2}$, b: $\langle (\bar{u}_2')^2 \rangle^{1/2}$
 c: $\langle (\bar{u}_3')^2 \rangle^{1/2}$

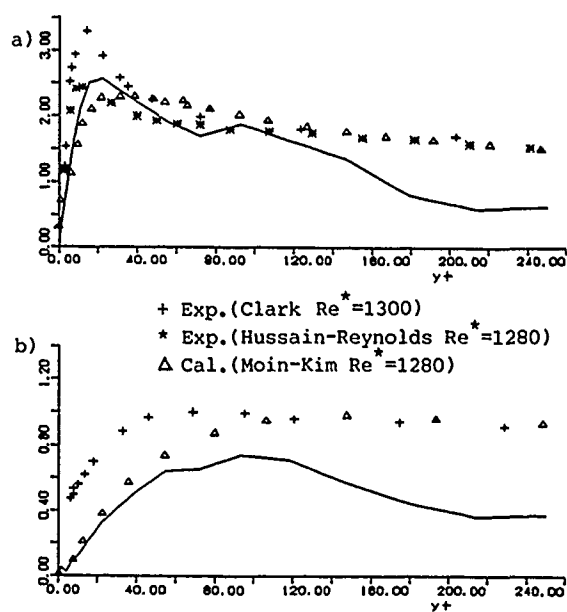


Fig.4-b Turbulence intensities $\alpha = 0.06$
 $t = 10$, $Re^* = 500$
 a: $\langle (u_1'')^2 \rangle^{1/2}$, b: $\langle (\bar{u}_2')^2 \rangle^{1/2}$
 c: $\langle (\bar{u}_3')^2 \rangle^{1/2}$

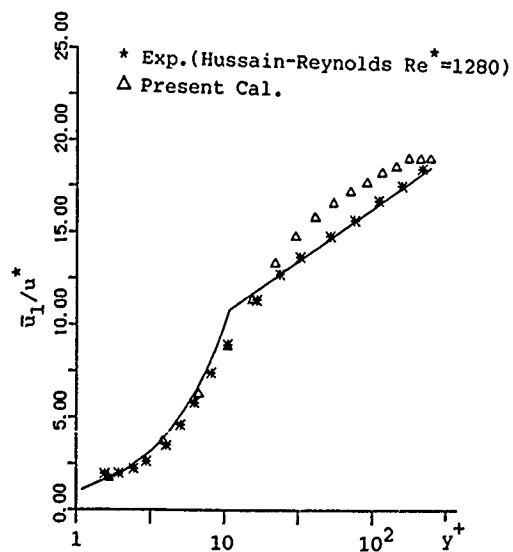


Fig.5-a Mean velocity profile $\alpha = 0.03$
 $t = 10.5$, $Re^* = 500$

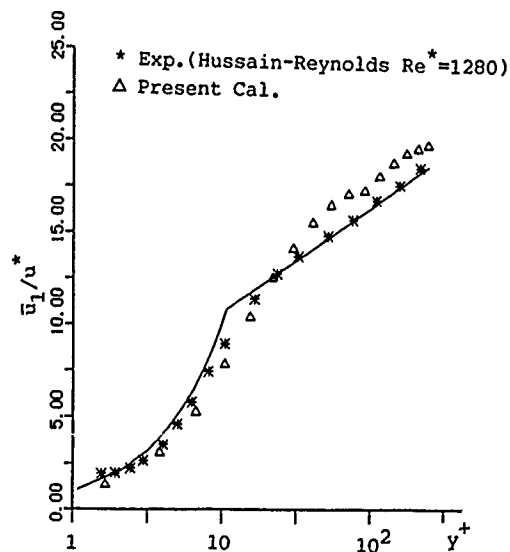


Fig.5-b Mean velocity profile $\alpha = 0.06$
 $t = 10$, $Re^* = 500$

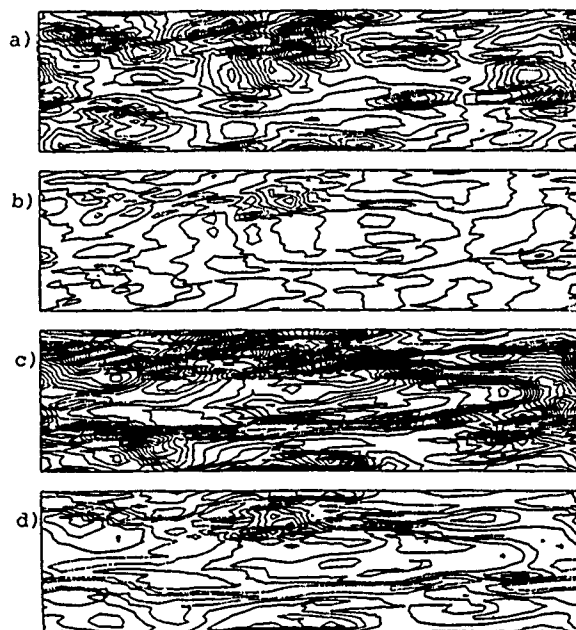


Fig.6-a Contour lines of each term in the streamwise momentum equation on x_1-x_3 plane,
 $\alpha = 0.03$, $y^+ = 22.2$, $t = 9.5$, $Re^* = 500$,
 a: convection terms interval 50,
 b: artificial dissipation terms interval 2
 c: SGS model terms interval 2, d: viscous terms interval 10

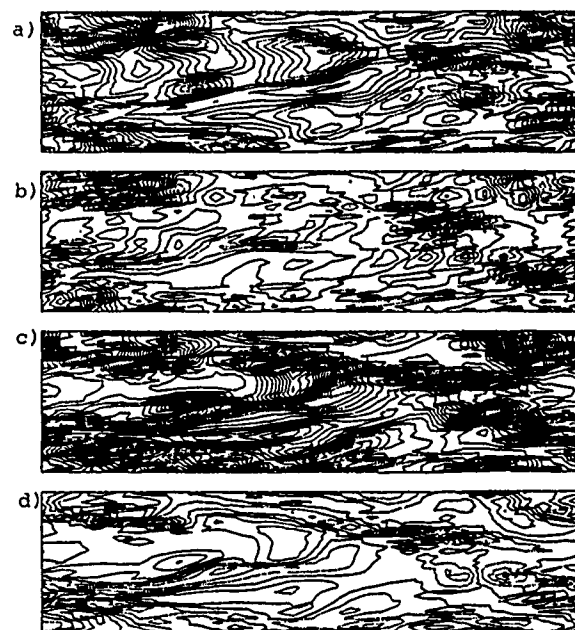


Fig.6-b Same as Fig.6-a
 $\alpha = 0.06$, $y^+ = 22.2$, $t = 10$, $Re^* = 500$,
 a: convection terms interval 50,
 b: artificial dissipation terms interval 2
 c: SGS model terms interval 2, d: viscous terms interval 10

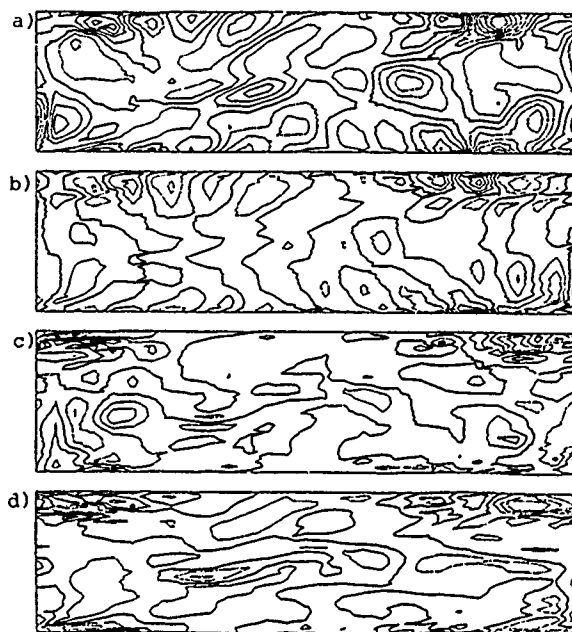


Fig.7-a Same as Fig.6-a
 $\alpha = 0.03$, $y^+ = 250$, $t = 9.5$, $Re^* = 500$,
 a: convection terms interval 50,
 b: artificial dissipation terms interval 2
 c: SGS model terms interval 2, d: viscous terms interval 10

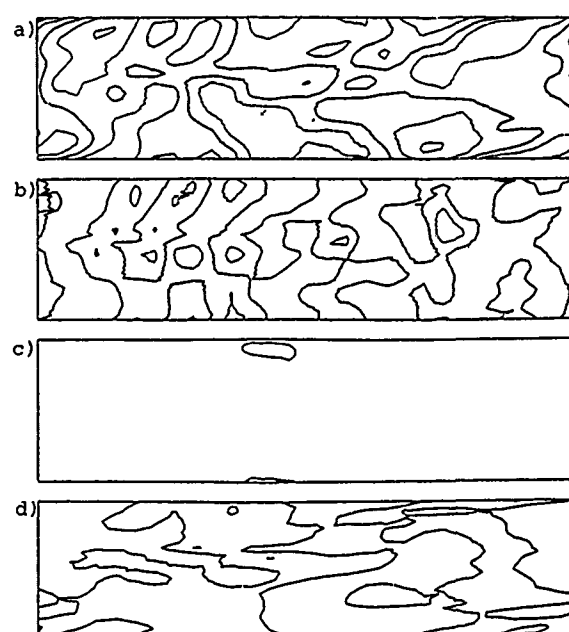


Fig.7-b Same as Fig.6-a
 $\alpha = 0.06$, $y^+ = 250$, $t = 10$, $Re^* = 500$,
 a: convection terms interval 50,
 b: artificial dissipation terms interval 1
 c: SGS model terms interval 1, d: viscous terms interval 1

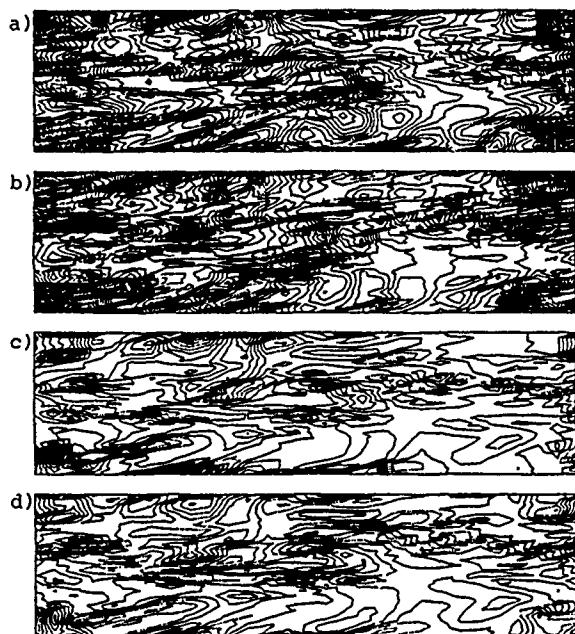


Fig.8-a Contour lines of each term in the stream wise momentum equation calculated by Euler method,
 $\alpha = 0.15$, $y^+ = 22.2$, $t = 9.5$, $Re^* = 500$,
 a: convection terms interval 50,
 b: artificial dissipation terms interval 5
 c: SGS model terms interval 5, d: viscous terms interval 10

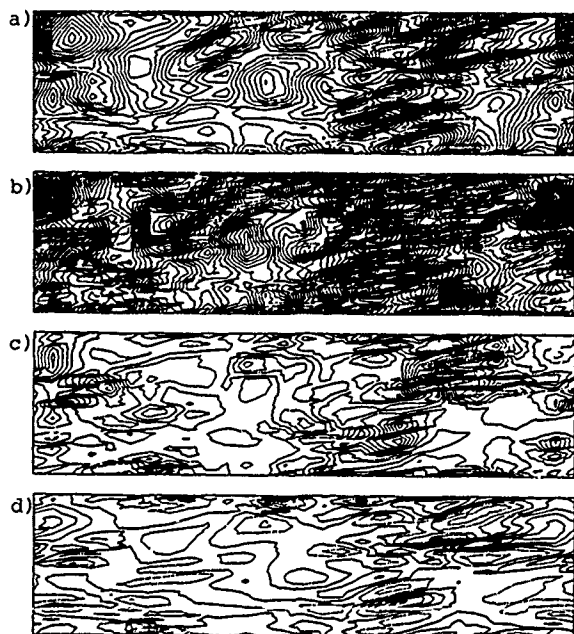


Fig.8-b Same as Fig.8-a
 $\alpha = 0.15$, $y^+ = 250$, $t = 9.5$, $Re^* = 500$,
 a: convection terms interval 50,
 b: artificial dissipation terms interval 2
 c: SGS model terms interval 2, d: viscous terms interval 10

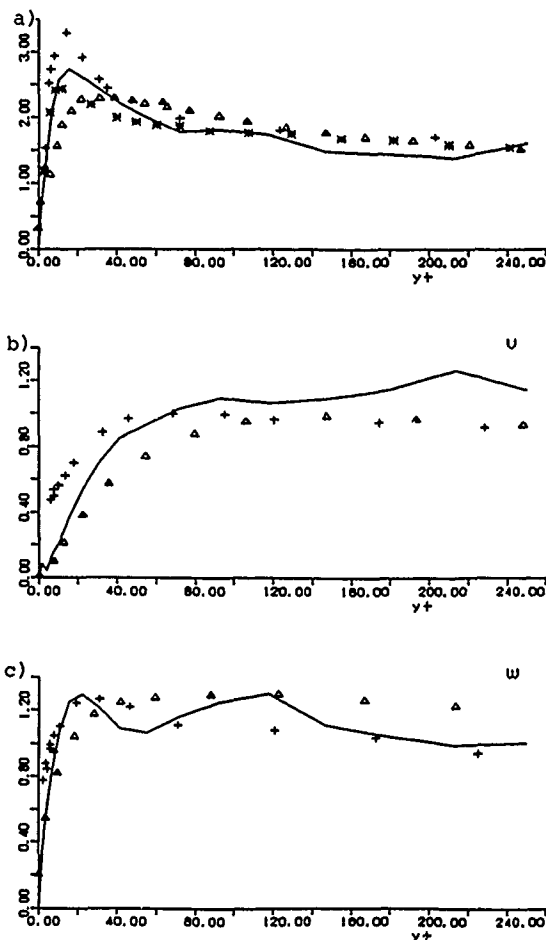


Fig.9 Turbulence intensities calculated by Euler method, $\alpha = 0.15$
 $t = 9.5$, $Re^* = 500$
 a: $\langle (u_1'')^2 \rangle^{1/2}$, b: $\langle (\bar{u}_2')^2 \rangle^{1/2}$
 c: $\langle (\bar{u}_3')^2 \rangle^{1/2}$

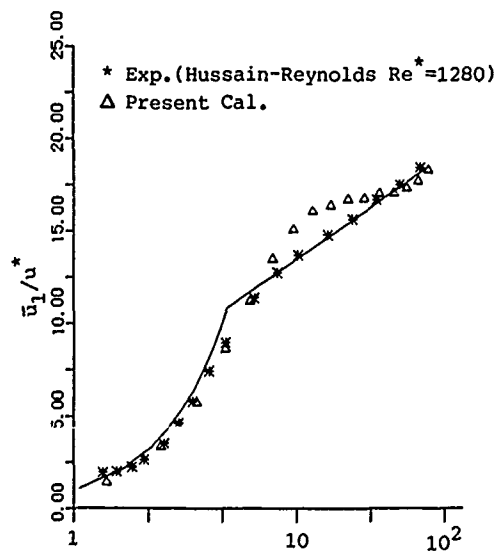


Fig.10 Mean velocity profile calculated by Euler method, $\alpha = 0.15$
 $t = 9.5$, $Re^* = 500$

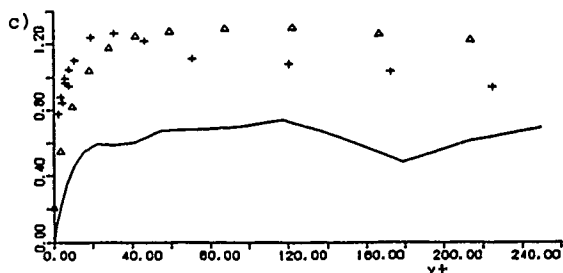
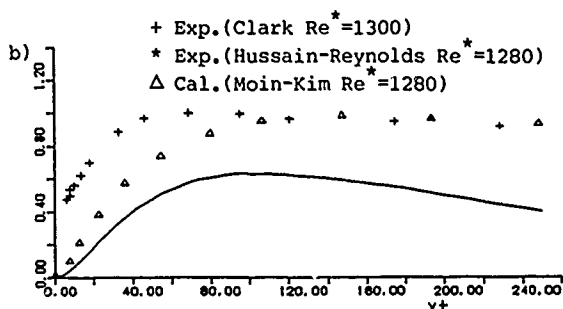
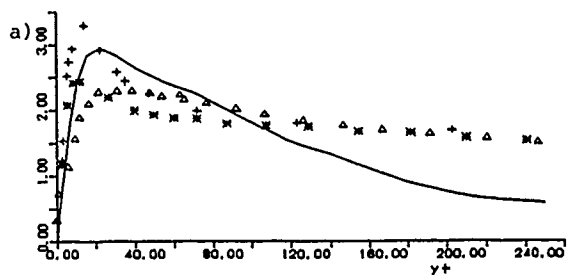


Fig.11 Turbulence intensities calculated by Euler method $\alpha = 0.6$
 $t = 9.5, Re^* = 500$
 $a: \langle (u_1'')^2 \rangle^{1/2}, b: \langle (\bar{u}_2)^2 \rangle^{1/2}$
 $c: \langle (\bar{u}_3)^2 \rangle^{1/2}$

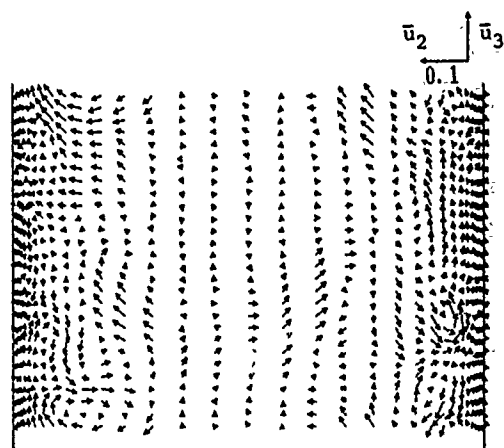


Fig.12-a Velocity vectors on x_2-x_3 plane calculated by Adams-Bashforth method
 $\alpha = 0.03, t = 9.5, x_1 = 1.5, Re^* = 500$

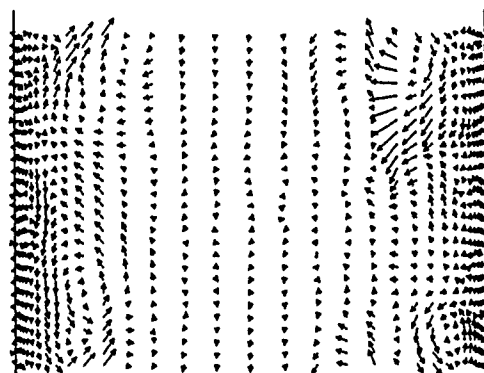


Fig.12-b Same as Fig.12-a
 $\alpha = 0.06, t = 10.0, x_1 = 1.5, Re^* = 500$

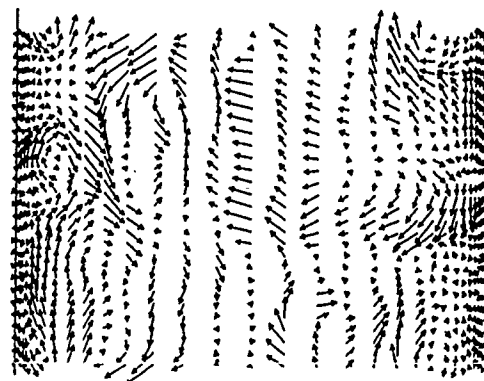


Fig.12-c Velocity vectors on x_2-x_3 plane calculated by Euler method
 $\alpha = 0.15, t = 9.5, x_1 = 1.5, Re^* = 500$

Computation of the Flow past Shiplike Hulls

J. Piquet and M. Visonneau
ENSM
Nantes, France

Abstract

The present work first details the implementation problems of a numerical procedure for the solution of the Reynolds-averaged Navier-Stokes equations in boundary-fitted coordinates. The procedure is validated using well documented experiments on the HSVA tanker and the comparisons demonstrate the ability of the method to predict ship stern flows.

1. Introduction

For a long time, wind tunnel or towing tank experiments have been the own practical way to get information on ship performances because of the restrictions of inviscid or boundary layer models. With the development of computers, it becomes possible to obtain numerical information with an answer turnover and a level of details which are hardly possible with experiments. The prediction of shiplike afterbody flows, which is considered hereafter, is necessary for the knowledge of viscous resistance and, more importantly, for propeller and control surface design as both are immersed in regions where viscous effects are significant. Classically, such problems were handled solving first a potential problem with panel methods. The inviscid flow field on the body was used as a boundary condition for thin boundary layer equations, the solution of which allowed the determination of viscous corrections. Unfortunately, it was demonstrated during the SSPA-ITTC workshop on ship boundary layers [1] that such a procedure failed in the stern region because of the rapid thickening of the boundary layer in this zone. The limited success of generalizations of thin boundary layer equations involving high order corrections, see e.g. [2][3][4], was subsequently demonstrated so that the tendency towards computing the full solution of the Navier-Stokes equations became stronger and stronger for increased computer resources became more and more available at continuously decreasing costs. However, significant obstacles to progress in the treatment of such three-dimensional flows remain, the most important being the difficulty in describing with enough resolution the geometry of the physical domain in which the body is immersed, even if, as here, no free surface effect is considered. Another important difficulty is the need of reliable data to validate computations insofar as the comparisons between the experiments and the computations involve systematic interpolation procedures.

Table 1 summarizes the main characteristics of the presently available methods which share several common

features as well as differences among which the following appear important. (i), used coordinates and grid generation techniques, adaptivity of the mesh ; (ii), type of master equations and retained approximations - all of which depart from thin boundary layer assumptions - ; (iii), turbulent models, how are they used and with what specific boundary conditions ; (iv), discretization schemes, pressure velocity coupling methods, iterative modes , solution methods used for the linear systems ; (v), acceleration means ; (vi), initial and boundary conditions.

All the methods (including this one) that have been published, but [5][6][7], rest on the use of Reynolds averaged Navier-Stokes equations (hereafter called RANSE) presented in §2 and written in a body-fitted curvilinear coordinate system. Except works [8][9][10][11], only the independent variables are transformed from the physical coordinates x (horizontal along the axis of the body), y (horizontal, orthogonal to the axis of the body), z (vertical) to the curvilinear coordinates $\lambda^i = (\lambda, \eta, \zeta)$ while the dependent variables are retained in the physical domain : the velocity components are the components in a cartesian frame with the noticeable exception of [12][13][14], where cylindrical velocity components are preferred. In order to allow more easily comparison with experiments, the coordinate planes $\lambda = \text{const.}$ are identified with $x = \text{const.}$ planes. In the following (§2.2), η will refer to the coordinate away from the wall such that the equation of the wall is $\eta = 1$; ζ will refer to the girthwise coordinate. The other alternative [8][9][10][11] uses contravariant coordinates. This simplifies the continuity equation but introduces Christoffel symbols in the momentum equations, the full treatment of which is cumbersome (usually a lot of terms are omitted) and either time or storage consuming.

Now, considering the master equations, ie. those which are discretized numerically, they usually involve a $k-\epsilon$ type of closure with a wall-function approach which avoids numerical troubles often associated to the sink-source terms in the ϵ equation while saving storage for the nodal unknowns. Some works depart from this trend by the use of either a classical mixing length model [8][9] or of a subgrid scale model [15]. Considering more sophisticated Reynolds stress models does not seem to improve significantly the results [16]. In the following, a $k-\epsilon$ model is retained but the wall function approach is avoided (§2.4) Only the ϵ equation is bypassed close to the wall. For a significant increase in numerical troubles and in

Authors	Main References	Turbulence	law reg	grid generation	Pressure solver	accrete	momentum eq.	sober	space Δ	time Δ	start	inlet	far field	grid	test cases	remarks
Abd El Maguid et al - 1971 - 1980 -	[22][23]	K-ε model	wall fn.	algebraic	SIMPLE : SLUR-TDMA	no	staggered grid cartesian vel.	TDMA-PP	hybrid	implicit	potential	U: 1/7 power equil. turbulence	uniform	35x12x12 25/15/9	SSPA 720 MSVA iter	first obtained on CDC 6500
Jansson & Larsson - 1985 -	[24]	K-ε model	wall fn.	algebraic	SIMPLE : SLUR-TDMA	Δt(t)	staggered grid cartesian vel.	TDMA-PP	hybrid	implicit	potential	U: 1/7 power equil. turbulence	uniform	1830 to 4410 cells	SSPA 720	coarse grid small domain, p field incorrect
Levan & Hoekstra - 1985 -	[9][10]	mbg length Cabeci-Smith	no	Schwarz- Christoffel	p from normal momentum partially staggered grid coupled variables unstagg SLUR type iteration for p	partial cancel.	contravariant velocities : v special v physical	Coupled SLUR pp	3pt. backwd. p _u 2pt formed.	implicit	potential	thin B.L. or exp. data no crossflow	potential	50x40x21	Wigley	very good results outer convergence rapid (11 avg). underrelax in case
Hoekstra & Raven	[8]	-	no	-	P _u : quick downstream V _u : quick upstream no (work with velocity)	grid seq P-MG TD n & c physical	z contrav. v _u & c physical	-	-	-	-	-	-	-	-	-
Mori & Ito 1985	[54]	K-ε model	no	elliptic	no (work with velocity)	no	vorticity	no	hybrid	explicit	potential	missing length Major crossflow	uniform	30x18x18 2hr. / 7500 PIVAC M200	SSPA 720	no slip at wall laminar profiles convergence plims
Murphy, 1980	[25][26]	K-ε model	wall fn.	algebraic	SIMPLE : SLUR-TDMA	no	staggered grid polar components	TDMA-PP	hybrid	implicit	uniform	U: 1/7 power equil. turbulence	uniform	31x12x12	Ship liner	outlet station too close, coarse grid
Murakami & Nakase	[16]	K-ε model	wall fn.	conformal mapping	SIMPLE : SLUR-TDMA	no	staggered grid	TDMA-PP	hybrid	implicit	rest	thin B.L. equil. turbulence	potential	450x20	SSPA 720	good results with SSPA iter.
Tzabaras & Loukakis 1985	[19][21]	Reyn. Str.	wall fn.	elliptic	SIMPLER : SLUR-TDMA	no	staggered grid polar components	fully ell.	hybrid	implicit	uniform	U: 1/7 V-W-U V.W updated	uniform	30x15x10 30x15x14	Wigley	good results with SSPA iter.
Chen & Patel 1984 1985	[12][13][46]	K-ε model	wall fn.	elliptic	-	-	-	TDMA-PP	finite analytic	implicit	uniform	-	-	74x30x21 110 x 110 x 110 30° Cray T3E	SSPA 720 SSPA 720 SSPA 720	MSVA iter. Series SSPA iter. Series Wigley iter. Series complete set of compacts.
Patel 1988	[14][41]	-	-	-	-	-	-	fully ell.	-	-	-	-	-	60x21x15	SSPA 720	velocity profiles MSVA iter
Broberg et al 1988	[11]	K-ε model	wall fn.	elliptic	PISO : SLUR-TDMA	no	staggered grid contravariant vel. compns.	TDMA-PP	finite analytic	implicit	uniform	U: 1/7 V-W-U V-W than upld	uniform	85x30x13 40 sweeps 85x30x21	SSPA 720	results without wall functions
Piquet et al 1987	[18][50]	K-ε model	no	elliptic	SIMPLER : ILL for P SLUR-TDMA for P'	SCG loc. At	staggered grid cartesian comp	ILL-SCG	finite analytic	implicit	uniform	U: W thin B.L. V-W than upld	uniform	115x30x30 170x30x20	Wigley DM Wigley FS	comparison double model & free surf. cases, preliminary
Piquet et al 1989	[15]	SGS model	no	elliptic with free surf	MAC type (Poisson eq.)	no	contravariant vel. compns. rotational fin	TDMA	conver	explicit	uniform	start upstream	uniform	54x15x18	Wigley	discussion of grid effects
Miyata et al 1987	[39]	K-ε model	wall fn.	algebraic	SIMPLE - checkerboard SLUR-TDMA	no	staggered grid cartesian comp	TDMA-PP	hybrid	implicit	potential	start upstream	uniform	54x15x18	Wigley	1700 time steps to converge. Pressure oscillations.
Mazuko & Shirone	[39]	K-ε model	no	elliptic	anti. compressibility approxim. factorization	no	collocated grid cartesian comp	coupled with P	5 point	weighted	near U	start upstream	uniform	54x15x18	Wigley	1700 time steps to converge. Pressure oscillations.

Table 1 - Main characteristics of the Available Methods

computing time, the delicate problem of the three-dimensional orientation of the log law specification, dealt with only in [14], is avoided, as well as significant overestimations of the velocity profiles, close to the wall, in the propeller disk region. [17][18].

From the closed RANSE, the master equations are almost invariably obtained -except [14][19]- using the so-called partially parabolic approximation in which longitudinal λ -transport due to viscosity and turbulence is neglected (ie, if ϕ is the advected quantity, only the $\phi\lambda\lambda$ terms are dropped). This approximation is usually developed for viscous flow fields in which pressure is the dominant transmitter of influence in the upstream direction. In certain conditions, it does not forbid the presence of -seldomly present- longitudinal flow reversal (along λ) which may occur close to transom sterns or when a propeller is in operation. In this work, the master equations do not involve such an approximation for reasons which will be made clear; therefore the fully elliptic equations are used.

Turning now to the numerical aspects which are studied in §3, a general prerequisite is a method for generating the body-fitted grids. The most common choice, including ours already detailed in §2.3, rests on elliptic solvers [20] because they are easy to use and because they allow a priori controls of the quality of the grid close to the body. A possible alternative has been proposed in [8][9][10][19][21] where twodimensional grids, generated via conformal transformation designed, for instance, from the Schwarzian derivative theorem, are stacked in the λ direction. Such grids build-in transverse orthogonality to the price of distortion problems in the λ direction, close to the aft sections. Other algebraic techniques have also been used [22][23][24][25][26] but they appear often abandoned.

The most important aspect of the numerics lies in the way the incompressibility constraint is enforced. This may be done in three ways. A *first category* of methods includes those where the pressure-velocity coupling is simulated with a suitable modification of the continuity equation. Compressible flow methods used for low Mach numbers belong to this category, although severe difficulties are usually found in the limit of vanishing Mach numbers. The artificial compressibility method [27], systematically used in some institutes (see e.g. [28]), and applied to ship flows in [29][30], gives also rise to convergence problems and needs a careful selection of numerical parameters such as the pseudocompressibility factor. The *second category* includes methods in which the continuity equation is satisfied identically at each iteration. Apart from unsegregated methods [31], such methods follow the boundary layer practice in which the flow domain is swept from upstream to downstream, implicit differencing of momentum being used for marching stability. Upstream influence through the pressure field has to be accounted for, and this is done introducing some form of forward differencing for the streamwise pressure gradient which allows departure-free behavior [32]. For ship applications, such methods have been mainly developed in the framework of the partially parabolic approximation in [8][9][10]. In this work, we have followed (§3.2) the most common so-called *pressure correction methods* in which the pressure velocity coupling is solved iteratively, updating successively the velocity variables in the momentum equations and the pressure in a

pressure equation, in such a way that solenoidality is satisfied at convergence. In the ship applications, both the advection and the diffusion of momentum are implicit in time; the updating procedure being handled on each equation by the well known "SIMPLE" [33], "SIMPLER" [34], or "PISO" [35] methods. One of the dominant aspects of such techniques lies in the way the pressure equation is handled as the pressure solver controls the global convergence of the method (and therefore, its robustness on fine grids), and as it generates the greatest part of the computational cost. The present work strongly differs from similar computations [12][13][14] by the characteristics of the pressure and pressure correction solvers which become critical as soon as grid clustering is strongly increased by the removal of the the wall function approach.

Such modifications are necessary for the following reason. Because only the independent variables are transformed, the directions of the velocity components differ from the direction of the curvilinear coordinates. As a first consequence, the projection phase of the pressure-velocity coupling does not connect always the driving component of the pressure gradient to the corrected velocity component. Because of the strong grid clustering, the stiffness of the "three-dimensional" pressure matrix is so much increased that standard relaxation techniques usually retained do not converge anymore. This argument will be clarified in (§3.3) As a second consequence, the possibility of pressure odd-even oscillations is recovered even if the grid is staggered (the most common choice, see Table 1). They are classically avoided, as when, as here, collocated grids are used, with weighted averages of coefficients defined during the projection phase. For the methods belonging to the third category, the discretization of the advective terms rests often on strongly diffusive classical hybrid schemes. In this work, we use (§2.1) the so-called finite-analytic method of [37] applied, for instance, in [13][14][15][18].

This quick review of methods would stay incomplete without consideration of initial and boundary conditions. They will be specified in §4, when the results are studied. While the iterative procedure is usually initialized from rest, from uniform flow, or from potential theory, the considered domain boundaries usually extend from a midship station to several lengths behind the body. [5][6][7][15][38][39] depart from this choice on model ships and start from a uniform flow field far upstream. In this work, we follow the common practice which considers that the inlet flow at midship stations can be characterized by some simple integral parameters and that the crossflow at midship can be neglected. These integral parameters are obtained either from experiments or from thin boundary layer assumptions used upstream. This allows to save computer resources and to avoid transition problems in the fore part of ship models. The flow domain extends usually to some ship lengths downstream and to one ship length away from the axis of the ship. Symmetry conditions are retained on the vertical plane -the so-called keel plane- (only one side of the ship is handled) as well as on the horizontal plane -the water plane-. Only the so-called double-model problem is therefore treated, except in [5][6][7][15][38] where free surface effects are considered. Related to the flow domain choice, is the wake topology which involves, the most often, a singularity line either of the polar type or of the parabolic type. In the former case, transverse grids are topologically equivalent to concentric circles ($\eta = \text{const.}$) and their radii ($\zeta =$

const.). In the latter case, the singular line starts from the bottom of the ship, in its vertical plane of symmetry into the wake, defining a line of separation between the upper part of this vertical plane of symmetry (the "fictive rudder") which is a (symmetry) surface $\eta=1$ that extends the wall surface ($\eta=1$) in the wake, and its bottom part which is a (symmetry) surface $\zeta=2$.

Among the available experimental information which has been extensively reviewed in [40][41], we shall mainly focus (§4) on the HSVA tanker [44][45]. For this case, very detailed mean flow measurements are provided in several $x = \text{const.}$ planes ; this minimizes interpolation processing. Moreover, the data are free from blockage effects because a wind tunnel with slotted walls was used. Uncertainties on the inlet conditions appear therefore to be an admissible penalty. The paper is outlined as follows. §2 presents the equations and the main features of the used method ; §3 focusses on the numerical aspects ; §4 discusses the results and presents significant comparisons with the HSVA experiments.

2. The Master Equations

2.1. The Primitive Form.

The full RANSE (2.1) for the mean velocity field U and for the mean pressure deviation P

$\nabla \cdot U = 0$, $\partial U / \partial t + (U \cdot \nabla)U + \nabla P = \text{Re}^{-1} \nabla^2 U - \nabla \cdot \bar{u}\bar{u}$ (2.1)
need a closure assumption for the Reynolds stresses $\bar{u}\bar{u}$ which is taken under the isotropic form (2.2)

$$\bar{u}\bar{u} = 2k/3 - v_T [\nabla U + \nabla^T U] \quad (2.2)$$

where $v_T = C_\mu k^2 / \epsilon$ is the turbulent viscosity, k is the turbulent kinetic energy and ϵ the so-called dissipation of turbulent kinetic energy. k and ϵ are governed by the standard following transport equation (2.3) and (2.4)

$$\partial k / \partial t + U \cdot \nabla k = G - \epsilon + \nabla \cdot [R_k^{-1} \nabla k] \quad (2.3)$$

$$\partial \epsilon / \partial t + U \cdot \nabla \epsilon = C_{\epsilon 1} G / k - C_{\epsilon 2} \epsilon / k + \nabla \cdot [R_\epsilon^{-1} \nabla \epsilon] \quad (2.4)$$

G is the rate of production of turbulent kinetic energy - $\bar{u}\bar{u} : \nabla U$, R_{eff} is the effective Reynolds number defined by $R_{\text{eff}}^{-1} = \text{Re}^{-1} + v_T$ while $R_k^{-1} = \text{Re}^{-1} + v_T / \sigma_k$ and $R_\epsilon^{-1} = \text{Re}^{-1} + v_T / \sigma_\epsilon$. Unless specified, model "constants" are given by their standard values :

$$C_\mu = 0.09, C_{\epsilon 1} = 1.44, C_{\epsilon 2} = 1.92, \sigma_k = 1, \sigma_\epsilon = 1.3 \quad (2.5)$$

2.2 Physical space and computational space

2.2.1 The problem. The physical domain Ω , where the flow is studied, is bounded by the ship hull B of surface ∂B , by the outer boundary Σ , by the inlet station U , by the outlet station D and by the vertical V and horizontal H planes of symmetry. Equations (2.1 to 4) which classically involve the cartesian velocity components $\{U^\alpha\} \equiv \{U, V, W\}$ are partially transformed from the cartesian rectilinear coordinates $\{x^\alpha\} \equiv \{x, y, z\}$ in the physical space, to the curvilinear coordinates $\lambda^i \equiv \{\lambda, \eta, \zeta\}$ in the so-called computational space. The coordinate transformation is designed in order that the boundaries ∂B and Σ become $\eta = \text{const.}$ surfaces, that the boundaries U and V become $\lambda = \text{const.}$ surfaces and that the planes of symmetry become $\zeta = \text{const.}$ surfaces. The domain Ω

becomes a parallelepiped in the computational space in which the discretization consists in stacked unit cubes of sides $\Delta \lambda = \Delta \eta = \Delta \zeta = 1$. Each unit cube of the computational space is a curvilinear hexahedron in the physical space, the "sides" of which are measured by the moduli of the covariant vectors $a_i = \partial r / \partial \lambda^i$.

2.2.2. Useful Relationships. The transformation necessarily involves byproducts from the basis a_j . Of particular interest are [20] :

(i) The area vectors $b^i = a_j \times a_k$ (i, j, k in cyclic order) which measure the oriented area of a small surface of unit sides along λ^j and λ^k on a $\lambda^i = \text{const.}$ surface in the computational space. b^i appears as built with two small triangle-like surfaces in the physical space.

(ii) The Jacobian J of the transformation from the computational space of the coordinates $\{\lambda^i\}$ to the physical space of the coordinates $\{x^\alpha\}$. J measures the "physical" volume of a parallelepiped of unit sides in the computational space ; this parallelepiped appears as an hexaedron-like volume in the physical space.

(iii) The covariant and contravariant metric tensors $g_{ij} = a_i \cdot a_j$; $g^{ij} = b^i \cdot b^j / \det g_{ij}$ where the determinant of g_{ij} is the square J^2 of the foredefined jacobian.

An important relationship to be used is the following simple restatement (2.6) of the chain-rule derivative formula :

$$\partial \lambda^k / \partial x^\alpha = J^{-1} b_\alpha^k \quad (2.6)$$

which allows the computation of the standard following operators :

$$\nabla \cdot U = J^{-1} \partial (J U^i) / \partial \lambda^i = J^{-1} \partial [b_\alpha^i U^\alpha] / \partial \lambda^i \quad (2.7)$$

where U^α and $[\nabla \phi]_\alpha$ are the physical components in the cartesian orthonormalized physical space.

$$[\nabla \phi]_\alpha = J^{-1} b_\alpha^k \partial \phi / \partial \lambda^k \quad (2.8)$$

$$\nabla^2 \phi = \text{div} \left[g^{ik} \frac{\partial \phi}{\partial \lambda^k} \right] = \frac{1}{J} \frac{\partial}{\partial \lambda^i} \left[J g^{ik} \frac{\partial \phi}{\partial \lambda^k} \right] \quad (2.9)$$

2.2.3. The Grid generation method. Because the values of the curvilinear coordinates λ^i are specified on $\partial \Omega$, the values of λ^i inside Ω result from a boundary value problem in which the dependent variables are the $\{\lambda^i\}$ and the independent (unknown) variables are the $\{x^\alpha\}$, the correspondance between $\{x^\alpha\}$ and $\{\lambda^i\}$ being one-to-one. If (2.9) is written for $\nabla^2 x = \nabla^2 y = \nabla^2 z = 0$, the resulting partial differential equations (2.10) may be used to generate the coordinates :

$$\nabla^2 \phi = g^{ik} \frac{\partial^2 \phi}{\partial \lambda^i \partial \lambda^k} + \frac{1}{J} \frac{\partial [J g^{ik}]}{\partial \lambda^i} \frac{\partial \phi}{\partial \lambda^k} \text{ with } \phi = x^\alpha \equiv (x, y, z) \quad (2.10)$$

Because the coefficient of the first order derivative, in (2.10), is the laplacian of the curvilinear coordinate :

$$f^k = \nabla^2 \lambda^k = \frac{1}{J} \frac{\partial [J g^{ik}]}{\partial \lambda^i} [J g^{ik}] \quad (2.11)$$

The common practice is to specify it as a grid clustering control $f^k = \nabla^2 \lambda^k$. In this case, (2.10) becomes (2.12)

$$\nabla^2 \phi = g^{ik} \frac{\partial^2 \phi}{\partial \lambda^i \partial \lambda^k} + f^j \frac{\partial \phi}{\partial \lambda^j} \quad (2.12)$$

Now, if $\nabla^2 \alpha$ is computed with (2.11) rather than with (2.10), f^k must be equal to the rhs. of (2.12). Therefore, when (2.12) is used to compute the diffusion terms (for $\phi = U, V, W, k, \epsilon$), the iterative method for solving the mesh must be solved to convergence. In all that follows, only the special case $\lambda = \lambda(x)$ is considered so that $f^1 = -g^{11} x_{\lambda} \lambda / x_{\lambda} = -2ag^{11}$ [12][46] results from the assumed longitudinal grid distribution $x(\lambda)$. Thus, only the equations for y and z need to be solved, once control functions f^2 and f^3 have been specified.

f^2 and f^3 are connected to g^{ij} in such a way that $2b = -f^2/g^{22} \equiv S_{\eta\eta}/S_{\eta}$ and $2c = -f^3/g^{33} \equiv \phi \zeta \zeta / \phi \zeta$ (as well as $2a$) are frozen during the iterative use of (2.12) for $\phi = y, z$. They are prescribed according to (2.13) where S is the curvilinear abscissa along the $\zeta = \text{cte}$ lines and ϕ is the polare angle in the $x = \text{const.}$ correction.

$$f^2 = F_A(\eta, \zeta) \text{ for } \lambda \leq \lambda_A; F_A = -g^{22} \frac{S_{\eta\eta}}{S_{\eta}} | \lambda = \lambda_A \quad (2.13a)$$

$$f^2 = F_B(\eta, \zeta) \text{ for } \lambda \geq \lambda_B; F_B = -g^{22} \frac{S_{\eta\eta}}{S_{\eta}} | \lambda = \lambda_B \quad (2.13b)$$

$$f^2 = F_C(\lambda, \eta, \zeta) \text{ for } \lambda_A \leq \lambda \leq \lambda_B; \quad (2.13c)$$

$$F_C = \frac{(\lambda - \lambda_B)F_A - (\lambda - \lambda_A)F_B}{\lambda_A - \lambda_B}$$

a, b, c are fixed from an initial guess taylored to the problem (see §3). The numerical solution of the grid equations uses exponential schemes similar to (3.6) - see infra - in both directions; it considers crossed second-order derivatives as source terms which are discretized, as well as metric components, with centered schemes. The solution of the resulting linear systems endly results from SLOR alternate η and ζ sweeps. The grid generation procedure thus defined has two aims: it first allows a correct clustering of grid points close to the wall, and, as important, it smoothes the grid. So, zero machine convergence of the procedure is not necessary. The f^2 and f^3 functions that result from (2.13) after SLOR sweeps are not used in the Navier-Stokes solver. Rather, the discrete equations corresponding to the Poisson operators are considered as a 2×2 linear system whose solution gives the needed f^2 and f^3 .

2.3 The Flow Equations

Apart from the continuity equation - see (2.7) -, the transport equations for the mean momentum, for k and ϵ can be written under the following *Master Equation* (2.14) for Φ :

$$g^{11} \Phi_{\lambda\lambda} + g^{22} \Phi_{\eta\eta} + g^{33} \Phi_{\zeta\zeta} = 2A_{\phi} \Phi_{\zeta} + 2B_{\phi} \Phi_{\eta} + 2C_{\phi} \Phi_{\lambda} + R_{\phi} \Phi_t + S_{\phi} \quad (2.14)$$

where

$$2A_{\phi} = \frac{R_{\text{eff}}}{J} [b_j^3 \alpha_{\phi}^j] - f^3$$

$$2B_{\phi} = \frac{R_{\text{eff}}}{J} [b_j^2 \alpha_{\phi}^j] - f^2$$

$$2C_{\phi} = \frac{R_{\text{eff}}}{J} [b_j^1 \alpha_{\phi}^j] - f^1 \quad (2.15)$$

$$R_{\phi} = a_{\phi} R_{\text{eff}}; S_{\phi} = s_{\phi} - 2 [g^{12} \Phi_{\lambda\eta} + g^{13} \Phi_{\lambda\zeta} + g^{23} \Phi_{\eta\zeta}]$$

and

$$\alpha_{\phi}^1 = a_{\phi} U J^{-1} [b_1^1 v_{T,\lambda} + b_1^2 v_{T,\eta} + b_1^3 v_{T,\zeta}] \quad (2.16a)$$

$$\alpha_{\phi}^2 = a_{\phi} V J^{-1} [b_2^1 v_{T,\lambda} + b_2^2 v_{T,\eta} + b_2^3 v_{T,\zeta}] \quad (2.16b)$$

$$\alpha_{\phi}^3 = a_{\phi} W J^{-1} [b_3^1 v_{T,\lambda} + b_3^2 v_{T,\eta} + b_3^3 v_{T,\zeta}] \quad (2.16c)$$

The index ϕ refers to any of the advected quantities, namely U, V, W, k, ϵ ; the indices λ, η, ζ refer to the partial derivatives; coefficient a_{ϕ} is equal to 1 except $a_k = \sigma_k, a_{\epsilon} = \sigma_{\epsilon}$. Source terms s_{ϕ} for U, V, W, k, ϵ are obtained from (2.17) written with cartesian derivatives indexed x, y, z .

$$S_U = R_{\text{eff}} [p_x - \text{grad} v_T \cdot \frac{\partial U}{\partial x}] \quad (2.17a)$$

$$S_V = R_{\text{eff}} [p_y - \text{grad} v_T \cdot \frac{\partial U}{\partial y}] \quad (2.17b)$$

$$S_W = R_{\text{eff}} [p_z - \text{grad} v_T \cdot \frac{\partial U}{\partial z}] \quad (2.17c)$$

$$S_k = -\sigma_k R_{\text{eff}} (G - \epsilon) \quad (2.17d)$$

$$S_{\epsilon} = -\sigma_{\epsilon} R_{\text{eff}} \left(C_{\epsilon 1} \frac{\epsilon}{k} G - C_{\epsilon 2} \frac{\epsilon^2}{k} \right) \quad (2.17e)$$

2.4 The Turbulent Model

Two reasons for the eviction of the wall function approach have been already mentionned in the introduction, namely the problem of specifying the directional dependence of U_{τ} and the practical overestimation of velocity profiles. A third reason is the noticed strong dependence of the pressure level on the location of the grid points close to the surface. As, at least the ϵ equation is avoided close to the wall, it is necessary to specify the closure assumptions to supply. For the HSVA case (§3), a one equation is used in the inner zone in order to make the closure problem free from the estimation of U_{τ} (whose sign may vary in the domain). The closure assumptions (2.18, 2.19) follow the choices of [47]

$$\epsilon = k^3/2l_{\epsilon}; v_T = C_{\mu} \sqrt{k} l_{\mu} \quad (2.18a,b)$$

where the scales of the two equations differ [48]:

$$l_{\mu} = C_1 n [1 - \exp(-\text{Re} \sqrt{k} n / A_{\mu})];$$

$$l_{\epsilon} = C_1 n [1 - \exp(-\text{Re} \sqrt{k} n / A_{\epsilon})] \quad (2.19)$$

The constant C_1 results from log law assumptions, n is the normal distance to the wall, which give $C_1 = \kappa C_{\mu}^{-3/4}$; the

asymptotic behavior of v_T when $n \rightarrow 0$ fixes $A_E = 2C_1$; $\delta = 70$ allows to recover the 5.45 constant of the flat log law. The (straightforward) patching of the k model with the outer $k-\epsilon$ model is located $Re\sqrt{k} n \equiv 200-250$.

3. The Numerics

3.1 The Transport Equations

The numerical method for the treatment of (2.14) closely follows [12][14]. Coefficients of Φ derivatives are evaluated at the center P of the control volume and coordinates are normalized in the following way.

$$\lambda^* = \lambda / \sqrt{g}^{11}; \eta^* = \eta / \sqrt{g}^{22}; \zeta^* = \zeta / \sqrt{g}^{33} \quad (3.1)$$

so that the normalized form (3.2) is obtained:

$$\Phi \lambda^* \lambda^* + \Phi \eta^* \eta^* + \Phi \zeta^* \zeta^* = 2A \Phi \zeta^* + 2B \Phi \eta^* + 2C \Phi \lambda^* + R \Phi_t + (S_\phi)_P \quad (3.2)$$

with:

$$A = (A_\phi)_P / \sqrt{g}^{33}; B = (B_\phi)_P / \sqrt{g}^{22}; C = (C_\phi)_P / \sqrt{g}^{11} \\ R = (R_\phi)_P \quad (3.3)$$

for a parallelepipedic volume (in the computational space) whose sides are given by (3.3):

$$\Delta \lambda^* = 1 = 1 / \sqrt{g}^{11}; \Delta \eta^* = k = 1 / \sqrt{g}^{22}; \Delta \zeta^* = h = 1 / \sqrt{g}^{33}$$

Now, the equation (3.1) is splitted as follows [14]:

$$2C \Phi \lambda^* - \Phi \lambda^* \lambda^* + R \Phi_t + S_\phi = G(\lambda^*, \eta^*, \zeta^*, t) \quad (3.4)$$

$$\Phi \eta^* \eta^* + \Phi \zeta^* \zeta^* - 2A \Phi \zeta^* - 2B \Phi \eta^* = G \quad (3.5)$$

Assuming that G and S_ϕ are constant on each element, a backward time derivative reduces (3.4) and (3.5) to a one dimensional and a two dimensional advection-diffusion equation, respectively. The solution of (2.4) is written as:

$$\Phi = a [\exp(2c\lambda^*) - 1] + b\lambda^* + c \quad (3.6)$$

Substituting (3.6) into (3.4), one is left with:

$$g = [2C\Phi \lambda^* - \Phi \lambda^* \lambda^* + R \Phi_t + S_\phi]_P \\ = (C_U + C_D)\Phi_P - C_U\Phi_U - C_D\Phi_D + \tau^{-1}R(\Phi_P - \Phi_P^{n-1}) + (S_\phi)_P \quad (3.7)$$

with

$$C_U = \frac{C \exp(C)}{1 \sinh C}; C_D = \frac{C \exp(-C)}{1 \sinh C}$$

τ is the time step, the index $n-1$ refers to the known state, indices U and D refer to upstream and downstream nodal values respectively. The resolution of (3.5) is classical and the result can be written under the form (3.8)

$$\Phi_P = \sum_{nb} C_{nb} \Phi_{nb} - C_P g \quad (3.8)$$

The index nb refers to neighbouring nodes NE, NW, SE, SW, NC, SC, EC, WC (fig.1). If the relationship (3.8) characterizes compact schemes (the molecule of which involves at most three points per direction), the values of influence coefficients C_{nb} , C_U , C_P depend on the type of discretization in the plane η, ζ . Following [12][37][40], we use the finite analytic discretization. The resulting values of C_{nb} are omitted here. Combining (3.7) and (3.8) gives (3.9).

$$\left[1 + C_P (C_U + C_D) + C_P \frac{R}{\tau} \Phi_P \right] = \sum_{nb} C_{nb} \Phi_{nb} + C_P \left[C_U \Phi_U + C_D \Phi_D + \frac{R}{\tau} \Phi_P^{n-1} - (S_\phi)_P \right] \quad (3.9)$$

3.2. The Pressure Velocity Coupling.

3.2.1. The algebraic problem. The discrete solution of RANSE is written

$$(E-A) \mathbf{V} + G \mathbf{P} = \mathbf{f}; D \mathbf{V} = \mathbf{g} \quad (3.10)$$

where \mathbf{V} and \mathbf{P} are the vectors of nodal unknowns for the velocity and the pressure. Boundary conditions and known iterates from time t^{n-1} are gathered in \mathbf{f} and \mathbf{g} . D and G refer to the discrete form of the divergence and of the gradient operator which may involve interpolation procedures so that, in general, $D \neq G^T$. E-A gathers the implicit part of the advection and diffusion terms in (3.9), E being the diagonal matrix of the coefficients C at node P. The concrete form of E and A is not important for the argument; let us only mention that, with the finite analytic method, diagonal dominance implies that the spectral radius of $E^{-1}A$ is less than one so that an iterative method which gives \mathbf{V} from \mathbf{P} through (3.11)

$$\mathbf{V} = (E-A)^{-1} (\mathbf{f} - G\mathbf{P}) \quad (3.11)$$

converges quickly. If (3.11) is substituted into (3.10), the pressure is obtained with (3.12)

$$[D(E-A)^{-1}G] \mathbf{P} = D(E-A)^{-1}\mathbf{f} - \mathbf{g} \quad (3.12)$$

Pressure correction techniques rest on the use of the approximate inverse E^{-1} for $(E-A)^{-1}$.

3.2.2. The "PISO" Procedure [35]. It consists in the following steps, starting from a guessed solution $(\mathbf{V}^{n-1}, \mathbf{P}^{n-1})$ from which $(\mathbf{V}^n, \mathbf{P}^n)$ is computed in the following way.

(i) *prediction step.* The velocity predictor \mathbf{V}^* is first computed solving -step 4 - (3.13):

$$(E-A)\mathbf{V}^* = \mathbf{f} - G\mathbf{P}^{n-1} \quad (3.13)$$

\mathbf{V}^* does not satisfy the continuity equation ($D\mathbf{V}^* \neq \mathbf{g}$) and must be corrected. Two correction steps are used to generate $(\mathbf{V}^n, \mathbf{P}^n)$.

(ii) *first correction step.* The first corrected field $(\mathbf{V}^{**}, \mathbf{P}^*)$ to be computed is such that:

$$E\mathbf{V}^{**} - A\mathbf{V}^* + G\mathbf{P}^* = \mathbf{f}; D\mathbf{V}^{**} = \mathbf{g}; \text{step 1} \quad (3.14a,b)^1$$

The momentum equation (3.14) specifies \mathbf{V}^{**} from \mathbf{V} defined by (2.15a)

$$\hat{\mathbf{V}} = E^{-1} (A\mathbf{V}^* + \mathbf{f}) \quad (3.15a)^1$$

according to the following projection form - step 2 -:

$$\mathbf{V}^{**} = \hat{\mathbf{V}} - E^{-1}G\mathbf{P}^* \quad (3.15b)^1$$

while the pressure equation for \mathbf{P}^* is obtained from a substitution of (3.15b) into (3.14) - step 3 -:

$$DE^{-1}G\mathbf{P}^* = D\hat{\mathbf{V}} - \mathbf{g} \quad (3.16)^1$$

(iii) *second (mandatory) correction step.* The second corrected field $(\mathbf{V}^{***}, \mathbf{P}^{**}) \equiv (\mathbf{V}^n, \mathbf{P}^n)$ satisfies

$$E\mathbf{V}^{***} - A\mathbf{V}^{**} + G\mathbf{P}^{**} = \mathbf{f}; D\mathbf{V}^{***} = \mathbf{g} \quad (3.14a,b)^2$$

Therefore, equations (3.15a,b)² and (3.16)² result from (3.15a,b)¹ and (3.16)¹ if the following substitution is performed: $\mathbf{V}^* \rightarrow \mathbf{V}^{**}$, $\mathbf{V}^{**} \rightarrow \mathbf{V}^{***}$, $\mathbf{P}^* \rightarrow \mathbf{P}^{**}$. In our implementation, where only the steady state is looked for, the second correction step is not performed so that $\mathbf{V}^n = \mathbf{V}^*$, $\mathbf{P}^n = \mathbf{P}^*$.

3.3 Implementation problems.

-Step 1- In the cell-centered colocated grid approach, where velocity components pressure and turbulent quantities are defined at the center of the control volume, the momentum equations (3.9) can be written under the form (3.17).

$$U_d = \frac{1}{1 + C_C(C_U + C_D)} \left\{ \sum_{nb} C_{nb} U_{nb} + C_C \left[C_U U_u + C_D U_d + \frac{R}{\tau} (U_d^{n-1} - U_d) - S_U \right] \right\}$$

$$V_n = \frac{1}{1+C_C(C_U+C_D)} \left\{ \sum_1^8 C_{nb} V_{nb} + C_C \left[C_U V_u + C_D V_d + \frac{R}{\tau} (V_n^{n-1} - V_n) - S_V \right] \right\}$$

$$W_e = \frac{1}{1+C_C(C_U+C_D)} \left\{ \sum_1^8 C_{nb} W_{nb} + C_C \left[C_U W_u + C_D W_d + \frac{R}{\tau} (W_e^{n-1} - W_e) - S_W \right] \right\}$$

C_C is the finite analytic coefficient computed at the collocated velocity node (in the standard MAC method [49] C_d , for U_d , C_n , for V_n , C_e , for W_e are computed at the staggered velocity nodes). The matrix E is built with coefficients like $1+C_C(C_U+C_D)$, etc... The matrix A gathers terms like C_{nb} , $C_C C_U$, $C_C C_D$, ... Terms like R/τ are in f . The G matrix for pressure contributions is inside source terms (S_U) , (S_V) ...

-Step 2- Equation (3.15b) can be written

$$U = \hat{U} - J^{-1} D (b_1^1 P_\lambda + \underline{b_1^2 P_\eta} + \underline{b_1^3 P_\zeta})$$

$$V = \hat{V} - J^{-1} D (b_2^1 P_\lambda + \underline{b_2^2 P_\eta} + \underline{b_2^3 P_\zeta})$$

$$W = \hat{W} - J^{-1} D (b_3^1 P_\lambda + \underline{b_3^2 P_\eta} + \underline{b_3^3 P_\zeta}) \quad (3.18)$$

where

$$D = \frac{C_C R}{1 + C_C(C_U + C_D)}$$

The underlined terms in (3.18) are generated by the misalignment between the coordinate lines and the directions of the velocity components. With respect to the staggered grid approach, it is seen that the D coefficient for the pressure gradient does not depend now on the corresponding velocity component.

-Step 3 - Substituting (3.18) into the continuity equation (3.19) :

$$[b_1^1 U + b_2^1 V + b_3^1 W]_\lambda + [b_1^2 U + b_2^2 V + b_3^2 W]_\eta + [b_1^3 U + b_2^3 V + b_3^3 W]_\zeta = 0 \quad (3.19)$$

gives the pressure field (3.16) which can be viewed also as the solution of the continuous equation (3.20)

$$\frac{\partial}{\partial \lambda} \left[a^{ij} \frac{\partial P}{\partial \lambda_j} \right] = - \text{div } \hat{V}; a^{ij} = DJ g^{ij} = DJ^{-1} \sum_{k=1}^3 b_k^i b_k^j \quad (3.20)$$

Equation (3.20) is now discretized with a centered scheme. Usually, this gives a 27 node pressure molecule (9 in the upstream plane, 9 in the central plane, 9 in the downstream plane). Seven points : U, D, N, S, E, W, P come from second order derivatives $\partial^2 / \partial \lambda^i \partial \lambda^j, i=j$; the other twenty points come from the crossed second - order derivatives $\partial^2 / \partial \lambda^i \partial \lambda^j, i \neq j$. Because of the retained discretization, the pressure molecule involves only 19 points (five points in U and D planes). Among the whole set of contributions to the pressure matrix, it is necessary to keep all the fluxes in order to allow a complete construction of the a_{ij} coefficients, $i=j$, because of the misalignment problem. Extradiagonal coefficients $i \neq j$ arising from crossed second order derivatives are connected to the level of non orthogonality of the grid. They are not retained implicitly but rather treated as source terms. As a result diagonal dominance and symmetry of the discretized pressure matrix is easily obtained. 18 velocity

components have to be specified in (3.20) for the evaluation of $\text{div } \hat{V}$ in each control volume

$$\text{div } \hat{V} = (b_1^1 \hat{U} + b_2^1 \hat{V} + b_3^1 \hat{W})_d - (b_1^1 \hat{U} + b_2^1 \hat{V} + b_3^1 \hat{W})_u + (b_1^2 \hat{U} + b_2^2 \hat{V} + b_3^2 \hat{W})_n - (b_1^2 \hat{U} + b_2^2 \hat{V} + b_3^2 \hat{W})_s + (b_1^3 \hat{U} + b_2^3 \hat{V} + b_3^3 \hat{W})_e - (b_1^3 \hat{U} + b_2^3 \hat{V} + b_3^3 \hat{W})_w \quad (3.21)$$

Because of the definition of the control volume, the whole set of velocity components has to be reconstructed from the known centered velocity components. A simple interpolation is used for that purpose. Because of the structure of the retained discrete molecule, the discrete pressure matrix is symmetric.

-Step 4- The computation of the non solenoidal V^* field uses (3.17), the pressure field resulting from step 4 being present in source terms. The correction procedure starts only when the field V^* has been computed throughout the complete domain.

3.4 Solution of the linear Systems

3.4.1 The Problem

Before discussing the technical solutions which have allowed correct solutions to be obtained, let us point out the origin of the difficulties. Pressure equations and pressure correction equations are almost invariably solved with SLOR type methods applied to the seven point molecule induced by the treatment of under lined terms in (3.18,19) as source terms. The main interest of this approach is, as already seen, that the P matrices are now symmetric and, usually, diagonally dominant. SLOR methods can therefore be expected to converge. Moreover, the coding of the needed tridiagonal matrix algorithm is straightforward. Unfortunately, due to the problem of misalignment, dominant terms are omitted in the system and treated as source terms. As a consequence, global convergence of the method is made more difficult. Unless strong departure from orthogonality is admitted for the grid, this is not dramatic when wall functions are used because grid clustering in the direction η remains rather weak : the first points away from the wall being located so that $50 < y^+ < 200$. When wall functions are avoided, strong grid clustering implies a dramatic increase of the pressure matrix stiffness so that, for three dimensional problems, divergence of the iterative procedure occurs, mainly through a too important pressure correction in the wake. If the pressure matrix is enriched, [18], (using e. g. nine points at the current station $\lambda = \lambda_i$) it becomes more difficult to invert. Thus, improving at least the pressure solver is necessary.

3.4.2 The pressure solver

It has been found [50] that convergence was systematically achieved in practice with an incomplete LU preconditioned biconjugate gradient (PBCG method). Conjugate gradient techniques are used as acceleration methods in which the elements of the pressure matrix (hereafter called A) are generated at each iteration, without any need of storing the full matrix. The CG method satisfies a minimisation property so that a monotone decrease of the error is possible as well as a convergence disruption to which is associated a monotonic decrease of the error. This is not verified in practice because it is not the full pressure matrix that is solved. Because the spectrum of the A matrix is continuously distributed, preconditioning is necessary as a means of improving the convergence of the BCG method : the system to solve $Ax = b$ is replaced by the equivalent system $By = c$ where $\kappa(B) \ll \kappa(A)$, where κ is the condition number of the

matrix, so that eigenvalues of B are more clustered than those of A. What is needed is an approximate inverse A for A such that $AAx = Ab$ or $By = c$ where $B = AA$; $c = Ab$. B being "not too far" from the identity, the CG method for B converges quickly.

The \tilde{A} matrix is selected so as to preserve the sparsity of A. Here, an incomplete LU decomposition [51] [52] -no fill in- is used - the so-called LU (1, 2) decomposition performed worse than the retained classical LU (1, 1) decomposition - . The solution of the LU systems involves recursions which cannot be easily vectorized so that the solutions of these triangular systems is time consuming. Fortunately, a Neumann series method applied to the L and U systems has been found to converge nicely. The argument is presented for L. If L is written under its Jacobi splitting $L = D_L + E_L$, $L = D_L [1 - l]$ where $l = D_L^{-1}E_L$. It appears in practice that l is a convergent matrix. A classical theorem of linear algebra then indicates that $1-l$ is regular and $(1-l)^{-1} = 1+l+l^2+\dots$. The Neuman serie is truncated to m terms and the resulting approximate inverse of $1-l$ can be computed with the Horner scheme. The whole set of computations can be vectorized with a speedup ratio higher than 30. Further information on the PBCG algorithm are given in [51].

4. The Results. HSYA Tanker.

The flow domain covers $0 < X < 6$ where X is adimensionalized with L, the ship being from $X = -1$ to $X = 1.05$; $r_s < r < L$ where r is the radial distance from the axis of the ship $y = z = 0$ and r_s is the radial location of the hull. The flow domain is discretized with 80, 40, 31 points in the axial, radial and girthwise directions. Starting from an a-priori specified surface grid distribution, a volumic grid is firstly generated using a transfinite interpolation procedure [20][55] which is modified in order to allow clustering of points in areas of strong concavity. The resulting grid is irregular as the discontinuities on the body surface are propagated throughout the domain. The elliptic grid generation method is used to smooth out the grid irregularities. Fig.3 presents a perspective view of the grid which appears to behave correctly.

Inlet conditions, written at $X = 0$, are estimated in such a way that results at $X = .291$ roughly match with experiments [1]. The main undetermination lies in the fact that specified data [1][44] involve θ_{11} , δ_1 , C_f and H_{12} , where :

$$\theta_{11} = \int_0^\infty \left[\frac{U_c - U}{Q_c} \right] \frac{U}{Q_c} dy ; \delta_1 = \int_0^\infty \left[\frac{U_c - U}{Q_c} \right] dy \quad (4.1)$$

$$H_{12} = \theta_{11} / \delta_1 ; C_f = \tau_w / \frac{1}{2} \rho U_\infty^2$$

from which needed values for δ , U_τ and Q_c are estimated ($\beta_w \approx 0$). These estimations allow the generation of inlet velocity profiles by the method of Coles & Thompson [53]. It is therefore necessary to briefly mention the results of the sensitivity analysis of δ , U_τ and Q_c data. It is found that, if the influence U_τ is very weak, the result of the computations depend on the level of the overshoot of Q_c with respect to 1, and of the location δ of this overshoot. We consider that this is the most serious weakness of this approach and this justifies recent attempts [6] [29] [30]

[39] to compute the flow past a complete full shape, starting from far upstream. Apart from difficulties connected to the transition specification - a problem on ship models, not on full scale ships -, the flow becomes then somewhat sensitive to the level of the turbulent viscosity outside the viscous zone so that consideration of these aspects is left for a future study. Other boundary conditions are either wall-type conditions or symmetry conditions. Neumann boundary conditions are used for the pressure, except for $r = L$ where P is taken equal to zero.

120 global iteration are used with a local time stepping procedure. Local time step is divided to ensure a fixed amount of diagonal dominance will respect to discretized momentum equations.

Fig.4 presents longitudinal pressure distributions. A sensible grid effect in the longitudinal direction is present in this case. Girthwise distributions agree reasonably well with experiments although some more resolution should be necessary (fig.5). Comparison of secondary velocities with experiments [44] is given in fig.6. The convergence of streamlines, which starts to develop at midship, increases more downstream and gives rise to a counterclockwise primary vortex in the hollow of the stern. The primary vortex is close to the keel plane both in the computation and in the experiments which indicate a "blind" zone for $x/L > .95$, where the longitudinal velocity component is too small to allow significant measurements. The longitudinal vortex where the hull terminates is also found to agree with experiments. If isowakes are now considered (fig. 7) - they are defined as isovalues of the component U in crossplanes -, it is found that the experimental trends are correctly captured (except, of course, for string effects which are not present in the computation, see e.g. $x = 38$ mm, 0 mm, 100 mm, in [44] data-). It must be mentioned that a bilinear interpolation is used to specify isowakes so that it is misleading to compare isowakes .95, 1, or 1.05 as corresponding velocity profiles are usually very "flat" close to $U = 1$. The apparent overestimation of the viscous thickness close to the waterline is probably due to the fact that the inlet viscous thickness does not depend on girth, while it should thicken from the keelplane to the waterplane.

Velocity components U, V, W as well as pressure data can be compared more extensively (fig. 8a to e). U and V are presented on the upper left and right sides, respectively, W and P are presented on the lower left and right sides, respectively. For each series of plots, the evolution is considered with respect to y at a given station $X = \text{const.}$, for several depths $z = \text{const.}$. In general, it is seen that the calculations are in correct agreement with the data, especially on V and W, except, for U, in small regions close to the hull or in the neighborhood of the wake centerplane. This discrepancy is believed to be due to the hull shape modifications. Due to the large amount of grid points which would have been necessary to account for the hub support boss located for -19 mm. $< x < 0$ mm. (in [40] data), this detail of the geometry has been eliminated (fig. 9). Also, coordinate lines (L) : $\eta = 1$, $\zeta = \text{const.}$ evolve continuously from the ship hull into the vertical plane V of symmetry of the wake. They define a family of curves that describe the hull surface for $\lambda < \lambda_w(X)$ where $\lambda_w(X)$ defines parametrically the intersection of the hull-surface ∂B with V ; this intersection is located for $.95 < X < 1.05$. For $\lambda < \lambda_w(X)$, lines (L) are almost rectilinear in V, ie. $z(\eta = 1, \zeta \text{ given})$ depends only weakly on λ . In V, the line $\lambda < \lambda_w(X)$ usually

consists of a vertical line located at $X = .95$ for $z_b \leq z \leq z_r$. For $z_r \leq z \leq 0$, the line $\lambda < \lambda_w(X)$ (which is a piecewise linear function of X) is rather close to a straight line, the equation of which can be written : $z/z_r = 1 + 10 [.95 - X]$

so that the hull has disappeared in the cross plane $X = 1.05$. Now, the approximate hull profile in V is not described exactly by $\lambda < \lambda_w(X)$ but rather by a "stair" function (fig.9) consisting of a succession of lines $X = \text{const.}$, each of them separated by a line close to $z = \text{const.}$. The no-slip condition is evidently written on the resulting "stair surface" ∂B_s which is a crude approximation of the "longitudinal geometry" while crossplanes are correctly body-fitted. As a result, the description of the viscous layer is rather poor. Nevertheless, a comparison with [14] -where a similar treatment is present- indicates that the slight improvement obtained on the secondary flow can be attributed to the fact that wall functions are not used here. The discrepancy between the computed and measured U components is important, especially in the wake. Apart from the fact that this discrepancy is already present upstream, another possible explanation could be the incorrect account of the loss of no-slip which results from the turbulent model.

Fig. 10 presents the comparisons between the computed and measured longitudinal vorticity component isolevels. In spite of the uncertainties involved in processing both the measured and computed data, such a comparison allows examination of differences of velocity gradients rather than velocity themselves. This test is therefore more stringent. As a result, it is found that the computations reproduce both the general features of the contours and the magnitudes. It is also evident that the diffusivity which is present in the viscous region is more correct, with respect to experiments, than that which would result from the use of wall functions [14]. The differences in the shape of the isovalues, in the wake, could be foreseen from the differences in the velocity distributions. Fig.11 presents a color picture of lines of wall friction, the hull is coloured with the pressure field, high C_p and low C_p being associated to red and blue colours respectively. The flow which looks clearly twodimensional at midship enters an oblique low pressure region which deviates the wall streamlines. The resulting convergence of these friction lines implies a thickening of the viscous layer, close to the aft, that makes thin boundary layer methods breakdown [1]. A vertical convergence separation line seems also present, close to $\lambda = \lambda_w (= .95)$. Due to the approximate characteristics of the hull geometry and to the fact that the U velocity component is very low here, the materiality of this result remains to be confirmed from experiments. The maximum pressure levels are found on the hull $X \approx 1-1.025$. More downstream, the vortical structure of the flow is confirmed : streamlines associated to the secondary velocity components V and W are drawn for two crosssections $X = \text{const.}$

5. Conclusion

A fully elliptic numerical method for the solution of the full Reynolds-averaged Navier-Stokes equations has been applied to the computation of the flow past a shiplike hull. The method uses a system of numerically generated curvilinear coordinates and retains the cartesian velocity components as independent variables. The turbulent closure of the equations is handled with the well-known

$k-\epsilon$ model. The use of wall functions is avoided ; instead, a one equation model is used close to the wall. Bypassing the wall functions implies a very high grid resolution in the direction normal to the wall as well as high aspect ratios for the discrete molecules. Due to the resulting increased stiffness of the pressure matrix, it has been found necessary to improve the pressure solver in order to get rid of convergence problems. The numerical method has been described and evaluated on one ship hull for which experimental data are available. From the presented results, the following conclusions can be drawn.

With respect to the modelling of physical flow characteristics, the main features of ship stern flows appear correctly captured. In particular, the viscous inviscid interaction gives rise to a pressure field in good agreement with experiments. The method allows also a correct description of the mean velocity flowfield in the thin boundary layer, provided suitable initial conditions are available [51]. In the thick region, close to the aft, where thin boundary layer methods systematically breakdown, the overall features of the flow are also captured : secondary velocities and even longitudinal vorticity components are correctly predicted. Where discrepancies are found, they may be attributed to the technique which has been used to approximate geometrical details in the framework of a monoblock structured grid. Improvements in the description of the flow close to the propeller disk region therefore require a more detailed resolution of the geometry.

With respect to the methodology, ship stern flows do not appear to involve too strong a viscous-pressure interaction. Therefore, the segregated approach seems well adapted. Apart from geometrical grid aspects, improvements could result from one of the following three points.

(i) *The convection diffusion scheme.* The finite analytic scheme only roughly accounts for the correct physical imbalances : pressure gradients vs. diffusion in the near field, pressure gradient vs. convection in the far field, for all the possible convection velocity directions. More particularly, the hypothesis of local uniformity of the influence coefficients and of the source terms, which allows locally (finite) analytic solutions to be computed, is probably too restrictive, especially in the direction away from the wall, where the convection velocity and the source terms vary rapidly, owing to strong gradients of turbulent quantities.

(ii) *The Poisson solver.* This is the most time-consuming part of the method, especially on three-dimensional grids where the aspect ratios can be very high. The conjugate gradient technique appears very well adapted to the problem in spite of its induced storage increase. It can be noticed that it may be somewhat unreasonable to compute the pressure -which is regular and does not vary significantly close to the walls- on a grid which appears rather well suited for the velocity distributions and for the turbulent quantities in that they especially vary close to the walls. Because less points are needed for the pressure, the use of a multigrid procedure should efficiently cut down cpu times. Because relaxation is a local procedure, a multigrid technique might be also a way of improving the solution in the boundary-unfitted region close to the aft.

(iii) *The Turbulent Model* is also a potential source of uncertainty for the description of near-wall flows where strong curvature effects are present. Although the flows considered are mainly pressure-controlled, improvements in the turbulence models might lead at least to improved length scale predictions (the turbulent kinetic energy is

known to be overpredicted in thick boundary layers [40]). Nevertheless, it is considered that improved results will be rather an outcome of a better treatment of the geometry and of a better convection-diffusion algorithm.

Acknowledgments : Authors gratefully acknowledge financial support of DRET through contract 86 / 104. Cpu on Cray2 was attributed by the Scientific Committee of CCVR. Cpu on VP200 was attributed by DS / SPI. The presented method has been developed from an earlier code version of the method [12].

Références

- [1] L. Larsson. (Ed.) *Proceedings of SSPA-ITTC on Ship Boundary Layers*. SSPA Report N°90 (1980)
- [2] L. Larsson and M.S. Chang, Numerical Viscous and Wave Resistance Calculations Including Interaction. *Proc. 13th ONR Symp. Naval Hydrodynamics*, Tokyo, (1980)
- [3] T. Nagamatsu, Calculation of Ship Viscous Resistance and its Application. *Journ. Soc. Naval Arch. Japan* 157, 47 (1985) - See also *Proc. 2nd Int Symp. Viscous Flow*. SSPA-Goteborg, (1985)
- [4] S. Soejima, Calculation of Three-dimensional Boundary Layers Around Ship Hull Forms. *Proc. 2nd. Symp. Num. Phys. Aspects of Aerod. Flows*, Long Beach, CA. (1985)
- [5] H. Miyata and S. Nishimura, Finite Difference Simulation of Non linear Ship Waves. *J. Fluid Mech.* 157, 327-357 (1985)
- [6] H. Miyata, S. Nishimura and A. Masuko, Finite Difference Simulation for Non linear Waves Generated by ships of Arbitrary Three-dimensional Configuration. *J. Comp. Phys.* 60, N°3, 391-396 (1985)
- [7] H. Miyata, H. Kajitani, S. Akifuji, M. Baba, M. Kanai, Wave Formation about a Ship Bow advancing in Head Seas. *Spring Meeting Soc. Nav. Arch. Japan* (1987)
- [8] M. Hoekstra, H.C. Raven, Application of a Parabolized Navier-Stokes Solution System to Ship Stern Flow Computation. *Proc. Osaka Int. Colloq. on Ships Viscous Flow*, 125-142 (1985)
- [9] M. Hoekstra and H.C. Raven, Ship Boundary Layer and Wake Calculation with a Parabolized Navier-Stokes Solution System. *Proc. 4th Int. Conf. Num. Ship Hydrodynamics*, Washington D.C. 470-491 (1985)
- [10] H.C. Raven and M. Hoekstra, A Parabolized Navier-Stokes Solution Method for Ship Stern Flow Calculations. *Proc. 2nd Int. Symp. Ship Viscous Resistance*, SSPA Goteborg (1985)
- [11] L. Broberg, Numerical Calculation of Ship Stern Flow. *PhD Thesis, Univ. Of Chalmers* (1988) ; also SSPA Rept. 2801-2 & 2803-1
- [12] H.C. Chen and V.C. Patel, Calculation of Trailing-Edge, Stern and Wake Flows by a time-Marching Solution of the Partially Parabolic Equations. *IIHR Rept N°285 Iowa City, Ia* (1985)
- [13] H.C. Chen and V.C. Patel, Numerical Solutions of the Flow over the Stern and in the Wake of Ship Hulls. *Proc. 4th. Num. Conf. on Numerical Ship Hydrodynamics*, Washington D.C. 492-511 (1985)
- [14] V.C. Patel, H.C. Chen and S. Ju, Ship Stern and Wake Flows : Solutions of the Fully-Elliptic Reynolds-Averaged Navier-Stokes Equations and Comparisons with Experiments. *IIHR Rept. 323 Iowa City, Ia* (1988)
- [15] H. Miyata, T. Sato and N. Baba, Finite Difference Solution of a viscous Flow with Free-surface Wave about an Advancing Ship. *J. Comp. Phys.* 72, 393-421 (1987)
- [16] G. Tzabiras, On the Calculation of the 3D Reynolds Stress Tensor by Two Algorithms. *Proc. 2nd. Int. Symp. Ship Viscous Flows*, Goteborg, Pap. 15 (1985)
- [17] J. Piquet, P. Queutey and M. Visonneau, Computation of Viscous Flows past Axisymmetric Bodies with and without Propeller in Operation. *Numerical Methods in Laminar and Turbulent Flows* (C. Taylor, W.G. Habashi, M.M. Hafez, Eds.) 5, Part 1, Pineridge Press, 644-655 (1987)
- [18] J. Piquet and M. Visonneau, Steady Three-dimensional Viscous Flow Past a Shiplike Hull. *Proc. 7th. GAMM Conf. Num. Methods in Fluid Dynamics. Notes on Numerical Fluid Dynamics*, (M. Deville, Ed.) 20, Vieweg, 294-301 (1988)
- [19] G.D. Tzabiras, Numerical and Experimental investigation of the Flow Field at the stern of Double Ship Hulls. *PhD Thesis, Nat. Tech. Univ. Athens* (1984)
- [20] J.F. Thompson, Z.U.A. Warsi and C.W. Mastin, *Numerical Grid Generation, Foundations and Applications*. North Holland Publ. New York (1985)
- [21] G. Tzabiras and T.A. Loukakis, A Method for Predicting the Flow Around the Stern of Double Ship Hulls. *Int. Ship. Progress* N°345 (1983)
- [22] A.M. Abd El Meguid, N.C. Markatos, D.B. Spalding, K. Muraoka, A Method of Predicting three-dimensional Turbulent Flows around Ships/Hulls. *Proc. 1st. Int. Symp. Ship Viscous Resistance*, SSPA Goteborg (1978)
- [23] A.M. Abd El Meguid, N.C. Markatos, K. Muraoka, D.B. Spalding, A comparison between the Parabolic and Partially-parabolic Solution Procedures for Three-dimensional Turbulent Flows around Ship's Hulls. *App. Math. Modelling* 3, 249 (1980)
- [24] C.E. Jansson and L. Larsson, Ship Flow Calculations using the Phoenix Computer Code. *Proc. 2nd. Int. Symp. on Ship Viscous Resistance* SSPA, Goteborg (1985)
- [25] K. Muraoka, Examination of a two-Equation Model of Turbulence for Calculating the Viscous Flow around Ships. *J. Society Naval Arch. Japan*, 147, 35 (1980)
- [26] K. Muraoka, Calculation of thick Boundary Layer and Wake of Ships by a Partially Parabolic Method. *Proc. 13th. ONR. Symp. Naval Hydrodynamics* Tokyo, 601-616 (1982)
- [27] R. Peyret and T.D. Taylor, *Computational Methods for Fluid Flow*. Springer-Verlag Ed., New-York. (Series in Comp. Phys.)
- [28] D.C. Kwak, J.L. Chang, S.P. Shanks, S. Chakravarthy, An incompressible Navier-Stokes Flow Solver in Three-dimensional Curvilinear Coordinate System Using Primitive Variables. *AIAA J.* 24, 390-396 (1986)
- [29] Y. Kodama, Computation of 3-D Incompressible Navier-Stokes Equations for Flow Around a Ship Hull Using an Implicit Factored Method. *Proc. Osaka Int. Symp. on Ship Viscous Flow*, 109-124
- [30] Y. Kodama, Computation of High Reynolds Number Flow past a Ship Hull using the IAF Scheme. *Proc. Soc. Naval Arch. Japan, Spring Meeting* (1987)
- [31] S.P. Vanka, Computations of Turbulent Recirculation Flows with Fully Coupled Solution of Momentum and Continuity Equations. *Argonne National Lab. Rep. ANL-83-74* (1983)
- [32] S.G. Rubin, Incompressible Navier-Stokes and Parabolized Navier-Stokes Formulations and Computational Techniques. *Computational Methods in Viscous Flows*, 3; Series : Recent Adv. in Num. Meth. Fluids, Habashi, Ed., Pineridge Press (1985)

[33] S.V. Patankar and D.B. Spalding, A Calculation Procedure for heat, Mass and Momentum Transfer in Three-Dimensional Parabolic Flows. *Int. J. Heat Mass Transfert* 15, 1787 (1972)

[34] S.V. Patankar, *Numerical Heat Transfer and Fluid Flow*, Hemisphere Publishing Corp. New-York.

[35] R.I. Issa, Solution of the Implicitly Discretized Fluid Flows Equations by Operator-Splitting, *J. Comp. Phys.*, 62, N°1, 40-65 (1986)

[36] M. Israeli and A. Lin, Iterative numerical solutions and Boundary Conditions for the Parabolized Navier-Stokes. *Comp. & Fluids* 13, N°4, 397-410 (1985)

[37] C.J. Chen and H.C. Chen, Finite Analytic Numerical Method for Unsteady Two-Dimensional Navier-Stokes Equations. *J. Comp. Phys.* 53, N°2, 209-226 (1984)

[38] T. Hino, Numerical Simulation of a Viscous Flow around a Ship Model, *Proc. Soc. Naval Arch. Japan*, Spring Meeting (1987)

[39] A. Masuko, Y. Shiroye and S. Ishida, Numerical Simulations of the Viscous Flow around Ships including Bilge Vortices, *Proc. 17th. Symp. Naval Hydrodynamics*, Den Haag (1988)

[40] V.C. Patel, Some Aspect of Thick Three-Dimensional Boundary Layers, *Proc. 14th. ONR Symp. Naval Hydro. Ann Arbor*, 999-1040 (1982)

[41] V.C. Patel, Ship Stern and Wake Flows : Status of Experiment and Theory, *Proc. 17th. Symp. Naval Hydrodynamics*, Den Haag (1988)

[42] L. Larsson, *Boundary Layers on Ships*, PhD Thesis, Univ. Chalmers (1975)

[43] L. Lofdahl and L. Larsson, Turbulence Measurements Near the Stern of a Ship Model, *J. Ship Research* 28, N°3 (1984)

[44] K. Wieghardt and J. Kux, Nomineller Nachstrom auf Grund von Windkanalversuchen, *Jahrb. Der Schiffbautechnischen Gesellschaft (STG)*, 303-318, (1980)

[45] K. Wieghardt, Zur Kinematik einer Nachlaufstromung, *Z. Flugwiss. Weltraumforsch.* 7, Heft 3 (1983)

[46] H.C. Chen and V.C. Patel, Calculation of Stern Flows by a Time Marching Solution of the Partially Parabolic Equations, *Proc. 15 th. ONR Symp. Naval Hydrodynamics*, Hamburg (1984)

[47] H.C. Chen and V.C. Patel, Near-Wall Turbulence Models for Complex Flows including Separation, *AIAA Paper* 87-1300

[48] M. Wolfshtein, The Velocity and Temperature Distribution in One-Dimensional Flow with Turbulent Augmentation and Pressure Gradient, *Int. J. Heat Mass Transfert* 12, 301-318 (1969)

[49] F.H. Harlow and J.R. Welsh, Numerical Calculation of Time Dependent Viscous Incompressible Flows of Fluid with a Free Surface, *Phys. Fluids* 8, 2182-2189 (1965). See also Los Alamos Rept. LA-3425 (1966)

[50] J. Piquet, P. Queutey and M. Visonneau, Computation of the Threedimensional Wake of a Shiplike Body, *Proc. 11th. Int. Conf. Num. Meth. Fl. Dyn.*, Lect. Notes Phys. Springer-Verlag (1989)

[51] J. A. Meijerink and H.A. Van Der Vorst, An Iterative Solution Method for Linear Systems of which the coefficient Matrix is a Symmetric M-Matrix, *Maths. Comp.* 31, N°137, 148-162 (1977)

[52] J.A. Meijerink and H.A. Van Der Vorst., Guidelines for the usage of Incomplete Decompositions in Solving Sets of Linear Equations as they occur in Practical Problems, *J. Comp. Phys.* 44 (1981)

[53] T. Cebeci, K.C. Chang and K. Kaups, A Three Dimensional General Method for Threedimensional Laminar and Turbulent Boundary Layers on Ship Hulls, *Proc. 12th. ONR Symp. Naval Hydrodynamics*, Washington (1978)

[54] K.H. Mori & N. Ito, Near-Wake Computations by Solving the Vorticity Transport Equation in a Body-fitted Coordinate System, *Proc 4th. Int. Conf. Num. Ship Hydro.*, Washington D.C., 512-528 (1985)

[55] L.E. Eriksson, Generation of Boundary Conforming grids around Wing-Body Configurations using Transfinite Interpolation, *AIAA Journ.*, 20, N°10, 1982.

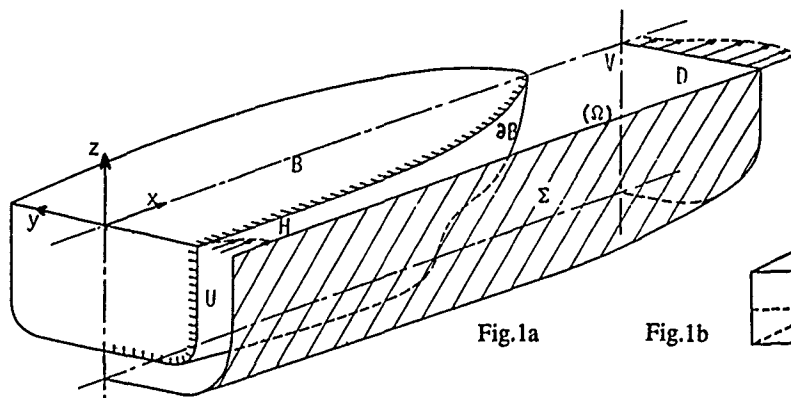


Fig.1a

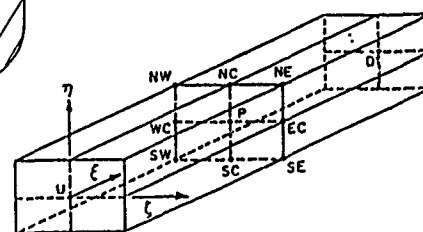


Fig.1b

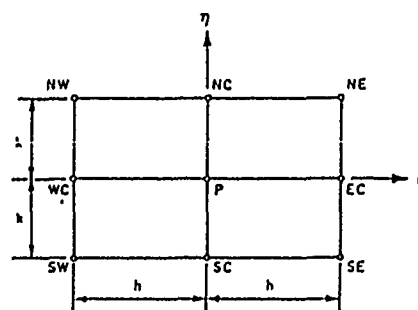


Fig.1c

Fig.1a - Physical Domain

Fig.1b - Computational Box

Fig.1c - Transverse plane in the Computational Domain.

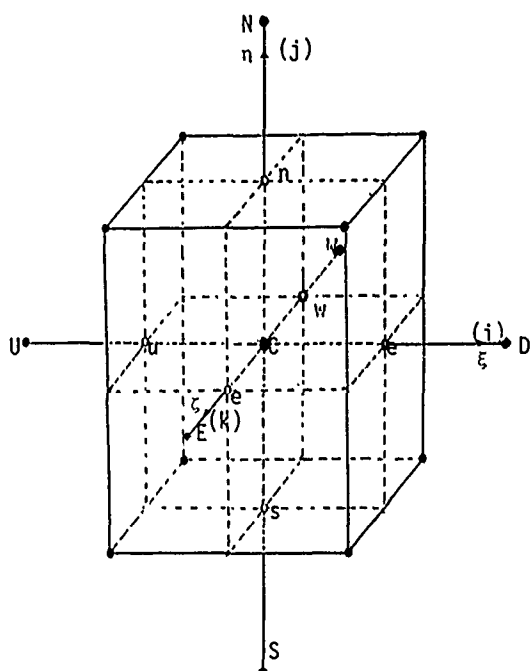


Fig.2 - Collocated grid. •, location of velocity components and of pressure.

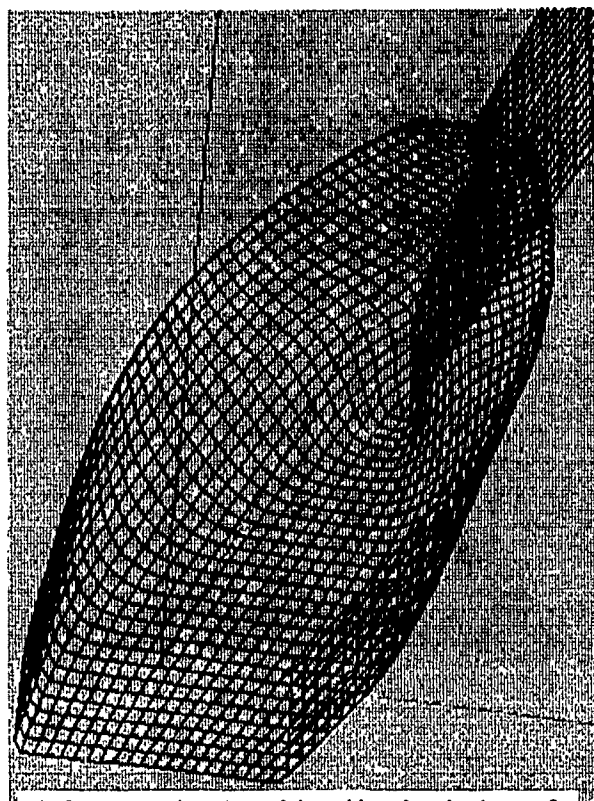


Fig.3 - Perspective view of the grid surface $j = 1$; $\eta = 0$.

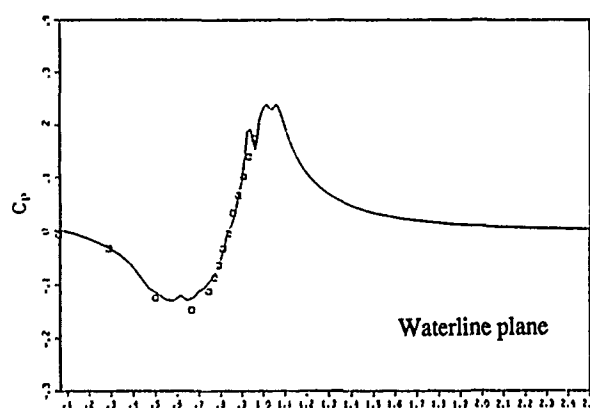
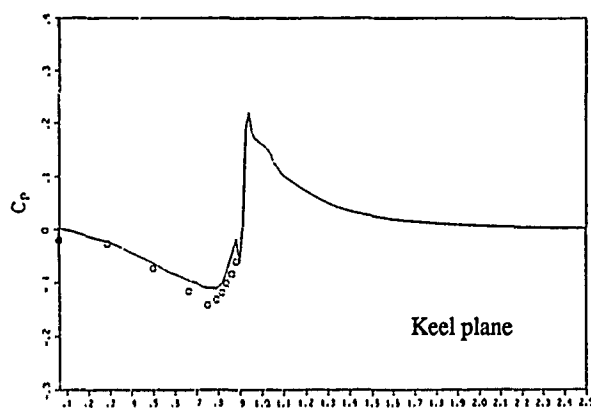


Fig.4 - Longitudinal Pressure Distributions. •, experiments
—, computations.

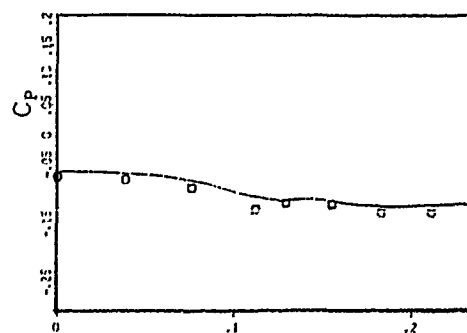
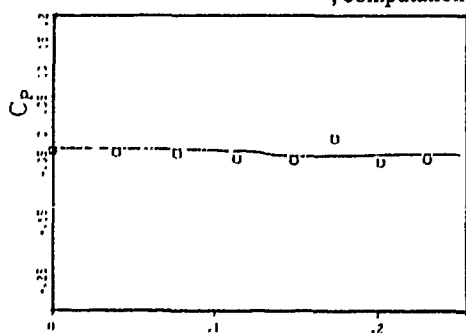


Fig.5 - Girthwise Pressure Distributions. •, experiments;
—, computations.

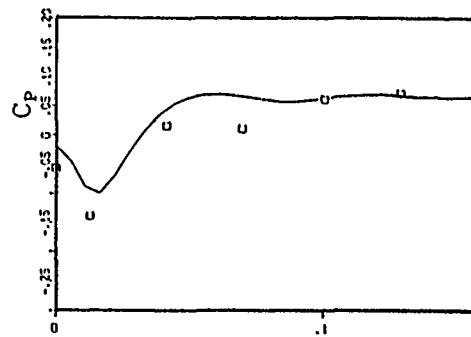
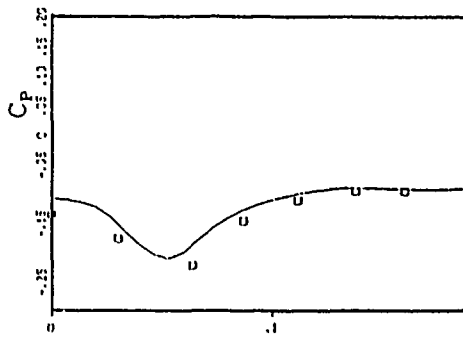


Fig.5 - Girthwise Pressure Distributions. \square , experiments ;
—, computations.

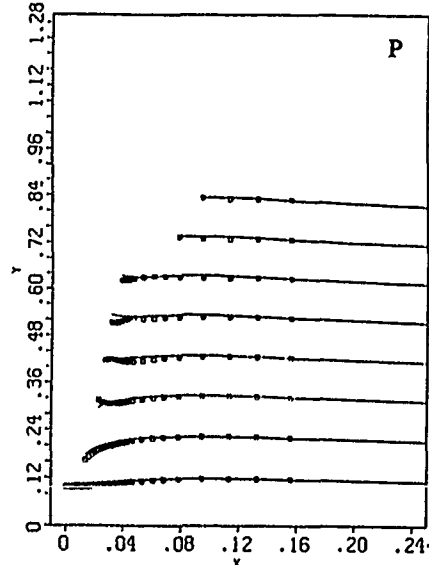
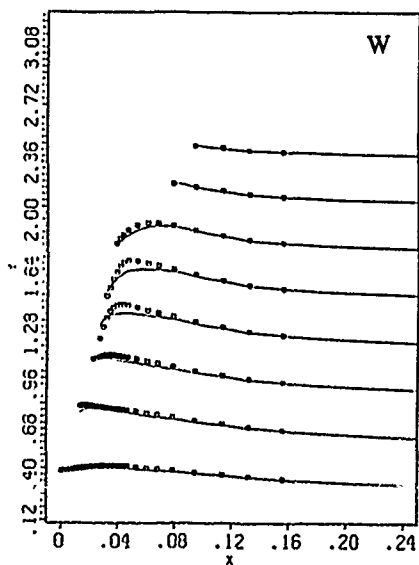
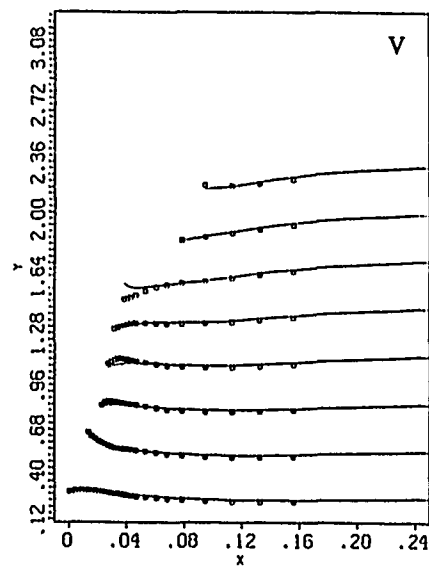
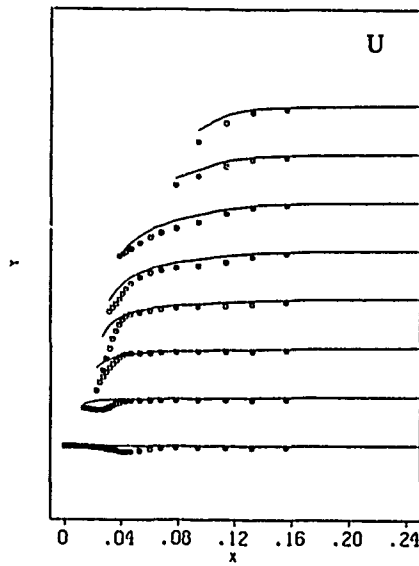


Fig.8a - Velocity components and Pressure at a given crosssection $X/L = .944$, for several depths $Z = \text{const.}$, as a function of Y . \square , experiments ; —, computations.

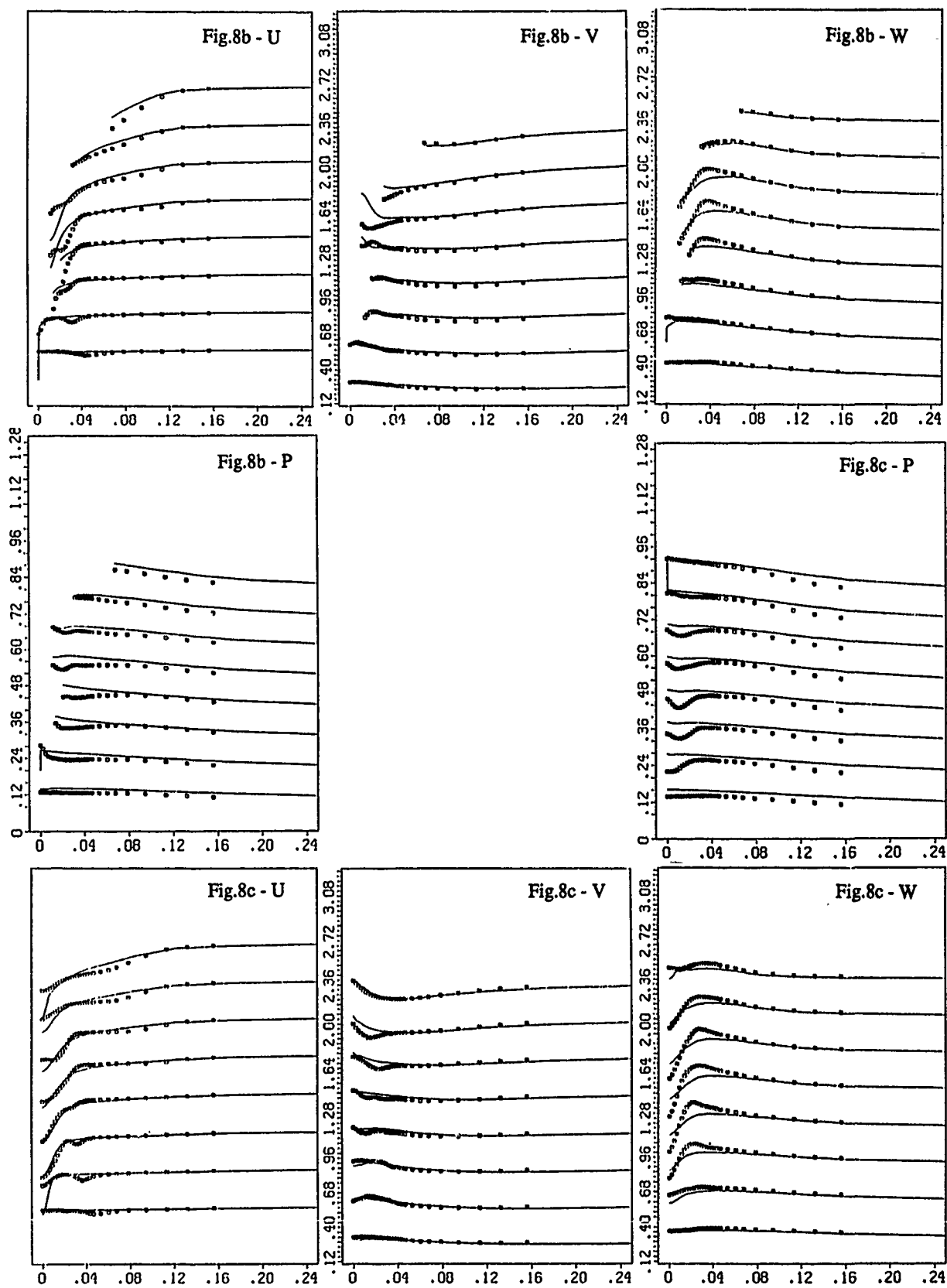


Fig.8b, c - Velocity components and Pressure as a function of Y, at given crosssections : $X/L = .962$ and $X/L = 1.007$, for several depths $Z = \text{const.}$, experiments ; —, computations.

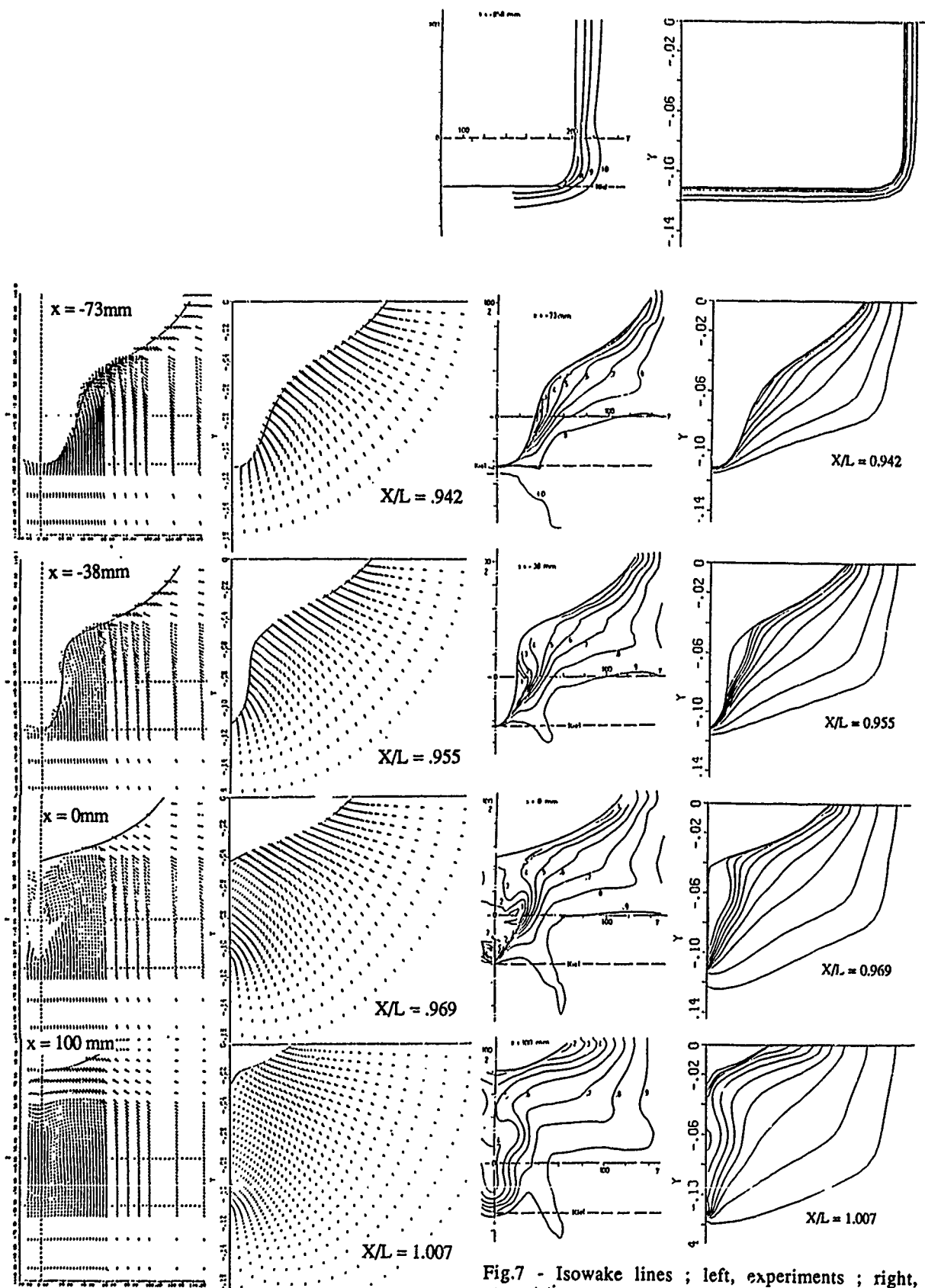


Fig.6 - Secondary velocities at several crosssections $X = \text{const}$; left, experiments ; right, computations.

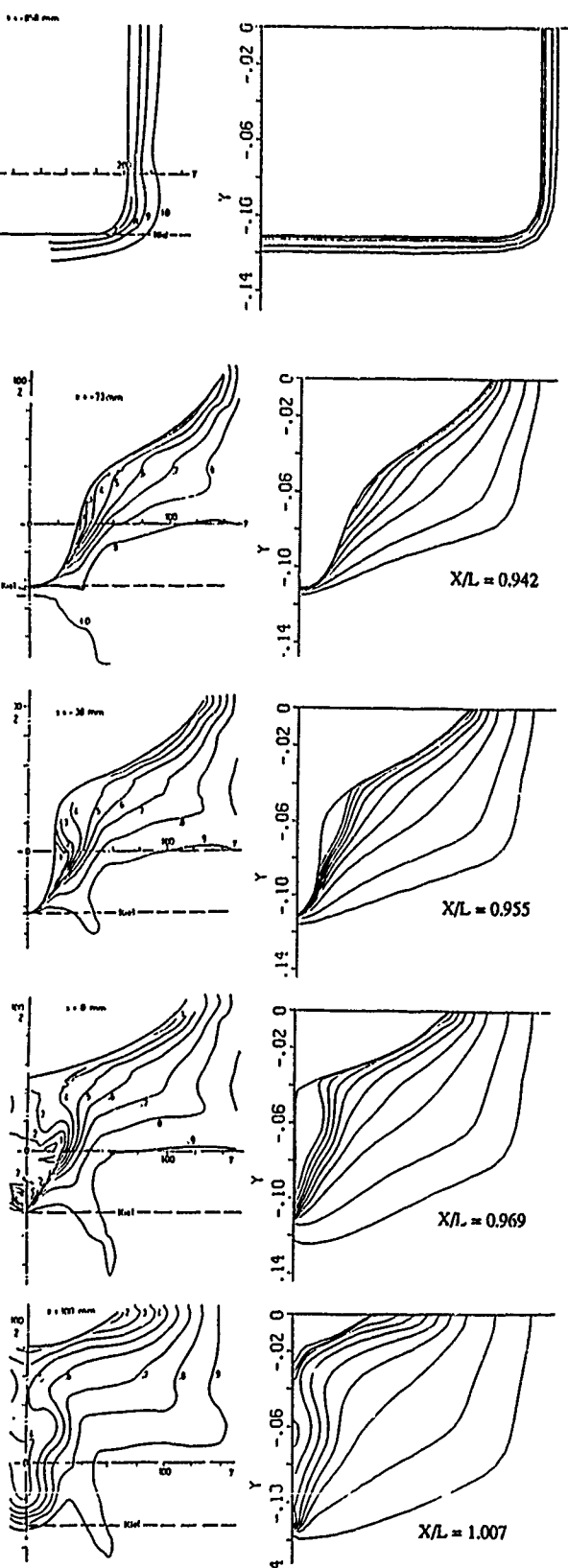


Fig.7 - Isowake lines ; left, experiments ; right, computations.

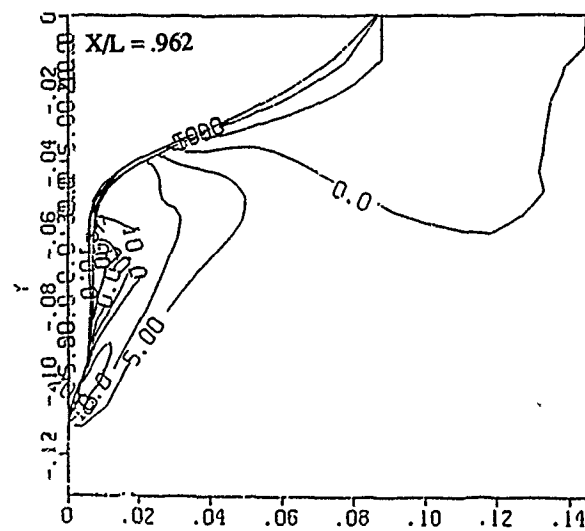
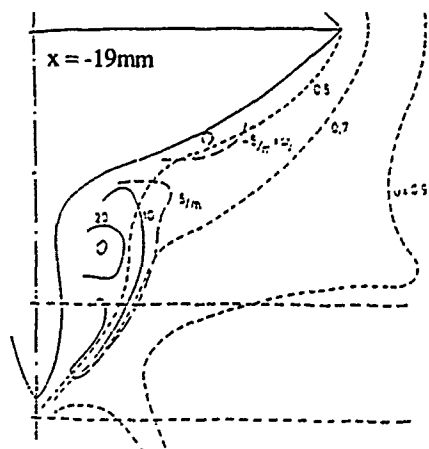
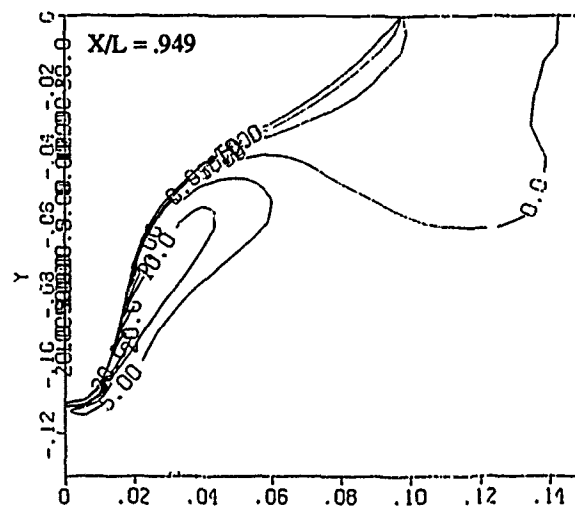
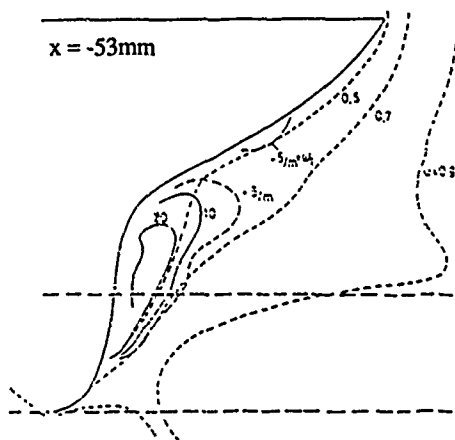
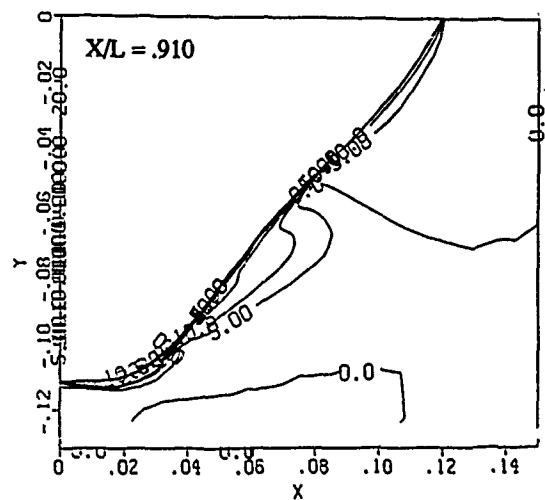
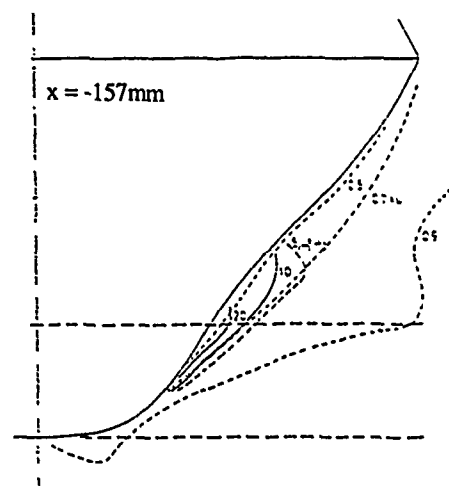


Fig. 10 - Contours of isolevels of the longitudinal component of the vorticity field in transverse crosssections. Left, experiments [44] ; right, computations.

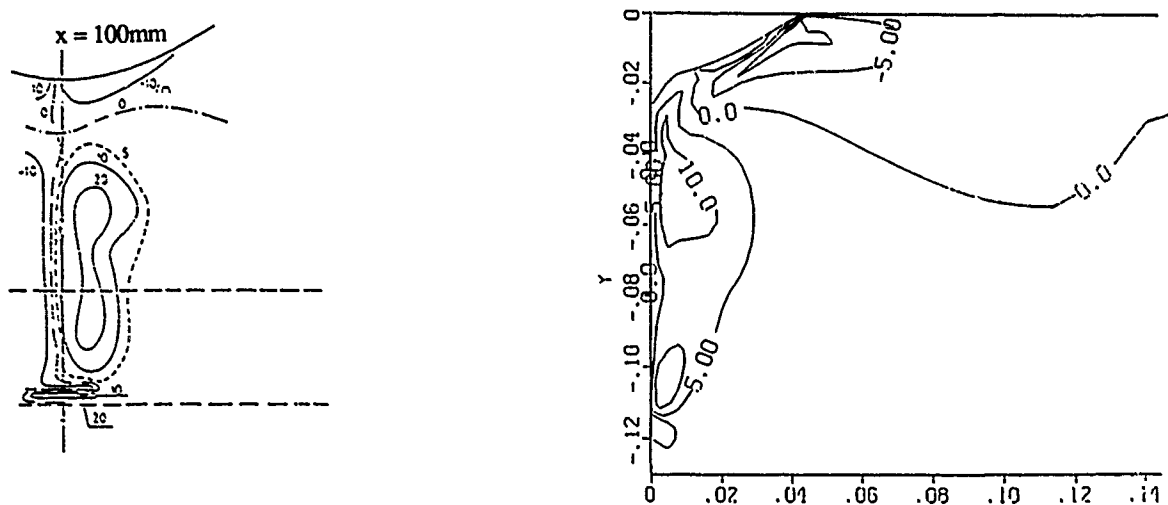


Fig.10 - Contours of isolvels of the longitudinal component of the vorticity field in transverse crosssections. Left, experiments [44] ; right, computations.

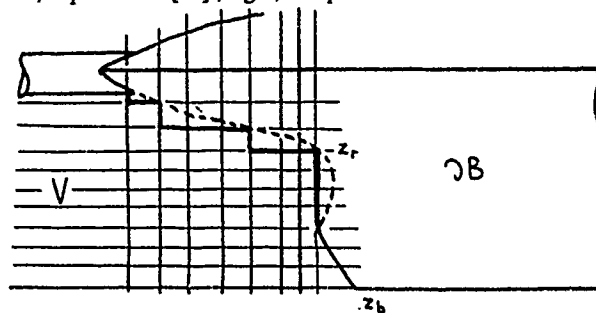


Fig.9 - Detailed view of the aft part of the HSVA tanker. ---, $\lambda(x)$ exact intersection between V and ∂B ; —, present approximate "stair" representation of this line (note : the sting is omitted in the computations).

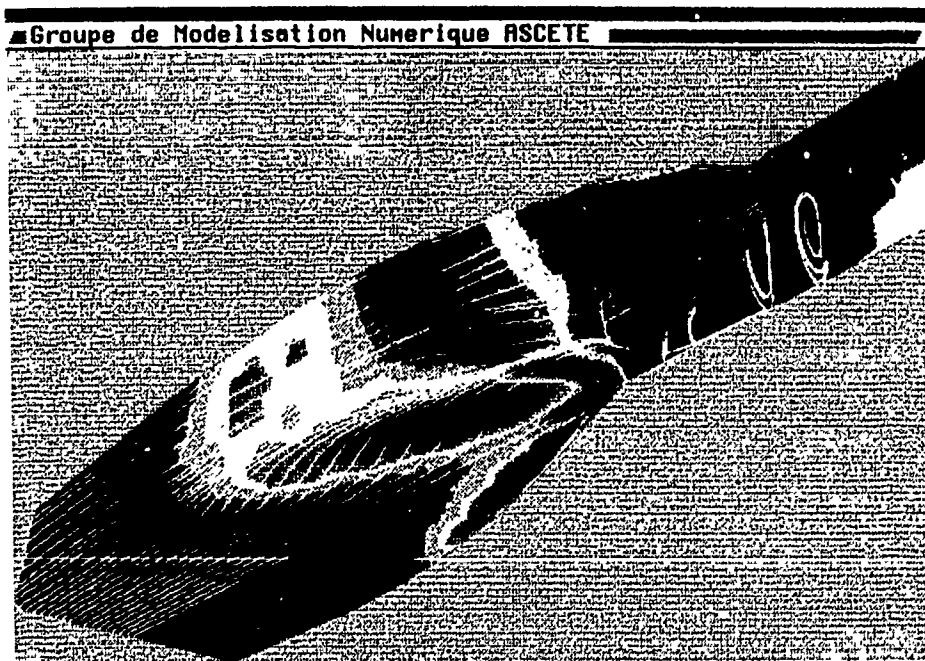


Fig.11 - Perspective view of the aft part of the HSVA tanker ; skin-friction lines.

DISCUSSION

by Y. Kodama

You used a non-aligned grid system near the stern, which greatly reduces load for grid generation and improves grid orthogonality. However, I think a special treatment should be needed in order to satisfy conservation there. Did you do those treatments there? If not, what is your opinion about the effect of possible violation of conservation there on the computed results?

Author's Reply

Because of the use of an H-grid associate to the constraint $x=x(\xi)$, the grid which has been built here is no more body-fitted in the intersection between the overhang and the plane of symmetry ($y=0$). This implies two consequences;

(i) the exact geometry is not well represented, so that the no slip condition is not written at the right place in the plane of symmetry.

(ii) the development of the boundary layer below the overhang is not correctly captured because of the lack of discretization points and a distribution law which is not in agreement with the strong variation of the velocity profiles in the plane $y=0$. Due to the used topology, this weakness is not easily surmountable because the grid lines which are supposed to describe the overhang symmetry line boundary layer come from the surface of the hull.

It is believed that the correct representation of the body surface is more important than conserving momentum on a geometry which is incorrectly reproduced in the symmetry plane. The best remedy to this fundamental weakness is to relax the constraint $x=x(\xi)$, working on more general (and less orthogonal) grids.

Simulations of Forces Acting on a Cylinder in Oscillatory Flow by Direct Calculation of the Navier-Stokes Equations

T. Kinoshita

University of Tokyo, Tokyo, Japan

M. Hinatsu

Ship Research Institute, Tokyo, Japan

S. Murashige

University of Tokyo, Tokyo, Japan

Abstract

Flow around floating vessels sometimes accompanies separations, and is unsteady in ocean waves. We select the flow around a circular cylinder in an oscillatory flow as a preliminary study for it.

In this paper, the two dimensional Navier-Stokes equations for it are directly computed using body-fitted coordinate, moving mesh technique, 3rd order upwind scheme, and the MAC method at the Reynolds number, $R_a=10^4$ and the Keulegan-Carpenter number, $K_c=5, 7$, and 10.

The computed results simulate the effect of the K_c number on the flow field in excellent agreement with published data both qualitatively and quantitatively.

Moreover, we examine the validity of this computational scheme. The good agreement with analytical solutions gives reliability of it, and we consider the effect of fineness of the grid and the effect of the Reynolds number minutely.

1. Introduction

The flow around a circular cylinder in an oscillatory flow is idealization of the flow around floating vessel like semi-submersible in ocean waves. It accompanies separations and is unsteady. Hence, we must sometimes understand mechanism of the separated vortices to estimate hydrodynamic forces acting on it.

Flow visualization gives a lot of valuable qualitative information for it. Williamson [1] oscillated a circular cylinder in water at rest at the Keulegan-Carpenter number, $K_c < 60$, and the frequency parameter, $\beta = 255$,

where $K_c = U_m T / D$, $\beta = R_a / K_c$, R_a is the Reynolds number, $R_a = U_m D / \nu$, U_m denotes the maximum velocity in a period, D the diameter of the circular cylinder, ν the kinematic viscosity of a fluid, and T the period of oscillation. He related the position and strength of vortices around it to K_c . For example, a very interesting half Karman vortex street in the transverse direction was observed in the range of $7 < K_c < 13$. Honji [2] performed the same experiment as Williamson at $K_c < 4$ and $70 < \beta < 700$, and indicated that structures of flow field become three dimensional in special range of K_c and β . Tatsuno et al. [3] performed the same experiment as them in the more wide range of K_c than Honji at $K_c < 15$ and $\beta < 150$, and classified the flow patterns minutely.

For the small sectional size of cylindrical bodies compared with wave length, in-line force per unit length, F_{in} , is commonly predicted by the following equation.

$$F_{in} = \frac{1}{2} \rho C_d D u |u| + \frac{1}{4} \pi \rho C_m D^2 \frac{du}{dt} \quad (1)$$

where the coefficients C_d and C_m denote the drag and inertia coefficients, respectively, D the width of structures, ρ the density of fluid, t the time, and u the velocity of the ambient flow. First, Morison et al. [4] proposed it intuitively, and later Keulegan and Carpenter [5] evaluated it systematically. Equation (1) is called the Morison equation and means that the in-line force is assumed to be given by a linear sum of the viscous drag and inertia forces. According to Keulegan and Carpenter [5], assuming an odd-harmonic in-line force of $\theta = 2\pi t / T$, i.e. $F_{in}(\theta) = -F_{in}(\theta + \pi)$, expressing it in terms of a Fourier series, and neglecting the high frequency terms in them, we get the Morison equation (1). The coefficients C_d and C_m are

expressed under the condition of $U=U_m \sin \theta$ as follows:

$$C_d = \frac{3}{4} \int_0^{2\pi} \frac{F_{in} \sin \theta}{\rho D U_m^2} d\theta$$

$$C_s = \frac{2 U_m T}{\pi^3 D} \int_0^{2\pi} \frac{F_{in} \cos \theta}{\rho D U_m^2} d\theta \quad (2)$$

Sarpkaya[6] carried out an analysis of the experimental data of Keulegan and Carpenter[5] as well as his own data, and showed that the coefficients C_d and C_m depend on not only K_o but also R_o . In particular, it is interesting that C_d increases and C_m decreases with K_o in the range of about $5 < K_o < 15$, of which region corresponds to that of transverse half Karman vortex street observed by Williamson[1]. He also pointed out that the Morison equation (1) cannot express the experimental data well in the range of $8 < K_o < 25$.

Experimental estimation of the coefficients C_d and C_m as well as lift force coefficient, C_l , requires considerable number of trial, because the ambient flow field is affected by plural parameters.

For this problem, some analytical solutions have been obtained. Stokes[7] was the first to show that the force acting on a cylinder oscillating sinusoidally in a viscous fluid depends on both K_o and R_o or β . The force is expressed in terms of the Morison equation (1) by noting that $|\cos \theta| \cos \theta$ is approximated by $(8/3\pi) \cos \theta$ over a period, and the coefficients are expressed as follows:

$$C_d = \frac{3\pi^3}{2K_o} \{ (\pi\beta)^{-\frac{1}{2}} + (\pi\beta)^{-1} + O(\pi\beta)^{-\frac{3}{2}} \} \quad (3)$$

$$C_s = 2 + 4(\pi\beta)^{-\frac{1}{2}} + O(\pi\beta)^{-\frac{3}{2}} \quad (4)$$

Equations (3) and (4) are valid only for large values of β . Wang[8] extended this analysis to $O[(\pi\beta)^{-3/2}]$ using the method of matched asymptotic expansion. His solution, which is valid for $K_o \ll 1$, $R_o \times K_o \ll 1$, and $\beta \gg 1$, may be reduced to

$$C_d = \frac{3\pi^3}{2K_o} \{ (\pi\beta)^{-\frac{1}{2}} + (\pi\beta)^{-1} - \frac{1}{4}(\pi\beta)^{-\frac{3}{2}} \} \quad (5)$$

$$C_s = 2 + 4(\pi\beta)^{-\frac{1}{2}} + (\pi\beta)^{-\frac{3}{2}} \quad (6)$$

The equations (5) and (6) differ from (3) and (4) only in the last terms. Stokes and Wang's solutions are

virtually identical in the range of their validity, i.e. for large β . On the other hand, Bessho[9] obtained the analytical solutions for this problem using Oseen's scheme and showed the coefficients C_d and C_m as follows:

$$C_d = \frac{3\pi^3}{2K_o} (\pi\beta)^{-\frac{1}{2}} \{ 1 + \frac{1.15}{\pi^2} K_o \} \quad (7)$$

$$C_s = 2 + 4(\pi\beta)^{-\frac{1}{2}} \{ 1 - \frac{0.8}{\pi^2} K_o \} \quad (8)$$

Numerical analysis is another way to this problem. Recent advances of a super computer have enabled direct calculation of the Navier-Stokes equations, and some flow fields have been solved. Baba and Miyata[10] carried out an analysis of a flow around a circular cylinder in an oscillatory flow at $R_o=1000$ and $K_o=5$ and 7 using the finite difference method and showed qualitative agreement with observations.

Objective of this paper is to accurately simulate instantaneous unsteady flow field around an oscillating circular cylinder and to estimate hydrodynamic forces acting on the circular cylinder quantitatively at $R_o=10000$ and $K_o=5 \sim 10$. Namely, increase of C_d and decrease of C_m with K_o in this range as well as drastic change of the flow pattern are simulated. For these purposes, the authors adopt direct simulation of the Navier-Stokes equations. Although the number of mesh is limited, we consider that simulation of newly generated predominant vortices which mainly affect the flow field is only required, while energy cascade to very small vortices is less important to this problem.

In this paper, the Navier-Stokes equations are solved for flow around a sinusoidally oscillating circular cylinder in a fluid at rest, using the finite difference method. The flow is identical with flow around a circular cylinder fixed in an sinusoidally oscillating flow except for the constant gradient pressure (see Appendix). In the former case, we need the moving mesh technique which moves a computational grid with bodies, because the circular cylinder moves every moment. In addition to this problem, the moving mesh technique enables computation of a flow around bodies which instantaneously change their shapes like fish. Accordingly, the present computational procedure can be widely applicable.

All problems are two-dimensionally solved. Although three dimensional

computations are necessary to take into account the three dimensional coherent structure of the shed vortex sheets, they remain as a next step of the research. This paper shows two dimensional solution to this problem.

In order to use the present computational scheme as a practical tool, we must determine the validity of it. We compare the computed results with the analytical solutions and examine effects of total number of grid points, minimum grid size, time increment, and the Reynolds number on the computed results.

2. Governing Equations

The two dimensional Navier-Stokes equations are written in the normalized form as follows:

$$\begin{aligned} \frac{1}{K_c} \frac{\partial u}{\partial t} + u \frac{\partial u}{\partial x} + v \frac{\partial u}{\partial y} - \\ - \frac{\partial p}{\partial x} + \frac{1}{Re} \left(\frac{\partial^2 u}{\partial x^2} + \frac{\partial^2 u}{\partial y^2} \right) \\ \frac{1}{K_c} \frac{\partial v}{\partial t} + u \frac{\partial v}{\partial x} + v \frac{\partial v}{\partial y} - \\ - \frac{\partial p}{\partial y} + \frac{1}{Re} \left(\frac{\partial^2 v}{\partial x^2} + \frac{\partial^2 v}{\partial y^2} \right) \end{aligned} \quad (9)$$

where u and v denote the velocity in the x -direction and the velocity in the y -direction, respectively, and p the pressure. The velocity is normalized by the maximum velocity of oscillation in a period, U_m^* , the pressure by ρU_m^{*2} , the length by the diameter of a circular cylinder D^* , and the time by the period of the oscillation T^* . A superscript of asterisk denotes the dimensional value.

The continuity equation is written in the normalized form as follows:

$$\frac{\partial u}{\partial x} + \frac{\partial v}{\partial y} = 0 \quad (10)$$

3. Computational Procedure

3.1 Body-fitted Coordinate System and Moving Mesh

Body-fitted coordinate system makes it easy to compute flow around a body of arbitrary shape, especially to treat boundary conditions through coordinate transformation. In this simulation, the grid is generated as shown in Fig.1 and the system is an 'O-grid'. In this grid, a circular cylinder of unit diameter forms the inner boundary. The outer boundary is a circle whose diameter is 40 times that of the inner

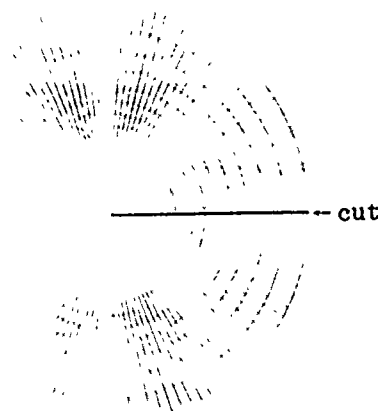


Fig.1 Grid

circle. The number of grid divisions are 120 in the circumference direction and 50 in the radius direction. The grid is clustered near body surface using geometric series to obtain high resolution. The minimum space adjacent to the body is set to 0.005.

Introducing a cut line along the positive part of the x -axis in the physical plane (x, y) as shown in Fig.1, we transform the plane (x, y) into the computational plane (ξ, η) whose grid increment is set to be constant and unity for each direction as shown in Fig.2.

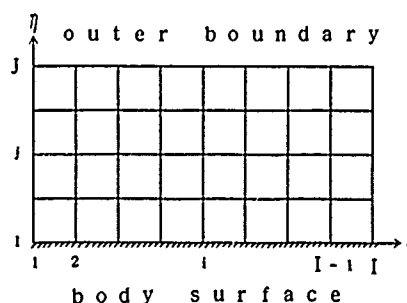


Fig.2 Computational plane

Actual computation is performed in this computational plane (ξ, η).

As noted in the introduction, the moving mesh technique is adopted. Now we can consider two ways to move the grid as follows: (1) the way to fix the outer boundary and move only the inner boundary, (2) the way to move the outer boundary with the inner boundary simultaneously. Case (1) requires longer computational time than case (2), because the grid must be regenerated every moment. Hence, case (2) is adopted in this paper. The relations of partial differential

operators between the physical plane (x,y) and the computational plane (ξ,η) are written as follows:

$$\begin{aligned}\partial_x &= a\partial_\xi + b\partial_\eta \\ \partial_y &= c\partial_\xi + d\partial_\eta \\ \partial_{xx} + \partial_{yy} &= \hat{a}\partial_{\xi\xi} + \hat{b}\partial_{\xi\eta} + \hat{c}\partial_{\eta\eta} \\ &\quad + \hat{d}\partial_\xi + \hat{e}\partial_\eta \\ \partial_t &= -(ax_\tau + cy_\tau)\partial_\xi - (bx_\tau + by_\tau)\partial_\eta + \partial_\tau\end{aligned}\quad (11)$$

where t denotes the time in the physical plane (x,y), τ the time in the computational plane (ξ,η), and

$$\begin{aligned}a &= \xi_x - Jy_\eta, \quad b = \eta_x - Jy_\xi \\ c &= \xi_y - Jx_\eta, \quad d = \eta_y - Jx_\xi \\ \hat{a} &= a^2 + c^2, \quad \hat{b} = 2(ab + cd) \\ \hat{c} &= -b^2 + d^2 \\ \hat{d} &= aa_\xi + ba_\eta + cc_\xi + dc_\eta \\ \hat{e} &= ab_\xi + bb_\eta + cd_\xi + dd_\eta \\ J &= \begin{vmatrix} \xi_x & \xi_y \\ \eta_x & \eta_y \end{vmatrix} = \frac{1}{\begin{vmatrix} x_\xi & x_\eta \\ y_\xi & y_\eta \end{vmatrix}}\end{aligned}$$

All physical quantities, i.e. velocity and pressure, are estimated at each intersection point of grid, which is so-called 'regular mesh'.

3.2 Boundary Conditions

Indices (i,j) of grid points in the computational plane (ξ,η) are shown in Fig.2. Each boundary condition is as follows:

(1) Body Surface (j=1)

*The velocity is set to that of a circular cylinder.
*The first derivative of the pressure is derived through the Navier-Stokes equations (9) and the orthogonality of the grid on the body surface as follows:

$$\begin{aligned}\frac{\partial p}{\partial \eta} &= \frac{1}{JEK_c}(y_\xi U_t - x_\xi V_t) \\ &\quad - \frac{1}{JEK_c}(bU + dV)(y_\xi u_\eta - x_\xi v_\eta) \\ &\quad + \frac{1}{JE}(bU + dV)(y_\xi u_\eta - x_\xi v_\eta) \\ &\quad + \frac{1}{ReJE}(-y_\xi(\hat{c}u_{\eta\eta} + \hat{e}u_\eta) + x_\xi(\hat{c}v_{\eta\eta} + \hat{e}v_\eta))\end{aligned}\quad (12)$$

where U and V denote the motion velocity in the x-direction and that in the y-direction of the circular cylinder, respectively, and $E = x_\xi^2 + y_\xi^2$.

(2) Outer Boundary (j=J,J+1)

*The velocity is set to zero.

*Using linear extrapolation, the pressure is set as follows:

$$\begin{aligned}p_J &= 2p_{J-1} - p_{J-2} \\ p_{J-1} &= 2p_J - p_{J-1}\end{aligned}\quad (13)$$

(3) Outside of Cut (i=-1,0,I,I+1)

*The velocity and pressure are set as follows:

$$\begin{aligned}q_{-1} &= q_{I-2} \\ q_0 &= q_{I-1} \\ q_I &= q_1 \\ q_{I+1} &= q_2\end{aligned}\quad (14)$$

where q denotes velocity or pressure. This condition is called 'periodic condition'.

3.3 MAC Method and Discretization

In the present computation, the MAC method[11] is adopted as a computational algorithm. In this method, pressure p is obtained by solving the Poisson equation which is derived by taking the divergence of the Navier-Stokes equations as follows:

$$\nabla^2 p = -\nabla \cdot \{(\bar{u} \cdot \nabla) \bar{u}\} - \frac{1}{K_c} \frac{\partial \varepsilon}{\partial t} + \frac{1}{Re} \nabla^2 \varepsilon\quad (15)$$

where \bar{u} denotes the velocity vector and ε is written as

$$\varepsilon = \frac{\partial u}{\partial x} + \frac{\partial v}{\partial y}\quad (16)$$

The condition of the continuity is imposed as follows:

$$\frac{\partial \varepsilon}{\partial t} \sim -\frac{\varepsilon^n}{\Delta t} \quad (\varepsilon^{n+1}=0)\quad (17)$$

where Δt denotes the time increment, and n the time step. The reason why the local dilation term of the n-th time step is left is that it prevents the accumulation of numerical errors. Velocity is obtained by solving the Navier-Stokes equations (9) using the Euler explicit time differencing scheme. The flow chart of computation is shown in Fig.3.

The governing equations are discretized as follows:

(1) Space differencing

The terms except the convective term are discretized by 3-points central differencing scheme for all regions. The convective term is discretized by 1st order upwind differencing scheme (18) for j=2 and 3rd order upwind differencing scheme (19) for j ≥ 3

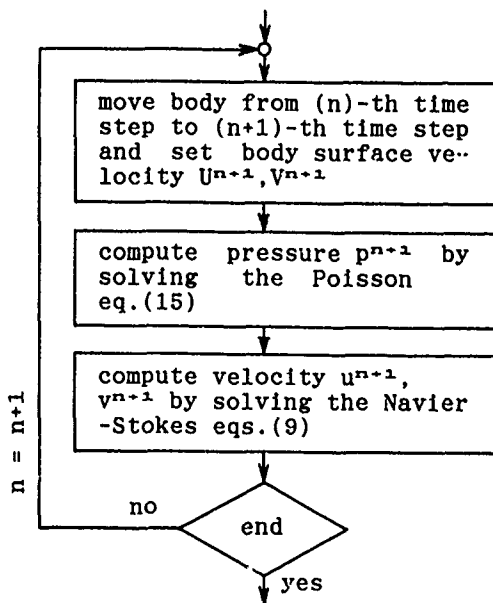


Fig.3 Flow chart

$$u \left(\frac{\partial u}{\partial \xi} \right)_i \sim u_i \frac{(-u_{i-1} + u_{i+1})}{2h} - |u_i| \frac{(u_{i-1} - 2u_i + u_{i+1})}{2h} \quad (18)$$

$$u \left(\frac{\partial u}{\partial \xi} \right)_i \sim u_i \frac{(u_{i-2} - 8u_{i-1} + 8u_{i+1} - u_{i+2})}{12h} + |u_i| \frac{(u_{i-2} - 4u_{i-1} + 6u_i - 4u_{i+1} + u_{i+2})}{4h} \quad (19)$$

where h denotes the grid increment.

(2) time differencing

The Euler explicit method is used as follows:

$$\frac{\partial u}{\partial t} \sim \frac{(u^{n+1} - u^n)}{\Delta t} \quad (20)$$

3.4 Stability

The limitation of the time increment is given by the von Neumann method, as follows:

$$\Delta t \leq \frac{\Delta x}{K_c \times u} \quad (21)$$

where Δt denotes the time increment, Δx the local grid increment and u the local velocity.

In the case of $K_c=5$ and $u=1.0$, the limitation of the time increment is given as follows:

$$\Delta t \leq 0.001 \quad (22)$$

Since the von Neumann method is valid only for linear equations, the

time increment must be set lower than the above value in actual computation.

In this computation, it is set as follows:

$$\begin{aligned} \Delta t &= 0.0002 & \text{for } K_c = 5 \text{ and } 7 \\ \Delta t &= 0.0001 & \text{for } K_c = 10 \end{aligned} \quad (23)$$

4. Computational Results

The computations are performed at $R_\infty=10000$ and $K_c=5, 7$ and 10 . In order to realize asymmetric flow field, sinusoidal motion of a circular cylinder in the direction vertical to the oscillation is superposed on the oscillation at the first quarter period of the oscillation as follows:

$$\begin{aligned} U &= \sin(2\pi t) \\ V &= 0.1 \times \sin(4\pi t) & \text{for } t = 0.0 \sim 0.25 \\ &= 0.0 & \text{for } t > 0.25 \end{aligned} \quad (24)$$

where U and V denotes the motion velocity of a circular cylinder in the x -direction and that in the y -direction, respectively. The amplitude and period of the superposed sinusoidal motion are $1/10$ th and half of the oscillation, respectively.

For all computational conditions, the circular cylinder is oscillated for eight periods, and the results are discussed for the data in the 8-th period.

4.1 Hydrodynamic Forces Acting on a Circular Cylinder

(1) In-Line Force

Published experimental data of hydrodynamic forces are arranged by the drag coefficient, C_d , and the inertia coefficient, C_m , or the added mass coefficient, C_a , where $C_m=1+C_a$ (see Appendix). Before describing the computed results, we should note that there are scatters between the data published by different researchers as shown in Fig.4.1. The time history of in-line force shows a qualitatively same pattern in each cycle, but the magnitude and phase vary to some degree. The differences yield the scatters. For example, Kato et al.[12] showed the time history of pressure distributions, in which the magnitude differs more than 50 per cent in some cycle. Thus, since the value of the coefficients depends on how to average and estimate them, they may scatter even in the same experimental facility. Besides the differences of experimental method and conditions, the reasons of

the differences of the magnitude and phase in each cycle are considered as follows. With progression of R_a and/or K_a , irregularity of shed vortex sheet which has three dimensional coherent structures[2][3] is superposed on that which has two dimensional coherent structures. As a result, complicated flow field which shows strong irregularity is formed. Hence, the scatters are not only due to errors but also due to essential nature of flow field. Furthermore, the coefficients C_a and C_m (or C_a) are considerably varied by even a little phase shift of hydrodynamic force time history.

The computed results of C_a and C_m are shown in Figs.4.1 and 2 with experimental data of Sarpkaya[6] and Tanaka et al.[13] and the analytical solutions[8][9] which are rewritten by equations (5) ~ (8) by noting $C_m = 1 + C_a$. These figures show that these computational results simulate very well the effect of the K_a number on the drag coefficient C_a and the added mass coefficient C_m .

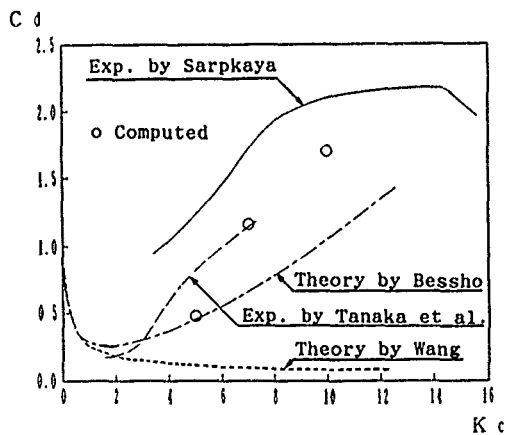


Fig.4.1 Drag coefficient, C_d

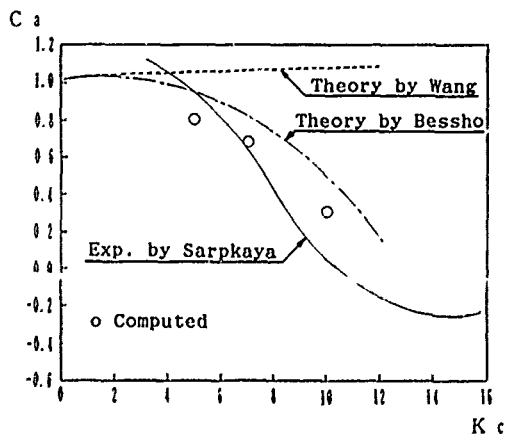


Fig.4.2 Added mass coefficient, C_m

Next, in order to examine that the present computation simulates unsteady phenomena accurately every moment, time histories of in-line force are shown in Figs.5.1,2 and 3.

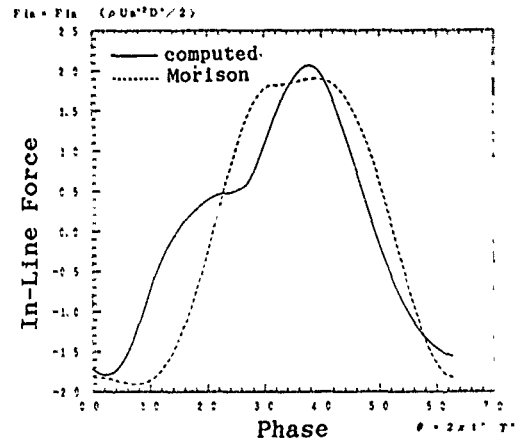


Fig.5.1 Time history of in-line force ($K_a=5$)

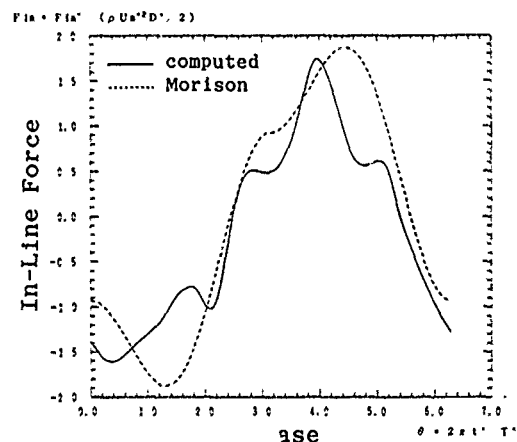


Fig.5.2 Time history of in-line force ($K_a=7$)

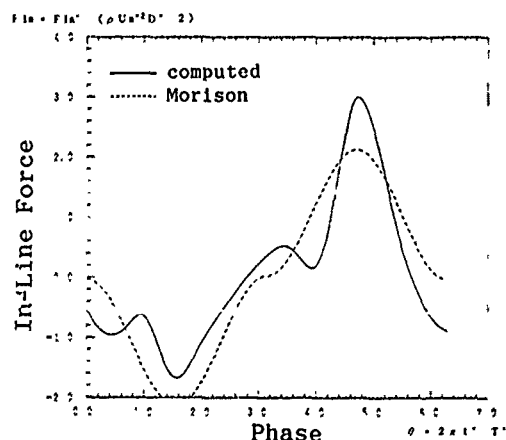


Fig.5.3 Time history of in-line force ($K_a=10$)

Almost no experimental data of time histories of in-line force have been published, but we can get the approximation for them by substituting the experimental data of the coefficients into C_d and C_m in the Morison equation (1). The broken lines in these figures denote the approximation. Here it should be noted that the Morison equation assumes an odd-harmonic in-line force, neglects higher frequency components and cannot express the experimental data in the range of $K_o = 8 \sim 25$. The first assumption means that the flow field repeats every half period of the oscillation. At $K_o = 5$ and 7, the computed results are in very good agreement with the approximation by the Morison equation as shown in Figs. 5.1 and 2. While at $K_o = 10$, they are not in so good agreement with them as at $K_o = 5$ and 7 and are not odd-harmonic definitely as shown in Fig. 5.3. This matter is discussed in Chapter 4.2 more minutely.

(2) Transverse Force

The comparison of the computed results of the maximum value of transverse force, $F_{tran.max}$ with experimental data of it [6] is shown in Fig. 6.

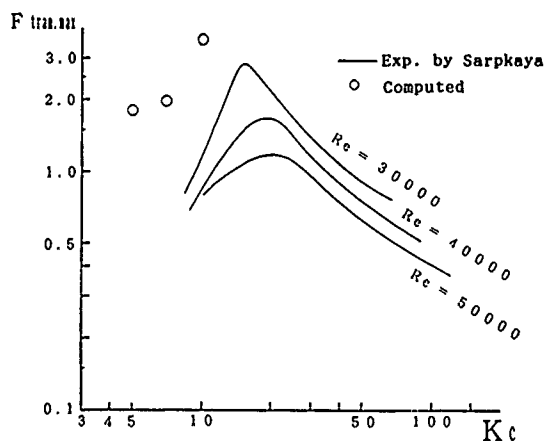


Fig. 6 Maximum value of Transverse force, $F_{tran.max}$

The experiment was not performed at $R_o = 10000$, but the computed results seem to show dependence of it on K_o and R_o fairly well. The experiment shows that the ratio of the frequency of fluctuation of transverse force to the frequency of the oscillation of the cylinder is two in the region of the K_o number set in this computation. Time histories of transverse force in Figs. 7.1, 2 and 3 shows that.

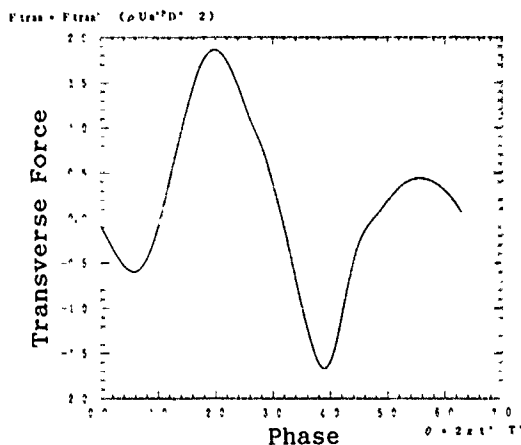


Fig. 7.1 Time history of transverse force ($K_o = 5$)

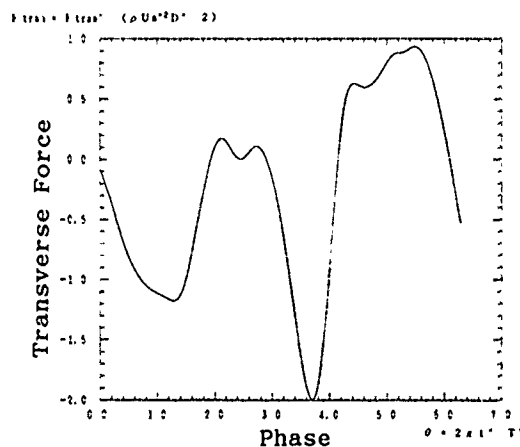


Fig. 7.2 Time history of transverse force ($K_o = 7$)

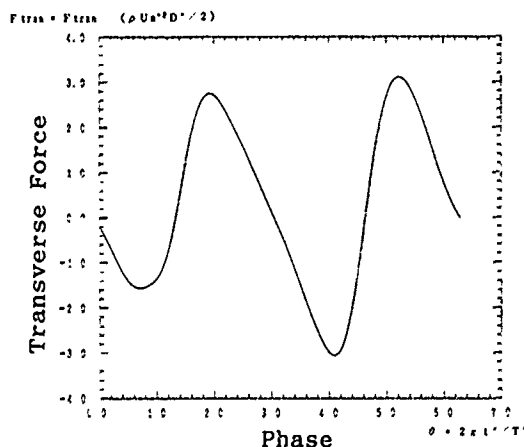


Fig. 7.3 Time history of transverse force ($K_o = 10$)

We consider that a transverse force depends on positions of vortices strongly. Time history of transverse force is a good measure of periodicity of the flow field.

4.2 Time Evolution of Vorticity

Time evolution of vorticity is shown in Figs.8.1 and 2 where the time increment is set to 0.1, contour pitch 2.0, a solid line denotes a counterclockwise vortex, and a broken line a clockwise vortex. The circular cylinder is oscillated from side to side along the x-axis, a black circle in each figure shows the position of an oscillating circular cylinder, and it is located on the left end at $t=7.0$.

Williamson[1] classified aspects of vortices around the circular cylinder into some groups by K_α for R_α of the order 10^3 , and in the range of $K_\alpha < 13$ they are summarized as follows:

(a) $K_\alpha < 7$

Vortices which are generated in a half period become a pair with vortices which are generated in the last half period. He called it 'pairing of attached vortices', although one of the pair is not attached but shed.

(b) $7 < K_\alpha < 13$

The pairing of shed vortices is formed, and a street of vortices moves away from the cylinder roughly vertically to the oscillation. He called it 'transverse street'.

The computed results are as follows:

(1) $K_\alpha = 5$ (Fig.8.1.(0) ~ (9))

At $t=7.0$, the vortices A and B which grow at $t=7.0 \sim 7.5$ are already generated in the vicinity of the cylinder surface. Vortices C and D at $t=7.2$ and vortices E and F at $t=7.8$ are typical examples of 'pairing of attached vortices'. It is noticed that the flow field is asymmetric.

(2) $K_\alpha = 10$ (Fig.8.2.(0) ~ (9))

At $t=7.0$, vortex A which grew at $t=6.5 \sim 7.0$ turns to the opposite side and is divided by vortex A'. Vortex B' was shed at $t=6.5 \sim 7.0$, moves away from the cylinder nearly vertically to the oscillation at $t=7.0 \sim 7.3$, and become 'transverse street'. At $t=7.2$, vortex A amalgamates vortex D. At $t=7.4$ and 7.5 , vortex D is shed.

The flow patterns are not clarified yet at $R_\alpha = 10000$, but it is interesting that the computed results agree with Williamson's observation at Re of the order 10^3 very well. As mentioned in section 4.1 (1), increase of C_d and decrease of C_m with K_α are simulated very well in this range of K_α . We consider that the changes of C_d and C_m are due to these drastic changes of

aspects of vortices.

Further it is noticed in Fig.8.2 that the aspect of vortex shedding is different between in the first half and in the last half period at $K_\alpha = 10$. In the first half period, two vortices shed, i.e. vortex D' sheds at $t=7.3$ and vortex D shed at $t=7.4$. While, in the last half period, one vortex sheds, i.e. vortex E sheds at $t=7.9$. It affects in-line force. The computed results of in-line force time history is not odd-harmonic as shown in Fig.5.3. The peak value in the first half period is lower than that in the last half period. It means that the Morison equation can not express the experimental data well in this range of K_α as pointed out by Sarpkaya, who says that the range is $8 < K_\alpha < 25$ at R_α of the order 10^4 . Figs.5.1, 2, and 3 show that in-line force becomes less odd-harmonic with the progress of K_α . They show the same tendency as Williamson's observation at R_α of the order 10^3 .

Tatsuno et al.[3] pointed out recently that the flow field patterns are classified by periodicity and three dimensional coherent structures of flow field more minutely with β and K_α than Williamson's classification. For estimating in-line force more correctly, we must understand in what period the flow field repeats. The period is not necessarily an integer.

5 Discussions

In order to examine the validity of the present computation, we consider the following six points.

(1) Comparison of computed results with analytical solutions

The computed results obtained without the initial disturbance, which is the oscillation in the y-direction in the first quarter period, must agree with analytical solutions in the range where the theories are valid, $K_\alpha \ll 1$, $R_\alpha \times K_\alpha \ll 1$, $\beta \gg 1$. When the Reynolds number is fixed to 10^4 , the valid range is $K_\alpha \ll 1$. Figure 9.1 and 2 show that the computed results are close to the analytical solutions in this range and that the present computation is reliable.

(2) Effect of initial disturbance

For examination of the effect of the degree of the initial disturbance on the flow field, we carried out the computation using the following equation instead of equation (24).

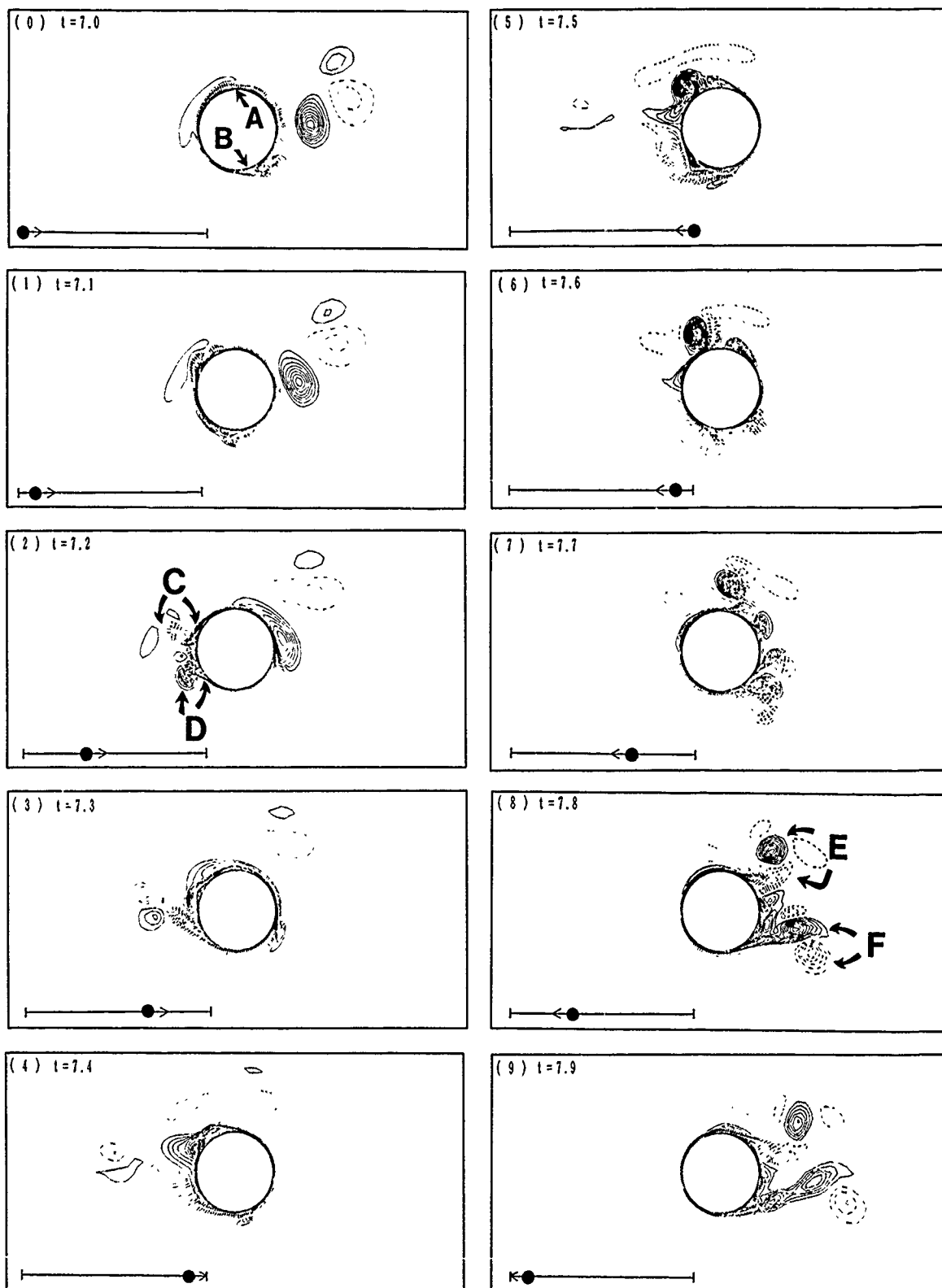


Fig.8.1 Vorticity contour, pitch=2.0, $K_\alpha=5$
solid line: counterclockwise, broken line: clockwise

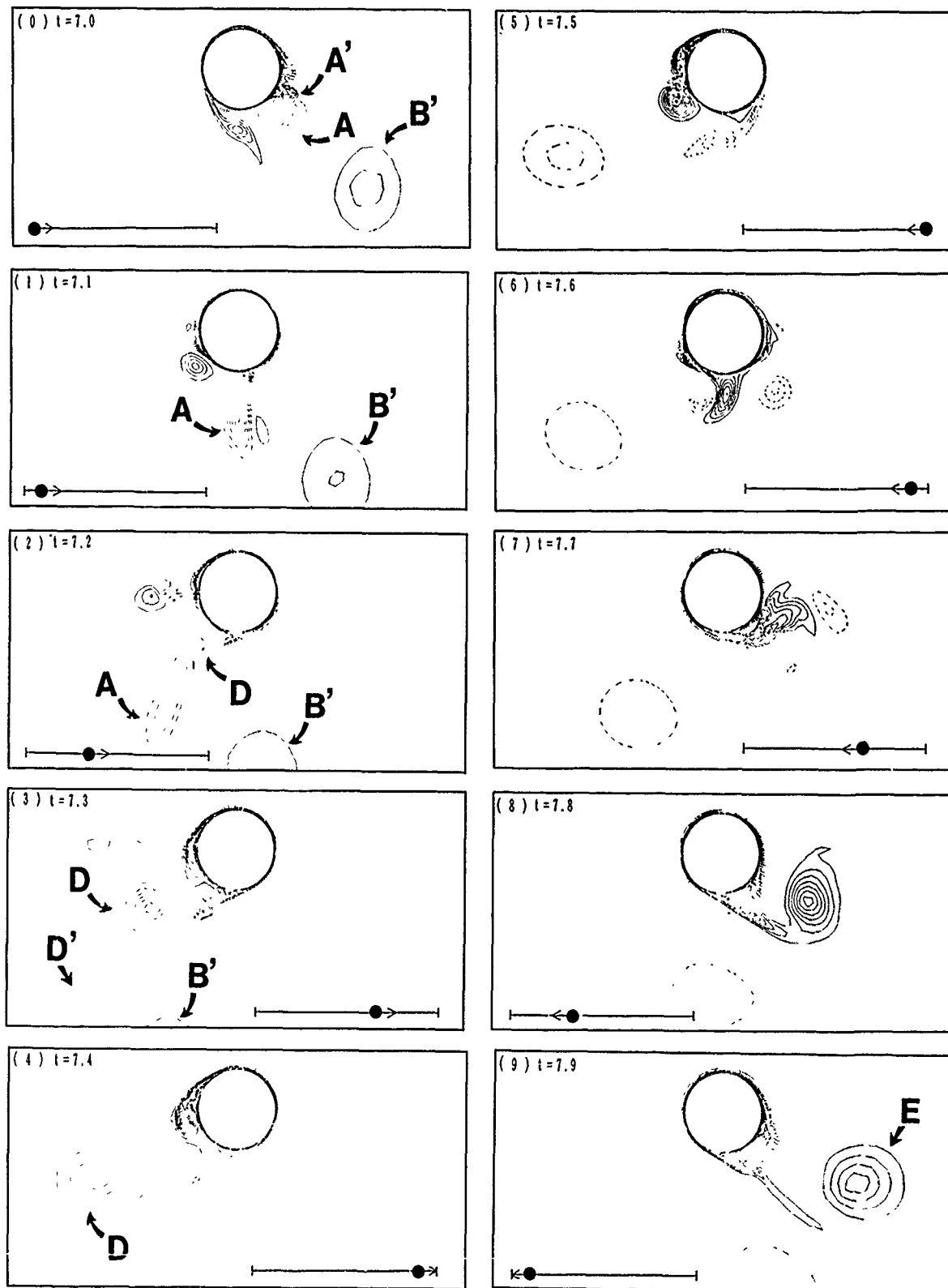


Fig.8.2 Vorticity contour, pitch=2.0, $K_a=10$
solid line: counterclockwise, broken line: clockwise

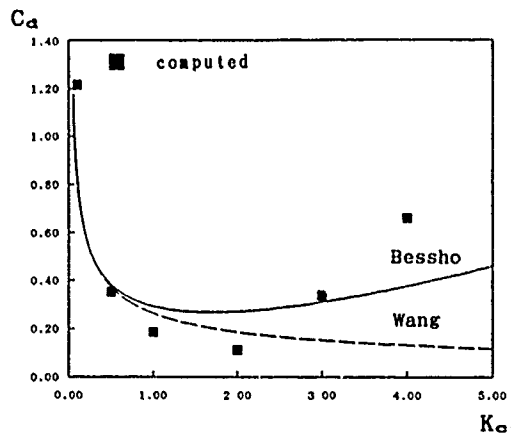


Fig.9.1 Comparison of drag coefficient, C_d between computed results and analytical solutions

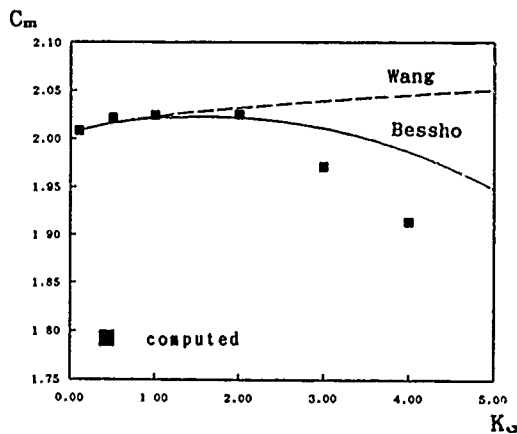


Fig.9.2 Comparison of inertia coefficient, C_m between computed results and analytical solutions

$$\begin{aligned}
 U &= \sin(2\pi t) \\
 V &= 0.01 \times \sin(4\pi t) \quad \text{for } t = 0.0 \sim 0.25 \\
 &= 0.0 \quad \text{for } t > 0.25
 \end{aligned}
 \quad (25)$$

In equation (25), the amplitude of superposed sinusoidal motion in the y-direction is set to 1/10th of equation (24) and the period the same as equation (24). There are differences between the two results qualitatively. Time histories of in-line force are shown in Fig.10. Here it should be noted that it is difficult to get the same disturbance in different water tanks, even though same experiments are performed. This is one of the reasons why experimental data scatter. Although it is almost impossible to express the disturbance in the tank numerically, we consider

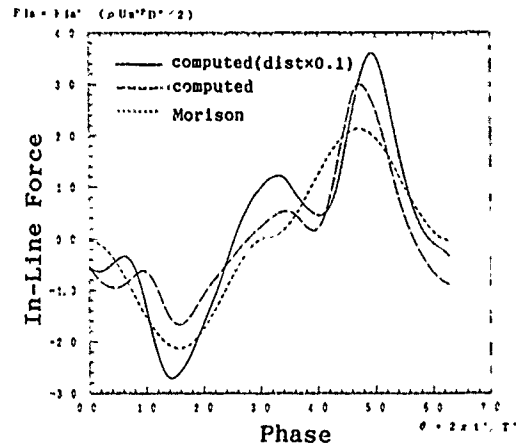


Fig.10 Effect of initial disturbance

that the difference between computed results with the different initial disturbances as shown in Fig.10 may be obtained under different experimental conditions.

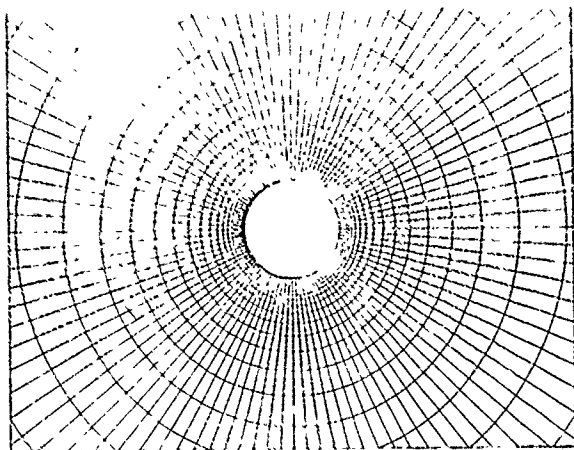
(3) Effect of total number of grid points on C_d , C_m , and flow field

The grid used in the present computation is determined by the total number and the minimum increment. Resolution of flow field by finer grid is higher, while stability of the solution is lower if the same time increment is used. Since we cannot compute so long, minimum time increment is limited. Hence, we cannot make the grid infinitely fine. Table 1 shows that C_d and C_m computed by the grid 120×50 and 140×60 are in the range of scatters of experimental data, but that those by the grid 100×30 are clearly not in the range.

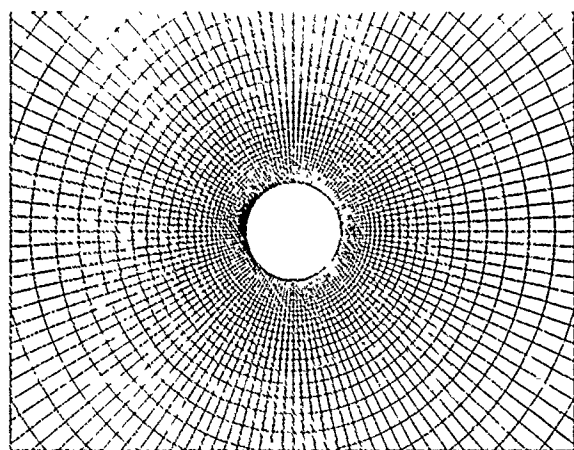
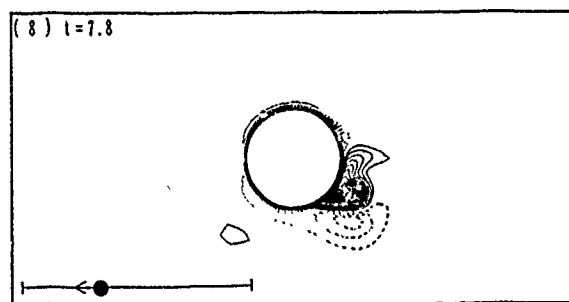
Table 1 Effect of total number of grid points on C_d and C_m
($K_o=5$, $R_o=10^4$)

	100 × 30	120 × 50	140 × 60
C_d	1.031	0.480	0.664
C_m	0.649	0.795	0.809

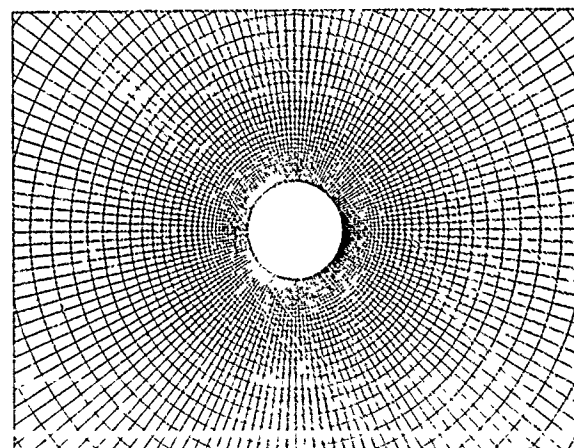
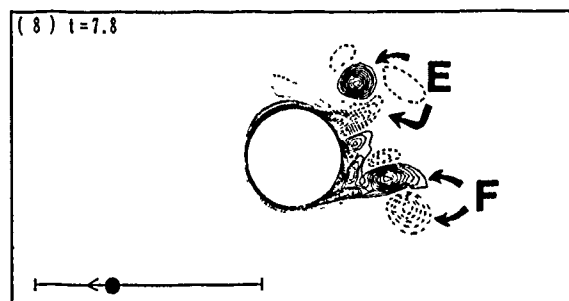
Figure 11 shows that the computed results by the grid 120×50 and 140×60 qualitatively agree with experimental data very well, but that those by the grid 100×30 do not agree with them.



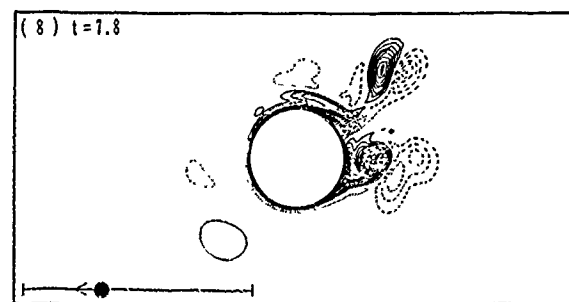
(a) 100×30



(b) 120×50



(c) 140×60



Grid near the cylinder surface

Vorticity contour

Fig.11 Effect of total number of grid points on flow field
($K_0=5$, $R_0=10^4$, $t=7.8$)

(4) Effect of minimum grid increment on C_d and C_m

We can do the same consideration as the total number of grid points. Finer grid increment near the surface of the cylinder makes the resolution of boundary layer higher, but the stability of the solution lower if the same time increment is used. Table 2 shows that the coarser and finer minimum increments than that used in the present computation do not give good results of C_d and C_m .

Table 2 Effect of minimum grid increment on C_d and C_m
($K_0=5$, $R_0=10^4$)

	$\Delta x=0.003$	$\Delta x=0.005$	$\Delta x=0.007$
C_d	0.703	0.480	0.703
C_m	0.469	0.795	0.469

(5) Effect of time increment on C_d and C_m

Through the consideration of the stability, finer time increment makes the stability of the solution higher and give a solution closer to the true one. But finer time increment makes time derivative of the residual of the continuity equation larger and the results may not suffice for the mass conservation law. Table 3 shows that C_d and C_m using $\Delta t=0.0001$ are not in the range of scatters of experimental data.

Table 3 Effect of time increment on C_d and C_m
($K_0=5$, $R_0=10^4$)

	$\Delta t=0.0001$	$\Delta t=0.0002$	$\Delta t=0.0004$
C_d	0.814	0.480	0.654
C_m	0.668	0.795	0.739

(6) Effect of the Reynolds number on C_d and C_m

The experimental data by Sarpkaya[6] and Tanaka et al.[13] indicate that C_d decreases and C_m does not vary with progression of the R_0 number. Figures 12.1 and 2 show that the computed results do not simulate the tendency.

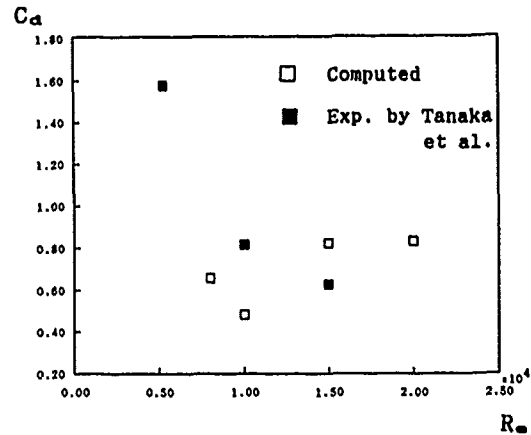


Fig.12.1 Effect of the Reynolds number on drag coefficient, C_d

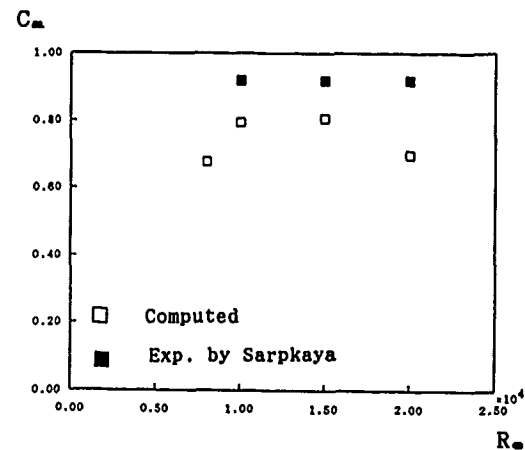


Fig.12.2 Effect of the Reynolds number on added mass coefficient, C_m

Why can we get very good solutions at $R_0=10^4$? We can consider the reason as follows. As noted earlier, the big vortices generated every half period are predominant for the flow field. Hence, in the computation at $R_0=10^4$, we can consider that 3rd order upwind scheme controls the transition to turbulence near the surface of the cylinder and the flow field outside it, including predominant vortices, is correctly estimated. For this reason, we can obtain very good results at $R_0=10^4$. Then we need to consider the effect of numerical dissipation on the solutions. At the higher Reynolds number, the local effective Reynolds number near the surface of the cylinder becomes too high for 3rd order upwind scheme to control the transition to turbulence there, and, as a result, the numerical dissipation makes the Reynolds number lower. We need to consider the cause of some errors in more detail to estimate the dependence of the Reynolds number on the flow

field.

For more precise estimate of hydrodynamic forces acting upon a circular cylinder in an oscillatory flow, the following is hereafter required;

*observations of phenomena for long periods

*simulation of three dimensional coherent structures of the flow field.

In this paper, all computation is performed using FACOM VP-100, and it takes about 70 minutes for 8 periods of the oscillation under the condition of the time increment $\Delta t = 0.0002$ which is 40000 time steps.

6 Conclusions

(1) Solutions for the flow around an oscillating circular cylinder at $R_\infty = 10000$ and $K_\infty = 5, 7$ and 10 are obtained by the direct calculation of the Navier-Stokes equations using body-fitted coordinates system, moving mesh technique, and the MAC method. The results are in excellent agreement with published experimental data quantitatively.

(2) The computed flow patterns show the 'pairing of attached vortices' and 'transverse street' at this range of K_∞ , where C_d increases and C_m decreases drastically. The change of aspects of vortices is very similar to Williamson's observation at R_∞ of the order 10^3 .

(3) Time histories of the computed inline force are in good agreement with those which are given by the Morison equation and published experimental data of C_d and C_m at $K_\infty = 5$ and 7 . They show that this computation simulates unsteady phenomena accurately every moment.

(4) Time history of the computed inline force is not odd-harmonic at all at $K_\infty = 10$.

(5) The reliability of the present computation is confirmed by the comparison of it with the analytical solutions. On the other hand, the computed results vary with total number of grid points, minimum grid increment, and time increment. But we cannot determine the best ones before getting solutions and comparing them with experimental data. In order to estimate the effect of the Reynolds number on the flow, we need to consider the cause of some errors in more detail.

(6) For more precise estimate of hydrodynamic forces around an oscillating circular cylinder, structures of the flow field must be observed for long period and regularity of it must be investigated. Since three dimensional coherent structures of the flow field may affect the regularity, we need three dimensional simulation to discuss them more completely.

The authors acknowledge some useful comments by Prof. Y. Ikeda of the University of Osaka Prefecture and Dr. Y. Kodama and Dr. T. Hino of Ship Research Institute.

References

1. Williamson, C.H.K., "Sinusoidal flow relative to circular cylinders", J. Fluid Mech. Vol.155, p.141 (1985)
2. Honji, H., "Streaked flow around an oscillating circular cylinder", J. Fluid Mech. Vol.107, p.509 (1981)
3. Tatsuno, M., and Bearman, P.W., "Flows induced by a cylinder performing oscillations at large amplitudes", J. the Flow Visualization Society of Japan. Vol.8, No.30, p.357 (1988)
4. Morison, J.R. et al., "The force exerted by surface waves on piles", J. Petroleum Tech. Vol.189, No.2, p.149 (1950)
5. Keulegan, G.H., and Carpenter, L.H., "Forces on cylinders and plates in an oscillating fluid. J. Research of the National Bureau of Standards", Vol.60, No.5, p.423 (1958)
6. Sarpkaya, T., and Isaacson, M., "Mechanics of Wave Forces on Offshore Structures", Van Nostrand Reinhold Company (1981)
7. Stokes, G.G., "On the effect of the internal friction of fluids on the motion of pendulums", Trans. Camb. Phil. Soc. Vol.9, p.8 (1851)
8. Wang, C.Y., "On the high frequency oscillating viscous flows", J. Fluid Mech. Vol.32, p.35 (1968)
9. Bessho, M., "Study of viscous flow by Oseen's scheme (4th report, two-dimensional oscillating flow without uniform velocity)", J. the Society of the Naval Architects of Japan. Vol. 161, p.42 (1987)
10. Baba, N., and Miyata, H., "High-order accurate difference solution of vortex generation from a circular cylinder in an oscillatory flow", J. Comput. Phys. Vol.69, No.2, p.362 (1987)
11. Harlow, F.H., and Welch, J.E., "Numerical calculation of time dependent viscous incompressible flow of fluid with free surface", The

Physics of Fluids. Vol.8. No.12, p.2182 (1965)

12. Kato, S., and Ohmatsu, S., "Hydrodynamic forces and pressure distributions on a vertical cylinder oscillating in low frequencies", OMAE (1989)

13. Tanaka, N., Ikeda, Y., Himeno, Y., and Fukutomi, Y., "Experimental study on hydrodynamic viscous force acting on oscillating bluff body", J. the Kansai Society of Naval Architects. Vol.179, p.35 (1980)

Appendix Relations Between Flow Around an Oscillating Circular Cylinder in a Fluid at Rest and Flow Around a Circular Cylinder Fixed in an Oscillating Flow (All quantities are dimensionally defined)

(a) Flow around an Oscillating Circular Cylinder in a Fluid at Rest

Assuming that a circular cylinder oscillates in the x-direction, the governing equations are written as follows:

$$\begin{aligned} \frac{dU}{dt} + \frac{\partial u'}{\partial t} + u' \frac{\partial u'}{\partial x} + v' \frac{\partial u'}{\partial y} \\ - \frac{1}{\rho} \frac{\partial p}{\partial x} + \nu \left(\frac{\partial^2 u'}{\partial x^2} + \frac{\partial^2 u'}{\partial y^2} \right) \\ \frac{\partial v'}{\partial t} + u' \frac{\partial v'}{\partial x} + v' \frac{\partial v'}{\partial y} \\ - \frac{1}{\rho} \frac{\partial p}{\partial y} + \nu \left(\frac{\partial^2 v'}{\partial x^2} + \frac{\partial^2 v'}{\partial y^2} \right) \end{aligned} \quad (26)$$

$$\frac{\partial u'}{\partial x} + \frac{\partial v'}{\partial y} = 0 \quad (27)$$

where $U=U(t)$ denotes the velocity of the circular cylinder, a superscript of prime the value in the coordinate system which moves with the circular cylinder, and ν the kinematic viscosity.

Boundary conditions are written as follows:

$$\begin{aligned} \begin{cases} u' = -U \\ v' = 0 \end{cases} \quad \text{at } r \rightarrow \infty \\ \begin{cases} u' = 0 \\ v' = 0 \end{cases} \quad \text{at } r = a \end{aligned} \quad (28)$$

where r denotes the distance from the center of the circular cylinder and a the radius of the circular cylinder.

(b) Flow around a Circular Cylinder Fixed in an Oscillatory Flow

Assuming that the ambient flow oscillates in the x-direction, the governing equations are written as follows:

$$\begin{aligned} \frac{\partial u}{\partial t} + u \frac{\partial u}{\partial x} + v \frac{\partial u}{\partial y} \\ - \frac{1}{\rho} \frac{\partial p}{\partial x} + \nu \left(\frac{\partial^2 u}{\partial x^2} + \frac{\partial^2 u}{\partial y^2} \right) \\ \frac{\partial v}{\partial t} + u \frac{\partial v}{\partial x} + v \frac{\partial v}{\partial y} \\ - \frac{1}{\rho} \frac{\partial p}{\partial y} + \nu \left(\frac{\partial^2 v}{\partial x^2} + \frac{\partial^2 v}{\partial y^2} \right) \end{aligned} \quad (29)$$

$$\frac{\partial u}{\partial x} + \frac{\partial v}{\partial y} = 0 \quad (30)$$

where $U=U(t)$ denotes the velocity of the oscillatory flow.

Boundary conditions are written as follows:

$$\begin{aligned} \begin{cases} u = -U \\ v = 0 \end{cases} \quad \text{at } r \rightarrow \infty \\ \begin{cases} u = 0 \\ v = 0 \end{cases} \quad \text{at } r = a \end{aligned} \quad (31)$$

In infinitely far field from the circular cylinder, the velocity is written as

$$\begin{cases} u = -U(t) \\ v = 0 \end{cases} \quad (32)$$

Thus, equation (29) in the far field becomes the following equations:

$$\frac{dU}{dt} = \frac{1}{\rho} \frac{\partial P_{inf}}{\partial x} \quad (33.a)$$

$$\frac{\partial P_{inf}}{\partial y} = 0 \quad (33.b)$$

where P_{inf} denotes the pressure in the far field, i.e. the pressure in the uniformly oscillatory flow. Equation (33.b) represents that the pressure in the oscillatory flow, P_{inf} , is a function of only x and t , i.e. $P_{inf} = P_{inf}(x, t)$.

The pressure is divided into two parts as follows:

$$p = P_{inf} + P_{dist} \quad (34)$$

where P_{dist} denotes the pressure due to the disturbance caused by a circular cylinder. Using equations (33) and

(34), equation (29) is rewritten as follows:

$$\begin{aligned} \frac{dU}{dt} + \frac{\partial U}{\partial t} + u \frac{\partial U}{\partial x} + v \frac{\partial U}{\partial y} \\ = - \frac{1}{\rho} \frac{\partial P_{dist}}{\partial x} + \nu \left(\frac{\partial^2 U}{\partial x^2} + \frac{\partial^2 U}{\partial y^2} \right) \\ \frac{\partial V}{\partial t} + u \frac{\partial V}{\partial x} + v \frac{\partial V}{\partial y} \\ = - \frac{1}{\rho} \frac{\partial P_{dist}}{\partial y} + \nu \left(\frac{\partial^2 V}{\partial x^2} + \frac{\partial^2 V}{\partial y^2} \right) \end{aligned} \quad (35)$$

Equation (26) is the same form as equation (25). The only difference between the flow(a) and the flow(b) is that the pressure includes the additional term P_{int} whose gradient is required to accelerate the undisturbed flow in the flow(b). Integrated around the cylinder, P_{int} gives rise to an inertia force, which is $\rho (\pi a^2) \partial U / \partial t$ per unit length. The inertia coefficient, C_m , which is defined in the flow(b), is related to the added mass coefficient, C_a , which is defined in flow(a) as follows:

$$C_m = 1 + C_a \quad (36)$$

Numerical and Analytical Investigations of a Stationary Flow past a Self-Propelled Body

N. P. Moshkin
Institute of Theoretical and Applied Mechanics
Novosibirsk, USSR
V. V. Pukhnachov and V. L. Sennitskii
Lavrentyev Institute of Hydrodynamics
Novosibirsk, USSR

Abstract

A stationary viscous incompressible liquid flow past a body is considered. The liquid velocity distribution on the surface of the body is prescribed so that the total discharge through it equals zero. The velocity vector tends to a nonzero constant vector at infinity. The following equations are to be fulfilled:

$$\begin{aligned} \vec{S} &= 0, & (*) \\ \vec{T} &= 0, & (**) \end{aligned}$$

Here \vec{S} and \vec{T} are, respectively, the momentum and the moment of momentum, transferred by the body to the liquid (for two-dimensional flows, \vec{S} and \vec{T} are the above-mentioned values, related to the unit length). These conditions form the boundary-value problem for the Navier-Stokes equations, which we call the problem of stationary flow past a self-propelled body. Though the problem of the flow past of a self-propelled body has a natural origin (self-propulsion executes inhabitants, ships and airplanes) and though it has a practical importance, the number of works concerning it is very limited. This work contains the results of investigations of different models of a self-propulsion of a body in a liquid obtained by analytical, numerical and experimental methods.

§ 1.

1.1 Let Σ be the bounded closed surface in R^3 and Ω be the domain external with respect to Σ . The problem of defining vector-function $\vec{v}(\mathbf{x})$ (the difference between flow velocity at the point \mathbf{x} , and constant velocity at infinity, $\vec{e}_1 = (1, 0, 0)$) and scalar function $p(\mathbf{x})$ (pressure) which satisfy the stationary system of Navier-Stokes equations in the domain Ω :

$$\Delta \vec{v} - \text{Re } \partial \vec{v} / \partial x_1 - \nabla p = \text{Re } \vec{v} \cdot \nabla \vec{v}, \quad (1.1)$$

$$\nabla \cdot \vec{v} = 0,$$

and the following boundary conditions:

$$\vec{v} = \vec{a}(\mathbf{x}), \quad (1.2)$$

$$\vec{v} \rightarrow 0 \quad (1.3)$$

when $\mathbf{x} \rightarrow \infty$.

Here \vec{a} is the vector-function satisfying the condition

$$\int_{\Sigma} \vec{a} \cdot \vec{n} d\Sigma = 0, \quad (1.4)$$

whilst still arbitrary in other respects,

\vec{n} is the unit vector of the external normal to the boundary of the domain Ω . Equations (1.1) have been written down in dimensionless variables, so that $\text{Re} = V_{\infty} l / \nu$ is the Reynolds number, ν is the kinematic viscosity coefficient, l is the characteristic linear scale (e.g., $l = \text{diam. } \Omega$). The value of V_{∞} (velocity of flow past) is a natural velocity scale, and the pressure scale is assumed equal to $\rho V_{\infty} \nu / l$, where ρ is the liquid density.

Further the surface of Σ will be assumed to belong to the Hölder class $C^{2+\alpha}$, $0 < \alpha < 1$, and the components of vector \vec{a} - to belong to the class $C^{2+\alpha}(\Sigma)$. Problem (1.1)-(1.4) with the fixed function \vec{a} was considered in a great number of works. The most significant results were obtained by R. Finn [8] and K.I. Babenko [2]. If $\vec{a} = -\vec{e}_1$, we come to a classic problem of a flow past a body with an unmovable impermeable boundary Σ . It is well-known that in this case the resistance force of the liquid exerted on the body differs from zero. Thus, to realize a stationary regime of flow past a body, it is necessary to confine it to the liquid flow by external forces. The classic problem of flow

past a body therefore should be called the problem of flow past a towered body.

Here our particular emphasis will be placed on the problem of momentumless flow past a body, or problem (1.1) - (1.4) with the additional condition (*). In the terms \vec{v} , p the latter is expressed by the equality

$$\vec{F} \equiv \int_{\Sigma} [-P\vec{v} \cdot \vec{n} + \text{Re}\vec{v}(\vec{v} + \vec{e}_1) \cdot \vec{n}] d\Sigma = 0 \quad (1.5)$$

Here \vec{F} is the resistance force, $P\vec{v}$ is the stress tensor corresponding to the velocity and pressure fields (\vec{v} and p , respectively), having the elements $(Pv)_{ij} = -p\delta_{ij} + \partial v_i / \partial x_j + \partial v_j / \partial x_i$ (1, $j = 1, 2, 3$).

It is clear that in the model under consideration condition (*) may be provided only by the mobility and (or) the permeability of the body boundary Σ . In the latter case it is natural to be expected that the total discharge of a liquid through the body surface is equal to zero, that is expressed by (1.4). The condition of momentumless flow past a body (**) is not imposed here upon the solution.

It is well-known that with fixed \vec{a} problem (1.1)-(1.4) has at least one solution for any Reynolds number, $\text{Re} \geq 0$ [2, 8, 14]. With low Re , its solution is unique [2]. From here it follows that the problem of momentumless flow past a body, (1.1)-(1.5) is solvable, generally speaking, only if the additional conditions on the function $\vec{a}(\vec{x})$ are fulfilled. In other words, this problem is to be considered as a problem of a joint definition of functions \vec{v} , p and \vec{a} from the relations (1.1)-(1.5). In this case condition (1.5), equivalent to three scalar relations, admits a wide arbitrariness in choosing the function \vec{a} , which may be considered as a determining function. It should be noted that by virtue of the law of momentum, condition (1.5) is equivalent to the equality to zero of the liquid pulse flow through any control surface covering Σ , in particular, an infinitely distanced control surface [18].

1.2. The existence of the solution to the problem of momentumless flow past a body has not been considered so far. The existence problem may be solved rather effectively in the simplest case when the Reynolds number is equal to zero [19]. Let us denote system (1.1) when $\text{Re} = 0$ (Stokes system) by (1.1) and the relation (1.5) when $\text{Re} = 0$ by (1.5)°. System (1.1)°, conditions (1.2)

- (1.4) and equality (1.5)° form the problem which will be denoted by (1.1)°-(1.5)° and called the problem of momentumless flow past a body in the Stokes approximation.

In contrast to (1.1)-(1.5), problem (1.1)°-(1.5)° is linear, and the Stokes operator generated by system (1.1)° is a self-conjugated one [14]. The above-mentioned circumstances make it possible to find an effective solution of problem (1.1)°-(1.5)° in terms of eigenfunctions of some spectral problem. It may be formulated as follows.

It is required to find number λ and vector-function $\vec{\phi}(\vec{x}) \neq 0$, determined on the surface Σ , which satisfies condition (1.4), from the relation

$$\Delta \vec{\phi} = \lambda \vec{\phi}$$

Here Δ denotes a linear operator, which puts in correspondence with function $\vec{\phi}$ the value of the trace of the stress vector $P\vec{v}$ on the surface Σ , calculated from the solution \vec{v} , p of problem (1.1)°-(1.5)°, where $\vec{a} = \vec{\phi}$. Operator Δ , initially determined on the functions $\vec{\phi} \in C^{2+\alpha}(\Sigma)$, admits a self-conjugated expansion up to the operator, acting to $H^{-1/2}(\Sigma)$ from $H^{1/2}(\Sigma)$. A totality of the trace of the functions $\vec{u} \in H^1(\Omega)$ on the surface Σ are denoted by $H^{1/2}(\Sigma)$ and the closure in the Dirichlet integral norm of a set of solenoidal vector-functions, smooth in Ω , and equal to zero at sufficiently high values of $|\vec{x}|$ is denoted by $H^{1/2}_0(\Sigma)$. The space $H^{-1/2}(\Sigma)$ is conjugate with respect to $H^{1/2}(\Sigma)$. Using the theory, developed in [15], it is possible to find the following properties of operator Δ : (i) it has an inverse Δ^{-1} , which is continuous and self-conjugated; (ii) the spectrum of operator Δ is discrete and finite-fold; (iii) all the eigenvalues $\lambda_1 < \lambda_2 < \lambda_3 \dots$ are positive; (iv) $\lambda_k \rightarrow \infty$ when $k \rightarrow \infty$; the eigenfunctions $\vec{\phi}_k$ and $\vec{\phi}_l$ corresponding to the eigenvalues λ_k and $\lambda_l \neq \lambda_k$, are orthogonal both in matrix $L_2(\Sigma)$ and that generated by a scalar product $(\Delta^{1/2}\vec{\phi}, \Delta^{1/2}\vec{\phi})$. The totality of eigenfunctions $\{\vec{\phi}_k\}$ forms a full system both in $L_2(\Sigma)$ and $H^{1/2}(\Sigma)$.

Now it is not difficult to formulate the solution algorithm for the problem of momentumless flow past a body in the Stokes approximation. Let $a_k = (\vec{a}, \phi_k)$ denote the Fourier coefficients of expansion of the function $\vec{a}(\vec{x})$ in basis $\{\vec{\phi}_k\}$, orthonormalized to $L_2(\Sigma)$. Then the condition (1.5)° may be written as follows:

$$\sum_{k=1}^{\infty} (\lambda_k a_k \int_{\Sigma} \varphi_{k,i} d\Sigma) = 0 \quad (i = 1, 2, 3), \quad (1.6)$$

where $\varphi_{k,i}$ is the i -th component of vector $\vec{\varphi}_k$. Condition (1.4) means that

$$\sum_{k=1}^{\infty} (a_k \int_{\Sigma} \vec{\varphi}_k \cdot \vec{n} d\Sigma) = 0. \quad (1.7)$$

Let us choose an arbitrary element $\vec{a} \in H^{1/2}(\Sigma)$ satisfying conditions (1.6), (1.7) and then solve problem (1.1) - (1.5). In so doing the velocity vector \vec{v} is defined one-valued, and the pressure p is defined accurate to the additive constant. Thus, in the solution of (1.1) - (1.5), being the problem of determining functions \vec{v} , p and \vec{a} , there is a functional arbitrariness. Therefore, determining the function \vec{a} from the condition of minimum power functional is considered to be natural:

$$J = \int_{\Sigma} \vec{v} \cdot P\vec{v} \cdot \vec{n} d\Sigma.$$

The value of J is equal to the work expended per unit line in sustaining a stationary self-motion regime.

In the general case the problem of determining minimum J under certain natural restrictions upon the function \vec{a} is solved by the method of Lagrange indefinite coefficients. Let us consider the examples of such restrictions: the function $\vec{a} + \vec{e}_1$ has the support Σ which does not coincide with the whole surface of Σ (physically the case when the region $\Sigma' \subset \Sigma$ is sufficiently small is of interest); function $\vec{a} + \vec{e}_1$ has a zero normal component (the boundary of a self-moving body is impermeable); function $\vec{a} + \vec{e}_1$ has a zero tangential component (the body surface is unmovable). If the surface Σ is a sphere, the minimization problem of functional J for the second and third type of the above-mentioned restrictions is solved explicitly with the use of the results obtained in [10]. In both cases the minimum of J is achieved on the functions \vec{a} , corresponding to the regime of potential flow past a body. It is unknown if this property of extremals of functional J holds for an arbitrary surface Σ .

The matter of solvability of problem (1.1) - (1.5) when $Re > 0$ is rather complicated. However, it is hoped that its solution may be positive for low Reynolds numbers. The solution asymptotics for a classical problem of flow past a body ($\vec{a} = -\vec{e}_1$) when $Re \rightarrow 0$ [9] is the basis for such an optimism.

1.3. Now let us consider an asymptotical behaviour of the solution to problem (1.1) - (1.5) when $r = |\vec{x}| \rightarrow \infty$. For now, let us ignore the additional condition (1.5) and recall that the existence theorem for (1.1) - (1.4) "as a whole" is solid in the class of vector-functions \vec{v} having Dirichlet finite integral [14],

$$\int_{\Omega} \nabla \vec{v} : \nabla \vec{v} dx < \infty \quad (1.8)$$

In [2] it was established that any solution of the above-mentioned problem satisfying the inequality (1.8) admits the estimate

$$|\vec{v}(\mathbf{x})| \leq Cr^{-1/2-\varepsilon} \text{ when } r \rightarrow \infty \quad (1.9)$$

with some positive constants C and ε . As was shown in [8], any solution of problem (1.1) - (1.4) satisfying inequality (1.9) has an asymptotical behaviour

$$\vec{v}(\mathbf{x}) = \vec{F} \cdot \mathbf{E}(\mathbf{x}) + \vec{\zeta}(\mathbf{x}). \quad (1.10)$$

Here \vec{F} is constant vector determined by the formula (1.5), and $\vec{\zeta}(\mathbf{x})$ is the remaining term, for which the following estimate has been obtained (r is high):

$$|\vec{\zeta}| \leq C_1 r^{-3/2+\varepsilon} (1+s)^{-1+\varepsilon}, \quad (1.11)$$

Here $s = r - x$, $\varepsilon > 0$ is arbitrarily small, and $C_1 = \text{const.} > 0$. Symbol $\mathbf{E}(\mathbf{x})$ denotes the fundamental tensor of Oseen system, corresponding to (1.1). The expressions for the elements of tensor \mathbf{E} may be found in [8].

It follows from (1.10), (1.11) that there is a paraboloidal region of the wake in the direction of \vec{e}_1 , inside of which $\vec{v} = O(r^{-1})$. Beyond any circular cone having the axis directed along \vec{e}_1 , $\vec{v} = O(r^{-2})$. The field asymptotics terms $\vec{v}(\mathbf{x})$ of the order of $r^{-3/2}$ obtained in [3] on the assumption of the collinearity of vectors \vec{F} and \vec{e}_1 . (This assumption is fulfilled, for example, in the case of axisymmetrical flow past a surface of revolution Σ , thereby the condition (**) being also fulfilled). In [3, 6] the velocity vortex behaviour at great distances from the body is investigated, and the vortex is shown to decrease exponentially outside the wake.

Formula (1.10) means that far from the towed body, the velocity field disturbance (accurate to the smalls of higher order) will be as that of Oseen flow "flowing past" a concentrated force \vec{F} .

The velocity field asymptotics in the problem of momentumless flow past a body proved to be determined by a much higher number of functionals

characterizing both the body shape and the way of realization of self-motion regime. The basic result may be formulated as follows [20].

Let \vec{v} , p be the solution of problem (1.1)-(1.4) from the class (1.8) satisfying the additional condition (1.5). Then when $r \rightarrow \infty$ the asymptotical representation of $\vec{v}(x)$ in the form

$$\vec{v}(x) = R : DE(x) + Q : \nabla E(x) + \vec{\eta}(x). \quad (1.12)$$

is valid. Here $R = (R_{ij})$, $Q = (Q_{ij})$ are the constant tensors ($i, j = 1, 2, 3$). The elements of tensor R are expressed explicitly in the terms of function $\vec{a}(x)$. Symbols DE and ∇E denote the third-rank tensors having the elements

$$(DE)_{ijk} = \frac{1}{2} \left(\frac{\partial E_{ik}}{\partial x_j} + \frac{\partial E_{jk}}{\partial x_i} \right),$$

$$(\nabla E)_{ijk} = \frac{\partial E_{jk}}{\partial x_i},$$

$i, j, k = 1, 2, 3$. Summarizing in consolidation $R : DE$, $Q : \nabla E$ is made with respect to indices i and j . Function $\vec{\eta}(x)$ admits the estimate

$$|\vec{\eta}(x)| \leq C_2 r^{-2+\varepsilon} (s+1)^{-1/2} \quad (1.13)$$

when $r \rightarrow \infty$, where ε and C_2 are the positive constants, ε being arbitrarily small, $s = r - x$.

Formula (1.12) is derived on the basis of integral representation of problem (1.1)-(1.3) obtained in [9]. To estimate the volume integral

$$\vec{N}(x) = \int_{\Omega} \vec{v}(y) \cdot \vec{v}(y) \cdot \nabla E(x - y) dy$$

when $r \rightarrow \infty$, the results of [3] have been used.

According to (1.12), (1.13), in the regime of momentumless flow past a body we have $\vec{v} = O(r^{-3/2})$ in a paraboloidal region of the trail and $\vec{v} = O(r^{-5/2+\varepsilon})$ beyond any cone having the axis \vec{e}_1 . Thus, a quicker decrease in velocity disturbance at great distances from a self-moving body, as compared to towed one, is evident. Representation (1.12) also means that (at least over the wake region) the main terms of velocity field asymptotics in the problem of momentumless flow past a body are characterized by 18 parameters, they are the elements of tensors R and Q .

In an axisymmetrical case the number of these parameters decreases to eight. Identification of the elements of tensor

Q being some functionals of the solution to problem (1.1)-(1.5) is of particular interest. This problem has not been solved so far.

One of paradoxical results, related to the classical problem of flow past a body for the Navier-Stokes equations, is as follows. Let in (1.2) $\vec{a} = -\vec{e}_1$ (This means immobility and impermeability of the body boundary). Then for any solution \vec{v} , p of problem (1.1)-(1.3) satisfying the condition (1.8) we have

$$\int_{\Omega} |\vec{v}|^2 dx = \infty$$

Such a statement related to the energy of disturbed motion in the problem of viscous flow past a body first appeared in [7].

It is obvious that a self-moving cannot contribute such a great disturbance into a flow. An appropriate exact formulation is as follows. Let \vec{v} , p be the solution of problem (1.1)-(1.4) satisfying the additional conditions (1.5), (1.8). Then

$$\int_{\Omega} |\vec{v}|^2 dx < \infty \quad (1.14)$$

The property of the solution of the problem of momentumless flow past a body expressed by inequality (1.14) distinguishes it among all the possible solutions of problem (1.1)-(1.4) if function \vec{a} entering it is varied. We hope that this property may be used to investigate the existence of the solution of problem (1.1)-(1.5), if the latter is considered as some optimization problem.

The two notes are to be made in connection with the velocity field asymptotics at great distances from a self-moving body. The first of them deals with the velocity vortex behaviour with increasing the distance from a body. When $r \rightarrow \infty$, the vorticity in the solution of problem (1.1)-(1.5) decreases quicker than in a classical problem of flow past a body both inside and outside of the wake [6]. In the exceptional cases the wake may be absent. In [16] such a situation is illustrated by a plane potential viscous flow past a self-moving "body". Its boundary consists of two symmetric coupled components, on each of them a normal velocity component being equal to zero, and a tangential one being constant.

The second note is connected with the velocity asymptotics in a turbulent flow regime. In this case, based on the consideration of [20] and additional assumptions related to the Reynolds stress behaviour when $r \rightarrow \infty$ (for a self-moving body these assumptions are discussed in [5]), it is possible to obtain representation (1.12) for the averaged velocity field. However, here the elements of tensors R and Q are the functionals of the solution of unclosed system of Reynolds equations. These equations are treated as the Navier-Stokes equations with the density of external mass forces $\vec{g} = -2 \cdot Re \cdot \text{div } \Pi$ where Π is the Reynolds stress tensor having the elements $\Pi_{ij} = \overline{v_i' v_j'}$ ($i, j = 1, 2, 3$). Here condition (*) changes its form in comparison with (1.15) and is as follows:

$$\int_{\Sigma} [-P \vec{n} \cdot \vec{n} + Re \vec{v} \cdot (\vec{v} + \vec{e}_1) \cdot \vec{n} + Re \Pi \cdot \vec{n}] d\Sigma = 0.$$

§ 2.

2.1. Liquid flows at great distances from self-propelled and non-self-propelled bodies can be significantly different.

Let us consider the problems of a stationary flow of a viscous incompressible liquid past self-propelled bodies [21, 22].

a). The body is a circular cylinder with a moving body. The cylinder axis coincides with the axis Z of the system of the rectangular coordinates X, Y, Z . The liquid flow is plane and symmetrical in relation to the axis X in the plane X, Y . The body boundary moves so that the correlation (*) is fulfilled. The correlation (**) is fulfilled by the reason of the symmetry of the flow in relation to the axis X .

The Navier-Stokes and the continuity equations and the conditions on the cylinder boundary and at infinity have the following form:

$$\begin{aligned} (\vec{v} \cdot \nabla) \vec{v} &= -p + \frac{1}{Re} \Delta \vec{v}, \quad \nabla \cdot \vec{v} = 0, \\ \vec{v} &= \lambda f \vec{e} \text{ for } r = 1, \quad \vec{v} \rightarrow \vec{i} \text{ for } r \rightarrow \infty, \end{aligned} \quad (2.1)$$

where $\vec{v} = \vec{V}/V_\infty$ (\vec{V} is the liquid velocity; V_∞ is the X -component of the liquid velocity \vec{V} at infinity ($\vec{V} = (V_\infty, 0, 0)$; $V_\infty > 0$); $p = P/(\rho V_\infty^2)$ (P is the pressure in the liquid; ρ is the liquid density); $r = \sqrt{X^2 + Y^2}/a$ (a is the radius of the cylinder);

$\vec{i} = (1, 0, 0)$; $Re = a V_\infty / \nu$ is the Reynolds number (ν is the kinematic coefficient of the liquid viscosity); λ is a function of Re ; f is an odd function of the angle θ between the vectors \vec{i} and $X \vec{i} + Y \vec{j}$ ($\vec{j} = (0, 1, 0)$; $f = \sum_{m=1}^{\infty} f_m \sin m \theta$; f_m are constants; $f_1 \neq 0$; $f_2 \neq 0$); $\vec{e} = \vec{k} \times \vec{n}$ ($\vec{k} = (0, 0, 1)$; \vec{n} is the unit external normal to the cylinder boundary).

The dependences f on θ and λ on Re are prescribed so that $\vec{S} = 0$.

In [21] the problem (2.1) was solved approximately for low Re . The following asymptotical formula for the liquid velocity at great distances from the body was obtained:

$$\vec{v} \sim \vec{i} \left[1 + \frac{2 \pi^{1/2} f_1 a V_\infty^{1/2}}{X^{3/2}} \left(1 - \frac{V_\infty Y^2}{2 \nu X} \right) \exp \left(- \frac{V_\infty Y^2}{4 \nu X} \right) \right] \quad (2.2)$$

for $X/a \rightarrow +\infty$ and constant $Y^2/(aX), Re$. In accordance with (2.2) for the plane flow past a self-propelled body, the disturbance of the liquid velocity vanishes by the law $X^{-3/2}$ (for the plane flow past a body which receives from the liquid per unit length per unit time a non-zero momentum the disturbance of the liquid velocity vanishes by the law $X^{-1/2}$ [5]). The formula (2.2) has such a form as the formula for the velocity of plane liquid flow far from a self-propelled body founded in [5].

b). The body is a ball with a liquid-permeable boundary. The ball centre coincides with the origin of the coordinates X, Y, Z . The liquid flow is symmetrical in relation to the axis X and is non-swirling around it. On the body boundary the liquid velocity component normal to it is distributed so that the liquid mass flux through this boundary equals zero and the correlation (*) is fulfilled. The correlation (**) is fulfilled by the reason of the non-swirling of the flow around the axis X .

The Navier-Stokes and the continuity equations and the conditions on the ball boundary and at infinity have the following form

$$(\vec{v} \cdot \nabla) \vec{v} = -\nabla p + \frac{1}{Re} \Delta \vec{v}, \quad \nabla \cdot \vec{v} = 0, \quad (2.3)$$

$\vec{v} = \lambda f \vec{n}$ for $r = 1$, $\vec{v} \rightarrow \vec{i}$ for $r \rightarrow \infty$, where $r = \sqrt{X^2 + Y^2 + Z^2}/a$ (a is the radius of the ball); λ is a function of Re ; f is a function of the angle θ between the vectors \vec{i} and

$X\vec{i} + Y\vec{j} + Z\vec{k}$ ($f = \sum_{m=0}^{\infty} f_m P_m(\cos \theta)$); f_m - are constants; $f_1 \neq 0$; $f_2 \neq 0$; P_m are the polynomials of Legendre).

The dependences f on θ and λ on Re are prescribed so that $S = 0$.

In [22] the problem (2.3) was solved approximately for low Re . The following asymptotical formula for the liquid velocity at great distances from the body was obtained:

$$\vec{V} \sim \vec{V}_{\infty} \left[1 + \frac{3 f_2 a^2}{f_1 X^2} \left(1 - V_{\infty} \frac{Y^2 + Z^2}{4 v X} \right) \times \right. \\ \left. \times \exp \left(- V_{\infty} \frac{Y^2 + Z^2}{4 v X} \right) \right], \quad (2.4)$$

for $X/a \rightarrow +\infty$ and constant $(Y^2 + Z^2)/(aX)$, Re .

In accordance with (2.4) for the axisymmetrical flow past a self-propelled body the disturbance of the liquid velocity vanishes by the law X^{-2} (for the axisymmetrical flow past a body which receives from the liquid per unit time a non-zero momentum the disturbance of the liquid velocity vanishes by the law X^{-1} [5]).

2.2. A propeller work can significantly affect a liquid flow near a body at distances which do not exceed its several transverse dimensions. This may be used to organize required liquid flow around a body (for example, a flow with closed streamlines).

Let us consider the problem of a stationary flow of viscous incompressible liquid past a pair of rotating cylinders (a pair of identical parallel circular cylinders rotating around their axes with opposite angular velocities) [23]. The axes of the cylinders are parallel to the axis Z and intersect the plane X, Y at points $X = 0, Y = h$ and $X = 0, Y = -h$. The liquid flow is plane and symmetrical in relation to the axis X in the plane X, Y .

The Navier-Stokes and the continuity equations and the conditions on the boundaries of the cylinders and at infinity have the following form:

$$(\vec{V} \cdot \nabla) \vec{V} = -\nabla p + \frac{1}{Re} \Delta \vec{V}, \quad \nabla \cdot \vec{V} = 0, \\ \vec{v} = -k \times \vec{r}_+ \text{ for } |\vec{r}_+| = 1, \vec{v} = k \times \vec{r}_- \quad (2.5)$$

for $|\vec{r}_-| = 1, \vec{V} \rightarrow \varepsilon \vec{i}$ for $r \rightarrow \infty$,

where $\vec{v} = \vec{V}/(\Omega a)$ (Ω is the module of the angular velocities of the cylinders; a is the radius of the

cylinders); $p = P/(\rho \Omega^2 a^2)$; $r = \sqrt{X^2 + Y^2}$ ($x = X/a, y = Y/a$); $\vec{r}_+ = \vec{r} + (y - 1/(2\varepsilon))\vec{j}$; $\vec{r}_- = \vec{r} + (y + 1/(2\varepsilon))\vec{j}$; $\varepsilon = a/(2h)$; $Re = a^2 \Omega / \nu$ is the Reynolds number.

In [23] the problem (2.5) was solved approximately for small ε . It was ascertained that in the considered approximation the pair of rotating cylinders is a self-propelled body.

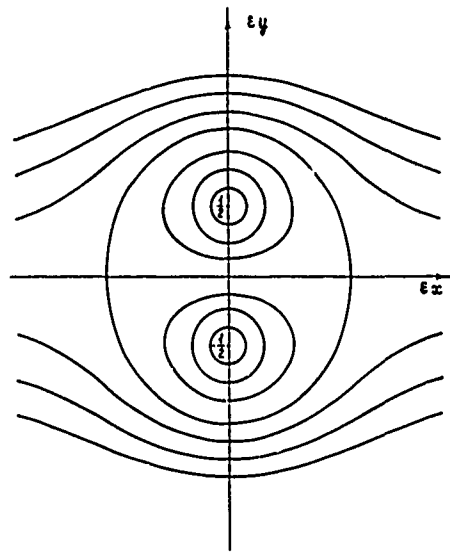


Fig. 1

In Fig. 1 the pattern of streamlines of the flow around the cylinders is displayed (the sections of the cylinders by the plane $\varepsilon X, \varepsilon Y$ are represented by the points $\varepsilon X = 0, \varepsilon Y = 1/2$ and $\varepsilon X = 0, \varepsilon Y = -1/2$; the cylinders are surrounded by the liquid layer which is streamed continuously by the liquid moving from infinity). This flow around the cylinders is realized by the motion of their boundaries, i.e. by the propeller work.

The problem of a stationary flow of a viscous incompressible liquid past a pair of rotating cylinders was considered in [23] in connection with the problem of decreasing the energy required for a body to propel in a liquid. In connection with the latter problem the motion of a pair of rotating cylinders in a liquid was also investigated experimentally [24, 25]. The measurements showed that the self-propelling of the cylinders was energetically non-profitable and a reduction of the energy which was necessary for their propelling

could be achieved when the cylinders simultaneously rotated and were affected by an external force (the propeller worked but not in a self-propelling regime).

The power N which is necessary for a pair of cylinders to propell is the sum of two quantities:

$$N = FQ + W,$$

where F is the external force acting onto the cylinders; Q is the velocity of the pair of cylinders; W is the power which is necessary for the cylinders to rotate.

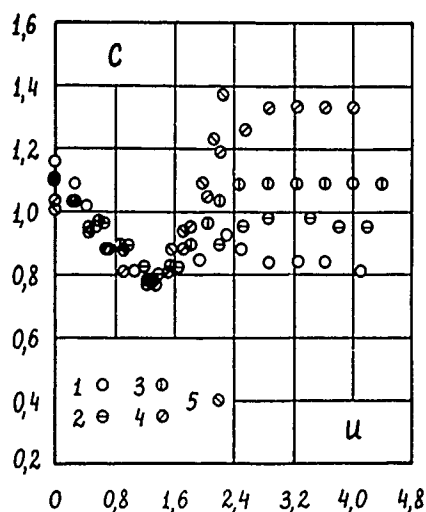


Fig. 2

In Figs. 2, 3 the data obtained by measurements on the dependences $c = F/(2La\rho Q^2)$ and $w = W/(2La\rho Q^3)$ on $u = \Omega a/Q$ are displayed (L is the length of the cylinders; symbols 1-5 correspond to $\varepsilon = 0.45; 0.4; 0.35; 0.3; 0.25$) [25]. In accordance with these data, the most energy profitable propelling is realized at $u \approx 1.3$. The power which is necessary for this propelling of the cylinders is approximately, 30% of the power required for the propelling of the non-rotating cylinders.

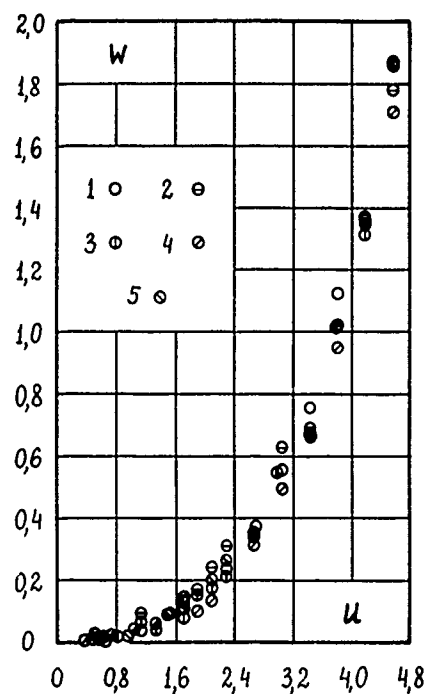


Fig. 3

§ 3

3.1. Let us come over to the problem of numerical modelling of momentumless flow past a body. It is based on the Navier-Stokes equations with the use of numerical methods [1,4,11,13]. The two cases are considered when relation (*) is fulfilled. In one of them (downstream), there is a surface S behind the ball (a part of sphere with a greater radius). The liquid flows over S and gets thereby an additional pulse. In the other case the ball surface is permeable. On one its part, between two cones with the divergence semi-angles Q_1 , Q_2 and a mutual axis $\theta = \pi$, the liquid is sucked in, and on the other its part, "cut" by a cone $Q_3 \leq \pi$ the same quantity of the liquid is returned to the flow.

The other way to fulfil the condition (*) are also possible, for example, by prescribing a self-consistent distribution of volume forces, localized in a small region behind the body. A numerical solution of the problem of momentumless flow past an extended ellipsoid of

revolution was obtained in this state-
ment in [12].

The solution of the problem of flow
past a self-moving body becomes more
complicated due to nonlocality of con-
dition (*). In the present paper a sta-
tionary solution was found when solving
the nonstationary Navier-Stokes equa-
tions. In the spherical coordinate sys-
tem they have the form:

$$\begin{aligned} \frac{\partial u}{\partial t} + (u - \cos \theta) \frac{\partial u}{\partial r} + \frac{(v + \sin \theta) \partial u}{r \partial \theta} - \frac{v(v + \sin \theta)}{r} - \\ - r^2 \frac{W^2}{r} = \frac{\partial P}{\partial r} + \frac{1}{Re} \left[\Delta u - \frac{2u}{r^2} - \frac{2}{r^2 \sin \theta} \frac{\partial}{\partial \theta} \times \right. \\ \times (\sin \theta \cdot v) \left. \right], \frac{\partial v}{\partial t} + (u - \cos \theta) \frac{\partial v}{\partial r} + \frac{v + \sin \theta}{r} \frac{\partial v}{\partial \theta} + \\ + \frac{u(v + \sin \theta)}{r} - r^2 \frac{W^2 \cot \theta}{r} - \frac{1}{r} \frac{\partial P}{\partial \theta} + (3.1) \\ + \frac{1}{Re} \left[\Delta v - \frac{2v}{r^2 \sin^2 \theta} + \frac{2}{r^2} \frac{\partial u}{\partial \theta} \right], \frac{\partial W}{\partial t} + (u - \cos \theta) \frac{\partial W}{\partial r} + \\ + \frac{v + \sin \theta}{r} \frac{\partial W}{\partial \theta} + \frac{u - \cos \theta}{r} \frac{\partial (v + \sin \theta) W \cot \theta}{r} - \frac{1}{Re} \times \\ \times (\Delta W - \frac{W}{r^2 \sin \theta}), \frac{1}{r^2} \frac{\partial}{\partial r} (r^2 u) + \frac{1}{r \sin \theta} \frac{\partial}{\partial \theta} \times \\ \times (\sin \theta \cdot v) = 0, Re = \frac{a V_\infty}{\nu}; \Gamma = \frac{a \omega}{V_\infty}, \\ (\Delta = \frac{1}{r^2} \frac{\partial}{\partial r} (r^2 \frac{\partial}{\partial r}) + \frac{1}{r^2 \sin \theta} \frac{\partial}{\partial \theta} \times \\ \times (\sin \theta \frac{\partial}{\partial \theta})), \end{aligned}$$

Here u, v and W are the projections
of the velocity vector to r, θ and
 ϕ directions, respectively, a is the
sphere radius, V_∞ is the modulus of
inflowing flow velocity, ω is the
characteristic value of swirling by the
propeller model. Equations (3.1) have
been written down in dimensionless va-
riables. The values of $a, V_\infty, \rho V_\infty^2,$
 $a \omega$ have been chosen as the scales
of length, velocity, pressure and
swirling. The boundary conditions are
prescribed as follows:

The sphere surface $r = 1$;

$$u = u_0(\theta) + \cos \theta, \quad (3.2)$$

$$v = -\sin \theta, W = W_0(\theta)$$

The axis of symmetry $\theta = 0, \theta = \pi$:

$$\partial u / \partial \theta = 0, v = 0, W = 0; \quad (3.3)$$

The conditions on the sphere having a
large enough radius $r = r_s$:

$$v = 0, W = 0, p = 0; \quad (3.4)$$

The conditions on the surface

$$S = \{ (r, \theta): r = r_s, \theta_s \leq \theta \leq \pi \};$$

$$\begin{aligned} v^+ = v^- = -\sin \theta, u^+ = u^-, \\ p^+ - p^- = [p], W^+ = W^- = W_s(r_s, \theta). \end{aligned} \quad (3.5)$$

Here an upper index + or - states to
the side of the surface S (e.g.

$$v^+(r_s, \theta) = \lim_{r \rightarrow r_s + 0} v(r, \theta)).$$

The considerations dealing with the va-
lidity of such a statement can be

found in [13].

3.2. To solve numerically the model
problem under consideration [11], the
methods such as MAC, SUMAC and other
similar ones were generalized [1,4,11].
The main differences are due to a spe-
cial way of prescribing conditions
(3.4) when $r = r_s$ and the presence of
surface S having the pressure jump. The
unknown values were calculated in the
nodes of displaced network (u, v
in the middles of the cell sides; $P,$
 W at the centers of them). The radi-
al velocity component u on the sphe-
re with a large radius was determined
from a difference analogy of the con-
tinuity equation. Surface S passed
through the centers of the cells. The
velocity components v and W pres-
cribed on S were found with the use of
(3.5), i.e. the equation at these points
was not used. When the problem with
surface S is considered, two pressures
 P^+ and P^- , are to be determined at
points of this surface, one of them be-
ing excluded with the help of $P^+ - P^- =$
[p]. In the Poisson difference equation
for pressure, which is derived in a
usual way, in its righthand part there
appears an additional term $\text{const} \cdot [p]$
differing from zero only at the points
near surface S . The pressure equation
was solved by the method of upper re-
laxation. Fulfillment of (3.5) was ac-
hieved by correction of the pressure
jump [p], prescribed on S , or the volu-
me of liquid flowing over the body sur-
face. The pressure jump or discharge
variations were made within the general
iteration process. The flow region was
mapped onto the rectangle by transfor-
mation $r = \exp Z, \theta = \theta'$. The dimension-
al network was introduced in plane
(Z, θ')

3.3. We made some calculations in or-
der to compare the basic hydrodynamical
characteristics for towed or self-
moving sphere. The numerical experi-
ments were made under the following
boundary conditions. In the problem
with surface S we have

$$u_0(\theta) \equiv 0, W_0(\theta) \equiv 0, \quad (3.6)$$

$$W_s(r_s, \theta) = \begin{cases} (1 - e^{-B R_s^2 \sin^2 \theta}) / (R_s \cdot \sin \theta), \\ \theta_s \leq \theta \leq \pi, \\ 0, \text{ for other } \theta \end{cases} \quad (3.7)$$

(here R_s is the dimensionless radius
of surface S). If self-motion is model-
led by the liquid flow over the sphere
surface, conditions (3.5) on S are not
used. Functions $u_0(\theta)$ and $W_0(\theta)$ were

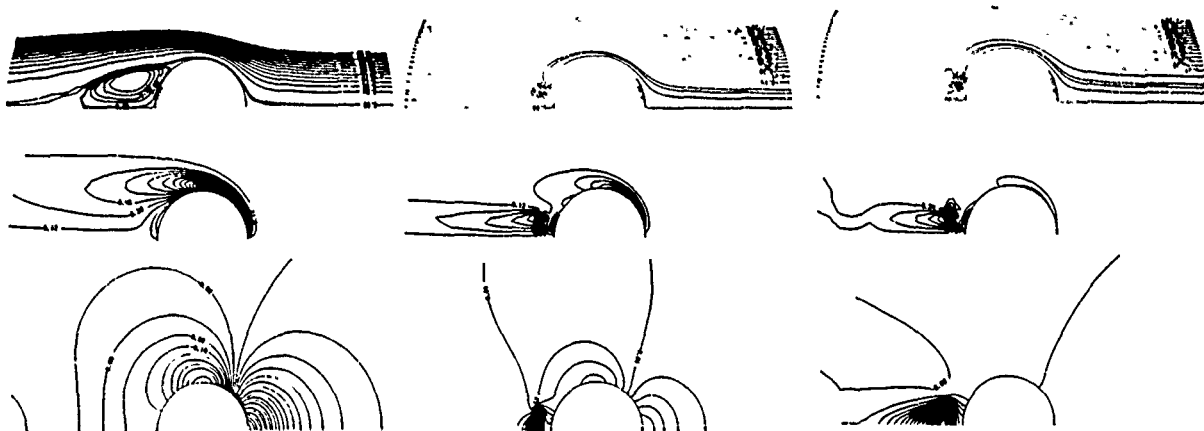


Fig. 4a

Fig. 4b

Fig. 4c



Fig. 4d

prescribed in the following way:

$$u(\theta) = \begin{cases} -E f_1(\theta), & \theta \leq \theta_1, \\ E f_1'(\theta), & \theta_1 \leq \theta \leq \pi, \\ 0 & \text{for other } \theta, \end{cases} \quad (3.8)$$

$$E_1 = \kappa \left(\int_{\theta_1}^{\pi} f_1(\theta) \sin \theta d\theta \right)^{-1},$$

$$E_2 = \kappa \left(\int_{\theta_3}^{\pi} f_2(\theta) \sin \theta d\theta \right)^{-1},$$

where $f_1(\theta) = (\theta - \theta_1)(\theta_2 - \theta)$, $f_2(\theta) = \theta(\theta - \theta_3)$,

$$w_0(\theta) = \begin{cases} (1 - e^{-B \sin^2 \theta}) / \sin \theta, & \theta_3 \leq \theta \leq \pi, \\ 0, & \text{for other } \theta. \end{cases} \quad (3.9)$$

(3.7), (3.9) mean that the flow is swirling only after it has passed through the unit which models a propeller.

Presented in Fig. 4 are the isolines of the stream function, swirling and pressures for $Re = 50$. Fig. 4a illustrates the towed sphere, and Figs. 4b, c illust-

rate the self-moving sphere. The propeller is modelled by the surface having the pressure jump $r_s = 1.4$; $\theta_s = 162^\circ$. Fig. 4b illustrates the flow rotation when $\Gamma = 0$; $[p] = 3.00$. Fig. 4c corresponds to $\Gamma = 15$, $[p] = 4.38$. Figs. 4d, e represents a self-moving sphere with a permeable surface. The case when $\Gamma = 0$, $\theta_1 = 108^\circ$; $\theta_2 = 132^\circ$; $\theta_3 = 156^\circ$ is shown in Fig. 4d. Fig. 4e corresponds to the case when $\Gamma = 20$; $\theta_1 = 1125^\circ$; $\theta_2 = 135^\circ$; $\theta_3 = 157^\circ$.

The calculations were made with the use of different networks. The most detailed network consisted of 40 nodes in a radial direction and 60 nodes in an angle. In all the calculations $r_s = 12.1$ ($Z_s = 2.5$). The number of iterations required for a stationary distribution of parameters to be achieved was dependent on the choice of initial values of $[p]$ and κ . When the rest state was assumed to be an initial state, not more than 1500 iterations were to be found. Continuation in the number Re reduced the required number of iterations by a factor of 1.5 or 2.

3.4. The problem of stationary motion of an arbitrary body with a constant velocity is tightly connected with the estimate of the consumption of energy necessary for providing the motion regime under consideration. In the case of towed body the required power N is simply expressed through the resistance R ;

$N = \vec{F} \cdot \vec{V}$. In the case of momentumless flow $\vec{F} \equiv 0$. One can judge about the value of required power by the losses of mechanical energy, associated with dissipation,

$$\Phi = 2 \rho \nu \int_{\Omega} D: D dx$$

where D is the strain velocity tensor; Ω is the flow region which is unbound in the case of external problem of flow past a body. Fig. 5 gives the values of dimensionless dissipation Φ ($\Phi = \Phi / (2 \rho \nu V_{\infty}^3 a^3)$) for different cases of stationary motion of a sphere having the radius a with a constant velocity V_{∞} in the liquid having the density ρ for different Reynolds numbers $Re = V_{\infty} a / \nu$.

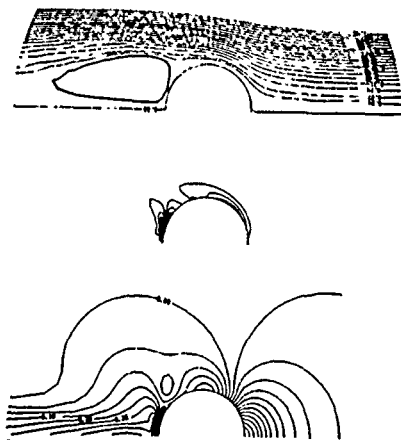


Fig. 4e

The solid line denotes the data for the towed sphere ($\Phi = C_d / 4$). A dashed line denotes the data for a linear problem (Stokes approximation). The calculated values of dissipation for different rotations for the problem with a permeable surface of the sphere, $\theta_1 = 112.5^\circ$; $\theta_2 = 135^\circ$; $\theta_3 = 157.5^\circ$ are denoted by rectangles. The problem with the surface S ($T_s = 1.4$; $\theta_s = 162^\circ$) is denoted by circles. Non-shaded circles correspond to the problem with zero rotation. It is easily seen that the flow rotation amplification is accompanied by the increase in dissipation of mechanical energy, and, consequently, the increase in required power.

For the problem with surface S the resistivity coefficients C_p and C_f may be calculated in the usual way. Fig. 6 presents the values of C_p , C_f for different Re . It is interesting to note that if $C_f > C_p$ for a towed sphere, C_f may be less than C_p for a self-moving one in the Re range under

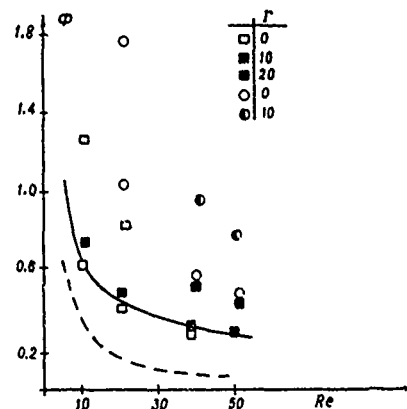


Fig. 5

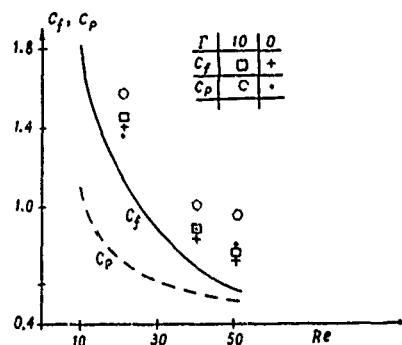


Fig. 6

consideration.

References

1. Amsden, A.A., Harlow, F.H. "A simplified MAC technique for incompressible fluid flow calculations", J. of Comput. Vol.6, pp.322-325 (1970).
2. Babenko, K.I. "On stationary solutions of the problem of viscous incompressible liquid flow past a body", Matematicheskii sbornik. Vol. 91(133), No.1(5).
3. Babenko, K.I., Vasiliev, M.M. "An asymptotical behaviour of the solution of the problem of viscous liquid flow past a finite body! Moscow - Reprint, Institute of Applied Mathematics, USSR Academy of Sciences, No.84 (1971).
4. Belotserkovsky, O.M., Gushin, V.A., Shchennikov, V.V. "Splitting method applied to the problem of viscous incompressible liquid dynamics", ZhVMI NF Vol.15, No.1, pp.197-207 (1975).

5. Birkhoff, G., Zarantonello, E.H. "Jets, wakes and cavities", New York Academic Press, (1957).
6. Clark, D.C. "The vorticity at infinity for solutions of the stationary Navier-Stokes equations in exterior domains", Indiana Univ.Math.J. Vol.20, No.7, pp.633-654 (1971).
7. Finn, R. "An energy theorem for viscous fluid motions", Archive for Rational Mech. and Anal., Vol.6, No.5, pp.371-381 (1960).
8. Finn, R. "On the exterior stationary problem for the Navier-Stokes equations, and associated perturbation problems", Arch. for Rational Mech. and Anal. Vol.19, No.5, pp.363-406 (1965).
9. Fischer, T.M., Hsiao, G.C., Wendland, W.L. "Singular perturbations for the exterior three-dimensional slow viscous flow problem", J.of Math.Anal. and Applications Vol.110, No.2, pp. 583-603 (1985).
10. Happel, T., Brenner, H. "Low Reynolds number hydrodynamics", Prentice-Hall (1965).
11. Harlow, F.H., Welch, J.E. "Numerical calculation of time-dependent viscous incompressible flow of fluid with free surface", Phys. of Fluids, Vol.8, No.12, pp.2182-2189 (1965).
12. Iztelevov, M.I. "Calculation of momentumless flow past an ellipsoid", Problemy dinamiki vyazkoi zhidkosti, Novosibirsk (1985), (in Russian).
13. Kuznetsov, B.G., Moshkin, N.P. "Viscous flow in an angular cylindrical tube with flowing through an inner boundary", Problemy dinamiki vyazkoi zhidkosti:Trudy X Vsesoyuznoi konferentsii, Novosibirsk, pp.188-191 (1985), (in Russian).
14. Ladyzhenskaya, O.A. "Mathematical problems of viscous incompressible liquid dynamics", Moscow, Nauka Publishers (1970), (in Russian).
15. Lions, J.-L., Magenes, E. "Problems aux limites non homogenes et applications", Paris, Dunod (1968).
16. Lugovtsov, A.A., Lugovtsov, B.A. "The example of viscous incompressible flow past a body with a moving boundary", Dinamika sploshnoi sredy, Novosibirsk, vyp. 8 (1971).
17. Moshkin, N.P., Pukhnachov, V.V. "A momentumless viscous incompressible flow over a body", Book of Abstracts, Soviet Union - Japan symposium on computational fluid dynamics (USSR, Novosibirsk, Sept. 9-16, 1988), pp.84-85 (1988), (in Rus.)
18. Pukhnachov, V.V. "On some modification of flow past a body", Problemy matematiki i mehaniki, Novosibirsk:Nauka Publishers (1983).
19. Pukhnachov, V.V. "Stokes approximation in the problem of flow past a self-moving body", Boundary value problems in mathematical physics and their approximations, Kiev, Naukova Dumka Publishers (1989), (in Russian).
20. Pukhnachov, V.V. "Velocity field asymptotics at great distances from a self-moving body", PMTF, No. 2, pp.52-60 (1989), (in Russian).
21. Sennitskii, V.L. "Liquid flow around a self-propelled body", Zhurnal Prikladnoi Mekhaniki i Tekhnicheskoi Fiziki, No.3, pp.78-83 (1978) (in Russian).
22. Sennitskii, V.L. "Example of flow of an axisymmetric liquid stream over a self-propelled body", Zhurnal Prikladnoi Mekhaniki i Tekhnicheskoi Fiziki, No.4, pp.31-36 (1984), (in Russian).
23. Sennitskii, V.L. "Rotating cylinders in a viscous liquid", Part 1, Dinamika sploshnoi sredy, Novosibirsk, Vol. 21, pp.70-83 (1975); Part 2, Dinamika sploshnoi sredy, Novosibirsk, Vol. 23, pp.169-181 (1975) (in Russian).
24. Sennitskii, V.L. "On the propelling of a pair of rotating circular cylinders in a liquid", Dinamika sploshnoi sredy, Novosibirsk, Vol. 47, pp.145-153 (1980) (in Russian).
25. Sennitskii, V.L. "On the drag force acting on a pair of circular cylinders streamed by water", Dinamika sploshnoi sredy, Novosibirsk, Vol.52, pp.178-182 (1981) (in Russian).

Time-Domain Calculation of the Nonlinear Hydrodynamics of Wave-Body Interaction*

C. Yang, Y. Z. Liu
Shanghai Jiao Tong University,
Shanghai, China
N. Takagi
Nihon University
Chiba, Japan

Abstract

The boundary element method coupled with time-marching finite difference is adopted and improved to calculate the nonlinear hydrodynamics of wave-body interaction. The radiation condition and initial condition have been studied through specially chosen examples such as the cylinder undergoing forced heave motion or forced sway motion and the body floating or standing in periodic waves with wave front, and steady solution of practical interest has been obtained in a definite calculation domain by less computer time. A few comparisons are made with available solution and model test results. It is concluded that the method is capable of predicting forces due to nonlinear wave quite accurately with requirement of medium computer.

Nomenclature

oxyz	frame of reference, with z pointing upward and z=0 the still water surface
ϕ	velocity potential
S_b	immersed body surface
S_f	free surface
S_c	outer open boundary surface
\hat{n}	unit normal vector directed outward from the fluid region $\hat{n}=(n_x, n_y, n_z)$
V_n	normal velocity of the body surface
g	acceleration of gravity
t	time variable
Δt	time increment
$\eta(x, y, t)$	elevation of the free surface for 3-D case
$\eta(x, t)$	elevation of the free surface for 2-D case
\bar{x}	field point

\bar{z}	source point
u_G	horizontal velocity of the body
w_G	vertical velocity of the body
H	wave height
C	wave velocity
ω	wave frequency or oscillating frequency of the body undergoing forced motion
T	wave period
h_0	oscillating amplitude of the body undergoing forced motion
a	radius of circular cylinder
DF	mean water draft of the body
d	still water depth
R	radius of the outer open boundary
ρ	mass density of fluid

1. Introduction

In many design cases, the application of linear diffraction theory is not entirely appropriate for the prediction of wave forces on large offshore structures of general form. For 3-D nonlinear free surface problem, basically there are two approaches commonly used in literature. One is based on finite difference method, in which the solution of Navier-Stokes equations by MAC and its various modifications SMAC, SUMMAC, ABMAC, IMP and recently TUMMAC (1)(2)(3) are relatively popular. This approach appears to have the capacity to cope with large amplitude nonlinear waves and even breaking, but considerable further development will be necessary to be realistically used due to its high cost and need of supercomputer. The other approach is based on boundary element method coupled with finite difference time-marching method, first introduced by Longuet-Higgins and Cokelet (4) and then followed by Faltinsen (5), Vinje et al. (6), Isaacson (7), Lin et al. (8), and others. This approach is more suitable to deal with the wave diffraction of large offshore structures for engineering use and is

*The Project Supported Partly by National Natural Science Foundation of China.

adopted in this paper.

The work of this paper is to solve 2-D and 3-D nonlinear problems with free surface. The wave-body interaction is treated as a transient problem with known initial condition and is solved by integral-equation method based on Green's theorem. It is emphasized to deal with the following aspects through different model problems in the paper: (a) the radiation condition. (b) the point at the junction of the body and the free surface, (c) the initial condition for a body floating or standing in periodic wave. Only after describing these three aspects correctly is the solution stable and practical.

Numerical calculation should be truncated at finite distance and the smaller the domain the better, while the physical domain is infinite. Therefore a numerical radiation condition should be posed so as no reflected waves from the truncated surface, i.e. outer open boundary. For an axisymmetrical cylinder heaving in still water, several approaches for the formulation of the radiation condition have been tested, and it is found that the usual one-dimensional Sommerfeld condition is the simplest and can give reasonable results both for the wave pattern and wave force. For the cylinder sway in still water, the Sommerfeld condition is extended to 2-D case and the wave direction is determined only by wave itself. The numerical results show good agreement with the tested ones done in Nihon University, Japan. For the diffraction of a solitary wave upon a fixed vertical circular cylinder, the Sommerfeld condition is further extended as a radiation condition by assuming that the scattering of the outgoing wave is small at the outer open boundary. The numerical results is appropriate compared with Isaacson's [7] analytical solution. The same works have been done for the diffraction of a periodic wave upon a fixed cylinder.

In the numerical calculation, Lagrangian free surface condition is used. The point at the junction of the body and the free surface is determined by extrapolation for axisymmetrical flow and by satisfying both the conditions on the free surface and on the body for general 3-D flow, that is, according to the body condition we can obtain the velocity of the intersection point, by which the new position of intersection point can be determined through satisfying the free surface condition.

In order to shorten initial transient process, appropriate initial boundary condition should be posed. Numerical tank is good for this purpose, and it can make the vicinity of the body be still water. The another advantage of the numerical tank is capable to produce waves with any water depth and any water bottom condition. The approach of numerical tank is described in detail in the doctoral thesis by C. Yang [9]. A 2-D nonlinear Stokes wave with wave front is also suitable for the initial condition. The details are described in subsequent section.

2. Formulation of the Problem

2.1 Basic Equations

The basic assumptions are that the fluid is inviscid, incompressible and the flow is irrotational. Select the coordinate system and computation domain as shown in Fig.1, the velocity potential $\phi(x,y,z,t)$ satisfies

$$\nabla^2 \phi(x,y,z,t) = 0 \quad \text{in fluid domain} \quad (1)$$

$$\frac{\partial \phi}{\partial n} = 0 \quad \text{on } S_d \quad (2)$$

$$\frac{\partial \phi}{\partial n} = V_n \quad \text{on } S_b \quad (3)$$

$$\left. \begin{aligned} \frac{Dx}{Dt} &= \frac{\partial \phi}{\partial x} \\ \frac{Dy}{Dt} &= \frac{\partial \phi}{\partial y} \\ \frac{Dz}{Dt} &= \frac{\partial \phi}{\partial z} \end{aligned} \right\} \quad \text{on } S_f \quad (4)$$

$$\frac{D\phi}{Dt} = -g\eta + 0.5\nabla\phi \cdot \nabla\phi \quad \text{on } S_f \quad (5)$$

Here the conditions on the free surface are expressed in Lagrangian form. These equations are solved with suitable initial and radiation conditions.

2.2 Time-marching Procedure

The free surface and the velocity potential on it are calculated by finite difference time-marching method and they can be expressed in the form

$$\left. \begin{aligned} x^{n+1} &= x^n + 0.5\Delta t \left(3\left(\frac{\partial \phi}{\partial x}\right)^n - \left(\frac{\partial \phi}{\partial x}\right)^{n-1} \right) \\ y^{n+1} &= y^n + 0.5\Delta t \left(3\left(\frac{\partial \phi}{\partial y}\right)^n - \left(\frac{\partial \phi}{\partial y}\right)^{n-1} \right) \\ z^{n+1} &= z^n + 0.5\Delta t \left(3\left(\frac{\partial \phi}{\partial z}\right)^n - \left(\frac{\partial \phi}{\partial z}\right)^{n-1} \right) \end{aligned} \right\} \quad (6)$$

$$\begin{aligned} \phi^{n+1} &= \phi^n + 0.5\Delta t \left(3(-g\eta + 0.5\nabla\phi \cdot \nabla\phi)^n \right. \\ &\quad \left. - (-g\eta + 0.5\nabla\phi \cdot \nabla\phi)^{n-1} \right) \end{aligned} \quad (7)$$

Where superscript n denotes the value at $t=n\Delta t$. Eq.(7) can be rewritten as follows

$$\begin{aligned} \phi^{n+1} &= F_1(\phi^n, \phi^{n-1}, \left(\frac{\partial \phi}{\partial n}\right)^n, \left(\frac{\partial \phi}{\partial n}\right)^{n-1}) \\ &\quad \text{on } S_f^{n+1} \end{aligned} \quad (8)$$

Where F_1 is a known function.

According to the mode in which body moves we can obtain

$$\begin{aligned} \left(\frac{\partial \phi}{\partial n}\right)^{n+1} &= F_2(\phi^n, \phi^{n-1}, \left(\frac{\partial \phi}{\partial n}\right)^n, \left(\frac{\partial \phi}{\partial n}\right)^{n-1}, \phi^{n+1}) \\ &\quad \text{on } S_b^{n+1} \end{aligned} \quad (9)$$

where F_2 is a known function for forced motion and it can be obtained by solving Newton's Law of momentum simultaneously with the solution of the velocity potential ϕ for freely motion, because implicit scheme is usually used in the Bernoulli's equation [9] for this case.

With suitable radiation condition the velocity potential on the outer open boundary can be described as

$$\phi^{n+1} = F_3(\phi^n, \phi^{n-1}, (\frac{\partial \phi}{\partial n})^n, (\frac{\partial \phi}{\partial n})^{n-1}) \quad \text{on } S_c^{n+1} \quad (10)$$

where F_3 is also a known function and can be obtained in section 3.

Once the free surface S_f^n , immersed body surface S_b^n , outer open boundary S_c^n and the velocity potential ϕ^n , normal velocity $(\partial \phi / \partial n)^n$ on them are known (of course before time $t = n\Delta t$ all of these quantities are also known), S_f^{n+1} and ϕ^{n+1} on S_f^{n+1} can be obtained from Eqs.(6),(7). S_b^{n+1} and $(\partial \phi / \partial n)^{n+1}$ on S_b^{n+1} can be determined in terms of the new points at the junction of the body and the free surface and Eq.(9) separately. S_c^{n+1} and ϕ^{n+1} on S_c^{n+1} can be determined in terms of the radiation condition Eq.(10). From Green's third formula, we have

$$\phi(\vec{x}) = \frac{1}{\alpha(\vec{x})} \int_S (G(\vec{x}, \vec{\xi}) \frac{\partial \phi}{\partial n}(\vec{\xi}) - \frac{\partial G(\vec{x}, \vec{\xi})}{\partial n} \phi(\vec{\xi})) ds \quad (11)$$

where $S = S_f + S_b + S_c$. Both points \vec{x} and $\vec{\xi}$ are on the boundary S . $\alpha(\vec{x}) = 2\pi$ for a smooth surface at point \vec{x} . Rankine source with suitable images is used as the Green function $G(\vec{x}, \vec{\xi})$, which is so chosen that the bottom condition are satisfied automatically.

Now the integral equation (11) can be solved numerically at time $t = (n+1)\Delta t$, and we can obtain $(\partial \phi / \partial n)^{n+1}$ on S_f^{n+1} and S_c^{n+1} , ϕ^{n+1} on S_b^{n+1} . In this way we can go further to time $t = (n+2)\Delta t$ and calculations can be advanced over a sufficient duration.

Once the values of the velocity potential on the body surface are known, the pressure on the body surface can be obtained from Bernoulli equation represented in a frame of reference fixed on the body.

$$p = -\rho(\frac{\partial \phi}{\partial t} - \vec{v}_e \cdot \nabla \phi + 0.5 \nabla \phi \cdot \nabla \phi + gz) \quad (12)$$

where $(\partial \phi / \partial t)^{n+1} = (\phi^{n+1} - \phi^n) / \Delta t$, ϕ^{n+1} and ϕ^n are the values of the velocity potential on the same point of the body at different time steps and \vec{v}_e is the velocity of the body at that point. The hydrodynamic forces on the body are calculated from the formula

$$F_k = \int_{S_b} p n_k ds \quad (13)$$

3. Radiation Condition

3.1 Forced Motion

Assuming that a cylinder starts to move in still water, initial condition could be satisfied easily, so we specially choose the examples of forced heave motion and forced sway motion as the calculation models to find out the appropriate radiation condition.

In numerical calculations we use a cylindrical coordinate system (r, θ, z) on the outer open boundary S_c and make $r = R = \text{const}$ represent S_c .

First let a circular cylinder undergo a forced heave motion in still water, here the flow is axisymmetric. Before the wave reaches the S_c we have

$$\phi = 0 \quad \text{on } S_c \quad (14)$$

With such radiation condition we have tried different radius R , i.e. expanding the open boundary gradually to find out how the scale of the outer open boundary affects the numerical solution. Then we assume that the wave near the outer boundary satisfies Sommerfeld radiation condition [10]

$$\frac{\partial \phi}{\partial t} + C_\phi \frac{\partial \phi}{\partial r} = 0 \quad \text{on } S_c \quad (15)$$

The phase velocity C_ϕ varies only with time on S_c , and it can be determined by ϕ^{n+1} and $(\partial \phi / \partial n)^n$ on S_f near S_c . Then ϕ^{n+1} on S_c can be obtained according to C_ϕ . Eq.(15) can make the wave on S_c be propagating outward along \vec{r} direction.

Next let a circular cylinder undergo forced sway motion. Now the flow is non-axisymmetric and Sommerfeld condition is described as

$$\frac{\partial \phi}{\partial t} + C_\phi \frac{\partial \phi}{\partial l} = 0 \quad \text{on } S_c \quad (16)$$

Here \vec{l} is an unknown direction of outgoing wave on the outer boundary, phase velocity C_ϕ varies with time t and angle θ and is equal at the same vertical line. From Eq.(16) we have

$$\frac{\partial \phi}{\partial t} + C_\phi (k_r \frac{\partial \phi}{\partial r} + k_\theta \frac{\partial \phi}{\partial \theta}) = 0 \quad (17)$$

where

$$\begin{aligned} k_r &= \cos(\vec{l}, \vec{r}) \\ k_\theta &= \cos(\vec{l}, \vec{\theta}) \end{aligned} \quad (18)$$

The solution of Eq.(17) can be expressed as

$$\phi = \phi(k_r r + k_\theta R\theta - C_\phi t) \quad (19)$$

where

$$k_r = \alpha \frac{\partial \phi}{\partial r} / ((\frac{\partial \phi}{\partial r})^2 + (\frac{\partial \phi}{\partial \theta})^2)^{1/2} \quad (20)$$

$$k_\theta = \alpha \frac{\partial \phi}{\partial \theta} / ((\frac{\partial \phi}{\partial r})^2 + (\frac{\partial \phi}{\partial \theta})^2)^{1/2} \quad (21)$$

$$\alpha = \begin{cases} 1 & \text{if } \frac{\partial \phi}{\partial r} > 0 \\ -1 & \text{if } \frac{\partial \phi}{\partial r} < 0 \end{cases}$$

such α can make the wave at outer boundary be outgoing propagating wave.

Substituting Eq.(20) into Eq.(17), we have

$$\frac{\partial \phi}{\partial t} + \alpha C_\phi ((\frac{\partial \phi}{\partial r})^2 + (\frac{\partial \phi}{\partial \theta})^2)^{1/2} = 0 \quad (22)$$

Up to now by Eq.(22) we can determine C_ϕ in terms of ϕ^{n+1} and $(\partial \phi / \partial n)^n$ on S_f near S_c , and obtain ϕ^{n+1} on S_c according to C_ϕ .

3.2 Wave Diffraction Problem

For the diffraction of a solitary wave or periodic wave upon a fixed or floating vertical cylinder, the Sommerfeld condition is further extended as a radiation condition by assuming that the scattering of the outgoing wave is small on the outer open boundary. Replacing ϕ in Eq.(22) by ϕ_s , we can also obtain ϕ^{n+1} on S_c , here

$$\phi_s = \phi - \phi_w \quad (23)$$

and ϕ is total velocity potential and ϕ_w is velocity potential of incoming wave.

4. Description of the Initial Condition

4.1 Radiation Problem

For forced heave motion mentioned above we have

$$\phi(x, y, z, 0) = 0 \quad \text{on } S_f |_{t=0} \quad (24)$$

$$\frac{\partial \phi}{\partial n}(x, y, z, 0) = (\dot{z}_{Gn}) \Big|_{t=0^+} \quad \text{on } S_b |_{t=0} \quad (25)$$

$$\phi(x, y, z, 0) = 0 \quad \text{on } S_c |_{t=0} \quad (26)$$

For forced sway motion, the formulas of initial conditions on S_f and S_c are similar with Eqs.(24),(26) and that on S_b becomes

$$\frac{\partial \phi}{\partial n}(x, y, z, 0) = (\dot{x}_{Gn}) \Big|_{t=0^+} \quad \text{on } S_b |_{t=0} \quad (27)$$

4.2 Body Standing on Floating in Waves

If the incoming wave is a solitary wave,

as used by Isaacson [7], because it decays rapidly away from its crest, the flow near the body can be taken zero as initial condition. If the incident wave is periodic Stokes or Conoidal waves and the body is assumed to be stationary at certain instant (as initial time), there must be a transient period before a steady state is approached. Sometimes as reported by Vinje, Xie and Brevig [11], even numerical troubles occur. In order to formulate the initial condition properly, a numerical tank is set up using the same procedure. A 2-D cylinder with different cross-section heaving can produce the required wave profile, see Fig.2 and Fig.3. The details are in doctoral thesis by C.Yang [9]. With such a incident wave, the solution can approach steady rapidly and initial condition can be described as

$$\phi|_{t=0} = \phi_w|_{t=0} \quad \text{on } S_f |_{t=0} \quad (28)$$

$$\phi|_{t=0} = \phi_w|_{t=0} \quad \text{on } S_c |_{t=0} \quad (29)$$

The numerical tank can be applied to any water depth and any type of water bottom boundary. Another expression of the incident wave is a 2-D nonlinear Stokes wave with wave front, it can be described as

$$\eta(x, y, t) = A(\bar{x}) \left(\frac{H}{2} \cos \theta + \frac{H^2 k}{16} \frac{\text{ch}(kd)}{\text{sh}^3(kd)} (2 + \text{ch}(2kd)) \cos 2\theta \right) \quad (30)$$

$$\phi(x, y, t) = A(\bar{x}) \left(\frac{H\omega}{2k} \frac{\text{ch}(ks)}{\text{sh}(kd)} \sin \theta + \frac{3H^2 \omega}{32} \frac{\text{ch}(2ks)}{\text{sh}^4(kd)} \sin 2\theta \right) \quad (31)$$

Where

$$\theta = kx - \omega t, \quad s = z + d, \quad \bar{x} = \bar{k}(x - C_g t) \quad (\bar{k} < k) \quad (32)$$

$$C_g = \frac{C}{2} \left(1 + \frac{2kd}{\text{sh}(2kd)} \right), \quad C = \left(\frac{g}{k} \text{th}(kd) \right)^{1/2}$$

$$A(\bar{x}) = \begin{cases} 1 - \exp(\bar{x} \bar{k} a) & \text{if } \bar{x} \bar{k} a < 0 \\ 0 & \text{if } \bar{x} \bar{k} a \geq 0 \end{cases} \quad (33a)$$

$$\text{or,} \quad A(\bar{x}) = \begin{cases} 1 & \text{if } \bar{x} + \bar{k} a \leq \pi \\ 0.5(1 - \cos(\bar{x} + \bar{k} a)) & \text{if } -\pi < \bar{x} + \bar{k} a < 0 \\ 0 & \text{if } \bar{x} + \bar{k} a \geq 0 \end{cases} \quad (33b)$$

This Stokes wave by Eqs.(30),(31) can ensure no wave in the vicinity of the body, and is also suitable for the initial condition in some cases.

5. Numerical Procedure

In order to make the computer program be extended easily to arbitrary 3-D body, we use the whole cylinder and fluid region as computation domain. The boundary $S = S_b + S_f + S_c$ are discretized into element and on each element $(\partial \phi / \partial n)_j$ and ϕ_j are assumed to be constant

for 3-D case or linearly distributed for 2-D case, as in typical boundary method, the above Green's formula Eq.(11) becomes

$$\sum_{j=1}^{NB} A_{ij} \phi_j + \sum_{j=1}^{NF} B_{ij} \left(\frac{\partial \phi}{\partial n} \right)_j + \sum_{j=1}^{NC} C_{ij} \left(\frac{\partial \phi}{\partial n} \right)_j = D_i \quad i=1, 2, \dots, NN \quad (34)$$

where

$$\left. \begin{aligned} A_{ij} &= - \int_{S_j} \frac{\partial G}{\partial n} (\bar{x}_i, \bar{r}) ds - \alpha_i \delta_{ij} \\ B_{ij} &= \int_{S_j} G(\bar{x}_i, \bar{r}) ds \\ C_{ij} &= B_{ij} \\ D_i &= - \sum_{j=1}^{NB} B_{ij} \left(\frac{\partial \phi}{\partial n} \right)_j - \sum_{j=1}^{NF} A_{ij} \phi_j - \sum_{j=1}^{NC} A_{ij} \phi_j \\ \delta_{ij} &= \begin{cases} 1 & i=j \\ 0 & i \neq j \end{cases} \end{aligned} \right\} \quad (35)$$

and $NN=NB+NF+NC$ is total number of elements (for 3-D) or nodes (for 2-D) on boundary $S=S_b+S_f+S_c$, and NB on S_b , NF on S_f , NC on S_c respectively. These algebraic equations can be solved either by direct or iterative method.

The junction point of the body and free surface is determined in the paper by extrapolation for axisymmetric flow and by satisfying both the conditions on the body and on the free surface for general 3-D flow, that is, according to the body condition we can obtain the velocity of the intersection point, by which the new position of intersection point can be determined through satisfying the free surface condition.

6. Numerical Examples and Conclusion

6.1 Forced Heave Motion

As an example, we consider the forced heave motion of a floating truncated vertical cylinder of radius a and mean draft $a/2$. The vertical velocity of the body is prescribed to be

$$\dot{z}_G = h_0 \omega \sin \omega t \quad (36)$$

with body draft

$$\bar{H}(t) = -\frac{a}{2} h_0 \cos \omega t \quad (37)$$

In order to make our computation comparable to Lin's (8) results, we also choose that $a=1$, $\rho=1$ and $g=1$, the other initial input data for calculation is $\omega=\pi/2$, $h_0=0.05$, $d=8$, $\Delta t=0.1$. Besides the radius of the outer boundary and the radiation condition for calculation are divided into following three groups

- (1) $\begin{cases} R=11 \\ \text{Rad. Cond. Eq. (14)} \end{cases}$
- (2) $\begin{cases} R=4.7 \\ \text{Rad. Cond. Eq. (14)} \end{cases}$
- (3) $\begin{cases} R=4.7 \\ \text{Rad. Cond. Eq. (15)} \end{cases}$

Fig.4, Fig.5 and Fig.6 show respectively the time history of free surface profiles consisting with above three cases. From Fig.6 we can observe the wave reflecting from the outer boundary, Fig.7 shows the comparison of heave force of case(3) with Lin's (8), and Fig.8 shows the effect of water depth on heave forces in which the calculation method is similar to case(3).

6.2 Forced Sway Motion

Let a floating truncated cylinder undergo forced sway motion. The radius of the cylinder is a , the mean draft of it is $a/2$ and the water depth is a . The gravity center of the body can be described as

$$x_G = h_0 \sin \omega t \quad (38)$$

here $h_0=0.05a$ and $\omega/(a/g)^{1/2}=0.8028$. Comparison has been made between the calculations and experiments by Dr. N.Takaki in Nihon University, Japan. Fig.9 shows good agreement of the results of the free surface elevations at the fixed point. Fig.10 gives the free surface profiles at some fixed time.

6.3 Diffraction Problem

The diffraction problems of a vertical circular cylinder standing on the seabed and piercing the free surface by a solitary wave has been calculated. Fig.11 shows the comparison of hydrodynamic coefficients among present results, Li's (12) difference solution and Isaacson's (7) closed-form solution.

Fig.12 gives numerical calculation model of diffraction problem, in which the 2-D incoming wave is obtained by the forced heave motion of a 2-D cylinder, i.e. numerical tank. Fig.13 is the time history of incoming wave elevation and velocity potential of incoming wave at point $x=-R$, $y=0$ (see Fig.12 point A). Fig.14 is the time history of horizontal wave force.

The interaction of the 2-D floating rectangular cylinder and the wave has been calculated, where the cylinder is only with one degree of freedom in z direction and the wave is also produced by the numerical tank which ensure no wave in the vicinity of the cylinder. Fig.15 is the free surface elevations at point $x=-R$. Fig.16 is the variations of horizontal wave force and vertical wave force. Fig.17 shows the variations of the body center and the body velocity in z direction.

Fig.18 and Fig.19 show the results of a 2-D periodic Stokes wave (described by Eq.(30) and Eq.(31)) upon a fixed circular cylinder and a truncated fixed circular cylinder at

the free surface.

6.4 Conclusions

From above examples the following conclusions are obtained:

- (a) The boundary element method coupled with time-marching finite difference shows good prospect for practical use with reasonable cost and requirement of medium computer.
- (b) Sommerfeld condition with varying wave speed used approximately as radiation condition for radiation and diffraction potential in nonlinear case seems to be acceptable, at least for the case we have dealt with.
- (c) Numerical tank is good for establishment of initial boundary condition with shorter transient process, and it can be applied to any water depth and any water bottom condition. A 2-D nonlinear Stokes wave with wave front is also suitable for initial condition.
- (d) The determination of the location of the intersection points at the free surface and the body is serious problem, the approach we used is succeeded in our cases.

References

1. Bourianoff, G.I., Penumalli, B.R., "Numerical simulation of ship motion by Eulerian hydrodynamic techniques", Proc. of Second Int'l Conf. on Numerical Ship Hydrodynamics (1977).
2. Miyata, H. and Nishimura, S., "Finite-difference simulation of nonlinear ship waves", J. Fluid Mech. Vol.157, pp.327-357 (1985).
3. Nishimura, S., Miyata, H. and Kajitani, H., "Finite-difference simulation of ship waves by the TUMMAC-IV method and its application to hull-form design", J. Soc. Nav. Archit. Japan, Vol.157, pp.1-14 (1985).
4. Longuet-Higgins, M.S. and Cokelet, E.D., "The deformation of steep surface waves on water", Proc. Roy. Soc. Series A, Vol.350 (1976).
5. Faltinsen, O., "Numerical solutions of transient nonlinear free surface motion outside or inside moving bodies", Proc. Second Int'l Conf. on Numerical Ship Hydrodynamics (1977).
6. Vinje, T. and Brevig, P., "Nonlinear ship motion", Proc. Third Int'l Conf. on Numerical Ship Hydrodynamics (1981).
7. Isaacson, M. de St Q., "Nonlinear-wave effects on fixed and floating bodies", J. Fluid Mech. Vol.120, pp.267-281 (1982).
8. Lin, V.M., Newman, J.N. and Yue, D.K., "Nonlinear forced motion of floating body", Proc. of 15th Symp. on Naval Hydrodynamics (1984).
9. Yang, C., "Time domain calculation of three dimensional nonlinear wave forces", Doctoral thesis, Shanghai Jiao Tong University, China (1987).
10. Olanski, L., "A simple boundary condition for unbounded hyperbolic flows", J. Comp. Phys. Vol.21 (1976).
11. Vinje, T., Xie, M.G. and Brevig, T., "A numerical approach to nonlinear ship motion", Proc. of 14th Symp. on Naval Hydrodynamics (1982).
12. Lin, B.Y. and Lu, Y.L., "A numerical model for nonlinear wave diffraction around large offshore structure", Proc. Second Asian Congress on Fluid Mech. (1986).

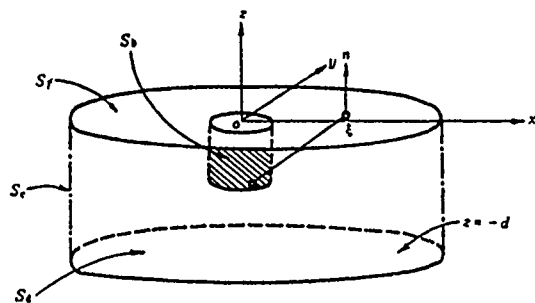


Fig.1 Frames of reference and integration surface (show with $\eta=0$)

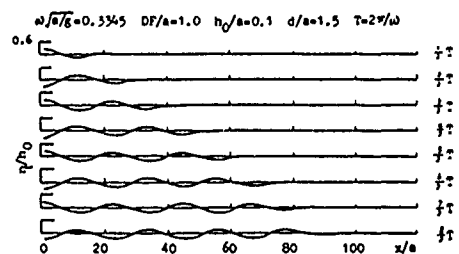


Fig.2 Free surface elevations at various times

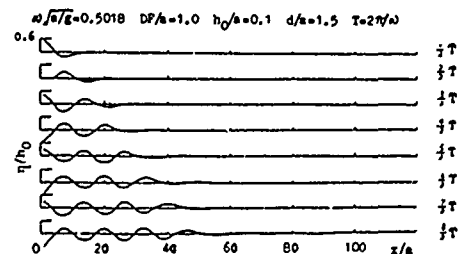


Fig.3 Free surface elevations at various times

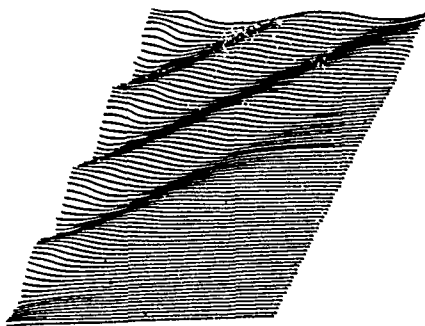


Fig.4 Nonlinear free surface profiles for case (1)
($1 \leq t \leq 5.5$, $t=0, 0.5, 0.1, \dots$)

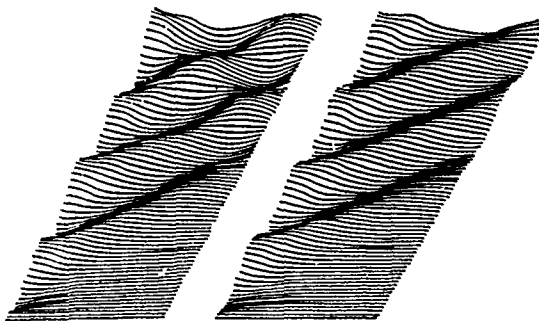


Fig.5 Nonlinear free surface profiles for case (2)
($1 \leq t \leq 1.7$, $t=0, 0.5, \dots$)

Fig.6 Nonlinear free surface profiles for case (3)
($1 \leq t \leq 1.7$, $t=0, 0.5, \dots$)

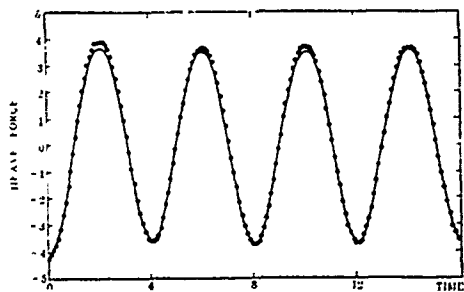


Fig.7 Heave force variation($h_0=0.05$)
— case(3)
... Lin's results

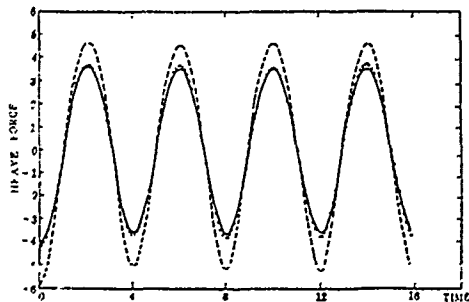


Fig.8 Heave force variation for different water depths
--- d=1 +++ d=2 — d=8

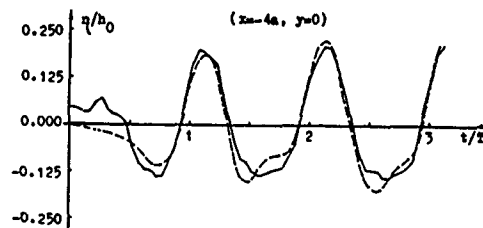
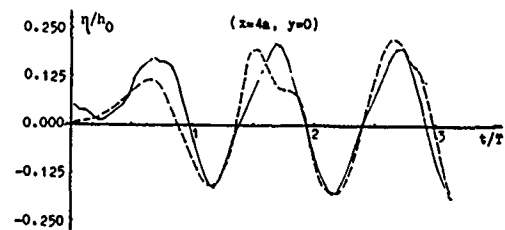
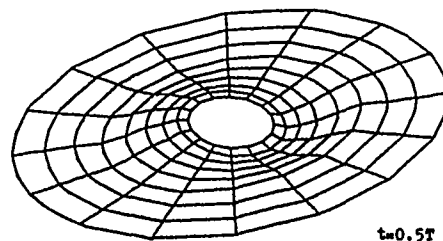
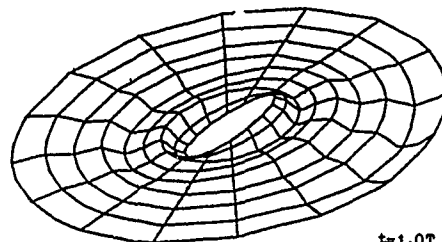


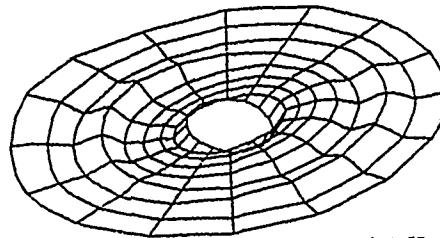
Fig.9 Free surface elevations at the fixed point
— model test results
--- numerical results



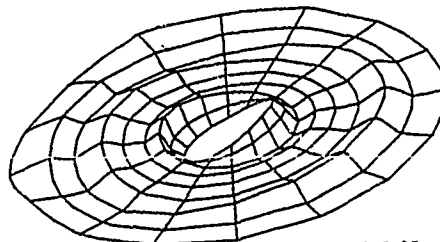
$t=0.5T$



$t=1.0T$



$t=1.5T$



$t=2.0T$

Fig.10 Free surface profiles

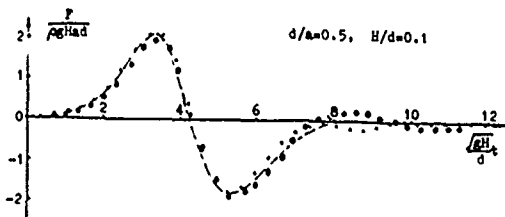


Fig. 11 Horizontal wave force variation
ooo present results
... Li's results
--- Isaacson's results

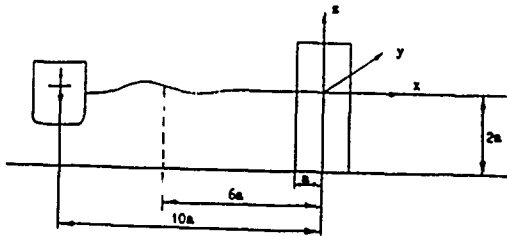


Fig. 12 Numerical calculation model

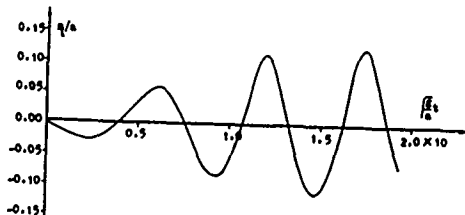


Fig. 13a Incoming wave elevation for
3-D fixed circular cylinder
at point A ($x=-R, y=0$)

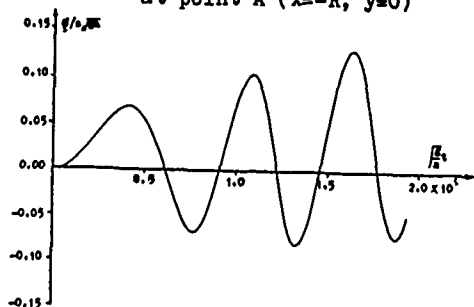


Fig. 13b Velocity potential of incoming
wave for 3-D fixed circular
cylinder at point A ($x=-R, y=0$)

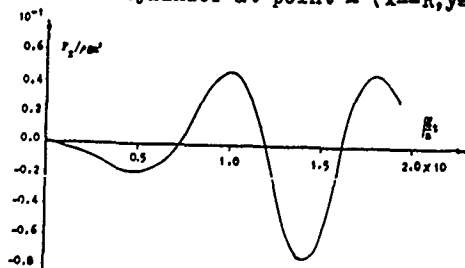


Fig. 14 Horizontal wave-force variation
for 3-D fixed circular cylinder

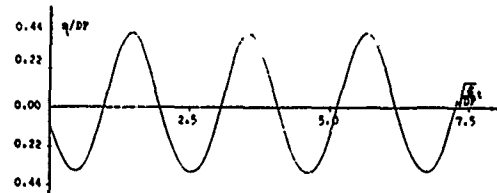


Fig. 15 Incoming wave elevation at $x=-R$ for
2-D floating rectangular cylinder
($d/DF=4, a/DF=5.6, R/DF=26$)

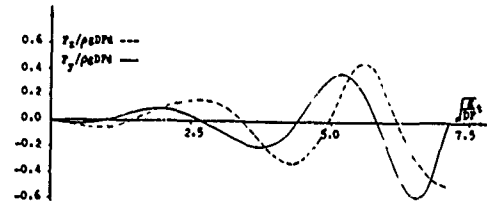


Fig. 16 Horizontal and vertical wave-
force variations for 2-D
floating rectangular cylinder
($d/DF=4, a/DF=5.6, R/DF=26$)

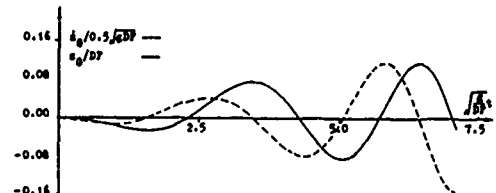


Fig. 17 Variations of the body center and
the body velocity for 2-D floating
rectangular cylinder in z direction
($d/DF=4, a/DF=5.6, R/DF=26$)

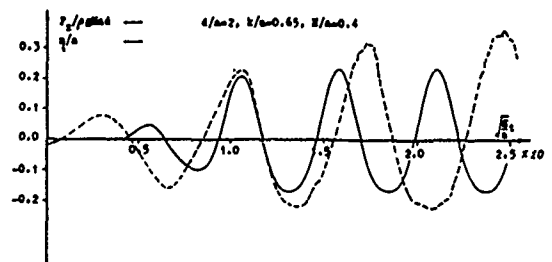


Fig. 18 Incoming wave elevation at $x=0$ and
horizontal wave-force for 3-D
fixed circular cylinder

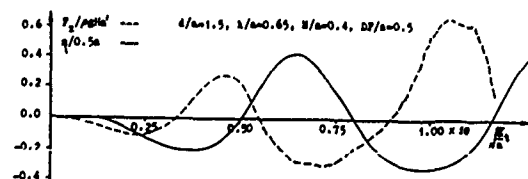


Fig. 19 Incoming wave elevation at $x=0$ and
horizontal wave-force for 3-D
truncated circular cylinder at the
free surface

DISCUSSION

by K.J. Bai

First of all, the authors should be congratulated on the impressive numerical work reported in the present paper. This paper is a most welcome addition to the literature on numerical computations for the nonlinear free surface flow problem. In the following, I would like to make three comments:

(1) the radiation condition given in Eq.(15) is true only for linear (or nonlinear) hyperbolic-type wave. However, in the water wave problem there exists local disturbance term besides the propagating waves. Therefore this radiation condition should be imposed at a sufficient distance away from the heaving vertical cylinder. Specifically, for this heave motion, the local term in the potential behaves like a pulsating free-space (Rankine) source. In some cases, at the sufficient distance away from the heaving cylinder where the local disturbance term is negligible, the propagating waves may be treated as linear. This is because the nonlinear three-dimensional wave will be linear as it spreads out. Recently we have made some numerical tests on the matching of the Kelvin source distribution and the local nonlinear numerical scheme along the numerical radiation boundary, which replaces the radiation condition in Eq.(15). This matching procedure worked very well in our numerical test. I wonder if you have ever tested this scheme. I would like to know how far one should take the radiation boundary in order to use the radiation condition Eq.(15).

(2) Similarly to the above question, I do not understand the radiation condition given in Eq.(22) for the sway motion of a vertical cylinder. I think that for this asymmetric motion for the swaying cylinder, the wave number vector should be radial vector. It may be seen from the fact that the potential for the swaying vertical cylinder can be expressed in a Fourier-Bessel series in a sufficient distance away from the cylinder.

(3) I do not understand the validity of the equation in (23)' which is entirely based on the linearity. Even though the diffracted waves become small at the radiation boundary, I do not see the logic behind the linear superposition of the local nonlinear part (i.e., the incoming wave, I guess) and the linear part.

Author's Reply

(1) Although Olanski condition is just only an approximation as radiation condition for radiation and diffraction problems in nonlinear case, the numerical results have shown that this radiation condition can absorb the reflected wave on the open boundary. Besides because of the Sommerfeld radiation condition with varying phase velocity every time step, this condition is acceptable in nonlinear case so long as the distance between open boundary and body is large enough. Of course that nonlinear solution matching with linear Green's function on the open boundary is also usable as an approximation, but Sommerfeld condition is easier.

(2) If the vertical circular cylinder undergoes forced sway motion, the flow would be non-axisymmetric in the vicinity of the body, and we should solve this problem in 3-D flow, and it is different from the heave motion of a circular cylinder. Because the distance between the open boundary and body is just only large enough, the direction of the reflected wave on open boundary and body is just only large enough, the direction of the reflected wave on open boundary is an unknown quantity which can be determined by Eq.(20). If the open boundary is very far away from the body, the direction of the reflected wave will be along r direction, and it can be obtained from Eq.(20).

(3) in the wave diffraction problem we use $\Phi_S = \Phi - \Phi_W$ just only on the open boundary. On the free surface we let Φ satisfy nonlinear free surface condition, and Eq.(23) only used as satisfying radiation condition on open boundary.

DISCUSSION

by R.C. Ertekin

The authors should be commended for their paper which initiates one of the first steps in solving the exact nonlinear diffraction/radiation problems governed by the potential theory. I have a few questions on the formulation and results.

1) What is the form of the Green function which satisfy $\partial\Phi/\partial n=0$ on the sea floor? I know of a way of placing image singularities if the sea floor is horizontal so that $\partial\Phi/\partial z=0$ there. But not the form of Green function if it is arbitrary so that $\partial\Phi/\partial n=0$.

2) How did you deal with the 3-D problem of neighboring panel compatibility, i.e. that the surface elevation is continuous in passing from one panel to another and having a common boundary (without holes) between adjacent elements? If the problem is axisymmetric, one can use cubic spline interpolation, for instance, to deal with this problem, as it was done by Brown University researchers to solve the problem of rain drop collision with a free surface using the BEM (Symp. on Fluid Dynamics, California Institute of Technology, Pasadena, 1989). I can see the resolution of this difficulty in the case of a heaving cylinder, but not so easily, in swaying cylinder case in 3-D.

3) Wang, Wu and Yates solved the solitary wave diffraction by a vertical cylinder using Boussinesq equations (17th ONR symp., The Hague, 1988) and compared their results with Isaacson's that you cited. They found considerable discrepancy especially behind the cylinder. Whereas your results agree well with Isaacson's. Can you explain what you think might be the reason for this?

4) Could you comment on the accuracy and efficiency of your time stepping method?

Author's Reply

1) Here Green Function is so chosen that it can satisfy $\partial G / \partial n = 0$ on the sea floor when sea floor is flat, that is $G = 1/r + 1/r'$. If it is not flat, Green function can be described as $G = 1/r$. We must place singularities along

the sea floor. At this time $\partial G / \partial n \neq 0$, and the sea floor will become one part of the integration surface.

2) In the numerical calculation we can follow the fluid particles at every time step by use of Lagrangian free surface condition and time stepping scheme, then we can determine the free surface elevations and the shape of panel. If the shape of panel is very different from the initial shape, we can redivide the free surface element in terms of some regulations.

3) The diffraction problem of a vertical circular cylinder standing on the seabed and piercing the free surface by a soliton wave has been calculated. There are only small differences between our results and Isaacson's. I think that the different methods by which the radiation condition and the intersection points of the body and the free surface can be described will affect the numerical results.

4) The accuracy of time stepping method will depend on the discretion of the elements, the quantities of the time step and element size, the scheme of finite difference and the method of integration. If the radiation condition and the determination of intersection point are not appropriate, the calculation will diverge after a few time steps. If the free surface has very serious nonlinear, for examples, the body enter into the water suddenly the usual method to deal with the free surface elevation could not be very efficient.

Two-Dimensional Numerical Modelling of Large Motions of Floating Bodies in Waves

D. Sen

Memorial University of Newfoundland, Newfoundland, Canada

J. S. Pawlowski

NRC and Memorial University of Newfoundland, Newfoundland, Canada

J. Lever and M. J. Hinchey

Memorial University of Newfoundland, Newfoundland, Canada

Abstract

A numerical method is described, which simulates in the time domain the propagation of steep two dimensional periodic waves and the large motions induced by the waves on free floating bodies. The method allows for mild transient phenomena. The algorithm is based on Green's formula for harmonic functions applied in a finite control fluid domain, together with the fundamental solutions of Laplace's equation. A lowest order boundary element discretization is used. In addition to several numerical results, computations of the sway forces and the roll and heave motions induced by steep periodic waves on a floating body restrained in the sway mode are presented and compared with the results of specially conducted model tests.

1. Introduction

The increasing accessibility of computers of high capacity and the parallel development of computing techniques lead to the feasibility of algorithmic solutions of complicated hydrodynamic problems through a discretization of the corresponding governing equations in their fundamental form. In this paper, a solution of this type is discussed for the problem of motions induced by steep water waves on a floating body. The problem is formulated in two dimensions, in the time domain and potential fluid flow is assumed.

A number of numerical models of the same problem have been developed since the appearance of the integral equation formulation combined with the time stepping scheme for the non-linear free surface conditions originally employed by Longuet-Higgins and Cokelet [1] in a study of the propagation of steep waves. Faltinsen [2] considered forced heave motions of a two-dimensional circular cylinder, as well as a related problem of sloshing [3]. Vinje and co-workers extended their earlier work on breaking wave simulation (Vinje and Brevig [4]) to include submerged and surface-piercing bodies in the fluid [5,6], and next attempted

the problem of motions of floating bodies [7,8]. Subsequently, the simulation of a capsizing of Salter's duck, an ocean energy extracting device, was reported in [9]. For this latter study, experimental results supplemented the numerical simulation.

Following largely the techniques of Vinje and co-workers, with an important modification in the consideration of the body-free surface intersection point, Lin [10] simulated two-dimensional waves generated by a wave-maker in a finite rectangular tank. This study was followed by an extension to forced oscillations of axi-symmetric three-dimensional cylinders, [11]. Subsequently, Dommermuth and Yue [12,13] investigated the three-dimensional axi-symmetric problem and were able to simulate forced heave oscillations of large amplitude of cylinders and inverted cones in an otherwise undisturbed free surface. Greenhow and co-workers also employed the approach of Vinje and applied the method in a study of the two-dimensional impact problem [14,15,16]. In the adaptation, specific improvements and developments of the algorithm were made to make it suitable for the particular application. Isaacson [17,18] reported on a similar method for studying two and three-dimensional fixed and floating body problems. In spite of those efforts, to the knowledge of the authors, a fully satisfactory solution of the problem has not been achieved.

The study presented here was undertaken to investigate the possibility of developing a relatively simple but robust numerical model of the problem, which would be as suitable as possible for future generalizations to three dimensions. This in particular lead to the requirement that the wave excitation in the control fluid domain and the radiation condition for the outgoing waves be implemented in forms which would not preclude an efficient modelling of open water conditions. Similarly, the modelling of wave breaking was excluded in order to ensure long periods of simulation for steep wave conditions. In this way the presented model acquired its characteristic features which distinguish it from the models

described above.

The computer codes used in the study were written in FORTRAN and the computations were performed on DEC-VAX 8800 and -VAX 8530 cluster at Memorial University of Newfoundland. The study as presented here was completed in April 1988.

2. The Governing Equations and Their Boundary Element Formulation

2.1 The Governing Equations

A finite two-dimensional control domain, D , containing fluid is considered. The domain is bounded by a piecewise smooth contour ∂D , as shown in Fig. 1. The boundary ∂D is composed of the free surface ∂D_f , an impermeable bottom ∂D_b , and the wetted contour ∂D_s of a partially or fully submerged impermeable rigid body B . The remaining part of ∂D consists of two vertical geometrical control boundaries ∂D_{C1} and ∂D_{C2} , separated by such a distance that D contains the submerged part of B . A Cartesian coordinate system Oxz is chosen, with the z axis directed vertically upwards and origin O coinciding with the intersection of ∂D_{C1} with the undisturbed free surface.

The fluid in D is considered to be inviscid, incompressible and homogeneous, and the flow is assumed to be irrotational. If B is completely submerged, thereby rendering D a multiply connected domain, the flow is assumed to be acyclic. Therefore the flow in D is described by a single valued velocity potential $\phi(\vec{x}, t)$, where \vec{x} denotes the radius vector and t denotes time. The continuity of flow requires that the potential should satisfy Laplace's equation in D :

$$\frac{\partial^2 \phi}{\partial x^2} + \frac{\partial^2 \phi}{\partial z^2} = 0 \quad (1)$$

On the free surface ∂D_f the kinematic condition:

$$\frac{\partial \eta}{\partial t} = \frac{\partial \phi}{\partial z} - \frac{\partial \phi}{\partial x} \frac{\partial \eta}{\partial x} \quad (2)$$

and the dynamic condition:

$$\frac{\partial \phi}{\partial t} = - \left(\frac{p_a}{\rho} + g\eta + \frac{1}{2} (\nabla \phi)^2 \right) \quad (3)$$

are imposed, where η denotes the free surface elevation, g denotes the acceleration of gravity, and ∇ represents the gradient operator: $\nabla = \partial/\partial x$; p_a is the applied pressure on the free surface, set equal to 0 in the sequel, and ρ signifies fluid density. On ∂D_b the impermeability condition is applied

$$\frac{\partial \phi}{\partial n} = 0 \quad (4)$$

where $\partial/\partial n = \vec{n} \cdot \partial/\partial \vec{x}$, and \vec{n} designates the unit normal vector on ∂D directed outwards of D . The same condition imposed on the wetted body surface ∂D_s gives:

$$\frac{\partial \phi}{\partial n} = V_n \quad (5)$$

where V_n is the velocity component of ∂D_s along its (outward to D) normal. For bodies fixed in space, $V_n = 0$.

In addition, boundary conditions on control boundaries ∂D_{C1} and ∂D_{C2} are assumed to be applied in such a form that either ϕ or $\partial \phi/\partial n$ are known at all time instants $t \geq 0$. The imposed conditions are described later in connection with specific applications.

2.2 The Boundary Element Formulation and Its Discretization

2.2.1 The Boundary Integral Formulation

The application of Green's second identity to ϕ and the fundamental solution $\ln r(P, Q)$, with point P located in D or on ∂D , results in the well known Green's formula for harmonic functions [19]:

$$\Omega(P)\phi(P) - \int_{\partial D} [\phi(Q) \frac{\partial}{\partial n_{(Q)}} \ln r(P, Q) - \frac{\partial}{\partial n_{(Q)}} \phi(Q) \ln r(P, Q)] dS(Q) \quad (6)$$

with point Q located on ∂D . Here $r(P, Q) = |\vec{x}(P) - \vec{x}(Q)|$ is the distance between points P and Q ; the subscript of $\partial/\partial n$ indicates the point at which the differentiation is taken; $\Omega(P) = 2\pi$ for P located inside D but not on ∂D . For P located on ∂D , $\Omega(P)$ is the angle subtended inside D by the tangents to ∂D at P , which is equal to π when the normal to ∂D is continuous at P and the Cauchy principal value of the integral over ∂D is taken.

Formula (6) expresses the potential ϕ at any point P inside D in terms of its boundary values and those of its normal derivative. When P is placed on ∂D and values of ϕ are prescribed on a part of ∂D and those of $\partial \phi/\partial n$ are imposed on the remaining part, (6) represents two coupled Fredholm's integral equations of the second kind with respect to $\phi(P)$ as the unknown, and of the first kind with respect to $\partial \phi(P)/\partial n$ as the unknown. Formula (6) is valid at any instant of time, and therefore for solutions advancing in time, this relation can be applied at every consecutive time step.

2.2.2 Discretization

It is assumed that ∂D consists of N_s piecewise smooth open contours:

$$\partial D \sim \bigcup_{k=1}^{N_s} \partial D_k \quad (7)$$

The open contours ∂D_k are further subdivided into a finite number of segments, each approximated by a straight line between its end points:

$$\partial D_k = \bigcup_{i=1}^{M_k} \delta S_i^k \quad (8)$$

A collocation point Q_i^k is chosen on each of the segments δS_i^k . The functions ϕ and $\partial\phi/\partial n$ on ∂D are approximated by constant values on each segment and the values are determined at the corresponding collocation points Q_i^k . Following the usual practice, the collocation points are placed at the centre of each segment. However, in principle Q_i^k need not be located centrally in δS_i^k . The discretization scheme maintains a consistent order of approximation (see e.g. [20]) and represents an application of the lowest order boundary element method or b.e.m., [21]. A system of linear algebraic equations is thus obtained from (6), (7) and (8), with respect to the unknown ϕ_i^k or $\partial\phi_i^k/\partial n_i$ values at collocation points Q_i^k . The influence coefficients in this system depend only on the geometry of the boundary contour and can be determined explicitly (see e.g. [3]) for the present type of straight line segments.

The bottom condition (4) permits exclusion of ∂D_0 from the contour of integration in the integrand in (6) if ∂D_0 is horizontal, by augmenting the fundamental singularity with its symmetric image with respect to ∂D_0 . Thus, when the bottom is horizontal at a depth d , $\ln r(P, Q)$ in (6) is replaced by $\ln r(P, Q) + \ln r(P, Q')$, and ∂D_0 is discarded from ∂D . Here Q' is the symmetric image of Q with respect to ∂D_0 . This results in a reduction of the system of linear equations by the number of segments used in discretizing ∂D_0 . The influence coefficients then contain additional integrations over the image segments.

It is possible to apply a higher order formulation of the b.e.m., for example, an isoparametric representation of ϕ_i^k and $\partial\phi_i^k/\partial n_i$ over the segments, δS_i^k (see e.g. [21]). Such refinements are achievable at the expense of additional algorithmic complexities. In particular, complications arise in the treatment of the point at which the normal to ∂D is discontinuous or at the intersection of two parts of the boundary on each of which different conditions (i.e. ϕ or $\partial\phi/\partial n$) are imposed, which in the present application are the features of the body-free surface intersection point. In addition to a discontinuity of the normal at this point, conditions posed on the body and the free surface are different (Neumann condition on the body boundary and Dirichlet condition on the free surface). In this respect, the central collocation discretization scheme adopted here

avoids an explicit occurrence of the problems and as a result is the most straightforward for numerical implementation. In addition, higher order applications of b.e.m., which lead to a better resolution with lesser number of segments (see e.g. [22]), are known to be more susceptible to numerical instability [24] which is a major concern in the considered application.

The present choice of discretization scheme is founded in the belief that a 'workable' model can be developed based on this simplest scheme, for the final task of the simulation of large motions of floating bodies in steep waves, since it is supposed that several of the anticipated problems may not necessarily be remedied by applying more refined discretizations but initially may even be obscured by the inherent difficulties of such applications. More refined discretizations can, in principle, be adopted later.

2.3 The Basic Algorithm of Solution

The general discretization scheme described above is applied to the boundary value problem (1) to (5) by identifying the open contours ∂D_k with the free surface ∂D_f , the bottom ∂D_0 , the body contour ∂D_b and the control boundaries ∂D_{c1} and ∂D_{c2} . The simulation sought for is accomplished through a time marching procedure. Initial conditions provide the boundary data on ∂D at $t = 0$: ϕ on ∂D_f , $\partial\phi/\partial n$ on ∂D_0 and ∂D_b , and either ϕ or $\partial\phi/\partial n$ on ∂D_{c1} and ∂D_{c2} . From the solution of the appropriately rearranged system of linear equations, $\partial\phi/\partial n$ on ∂D_f and ϕ on ∂D_b for that time instant are determined. The boundary conditions are then invoked to obtain the required boundary data for the next time level. In particular, appropriate evolution equations for the free surface, deduced from (2) and (3), and for the control boundaries, if applicable, are integrated in time to determine the updated free surface contour (i.e. the configuration of ∂D_f for the advanced time level) and the values of ϕ or $\partial\phi/\partial n$ on the updated boundaries. On the body, $\partial\phi/\partial n$ on ∂D_b is related to the body velocity by virtue of (5), which in turn is related to ϕ through the body equations of motion and Bernoulli's equation. The boundary contour ∂D as well as the boundary data for the advanced time level are now established and the solution process can be repeated.

The potential ϕ at any desired location in D can be calculated from the discretized form of relation (6). Other information, e.g. fluid velocity and pressure are calculable from ϕ by utilizing Bernoulli's equation and employing numerical difference techniques in space and time. The evolution of the free surface and the motion of the body, which constitute necessary information for advancing the solution in time, are extracted as the simulation proceeds.

The system of linear equations to be solved, in general corresponds to a full coefficient matrix and thus benefits admissible in solutions of matrices with special features are not available. In the present algorithm, a standard IMSL (International Mathematical and Statistical Library) routine is utilized which employs a Gaussian elimination technique for matrix inversion [25].

The evolution equations for the free surface can be put in the following general form:

$$\frac{dy}{dt} = f(y, t) \quad (9)$$

In the present algorithm, a 4th order implicit Adams-Bashforth-Moulton (A-B-M) scheme is adopted and is found to be convergent for all required integrations. To achieve convergence to the third significant figure, usually not more than one corrector step is necessary. This scheme requires information at the preceding four steps. In the initiation of the solution, the first three steps are therefore treated by means of successively lower order schemes with a greater number of iterations.

A variety of other schemes exists for the integration of equations of the form (9), e.g. Runge-Kutta schemes, Hamming's method, etc. Fourth order Runge-Kutta starters are popular for analogous initial-value problems (e.g. [1, 2 and 13]). However, the starter scheme employed here is found adequate for the applications considered. Limited numerical experiments with other schemes were also performed and the algorithm appeared insensitive to the choice of any particular scheme.

3. Applications to Linear Free Surface Flow Problems

3.1 General Considerations

A simple means of partly testing the effectiveness and reliability of the algorithm is to apply it to problems which involve small amplitude free surface elevations. The simulation of the propagation of small amplitude waves allows one to linearize the free surface conditions and therefore reduces the possible sources of numerical errors. It also allows us to examine and solve the remaining numerical problems as discussed below. In addition, solutions of linearized flows are usually available in closed forms thereby providing an exact basis for comparison.

Upon applying the usual approximations, the free surface conditions (2) and (3) take the following linearized forms:

$$\frac{\partial \eta}{\partial t} = \frac{\partial \phi}{\partial z} \quad (10)$$

$$\frac{\partial \phi}{\partial t} = -g\eta \quad (11)$$

and are applied on the undisturbed free surface $z = 0$. In addition, for the applications considered in this section, the fluid domain is represented by the rectangular area depicted in Fig. 1, with the body contour removed. The bottom surface is taken to be at a constant depth d . The free surface part of the boundary on which the integrand in (6) is to be evaluated remains undisturbed at all time instants, and $\partial/\partial n = \partial/\partial z$ on ∂D_f . The entire boundary ∂D is therefore independent of time and consequently the influence coefficients in the resulting system of linear equations remains unchanged in time.

3.2 The Simulation of Airy Waves

As a test case, the method was applied to simulate the propagation of steady Airy waves in the control domain. In the simulation, the initial values of the potential on the undisturbed free surface $z = 0$ were specified according to the Airy wave potential:

$$\phi(\bar{x}, t) = \frac{H\lambda}{2T} \frac{\cosh[2\pi(z+d)/\lambda]}{\sinh 2\pi d/\lambda} \sin \frac{2\pi}{\lambda} (x - ct) \quad (12)$$

with $t = 0$. This corresponds to a wave of height H , length λ and period T , progressing in the positive x direction with celerity c . For the linearized simulations, either ϕ or $\partial\phi/\partial n$, computed from (12), were applied on the control boundaries.

The following notation is used in the discussion of computed results: Δx denotes the length of the segments (or the spatial grid size), suffixed appropriately to indicate the part of ∂D on which they are chosen, viz. Δx_f , Δx_{c1} , Δx_{c2} are the segment sizes on ∂D_f , ∂D_{c1} and ∂D_{c2} respectively. The time step size is denoted by Δt . N_t represents the time step level of computation: $N_t = t/\Delta t$. The distance between the control boundaries ∂D_{c1} and ∂D_{c2} , i.e. the horizontal extent of the free surface, is denoted by L . In the linearized simulations, the spatial grid sizes are kept constant on each part of the boundary, and Δt is constant over the entire time of simulation.

As an example, in Figs. 2(a) and (b), the free surface elevations are shown for a simulation where Neumann conditions were imposed on both the control boundaries. The control domain was relatively long, $L = 7\lambda$, with water depth $d = 0.4\lambda$. Other parameters were: Δx_f , Δx_{c1} , $\Delta x_{c2} = \lambda/25$ and $\Delta t = T/40$. The comparison with theoretical free surface contours clearly demonstrates that the algorithm is capable of following the wave motion with acceptable degree of precision over long periods of simulation time.

Computations were also performed for a wide variety of combinations of the spatial and

temporal grid sizes, for different values of L/λ and d/λ , and for different initial distributions of the free surface potential (i.e. initial values of ϕ on ∂D_f given by (12) with values of t different than 0). In all computations, the quality of agreement between the numerical and theoretical results was similar to the presented examples. The numerical solutions did not exhibit any discernible evidence of degeneration even after, for example, 400 time steps or up to 10 wave periods.

3.3 The Unsteady Wave Propagation

The simulation of the propagation of unsteady waves is achieved by specifying an exciting wave potential on one of the control boundaries. The fluid in D is initially at rest with $z = 0$ as the initial contour of ∂D_f . The potential given by (12), which corresponds to an Airy wave propagating in the positive x direction, is applied in a modulated form on ∂D_{C1} at all time instants $t \geq 0$. Therefore, a disturbance is introduced at one end of the control domain to excite a fluid motion in the initially unperturbed fluid in D . For this simulation, the boundaries ∂D_{C1} and ∂D_{C2} can be referred to as upstream and downstream boundaries respectively.

For the initially unperturbed state of fluid $\phi(\vec{x}, t)|_{t=0} = 0$ in the entire of D , including ∂D (the value of ϕ could strictly be any constant, but it is convenient to make this constant 0 by redefining ϕ , see e.g. [26]). What is not so apparent is the requirement that

$\partial\phi(\vec{x}, t)/\partial t|_{t=0} = 0$ be maintained simultaneously. Examining eqn. (3), it can be noticed that $\eta|_{t=0} = 0$ and $\phi|_{t=0} = 0$ imply $\partial\phi/\partial t|_{t=0} = 0$ on ∂D_f . It follows that $\partial\phi/\partial t$ on ∂D_{C1} must have a zero value at $t = 0$ for the compatibility of the initial boundary data, at the intersection of ∂D_{C1} and ∂D_f . The potential given by (12) maintains $\phi|_{t=0} = 0$ on ∂D_{C1} but $\partial\phi/\partial t|_{t=0}$ has a finite value. Simulations which did not impose $\partial\phi/\partial t|_{t=0}$ on ∂D_{C1} were not successful due to a numerical instability which started at the origin (at $\partial D_{C1} \cap \partial D_f$) and slowly spread over the entire domain. Although this instability is of a weak type, in the sense that the solution can still be continued, the free surface contour shows undesired 'zigzag' patterns and eventually diverges from the required Airy wave profile.

In the present formulation, a modified excitation potential ϕ^* is used, defined by introducing a modulation function $M(t)$:

$$\phi^*(t) = M(t)\phi(t) \quad (13)$$

with:

$$M(t) = \begin{cases} 0.5(1 - \cos(\pi t/\beta)) & t < \beta \\ 1 & t \geq \beta \end{cases} \quad (14)$$

where $\beta > 0$. This function has the property that $M(t)|_{t=0} = 0$ and $\partial M(t)/\partial t|_{t=0} = 0$. Therefore, regardless of the form of ϕ on ∂D_{C1} , the initial values of $\partial\phi^*/\partial t$ are equal to zero by virtue of (13) and:

$$\frac{\partial\phi^*(t)}{\partial t} = M(t) \frac{\partial\phi(t)}{\partial t} + \frac{\partial M(t)}{\partial t} \phi(t) \quad (15)$$

The time span over which the excitation potential is modulated can be controlled by selecting an appropriate value of the parameter β . When (13) is applied with a sufficiently large value of β in $M(t)$, the instability disappears. With $\beta/T = 1.0$, the existence of some undesired behaviour was still detected. With further increase of β/T to 2, waves evolved smoothly although no numerical smoothing was applied. By inserting (13) in Bernoulli's equation it is found that the modulation excludes an impulsive application of pressure on ∂D_{C1} at $t=0$. These considerations appear to parallel a recent study of the impulsive wave-maker problem, [27].

3.4 Computed Examples

Examples of computed results in terms of the free surface elevations are shown in Fig. 3. For these computations, the downstream boundary was placed at the distance of 2λ from the upstream boundary. The discretization parameters were: $\Delta x_f = \lambda/24$ and $\Delta t/T = 1/36$, where λ and T refer to the length and period of the excitation wave. The downstream boundary was considered to be a rigid wall, thus the condition posed on ∂D_{C2} was $\partial\phi(t)/\partial n = 0$ at all time instants. The water had a depth of $d = 0.5\lambda$, and the excitation potential was modulated over $2T$, i.e. $\beta/T = 2$. Fig. 3. shows plots of the evolutions of free surface elevations at four stations situated at $x = 0.26\lambda, 0.50\lambda, 0.74\lambda$ and 0.98λ , together with the theoretical Airy wave evolutions computed from (12) at the corresponding stations. For comparative purposes, the Airy wave evolutions are also modulated by the same modulation function. It is clear that for $t/T \leq 5$, the reflected waves do not reach the locations $x/\lambda = 0.98$. At locations $x/\lambda = 0.24$ and 0.50 , more than two periods of steady state results are achieved.

The algorithm was also applied to simulate wave generation by piston and flapper types of wave-makers. The corresponding Neumann boundary conditions were imposed on a ∂D_{C1} fixed at the mean position of the wave-maker board. In both cases, the normal velocity values were modified by the modulating function (14). Stable propagating waves were simulated. The gain functions (wave amplitude to half stroke ratios) were found to be within 0.2% and 1% relative error when compared to the linear theory values [28].

The presented results exemplify the robustness of the numerical time domain

simulation algorithm for fluid flow problems that include a free surface. Computations were performed for a number of other combinations of parameters, and showed a similar quality of agreement with theoretical solutions. No rigorous rule could be established for the minimum size of Δx . As a rough guide, a size of $\Delta x = \lambda/12$ was found to describe adequately the evolution of the free surface for most of the simulations. Further relaxation resulted in a lack of resolution, although the fluid motion could still be followed (which means the solution did not break down). For temporal grid size, the Courant-Friedrichs-Lewy (C-F-L) type of condition, [29]:

$$N_{CFL} = |c \frac{\Delta t}{\Delta x}| \leq 1 \quad (16)$$

with c representing the wave celerity, was used for guidance, although no formal stability analysis of the algorithm was carried out. In the present computations, for most of the cases, a value of N_{CFL} between 0.5 and 0.7 was used.

However, the solutions were found to exhibit a tendency towards numerical instability upon successive refinements of the spatial mesh sizes. When a collocation point was located very close to a corner where the boundary undergoes a sharp change in curvature, such as the intersections of ∂D_f with ∂D_{C1} and ∂D_{C2} , relatively large errors occurred in the computed velocities at these locations, in comparison with points far from such corners. These non-uniform differences appeared to introduce numerical instability when the grid size was very fine, typically when $\Delta x/\lambda \leq 1/100$. A similar behaviour of solutions near corners in applications of boundary element methods is documented in literature [24]. This instability is thought not to be a serious limitation in the applications of the algorithm but serves to indicate a lower bound on the grid sizes.

In addition to the 4th order A-B-M scheme, other schemes for the integration of eqns. (10) and (11) were also tried. First order implicit schemes were found to be inadequate in that the solution showed poor convergence characteristics and contained large errors. In contrast, 2nd order schemes lead to substantial improvements. Further improvements were achieved by using 3rd and 4th order schemes, although the relative improvements between those two latter orders were practically insignificant (the numerical values differed only in the sixth significant figure). In no case was more than one corrector level required for a convergence to the third significant figure. It is observed here that, from a computational point of view, higher order schemes do not necessarily require additional computational effort. To start the 4-th order A-B-M schemes, lower order A-B-M schemes were found to be adequate.

4. The Unsteady Propagation of Steep Waves

4.1 The Evolution Equations for The Free Surface

For the simulation of the propagation of steep waves, it is necessary to consider the non-linear free surface conditions (2) and (3) without the linearizing approximations. These equations are to be satisfied on the exact location of the free surface and therefore the evolution of the free surface within the control domain must be followed. As a result the fluid domain must be redefined at every consecutive time instant. In addition the evolution of the boundary data on the free surface must also be determined.

In the present work, an Eulerian formulation of the free surface conditions is used. Assuming the free surface elevation η to be a single valued function of coordinate x , the evolutions of η and ϕ on the instantaneous free surface are followed at image points of the undisturbed free surface, obtained by the projection along the vertical axis. The variation of the potential at the image points on the free surface, which undergo vertical displacements, is determined by (see e.g. [3]):

$$d\phi = \frac{\partial \phi}{\partial t} dt + \frac{\partial \phi}{\partial z} d\eta \quad (17)$$

since $\phi = \phi(z, t)$ at these points. Here $d\eta$ is the differential of the vertical displacement of the image point:

$$d\eta = \frac{\partial \eta}{\partial x} dx \quad (18)$$

From (2), (3), (17) and (18), the evolution equation for ϕ is obtained as:

$$\frac{d\phi}{dt} = -g\eta - \frac{1}{2} \left[\left(\frac{\partial \phi}{\partial x} \right)^2 + \left(\frac{\partial \phi}{\partial z} \right)^2 \right] - \frac{\partial \phi}{\partial x} \frac{\partial \phi}{\partial z} \frac{\partial \eta}{\partial x} \quad (19)$$

which defines the rate of change of the potential at the image points. In the present method, therefore, eqns. (2) and (19) respectively are the evolution equations to be integrated in time in order to determine the instantaneous free surface contour and potential.

The above method of following the evolution of free surface is different from the Lagrangian method utilized in most of the previous investigations of non-linear water waves, which were also based upon boundary integral formulations (e.g. [1,5,11,13,30 and 31]). The attractiveness of the Lagrangian method follows from its ability to describe multivalued free surface contours. In contrast, the applicability of the present method is restricted to single-valued free surface contours. The possibility of simulating extreme wave conditions, pertinent

to wave breaking, is therefore excluded. However, the present method provides several computational advantages. The image points on the free surface, which through the discretization are identified with collocation points, are not allowed to cluster. So, the scheme avoids the adverse numerical effects often inherent in the Lagrangian methods in which the particles tend to concentrate in some regions. From the previous experience of other workers, it is known that some form of control of the Lagrangian points is necessary to prevent them from clustering, e.g. the introduction of a 'tangential' velocity component as discussed by Baker in [30] or a regridding of the free surface points at every time step, as employed in [13]. The present method of following the free surface is free from such complications. In addition, the collocation points cannot leave the computational domain at any time, therefore the additional task of tracing such points is avoided. Computational experience gained from performed simulations suggests that in the presented method numerical difficulties arise when a collocation point is situated very close to one of the vertical control boundaries. By preventing horizontal displacements of the collocation points, such problems are also minimized.

Yet another point with regard to the applicability of the present method needs to be mentioned. The ultimate objective is to be able to simulate the motion of a floating body in steep waves, for a sufficiently long time, preferably over a number of periods of oscillation. It must be noted that in the Lagrangian method the simulation cannot be extended much beyond the time when the wave breaks. Similar restrictions in applications are typical of most finite-difference algorithms (see e.g. [32]).

4.2 The Simulation Procedure and Wave Excitation

The simulation of the unsteady propagation of steep waves is accomplished by a procedure similar to the one described in §3.3. A wave potential, representing an oncoming wave travelling in the positive x direction, is imposed on ∂D_1 at $t \geq 0$. This applied potential is hereinafter called the excitation potential, since it provides the necessary excitation of fluid motion in D . It was found through numerical results that the form of the excitation potential has negligible influence on the generated numerical wave at points in the interior of D , provided they are sufficiently far from the upstream boundary.

An alternative way of simulating waves is to provide a moving wave-maker at one end of the control domain. Such a procedure was applied in earlier works, e.g. [10,11,14]. In the present method of following the evolution of the free surface, such an approach would necessitate either a redistribution of the free

surface grid or a successive introduction and deletion of collocation points, since the wave-maker enters and withdraws from the free surface grid. It could cause collocation points to come very close to the wave-maker and thus generate numerical difficulties, as it was explained above.

4.3 The Non-reflective Downstream Boundary

The application of the impermeability condition at the downstream boundary ∂D_2 , as it was done in the applications presented above, is not satisfactory for simulations of long duration. An appropriate open boundary, or radiation condition must be specified, which makes the boundary sufficiently transmissive to allow wave patterns generated in D to pass through the boundary without causing appreciable reflection effects. In the present algorithm, a simple open boundary condition is adopted on ∂D_2 , which assumes that the potential at this boundary can be written as a wave form of the same celerity as that of the applied excitation potential on ∂D_1 :

$$\phi(x,t) = \phi(x - ct) \quad (20)$$

where c represents the celerity of the excitation wave (cf. eqn. (12)). This results in the following relation:

$$\frac{\partial \phi}{\partial t} = -c \frac{\partial \phi}{\partial n} \quad (21)$$

in which $\partial/\partial n = \partial/\partial x$ on ∂D_2 was used. Eqn. (21) has a form similar to Orlandi's radiation condition but its application here is not strictly equivalent. In [33] and in many finite-difference algorithms (see e.g. [34]), the value of c is taken as the celerity of the local waves approaching the downstream boundary, and c is determined by a numerical differentiation at the neighbouring grid points. In [35], a similar simple form is adopted with c determined from:

$$c = \sqrt{gd} \quad (22)$$

where d denotes the local water depth at the downstream boundary. Eqn. (22) represents the shallow water approximation of the phase velocity and is therefore different from the condition applied in the present method (both methods become equivalent in the limiting situation of $d/\lambda \ll 1$).

The evolution of ϕ is now easily determined by the time-integration of eqn. (21), using the same scheme as the one used for integrating (2) and (19). Simple as it appears, in the considered applications this procedure results in minimal reflection effects on ∂D_2 , as the results presented below illustrate.

4.4 Specific Considerations

4.4.1 Spatial Derivatives on The Free Surface

The evolution equations (2) and (19) require the evaluation of spatial derivatives of η and ϕ at the collocation points. To determine $\partial\eta/\partial x$, η as a function of x is approximated by a cubic spline. From this approximation, the components of the outward normal vector can be calculated. For the spatial derivatives of ϕ :

$$\frac{\partial\phi}{\partial s} = n_2 \frac{\partial\phi}{\partial x} \quad (23)$$

since $1/(ds/dx) = n_2$, where $\partial/\partial s$ denotes the tangential derivative. To determine $\partial\phi/\partial x$, in turn ϕ as a function of x is approximated by a cubic spline. From $\partial\phi/\partial s$ and $\partial\phi/\partial n$ and the outward normal vector, other components of the spatial derivatives can be determined. In the software, an IMSL routine for cubic splines with natural end conditions is used in which no conditions are prescribed at the end points and continuity of second derivatives is enforced at the penultimate points [36].

4.4.2 The Instability at The Intersection of ∂D_{C1} and ∂D_f

When a time-modulated excitation Airy potential is applied on ∂D_{C1} in the described algorithm, an instability is found to originate at the intersection of ∂D_{C1} and ∂D_f . The form of the instability is qualitatively similar to that observed in the analogous linear application when the modulation function was not used. The solution breaks down, typically within 10 time steps irrespective of the step size.

The occurrence of these oscillations can be attributed to the incompatibility of the excitation wave potential and elevation applied externally on ∂D_{C1} with the wave potential and free surface elevation induced in D in the vicinity of ∂D_{C1} . In other words, the free surface conditions implicitly satisfied on the left of ∂D_{C1} (i.e. by the exciting wave potential) are inconsistent with the conditions on ∂D_f immediately to the right of ∂D_{C1} . On the basis of conducted numerical experiments, this discontinuity is believed to cause large velocity gradients across the vertical boundary and these initiate the instability. The application of other, 'non-linear' excitation potentials, e.g. Stokes second order potential, were tried without success. Difficulties originating from analogous discontinuities were known earlier, e.g. similar problems were discussed in [37] and in [11], the discontinuity was identified with the difficulty of the matching of non-linear interior with linear exterior solutions, reported in [8].

In order to achieve a smooth variation of the free surface elevation and potential across ∂D_{C1} , the matching procedure, described below, was developed. Another vertical boundary ∂D_{C1}^* in the interior of the control domain D is introduced at a short distance l from ∂D_{C1} . The free surface elevation and potential

evaluated without the matching procedure are represented by $f_2(x)$. A transfer function $g(x)$ is introduced to redefine $f_2(x)$ as $f_2^*(x)$ in the 'matching zone' between ∂D_{C1} and ∂D_{C1}^* :

$$f_2^*(x) = g(x) f_1(x) \quad (24)$$

where $f_2^*(x)$ is defined in $x_1 \leq x \leq x_1 + 1$, $f_1(x)$ indicates the theoretical wave elevation or potential corresponding to the excitation potential applied on ∂D_{C1} , and x_1 represents the x coordinate of ∂D_{C1} . A quadratic polynomial is chosen for $g(x)$ whose coefficients are determined from the conditions:

$$\begin{aligned} f_2^*(x_1) &= f_1(x_1) \\ f_2^*(x_1 + 1) &= f_2(x_1 + 1) \end{aligned} \quad (25)$$

$$\frac{\partial}{\partial x} f_2^*(x_1 + 1) = \frac{\partial}{\partial x} f_2(x_1 + 1)$$

The above procedure requires the evaluation of $\partial[f_2(x_1 + 1)]/\partial x$ and this is determined from a second order central difference scheme. A linear form of $g(x)$ was found not as satisfactory. The quadratic function for $g(x)$ is however very effective in suppressing the instability and enables the fluid motion to be followed without further problems originating at the intersection point.

On the downstream boundary ∂D_{C2} it is necessary to determine the intersection of ∂D_f with ∂D_{C2} . This is determined via a second order Lagrangian scheme using the data at the three preceding collocation points on ∂D_f .

4.4.3 The Instability on The Free Surface

In addition to the instability originating at the upstream end of the free surface, another instability was found to develop on the entire free surface as the solution progressed. Saw-tooth instabilities of this type have been reported by earlier investigators. Numerical experiments with various combinations of the spatial and temporal grid sizes were performed with the hope of identifying a stability criterion related to these discretization parameters. However no such criterion could be established. In the present formulation, in which collocation points on the free surface are restricted to move vertically, the arc lengths between the adjacent collocation points never reduce below the horizontal grid spacing. Consequently, the relation between the time step size and the horizontal projection of the free surface segments is easily controlled. In all computations, the C-F-L type condition, see eqn. (16), was satisfied in the entire fluid domain and throughout the whole simulation period. A form of stability criterion based upon a linear von Neumann stability analysis for a 4th order Runge-Kutta scheme was provided in [13]:

$$\left| \frac{\pi c \Delta t^2}{8 \Delta x_f} \right| \leq 1 \quad (26)$$

This condition was also maintained in the discussed computations.

The present computational experience indicates that the instability is closely associated with the shape of the free surface elevation. It becomes more pronounced as the wave steepens. It should be observed that in the analogous linear application, no such problem was encountered. Computations with successively higher levels of iteration in the time-integration of the free surface conditions and a close examination of the computed free surface profiles and boundary data suggest an insensitivity of the instability to the time-integration schemes. Therefore, the violation of a stability condition of the above type might not be the root mechanism in the initiation of the instability.

To suppress this instability, the smoothing scheme originally employed by Longuet-Higgins and Cokelet [1] was adopted. In view of their computational experience, the five-point scheme was used instead of a seven-point scheme. The formula provided in [1] is inapplicable for the special cases of the first and last two collocation points on the free surface and a modified scheme had to be applied there. The smoothing scheme is applied at regular time intervals. Usually, the application at every 4th time step was found effective in eliminating the unwanted oscillations. It is possible to employ a variety of other available smoothing schemes. A third degree five point least squares smoothing scheme was also tested and was found to be equally effective.

Although the application of artificial smoothing is known to cause a loss of the local accuracy of the solution, the global solution fortunately remained within acceptable limits of accuracy, which was demonstrated by the computed results. This feature of the artificial smoothing was also noted by earlier workers (e.g. [11, 14 and 38]).

4.5 Computed Results

In the present context, the notation described above applies with the exception that Δx_f denotes the spacing of the free surface collocation points along the x axis, instead of the actual lengths of the segments. Unless otherwise specified, the applied excitation potential on ∂D_{C1} is the Airy potential. The normalizing parameters for horizontal and vertical length scales and time scale are respectively the length λ , height H and period T of the Airy wave corresponding to the excitation potential (cf. eqn. (12)). In all presented computations, Δx_f , Δx_{C1} , Δx_{C2} and Δt are constants. However, due to wave run up, ∂D_{C2} continuously changes in length. Since the left hand side of eqn. (21) is an Eulerian time derivative, the collocation points on this

boundary are generally kept fixed in space, except for the uppermost segment. Depending on the length of ∂D_{C2} , a segment is deleted or an additional segment is introduced so that the length of the segment in comparison with the length of the adjacent segment on ∂D_f maintains a ratio between 0.5 and 2.0.

Numerical experiments carried out to investigate the effectiveness of the matching procedure showed that the number n of collocation points in the matching zone is the dominant factor in comparison with the length l of the zone. The choice of $n = 4$ was very effective in removing the oscillations, regardless of the grid sizes and wave heights. The subsequent results are all computed with this value of $n = 4$.

The convergence characteristics of the solution in the entire fluid domain was studied. The chosen fluid domain extended horizontally over $L = 2\lambda$ and vertically over $d = 0.5\lambda$, and the applied excitation corresponded to a large nominal wave steepness of $H/\lambda = 0.10$. For these computations, the segment sizes were: Δx_f , Δx_{C1} , $\Delta x_{C2} = \lambda/16$, $\lambda/20$, $\lambda/24$, $\lambda/28$, $\lambda/32$ and $\lambda/40$. The time step size was $\Delta t/T = 1/40$ for the first five values of N , while for $N = 120$, it was halved to $\Delta t/T = 1/80$. This was necessary because of the reduced segment sizes. Otherwise for $\Delta t/T = 1/40$, which corresponds to $N_{eff} = 1$ (cf. eqn. (16)), the solution exhibited an instability. Free surface smoothing was applied at every fourth step, $\beta/T = 1$ was taken in the modulation function, and $n = 4$ was used for the matching region. Except for the value of $N = 48$, the results demonstrated good convergence characteristics. For this value of N , the results were affected by comparatively poorer resolution. These computations (and many others) indicated that the value of $\Delta x_f = \lambda/24$ and comparable values for Δx_{C1} , Δx_{C2} were adequate for describing the fluid motion without appreciable effects of the lack of resolution.

The effectiveness of the open boundary condition (21) was examined by selecting a range of values of the celerity of the outgoing waves. Taking c in eqn. (21) as c' , with $c' = \alpha c$, where c represents the celerity of the exciting wave at ∂D_{C1} (as in eqn. (12)), computations covered a variation of α from 0 to 1, with specific values of $\alpha = 0$, 0.25, 0.50, 0.75, 0.90 and 1.00. The other parameters were chosen as: $L = 2\lambda$; $d/\lambda = 0.5$; $H/\lambda = 0.10$; Δx_f , Δx_{C1} and $\Delta x_{C2} = \lambda/24$, and $\Delta t/T = 1/40$. The free surface elevations at the simulation time of $t/T = 8.75$ are shown in Fig. 4. It is apparent that the reflection effects at the downstream boundary increase with the difference between α and 1. Results for $\alpha = 1$ indicate that the wave passes through ∂D_{C2} with imperceptible reflection. From these and other computations the effectiveness of choosing $\alpha = 1.0$ for making the downstream boundary transmissive was evident, although

values slightly less than 1 also appeared to work well. Computations were also attempted for values of α greater than 1, but even for a value moderately greater than one, e.g. $\alpha = 1.05$, the solution broke down after about $t = 5T$, which was approximately the time for the wave to grow fully at the downstream boundary. This breakdown resulted from an instability originating at the downstream intersection of ∂D_1 and ∂D_2 . In view of the success of $\alpha = 1.0$ in making the boundary sufficiently non-reflective, this aspect was not pursued any further.

A comparison of evolutions of wave elevation, for $H/\lambda = 0.10$ at $x/\lambda = 0.98$, with theoretical profiles for the Airy wave given by (12), Stokes second order wave and Miche's second order theoretical profile [39] are shown in Fig. 5. The numerically simulated wave compares well with the second order profiles, but displays stronger non-linear characteristics. The comparatively more peaky crest and shallower trough of the computed wave are visible.

To investigate the influence of the excitation potential on the interior solution, computations were performed with a Stokes second order potential as the excitation instead of the Airy wave potential. The applied excitations had a value of $H/\lambda = 0.10$, for which the second order correction in wave amplitude is almost 10% of the first order amplitude, but both excitations have the same average energy density. The fluid domain chosen and the discretization parameters were: $L = 2\lambda$, $d = 0.5\lambda$, $\Delta x_f = \lambda/24$, $\Delta t = T/40$. The evolutions of wave elevation in time at $x/\lambda = 0.48$ and 1.48 are shown in Figs. 6 (a) and (b). The differences between the two simulations are undetectable.

The results presented above show that the simulation of unsteady steep wave propagation can be achieved by imposing an excitation potential on one of the vertical control boundaries encompassing a rectangular fluid domain. The interior solution appears to be not sensitive to the exact form of the potential. The simulated wave profile displays typical non-linear characteristics of relatively more peaky crest and shallower trough in comparison with linear waves. As expected, the non-linearities are more pronounced for steeper waves. Very steep waves were simulated for time durations of over 20 wave periods, for which a steady state behaviour occurred in the entire domain.

The simple outgoing wave condition (21) produced good results over the entire period of each computation as well as for all combinations of H , T , L and d for which computations were performed. The interior wave was not observed to be contaminated by numerical reflection effects even after long times of simulation and at locations close to the downstream boundary. This demonstrated the

effectiveness of (21) in the modelling of the propagation of nonlinear periodic waves.

5. The Floating Body Problem

5.1 The Governing Equations

In order to simulate motions of a floating body in steep waves, a floating body B is introduced in the fluid, such that its wetted contour ∂D_B is completely contained in D (see Fig. 1). The objective is to expose B to an incident steep wave train and subsequently to follow the induced motion of B . A propagating steep wave is generated in D in the manner described above. For such simulations, it is necessary to know the exact location of ∂D_B at every time instant. In addition, a relation between ϕ and $\partial\phi/\partial n$ on ∂D_B must be established such that the evolution of boundary data on ∂D_B can be followed. The required information is obtained by invoking the equations of rigid body motion and the impermeability condition.

For the following considerations an additional coordinate system fixed with the body is introduced. A rectangular Cartesian coordinate system $Gx'z'$ is used with its origin G located at the body centre of gravity CG , and Gz' axis directed vertically upwards in the undisturbed position of the body. The axis through G perpendicular to the x' and z' axes is assumed to coincide with a principal axis of inertia of the body. The body geometry is invariant in the coordinate system and therefore the instantaneous wetted contour ∂D_B is completely defined by the location and orientation of $Gx'z'$ system with respect to the Oxz system and wave elevation. The components in the $Gx'z'$ system denoted by $(\bar{x})'$, of the radius vector of a point fixed with the body, are related to the components in the fixed in space system, of the radius vectors of the same point and of CG , denoted by (\bar{x}) and (\bar{x}_G) respectively, by the following relation:

$$(\bar{x} - \bar{x}_G) = [R]^T (\bar{x})' \quad (27)$$

where matrix $[R]$ represents the tensor of rotation and the superscript T indicates a transpose. $[R]$ is given by:

$$[R] = \begin{bmatrix} \cos \theta & \sin \theta \\ -\sin \theta & \cos \theta \end{bmatrix} \quad (28)$$

where θ denotes the angular displacement of $Gx'z'$ system with respect to Oxz system, measured as positive counterclockwise. The equations of motion for the body are written in the Newtonian form:

$$(F_x, F_z, M_B) = (M_B \ddot{x}_G, M_B \ddot{z}_G, I_G \ddot{\theta}) \quad (29)$$

where F_x and F_z are the components of the force \bar{F} acting upon the body, whereas x_G and z_G are

those of \vec{x}_G , in x and z directions correspondingly; M_θ represents the moment of force \vec{F} about the axis passing through G and orthogonal to Gx' and Gz' ; M_B denotes the body mass and I_θ denotes the body moment of inertia about the axis with respect to which M_θ is defined, and dots indicate differentiation with respect to time.

The external forces and moment exerted on B can be obtained by a direct integration of fluid pressure p on ∂D_B :

$$F_x = \int_{\partial D_B} p n_x dS \quad (30)$$

$$F_z = \int_{\partial D_B} p n_z dS - g M_B \quad (31)$$

$$M_\theta = \int_{\partial D_B} p [-(z-z_G)n_x + (x-x_G)n_z] dS \quad (32)$$

where n_x and n_z denote the components of the normal vector on ∂D_B in the fixed in space system of reference. The pressure p is computed from unsteady Bernoulli's equation:

$$p = -\rho(gz + \frac{\partial \phi}{\partial t} + \frac{1}{2} (\nabla \phi)^2) \quad (33)$$

On the body surface, the fluid normal velocity $\partial \phi / \partial n$ is equal to the normal component of the body velocity by virtue of impermeability condition (5). Therefore, from (5) and (27), the following form of the impermeability condition is obtained:

$$\frac{\partial \phi}{\partial n} = n_x \dot{x}_G + n_z \dot{z}_G + \dot{\theta} [-(z-z_G)n_x + (x-x_G)n_z] \quad (34)$$

to be satisfied on ∂D_B . The above expression provides $\partial \phi / \partial n$ at any point on ∂D_B in terms of the body configuration, velocity and geometry.

5.2 The Algorithm for The Computation of Hydrodynamic Forces

The solution algorithm described in §2.3 can now be adapted for the simulation of motions of B . At any instant, presuming $\partial \phi / \partial n$ to be known on ∂D_B , the other boundary data are determined from the solution of the integral relation (6). From this, the fluid pressure p exerted on the body is determined by utilizing Bernoulli's equation (33). Subsequently, the fluid excitation loads on B are determined by a direct integration of pressure over the wetted body surface, (30) to (32). To establish the boundary data for the next time level, the equations of motion are invoked. By integrating (29), \vec{x}_G , \vec{v}_G , θ and $\dot{\theta}$ at the advanced time are determined. The necessary boundary data ($\partial \phi / \partial n$) on the body surface are then established from (34) and the computation for the next time step can begin.

The use of Bernoulli's equation (33) requires the evaluation of $\partial \phi / \partial t$ on the body. To this end the following relation:

$$\frac{d\phi}{dt} = \frac{\partial \phi}{\partial t} + \vec{v} \cdot \frac{\partial \phi}{\partial \vec{x}} \quad (35)$$

is applied, where d/dt signifies the rate of change of any quantity following a material point of the rigid body and \vec{v} denotes the velocity of the point. The quadratic term in Bernoulli's equation is readily obtainable from:

$$(\nabla \phi)^2 = \left(\frac{\partial \phi}{\partial n}\right)^2 + \left(\frac{\partial \phi}{\partial s}\right)^2 \quad (36)$$

At a collocation point i the tangential derivative $\partial / \partial s$ of ϕ , is determined in the form:

$$\left(\frac{\partial \phi}{\partial s}\right)_i = \left(\frac{\partial \phi}{\partial i}\right)_i / \left(\frac{\partial s}{\partial i}\right)_i = \frac{1}{\Delta S_i} \left(\frac{\partial \phi}{\partial i}\right)_i \quad (37)$$

since for the straight line segments, $(\partial s / \partial i)_i = \Delta S_i$ which denotes the length of the segment. To determine $(\partial \phi / \partial i)_i$, appropriate second-order difference formulae are employed. This is permissible despite large variations in ∂D_B , since ϕ on the surface is in general a smoothly varying continuous function, which was confirmed by plotting ϕ_i against i for several conditions. In the present algorithm, Simpson's rule was applied for the evaluation of force and moment expressions (30) to (32).

To carry out the computations on the wetted body surface ∂D_B , it is convenient to describe the body geometry with respect to the $Gx'z'$ system, in which it is invariant. Denoted by $\partial D'_B$, it can be subdivided into segments once and for all. To determine the wetted contour ∂D_B ($\partial D_B \subseteq \partial D'_B$), the intersection points $\partial D'_B \cap \partial D_B$ need to be found. This is achieved using an extrapolation scheme in which a second order polynomial is fitted to the three points on $\partial D'_B$ adjacent to $\partial D'_B \cap \partial D_B$. However, the application of a fixed discretization of $\partial D'_B$ through the determination of $\partial D'_B \cap \partial D_B$ and the subsequent consideration of only those segments of $\partial D'_B$ which belong to ∂D_B , produced an instability in the force computation and a resulting divergence of the solution. This was caused by the introduction or deletion of segments on the body near the intersection point with the free surface, which in turn produced a large variation of pressure in the computation of the dynamic part of the pressure distribution. This problem is overcome by redistributing the collocation points on the body at every time step such that the segment sizes vary smoothly in time. Because of the redistribution of the collocation points, a spatial interpolation of ϕ becomes necessary in the computation of $d\phi/dt$. In general, this spatial interpolation introduces very small approximation errors, since the changes of collocation points between two consecutive time steps are very small.

Computations using linear and second order interpolation rules produced practically indistinguishable results. In the present algorithm, the second order rule is applied.

On the free surface, a similar redistribution of the collocation points becomes necessary. Except for a wall-sided body in heave motion, any other combination of the body geometry and modes of motion causes a change in the size of the segments adjacent to the body, eventually leading to a deletion or introduction of a collocation point. For the same reason as on the body, this destabilizes the force computations. Therefore the original locations of the collocation points cannot be retained, and collocation points must be redistributed at every time step. This necessitates an interpolation of η and ϕ in space for the integration of the free surface evolution equations. Instead of storing and interpolating between η and ϕ values, the values of the right hand sides of (2) and (19) are stored for the required number of past time steps (four steps for the integration scheme employed) and interpolated. This results in a slight reduction of the computation. A cubic spline interpolation is employed. With regard to the associated numerical inaccuracies, the above comments on the discretization of ∂D_B apply.

5.3 The Integration of The Equations of Motion

In order to integrate them in time, the equations of motion (29) are transformed into six ordinary differential equations of the first order:

$$\begin{aligned} (\dot{u}_G, \dot{x}_G, \dot{v}_G, \dot{z}_G, \dot{\omega}, \dot{\theta}) = \\ \left(\frac{F_x}{M_B}, u_G, \frac{F_z}{M_B}, v_G, \frac{M_\theta}{I_\theta}, \omega \right) \end{aligned} \quad (38)$$

A number of standard techniques are available for integrating the above system of equations. For convenience, as well as to be consistent with the integration of the free surface conditions, a 4th order A-B-M scheme was originally used. However, the solution was divergent, and this could not be remedied by increasing the number of iterations per time step. The problem was found to be caused by the computation of the $d\phi/dt$ term. When an implicit scheme is used for the equations of motion, this term can only be computed from a backward difference scheme in time in the corrector part of the algorithm and this leads to the instability.

In the present algorithm, the instability is avoided by computing the predicted values by using a backward difference scheme for $d\phi/dt$ in the force evaluation, and an explicit scheme for integrating the equations of motion. For the second and higher iterations, the scheme returns to the preceding time step and corrects the forces, this time utilizing a central difference scheme for $d\phi/dt$, and once more

integrates the equations of motion using the explicit scheme. In this way, it is possible to use a stable difference formula for the dynamic pressure term in the force calculation, in exchange for an explicit scheme of the integration of the equations of motion.

Although the adopted procedure was more stable and not divergent at the initial time steps, after sufficient time, in particular when surge and/or roll motions were involved, another 'saw-tooth' type instability was found in the time variation of the forces, velocities and displacements. These appeared first in the force computations and gradually contaminated the velocities and displacements. The mechanism which initiates this instability was not identified, but the singularity at the body and free surface intersection point, associated with larger horizontal velocity components in these modes, is probably a factor. This problem is circumvented by smoothing the forces in time. The smoothing formulae applied are the same as those used on the free surface (notice that the smoothing here is in time). For the chosen integration rules, forces over only the past four steps need to be smoothed.

6. The Evaluation Against Experimental Data

6.1 The Experimental Program

An experimental program was undertaken to validate the numerical model. This was considered necessary due to the inadequacy of published analytical, numerical or experimental data on two-dimensional motions of floating bodies in steep waves. To the authors knowledge, no systematic two-dimensional experimental data are readily available in open literature, in which a floating body is subjected to an incident wave train such that the motions and/or waves contain significant non-linear characteristics. The only exception appears to be the experiment by Kyojuka [40] who conducted an experiment on a body of Lewis form by subjecting it to oncoming waves and presented the results in the frequency domain.

The experiments were performed in the Memorial University wave tank which has interior dimensions of 54.74 m x 4.8 m x 3.04 m and is equipped with a piston type wave-maker and a parabolic beach (for more details on the tank, see [41]). The arrangement where the body is completely free to float was considered not to be favourable for experimental purposes, since it would be difficult to prevent the body from undergoing motions in the transverse plane (yaw and pitch). This led to the choice of experiments in which the body was restricted from swaying. The body chosen for testing was of rectangular 40 cm x 40 cm cross section, and its length was 120 cm. To avoid sharp corners and minimize resulting flow separation, a bilge radius of 2.5 cm was provided. The body was ballasted to a draft of 20 cm. To achieve two-dimensionality of the flow, a channel within the wave tank was constructed by erecting

vertical walls. The channel length was 6.1 m. For the period for which test results were collected, reflected waves from either end of the tank did not reach the test site. Experiments were performed in a water depth of 0.9 m. The wave field was monitored using standard twin wire wave probes of resistor type. The collected data were therefore the wave heights, the horizontal force exerted on the body and roll and heave displacements of the body.

Prior to the testing of body motions, a series of preliminary tests were performed in which waves were generated and wave heights were measured at four locations along the centre line of the channel. One of them coincided with the designed location of the body. The purpose of these tests was to determine the range of frequencies and heights for which waves of acceptable quality could be generated in the channel. Also, the data generated were needed for the comparison with the simulation.

The tests with the model were conducted in two series. In one the model was free to heave but restrained from rolling. The roll moment was not measured in these tests. In the other, the model was free to heave and roll but restrained from swaying. The steepest waves generated in the preliminary wave test series could not be applied in the main series of the tests because they caused significant flooding. Altogether 39 tests were performed covering the range of wave periods $0.054 \leq \bar{\omega} \sqrt{(b/2g)} \leq 1.08$, with $\bar{\omega} = 2\pi/T$ and b denoting the breadth of the body cross-section, and of wave steepness $0.068 \leq H/\lambda \leq 0.013$. The tests with the body free to roll were carried out for two radii of gyration 0.29b and 0.36b, and for $GM/b = 0.054$.

For all body motion tests, data were recorded which included the transient information. Except for the horizontal force measurement, all other measurements (wave heights, heave and roll motions) had insignificant amount of noise content. The noise was removed by a five point averaging technique. For the force measurement, however, the time records contained a relatively large proportion of high frequency noise. The noise was subsequently removed by applying a digital filtering technique. A majority of the tests was conducted twice to verify repeatability of the tests. The results showed very good repeatability, with the exception of the sway forces.

6.2 The Comparison of Experimental and Numerical Results

6.2.1 General Comments

In order to establish a proper basis for the comparison of the experimental data with the corresponding results of computation, it is necessary to replicate the experimental wave

conditions in the numerical simulation as close as possible. Previous computed results (cf. §4) showed that the height of the generated waves inside the control domain is closely comparable to the height (H) of the Airy wave describing the excitation potential. Also, the fundamental period of the generated wave was shown to be very close to the excitation period. Ideally, the excitation potential should be selected such that the waves simulated at the location of the body match the test wave conditions but this would lead to a trial-and-error search for the correct excitation potential. Considering the simulation time and the number of experimental conditions that were to be simulated, this process would have been prohibitively expensive and time consuming. Instead, the application of the Airy excitation potential with H and T taken from the test conditions was found to give close enough simulations of the experimental waves.

All of the numerical results, used in the comparisons with the experimental data, unless specifically mentioned, were computed for a standardized control domain extending over $L = 4.0\lambda$. The CG of the body at rest was located at $L_1 = 2.5\lambda$ from the boundary ∂D_{C1} . The two values of time variable T_1 and T_2 indicate approximately the time at which the fully developed wave pattern reached the location of the body (T_1), and the time at which the reflected from the body wave pattern reached the excitation boundary (T_2). The values provide a guidance for the time interval within which the comparisons are meaningful. For the size of the domain chosen, about 3 to 5 wave periods could be obtained within the interval between T_1 to T_2 for most of the tests.

Considering the wide range of wavelengths λ for which numerical results were to be generated, the grid sizes were not standardized. The spatial grid sizes were chosen such that a reasonably good description of the entire boundary can be obtained, Δt for each computation was chosen such that it satisfied the condition given by eqn. (16). The other relevant parameters were: $\beta/T = 1$ and $n = 4$ for all computations (this corresponded to the matching length between 0.1λ to 0.13λ). The shape of the body in the numerical model was rectangular.

The comparison between the numerical and experimental time records were presented in the following manner. The numerical wave elevation was monitored at a station inside the control domain, located at a distance of 0.5λ from the excitation boundary. The station was about 0.4λ outside of the matching region on the average, therefore the time history for the free surface elevation remained uninfluenced by reflections from the body for a relatively long time. For the experimental input conditions, the wave elevation records from the preliminary test series without the presence of the body were taken as the experimental

input conditions. The comparison of these two records provided the comparison of the oncoming wave conditions. For presentation, these two records were synchronized. The synchronization was standardized by matching the peak of the simulated wave in the time interval $3 \leq t/T \leq 4$ with the peak of the experimental wave record.

The primary outputs of the experimental and numerical model were the two displacements, heave and roll, and the horizontal (sway) force. These results were plotted after their records were synchronized with respect to the undisturbed wave pattern at the horizontal location of the body CG at rest. The synchronization was achieved by first presenting the experimental records relative to the undisturbed wave pattern at the CG location. The undisturbed wave pattern was obtained from a reference probe record and the phase difference between the reference probe and the probe at the location of the body CG, measured in the absence of the model. Subsequently the records of the responses determined by the numerical model were adjusted for the phase difference between the experimental and simulated wave patterns at the location of the reference probe. The error inherent in this procedure was estimated within ± 15 deg.

6.2.2 The Comparison of Sway Forces and Heave Motions

A detailed review of the comparison of the experimental and computed records is beyond the scope of the present discussion, only a brief summary and some examples can be presented here.

With the exception of three instances over the whole experimental range, the sway force differences of peak-to-peak values were contained within $\pm 10\%$ with respect to the experimental data, for the steady responses. However, relatively large, on the average $\pm 20^\circ$, phase differences were observed, larger for the model restrained from rolling, on the average $\pm 26^\circ$. It should be noticed that the experimental peak-to-peak values were assessed to be repeatable within not less than $\pm 4\%$ error.

The differences of steady peak-to-peak heave responses, between the experiment and computation were well below $\pm 5\%$ for the model free to roll and occasionally above that value for the model restrained from rolling. The phase differences were within ± 15 deg, with the exception of three tests. In the range of heave resonance the numerical values consistently overpredicted the experimental data. The repeatability of the experimental data was estimated within $\pm 2\%$.

6.3 The Comparison of Roll Motions

With the exception of the lowest experimental frequency in the vicinity of roll natural frequency, the body displayed very small roll displacements in all other tests. The roll amplitudes were mostly less than 4 deg. The numerical method predicted a similar behaviour.

Large roll amplitudes were obtained experimentally for the frequency $\bar{\omega}/(b/2g) = 0.54$ with the radius of gyration $0.033b$. At this frequency, experimental data was gathered for three different wave steepnesses, $H/\lambda = 0.013, 0.023$ and 0.028 . A larger steepness could not be achieved due to the limitation of the dynamometer (maximum allowable roll of ± 30 deg.) as well as due to water spilling inside the body. For these tests, although the agreement of measured and computed phases was very good, with phase differences within ± 15 deg, the roll amplitudes were considerably over-predicted, with peak-to-peak values differing by between 17% to 32%. The peak-to-peak sway forces were under-predicted on the average by 19%. The heave motions correlated well, with peak-to-peak values over-predicted on the average by 5% and approximately zero phase difference.

The over-predictions of roll amplitudes is believed to result from effects of fluid viscosity which were not accounted for in the numerical model. The significant influence of fluid viscosity on the damping of roll is well documented in literature (see e.g. [42]). Therefore, the incorporation in the numerical model of the viscous effects upon roll damping is expected to improve the predictions.

In order to include the viscous damping of roll in the numerical model, the equation of roll motion was modified to the form:

$$I\ddot{\theta} = M_{\theta} - b_{\theta}(\dot{\theta}) \quad (39)$$

where the second term on the right-hand side of (39) represents the contribution of viscous damping to the roll moment and is considered

as a function of angular speed $\dot{\theta}$. It should be observed that moment M_{θ} includes the effects of roll damping resulting from wave scattering. The expression for the viscous damping moment was identified from free rolling numerical and physical experiments in the form:

$$b_{\theta}(\dot{\theta}) = B_1\dot{\theta} + B_2|\dot{\theta}|\dot{\theta} \quad (40)$$

where B_1 and B_2 denote constant coefficients derived from the identification. In the identification the assumption was made that the damping contribution of wave scattering to the

roll moment is linear with respect to $\dot{\theta}$.

The numerical results obtained by the described above procedure showed a significant improvement of the predicted roll motion. The changes of computed sway force and heave motion were marginal. Figs. 7 and 8 show the comparisons of the computed and measured records, obtained without and with the inclusion of viscous roll damping respectively. The results are for the largest wave steepness $H/\lambda = 0.028$ at which the worst agreement between the experiment and computation was observed. For all three wave steepnesses the differences between computed and measured peak-to-peak roll values remained below 6% for the simulations in which eqn. (39) was applied.

6.4 Summary

Taking into account the experimental errors and inaccuracies of the comparison resulting from the unsteady characteristics of the experimental and computed data, the predictions by the numerical model show good agreement with experimental records. The observed differences between computed and measured sway forces and heave motions result, at least partly, from the absence of viscous effects in the numerical model. A similar remark applies to the roll motions where the inclusion of the viscous roll damping is semi-empirical.

It should be observed that the experimental data used in the comparison included three kinds of non-negligible non-linear phenomena. For the shorter waves with higher steepness, the waves near the body approached the breaking limit. In a number of tests, a foam formation was observed. Large heave and relative motions of the body with respect to waves were observed in several tests. For these tests, the video records showed that the run-up profiles resembled closely those generated by the simulation. In addition, the tests included the occurrence of roll amplitudes up to 20 deg. combined with large motions relative to waves.

The comparison confirmed the validity of the numerical method in the presence of the described phenomena. It also demonstrated that the method can provide realistic estimates of roll motions within the specified range if a semi-empirical model of viscous roll damping is included in the algorithm.

7. Conclusion

The numerical results presented above show that the propagation of steep long-crested periodic waves, which may include mild transients, can be modelled numerically in the time domain by means of a relatively simple, low order boundary element method algorithm. The efficiency of a radiation condition of Orlanski's type is also demonstrated. The use of the condition makes possible the avoidance of other means of eliminating the reflection of waves at the downstream boundary, such as e.g. the introduction of an artificial wave damping in the free surface conditions, which

are not compatible with open water conditions. Similar comments apply to the wave excitation in the control fluid domain, achieved in the algorithm by a matching of an imposed exciting wave potential with the flow in the control domain, in the vicinity of the upstream control boundary. The procedure is different from the more usual simulation of a physical wave-maker, and corresponds better to open water conditions. However, in the procedure the exciting wave potential must be modulated in time to enforce the compatibility of the initial conditions at the boundary and in the control domain. The problem parallels similar difficulties encountered in the modelling of the wave-maker.

Another characteristic feature of the algorithm constitutes the use of an Eulerian form of the nonlinear free surface conditions, based on the assumption of a single-valued wave elevation. At present this form of the conditions appears to be more suitable for the extended in time modelling of motions of floating bodies in steep waves, than its Lagrangian counterpart, although the latter is capable of modelling wave breaking. The application of the Eulerian free surface conditions makes possible a strict observance of local stability condition of Courant type, without the use of procedures (such as e.g. a regridding of collocation points) which may introduce a numerical smoothing. The results presented above suggest that the violation of a Courant type stability condition may not be the reason of the occurrence of the typical instability in the free surface data.

The extension of the basic steep wave propagation algorithm, which includes the presence of a free floating body in the control fluid domain, provided time domain simulations of body motions. In the simulations steady state motions of the body excited by steep periodic waves, preceded by short transients, were achieved. The computed records compare well with experimental data, thus illustrating the applicability of the extended algorithm. The experimental data were obtained from specially performed model tests, with a body model restrained in the sway mode. In several of those tests significant nonlinear phenomena related to the wave propagation and interaction with the body were observed. In the numerical simulations no significant wave reflection at the downstream boundary was detected. However, for the form of the algorithm presented here, simulation times are limited by the reflection of waves scattered by the body from the upstream control boundary. To ensure the stability of the computation of hydrodynamic forces and of the integration of the equations of body motion, special procedures were developed which include a smoothing of the hydrodynamic forces in time.

References

1. Longuet-Higgins, M.S. and Cokelet, E.D., "The deformation of steep surface waves on water: I. a numerical method of computation." *Proc. R. Soc. Lond., Series A*, 350, pp. 1-26 (1976).
2. Faltinsen, O.M., "Numerical solution of transient nonlinear free-surface motion outside or inside moving bodies." *Proc. 2nd Int. Conf. Num. Ship Hydro.*, Berkeley, CA, pp. 347-357 (1977).
3. Faltinsen, O.M., "A numerical nonlinear method of sloshing in tanks with two dimensional flow." *J. Ship Res.*, 22, 3, pp. 193-202 (1978).
4. Vinje, T. and Brevig, P., "Numerical simulation of breaking waves." *Adv. Water Resources*, 4, pp. 77-82 (1981).
5. Vinje, T. and Brevig, P., "Numerical calculation of forces from breaking waves." *Int. Sym Hydro. Ocean Eng.*, Norwegian Inst. Tech., Trondheim, pp. 547-565 (1981).
6. Brevig, P., Greenhow, M. and Vinje, T., "Extreme wave forces on submerged energy devices." *Appl. Ocean Res.*, 4, 4, pp. 219-225 (1982).
7. Vinje, T. and Brevig, P., "Nonlinear ship motions." *Proc. 3rd Int. Conf. Num. Ship Hydro.*, Paris, pp. 257-268 (1981).
8. Vinje, T., Maogang, X. and Brevig, P., "A numerical approach to nonlinear ship motion." *Proc. 14th ONR Symp. Naval Hydro.*, National Academy Press, pp. 245-278 (1982).
9. Greenhow, M., Vinje, T., Brevig, P. and Taylor, J., "A theoretical and experimental study of the capsize of Salter's duck in extreme waves." *J. Fluid Mech.*, 118, pp. 221-239 (1982).
10. Lin, W. M., "Nonlinear motion of the free surface near a moving body." *Ph.D. Thesis*, Dept. Ocean Eng., MIT, 127 p. (1984).
11. Lin, W. M., Newman, J. N. and Yue, D.K.P., "Nonlinear forced motions of floating bodies." *Proc. 15th ONR Symp. Naval Hydro.*, National Academy Press, Washington, D.C., pp. 33-49 (1989).
12. Dommermuth, D.G. and Yue, D.K.P., "Study of nonlinear axisymmetric body-wave interactions." *Proc. 16th ONR Symp. Naval Hydro.*, National Academic Press, Washington, D.C., pp. 116-136 (1986).
13. Dommermuth, D. G. and Yue, D.K.P., "Numerical simulations of non-linear axisymmetric flows with a free surface." *J. Fluid Mech.*, 178, pp. 195-219 (1987).
14. Greenhow, M. and Lin, W. M., "Numerical simulation of free surface flows generated by wedge-entry and wave-maker motions." *Proc. 4th Int. Conf. Num. Ship Hydro.*, National Academy of Sciences, Washington, D.C. pp. 94-106 (1985).
15. Greenhow, M., "Water entry and exit of a horizontal cylinder." *Proc. Second International Workshop on Water Waves and Floating Bodies*, Rep. No. AM-87-6, Univ. Bristol, pp. 25-28 (1987).
16. Greenhow, M., "Wedge entry into initially calm water." *Appl. Ocean Res.*, At press (1988).
17. Isaacson, M. St. Q., "Nonlinear wave-effects on fixed and floating bodies." *J. Fluid Mech.*, 120, pp. 267-281, also *Corrigendum*, 133, pp. 469 (1982).
18. Isaacson, M. St. Q., "Steep wave forces on large offshore structures." *Soc. Petro. Eng. J.*, 23, 1, pp. 184-190 (1983).
19. Krzyzanski, M., "Partial Differential Equations of Second Order." Vol. 1, Polish Scientific Publishers (1971).
20. Hess, J. L., "Higher order numerical solution of the integral equation for the two-dimensional Neumann problem." *J. Comp. Meth. Appl. Mech. Eng.*, 2, pp. 1-15 (1973).
21. Wardle, L.J., "An Introduction to the Boundary Element Method." Numerical solution of partial differential equations, J. Noye ed., North-Holland, pp. 289-312 (1982).
22. Hess, J. L., "The use of higher order surface singularity distributions to obtain improved potential flow solutions for the two-dimensional lifting airfoils." *J. Comp. Meth. Appl. Mech. Eng.*, 5, pp. 11-35 (1975).
23. Breit, S. R., Newman, J. N. and Sclavounos, P.D., "A new generation of panel programs for radiation-diffraction problems." *Proc. 3rd Int. Conf. Beh. Off. Str. (BOSS)*, Elsevier Sc. Pub. B.V., pp. 531-544 (1985).
24. Schultz, W.W., "A complex-valued integral method for free surfaces with intersecting bodies." *Proc. Second International Workshop on Water Waves and Floating Bodies*, Rep. No. AM-87-06, Univ. Bristol, pp. 101-103 (1987).
25. Forsythe, G. and Moler, C.B., "Computer solution of linear algebraic equations." Chapter 9, Prentice-Hall, Inc., Englewood, Cliff., N.J. (1967).
26. Lamb, Sir H., "Hydrodynamics." 6th Printing, Dover Pub., (1945).

27. Cointe, R., Jami, A. and Molin, B., "Nonlinear impulsive problems." Proc. Second Int. Workshop on Water Waves and Floating Bodies, Rep. No. AM-87-06, Univ. Bristol, pp. 13-16 (1987).
28. Biesel, F., "Les Appareils Generateurs de houle en Laboratoire." La Houille Blanche, 6, pp. 147-165 (1951).
29. Roache, P., "Computational Fluid Dynamics." Hermosa Pub. (1972).
30. Baker, J. R., Meiron, D. I. and Orszag, S.A., "Applications of a generalized vortex method to nonlinear free-surface flows." Proc. 3rd Int. Conf. Num. Ship Hydro., Paris, pp. 179-191 (1981).
31. New, A. L., McIver, P. and Peregrine, D. H., "Computation of overturning waves." J. Fluid Mech., 150, pp. 233-251 (1985).
32. Telste, J. C., "Calculation of fluid motion resulting from large amplitude forced heave motion of a two-dimensional cylinder on a free surface." Proc. 4th Int. Conf. Num. Ship Hydro., National Academy of Sciences, pp. 81-93 (1985).
33. Orlanski, J., "A simple boundary condition for unbounded hyperbolic flows." J. Comp. Phy., 21, pp. 251-269 (1976).
34. Chan, R.K-C. and Chan, F.W-K., "Numerical solution of transient and steady free surface flows about a ship of generalized hull shape." Proc. 13th ONR Symp. Naval Hydro., Tokyo, pp. 257-280 (1980).
35. Wu, D-M. and Wu, T.Y., "Three dimensional nonlinear long waves due to a moving surface pressure." Proc. 14th ONR Symp. Naval Hydro., National Academy Press, pp. 103-125 (1982).
36. Ahlberg, J., Nilson, E. and Walsh, H., "The theory of splines and their applications." Academic Press, New York. (1967).
37. Han, F. S. and Stansby, P.K., "On the application of the boundary element method to two-dimensional free surface interactions with bodies." Proc. Second International Workshop on Water Waves and Floating Bodies, Report. No. AM-87-06, Univ. of Bristol, pp. 39-42 (1987).
38. Dold, J.W. and Peregrine, D.H., "An efficient boundary-integral method for steep unsteady water waves." In Numerical Methods for Fluid Dynamics II. Ed. K.W. Morton and M.J. Baines, Oxford Univ. Press., pp. 671-679 (1986).
39. Miche, R., "Mouvements ondulatoires de la mer en profondeur croissante ou décroissante." Annales des Ponts et Chausses (1944).

40. Kyoizuka, Y., "Experimental study on second-order forces acting on cylindrical bodies in waves." Proc. 14th Symp. Naval Hydro., Tokyo, pp. 319-382 (1982).
41. Muggeridge, D.B. and Murray, J.J., "Calibration of a 58 m. wave flume." Can. J. Civil Eng., 8, 4, pp. 449-455 (1981).
42. Himeno, Y., "Prediction of ship roll damping - a state of the art." University of Michigan Dept. of Naval Arch. Rep. No. 239, 65 pp (1981).

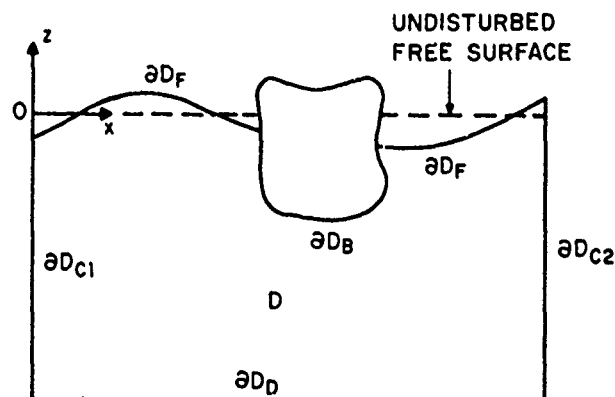
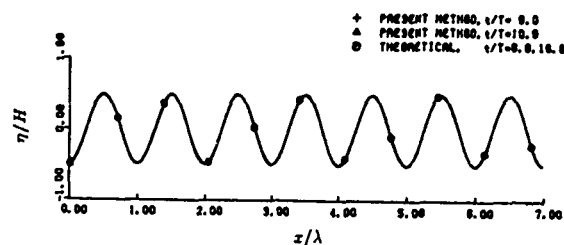
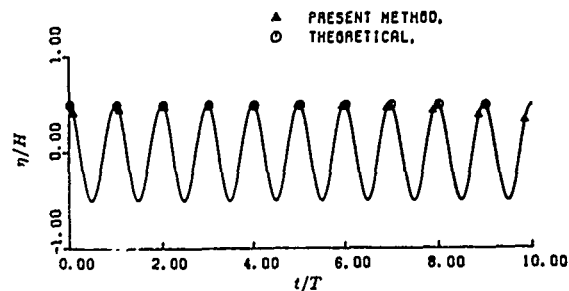


Fig. 1 Definition diagram.



(a) Free surface elevations



(b) Evolution of the free surface in time at the center of the domain $x = 3.5\lambda$

Fig. 2 Propagation of a linear steady progressive wave: $(L/\lambda = 7, d/\lambda = 0.4, \Delta x_F/\lambda = 1/25 \text{ and } \Delta t/T = 1/40)$.

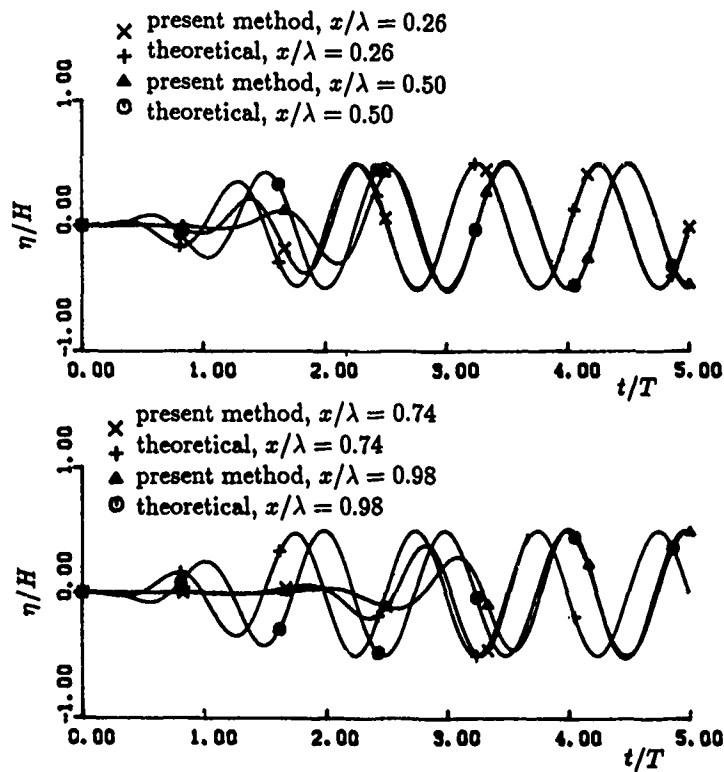


Fig. 3 The evolution in time of a free surface elevation started from rest.

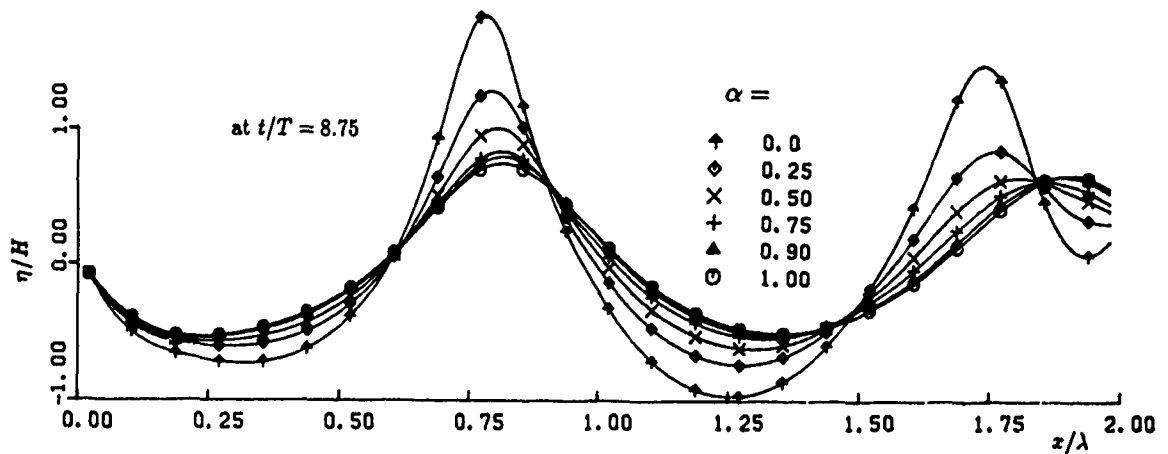


Fig. 4 Free surface elevations for different values of α :
($L=2\lambda$, $d/\lambda=0.5$, $H/\lambda=0.1$, $\Delta x_f/\lambda = 1/24$ and $\Delta t/T=1/40$).

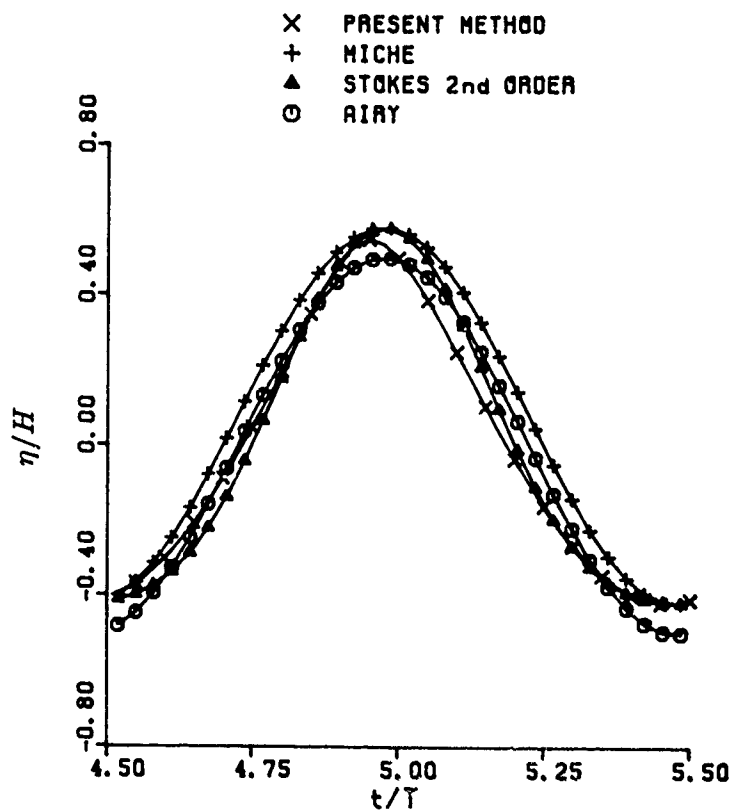


Fig. 5 Comparison of theoretical and numerical time histories of wave elevation.

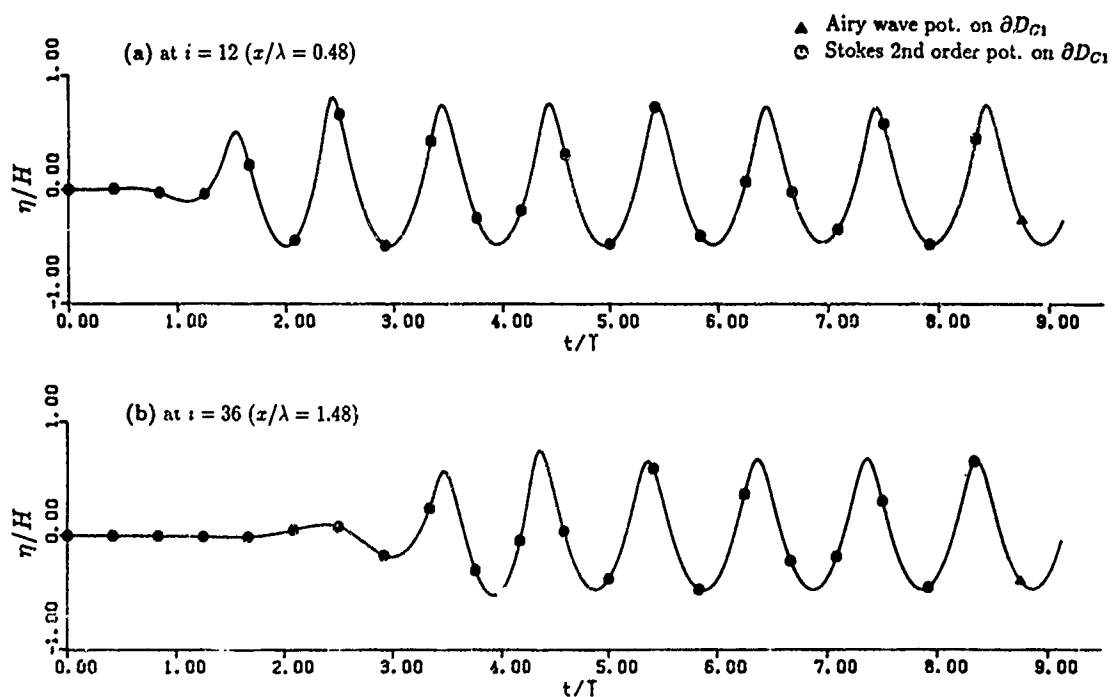


Fig. 6 The evolution in time of free surface elevations induced by different excitation potentials.

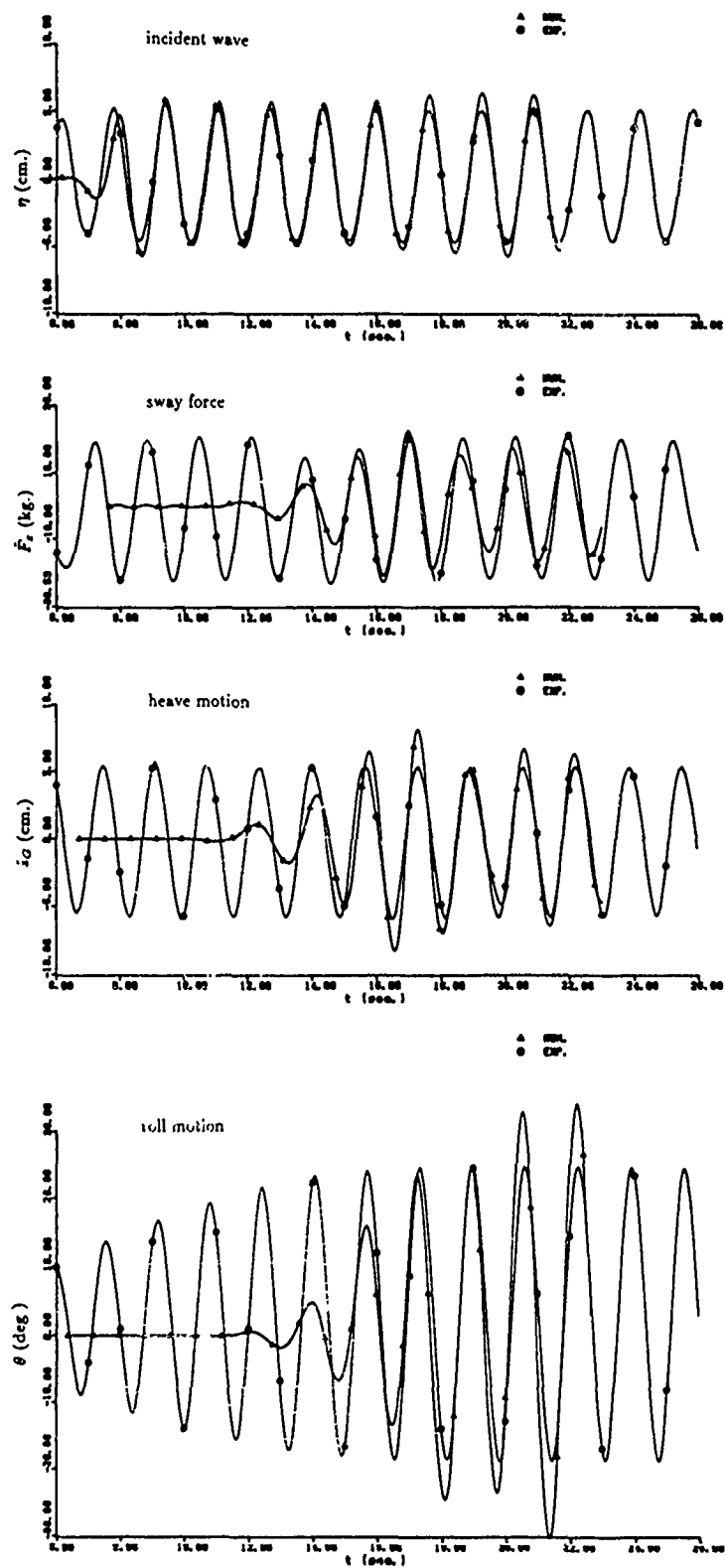


Fig. 7 Comparison of experiment and theory for $\tilde{\omega}/b/2g = 0.54$ and $H/\lambda = 0.028$: ($T_1=14.5$ sec and $T_2=21.0$ sec).

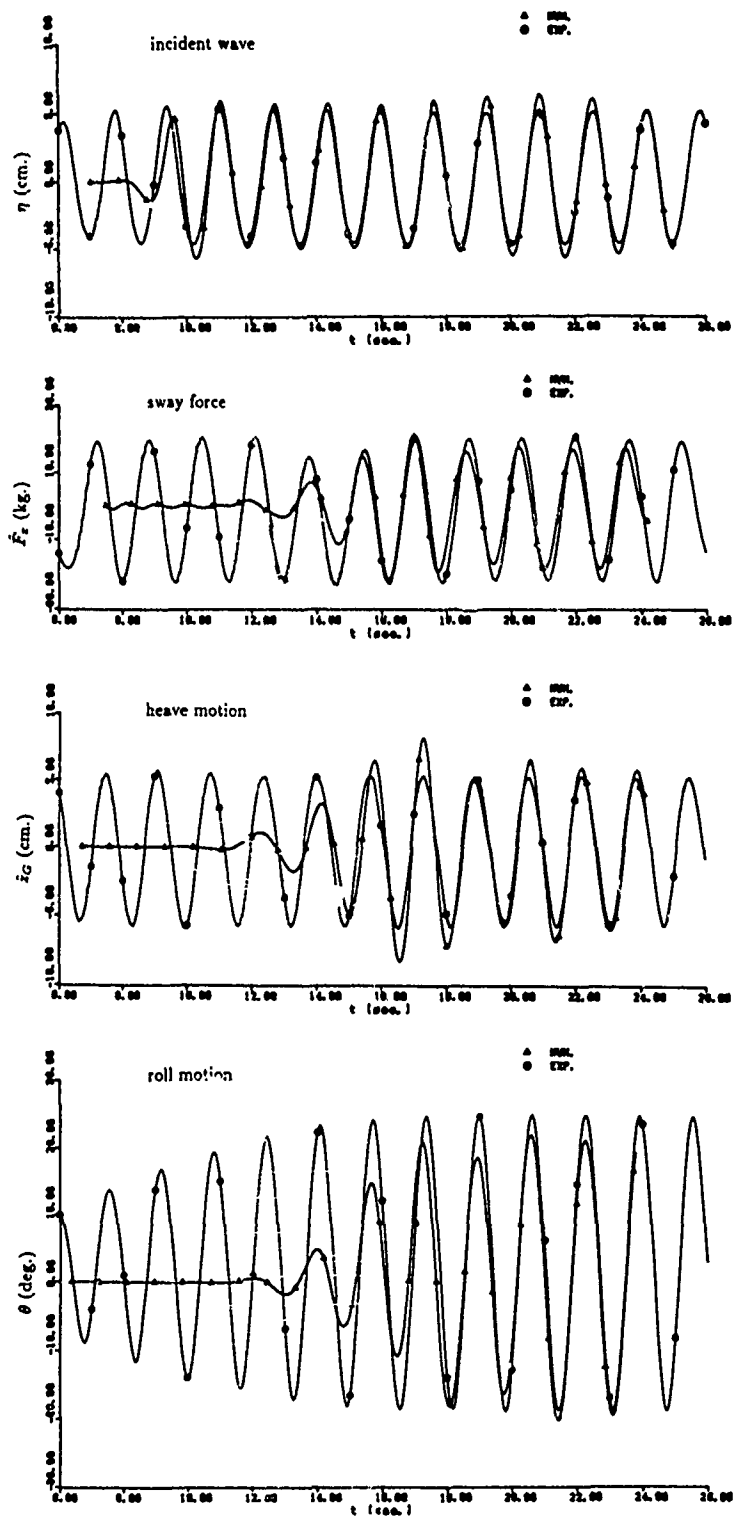


Fig. 8 Comparison of theory and experiment for $\tilde{\omega}/b/2g = 0.54$ and $H/\lambda = 0.028$ when roll viscous damping is included in the simulation: ($T_1 \approx 14.5$ sec and $T_2 \approx 21.0$ sec).

DISCUSSION

by R. Cointe

I would like to congratulate the authors for a very interesting and extensive work. We are now working on a similar problem and we find it very difficult to accurately compute the free motions of the body using finite differences in time to evaluate the $\partial\Phi/\partial t$ term in Bernoulli's equation. An alternative method consists in evaluating this term by solving the corresponding boundary integral equation. Would the authors discuss their experience on this problem?

Author's Reply

The work presented by Dr. Cointe at this conference [A1], addresses several problems which are either identical or analogous to the ones we have addressed in our paper. The main differences between the two works result from the assumed directions of approach, with the "numerical flume" approach taken by Dr. Cointe, and "open water" approach chosen by us. As a result certain comparisons between the achieved results may be instructive.

In particular I believe, it is worthwhile to notice that the wave damping condition employed in [A1] at the downstream boundary, is tuned to the dominant wave frequency, and our application of the radiation condition depends on the use of an appropriate wave celerity.

It could also be interesting to see how an introduction of the compatibility of the initial condition on the exciting boundary and free surface, which we impose through a modulation function, would affect the performance of Dr. Cointe's algorithms.

Referring directly to Dr. Cointe's question, we could not avoid the necessity to solve the boundary value problem twice in order to advance the simulation of motion of a floating body in time. The technique used is described in section 5.3, and it relies on using a central difference scheme to obtain time derivatives of the potential on the body surface.

We very much appreciate Dr. Cointe's question and wish him success in finalizing the development of his model.

[A1] R. Cointe, "Nonlinear Simulation of Transient Free Surface Flows", 5th International Conference on Numerical Ship Hydrodynamics, Hiroshima, 1989.

DISCUSSION

by R.C. Ertekin

The authors should be commended for a very careful and detailed analysis carried out in their paper. It was a pleasure to read it.

By using the plane speed obtained from the potential for Airy Waves, you appear to be assuming, at least implicitly, that downstream waves are linear. And by setting $c' = \alpha c$ and varying α , aren't you basically determining the value of the phase speed which you would have if you numerically calculated it?

We have recently solved the problem of diffraction of nonlinear waves by 2-dimensional submerged objects by using the BEM. The results will be presented in the next OMAE conference in Houston (1990, 9th meeting). We have used Crank-Nicholson scheme in time stepping and found no saw-tooth waves that you have seen in your results by using the A-B-M method. We have not filtered our results. This makes us believe that your time stepping algorithm is causing the problem. It is not very unheard of that a multistep method is associated with such difficulties (Burden & Faires, "Numerical Analysis", 1985, Prindle & Weber). One way of handling this difficulty is by using adaptive time stepping in the algorithm.

I would like to also point out that Shapiro, R. ("Linear filtering", Mats. Comput., Vol. 29, 1975) presented filtering formulas for any number of points earlier.

Finally, could you explain why sway forces could not have been repeated in the experiments?

Author's Reply

The comments by Professor Ertekin are appreciated. Considering the formulation presented in the paper, the upstream boundary can be used as a permeable boundary for oncoming waves which satisfy fully the non-linear free surface conditions. However, applications on that boundary, of wave potentials which do not conform to the conditions, are equivalent to wave excitations by a wave maker. As much as the kinematics of a wave maker board does not imply the linearity of the generated waves, since they satisfy the non-linear free surface conditions, the application of an Airy wave potential on the upstream boundary does not imply the linearity of the wave generated in the control fluid domain. A wave excitation

of this type, by a wave potential which includes a wave celerity c in its definition, makes it convenient to use the same celerity in the radiation condition. This procedure appeared to be effective in the performed simulations. Otherwise the celerity would have to be determined numerically from the solution in the control fluid domain.

The source of the saw-tooth instability in the wave propagation simulation is not entirely clear. In our simulations it was related to the use of the non-linear free

surface conditions and to wave steepness, and therefore the accuracy of the computation of the spatial derivatives in the free surface conditions seems to be the probable source of the instability.

Finally, the measurements of sway forces were repeated in all the tests carried out twice. However the peak-to-peak values from those measurements showed a variation of at least $\pm 4\%$ between the original and repeated test records. The cause of these variations was not fully determined.

for the Green's functions involved. The solution of the boundary integral equations comes from a very effective iterative solver. The calculation of the wave drift forces is done in two alternative ways, one is the integration of the pressures over the mean wetted surface of the body and secondly using the Maruo expression for the wave drift forces corrected for the small forward speed parameter. The nature of the non-uniformity in the asymptotic expansions will be studied in this paper and extended to uniform expansions. We keep in mind that one of our goals is to arrive at a formulation that makes use of the zero speed source potential.

In this paper we present a uniform approximation valid for small values of the small parameter but also for fixed finite values of τR .

2. Mathematical Formulation

We first derive the equations for the potential function $\Phi(\underline{x}, t)$, such that the fluid velocity $\underline{u}(\underline{x}, t)$ is defined as $\underline{u}(\underline{x}, t) = \text{grad } \phi(\underline{x}, t)$. The total potential function will be split up in a steady and a non-steady part in a well-known way:

$$\phi(\underline{x}, t) = Ux + \bar{\phi}(\underline{x}; U) + \tilde{\phi}(\underline{x}, t; U) \quad (1)$$

In this formulation U is the incoming unperturbed velocity field, obtained by considering a coordinate system fixed to the ship moving under a drift angle α . In our approach this angle need not be small. The time dependent part of the potential consists of an incoming wave at frequency ω and a diffracted and/or radiated wave contribution. To compute the wave drift forces all these components will be taken into account.

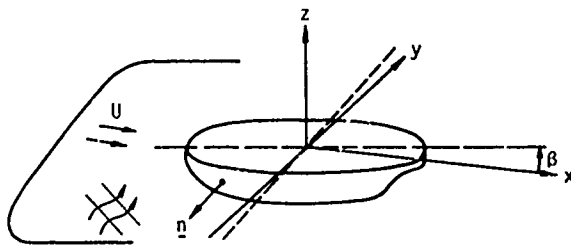


Fig. 1. Axis of coordinate system

The equations for the total potential ϕ can be written as:

$$\Delta\phi = 0 \text{ in the fluid domain } D, \quad (2)$$

At the free surface we have the dynamic and kinematic boundary condition

$$\left. \begin{aligned} g\zeta + \phi_t + \frac{1}{2}\nabla\phi \cdot \nabla\phi &= \text{constant} \\ \phi_z - \phi_x\zeta_x - \phi_y\zeta_y - \zeta_t &= 0 \end{aligned} \right\} \text{ at } z = \zeta \quad (3)$$

We assume that the waves are high compared to the Kelvin wave pattern, but that they are both small in nature, hence the free surface boundary condition can be expanded at $z = 0$. Elimination of ζ leads to the following non-linear condition:

$$\begin{aligned} \frac{\partial^2}{\partial t^2}\phi + g\frac{\partial}{\partial z}\phi + \frac{\partial}{\partial t}(\nabla\phi \cdot \nabla\phi) \\ + \nabla\phi \cdot \nabla\left[\frac{\nabla\phi \cdot \nabla\phi}{2}\right] = 0 \text{ at } z = 0 \end{aligned} \quad (4)$$

To compute the wave resistance at low speed the free surface elevation must be treated more carefully, because the wave height is of asymptotically smaller order. This problem has been studied extensively by Eggers [13], Baba [14], Hermans [15] and Brandsma [16]. The velocity field is well described by the double body potential with a small wave pattern. Therefore we take the double body potential into account and we neglect the stationary wave pattern. For the wave potential $\tilde{\phi}(\underline{x}, t; U)$ the free surface condition now becomes:

$$\begin{aligned} \tilde{\phi}_{tt} + g\tilde{\phi}_z + 2U\tilde{\phi}_{xt} + \\ + 2\nabla\bar{\phi} \cdot \nabla\tilde{\phi}_t + (U^2 + 2U\bar{\phi}_x + \bar{\phi}_x^2)\tilde{\phi}_{xx} + \\ + 2(U + \bar{\phi}_x)\bar{\phi}_y\tilde{\phi}_{xy} + \bar{\phi}_y^2\tilde{\phi}_{yy} \\ + (3U\bar{\phi}_{xx} + \bar{\phi}_x\bar{\phi}_{xx} + \bar{\phi}_y\bar{\phi}_{xy})\tilde{\phi}_x + \\ + (2U\bar{\phi}_{xy} + \bar{\phi}_x\bar{\phi}_{xy} + \bar{\phi}_y\bar{\phi}_{yy})\tilde{\phi}_y + \mathcal{L}^{(2)}\{\tilde{\phi}\} = 0 \\ \text{at } z = 0 \end{aligned} \quad (5)$$

The boundary conditions on the hull can be written in a similar way for all radiating and diffracted modes. We therefore treat the following general form, keeping in mind that the actual form has to be used in the computations. Generally we have the condition:

$$(\nabla\tilde{\phi} \cdot \underline{n}) = V(\underline{x})e^{-i\omega t} \underline{x} \in S \quad (6)$$

where S is the mean wetted area of the ship hull.

The non-linear operator $\mathcal{L}^{(2)}$ on $\tilde{\phi}$ will be neglected as well. The first term in equation (5) contains linear terms in U .

The Effect of the Steady Perturbation Potential on the Motions of a Ship Sailing in Random Seas

R. H. M. Huijsmans
Maritime Research Institute Netherlands
Wageningen, The Netherlands
A. J. Hermans
Technical University of Delft
Delft, The Netherlands

Abstract

In this paper results will be presented of model tests and calculations of the wave drift force on a 200 kDWT tanker and half immersed sphere. The theory of small forward speed motion computations is extended in order to allow larger horizontal distances in the Green's functions by deriving a proper asymptotic expansion of the low speed Green's function. Also an alternative formulation for the wave drift forces has been derived, based on the momentum balance as e.g. derived by Newman or Maruo. This alternative formulation is derived for the small forward speed case.

1. Introduction

Recently we derived a formulation for the description of the motions of a floating body with a small velocity. The reason for such a formulation is related to the wave drift damping phenomena. Large moored tankers offshore exhibit low frequency resonance behaviour. These resonant forces are associated with the slowly varying wave drift forces. These forces can be computed with the help of linear diffraction theory and taking into account the second order effects of the pressure and the wave height. An extensive study among many other studies was published by Pinkster [1]. Also second order wave excitation may be taken into account in an approximative way, see Benschop et al. [2]. In an early paper Remery and Hermans [3] indicated that for an accurate description of the low frequency motions not only the drift forces are important but also the accurate prediction of the damping coefficient near resonance. In a later study by Wichers [4] he showed that this damping coefficient was quadratic with respect to the wave height, thus leading to the concept of wave drift damping coefficient, which have been shown by Wichers et al. [5]

to be related with the forward speed dependency of the wave drift forces. The effect of the varying wave drift forces with speed has been described by a number of authors nowadays, beginning from Hermans and Huijsmans [6] to the more recent publication by Nossen et al. [7], Sclavonous [8] and Hu and Eatock Taylor [9]. In the paper of Hermans and Huijsmans the speed was restricted to be low, due to non-uniform character of the asymptotic expansion scheme. In the paper of Sclavonous the problem was solved by deriving explicit Green's functions for the wave drift damping, with a proper account of the disturbance of the steady potential ϕ_s . In order to solve the forward speed problem Zhao and Faltinsen [10] showed that the treatment of the speed dependent boundary conditions (depending on the steady potential ϕ_s) have to be handled carefully. As soon as one tries to use the expansion scheme in [11] for the unsteady potential with respect to forward speed at a small but fixed forward speed one is confronted with the non-uniformities in the asymptotic expansion. In short one finds for a point source that the second order results behave like $(\tau R)^{\frac{1}{2}}$ where $\tau = \frac{U\omega}{g}$ is the small parameter and R is the distance to the point source.

In former studies only the speed effect due to a uniform flow has been attempted. However the influence of the steady perturbation potential resulting from the stationary fluid flow around the ship, on the ship motion problem is not well understood. For the case the current is head on or the ship's course is at zero drift angle, then the influence can be neglected. In case of a ship moving at a certain drift angle it then appears to be of considerable influence, see Huijsmans et al. [12]. In our study we have incorporated the steady forward speed perturbation potential into the ship motion problem. The forward speed ship motion problem is solved using an efficient algorithm

Our Ansatz is that in order to obtain the first order approximation with respect to U the higher order terms in U may be neglected in the free surface condition. In the next section we show that in general this is true, but first we discuss the construction of the regular part of the perturbation problem, with the complete linear free surface condition.

We assume $\tilde{\phi}(\underline{x}, t; U)$ to be oscillatory.

$$\tilde{\phi}(\underline{x}, t; U) = \phi(\underline{x}; U) e^{-i\omega t} \quad (7)$$

The free surface condition is then written as:

$$\begin{aligned} -\omega^2 \phi - 2i\omega U \phi_{xx} + U^2 \phi_{xx} + \\ g\phi_z = D(U; \bar{\phi}) \{ \phi \} \text{ at } z=0 \end{aligned} \quad (8)$$

where $D(U; \bar{\phi})$ is a linear differential operator acting on ϕ as defined in equation (5).

We apply Green's theorem to a problem in D_i inside S and to the problem in D_e outside S , where S is the ship's hull. The potential function inside S obeys condition (8) with $D = 0$, while the Green's function fulfills the homogeneous adjoint free surface condition:

$$\begin{aligned} -\omega^2 G + 2i\omega U G_\xi + \\ + U^2 G_{\xi\xi} + gG_\zeta = 0 \quad \text{at } \zeta = 0 \end{aligned} \quad (9)$$

This Green's function has the form

$$G(\underline{x}, \underline{\xi}; U) = -\frac{1}{\underline{r}} + \frac{1}{\underline{r}'} - \psi(\underline{x}, \underline{\xi}; U) \quad (10)$$

where $\underline{r} = |\underline{x} - \underline{\xi}|$ and $\underline{r}' = |\underline{x} - \underline{\xi}'|$, where $\underline{\xi}'$ is the image of $\underline{\xi}$ with respect to the free surface.

Combining the formulation inside and outside the ship we obtain a description of the potential function defined outside S by means of a source and a vortex distribution of the following form:

$$\begin{aligned} 4\pi\phi(\underline{x}) = \\ - \iint_S \gamma(\underline{\xi}) \frac{\partial}{\partial \underline{n}} G(\underline{x}, \underline{\xi}) dS_\xi - \frac{2i\omega U}{g} \int_{WL} \gamma(\underline{\xi}) G(\underline{x}, \underline{\xi}) d\eta + \\ - \iint_S \sigma(\underline{\xi}) G(\underline{x}, \underline{\xi}) dS_\xi + \frac{U^2}{g} \int_{WL} \left[\gamma(\underline{\xi}) \frac{\partial}{\partial \xi} G(\underline{x}, \underline{\xi}) + \right. \\ \left. - \{ \alpha_t \gamma_t(\underline{\xi}) + \alpha_T \gamma_T(\underline{\xi}) \} G(\underline{x}, \underline{\xi}) \right] d\eta + \\ + \frac{U^2}{g} \int_{WL} \alpha_n \sigma(\underline{\xi}) G(\underline{x}, \underline{\xi}) d\eta + \\ \frac{i\omega}{g} \iint_S G(\underline{x}, \underline{\xi}) D \{ \phi \} dS_\xi \end{aligned} \quad (11)$$

with $\alpha_t = \cos(Ox, \underline{t})$, $\alpha_T = \cos(Ox, \underline{T})$ and $\alpha_n = \cos(Ox, \underline{n})$, where \underline{n} is the normal and \underline{t} is the tangent to the waterline and $T = \underline{t} \times \underline{n}$ the binormal. It is clear that the choice of $\gamma(\underline{\xi}) = 0$ for the integral along the waterline will give no contribution up to order U . The source distribution we obtain in this way is not a proper distribution, because it expresses the function ϕ in a source distribution along the free surface with a strength proportional to derivatives of the same function ϕ . However this formulation is linear in U and moreover the integrand tends rapidly to zero for increasing distances R . So finally we arrive at the formulation:

$$\begin{aligned} -2\pi\sigma(\underline{x}) - \iint_S \sigma(\underline{\xi}) \frac{\partial}{\partial \underline{n}_x} G(\underline{x}, \underline{\xi}) dS_\xi \\ + \frac{U^2}{g} \int_{WL} \alpha_n \sigma(\underline{\xi}) \frac{\partial}{\partial \underline{n}_x} G(\underline{x}, \underline{\xi}) d\eta + \\ + \frac{i\omega}{g} \iint_{FS} \frac{\partial}{\partial \underline{n}_x} G(\underline{x}, \underline{\xi}) D \{ \phi \} dS_\xi = 4\pi V(\underline{x}), \\ \underline{x} \in S \end{aligned} \quad (12)$$

and

$$\begin{aligned} 4\pi\phi(\underline{x}) = \\ - \iint_S \sigma(\underline{\xi}) G(\underline{x}, \underline{\xi}) dS_\xi + \\ + \frac{i\omega}{g} \iint_{FS} G(\underline{x}, \underline{\xi}) D \{ \phi \} dS_\xi \quad \underline{x} \in D_e \end{aligned} \quad (13)$$

where $D \{ \phi \} = 2\nabla \bar{\phi} \cdot \nabla \phi$.

We now consider small values of U , keeping in mind that there are two dimensionless parameters that play a role in the limit. We consider $\tau = \frac{\omega U}{g} \ll 1$ and $\nu = \frac{g L^3}{U^2} \gg 1$.

It turns out that the source strength and potential function can be expanded as follows:

$$\sigma(\underline{x}) = \sigma_0(\underline{x}) + \tau \sigma_1(\underline{x}) + \tilde{\sigma}(\underline{x}; U) \quad (14)$$

$$\phi(\underline{x}) = \phi_0(\underline{x}) + \tau \phi_1(\underline{x}) + \tilde{\phi}(\underline{x}; U) \quad (15)$$

where σ and ϕ are $\mathcal{O}(\tau^2)$ as $\tau \rightarrow 0$, while the expansion of the Green's function is less trivial.

3. The Green's Function

In this section we present an asymptotic expansion of the Green's function. The Green's function follows from the source function presented in Wehausen and Laitone [17]. In case of $\tau < 1/4$ the function $\psi(\underline{x}, \underline{\xi}; U)$ is written as follows:

$$\begin{aligned}\psi(\underline{x}, \xi; U) &= \frac{2g}{\pi} \int_0^{\pi/2} d\theta \int_{\mathcal{L}_1} dk F(\theta, k) + \\ &+ \frac{2g}{\pi} \int_{\pi/2}^{\pi} d\theta \int_{\mathcal{L}_2} dk F(\theta, k) \quad (16)\end{aligned}$$

where:

$$\begin{aligned}F(\theta, k) &= \frac{k \exp(k[z + \zeta + i(x - \xi) \cos \theta])}{gk - (\omega + Uk \cos \theta)^2} \cdot \\ &\cdot \cos[k(y - \eta) \sin \theta] \quad (17)\end{aligned}$$

The contours \mathcal{L}_1 and \mathcal{L}_2 are given as follows:

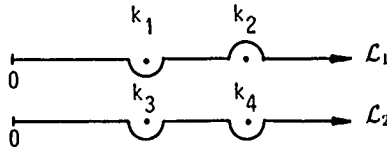


Fig. 2. Contours of integration

The contours are chosen such that the radiation conditions are satisfied. The radiated waves are outgoing and the Kelvin pattern is behind the ship. For small values of τ the poles of equation (17) behave as:

$$\sqrt{gk_1}, \sqrt{gk_3} \approx \omega + \mathcal{O}(\tau) \text{ as } \tau \rightarrow 0 \quad (18)$$

$$\sqrt{gk_2}, -\sqrt{gk_4} \approx \frac{\omega}{\tau \cos \theta} + \mathcal{O}(1) \text{ as } \tau \rightarrow 0 \quad (19)$$

A careful analysis of the asymptotic behaviour of $\psi(\underline{x}, \xi; U)$ for small values of U leads to a regular part and an irregular part:

$$\begin{aligned}\psi(\underline{x}, \xi; U) &= \psi_0(\underline{x}, \xi) + \tau \psi_1(\underline{x}, \xi) + \dots \\ \dots \tilde{\psi}_0(\underline{x}, \xi) &+ \nu^{-1} \tilde{\psi}_1(\underline{x}, \xi) + \dots \quad (20)\end{aligned}$$

where

$$\begin{aligned}\psi_0(\underline{x}, \xi) &= \\ 2k_0 \int_{\mathcal{L}_2} \frac{k \exp k(z + \zeta)}{k - k_0} J_0(kR) dk \quad (21)\end{aligned}$$

$$\begin{aligned}\psi_1(\underline{x}, \xi) &= \\ 4ik_0 \cos \theta' \int_{\mathcal{L}_2} \frac{k^2 \exp k(z + \zeta)}{(k - k_0)^2} J_1(kR) dk \quad (22)\end{aligned}$$

where $R^2 = (x - \xi)^2 + (y - \eta)^2$ and $\theta' = \arctan\{\frac{y - \eta}{x - \xi}\}$ and

$$\begin{aligned}\tilde{\psi}_0(\underline{x}, \xi) &= \\ -4\nu \int_0^{\pi/2} \exp[\nu(z + \zeta) \sec^2 \theta] \sin[\nu(x - \xi) \sec \theta] \cdot \\ \cdot \cos[\nu(y - \eta) \sin \theta \sec^2 \theta] \sec^2 \theta d\theta \quad (23)\end{aligned}$$

The expression in equation (23) gives the interaction of the translating part of the Green's function with the oscillatory part. In Hermans and Huijsmans [6] it is shown that due to the highly oscillatory nature the influence of equation (23) may be neglected in our first order correction for small values of τ .

The non-uniformity character of equation (20) for large values of R becomes clear, if we analyse $\psi_1(\underline{x}, \xi)$ a little bit further. The contour of integration \mathcal{L}_2 is chosen well underneath the singularity $k_0 = \omega^2/g$ and performs a partial integration of equation (22).

The end points give zero contribution. Hence we find:

$$\begin{aligned}\psi_1(\underline{x}, \xi) &= \\ 4ik_0 \cos \theta' \int_{\mathcal{L}_2} \frac{1}{(k - k_0)} \frac{d}{dk} [k^2 e^{k(z + \zeta)} J_1(kR)] dk \quad (24)\end{aligned}$$

We are mainly concerned with small values of $\tau(z + \zeta)$ because the pressure is calculated at the ship's hull and we assume the horizontal length scales large compared to the vertical length scale.

To get more insight in the structure of the source function we deform the contour \mathcal{L} in the complex plane.

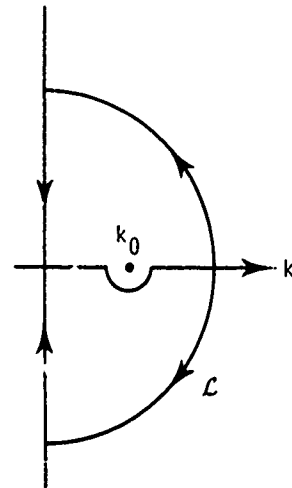


Fig. 3. Contours in complex plane

We use the relation $J_n(z) = \frac{1}{2} \{H_n^{(1)}(z) + H_n^{(2)}(z)\}$. For large values of z the Hankel functions behave like

$$\begin{aligned} H_n^{(1)} &\approx \sqrt{\frac{2}{\pi z}} e^{i(z - \frac{1}{2}n\pi - \pi/4)} \text{ and} \\ H_n^{(2)} &\approx \sqrt{\frac{2}{\pi z}} e^{-i(z - \frac{1}{2}n\pi - \pi/4)} \end{aligned} \quad (25)$$

We find as an approximation of equation (20)

$$\begin{aligned} \psi &\approx \psi_0 + \tau \psi_1 = 2\pi i \left\{ k_0 e^{k_0(z+\zeta)} H_0^{(1)}(k_0 R) + \right. \\ &+ 2\tau i \cos \theta' \frac{d}{dk} \left[k^2 e^{k(z+\zeta)} H_1^{(1)}(kR) \right]_{k=k_0} \left. \right\} + \\ &+ \frac{2}{\pi} \int_0^\infty k \left\{ \frac{e^{ik(z+\zeta)}}{k + ik_0} + \frac{e^{-ik(z+\zeta)}}{k - k_0} \right\} K_0(kR) dk + \\ &- \frac{4\tau \cos \theta'}{\pi} \int_0^\infty k^2 \left\{ \frac{e^{ik(z+\zeta)}}{(k + ik_0)^2} - \frac{e^{-ik(z+\zeta)}}{(k - k_0)^2} \right\} \cdot \\ &\cdot K_1(kR) dk \end{aligned} \quad (26)$$

This expression is then studied for large values of R .

The two integrals can be expanded with the help of the following integral representation of the function $K_n(z)$:

$$K_n(z) = \int_0^\infty e^{-z \cosh t} \cosh nt dt \quad (27)$$

We first apply the method of steepest descent with respect to the t integral and perform a partial integration with respect to k . It then turns out that both integrals behave like $\mathcal{O}(R^{-3/2})$, hence they lead to uniform expansions with respect to τ . The integrals are $\mathcal{O}(1)$ as $\tau \rightarrow 0, \forall R \in [0, \infty)$.

The terms that follow from the residues give rise to the expected non-uniform behaviour. The second term in equation (26) may be written in the form:

$$\begin{aligned} \tau \psi_1(\underline{x}, \underline{\xi})|_{Rcs} = \\ 2\pi i * 2i\tau \cos \theta' \left[k_0 H_1^{(1)}(k_0 R) + \right. \\ \left. + (z + \zeta) k_0^2 H_1^{(1)}(k_0 R) + R k_0^2 H_1^{(1)}(k_0 + R) \right] e^{k_0(z+\zeta)} \end{aligned} \quad (28)$$

The second term gives rise to non-uniform behaviour of large values of $z + \zeta$, however we restrict ourselves to finite values of $z + \zeta$.

Our main concern is the last term. We compare this term with the first one in equation (26)

$$\begin{aligned} \psi_{Rcs} &\approx 2\pi i k_0 e^{k_0(z+\zeta)} H_0^{(1)}(k_0 R) \\ \{1 + 2i\tau k_0 R \cos \theta'\} &+ \mathcal{O}(\tau^2), \forall R \in [0, \infty) \end{aligned} \quad (29)$$

and for large values of R we have:

$$\begin{aligned} \psi &\approx 2\pi i \sqrt{\frac{2}{\pi k_0 R}} k_0 e^{k_0(z+\zeta)} e^{i(k_0 R - \pi/4)} \\ \{1 + 2i\tau k_0 R \cos \theta'\} &+ \mathcal{O}(R^{-3/2}) + \mathcal{O}(\tau^2) \end{aligned} \quad (30)$$

The origin of the non-uniformity is now clear. It is the well-known phase shift of the wave numbers of the PLK method. The residue of the exact source functions leads to the exact phase shift, in our case we have approximated:

$$\exp(2ik_0\tau(x - \xi)) \text{ by } 1 + 2ik_0\tau(x - \xi) \quad (31)$$

This term originates from the x, t derivatives in the free surface boundary condition. Before treating methods to obtain uniform expansions we must keep in mind the way we like to use the Green's function. This leads to the insight that we need two different approaches. One for the computation of the far field wave and one for the computation of the integral equation. In the far field the exact value of the wave number has to be taken into account, while in the latter case a first order correction of the wave number is sufficient to arrive at solutions valid up to second order.

4. Expansion of Source Strength

In this section an approximate solution of equation (12) will be derived. Inserting (14) and (15) into (20) one obtains for like powers of τ the following set of equations:

$$\begin{aligned} -2\pi\sigma_0(\underline{x}) - \iint_S \sigma_0(\underline{\xi}) \frac{\partial}{\partial \underline{n}_x} G_0(\underline{x}, \underline{\xi}) dS_\xi \\ = 4\pi V_0(\underline{x}), \underline{x} \in S \end{aligned} \quad (32)$$

and

$$\begin{aligned} -2\pi\sigma_1(\underline{x}) - \iint_S \sigma_1(\underline{\xi}) \frac{\partial}{\partial \underline{n}_x} G_0(\underline{x}, \underline{\xi}) dS_\xi = \\ - \iint_S \sigma_0(\underline{\xi}) \frac{\partial}{\partial \underline{n}_x} \psi_1(\underline{x}, \underline{\xi}) dS_\xi + 4\pi V_1(\underline{x}) + \\ \frac{2i\omega}{g} \iint_{FS} \frac{\partial}{\partial \underline{n}_x} G_0(\underline{x}, \underline{\xi}) \nabla \bar{\phi}(\underline{\xi}) \cdot \nabla \phi_0(\underline{\xi}) dS_\xi \end{aligned} \quad (33)$$

where $G_0(\underline{x}, \underline{\xi}) = -\frac{1}{r} + \frac{1}{r'} - \psi_0(\underline{x}, \underline{\xi})$ is the zero speed pulsating wave source and

$$V(\underline{x}) = V_0(\underline{x}) + \tau V_1(\underline{x}) + \mathcal{O}(\tau^2) \quad (34)$$

The potential functions in (14) now become:

$$\phi_0(\underline{x}) = -\frac{1}{4\pi} \iint_S \sigma_0(\underline{\xi}) G_0(\underline{x}, \underline{\xi}) dS_{\xi} \quad (35)$$

$$\begin{aligned} \phi_1(\underline{x}) = & -\frac{1}{4\pi} \iint_S \sigma_0(\underline{\xi}) \psi_1(\underline{x}, \underline{\xi}) dS_{\xi} \\ & -\frac{1}{4\pi} \iint \sigma_1(\underline{\xi}) G_0(\underline{x}, \underline{\xi}) dS_{\xi} + \\ & + \frac{i\omega}{2\pi g} \iint_{FS} G_0(\underline{x}, \underline{\xi}) \nabla \bar{\phi}(\underline{\xi}) \cdot \phi_0(\underline{\xi}) dS_{\xi} \end{aligned} \quad (36)$$

In principle the solution of the problem is now solving $\phi_0(\underline{x})$ and $\phi_1(\underline{x})$ using the steady perturbation potential. The steady perturbation potential $\bar{\phi}$ is determined using a boundary integral technique for the steady double body flow, which originally comes from a Hess and Smith type of algorithm. The steady double body flow is calculated separately and is then incorporated into the free surface integral.

In reference [6] it is shown that the non-uniform term with respect to ν in the Green's function leads to contributions that are asymptotically small compared to the terms we have taken into account.

5. Uniform Asymptotic Expansions

In principle we have to solve (32) and (33) where the source function suffers non-uniform behaviour. If the size of the ship is order one with respect to τ it is sufficient to use (10) with (20). The question remains how to compute the far field. This will be dealt with in part 1 of this section.

If the size of the vessel becomes large with respect to τ , $\tau R = \mathcal{O}(1)$, we have to modify (20) in order to obtain proper approximations of the source strength from (32) and (33). This problem is stated in part 2 of this section.

5.1 The Far Field

In the case where $\sigma_0 + \tau\sigma_1$ is known, the far field may be computed with the aid of equation (13). Because for R large we cannot use (10) with (16). As explained before the contribution of the "Kelvin" residues from k_2 and k_4 are neglected. Contributions of the wave residues are dominant but first we apply the method of stationary phase to the integral with respect to θ . The integrand $F(\theta, k)$ for large values of R with the notation $x = R \cos \bar{\theta}$, $y = R \sin \bar{\theta}$:

$$F(\theta, k) =$$

$$\begin{aligned} & \frac{k}{2} \frac{\exp(k(z + \zeta))}{gk - (\omega + kU \cos \theta)^2} \\ & \left\{ \exp[-ik(\xi \cos \theta + \eta \sin \theta)] \cdot \exp[ikR \cos(\theta - \bar{\theta})] + \right. \\ & \left. \exp[-ik(\xi \cos \theta - \eta \sin \theta)] \exp[ikR \cos(\theta + \bar{\theta})] \right\} \end{aligned} \quad (37)$$

We have to distinguish between the four quadrants at infinity. We choose $0 \leq \bar{\theta} \leq \pi/2$. All other quadrants can be treated in a similar way, the results are the same. We obtain:

$$\begin{aligned} \Psi(\underline{x}, \underline{\xi}; U) \approx & \frac{g}{\pi} \sqrt{\frac{2\pi}{R}} e^{-\frac{\pi i}{4}} \\ & \left[\int_{\mathcal{L}_1} \frac{\sqrt{k} \exp\{k(z + \zeta) - ik(\xi \cos \bar{\theta} + \eta \sin \bar{\theta}) + ikR\}}{gk - (\omega + Uk \cos \bar{\theta})^2} dk \right. \\ & \left. + \int_{\mathcal{L}_2} \frac{\sqrt{k} \exp\{k(z + \zeta) + ik(\xi \cos \bar{\theta} + \eta \sin \bar{\theta}) - ikR\}}{gk - (\omega - Uk \cos \bar{\theta})^2} dk \right] \end{aligned} \quad (38)$$

The first integral may be closed in the upper quarter plane whilst the second one may be closed in the lower quarter plane. The integrals along the imaginary axis are of $\mathcal{O}(R^{-3/2})$.

We now finally obtain:

$$\begin{aligned} \Psi(\underline{x}, \underline{\xi}; U) \approx & 2\pi i \sqrt{\frac{2}{\pi R}} \left\{ \frac{e^{i(k_1(\theta)R - \pi/4)}}{(1 - \frac{2U}{g} \cos \bar{\theta}(\omega + k_1(\theta)U \cos \bar{\theta}))} \right\} \\ & \sqrt{k_1(\theta)} \exp\{k_1(\theta)(z + \zeta) - ik_1(\theta)(\xi \cos \bar{\theta} + \eta \sin \bar{\theta})\} \end{aligned} \quad (39)$$

with

$$k_1(\theta) = \frac{g - 2\omega U \cos \bar{\theta} - g\sqrt{(1 - 4\tau \cos \bar{\theta})}}{2U^2 \cos^2 \bar{\theta}} \quad (40)$$

Hence, to obtain the potential in the far field we use (13) with

$$G(\underline{x}, \underline{\xi}) = -\frac{1}{r} + \frac{1}{r'} - \bar{\psi}(\underline{x}, \underline{\xi}; U) \text{ and} \quad (41)$$

$$\sigma(\underline{\xi}) = \sigma_0(\underline{\xi}) + \tau\sigma_1(\underline{\xi}) \quad (42)$$

5.2 Large Vessels

In the case of large vessels (41) is not a good approximation for the source strength. We now have to take care of the non-uniformity as described in (30). A practical requirement is that we want to make use of the zero speed oscillatory Green's function and its derivatives. The function $\psi_1(\underline{x}, \underline{\xi})$ can be computed for the major part using algorithms as e.g. developed by Newman [18] or Noblesse [19]. One minor contribution has to be evaluated separately. Keeping in mind that the PLK method requires the omission of the most severe secular term to obtain uniform expansions we may conclude that the procedure only needs to avoid approximations as (31). The following procedure makes it possible to use the zero speed algorithms with a slight modification. A proof of the validity can be given rigorously with the same analytic manipulations as described in Section 3. For instance the following correction may be performed:

$$\psi_{Res} \approx (\psi_{0, res} + \tau\psi_{1, res}) \frac{\exp(2i\tau k_0(x - \xi))}{1 + 2i\tau k_0(x - \xi)} \quad (43)$$

It can be shown by inspection that this multiplicative correction yields the correct uniform asymptotic expansion up to $\mathcal{O}(\tau^2 R)$ as $\tau \rightarrow 0$ [20]. The interval of validity is properly extended. It is also possible to apply the correction to $\psi_{0, res}$ alone and to show that:

$$\begin{aligned} \psi_{res} &= (\psi_{0, res}(1 - 2ik_0\tau(x - \xi)) + \tau\psi_{1, res}) \\ &\exp(2i\tau k_0(x - \xi)) + \mathcal{O}(\tau^2 R) \end{aligned} \quad (44)$$

The correction is only needed for large values of $K_0 R$, therefore the correction may be performed at asymptotic level. This leads to the following simplified results for the total ψ . This result is rewritten in asymptotic form where we made use of the explicit form of the residues

$$\psi \approx \bar{\psi}_0 + \tau\bar{\psi}_1 \quad (45)$$

where

$$\bar{\psi}_0 =$$

$$\psi_0 - 2\pi k_0 e^{k_0(z+\zeta)}.$$

$$\cdot \sqrt{\frac{2}{\pi k_0 R}} \left[e^{i(k_0 R - \pi/4)} \{1 - \exp(2ik_0\tau(x - \xi))\} \right] \quad (46)$$

and

$$\bar{\psi}_1 =$$

$$\psi_1 - 2\pi k_0 e^{k_0(z+\zeta)}.$$

$$\cdot \sqrt{\frac{2}{\pi k_0 R}} \left[e^{i(k_0 R - \pi/4)} \{2ik_0(x - \xi)\} \right] \quad (47)$$

The correction of ψ_0 can easily be performed in the zero speed Green's function algorithm, while the correction of ψ_1 can be performed either analytically or numerically. It can be shown by inspection also that:

$$\psi \approx \bar{\psi}_0 + \tau\bar{\psi}_1 + \mathcal{O}(\tau^2 R) \quad (48)$$

Hence the region of validity is extended in a proper way.

If one wants to higher order approximations the procedure has to be reconsidered. Corrections can be obtained along the same line. However the advantage of reduction to the zero speed algorithms is not available anymore. One has to devise a fast algorithm for ψ_2 .

6. Wave Drift Forces

In Hermans and Huijsmans [6] we described a way to compute the first order forces and the second order wave drift forces. The method we used there was based on a direct pressure integration of the first and second order pressures respectively. It has been shown before (e.g. see Pinkster [1]) that this method works well and is even necessary in order to compute the slowly varying wave drift forces.

At this moment we are mainly interested in the constant component of the wave drift force. In this section we recapitulate a method that leads to results that possibly are more accurate numerically, because when using the pressure integration technique one has to use derivatives of the potential function over the mean wetted surface. This is even more the case if one uses pressure integration in the case of ship motions with forward speed (see Huijsmans [21]). Newman [22] and Maruo [23] have derived an expression for the wave drift forces and moments.

The mean forces and moments may be expressed as [22]:

$$\bar{F}_x = - \iint_{S_\infty} [p \cos \theta + \rho V_R (V_R \cos \theta - V_\theta \sin \theta)] R d\theta dz \quad (49)$$

$$\bar{F}_y = - \iint_{S_\infty} [p \sin \theta + \rho V_R (V_R \sin \theta + V_\theta \cos \theta)] R d\theta dz \quad (50)$$

$$\bar{M}_z = - \iint_{S_\infty} V_R V_\theta R^2 d\theta dz \quad (51)$$

where p is the first order hydrodynamic pressure, \underline{V} is the fluid velocity with radial and tangential components V_R, V_θ and S_∞ is a large cylindrical control surface with radius R in the ship-fixed coordinate system. Faltinsen and Michelsen [24] derive from these formulas expressions in terms of the source densities of the first order potentials. From:

$$\sigma(\xi) = \sigma^{(7)}(\xi) + \sum_{j=1}^6 \sigma^{(j)}(\xi) \bar{\alpha}_j \quad (52)$$

where $\alpha_j = \bar{\alpha}_j e^{-i\omega t}$ $j=1,6$ are the six modes of motion and superscript 7 refers to the diffraction component of the source strength. In our case we follow the same reasoning to obtain similar results for the slow forward speed case. Our velocity potential has the form:

$$\begin{aligned} \Phi(\underline{x}, t) = & Ux + \bar{\phi}(\underline{x}; U) + \phi(\underline{x}, U) e^{-i\omega t} \\ = & Ux + \bar{\phi}(\underline{x}; U) + \\ & \left\{ \phi^{(0)}(\underline{x}; U) + \phi^{(7)}(\underline{x}; U) + \sum_{j=1}^6 \phi^{(j)}(\underline{x}; U) \bar{\alpha}_j \right\} e^{-i\omega t} \end{aligned} \quad (53)$$

where the potentials $\phi^{(j)}(\underline{x}; U)$, $j=1,7$ have the form (13) and are the potentials due to the motions and diffraction effects. We assume that they are all determined by means of a source distribution where $\sigma^{(j)}(\underline{x}) = \sigma_0^{(j)}(\underline{x}) + \tau \tau_1^{(j)}(\underline{x})$.

In the far field $R \gg 1$ we neglect the influence of the stationary potential $\bar{\phi}(\underline{x}; U)$ in (53) hence we approximate (53) by:

$$\phi(\underline{x}, t) =$$

$$\begin{aligned} & Ux + \frac{g\zeta_a}{\omega} e^{i\{k_1(\beta)z + i(k_1(\beta)(x \cos \beta + y \sin \beta) - \omega t)\}} \\ & + F(\theta) e^{iS(\theta)} \sqrt{\frac{1}{R}} e^{i(k_1(\theta)z + i(k_1(\theta)(x \cos \theta + y \sin \theta) - \omega t)} \end{aligned} \quad (54)$$

here ζ_a is the amplitude of the incoming wave and $F(\theta) e^{iS(\theta)}$ results from the asymptotic expansion of the far field potentials in (53) with

$$\begin{aligned} & 4\pi\phi^{(j)}(\underline{x}; U) = \\ & - \iint_S \sigma^{(j)}(\xi) G(\underline{x}, \xi) dS_\xi \\ & + \frac{2i\omega}{g} \iint_{FS} \nabla \bar{\phi} \cdot \nabla \phi^{(j)} G(\underline{x}, \xi) dS_\xi \end{aligned} \quad (55)$$

where $G(\underline{x}, \xi)$ is approximated by (30). Due to the fact that the function $\nabla \bar{\phi}(\xi)$ decays rapidly as $|\xi| \rightarrow \infty$ we assume that $R = |\underline{x}|$ is large enough to take the asymptotic expansion of $G(\underline{x}, \xi)$ in the last term as well. The function $\nabla \phi^{(j)}$ may be replaced by $\nabla \phi_0^{(j)}$. This leads to

$$\begin{aligned} & F(\theta) e^{iS(\theta)} = \\ & \sqrt{\frac{k_1(\theta)}{2\pi}} \left[\frac{e^{-3\pi i/4}}{1 - \frac{2U}{g} \cos \theta (\omega + k_1(\theta) U \cos \theta)} \right] \cdot \\ & \cdot \left[\iint_S \sigma(\xi) \exp \{k_1(\theta) \zeta - i k_1(\theta) (\xi \cos \theta + \eta \sin \theta)\} dS_\xi \right. \\ & \left. - \frac{2i\omega}{g} \iint_{FS} \nabla \bar{\phi} \cdot \nabla \phi_0^{(7)} \exp \{-i k_1(\theta) (\xi \cos \theta + \eta \sin \theta)\} dS_\xi \right] \end{aligned} \quad (56)$$

where:

$$\phi_0^{(7)}(\xi) = \phi_0^{(7)}(\xi) + \sum_{j=1}^6 \phi_0^{(j)}(\xi) \bar{\alpha}_j \quad (57)$$

This result is of $\mathcal{O}(\tau^2)$ as $\tau \rightarrow 0 \forall R \in [0, \infty)$.

The upper integration boundary in (49), (50) and (51) is the free surface

$$\zeta = \frac{1}{g} \text{Re} \left[(i\omega \phi(x, y, 0) - U \phi_x(x, y, 0)) e^{-i\omega t} \right] \quad (58)$$

It follows from the pressure term that we may write:

$$\int_{-\infty}^{\zeta} p dz = \frac{\rho g}{2} \zeta^2 - \frac{\rho}{2} \int_{-\infty}^0 (|\underline{V}|^2 - U^2) dz \quad (59)$$

We find the following expression for \bar{F}_x :

$$\begin{aligned}\bar{F}_x = & -\frac{\rho}{4} \int_0^{2\pi} \{k_0 \phi \phi^* + 2\tau \text{Im}(\phi \phi_x^*)\} R \cos \theta d\theta \\ & + \frac{\rho}{4} \int_0^{2\pi} \int_{-\infty}^0 \left[\left(\frac{1}{R^2} \phi_\theta \phi_\theta^* - \phi_R \phi_R^* + \phi_z \phi_z^* \right) R \cos \theta + \right. \\ & \left. + \frac{1}{R} (\phi_R \phi_\theta^* + \phi_R^* \phi_\theta) R \sin \theta \right] d\theta dz\end{aligned}\quad (60)$$

and for \bar{F}_y :

$$\begin{aligned}\bar{F}_y = & -\frac{\rho}{4} \int_0^{2\pi} \{k_0 \phi \phi^* + 2\tau \text{Im}(\phi \phi_x^*)\} R \sin \theta d\theta \\ & + \frac{\rho}{4} \int_0^{2\pi} \int_{-\infty}^0 \left[\left(\frac{1}{R^2} \phi_\theta \phi_\theta^* - \phi_R \phi_R^* + \phi_z \phi_z^* \right) R \sin \theta + \right. \\ & \left. - \frac{1}{R} (\phi_R \phi_\theta^* + \phi_R^* \phi_\theta) R \cos \theta \right] d\theta dz\end{aligned}\quad (61)$$

and for \bar{M}_z :

$$\begin{aligned}\bar{M}_z = & + \frac{\rho}{4} \int_0^{2\pi} \int_{-\infty}^0 R (\phi_R \phi_\theta^* + \phi_R^* \phi_\theta) d\theta dz\end{aligned}\quad (62)$$

The integration with respect to z needs some extra attention due to the fact that the exponential behaviour of the incident wave and the radiated or diffracted wave is different, due to the dependence of the wave number on β and θ , respectively see (54).

The asteriks in equation (60) denote the complex conjugate and

$$\begin{aligned}\phi = & \frac{g\zeta}{\omega} \exp(k_1(\beta)z + ik_1(\beta)(x \cos \beta + y \sin \beta)) \\ & + F(\theta) e^{iS(\theta)} \sqrt{\frac{1}{R}} \exp\{k_1(\theta)z + ik_1(\theta)R\}\end{aligned}\quad (63)$$

We formally write (63) as sum of two components:

$$\phi = \phi_i + \phi_R \quad (64)$$

For the wave number $k_1(\theta)$ we can write neglecting U^2 terms in the wave number depending on θ :

$$k_1(\theta) = k_0(1 + 2\tau \cos \theta) \quad (65)$$

The first term is related to the incoming wave field while the second one describes the diffraction and radiation effects.

A closer look at (63) and (60) shows that the contribution to \bar{F}_x consists of two parts. The first one, $F_x^{(1)}$, originates from those parts of the cross products that behave like $R^{-1/2}$ while the second one, $F_x^{(2)}$, originates from those square terms of the second part of (63) they behave like R^{-1} . We formally write:

$$\bar{F}_x = F_x^{(1)} + F_x^{(2)} \quad (66)$$

We now can write:

$$\begin{aligned}F_x^{(1)} = & -\frac{\rho\omega\zeta_a}{4} R^{1/2} \int_0^{2\pi} F(\theta)(\cos \theta + \cos \beta) \cdot \\ & \cdot \cos\{(k_1(\beta)\cos(\theta - \beta) - k_1(\theta))R - S(\theta)\} d\theta + \\ & + \tau \frac{\rho\omega\zeta_a}{2} R^{1/2} \int_0^{2\pi} F(\theta)[(\cos \theta + \cos \beta)\cos \theta \\ & + \frac{1}{2}(\cos^2 \theta - \sin^2 \theta) - \sin \theta \sin \beta] \cdot \\ & \cdot \cos\{(k_1(\beta)\cos(\theta - \beta) - k_1(\theta))R - S(\theta)\} d\theta \\ & + O(\tau^2)\end{aligned}\quad (67)$$

We now apply the method of stationary phase for large values of R . To do so we have to determine the stationary points of the integrands. We determine the point where:

$$\frac{d}{d\theta} \{k_1(\beta)\cos(\theta - \beta) - k_1(\theta)\} = 0 \quad (68)$$

We find two points,

$$\theta_1 = \beta + 2\tau \sin \beta \text{ and } \theta_2 = \beta + \pi + 2\tau \sin \beta \quad (69)$$

The second point gives a zero contribution, where we remark that the last term in (67) is cancelled by the τ -dependent contribution of the last term. It is obvious that the other terms give zero contribution due to the factor π in θ_2 . We use the asymptotic result:

$$\begin{aligned}& \int_0^{2\pi} l(\theta) \cos\{(k_1(\beta)\cos(\theta - \beta) - k_1(\theta))R - S(\theta)\} d\theta \\ & \approx \left[\frac{2\pi}{Rk_0} \right]^{1/2} \frac{1}{(1 - 2\tau \cos \beta)^{1/2}} \{l(\beta + 2\tau \cos \beta) \cdot \\ & \cdot \cos(S(\beta + 2\tau \cos \beta) + \pi/4)\}\end{aligned}\quad (70)$$

As mentioned before the second contribution is zero. A critical reader will notice that formally we have to deal with a non-uniformity due to the fact that we have a first order 'uniform' solution. The phase correction is of first order. Hence in our asymptotic result of (70) we neglect the second order phase correction. The only

way to do the analysis properly is to use the exact value of the wave number in (40) instead of our asymptotic approximation.

Summarizing we now have:

$$\begin{aligned}
 F_x^{(1)} &\approx \\
 A \left[\frac{2\pi}{k_0} \right]^{1/2} &\cos(S(\beta^*) + \pi/4) \\
 \cdot F(\beta^*) \{ \cos \beta^* + \cos \beta + & \\
 -2\tau \cos(2\beta) \} & \quad (71)
 \end{aligned}$$

where $A = -\frac{\rho \omega \zeta_0}{4}$ and $\beta^* = \beta + 2\tau \sin \beta$.

A similar analysis can be followed for the sway force and leads to the following result:

$$\begin{aligned}
 F_y^{(1)} &\approx \\
 A \left[\frac{2\pi}{k_0} \right]^{1/2} &\cos(S(\beta^*) + \pi/4) \\
 \cdot F(\beta^*) \{ \sin \beta^* + \sin \beta + & \\
 -2\tau \sin(2\beta) \} & \quad (72)
 \end{aligned}$$

The second part of the wave drift force may now be written as:

$$\begin{aligned}
 F_x^{(2)} = & \\
 -\frac{\rho}{4} k_0 \int_0^{2\pi} F^2(\theta) \{ \cos \theta - 2\tau \cos(2\theta) \} d\theta & \quad (73)
 \end{aligned}$$

For the sway force this leads to:

$$\begin{aligned}
 F_y^{(2)} = & \\
 -\frac{\rho}{4} k_0 \int_0^{2\pi} F^2(\theta) \{ \sin \theta - 2\tau \sin(2\theta) \} d\theta & \quad (74)
 \end{aligned}$$

7. Numerical Results

For the validation of the mathematical model presented in the previous sections computations have been performed on a fully loaded 200 kDWT tanker and a half immersed sphere.

The description of the tanker can be found in Huijsmans et al. [12]. The numerical results of the wave drift forces on the tanker have been validated against results of model test experiments. The calculations for the 200 kDWT tanker are applicable to the situation of a tanker in both head-on current and waves as well as the case of the waves and current parallel under 135 degrees, as displayed in the next figure.

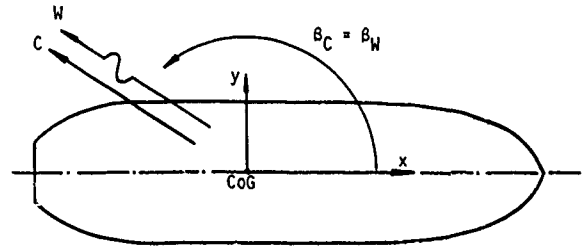


Fig. 4. Definition of waves and current

The calculated steady double body flow using the Hess and Smith algorithm apply to the situation of a tanker under a drift angle of 135 degrees (in principle the solution can be made applicable to any drift angle α_c).

The boundary conditions on the mean wetted hull for the radiation problem have been applied with the steady perturbation potential set to zero, which then results in the well-known expression for the m-terms of the radiation boundary condition. A more proper way of handling the radiation boundary condition as published by Zhao et al. [10] was not attempted here due to the difficulty of the splitting the boundary conditions into linear forward speed dependent boundary conditions.

For the results of computation for the wave drift force on the sphere a comparison was made with results of computations as was obtained by Nossen et al. [7].

The panel discretization of the tanker amounted to 238, 720 and 1610 panels in order to check the numerical accuracy of the pressure integration technique. The result of the computation are depicted in Fig. 15. The number of panels for the sphere amounted to 744.

To solve the integral equations for the source strength $\sigma_0^{(j)}(\underline{x})$ and $\sigma_1^{(j)}(\underline{x})$ large algebraic equations have to be solved.

In the present solver use is made of a newly developed iteration scheme. Details of this new solver for Boundary Integral Equations will be published in the near future. To solve a large system of 1610 unknowns for the radiated and diffracted modes only required 4 to 6 iteration steps to gain an accuracy of 10^{-4} in the Euclidian norm. The timing was approximately 28 CPU seconds per wave frequency for 1610 panels on an ETA 10P mini supercomputer from ETA systems. The analysis of the results of the wave drift forces using the pressure distribution integration, as shown in

Figs. 9 to 12 leads to the observation that the numerical accuracy of the pressure distribution integration greatly depends on the panel discretization. Detailed results are presented in Table 1 for the frequencies of 0.5 and 0.7 rad/s.

Table 1

F_x for 180 deg. waves and current			
ω	238	720	1610
0.5	15.5	17.3	14.9
0.7	11.2	15.3	15.1

7.1 Half Immersed Sphere

The results of computation for the sphere are presented for the mean wave drift force. The mean drift force on the sphere has been calculated in two ways, i.e. one describing the correct influence of the steady perturbation potential and the other is using the slenderness approximation in which the influence of the steady perturbation potential has been neglected.

The region of integration over the free surface was from $r = R$ to $r = 3R$, where R is the radius of the sphere. The number of free surface panels amounted to 810 panels.

These results are presented in the following Figs. 5 to 7.

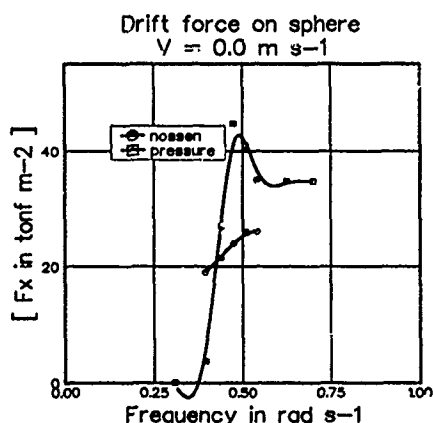


Fig. 5. Zero speed wave drift forces

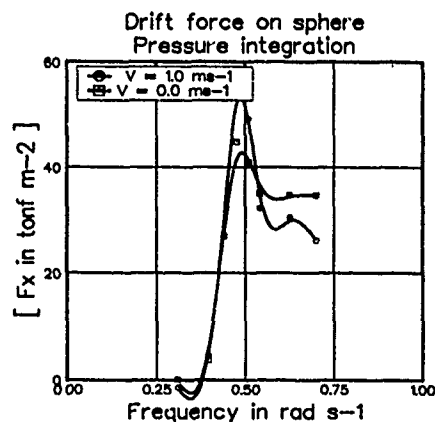


Fig. 6. Forward speed wave drift forces

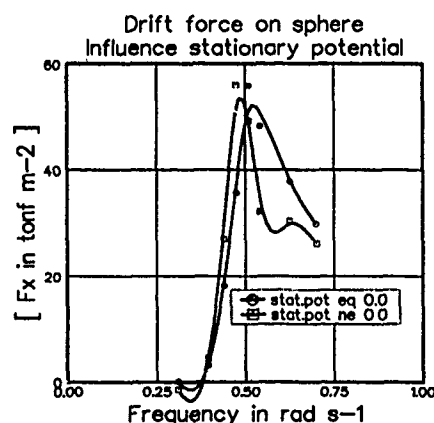


Fig. 7. Influence of steady potential

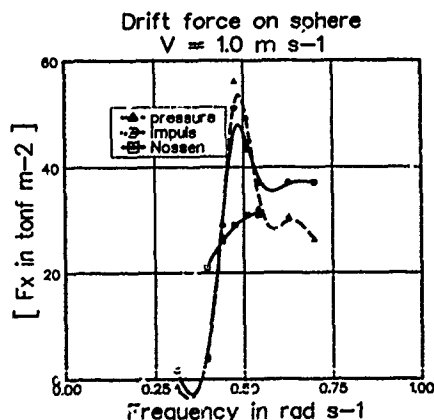


Fig. 8. Forward speed results Nossen

In Fig. 8 the results of computation are presented for $Fn = 0.032$ against other results as obtained by Nossen et al. [7].

The observed difference between the results of Nossen and ours is due to the fact that the results of Nossen apply to a fixed cylinder in waves whereas our results apply to the free floating case. In the range where diffraction dominates, the results tend to be the same.

The zero speed wave drift forces on the sphere are calculated in two ways; i.e. one using a pressure distribution integration technique and the other one uses the momentum flux analysis (Maruo [23]).

For the forward speed case this was also done, however now the equations (71) and (73) have to be used for the momentum flux analysis.

One can see from Figs. 5 to 7 that the calculations using the momentum balance are not so much influenced by the panel discretization. This can be made plausible by observing that the expression for the wave drift forces from the momentum balance only simple source distribution integration over the mean wetted hull is required. It is our opinion that due to the integration of higher order derivatives in the pressure distribution for the forward speed case the results are more sensitive for the way the integration is performed.

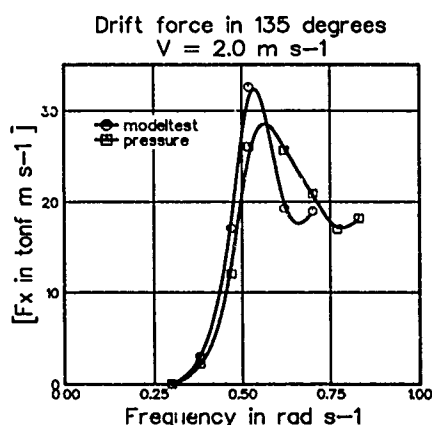


Fig. 9. Mean surge drift force

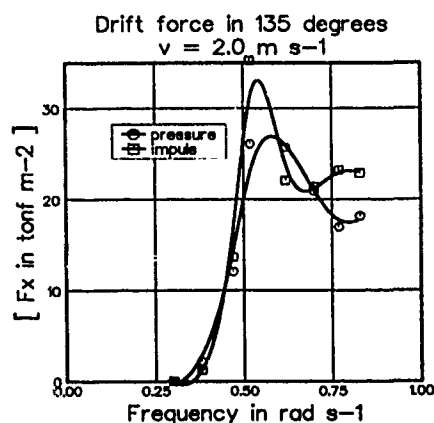


Fig. 11. Mean surge drift force

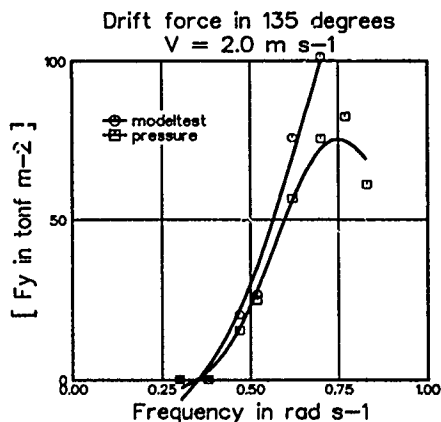


Fig. 10. Mean sway drift force

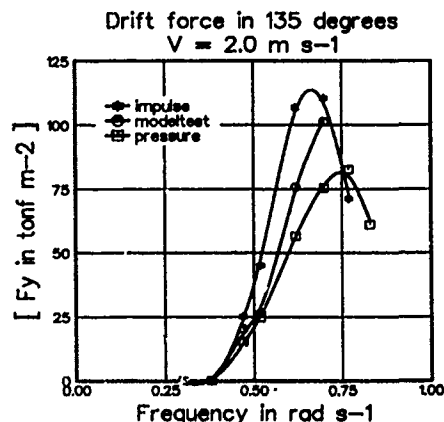


Fig. 12. Mean sway drift force

7.2 Tanker

At MARIN a number of tests have been conducted. The test comprise in short regular wave test on a stationary moored 200 kDWT tanker in 82.5 metres of water depth with waves and current parallel to each other. The results of model tests and computations for head waves and 2 knots current have been extensively described by Wichers [25] and Huijsmans [21]. The results of model tests for the tanker with the waves and current coming from 135 degrees are presented in Figs. 9 and 12 for the mean surge and sway drift force respectively.

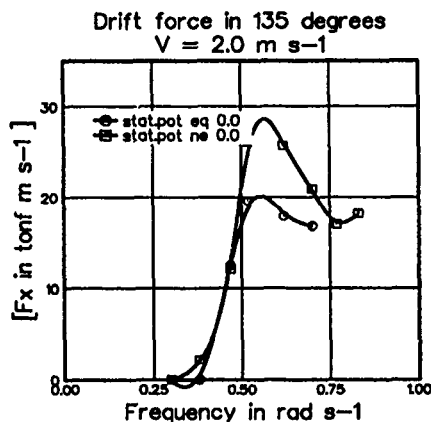


Fig. 13. Influence of steady potential

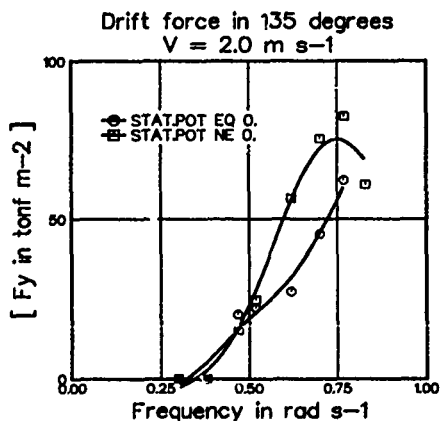


Fig. 14. Influence of steady potential

The resulting drift forces are calculated in two ways; i.e. one using the pressure integration technique and one using the momentum flux analysis. The results have been presented in Figs. 11 and 12 for the surge and sway wave drift force respectively. The influence of the stationary potential on the wave drift forces has been studied. The results are displayed in Figs. 13 and 14. From these results one is tempted to conclude that the influence of the stationary potential on the drift forces in this case is restricted to the sway drift force results, however, previous observations also indicate that the use of a pressure integration for the calculation of the wave drift forces with forward speed are somewhat doubtful, due to the large dependency on the panel discretization of the body.

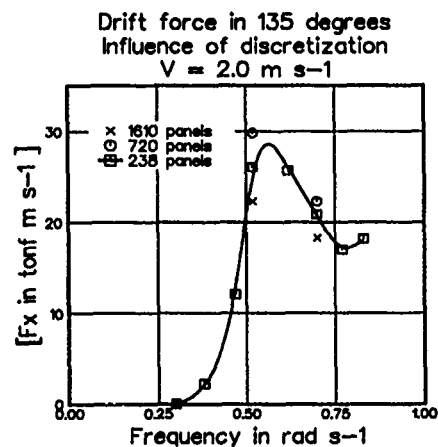


Fig. 15. Influence of panel discretization

References

- [1] Pinkster, J.A., *Low frequency second order wave exciting forces on floating structures*, PhD thesis, University of Delft (1980).
- [2] Benschop, A., Hermans, A.J. and Huijsmans, R.H.M., "Second order diffraction forces on a ship in irregular waves", *Journal of Applied Ocean Research*, Vol. 9 (1987).
- [3] Remery, G.F.M. and Hermans, A.J., "Slow drift oscillations of a moored object in random seas", *Proceedings of the Offshore Technology Conference*, Houston, Paper 1500 (1971).

- [4] Wichers, J.E.W., "On the low frequency surge motions of vessels moored in high seas", *Offshore Technology Conference*, Houston, Paper 4437 (1982).
- [5] Wichers, J.E.W. and Huijsmans, R.H.M., "On the low frequency hydrodynamic damping force acting on offshore moored vessels", *Offshore Technology Conference*, Houston, Paper 4813 (1984).
- [6] Hermans, A.J. and Huijsmans, R.H.M., "The effect of moderate speed on the motions of floating bodies", *Schiffstechnik* (March 1987).
- [7] Nossen, J., Palm, E. and Grue, J., "On the solution of the radiation and diffraction problems for a floating body with a small forward speed", *International Workshop on Water Waves and Floating Bodies*, Oslo (1989).
- [8] Sclavonous, P., "The slow drift wave damping of floating bodies", *International Workshop on Water Waves and Floating Bodies*, Oslo (1989).
- [9] Hu, C.S. and Eatock Taylor, R., "A small forward speed perturbation method for wave-body problems", *International Workshop on Water Waves and Floating Bodies*, Oslo (1989).
- [10] Zhao, R. and Faltinsen, O., "A discussion of the m-terms in the wave-body interaction problem", *International Workshop on Water Waves and Floating Bodies*, Oslo (1989).
- [11] Huijsmans, R.H.M. and Hermans, A.J., "A fast algorithm for the calculation of 3-D ship motions at moderate forward speed", *Proceedings of 4th Numerical Ship Hydrodynamic Conference*, Washington (1985).
- [12] Huijsmans, R.H.M. and Wichers, J.E.W., "Considerations on wave drift damping of a moored tanker for zero and non-zero drift angles", *Proceedings of the PRADS Symposium*, Trondheim (1987).
- [13] Eggers, K., "Non-Kelvin dispersive waves around non slender ships", *Schiffstechnik*, Vol. 8, (1981).
- [14] Baba, E., *Wave resistance of ships in low speed*, Technical Report 109, Mitsubishi Technical Bulletin (1976).
- [15] Hermans, A.J., *The wave pattern of a ship sailing at low speed*, Technical Report 84A, University of Delaware (1980).
- [16] Brandsma, F.J. and Hermans, A.J., "A quasi-linear free surface condition in slow ship theory", *Schiffstechnik* (April 1985).
- [17] Wehausen, J. and Laitone, E., *Surface Waves*, Volume 9 of *Handbuch der Physik*, Springer Verlag (1960).
- [18] Newman, J.N., "The evaluation of free-surface Green's functions", *Proceedings of the 4th International Conference on Numerical Ship Hydrodynamics*, Washington (1985).
- [19] Telste, J. and Noblesse, F., "Numerical evaluation of Green's functions of water wave diffraction and radiation", *Journal of Ship Research*, Vol. 1111 (1987).
- [20] Hearn, G., Priv. Communication (1989).
- [21] Huijsmans, R.H.M., "Wave drift forces in current", *16th Conference on Naval Hydrodynamics*, Berkeley (1986).
- [22] Newman, J.N., "The drift force and moment on a ship in waves", *Journal of Ship Research*, Vol. 10 (1967).
- [23] Maruo, H., "The drift of a body floating on waves", *Journal of Ship Research*, Vol. 4 (1960).
- [24] Faltinsen, O. and Michelsen, F., "The motions of large structures in waves at zero Froude number", *Symposium on the Dynamics of Marine Vehicles and Structures in Waves*, London (1974).
- [25] Wichers, J.E.W., "Progress in computer simulations of SPM moored vessels", *Offshore Technology Conference*, Houston, Paper 5175 (1986).

DISCUSSION

by R. Zhao

- (1) Discuss about direct pressure integration method
- (2) Discuss about wave drift damping

Author's Reply

The direct pressure integration method is based on the integration of local hydrodynamic quantities like water velocities and gradients of pressures over the mean wetted hull. This procedure is demonstrated in our papers presented at the ONR Conference in 1986, [A1] and at the UTAM symposium, [A2].

One of the main problems in using the direct pressure integration method is based on the accuracy of the underlying hydrodynamic data. In the zero speed case there is sufficient evidence that this procedure, using 3-D diffraction theory results, will lead to meaningful results. In the non-zero speed case however this evidence is lacking and to the author's opinion the accuracy of the first order results based on 3-D diffraction results with forward speed must be even more accurate

than the zero speed results due to the fact that in the evaluation of the pressure distribution, gradients of the water velocity distribution are required. In pursuing the direct pressure integration one has to resort to e.g. higher order panel methods to obtain the required accuracy.

The question regarding the wave drift damping has not been addressed in this paper, however information can easily be obtained using the results of our paper. At the moment we only calculated the drift force at two speeds, which is in principle enough to obtain wave drift damping data. However, if one wants to obtain reliable results for the wave drift damping coefficient several more speeds (also negative speeds) have to be calculated. This will be done in the near future.

[A1] R. H. M. Huijsmans, "Wave Drift Forces in Current", 15th ONR Symposium, Berkeley, 1986.

[A2] R. H. M. Huijsmans, "Slowly Varying Wave Drift Forces in Current", IUTAM Symposium on non-linear water waves, Tokyo, 1987.

Numerical Prediction of Semi-Submersible Non-Linear Motions in Irregular Waves

X. B. Chen and B. Molin
Institut Français du Pétrole
Rueil-Malmaison, France

Abstract

A numerical model to predict non-linear vertical motions of a semi-submersible in regular and irregular waves is presented. Non-linear second-order forces are evaluated by using Molin's method which permits to obtain them without explicitly solving for the second-order potential. Non-linear low frequency motions being large in magnitude, variations of second-order forces with the motion of the body mean position are considered in the time simulation. As application cases, two floating bodies with small waterplane areas are taken into account. Comparisons of calculations with experimental results show that this theory correctly predicts the low frequency motions.

1. Introduction

The nonlinear behavior of floating offshore structures in regular and irregular waves is an interesting and important topic in ocean engineering. The problem of dynamic interaction of ocean waves and a floating structure is intrinsically nonlinear. Even though potential flow is assumed, direct solution to the three-dimensional problem has not been achieved yet. For small amplitude waves, the perturbation method is often used to separate it into first- (linear) and second-order problems. The first-order problem can be solved by using a singularity method. The second-order problem is quite more complicated. The second-order problem is important as it yields the second-order loads whose frequencies, disjointed from those of the first-order, may be close to the resonant frequencies of the fluid-structure system. These exciting loads are not very large in magnitude but significant amplification may be induced due to the small system damping.

The large low-frequency motions of floating bodies excited by second-order low frequency loads are dealt with in this paper. In recent years, numerous contributions (Newman^[2] 1974; Pinkster and Huijsmans^[3] 1982; Molin^[4] 1993 etc.) have been published. Although horizontal low-frequency motions for a moored floating structure are often evaluated and in reasonable agreement with experiments, vertical resonant motions have been little studied and poorly predicted (Pinkster et Dijk^[5] 1985). A time simulation model based on separation of mean large slow motions of bodies and their first-order motions by two time scales is presented. Triantafyllou's^[6] (1982) theory on the horizontal surge, sway and yaw motions is extended, in this model, to full six degrees low frequency motions. Specifically the variation of the second-order loads with body mean position is

studied and some interesting remarks are deduced.

Exact second-order loads are obtained by applying Molin's^[1] (1979) method and using two identities to transform Haskind integrals (Chen^[10] 1989) for second-order potential contributions, besides first-order quantities contributions which are evaluated straightforwardly after solving the first-order problem. The system damping being an important factor is composed of radiation part and viscous part. At low frequencies as the radiation damping is negligible, the viscous part, presented by linear and quadratic model is used in time simulation.

The validation of numerical model is made by comparison with experiment results. Two floating bodies having low vertical resonant frequency idealizing characteristic offshore structures which have large submerged volumes with comparatively small waterplane areas, are used in experiments undertaken at the Ship Research Institute of Japan by Molin^[11] (1982). Comparisons of numerical calculations with experimental results show that this theory predicts correctly the large low frequency vertical motions.

2. Low Frequency Motions Theory

A floating body is assumed to be submitted to bichromatic waves of amplitudes a_1, a_2 and frequencies ω_1, ω_2 . It responds oscillatorily with small amplitudes at the frequencies ω_1 and ω_2 around its mean position which moves with large amplitude at the low frequency $(\omega_1 - \omega_2)$. As illustrated by figure 1, three reference systems are defined: (1) A three-dimensional Cartesian coordinate system $o_o x_o y_o z_o$ fixed in space with the z_o -axis vertically upwards. (2) System $oxyz$ following the large low frequency motion which has its origin at the body gravity center G . and (3) Another coordinate system $OXYZ$ tied to the body which coincides with $oxyz$ in the absence of small high frequency motions. The three systems coincide at the initial time.

Assuming a vector $\vec{F}_o(t)$ with six components of surge, sway, heave, roll, pitch and yaw which designate the six degrees of freedom of the body:

$$\vec{F}_o(t) = [x_o(t), y_o(t), z_o(t), \phi_o(t), \theta_o(t), \psi_o(t)]^T \quad (1)$$

Two small parameters ε and ϵ are introduced to express this vector into two parts:

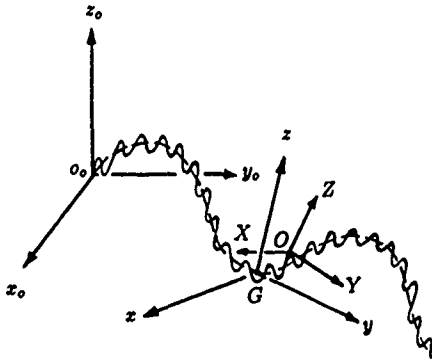
$$\vec{F}_o(t) = \vec{F}_G(t) + \epsilon \cdot \vec{F}(t, t/\epsilon) \quad (2)$$

Where ε , a perturbation parameter, is proportional to the ratio of wave amplitude to wave length while ϵ represents the ratio between the two time scales of motions: a high frequency mo-

¹Reference number at end of paper

tion with small amplitude around its mean position and a low frequency motion of the body mean position of large amplitude because of low resonant frequencies of the system. (More strictly

Figure 1 — Reference Systems



we should take six ratios of time scales since the six low resonant frequencies are not the same).

It was shown by Triantafyllou^[6], in the inviscid, irrotational and incompressible fluid, that the two potential problems relating these two-scales motions can be separated and that the first-order problem is the same as if no low frequency motions exist and high frequency first-order forces and motions are only parametrically dependent on the low frequency motions. We shall emphasize this 'parametrical' dependence by representing the low frequency forces as a function of the body mean position.

The high frequency motions excited by first-order forces can easily be derived by classical means of using motion transfer function and those from second-order high frequency excitation are of order ϵ^2 and negligible. As these high frequency motions are supposed to be small as compared to the low frequency motions, our efforts are concentrated on the evaluation of the large mean position motions:

$$\vec{r}_G(t) = [x_G(t), y_G(t), z_G(t), \phi_G(t), \theta_G(t), \psi_G(t)]^T \quad (3)$$

We shall first establish the low frequency motion equation, in the following, assuming the dependence on the mean position of the second-order low frequency forces and proceed the time simulation and frequential analyses. The complete second-order forces are evaluated in the last paragraph of this section.

2.1 Low Frequency Motion Equation

The complex notations are afterward admitted in following analytical expressions. For example, a real harmonic function $H(t)$ of frequency ω having an amplitude h and a phase β is represented by:

$$\begin{aligned} H(t) &= h \cdot \cos(\omega t + \beta) \\ &= h \cos \beta \cdot \cos(\omega t) - h \sin \beta \cdot \sin(\omega t) \\ &= \Re \{ h \cdot e^{-i\omega t} \} \end{aligned} \quad (4)$$

and so:

$$h = h \cos \beta - i \cdot h \sin \beta = h \cdot e^{-i\beta} \quad (5)$$

where $i = \sqrt{-1}$ and $\Re\{F\}$ designates the real part of the complex function F .

Assuming the mass-inertia matrix of system and added mass-inertia matrix $M + m$, damping matrix B , restoring matrix K and exciting low frequency forces $\vec{F}(\vec{r}_G, t)$, the motion equation can be written:

$$(M + m) \frac{d^2}{dt^2} \vec{r}_G(t) + B \frac{d}{dt} \vec{r}_G(t) + K \vec{r}_G(t) = \vec{F}(\vec{r}_G, t) \quad (6)$$

In this equation, the exciting low frequency forces can be caused by wind, current and waves. For the sake of simplicity, $\vec{F}(\vec{r}_G, t)$ only includes the wave effects. Using Taylor's series, these low frequency forces can be expressed by:

$$\vec{F}(\vec{r}_G, t) = \vec{F}(\vec{r}_{0G}, t) + [(\vec{r}_G - \vec{r}_{0G}) \cdot \nabla] \vec{F}(\vec{r}_{0G}, t) + \dots \quad (7)$$

By denoting:

$$\vec{F}_0(t) = \vec{F}(\vec{r}_{0G}, t) \quad (8)$$

and

$$F_1(t) = \nabla \vec{F}(\vec{r}_{0G}, t) \quad (9)$$

noting that $F_1(t)$ is a 6×6 matrix, the equation (7) can be then written as:

$$\vec{F}(\vec{r}_G, t) = \vec{F}_0(t) + F_1(t) \cdot (\vec{r}_G - \vec{r}_{0G}) + \dots \quad (10)$$

Substituting the equation (10) in which the first two terms are used and the vector \vec{r}_{0G} , representing the origin position of the body, is taken as zero vector into the equation (6), the latter can be rewritten as:

$$(M + m) \frac{d^2}{dt^2} \vec{r}_G(t) + B \frac{d}{dt} \vec{r}_G(t) + [K - F_1(t)] \vec{r}_G(t) = \vec{F}_0(t) \quad (11)$$

This equation resembles Mathieu's equation if $F_1(t)$ is periodic. The solutions to this equation will be discussed in detail for the cases of regular, bichromatic and irregular waves.

Motion In Regular Waves

A regular wave with an amplitude a and a phase β of frequency ω , in the direction of angle θ with the axis x is represented by the following form:

$$\begin{aligned} \eta(t) &= a \cos(kx \cos \theta + ky \sin \theta - \omega t - \beta) \\ &= \Re \{ a \cdot e^{-i\omega t} \} \end{aligned} \quad (12)$$

with:

$$a = a \cdot e^{ik(x \cos \theta + y \sin \theta) - i\beta} \quad (13)$$

The low frequency forces contain only the steady forces which are function of wave frequency and mean position:

$$\vec{F}(\vec{r}_G, t) = \vec{F}_{d0} + F_{d1} \cdot \vec{r}_G \quad (14)$$

in which \vec{F}_{d0} is the steady forces at the origin position and F_{d1} their first derivatives with regard to mean position displacement. They are expressed in complex form:

$$\vec{F}_{d0} = \Re \left\{ \frac{1}{2} a a^* \vec{F}_{20}(\omega, -\omega) \right\} \quad (15)$$

and:

$$F_{d1} = \Re \left\{ \frac{1}{2} a a^* F_{21}(\omega, -\omega) \right\} \quad (16)$$

where a^* is complex conjugate of a , the complex amplitude of wave at the original point (x_G, y_G) and $\vec{F}_{20}(\omega_j, -\omega_l)$ is the transfer function of the second-order low frequency forces in bichromatic wave of frequencies ω_j and ω_l (here we impose $\omega_j = \omega_l = \omega$). $F_{21}(\omega_j, -\omega_l)$ is the gradient matrix of $\vec{F}_{20}(\omega_j, -\omega_l)$. Introducing these equations (14, 15, 16) into (11), we obtained a new formula to calculate the mean displacement of the body:

$$\bar{r}_{G0} = \left[K - \Re \left\{ \frac{1}{2} a a^* F_{21}(\omega, -\omega) \right\} \right]^{-1} \Re \left\{ \frac{1}{2} a a^* \bar{F}_{20}(\omega, -\omega) \right\} \quad (17)$$

instead of the classical formula:

$$\bar{r}_{G0c} = K^{-1} \cdot \Re \left\{ \frac{1}{2} a a^* \bar{F}_{20}(\omega, -\omega) \right\} \quad (18)$$

The formula (17) indicates that mean displacement of a floating body in regular wave is not strictly proportional to the square of the wave amplitude and that it depends also on the derivative of the steady forces. For example in the case of heave motion, the vertical steady force and its derivative being usually of the same sign, the mean displacement predicted by (17) may be much larger than (18) which is classically used. Another interesting remark can be obtained by considering the free motion of the system represented by the equation (11). The natural resonant frequency of heave motion, assumed to be decoupled from the other degrees of freedom, is given by:

$$\omega_{Rz} = \sqrt{\frac{K_{33} - \Re \left\{ \frac{1}{2} a a^* F_{21z}(\omega, -\omega) \right\}}{(M + m_{33})}} \quad (19)$$

This shows that the natural frequency in still water is different from that in a regular wave. The natural frequency may be smaller when wave amplitude increases and it depends in addition on wave frequency. In fact, the derivatives of steady forces play a role like a supplement (or decrease) of the restoring forces in the system.

Motion In Bichromatic Waves

Free surface elevation of bichromatic wave is represented, at first-order form, as:

$$\eta(t) = \eta_1(\theta, \omega_1, \beta_1, t) + \eta_2(\theta, \omega_2, \beta_2, t) \\ = \Re \{ a_1 \cdot e^{-i\omega_1 t} \} + \Re \{ a_2 \cdot e^{-i\omega_2 t} \} \quad (20)$$

here a_1 and a_2 are complex amplitudes of waves including the directional angle θ and their phases β_1 and β_2 , and corresponding frequencies ω_1 and ω_2 .

In this bichromatic wave system, the low frequency forces are composed of a steady part and an oscillatory part which has a difference frequency $(\omega_1 - \omega_2)$:

$$\bar{F}(\bar{r}_G, t) = \bar{F}_d(\bar{r}_G) + \bar{F}_2(\bar{r}_G, t) \quad (21)$$

and they are written by:

$$\bar{F}_d(\bar{r}_G) = \bar{F}_{d0} + F_{d1} \cdot \bar{r}_G \quad (22)$$

$$\bar{F}_2(\bar{r}_G, t) = \bar{F}_{20}(t) + F_{21}(t) \cdot \bar{r}_G \quad (23)$$

Introducing above identities into the equation (11), we have the motion equation as:

$$(M + m) \frac{d^2}{dt^2} \bar{r}_G(t) + B \frac{d}{dt} \bar{r}_G(t) + [K - F_{d1} - F_{21}(t)] \bar{r}_G(t) \\ = \bar{F}_{d0} + \bar{F}_{20}(t) \quad (24)$$

in which the low frequency forces can be rewritten in complex form including their transfer functions:

$$\bar{F}_{d0} = \Re \left\{ \frac{1}{2} a_1 a_1^* \bar{F}_{20}(\omega_1, -\omega_1) + \frac{1}{2} a_2 a_2^* \bar{F}_{20}(\omega_2, -\omega_2) \right\} \quad (25)$$

$$F_{d1} = \Re \left\{ \frac{1}{2} a_1 a_1^* F_{21}(\omega_1, -\omega_1) + \frac{1}{2} a_2 a_2^* F_{21}(\omega_2, -\omega_2) \right\} \quad (26)$$

$$\bar{F}_{20}(t) = \Re \left\{ a_1 a_2^* \bar{F}_{20}(\omega_1, -\omega_2) \cdot e^{-i(\omega_1 - \omega_2)t} \right\} \quad (27)$$

$$F_{21}(t) = \Re \left\{ a_1 a_2^* F_{21}(\omega_1, -\omega_2) \cdot e^{-i(\omega_1 - \omega_2)t} \right\} \quad (28)$$

The evaluation of the transfer function of second-order low frequency forces will be considered in the next paragraph (2.2). It is assumed to be known now.

The exact solution to the equation (24) can be obtained by time simulation method. We integrate this equation, supposing a starting point of $\bar{r}_G(0) = \frac{1}{2} \bar{F}_G(0) = 0$, by a standard fourth-order Runge-Kutta method. The motion simulated becomes stable after some transient periods.

The frequency domain analysis, in bichromatic wave case, is possible if the following assumption is admitted:

$$\bar{r}_G(t) = \bar{r}_{G0} + \Re \left\{ \bar{r}_{G1} e^{-i(\omega_1 - \omega_2)t} \right\} + \Re \left\{ \bar{r}_{G2} e^{-i2(\omega_1 - \omega_2)t} \right\} \quad (29)$$

Introducing above equation into the equation (24), each mode of motion can be approximatively obtained by below identities:

$$\bar{r}_{G0} = [K - F_{d1}]^{-1} \cdot F_{d0} \quad (30)$$

$$\bar{r}_{G1} = [-(M + m)(\omega_1 - \omega_2)^2 - iB(\omega_1 - \omega_2) + K - F_{d1}]^{-1} \\ \cdot a_1 a_2^* [\bar{F}_{20}(\omega_1, -\omega_2) + F_{21}(\omega_1, -\omega_2) \bar{r}_{G0}] \quad (31)$$

$$\bar{r}_{G2} = [-4(M + m)(\omega_1 - \omega_2)^2 - i2B(\omega_1 - \omega_2) + K - F_{d1}]^{-1} \\ \cdot \frac{1}{2} a_1 a_2^* [F_{21}(\omega_1, -\omega_2) \bar{r}_{G1}] \quad (32)$$

The formula (30) for mean displacement is the same as (17). The oscillatory amplitude of frequency $(\omega_1 - \omega_2)$ is determined by (31). It depends not only on the low frequency forces but also on the mean displacement (\bar{r}_{G0}) and derivatives of steady forces (F_{d1}). Since the second-order forces are proportional to the square of the wave amplitudes, the amplitude of the low frequency is thought to be the same too. It may not be true because the 'supplement' stiffness (F_{d1}) increases with the square of wave amplitudes. For instance, in case of heave motion, F_{d1z} being positive, the motion amplitude does not increase parabolically as wave amplitude increases. The motion amplitude should be less than proportional to wave amplitude square when the difference frequency is larger than that of resonance and more when the difference frequency is smaller. We keep the double difference frequency $2(\omega_1 - \omega_2)$ term because this frequency may be closer to the resonant frequency of the system when the different frequency $(\omega_1 - \omega_2)$ is much lower.

Motion In Irregular Waves

The unidirectional irregular wave is often represented by a finite series of elementary Airy components whose amplitudes are deduced from the wave power spectrum $S_{\eta\eta}(\omega)$:

$$\eta(t) = \sum_{j=1}^N a_j \cos(k_j x \cos \theta + k_j y \sin \theta - \omega_j t - \beta_j) \quad (33)$$

and:

$$a_j = \sqrt{2 S_{\eta\eta}(\omega_j) \delta \omega_j} \quad (34)$$

where θ is the wave direction angle. Phase angles β_j ($j = 1, 2, \dots, N$) are determined at random between $(0, 2\pi)$ and $\delta \omega_j$ is the j th discretization step of power spectrum frequency width. If we use the complex presentation, the wave system is rewritten by:

$$\eta(t) = \Re \left\{ \sum_{j=1}^N a_j \cdot e^{-i\omega_j t} \right\} \quad (35)$$

with:

$$a_j = \sqrt{2S_{\eta\eta}(\omega_j)} \delta\omega_j \cdot e^{ik_j(x \cos \theta + y \sin \theta) - i\beta_j} \quad (36)$$

If all discretization steps $\delta\omega_j$ ($j = 1, \dots, N$) are equal ($= \delta\omega$) and the largest low frequency considered ω_m is:

$$\omega_m \leq n \cdot \delta\omega \quad n \leq N \quad (37)$$

we can then express the second-order steady part and the oscillatory part of the low frequency forces by following simple and double summation forms:

$$\bar{F}_{d0} = \Re \left\{ \sum_{j=1}^N \frac{1}{2} a_j a_j^* \bar{F}_{20}(\omega_j, -\omega_j) \right\} \quad (38)$$

$$\bar{F}_{d1} = \Re \left\{ \sum_{j=1}^N \frac{1}{2} a_j a_j^* F_{21}(\omega_j, -\omega_j) \right\} \quad (39)$$

$$\bar{F}_{20}(t) = \Re \left\{ \sum_{\ell=1}^n \sum_{j=\ell+1}^N a_j a_{j-\ell}^* \bar{F}_{20}(\omega_j, -\omega_{j-\ell}) \cdot e^{-i(\omega_j - \omega_{j-\ell})t} \right\} \quad (40)$$

$$F_{21}(t) = \Re \left\{ \sum_{\ell=1}^n \sum_{j=\ell+1}^N a_j a_{j-\ell}^* F_{21}(\omega_j, -\omega_{j-\ell}) \cdot e^{-i(\omega_j - \omega_{j-\ell})t} \right\} \quad (41)$$

As we see the above expressions of oscillatory part of low frequency forces, two remarks have to be pointed out: one is that the number N of element wave frequencies should be large enough to represent correctly irregular waves and to evaluate the low frequency forces at the difference frequencies ($\omega_j - \omega_{j-\ell}$) for $\ell = 1, \dots, n$ and $j = 1, \dots, N$ (N is typically between 100 and 200). Another is that the double summations of low frequency forces at each time step need more computing time as the number N is large. Prior to doing the simulation by same equation (24) as in bichromatic wave case, two special files have to be built up. First file containing the second-order force transfer function at origin mean position can be obtained by running repeatedly a first-order diffraction-radiation code for a number (m) of frequencies (m may be equal to $N/10$ or $N/5$) which cover the whole frequency range and successively a second-order code for repeating $m(m+1)/2$ times. The first- and second-order solutions for other frequencies can then be obtained by an interpolation method. Second file containing the derivatives of second-order force transfer function can be achieved by establishing two files at two or three different mean positions and using the finite difference method.

2.2 Low Frequency Forces

The low frequency forces, obtained by integrating the second-order hydrodynamic pressure on the body wetted surface, consist of one part which depends only on first-order quantities (potential, velocity and motions etc.) and another part which depends on the second-order velocity potential. They can then be written as:

$$\bar{F}_{20}(\omega_j, -\omega_\ell) = \bar{F}_{21}(\omega_j, -\omega_\ell) + \bar{F}_{22}(\omega_j, -\omega_\ell) \quad (42)$$

The first part forces $\bar{F}_{21}(\omega_j, -\omega_\ell)$ are formulated by integrating the hydrodynamic pressure which corresponds to quadratic terms in Bernoulli's equation and corrective terms due to the in-

tegration over the average surface instead of instantaneous surface (supposing a given mean position). These forces consisting of four terms are presented by:

$$\begin{aligned} \bar{F}_{21}(\omega_j, -\omega_\ell) = & -\frac{\rho g}{2} \oint_{\Gamma_0} (\eta_j - \xi_j) \cdot (\eta_\ell^* - \xi_\ell^*) N d\Gamma \\ & + \frac{\rho}{2} \iint_{S_{co}} \nabla \phi_j^{(1)} \cdot \nabla \phi_\ell^{(1)*} N dS \\ & + \frac{i\rho}{2} \iint_{S_{co}} (M \bar{O} M_j \omega_\ell \nabla \phi_\ell^{(1)} - M \bar{O} M_\ell^* \omega_j \nabla \phi_j^{(1)*}) N dS \\ & + \frac{1}{2} (\mathbf{R}_j \cdot \bar{\mathbf{F}}_{In\ell} + \mathbf{R}_\ell^* \cdot \bar{\mathbf{F}}_{Inj}) \end{aligned} \quad (43)$$

where ρ is water density and g is the acceleration due to gravity. The indices j and ℓ represent the first-order quantities corresponding the wave frequencies ω_j and ω_ℓ and the sign $*$ designates the conjugate complex. N is the general normal vector of body surface towards the fluid. The first contribution is an integral of relative water elevation (difference of water elevation η and vertical displacement ξ) on the average waterline Γ_0 . The second contribution is the integral of pressure due to the fluid quadratic velocity ($\phi^{(1)}$ being first-order velocity potential). The third one comes from the corrective term of the first-order pressure on the average surface instead of instantaneous surface ($M \bar{O} M$ being translation of one point M on body surface) and the fourth one is a correction of first-order inertia forces $\bar{\mathbf{F}}_{In}$ due to the first-order rotations \mathbf{R} .

All these contributions can be evaluated directly once the first-order problem is solved. In fact, the first-order velocity potential obtained by a singularity method is used to have the first-order excitation forces and motions by mechanical equations. A source distribution which is kinematically equivalent to the body responding in waves can be obtained by considering first-order motions and used to evaluate first-order quantities (potential and its spatial derivatives on body's surface and the water elevation on the waterline) that are needed for the first part of the second-order forces.

The second-order velocity potential $\phi^{(2)}(x, y, z, t)$ is assumed to have incident, diffraction and radiation parts in the same manner as the first-order potential:

$$\phi^{(2)}(x, y, z, t) = \Re \left\{ a_j a_\ell^* (\phi_I^{(2)} + \phi_D^{(2)} + \phi_R^{(2)}) \cdot e^{-i(\omega_j - \omega_\ell)t} \right\} \quad (44)$$

in which the incident potential $\phi_I^{(2)}$ is known:

$$\begin{aligned} \phi_I^{(2)} = & \frac{ig^2}{g[k_j - k_\ell] \tanh(k_j - k_\ell H) - (\omega_j - \omega_\ell)^2} \\ & \cdot \frac{\cosh[k_j - k_\ell](z + H)}{\cosh(k_j - k_\ell H)} A^- e^{i(k_j - k_\ell)(x \cos \theta + y \sin \theta)} \end{aligned} \quad (45)$$

where:

$$\begin{aligned} A^- = & \frac{\omega_j - \omega_\ell}{\omega_j \omega_\ell} k_j k_\ell [1 + \tanh(k_j H) \tanh(k_\ell H)] \\ & + \frac{1}{2} \left[\frac{k_j^2}{\omega_j \cosh^2(k_j H)} - \frac{k_\ell^2}{\omega_\ell \cosh^2(k_\ell H)} \right] \end{aligned} \quad (46)$$

in which H is the waterdepth.

The second-order radiation potential is supposed to satisfy the same equations as the first-order radiation potential. The only difference corresponds to low frequency ($\omega_j - \omega_\ell$) instead of the frequencies ω_j or ω_ℓ . The solution by using the same singularity method gives us the potential damping and added mass for one low frequency.

All nonhomogeneous properties of the second-order prob-

lem are tied with the second-order diffraction potential which satisfies not only Laplace's equation, the sea bed condition equation and a proper radiation condition but also the nonhomogeneous free surface condition and the nonhomogeneous body surface condition. These two latter conditions are written as:

$$-(\omega_j - \omega_l)^2 \phi_D^{(2)} + g \frac{\partial}{\partial z} \phi_D^{(2)} = a_{LD}^{(2)} \quad (47)$$

on the free surface and:

$$\frac{\partial}{\partial n} \phi_D^{(2)} = -\frac{\partial}{\partial n} \phi_I^{(2)} + a_C^{(2)} \quad (48)$$

on the body surface.

The nonhomogeneous terms $a_{LD}^{(2)}$ and $a_C^{(2)}$ being functions of the first-order potentials are expressed by:

$$\begin{aligned} a_{LD}^{(2)} = & i(\omega_j - \omega_l)(\nabla \phi_j^{(1)} \cdot \nabla \phi_{Pl}^{(1)*} + \nabla \phi_{Pl}^{(1)*} \cdot \nabla \phi_j^{(1)}) \\ & - \frac{i\omega_j}{2g} \left[\phi_j^{(1)} \left(-\omega_l^2 \frac{\partial}{\partial z} \phi_{Pl}^{(1)*} + g \frac{\partial^2}{\partial z^2} \phi_{Pl}^{(1)*} \right) \right. \\ & \quad \left. + (-\omega_l^2 \frac{\partial}{\partial z} \phi_{Pl}^{(1)*} + g \frac{\partial^2}{\partial z^2} \phi_{Pl}^{(1)*}) \phi_j^{(1)} \right] \\ & + \frac{i\omega_l}{2g} \left[\phi_l^{(1)*} \left(-\omega_j^2 \frac{\partial}{\partial z} \phi_{Pj}^{(1)} + g \frac{\partial^2}{\partial z^2} \phi_{Pj}^{(1)} \right) \right. \\ & \quad \left. + (-\omega_j^2 \frac{\partial}{\partial z} \phi_{Pj}^{(1)} + g \frac{\partial^2}{\partial z^2} \phi_{Pj}^{(1)}) \phi_l^{(1)*} \right] \quad (49) \end{aligned}$$

and:

$$\begin{aligned} a_C^{(2)} = & (\vec{V}_{Ej} - \nabla \phi_j^{(1)}) \mathbf{R}_j^* \cdot \vec{n}_0 + (\vec{V}_{El} - \nabla \phi_l^{(1)*}) \mathbf{R}_j \cdot \vec{n}_0 \\ & - (M \vec{\omega}_j \cdot \nabla) \nabla \phi_l^{(1)*} \cdot \vec{n}_0 - (M \vec{\omega}_l \cdot \nabla) \nabla \phi_j^{(1)} \cdot \vec{n}_0 \quad (50) \end{aligned}$$

in which $\phi_j^{(1)}$ is the first-order incident potential and $\phi_P^{(1)}$ is the sum of the first-order diffraction and radiation potentials. \vec{V}_E is the velocity of the point Mo on the body surface.

It is important to note in the above expressions the double spatial derivatives of the first-order velocity potential. For a three dimensional body of arbitrary form, because of the singularity of Green function as shown by [09], the double spatial derivatives near the body surface are not possible to be evaluated accurately by using a numerical method. The nonhomogeneous terms can not be then obtained directly. But we are going to try to calculate the integrals containing these terms.

The second part of the low frequency forces are written by:

$$\vec{F}_{22}(\omega_j, -\omega_l) = i(\omega_j - \omega_l) \rho \int \int_{S_{co}} (\phi_j^{(2)} + \phi_D^{(2)}) \mathbf{N} dS \quad (51)$$

The contribution of the incident potential is easily obtained as the second-order incident potential is known (see equation 45). In order to evaluate the contribution of the diffraction potential, additional potentials ψ_l ($l = 1, \dots, 6$) are introduced. These additional potentials satisfy Laplace's equation, the sea bed and the radiation conditions and the two following boundary conditions:

$$\begin{aligned} -(\omega_j - \omega_l)^2 \psi_l + g \frac{\partial}{\partial z} \psi_l &= 0 \quad z=0 \quad (52) \\ \frac{\partial}{\partial n} \psi_l &= N_l \quad \text{on } S_{co} \quad (53) \\ l &= 1, 2, \dots, 6 \end{aligned}$$

these equations being the same as in the first-order radiation problem, these additional potentials are obtained in the same way.

Green's second identity is applied to transform the volume

integral in fluid domain including the Laplace operator on $\phi_D^{(2)}$ and ψ_l into boundary surface integrals. By analysing asymptotic expressions of the velocity potentials and using the stationary phase theorem for the surface integral at infinity, Molin^[6] (1979) has shown that the following identity is true:

$$\begin{aligned} \int \int_{S_{co}} \phi_D^{(2)} N_l dS &= \int \int_{S_{co}} \left[-\frac{\partial}{\partial n} \phi_l^{(2)} + a_C^{(2)} \right] \psi_l dS \\ &\quad - \frac{1}{g} \int \int_{z=0} a_{LD}^{(2)} \cdot \psi_l dS \quad (54) \end{aligned}$$

where:

$$l = 1, 2, \dots, 6$$

Introducing this identity in the expression (51), we have the complete formula for the l th component of the low frequency forces:

$$F_{22l}(\omega_j, -\omega_l) = F_{21l}(\omega_j, -\omega_l) + F_{2cl}(\omega_j, -\omega_l) + F_{2il}(\omega_j, -\omega_l) \quad (55)$$

in which we name the incident integral:

$$F_{21l}(\omega_j, -\omega_l) = -i(\omega_j - \omega_l) \rho \int \int_{S_{co}} \phi_l^{(2)} N_l dS \quad (56)$$

the Haskind integral on the body surface:

$$F_{2cl}(\omega_j, -\omega_l) = i(\omega_j - \omega_l) \rho \int \int_{S_{co}} \left[\frac{\partial}{\partial n} \phi_l^{(2)} - a_C^{(2)} \right] \psi_l dS \quad (57)$$

and the Haskind integral on the free surface:

$$F_{2il}(\omega_j, -\omega_l) = i(\omega_j - \omega_l) \frac{\rho}{g} \int \int_{z=0} a_{LD}^{(2)} \psi_l dS \quad (58)$$

With these three integrals including only terms function of the first-order velocity potential, the complete low frequency forces may be evaluated without explicitly knowing the second-order velocity potential which is more difficult to have, on condition that the difficulty of the double derivatives of the first-order velocity potential can be overcome.

An identity deduced from Stokes' theorem can be derived by making the vectorial analysis:

$$\begin{aligned} \int \int_S (\vec{G} \cdot \nabla) \nabla \phi \cdot \vec{n}_0 dS &= \oint_{\Gamma} (\nabla \phi \wedge \vec{G}) d\vec{\Gamma} \\ &\quad + \int \int_S [(\nabla \phi \cdot \nabla) \vec{G} + \nabla \phi \cdot \text{div}(\vec{G})] \cdot \vec{n}_0 dS \quad (59) \end{aligned}$$

By using this identity into (57) and supposing $\vec{G} = \psi_l \cdot M \vec{\omega}_l$, the Haskind integral on the body surface is transformed into integrals which don't contain any more the double spatial derivatives and can so be evaluated accurately.

In order to evaluate the Haskind integral on the free surface, we divide the unlimited free surface into two regions: an inner region S_{inn} which is limited by the waterline and a boundary circle line some distance far away from the body and an outer region S_{out} which is the surface extending from the boundary circle line to infinity.

In the inner region, since the Haskind integral contains the double spatial derivative of the first-order potential, another identity derived from Riemann's theorem is developed as:

$$\begin{aligned} \int \int_S G \cdot \frac{\partial^2}{\partial x^2} \phi dS &= - \oint_{\Gamma} G \cdot \left[\frac{\partial}{\partial y} \phi \cdot \mathbf{n}_y + \frac{\partial}{\partial x} \phi \cdot \mathbf{n}_x \right] d\Gamma \\ &\quad + \int \int_S \left[\frac{\partial}{\partial x} G \cdot \frac{\partial}{\partial x} \phi + \frac{\partial}{\partial y} G \cdot \frac{\partial}{\partial y} \phi \right] dS \quad (60) \end{aligned}$$

Using this identity, the Haskind integral on the inner region can be transformed into integrals in which double derivative does not appear any more and may be so calculated numerically by using

classical quadratic method.

In the outer region, the asymptotical form of the non-homogeneous term $a_{LD}^{(2)}$, in the cylindrical reference (r, θ, z) , is derived by using the development of Kochin's function in the presentation of the first-order velocity potential. This asymptotic expression of $a_{LD}^{(2)}$ as form of a product of Fourier series in θ and oscillatory radial functions in r and the similar expression for ψ_1 are introduced into the Haskind integral. This integral is then separated into a product of two line integrals: first integral in θ which is not difficult to be calculated by applying the orthogonality properties of Fourier series product and another integral in the radial distance r which is easily obtained by analytical results of Fresnel integral.

The value of the Haskind integral on the free surface is the sum of integral results on the inner region and on the outer region. This value varies oscillatorily with the radial distance of the boundary circle line which separates the inner and outer regions. As shown in [10], the oscillatory value converges much more rapidly than that without the outer region integral and the final result is very close to the average value of oscillation. In a test case of a vertical cylinder (height/radius=5.) for which we have analytical results, the inner region is discretized by 36 points in circumference direction and 10 points in radial direction per composite wave length λ_c which is defined by:

$$\lambda_c = \frac{2\pi}{k_j - k_l + k_{jl}} \quad (61)$$

where k_{jl} satisfies:

$$(\omega_j - \omega_l)^2 = g k_{jl} \cdot \tanh(k_{jl} H) \quad (62)$$

A good agreement between numerical and analytical results is obtained when the radial distance is more than three λ_c . The average value of integral results for the radial distances between $4\lambda_c$ and $5\lambda_c$ is taken as the final result of the Haskind integral. The error between the numerical result and the analytical result is less than five per cent.

The computing time for the low frequency forces is dominated by the evaluation of the Haskind integral on the free surface, since other contributions are just in form of simple additions of the first-order quantities which are obtained once the first-order problem is solved completely. In the same case of a vertical cylinder whose one quarter surface is divided into 108 panels, the first-order solution costs about 3 minutes on Vax8700 computer while the free surface Haskind integral is obtained after 10 minutes calculus for one frequency. When the system responds to only some frequencies, it is necessary to evaluate completely the low frequency forces for these frequencies. But it is also reasonable, when the frequencies considered are numerous, to take the approximation which consists of neglecting purely and simply the free surface integral. This economical approximation is adequate when the diffraction effects are weak. For instance, the submersible or semi-submersible with small waterplane areas are the cases where the approximation can be used. This is shown by Matsui^[9] who considered the ITTC semi-submersible platform. The work in [9] has the same conclusion.

3. Model Test Presentation

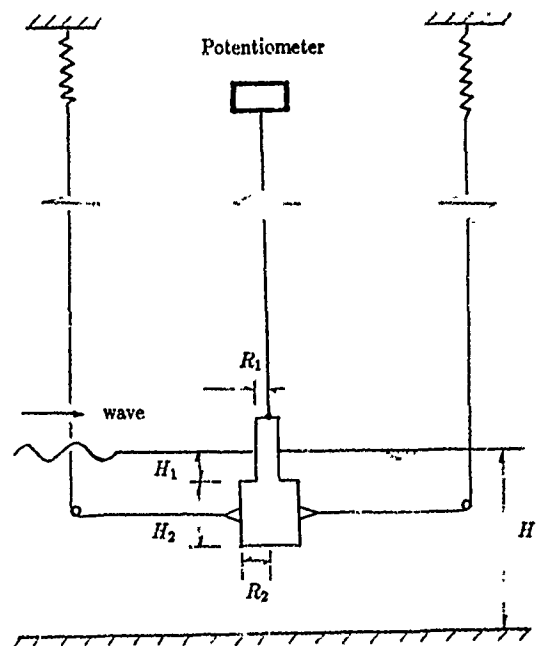
The model tests were carried out at the Ocean Basin of the Ship Research Institute of Japan, while the second author was on sabbatical leave in 1981-1982. Two bottle-shaped models were considered, with different neck diameters. Table 1 presents some characteristics of both models.

Table 1 — Characteristics of the Models

Designation	Model No.1	Model No.2
R1 Neck diameter	11.5 cm	21.6 cm
H1 Neck height	20.0 cm	20.0 cm
R2 Bottle diameter	63.0 cm	63.0 cm
H2 Bottle height	70.0 cm	70.0 cm
M Displacement	220.3 Kg	225.5 Kg
Cg Center of gravity	33.8 cm	34.7 cm
Cb Center of body	35.4 cm	36.4 cm
Kz Vertical Stiffness	113.3 N/m	370.6 N/m

The test set-up is described on figure 2. The mooring system was constituted by two linear springs. The ballasts of the models were adjusted to ensure large natural periods in roll and pitch. In all tests it appeared that the pitch response was negligibly small. The heave motion of the models was measured by a potentiometer. It was checked during the tests that the surge motion was always small enough to ensure an accurate measurement.

Figure 2 — Test set-up



Tests in regular waves were first undertaken for the purpose to evaluate the vertical steady force. The mean vertical displacements were measured for wave periods ranging from 0.6 to 2.0 seconds and double wave amplitudes of 4. and 6. centimeters.

Extinction tests were made in still water and in regular waves, in order to estimate the heave damping, which is an important quantity in the evaluation of low frequency motion. In this series of tests, the model was given a vertical downward displacement (10 to 20 cm) and released. The heave damping was classically estimated from the record of the decaying motion. The tests showed that the damping increases under the effect of wave superimposition. Another feature observed in regular waves, is that the zero down-crossing intervals decreased as the heave motion decayed to zero. This variation of natural periods is taken into account by the equation (19).

A large proportion of the tests undertaken were in bichro-

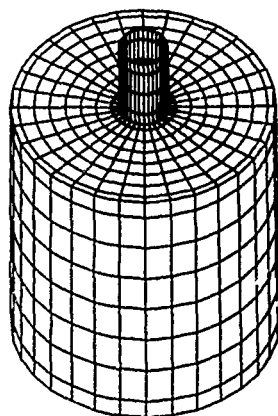
matic waves. In these experiments, two regular waves of equal amplitudes were superimposed. One pulsation was kept constant and different beat frequencies were achieved by varying the other. Another kind of tests was also made at constant beat frequency and varying wave amplitude. Tests in irregular waves plus current were also undertaken.

In next section, the tests results and analysis are presented in the comparison with the numerical predictions.

4. Numerical Predictions and Comparisons

For the purpose of the numerical solution to the diffraction-radiation problems that is needed to evaluate the low frequency forces, the body wetted surface is meshed by quadrilateral panels. The principle of discretization is that the panels close to the free surface and near the corners of body surface are finer than the others. Figure 3 presents the mesh used in the full numerical calculus. The total number of panels is 880.

Figure 3 — Mesh of the body surface

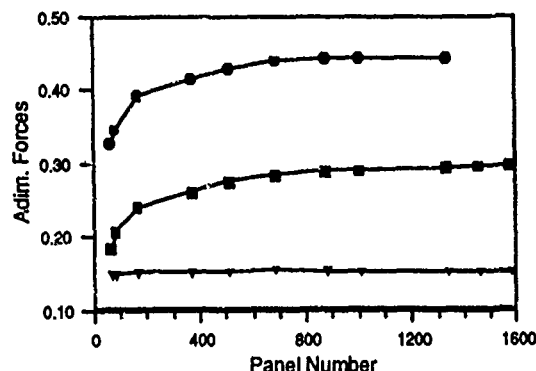


The numerical accuracy depends directly on the representation of the body form, that is, the size of the discretization. A mesh giving an accurate solution to the first-order problem may not be refined enough for the second-order problem. The convergence with discretisation was so investigated first. Model No.1 is chosen to evaluate the first-order vertical force and the second-order steady force in a regular wave of frequency ($\omega = 6.283 \text{ rad./sec.}$) and the low frequency vertical force in bichromatic waves of frequencies ($\omega_1 = 7.222 \text{ rad./sec.}$ and $\omega_2 = 6.283 \text{ rad./sec.}$). Figure 4 presents the numerical results with respect to the panel number in which the first-order vertical force $F_{1z}(\omega)$ with the markers (\bullet) is adimensionalized by $\rho g L a$ (here the reference length $L = 1 \text{ m}$), the second-order steady force $F_{2z}(\omega, -\omega)$ with the markers (\blacksquare) by $(\rho g L a a/2)$ and the low frequency force $F_{2z}(\omega_1, -\omega_2)$ with the markers (\blacklozenge) by $(\rho g L a_1 a_2)$.

From the figure 4 we see that the first-order forces have converged with 100 panels, while the second-order forces need over 800 panels. If the criterion of panel size for the first-order is one sixth of wave length, that of the second-order should be one fifteenth of the average wave length (about 800 panels on the whole surface). In order to achieve a good accuracy for the low frequency forces, we have then chosen the discretisation of 880 panels presented by the figure 3. The computer times on the series of Vax8000 computer, for one frequency, are about

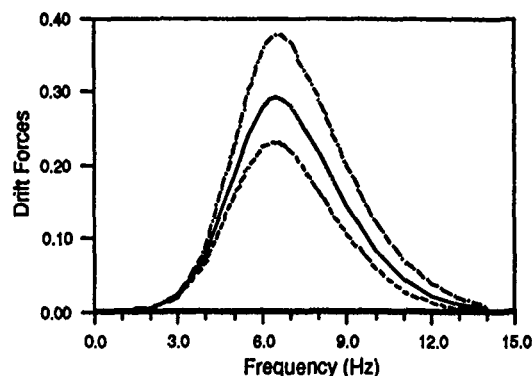
9 minutes for the first-order problem and 30 minutes for the evaluation of the low frequency forces.

Figure 4 — Convergence with discretisation



In the regular waves, the second-order steady forces of model No.1 are evaluated for 16 frequencies from 2 rad./sec. to 14 rad./sec. at three vertical position of the body: the origin position (neck height $H_1=20 \text{ cm}$), the higher position (neck height $H_1=18 \text{ cm}$) and the lower position (neck height $H_1=22 \text{ cm}$). The results are presented by the figure 5 in which the curve (—) describes the steady forces as a function of the wave frequencies at the origin position, the curve (---) at the higher position and the curve (- - -) at the lower position.

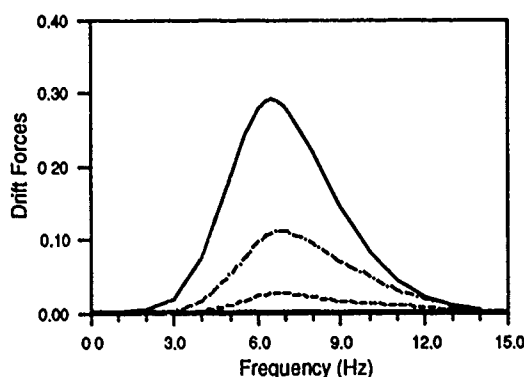
Figure 5 Vertical drift forces at three reference positions



As the first-order vertical body motions are small, the drift forces dominated by the contribution of the quadratic term of the fluid velocity (see the equation 43) are always positive upward because the fluid motion is larger above the model than underneath. For the same reason the drift forces are higher at the higher position and lower at the lower position, as compared to the origin position, and they have a peak for a frequency equal to about 6.5 rad./sec.

Figure 6 presents the derivatives of vertical drift forces with respect to the mean vertical position. These derivatives are obtained by finite differences. The adimensionalized vertical drift forces F_{20z} at the origin mean position are drawn by the curve (—) and their first derivatives F_{21z} by the curve (---) which are adimensionalized by $(\rho g L a a/2 * L/3 \text{ cm})$. The second derivatives adimensionalized by $(\rho g L a a/2 * 2L^2/9 \text{ cm}^2)$ are also presented by the curve (- - -).

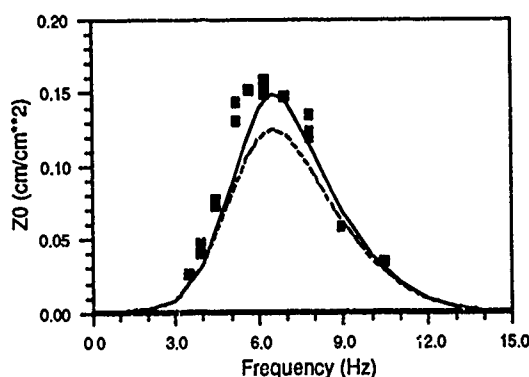
Figure 6 — Derivatives of the vertical drift forces



The derivatives shown by the figure have similar shapes (a peak for a frequency equal to 6.5 rad./sec.) as the drift forces at the origin position. The values of the first derivatives are smaller than those of the drift forces and the second derivatives are much smaller than the first derivatives (with the adimensionalizations given above). So it is legitimate to use only the first term in the Taylor series of the steady forces (see the equation 7).

Using the vertical drift forces and their first derivatives evaluated numerically, the vertical mean displacements of the model in regular waves are obtained by the equation (24). Figure 7 presents this result as the curve (—) and the comparison with the model tests undertaken at the Ship Research Institute of Japan (markers ■ ■ ■) and with the results calculated by the classical method of the equation (18) (the curve - - -).

Figure 7 — Vertical mean displacements

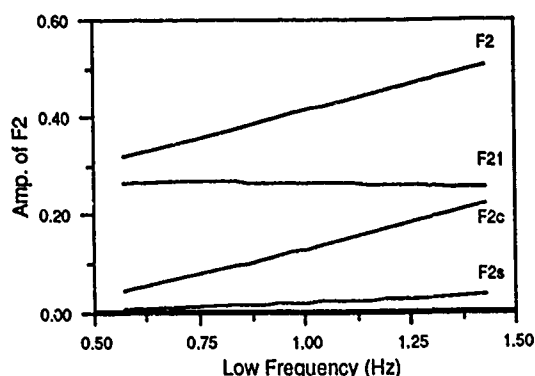


The vertical mean displacements are adimensionalized by the square of the wave amplitude. The comparison from the figure 7 shows a good agreement between the experiments and the numerical predictions. But the classical method underestimates the vertical mean displacement.

In the bichromatic waves tests for model No.2, the second wave frequency $\omega_2 = 5.712$ rad./sec. is kept constant while the first frequency ω_1 varies from 6.283 rad./sec. to 7.140 rad./sec., which covers the whole frequency range used in the model tests. The second-order low frequency forces at the origin mean position are presented on figure 8. The top curve describes the amplitude of total low frequency forces which consist of the first

part (see equation 42) shown in the middle, the second-order incident contribution and the Haskind integral on the body surface shown underneath, and the contribution of the Haskind integral over the free surface (bottom curve).

Figure 8 — Low frequency forces



The second-order low frequency forces are dominated by the first part. But it is not correct to take only this part as an approximation of the low frequency forces because the contribution of second-order potential (set-down effect) is important and increases with the difference frequency. Nevertheless the contribution of the Haskind free surface integral is very small as compared to the other contributions. The approximation which consists in neglecting this small but expensive contribution is justified.

The steady forces are evaluated as the sum of the steady forces in two regular waves of two different frequencies. The first derivatives of the low frequency forces and the steady forces are obtained by the same procedure as those of the steady forces in regular waves, applying the finite difference method to the results at three different mean positions. The obtained low frequency forces and the steady forces and their first derivatives are used in equation (24) for the motion simulation. Figure 9 presents one of the bichromatic wave which was used in the model tests ($\omega_1 = 6.756$ rad./sec. and $\omega_2 = 5.712$ rad./sec.) with a beat amplitude equal to 4 cm ($a_1 = a_2 = 2$ cm). The low frequency motion simulation is shown on figure 10.

In the equation (17), the added mass is taken as the numerical result at the frequency equal to 1.044 rad./sec. and the linear heave damping is derived from the extinction tests. The simulation is started at an initial point such that the displacement and the velocity are zero. The simulated motion is stable after less than ten periods. The low frequency motion amplitude and the mean displacement are measured from the stable simulation.

In the same bichromatic wave, the simulations are worked out for double beat amplitudes from 2 cm to 8 cm. The results are shown by the curve (—) in figure 11. The markers (■ ■ ■) are the experimental points and the curve (- - -) designates the classical calculus without the first derivatives of the second-order low frequency forces.

According to the frequency domain analysis in the above section 2, the amplitude curve of classical method is parabolic because the second-order motions are simply proportional to the square of the wave amplitude. But the motion simulation which takes account of the variation of the second-order forces with respect to the mean position is not the same. When the beat frequency is larger than the natural frequency, the simulation

Figure 9 — Bichromatic wave

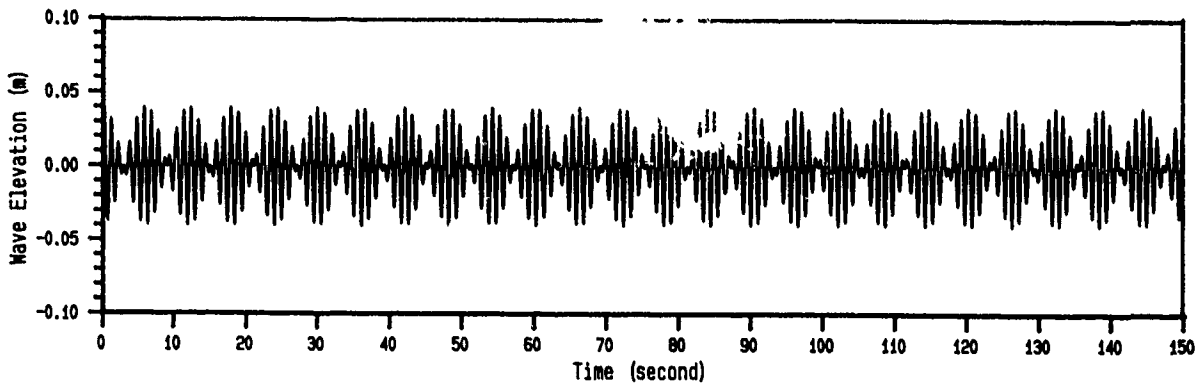
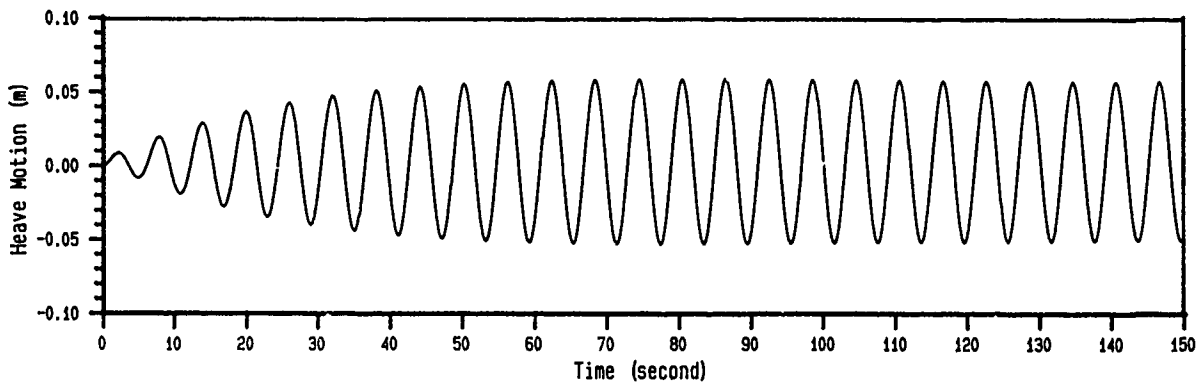
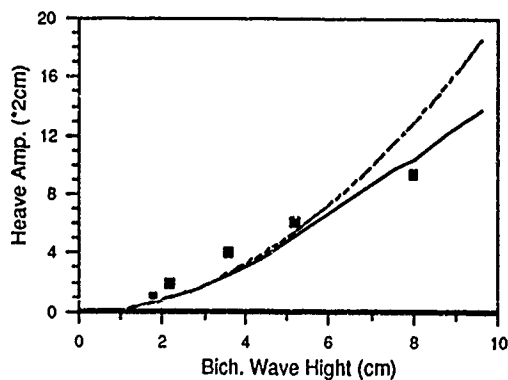


Figure 10 — Low frequency motion



amplitude is less than a square function of the wave amplitude. The difference between the two increases with the wave amplitude. The comparison shows that the simulation amplitude curve is much closer to the experimental results than that from using the classical method.

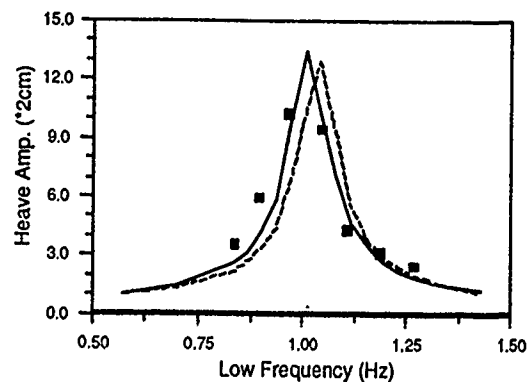
Figure 11 — Heave amplitude as a function of wave amplitude



The whole low frequency motions are obtained for the frequency range of the resonance by the same way. The figure 12 presents the results of the double heave amplitude with respect

to the beat frequency. The markers (■ ■ ■ ■) are the points of the model tests results. The continuous line (—) is derived from the motion simulation while the dotted line is obtained by using the classical method.

Figure 12 — Heave amplitude of model No.2

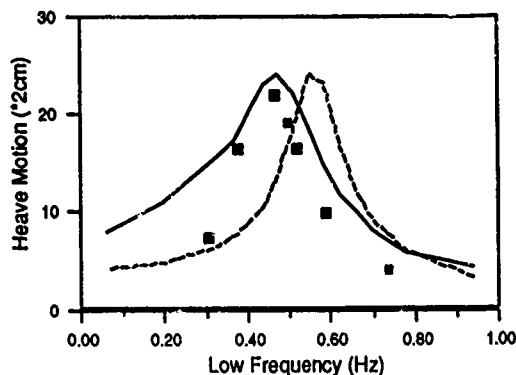


The heave amplitude of the motion simulation is in good agreement with the experimental results. The classical method underestimates the heave motion for frequencies lower than that of resonance while it over-estimates the heave motion at larger

frequencies. Moreover the motion simulation predicts correctly the resonant frequency of the system.

For model No.1 in bichromatic waves, the numerical computations are carried out for frequencies ω_1 varying from 6.347 rad./sec. to 7.221 rad./sec. and fixed $\omega_2 = 6.283$ rad./sec. The double beat amplitude is 5.7 cm ($a_1 = a_2 = 2.85$ cm). Same procedures are used as for the model No.2. The results are presented on figure 13.

Figure 13 — Heave amplitude of model No.1



Again the classical method does not predict well the low frequency heave motions. The motion simulation predicts correctly the resonant frequency of the body in bichromatic waves.

Table 2 — Resonant frequency prediction

Model	Classical	Simulation	Experiment
Model No.1	0.57 rad/sec	0.47 rad/sec	0.45 rad/sec
Model No.2	1.04 rad/sec	1.00 rad/sec	1.00 rad/sec

Although the numerical prediction gives the correct frequency of resonance, the agreement with the experimental results for model No.1 is not excellent. It is necessary to note that the heave damping in the simulation using the equation (24) takes the form as:

$$B = B_0 + B_1 \cdot \left| \frac{d}{dt} z_G(t) \right|$$

in which the linear damping B_0 is derived from the extinction tests and the quadratic damping B_1 is computed by the following formula:

$$B_1 = \frac{1}{2} \rho S C_d$$

where S is the bottom area and the drag coefficient C_d is taken equal to 3. It is possible that the unsatisfactory comparison with the model tests arises from the unclear determination of the heave damping. Further investigation on the viscous damping of the system is necessary.

5. Conclusions

Using the Haskind integral relations, the second-order low frequency forces can be completely evaluated by the aid of two transformation identities, without explicitly solving for the second-order potential. The numerical results show that for floating semi-submersible bodies, the Haskind integral on the free

surface can be negligible.

A simulation model for the prediction of low-frequency motions taking account of the variation of the second-order low frequency forces with regard to the mean position has been presented. Even though satisfactory comparisons with the model tests results are obtained for the heave motions in bichromatic waves, the system damping for low frequency motion is needed for further investigations.

Reference

1. B. Molin 1979 "Second order diffraction loads upon three-dimensional bodies" *Applied Ocean Research*. Vol:1 No:4 pp197-202.
2. J.N. Newman 1974 "Second-order, slowly-varying forces on vessels in irregular waves" *Proceedings of International Symposium on the Dynamics of Marine Vehicles and Structures in Waves*. pp193-197.
3. J.A. Pinkster and R.H.M. Huijsmans 1982 "The low frequency motions of a semi-submersible in waves" *Proceeding of Conference on Behaviour of Offshore Structure*. pp447-466.
4. B. Molin 1983 "Three-year experience in the numerical prediction of the slow-drift motion of moored tankers" *Proceeding of 15th OTC*. pp187-191.
5. J.A. Pinkster and A.W. van Dijk 1982 and 1985 "Low frequency behavior of semi-submersibles" and "Wave drift forces on large semi-submersibles" *Joint Industry Projects NSMB*.
6. M.S. Triantafyllou 1982 "A consistent hydrodynamic theory for moored and positioned vessels" *Journal of Ship Research*. Vol:26 No:2 pp97-105.
7. B. Molin 1989 "Comportements non-linéaires des plateformes semi-submersibles" *Actes des 2èmes Journées de l'Hydrodynamiques*. pp123-140.
8. T. Matsui 1987 "Second-order hydrodynamic forces on moored vessels in random waves" *IUTAM symposium* pp202-300.
9. X.B. Chen 1988 "Etude des réponses du second-ordre d'une structure soumise à une houle aléatoire" *Thèse de Doctorat de ENSM*.
10. X.B. Chen 1989 "Evaluation des efforts de basse fréquence sur une structure soumise à une houle irrégulière: comparaison de différentes approximations" *Actes des 2èmes Journées de l'Hydrodynamique*. pp141-156.
11. B. Molin 1982 "Some experiments on the low-frequency heave motion of floating bodies with small waterplane areas" *IFP report*. Reference number: 30 166.

DISCUSSION

by R. H. Huijsmans

I like to congratulate the authors with their fine paper and their treatment of the mean position dependency of the second order forces, which resembles the way the wavedrift damping concept has been introduced.

I have a question regarding the low-frequency drift forces depending on the second order potential F_{22} . In using Lighthill's transformation to the Haskind integral we showed [A1] that the simplified analysis of this integral as was proposed by Pinkster [A2] was valid for a wide frequency range. This simplified analysis has the benefit of small computational efforts. Would the authors comment on this?

A next question concerns the Fig.8 of your paper. It seems to me that for practical irregular waves notably JONSWAP type wave spectra, these only exists a small frequency band where the envelope spectrum has some significance. Therefore larger difference frequencies need not to be regarded extensively. Can the authors comment on this.

[A1] A. Benschop, A.J. Hermans, R.H.M. Huijsmans, "Second order diffraction forces on a ship in irregular waves", Applied Ocean Research, 9, 1987.

[A2] J.A. Pinkster, "The low frequency excitation forces on ships", PhD Thesis, University Delft, 1980.

Author's Reply

1. The contribution of the second-order diffraction potential to the second-order loads consists of two Haskind integrals: one on the free surface that involves the second-order correction to the free surface equation, the other over the hull that involves the second-order correction of the body surface equation. For difference frequency problems it is generally accepted that the free-surface integral is small, which has been confirmed both by the discussor's results [A1] and by ours. However, if the body is allowed to respond to waves, the body surface integral is not small, even for the difference frequency case. Thus Pinkster's approximate method, which only takes account of the second-order incident potential on the body surface, may not be valid.

2. We are thankful to the discussor that this second comment has made us aware that all

figures in the paper are incorrectly labeled. The low frequencies on the horizontal axes are not expressed in Hertz but in radian per second (as it is written in the text). We apologize for that error.

DISCUSSION

by R. Eatock Taylor

It appears that the second order correction due to the body motions involves the large low frequency motions (eq.7) and the small wave frequency motions (eq.43). This presumably results from the two time scale approach, although the details are not given. Is this consistent with including terms from the second order potential for the low frequency forces? My memory of Triantafyllou's argument is that the corresponding forces are of third order, because of the small parameter which results from taking the derivative of the potential with respect to the slow time [i.e., the factor $(\omega_j - \omega_L)$].

This leads to a second question. The expression for the second order incident potential given in eq.45 does not appear to be valid at very small difference frequencies. I suggested this at the Water Waves Workshop in Norway earlier this year, and I would like to ask the authors whether their formulation leads to a discontinuity in the vertical force as $\omega_j \rightarrow \omega_L$; i.e. do they reach the regular wave result in the limit?

Author's Reply

We agree that our method can be rigorously justified only in the case when the time scale of the low frequency motion is very long compared to the wave motion time scale. Obviously this is not the case for the vertical motion of more traditional semi-submersible platform. but still we contend that variation of the low frequency exciting forces with the low frequency vertical motion should be account for, just as the low frequency horizontal velocity affects the low frequency horizontal loads.

The discrepancy between the vertical drift force and the $\omega_j \rightarrow \omega_L$ limit of difference frequency vertical force had already been noted in [9]. In the present case it does not appear as our numerical model is restricted to the infinite water depth case.

DISCUSSION

by R. Zhao

(1) Discuss about vertical drift force by using direct pressure integration or based on momentum and energy relations.

Author's Reply

In an earlier paper[A3] of the author computed the vertical drift forces on the same models, using both the momentum method and the direct pressure integral method. Numerical results showed excellent agreements. This

success however may have been partially due to the fact that the diffraction-radiation problem was solved with a fluid finite elements technique, which allows for an accurate evaluation of the fluid particle velocities.

[A3] B. Molin and J. P. Hairault, "On Second-Order Motion and Vertical Drift Forces for Three-Dimensional Bodies in Regular Waves", Proc. Int. Workshop on Ship and Platform Motions, Berkeley, 1983.

Numerical Computations for a Nonlinear Free Surface Flow Problem

K. J. Bai and J. W. Kim
Seoul National University
Seoul, Korea
Y. H. Kim

Dae Woo Shipbuilding and Heavy Machinery Co.
Jangseungpo, Korea

ABSTRACT

A finite-element method is presented for solving a nonlinear free surface flow problem for a ship moving in a towing tank. This problem is formulated as an initial/boundary value problem governed by Laplace's equation. The variational functional used in the present paper is basically similar to the variational functional given by Luke (1967).

In the numerical procedure, the variational problem is reduced to a set of nonlinear ordinary differential equation where the unknown functions appear as the first derivatives with respect to time. In this numerical procedure, the governing equation, i.e., Laplace's equation, is treated as a constraint to the ordinary differential equation. In solving this problem, we employed the lumping and the upwinding schemes to maintain the numerical stability in the integration with respect to time. To illustrate this method, a simple wedge-shape ship stretched to the bottom is treated. Computations are made for the range of depth Froude number, $F_h = 0.7 \sim 1.1$. The computed results show a good agreement with the previous results obtained by other methods. Even though the present computations are made mainly in the neighborhood of $F_h = 1$, this method can be applied to general Froude number.

1 Introduction

A free surface flow of an inviscid, incompressible fluid past a ship moving with a constant velocity in a towing tank is described by an initial/boundary value problem governed by Laplace's equation with a free surface as a part of solution.

In the past, the problems of this type were generally treated after the boundary condition on the free surface was linearized. Recently, however, there are growing interests in treating the nonlinear free surface flow problems by various

numerical schemes. For example, two-dimensional problem was treated by Washizu *et al.* (1977), Hess (1977), Korving & Hermans (1977), Salvesen & von Kerczek (1978), Yen, Lee & Akai (1977) and Mori & Shin (1988). Recently, a three dimensional nonlinear problem is treated by Dommermuth & Yue (1988).

There is another line of investigations on the nonlinear free surface flow problem based on the shallow water approximation which results in the Korteweg-de Vries, Boussinesq and Kadomtsev-Petviashvili equations and Green-Naghdi formulation. Many references along this approach can be found in Choi & Mei (1989). To name few, Choi & Mei (1989), Ertekin, Webster & Wehausen (1984,1986) treated three-dimensional problems.

In the present paper, we initially planned to investigate two different computational methods, i.e., the finite-element method and the fundamental singularity-distribution method for a three dimensional nonlinear problem. However, the progress along the second approach is not quite satisfactory at this time. Thus we describe only the application of a finite element method in this paper. One may find the application of fundamental source distribution method for a sloshing problem in three dimensional rectangular tank in Kim (1989). To illustrate the present numerical method, computations are made for a wedge-shape ship extended from the bottom to the free surface. Main computational efforts are made for the critical Froude number, i.e., $F_h = 1.0$, just because of less computation time compared to the small depth Froude numbers. To treat the case of small Froude number, one simply has to take more finite elements. The computed results show two dimensional solitons periodically generated in the upstream and complicated three dimensional waves in the downstream. The comparisons show a good agreement with the previous results.

2 Mathematical Formulation

We adopt a moving coordinate in this paper. Let $Oxyz$ be a coordinate system with Oz opposing the direction of gravity and $z = 0$ coincides the undisturbed free surface. The origin O is placed inside the body which moves with velocity U in the negative x -direction. We assume that the fluid is inviscid and incompressible and its motion is irrotational such that the velocity field of the fluid \vec{u} can be defined as

$$\vec{u}(x, y, z, t) = \nabla\phi(x, y, z, t) \quad (1)$$

where ϕ is the velocity potential and satisfies the Laplace equation

$$\nabla^2\phi(x, y, z, t) = 0 \quad (2)$$

in fluid domain D and the boundary condition

$$\phi_n = -Un_x \quad (3)$$

on the body surface S_O where $\vec{n} = (n_x, n_y, n_z)$ denotes the outward unit normal vector on the boundaries.

If the free surface is represented by $z = \zeta(x, y, t)$ the kinematic and dynamic boundary conditions on the free surface S_F can be given as

$$\zeta_t = -U\zeta_x + \frac{1}{n_x}\phi_n \quad (4)$$

$$\phi_t = -U\phi_x - \frac{1}{2}|\nabla\phi|^2 - g\zeta - \frac{p}{\rho} \quad (5)$$

where g and ρ denote the gravity constant and the density of fluid and $p = p(x, y, t)$ is taken zero when the pressure distribution is absent.

By assuming that the fluid is initially at rest, the initial condition may be given as

$$\phi = \phi_t = 0 \quad \text{at } t = 0 \quad (6)$$

and the resulting radiation condition is given as

$$\phi \rightarrow 0 \quad \text{as } x^2 + y^2 \rightarrow \infty. \quad (7)$$

It should be noted that a modified radiation condition was treated in the computations for the downstream boundary.

For the fluid domain of finite depth h with the side walls at $y = \pm B$ the additional boundary conditions are given as

$$\phi_n = 0 \quad \text{on } z = -h \quad (8)$$

$$\phi_n = 0 \quad \text{on } y = \pm B. \quad (9)$$

To put our formulations in a scale-independent form we nondimensionalize all physical variables by h , ρh^3 and $\sqrt{\frac{h}{g}}$ for length, mass and time scales, respectively. With some abuse of notations we can re-write the above governing equation and boundary conditions as

$$\nabla^2\phi(x, y, z, t) = 0 \quad \text{in } D \quad (10)$$

$$\phi_n = -F_h n_x \quad \text{on } S_O \quad (11)$$

$$\zeta_t = -F_h \zeta_x + \frac{1}{n_x}\phi_n \quad \text{on } S_F \quad (12)$$

$$\phi_t = -F_h \phi_x - \frac{1}{2}|\nabla\phi|^2 - \zeta - p \quad \text{on } S_F \quad (13)$$

$$\phi_n = 0 \quad \text{on } z = -1 \quad (14)$$

$$\phi_n = 0 \quad \text{on } y = \pm B \quad (15)$$

where $F_h = \frac{U}{\sqrt{gh}}$ is the depth Froude number and all variables are redefined as nondimensionalized ones.

3 Method of Solution

3.1 Variational formulation

For the convenience of the formulation we start with a homogeneous problem; $F_h = 0$ and all boundaries except free surface are rigid walls. Then we introduce a variational form of the above problem based on a functional J and a Lagrangian L defined as

$$J = \int_0^{t^*} L \, dt \quad (16)$$

$$L = \iint_{\bar{S}_F} \phi \zeta_t \, dS \quad (17)$$

$$- \frac{1}{2} \iint_{\bar{S}_F} \zeta^2 \, dS - \frac{1}{2} \iiint_D |\nabla\phi|^2 \, dV$$

where \bar{S}_F is the projection of S_F on Oxy plane and t^* is the final time.

Taking the variations on J , first with respect to $\delta\zeta$, the variation on ζ , denoting δJ_ζ , and with respect to $\delta\phi$, denoting δJ_ϕ , respectively, we obtain

$$\begin{aligned} \delta J_\zeta &= \int_0^{t^*} dt \left[\iint_{\bar{S}_F} (\phi \delta \zeta_t - \zeta \delta \zeta) \, dS \right. \\ &\quad \left. - \frac{1}{2} \iint_{\bar{S}_F} |\nabla\phi|^2 \delta \zeta \, dS \right] \\ &= \iint_{\bar{S}_F} [\phi \delta \zeta]_{t=0}^{t=t^*} \, dS - \iint_{\bar{S}_F} [\phi \delta \zeta]_{t=0} \, dS \quad (18) \\ &\quad - \int_0^{t^*} \left[\iint_{\bar{S}_F} (\phi_t + \frac{1}{2}|\nabla\phi|^2 + \zeta) \delta \zeta \, dS \right] dt \end{aligned}$$

and then with respect to $\delta\phi$,

$$\begin{aligned}\delta J_\phi &= \int_0^{t^*} dt \left[\iint_{\bar{S}_F} \zeta_t \delta\phi dS \right. \\ &\quad \left. - \iiint_D \nabla\phi \cdot \nabla\delta\phi dV \right] \\ &= \int_0^{t^*} dt \left[\iint_{\bar{S}_F} \left(\zeta_t - \frac{1}{n_x} \phi_n \right) \delta\phi dS \right. \\ &\quad \left. + \iiint_D \nabla^2\phi \delta\phi dV \right].\end{aligned}\quad (19)$$

Here, $\delta J = \delta J_\zeta + \delta J_\phi$.

Equation (18) shows that the stationary condition on J for the variation of ζ recovers the dynamic free surface boundary condition in each time and that the wave elevation at $t = 0, t^*$ should be specified as the constraints.

Equation (19) shows that the stationary condition on J for the variation of ϕ recovers the kinematic condition on S_F and the governing equation.

The variational form written above is previously given by Miles (1977) and is slightly different from that given by Luke (1967). In the present variational formulation the wave elevation ζ is assumed to be known at $t = 0, t^*$, whereas Luke assumed the potential ϕ to be known at both initial and final times additionally. Specifically, the present variational form is obtained from Luke's form by subtracting the volume integral of the potential resulted in the process of the integration by parts with respect to time. The present variational functional has more advantage over the original Luke variational functional in treating the nonlinear free surface boundary conditions.

3.2 Finite-Element Discretization.

The original initial/boundary value problem is well defined for ϕ of which the admissible solution should be twice continuously differentiable in space. However, in the above variational method, it suffices that the admissible trial functions have the square integrable properties of the function ϕ and only their first derivatives in space. This enables us to look for an approximate solution in a wider class in the variational method.

As in usual finite element analysis we discretize the fluid domain into finite number of finite elements. In the present computations, the finite elements are generated such that the projections on the horizontal plane, i.e. $z=0$, is unchanged while the other coordinate, i.e. the z -axis, is allowed to change in time. This simplifies the mesh generation and the computations considerably. However, this restriction is

not necessary for the present method in applying to a general problem. Then we approximate ϕ in N dimensional function space whose basis is continuous in D and has continuous derivatives in each element. However, it is allowed to have a finite discontinuity in the normal derivative across the common boundaries of the adjacent elements. We denote the basis of this space by $\{N_i\}_{i=1,\dots,N}$ and approximate ζ by the span of the restrictions of $\{N_i\}_{i=1,\dots,N}$ on S_F which is also continuous and piecewise differentiable on \bar{S}_F ;

$$\phi(x, y, z, t) = \phi_i(t) N_i(x, y, z; \zeta) \quad (20)$$

$$\zeta(x, y, t) = \zeta_k(t) M_k(x, y) \quad (21)$$

where

$$M_k(x, y) = N_{i_k}(x, y, z; \zeta)|_{z=\zeta} \quad k = 1, \dots, N_F \quad (22)$$

and N_F is the number of nodal points on S_F and i_k is the nodal number of the basis function N_i of which the node coincides with that of the free surface node k . Summation conventions for the repeated indices are used here. It should be noted that the basis function $\{N_i\}_{i=1,\dots,N}$ is dependent on the free surface shape $z = \zeta(x, y, t)$ but its restriction on S_F is the function of (x, y) and independent of ζ . This special property of $\{M_k\}_{k=1,\dots,N_F}$ is due to the simplicity of the fluid domain D which has no variation in z -direction such that we can change the position of the nodal points only in the z -direction in each time step.

Once the trial function is approximated by using the above basis function, we obtain the Lagrangian L for this trial solution as

$$\begin{aligned}L &= \phi_{i_k} T_{kl} \dot{\zeta} \\ &\quad - \frac{1}{2} \phi_i K_{ij} \phi_j - \frac{1}{2} \zeta_k P_{kl} \dot{\zeta}\end{aligned}\quad (23)$$

where

$$\begin{aligned}T_{kl} &= \iint_{\bar{S}_F} M_k M_l dS \\ K_{ij} &= \iiint_D \nabla N_i \cdot \nabla N_j dV \\ P_{kl} &= \iint_{\bar{S}_F} M_k M_l dS.\end{aligned}\quad (24)$$

The tensors K_{ij} , P_{kl} are the kinetic and potential energy tensor and T_{kl} is a tensors obtained from the free surface integral, which can be interpreted as a tensor related to the transfer rate between these two energies. It is of interest to note that in Eq. (24), $T_{kl} = P_{kl}$. However T_{kl} will be defined differently from this in the computation through lumping.

The stationary condition on $J = \int L dt$ is equivalent to the following Euler-Lagrange equation

$$T_{kl} \dot{\Omega} = K_{ikj} \phi_j, \quad (25)$$

$$T_{kl} \dot{\phi}_i = -\frac{1}{2} \phi_i \frac{\partial K_{ij}}{\partial \zeta_k} \phi_j - P_{kl} \Omega, \quad (26)$$

for $k = 1, \dots, N_F$

$$K_{ij} \phi_j = 0, \quad i \neq i_k. \quad (27)$$

Here Eq. (25) and Eq. (26) are the nonlinear ordinary differential equation for $\{\zeta_k, \phi_{i_k}\}_{k=1, \dots, N_F}$ and Eq. (27) is the algebraic equations for $\{\phi_i\}_{i \neq i_k}$ which is the constraints for the above two equations.

It can be easily shown that the solution of the above discretized problem satisfies the conservation of mass and total energy, i.e.

$$\frac{d}{dt} \left(\sum_{k,l} P_{kl} \Omega \right) = 0 \quad (28)$$

$$\frac{d}{dt} \left(\sum_{i,j} \phi_i K_{ij} \phi_j + \sum_{k,l} \zeta_k P_{kl} \Omega \right) = 0. \quad (29)$$

This property of the conservations is independent of the tensor T_{kl} if it satisfies

$$\sum_k T_{kl} = \sum_k P_{kl}. \quad (30)$$

It should be also pointed out that the direct use of (26) leads to some difficulty in the computations. This difficulty arises from the first term in the right-hand side which is the derivative of the kinetic energy tensor with respect to the wave elevation. We have avoided this difficulty by utilizing the fact that (26) is equivalent to the condition of vanishing of the right-hand side in Eq. (18). In Eq. (18) $\delta \zeta$ can be regarded as test functions on \bar{S}_F . Then Eq. (26) can be given as

$$\begin{aligned} T_{kl} \dot{\phi}_i = & - \iint_{\bar{S}_F} M_k \phi_x \Omega \, dS \\ & - \frac{1}{2} \iint_{\bar{S}_F} M_l |\nabla \phi|^2 \, dS \\ & - P_{kl} \Omega. \end{aligned} \quad (31)$$

If the integrals in Eq. (26) and (31) are evaluated exactly, they are equivalent. However, in the present computation these integrals are calculated by integral quadrature rules. Therefore, the conservation of energy may not be satisfied exactly due to the error caused by the numerical integration. This test result is given in the next section.

3.3 Numerical Dispersion Relation.

If one solves the above variational formulation numerically, one encounters the effect of numerical dispersion depending on the specific numerical schemes employed. However, it is difficult to analyze the numerical dispersion effect in the above nonlinear three-dimensional problem. Therefore, we restrict ourselves to a linear problem and test the numerical dispersion in the following. The linear version of the Eq.'s (25)~(27) is given as

$$T_{kl} \dot{\Omega} = K_{ikj}^0 \phi_j \quad (32)$$

$$K_{ij}^0 \phi_j = 0, \quad i \neq i_k \quad (33)$$

$$T_{kl} \dot{\phi}_i = -P_{kl} \Omega \quad (34)$$

for $k = 1, \dots, N_F$ where K_{ij}^0 is the linearized kinetic energy tensor evaluated in the undisturbed fluid domain.

We use the 8-node brick element with linear interpolation along each coordinate. Then by separation of variables the velocity potential $\phi(x, y, z, t)$ can be represented as a product of the following three sets of functions:

$$\varphi^x(x, t) = \varphi_i^x(t) X_i(x), \quad i = 1, \dots, N_x, \quad (35)$$

$$\varphi^y(y, t) = \varphi_j^y(t) Y_j(y), \quad j = 1, \dots, N_y, \quad (36)$$

$$\varphi^z(z, t) = \varphi_k^z(t) Z_k(z), \quad k = 1, \dots, N_z \quad (37)$$

where $X_i(x), Y_j(y), Z_k(z)$ are the one dimensional basis functions and N_x, N_y, N_z are numbers of nodal points in x, y and z coordinates, respectively. Taking Fourier transformation from the frequency domain to the frequency domain, ω , we have the following set of eigen-value problems.

$$\int (X_i' X_j' - k_x^2 X_i X_j) dx \varphi_j^x = 0 \quad (38)$$

$$\int (Y_i' Y_j' - k_y^2 Y_i Y_j) dy \varphi_j^y = 0 \quad (39)$$

$$\omega^2 \varphi_1^z \delta_{i1} - \int_{-1}^0 (Z_i' Z_j' + k_z^2 Z_i Z_j) dz \varphi_j^z = 0 \quad (40)$$

where $\varphi_1^x = \varphi^x(0)$ and $k^2 = k_x^2 + k_y^2$. Here $\delta_{i1} = 1$ if $i = 1$ and zero otherwise. It is understood that the time dependent terms are now functions of frequencies without changing their notations.

Moreover, we can treat a two-dimensional wave propagating in the x direction without loss of generality since the linear wave is isotropic in Oxy plane as long as we use the same mesh size in x and y directions. To obtain the dispersion relation, we assume the type of solution for φ^x as

$$\varphi^x(x, \omega) = A e^{i \theta_n x} \quad (41)$$

where A is a constant amplitude and

$$\theta_n = \frac{\pi}{n\Delta x}, \quad n = 1, 2, 3, \dots \quad (42)$$

is the discrete wave numbers and Δx is the horizontal mesh size. By solving Eq. (38) and (40) after substituting Eq. (41) into Eq. (38), the dispersion relation can be obtained as

$$k_n^2 = \frac{6}{\Delta x^2} \frac{1 - \cos(\theta_n \Delta x)}{2 + \cos(\theta_n \Delta x)} \quad (43)$$

$$\omega = W(\theta_n) \quad (44)$$

$$= \Delta z \frac{\beta_1^{N-1} G_1 F_2 - \beta_2^{N-1} G_2 F_1}{\beta_2^N F_1 - \beta_1^N F_2}$$

where

$$\beta_{1,2} = \frac{6 + 2\mu^2 \pm 3\sqrt{\mu^4/3 + 4\mu^2}}{6 - \mu^2} \quad (45)$$

$$F_i = 1 + \mu^2/3 - \beta_i \left(1 - \frac{\mu^2}{6}\right), \quad (46)$$

$$G_i = 1 - \mu^2/6 - \beta_i \left(1 + \frac{\mu^2}{3}\right), \quad i = 1, 2 \quad (47)$$

with the number of elements in x -direction $N = N_x - 1$ and $\mu = k_n \Delta x$ with vertical mesh size $\Delta z = 1/N$.

The well-known exact linear dispersion relation corresponding to Eq. (43), (44) is

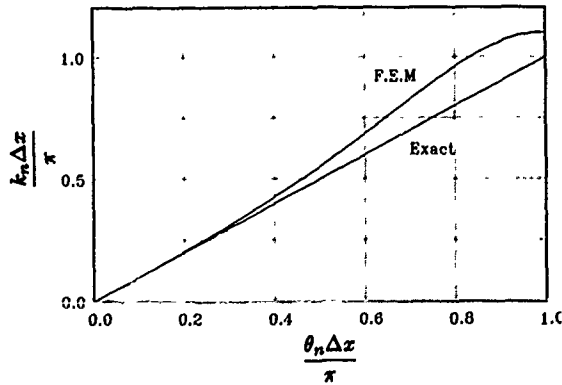
$$k_{exact}^2 = \theta_n^2 \quad (48)$$

$$\omega_{exact}^2 = k \tanh k. \quad (49)$$

The comparisons between these numerical and exact dispersion relations are shown in Fig. 1. It can be shown that for $\Delta x \ll 1$ with θ_n held fixed

$$k_n^2 = k_{exact}^2 (1 + O(\Delta x^2)), \quad (50)$$

which means that $\omega(\theta_n)$ has an error of $O(\Delta x^2)$, however small values of Δy we choose.



(a)

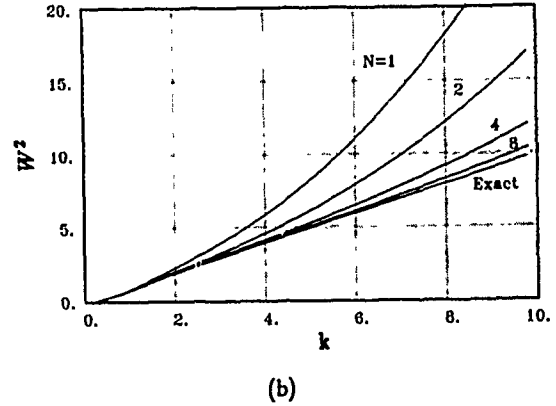


Fig. 1 Comparison of numerical and exact dispersion relations.

(a): Eq. (43) and Eq. (48)

(b): Eq. (44) and Eq. (49)

N : No. of elements in vertical direction.

Fig. 1 shows that the numerical dispersion relation predicts higher values for ω than the exact values. This inherent property of finite element method based on variational formulation restricts the numerical stability in time-domain analysis. A simple remedy to correct this inherent drawback is the use of the so-called 'lumping' in the tensor T_M which is originally equal to P_M as in Eq. (24). The lumped tensor \bar{T}_M is given as

$$\bar{T}_M = \delta_{kl} \sum_m P_{km} \quad (51)$$

where δ_{kl} is Kronecker's delta. Then the dispersion relation corrected by this lumping is

$$\begin{aligned} \omega &= \bar{W}(\theta_n) \\ &= \frac{2 + \cos(\theta_n \Delta x)}{3} W(\theta_n). \end{aligned} \quad (52)$$

The order of correction term in Eq. (52) is $O(\Delta x^2)$ which is same as the error in $W(\theta_n)$. For the shortest wave length $2\Delta x$, $\bar{W}(\theta_n)$ of the lumped case predict one third of the values of $W(\theta_n)$ of the unlumped case. This means that with lumping we can take time step three times larger than the standard finite element method without loss of the order of accuracy in the dispersion relation. The dispersion correction given in Eq. (51) by the lumping also preserves the conservation of the mass and energy, since Eq. (30) is satisfied when T_M is replaced by \bar{T}_M defined in Eq. (51).

3.4 Treatment of the Convective Term.

We assume that a ship is moving with a Froude number F_h . Then the pure convection terms are added to free surface boundary conditions. Since the presence of convection term due to the introduction of a moving coordinate does

not change the original dispersion and nonlinearity, we analyze them separately and then add it to the original problem. Therefore it suffices to consider a pure convection problem separately here.

Let a convection problem for ζ be given as

$$\zeta_t = -F_h \zeta_x \quad \text{on } \bar{S}_F. \quad (53)$$

The numerical scheme based on a direct weak formulation for the above equation is known to have a considerable phase error for short waves. To reduce the contamination of the phase errors in the computational domain caused by the short wave components, an upwinding scheme by using asymmetric test function has been successfully employed as in Hughes & Brooks (1982). The discretized form of Eq. (53) based on this scheme is obtained as

$$T_{k\Omega} \dot{\zeta}_i = -F_h \iint_{\bar{S}_F} (M_k + \frac{\alpha \Delta x}{2} \frac{\partial}{\partial x} M_k) \frac{\partial}{\partial x} M_i dS \quad (54)$$

where α is the upwinding parameter and has a value between 0 and 1. If $\alpha = 0$, it is equivalent to the standard Galerkin method based on symmetric test functions. If $\alpha = 1$, the right-hand side of equation (54) is equivalent to the forward-difference formula in finite difference method.

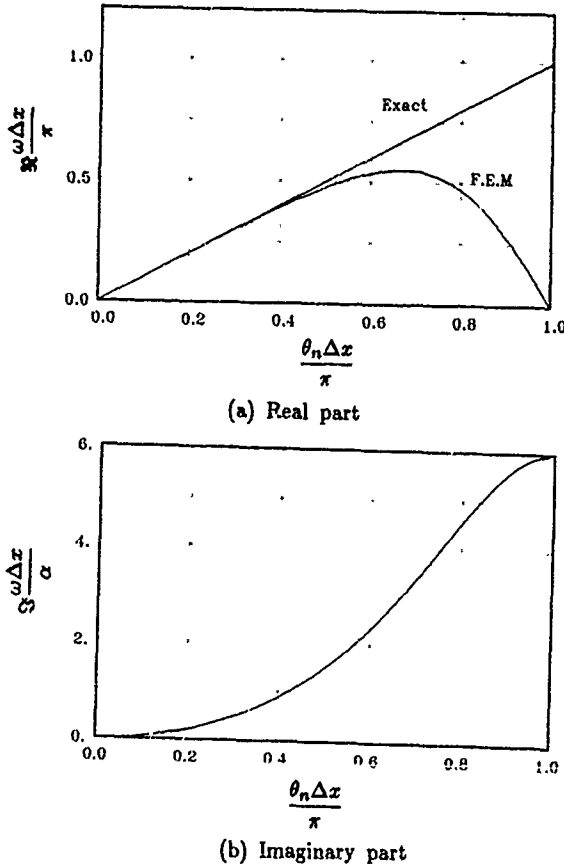


Fig. 2 Numerical dispersion relation due to the convective term for $F_h = 1$. (Eq. (55))

In a similar procedure given in Eq. (41) through Eq. (43), the following numerical dispersion relation is obtained for $F_h = 1$:

$$\omega = \frac{3}{\Delta x} \frac{\sin(\theta_n \Delta x)}{2 + \cos(\theta_n \Delta x)} + i \frac{3\alpha}{\Delta x} \frac{1 - \cos(\theta_n \Delta x)}{2 + \cos(\theta_n \Delta x)}. \quad (55)$$

The real and imaginary parts of the above equations are plotted in Fig. 2a and 2b, respectively. In Fig. 2a the real part of ω is compared with the exact relation

$$\omega = \theta_n. \quad (56)$$

In Eq. (55) it can be seen that the upwinding procedure has no effect on the real part of ω . The additional term in the imaginary part due to the upwinding behaves as a diffusion term and plays a role of damping mainly to the short wave component in time. The computations based on Eq. (54) are made for several values of α to test the effect of the numerical damping. The result is given in the next section.

3.5 Treatment of the Radiation Condition.

In the present computations, the computation domain is taken sufficiently large in the upstream direction so that the generated solitons travelling upstream does not hit the upstream boundary at the final time of computations. However, along the downstream radiation boundary, we used a simple boundary condition in a moving frame of reference as

$$\phi_n = 0 \quad \text{at } x = x_R \quad (57)$$

where $x = x_R$ is the radiation boundary at downstream. This can be interpreted as the disturbance convected away with the negative velocity of the moving coordinate. The present computed flow cases are such that the Froude number is around one. Accordingly, the velocity of the moving frame of reference is the critical speed. If there are any reflected waves from the downstream radiation boundary, then the speed of the reflected waves will not be larger than the critical speed. Therefore one may expect the reflected wave cannot contaminate the solution in the computation domain. Strictly speaking this is true only for a linear problem. However, even in nonlinear case the speed of waves at downstream do not exceed the critical speed in most cases. This simple numerical treatment of the downstream radiation boundary condition is tested successfully and the result is given in the next section.

3.6 Time Integration on the Free Surface.

Up to the previous subsections, we presented the numerical treatments of the governing equations, the convective terms and the radiation conditions as boundary value problem. Once we discretize the computation domain by the

finite elements and obtain the discretized form of matrix equation after integrating out all the space variables, then the problem is reduced to a set of nonlinear ordinary differential equations to solve. In this reduced equations, the time derivatives are present in the potential and the free surface elevation, both defined on the free surface. The reduced set of ordinary differential equations becomes the following form:

$$\bar{T}_M \dot{\Omega} = -F_h C_{M\Omega}^i \Omega + K_{ijk} \phi_j + f_{ik}, \quad (58)$$

$$\bar{T}_M \dot{\phi}_i = -F_h C_{kj}^i \phi_j - P_M \Omega - \phi_i D_{ikl}^1 \dot{\Omega} - \frac{1}{2} \phi_i D_{ikj}^2 \phi_j, \quad (59)$$

$$f_{ik} = -f_i, \quad i \neq i_k, \quad \text{for } k = 1, \dots, N_F, \quad (60)$$

where

$$\begin{aligned} C_{M\Omega}^i &= \iint_{\bar{S}_F} (M_k + \frac{\alpha \Delta x}{2} \frac{\partial}{\partial x} M_k) \frac{\partial}{\partial x} M_l dS \\ C_{kj}^i &= \iint_{\bar{S}_F} (M_k + \frac{\alpha \Delta x}{2} \frac{\partial}{\partial x} M_k) \frac{\partial}{\partial x} N_j dS \\ D_{ikl}^1 &= \iint_{\bar{S}_F} M_k M_l \frac{\partial}{\partial z} N_i dS \\ D_{ikj}^2 &= \iint_{\bar{S}_F} M_k \nabla N_i \cdot \nabla N_j dS \\ f_i &= F_h \iint_{S_0} N_i n_x dS. \end{aligned} \quad (61)$$

It should be pointed out that Eq. (60) can be interpreted as a constraint to Eq. (58) and (59). Equation (60) is obtained from the boundary value problem for Laplace equation with an essential condition on free surface and a natural condition on the body surface.

In the solution procedure for this problem, the constraint, i.e., Eq. (60) is first solved by the Jacobi conjugate gradient method. Then the matrix \bar{T}_M is inverted. Here the other matrices, which are dependent on the free surface shape, are treated as known from the previous time step. The final form in Eq. (58) and (59) is solved by the fourth-order Runge Kutta method.

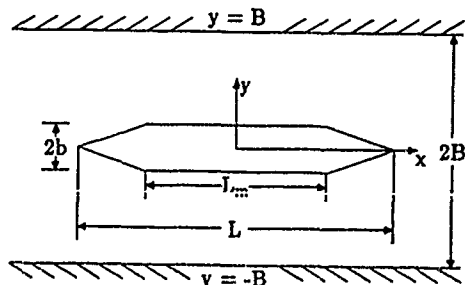


Fig. 3 Sketch of ship model and tank in horizontal plane view. Here the x-axis is against the gravity.

4 Numerical Results and Discussions

The computed model as shown in Fig. 3, is a vertical-sided wedge-shaped ship extended from the free surface to the bottom of the tank. The length of the wedge ship, the length of the parallel middle body, and the beam are denoted by L , L_m , and $2b$, respectively. The tank has the width of $2B$ and the mean water-depth of h . The ship is assumed to move with a constant velocity of $-U$ along the centerline of the tank. In presenting our computed results, all the physical quantities are nondimensionalized by h , ρh^3 and $\sqrt{\frac{h}{g}}$ for the length, mass, and time, respectively as mentioned previously.

Before we made the computations for the ship in the tank, we tested the case of a two-dimensional free oscillations in a three dimensional rectangular tank as an initial-value problem. The results are given in Fig. 4. Here the motion started from an initial hump on the free surface and let the time increases. The normalized tank length is 40 and the final time in nondimensional scale is 60 with the time step of 0.2. Fig. 4a and 4b show the results of 15 wave elevations with time increment of 4. The computed wave elevation and the speed of propagation agreed well with the approximate theoretical results for the amplitude and speed of the wave, which is given in Appendix A.

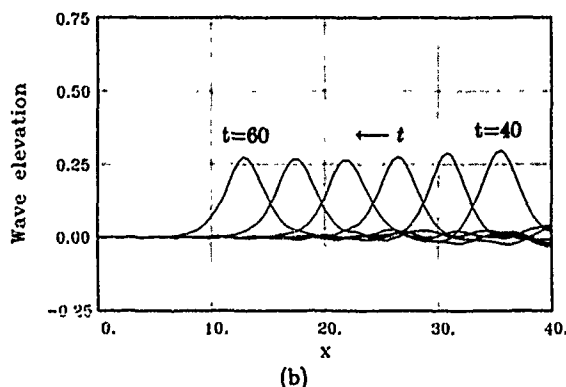
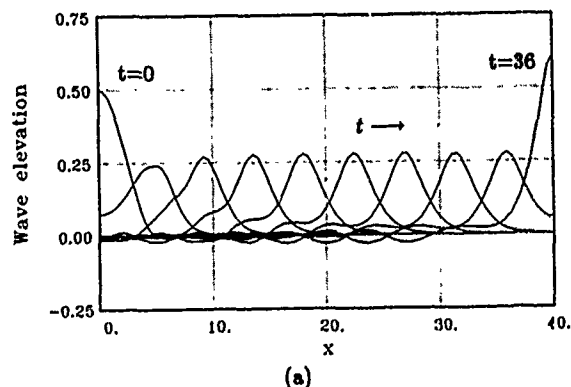


Fig. 4 Numerical test of free oscillation in a tank started from an initial hump at $t=0$. Tank length = 40, $\Delta x = 0.4$ and $\Delta t = 0.2$

Fig. 5 shows the test results of the conservation of the total energy, E , which is sum of the kinetic energy K and the potential energy P . The computed case is same as Fig. 4. Here the energy is normalized by the initial energy. This result shows that the total energy is conserved fairly well throughout computations.

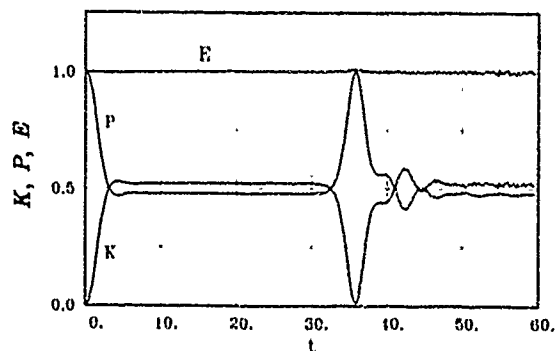
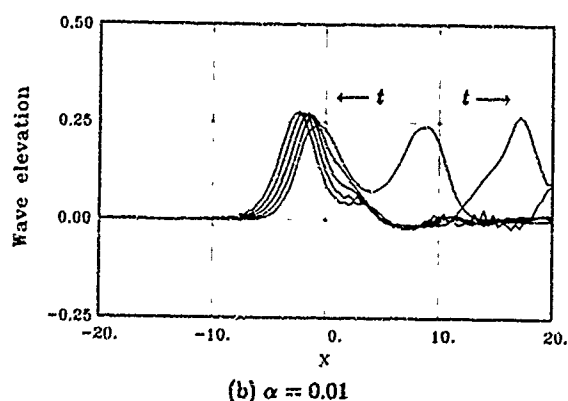
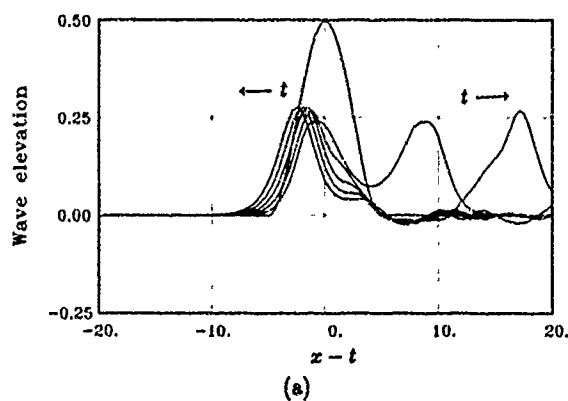
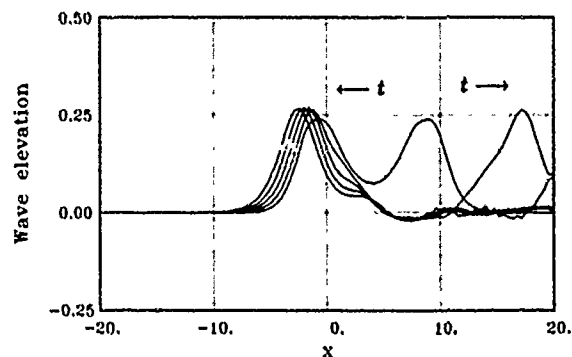


Fig. 5 Numerical test of energy conservation for the case of Fig. 4.

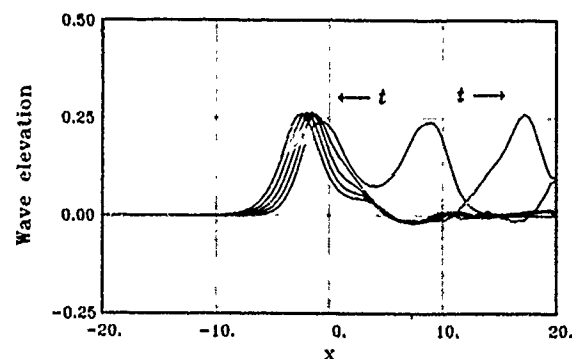
K : kinetic energy
P : potential energy
 $E = K + P$: total energy



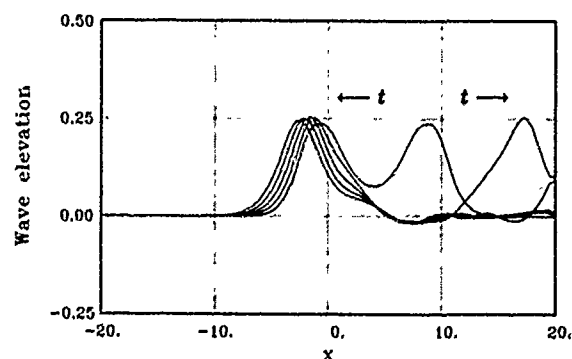
(b) $\alpha = 0.01$



(c) $\alpha = 0.03$



(d) $\alpha = 0.05$



(e) $\alpha = 0.1$

Fig. 6 Numerical test of the effect of upwinding parameter α for the convective term across the radiation boundary. The initial disturbance is same as in Fig. 4.

(a): Computed in the inertial coordinates.
(b)~(e): Computed in the coordinates moving with velocity -1 .

Fig. 6 shows the numerical test of the effect of the upwinding parameter, α , for the convective term across the radiation boundary. The initial disturbance is same as in Fig. 4. Fig. 6a shows the wave profiles first computed from

the formulation defined in the inertial coordinates and the results are shifted to $-\sqrt{gh}t$ to compare those given in Fig. 6b through Fig. 6e. Fig. 6b through Fig. 6e are obtained from the results computed in the coordinates moving with the velocity of -1 for four values of the upwinding parameter, $\alpha = 0.01, 0.03, 0.05, 0.1$. These comparisons show the dual roles of upwinding on the numerical damping and stability. This means that too much upwinding would give too much numerical damping effect in the numerical results. In the moderate range of the values of α , the upwinding works favorably to the stability.

Fig. 7 through Fig. 12 are the results for the following computation conditions:

Wedge model: $L=8, b=0.4, L_m=4$
 Computation Domain: $x=(-30, 30)$,
 $y=(-4, 0)$ (Symmetry is used)
 Finite Element Meshes: $150 \times 10 \times 1$ elements
 Upwinding Parameter: $\alpha = 0.05$
 Mesh sizes: $\Delta x=0.4, \Delta y=0.4, \Delta t=0.2$

Fig. 7 throughout Fig. 10 shows the results of wave profiles as time increases with the time increment of 20, for the cases of $F_h = 1.0, 0.9, 0.8, 0.7$, respectively. The generation of the upstream solitons are pronounced as the F_h approaches to 1. For $F_h = 0.7$, the generation of upstream solitons is barely noticeable. Fig. 11 shows the results of supercritical Froude number, i.e., $F_h=1.05$. It is of interest to note that the numerical instability shows up when $t=60$. Further computations for t larger than 60 showed that the water surface hit the bottom locally. At present, our program cannot incorporate with a local dry bottom. This can be easily incorporated in the near future.

Fig. 12a and 12b show the computed wave resistance for $F_h=0.9$ and 1.0, respectively. Fig. 13a and 13b show the time record of wave elevations for $F_h = 0.9$ and 1.0, respectively. This shows that the time-dependent hydrostatic pressure is not negligible in the resistance computations.

Fig. 14a and 14b show the computed results of wave resistance for two different tank conditions: Fig. 14a is for the case of the tank and ship geometry being reduced to one half in the direction of the y-direction. Fig. 14b is for the case of those geometry reduced to one-tenth in that direction. Thus the wave resistances are shown by multiplied by the factor of two and ten, in Fig. 14a and 14b, respectively.

Table 1 shows the amplitude, speed and the generation period of solitons for the blockage coefficient, $S = 0.1$. Here the blockage coefficient, S is defined as in Ertekin *et al.* (1986). The amplitude A is taken from the first solitons. The period is measured from the computed results at the F.P. Also shown are the computed results by Ertekin *et al.* who treated a pressure patch in Table 1.

Table 2 shows the amplitude, speed and the generation period of solitons obtained in the tank reduced to one half of the tank width for several values of the blockage coefficients when $F_h = 1$. The amplitudes and the speed increases whereas the generation period decreases as the blockage coefficient increases. This trend agrees well with the previous experimental results of Ertekin.

Table 1. Amplitude, Speed and generation period of solitons for the blockage coefficient, $S=0.1$. The values in the parentheses are obtained from Ertekin *et al.* (1986).

U/\sqrt{gh}	A/h	C/\sqrt{gh}	UT_g/h
0.7	0.139	1.06	14.6
0.8	0.240	1.10	19.4
0.9	0.375	1.16	24.1
	(0.5101)	(1.224)	(20.0)
1.0	0.553	1.24	30.0
	(0.6248)	(1.280)	(29.6)
1.05*	0.677	1.27	34.7
1.1*	0.806	1.32	39.1
	(0.7729)	(1.390)	39.3

* The values are obtained from the narrow tank reduced to the 1/10 in y-direction.

Table 2. Amplitude, Speed and generation period of solitons obtained in the tank reduced to one half of the tank width for $U/\sqrt{gh} = 1$.

Block. coeff.	A/h	C/\sqrt{gh}	UT_g/h
0.06	0.404	1.18	44.2
0.08	0.475	1.22	36.2
0.1	0.545	1.24	29.8
0.12	0.604	1.26	27.0

As a concluding remark the accuracy of the present computations could be improved by employing finer meshes. The computation time for a typical model of 1500 elements was 260 seconds for each time step by IBM PC/XT with T800 Monoputer. A typical number of the total time steps was 500.

ACKNOWLEDGEMENTS.

This work has been supported by the Nonlinear Ship Hydrodynamics Program supported by the Korean Science & Engineering Foundation.

REFERENCES

- Choi, H. S. & Mei, C. C. 1989 Wave resistance and squat of a slender ship moving near the critical speed in restricted water. *Proc. 5th Int. Conf. on Num. Ship Hydrodynam., Hiroshima*.
- Dommermuth, D. G. & Yue D. 1988 The non-linear three-dimensional waves generated by a moving surface disturbances. *Proc. 17th Symp. Naval Hydrodynam., Hague*.
- Ertekin, R. C. 1984 Soliton generated by moving disturbances in shallow water: theory, computation and experiment. Ph.D. dissertation, University of California, Berkeley.
- Ertekin, R. C., Webster, W. C. & Wehausen, J. V. 1984 Ship-generated solitons. *Proc. 15th Symp. Naval Hydrodynam., Hamburg*, pp. 347-364.
- Ertekin, R. C., Webster, W. C. & Wehausen, J. V. 1986 Waves caused by a moving disturbance in a shallow channel of finite width. *J. Fluid Mech.*, **169** pp. 347-364.
- Green, A. E. & Naghdi, P. M. 1976 A derivation of equations for wave propagation in water of variable depth. *J. Fluid Mech.* **78** pp. 237-246.
- Hess, J. 1977 Progress in the calculation of nonlinear free-surface problems by surface-singularity techniques. *Proc. 2nd Int. Conf. on Num. Ship Hydrodynam., Berkeley*, pp. 278-284.
- Hughes, T. J. R. & Brooks, A. 1982 A theoretical framework for Petrov-Galerkin Methods with discontinuous weighting Functions: Application to the Streamline-upwind procedure *Finite Elements in Fluids*, vol. 4, John Wiley & Sons Ltd., pp. 47-65.
- Kim, Y. H. 1989 A numerical analysis of free surface wave problems by source distribution method. M.S. Thesis, Seoul Nat'l Univ. (in Korean).
- Korving, C. & Hermans, A. J. 1977 The wave resistance for flow problems with a free-surface. *Proc. 2nd Int. Conf. on Num. Ship Hydrodynam., Berkeley*, pp. 285-291.
- Luke, J. C. 1967 A variational principle for a fluid with a free surface. *J. Fluid Mech.* **27** pp. 395-397.
- Miles, J. W. 1977 On Hamilton's principle for surface waves. *J. Fluid Mech.* **83** pp. 395-397.
- Mori, K. & Shin, M. 1988 Sub-breaking wave: it's characteristics, appearing condition and numerical simulation. *Proc. 17th Symp. Naval Hydrodynam., Hague*.
- Salvesen, N. & von Kerczek, C. 1978 Nonlinear Aspects of Subcritical Shallow- Water Flow Past Two-Dimensional Obstructions. *J. Ship Res.* vol. 22, No. 4, pp. 179-200.
- Washizu, K., Nakayama, T. & Ikegawa, M. 1977 Application of the finite element method to some free surface fluid problems. *Finite Elements in Water Resources*, Pentech Press, London, pp. 4.247-4.226
- Wu, T. Y. 1981 Long waves in ocean and coastal waters. *J. Engng Mech. Div. ASCE* **107** pp. 501-522.
- Wu, D. M. & Wu, T. Y. 1982 Three-dimensional nonlinear long waves due to moving surface pressure. *Proc. 14th Symp. Naval Hydrodynam., Ann Arbor, Mich.*, pp. 103-129.
- Yen, S. M., Lee, K.D. & Akai, T.J. 1977 Finite-element and finite-difference solutions of nonlinear free-surface wave problems. *Proc. 2nd Int. Conf. on Num. Ship Hydrodynam., Berkeley*, pp. 305-318.

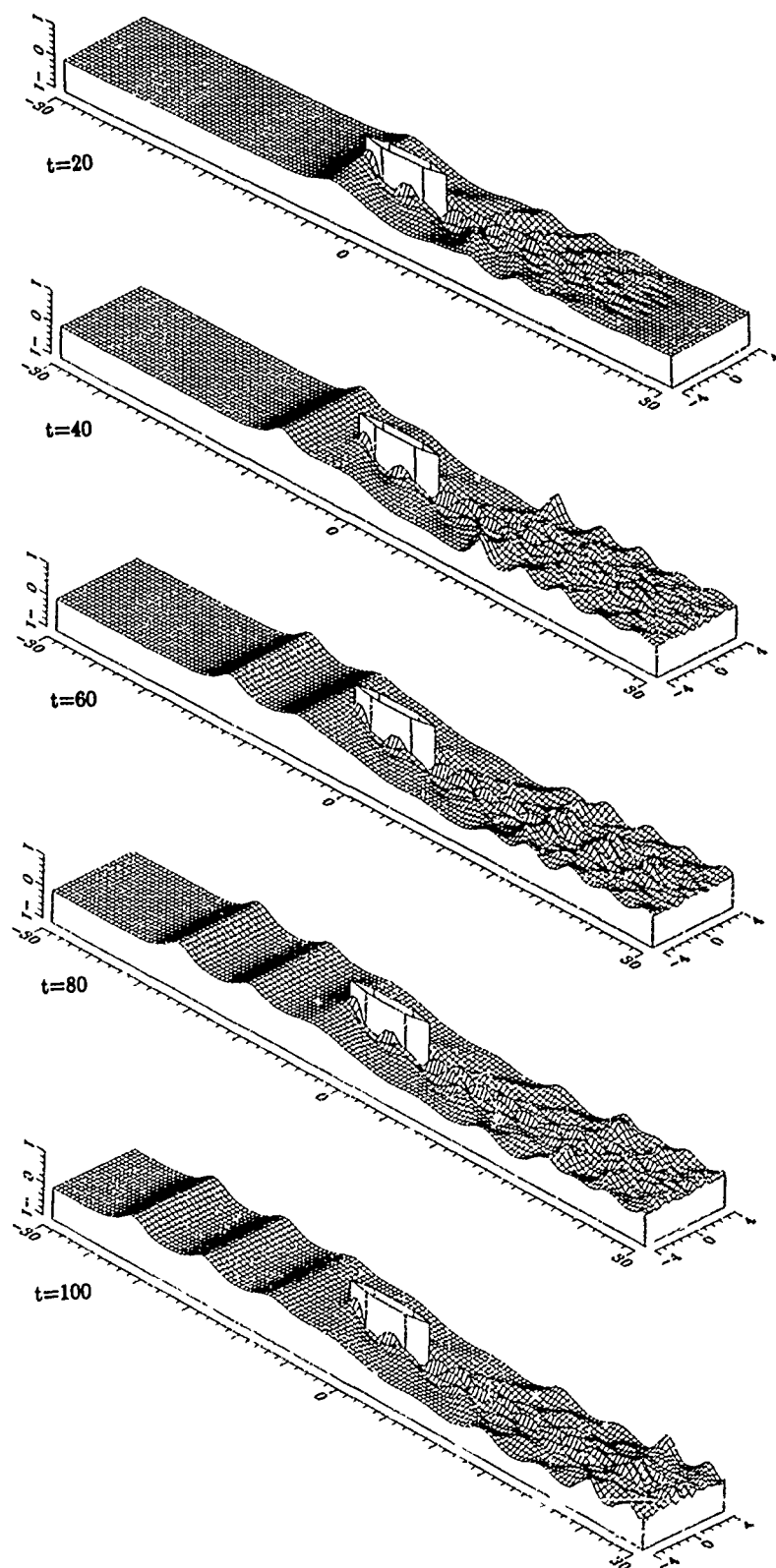


Fig. 7 Computed free surface for $F_h = 1$

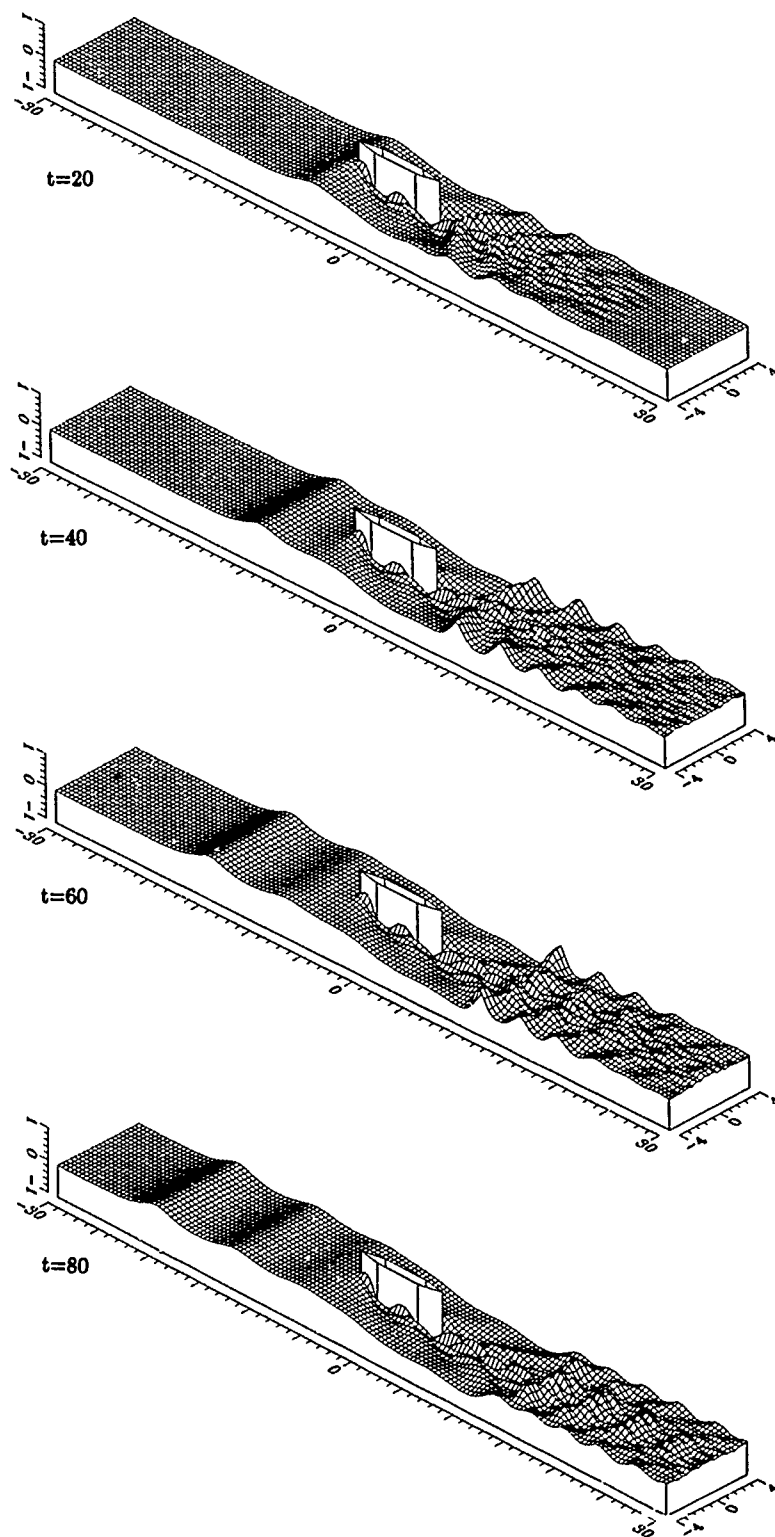


Fig. 8 Computed free surface for $F_h = 0.9$

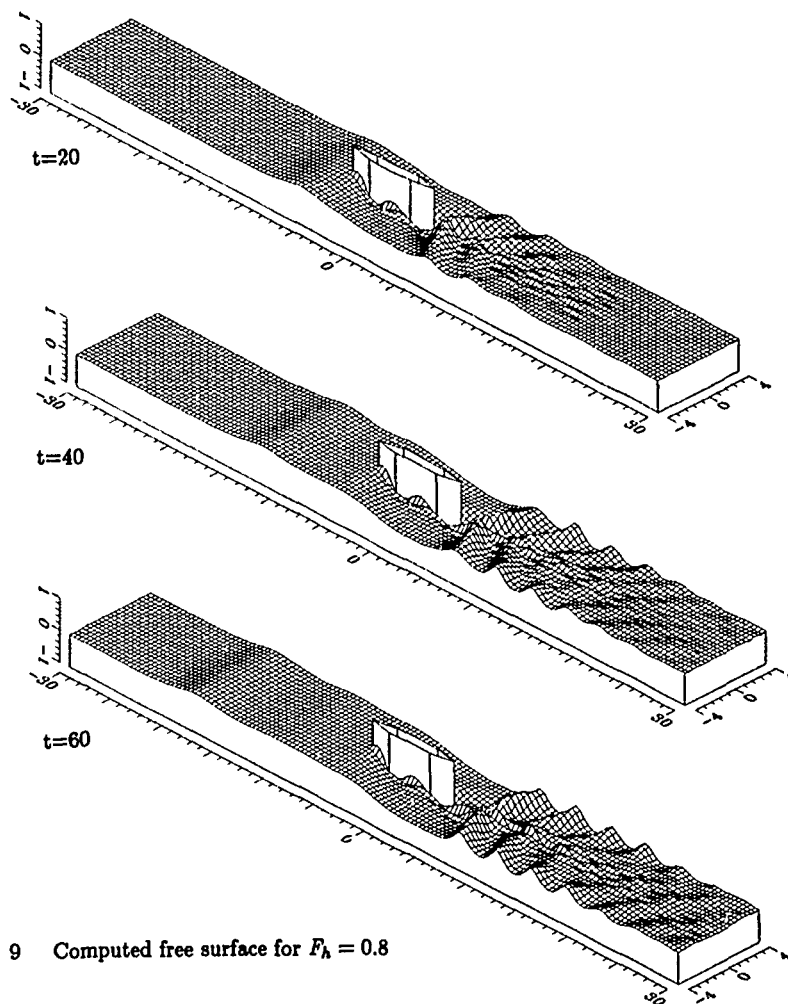


Fig. 9 Computed free surface for $F_h = 0.8$

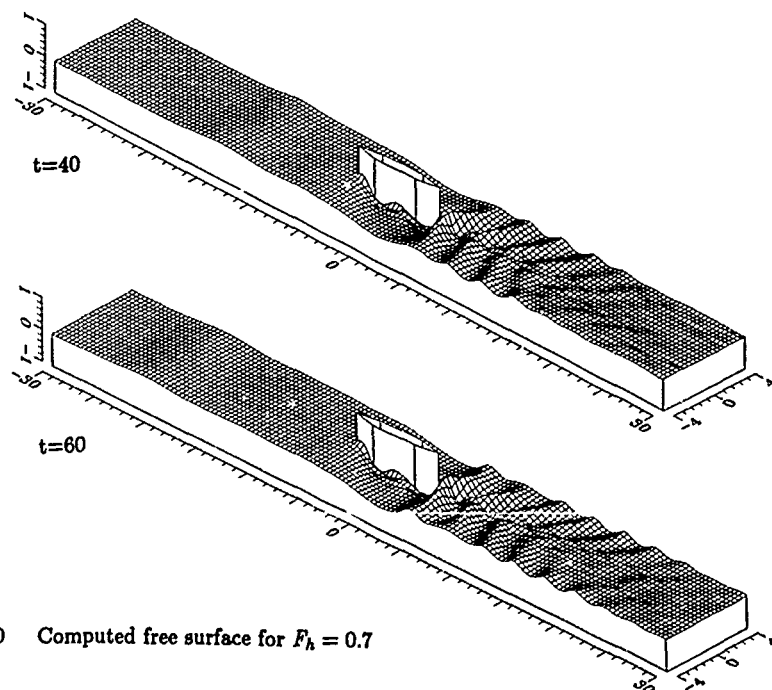


Fig. 10 Computed free surface for $F_h = 0.7$

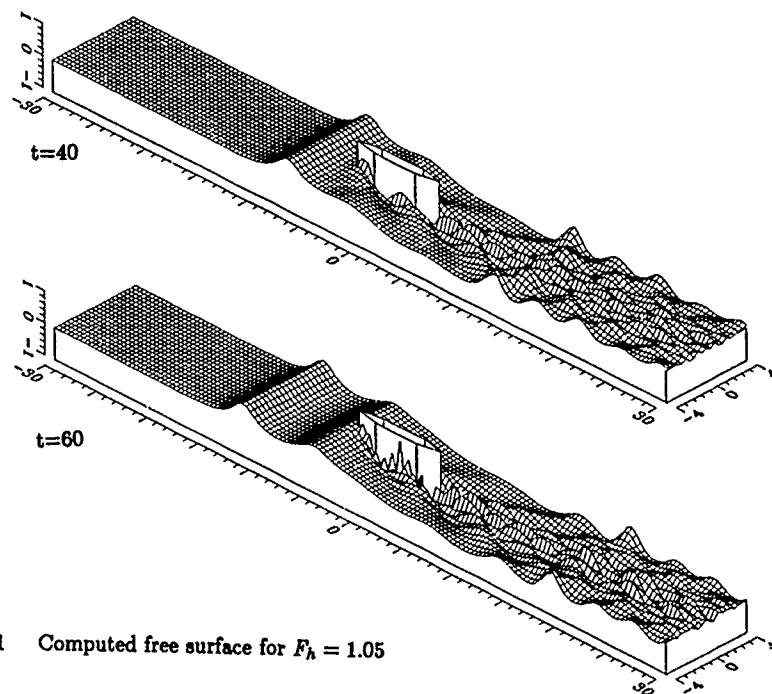
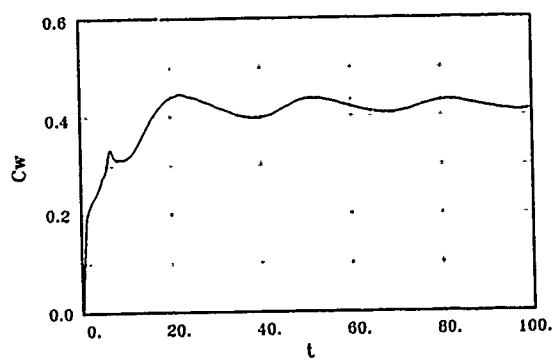
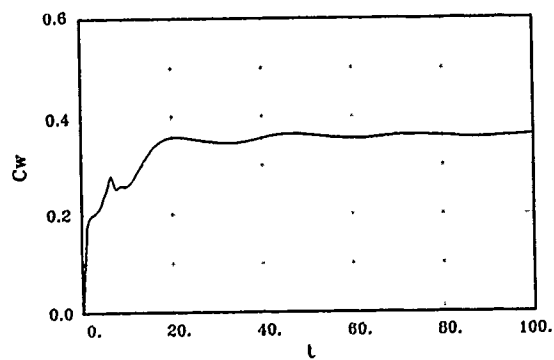


Fig. 11 Computed free surface for $F_h = 1.05$



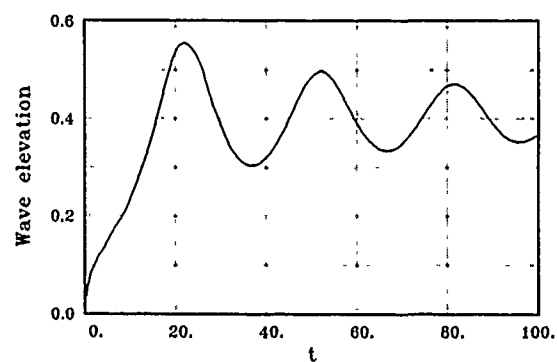
(a)



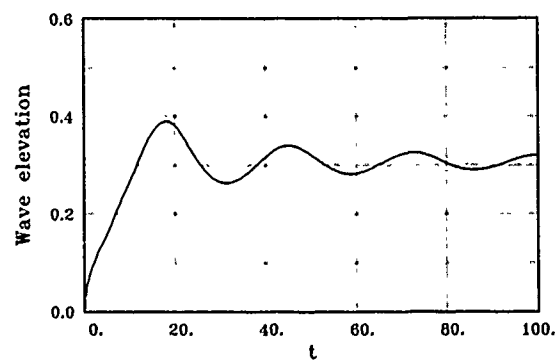
(b)

Fig. 12 Wave resistance for different Froude numbers ($B = 4$, $b = 0.4$).

- (a) $F_h = 1$
(b) $F_h = 0.9$



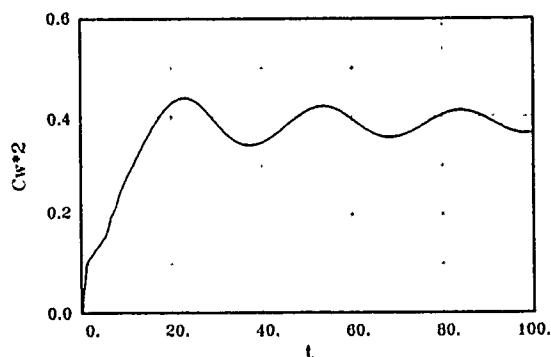
(a)



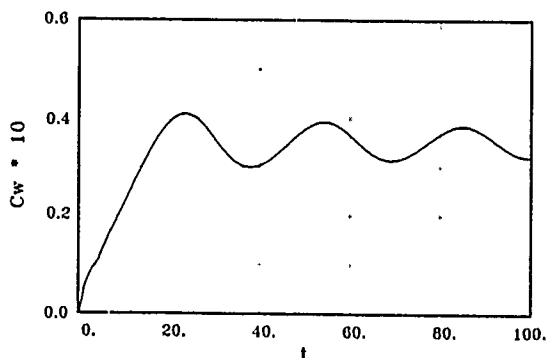
(b)

Fig. 13 Wave elevation at F.P of a wedge.

- (a) $F_h = 1$
(b) $F_h = 0.9$



(a)



(b)

Fig. 14 Wave resistance for different tank and hull geometry ($F_h = 1$).
(a) $B = 2$, $b = 0.2$
(b) $B = 1$, $b = 0.1$

Appendix

A Comparisons with Other Theories.

The comparisons are made on the linear dispersion relation and the speed of the nonlinear wave of permanent form among several different approximate theories. We present the results obtained by the equations derived by Green & Naghdi (1976) (hereafter the GN equation) and Wu (1981). Since both equations are derived with the assumption of shallow-water limit or equivalent assumption on the velocity field, we compare them with the result of finite element method with one element in depth-wise direction. For the

finite element method we present two different approximation in depth-wise direction. In the first approximation a linear interpolation is used. The results presented in the section 4 were obtained by using this element. In the second, we use a quadratic interpolation which satisfies the boundary condition on the bottom. The above two approximations will be referred to L1 and L2, respectively, hereafter. The approximate velocity potentials of L1 and L2 schemes in two dimensions are given as

$$L1: \phi_1(x, z, t) = f_1^1(x, t) + z f_2^1(x, t) \quad (A.1)$$

$$L2: \phi_2(x, z, t) = f_1^2(x, t) + (z+1)^2 f_2^2(x, t). \quad (A.2)$$

A.1 Linear Dispersion Relation

The linear dispersion relations of GN and Wu equations are identical and can be found in Ertekin (1984). The relations for L1 and L2 scheme can be derived from Eq. (40) with appropriate basis functions. The results are

$$GN, Wu: \omega^2 = \frac{3k^2}{3+k^2} \quad (A.3)$$

$$L1: \omega^2 = \frac{k^2(12+k^2)}{12+4k^2} \quad (A.4)$$

$$L2: \omega^2 = \frac{k^2(15+k^2)}{15+6k^2}. \quad (A.5)$$

The above relations are plotted in Fig. 15 compared with the exact relation. It can be found that the finite element method gives the upper bound for the exact values of ω , whereas GN and Wu equation gives the lower bound. The L2 scheme predicts more closely to the exact values of ω whereas the L1 scheme deviates more than others.

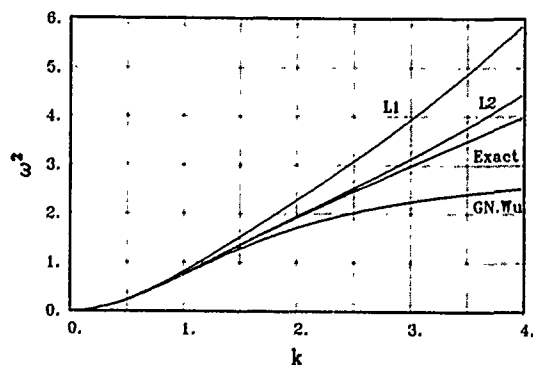


Fig. 15 Linear dispersion relations in various schemes.

A.2 Speed of Permanent Wave Form

The speed of solitary waves for a given amplitude can be found in Ertekin (1984) for GN equation. The speed for Wu's equation is given only in limiting case of small amplitude in Wu & Wu (1982). But one can derive the relation using the integral invariants of Wu's equation in steady state. For L1 and L2 schemes the speed of permanent wave form can be derived using the dynamic free-surface condition and their two integral invariants, i.e., mass and momentum flux. They are given below:

$$\text{GN} : C^2 = 1 + A \quad (\text{A.6})$$

$$\text{Wu} : C^2 = \frac{6(1+A)^3}{A^2(3+2A)} \left(\log(1+A) - \frac{A}{1+A} \right) \quad (\text{A.7})$$

$$\text{L1} : \frac{C^2 A^2}{1+A} + \frac{(1+A)H^2}{3} - A^2 = 0 \quad (\text{A.8})$$

$$\text{L2} : \frac{C^2 A^2}{1+A} + \frac{(1+A)H^2}{5} - A^2 = 0. \quad (\text{A.9})$$

where

$$u = \frac{CA}{1+A} \quad (\text{A.10})$$

$$H = -\frac{C}{1+A} + \sqrt{C^2 - 2A}$$

and where C and A are the normalized speed and amplitude. The above results are plotted in Fig. 16. It is of interest to note that in the speed-amplitude relation for L1 and L2 schemes two different speeds are present at an amplitude (note the dotted lines), or vice versa. Presumably this is due to the presence of waves other than the solitary waves. Fig. 16 also shows that the L1 (or L2) scheme gives the bounded amplitude and speed of permanent wave form with $A \approx 0.600$ (or 0.714) for the maximum amplitude, and $C^2 = 1.473$ (or 1.591) for the maximum speed.

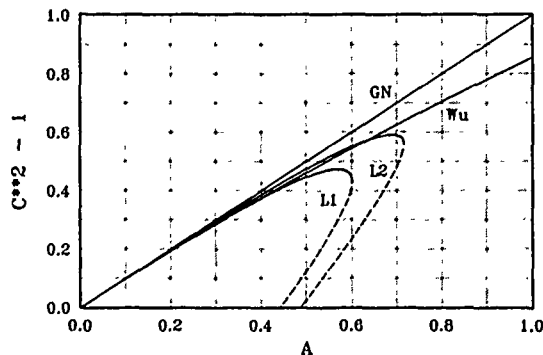


Fig. 16 Speed of the permanent wave form in various schemes.

DISCUSSION

by R.C. Ertekin

I think this paper presents an excellent example of how micro computers can be effectively utilized to solve complicated problems in time domain. Their method of solution to the problem is impressive. I would like to comment on some points in the paper.

The Green-Naghdi equations that you refer to are the simplest equations in a series of equations (or theories) that can be obtained by the Theory of Directed Fluid Sheets. Shields (Ph. D. Thesis, U. C. Berkely, 1985) have derived the theory II and III equations. Their derivations (with Prof. W. C. Webster), in some sense, resemble the Pohlhausen method in laminar boundary layer theory. I think the higher theory Green-Naghdi equations show double valued phase speed (your Fig.16) like L1 and L2. This double-value of c is not very surprising since the highest wave is not the fastest one as shown by Cokelet and Longuet-Higgins in a J. Fluid Mech. article in 70's. If you used a cubic interpolation function, I believe the maximum amplitude would become closer to $A \approx 0.78$ as shown by Fenton in also a JFM article who used a very high order perturbation expansion.

As you commented the Green-Naghdi equations can be obtained by variational methods. Solomon and Miles(1985) derived the G-N equations by using Hamilton's principle (J. Fluid Mechanics). I will be happy to furnish these references in a more complete form if you wish.

I am not sure that "dry mode" is a good

idea. I am not even sure that it happens in nature. We have experienced such difficulties also. By changing $x, \Delta y$ and Δt we solved the problem. If you reduce your space and time increments your problem of stability may disappear.

In free oscillation tests (Fig.4), the oscillations in the trailing part of the waves are perhaps partially numerical. I remember the thesis of H. Schember (Cal. Inst. of Technology, Ph. D. thesis, 1982) who studied a similar problem on these oscillations.

Author's Reply

Thank you for your nice comments. We have admired your pioneering research on the Green-Naghdi method applied to the nonlinear free-surface flow problems.

We were the comment on the dry mode, we partly agree with Professor Ertekin on the possibility of dry bottom due to the numerical instability. However, we have observed the dry bottom in the experiments when we moved a vertical flat plate in the direction normal to the plate and along the centerline of the tank in a shallow water in a wave tank (22cm X 20cm X 110cm). The dry bottom was possible in nature when the flat plate is moving so fast that the water behind cannot fill the empty space fast enough. Then there should be locally dry bottom in nature.

On the last comment about Fig.4 for the free oscillation test, we believe that the trailing part of the smaller waves is due to the dispersion of the initial free-surface elevation (hump) into waves of different wave numbers.

Numerical Grid Generation and Upstream Waves for Ships Moving in Restricted Waters

R. C. Ertekin and Z. -M. Qian
University of Hawaii
Honolulu, USA

Abstract

The shallow-water wave equations of Boussinesq type are employed to numerically solve the problem of a vertical strut moving in a channel. Since the most important parameter in soliton generation by moving disturbances is the blockage coefficient, a strut can be made equivalent to a finite draft ship. A boundary-fitted curvilinear coordinate system based on elliptic equations is generated to deal with the difficulties due to the body-boundary conditions in a channel containing an arbitrarily-shaped ship boundary which extends to sea floor. The strut problem is solved numerically in a transformed computational plane which contains uniform grid size. A finite-difference method is applied to the equations to march in time. The surface elevation and wave resistance are computed and compared with the available experimental data. The agreement between the calculations and experimental data is, in general, very good.

1. Introduction

The phenomenon of ship-generated solitons was rediscovered experimentally (see Huang et al. [12]) during the experiments done by Sibul et al. [28] on an unrelated subject. Huang et al. [12] observed that when a ship model is set into motion, starting from rest and quickly reaching a constant velocity, two-dimensional waves that precede the model are generated one after the other in addition to the usual three-dimensional waves behind the model. The waves that move ahead of the model were completely above the still water line and their speeds were critical or supercritical. These waves have been termed solitons or solitary waves which, unconventionally, refer to individual waves in a train of waves. The subcritical, critical and supercritical

wave speed refer to the depth Froude number, $F_h = U/\sqrt{gh}$, being less than, equal to and greater than 1.0, respectively, where U is the ship-model speed, g is the gravitational acceleration and h is the undisturbed water depth which is constant. No published mention of the phenomenon of ship-generated solitons could be found until the reports by Thews and Landweber [30], Sturtzel and Graff [29], and Graff [9] that describe the continuous solitary wave generation experimentally were brought to attention in 1984.

Wu and Wu [35] reported first on some numerical calculations of a two-dimensional pressure distribution moving steadily over the water surface in which the same phenomenon of soliton generation was predicted. These calculations were based on generalized Boussinesq equations derived earlier by Wu [34]. Some of the calculations were also reported in Huang et al. [13].

The most striking feature of these nonlinear waves is that they are almost perfectly two-dimensional, spanning the tank walls, even though the generating source is a three-dimensional ship model. Only a few qualitative features of these solitons could be observed during the experiments of Huang et al. [12] since the experiments were not systematic. Ertekin [3] carried out a series of experiments in which certain parameters such as water depth, model draft and tank width were changed systematically. During the experiments, a ship model (Series 60, Block 80) was towed along the centerline of the tank with a constant velocity. The total resistance experienced by the model and the run-away-soliton amplitudes were measured simultaneously in these experiments.

The experimental results of Ertekin [3] and Ertekin et al. [4] showed some very important qualities of the ship-generated solitons. Among several are: the dependence of soliton amplitudes on the blockage coefficient (the ratio of the cross-sectional area of the model at midships to the cross-sectional area of the water mass, see Eq. (3)); the phenomenon is not associated with equipment malfunctioning; at critical and supercritical speeds a steady-state flow cannot, in general, be obtained; below critical speed soliton amplitudes die out leaving a shelf in front of the ship model; and no solitons can be generated as blockage coefficient goes to zero. The last feature of the phenomenon implies that as the tank width or the water depth goes to infinity, no upstream waves can be generated. However, we note that a recent work by Pedersen [24] challenges this conjecture by an argument related to the existence of Mach stems as discussed in Ertekin [3].

Ertekin [3] also investigated the theoretical cases of a two-dimensional pressure distribution, and a two-dimensional bump on the sea floor moving with a constant velocity. Both the Green and Naghdi [10] equations for a thin fluid sheet (see also, Ertekin [6]), and the shallow-water equations derived by Wu [34] were used. Some of the results were included in Ertekin et al. [4]. Akylas [1] and Cole [2] have considered a two-dimensional bottom bump by using the Korteweg de Vries equation (KdV). Lee [16] and Lee et al. [17] considered a two-dimensional bottom bump both experimentally and numerically. Some of their preliminary results were included in the Discussion Section of Ertekin et al. [4].

First attempts to consider a three-dimensional disturbance in computations are due to Mei and Choi [18], Mei [19], Ertekin et al. [5] and Mei and Choi [20]. Mei [19] considered a vertical strut which is slender so that the rigid-boundary condition on the body can be applied at the center-line of the strut within the order of perturbation expansion. This approximation has resulted in two-dimensional waves in both the upstream and downstream regions since the modified KdV equation derived is two-dimensional only. A remark may be necessary with regard to the terminology used here for the number of dimensions. In three-dimensional Cartesian coordinates where x and y are in the horizontal still-water plane and z is vertical pointing up, we use the terminology two-dimensional for flows confined to the x - y plane and three-dimensional for flows confined to

both the x - z plane and the x - y plane even though some flow quantities, such as the velocity potential, do not depend on the vertical coordinate z because of the mean-layer approximation. Going back to the discussion on Mei's results, we note that the two-dimensionality of downstream waves as calculated by Mei [19] was not observed, in general, in the experiments of Ertekin [3].

Ertekin et al. [5] considered a three-dimensional pressure distribution and solved the Green-Naghdi (G-N) equations in the time domain. The solution of this nonlinear initial-boundary-value problem also showed three-dimensional downstream waves, qualitatively agreeing with the experimental results. This confirmed that the application of Mei's formulation has a limited range, at least, as far as the downstream waves are concerned. The wave resistance is also found to be in qualitative agreement with the experimental data. More recently, Katsis and Akylas [14] and Wu and Wu [36] obtained results for a three-dimensional moving surface-pressure distribution by using forced nonlinear Kadomtsev-Petviashvili (K-P) and generalized Boussinesq (gB) equations, respectively. The stability of the forced KdV equation as it relates to run-away solitons is investigated by Wu [37].

In the present study, we investigate the nonlinear waves generated by a vertical strut by using the generalized Boussinesq equations as derived by Wu [34]. The no-flux boundary condition is satisfied by means of a numerical grid-generation technique (see for instance, Thompson et al. [31]). The nonlinear and unsteady results are directly compared with the experimental data. In Section 2, we formulate the fluid-dynamics problem to be solved with all the boundary and initial conditions to be satisfied. We also transform the equations from earth-bound coordinates to moving coordinates in this Section. In Section 3, the numerical grid-generation technique used is discussed and the equations of Section 2 are transformed to a regular rectangular computational domain. In Section 4, the numerical-solution method is given and wave resistance experienced by the strut is discussed. The finite-difference method employed is presented and sample results are shown. Preliminary results are also given in Ertekin and Qian [8], and the detailed derivations of the equations presented here and some other results can be found in Qian [25], and Ertekin and Qian [7].

2. Formulation of the problem

In order to clarify the physical problem let us consider Fig. 1. This shows a ship model moving along the centerline of a shallow-water channel. The dimensionless speed of the ship-model is given by the depth Froude number, F_h , which is not necessarily critical. The boundaries consist of the tank walls, the center-plane symmetry axis if only half of the physical region is to be considered due to symmetry (mirror-image problem), the two inlet and outlet boundaries (or "open" boundaries) ahead of and behind the model, and the no-flux condition on the model. The channel floor and the free-surface boundary conditions are not discussed since these are either exactly (in the case of G-N equations) or approximately (in the case of gB, KdV or K-P type equations) satisfied by the particle velocity vector. Then the problem can be solved by using a nonlinear and unsteady shallow-water wave equation to obtain the unknown particle velocities created by the movement of the model. One can use neither linear nor steady-state equations because of the nature of the phenomenon. In fact, it can be shown (Ertekin [3]), perhaps unsurprisingly, that the steady form of the gB equations used in this study predicts no disturbance in the upstream region. The same is true for other shallow-water wave equations.

2.1 Boussinesq equations

The two different sets of shallow-water equations that have been applied frequently to soliton-generation problems in the past, namely the Green-Naghdi equations and the generalized Boussinesq equations, have both advantages and disadvantages compared with the other. Even though the derivation of both of these equations can start with the assumption that the fluid is incompressible and inviscid, only the gB equations require that the flow be irrotational. This feature of the gB equations allows one to consider the layer mean value of the velocity potential and the surface elevation as the unknowns to be determined. On the other hand, such a potential does not exist in the case of the G-N equations since the flow is, in general, rotational. As a consequence, the G-N equations are expressed in terms of the unknown velocity components and the surface elevation. The apparent advantages of the G-N equations over the gB equations were discussed in Ertekin et al. [4, 5]. In a three-dimensional problem with a large domain, the gB equations are more efficient to solve computationally. Therefore, we choose

to solve the following set of gB equations for a constant water depth and zero atmospheric pressure (Wu [34]):

$$\zeta_o + \bar{\nabla} \cdot \{ (h + \zeta_o) \bar{\nabla} \phi_o \} = 0, \quad (1)$$

$$\phi_o + \frac{1}{2} |\bar{\nabla} \phi_o|^2 + g \zeta_o - \frac{h^2}{3} \nabla^2 \phi_o = 0, \quad (2)$$

where (x^o, y^o) are the coordinates of the fixed coordinate system in which x^o specifies the direction opposite to the movement of the ship, ζ_o is the surface elevation of the wave, ϕ_o is the layer mean value of the velocity potential defined by $\bar{u}^o = \bar{\nabla} \phi_o$ in which $\bar{u}^o = (u^o, v^o)$, h is the undisturbed water depth (constant) of the channel and $\bar{\nabla}$ is the two-dimensional gradient vector in the horizontal plane. Eqs. (1) and (2) are the statements of conservation of mass and momentum, respectively.

The general form of these equations in which the sea floor topography may depend on the x^o, y^o coordinates and time t^o were obtained under the assumption that the Ursell number is of order unity (Ursell [32]). However, they seem to be valid in a wide range of Ursell numbers as shown by Lee [16]. The velocity potential and the surface elevation in these equations depend on x^o, y^o and t^o . These equations satisfy approximately the nonlinear free-surface condition and the sea-floor condition. The configuration of the physical region is shown in Fig. 2.

Before elaborating on the boundary conditions and initial conditions to be satisfied, we need to justify the use of a vertical strut to model the conditions of the experiments done by Ertekin [3]. In those experiments, the tank width, the model draft and the water depth were systematically changed to obtain 27 different blockage coefficients, S_b :

$$S_b = \frac{A_o}{2Wh}, \quad (3)$$

where A_o is the cross-sectional area of the underwater portion of the full model at midships at a given draft and W is the half-width of the tank. Also, F_h is varied to cover the range of 0.5-1.3. The most striking finding of these experiments was the dependence of the soliton amplitude, speed and the period of generation (the time that it takes for the second soliton to generate) on the blockage coefficient, S_b . Typical experimental results have been given in Ertekin et al. [4]. Therefore, it is clear that one can use a vertical strut

to model the same conditions which existed during the experiments, i.e., hull form is of secondary importance.

Now, we can go back to the discussion of the boundary conditions and initial conditions. Because we assume that (see Fig. 2) AO and BC are part of the symmetry axis, only half of the physical domain needs to be considered. The computational advantage of this scheme is obvious. We then have the following boundary conditions. On the symmetry axis AO and BC, and the channel wall DE, the no-flux condition is

$$\phi_{y^0}^0 = 0. \quad (4)$$

On the ship boundary, which is moving in the negative x^0 direction, we have

$$\phi_{x^0}^0 n_{x^0} + \phi_{y^0}^0 n_{y^0} = -U^0 n_{x^0}, \quad (5)$$

where U^0 is the speed of the moving boundary and $\vec{n} = (n_{x^0}, n_{y^0})$ is the unit normal vector of the ship boundary pointing into the fluid. On the upstream and downstream open boundaries, we use Sommerfeld's radiation condition with constant shallow-water wave celerity, i.e.,

$$\zeta_{x^0}^0 \mp \sqrt{gh} \zeta_{x^0}^0 = 0, \quad (6)$$

$$\phi_{x^0}^0 \mp \sqrt{gh} \phi_{x^0}^0 = 0$$

on EO (-) and CD (+). The initial conditions are chosen such that there is no motion at time $t=0^-$:

$$\zeta^0 = 0, \quad \phi^0 = 0, \quad (7)$$

for all x^0 and y^0 . The governing equations (1) and (2) will be solved subject to the boundary and initial conditions (4)-(7).

Since we will use a numerical grid-generation technique to map the physical plane onto a regular rectangular computational plane to avoid interpolations as much as possible in satisfying the body-boundary condition, we must first transform the gB equations and the boundary and initial conditions to a moving coordinate system as shown in Fig. 3.

2.2 Equations in moving coordinates

The equations of last section will be transformed from the fixed coordinate

system (x^0, y^0) to the left moving coordinate system (x', y') whose velocity is $-U^0$. Since

$$t^0 = t', \quad x^0 = x' - U^0 t^0, \quad y^0 = y', \quad (8)$$

the continuity equation (1) becomes

$$\zeta_t' + \vec{\nabla} \cdot [(\zeta' + h) \vec{\nabla} \phi'] = 0, \quad (9)$$

and the momentum equation (2) becomes

$$\phi_t' + \frac{1}{2}(\phi_{x'}^2 + \phi_{y'}^2 - U^{02}) + g\zeta' = \frac{h^2}{3}(\nabla^2 \phi_t' + U^0 \nabla^2 \phi_{x'}'). \quad (10)$$

Referring to Figs. 2 and 3, the boundary conditions and the initial conditions become

$$\phi_{y'}' = 0 \quad \text{on AO, BC and DE}, \quad (11)$$

$$\phi_{x'}' n_{x'} + \phi_{y'}' n_{y'} = 0 \quad \text{on AB}, \quad (12)$$

$$\zeta_t' + (U^0 \mp \sqrt{gh}) \zeta_{x'}' = 0, \quad (13)$$

$$\phi_t' + (U^0 \mp \sqrt{gh})(\phi_{x'}' - U^0) = 0,$$

on EO (-) and CD (+), and

$$\zeta' = 0, \quad \phi' = U^0 x', \quad \text{at } t=0^-. \quad (14)$$

Next, we nondimensionalize these equations in the moving coordinates by the new dimensionless variables given by

$$x = \frac{x'}{h}, \quad y = \frac{y'}{h}, \quad \zeta = \frac{\zeta'}{h}, \quad (15)$$

$$t = \frac{t'}{h} \sqrt{gh}, \quad U = \frac{U^0}{\sqrt{gh}}, \quad \phi = \frac{\phi'}{h\sqrt{gh}}.$$

The dimensionless forms of the continuity and momentum equations then become

$$\zeta_t + \vec{\nabla} \cdot [(1 + \zeta) \vec{\nabla} \phi] = 0, \quad (16)$$

$$\phi_t + \frac{1}{2}(\phi_x^2 + \phi_y^2 - U^2) + \zeta = \frac{1}{3}(\nabla^2 \phi_t + U \nabla^2 \phi_x). \quad (17)$$

And the dimensionless boundary and initial conditions (11)-(14) become

$$\phi_y = 0 \quad \text{on AO, BC and DE}, \quad (18)$$

$$\phi_x n_x + \phi_y n_y = 0 \quad \text{on AB}, \quad (19)$$

$$\zeta_t + (U \mp 1)\zeta_x = 0,$$

(20)

$$\phi_t + (U \mp 1)(\phi_x - U) = 0,$$

on EO (-) and CD (+), and

$$\zeta = 0, \phi = Ux, \text{ at } t = 0^+.$$

(21)

Eqs. (16)-(21) will be solved by a finite-difference method. Because we are dealing with a simply connected region which has a non-rectangular boundary in the plan view of the ship, it is preferable to use boundary-conforming coordinates in the fluid domain. In the next Section, we will describe the numerical generation of these boundary-conforming coordinates and transform the governing equations from the physical moving-plane onto a rectangular plane where a finite-difference method can be easily used within a uniform rectangular grid.

3. Numerical grid-generation

When there are irregular boundaries in a fluid domain, one can use several discretization schemes in a finite-difference method. One of them is the "irregular-star" technique which has been used for some time in ship-wave problems (see for instance, Ohring and Telste [22]), and another is the "staggered-mesh" system used by Miyata et al. [21] in a marker-and-cell method. Yet, another method suitable for the present problem is the numerical generation of boundary-conforming coordinates (see for instance, Thompson et al. [31]). In the first two schemes mentioned above, the difficulties in dealing with an irregular boundary are: the use of unequal grid size in different regions of the computational domain which brings additional complexities and inaccuracies, the heavy use of various interpolation techniques on irregular boundaries for the evaluation of the higher-order derivatives of a function being solved for, and as a consequence, the need to use very small grid size which results in an increased computational time, and finally, serious questions concerning the assumption of the existence of a function being extrapolated outside the fluid domain. The last difficulty is again related to irregular boundaries. These difficulties do not exist if one uses a numerically generated grid along with a finite-difference method. However, due to the addition of extra terms in the governing equations, numerical calculations become more complicated and intensive when one transforms the

equations from a physical plane to a rectangular computational plane with a uniform grid.

Depending on the boundary conditions, one can use several different grid-generation systems, such as the elliptic, parabolic, hyperbolic or algebraic generation systems. An elliptic generation system may be chosen in our case since Dirichlet boundary conditions are specified on all the boundaries enclosing the simply-connected physical region. The Dirichlet conditions are simply the boundary coordinates given in the physical problem.

3.1 Elliptic Generation System

Referring to Fig. 4, a uniform grid in the transformed plane can be generated by determining the coordinates $x(\xi, \eta)$ and $y(\xi, \eta)$, for $\Delta\xi = \Delta\eta = 1.0$. Because of the fact that the extrema of solutions of an elliptic system cannot occur inside the boundaries, one-to-one correspondence between points of the respective planes is guaranteed. This, of course, also ensures the single-valuedness of the coordinate functions. Then the equations of the elliptic generation system given by

$$\nabla^2 \xi = 0, \nabla^2 \eta = 0,$$

can be replaced by a set of nonlinear equations in terms of x and y to be solved in the transformed plane:

$$\alpha x_{\xi\xi} - 2\beta x_{\xi\eta} + \gamma x_{\eta\eta} = 0, \quad (22)$$

$$\alpha y_{\xi\xi} - 2\beta y_{\xi\eta} + \gamma y_{\eta\eta} = 0,$$

where

$$\alpha = x_\eta^2 + y_\eta^2, \beta = x_\xi x_\eta + y_\xi y_\eta, \gamma = x_\xi^2 + y_\xi^2. \quad (23)$$

The above equations can be solved by a finite-difference method based on second-order central-difference formulas, i.e.,

$$\alpha(x_{j+1,i} - 2x_{j,i} + x_{j-1,i}) - \frac{\beta}{2}(x_{j+1,i+1} - x_{j-1,i+1} - x_{j+1,i-1} + x_{j-1,i-1}) + \gamma(x_{j,i+1} - 2x_{j,i} + x_{j,i-1}) = 0, \quad (24)$$

and

$$\alpha(y_{j+1,i} - 2y_{j,i} + y_{j-1,i}) - \frac{\beta}{2}(y_{j+1,i+1} - y_{j-1,i+1} - y_{j+1,i-1} + y_{j-1,i-1}) + \gamma(y_{j,i+1} - 2y_{j,i} + y_{j,i-1}) = 0. \quad (25)$$

This results in a system of nonlinear

equations which we solve by a Successive Over Relaxation (SOR) method. The solution is accomplished by a point iteration in which the initial guess is chosen as a weighted average of the boundary points. The boundary values of x and y in the physical plane are specified. A typical result for a parabolic strut whose dimensionless equation is given by

$$y = 2A_w \left(1 - \frac{x}{L}\right) \frac{x}{L}, \quad (26)$$

where $A_w/2$ is the half-width of the strut and L is the length of the strut, is shown in Fig. 5. In this Figure $A_w/2 = 0.3$, $L = 8.0$, $S_p = 7.5\%$, and $\Delta x = \Delta y = 0.1$. However, only every fifth grid line is plotted for clarity.

The accuracy of the elliptic generation system used here has been checked against a simple ideal flow problem (doublet + uniform flow) which has an exact solution, and found to agree within a tolerance of 1×10^{-8} . We note that $x = \text{constant}$ lines and $\xi = \text{constant}$ lines coincide in their respective planes, and as a result, no coordinate contraction has been used. The purpose of this scheme is to preserve the symmetry boundary AO and BC. If we had allowed x to depend upon η also, then we would have had to solve the problem in the entire physical region, not just in half of it. In that case, the boundary points would not have been uniform.

3.2 Governing equations in the transformed plane

The purpose of transforming the equations from an earth-bound system to a moving system was to avoid the generation of a numerical grid at each time step, thereby not allowing the time derivatives to produce extra terms. If we now apply the differential relations between the derivatives of a function in (x, y) and (ξ, η) planes (see, Thompson et al. [31]), the continuity equation (16) becomes

$$\zeta_t = H, \quad (27)$$

where

$$H = -(\zeta + 1) \nabla^2 \phi - \nabla \zeta \cdot \nabla \phi$$

$$= -\frac{1}{J^2} (\zeta + 1) (\alpha \phi_{\xi\xi} - 2\beta \phi_{\xi\eta} + \gamma \phi_{\eta\eta}) -$$

$$\frac{1}{J^2} (y_\eta \phi_\xi - y_\xi \phi_\eta) (y_\eta \zeta_\xi - y_\xi \zeta_\eta) +$$

$$\frac{1}{J^2} (x_\eta \phi_\xi - x_\xi \phi_\eta) (-x_\eta \zeta_\xi + x_\xi \zeta_\eta),$$

and the Jacobian, J , of the transformation is $J = x_\xi y_\eta - x_\eta y_\xi$. Note that even though the general formulas are given here, x depends on ξ alone since $y = \text{constant}$ and $\eta = \text{constant}$ are parallel everywhere.

Similarly, the momentum equation (17) becomes

$$\phi_t + A \phi_{\xi\xi} + B \phi_{\xi\eta} + C \phi_{\eta\eta} = Q, \quad (28)$$

where

$$A = -\frac{\alpha}{3J^2}, \quad B = \frac{2\beta}{3J^2}, \quad C = -\frac{\gamma}{3J^2},$$

$$Q = -\zeta - \frac{1}{2} (\phi_x^2 + \phi_y^2 - U^2) + \frac{1}{3} U \nabla^2 \phi_x = -\zeta -$$

$$\frac{1}{2} \left\{ \left(\frac{y_\eta \phi_\xi - y_\xi \phi_\eta}{J} \right)^2 + \left(\frac{-x_\eta \phi_\xi + x_\xi \phi_\eta}{J} \right)^2 - U^2 \right\} + (A_1 \phi_{\xi\xi} +$$

$$B_1 \phi_{\xi\eta} + C_1 \phi_{\eta\eta} + D \phi_{\xi\xi\xi} + E \phi_{\xi\xi\eta} + F \phi_{\xi\eta\eta} + G \phi_{\eta\eta\eta}),$$

$$A_1 = \frac{2U}{3J^4} (JA_0 - J_0 \alpha), \quad B_1 = -\frac{2U}{3J^4} (JB_0 - 2J_0 \beta),$$

$$C_1 = \frac{2U}{3J^4} (JC_0 - J_0 \gamma), \quad D = \frac{U}{3J^3} y_\eta \alpha,$$

$$E = -\frac{U}{3J^3} (2y_\eta \beta + y_\xi \alpha),$$

$$F = \frac{U}{3J^3} (y_\eta \gamma + 2y_\xi \beta), \quad G = -\frac{U}{3J^3} y_\xi \gamma,$$

$$J_0 = J_\xi y_\eta - J_\eta y_\xi$$

$$= y_\eta^2 x_{\xi\xi} - 2y_\xi y_\eta x_{\xi\eta} + y_\xi^2 x_{\eta\eta} - x_\eta y_\eta y_{\xi\xi} +$$

$$(x_\xi y_\eta + x_\eta y_\xi) y_{\xi\eta} - x_\xi y_\xi y_{\eta\eta},$$

$$A_0 = \frac{1}{2} (y_\eta \alpha_\xi - y_\xi \alpha_\eta)$$

$$= x_\eta y_\eta x_{\xi\eta} - x_\eta y_\xi x_{\eta\eta} + y_\eta^2 y_{\xi\eta} - y_\eta y_\xi y_{\eta\eta},$$

$$B_0 = y_\eta \beta_\xi - y_\xi \beta_\eta = x_\eta y_\eta x_{\xi\xi} + (x_\xi y_\eta - x_\eta y_\xi) x_{\xi\eta} -$$

$$x_\xi y_\xi x_{\eta\eta} + y_\eta^2 y_{\xi\xi} - y_\xi^2 y_{\eta\eta},$$

$$C_0 = \frac{1}{2}(y_\eta y_\xi - y_\xi y_\eta)$$

$$= x_\xi y_\eta x_{\xi\xi} - x_\xi y_\xi x_{\xi\eta} + y_\xi y_\eta y_{\xi\xi} - y_\xi^2 y_{\xi\eta}.$$

And the dimensionless boundary and initial conditions (18)-(21) become as follows.

$$\phi_\eta = 0 \text{ on AO, BC and DE} \quad (29)$$

$$-\beta\phi_\xi + \gamma\phi_\eta = 0 \text{ on AB.} \quad (30)$$

$$\zeta_t = Z_{1,2}, \quad (31)$$

$$\phi_t = P_{1,2},$$

where

$$Z_{1,2} = -\frac{(U \mp 1)}{J}(y_\eta \zeta_\xi - y_\xi \zeta_\eta),$$

$$P_{1,2} = -(U \mp 1) \left\{ \frac{1}{J}(y_\eta \phi_\xi - y_\xi \phi_\eta) - U \right\},$$

on EO (subscript 1) and CD (subscript 2),

$$\zeta = 0, \quad \phi = Ux(\xi), \text{ at } t=0^-. \quad (32)$$

As before, the subscripts ξ and η denote the derivatives with respect to these variables. We are now ready to solve equations (27) and (28) subject to the boundary conditions (29)-(32).

4. Numerical solution of gB equations and wave resistance

In this Section, we present the method employed to solve the nonlinear and unsteady shallow-water equations as given in the last Section, and also, give the formulation for wave resistance. Some of the results obtained will be presented and compared directly with the available experimental data. The accuracy of the equations and the numerical method will be revealed when we discuss the speed, amplitude and the period of generation of solitons, and wave resistance.

4.1 Finite-difference method

Because of the success of the Modified Euler Method in previous applications, we use this two-step method to march in time. The spatial derivatives are approximated by second-order central-difference formulas. The truncation error of the resulting equations is $O(\Delta x^2, \Delta y^2, \Delta t^2)$. In this method, the values of ζ and ϕ at the

present time step, indicated by the superscript (2), may be obtained by modifying the values obtained in the middle step, indicated by the superscript (m). The middle-step values are evaluated by modifying the previous-time-step values, indicated by the superscript (1).

With these preliminaries, the continuity equation (27) becomes

$$\zeta^{(m)} = \zeta^{(1)} + \Delta t H^{(1)}, \quad (33)$$

$$\zeta^{(2)} = \zeta^{(1)} + \frac{\Delta t}{2}(H^{(1)} + H^{(m)}), \quad (34)$$

where Δt is the time interval and H was given by (27). Similarly the momentum equation (28) becomes

$$\begin{aligned} \phi^{(m)} + A\phi_{\xi\xi}^{(m)} + B\phi_{\xi\eta}^{(m)} + C\phi_{\eta\eta}^{(m)} = \\ \phi^{(1)} + A\phi_{\xi\xi}^{(1)} + B\phi_{\xi\eta}^{(1)} + C\phi_{\eta\eta}^{(1)} + \Delta t Q^{(1)}, \end{aligned} \quad (35)$$

$$\begin{aligned} \phi^{(2)} + A\phi_{\xi\xi}^{(2)} + B\phi_{\xi\eta}^{(2)} + C\phi_{\eta\eta}^{(2)} = \phi^{(1)} + A\phi_{\xi\xi}^{(1)} + \\ B\phi_{\xi\eta}^{(2)} + C\phi_{\eta\eta}^{(2)} + \frac{\Delta t}{2}(Q^{(1)} + Q^{(m)}), \end{aligned} \quad (36)$$

where A , B , C and Q were defined by (28).

The upstream and downstream open-boundary conditions become

$$\zeta^{(m)} = \zeta^{(1)} + \Delta t Z_{1,2}^{(1)}, \quad (37)$$

$$\zeta^{(2)} = \zeta^{(1)} + \frac{\Delta t}{2}(Z_{1,2}^{(1)} + Z_{1,2}^{(m)}), \quad (38)$$

$$\phi^{(m)} = \phi^{(1)} + \Delta t P_{1,2}^{(1)}, \quad (39)$$

$$\phi^{(2)} = \phi^{(1)} + \frac{\Delta t}{2}(P_{1,2}^{(1)} + P_{1,2}^{(m)}). \quad (40)$$

The right-hand-side terms of these equations are calculated from the previous time step, and then considered as known variables in the present time step. During each time step, ζ can be directly solved from (33) for the middle step, and from (34) for the present step. ζ and ϕ can also be found directly on the open boundaries from (37) and (39) for the middle step, and from (38) and (40) for the present step as the solution of the initial-value problem. ϕ will then be determined iteratively from (35) for the middle step, and from (36) for the present step as the solution of the boundary-value problem.

As in the case of the numerical grid generation, we use the SOR method to solve the set of simultaneous equations which resulted by the application of the Modified Euler Method. A five-point filtering formula (see Shapiro [27],

Haussling [11], and Ertekin et al. [5]) is applied to reduce the effect of the numerical errors which are caused by high-frequency cross-channel waves. ξ and ϕ are filtered in the ξ and η directions in the transformed plane after each time step. The SOR parameter varied between 1.5 and 1.9 in our calculations.

4.2 Wave resistance

The wave resistance, R , experienced by the vertical strut can be obtained by evaluating the pressure, p_g , on the strut, i.e.

$$C_R(t) = \frac{R(t)}{\rho g h^3} = 2 \int_0^L \left\{ \int_{-h}^t p_g dz \right\} y_x dx. \quad (41)$$

The pressure on the strut can be obtained from Euler's integral once the velocity potential and the surface elevation are determined. Following Wu [34] and Wang et al. [33], we obtain

$$\int_{-h}^t p_g dz = \frac{1}{2} (1 + \xi) \{ 1 + \xi + (\xi^2 + 2\xi - 2) \left(\phi_t + \frac{1}{2} (\phi_x^2 + \phi_y^2 - U^2) + \xi \right) \}, \quad (42)$$

in the moving coordinates. Equation (42) is obtained by expanding the pressure in a perturbation series where the error term is $O(\epsilon^5)$, and ϵ is the dispersion parameter. One can now substitute (42) into (41) and obtain the wave resistance as a function of time after transforming the variables from the (x, y) system to (ξ, η) system.

4.3 Discussion on the numerical accuracy and results

When the water depth, h , is constant, the conservation of mass statement given by (1) is exact. Therefore, this equation can serve as a check on the numerical accuracy of the results. We note that the same argument cannot be made by using the conservation of linear momentum statement given by (2) since this equation is approximate. The dimensionless water mass, $m/\rho h^3$, given by

$$\int_{A_{\xi\eta}} (1 + \xi) J dA_{\xi\eta} + \int_0^t \left\{ \int_{l_L} S d\eta - \int_{l_R} S d\eta \right\} dt, \quad (43)$$

where

$$S(\xi, \eta, t) = \frac{\sqrt{a}}{J} (1 + \xi) (y_\eta \phi_\xi - y_\xi \phi_\eta),$$

and l_L, l_R represent the left and the right open boundaries, respectively, and

$A_{\xi\eta}$ denotes the surface of the computational region, remains constant within 1%, showing that numerical accuracy is very high.

The gB equations are solved by a computer program which uses the grid points generated by another computer program. Two sets of numerical tests are conducted and the parameters of the problem are selected to approximately correspond to the experiments done by Ertekin [3].

In the first set of the numerical tests, two different blockage coefficients, 7.5% and 12.5%, are selected. The grid size on boundaries is chosen as $\Delta x = \Delta y = 0.1$, and the time interval is chosen as $\Delta t = 0.05$ even though Von Neumann's stability method applied shows that Δt can be the same as Δx without any stability problems. Two different speeds, $F_h = U = 0.9$ and 1.0 , are used so that precursor solitons can be generated quickly. The perspective plots (see Fig. 6 a,b) as well as the contour plots (see Fig. 7 a,b) are shown here for Case 3. For other results see Qian [25]. In perspective plots the strut below the lowest wave surface could not be plotted because of the limitation of the graphics software that we used. The period between the first and second soliton or the period of generation, the amplitude and the speed of the first and second solitons are calculated (see Tables 1-3). The period of generation is obtained from the numerical moving-gauge results as shown in Fig. 8 (continuous lines). In Fig. 8 the location of the numerical gauges are at distances of $0.625L$ (Gauge 2) and L (Gauge 3) ahead of the strut on the symmetry axis. Note that in the first set of numerical tests (Cases 1, 2 and 3), $W=4$, $L=8$ and $l_R - l_L = 64$. Comparisons with the experiments (Ertekin [3] and Ertekin et al. [4]) are also made in Tables 1-3.

To understand the effect of ship length on the computational results, we conducted another numerical test by increasing the ship length to 15.2 but leaving all other parameters of the problem the same. This test is referred to as Case 4. Case 4 results are shown in Figs. 6 c,d and 7 c,d, and in Fig. 8 (dotted lines). As can be seen from these Figures, shorter strut has considerably more wave build-up around the bow and stern than the longer strut, and also, the downstream waves are smaller in the longer strut case. From Fig. 8 we see that it takes longer to generate the first soliton in the longer strut case than the shorter strut case. Also the amplitude of the first soliton is smaller, and the amplitude of the

second soliton is larger in Case 4 compared with Case 3 (see also, Tables 1-3).

In the second set of numerical tests, we used exactly the same $S_b=14.2$, $W=6.1$ and $L=15.2$ used in one set of the experiments of Ertekin [3]. In the experiments, $h=10$ cm, $d=7.5$ cm and $F_h=1.0$ were used (Test No. 1936). The location of the moving gauges were given in Ertekin et al. [4]. This numerical test is called Case 5. In Case 5, $\Delta x=\Delta y=0.15$ and $\Delta t=0.08$ are used since the computational region is larger than before. Also $l_R-l_L=137.25$ in this case. The perspective plots of Case 5 results are shown in Fig. 9, and the contour plots in Fig. 10. The numerical wave-gauge results and the wave resistance results are shown in Fig. 11. The corresponding experimental results are shown in Fig. 12. The numerical results in Fig. 11 are shifted in time so that the moment the towing carriage started moving in Fig. 12 (see the sudden increase in resistance at $t=2.5$ s) corresponds to $t=0$ s in calculations. This shift in time in experiments is due to starting data acquisition before the carriage is put into motion. The quantitative differences between the experiments and calculations in Case 5 are given in Tables 1-3. The agreement can be considered quite good.

The average total resistance measured during the experiments was 9.3 newtons for Case 5. In the calculations the average wave resistance is obtained as 9.6 newtons. We estimate the frictional resistance as 1.4 newtons from Schoenherr's flat plate skin friction formula. Of course, the eddy or form resistance must be included also. Thus, one can conclude that the total resistance predicted is slightly higher than the experimental datum. Some other cases which are not presented here also support this conclusion.

In conjunction with the numerical schemes used in this study, we mention that the surface elevation and the velocity potential are filtered along both the ξ and η directions at each time step. The average number of iterations is 15 for the first-step solution (for a tolerance of 8×10^{-7}) and 6 for the modified or second-step solution (for a tolerance of 5×10^{-7}). The computations, which were performed on the X-MP/48 Cray Computer of the San Diego Supercomputer center, took about 90 minutes of CPU time for 2200 time steps in Case 3. Single precision is used on this 64 bit machine. Filtering was absolutely necessary in our calculations. Removal of the filtering scheme caused very high waves at the

stern, and eventually, the computations could not be continued. The unphysical waves in the absence of filtering occurred for various grid sizes and time intervals.

From the results presented here, we see that general appearance of the waves agree with the results of earlier research (e.g., Huang et al. [13], Ertekin [3], and Ertekin et al. [5]). For each soliton, including the first and the second one in all cases, the amplitude increases rapidly while the speed increases. The relation between the amplitude and speed of the solitons (computed) satisfies approximately the dispersion relation for a general two dimensional soliton propagation, such as the second-order formula proposed by Laitone [15], and a formula derived by Schemmer [26]. However, solitons generated by ships do not have an exact permanent form. The amplitude of each soliton gradually increases after generation. This, of course, may be partially due to the governing equations which satisfy the free-surface conditions only approximately. Also, the rather small differences between the computations and experiments may be also due to the neglect of viscosity (although this effect must be very small), and, of course, computational as well as experimental errors, especially in the case of period of soliton-generation.

The soliton generation clearly depends on the blockage coefficient and speed of the moving strut, but it also slightly depends on the length of the strut. An increase in the Froude number, or the speed of the ship, can delay the generation of the first soliton, and thus increase the period between the first and second solitons. Soliton amplitudes and speeds increase correspondingly. Fast movement of the disturbance increases the period of soliton generation and larger blockage coefficient decreases the period of soliton generation. The second soliton almost always comes out with a smaller amplitude and speed than the first soliton. As can be seen in Table 2, the agreement between the experiments and computations for the amplitude and speed of the second soliton is very good.

5. Conclusions

The waves generated by a ship in a shallow-water channel can be modeled by numerical calculations of Boussinesq equations, and two-dimensional solitons may be generated ahead of the ship. The shallow-water equations of gB type can successfully simulate this phenomenon. The generation of a boundary-fitted curvilinear coordinate system is very

effective for the configuration containing the ship boundary. The physical problem is solved in the transformed plane with a uniform grid size. The boundary conditions, especially on the ship boundary, can be satisfied without the need for a special treatment of the boundary values. However, all equations become more complicated after the transformation, and thus computations become much more intensive. Since the grid size is chosen to be uniform on the physical boundaries, equal ξ lines become straight and are perpendicular to the symmetry boundary and wall boundary. On the symmetry boundary and wall boundary, the no-flux boundary condition can be simplified, and also the symmetry condition can be used to deal with the third-order derivatives. If we use coordinate system control (attraction) for the grid generation, the grid lines will not be generally straight, and the no-flux boundary condition will become more complicated on all solid boundaries, and also, no symmetry condition can be used.

The constant wave celerity used on the open boundaries work out perfectly. Therefore, it seems that one cannot easily justify the use of a numerical scheme in which the phase speed is calculated (see for instance, Orlanski [23]).

More efficient methods of numerical grid generation can be investigated and used with three-dimensional ship surfaces to reduce the errors introduced by numerical grid generation. Coordinate-system control is recommended in order that the coordinate lines can be attracted by the boundaries, especially around the ship boundary, so that the boundary effects can be considered more accurately. This obviously requires that we can deal successfully with the higher-order derivatives on the boundaries. Nevertheless, the symmetry boundaries will be destroyed in this case, causing the necessity to solve the problem in the entire physical domain.

Acknowledgements

We are grateful to Prof. John V. Wehausen for his invaluable comments throughout this research. Our appreciation also goes to Prof. Theodore Y.-T. Wu who made a very timely comment on the resistance formulation. We would like to thank the International Business Machines Corporation for providing the computer equipment used in this study. This material is based upon work supported by the National Science Foundation under Grant Numbers

MSM-8706910 and BCS-8958346. The computer time was provided under Account Numbers 941 HAW and 234 HAW awarded by the San Diego Supercomputer Center.

References

1. Akylas, T.R., "On the Excitation of Long Nonlinear Water Waves by a Moving Pressure Distribution," *J. of Fluid Mech.*, Vol. 141, pp. 455-466, 1984.
2. Cole, S.L., "Transient Waves Produced by Flow Past a Bump," *Wave Motion*, Vol. 7, pp. 579-587, 1985.
3. Ertekin, R.C., "Soliton Generation by Moving Disturbances in Shallow Water: Theory, Computation and Experiment," Ph.D. Thesis, University of California, Berkeley, 1984.
4. Ertekin, R.C.; Webster, W.C. and Wehausen, J.V., "Ship-Generated Solitons," *Proc. 15th. Symposium on Naval Hydrodynamics*, Hamburg, pp. 347-361; Disc. pp. 361-364, 1984, (ONR, National Academy Press, Washington, D.C., 1985).
5. Ertekin, R.C.; Webster, W.C. and Wehausen, J.V., "Waves Caused by a Moving Disturbance in a Shallow Channel of Finite Width," *Journal of Fluid Mechanics*, Vol. 169, pp. 275-292, 1986.
6. Ertekin, R.C., "Nonlinear Shallow Water Waves: The Green-Naghdi Equations," *Proc. Pacific Congress on Marine Science and Technology*, PACON '88, Honolulu, Hawaii, May, pp. OST6/42 - OST6/52, 1988.
7. Ertekin, R.C. and Qian, Z.-M., "Soliton Generation and Ship Wave Resistance in Shallow Waters. Part I: Vertical Strut," *Univ. of Hawaii, Dept. of Ocean Engng., Report No. UHMOE-88101*, December, ii+50 pp., 1988.
8. Ertekin, R.C. and Qian, Z.-M., "Solitary Waves Generated by Ships in Restricted Waters," *The 4th. Asian Congress of Fluid Mechanics*, August, Hong Kong, 4 pp., 1989.
9. Graff, W., "Untersuchungen uber die Ausbildung des Wellenwiderstandes im Bereich der Stauwellengeschwindigkeit in flachem, seitlich beschränktem rahrwasser," *Shiffstechnik*, Vol. 9, pp. 110-122, 1962.
10. Green, A.E. and Naghdi, P.M., "A Derivation of Equations for Wave Propagation in Water of Variable Depth," *Journal of Fluid Mechanics*, Vol. 78, part 2, pp. 237-246, 1976.
11. Haussling, H.J., "Solution of nonlinear wave problems using boundary-fitted coordinate systems," In *Numerical Grid Generation* (Ed. J.F. Thompson), Elsevier Science Publishing Company, New York, pp. 385-407, 1982.

12. Huang, De-Bo; Sibul, O.J. and Wehausen, J.V., "Ships in Very Shallow Water," Festkolloquium - Dedicated to Professor Karl Wieghardt, March, Institut für Schiffbau der Universität Hamburg, 1982.
13. Huang, De-Bo; Sibul, O.J.; Webster, W.C.; Wehausen, J.V.; Wu, De-Ming and Wu, T.Y., "Ships Moving in the Transcritical Range," Proc. Conference on Behavior of Ships in Restricted Waters, November, Varna, Bulgaria, Vol. II, pp. 26-1 to 26-10, 1982.
14. Katsis, C. and Akylas, T.R., "On the Excitation of Long Nonlinear Water Waves by a Moving Pressure Distribution. Part 2: Three Dimensional Effects.," J. Fluid Mech., Vol. 177, pp. 49-65, 1987.
15. Laitone, E.V., "The Second Approximation to Cnoidal and Solitary Waves," J. Fluid Mech., Vol. 9, pp. 430-444, 1960.
16. Lee, S.-J., "Generation of Long Water Waves by Moving Disturbances," Ph.D. Thesis, California Institute of Technology, Pasadena, California, 1985.
17. Lee, S.-J.; Yates, G.T. and Wu, T.Y., "A Theoretical and Experimental Study of Precursor Solitary Waves Generated by Moving Disturbances," IUTAM Symp. on Nonlinear Water Waves, Tokyo, pp. 62-63, 1987.
18. Mei, C.C. and Choi, H.S., "Forces on a Slender Ship Advancing Near Critical Speed in a Shallow Channel," 4th. Int. Conf. on Numerical Ship Hydrodynamics, September, National Academy of Sciences, Washington, D.C., pp. 359-367, 1985.
19. Mei, C.C., "Radiation of Solitons by Slender Bodies Advancing in a Shallow Channel," J. of Fluid Mech., Vol. 162, pp. 53-67, 1986.
20. Mei, C.C. and Choi, H.S., "Forces on a Slender Ship Advancing Near the Critical Speed in a Wide Canal," J. Fluid Mech., Vol. 179, pp. 59-76, 1987.
21. Miyata, H.; Nishimura, S. and Masuko, A., "Finite Difference Simulation of Nonlinear Waves Generated by Ships of Arbitrary Three-Dimensional Configuration," J. of Comput. Phys., Vol. 60, pp. 391-436, 1985.
22. Ohring, S. and Telste, J., "Numerical Solutions of Transient Three-Dimensional Ship-Wave Problems," Proc. 2nd Int. Conf. on Numerical Ship Hydrodyn., Berkeley, pp. 88-103, 1977.
23. Orlanski, I., "A Simple Boundary Condition for Unbounded Hyperbolic Flows," J. Comput. Phys., Vol. 21, pp. 251-269, 1976.
24. Pedersen, G., "Three-dimensional Wave Patterns Generated by Moving Disturbances at Critical Speeds," J. Fluid Mech., Vol. 196, pp. 39-63, 1988.
25. Qian, Z.-M., "Numerical Grid Generation and Nonlinear Waves Generated by a Ship in a Shallow-Water Channel," M.S. Thesis, University of Hawaii at Manoa, Dept. of Ocean Engineering, x+121 pp., 1988.
26. Schemmer, H. R., "A New Model for Three-Dimensional Nonlinear Dispersive Long Waves," Ph.D. Dissertation, California Institute of Technology, Pasadena, California, 1982.
27. Shapiro, R., "Linear filtering," Maths. Comput. Vol. 29, pp. 1094-1097, 1975.
28. Sibul, O.J.; Webster, W.C. and Wehausen, J.V., "A Phenomenon Observed in Transient Testing," Schiffstechnik, Vol. 26, pp. 179-200, 1979.
29. Sturtzel, W. and Graff, W., "Untersuchungen der in stehendem und stromendem Wasser festgestellten Änderungen des Schiffswiderstandes durch Druckmessungen," Forschungsberichte des Wirtschafts- und Verkehrsministeriums Nordrhein-Westfalen, Nr. 618, 34 pp., 1958.
30. Thews, J.G. and Landweber, L., "The Influence of Shallow Water on the Resistance of a Cruiser Model," U.S. Experimental Model Basin, Navy Yard, Washington, D.C., Report No. 408, 1935.
31. Thompson, J.F.; Warsi, Z.U.A. and Mastin, C.W., "Numerical Grid Generation," Elsevier Sci. Pub. Co., New York, xv + 483 pp., 1985.
32. Ursell, F., "The Long Wave Paradox in the Theory of Gravity Waves," Proc. Camb. Phil. Soc., Vol. 49, pp. 685-694, 1953.
33. Wang, K.H.; Wu, T.Y. and Yates, G.T., "Scattering and Diffraction of Solitary Waves by a Vertical Cylinder," 17th. Symp. on Naval Hydrodyn., The Hague, The Netherlands, pp. 37-46, 1988.
34. Wu, T.Y., "Long Waves in Ocean and Coastal Waters," Journal of Engng. Mech. Div., ASCE, Vol. 107, No. EM3, Proc. Paper No. 16346, June pp. 501-522, 1981.
35. Wu, D.-M. and Wu, T.Y., "Three-Dimensional Nonlinear Long Waves Due to Moving Surface Pressure," Proc. 14th. Symposium on Naval Hydrodynamics, Ann Arbor, pp. 103-125, 1982, (ONR, National Academy Press, Washington, D.C., 1983).

36. Wu, D.-M. and Wu, T.Y., "Precursor Solitons Generated by Three-Dimensional Disturbances Moving in a Channel," IUTAM Symp. on Nonlinear Water Waves, Tokyo, pp.

18-19, 1987.
37. Wu, T.Y., "Generation of Upstream Advancing Solitons by Moving Disturbances," J. Fluid Mech., Vol. 184, pp. 75-99, 1987.

Case No.	$\frac{U}{\sqrt{gh}}$	S_b (%)	$\frac{\Lambda_s}{h}$			$\frac{U_s}{\sqrt{gh}}$		
			C	E	D (%)	C	E	D (%)
1	0.8	7.5	0.18	0.15	20.0	1.05	1.07	-1.9
2	1.0	7.5	0.54	0.50	8.0	1.20	1.22	-1.6
3	0.8	12.5	0.29	0.27	7.4	1.12	1.11	0.9
4	0.8	12.5	0.25	0.27	-7.4	1.12	1.11	0.9
5	1.0	14.2	0.70	0.62	12.9	1.27	1.23	3.2

Table 1. Dimensionless amplitude and speed of the first soliton.

Case No.	$\frac{U}{\sqrt{gh}}$	S_b (%)	$\frac{\Lambda_s}{h}$			$\frac{U_s}{\sqrt{gh}}$		
			C	E	D (%)	C	E	D (%)
1	0.8	7.5	0.11	0.12	-8.8	1.02	1.03	-1.0
2	1.0	7.5	0.50	0.49	2.0	1.20	1.18	1.7
3	0.8	12.5	0.21	0.23	-8.7	1.09	1.09	0.0
4	0.8	12.5	0.24	0.23	4.3	1.09	1.09	0.0
5	1.0	14.2	0.69	0.56	23.2	1.27	1.23	3.2

Table 2. Dimensionless amplitude and speed of the second soliton.

Notes on the Tables:

C : Present computational results,
E : Experimental data (Ertekin [3]),
D : Difference between the calculations and experimental data,
 S_b : Blockage coefficient,
h : Depth of undisturbed water,
g : Gravitational acceleration,
U : Speed of the ship,
 Λ_s : Amplitude of the first or second soliton,
 U_s : Speed of the first or second soliton in earth-bound coordinates,
 T_g : Period of generation of solitons.

Case No.	$\frac{U}{\sqrt{gh}}$	S_b (%)	$\frac{UT_g}{h}$		
			C	E	D (%)
1	0.8	7.5	31	34	-8.8
2	1.0	7.5	44	47	-6.4
3	0.8	12.5	21	23	-8.7
4	0.8	12.5	20	23	-13.1
5	1.0	14.2	27	33	-18.2

Table 3. Dimensionless period between the first and the second soliton as observed in the moving coordinates.

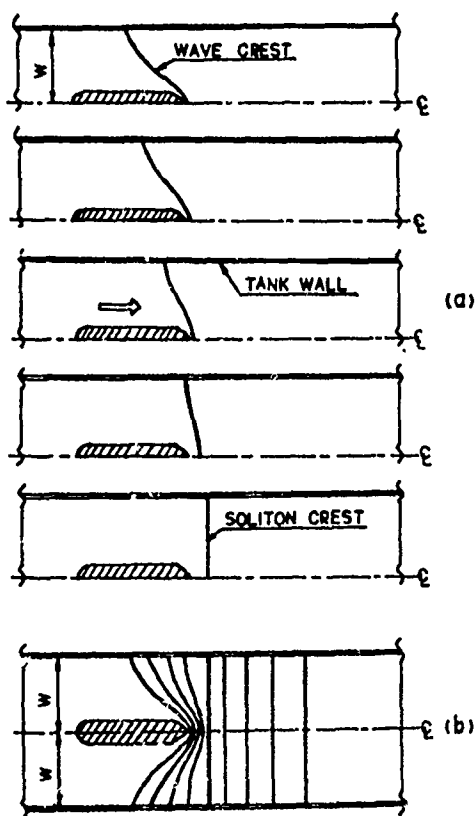


Figure 1. (a) Sketches of crest patterns during the emergence of a soliton in a moving reference of frame, (b) superposed sketches of (a) and a train of solitons (from Ertekin [3]).

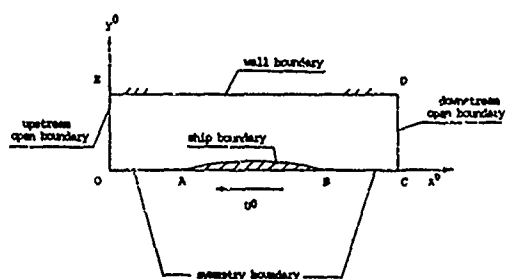


Figure 2. Configuration of the physical region.

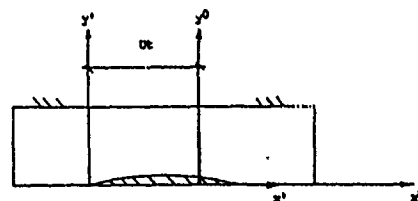


Figure 3. Fixed (x^0, y^0) and moving (x', y') coordinate systems.

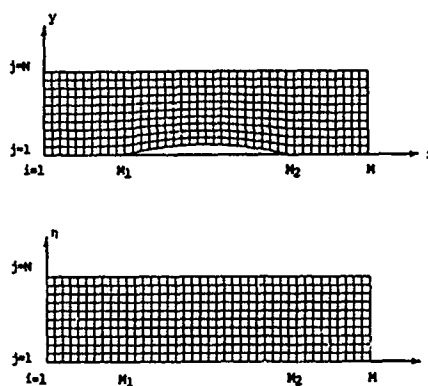


Figure 4. Physical (x, y) and computational (ξ, η) planes.

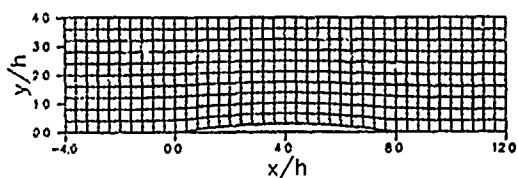


Figure 5. Numerically generated grid for the parabolic strut, Cases 1 and 2.

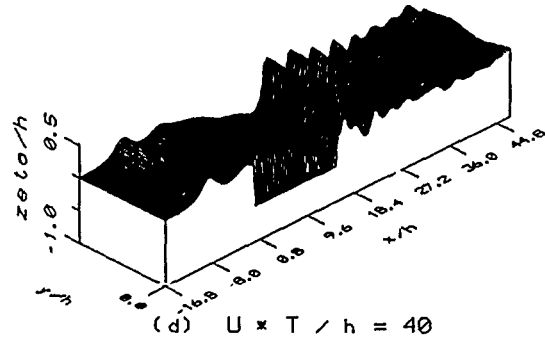
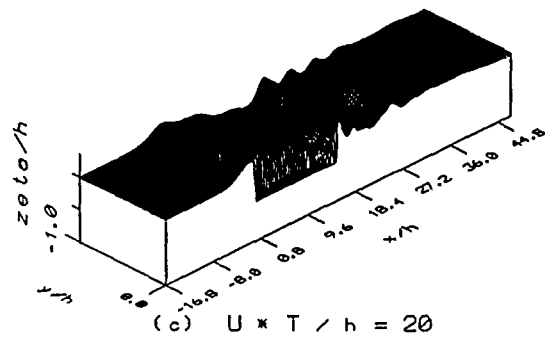
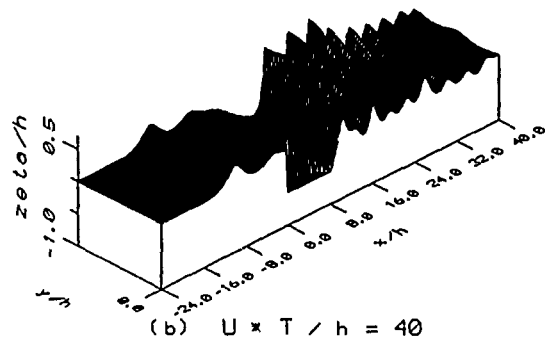
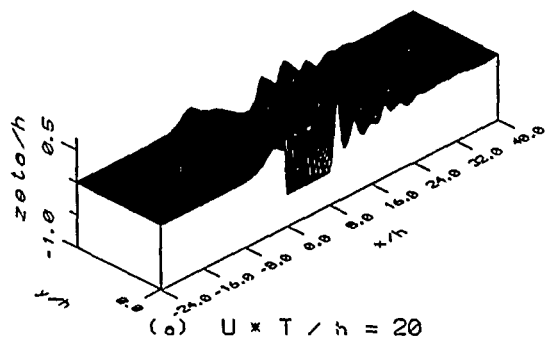


Figure 6. Perspective plots of computed surface elevation (a) and (b): Case 3 (shorter strut), (c) and (d): Case 4 (longer strut).

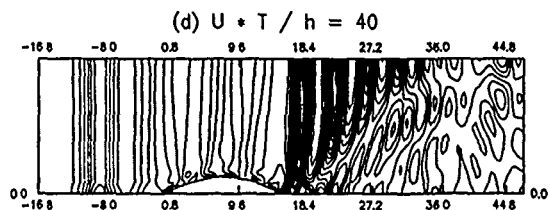
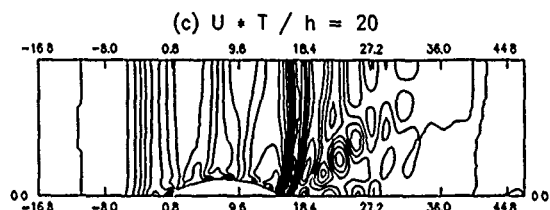
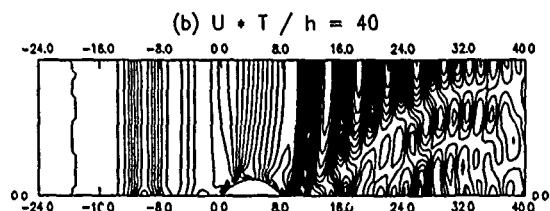
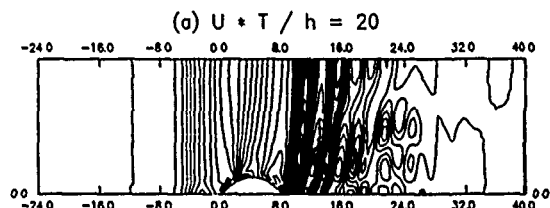


Figure 7. Contour plots of computed surface elevation (a) and (b): Case 3 (shorter strut), (c) and (d): Case 4 (longer strut).

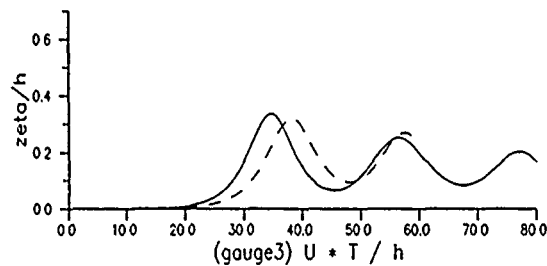
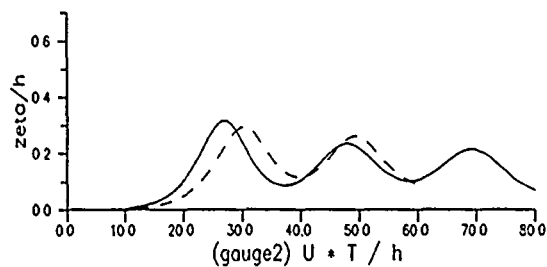


Figure 8. Computed surface elevation as observed by numerical moving-wave-gauges. (—): Case 3, (----): Case 4.

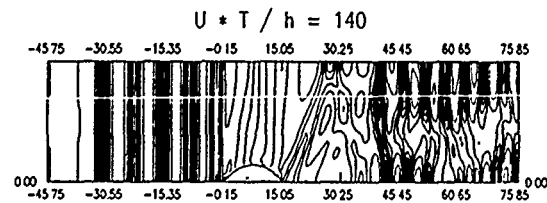
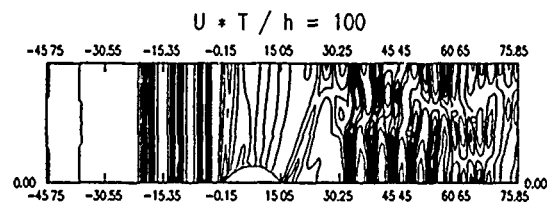
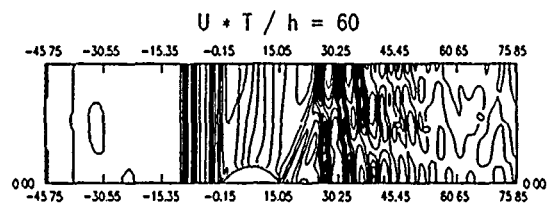


Figure 10. Contour plots of computed surface elevation, Case 5.

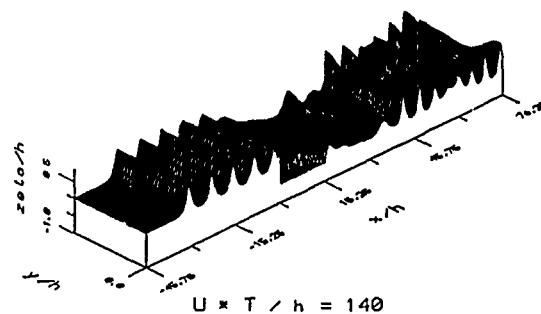
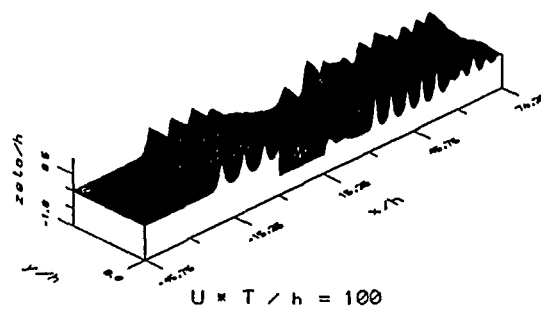
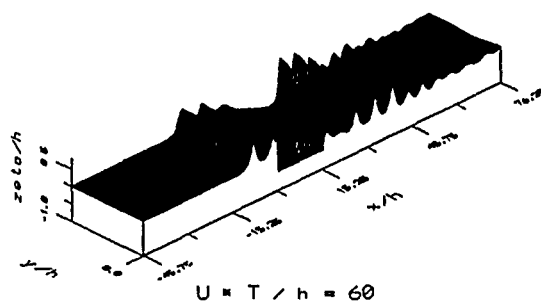


Figure 9. Perspective plots of computed surface elevation, Case 5.

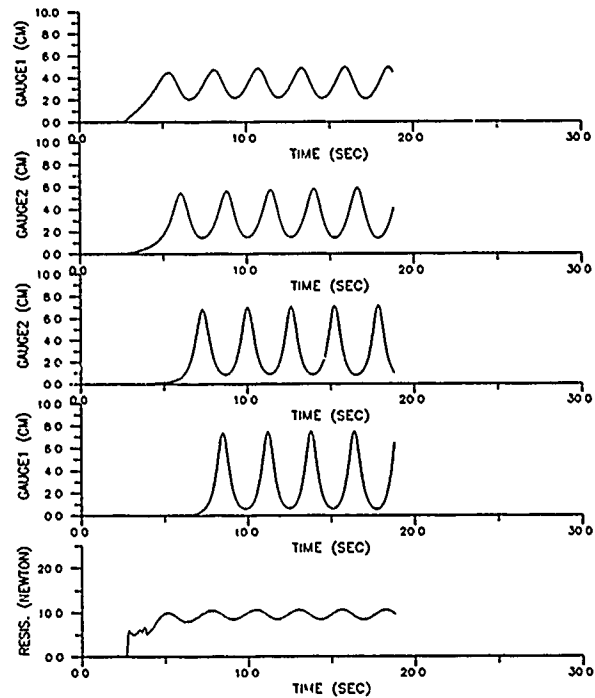


Figure 11. Computed surface elevation as observed at 4 numerical moving-wave-gauges and wave resistance, Case 5.

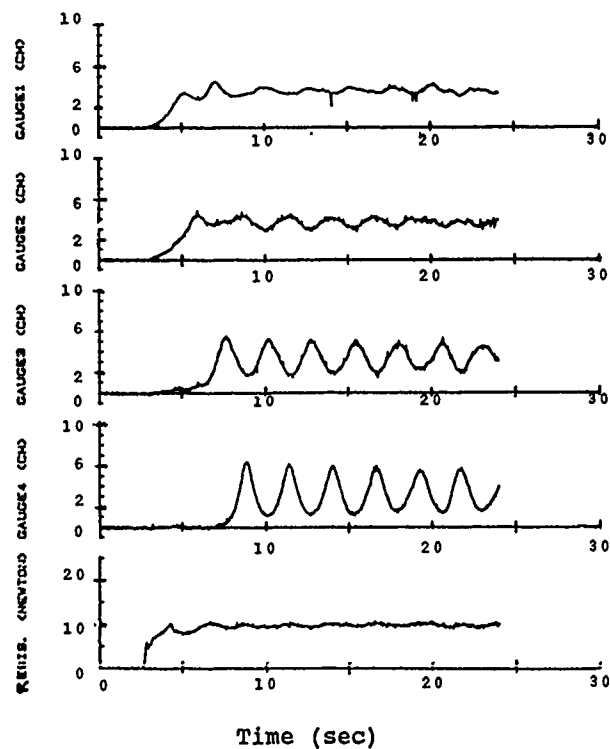


Figure 12. The experimental data of surface elevation and total resistance (Test No. 1936), $F_h=1.0$, $h=10$ cm, draft=7.5 cm, $W=61$ cm, moving gauges.

DISCUSSION

by J.W. Kim

The authors should be congratulated on their successful extension of Boussinesque type equation to 3-dimensional free-surface flow problems. We would like to make comments on the following two points.

The first is the time integration method adopted in the present paper. As pointed out in your earlier paper(1984) [A1] numerical solutions of the gB equation for a disturbance moving at near the critical speed show the gradual increase of the amplitude of upstream solitons whereas the GN equation shows nearly constant amplitude. We have also reproduced this numerical calculation based on the 4th order Runge Kutta method for the time integration and then we have obtained the constant amplitude for both equations. The only difference between ours and your previous calculation is in the time integration method, where you used the Modified Euler Method (MEM). In the present paper you also used MEM for the time integration. From our experience in both time integration methods, we believe that the difficulties you experienced in your present work before introducing the filtering process is mainly due to the inadequacy of MEM for this problem.

The second point I would like to discuss is on the treatment of the convection term. Although the gB equation given in your paper has no convection term explicitly, the perturbed velocity potential and wave elevation will have convection effect implicitly since the basic flow is uniform stream. For the convection operator it is well-known that the central difference scheme in spatial discretization has a considerable phase error on short waves with wave length comparable to the mesh size. We have also experienced similar difficulties in our calculation by the finite element method. As a remedy for this difficulty we used the partial upwinding scheme.

From the above two points, we believe that the filtering process in your computation scheme has presumably played a role of eliminating the overall combined effect of the two dif-

ficulties due to MEM and convection.

[A1] Ertekin, R.C., Webster, W.C. & Wehausen, J.V., Ship-generated Solitons, Proc. 15th Symp. Naval Hydrodynamics, Hamburg, 1984 pp.347-364.

Author's Reply

We would like to thank Mr. Kim for a very useful and timely discussion.

Your comments on the use of MEM and its effects on the numerical predictions are agreeable. It is clear to us that a fourth-order method such as the RK4 method used will produce more accurate results. However, it is not very clear that reducing the truncation errors by using a higher order scheme will totally eliminate the continuous amplitude increases observed when one uses the gB equations. One must keep in mind that the momentum and, therefore, the energy is not exactly conserved in gB equations even if the sea floor is flat. When the disturbance is small, the amplitude increase may be reduced, perhaps to a minimum. But we do not think that it can be eliminated when large disturbances are used. The same is not true when the Green-Naghdi equations are used since these equations satisfy the conservation of mass and energy exactly, even if the sea floor is not flat. On the other hand, one may justifiably argue that if the disturbance is large, then the assumptions behind the derivation of the gB equations are violated, and therefore one should not expect that the amplitude does not grow. We agree with this agreement.

It is true that the MEM causes high frequency waves because of the presence of central differencing. That is why we used filtering. Filtering eliminates high frequency waves which occur around and behind the hull. But, obviously, it does not effect the very low-frequency waves ahead of the hull in the upstream region. Since these waves are the primary concern to us, we did not worry about using MEM which proved to be a very valuable scheme because of its efficiency compared to a higher-order scheme.

Wave Resistance and Squat of a Slender Ship Moving Near the Critical Speed in Restricted Water

H. S. Choi
Seoul National University
Seoul, Korea
C. C. Mei
Massachusetts Institute of Technology
Cambridge, USA

Abstract

The wave resistance and implied squat of a slender ship advancing near the critical speed in restricted water are studied. Employing matched asymptotic expansion techniques, it is shown that the response can be described by the homogeneous Kadomtsev - Petviashvili (KP) equation with flux conditions on boundaries, when the channel is wide compared to the ship length. Numerical results show the generation and radiation of straight-crested solitons in a periodic manner ahead of the ship, when it moves at transcritical speeds with moderate blockage. The solitons are initially three dimensional, which are followed by a depressed region and a train of complicated ship-bound waves in the wake. Hydrodynamic forces are computed by using slender body approximation, and the implied sinkage and trim are estimated based on hydrostatic relations. These quantities vary with time and strongly depend on the ship's speed and blockage. Near the critical speed, the wave resistance and the trim oscillate around mean values in phase with the emission of solitons, while the sinkage takes place out of phase. The calculated results are in crude agreement with the measurements.

1. Introduction

A couple of investigators have reported the fascinating phenomenon observed during shallow tank tests that a ship model towed near the critical speed \sqrt{gh} (g = acceleration due to gravity, h = water depth) radiates a succession of upstream-propagating waves in an almost periodic manner (Thews & Landweber 1935 ; Izubuchi & Nagasawa 1937 ; Graff 1962 ; Huang et al. 1982). As a result, the ship experiences

considerable changes in resistance, trim and sinkage, or better known as squat. One of most exciting aspects in this now identified phenomenon is that a three-dimensional disturbance, such as a ship, generates 2 dimensional waves propagating upstream in a tank of finite width. In addition to it, the propagation speed of the upstream waves, named solitons, is faster than the constant towing speed so that a steady state cannot be attained.

Linear theories fail to predict the flow. Katsis and Akyas (1987) clarified it in the light of the linearized dispersion relation. Among all waves radiated from a disturbance advancing at a speed U , those which may remain stationary with the disturbance in the direction γ must have the wave number k such that $F kh \cos \gamma = (kh \tanh kh)^{1/2}$, where F is the depth Froude number ($=U / \sqrt{gh}$). It means that at a transcritical velocity, $F = 1 + O(kh)^2$, long waves must be in nearly the same direction as the moving disturbance, i.e. $\cos \gamma = 1 + O(kh)^2$. Furthermore the group velocity tends to vanish in the moving frame. Consequently the long waves become almost nondispersive and the associated wave energy cannot be radiated. It implies, in order to deal with the problem, we have to include a balanced interplay by the nonlinear and dispersive effects to the leading-order wave equation, and to keep it in mind that transient waves evolve slowly.

Wu and Wu(1982) were the first who calculated the generation and propagation of solitons for a moving disturbance spanning uniformly across the channel by using the generalized Boussinesq equation. Akyas (1984) also considered a two-dimensional pressure band travelling on the free surface but focused attention to the immediate neighborhood of the critical speed. He showed that the physics

can simply be described by an inhomogeneous Korteweg-de Vries (KdV) equation. In a joint theoretical and experimental study, Lee et al. (1989) found a broad agreement between the experiment and two theoretical models, the generalized Boussinesq and the forced KdV equations, for a moving two-dimensional bottom topography in a shallow water tank. All these works are concerning with 2 dimensional disturbances and thus one-dimensional wave fields.

For a rectangular patch of surface pressure whose width is comparable with the tank width, Ertekin et al. (1986) solved Green - Nagdhi's directed - sheet model numerically. Their calculations have yielded two-dimensional flow upstream and three-dimensional flow downstream, in qualitative agreement with the measurements they carried out systematically (Ertekin, 1984 and Ertekin et al., 1984). Wu and Wu (1987) obtained similar results using the generalized two-dimensional Boussinesq equation. Katsis and Akylas (1987) calculated some 3 dimensional long waves bounded by side walls using the Kadomtsev-Petviashvili (KP) equation. Quite recently, Lee and Grimshaw (1989) studied the three-dimensional slowly-varying evolution of wave fields ahead of a bottom topography in a horizontally unbounded fluid domain by using a forced KP equation. Meanwhile, Bai et al. (1989) applied finite element method to a vertical strut sliding in shallow water.

It is, however, as yet unclear how these methods with pressure distributions can be applied to three dimensional bodies such as a ship. In this respect, Mei and Choi (1987, hereinafter referred to as I) extended the theory of Mei (1986) to treat the transient forces on and responses of a slender ship. They found that the waves in the far field can be described by one-dimensional inhomogeneous KdV equation for a special class of channel width ($=2W$) and ship's slenderness parameter ($=\delta$) as follows; $W/L = O(\mu^{-m})$ with $0 \leq m \leq 1/2$ and $\delta = O(\mu^{2/5})$, where $2L$ stands for the ship length and $\mu = h/L = o(1)$ for the dispersion. It correctly predicts the upstream solitons, and the estimated sinkage and trim for a destroyer favourably compare with the time - averaged experimental values of Graff et al. (1964). But the theory fails to render three-dimensional waves in the wake. In viewing the result of Katsis and Akylas (1987), it strongly suggests us to modify our theory in their direction. In fact, it was already pointed out in I that the KdV equation is to be replaced by the KP equation, when the canal is much wider, i.e. $W/L = O(\mu^{-1})$. We have done it in this paper by following the same scheme described in I, but for a wider channel.

2. Formulation

We consider a ship advancing with a constant speed in a shallow channel. For simplicity, the ship is assumed to possess the lateral symmetry and to move amid the channel so that it is enough to take only the half of fluid domain into account. A rectangular coordinate system is introduced, which is fixed on the waterplane of the ship. The x^* -axis coincides with the longitudinal axis of the ship and the centerline of the channel (Fig.1). Under the usual assumptions of potential theory, fluid motions are described in terms of the velocity potential $\phi^*(x^*, y^*, z^*, t^*)$, which is the solution of the following initial - boundary value problem. The Laplace equation holds in the fluid region

$$\nabla^2 \phi^* = 0 \quad (-h \leq z^* \leq \zeta^*). \quad (1)$$

The kinematic and dynamic boundary conditions on the free surface at $z^* = \zeta^*$ are

$$\phi_{t^*}^* = \zeta_{t^*}^* + (U + \phi_{x^*}^*) \zeta_{x^*}^* + \phi_{y^*}^* \zeta_{y^*}^*, \quad (2)$$

$$g \zeta^* + \phi_{t^*}^* + U \phi_{x^*}^* + 1/2 (\nabla \phi^*)^2 = 0. \quad (3)$$

No net flux condition holds on the channel bottom

$$\phi_{z^*}^* = 0 \quad (z^* = -h), \quad (4)$$

on the channel wall

$$\phi_{y^*}^* = 0 \quad (y^* = W), \quad (5)$$

and also on the ship's hull $r^* = R^*(x^*, \theta)$

$$\phi_{n^*}^* = (U + \phi_{x^*}^*) R_{x^*}^* [1 + (R_{\theta}^*/R^*)^2]^{-1/2}, \quad (6)$$

where r^* and θ are polar coordinates on the (y^*, z^*) - plane. Under the assumption of slender body, the normal derivative on the ship surface has been approximated by that on the transverse plane at constant x^* along the ship. Before the initial instant $t^* = 0$, there was no disturbance

$$\phi^* = 0, \quad \zeta^* = 0 \quad (t^* = 0). \quad (7)$$

In order to solve the problem approximately, we employ perturbation techniques by defining two smallness parameters

$$\epsilon = A/h, \quad \mu = h/L, \quad (8)$$

and assume without loss of generality $\epsilon = \mu^2$ which implies that the nonlinearity and the dispersion are both important to the leading order solution of the problem. In eq.(8), A means a typical wave amplitude. Variables are normalized as below:

$$\zeta^* = A\zeta, \quad \phi^* = (gAL/U)\phi, \quad t^* = (L/\sqrt{gh})t. \quad (9)$$

Herein we rather focus our attention to the flow near the critical speed. Thus the Froude number is expanded

$$F^2 = 1 - 2\alpha\mu^2 \quad \text{with } \alpha = O(1). \quad (10)$$

To cope with the slow variation of flow, we have to rescale time

$$\tau = t/\mu^2, \quad (11)$$

The channel is assumed wide in comparison with the ship length

$$y'/L = 1/\mu\eta_0 \quad \text{with } \eta_0 = O(1). \quad (12)$$

As pointed out by Mei (1986), the blockage coefficient S_B must have a magnitude of $O(\mu^4)$

$$S_B \approx R_0^2 / 2Wh = O(\mu^4), \quad (13)$$

where R_0 denotes the characteristic transverse radius of ship and the blockage coefficient is simply the area ratio of the midship section to the channel cross-section. Consequently the slenderness parameter must be

$$\delta = R_0 / L = O(\mu^2). \quad (14)$$

It implies that the nonlinearity arises from the slenderness of disturbance.

Because of these vastly different length scales involved, it is relevant to divide the channel cross-section into three regions as:

(i) the far field ; $|x^*| < \infty, y^* = O(W) = O(L/\mu),$

$$z^* = O(h) = O(\mu L), \quad (15)$$

(ii) the intermediate field ; $x^* = O(L),$

$$(y^*, z^*) = O(h) = O(\mu L), \quad (16)$$

(iii) the near field ; $x^* = O(L),$

$$(y^*, z^*) = O(R_0) = O(\mu^2 L). \quad (17)$$

We shall first analyze each field separately and then conduct matching by following the line reported in I. Accordingly most parts must be very similar to those in I and it is already obvious that modifications which will appear are solely attributed to the different definition on the length scale of W/L . Nevertheless steps are explicitly given here in order to keep this paper self-contained.

3. The Far Field

In accordance with the scheme defined by eq.(15), the far field variables are made dimensionless

$$x^* = Lx, \quad y^* = Wy, \quad z^* = hz. \quad (18)$$

The normalization of other variables holds effective as defined in eqs.(9) - (11). In this field, the banks and the bottom of the channel directly affect the propagation of waves. However, the boundary condition on the ship hull is of no meaning and the forcing agency is not known. The governing equation and the boundary conditions are rewritten in terms of the dimensionless farfield variables:

$$\mu^2(\phi_{xx} + \mu^2\eta_0^2\phi_{yy}) + \phi_{zz} = 0 \quad (-1 \leq z \leq \mu^2\zeta), \quad (19)$$

$$\phi_z = \mu^2[(1 - 2\alpha\mu^2)\zeta_x + \mu^2\sqrt{1 - 2\alpha\mu^2}\zeta_\tau + \mu^2\phi_x\zeta_x + \mu^4\eta_0^2\phi_y\zeta_y] \quad (z = \mu^2\zeta), \quad (20)$$

$$(1 - 2\alpha\mu^2)(\zeta + \phi_x) + \mu^2\sqrt{1 - 2\alpha\mu^2}\phi_\tau + \frac{1}{2}[\mu^2(\phi_x^2 + \mu^2\eta_0^2\phi_y^2) + \phi_z^2] = 0 \quad (z = \mu^2\zeta), \quad (21)$$

$$\phi_z = 0 \quad (z = -1), \quad (22)$$

$$\phi_y = 0 \quad (y = 1), \quad (23)$$

Substituting the expansions

$$\phi \sim \phi^{(0)} + \mu^2 \phi^{(2)} + \mu^4 \phi^{(4)} + \dots, \quad (24)$$

$$\zeta \sim \zeta^{(0)} + \mu^2 \zeta^{(2)} + \mu^4 \zeta^{(4)} + \dots, \quad (25)$$

into eq.(19), we obtain

$$\phi_{xx}^{(0)} = 0, \quad (26a)$$

$$\phi_{xx}^{(2)} = -\phi_{xx}^{(0)}, \quad (26b)$$

$$\phi_{xx}^{(4)} = -(\phi_{xx}^{(2)} + \eta_0^2 \phi_{yy}^{(0)}). \quad (26c)$$

With help of no flux condition on the channel bottom, the general solution straightforwardly yields to

$$\phi^{(0)} = \psi^{(0)}(x, y, \tau), \quad (27a)$$

$$\phi^{(2)} = \psi^{(2)}(x, y, \tau) - \frac{1}{2}(z+1)^2 \psi_{xx}^{(0)}, \quad (27b)$$

$$\begin{aligned} \phi^{(4)} = & \psi^{(4)}(x, y, \tau) - \frac{1}{2}(z+1)^2 (\psi_{xx}^{(2)} + \eta_0^2 \psi_{yy}^{(0)}) + \\ & + \frac{1}{4!}(z+1)^4 \psi_{xxxx}^{(0)}, \end{aligned} \quad (27c)$$

where $\psi^{(n)}$ are unknown functions to be determined later by matching with the intermediate field potential. The free surface elevation is derived from the dynamic condition, eq.(21)

$$\zeta^{(0)} = -\psi_x^{(0)} \quad (z=0), \quad (28a)$$

$$\zeta^{(2)} = -\psi_x^{(2)} - \psi_\tau^{(0)} - \frac{1}{2}\psi_{xxx}^{(0)} - \frac{1}{2}(\psi_x^{(0)})^2 \quad (z=0). \quad (28b)$$

Utilizing the above relations, the kinematic condition of $O(\mu^4)$ on $z=0$ turns out to be

$$\phi_z^{(4)} = \zeta_x^{(2)} + \zeta_\tau^{(0)} - 2\alpha \zeta_x^{(0)} - 2\zeta^{(0)} \zeta_x^{(0)} \quad (z=0). \quad (29)$$

Combining eqs.(27) - (29) and differentiating with respect to x , we finally get the leading order wave equation

$$\zeta_{xx}^{(0)} - \alpha \zeta_{xx}^{(0)} - \frac{3}{4}(\zeta^{(0)})_{xx}^2 - \frac{1}{6}\zeta_{xxxx}^{(0)} =$$

$$-\frac{1}{2}\eta_0^2 \zeta_{yy}^{(0)} = 0 \quad (z=0). \quad (30)$$

It is the homogeneous KP equation, which is the three-dimensional counterpart of the KdV equation, since it contains the transverse dispersion as well as the longitudinal dispersion. If $\zeta_{yy}^{(0)}=0$, the KdV equation is recovered.

An observer in the far field is too far away from the ship so that he just observes waves without knowing the details of wave generation, which can only be found through matching with the intermediate field. For this purpose, we need the inner expansion of the far field potential for small y

$$\begin{aligned} \phi = & \psi^{(0)}(x, 0, \tau) + y \psi_y^{(0)}(x, 0, \tau) + \mu^2 [\psi^{(2)}(x, 0, \tau) - \\ & - \frac{1}{2}(z+1)^2 \psi_{xx}^{(0)}] + O(\mu^3). \end{aligned} \quad (31)$$

4. The Near Field

In a fluid domain close to the ship, the characteristic length is R_0 and thus let us nondimensionalize the near field variables

$$\begin{aligned} y^* = R_0 \bar{y}, \quad z^* = R_0 \bar{z}, \\ r^* = R_0 \bar{r}, \quad R^* = R_0 \bar{R}, \end{aligned} \quad (32)$$

but retain the rest of the normalizations. The Laplace equation is now transformed for $-\infty < \bar{z} \leq (\mu^3/\delta)\bar{\zeta}$

$$\delta^2 \phi_{xx} + \phi_{yy} + \phi_{zz} = 0. \quad (33)$$

On the free surface at $\bar{z} = (\mu^3/\delta)\bar{\zeta}$, we have

$$\begin{aligned} \phi_{\bar{z}} = & \mu^3 \delta \sqrt{1-2\alpha\mu^2} \bar{\zeta}_{\bar{\tau}} + \mu \delta (1-2\alpha\mu^2) \bar{\zeta}_{\bar{x}} + \\ & + \mu^3 \delta \phi_{\bar{x}} \bar{\zeta}_{\bar{x}} + (\mu^3/\delta) \phi_{\bar{y}} \bar{\zeta}_{\bar{y}}, \end{aligned} \quad (34)$$

$$\begin{aligned} (1-2\alpha\mu^2)(\bar{\zeta} + \phi_{\bar{x}}) + \mu^2 \sqrt{1-2\alpha\mu^2} \phi_{\bar{\tau}} + \\ + \frac{1}{2}\mu^2 [\bar{\phi}_{\bar{x}}^2 + (\bar{\phi}_{\bar{y}}^2 + \bar{\phi}_{\bar{z}}^2)\delta^2] = 0. \end{aligned} \quad (35)$$

On the ship hull $\bar{r} = \bar{R}(x, \theta)$, the condition is

$$\phi_{\bar{r}} = (\delta/\mu)^2 (1-2\alpha\mu^2 + \mu^2 \phi_{\bar{x}}) \bar{R}_{\bar{x}} [1 + (\bar{R}_0/\bar{R})^2]^{-1/2}. \quad (36)$$

As already discussed, the slenderness parameter is a small quantity of $O(\mu^2)$ and thus we suppose the following expansions:

$$\phi \sim \bar{\phi}^{(0)} + \mu \bar{\phi}^{(1)} + \mu^2 \bar{\phi}^{(2)} + \dots, \quad (37)$$

$$\xi \sim \bar{\xi}^{(0)} + \mu \bar{\xi}^{(1)} + \mu^2 \bar{\xi}^{(2)} + \dots \quad (38)$$

Then the Laplace equation and the boundary conditions are readily expressed as below:

$$\bar{\phi}_{yy}^{(n)} + \bar{\phi}_{zz}^{(n)} = 0 \quad (-\infty < \bar{z} \leq 0, n=0,1,2), \quad (39)$$

$$\bar{\phi}_{\bar{z}}^{(n)} = 0 \quad (\bar{z}=0, n=0,1,2), \quad (40)$$

$$\bar{\xi}^{(0)} = -\bar{\phi}_x^{(0)} \quad (\bar{z}=0), \quad (41)$$

$$\bar{\phi}_{\bar{r}}^{(n)} = 0 \quad (\bar{r}=\bar{R}, n=0,1), \quad (42a)$$

$$\bar{\phi}_{\bar{r}}^{(2)} = \bar{R}_x [1 + (\bar{R}_0 / \bar{R})^2]^{-1/2} \quad (\bar{r}=\bar{R}), \quad (42b)$$

From eqs.(39) and (40), it is clear that $\bar{\phi}^{(1)}$ may be absorbed by $\bar{\phi}^{(0)}$. The leading-order problem is of homogeneous Neumann type, of which solution formally takes the form

$$\bar{\phi}^{(0)} = f^{(0)}(x, \tau), \quad (43)$$

The next-order solution contains a particular part owing to the inhomogeneous term in eq. (42b)

$$\bar{\phi}^{(2)} = f^{(2)}(x, \tau) + \bar{\phi}_p^{(2)}(x, y, z, \tau). \quad (44)$$

The particular solution represents the disturbed flow due to the motion of the ship, of which outer approximation for large \bar{r} will prove to be more meaningful in the viewpoint of matched asymptotic expansions. For large \bar{r} , the ship shrinks to a line source and thus $\bar{\phi}_p^{(2)}$ is expressed

$$\bar{\phi}_p^{(2)} = \frac{1}{\pi} q(x, \tau) \ln \bar{r} + c(x, \tau), \quad (45)$$

where q stands for the source strength and c may be regarded as a part of $f^{(2)}(x, \tau)$.

Applying the law of mass conservation to the fluid domain surrounded by the ship, the free surface and a control surface located far away from the ship, the source strength is readily

determined

$$q = \frac{2}{\eta_0} \frac{F^2}{\delta^2} S_B S_x(x), \quad (46)$$

where S_B is referred to the blockage coefficient and $S(x)$ to the longitudinal distribution of the cross-section area of the ship. It is reminded that the blockage coefficient has a magnitude of $O(\mu^4)$ near the critical speed, i.e. $F = 1 + O(\mu^2)$. For the sake of matching with the intermediate field solution, it is necessary to expand eq.(44) for large \bar{r}

$$\phi \sim f^{(0)}(x, \tau) + \mu^2 [f^{(2)}(x, \tau) + \frac{q}{\pi} \ln(\frac{\delta}{\mu} \bar{r})] + \dots \quad (47)$$

5. The Intermediate Field

Here the proper reference length for y^* and r^* is h , hence we introduce the dimensionless intermediate coordinates

$$y^* = h\bar{y}, \quad r^* = h\bar{r}, \quad (48)$$

and keep all other normalized variables defined in eqs.(9)-(11) and (18). The nondimensional equations are

$$\mu^2 \phi_{xx} + \phi_{yy} + \phi_{zz} = 0 \quad (-1 \leq z \leq \mu^2 \zeta), \quad (49)$$

$$\phi_z = \mu^4 \sqrt{1-2\alpha\mu^2} \zeta_\tau + \mu^2 (1-2\alpha\mu^2) \zeta_x + \mu^4 \phi_x \zeta_x + \mu^2 \phi_y \zeta_y \quad (z = \mu^2 \zeta), \quad (50)$$

$$(1-2\alpha\mu^2)(\zeta + \phi_x) + \mu^2 \sqrt{1-2\alpha\mu^2} \phi_\tau + \frac{1}{2} [\mu^2 \phi_x^2 + \phi_y^2 + \phi_z^2] = 0 \quad (z = \mu^2 \zeta), \quad (51)$$

$$\phi_z = 0 \quad (z = -1), \quad (52)$$

$$\phi_{\bar{r}} = (\delta/\mu)(1-2\alpha\mu^2 + \mu^2 \phi_x) \bar{R}_x [1 + (\bar{R}_0 / \bar{R})^2]^{-1/2} \quad (\bar{r} = \frac{\delta}{\mu} \bar{R}). \quad (53)$$

In anticipation of matching with the near field, we introduce expansions in the form of eqs.(37) and (38), with $\bar{\phi}$ and $\bar{\xi}$ replaced by ϕ and ξ , respectively, it then follows

$$\hat{\phi}_{yy}^{(n)} + \hat{\phi}_{xx}^{(n)} = 0 \quad (-1 \leq z \leq 0, n=0,1), \quad (54a)$$

$$\hat{\phi}_{yy}^{(2)} + \hat{\phi}_{xx}^{(2)} = -\hat{\phi}_{xx}(0). \quad (54b)$$

From the Taylor expansions of the conditions on the free surface, we get

$$\hat{\phi}_z^{(n)} = 0 \quad (z=0, n=0,1), \quad (55a)$$

$$\hat{\phi}_z^{(2)} = \hat{\zeta}_x^{(0)} \quad (z=0). \quad (55b)$$

It is immediate to have

$$\hat{\phi}^{(0)} = f^{(0)}(x, \tau), \quad (56a)$$

$$\hat{\phi}^{(2)} = f^{(2)}(x, \tau) - \frac{1}{2}(z+1)^2 f_{xx}^{(0)} + \hat{\phi}_p^{(2)}. \quad (56b)$$

The particular solution $\hat{\phi}_p^{(2)}$ again corresponds to the response to a line source at the ship's centerline, hence takes the following form for small \hat{r}

$$\hat{\phi}_p^{(2)} = \frac{1}{\pi} \hat{q}(x, \tau) \ln \hat{r} = \frac{\hat{q}}{\pi} \ln \left(\frac{\delta}{\mu} \bar{r} \right). \quad (57)$$

The solution has the inner expansion

$$\begin{aligned} \phi \sim f^{(0)}(x, \tau) + \mu^2 [f^{(2)}(x, \tau) - \frac{1}{2} f_{xx}^{(0)} + \\ + \frac{\hat{q}}{\pi} \ln \left(\frac{\delta}{\mu} \bar{r} \right)] + \dots \end{aligned} \quad (58)$$

Matching with the outer expansions of the near field results in the relations

$$q = \hat{q}, \quad (59)$$

$$f_p^{(0)}(x, \tau) = f^{(0)}(x, \tau), \quad (60a)$$

$$f_p^{(2)}(x, \tau) = f^{(2)}(x, \tau) - \frac{1}{2} f_{xx}^{(0)}. \quad (60b)$$

The source strength measured in the intermediate field is indeed identical with that in the near field. From mass conservation, the approximation for $\hat{\phi}_p^{(2)}$ must be

$$\hat{\phi}_p^{(2)} \sim \frac{1}{2} \hat{q} \hat{y} \quad (\hat{y} \gg 1), \quad (61)$$

so that the outer expansion of the intermediate field is, in terms of the far field variables

$$\phi \sim f^{(0)}(x, \tau) + \frac{\hat{q}}{2\eta_0} y + \mu^2 [f^{(2)} - \frac{1}{2}(z+1)^2 f_{xx}^{(0)}] + \dots \quad (62)$$

Matching provides useful information :

$$\psi^{(0)}(x, 0, \tau) = f^{(0)}(x, \tau) = f^{(0)}(x, \tau), \quad (63)$$

$$\psi_y^{(0)}(x, 0, \tau) = \frac{\hat{q}}{2\eta_0} = \frac{\beta}{\eta_0^2} S_x, \quad \beta = \frac{S_B}{\mu^4}. \quad (64)$$

Differentiating eq.(64) with respect to x and recalling the relation of eq.(28a), we finally get the boundary condition for $\zeta^{(0)}$ at $y=0$

$$\zeta_y^{(0)}(x, 0, \tau) = -\frac{1}{2} \beta S_{xx}(x). \quad (65)$$

We realize that the result thus obtained is basically the same as those Katsis and Akyas (1987) derived.

Once $\zeta^{(0)}$ is calculated, $\psi^{(0)} = f^{(0)} = f^{(0)}$ is known. Since the leading-order dynamic pressure is linearly proportional to the surface elevation, the forces and moment acting on the ship can easily be evaluated by invoking the slender body approximation. The implied sinkage and trim may be estimated from the hydrostatic relations (Tuck, 1966), which are given in I.

6. Numerical Results

To further investigate the wave field and resulting hydrodynamic forces, we have to rely on numerical computations for the homogeneous KP equation with proper boundary conditions. In contrast to the KdV equation, only a few literatures are available, in which numerical methods for the KP equation have been discussed. Katsis and Akylas (1987) applied an explicit finite-difference method for the standard KP equation and investigated the wave patterns due to normally distributed pressures in shallow water laterally bounded and unbounded. We adopted their scheme. To facilitate calculations, it is convenient to integrate eq.(30) with respect to x

$$\zeta_\tau^{(0)} = \alpha \zeta_x^{(0)} + \frac{3}{2} \zeta^{(0)} \zeta_x^{(0)} + \frac{1}{6} \zeta_{xxx}^{(0)} + \frac{1}{2} \eta_0^2 \int_{-\infty}^x \zeta_{yy}^{(0)} dx, \quad (66)$$

where use has been made that $\zeta^{(0)}$ and its derivatives must vanish far upstream. If the integral term on the right hand side of the above equation is neglected, it becomes the standard KdV equation.

In the discretization, simple forward differences are implemented for time derivatives, and central differences for spatial derivatives. But at the wall and the centerline of channel, one-sided differences are used instead of the central difference, and the boundary conditions, eqs.(23) and (65), have been incorporated. Integrals are evaluated by trapezoidal rule. From diverse numerical tests, the scheme has proven to be stable for

$$\Delta x = 0.1, \quad \Delta y = 0.1, \quad \Delta \tau = 0.00002$$

with the ship's length as 2.0 spanning from $x = -1.0$ for bow to $x = 1.0$ for stern. These values have been used for all computations in this work. As Katsis and Akylas pointed out, reflected waves from the numerical boundaries far upstream and downstream seriously deteriorates the result. Several devices for radiation condition have been tried without success. Thus the computation domain is taken as large as possible and the portion is discarded, where numerically reflected waves are apparent. To save computing time, it is advised to begin with a small domain and to enlarge it continuously as time passes.

Our primary concern is to examine the generation and propagation of solitons by a ship. For this purpose, let us consider a slender ship whose cross-sectional area varies parabolically

$$S(x) = 1 - x^2 \quad (|x| \leq 1).$$

In Fig.2, the evolution of the wave field at the critical speed is illustrated with time interval $\Delta \tau = 0.2$ up to $\tau = 1.0$. The parameters are chosen as below :

$$\mu = h/L = 0.25, \quad W/L = 1.0 \quad (\eta_0 = 4.0),$$

$$S_B = 0.105 \quad (\beta = 25.6), \quad F = 1.0 \quad (\alpha = 0.0).$$

The blockage coefficient seems somewhat too large for our theory to be valid. Nevertheless this case is taken up, because it is possible to compare with the experimental and numerical results of Ertekin et al. (1984 and 1986). They calculated Green-Nagdhi's model for a rectangular pressure patch, which should be roughly equivalent to a ship with blockage coefficient, $S_B = 0.105$, in the viewpoint of the hydrostatically displaced free surface. The figures are exaggerated vertically by 2.5 times. It is to note that 1τ corresponds to their nondimensional time $UT/h = 64$. During this time span, the ship advances a distance of 8 times the ship's length.

At $\tau = 0.2$, three-dimensional waves emerge ahead of the ship. A depressed region is built therebehind, which is followed by a train of complicated ship-bound waves in the wake and also reflected transverse waves far downstream. As time elapses, the upstream waves develop further and gradually become straight-crested as they are reflected from the wall. The first soliton almost completes its formation and becomes two-dimensional at $\tau = 0.4$. The second soliton starts to take its shape at $\tau = 0.6$, while the first soliton steadily propagates upstream and the depression is being elongated. At $\tau = 1.0$, the second soliton is completed and the third one begins to appear. Such a trend can also be recognized in Ertekin et al., but the waves downstream here look more ship-bound.

In Table 1, a comparison is made for the amplitude, propagation speed of the first soliton and the period of first two solitons. It is to note that the amplitude was taken at $\tau = 1.0$ ($UT/h = 64$), since it continuously increases during the developing phase. Let us first compare present results with those of Ertekin. The propagation speed agrees excellently, but significant deviations exist in amplitude and period. It is not probable that these are caused simply by numerical round-off errors. It was concluded in the works of Ertekin et al. that the amplitude increases and the period is shorter as the blockage is

larger, and the details of the disturbance is less important. The blockage coefficient is identical in both cases, but the presumed ship of Ertekin is much fuller than our slender ship. It might act as a stronger forcing agency and result in higher amplitudes. If it is true, then the present period should have been longer in order not to contradict the measurements. But it is not the case and let us leave it as open question. Now we turn to Bai et al.(1989) who applied finite element method to a vertical strut sliding in a shallow channel. Their result is closer to the present for amplitude, but to Ertekin for period. The propagation speed is slower than both. We may postulate that it is attributed to the different mathematical models. But no clear-cut conclusion can be drawn at this stage.

Table 1 Soliton amplitude, propagation speed and period for $\beta=25.6$ at $\alpha=0.0$

	A/h	c/\sqrt{gh}	UTg/h
Bai	0.553	1.24	30.0
Ertekin	0.6248	1.280	29.6
Present	0.5625	1.281	28.8

Fig.3 shows the wave profiles along the centerline and the wall of the channel at $\tau=1.0$. The completed first soliton assimilates each other closely. But there is a slight difference on the rear side of the second soliton, because a new soliton is just about to burst. A train of modulated wave packets follows a depressed region, which is directly responsible for the sinkage and trim of ships. The downstream configurations are in general quite dissimilar.

The time evolution of the wave resistance, sinkage and trim is depicted in Fig.4. The wave resistance and sinkage are normalized by the displacement and half length of the ship, respectively, while the trim is in degrees. Positive values indicate resistance, downward sinkage and trim by stern. The computed sinkage and trim are of qualitative meaning only, because no dynamic effects are included. Caution should be paid on three differently-scaled ordinates. All these quantities rise initially from zero to first maximum and then oscillate around mean values. The oscillation period is approximately $\tau g=0.45$ in coincidence with that of soliton. It reflects the fact that hydrodynamic forces and their effects on

the ship are dominated by the generation and radiation of solitons. The wave resistance and the trim fluctuate in phase with the periodic soliton emission, while the sinkage takes place out of phase. It seems unlikely that a steady state will be attained in time.

To assess the effect of ship's speed, we consider the same slender ship as above but in a slightly deeper channel

$$\mu=0.333, \quad \eta_0=3.0 \quad (W/L=1.0),$$

$$\beta=5.0 \quad (S_B=0.062)$$

for five speeds : two subcritical speeds $\alpha=2.5$ ($F=0.667$) and $\alpha=1.0$ ($F=0.882$), critical speed $\alpha=0.0$ ($F=1.0$), two supercritical speeds $\alpha=-1.0$ ($F=1.106$) and $\alpha=-2.5$ ($F=1.247$). The wave resistance, sinkage and trim are plotted in Fig.5,6 and 7 in this order. At transcritical speeds, the wave resistance indeed oscillates. The amplitude of oscillation reaches its maximum not at the critical but at a slightly faster speed, and the period becomes longer as speed increases, which supports the experimental findings. At the low subcritical speed, the wave resistance increases upto a certain threshold with an intermediate step, and it arrives at a near - steady state. At the high supercritical speed, the wave resistance initially reaches a maximum and then diminishes with time to a small steady value.

Similar trends are to be observed for the sinkage and trim in Fig.6 and 7. It is to note that the sinkage oscillates around zero at the critical speed and it becomes negative (lift up) at supercritical speeds. Generally speaking, the overall behaviour of the wave resistance, sinkage and trim is quite similar to two-dimensional cases described in I, as long as the channel width is not too wide and thus the flow around a ship is chiefly affected by upstream solitons.

The variation of soliton amplitude, propagation speed and period according to ship's speed is listed in Table 2. The amplitude given here is referred to the computed value at $\tau=3.0$ for the first soliton. The numbers in parentheses designate the experimental counterparts. The difference in emission period is again remarkable. However, it can be said that theory provides at least crude predictions.

Table 2 Variation of soliton amplitude, propagation speed and period for three ship's speeds

	A/h	c/\sqrt{gh}	UTg/h
$\alpha = -1.0$	0.64 (0.60)	1.31 (1.26)	50.8 (53.7)
$\alpha = 0.0$	0.45 (0.49)	1.21 (1.20)	40.5 (49.5)
$\alpha = 1.0$	0.29 (0.26)	1.13 (1.12)	31.0 (41.6)

Next we examine the wall effect on the response at the critical speed. Three channel widths are chosen as $w/L=0.5, 1.0$ and 3.0 , while the channel depth and the ship are kept unchanged ($\mu=0.333$). It implies that the corresponding blockage coefficients are $0.123, 0.062$ and 0.021 . Fig.8 a - c show the wave fields at $\tau=1.0$, when the ship moved a distance of 4.5 times the ship's length. The vertical scale is stretched by 3.2 times in comparison with those on the horizontal plane. Since the lateral coordinate is normalized by the half width of the channel in all cases, the banks are designated by -1.0 and 1.0 . For a wider channel, it is necessary to reduce Δy for a better resolution. For $w/L=0.5$, there is an indication that the second upstream wave develops on the back of the front waves, whose crest line is spear-headed. The depressed region is relatively long and the downstream waves are pronounced. For $w/L=3.0$, there is no sign for upstream-propagating waves and diverging waves with large run angle prevail. The downstream waves are hardly two-dimensional. Katsis and Akylas (1987) suggested that the maximum canal width for which the downstream waves remain to a reasonable approximation two-dimensional depends on crudely the source characteristics. They found that the maximum channel width is about $20 h$ for an elongated pressure distribution. Since we are dealing with a slender ship, it may be possible that the downstream waves remain practically two dimensional upto a certain range of channel width. But we have not attempted to confirm it.

The wave resistance, sinkage and trim are summarized in Table 3. Again the resistance and sinkage are made dimensionless with the displacement and the half length of the ship. Trim is in degrees. First two extremes are given with the nondimensional time in parenthesis at which they occur. For resistance and trim, the first

extreme corresponds to the first maximum and the second extreme to the first local minimum. The extremes and their deviations take greater values as the channel becomes narrower. For sinkage, the first extreme represents lift up for $w/L=0.5$ and 1.0 , but downward sinkage for $w/L=3.0$. The ship sinks more in average in a wider channel. The time intervals between two extremes for all three quantities are consistently 0.4 and 1.7 for $w/L=0.5$ and 1.0 , respectively. But there is no such a correlation for $w/L=3.0$.

Hang S.Choi would like to thank the Korean Science & Engineering Foundation for financial support. He also wishes to thank I.H.Cho, a graduate student at Seoul National University, for his drawing pictures.

References

- Akylas, T.B. 1984 On the excitation of long nonlinear water waves by a moving pressure distribution. *J.Fluid Mech.* 141, 455-466.
- Bai, K.J., Kim, J.W. and Kim, Y.H. 1989 Numerical computations for a nonlinear free surface flow problem. to be presented at the 5th Intern. Conf. on Numerical Ship Hydrodyn. September, Hiroshima.
- Ertekin, R.C. 1984 Soliton generation by moving disturbances in shallow water : theory, computation and experiment. Ph.D. Thesis, Univ. Calif. Berkeley.
- Ertekin, R.C., Webster, W.C. & Wehausen, J.V. 1984 Ship - generated solitons. *Proc. 15th Symp. Naval Hydrodyn.* Hamburg, 347-364.
- Ertekin, R.C., Webster, W.C. & Wehausen, J.V. 1986 Waves caused by a moving disturbance in a shallow channel of finite width. *J.Fluid Mech.* 169, 275-292.
- Graff, W. 1962 Untersuchungen ueber die Ausbildung des Wellenwiderstandes im Bereich der Stauwellengeschwindigkeit im flachem, seitlich beschraenktem Fahrwasser. *Schifftechnik*, Bd.9, Heft 47, 110-122.
- Graff, W., Kracht, A. & Weinblum, G. 1964 Some extension of D.W.Taylor's standard series. *Trans.Soc.Naval Arch. & Marine Engrs.* 72, 374-401.
- Huang, D.-B., Sibul, O.J. & Wehausen, J.V. 1982 Ships in very shallow water. Festkolloquium zur Emeritierung von Karl Wiegardt, Institut fuer Schiffbau, Hamburg Univ. Bericht Nr.427, 29-49.

Izubuchi, T. & Nagasawa, S. 1937 Experimental investigation on the influence of water depth upon the resistance of ships. (in Japanese) *Japan Soc. Naval Architects*, 61, 165-206.

Katsis, C. & Akylas, T.R. 1987 On the excitation of long nonlinear water waves by a moving pressure distribution. Part 2. Three-dimensional effects. *J. Fluid Mech.* 177, 49-65.

Lee, S.-J., Yates, G.T. and Wu, T.Y. 1989 Experiments and analyses of upstream-advancing solitary waves generated by moving disturbances. *J. Fluid Mech.* 199, 569-593.

Lee, S.-J. and Grimshaw, R.H.J. 1989 Upstream-advancing waves generated by three-dimensional moving disturbances. to appear in *Physics of Fluid*.

Mei, C.C. 1986 Radiation of solitons by slender bodies advancing in a shallow channel. *J. Fluid Mech.* 162, 53-67.

Mei, C.C. & Choi, H.S. 1987 Forces on a slender ship advancing near the critical speed in a canal. *J. Fluid Mech.* 179, 59-76.

Thews, J.G. & Landweber, L. 1935 The influence of shallow water on the resistance of a cruiser model. US Exp. Model Basin, Navy Yard Rep. 408.

Tuck, E.O. 1966 Shallow-water flows past slender bodies. *J. Fluid Mech.* 26, 81-95.

Wu, D.M. & Wu, T.Y. 1982 Three-dimensional nonlinear long waves due to moving surface pressure. *Proc. 14th Symp. Naval Hydrodyn.* Ann Arbor, 103-129.

Wu, D.M. & Wu, T.Y. 1987 Precursor solitons generated by three-dimensional disturbance moving in a channel. *Proc. IUTAM Symp. on Nonlinear Water Waves*, Tokyo, 69-76.

Table 3 First two extreme values of wave resistance, sinkage & trim for a slender ship in channels with different width ($\alpha = 0.0$, $\mu = 0.333$)

W/L	0.5	1.0	3.0
R _w	0.140 (0.7)	0.105 (1.1)	0.085 (2.1)
	0.101 (1.0)	0.074 (1.8)	0.082 (2.8)
s	-0.008 (0.5)	-0.005 (0.8)	0.017 (0.5)
	0.013 (0.9)	0.014 (1.5)	0.011 (1.9)
θ_T	12.082 (0.6)	8.827 (1.0)	7.900 (1.7)
	8.334 (1.0)	6.456 (1.7)	5.894 (3.9)

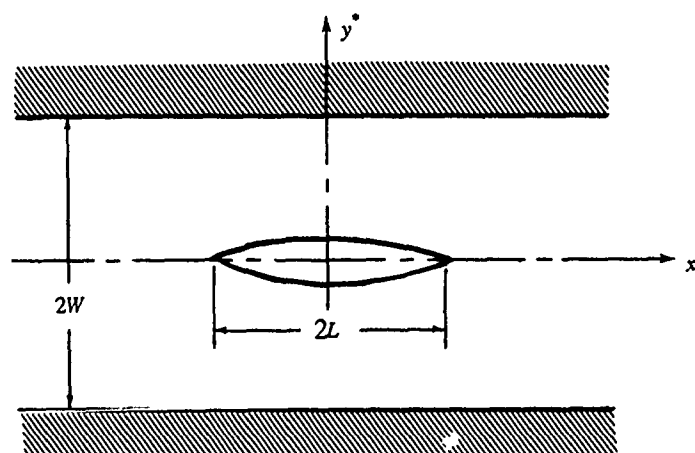


Fig.1 Definition sketch of a slender ship advancing in a channel

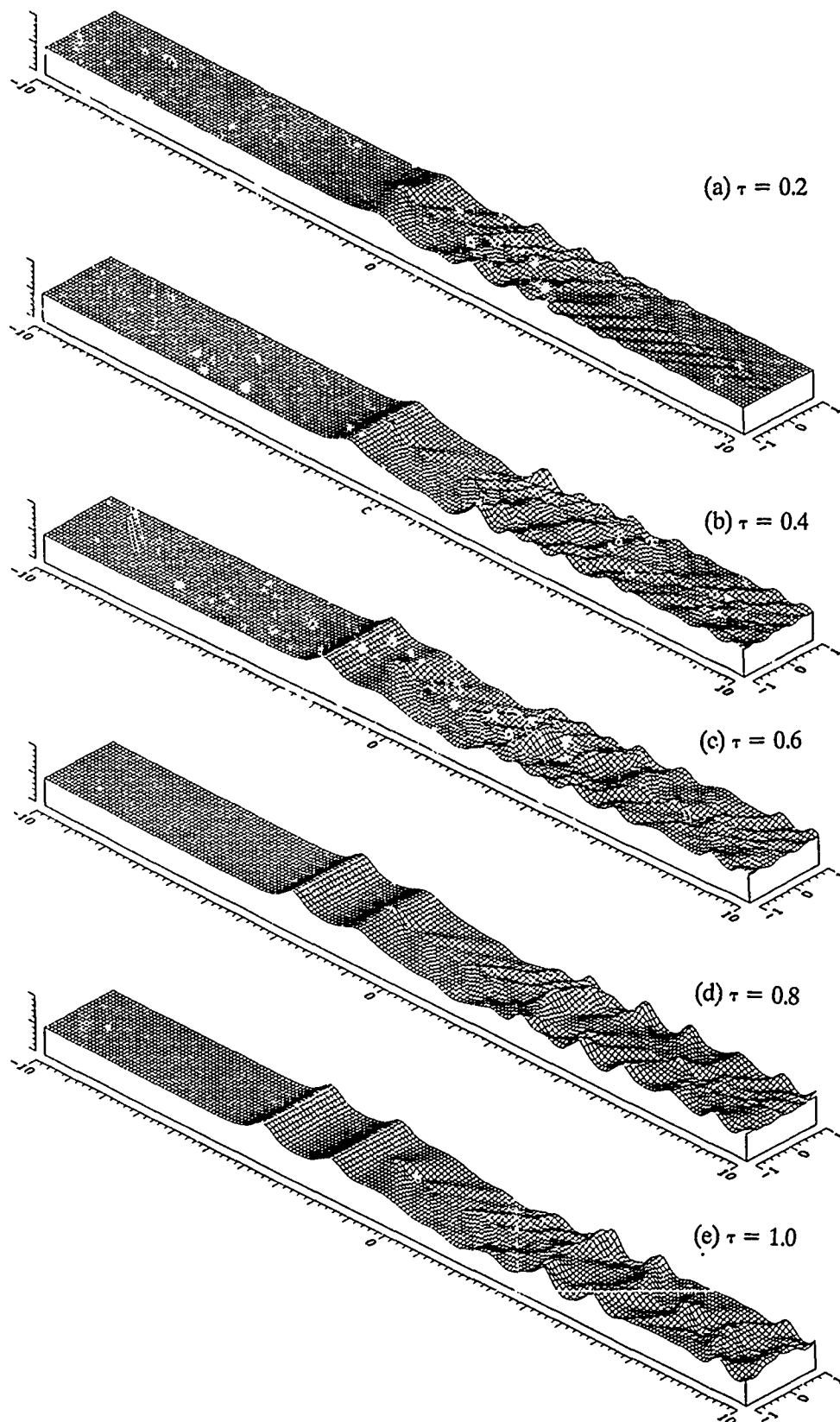
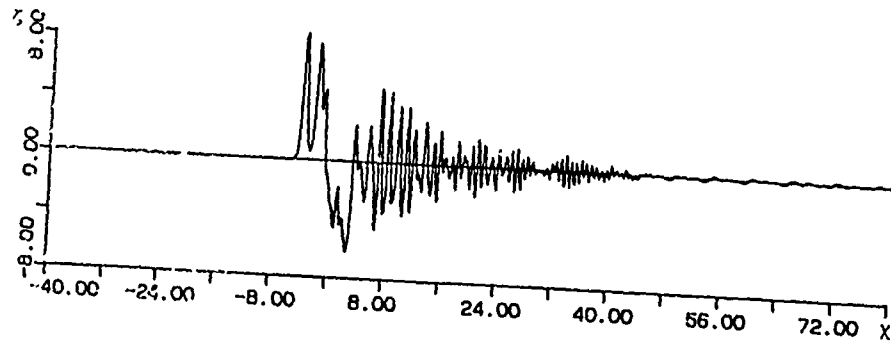
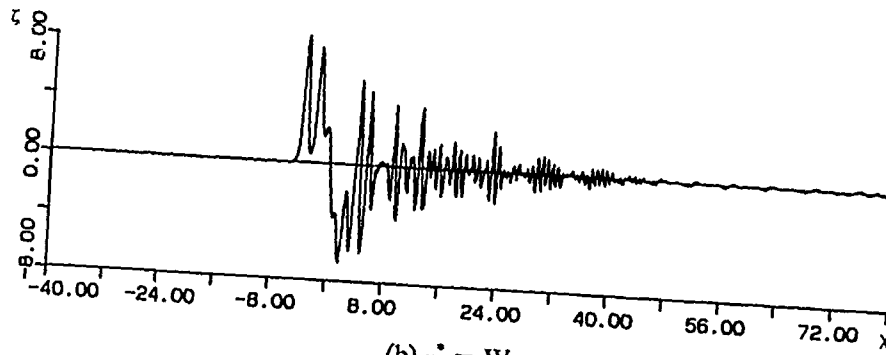


Fig.2 Evolution of wave field generated by a slender ship



(a) $y^* = 0$



(b) $y^* = W$

Fig.3 Wave profiles along the centerline & the wall of channel at $\tau = 1.0$

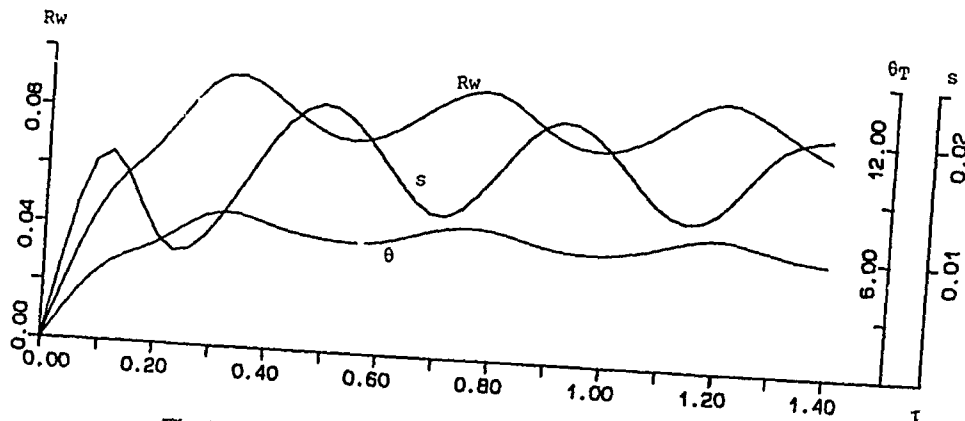


Fig.4 Evolution of wave resistance, sinkage and trim for a slender ship
($\alpha = 0.0$, $\beta = 26.5$, $\eta_s = 4.0$, $\mu = 0.25$)

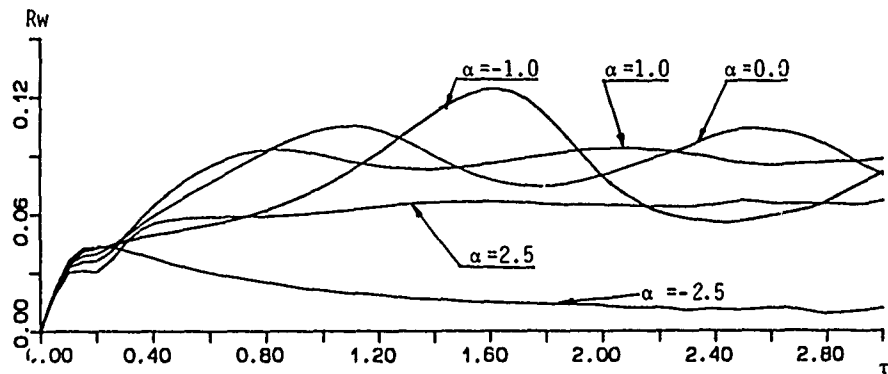


Fig.5 Evolution of wave resistance on a slender ship
for five different speeds
($\beta = 5.0$, $\eta_o = 3.0$, $\mu = 0.333$)

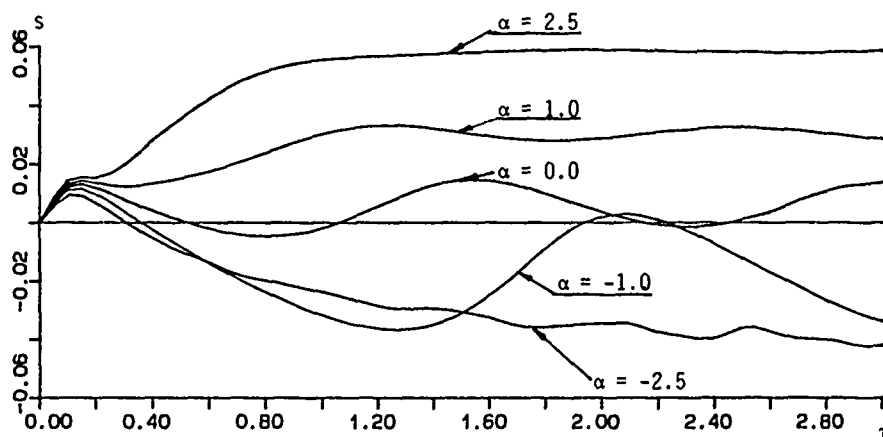


Fig.6 Evolution of sinkage for a slender ship
for five different speeds
($\beta = 5.0$, $\eta_o = 3.0$, $\mu = 0.333$)

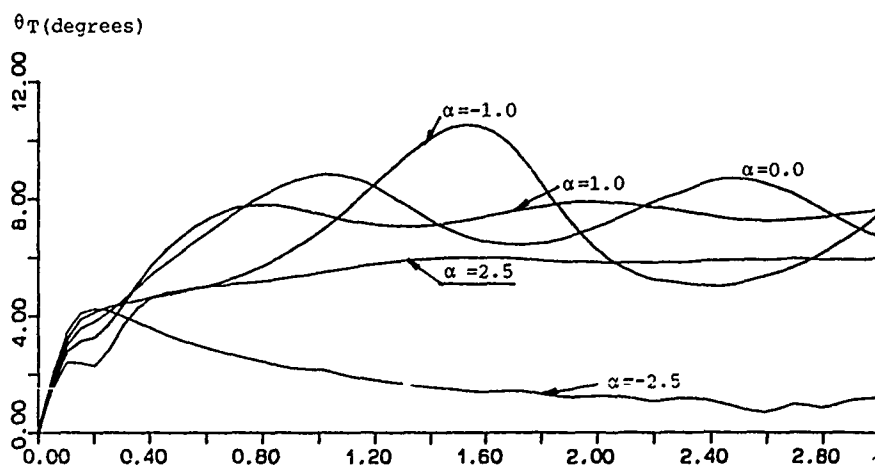


Fig.7 Evolution of trim for a slender ship
for five different speeds
($\beta = 5.0$, $\eta_o = 3.0$, $\mu = 0.333$)

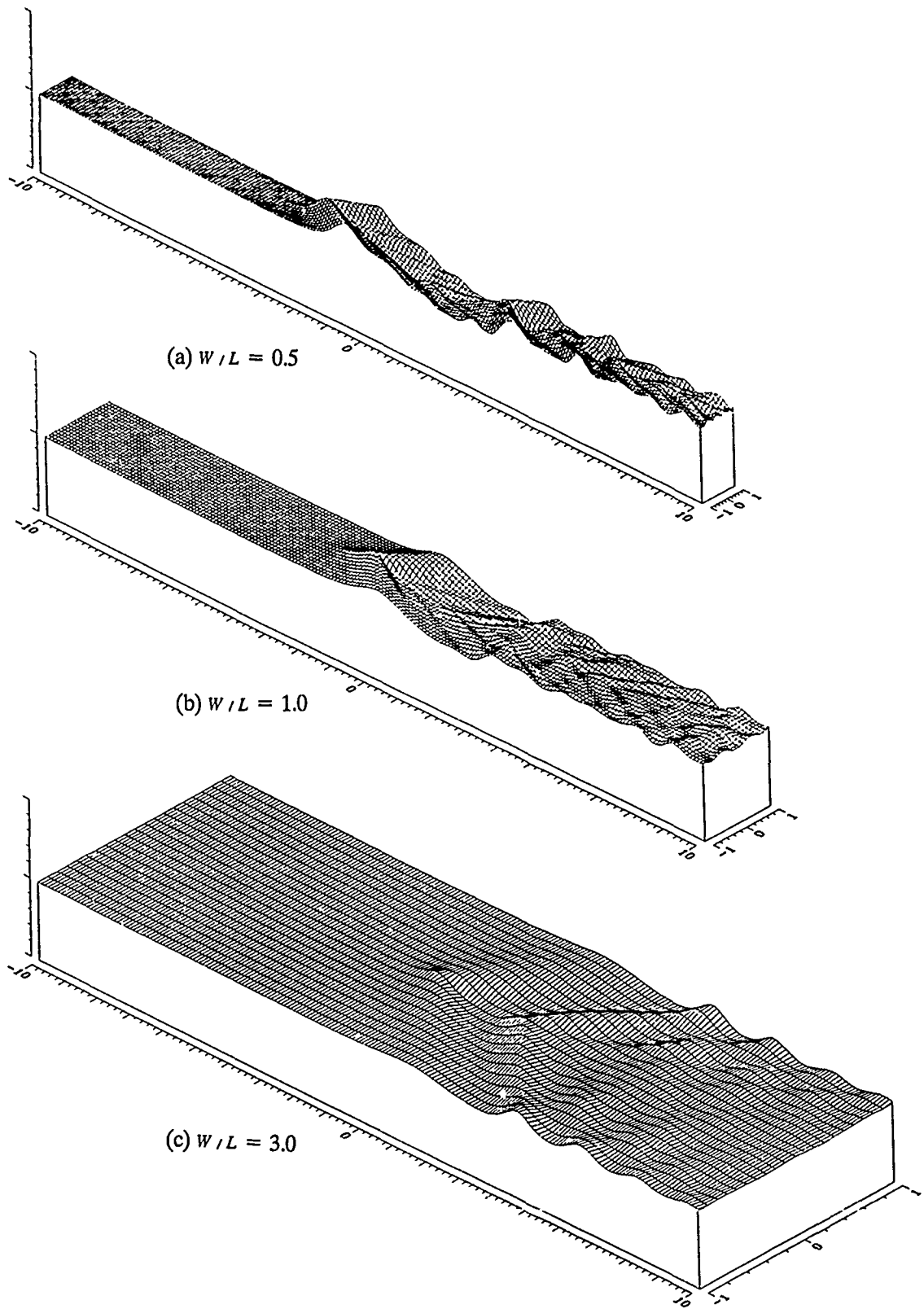


Fig.8 Wave pattern generated by a slender ship
for three different channel widths at $\tau = 1.0$ ($\alpha = 0.0$, $\mu = 0.333$)

DISCUSSION

by R.C. Ertekin

I would like to make a few comments before asking some questions on the points that are not clear to me.

Precursor soliton generation is not restricted to the critical speed. These waves have been observed and reported for Froude numbers as low as 0.2. The theory you used may be restricted to critical speeds but the phenomenon is not.

Soliton speeds are not necessarily faster than the towing speed always. As $Fr \rightarrow 1.3$ solitons form a bore attached to the bow. Around critical speed if the soliton amplitude is very low it is also possible that the soliton and model speeds are almost the same. For all subcritical speeds it is not clear that steady state cannot be reached, since soliton amplitudes (if 2nd, 3rd, etc. solitons) decrease as the ship continues to move forward. In some cases, solitons would not have been generated if we had a model tank which is very long.

I am surprised that Sommerfeld's condition did not work in your case. We have had no problem so far at the open boundaries. Perhaps something went wrong in the implementation process.

I am curious why you have not compared your resistance results with the experimental data. Could you please comment on this?

Your theory seems to be valid at $Fr=1$. However, most practical ship speeds are well below that. Can you extend the theory for subcritical speeds which may be low? If you can, your method will be much more efficient than a numerical method which is valid for all Froude numbers.

Author's Reply

Prof. Ertekin's discussions are highly appreciated. Since we have no experimental experience, your comments on the phenomena observed during tank tests will be much helpful for our further research.

It is not to mention that the Boussinesq equations are effective over a wide range of speed in shallow water, once the corresponding Ursell number is close to unity. It is also true that the expressions are rather complicated and an immense computation is required. For a simplification, we need an

additional assumption that the depth Froude number is expandable near the critical value. We have done it to obtain the two-dimensional Kdv equation or KP equation. Consequently it is obvious that our theory is valid for transcritical speeds.

In reply to the question about the comparison of wave resistance with experimental data, we tried to calculate for a destroyer model. But still more computations are necessary before we are able to arrive at a conclusion.

DISCUSSION

by T. Inui

This morning's Session (Session 7) reminded me my undergraduate diploma thesis (1943) on "Restricted Water Effect on Ship's Wake" (1943).

We measured the wake at two lengthwise positions, i.e. at midship and at the propeller position, and we also traversed in beamwise direction at midship. For the midship wake, which is approximately "potential" wake, we found an unexpectedly good agreement between our measurements and Kreitner's simple 1-D theory. The three different flow stages, i.e. subsonic, transonic, and supersonic, were clearly obtained.

Couple years later, I applied linear wave-making theory to this phenomena (1946), and found that

- i) For purely shallow water dR_w/dV is discontinuous at $F_h=1$, and
- ii) For restricted water R_w is discontinuous at $F_h=1$.

However, naturally, I could not succeed to get theoretically the transonic region. Since then it was my dream to bridge this gap by CFD, because it is essential to take into account the bodily sinkage and squat for the hull boundary condition.

The authors already obtained the first approximation for this. Then you may have a sufficient possibility by applying iteration. The authors' comments are highly appreciated.

Author's Reply

We thank Professor Inui for the comments on his own research. In response to it, we would like to emphasize once again that both the nonlinearity and the dispersion are important to the leading-order solution for the flow caused by a moving disturbance near

the critical speed in shallow water, and that a steady state can hardly be attained.

To the question, direct approaches such as the works Prof. Bai and Prof. Ertekin presented at this conference may give a better answer by taking the instantaneous hull-boundary condition exactly into their numerical schemes at the expense of a rapidly increased amount of computing time. In our slender-body approximation, it can be done only indirectly, if we include the temporal variation of the longitudinal distribution of ship's cross section in terms of source strength.

Some Numerical Computations about Free Surface Boundary Layer and Surface Tension Effects on Nonlinear Waves

E. Campana
Università "La Sapienza"
Roma, Italy

F. Lalli and U. Bulgarelli
Istituto Nazionale per Studi ed Esperienze di Architettura Navale
Roma, Italy

Abstract

This paper is a first approach to the development of a full nonlinear numerical method implementing the exact boundary conditions, taking into account viscosity and surface tension effects at the free surface. At this step, the following results have been obtained, maintaining the simplicity of the collocation method proposed by Dawson [5]:

1) effective fully nonlinear numerical procedure, taking into account the effects of viscosity at the free surface on potential flow;

2) simple preliminary results for the linear gravity-capillarity problem.

All the obtained numerical results have been tested with analytical solutions or experimental results.

\mathbf{q} = fluid velocity vector
 $\boldsymbol{\zeta}$ = vorticity vector
 ρ = density
 T = surface tension
 k = wave number
 \mathbf{v} = group velocity
 ν = kinematic viscosity
 \mathbf{g} = acceleration of gravity
 p = pressure
 R_w = wave resistance
 ϕ = velocity potential
 ϕ^* = perturbation potential
 ρ^* = simple layer density
 r = $|\mathbf{p}-\mathbf{q}|$
 r^* = $|\mathbf{p}-\mathbf{q}^*|$
 \mathbf{p} = field point
 \mathbf{q} = source point
 \mathbf{q}^* = image source point

List of symbols

Oxy = frame of reference fixed with the body : Ox is oriented in the opposite direction of the body velocity \mathbf{V} , Oy is vertical upwards
 $\partial\phi$ = body surface
 L = characteristic body length (chord)
 h = depth of the body center
 S = free surface
 \mathbf{n} = unit vector normal to S
 $\eta(x)$ = cartesian equation of the free surface
 K = curvature of the free surface
 l = curvilinear abscissa defined along S
 δ = free surface boundary layer thickness
 $\mathbf{V}(U,0)$ = body velocity vector

1. Introduction

The Rankine source method has been successfully adopted in recent years for the numerical solution of potential free surface flows.

In the usual approach the free surface boundary conditions are linearized and applied on the undisturbed free surface. Then, using the simple layer potential function, the boundary value problem is reduced to an integral equation which can be solved numerically.

With this approach, in 1977 Dawson [5] proposed a simple and effective procedure for computing the wave resistance of ships in the steady-state case. Such procedure was based on the idea of writing the above mentioned linearized boundary conditions along the zero Froude number flow streamlines on the undisturbed free surface.

In the wake of Dawson's paper several studies have then appeared in literature; some Authors deal with the linear problem, discussing about the consistency of different kinds of

linearizations [9,13], the numerical implementation of the radiation condition [10,12,14] or the numerical stability [12]. On the other hand some Authors, maintaining more or less the simplicity of the collocation method, and the use of an upstream finite differences scheme [5] for the radiation condition, proposed some kinds of iterative procedures to solve the nonlinear problem [6,11,15].

The present paper is a first approach to our future aim to develop a full nonlinear method, implementing the exact boundary conditions taking into account viscosity and surface tension effects at the free surface.

This combined gravity-capillarity problem is interesting because can give some more informations on nonlinear waves behavior, with respect to the classical model which neglects surface tension. As a matter of fact, Longuet-Higgins [2] proposed a model for the nonlinear transfer of energy from steep gravity waves to capillary ripples, which "ride" on the forward faces of the long waves. In this case the surface tension can be locally important and play a significant role in the generation of waves by wind. Furthermore capillary waves, taking energy from gravity waves and loosing it by viscosity, tend to delay the onset of breaking.

On the other hand Maruo and Ikehata, in an experimental work [8], pointed out the importance of surface tension on the shape of the wave pattern around the model, in particular at the forebody; how wave resistance coefficient depends also on the Weber number is furthermore shown in [8].

Among the free surface phenomena, the presence of a thin boundary layer can also be considered. All real fluid motions are of course rotational; even in nearly irrotational flows the relatively small amount of vorticity present in thin layers, can be crucial in determining the main flow characteristics, as it's well known. The condition of vanishing of the tangential stress at a perturbed free surface cannot be satisfied by an irrotational motion. Consequently we regard the incompressible flow as a combination of a thin rotational free surface layer and a potential flow region. The exact amount of the vorticity jump generated at the free surface can be written as a function of its curvature and of the potential velocity [4].

So we obtain a nonlinear dynamic boundary condition including viscosity effect at S ; of course in the limiting

case of $Re \rightarrow \infty$, the usual Bernoulli condition is obtained.

Numerical results have been computed for the full nonlinear formulation in the presence of a free surface boundary layer, while simple linear results are presented for the gravity-capillarity inviscid problem.

In order to validate the capability of the proposed model, numerical simulations of some typical test problems are described and discussed.

2. Mathematical formulations

We consider the following mathematical formulation for a 2D steady state potential flow, due to the motion of a submerged non-lifting body in a fluid of infinite depth. The extension to the 3D case can be easily obtained. The velocity $\underline{v}=(U,0)$ of the body is directed in the negative x direction, the y axis is positive upwards and the undisturbed free surface level is given by $y=0$. Consequently the fluid domain \mathcal{D} is bounded on the upper part by a free boundary S , and it is unbounded in the other directions. We assume that the fluid velocity, $\underline{q}=(u,v)$, can be written as:

$$(1) \quad \underline{q} = \nabla \Phi$$

where

$$(1') \quad \Phi = Ux + \varphi$$

In (1') the term Ux is the undisturbed flow potential and the term $\varphi(x,y)$ takes into account the interaction between the free surface and the body. Let be $y = \eta(x)$ the cartesian equation of the free boundary S , and l a curvilinear abscissa defined along S .

The potential $\Phi(x,y)$ satisfies Laplace's equation inside \mathcal{D} , where $\mathcal{D} = \mathcal{B} \cup \mathcal{D} \subset \mathbb{R}^2$ is the body:

$$(2) \quad \nabla^2 \Phi(x,y) = 0, \quad (x,y) \in \mathbb{R}^2 \setminus \mathcal{B} \cap \{y: -\infty < y < \eta(x)\}$$

The following boundary conditions, which include the effects of surface tension T , must be associated to equation (2):

$$(3) \quad \Phi_x \eta_x - \Phi_y = 0 \quad \text{on } S$$

$$(4) \quad \eta = \frac{1}{2g} (U^2 - \Phi_z^2) + \frac{T}{\rho g} K \quad \text{on } S$$

$$(5) \quad \Phi_n = 0 \quad \text{on } \partial \Omega$$

$$(6) \quad \lim_{|x| \rightarrow \infty} |\nabla \Phi| \quad \text{bounded}$$

Here $K(1)$ is the curvature of S , considered negative when the centre of curvature lies on the fluid side of the free surface:

$$(7) \quad K = \frac{\eta_{xx}}{(1 + \eta_x^2)^{3/2}}$$

From now on, in every model we will present, an extra boundary condition must be imposed at the bottom of Ω whenever the domain is supposed to have finite depth.

We are going to consider different kinds of approximations for the problem previously described, in which the boundary conditions given on S , obtained from (3) and (4), are suitable for computational purposes. More precisely four models are delineated.

2.1 The linear formulation with $T=0$

Assuming $T=0$ in (4) and neglecting the nonlinear terms both in (3) and in (4), we get the linearized free surface conditions:

$$(3') \quad U \eta_x = \varphi_y \quad \text{on } y=0$$

$$(8) \quad \eta = -\frac{U}{g} \varphi_x \quad \text{on } y=0$$

and the well known Neumann-Kelvin condition:

$$(9) \quad \frac{U^2}{g} \varphi_{xx} + \varphi_y = 0 \quad \text{on } y=0$$

where, for the condition at infinity, we have (see 2.6):

$$(6') \quad \lim_{x \rightarrow -\infty} |\nabla \Phi| = U$$

Therefore, in this case, the linear model describing the motion of a submerged body is constituted by (2), (5), (6'), (9) and (8) or (3'). It is worth to notice that, for this formulation, theorems for solution existence and uniqueness have been given in [7].

2.2 The linear formulation with $T \neq 0$

Without neglecting surface tension, conditions (9) and (8) can be written as:

$$(10) \quad \frac{U^2}{g} \varphi_{xx} + \varphi_y = \frac{T}{\rho g} \varphi_{yxx} = -\frac{T}{\rho g} \varphi_{yy} \quad \text{on } y=0$$

$$(11) \quad \eta = -\frac{U}{g} \varphi_x + \frac{T}{\rho g} \eta_{xx} \quad \text{on } y=0$$

Hence, in this case, the linear model is given by (2), (5), (6), (10) and (11) or (3').

2.3 The nonlinear formulation with $T=0$

In the nonlinear case, with $T=0$, condition (9) becomes:

$$(12) \quad \Phi_z^2 \Phi_{zz} + g \Phi_y = 0 \quad \text{on } S$$

while the nonlinear Bernoulli equation give:

$$(13) \quad \eta = \frac{1}{2g} (U^2 - \Phi_z^2) \quad \text{on } S$$

Therefore the nonlinear model, neglecting surface tension, is given by equations (2), (5), (6), (12) and (13) or (3).

2.4 The nonlinear formulation with $T \neq 0$

Assuming $T \neq 0$, the unified free surface condition is obtained by eliminating η between (3) and (4):

$$(14) \quad \Phi_z^2 \Phi_{zz} + g \Phi_y = \frac{T}{\rho} \Phi_z K_z \quad \text{on } S$$

So the nonlinear model with surface tension is given by equations (2), (4), (5), (6), (14). It is worth to observe that conditions (9), (10), (12) can be easily deduced from (14).

In the sequel we confine ourselves to consider the models given in 2.3

and 2.2.

2.5 The effect of viscosity at the free surface

Let us consider the model described in 2.3, in which we will introduce, in the hypothesis of large Reynolds numbers, the modifying effect of viscosity.

The introduction of a boundary layer at the free surface can be considered as a first step of a zonal splitting of the global problem into several interacting ones:

- the irrotational subdomain;
- the boundary layer at the free surface;
- the boundary layer about the body
- the wake;

Furthermore the new dynamic boundary condition improves some convergence properties of the numerical procedure [15].

To deduce the above mentioned condition we start from the consideration that the irrotational motion does not fulfil the condition of zero tangential stresses at the free surface (if the free boundary has a non zero curvature). Consequently, we introduce into the model given in 2.3 a partition of the flow field into an inviscid region, free from vorticity, and a thin viscous layer at the free boundary. Across the second region a vorticity jump, connected with the curvature of S , is considered, as well as the consequent velocity jump, due to the viscous component inside the boundary layer. In fact, although a rigid boundary is the commonest source of vorticity, in the case of a free boundary the vanishing of the tangential stresses generates vorticity and consequently a viscous boundary layer. Across this layer the above mentioned finite jumps of the velocity and of the vorticity are generated.

To include the effects of the vorticity at the free surface, we start from the steady Navier-Stokes equation:

$$(15) \quad \rho(\underline{q} \cdot \nabla) \underline{q} = -\nabla p^* + \mu \nabla^2 \underline{q}$$

where $p^* = p + \rho g y$, p^* is the dynamic pressure, p is the atmospheric pressure and ρ is the fluid density. By using the following identities:

$$(16') \quad (\underline{q} \cdot \nabla) \underline{q} = \nabla \left(\frac{1}{2} \underline{q} \cdot \underline{q} \right) - \underline{q} \times \underline{\zeta}$$

$$(16'') \quad \nabla^2 \underline{q} = -\nabla \times \underline{\zeta}$$

and, for $y = \eta(x)$:

$$(17) \quad \nabla \left(\frac{1}{2} \underline{q} \cdot \underline{q} + g \eta \right) = \underline{q} \times \underline{\zeta} - \nu \nabla \times \underline{\zeta}$$

Since the integral on the left hand side of (17) is path independent, we can integrate both sides of (17) along S , which in the steady flow is a streamline. Requiring that:

$$\lim_{l \rightarrow \infty} |\underline{q}| = U$$

we obtain:

$$(18) \quad \eta(l) = \frac{U^2}{2g} - \frac{1}{2g} \underline{q} \cdot \underline{q} - \frac{\nu}{g} \int_{-\infty}^l \nabla \times \underline{\zeta} \cdot d\ell'$$

since $\underline{q} \times \underline{\zeta} \cdot d\ell' = 0$.

The kernel of the curvilinear integral can be transformed as follows:

$$(19) \quad (\nabla \times \underline{\zeta}) \cdot d\ell' = -\frac{\partial \zeta}{\partial n} d\ell'$$

where n is the unit vector normal to S , oriented outwards. By substituting (19) into (18), we can easily get:

$$(20) \quad \eta(l) = \frac{U^2}{2g} - \frac{1}{2g} \underline{q} \cdot \underline{q} + \frac{\nu}{g} \int_{-\infty}^l \frac{\partial \zeta}{\partial n} d\ell'$$

The normal derivative of ζ , if the viscous layer is sufficiently thin, can be expressed as the ratio between the vorticity jump across the boundary layer and its thickness δ :

$$(21) \quad \frac{\partial \zeta}{\partial n} \approx \frac{\Delta \zeta}{\delta}$$

Now we shall use Helmholtz decomposition and a boundary layer approximation to evaluate the above mentioned vorticity and velocity jumps, in terms of the velocity potential gradient and of the geometrical curvature of the free surface. The

expression of $\Delta\zeta$ can be readily evaluated [4] as:

$$(21') \Delta\zeta = 2K |\nabla\Phi|$$

Moreover an estimation of the oscillatory boundary layer thickness can be given [4] by:

$$(22) \delta = \left(\frac{U\nu}{g}\right)^{1/2}$$

Furthermore we observe that the velocity distribution in the fluid domain can be decomposed as:

$$\underline{q} = \nabla\Phi + \underline{q}_v$$

where \underline{q}_v is required to satisfy:

$$\nabla \cdot \underline{q}_v = 0 \quad \nabla \times \underline{q}_v = \underline{\zeta}$$

In particular the velocity at the free boundary can be thought as the sum of $|\nabla\Phi|$ and the jump $\Delta|\underline{q}_v|$ of the rotational component across the boundary layer. This jump can be estimated [4]:

$$(23) \Delta|\underline{q}_v| \approx \delta \Delta\zeta$$

hence, we have:

$$(23') |\underline{q}| = |\nabla\Phi| + \Delta|\underline{q}_v| \approx |\nabla\Phi| + \delta \Delta\zeta = |\nabla\Phi| + 2\delta K |\nabla\Phi|$$

By introducing (21), (22), (23') in (20), neglecting terms of order δ^2 we get:

$$(24) \eta(\ell) = \frac{U^2}{2g} - \frac{1}{2g} \Phi_\ell^2 (1 + 4\delta K) + 2 \frac{\nu}{g\delta} \int_{-\infty}^{\ell} K(\ell') \Phi_\ell' d\ell'$$

The unified free surface boundary condition is obtained from (3), (24):

$$(25) \Phi_\ell^2 \Phi_{\ell\ell} (1 + 4\delta K) + g \Phi_\ell + 2 \Phi_\ell^2 \left(\delta K_\ell \Phi_\ell - \frac{\nu}{\delta} K \right) = 0$$

We observe that the usual inviscid nonlinear dynamical condition can be

obtained from (25) in the limiting case of $\delta \rightarrow 0$ (i.e. $Re \rightarrow \infty$).

2.6 An integrodifferential formulation for the gravity-capillarity problem

Let's consider now the linear problem with surface tension described in 2.2. We are going to develop some mathematical calculations in order to obtain an integrodifferential formula, in which the third order derivative present in (10), that create some difficulties for numerical implementation, does not appear. Moreover, we intend to explore the behavior of the solution.

Solving (11) with respect to η , it follows:

$$(26) \eta_{xx} - \frac{\rho g}{T} \eta = \frac{\rho U}{T} \varphi_x = F(x)$$

that is:

$$(27) \eta(x) = e^{\alpha x} \left[A_1 + \frac{1}{2\alpha} \int_0^x e^{-\alpha \xi} F(\xi) d\xi \right] + e^{-\alpha x} \left[A_2 - \frac{1}{2\alpha} \int_0^x e^{\alpha \xi} F(\xi) d\xi \right]$$

where A_1 and A_2 are arbitrary constants, and $\alpha = \sqrt{\rho g / T}$. Since η is bounded for $|x| \rightarrow \infty$, we find:

$$A_1 = \frac{1}{2\alpha} \int_0^\infty e^{-\alpha \xi} F(\xi) d\xi$$

$$A_2 = -\frac{1}{2\alpha} \int_{-\infty}^0 e^{\alpha \xi} F(\xi) d\xi$$

and hence:

$$(28) \eta(x) = -\frac{1}{2\alpha} \left[e^{\alpha x} \int_x^\infty e^{-\alpha \xi} F(\xi) d\xi + e^{-\alpha x} \int_{-\infty}^x e^{\alpha \xi} F(\xi) d\xi \right]$$

At this point, three different formulations, involving respectively φ , φ_ξ and $\varphi_{\xi\xi}$ will be obtained. Substituting the expression of $F(\xi)$ and integrating by parts we get:

$$(29) \quad \eta(x) = -\frac{1}{2} \frac{\rho}{T} \left[e^{\alpha x} \int_x^{\infty} e^{-\alpha \xi} U \varphi d\xi - e^{-\alpha x} \int_{-\infty}^x e^{\alpha \xi} U \varphi d\xi \right]$$

From (29), deriving with respect to x and applying the kinematical condition (3'):

$$(30) \quad \varphi_y = -\frac{\rho U^2}{T} \varphi + \frac{\rho U^2}{2T} \left[e^{\alpha x} \int_x^{\infty} e^{-\alpha \xi} \varphi d\xi + e^{-\alpha x} \int_{-\infty}^x e^{\alpha \xi} \varphi d\xi \right]$$

The formulation involving $\varphi_{\xi\xi}$ follows directly from (28), deriving with respect to x and using again condition (3'):

$$(31) \quad \varphi_y = -\frac{\rho U^2}{2T} \left[e^{\alpha x} \int_x^{\infty} e^{-\alpha \xi} \varphi_{\xi\xi} d\xi - e^{-\alpha x} \int_{-\infty}^x e^{\alpha \xi} \varphi_{\xi\xi} d\xi \right]$$

Finally, to get the last expression with $\varphi_{\xi\xi\xi}$, we integrate by parts (28):

$$(32) \quad \eta(x) = -\frac{U}{g} \varphi_x - \frac{U}{2g} \left[e^{\alpha x} \int_x^{\infty} e^{-\alpha \xi} \varphi_{\xi\xi\xi} d\xi - e^{-\alpha x} \int_{-\infty}^x e^{\alpha \xi} \varphi_{\xi\xi\xi} d\xi \right]$$

and the unified condition is obtained as above:

$$(33) \quad \varphi_y = -\frac{\rho U^2}{T} \frac{1}{2\alpha} \left[e^{\alpha x} \int_x^{\infty} e^{-\alpha \xi} \varphi_{\xi\xi} d\xi + e^{-\alpha x} \int_{-\infty}^x e^{\alpha \xi} \varphi_{\xi\xi} d\xi \right]$$

The relations (30), (31) or (33) can be used instead of (10), to avoid the calculation of the third order derivative φ_{xxy} or φ_{yyy} in the numerical implementation.

We notice that from (32) we obtain (9) when $T \rightarrow 0$, that is $\alpha \rightarrow \infty$.

In order to study some properties of the solution, we consider the simple free wave problem, given by (2), (10), (11); by means of the separation of variables we can write, up arbitrary constants:

$$(34) \quad \varphi = \text{Re} \left\{ e^{k(y-ix)} \right\}$$

where k is the separation constant. Substituting (34) in (10) we get the dispersion relation:

$$(35) \quad k^2 - \frac{\rho U^2}{T} k + \frac{\rho g}{T} = 0$$

$$\text{with: } k_g = \frac{\rho U^2}{2T} \left(1 - \sqrt{1 - \frac{4gT}{\rho U^4}} \right)$$

$$k_c = \frac{\rho U^2}{2T} \left(1 + \sqrt{1 - \frac{4gT}{\rho U^4}} \right)$$

Hence, if g or $T \rightarrow 0$ we obtain respectively:

$$k_g = \frac{g}{U^2} \quad (\text{pure gravity waves})$$

$$k_c = \frac{\rho U^2}{T} \quad (\text{pure capillary waves})$$

Since we consider the steady case, the phase velocity is zero, while the group velocity is given by:

$$(36) \quad v = \left(\frac{g}{U^2 k} - \frac{1}{2} \right) U$$

which can be written:

$$(37) \quad v = \frac{-\left(1 - \frac{4gT}{\rho U^4}\right) \mp \sqrt{1 - \frac{4gT}{\rho U^4}}}{\frac{4kT}{\rho U^3}}$$

The positive sign must be chosen for gravity waves, and the negative one for capillary waves: it is easy to recognize that the group velocity is positive for the formers, and

negative for the latters. So it follows that gravity waves and capillary ripples propagate in opposite directions [1,2], as it is well known from experimental observation.

2.7 A simplified formulation for the linear gravity-capillarity problem

Now we reconsider the linear formulation described in 2.2. Let us assume:

$$\begin{aligned} \varphi &= \varphi^g + \varphi^c \\ (38) \quad \eta &= \eta^g + \eta^c \end{aligned}$$

where the superscripts G and C indicate the terms connected respectively to the gravity and capillary waves; in fact, as it has been shown in the preceding section, in the capillarity-gravity problem two wave systems are present: the capillary wave preceding the body, and the gravity one following it.

So we can write:

$$\begin{aligned} U(\eta_x^g + \eta_x^c) &= \varphi_y^g + \varphi_y^c \\ U(\varphi_x^g + \varphi_x^c) + g(\eta^g + \eta^c) - \frac{T}{\rho}(\eta_{xx}^g + \eta_{xx}^c) &= 0 \\ \lim_{x \rightarrow -\infty} \eta^g &= \lim_{x \rightarrow -\infty} |\nabla \varphi^g| = 0 \\ \lim_{x \rightarrow +\infty} \eta^c &= \lim_{x \rightarrow +\infty} |\nabla \varphi^c| = 0 \end{aligned}$$

Since the problem is linear, we can apply the superposition of the effects, solving two splitted problems:

$$\begin{aligned} (39) \quad U\eta_x^g &= \varphi_y^g \\ (40) \quad U\varphi_x^g + g\eta^g - \frac{T}{\rho}\eta_{xx}^g &= 0 \\ (41) \quad \lim_{x \rightarrow -\infty} |\nabla \varphi^g| &= 0 \\ (42) \quad U\eta_x^c &= \varphi_y^c \\ (43) \quad U\varphi_x^c + g\eta^c - \frac{T}{\rho}\eta_{xx}^c &= 0 \end{aligned}$$

$$(44) \quad \lim_{x \rightarrow +\infty} |\nabla \varphi^c| = 0$$

These formulations can be strongly simplified assuming:

$$\begin{aligned} (45) \quad \eta_{xx}^g &= -(k^g)^2 \eta^g \\ \eta_{xx}^c &= -(k^c)^2 \eta^c \end{aligned}$$

that is, the free surface is sinusoidal. Of course, hypothesis (45) can be a good approximation only for the far field: the solution available with this assumption can so be considered asymptotical. We have:

$$(46) \quad U\varphi_x^g + \left(g + \frac{T}{\rho}(k^g)^2\right)\eta^g = 0$$

$$(47) \quad U\varphi_x^c + \left(g + \frac{T}{\rho}(k^c)^2\right)\eta^c = 0$$

and, considering (35), we get finally:

$$(48) \quad \eta^g = -\frac{\varphi_x^g}{Uk^g}$$

$$(49) \quad \varphi_{xx}^g + k^g \varphi_y^g = 0$$

$$(50) \quad \eta^c = -\frac{\varphi_x^c}{Uk^c}$$

$$(51) \quad \varphi_{xx}^c + k^c \varphi_y^c = 0$$

In order to solve problem (48), (49) condition (41) must be considered, as well as condition (44) for problem (50), (51).

3. Numerical procedure and results

The numerical solution of the mathematical models given in 2.3, 2.5 and 2.7 is reached by means of a simple layer formulation:

$$(52) \varphi(p) = \int_{\partial B} [\sigma \log r + \log r'] ds + \int_S \sigma \log r^* ds_s$$

in which

$$\begin{aligned} r &= |p - q_s| \\ r' &= |p - q_s^*| \\ r^* &= |p - q_s^*| \end{aligned}$$

with p field point, $q_s \in \partial B$, $q_s^* \in \partial B^*$, $q_s \in S$ source points, being B^* the image of B with respect to the undisturbed free surface.

The surface ∂B and a local portion of S are discretized, by means of the classical collocation method [5], with segments tangent to the boundaries.

3.1 The nonlinear gravity problem

In the numerical procedure the free surface S is followed, step by step, updating its discretization and, of course, the influence matrices.

The iterative scheme consists of two cycles. An 'internal' one, in which the nonlinear problem given by (2), (5) and (12) is solved with an iterative procedure; when the solution of this system satisfies the required accuracy, the free surface is updated in the 'external' cycle by means of (13). At the first step, to initialize the procedure, the potential flow and the free surface configuration are computed with Dawson method.

The computational steps, for the double iteration scheme, can be summarized as in the following:

- 1 - solve the linear problem (2), (5), (6), (8), (9) to initialize the numerical procedure;
- 2 - external loop (index m): $\psi_i^{(m)}$, $\eta_i^{(m)}$ are known on each boundary element i ;
- 3 - internal loop (index j): solve the nonlinear system

$$I \quad \Phi_{n_i}^{(j+1)} = 0$$

$$II \quad \Phi_{\ell_i}^{2(j)} \Phi_{\ell_i}^{(j+1)} + g \Phi_{y_i}^{(j+1)} = 0$$

in which the quadratic terms are considered explicitly, and the condition II is imposed on the previous approximation (m) of the free surface configuration; when $\max_i |1 - \Phi_i^{(j)} / \Phi_i^{(j+1)}|$ is lower than a prefixed tolerance

- go to step 4;
- 4 - external loop (index m): calculation of the new approximation of S , with

$$III \quad \eta_i^{(m+1)} = \frac{1}{2g} (U^2 - \Phi_{\ell_i}^2)$$

when $\max_i |1 - \eta_i^{(m)} / \eta_i^{(m+1)}|$ is less than a required tolerance, the numerical procedure is considered to be concluded.

Near the downstream boundary, also if the damping zone suggested in [5] is present, an oscillatory behavior has been observed, though for all the other grid points convergence has been reached; this phenomenon becomes more evident as the Froude number increases, as it could be expected. Moreover we notice that convergence is reached more rapidly for wave resistance than for wave height; this behavior, rather obvious since the former is an average quantity, can be useful for practical applications.

The same numerical strategy has been used also for the nonlinear formulation (24), (25), which includes the effects of viscosity at the free surface; the use of such formulation instead of (12), (13) extends considerably the range of applicability of the method [5], though the terms involving viscosity are rather small.

We remark that the term $\Phi_{\ell\ell}$ in (12) or in (25) is discretized with the four points finite differences scheme proposed by Dawson; the downstream damping zone, in which a two points operator is used, is fixed equal to a quarter of the wave length.

To validate the present method, the numerical procedure has been applied to a submerged hydrofoil, whose geometrical characteristics and location in the fluid dynamic field can be found in fig.1; several experimental results for this case can be found in [3].

In all the examples the free boundary has been discretized by 250 panels, and the boundary of the body by 40 elements. The number of panels per wave length has been chosen equal to 40, and about 80 free surface elements have been placed upstream the body leading edge. In the first two examples we compute the wave pattern corresponding to two different Froude numbers (.4406 and .617), with the Froude number defined as U/\sqrt{gL} (L is the chord length). The wave pattern, computed by the nonlinear procedure described before, by means of (25), is compared with the experimental data

obtained in [3] and with the linear numerical solution computed by Dawson's method [5]. As it's shown in fig.2 and 3 the full nonlinear formulation gives a numerical solution which fits the experimental data better than the linear one. We notice that in this range of Froude number the inviscid nonlinear formulation gives almost the same results of (25), the only difference being a small damping in the wave amplitude for the viscous formulation, as it can be expected. This behavior is shown in fig.4 ($Fr=.704$), in which the typical steep wave shape can be recognized; the damping appears to be significant rather far from the body: at a distance about $10*L$ a 4 per cent attenuation is present.

In fig.5 the wave resistance as a function of the Froude number is plotted (for this figure, $Fr=U/\sqrt{g*h}$): also in this case the nonlinear method behaves better than the linear one, with respect to the experimental data.

We remark that the inviscid formulation gives practically the same results for the wave resistance, but its range of applicability is narrower with respect to (25), in fact for $Fr>.57$ the numerical procedure diverges [5], while the use of (25) allows one to obtain results up to $Fr=.65$.

3.2 The linear gravity-capillarity problem

We solve numerically both the splitted problems (2), (5), (48), (49), (41) and (2), (5), (50), (51), (44), by means of Dawson's method, noticing that for the capillarity problem the second derivative must be discretized with a downstream finite differences operator, in order to satisfy the radiation condition.

In fig.6 the wave pattern obtained with this procedure is shown: the dashed lines indicate the splitted solutions, while the continuous line indicate the superposition of them. In this case the body is a circular cylinder (diameter $d = 0.01$ m), with a depth of the center equal to the diameter. Surface tension value is $.074$ N/m; for the discretization, 20 panels per capillary wave length have been chosen, with a total number of 300 panels used.

Fig.7 shows the behavior of the wave lengths accuracy with respect to the discretization, in comparison with the analytical values.

Finally, in fig.8 the values of gravity and capillary wave lengths as functions of the velocity U are plotted, in comparison with the

dispersion relation (35); in this case, 30 panels per wave length have been used.

Conclusions

Both the proposed numerical models seem to be promising and suitable to have more investigations. At the present the introduction of viscosity effects is rather effective in order to get convergence with highly nonlinear boundary conditions. The model with surface tension can be a very deep tool for describing nonlinear energy transfer phenomena; the results obtained with the simplified linear model are preliminary steps for studying a radiation condition suitable also for the nonlinear model.

Acknowledgements

We wish to acknowledge Prof. P. Bassanini, Dept. of Mathematics, Univ. 'La Sapienza' of Rome, for the helpful suggestions and encouragements, and Eng. T. Coppola, who implemented the computational codes.

References

- 1 Lamb, H., Hydrodynamics, 6th ed., Cambridge University Press, 1945.
- 2 Longuet-Higgins, M. S., "The Generation of Capillary Waves by Steep Gravity Waves", Journal of Fluid Mechanics, vol. 16, 1963.
- 3 Salvesen, N., "On Second Order Wave Theory for Submerged Two-Dimensional Bodies", 6th Symposium on Naval Hydro., Washington, 1966.
- 4 Batchelor, G. K., An Introduction to Fluid Dynamics, Cambridge, 1967.
- 5 Dawson, C. W., "A Practical Computer Method for Solving Ship-Wave Problems", 2nd Int. Conf. Numerical Ship Hydro., Berkeley, 1977.
- 6 Daube, O., Dulieu, A., "A Numerical approach of the Nonlinear Wave Resistance Problem", 3rd Int. Conf. Numerical Ship Hydro., Paris, 1981.
- 7 Do, C., Guevel, P., "Waves on a Uniform Flow in a Channel of Constant Depth", Research Notes in Mathematics, 78, Vol I, Fasano & Primicerio Ed., London 1983.
- 8 Maruo, H., Ikehata, M., "Some discussions on the Free Surface Flow around the Bow", 16th Symposium on Naval Hydro., Berkeley, 1986.
- 9 Jensen, G., Mi, Z. X., Soding, H., "Rankine Source Methods for Numerical Solutions of the Steady

- Wave Resistance Problem", 16th Symposium on Naval Hydro., Berkeley, 1986.
- 10 Jensen, P. S., "On the Numerical Radiation Condition in the Steady-State Ship Wave Problem", Journal of Ship Research, Vol. 31, n.1., 1987.
 - 11 Rong, H., Liang, X., Wang, H., "A Numerical Method for Solving Nonlinear Ship-Wave Problem", ITTC, Kobe, 1987.
 - 12 Sclavounos, P. D., Nakos, D. E., "Stability Analysis of Panel Methods for Free-Surface Flows with Forward Speed", 17th Symposium on Naval Hydro., The Hague, 1988.
 - 13 Raven, H. C., "Variations on a Theme by Dawson", 17th Symposium on Naval Hydro., The Hague, 1988.
 - 14 Nakatake, K., Kawagoe, T., Andou, J., Kataoka, K., "Calculation of Hydrodynamic Forces Acting on Hydrofoils", SMSSH, Varna, 1988.
 - 15 Campana, E., Lalli, P., Pitolli, F., Bulgarelli, U., "Fully Nonlinear Free Surface Flow Computation by means of Moving Panels method", ISRP, Shanghai, 1989.

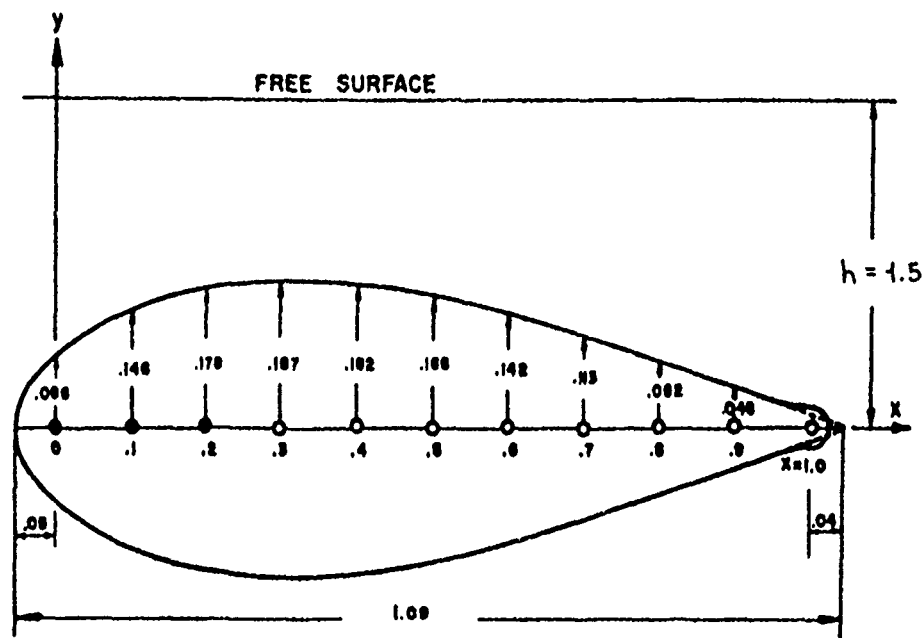


Fig.1: Cross section of the hydrofoil [3];
quantities expressed in ft.

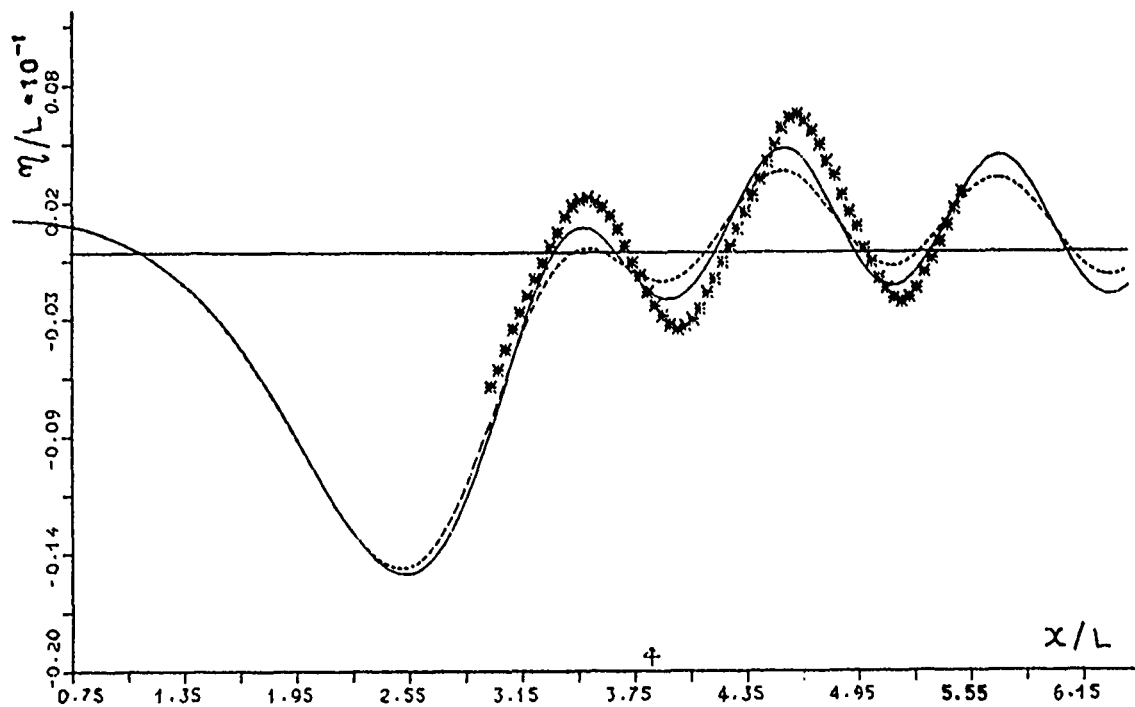


Fig.2: $U/\sqrt{g^*L} = .4406$

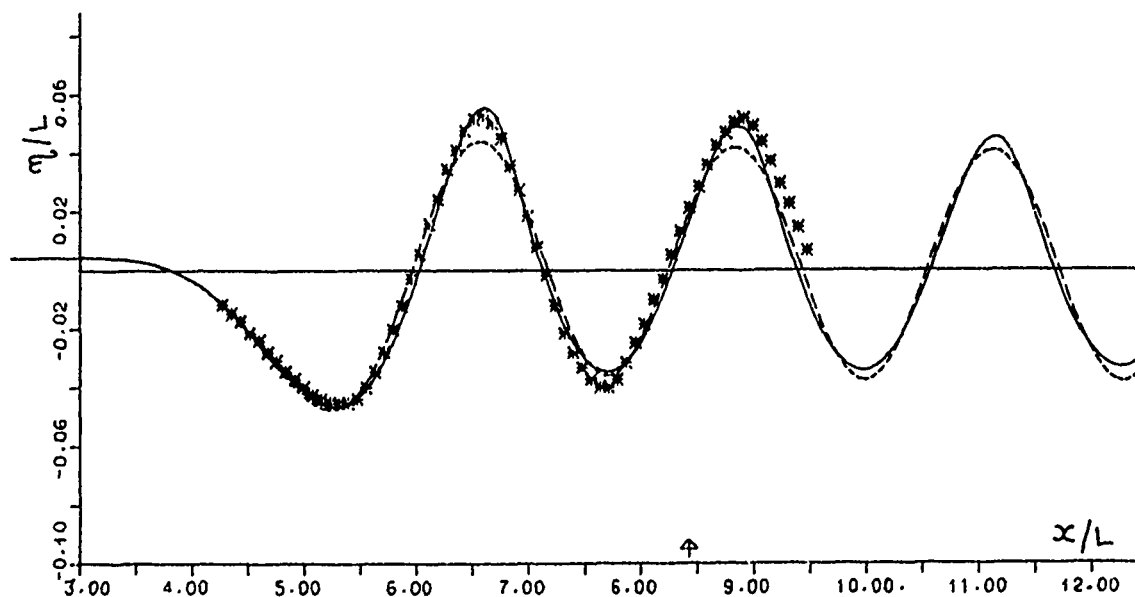


Fig.3: $U/\sqrt{g^*L} = .617$

Waves generated by the submerged hydrofoil, the arrows indicate the position of the trailing edge.

----- Dawson method
 ————— full nonlinear method
 ***** experimental [3]

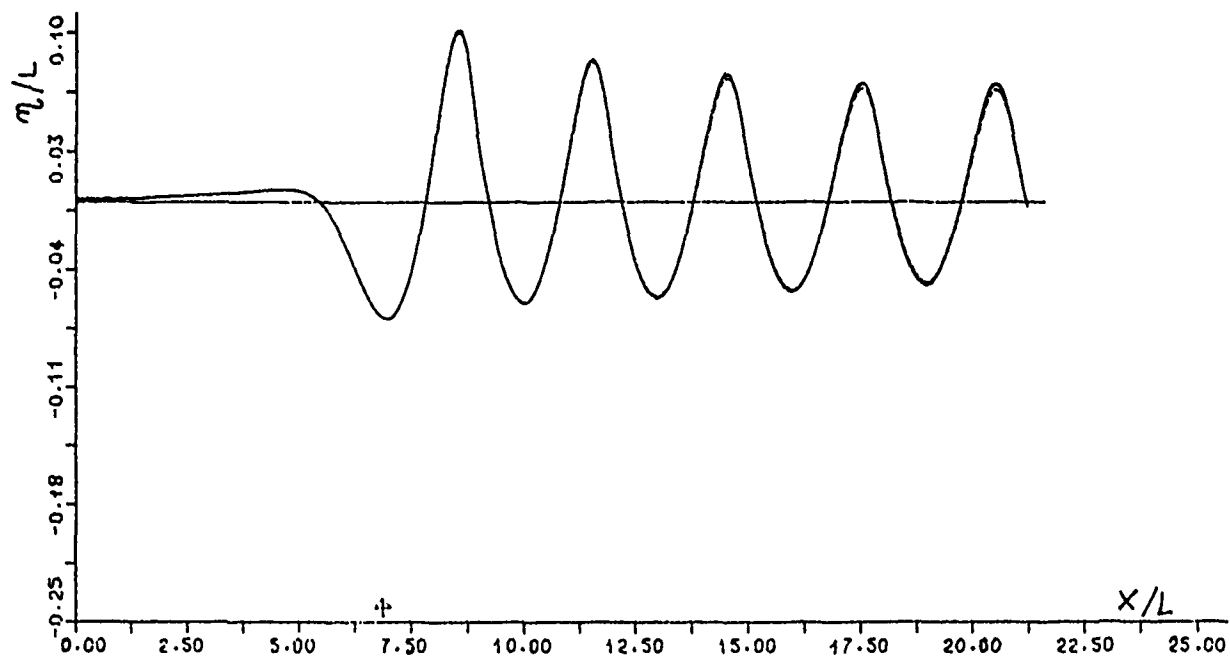


Fig.4: $U/\sqrt{g^*L} = .704$

— full nonlinear method
 - - - full nonlinear with viscous correction

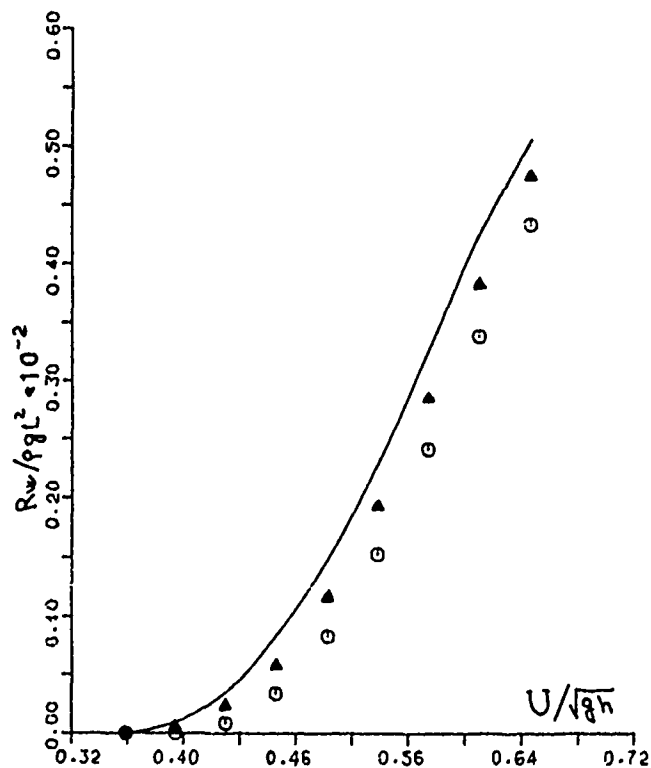


Fig.5: Wave resistance versus $U/\sqrt{g^*h}$

— experimental [3]
 ooooooo Dawson method
 ▲▲▲▲▲ full nonlinear method

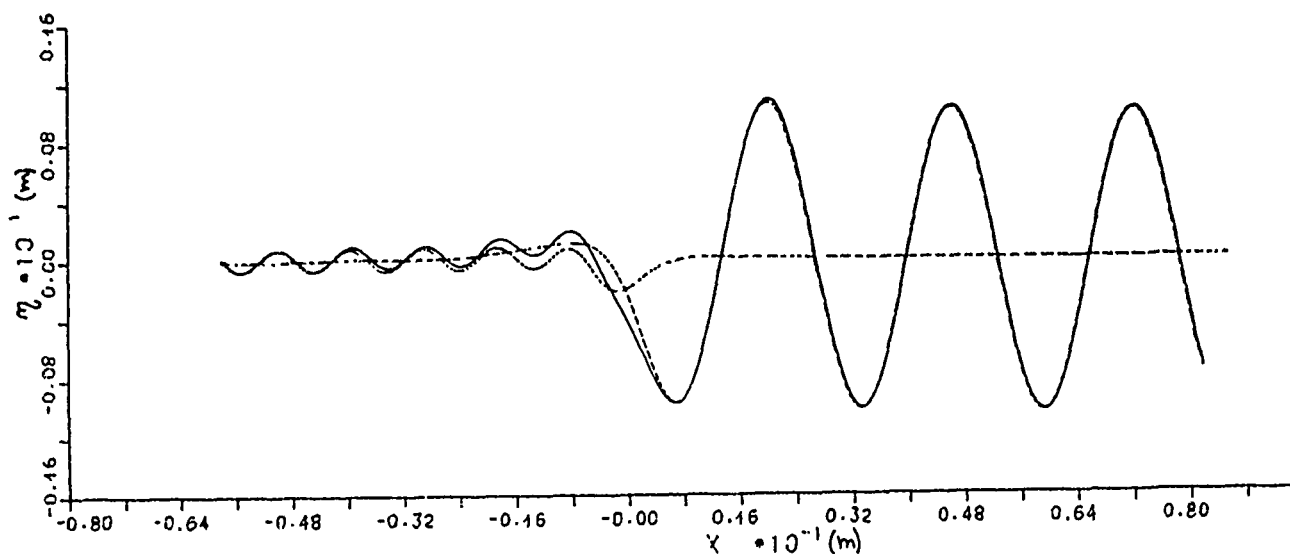


Fig.6: Gravity-capillarity steady free surface flow past a submerged circular cylinder:

----- gravity and capillary waves
 ————— superposition

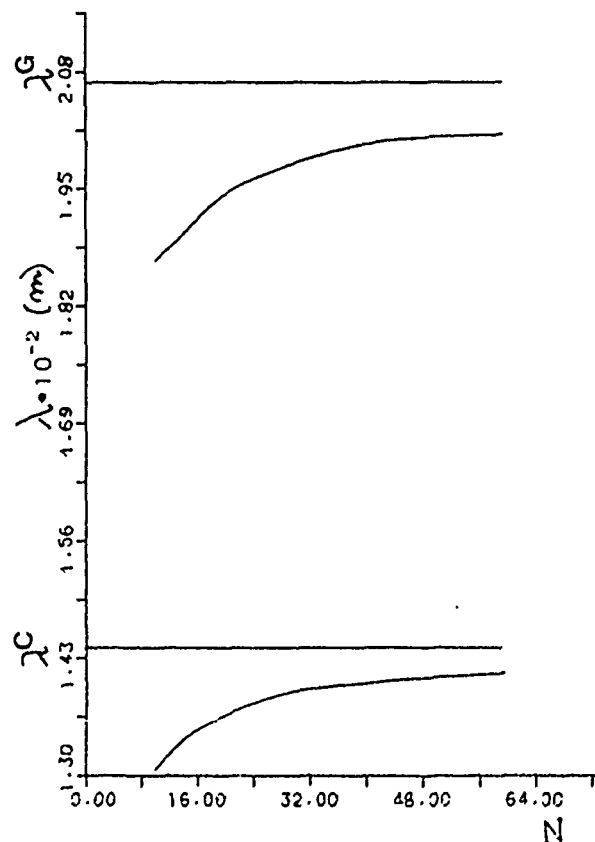


Fig.7: Wave lengths versus N = number of panels
 per wavelength;
 $U = .234$ m/s
 $L = .01$ m
 $h = .01$ m

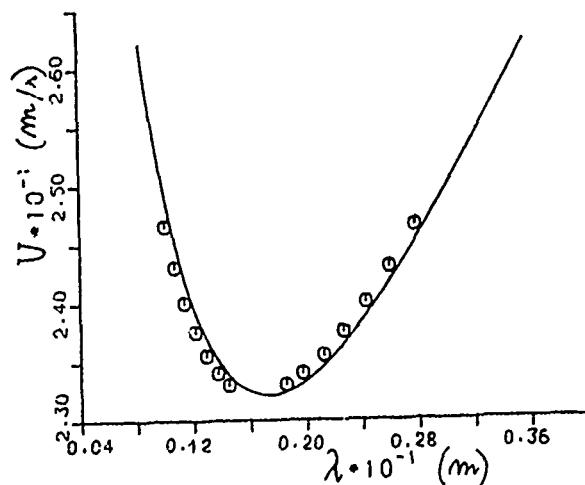


Fig.8: Dispersion relation (35)

$L = .01$ m

$h = .01$ m

———— analytical curve
 ooooooo numerical values

DISCUSSION

by K. Nakatake

I appreciate your results about capillary waves in front of the hydrofoil. I would like to know the way of decay of that kind of wave. And how large is the effect of surface tension on the wave behind the hydrofoil?

Author's Reply

I thank Prof. Nakatake for his kind appreciating comment about our work. I remark that our computations about gravity-capillary waves have been performed by means of a simplified linear model which, for its nature, cannot give any information about attenuation.

In the linear model, in fact, the capillary wave amplitude remain constant, as well as for the gravity wave. Anyway, since the attenuation increases with the curvature of the free surface, as it has been pointed out dealing with viscosity effects at the free boundary, the damping of capillary ripples must be much stronger with respect to the gravity waves.

For the 2nd part of the question, the effect of surface tension on the wave behind the body is easily evaluated. In fact, if the pure gravity wave length is equal to $2\pi F_r^2$, in the presence of surface tension the wave length become $(1 + \sqrt{1 - 4/W_0^2 F_r^2})\pi F_r^2$.

A Boundary Integral Formulation for Free Surface Viscous and Inviscid Flows about Submerged Bodies

C. M. Casciola

Istituto Nazionale di Studi ed Esperienze di Architettura Navale
Roma, Italy

R. Piva

Università di Roma "La Sapienza"
Roma, Italy

Abstract

The possibility to generate numerical models based on a boundary integral formulation for rotational free surface flows, either viscous or inviscid, is explored with the purpose to maintain some of the computational efficiency proper of potential flow approaches. A simple method for the simulation of the unsteady nonlinear behavior of the free surface has been derived, starting from a mathematical model which decouples the kinematical and the dynamical aspects of the flow field, without introducing the potential approximation. The strict relationship with the coupled models based on the integral formulation for viscous and inviscid flows, is discussed in details to extend the present method to these more general conditions. The mathematical and numerical aspects of the related integral equations are analyzed and an efficient numerical solution is proposed for the solution of the flow field generated by a moving submerged cylinder.

1 Introduction

Among the several methodologies adopted for the analysis of the free surface flow problems — usually nonlinear and unsteady — a special role is played by the potential flow approximation. This actually leads to a very appealing model consisting of a linear steady equation for the field and a nonlinear unsteady boundary condition on the free surface. The boundary integral equation method is particularly appropriate for the numerical solution of such problem for two main reasons. First, when applied to linear equations it reduces by one the space dimensions of the computational domain, second it provides a description of the complicated nonlinear boundary conditions more accurate than any other computational approach. This technique has been recently used for the numerical simulation of the wave pattern generated by the mo-

tion of a submerged cylinder with both linear and nonlinear free surface boundary conditions [6], yielding in a more efficient way the same results previously obtained by finite difference in curvilinear coordinates [5].

On the other hand, the viscous flow field about a submerged body and the interaction between the viscous phenomena and the free surface wave generation have been usually investigated by finite difference schemes of the Navier-Stokes equations in their differential form. The proper numerical approximation of the boundary conditions of the free surface, together with the need to confine the computational domain are the main difficulties connected with the use of this technique. In spite of these drawbacks, some interesting results have been presented recently for the unsteady flow about a submerged body, even in the case of breaking wave conditions [4].

The main purpose of the present work is to analyze the possibility to generate numerical models based on a boundary integral formulation for the simulation of rotational free surface flows either viscous or inviscid, which maintain some of the capabilities briefly discussed for the potential approximation. In this case the field equations — either Navier-Stokes or Euler — are both non linear and unsteady thus preventing the explicit confinement of the related terms into the free surface boundary conditions, as for the potential flow. In the past few years we investigated the integral equation approach for large Reynolds number flows about streamlined bodies [3]. We like here to extend the formulation to viscous free surface flows for the applications to ship hydrodynamics.

Following this idea, in section 2, the Navier-Stokes equations are written in integral form by using the fundamental solution for the unsteady Stokes operator and a representation formula for the velocity vector in the field in terms of the velocities and tractions at the boundary is obtained. The numerical solution of the

relevant integral equation presents some difficulties at large Reynolds numbers, mainly related to the tentorial singularity of the kernel. The limiting case of zero viscosity, that is the integral formulation for the Euler equation, is discussed in section 3 to better observe the critical behavior of these equations and to devise the proper way to recover simplified models for a quite general, but still sufficiently efficient, computational procedure. To this purpose we like to point out that the great advantage of the potential models in the framework of the free surface flows, is not as much connected to the introduction of the potential itself as it is to the decoupling between the kinematics (Laplace Eq.) and the dynamics (Bernoulli Eq.) of the problem. The Bernoulli equation which is non linear and unsteady has to be solved at the free surface (if the pressure is not required) to give the so called dynamical boundary condition. A further kinematical equation is required to describe, in its Lagrangian or Eulerian form, the motion of the free surface in time.

A brief review of the set of boundary conditions to be applied at the free surface for different approximations of the flow model, starting from the more general interface between two viscous fluids, is carried out in section 4 to understand the role of each of these conditions with regard especially to the coupling or decoupling of the field equations. More specifically, we like to understand how the free surface boundary conditions reduce for flow models still rotational, but simplified through a decoupling procedure analogous to the one for potential flows. We analyze this subject in section 5, where we derive directly from the Euler representation a decoupled model which recovers for the velocity the Poincaré kinematical formula. The role of dynamics in deriving the proper boundary conditions is discussed in connection with this point. The proposed model resulting from the above procedure, is consistent and well equipped to treat the nonlinear free surface behavior. It has a value in itself, as the numerical results shown in section 6 for the submerged cylinder may indicate. Further, starting from this model, for which we have studied the mathematical and numerical aspects of the solution, we intend to recover, through a backward procedure, the coupling aspects and the diffusion phenomena neglected at this moment. The direct connection between this model and the more general representations for the Euler and the Navier-Stokes equations, which has been described in the present paper, indicates the main lines to follow in the further investigations.

2 Integral formulation for viscous flows

As mentioned before, in this section the Navier Stokes

equations are recasted into an integral form. It is well known that the integral formulations for the Navier Stokes equations have been mostly used for studying the mathematical aspects of viscous flows. A typical example is the theory of hydrodynamic potentials which provides many important results for the linearized Navier Stokes equations. A detailed description of the method, introduced by Odqvist, is given in [1], where the direct integral representation for the steady state problem is also presented. The aim of Ladyzhenskaja's analysis, is devoted to the existence and uniqueness of solution for the Navier Stokes equations. It is on these theoretical topics that the integral formulation for viscous flow has found their best application, due to the simple analysis of the proper boundary conditions.

More recently, due to the developments of the boundary element methods, integral formulations have received new interest for the numerical simulation of viscous flows. Although these methods have their best application in linear problems, the advantages of integral formulations can be largely recovered in the numerical simulation of viscous flows about streamlined bodies when no massive separation occurs [3]. Actually in this case the nonlinear source term related to the vorticity in the field, is confined to a small region in the boundary layer and the wake, thus allowing for an efficient discretization procedure in terms of finite elements.

In this section the formulation, which has been previously described in [2] in full details, will be briefly reviewed in order to present an extension to free surface problems. In order to introduce the integral formulation, for the sake of clarity, the Navier Stokes equations are given here:

$$\frac{\partial \mathbf{u}}{\partial t} + \nabla \frac{u^2}{2} + \chi = -\frac{\nabla p}{\rho} + \nu \nabla^2 \mathbf{u} - \nabla \Pi \quad (1)$$

$$\nabla \cdot \mathbf{u} = 0$$

In equation (1) the term $\Pi = gz$ is the potential energy per unit mass related to the gravity force. The direct integral formulation for the system (1), as obtained in [2], gives the velocity of the fluid in terms of convolutions of the proper fundamental solutions which will be denoted in the following by $u_j^{(k)}$ and $p^{(k)}$ with the related traction given by $t_j^{(k)} = -p^{(k)}n_j + \mu(\frac{\partial u_j^{(k)}}{\partial z_i} + \frac{\partial u_i^{(k)}}{\partial z_j})$

$$u_k(x^*, t^*) = \int_{t_0}^{t^*} \int_{\Omega} (u_j t_j^{(k)} - \tilde{t}_j u_j^{(k)}) ds dt - \quad (2)$$

$$\int_{t_0}^{t^*} \int_{\Omega} \rho \nu u_j u_j^{(k)} ds dt +$$

$$\int_{t_0}^{t^*} \int_{\Omega} \chi_j u_j^{(k)} dv dt - \int_{\Omega} u_j u_j^{(k)} dv|_{t_0}$$

In deriving the integral representation formula (2) from the Navier Stokes equations in differential form, the term $\chi = -u \times \zeta$ ($\zeta = \nabla \times u$) has been assumed as a known forcing term; furthermore the traction vector $t_j^{(k)}$ is modified in the form

$$\tilde{t}_j = -Pn_j + \nu \left(\frac{\partial u_j}{\partial x_i} + \frac{\partial u_i}{\partial x_j} \right) \quad (3)$$

where:

$$P = \frac{p}{\rho} + \frac{1}{2}u^2 + \Pi \quad (4)$$

is the Bernoulli group. For the sake of clarity it is to be remarked the difference between the traction vector t_j involved in the boundary conditions and the modified traction vector \tilde{t}_j ($\tilde{t}_j = t_j + \frac{1}{2}u^2 + \Pi$).

As shown by (2) it appears that the solution u is given in terms of surface as well as volume integrals. The first surface integral gives the effect of the boundary values of the velocity and of the modified traction. Nonlinear terms are present in this integral through the modified tractions \tilde{t}_j .

The second surface integral accounts for the motion of the boundary, which moves with velocity ν_o (normal velocity component of a geometric point belonging to the boundary), and gives the effect of the momentum flux due to the boundary motion.

This integral gives a nonlinear contribution in free surface flows for the dependance of the boundary velocity ν_o on the fluid motion. The source of this nonlinearity are always confined to the boundary as the ones acting in potential flows.

Different is the case of the first volume integral which is related to the term χ and accounts for the rotational effects in the fluid. This source of nonlinearity, which directly comes from the field equation, is confined to the rotational flow region. In the general case it would require a large computational effort and it would penalize the computational procedure in comparison with other computational approaches. However for the flow about a submerged streamlined body, either attached or without a massive separation, this term can be efficiently treated by finite elements techniques retaining in this way a great deal of the computational efficiency of the boundary element method. In order to complete the description of (2) the last volume integral carries the information on the initial conditions.

The integral representation gives a boundary integral equation for the collocation point, at which the velocity is evaluated, approaching the boundary. To account for the jump properties of the double layer kernel $t_j^{(k)}$ a factor c ($= \frac{1}{2}$, for smooth boundaries) appears in the limit at the left hand side. The obtained integral equation is a constraint between the

values assumed by the velocity and the traction at the boundary. If we know one of them, for a given configuration of the domain representation (2) gives a Fredholm equation for the remaining one (either a first kind for the unknown traction or a second kind for the unknown velocity). The fundamental solutions $u_j^{(k)}$ and $p^{(k)}$ satisfy the equations:

$$\begin{aligned} \nabla \cdot u^{(k)} &= 0 \\ \mu \nabla^2 u^{(k)} - \nabla p^{(k)} - \rho \frac{\partial u^{(k)}}{\partial t} &= \delta^* e^{(k)} \end{aligned} \quad (5)$$

which must to be considered in the sense of distribution theory with $\delta(x - x^*)$ and $\delta(t - t^*)$ Dirac delta functions in space and time respectively. The explicit solution of (5) for the free space problem in two dimensions gives

$$\begin{aligned} u_j^{(k)} &= \delta_{ij} F - \frac{\partial^2 E}{\partial x_j \partial x_k} \\ p^{(k)} &= -\frac{\partial G}{\partial x_k} \delta(t^* - t) \end{aligned} \quad (6)$$

where:

$$\begin{aligned} G &= \frac{1}{2\pi} \ln(r) \\ F &= -\frac{1}{\rho} E(t^* - t) \frac{e^{-r^2/4\nu(t^*-t)}}{4\pi\nu(t^*-t)} \\ E &= -\frac{1}{4\pi\rho} E_1 \left(\frac{r^2}{4\nu(t^*-t)} \right) - G \\ \nabla^2 E &= F \end{aligned} \quad (7)$$

where E_1 is the exponential integral.

Looking at the fundamental solutions it appears that all the terms in the integral representation that contain a derivative with respect to x_k can be recasted in the form of a gradient ($\frac{\partial}{\partial x_k} = -\frac{\partial}{\partial x_k^*}$) by taking the derivative with respect to x_k^* out of the integrals. These terms give an irrotational contribution to the velocity field, while the rotational effect is related to the function F , which is not reducible to a gradient form. The function F is the fundamental solution for the heat transfer equation and it becomes sharper and sharper as the kinematical viscosity ν goes to zero.

The function E has the same behaviour as it appears from the last equation in system (7). The main difficulty in solving these equations for large Reynolds number flows is related to the crucial behaviour of the functions F and E , rather than to the evaluation of the volume integrals.

In order to gain a better insight on the properties of representation (2) in the case of large Reynolds numbers, we analyze the limiting case of Re infin-

ity. An integral formulation related to the differential model for inviscid flows (that is the Euler equations) is obtained in the next section.

3 The limiting case for inviscid flows

The Euler equations for an incompressible fluid are obtained from the Navier Stokes equations for the Reynolds number infinity. Consequently one of the boundary conditions for viscous flow should be relaxed, due to the lowering of the order of the partial differential equation. For this limiting case a boundary integral formulation is directly derived from the one valid for Navier Stokes equations, rather than from the differential model. Some introductory considerations on the proper boundary conditions to be applied is presented while the general discussion on the free surface boundary conditions for both viscous and inviscid models is given in the next section.

As a first step we obtain the limiting expressions for the fundamental solutions. As it appears from (6) the pressure fundamental solution $p^{(k)}$ doesn't depend on the kinematic viscosity ν , so that it retains the same expression as for the viscous case. This is not surprising since the pressure fundamental solution is related to the compressibility effects in the fluid, which in both cases is assumed of constant density. Looking at the limiting behavior of the function F in (7) the following relationship holds:

$$\lim_{\nu \rightarrow 0} \int_{\Omega} f(\mathbf{x}) F(\mathbf{x}, \mathbf{x}^*; t, t^*) d\mathbf{v} = -H(t^* - t) f(\mathbf{x}^*) \quad (8)$$

From (8) it directly follows the distributional limit for the function F as:

$$F = -H(t^* - t) \delta(\mathbf{x} - \mathbf{x}^*) \quad (9)$$

The limiting value for the function E (note that $\nabla^2 G = \delta(\mathbf{x} - \mathbf{x}^*)$) is given by

$$\nabla^2 E = -H(t^* - t) \delta(\mathbf{x} - \mathbf{x}^*) \quad (10)$$

Therefore we have:

$$E = -H(t^* - t) G \quad (11)$$

Finally the limiting expressions for the velocity fundamental solutions are

$$u_j^{(k)} = -\frac{H(t^* - t)}{\rho} \left(\delta_{ij} \frac{\partial^2 G}{\partial x_i \partial x_j} - \frac{\partial^2 G}{\partial x_j \partial x_i} \right) \quad (12)$$

with the corresponding traction vector given by:

$$t_j^{(k)} = \frac{\partial G}{\partial x_k} \delta(t - t^*) n_j \quad (13)$$

The direct combination of (12) and of (13) into the integral representation (2) readily gives the limiting formulation which is given below in vector notations with the explicit expressions of the surface integral while the remaining volume integrals are denoted by I_v

$$\begin{aligned} \mathbf{u}^* = & \int_{\partial\Omega(t^*)} (\mathbf{u} \cdot \mathbf{n}) \nabla G d\mathbf{s} + \\ & \int_{t_0}^{t^*} \int_{\partial\Omega(t)} P [(\mathbf{n} \cdot \nabla) \nabla G - \mathbf{n} \nabla^2 G] d\mathbf{s} dt + \\ & \int_{t_0}^{t^*} \int_{\partial\Omega(t)} \nu_{\sigma} [(\mathbf{u} \cdot \nabla) \nabla G - \mathbf{u} \nabla^2 G] d\mathbf{s} dt + I_v \end{aligned} \quad (14)$$

It clearly appears from (14) that the kernels in the second and third integrals have an hypersingular behaviour when the collocation point approaches the boundary. The formulation (14) does not present a direct computational interest, but it has great interest for the comparison it provides with the viscous case showing in particular the computational difficulties to be expected for large Reynolds number. In this case in fact the fundamental solutions do not present a real hypersingular behavior, but they are very difficult to be numerically evaluated in an accurate way for their close relationship with the hypersingular ones.

Moreover, the following analytical manipulations to set eq. (14) in a better form from the computational point of view will give some useful suggestions for an accurate treatment of the viscous equations. Following the procedure suggested for potential flows by Hsiao and Nedelec, eq. (14) can be rewritten through some known vector identities, in the form

$$\begin{aligned} \mathbf{u}^* = & \int_{\partial\Omega(t^*)} (\mathbf{u} \cdot \mathbf{n}) \nabla G d\mathbf{s} + \\ & \int_{t_0}^{t^*} \int_{\partial\Omega(t)} (\nabla P \times \mathbf{n}) \times \nabla G d\mathbf{s} dt \\ & + \nabla \cdot \times \int_{t_0}^{t^*} \int_{\partial\Omega(t)} 2\nu_{\sigma} (\nabla \times \mathbf{u}) G d\mathbf{s} dt \\ & - \nabla \cdot \times \int_{t_0}^{t^*} \int_{\partial\Omega(t)} \nu_{\sigma} (\mathbf{u} \times \nabla G) d\mathbf{s} dt + I_v \end{aligned} \quad (15)$$

where $\nabla \cdot = \mathbf{e}_k \frac{\partial}{\partial x_k}$. In the present form the hypersingular kernel doesn't appear any more and the contribution of the modified pressure P is closely related to that of a vortex layer of density $\gamma = \nabla P \times \mathbf{n}$. Further manipulations may be performed on (15) in order to show its close relationship with an uncoupled

model based on the Poincaré kinematic formula as it is shown in the next section. At the present stage it is of some interest to notice that eq. (15) could be used in the numerical simulation of nonlinear free surface flows with no difficulty other than the computation of the volume integrals. It is also worthwhile to notice that, for a two dimensional case, the velocity u at any point in the field is given in terms of two scalar valued functions at the boundary, instead of the two vector valued functions appearing in (2). This fact is strictly related to the lower order attained by the differential model for the limiting case. As a result only one integral constraint is expected among the two scalars as the collocation point approaches the boundary. Actually the boundary integral equation is given by the normal component of the vector formula (15). The other component gives, even on the boundary, a representation for the tangential velocity component in terms of given normal component and the modified pressure.

In the next section the proper boundary conditions for the free surface will be reviewed for both the viscous and the inviscid model. The kinematical description of the interface will also be presented.

4 Free surface boundary conditions for coupled models

In both the integral formulations presented in the previous sections the kinematical and dynamical parts of the flow problem are strictly coupled. The proper boundary conditions for the free surface problem in the coupled models is introduced here in some details in order to show the differences with the corresponding treatment in decoupled models (splitting of kinematics and dynamics) to be introduced in the next section.

The two possible kinematical descriptions of the free surface (Lagrangian and Eulerian) are also introduced and discussed at the end of this section. The boundary conditions which directly follow from the integral formulations are treated first. Let us consider the general case of an interface between two different fluids. Two different cases are considered. In the first one both fluids are assumed to be viscous while in the second one they are considered both inviscid. For a given position of the interface the boundary conditions are given by the dynamical balance of the free surface and by the no slip property of the viscous fluids. Neglecting surface tension effect, the boundary conditions are

$$u = u_u \quad (16)$$

$$t = t_u \quad (17)$$

where the subscript u stays for the upper fluid and the values of both members of (16) and (17) are unknown. From the integral representation (2) it follows that the boundary conditions are appropriate for the interface problem. Collocating the integral representation for the lower fluid at a point belonging to the free surface, one integral constraint between u and t is enforced. Analogously the other integral equation is obtained for u_u and t_u . In this way at each point of the interface we have four vector unknowns and four independent vector equations that is two boundary integral equations and two boundary conditions. In the case of no motion of the fluid acting upon the interface the problem is more simple and only one boundary condition, the dynamical one, has to be imposed, in the form, for instance, of a known pressure distribution:

$$t = -p_u n \quad (18)$$

In this case we have one unknown (the fluid velocity at the free surface) and one integral equation where the value specified by (18) for the traction vector is introduced.

A similar procedure leads to the boundary conditions to be used for the formulation (15) for the second case. Due to the inviscid character of the fluids it is expected to get a discontinuity in the tangential velocity component across the interface while only conditions on the normal velocity component and on the pressure may be used

$$u_n = u_{u,n} \quad (19)$$

$$p = p_u \quad (20)$$

We have now four scalar unknowns and four scalar equations: the two boundary conditions and the two integral equations relating the normal velocity component to the pressure. As in the viscous case, for no motion of the fluid acting upon the interface, a given pressure distribution is assigned.

In order to complete the formulation, the kinematical description of the interface has to be briefly recalled. As it is well known, for the geometrical analysis of a moving surface two possible descriptions are available. The Lagrangian one, gives the position of the geometrical points on the surface as a function of a Lagrangian parameter ξ . Denoting by x_ξ this function, once the velocity of the point labeled by ξ were known, the surface geometry may be determined solving the initial value problem:

$$\begin{aligned}\frac{dx_f}{dt} &= u_f \\ x(\xi, 0) &= x_0(\xi) \quad \xi \in D_\xi\end{aligned}\quad (21)$$

where D_ξ is the set of values of the Lagrangian parameter ξ and u_f is assumed to coincide with the local fluid velocity. Some problems are expected in the case of the interface between two inviscid fluids due to the discontinuity of the velocity across the interface. Some intermediate value for the tangential component should then be assumed to move the free surface.

In the Eulerian description the free surface configuration is defined by the implicit function $f(x, t) = 0$. In the restrictive hypothesis in which a single valued function is assumed for the free surface configuration, the geometric description is given in the more usual form $z = \eta(x, t)$. In this case the only normal component of the surface velocity (ν_σ) is defined. By equating its value to the normal fluid velocity the proper equation for the kinematic evolution of the free surface is attained.

The two geometrical formulations are equivalent. In fact the Lagrangian description is slightly more general than the Eulerian one, in which some regularity assumptions on the function f must be accepted. Moreover, whenever an Eulerian description exists, the two formulations are equivalent. Only in the computations some difference appears. Actually the Eulerian description doesn't modify significantly the dimensions of the boundary elements, while the Lagrangian one concentrates the elements near the crest of the waves where sharper velocity gradients appears and more computational accuracy is required. For these reasons the Lagrangian description is preferred in the computational model for the nonlinear free surface problem discussed in section 6.

From the previous analysis it clearly appears the simple use of the boundary conditions for free surface problems when using coupled formulations in integral form. Coupled models allow to impose the boundary conditions directly in terms of boundary velocity and tractions. The integral form allows for a simple use of the boundary conditions also in the discrete form, with no additional difficulty as in the numerical models based on the differential equations.

In the next section a decoupled model is introduced as a simplified version of the inviscid one. In this case the definition of the boundary conditions is not as direct as for the coupled models.

5 A general kinematical representation and the dynamical boundary condition

In this section a purely kinematical integral representation will be recovered as a simplified version of the integral formulation for inviscid flows. It follows a direct similarity between the two representations, in the sense that boundary integral equations with similar properties are attained in the two cases.

The procedure which leads from the inviscid integral formulation (15) to the present one is based on the idea of a back substitution of the Euler equations in differential form into the inviscid integral representation. In this way the dynamical variables are dropped out thus reducing (15) to a purely kinematical formula. In order to apply in a simple form the above procedure a quite drastic approximation is performed by considering the fluid domain Ω to be fixed in time. A more rigorous approach should reach the same conclusion through fairly more complex calculations without leading to a deeper understanding of the analogy between (15) and the present model. Under this assumption the surface integrals containing the boundary velocity ν_σ no longer appear and the representation (15) may reduce to a much simpler expression. Actually, by combining the Euler equations and the vorticity transport equation

$$\frac{\partial \mathbf{u}}{\partial t} + \nabla P + \chi = 0 \quad (22)$$

$$\frac{\partial \chi}{\partial t} + \nabla \times \chi = 0 \quad (23)$$

the following representation is attained from eq.(15) by a simple integration in time

$$\begin{aligned}\mathbf{u} &= \int_{\partial\Omega} (\mathbf{u} \cdot \mathbf{n}) \nabla G ds - \\ &\quad \int_{\partial\Omega} (\mathbf{u} \times \mathbf{n}) \times \nabla G ds - \\ &\quad \int_{\Omega} \chi \times \nabla G dv\end{aligned}\quad (24)$$

Representation (24) is the well known Poincaré formula when the velocity field is assumed solenoidal. This is a purely kinematical identity which can be used to obtain boundary integral equations for the kinematics of the flow. When the collocation point approaches the boundary, two equations follow from eq. (24) by performing the tangential and normal projections.

$$cu_r^* + \int_{\delta\Omega} u_r \frac{\delta G}{\delta n^*} ds = -\frac{\delta}{\delta \tau^*} \int_{\delta\Omega} u_n G ds + I_i^r \quad (25)$$

$$cu_n^* + \int_{\delta\Omega} u_n \frac{\delta G}{\delta n^*} ds = \frac{\delta}{\delta \tau^*} \int_{\delta\Omega} u_r G ds + I_i^n \quad (26)$$

where I_i stays for the contribution of the volume integrals. Equation (25) is a second kind Fredholm equation for the unknown u_r , or a first kind equation with Cauchy kernel for the unknown u_n . Analogously for eq. (26). The properties of the Fredholm equation are well known from the potential theory while matching properties can be found to hold for integro differential one (see ([7])). As expected the equations (25) and (26) are not independent, in the meaning that, whatever is the unknown, for a given data the solution of the first one is also a solution of the second one. When the boundary is a solid wall the value of u_n is assigned and u_r is the unknown. Different is the case of a free boundary, where u_n is the unknown. In this case to determine the boundary data u_r , the dynamical part of the model should be used. The procedure is strictly similar to that used for potential flows where the values of the potential ϕ are evaluated by means of the Bernoulli's equation. In the present case, due to the vorticity in the field, which has been retained, no potential function exists. The Euler equations must be used to obtain the relation between the tangential velocity component u_r and the known pressure distribution. In order to write the required equation we shall fix a point on the free surface, labeled by the Lagrangian variable ξ . Due to the boundary motion, the unit tangent vector τ_ξ , at the boundary point ξ will change in time. By projecting the Euler equation on this tangent vector we obtain

$$\frac{Du_r}{Dt} - \mathbf{u} \cdot \frac{\partial \tau_\xi}{\partial t} = -\frac{\partial P}{\partial \tau} \quad (27)$$

In order to simplify eq. (27) the second term on the left hand side is written as:

$$\mathbf{u} \cdot \frac{\partial \tau_\xi}{\partial t} = u_r \tau_\xi \cdot \frac{\partial \tau_\xi}{\partial t} + u_n \mathbf{n}_\xi \cdot \frac{\partial \tau_\xi}{\partial t} \quad (28)$$

Noting that $\tau_\xi \cdot \frac{\partial \tau_\xi}{\partial t} = 0$ the final expression is

$$\frac{Du_r}{Dt} = u_n \mathbf{n}_\xi \cdot \frac{\partial \tau_\xi}{\partial t} - \frac{1}{2} \frac{\partial u^2}{\partial \tau} - g \frac{\partial \eta}{\partial \tau} \quad (29)$$

where the dynamic boundary condition $p = \text{const}$ has been used. This nonlinear evolution equation for the tangential velocity component gives the free boundary condition for the two boundary integral equation (25) and (26).

It is worthwhile to add few more comments on the relationship between the present decoupled model and the coupled inviscid one. The normal component eq. (15) is very similar to (26). In the case of the coupled inviscid formulation the role of u_r is played by the tangential derivative of the dynamic pressure. A part from the integration in time the kernels are identical, so that the numerical methods for the two equations are expected to be essentially the same. The main difference between the two formulations is due to the fact that from (15) it follows only one integral equation, while in the kinematical decoupled model any of the two equations (25) and (26) may be selected. This feature of the kinematical model may be used to avoid the solution of the Cauchy type equation which is more difficult from the numerical point of view.

6 The numerical simulation for a submerged body

Some numerical results obtained by the formulation introduced in the previous section are presented for the unsteady flow about a submerged body. The flow field is assumed to be irrotational and the nonlinear free surface configuration is followed in time by the Lagrangian description. The evolution of the wave pattern generated from rest by a moving cylinder is simulated and the steady state configuration is reached in the case in which no breaking wave occurs.

The numerical procedure adopted makes use of the dynamical equation (29) and of the kinematical equation (21) to evaluate u_r on the free surface and the free surface configuration respectively. The following notations are used: $\delta\Omega_B$ and $\delta\Omega_f$ denote the body boundary and the free surface respectively. $\delta\Omega_\infty$ denote the fictitious boundary used to cut the computational domain at a finite distance from the submerged body. When treating the flow in a channel, the finite depth bottom is denoted by $\delta\Omega_b$, while $\delta\Omega_\infty$ is given by an inflow part ($\delta\Omega_i$) and an outflow part ($\delta\Omega_o$). As a boundary condition to be used in the boundary integral equation, the normal inflow velocity, time dependent in general, is assigned on $\delta\Omega_i$. The zero normal velocity condition is assigned on the bottom boundary for both the channel flow or the infinite depth case. At the outflow boundary the normal velocity component is also given or a suitable radiation condition is applied. On the free surface the tangential velocity component is evaluated by the dynamic equation (29). The reference frame is assumed connected with the body, which is moving at a constant depth beneath the undisturbed free surface. The dynamic equation is used in the inertial frame connected to the undisturbed fluid and the proper value of u_r is evaluated by changing the reference frame to that

fixed to the body.

As shown in the previous section any of the two boundary integral equation either (26) or (25) can be used to determine the unknown velocity component. The most efficient choice, from the computational point of view, is the use of the second kind Fredholm equation, in order to avoid the variational techniques required for an accurate solution of the Cauchy type equation. To this purpose a mixed approach is used here by assuming the normal component (26) to hold on the free surface and the tangential component (25) on the other boundaries. The equation which follows from this mixed formulation does not present a Cauchy type singularity and can be easily solved by numerical methods. In the case of multi-connected regions, some attention must be devoted to the eigenvalue related to the circulation around the body which in the present numerical study will be assumed to be zero.

In the computational procedure standard finite elements techniques are used to discretize the equation. In more details, piecewise linear shape functions are used to describe the geometry while piecewise constant functions are used for the unknown. In order to assure the solution uniqueness the condition of zero circulation around the body is imposed. The computational procedure is splitted in two parts. The boundary unknowns are evaluated first by solving the boundary integral equation. With the velocity distribution on the free surface completely known the configuration of the domain and the values of u_r are updated. The second order accurate Adams Bashforth scheme is used to perform this calculation. No redistribution procedure is used for the free surface panels which tends to concentrate near the crest of the waves. Due to the mean motion, at each time step a new panel is added at the inflow side and one is canceled at the outflow, where a Sommerfeld radiation condition is used.

By the described numerical technique the simulation of the transient wave system due to the motion of a circular cylinder has been performed. The obtained results are compared with those presented by Haussling and Coleman [5] and with those of Liggett and Liu [3] for the potential flow equation. Haussling and Coleman use a finite difference approach in generalized curvilinear coordinates and Liggett and Liu a boundary element approach. Both use an Eulerian description for the free surface. Although these approaches are completely different the three solutions show a good agreement (fig. 1). It could be noted that the present solution shows clearly the effects of non-linearity given by the adopted Lagrangian description of the free surface. In fact, with the present method a steady state solution couldn't be reached due to the steeping of the wave crest, which cause the solution

to break before the last instant showed by Liggett and Liu. In the case, shown in fig. 3, although the Froude number is higher than in the previous one, a steady state solution has been attained due to the greater submergence of the body. Fig. 4 shows the time history of the forces acting on the cylinder. Although the free surface configuration appears to reach the steady state, both lift and drag are oscillating around the presumed steady value. In fig. 8 a simulation with a smaller channel depth shows the evolution towards the breaking of the wave, which is attained by an overturning of the front face of the first crest behind the body.

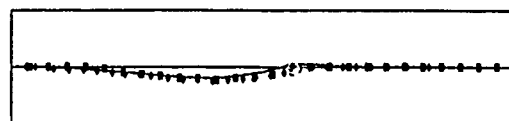
7 Concluding remarks

A computational method for unsteady free surface flows has been derived from a mathematical model which decouples the kinematical and the dynamical aspect of the flow field. The method, valid in general for rotational flows, has been shown to have the same computational efficiency of the potential based approaches. The strict relationship with the coupled models based on the integral formulation for viscous and inviscid flows, have been discussed. While the numerical solution of the Fredholm integral equation gives very satisfactory results, the numerical technique for an efficient as well as accurate resolution of the Cauchy type equation is to be completed. This is the crucial point for the numerical implementation of the limiting coupled formulation for inviscid flows. The viscous model, should be treated in similar way by recasting the equation in terms of vortex layers as shown for the inviscid case.

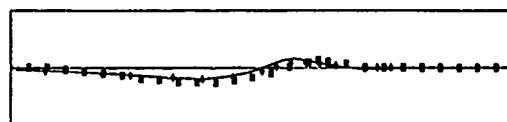
References

- [1] Ladyzhenskaja, O.A., (1986): *The Mathematical Theory of Viscous Incompressible Flows*, Gordon & Breach, New York, NY, USA.
- [2] Piva, R. and Morino, L., (1987): "Vector Green's Function Method for Unsteady Navier Stokes Equations", *Meccanica*, Vol. 22, pp. 76-85.
- [3] Piva, R., Graziani, G., and Morino, L., (1987): "Boundary Integral Equation Method for Unsteady Viscous and Inviscid Flows", Ed.: T.A. Cruse, *Advanced Boundary Element Methods*, Springer Verlag, New York, NY, USA.
- [4] Miyata H., Sato T., Baba N. "Difference Solution of a Viscous Flow with Free Surface Wave about an Advancing Ship", *J. Comput. Phys.*, 72 (1987), 393

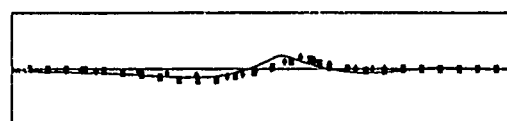
- [5] Haussling, H.J., and Coleman, R.M., (1977): "Finite-Difference Computations Using Boundary Fitted Coordinate Systems for Free-Surface Potential Flows Generated by Submerged Bodies", Eds.: J.V. Wehausen and N. Salvesen, The Proceedings of the Second International Conference on Numerical Ship Hydrodynamics.
- [6] Liu, P.L-F. and Liggett J.A., (1982): "Applications of the Boundary Element Method to Problems of Water Waves", Eds.: P.K. Banerjee and R.P. Shaw, Developments in Boundary Element Methods - 2, Applied Science Publishers, London.
- [7] Casciola, C.M., Lancia, M.R., and Piva, R., (1989): "A General Approach to Unsteady Flows in Aerodynamics: Classical Results and Perspectives", ISBEM 89, East Hartford Usa.
- [8] Nedelec, J.C., (1977): "Integral Equations with Non Integrable Kernels", Integral Equations and Operator Theory, Vol. 5, pp. 562-572.
- [9] Hsiao, G.C., (1986): "On the Stability of Integral Equations of the First Kind with Logarithmic Kernels", Archive for Rational Mechanics and Analysis, Vol. 94,2 pp.179-192, Springer Verlag, Berlin.



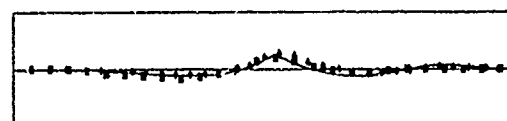
$t = 4.5$



$t = 6.$



$t = 7.5$



$t = 9$

Fig. 1. Free - surface configurations after the start of a submerge cylinder. Submergence $h = 2$.

$Fr = .566$ $D = 1$

— present solution

◊ Liggett and Liu

■ Haussling and Coleman

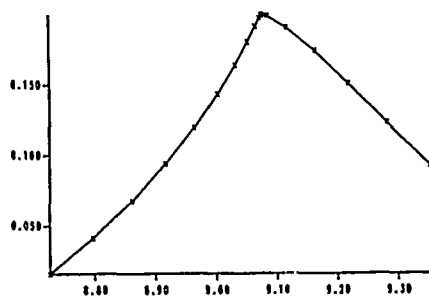


Fig. 2. Steeping of the wave for the same case as in Fig. 1. $t = 10$.

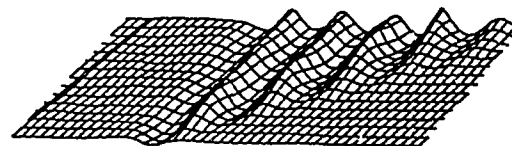


Fig. 3. Free surface configuration vs time
 $Fr = .95$ $D = 1$
 Submergence $h = 3$
 $Dt = .25$



$t = 15$



$t = 75$



$t = 30$



$t = 80$



$t = 45$



$t = 85$



$t = 60$



$t = 90$

Fig. 4. Configurations of the computational domain for the same case as in Fig. 3.

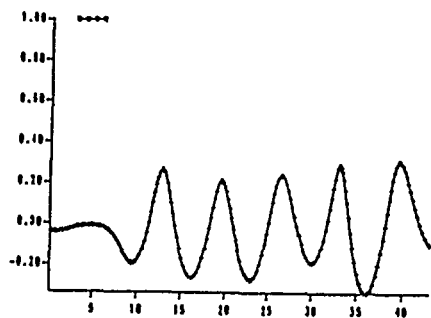


Fig. 5. Wave elevation.
 $Fr = .95$
 Submergence $h = 3$.
 $Dt = .25 \quad t = 85$

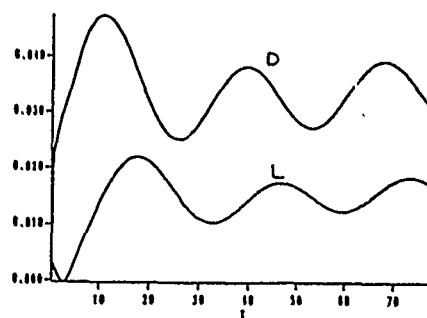


Fig. 6. Time History of the forces on the cylinder.
 Same case as in Fig. 5 (forces adimensionalized by $\rho U^2 D$)

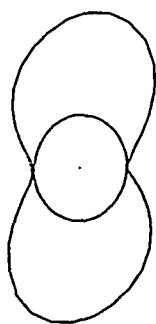


Fig. 7. Pressure distribution on the cylinder. Same case as in Fig. 5. $t = 85$

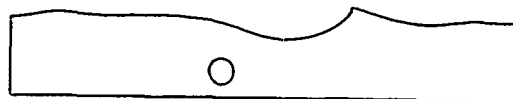


Fig. 8. Wave overturning. $D = 1$
 $Fr = .95$
 Submergence $h = 3$
 Channel depth $H = 4$
 $t = 14.25$
 $Dt = .25$

Development of a New Velocity Measurement System by Using Computerized Flow Visualization and Numerical Method

K. Mori and S. Ninomiya
Hiroshima University
Hiroshima, Japan

Abstract

A hybrid method is developed to measure 3-dimensional flows where the image processing method and numerical computational method are complementarily used; the 3-dimensional flow field is reproduced by the numerical calculations by making use of several scanned plane flows which have been obtained by the flow visualization and image processing.

The combination of the numerical computation has made the flow visualization system much less sophisticated. The method is applied to measure the flow field around the Wigley model to conclude that the method is promising although the used system is rather primitive.

1. Introduction

It is common to measure velocity fields by traversing an anemometer at one position after another even in a 3-dimensional domain. Needless to say, it is time-consuming and requires much labor. Even more, there are some cases where the velocity field cannot be measured by the conventional method due to reverse flows, abrupt changes of the velocity or stagnant flows.

The flow visualization has ever been a qualitative method which is useful to understand the flow field globally. However, owing to the advent of a new era of image processing techniques, it can be even quantitative.

There are some pioneering researches where the velocity field is determined

by the image processing techniques [1][2]. Most of them are for 2-dimensional flows but some are intended to be 3-dimensional flows where the tracers are tracked 3-dimensionally by making use of several cameras [3][4]. However, the instruments for measurements and the algorithm for analysis are complicated.

On the other hand, recent developments in computational fluid dynamics to simulate flow fields by solving the N-S equations are remarkable. However, there are still limitations in the hardwares of computers to have reliable results even by modern computers of high-speed and large memory storage; the computing domain and the grid size can not be taken enough for required.

The present method is a kind of hybrid methods of the image processing and the computational fluid dynamics; a 3-dimensional flow is reproduced by numerical computations from several scanned plane flows obtained by the flow visualization and image processing. It consists of five stages, as the block diagram shown in Fig.1; 1) flow visualization, 2) image processing, 3) image analysis, 4) numerical computation and 5) graphic display. The method is called "Three-dimensional Anemometer System by complementarily use of Computational and Optical Methods" (TASCOM).

Although the method is still under development and the instruments used here are rather primitive, the system may be much improved by an introduction of more sophisticated machines or higher-version of softwares.

2. Plane Flow Analysis

2.1 Flow visualization

The arrangement for the measurements is shown in Fig.2. A laser light sheet is used to scan a plane flow field which is traversed in z direction whose velocity component w is presumed the smallest among the three components. A 25 mW He-Ne laser beam and a circular cylindrical lens are used to realize a light sheet in the present experiment.

Hydrogen bubbles are used as tracers which are generated by the electrolysis of water. The reasons for the use of the hydrogen bubbles are, first, that they can trace flows without inertia and both their size and brightness can be controlled. Secondly, but essentially important, they do not pollute the water. They can be used in towing tanks also. Of course, they do not work well for the flows whose velocity is so small that the buoyant effect is relatively large.

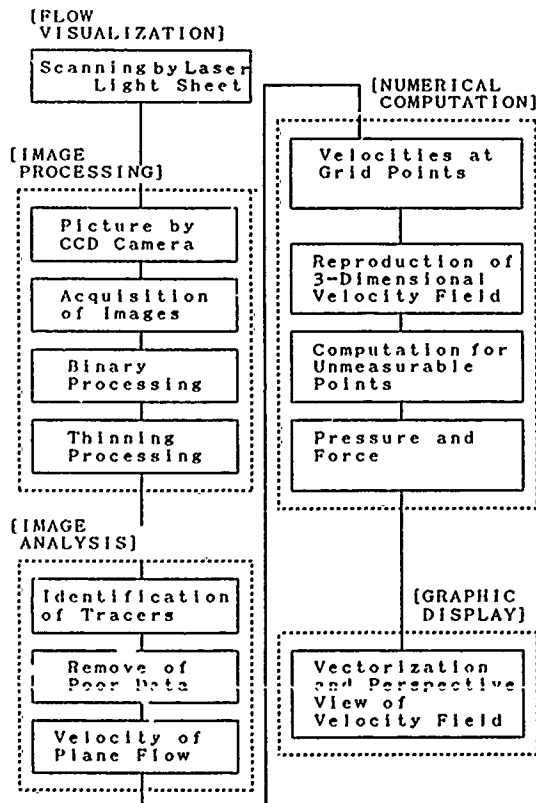


Fig.1 Block diagram of the present measuring system, TASCOT

The electrode is made of platinum wires which are formed ladder-like as shown in Figs.2 and 10. They can produce vertical segments of bubbles which cut the laser light sheet without fail.

In general, there are some regions where tracers do not get into; we call such regions "unmeasurable region" here. We do not pay special attentions for such regions and we expect the velocity there will be supplied by numerical computations.

2.2 Method of image processing

The process of the present image processing is shown schematically in Fig.1. This process consists of the following three steps.

1) freezing images of tracers:

The path lines of tracers on the scanned plane are recorded by a CCD camera (384 x 491 pixels), as shown in

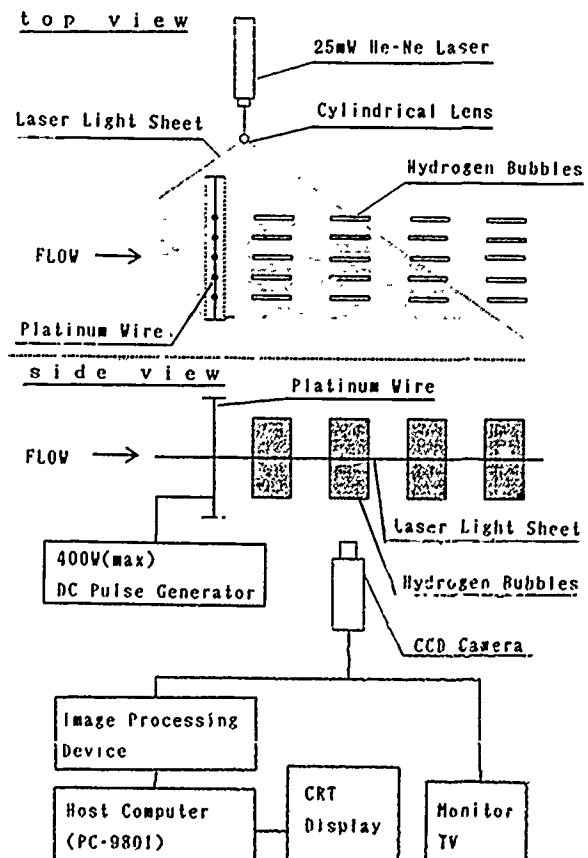


Fig.2 Arrangement of the system

Fig.2. The acquired analogue image signals are converted to digital data by making use of a image processing device (256 x 256 pixels, 8 bit). The device can freeze successive four frames at once at the time interval of 50 msec.

2) binary processing:

The 8-bit value of brightness of each pixel are binarized based on discriminating level. It is important how to set the value of the level, for the optimum value depends much on experimental conditions such as brightness of tracers, velocity and so on. Here it is set by a trial and error method.

3) thinning processing:

In order to have more reliable data of the tracers such as the length and the positions of start and termination, the thinning process is essential. As shown in Fig.3, the thinned line C_i is determined as the centerline of the segment A_i-B_i .

2.3 Calculation of plane velocity

As shown in Fig.4, the plane velo-

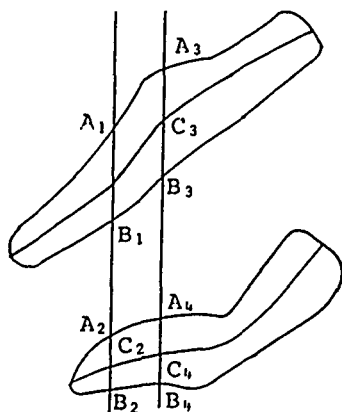


Fig.3 Thinning process of images

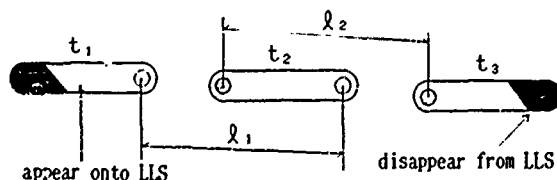


Fig.4 Calculation of the velocity

city (u, v) is evaluated from the two distances, l_1 and l_2 , between the three images of the same tracer at the three sequential times, t_1 , t_2 and t_3 . The three images have been identified to be the images of a single tracer. The plane flow velocity components are determined from the components of the distances in their directions.

1) identification of tracers:

The algorithm of identification of tracers is schematically shown in Fig.5. A priority is given to the image to be identified when it lies within a certain distance and fan angle; the image A_2 on the frame at time t_2 is identified with A_1 because A_2 lies within the fan angle of $a-a''$ and $a-a'''$ and within a given distance. At the next time step t_3 , A_3 is identified. Thus all the images are identified as $B_1-B_2-B_3$, $C_1-C_2-C_3$, and so on.

Through the above processes, if a tracer could not be identified, the tracer is assumed "stray" and is neglected in the following analysis. The distance and the fan angle are empirically given here.

2) selection:

There are still some possibilities to identify wrong images. If the two distances between the three identified images, l_1 , l_2 in Fig.4, are extremely

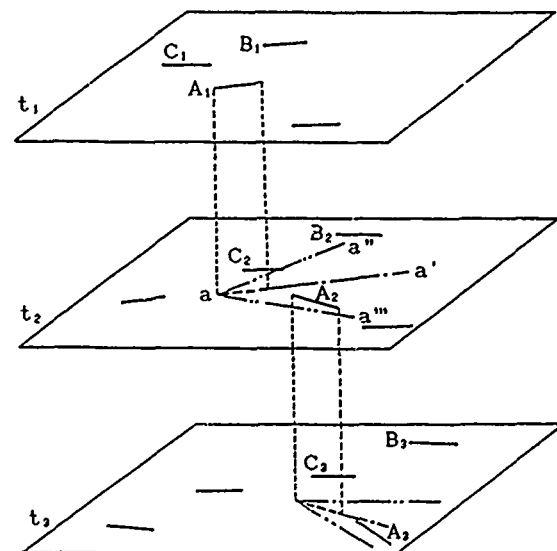


Fig.5 Identification of the images on three different frames

different each other or their average differs much from the surroundings, the set of images is assumed wrong and removed from the stored data.

3) calculation of the velocity components:

The plane velocity component (u_i , v_i) is calculated from the distances between the identified images on the three sequential frames by the following equations;

$$\begin{aligned} u_i &= \frac{\Delta x}{\Delta t} \\ v_i &= \frac{\Delta y}{\Delta t} \end{aligned} \quad (1)$$

where Δt is the interval time between the frames and Δx and Δy are the x- and y-components of the length Δl .

4) interpolation of the velocity:

It is necessary to have the velocity on assigned matrix points, which can be realized by the weighed interpolation of the original data at arbitrary points. The velocity vector $q(x,y)$ at (x,y) is calculated by

$$q(x,y) = \frac{\left\{ \sum_{i=1}^N \frac{q(x_i, y_i)}{r_i} \right\}}{\left\{ \sum_{i=1}^N \frac{1}{r_i} \right\}} \quad (2)$$

where r_i is the distance to the data interpolated, and N is the number of the possible data for interpolation. The maximum r_i is properly chosen and if N is less than 3, the velocity at the point is regarded as "not measured".

3. Accuracy Analysis of the Measuring System

It is important to estimate the accuracy of the measuring system. The nominal accuracy of the image analysis is given in terms of the density of the pixels of CCD camera and the sampling interval time.

The resolving power of the image processing, denoted by d , is given by

$$d = \frac{L}{n} \quad (3)$$

where n is the number of pixels and L is the actual size of the object to be pictured.

In the present system, the number of pixels is 256×256 and the size of the picture is about $100 \text{ mm} \times 100 \text{ mm}$. Then the resolving power d is 0.4 mm/pixel and the accuracy of positioning may be $\pm 0.2 \text{ mm/pixel}$.

The minimum velocity, which can be resolved, U_{\min} , is given by

$$U_{\min} = \frac{d}{\Delta t} \quad (4)$$

where Δt is the sampling interval time. In the present system 10 frames (pictures) are frozen per a second and the accuracy of the measured velocity is $\pm 2 \text{ mm/sec}$. The optimum sampling interval time should be determined depending on the uniform flow velocity and the density of pixels.

In practice, the final accuracy must include the errors which arise during the image processings due to non-uniformity of image brightness, wrong identifications and so on.

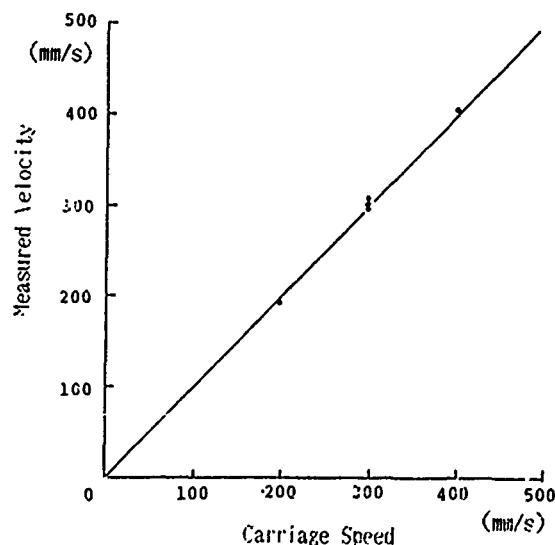


Fig.6 Accuracy analysis of the image processing

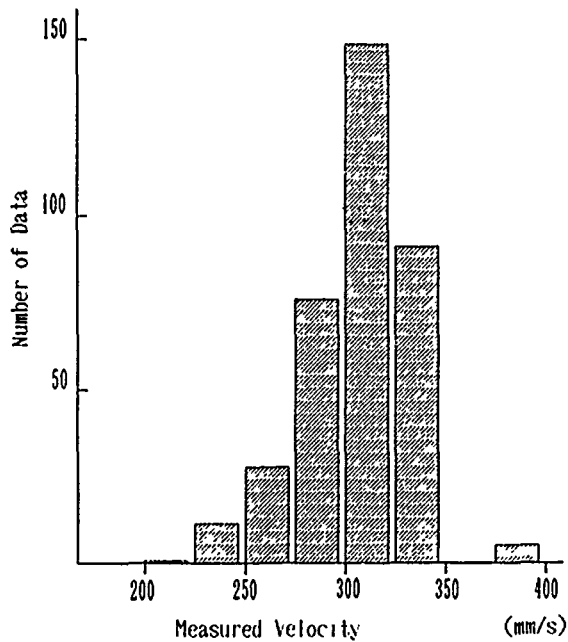


Fig. 7 Histogram of the measured velocity for the uniform flow

To confirm the total accuracy of the present system, two measurements are carried out in advance. One is to analyze the velocity of a pin-hole light which moves as a constant speed; this is realized by fixing the light onto the towing carriage. The other is to measure the uniform flow velocity of water circulating channel.

Fig. 6 shows the results of the first experiment; the abscissa gives the carriage speed and the coordinate, the analyzed velocity by the present method. The mean curve seems to be giving a good correlation and the error of measurement is smaller than the resolving power of the image processing.

Fig. 7 is the results of the second experiments; the measured velocity of the uniform flow of circulating water channel. 367 measured data are shown in histogram. The nominal velocity of the uniform flow by the indicator is 300 mm/sec and the nominal uniformity of the flow is about 96%. The total average of the measured data is 307.1 mm/sec. 64% of the measured data lies within 300 ± 25 mm/sec of the uniform flow velocity.

4. Reproduction of the 3-Dimensional Flow Field

4.1 Invoked equations and the scheme

The reproduction of the 3-dimensional flows from the scanned plane velocity fields is achieved numerically by a variational method to satisfy the continuity equation [5]. There the measured plane flow velocities (u_0, v_0) on the scanned planes are used as initial values.

The reason why the variational method is invoked is that the scheme must be robust or tough enough even if the initial values, provided by the scanned plane flows, are contaminated by measurement errors. The use of the variational method is expected to correct the given boundary values to satisfy the continuity equation.

The functional, F , is defined as

$$F(u, v, w, \lambda) = \int_V \left\{ \alpha_1^2 (u - u_0)^2 + \alpha_2^2 (v - v_0)^2 + \alpha_3^2 (w - w_0)^2 + \lambda \left[\frac{\partial u}{\partial x} + \frac{\partial v}{\partial y} + \frac{\partial w}{\partial z} \right] \right\} dV \quad (5)$$

where λ is the Lagrangian multiplier, and α_1, α_2 and α_3 are weighing constants. The problem is to find (u, v, w) to minimize F in the computing domain V .

The first variation of F is given by

$$\begin{aligned} \delta F(u, v, w, \lambda) = & \int_V \left[\left\{ 2\alpha_1^2 (u - u_0) - \frac{\partial \lambda}{\partial x} \right\} \delta u + \left\{ 2\alpha_2^2 (v - v_0) - \frac{\partial \lambda}{\partial y} \right\} \delta v + \left\{ 2\alpha_3^2 (w - w_0) - \frac{\partial \lambda}{\partial z} \right\} \delta w + \left[\frac{\partial u}{\partial x} + \frac{\partial v}{\partial y} + \frac{\partial w}{\partial z} \right] \delta \lambda \right] dV \\ & + \int_S \left\{ \lambda \delta u n_x + \lambda \delta v n_y + \lambda \delta w n_z \right\} dS \end{aligned} \quad (6)$$

where δ is the first variation, (n_x, n_y, n_z) are the components of the normal on S which is the computing boundary surface of V .

The condition of $\delta F=0$ yields a set of following equations;

$$u = u_0 + \frac{1}{2\alpha_1^2} \cdot \frac{\partial \lambda}{\partial x} \quad (7)$$

$$v = v_0 + \frac{1}{2\alpha_2^2} \cdot \frac{\partial \lambda}{\partial y} \quad (8)$$

$$w = w_0 + \frac{1}{2\alpha_3^2} \cdot \frac{\partial \lambda}{\partial z} \quad (9)$$

$$\left[\frac{\partial u}{\partial x} + \frac{\partial v}{\partial y} + \frac{\partial w}{\partial z} \right] = 0 \quad (10)$$

$$\int_S \left\{ \lambda \delta u n_x + \lambda \delta v n_y + \lambda \delta w n_z \right\} dS = 0 \quad (11)$$

Substituting (7), (8) and (9) into (10), we have

$$\begin{aligned} & \left[\frac{\alpha_3}{\alpha_1} \right]^2 \frac{\partial^2 \lambda}{\partial x^2} + \left[\frac{\alpha_3}{\alpha_2} \right]^2 \frac{\partial^2 \lambda}{\partial y^2} + \frac{\partial^2 \lambda}{\partial z^2} \\ & = -2\alpha_3^2 \left[\frac{\partial u_0}{\partial x} + \frac{\partial v_0}{\partial y} + \frac{\partial w_0}{\partial z} \right] \end{aligned} \quad (12)$$

(12) is the Poisson equation by which λ can be determined. It is solved by S.O.R. method under the boundary condition of (11). Then the velo-

city vectors (u,v,w) is calculated from (7), (8) and (9).

Because the velocity component w , normal to the scanned plane, is important in the present calculation, the ratio of α_1/α_3 and α_2/α_3 should be properly chosen.

The boundary condition of (11) can be satisfied by providing a suitable subsidiary conditions for $(\delta u, \delta v, \delta w)=0$ or $\lambda=0$ on the boundary S .

4.2 An example of reproduction of 3-dimensional flow

In order to confirm the present scheme to reproduce the 3-dimensional flow, the flow behind a sphere is analyzed.

The coordinates and the analyzed region is shown in Fig.8. The plane flows are provided on twenty horizontal planes by the potential flow calculation. The computation region is divided into $20 \times 20 \times 20$ cubic cells. This grid size may not be sufficient for enough accuracy, but the use of too fine grids does not always meet the experimental condition where the departures between the scanned planes can not be so small as expected in computation.

The boundary conditions for λ and $\delta u, \delta v$ and δw are given as follows:

$$\begin{aligned} & \text{on } x=0, \quad \partial \lambda / \partial z = 0, \\ & \quad \delta u, \delta v \text{ and } \delta w = 0, \\ & \text{on the other boundary planes,} \\ & \quad \lambda = 0, \end{aligned} \quad (13)$$

The boundary condition (13) satisfies (11).

The weighing constants α_1, α_2 , and α_3 are assumed as follows;

$$\begin{aligned} & \alpha_1, \alpha_2 = 10.0, \\ & \alpha_3 = 0.1 \end{aligned} \quad (14)$$

The Poisson equation (12) is solved by S.O.R., where 1.4 is used as the relaxation factor.

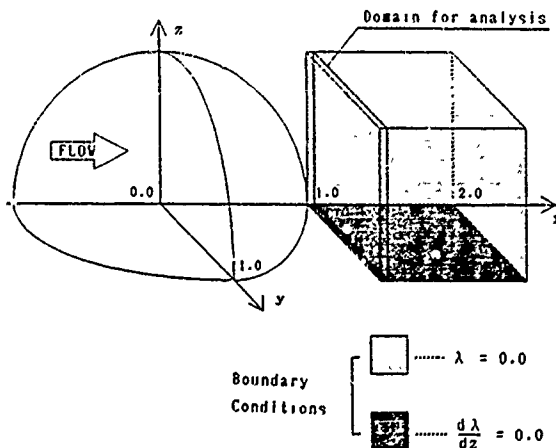


Fig.8 Computational domain for 3-dimensional reproduction

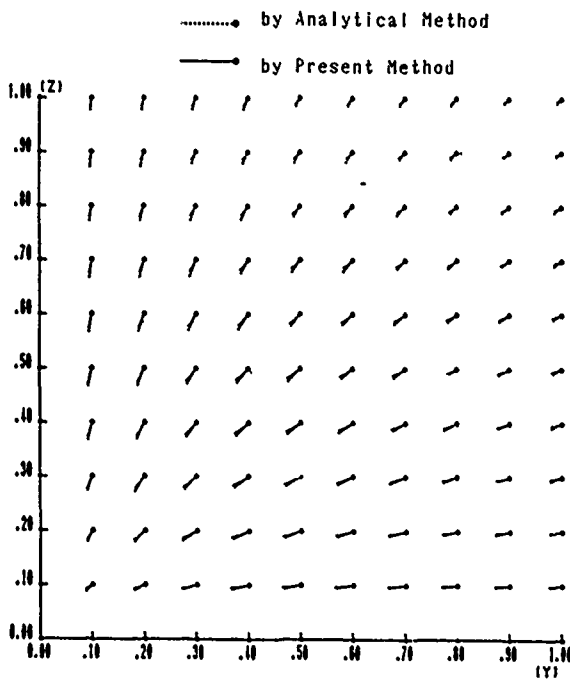


Fig.9 Comparison of reproduced 3-dimensional velocity vectors behind a sphere with the analytical

The reproduced y-z plane velocity vector is shown in Fig.9 together with the results calculated analytically. It is seen that the third z-component of the velocity is well reproduced, although there can be seen some discrepancies between them where velocity gradients are large just behind the sphere. The use of a finer grid has improved the results.

We can now conclude that the present variational method can be applicable to our analysis.

5. Measurement of the Stern Flow of Wigley Model

5.1 Arrangements and sampling

To study the applicability of the present method, a measurement of the stern flow of the 1.2m Wigley double hull model is carried out.

The arrangement of the measurement is shown in Fig.10. The laser light sheet is installed parallelly to the uniform flow; the x-y plane is scanned. In the present experiment, the model is traversed vertically for the plane flows to be scanned.

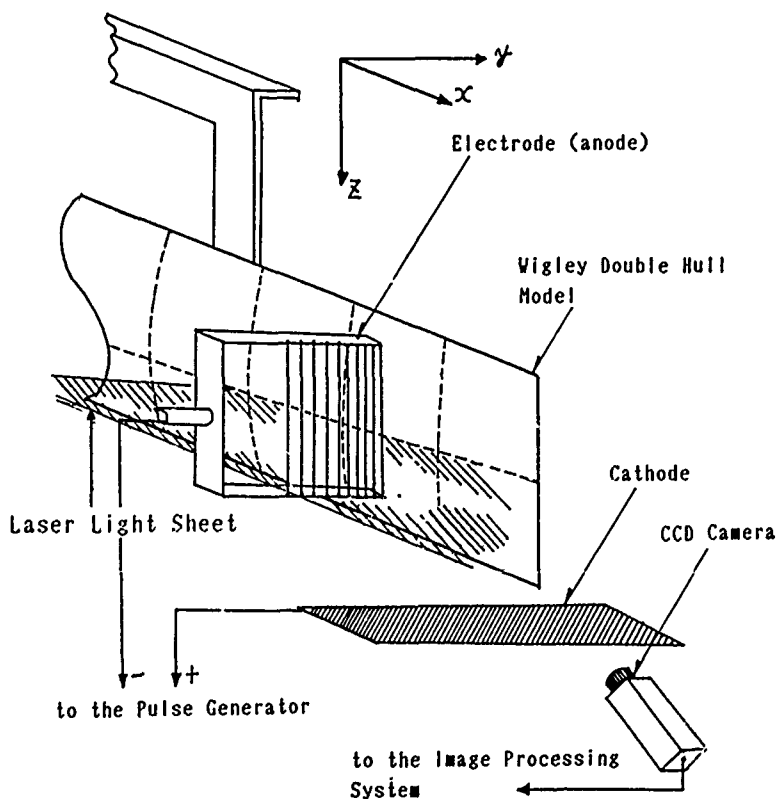


Fig.10

Arrangement for the measurements of the wake of Wigley model

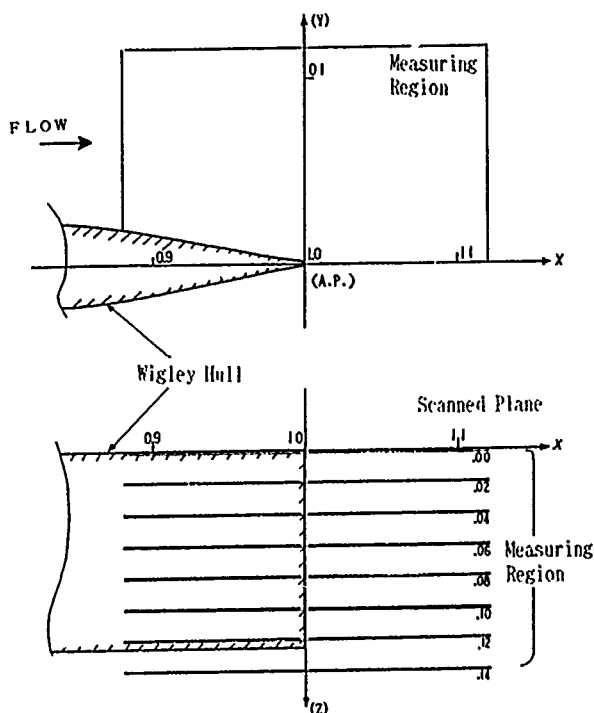


Fig.11 Measuring region and scanned planes for the Wigley model

As shown in Fig.11, eight planes are scanned at 0.02 intervals. Although the number of scanned planes may not be enough for the following calculation, the hardware of our system can not afford any more. The region for measurements, i.e., the scope of the camera, is determined to have a necessary accuracy. The maximum accuracy of the image processing unit here is ± 0.2 mm/pixel.

The experiment is carried out in the circulating water channel whose dimensions of the measuring section is as follows; $L \times B \times d = 2.0\text{m} \times 1.4\text{m} \times 0.9\text{m}$. The uniform flow speed is 100 mm/sec and the Reynolds number is about 1.2×10^5 .

One measuring plane has 60 pictures whose sampling time is 100 msec. This means that the determined velocity field is the mean velocity for 6 seconds.

5.2 Results of the plane flows

Fig.12 shows one example of tracer images on $z=0$ plane, the reflecting plane; (a) is the original binary pic-

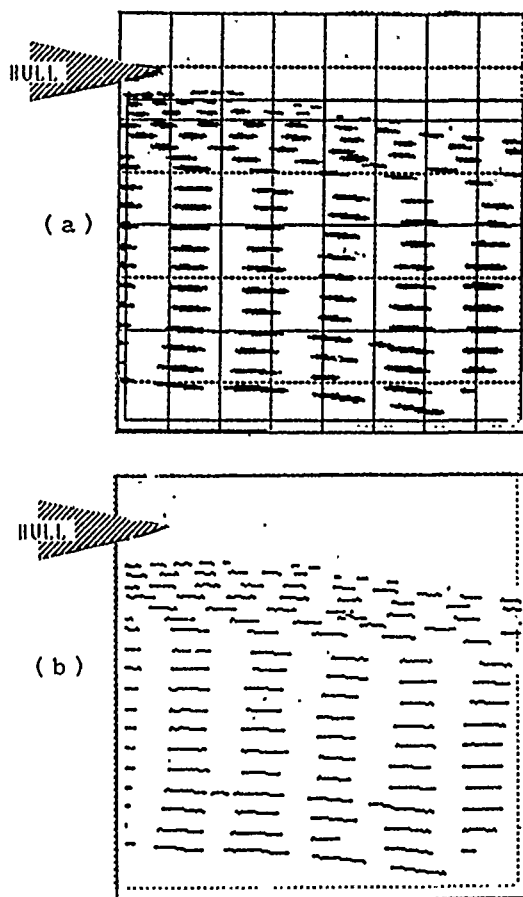


Fig.12 Frozen images on $z=0$ plane (a) and the thinned images (b)

ture from which background noises are removed by smoothing, while (b) is the thinned picture of (a).

From the picture (a), we can judge that the present technique of the flow visualization can stand for the quantitative analysis of the velocity and also that the images of the tracers are well frozen for the following processings. However, the pictures of the thinned images, (b), suggest that we have still some ill images when thinned due to noises or non-uniformity of the brightness of tracers. The wrong images are removed by estimating their length.

Fig.13 shows the plane velocity vectors analyzed by the procedure mentioned in 2.3. They are well measured. Thus we have 8 plane flow vectors where u and v are determined but w is assumed zero.

5.3 Results of 3-dimensional flow calculations

For the calculations to reproduce the 3-dimensional flows, 22 plane flows are presumed by the B-spline interpolation of the eight scanned plane velocity fields. This is because the departure between the plane flows of the present measurements is not small enough for the numerical calculations. More plane flows are expected to be scanned to have more accurate results.

The computing domain is $1.00 < x < 1.10$, $0.01 < y < 0.08$ and $0.0 < z < 0.14$. The boundary conditions are as follows;

on the reflecting plane (x-y plane, $z=0.0$);

$$\partial \lambda / \partial z = 0$$

on the other planes;

$$\lambda = 0 \quad (13)$$

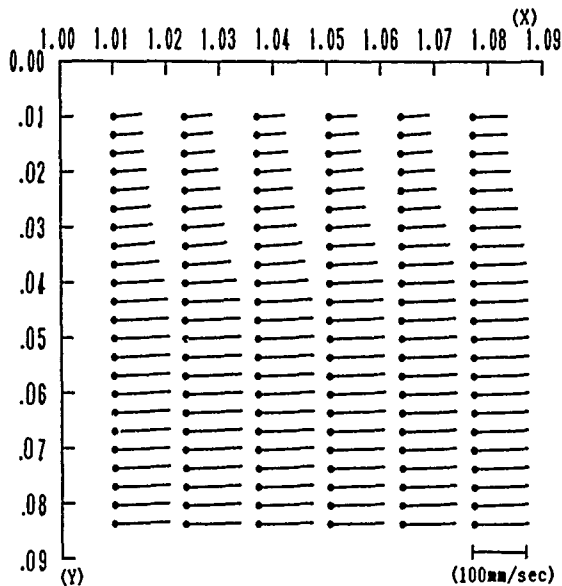


Fig.13 Plane flow vectors on $z=0$

The 3-dimensional velocity vectors at the section of A.P. is shown in Fig.14 compared with those measured by a 5-hole pitot tube. The calculation can be carried out on the same computers as real time.

Although the results do not always agree quantitatively with those by conventional method, the third velocity components are well reproduced. The computation was stable and robust as expected even if the measured plane flows contain some errors.

We can say through the present example that the method is applicable to 3-dimensional measurements. It can be also pointed out that an introduction of more qualified hardware will guarantee us to have more accurate results.

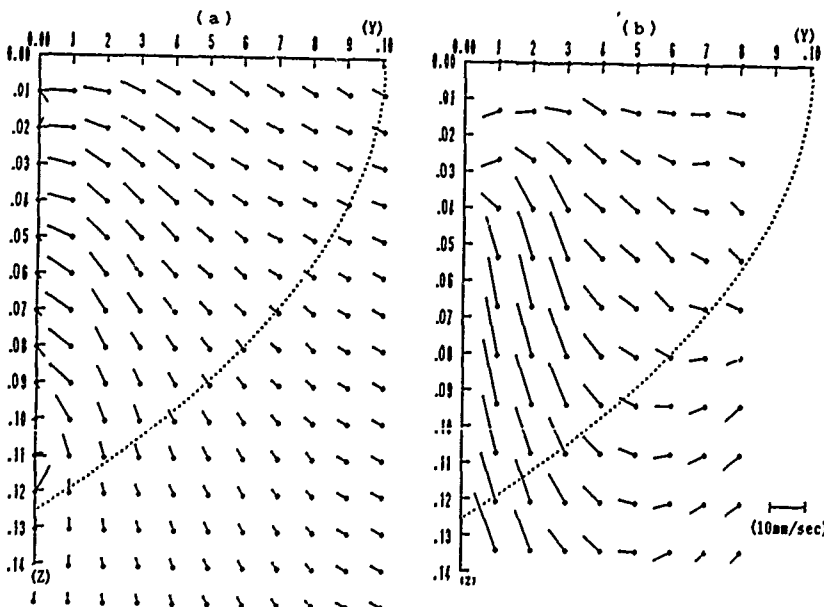


Fig.14

3-dimensional velocity vectors at the A.P. section

6. Conclusion

In the present paper, a new method to measure the 3-dimensional flow field by a complimentary use of the flow visualization and numerical computation, TASCUM, is demonstrated with some pilot examples. The attractive feature of the present method are the simplicity of the experimental apparatus and technique. The method is potentially applicable to the measurements in the towing tank also.

Through the present study following findings are summarized;

- 1) The use of the hydrogen bubble with the laser light sheet is practical and efficient for the image analysis. The vertical segment of the bubble always cuts the light sheet and leaves clear images. No pollution remains in the tank after the measurements.
- 2) The present algorithm for image processing, although primitive and directive, is efficient and accurate enough. The use of more sophisticated machines will assure more efficiency and accuracy.
- 3) 3-dimensional flow can be reproduced from several scanned plane flows to satisfy the continuity condition. The variational method is useful for the reproduction calculation where the measured plane flow components are contaminated by errors. This is because the method is tough enough through relaxation.

The authors wish to express their appreciations to Professors Y. Doi and T. Hotta at Hiroshima University for their variable discussions and advices.

The present research is partially supported by the Grant-in-Aid for Developmental Scientific Research of The Ministry of Education, Science and Culture.

References

1. Mori,K., Hotta,T. and Ninomiya,S. "Development of a Method to Measure Flow Field by Flow Visualization and Image Processing Techniques", J. of

the Society of Naval Architects of Japan, Vol.162, pp.81-89 (1987) (in Japanese).

2. Kobayashi,K., Saga,T., Segawa,S. and Tohnosu,S., "An Image Processing Technique for Determining Two-Dimensional Flow Fields with Reverse Flow", J. of the Flow Visualization Society of Japan, Vol.5, No.17, pp. 57-64 (1985) (in Japanese).
3. Doi,J. and Miyake,T., "Three-Dimensional Flow Measurement by Shape Reconstruction from Multiple Video Images", J. of the Flow Visualization Society of Japan, Vol.7, No.24, pp.46-52 (1987) (in Japanese).
4. Sata,Y.,Nishino,K. and Kasagi,N., "A New Algorithm of Three-Dimensional Particle Tracking For Whole Field Velocimeter", J. of the Flow Visualization Society of Japan, Vol.9, No.34, pp.237-240 (1989) (in Japanese).
5. Ishikawa,H., "Calculation of Three-Dimensional Wind Flows by Variational Method (WIND04)", JAERI-M 83-113 (1983) (in Japanese).

DISCUSSION

by T. Suzuki

This question is about the measurement principle, Fig.2. The laser sheet in Fig.2 shows us a cross section, x-y plane, of the hydrogen bubble sheet, so that you can get the velocity components u and v independently on w in this paper.

However, the hydrogen bubble sheets are inclining their vertical plane, even if the platinum wire is kept vertically, after the sheet streams down along the streamlines near the ship stern (see Fig.A1). In this case, one of the particles in the sheet should go upward (or downward) along the sheet and additional horizontal movement should occur. I think that this movement is not caught in this paper and it gives the error of v components.

Could you give me comments on this error and how it effects the w component?

Author's Reply

Thank you for your instructive discussion. It is a crucial point of our method. As you pointed out, if the hydrogen bubble segment have an inclination, there may be an error by $\Delta y / \Delta t$ in the u -component. This error can be minimized by keeping the bubble segment as vertical as possible.

In the present measurement, the platinum wire was moved parallelly to the main flow direction by every 50 mm step. In this case the maximum angle of inclination can be estimated about 9 degrees at most, then the maximum error in the u -component is about 2% under the assumption that w is $0.1u$.

Because the present study is still at the beginning, we didn't take this error so serious, but it can be corrected iteratively.

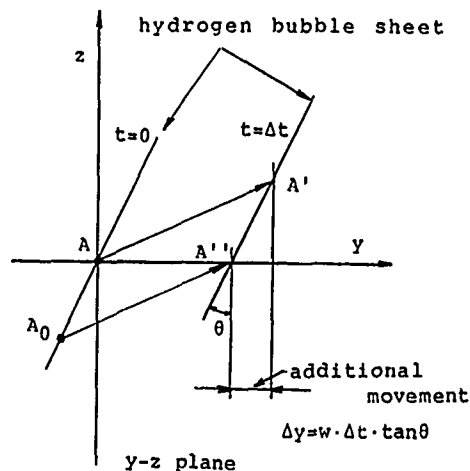


Fig.A1

Automatic Particle-Image Velocimetry Utilizing Laser-Induced Fluorescent Particles

T. C. Fu, R. Bing and J. Katz
The Johns Hopkins University
Baltimore, USA
T. T. Huang
David Taylor Research Center
Bethesda, USA

Abstract

Microscopic, neutrally buoyant particles containing fluorescing compound have been adapted as tracers for velocity measurements of large scale turbulent flows. This technique consists of illuminating a thin slice of the flow field with a laser sheet, which is pulsed following a specific illumination code. The multiple exposure image is recorded on photographic film and later enhanced while being digitized. Algorithms have been developed for analyzing the resulting images. They rely on the illumination code and the particle streak morphology in order to identify and compute the tracer velocity vectors. A one-inch diameter jet has been used as a flow field for preliminary tests.

Introduction

The present paper focuses on the development of a quantitative flow visualization system which is particularly suited for large scale towing tank experiments. Until recently, flow visualization has been utilized for providing only qualitative information, while quantitative data, namely the velocity field, has been determined by single point measurement techniques (hot wire anemometry, laser doppler velocimetry, etc.). Due to their nature, as well as cost, these techniques are limited to simultaneous sampling at a few spatial locations.

Early experiments with quantitative flow visualization have been performed by Kobayashi [1] and Marko & Rimai [2]. They have all used long exposure photography to record both the position and mean velocity of passive tracers within a fluid. High speed photography has also been adopted to record time series of tracer particle positions (Racca & Dewey [3]). A further refinement has been to identify particles in successive frames, and reconstruct the velocity with a time base equal to the framing time (Racca & Dewey [3]). Another approach has been to record multiple exposure images and measure the displacements of small suspended particles to obtain full-field velocity maps (Adrian [4]). Gharib & Willert [5] have performed a similar analysis. However, they have used a single extended exposure of particle streaks with prescribed variations in the intensity of the light emitted from each particle. The variation in intensity was achieved by utilizing fluorescing particles and by varying the wavelength of the illumination light. Finally, one should mention the work of Khalighi [6] who utilized digital image processing techniques to automatically analyze particle streak images and produce full-field velocity maps.

The primary factors affecting the capability to adapt particle displacement velocimetry to large scale complex

flows are the ability to handle large amounts of data, the required processing time, variations in velocity scales in the same flow field, the capability to record and identify fine details in large scale images as well as the availability of the appropriate particle tracers in large quantities. The approach opted for utilizes double exposed images of laser induced fluorescent particles which are analyzed automatically by digital image processing. This method enables one to resolve the entire velocity field simultaneously, thus allowing the identification of large scale flow structures as well as provide quantitative details about the velocity, circulation, etc. This technique is specifically suited for the study of large scale complex turbulent flows. Similar to the techniques of Gharib & Willert [5] and Khalighi [6], it consists of recording two exposures on a single frame. This approach minimizes the difficulty of identifying particle traces on successive frames, and still allow for short sampling intervals. Unlike the others, we have opted to identify the direction of flow by keeping one of the exposures longer than the other. The following paper focuses on this method.

An important assumption in all particle tracking techniques is that the seed particles follow the flow without slipping and do not alter the flow dynamics. This requirement prescribes the size, concentration and specific gravity of particles that can be used as tracers. Most of the past studies (Adamczyk and Rimai [7], Landeth, Adrian and Yao [8], Khalighi [6]), rely on the light reflected from the particles. This limitation has prohibited the use of very small particles, due to the low intensity of the reflected light. By utilizing tracers containing fluorescing material (Gharib and Willert [5]), the intensity of the emitted light is increased by several orders of magnitude, so that even microscopic particles can be used. The generation of particles with imbedded fluorescing material has been one of the critical problems, particularly when they are needed in large quantities.

Experimental Procedures

During the past two years we have constructed a large scale flow visualization facility with multiple light sheets in the 140 ft. towing basin at David Taylor Research Center (sketch is provided in Figure 1). While developing the flow visualization system in the towing tank, we have used water jets as the flow field in order to generate data for the imaging system. As a result the images provided in this paper have been recorded in a steady flow water jet facility located in a transparent test section. The jet was 1 inch in diameter. Thin sections (approximately 1 mm) of the flow field were

illuminated by a pulsed 300 mW argon ion laser. The water was seeded with microscopic (5-10 microns in diameter), neutrally buoyant particles, containing imbedded fluorescing dyes. These particles were invisible in most of the flow field, but responded with intense spontaneous fluorescence within the illuminated section. The production of these particles will be discussed later. The temporal light modulation followed a specific illumination code. Figure 2 shows the pattern used in the present work. The signal consisted of a long exposure (streak) followed by a shorter pulse (dot). The magnitude of the velocity was determined from the distance between the two traces of the same particle, while the flow direction could be determined by comparing the lengths of the two particles. As will be discussed later, the automatic image analysis algorithm could match between the traces as well as identify and remove streak patterns which did not resemble the illumination code.

The images were recorded on 35 mm film. We have opted for film since its resolution is much higher than that of video. As an example, Figure 3 contains two digitized images, both originated from the same negative. However, in the first one the entire negative was translated to a single video frame and then a portion of the frame was magnified. The second, on the other hand, was magnified prior to translation to video and as a result is clearer and sharper. A video frame has a resolution in the order of 500×500 lines, which is less than the resolution of 1 mm^2 of emulsion. Thus the translation to video should be performed carefully to avoid loss of details. Storing the original image in the form of a film negative allows variation in magnification while digitizing the image, and as a result enables us to control the resolution. While analyzing the image, one can focus a video camera on the negative and select the magnification depending on the desired detail. This is especially important when examining turbulent flows where wide ranges of velocities are present. For example, Figure 4 shows a typical image of the flow near the exit of a 1 inch diameter nozzle. Portions of the flow are unresolvable at this magnification. By focusing on a smaller portion of the negative (Figure 5), the magnification and hence the resolution are increased allowing for analysis of the originally unresolvable traces.

Image Analysis and Processing

As noted before, the image analysis and processing algorithms were developed with the specific objective of examining large scale real turbulent flows. As a result, the selected technique should be able to analyze images with a large numbers of particles at a wide range of velocities. Thus, it was necessary that the image resolution be such that both very small (low velocity) traces as well as long (high velocity) streaks could be clearly identified and handled efficiently. It was also necessary for the algorithms to be as simple as possible to maximize the speed of the analysis.

The images, recorded on film, were digitized by illuminating the negative from behind and by focusing a RCA video camera with a microscope objective zoom lens on a section of the film. The camera was linked to a high resolution video recorder as well as to an Imaging Technologies Inc. Series 100 Image processor and frame grabber which were installed in a Sun 4/260 workstation.

Each video frame was digitized to a 512×512 pixel, 8 bit array. Each pixel was assigned an intensity value, ranging from 0 to 255, corresponding to its relative brightness. The digitized image was then enhanced by color filtering, a smoothing convolution and contrast enhancement to reduce the noise. The use of fluorescing particles has the added benefit that the emitted light is of a wavelength which is higher

(in the yellow range) than the green light reflected from bubbles and contaminants. This feature allows significant enhancement of the input images by removing much of the reflected laser light through color filtering.

The filtered image was then sharpened by convolving with the following kernel:

-1	-1	-1
-1	12	-1
-1	-1	-1

Namely, each pixel value was multiplied by 12 and its eight nearest neighboring pixels were multiplied by -1. Then, the sum of these values was added to the original pixel intensity. Performing this process on the entire image effectively sharpens the edges of the traces (Figure 6). The image was then equalized, namely the intensity values of the entire image were normalized to range from 0 to 255, to improve contrast.

The next step was to "threshold" the image. Pixel values above a selected intensity level were set to 255 and values below it were set to 0. The threshold level was determined from an intensity histogram of the entire image. In an optimal situation the intensity histogram would be bimodal, with well separated peaks. That is, the particle traces would be easily distinguishable from the background and their edges would be distinct and clear. In practice this was not usually the case. In fact, it was not uncommon that the brightest background pixel would be brighter than the faintest pixel of a particle. This phenomenon occurred when the background illumination was not uniform. Therefore construction of an accurate binary image using threshold analysis required the use of local threshold intensity levels. Additional techniques could be utilized, if needed, to further aid in distinguishing particles from the background. These techniques include the use of gradient and Laplacian operators, to provide edge enhancement (Rosenfeld and Kak [9]) and examination of the slope of the thresholded average intensity vs. threshold curve (Prasad & Sreenivasan [10]).

The thresholded image was then reduced to a binary bit map of "0's" and "1's". The "0's" represented the background (pixels of value = 0) and the "1's" (pixels of value = 255) were parts of particle traces (Figure 7). This step reduced the needed computer memory space and processing time in that the image was now represented by an array of 1-bit integers. The bit map was then searched pixel by pixel, row by row until a pixel representing part of a particle trace was found (a "1"). Then the total size of the trace, as well as its length and orientation, were determined by examining connected pixels. The centroid of the trace was also found at this time. The program assumed that the trace found was the longer streak. The length and orientation of this trace, coupled with the illumination code, was then used to determine the probable location of the matching trace. In the photographs presented in Figures 3-6 the illumination code was such that the exposure time for the streak and the delay between exposures were 4 and 5 times the exposure time of the dot, respectively (Figure 2). Once the search distance and orientation of the streak were calculated, the matching dot was searched for only in a limited space. It was necessary however, to examine the image on both sides of the slot, since the flow direction was not known a priori. If a second trace was identified within the prescribed area, the ratio of the slot length to separation distance was then compared to the respective time ratios in order to insure that they were traces of the same particle. The last position of the center of the particle within the streak was then estimated by determining the width of the trace at three positions along the trace's major axis (Figure 8). The variation in their value

had to remain within a specified range for them to be accepted as the actual width of the trace. The position of the center of mass at the end of the streak was then determined to be at a half width from the edge of the trace and centered along its major axis (Figure 8). The same process was done for the shorter trace. The velocity was calculated from the estimated separation distance, center of mass to center of mass (Figure 8). This sequence was repeated until the entire image had been analyzed and a map of the entire velocity field (Figure 9) was produced.

Since both sides of the traces were searched there was a small possibility that dots which fulfill the above mentioned criteria would be found on both sides of the streak. If this situation occurred the velocities would be compared to neighboring values to determine the correct direction. If the correct direction and magnitude could not be inferred, this data point was not used for the final velocity map. The computer program also contains additional procedures to handle unmatched traces, variations in slopes, flow near the core of a vortex, etc.

The digitization, enhancement and processing phases were done interactively which allowed for operator control of the thresholding and scale of digitization. The analysis of the bit maps was done automatically with its output being the velocity vector for each particle trace found. A 512x512 pixel, 8 bit image was usually completely analyzed in approximately 2 minutes of CPU time. The more "trouble spots" (unmatched traces, multiple dots for one slot, noise, etc.) there were, the longer it took for the computer to complete the analysis. The entire process consisting of: selection of an image, digitization, enhancement, thresholding, and image analysis took approximately 10 minutes per image. More sophisticated automatic edge detection techniques as well as automatic thresholding are being implemented at the present time.

Particle Production

For the technique to be practical, particularly for large scale towing tank flows, an efficient method of manufacturing microscopic fluorescent particles was needed. A substantial effort has been invested in developing a reliable and controllable manufacturing process. The particles were composed of a specific mixture of acrylics and several fluorescing dyes. The mixture was adjusted to produce a neutrally buoyant substance. They were manufactured by dissolving the acrylics and then mixing the solution with the dyes. The mixture was atomized and the resulting "dust" (5-10 microns in diameter) was then collected and used as velocity tracers.

Error Estimation

An important aspect of the analysis is to estimate the error of the measurement. Geometric distortion due to the lenses can be corrected for by using the techniques described by Green [11]. Other errors are predominantly due to the digitization which sets the accuracy of each measurement to ± 0.5 pixels. The velocity is equal to the separation distance divided by the time lag between exposures. The separation distance is found by calculating the edge to edge distance between traces plus half the thickness of each trace. The error in edge to edge distance is 1 pixel and the error in estimating the center of the particle is 0.5 pixels, so the total error is 1.5 pixels. This is a rough analysis since filtering and enhancement may also introduce an error. As a result, future calibrations will be utilized for determining the error more accurately. In the future, the images will be digitized to provide generally a separation distance of 15 pixels, resulting in an error of

separation distance of 15 pixels, resulting in an error of approximately 10%. The error can be further reduced by reducing the digitization scale. For example, if the image is digitized such that the separation distance is increased to 60 pixels the error decreases to 2.5 %. However, the processing time increases accordingly. Thus, a judgement of what is the best digitization scale must be made. By recording the original image onto film, different digitization scales can be used for different portions of the image. This method provides the capability to optimize between the processing speed and the error. This feature is especially important if gradients of the velocity are desired, i.e. during vorticity analysis. Hesselink [12] estimated the maximum acceptable relative error to be less than 0.5% to insure an accurate vorticity determination. This error level is quite impractical for the technique presented in this paper. However, errors on the order of 1-10% can be achieved, depending on the length of the analysis. It should be noted here that to achieve an error of 1% the traces of a single particle should occupy the entire 512x512 frame.

Summary and Future Work

A particle displacement velocimetry technique utilizing digital image processing has been developed for examining large scale complex turbulent flows. The technique consists of illuminating a section of the flow field with a sheet of Argon ion laser while seeding the water with microscopic fluorescing neutrally buoyant particles. These tracers are invisible in most of the flow field, but respond with intense fluorescence within the illuminated section. By pulsing the laser twice while recording a single frame each particle leaves two traces on the same frame. The velocity is determined from the distance between the traces, and the direction of the flow is identified by keeping one of the pulses longer than the other. Each recorded film negative is analyzed by digitizing a portion of the frame, to a 512x512 pixel array which is then enhance, thresholded and then translated to a bit map. The analysis of the bit map consists of searching the array for traces. Once a trace is found, its position, orientation, width and length are determined. From this information, as well as the illumination code a search distance and direction of the matching second trace are calculated. If the second trace is found within the predetermined space the velocity is then determined from the separation distance. This procedure is repeated until the entire image is analyzed.

At present, the system is installed in a 140 foot towing tank at the David Taylor Research Center and is being utilized in the study of the three dimensional separated flows. Further refinement of the image processing and analysis procedures are also currently underway. In the future the image processing and analysis will be fully automated and expert systems will be utilized to determine proper levels of enhancement, thresholding and accuracy of analysis.

Acknowledgement

This work was sponsored in part by the Office of Naval Research Applied Hydrodynamic Research Program and in part by DARPA's Submarine Technology Program. Their support is gratefully acknowledged.

References

- 1 Kobayashi, T. 1983 Proc. 3rd Int. Symp. Flow Visualization Sept 6-9, Ann Arbor, Michigan, p. 261
2. Marko, K. A. and Rimai, L. 1985 Appl. Opt. 24, 3666-3672
3. Racca, R.G. and Dewey, J.M., 1988, Experiments in Fluids, Vol. 6, pp. 25-32.

4. Adrian, R. J, 1984 Appl Opt. 23, pp. 1690-1691
5. Gharib, M. and Willert, C., 1988 AIAA paper 88-3776-CP, pp. 1935-1943
6. Khalighi, B. 1989 Experiments in Fluids, Vol. 7, pp. 142-144
7. Adamczyk, A. A. and Rimai, L. 1988 Experiments in Fluids, Vol. 6, pp. 373-380
8. Landreth, C. C., Adrian, R. J. and Yao, C. S. 1988 Experiments in Fluids Vol. 6, pp. 119-128

9. Rosenfeld, A. and Kak, A. C. 1982 Digital Image Processing, 2nd edition New York: Academic Press.
10. Prasad, R. R. and Sreenivasan, K.R., 1989 Experiments in Fluids Vol. 7, pp. 259 -264.
11. Green, W. B., 1983 Digital Image Processing A Systems Approach, New York: Van Nostrand Reinhold.
12. Hesselink, L., 1988 Ann. Rev. Fluid Mech. Vol. 20, pp. 421-485

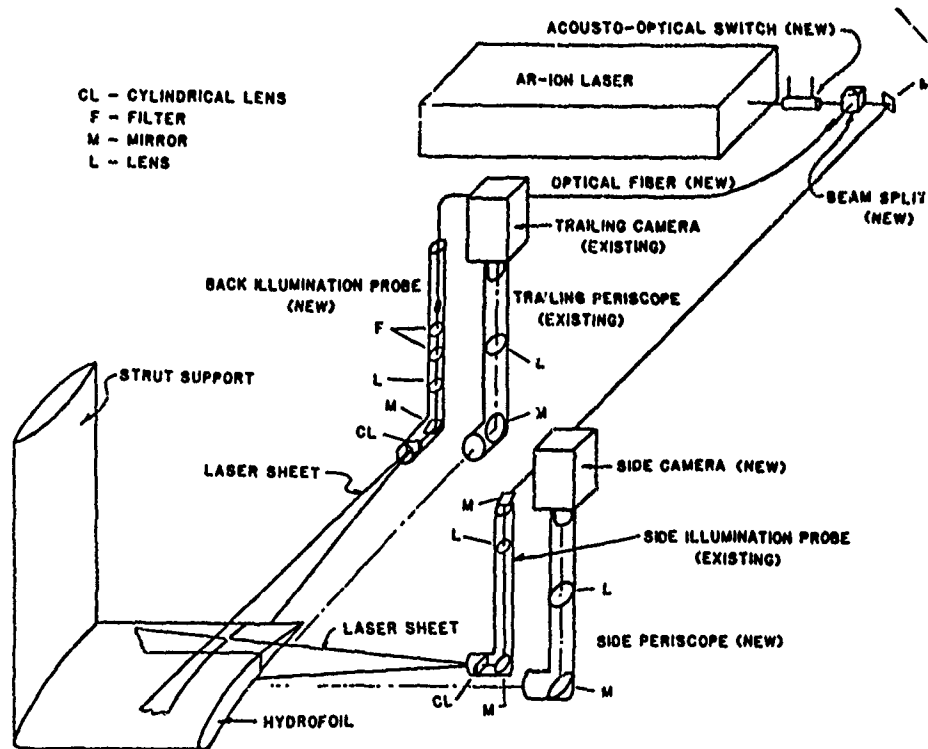


Figure 1: Sketch of the large scale flow visualization facility in the 140 ft. towing tank at the David Taylor Research Center.

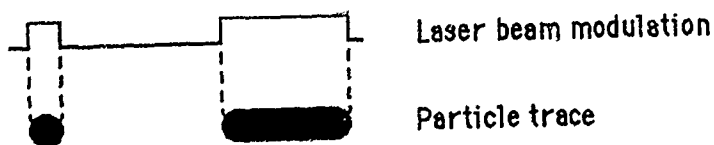


Figure 2: Incident illumination modulation code with a typical pair of traces of the same particle.



(a)



(b)

Figure 3: (a) Image of particle traces enlarged after digitization.
(b) Same image as (a) but magnified prior to digitization.



Figure 4: Typical double exposed image of the flow near a 1 inch diameter nozzle.



Figure 5: Enlarged section of Figure 4.

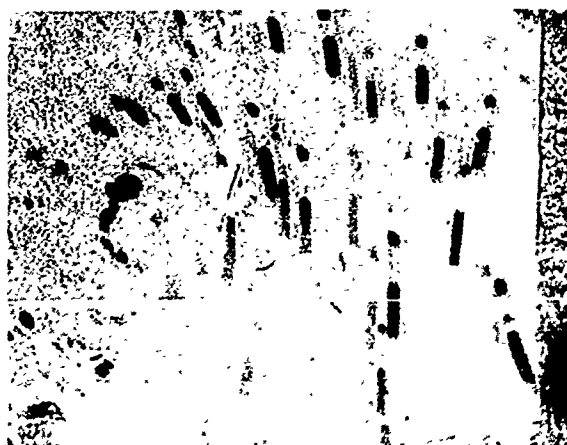


Figure 6: Figure 5 sharpened through convolution.

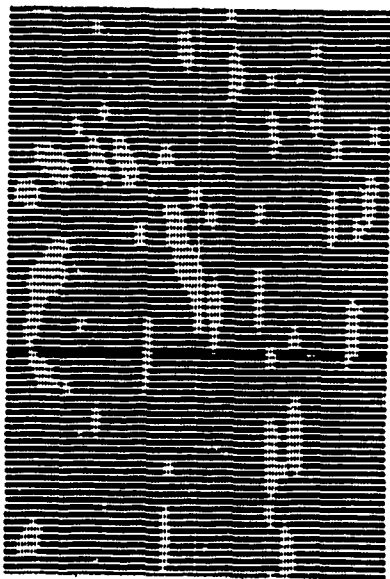
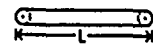


Figure 7: Binary bit map of Figure 6.

1) Measure trace length.



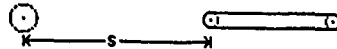
○

2) Determine trace width and center of particle.



○

3) Search for the partner trace.



○

4) Measure particle displacement.



- Figure 8: General sequence of image analysis steps.
- (1) Determine the length and orientation of the trace.
 - (2) Determine the width and the position of the center of the particle at the end of the trace.
 - (3) Search a small area at the calculated search distance.
 - (4) Measure the particle displacement.

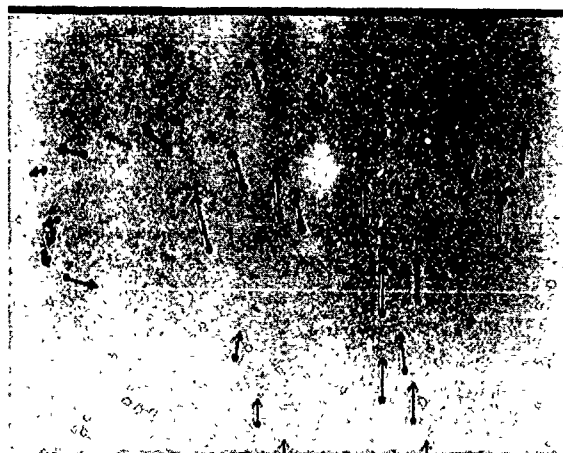


Figure 9: Map of the velocity field of the flow near a 1 inch nozzle, determined through analysis of Figure 7, by digital image processing.

Side-Wall Effects on Hydrodynamic Forces Acting on a Ship with Forward and Oscillatory Motions

M. Kashiwagi and M. Ghkusu
Kyushu University
Fukuoka, Japan

Abstract

A rational slender-ship theory is presented for predicting the side-wall effects on the added-mass and damping coefficients of a ship, moving with forward velocity and performing heave and pitch motions in a waterway with vertical and parallel side walls. Satisfaction of the side-wall boundary condition in the far-field solution is achieved by the method of mirror images, with a closed-form expression obtained of the resultant infinite series. The inner expansion of the far-field solution dictates the asymptotic behavior of the near-field solution, thereby determining the near-field homogeneous component. This component accounts for the side-wall interference in the inner region as well as the hydrodynamic interactions along the ship's length.

Computed added-mass and damping coefficients are presented for a half-immersed prolate spheroid. Validity of the proposed theory is confirmed by the comparison with the 3-D panel method for the special case of zero forward speed.

1. Introduction

Hydrodynamic forces acting on a ship model with forward and oscillatory motions are in most cases measured in a towing tank with limited width. When the forward speed and oscillation frequency of a ship model are relatively small, reflection waves from the side walls of a towing tank affect the measured hydrodynamic forces: they must be different from what we expect for a ship model in open water.

A diagram [1] is prepared for predicting whether the side-wall effect is expected or not, which gives the critical value of parameter $\tau = U\omega/g$ (where U is the forward speed, ω the oscillation frequency, and g the gravitational acceleration) as a function of the ratio of tank width to ship length. This diagram is, however, derived with heuristic ways and thus not entirely precise.

There have been a few theoretical studies concerning the side-wall effects on hydro-

dynamic forces acting on a ship moving at a finite forward speed in waves. The pioneering work of Hanaoka [2] based on the thin-ship theory is a rational theory of the side-wall effects, but did not give reliable information on the effects. Hosoda [3,4] and Takaki [5] are based on the strip-theory approach with a number of approximations in the mathematical evaluation of reflection waves from the side walls. Accuracy of their numerical results are therefore questionable despite their mathematically complicated expressions.

In the present paper, the slender-ship theory is applied to develop a rational method which is able to predict the effects of side-wall interference, particularly when a ship has a finite forward speed. The theory described in this paper may be regarded as an extension of Newman's unified theory [6] to the case of side-wall effects present.

In the inner region close to the ship hull, since the side walls and the radiation condition are absent, the inner solution can be identified with that in the unified theory for the open-sea problem. Namely it can be constructed by the superposition of the particular solution given by the strip theory plus a homogeneous solution giving three-dimensional effects. The latter component plays an important role in accounting not only for longitudinal flow interactions along the ship hull but also for the side-wall interference in the inner region.

In the outer region far from the ship, the ship may be seen as a segment on the longitudinal axis, but the side walls are present. Thus the solution is represented by a line distribution of 3-D wave sources with unknown strength along the ship's length. The velocity potential of 3-D wave source satisfying the side-wall boundary condition is derived by considering an infinite number of image singularities and a closed-form expression of the resultant infinite series.

The source strength in the outer solution and the coefficient of a homogeneous component in the inner solution are to be determined from the asymptotic matching procedure. The implementation of the asymptotic matching between the inner and outer solutions leads to an

integral equation for the strength of 3-D wave sources, the solution of which then settles the coefficient of the near-field homogeneous solution; thereby completing the velocity potential necessary for the calculations of added-mass and damping coefficients.

Solving the integral equation obtained requires the numerical evaluation of Cauchy's principal-value integrals involved in the kernel function representing the side-wall effects. Numerical implementation of these integrals is performed by firstly subtracting the singular behavior from the integrand, secondly integrating analytically the subtracted singular part, and finally integrating numerically the resultant non-singular part by means of an appropriate numerical technique. Clenshaw & Curtis quadrature is employed in this paper with a tolerance of absolute error less than 10^{-5} .

Computational results are presented of the heave and pitch added-mass and damping coefficients, for a half-immersed prolate spheroid of length-beam ratio 8.0 advancing at a Froude number 0.1 in the waterway of width twice the spheroid's length.

The appearance of side-wall effects is closely related to the wave pattern generated by an oscillating and translating ship and to its reflection from side walls of the waterway. Starting from the ring wave at $\tau=0$, the wave pattern changes to the complicated one dominated by the diverging-wave component, as the parameter τ increases across the critical value $1/4$. Corresponding to this complicated variation of the wave pattern, the added-mass and damping coefficients including the side-wall effects show complex variations.

In order to check the validity of the theory, numerical results for the special case of zero forward speed are compared with independent "exact" calculations based on the 3-D panel method, for example, by Kashiwagi [7]. The results of the present theory agree excellently with the 3-D panel-method predictions.

The present paper is restricted to the radiation problem of heave and pitch oscillations, but the diffraction problem may be analyzed in a similar manner with the knowledge of Slavounos' diffraction theory [11] for the case of open sea, which is left for future work.

2. Formulation of problem

As shown in Fig.1, we consider a ship in a waterway with vertical and parallel side walls. Let L , B , and d denote the length, breadth, and draft of a ship respectively, and B_T the breadth of a waterway. The ship is assumed to move at constant forward velocity U and to oscillate sinusoidally with circular frequency ω in heave and pitch; the depth of waterway is assumed deep enough, with no shallow-water effect in the water-wave phenomena.

A coordinate system used is shown in Fig.1. The x -axis is coincident with the centerline of the waterway and positive in the direction of the ship's forward velocity, the y -axis is

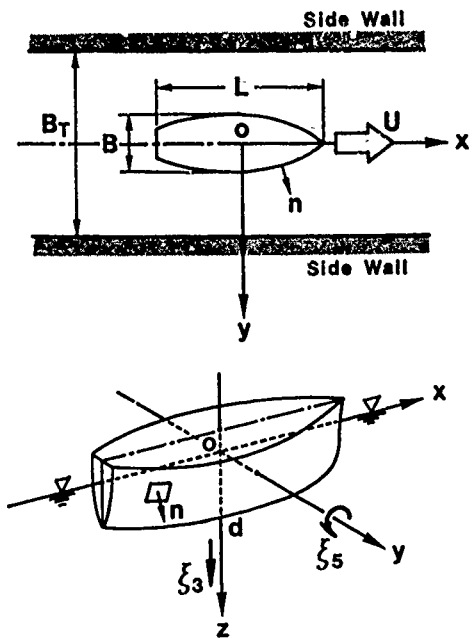


Fig.1 Coordinate system and notations

horizontal, and the z -axis is vertical and positive downward, with the origin placed at midships and on the undisturbed free surface. Assuming the flow to be inviscid with irrotational motion, the flow field can be described in terms of the velocity potential $\Phi(x, y, z, t)$ satisfying the Laplace equation of the form

$$[L] \quad \Phi_{xx} + \Phi_{yy} + \Phi_{zz} = 0 \quad (1)$$

in the fluid domain $z > 0$, $|y| < B_T/2$. In order to justify the linearization of the problem, the amplitudes of ship's oscillatory motions are assumed small. Then the velocity potential can be linearly decomposed as

$$\Phi = U[-x\chi(x, y, z)] + \text{Re} \left[\sum_{j=3,5} i\omega \xi_j \phi_j(x, y, z) e^{i\omega t} \right] \quad (2)$$

where $\chi(x, y, z)$ is the steady perturbation potential due to the forward motion of the ship, and the second line represents the unsteady part of the velocity potential. Mode index j is used, with $j=3$ for heave and $j=5$ for pitch, and ξ_j denotes the amplitude of the j -th mode of motion. Re means the real part of the expression to be taken and the time dependence $e^{i\omega t}$ will be hereafter understood and deleted in the analysis.

In this paper, we restrict the ship hull to be slender with small beam and draft compared to its length, and thus we are allowed on the free surface to neglect the contributions of steady perturbation potential. With this taken into account, the boundary conditions to be satisfied by the normalized unsteady velocity potential ϕ_j can be summarized as

$$\begin{aligned} [F] \quad & \phi_{jz} + K\phi_j + i2\tau\phi_{jx} - \frac{1}{K_0}\phi_{jxx} \\ [R] \quad & - i\mu(K\phi_j + i\tau\phi_{jx}) = 0 \end{aligned} \quad (3)$$

$$\text{where } K = \omega^2/g, \tau = U\omega/g, K_0 = g/U^2 \quad (4)$$

$$[B] \quad \phi_{jz} \rightarrow 0 \quad \text{as } z \rightarrow \infty \quad (5)$$

$$[W] \quad \phi_{jy} = 0 \quad \text{on } y = \pm B_T/2 \quad (6)$$

$$[H] \quad \phi_{jn} = n_j + \frac{U}{i\omega} m_j \quad \text{on ship hull} \quad (7)$$

Here μ in (3) is Rayleigh's artificial viscosity coefficient to ensure the appropriate radiation condition [R] being satisfied. The subscript n in (7) denotes normal differentiation, with the unit normal vector defined positive when pointing into the fluid domain (see Fig.1), and n_j is the components of the normal vector parallel to the x_j -axis with extended definition of $n_5 = zn_1 - xn_3$. m_j is the so-called m -terms representing the forward-speed effect due to the oscillatory motions in the steady flow, which has been originally derived in Timman and Newman [12] and can be explicitly written as

$$\left. \begin{aligned} (m_1, m_2, m_3) &= -(n \cdot \nabla) \nabla \chi \\ (m_4, m_5, m_6) &= -(n \cdot \nabla)(r \times \nabla \chi) \end{aligned} \right\} \quad (8)$$

In order to obtain a solution of the above three-dimensional boundary-value problem, we exploit a slender-ship theory. In this theory, the flow field to be analyzed will be divided into the inner and outer regions, and in each region the governing equation and boundary conditions may be simplified, making it possible to obtain the inner and outer solutions respectively with relative ease. However, both of these solutions include indeterminate coefficients, since nothing has been prescribed about the respective asymptotic behavior far away in the inner problem and close to the ship in the outer problem. These indeterminate coefficients can be settled by requiring the two solutions to be compatible in an overlap region between the inner and outer fields.

2.1 The outer problem

In the outer field far from the ship hull, the effects of three dimensionality and of side walls of the waterway must be accounted for. When the ship is seen from the outer field, it may be viewed as a segment on the x -axis, and thus the flow field is insensitive to the details of ship's hull geometry. Therefore the outer problem is defined by the 3-D Laplace equation [L], subject to the free-surface [F], radiation [R], sea-bottom [B], and side-wall [W] boundary conditions, that is, (3)-(6). Since these boundary conditions are homogeneous, the outer solution can be described in terms of the 3-D Green function with unknown wave sources distributed on the x -axis, in the form

$$\phi_j(x, y, z) = \int_L q_j(\xi) G(x - \xi, y, z) d\xi \quad (9)$$

Here $G(x, y, z)$ denotes the Green function or the potential of a "translating-pulsating" source with unit strength, and $q_j(x)$ is the strength of the source to be determined. The Green function appropriate to the present problem can be derived by applying Hanaoka's approach [2], in which the method of mirror images is utilized.

Considering the Fourier transform with respect to x of a unit source located at the origin and its mirror images with respect to both of the side walls of waterway, the Green function satisfying homogeneous boundary conditions (3)-(6) is given in the Fourier space as follows:

$$\begin{aligned} G^*(k; y, z) &= \int_{-\infty}^{\infty} G(x, y, z) e^{ikx} dx \\ &= \frac{1}{\pi} \int_0^{\infty} \frac{n \cos(nKz) - v \sin(nKz)}{n^2 + v^2} \frac{n}{\sqrt{n^2 + k^2}} \\ &\quad \cdot \sum_{p=-\infty}^{\infty} e^{-K|y - pB_T| \sqrt{n^2 + k^2}} dn \\ &+ \left[\begin{aligned} &\frac{-i \operatorname{sgn}(1 + k\tau)}{\sqrt{1 - k^2/v^2}} e^{-Kz} \\ &\cdot \sum_{p=-\infty}^{\infty} e^{-i \operatorname{sgn}(1 + k\tau) K|y - pB_T| \sqrt{1 - k^2/v^2}} \\ &\frac{1}{\sqrt{k^2/v^2 - 1}} e^{-Kz} \sum_{p=-\infty}^{\infty} e^{-K|y - pB_T| \sqrt{k^2/v^2 - 1}} \end{aligned} \right] \quad (10) \end{aligned}$$

$$\text{where } v = (1 + k\tau)^2, \quad \kappa = Kv = K(1 + k\tau)^2 \quad (11)$$

and the upper and lower expressions in brackets are to be taken according as $|k| < v$ and $|k| > v$, respectively.

The values of k satisfying $|k| = v$ give the branch points of the square-root function, which are written in the nondimensional form as

$$k_{1,2} = -2/(1 + 2\tau \pm \sqrt{1 + 4\tau}) \quad (12)$$

$$k_{3,4} = 2/(1 - 2\tau \pm \sqrt{1 - 4\tau}) \quad (13)$$

Note that for $\tau < 1/4$, k_3 and k_4 are real and positive, but complex-conjugate for $\tau > 1/4$. At zero forward speed ($\tau = 0$) k_2 and k_3 become -1 and $+1$ respectively, whereas k_1 and k_4 tend to respectively minus and plus infinity.

In connection with the infinite series appearing in (10), we can obtain their closed-form expressions under the condition $|y| < B_T/2$ as follows:

$$\begin{aligned} \sum_{p=-\infty}^{\infty} e^{-K|y - pB_T|} &= e^{-K|y|} \\ &+ \cosh(\ell Ky) \left[-1 + \coth\left(\frac{\ell KB_T}{2}\right) \right] \quad (14) \end{aligned}$$

$$\begin{aligned} \sum_{p=-\infty}^{\infty} e^{\pm iK|y - pB_T|} &= e^{\pm iK|y|} \\ &+ \cos(\ell Ky) \left[\frac{2\pi}{KB_T} \delta(\ell, \frac{2\pi}{KB_T}) - 1 \pm i \cot\left(\frac{\ell KB_T}{2}\right) \right] \quad (15) \end{aligned}$$

The function appearing as the first term in brackets on the right side of (15) denotes the infinite series of Dirac's delta function, defined by

$$\delta(\ell, \frac{2\pi}{KB_T}) = \sum_{m=-\infty}^{\infty} \delta(\ell - \frac{2\pi}{KB_T} m) \quad (16)$$

and therefore contributes only when $\ell = 2\pi m / KB_T$.

If we consider the limit of $B_T \rightarrow \infty$ in (14) and (15), it is relatively easy to confirm that the second line on the right-hand side of each equation vanishes and only the first term remains. Thus the side-wall effects are represented by the second line in (14) and (15); this suggests that the Green function can be expressed in an addition form of the open-sea Green function $G_O(x, y, z)$ plus the side-wall-effect part $G_T(x, y, z)$. The final expression of the Green function can be given by considering the inverse Fourier transform of the above expressions, with the following formula:

$$G(x, y, z) = G_O(x, y, z) + G_T(x, y, z) \\ = \frac{K}{2\pi} \int_{-\infty}^{\infty} \{G_O^*(k; y, z) + G_T^*(k; y, z)\} e^{-ikKx} dk \quad (17)$$

In the outer solution given by (9), the 3-D source strength $q_j(\cdot)$ is unknown but will be determined by requiring the inner expansion of (9) to be compatible with the outer expansion of an appropriate inner solution. For this matching procedure, the inner expansion of the Green function must be sought. Following the method of matched asymptotic expansions, we seek the inner expansion with the following order of magnitude:

$$Ky, Kz = O(\epsilon), \quad k = O(1), \quad \tau = O(1) \quad (18)$$

Considering that the side-wall effects will be expected when the forward velocity and oscillation frequency of a ship are relatively small, the assumption on the order of parameter τ in (18) seems reasonable. It should be noted, however, that this assumption does not necessarily mean the applicability of the present theory is restricted to the range under the critical value given by $\tau = 1/4$. The transitional value of the parameter τ where the theory becomes invalid may be determined from numerical computations and comparison of those with experiments.

The analysis for the inner expansion of the open-sea Green function is identical to that in the unified theory devised by Newman [6], and hence with the present notations the desired result can be expressed in the form

$$G_O^*(k; y, z) = G_{2D}(y, z) + \frac{1}{\pi} (1 - Kz) f_O^*(k) \\ + O(Kr(1-\nu), K^2 r^2) \quad (19)$$

where

$$G_{2D}(y, z) = G_O^*(0; y, z) \\ \sim -\frac{1}{\pi} \{ (1 - Kz)(\log Kr + \gamma) \\ + Kr(\cos\theta + \theta \sin\theta) \} - i(1 - Kz) \quad (20)$$

$$f_O^*(k) = \log \frac{2}{|k|} + \pi i \\ - \left[\frac{1}{\sqrt{1-k^2/\nu^2}} \{ \cosh^{-1}(\frac{\nu}{|k|}) + \pi i \operatorname{sgn}(1+k\tau) \} \right. \\ \left. - \frac{1}{\sqrt{k^2/\nu^2-1}} \{ \cos^{-1}(\frac{\nu}{|k|}) - \pi \} \right] \quad (21)$$

In (19) and (20), two-dimensional polar coordinates (r, θ) are used with the relation $(y, z) = (r \sin\theta, r \cos\theta)$, and γ is Euler's constant equal to 0.5772...

The expansion of the side-wall-effect part of the Green function can be obtained with comparatively simple reduction, in the form

$$G_T^*(k; y, z) = \frac{1}{\pi} (1 - Kz) f_T^*(k) \\ + O(Kr(1-\nu), K^2 r^2) \quad (22)$$

where

$$f_T^*(k) = \int_0^{\infty} \frac{n^2}{n^2 + \nu^2} \{ -1 + \coth(\frac{KB_T}{2} \sqrt{n^2 + k^2}) \} \\ \cdot \frac{dn}{\sqrt{n^2 + k^2}} \\ + \left[\frac{-\pi i \operatorname{sgn}(1+k\tau)}{\sqrt{1-k^2/\nu^2}} \{ \frac{2\pi}{KB_T} \delta(\sqrt{\nu^2 - k^2}, \frac{2\pi}{KB_T}) - 1 \} \right. \\ \left. - i \operatorname{sgn}(1+k\tau) \cot(\frac{KB_T}{2} \sqrt{1-k^2/\nu^2}) \right] \\ + \left[\frac{1}{\sqrt{k^2/\nu^2-1}} \{ -1 + \coth(\frac{KB_T}{2} \sqrt{k^2/\nu^2-1}) \} \right] \quad (23)$$

As in (10), the upper and lower expressions in brackets in (21) and (23) correspond to $|k| < \nu$ and $|k| > \nu$, respectively.

The final result of the inner expansion of the Green function will be obtained by substituting (19) and (22) into (17) and performing the inverse Fourier transform. Regarding the open-sea Green function (19), the analysis for the inverse Fourier transform shown in Newman and Sclavounos [9] can be directly applied. Therefore we have

$$G_O(x, y, z) \sim \delta(x) G_{2D}(y, z) + \frac{1}{\pi} (1 - Kz) \frac{d}{dx} F_O(Kx) \quad (24)$$

where

$$F_O(Kx) = \begin{cases} F_1(Kx) + F_2(Kx) & \text{for } x < 0 \\ F_2(Kx) & \text{for } x > 0 \end{cases} \quad (25)$$

$$F_1(X) = \left[-\int_{-\infty}^{k_1} + \int_{k_2}^{\infty} \right] e^{-ikX} \left[\frac{1}{\sqrt{1-k^2/\nu^2}} - 1 \right] dk/k \\ + E_1(i|k_1 X|) + E_1(i|k_2 X|) \quad (26)$$

$$F_2(X) = \frac{1}{2} \left[\int_0^{k_3} + \int_{k_4}^{\infty} \right] e^{-ikX} \left[\frac{1}{\sqrt{1-k^2/\nu^2}} - 1 \right] dk/k \\ + \frac{1}{2} \int_{k_3}^{k_4} e^{-ikX} \left[\frac{i}{\sqrt{k^2/\nu^2-1}} - 1 \right] dk/k \quad (27)$$

Function $E_1(z)$ in (26) denotes the exponential integral with complex argument. The expression (27) is applicable for $\tau < 1/4$, and should be understood for $\tau > 1/4$ with $k_3 = k_4$, where the wavenumbers k_j ($j=1, 2, 3, 4$) are given in (12) and (13).

The inverse Fourier transform of the side-wall-effect part (22) can be expressed as

$$G_T(x, y, z) \sim \frac{1}{\pi} (1-Kz) \frac{d}{dx} F_T(Kx) \quad (28)$$

where

$$\begin{aligned} F_T(X) = & \frac{i}{2\pi} \int_{-\infty}^{\infty} e^{-ikX} dk/k \\ & \cdot \int_0^{\infty} \frac{n^2}{n^2 + v^2} \{-1 + \coth(\frac{KB_T \sqrt{n^2 + k^2}}{2})\} \frac{dn}{\sqrt{n^2 + k^2}} \\ & + \frac{1}{2} \left(\frac{2\pi}{KB_T} \right) \sum_{p=1}^4 \cdot \sum_{m=0}^{\infty} \epsilon_m \left[\frac{\text{sgn}(1+k\tau)}{k|dv/dk - k/v|} e^{-ikX} \right]_{k=k_{pm}} \\ & - \frac{i}{2} \left[\int_{-\infty}^{k_1} + \int_{k_2}^{k_3} + \int_{k_4}^{\infty} \right] e^{-ikX} \frac{1}{\sqrt{1-k^2/v^2}} \\ & \cdot \cot\left(\frac{KB_T}{2} \sqrt{1-k^2/v^2}\right) dk/k \\ & + \frac{i}{2} \left[\int_{k_1}^{k_2} + \int_{k_3}^{k_4} \right] e^{-ikX} \frac{1}{\sqrt{k^2/v^2 - 1}} \\ & \cdot \coth\left(\frac{KB_T}{2} \sqrt{k^2/v^2 - 1}\right) dk/k \\ & - \frac{1}{2} \left[-\int_{-\infty}^{k_1} + \int_{k_2}^{k_3} + \int_{k_4}^{\infty} \right] e^{-ikX} \frac{1}{\sqrt{1-k^2/v^2}} dk/k \\ & - \frac{i}{2} \left[\int_{k_1}^{k_2} + \int_{k_3}^{k_4} \right] e^{-ikX} \frac{1}{\sqrt{k^2/v^2 - 1}} dk/k \quad (29) \end{aligned}$$

$$\text{and} \quad \epsilon_0 = \frac{1}{2}, \quad \epsilon_m = 1 \quad (m \neq 0) \quad (30)$$

The first term on the right-hand side of (29) represents the contribution of non-radiating local waves. The second term is obtained from the infinite series of delta function in (23) and physically the contribution of the outgoing waves at infinity. In this second term, k_{pm} denotes the values satisfying $KB_T \sqrt{v^2 - k^2} = 2\pi m$ ($m=0, 1, 2, \dots$), which exist at most four in number and when $m=0$ coincide with k_j ($j=1, \dots, 4$) given in (12) and (13).

A part of the radiated waves are reflected on the side walls, and changed in phase by the factor $\pi/2$ and represented as the third term in (29). In other words from the standpoint of hydrodynamic-force calculation, the third term is originally to be contributed to the damping force, as is the same as the second term, but by the phase shift of $\pi/2$ due to the side-wall effects, this term will contribute to the inertia force. The integrals in the third term must be treated as Cauchy's principal-value integral at the points of k satisfying $\sin(KB_T \sqrt{v^2 - k^2}/2) = 0$, namely at $k=k_{pm}$ defined in the second term.

The fifth and sixth terms in (29) are independent of B_T and thus to be cancelled out by some terms given in the open-sea expressions (25)-(27). However as discussed previously in connection with the infinite series of (14) and (15), these two terms play a role in cancelling out respectively the third and fourth terms of (29) in the limit of $B_T \rightarrow \infty$. When $\tau > 1/4$, the expressions from third to sixth terms should be understood with $k_3 = k_4$.

Since we got the desired inner expansion of the Green function, by substituting it in (9) we have readily the inner expansion of the outer solution in the following form:

$$\begin{aligned} \phi_j(x, y, z) \sim & q_j(x) G_{2D}(y, z) \\ & - \frac{1}{\pi} (1-Kz) \int_L q_j(\xi) \frac{d}{d\xi} [F_0(K(x-\xi)) \\ & + F_T(K(x-\xi))] d\xi \quad (31) \end{aligned}$$

2.2 The inner problem

Since the ship hull is assumed slender, changes of the flow in the x -direction are small in the region close to the ship hull, by comparison to changes in the transverse plane. Thus the flow in the inner region may be described by the 2-D Laplace equation subject to the free surface condition which is independent of forward velocity and applicable to the 2-D problem in the y - z plane; this can be mathematically justified by the coordinate stretching argument with the assumption of $x=O(1)$, $y=O(\epsilon)$, and $z=O(\epsilon)$. In the inner problem, the radiation condition and the side-wall boundary condition can not be specified, because the side walls are absent in the inner region. With these taken into account, the boundary-value problem can be written as

$$[L] \quad \phi_{jyy} + \phi_{jzz} = 0 \quad \text{for } z > 0 \quad (32)$$

$$[F] \quad \phi_{jz} + K\phi_j = 0 \quad \text{on } z=0 \quad (33)$$

$$[H] \quad \phi_{jN} = N_j + \frac{U}{i\omega} M_j \quad \text{on ship hull} \quad (34)$$

Here we note that the subscript N in (34) denotes the normal differentiation on the sectional contour in the 2-D transverse plane, and N_j and M_j denote the slender-body approximation of the 3-D quantities in (7) and (8), which are explicitly given as

$$\left. \begin{aligned} N_5 &= -xN_3 \\ M_3 &= -N_2 X_{zy} - N_3 X_{zz} \\ M_5 &= N_3 - xM_3 \end{aligned} \right\} \quad (35)$$

The inner boundary-value problem defined from (32) to (35) is the same as the conventional 2-D formulation except that the radiation condition is absent. Thus the inner solution can be identified with Newman's unified-theory solution [6], composed of a particular solution commonly used in the strip theory plus a homogeneous solution multiplied by a three-dimensional-effect coefficient. To be more specific,

$$\begin{aligned} \phi_j(x; y, z) = & \phi_j^P(y, z) + \frac{U}{i\omega} \hat{\phi}_j^P(y, z) \\ & + C_j(x) \phi_j^H(y, z) \quad (36) \end{aligned}$$

$$\phi_j^H(y, z) = \phi_j^P(y, z) - \overline{\phi_j^P(y, z)} \quad (37)$$

where the overbar denotes the complex conjugate, and ϕ_j^P and $\hat{\phi}_j^P$ are the particular solu-

tions determined to satisfy the following boundary conditions on the body profile at station x :

$$\phi_{jN}^P = N_j, \quad \hat{\phi}_{jN}^P = M_j \quad (38)$$

The coefficient of the homogeneous solution $C_j(x)$ in (36) is indeterminate at this stage, but may be settled by matching the outer expansion of (36) with the inner expansion of the outer solution already given by (31).

Far from the ship hull in the inner region, (36) reduces to

$$\begin{aligned} \phi_j(x; y, z) \sim & [\sigma_j(x) + \frac{U}{i\omega} \hat{\sigma}_j(x) \\ & + C_j(x) \{ \sigma_j(x) - \overline{\sigma_j(x)} \}] G_{2D}(y, z) \\ & - e^{-Kz} \cos(Ky) 2i C_j(x) \sigma_j(x) \end{aligned} \quad (39)$$

Here $\sigma_j(x)$ and $\hat{\sigma}_j(x)$ denote the 2-D effective source strengths; these can be given by solving the ϕ_j^P - and $\hat{\phi}_j^P$ -problems respectively. $G_{2D}(y, z)$ is the 2-D Green function and identical to the one shown in (20) or (31).

2.3 Matching

In the analysis described above, the unknowns are the 3-D source strength $q_j(x)$ in the outer solution and the coefficient $C_j(x)$ of a homogeneous component in the inner solution. These will be determined by the matching of the inner and outer solutions. Comparing (31) with (39) and equating the factors of G_{2D} , the following relation can be found:

$$q_j(x) = \sigma_j(x) + \frac{U}{i\omega} \hat{\sigma}_j(x) + C_j(x) \{ \sigma_j(x) - \overline{\sigma_j(x)} \} \quad (40)$$

Equating the remaining terms in (31) and (39) gives

$$\begin{aligned} i2\pi C_j(x) \sigma_j(x) = & \int_L q_j(\xi) \\ & \cdot \frac{d}{d\xi} [F_0\{K(x-\xi)\} + F_T\{K(x-\xi)\}] d\xi \end{aligned} \quad (41)$$

with the error of order $O(K^2 r^2)$.

Eliminating $C_j(x)$ from (40) and (41), we have an integral equation for the 3-D source strength $q_j(x)$ of the form

$$\begin{aligned} q_j(x) - \frac{i}{2\pi} [\sigma_j(x) / \overline{\sigma_j(x)} - 1] \int_L q_j(\xi) \\ \cdot \frac{d}{d\xi} [F_0\{K(x-\xi)\} + F_T\{K(x-\xi)\}] d\xi \\ = \sigma_j(x) + \frac{U}{i\omega} \hat{\sigma}_j(x) \end{aligned} \quad (42)$$

Once $q_j(x)$ is determined by solving (42) with an appropriate numerical method, the coefficient $C_j(x)$ can be readily determined from (40), and thus the inner solution will be completed.

In the case of no side-wall effects, i.e. $B_T \rightarrow \infty$, the function $F_T\{K(x-\xi)\}$ becomes zero as already mentioned, and the integral equation (42) reduces to the corresponding one in Newman's unified slender-ship theory in the open-sea case [6]. In the special case of zero

forward speed, Kinoshita and Saijo [8] derived an analogous equation to (42) in the study on a multi-body-type floating breakwater, consisting of an infinite array of slender bodies.

The inner solution (36) appears formally to be invariable regardless of whether the side walls are present or not. However, through the 3-D source strength $q_j(x)$, which includes the side-wall effects as a solution of (42), the coefficient of homogeneous solution $C_j(x)$ accommodates not only the 3-D interaction effects between transverse cross-sections but also the side-wall effects of the waterway.

3. Added-mass and damping coefficients

Since the inner solution has been determined, we proceed to the calculation of hydrodynamic pressure force and moment acting on a ship with forced heave and pitch motions. The linearized hydrodynamic pressure is given from Bernoulli's equation. Then the hydrodynamic force in the i -th direction due to the j -th mode of motion can be provided by integrating the pressure over the mean wetted surface of the ship hull, and can be expressed in terms of the added-mass (A_{ij}) and damping (B_{ij}) coefficients, in the form

$$F_i = - \sum_{j=3,5} \{ (i\omega)^2 A_{ij} + (i\omega) B_{ij} \} \xi_j \quad (i=3,5) \quad (43)$$

where

$$A_{ij} + B_{ij}/i\omega = \int_L [a_{ij}(x) + b_{ij}(x)/i\omega] dx \quad (44)$$

$$\begin{aligned} a_{ij} + b_{ij}/i\omega = & - \rho \int_C N_i \phi_j d\ell \\ & + i\rho \frac{U}{\omega} \int_C (N_i \hat{\phi}_j^P - M_i \phi_j^P) d\ell - \rho \left(\frac{U}{\omega} \right)^2 \int_C M_i \hat{\phi}_j^P d\ell \\ & - \rho C_j(x) \int_C (N_i - \frac{U}{i\omega} M_i) (\phi_j^P - \overline{\phi_j^P}) d\ell \end{aligned} \quad (45)$$

Here ρ is the fluid density, and in deriving the above, Tuck's theorem [13] has been used. a_{ij} and b_{ij} defined in (44) and (45) denote the 2-D added-mass and damping coefficients respectively, involving the 3-D interaction effects and the side-wall effects, and c to the integral sign in (45) denotes the submerged portion of the contour of the transverse section.

In order to perform the calculations of (45), the term M_3 defined by (35) and the related velocity potential ϕ_3^P must be known, besides the velocity potential ϕ_3^P commonly calculated in the strip theory. If ϕ_3^P and $\hat{\phi}_3^P$ are obtained, the remaining velocity potentials for pitch ($j=5$) follow from (35)

$$\left. \begin{aligned} \phi_5^P &= -x \phi_3^P \\ \hat{\phi}_5^P &= \phi_3^P - x \hat{\phi}_3^P \end{aligned} \right\} \quad (46)$$

Sclavounos [10] studied in the open-sea case the relative importance of the contributions from the M_3 -term and related velocity potential ϕ_3^P , by comparing the numerical results with experiments. His results reveal that the inclusion of the M_3 -term leads to a

substantial overprediction of the damping coefficients. This overprediction may be attributed to the inaccuracy of the m -terms near the ship ends, which have been evaluated with slender-body approximation. Therefore the m -terms should be evaluated from the 3-D precise calculation for the steady perturbation potential. Fortunately, according to his numerical study, a better agreement with experiments is provided by simply omitting the m -terms in the unified theory. Thus in the numerical calculations with side-wall effects presented here too, it was decided to neglect the M_{35} -term and consequently the velocity potential ϕ_5 in (45).

It should be noted that the last term in (45), multiplied by the coefficient $C_j(x)$, plays an important role in accounting for the unified-theory corrections in the open-sea case and for the effects of side-wall interference in the presence of waterway. Without this last term, the remaining expressions in (45) are identical to those in the strip theory.

4. Numerical calculation method

An important task in the present theory is to solve the integral equation (42) for the 3-D source strength $q_j(x)$. For this purpose, after dividing the ship's longitudinal axis into NX segments of equal length, the 2-D boundary-value problem for heave ($j=3$) in each divided transverse plane must be solved; which gives $\sigma_3(x)$ necessary in calculating the right side of (42). Since we neglect the contribution of steady perturbation potential, $\phi_3(x)$ becomes zero, and the 2-D effective source strength for pitch ($j=5$) can be evaluated directly from $\sigma_3(x)$, with the result of $\sigma_5(x) = -x\sigma_3(x)$ and $\phi_5(x) = \sigma_3(x)$.

The 3-D source strength $q_j(x)$, which is to be determined, has been assumed to vary linearly in x between adjacent nodal points, with the value of $q(x)$ at station $x=x_k$ denoted by q_k ,

$$q(x) = \sum_{k=2}^N \Lambda_k(x) q_k \quad (47)$$

where

$$\Lambda_k(x) = \begin{cases} (x-x_{k-1})/(x_k-x_{k-1}) & x_{k-1} < x < x_k \\ (x-x_{k+1})/(x_k-x_{k+1}) & x_k < x < x_{k+1} \\ 0 & \text{elsewhere} \end{cases} \quad (48)$$

With this approximation, the integral on the left-hand side of (42) is analytically evaluated over each segment. The remaining task after this procedure is the numerical evaluation of the integrals associated with the two functions, $F_0(K(x-\xi))$ and $F_T(K(x-\xi))$. In relation to the third term in $F_T(K(x-\xi))$ given by (29), Cauchy's principal-value integral must be numerically evaluated. In the numerical implementation of this integral, singular contributions are subtracted from the integrand and analytically integrated. For this manipulation we have used the following integral formula:

$$\int \frac{dv/dk - k/v}{\sin(\frac{KB_T}{2}\sqrt{v^2-k^2})} \cdot \frac{v}{\sqrt{v^2-k^2}} dk \\ = \frac{2}{KB_T} \log \left| \tan \frac{KB_T}{4} \sqrt{v^2-k^2} \right| \quad (49)$$

The resultant non-singular integral is evaluated using Clenshaw & Curtis quadrature with an absolute convergence requirement of 10^{-5} applied. This quadrature is known to give an accurate result even for highly oscillating functions with less computing time. Other single integrals, appearing in (29) and in (27) for the open-sea kernel function, are evaluated similarly with Clenshaw & Curtis quadrature, with appropriate truncation corrections based on asymptotic expansions of the integrand for large values of valuable k .

The double integral appearing as the first term in (29) is well-behaved, since its integrand rapidly reduces to zero as the radial distance in the n - k plane increases. Thus the evaluation of this integral is performed also by means of Clenshaw & Curtis quadrature for the double integral, with an absolute error less than 10^{-5} required.

After all these procedures, the integral equation (42) is transformed into a linear system of simultaneous equations for the discretized values of $q(x)$ at $NX-1$ nodal points. (The source strengths at end points $k=1$ and $k=NX+1$ have been postulated to vanish and thus treated as known.) The simultaneous equations obtained are solved by the matrix inversion with Gauss' elimination method.

Once the solution of the 3-D source strength $q_j(x)$ is obtained, it is straightforward to calculate from (40) the coefficient $C_j(x)$ of the near-field homogeneous solution and from (45) the 2-D added-mass and damping coefficients. The final results of the 3-D added-mass and damping coefficients can be obtained from (44), using the strip-wise integration along the x -axis.

5. Numerical results and discussion

5.1 Results of forward-speed problem

Numerical computations are performed for a prolate spheroid of length-beam ratio $L/B=8$, moving at the Froude number $F_n=0.1$ and oscillating sinusoidally with circular frequency ω in the waterway of width 16 times the ship's breadth, i.e. $B_T/B=16$. These ratios of ship and waterway dimensions are selected to correspond to a typical experiment situation, where a ship model of $L=2$ m and $B=0.25$ m is towed at the velocity $U=0.443$ m/s in a towing tank of 4 m in width.

The heave added mass (A_{33}) and damping (B_{33}) coefficients are shown respectively in Fig.2 and Fig.3, in the nondimensional form against the nondimensional wavenumber KL . With a similar style of representation, the added-moment of inertia (A_{55}) and damping (B_{55}) coefficients in pitch are presented in Fig.4 and Fig.5, respectively. The nondimensional

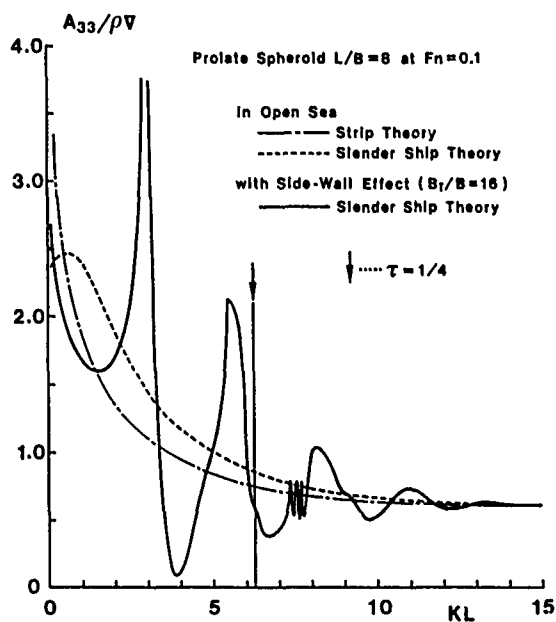


Fig.2 Heave added mass of a prolate spheroid ($L/B=8$) at $Fn=0.1$ in waterway of $B_T/B=16$

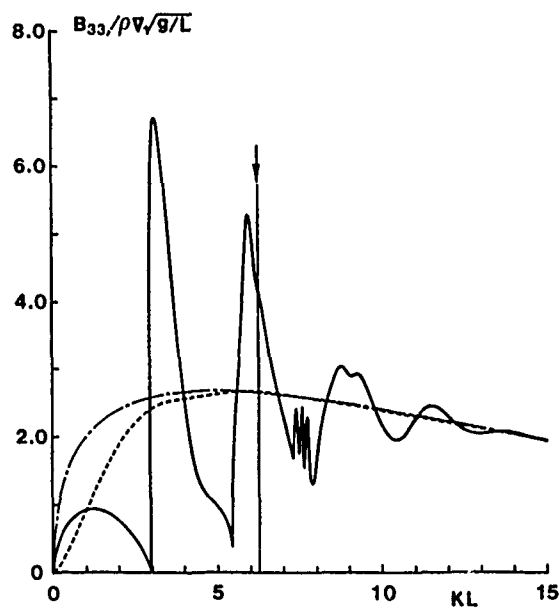


Fig.3 Heave damping coefficient of a prolate spheroid ($L/B=8$) at $Fn=0.1$ in waterway of $B_T/B=16$

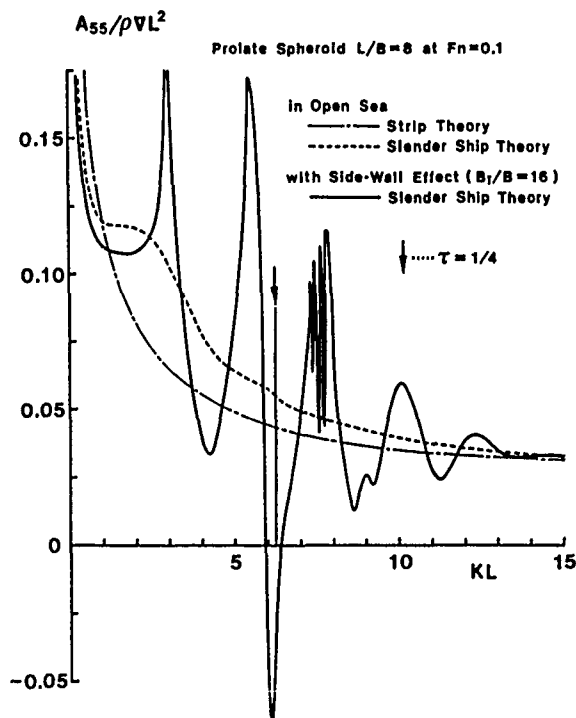


Fig.4 Pitch added moment of inertia of a prolate spheroid ($L/B=8$) at $Fn=0.1$ in waterway of $B_T/B=16$

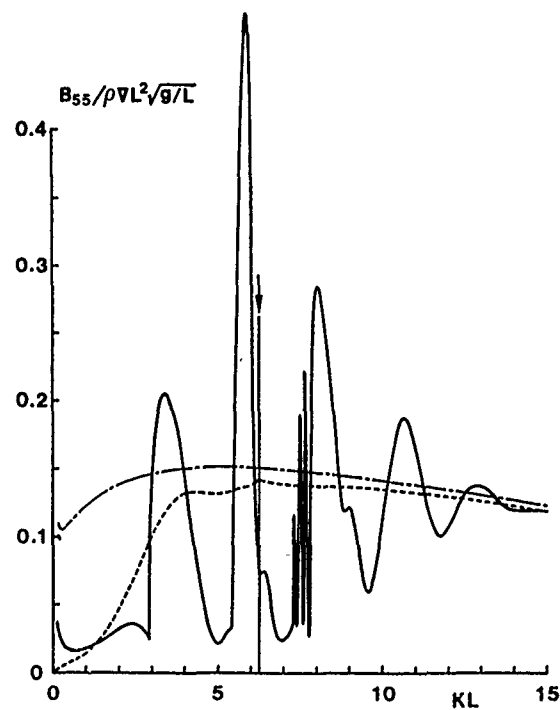


Fig.5 Pitch damping coefficient of a prolate spheroid ($L/B=8$) at $Fn=0.1$ in waterway of $B_T/B=16$

form of these coefficients are displayed in the ordinate of each figure.

In all of these figures, thick solid lines indicate the numerical results in the presence of side-wall effects, computed by the slender-ship theory described in this paper. In order to show the magnitude of side-wall effects, the values in open sea are shown by short-dashed lines, which were obtained with the side-wall-effect part of the kernel function $F_T\{K(x-\xi)\}$ set to be zero in the integral equation (42), and therefore must be identical to the unified-theory solutions [9]. Also shown in the open-sea case are the strip-theory predictions, which are indicated by dash-dotted lines. Comparing the predictions of the strip theory with those of the unified slender ship theory, we can understand that the effects of three dimensionality are prominent only in the low frequencies.

Since the forward velocity is present, with the increasing wavenumber KL , the parameter $\tau = U\omega/g = Fn/KL$ increases and takes the critical value $\tau = 1/4$ at $KL = 6.25$. The position of this critical wavenumber is shown by the vertical thin solid line with a downward arrow. In the frequencies less than $\tau = 1/4$, the effects of side walls are considerable not only in heave but also in pitch modes. In particular, A_{55} and B_{55} change drastically in the frequency range slightly less than the critical frequency $\tau = 1/4$, and A_{55} takes a negative value. It should be noted, however, that the damping coefficients B_{33} and B_{55} predicted by the present theory are definitely positive, although they vary greatly in magnitude and become nearly equal to zero at some frequencies. This non-negative damping force seems quite reasonable, judging from the consideration on the energy flux radiating in the longitudinal direction of the waterway. In some published results by a heuristic method [5], negative damping-force coefficients are predicted in the low frequencies; this is not the case.

It is known in the case of zero forward velocity that the wavenumbers corresponding to the tank-resonant mode in the transverse direction can be given by $KB_T = 2\pi m$ ($m = 1, 2, \dots$) and thus in the present case by $KL = \pi m$; at which the ratio of wavelength to tank width is equal to the inverse of an integer. When the forward velocity is present, the wavelength of the wave component radiating in the transverse direction is diminished in comparison to the wavelength at $U=0$, due to the effects of forward speed. With this knowledge, we can observe particularly in the range of $\tau < 1/4$ that the tank-resonant frequency is shifted to the lower frequency than the zero-speed tank-resonant frequency given by $KL = \pi m$.

The wave pattern generated by a ship with forward and oscillatory motions in open sea is known to change drastically, dependent on the value of τ [14]. In particular for τ close to but larger than $1/4$, the angle of the sector in which no radiating waves exist increases rapidly from zero to more than 90 degrees. This leads to the conjecture that, in the

range of $\tau > 1/4$, there exist the short waves which originate from the cusp part of the wave pattern and propagate in the transverse direction of the waterway. These waves reflect on the side walls and may exert a complicated influence on hydrodynamic forces on a ship. In the numerical results of the added-mass and damping coefficients shown from Fig. 2 to Fig. 5, we can observe fast variations in the short range of the wavenumber approximately between $KL = 7.3$ and 7.8 . The parameter τ corresponding to these wavenumbers takes the values ranging from 0.27 to 0.28 . Therefore the fast variations in the added-mass and damping coefficients might be attributed physically to a contribution of short waves originating from the cusp part of the wave pattern.

As the motion frequency increases across the range where the fast variations occur, the effects of side walls gradually decrease, and the added-mass and damping coefficients reduce to the corresponding values in open sea shown by short-dashed lines around the nondimensional wavenumber $KL = 14.0$. In this range, i.e. between $KL = 8.0$ and 14.0 , the diverging-wave component may be dominant in the side-wall effects on hydrodynamic forces on a ship.

We have a conventional diagram [1] which can be used to judge whether the side-wall effects are expected or not, by means of the parameter τ and the ratio of tank width to ship length B_T/L . In the present calculations the ratio of B_T/L is 2.0 and thus the critical angle of a sector, β_c , is given as

$$\beta_c = \tan^{-1}(B_T/L) = 63.4 \text{ deg.},$$

where the critical angle β_c is determined geometrically such that the wave emitted from the ship bow will strike the afterbody of the ship by the reflection from tank walls. This critical sector angle, on the other hand, is estimated from the calculations of the wave pattern generated by an oscillating and translating source [14], and is depicted in the diagram as a function of τ . Using this diagram with the critical angle β_c as the input, we get $\tau = 0.365$ as the predicted critical frequency. In the frequency range lower than this point the side-wall effects will be expected. For $Fn = 0.1$, the value $\tau = 0.365$ gives the critical wavenumber of $KL = 13.3$. Looking at the computed values shown in Figs. 2-5, this critical wavenumber turns out to be a good approximation.

5.2 Accuracy check and validation

The items to be checked for the accuracy of the present calculations are the 2-D solution in the transverse plane, numerical evaluation of the kernel function (25)-(27) and (29), and the solution of the integral equation (42). Since the 2-D boundary-value problem is well posed, no discussion is needed. Haraguchi & Ohmatsu's method [15] is utilized in the present work, which easily get rid of irregular frequencies and give an accurate solution.

Numerical integrations in (25)-(27) and (29) are, as described earlier, performed using Clenshaw & Curtis quadrature, with an absolute convergence requirement of 10^{-5} applied. Therefore the remaining thing to be checked is the accuracy of the solution of integral equation (42).

Fig.6 presents the added-mass and damping coefficients when the number of divisions in the x-direction NX was changed from 10 to 70, under the same computational conditions as in Figs. 2-5. Computed results are plotted with the values of $NX=70$ set to 1.0. The upper results in Fig.6 are for $KL=5.0$ ($\tau=0.224 < 1/4$), and the lower ones are for $KL=10.0$ ($\tau=0.316 > 1/4$).

For $\tau=0.224$, all computed coefficients appear to converge as the number of division increases, although the coefficients associated with the pitch mode dictate a finer discretization relative to that necessary for the heave-mode calculations. (Here we note that the relative error in B_{55} might be noticeable but its absolute error is not so large, because the value itself is small at $KL=5.0$ as seen in Fig.5.)

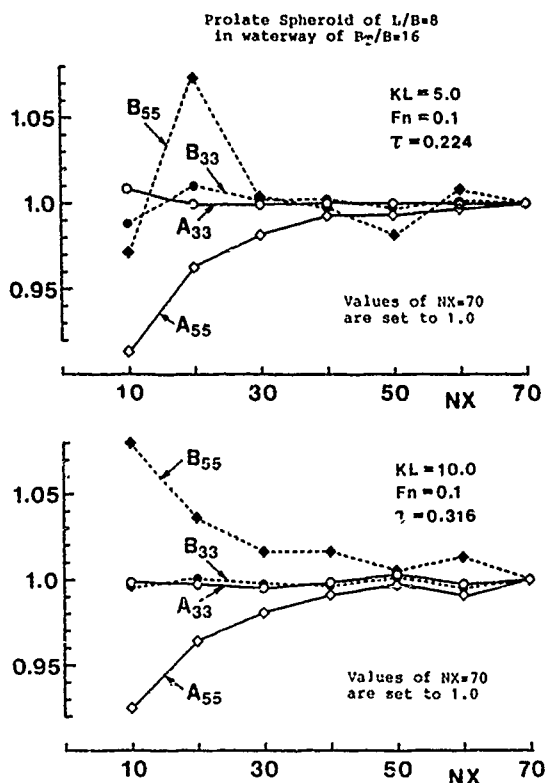


Fig.6 Number of division in the x-direction (NX) vs. added-mass and damping coefficients of a prolate spheroid, at $KL=5.0$ (upper) and $KL=10.0$ (lower). Results are plotted with the values at $NX=70$ set to 1.0.

For $\tau=0.316$, the results at $NX=60$ are slightly different from those at $NX=50$ or $NX=70$ with relative error of approximately 1.0 %. This suggests that the solution of the integral equation (42) tends to be unstable as the value of τ increases beyond $1/4$. Sclavounos [10] has found this kind of instability occurs in the unified theory for large values of τ , and proposed an alternative scheme, using the Chebyshev-polynomial expansion for the unknown source strength. However in the range of τ calculated here the instability seems not so serious, and Fig.6 reveals that 40 segments along the ship's length are sufficient to give a solution with relative error less than 2.0 %. On this basis, all of the computations shown in this paper have been carried out with $NX=40$.

In the special case of zero forward velocity, 3-D "exact" calculations based on the integral-equation method may be available, with the Green function modified to satisfy the side-wall boundary condition. A 3-D calculation method of this kind has been developed by Kashiwagi [7], in which almost perfect agreement is shown between the calculated and experimental values for a hemisphere and a ship model with fore-and-aft symmetry. If we compare the zero-speed results computed by the present theory with the corresponding ones by the 3-D integral-equation method, the validation for less complicated case can be accomplished.

Fig.7 and Fig.8 present respectively the heave added-mass (A_{33}) and damping (B_{33}) coefficients, for a prolate spheroid of $L/B=8$ floating at zero forward speed in the waterway of $B_T/B=16$. Similarly Fig.9 and Fig.10 show the pitch added-moment of inertia (A_{55}) and damping (B_{55}) coefficients under the same conditions. In these four figures, the same scale of the ordinates and the same line symbols are used as those in the corresponding figure for the forward-speed case shown from Fig.2 to Fig.5. Also included in Figs. 7-10 are the results of 3-D integral-equation (panel) method, which are presented by plus symbols for the case of open sea and by open circles for the case of side-wall effects present. A certain amount of inaccuracy should be expected in the results of 3-D panel method, too. However numerical accuracy is believed to be fairly good, because the hull surface of spheroid and the normal vector on it can be mathematically given and some analytical manipulations are thus used to improve the numerical accuracy. We see that very good agreement exists between the results of the slender-ship theory and of the 3-D panel method, showing the validity of the present theory.

6. Concluding remarks

We proposed a new rational theory for predicting the hydrodynamic forces on a ship, moving at constant forward speed and oscillating in heave and pitch in a restricted water-

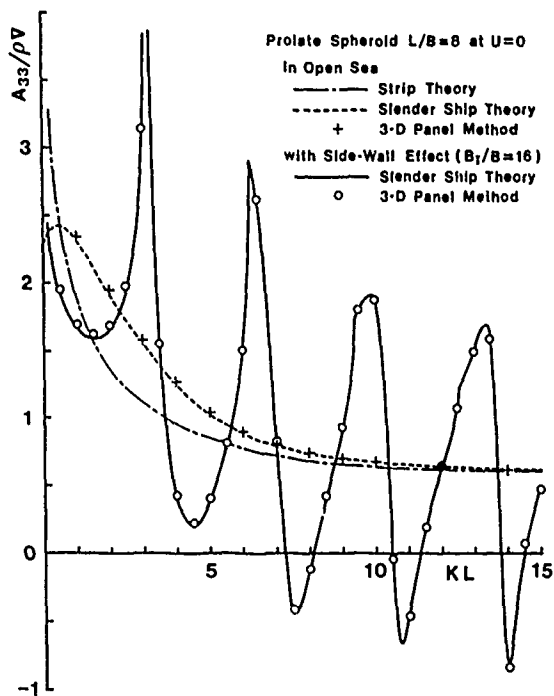


Fig.7 Heave added mass of a prolate spheroid, the same as Fig. 2 except for $Fn=0.0$. Comparison with the 3-D panel-method predictions.

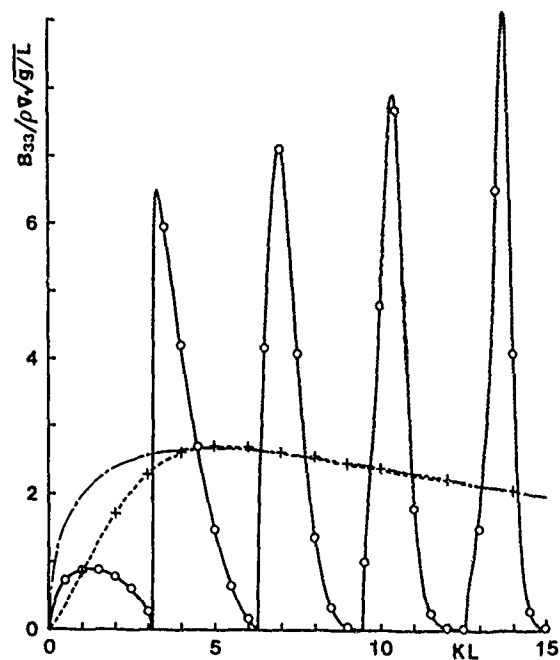


Fig.8 Heave damping coefficient of a prolate spheroid, the same as Fig. 3 except for $Fn=0.0$. Comparison with the 3-D panel-method predictions.

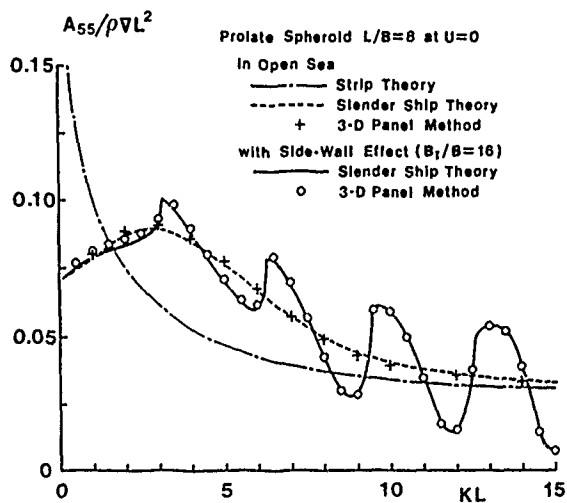


Fig.9 Pitch added moment of inertia of a prolate spheroid, the same as Fig. 4 except for $Fn=0.0$. Comparison with the 3-D panel-method predictions.

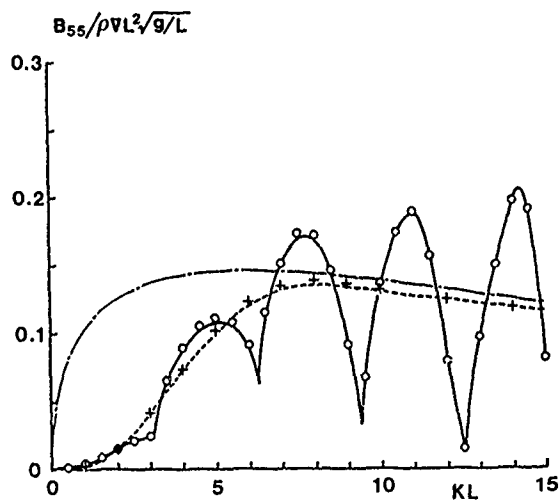


Fig.10 Pitch damping coefficient of a prolate spheroid, the same as Fig. 5 except for $Fn=0.0$. Comparison with the 3-D panel-method predictions.

way. Only the slenderness of the ship hull is assumed, and thus the proposed theory is valid for all frequencies and forward velocities of practical interest where the side-wall effects are prominent. Furthermore the theory is correct even for the case of a narrow waterway, because the side-wall effects are taken into account not only on outgoing waves but also on evanescent local waves.

Validity of the proposed theory is confirmed for the special case of zero forward velocity by comparison with the numerical results of 3-D panel method. In the case of non-zero forward velocity, however, the present theory may be the first one which is able to give precise predictions of the side-wall effects on hydrodynamic forces. Therefore with this theory, we are ready to make quantitative discussions on the effects of tank-wall interference included in the results of experiments for a ship model.

Computations were performed for the heave and pitch added-mass and damping coefficients of a prolate spheroid of length-beam ratio 8.0, moving at the Froude number 0.1 in the waterway of width twice the spheroid's length. The computed hydrodynamic forces show complex variations as the frequency increases. It is noted that these variations correspond to the appearance of complicated wave pattern, which starts from the pattern dominated by the ring wave and changes to the markedly different one dominated by the diverging wave, as the parameter $\tau = \omega U/g$ increases across the critical value $1/4$.

References

1. Vossers, G. and Swaan, W.A., "Some sea-keeping tests with a victory model", I. S. P. Vol.7, No.69, pp.189-206 (1960).
2. Hanaoka, T., "On the side-wall effects on the ship motions among waves in a canal", J. Soc. Nav. Arch. Japan No.102, pp.1-5 (1958).
3. Hosoda, R., "Side wall effects of towing tank on the results of experiments in waves (1)", J. Soc. Nav. Arch. Japan No.139, pp.23-30 (1976).
4. Hosoda, R., "Effect of side-wall interference of towing tank on the results of experiments in waves (2)", J. Soc. Nav. Arch. Japan No.143, pp.52-60 (1978).
5. Takaki, M., "Effects of breadth and depth of restricted waters on longitudinal motions in waves", J. Soc. Nav. Arch. Japan No.143, pp.173-184 (1979).
6. Newman, J.N., "The theory of ship motions" Adv. Appl. Mech. Vol.18, pp.221-283 (1978).
7. Kashiwagi, M., "3-D integral-equation method for calculating the effects of tank-wall interference on hydrodynamic forces acting on a ship", to be published in J. Kansai Soc. Nav. Arch. Japan No.212 (1989).
8. Kinoshita, T. and Saijo, K., "On the multi-body-type floating breakwater", J. Soc. Nav. Arch. Japan No.149, pp.54-64 (1981).
9. Newman, J.N. and Sclavounos, P.D., "The unified theory of ship motions", Proc. 13th Symp. on Nav. Hydrodyn. Vol.4, pp.1-22 (1980).
10. Sclavounos, P.D., "The unified slender-body theory: ship motions in waves", Proc. 15th Symp. on Nav. Hydrodyn., pp.177-192 (1984).
11. Sclavounos, P.D., "The diffraction of free surface waves by a slender ship", J. S. R. Vol.28, No.1, pp.29-47 (1984).
12. Timman, R. and Newman, J.N., "The coupled damping coefficients of symmetric ships", J. S. R. Vol.5, No.4, pp.34-55 (1962).
13. Ogilvie, T.F. and Tuck, E.O., "A rational strip theory for ship motions", Dept. Nav. Arch. Mar. Eng., Univ. Michigan, Rep.No.13, pp.1-92 (1969).
14. Hanaoka, T., "On the velocity potential in Michell's system and the configuration of the wave ridges due to a moving ship", J. Zosen Kiokai, No.93, pp.1-10 (1953).
15. Haraguchi, T. and Ohmatsu, S., "On an improved solution of the oscillation problem on non-wall-sided floating bodies and a new method for eliminating the irregular frequencies", Trans. West-Japan Soc. Nav. Arch., No.66, pp.9-23 (1983).

DISCUSSION

by C.M. Lee

I think that it is the first paper which presented a 3-D theory for an oscillating ship, including the side-wall effects. The authors should be congratulated for their excellent work.

Similar to the case of twin-hull ships, this paper shows negative added mass at certain frequencies. This kind of phenomenon does not occur in the open-sea case, and, therefore, induces puzzlement to those who cannot accept the motion of "negative added mass". My advice to those people has been that one should not get too excited by just observing unusual hydrodynamic coefficients alone but should wait until the computed results of ship motion in waves are shown.

My prediction is that although the hydrodynamic coefficients may look quite

different from those of the open-sea case, the motion results may not show significant differences, particularly for the tank width being twice the ship length as chosen in the sample calculations in this paper. I would like to encourage the authors to compute the ship motion to check if my prediction is correct.

Author's Reply

Thank you for your comment. We are now applying the proposed theory to the diffraction problem with side-wall effects. If the calculations of wave-exciting force and moment are completed, the ship motion in waves can be readily computed from them, using the added-mass and damping coefficients predicted by the present theory. Therefore, I think that the computed results of ship motions in waves can be shown in the foreseeable near future.

Interaction between Current, Waves and Marine Structures

R. Zhao and O. M. Faltinsen
Norwegian Institute of Technology
Trondheim, Norway

Abstract

A theoretical method to analyse current wave interaction on large-volume marine structures is presented. It is shown how to circumvent the problems associated with the m_j -terms. Numerical results for mean wave forces on floating vertical cylinders are discussed. The results are based on using both direct pressure integration and conservation of momentum.

Introduction

Zhao & Faltinsen [9] have presented a two-dimensional theory that hydrodynamically analyses the combined effect of waves and current on two-dimensional floating structures. Zhao et al. [10] generalized the theory to three-dimensional flow. A hemisphere was analysed and satisfactory agreement between numerical and experimental prediction of linear and mean wave forces was documented.

The theory is based on matching a local solution to a far-field solution. In the far-field the waves "ride" on the undisturbed current velocity, while in the near-field the waves "ride" on the local steady flow. The theoretical solution for the velocity potential is expressed as a series expansion in the wave amplitude ζ_a and the current velocity U . The problem is solved to first order in ζ_a and first order in U . It is assumed that the wave slopes of different wave systems and the Froude number are asymptotically small. In the free surface condition and the body boundary condition the interactions with the steady motion potential are taken care of. In addition a radiation condition is specified. In the numerical solution a boundary element method based on Green's second identity is incorporated. The far-field solution is represented by a sum of multipoles (including sources) with singularities inside the body. The multipoles satisfy the radiation condition and the far-

field free surface condition. For a general body several singularity points are used for the multipoles inside the body. The coefficients in the multipole expansion are determined by matching the local- and far-field solution.

In the main text we will outline the theory in more detail. We will focus our attention on the m_j -terms in the body boundary condition. The m_j -terms are due to interaction between the current and the oscillatory fluid motion. The same terms occur when ship motions at forward speed are analysed (Newman [8]). Numerical inaccuracies and unphysical effects of these terms can cause large errors in the numerical prediction, in particular for a body surface with sharp corners or local high curvature. It is shown numerically and analytically how problems with the m_j -terms can be avoided.

Numerical results for horizontal and vertical mean wave forces on floating vertical cylinders of finite length are presented. Both a direct pressure integration method and a method based on conservation of momentum are used. Convergence of the results are documented as a function of number of panels approximating the body surface, the free surface and the control surface. It is demonstrated that special care has to be shown in modelling the cylinder surface around sharp corners. This is particularly true when the direct pressure integration method is used.

Theory

Consider a structure in uniform current and regular incident waves with small amplitude in deep water. The structure is restrained from drifting, but is free to oscillate harmonically in six degrees of freedom. We choose a right-handed coordinate system (x,y,z) fixed in space. $z = 0$ is in the mean free surface, positive z -axis is upwards and goes through the centre of gravity of the structure when the body is at rest (see Fig. 1). Surge (η_1), sway (η_2) and heave (η_3) are

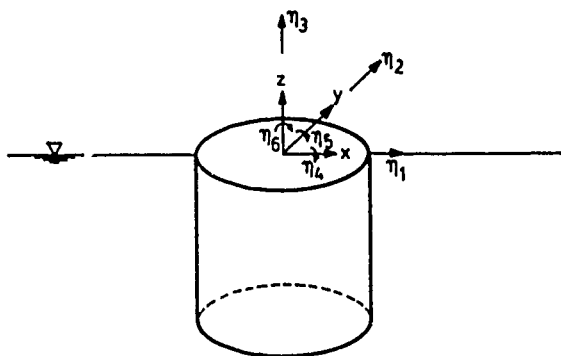


Fig. 1 Coordinate system and sign convention for translatory and angular displacements.

the translatory displacements of the body in the x-, y- and z-direction referred to the origin of the (x,y,z) coordinate system, when the body is at rest. Roll (η_4), pitch (η_5) and yaw (η_6) denote the angular displacements about the x-, y- and z-axis, respectively.

Consider the fluid to be incompressible and the fluid motion irrotational so that there exists a velocity potential ϕ which satisfies Laplace equation.

$$\nabla^2 \phi = 0 \quad (1)$$

In reality the flow is always rotational in a boundary layer close to the body. In addition the flow may separate from the body and invalidate a potential flow description also in parts of the flow outside the boundary layer. This depends for instance on the shape of body, the Reynolds number, the Keulegan-Carpenter number (KC), a non-dimensionalized frequency of oscillation, the roughness ratio and the ratio between the current velocity U and the maximum horizontal oscillatory ambient fluid velocity U_M in the current direction. Obviously the flow will always separate from a body with sharp corners in any type of ambient flow. This is also true for the flow around any blunt-sharped marine structures in current without waves. However, when the free stream velocity along the current changes direction with time, i.e. $U/U_M < 1$, the flow around bodies with curved surfaces will not separate for small KC-numbers (Zhao et al. [10]).

The potential flow solution will be written as a series expansion in the wave amplitude ζ_a of incident waves. It is assumed that ζ_a , the body motion and the steepness of the different wave systems are asymptotically small. We write

$$\phi = \phi_s + \phi_1 + \phi_2 + \dots \quad (2)$$

where ϕ_s is independent of ζ_a , ϕ_1 is linear

with respect to ζ_a , ϕ_2 is proportional to ζ_a^2 . Far away from the body

$$\phi_s \sim U(x \cos \alpha + y \sin \alpha) \quad (3)$$

Here α is the angle between the current direction and the x-axis. We assume that the current velocity U is small and solve the problem correctly to $O(U)$. A consequence of neglecting terms of $O(U^2)$ is that we disregard the effects of the steady wave system generated by the current flow past the body. In practice this is expected to be a good approximation. On the free surface, ϕ_s satisfies the rigid free surface condition, i.e.

$$\frac{\partial \phi_s}{\partial z} = 0 \quad \text{on } z = 0 \quad (4)$$

On the mean position of the body surface S_B , ϕ_s satisfies a zero-normal velocity condition, i.e.

$$\frac{\partial \phi_s}{\partial n} = 0 \quad \text{on } S_B \quad (5)$$

In general a numerical method has to be used to find ϕ_s . In our case we used Hess & Smith's method [2]. This is based on distributing sources over S_B .

Due to linearity we can decompose the first-order velocity potential ϕ_1 into separate components due to the rigid-body motions η_k , the incident waves and a diffraction potential $\phi_7 e^{i\omega t}$. We can write

$$\phi_1 = \phi_0 e^{i\omega t} + \phi_7 e^{i\omega t} + \sum_{k=1}^6 \phi_k \eta_k \quad (6)$$

The incident wave potential can be written as

$$\phi_0 e^{i\omega t} = \quad (7)$$

$$\frac{g \zeta_a}{\omega_0} e^{i(\omega t - kx \cos \beta - ky \sin \beta) + kz}$$

Here i is the imaginary unit, t the time variable, β the angle between the wave propagation direction and the x-axis, ω the circular frequency of oscillation and k the wave number. ω and k are connected through the relations

$$\omega = \omega_0 + kU \cos(\beta - \alpha) \quad (8)$$

$$k = \omega_0^2 / g \quad (9)$$

It is understood that the real part is to be taken in expressions involving $e^{i\omega t}$.

By using the dynamic and kinematic free surface conditions, it follows that ϕ_k , $k = 1, 6$ satisfy correctly to $O(U)$

$$-\omega^2 \phi_k + 2i\omega \nabla \phi_s \cdot \nabla \phi_k + i\omega \left[\frac{\partial^2 \phi_s}{\partial x^2} + \frac{\partial^2 \phi_s}{\partial y^2} \right] \phi_k + g \frac{\partial \phi_k}{\partial z} = 0, \text{ on } z = 0 \quad (10)$$

Also $(\phi_0 + \phi_7)e^{i\omega t}$ satisfies equation (10). Far away from the body equation (10) becomes

$$-\omega^2 \phi_k + 2i\omega U \left(\cos \alpha \frac{\partial \phi_k}{\partial x} + \sin \alpha \frac{\partial \phi_k}{\partial y} \right) + g \frac{\partial \phi_k}{\partial z} = 0, \text{ on } z = 0 \quad (11)$$

Equation (10) expresses the fact that the waves interact with the local steady flow ϕ_s around the body. Equation (11) resembles the classical free-surface condition with forward speed, which for $\alpha = 0$ can be written as

$$-\omega^2 \phi_k + 2i\omega U \frac{\partial \phi_k}{\partial x} + U^2 \frac{\partial^2 \phi_k}{\partial x^2} + g \frac{\partial \phi_k}{\partial z} = 0, \text{ on } z = 0 \quad (12)$$

The difference between equation (11) and (12) is that terms of $O(U^2)$ are neglected. Zhao & Faltinsen [9] found for two-dimensional flow that it is appropriate to use equation (11) when $\tau = \omega U/g < \sim 0.15$. In the three-dimensional flow case we expect a similar limitation. An example on calculations of the real part of the velocity potential due to a harmonically oscillating source satisfying either free surface condition (11) or (12) is shown in Fig. 2. The curves in the upper half plane correspond to calculations with equation (11). The τ -value is 0.1, $\omega \sqrt{|z_s|}/g = 0.6773$ where z_s is the z -coordinate of the source point. The calculations in Fig. 2 are for points on the mean free surface. We note a small phase difference between the wave systems when condition (11) or (12) is used. This is more evident on the upstream side of the source. The amplitudes are in good agreement. The consequence of neglecting terms of $O(U^2)$ in the free surface condition is that fewer wave systems occur far away from the body. However, the consequence of this is of no practical importance for small τ -values below 0.15. A further simplification of the source potential G is sometimes used. One writes

$$G = G_{U=0} + \tau \left. \frac{\partial G}{\partial \tau} \right|_{U=0} + \dots \quad (13)$$

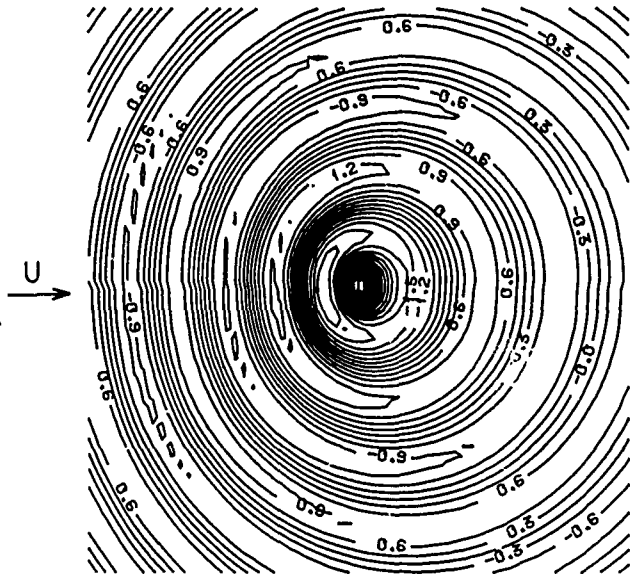


Fig. 2 Calculated values of the real part of the Green's function on the free surface. In the upper half part of figure equation (11) is used. In the lower half part the classical free surface condition (12) is used ($\tau = 0.1$, $\omega \sqrt{|z_s|}/g = 0.6773$) (The calculations in the lower half plane has been provided by J. Hoff).

This simplification can lead to large errors at some distance from the source point. This is illustrated in Fig. 3. The conditions are the same as in Fig. 2. The curves in the upper half plane correspond to that equation (13) has been used, while the curves in the lower half plane corresponds to that the free surface conditions (11) has been used.

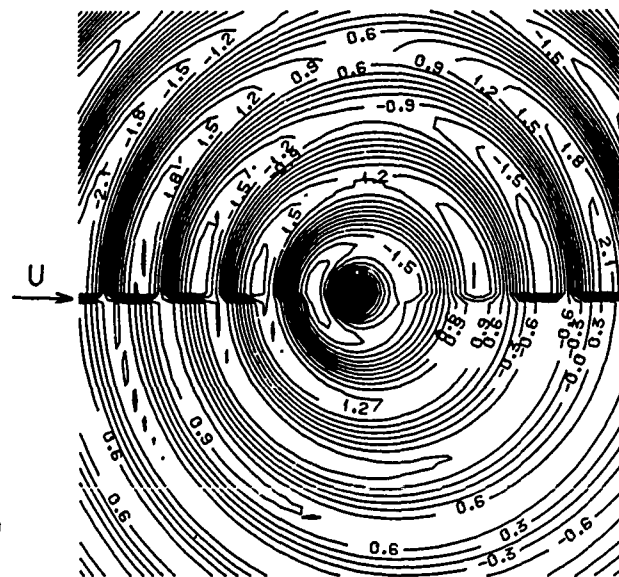


Fig. 3 Calculated values of the real part of the Green's function on the free surface. In the upper half part of the figure equation (13) has been used. In the lower half part free surface condition (11) has been used ($\tau = 0.1$, $\omega \sqrt{|z_s|}/g = 0.6773$).

The body boundary conditions can be written as

$$\frac{\partial \phi_k}{\partial n} = \begin{cases} i\omega n_k + m_k, & k = 1, 6 \\ -\frac{\partial \phi_0}{\partial n}, & k = 7 \end{cases} \quad (14)$$

Equation (14) applies on the mean wetted body surface S_B . The n_k - and m_k -components are defined by

$$\begin{aligned} \vec{n} &= (n_1, n_2, n_3) \\ \vec{r} \times \vec{n} &= (n_4, n_5, n_6) \\ \vec{m} &= -\vec{n} \cdot \nabla \vec{W} = (m_1, m_2, m_3) \\ -\vec{n} \cdot \nabla (\vec{r} \times \vec{W}) &= (m_4, m_5, m_6) \end{aligned} \quad (15)$$

where $\vec{W} = \nabla \phi_k$ and $\vec{r} = x\vec{i} + y\vec{j} + z\vec{k}$. Positive normal direction is into the fluid domain.

The m_k -terms in equation (14) arise because the steady motion potential does not satisfy the body boundary condition on the instantaneous body surface correct to $O(\zeta_a)$. The derivation is based on a Taylor expansion, which means the formulation is breaks down at sharp corners. This will lead to difficulties which will be further discussed later in the text.

It is also necessary to specify a radiation condition. When the free surface condition (11) is used, it means that the waves are propagating away from the body.

A solution to the boundary value problems for ϕ_k can be found by applying Green's second identity to the functions ϕ_k and $1/R$, in a fluid domain enclosed by the boundary S defined by $S_B \cup S_F \cup S_C \cup S_0$ (see Fig. 4). Then we obtain the following expression

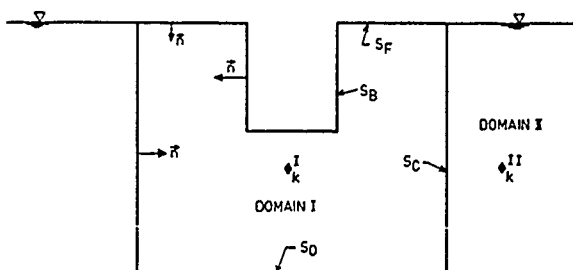


Fig. 4 Definition of surfaces used in the integration of equation (16).

$$4\pi\phi_k(x_0, y_0, z_0)$$

$$= \iint_S \left(\phi_k \frac{\partial}{\partial n} \frac{1}{R} - \frac{\partial \phi_k}{\partial n} \frac{1}{R} \right) ds(x, y, z) \quad (16)$$

where $R = \sqrt{(x-x_0)^2 + (y-y_0)^2 + (z-z_0)^2}$, S_C is a vertical cylindrical control surface, S_F is the mean free surface between S_C and S_B , S_0 is a bottom surface inside S_C .

We separate the total fluid domain into two parts. Part I is the fluid domain inside the boundary S while part II is outside S . In the outer domain (far-field) the free surface condition (11) is assumed valid, while in the inner domain (near-field) the complete free surface condition expressed by equation (10) is used.

We assume that the velocity potential ϕ_k in the outer domain can be represented by a sum of multipoles (including sources) with singularities inside the body (see Fig. 4).

$$\begin{aligned} \phi_k^{II}(x) &= \sum_{m=1}^k \left[A_{1m} G(x; x_m) \right. \\ &+ A_{2m} \frac{\partial G(x; x_m)}{\partial x_m} + A_{3m} \frac{\partial G(x; x_m)}{\partial y_m} \\ &+ A_{4m} \frac{\partial G(x; x_m)}{\partial z_m} + A_{5m} \frac{\partial^2 G(x; x_m)}{\partial x_m^2} \\ &+ A_{6m} \frac{\partial^2 G(x; x_m)}{\partial y_m^2} + A_{7m} \frac{\partial^2 G(x; x_m)}{\partial x_m \partial y_m} \\ &\left. + A_{8m} \frac{\partial^2 G(x; x_m)}{\partial x_m \partial z_m} + A_{9m} \frac{\partial^2 G(x; x_m)}{\partial y_m \partial z_m} + \dots \right] \end{aligned} \quad (17)$$

where $x_m = (x_m, y_m, z_m)$ is the coordinate of a singularity point. The Green's function G and its multipoles satisfy the far-field free surface condition (11) and the radiation condition.

In the numerical solution S_B , S_F , S_C and S_0 are divided into plane quadrilateral elements. The velocity potential is assumed constant over each element. At S_B the term $\partial \phi_k / \partial n$ is replaced by the body boundary condition (14). At S_F the term $\partial \phi_k / \partial n$ is replaced by the free surface condition (10) which includes the velocity potential and its first order derivatives along the free surface as unknowns. The first order derivatives of ϕ_k are numerically approximated by a Taylor expansion which are only function of ϕ_k on the free surface. The approximation is

correct to $O(\Delta^2)$, where Δ is a characteristic length of the elements. At S_c and S_0 the term $\partial\phi_k/\partial n$ is replaced by equation (17).

By letting the point (x_0, y_0, z_0) in equation (16) approach the mid-points of each element on the boundary surface S , we obtain a Fredholm integral equation of the second kind. This results in N number of equations. The total number of unknowns is $N+N_{II}$, where N_{II} is the number of terms used in the multipole expansion (17). The N_{II} additional equations are obtained by matching the inner and outer solutions at the control surfaces S_c and S_0 . This is done by a least square condition. It means we require the

$$\frac{\partial E_r}{\partial(\text{Re}(A_{nm}))} = 0 \quad \text{and} \quad \frac{\partial E_r}{\partial(\text{Im}(A_{nm}))} = 0 \quad (18)$$

where

$$E_r = \sum_{i=1}^{N_C} \{ [\text{Re}(\phi_k^{II} - \phi_k^I)]^2 + [\text{Im}(\phi_k^{II} - \phi_k^I)]^2 \}$$

Further ϕ_k^I is the inner domain solution, A_{nm} and ϕ_k^{II} are defined by equation (17) and N_C is the number of elements on $S_c \cup S_0$ which is going to match the outer solution. This leads to the following condition

$$\sum_{j=1}^{N_C} \{ -i\phi_k^I(x_j) \overline{G^{NI}(x_j; x_{MI})} \} \quad (19)$$

$$+ i \left[\sum_{m=1}^K \sum_{n=1}^L A_{nm} G^n(x_j; x_m) \right] \overline{G^{NI}(x_j; x_{MI})} \} = 0$$

where G^n is defined by writing equation (17) as

$$\phi_k^{II} = \sum_{m=1}^K \sum_{n=1}^L A_{nm} G^n(x; x_m)$$

and $\overline{G^{NI}(x_j; x_{MI})}$ is the conjugate of $G^{NI}(x_j; x_{MI})$. In the following equations the sign $\overline{}$ means the time average.

Equation (19) is satisfied for $NI = 1, L$ and $MI = 1, K$. This means a total of $N_{II} = L \times K$ number of equations. Number of multipole terms have to be much smaller than number of control surface elements. As an example with the results presenting in Fig. 10, $N_{II}=10$ and $N_C=56$.

The Green's function (source function) that we need should satisfy the far-field free

surface condition (11) and the radiation condition. The radiation condition is taken care of by introducing a Rayleigh viscosity μ . The Green's function $G e^{i\omega t}$ can be written as

$$G(x, y, z; x_0, y_0, z_0) = \frac{[(x-x_0)^2 + (y-y_0)^2 + (z-z_0)^2]^{-\frac{1}{2}} - [(x-x_0)^2 + (y-y_0)^2 + (z+z_0)^2]^{-\frac{1}{2}}}{2} + \frac{1}{\pi} \int_{-\pi}^{\pi} du \int_0^{\infty} d\lambda \frac{\lambda e^{\lambda(z+z_0+i\text{rcos}(u-\theta+\alpha))}}{\lambda - \frac{1}{g}(\omega^2 + 2\omega U \lambda \cos u - 2i\mu(\omega + U \lambda \cos u))}$$

where $x = r \cos \theta$ and $y = r \sin \theta$. Expression (20) can be simplified similarly as Grekas [1] did by using the residue theorem and introducing exponential integrals. The derivatives of the Green's function (Multipoles) were obtained by numerically evaluating the analytic expressions for the derivatives.

Having found the velocity potential by the method described in the previous text, the added mass, damping and first order excitation forces can be obtained by integrating the fluid pressure over the mean wetted body

surface correctly to $O(\zeta_a)$ and $O(U)$. When we have solved the equations of the first order motions, we can find the mean wave forces and moments correctly to $O(\zeta_a^2)$ and $O(U)$ either by directly integrating the pressure or by using the equations for conservation of momentum. We will show how this can be done if the equation for conservation of momentum is used.

We start with expressions given by Newman [7]. The rate of change of momentum $\vec{M}(t)$ in the fluid volume Ω inside $S = S_B \cup S_F \cup S_C \cup S_0$ (see Fig. 5) is

$$\frac{d}{dt} \vec{M} = - \rho \iint_S [(\frac{p}{\rho} + gz) \vec{n} + \vec{V} (V_n - U_n)] ds \quad (21)$$

Here \vec{V} is the fluid velocity vector, U_n is the normal velocity of surface S , \vec{n} is the normal vector to S (positive direction out of the fluid) and $V_n = \vec{V} \cdot \vec{n}$. The total fluid pressure is given by

$$p = -\rho g z - \rho \frac{\partial \phi_1}{\partial t} - \rho \nabla \phi_s \cdot \nabla \phi_1 - \frac{\rho}{2} |\nabla \phi_1|^2 - \rho \frac{\partial \phi_2}{\partial t} - \rho \nabla \phi_s \cdot \nabla \phi_2 + O(\zeta_a^3) + O(U^2) \quad (22)$$

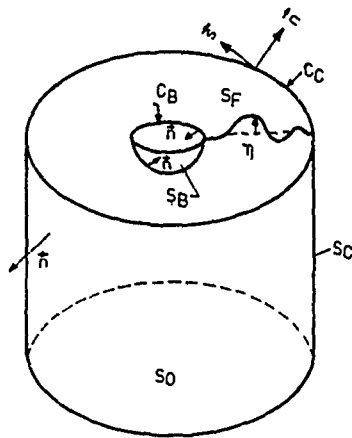


Fig. 5 Definitions used of surfaces in the calculation of mean wave forces.

By time averaging equation (21), assuming that S_0 is a horizontal plane at great depth and using boundary condition on S it follows that the mean wave drift forces can be written

$$\bar{F}_m = -\rho \iint_{S_C} \left(\frac{\partial}{\partial t} n_m + V_m V_n \right) ds \quad (23)$$

$$+ \begin{cases} 0, & m=1,2 \\ - \iint_{S_B+S_F} \rho g z n_3 ds, & m=3 \end{cases}$$

The integration is over the instantaneous surface S . We have to be careful when analysing the problem and keep all contributions

which are correctly to second order in the incident wave amplitude and first order in the current velocity. For the first term of the first integral in equation (23), we should first integrate up to the mean free surface, in which only the terms $-\frac{1}{2}\rho |\nabla \phi_1|^2 - \rho \nabla \phi_s \cdot \nabla \phi_2$ in equation (22) have contributions. In the integration from the mean free surface to the instantaneous free surface η , the first three terms of equation (22) have contributions. In the second term of the first integral, we can write $V_m = \partial(\phi_s + \phi_1 + \phi_2)/\partial x_m$ and $V_n = \partial(\phi_s + \phi_1 + \phi_2)/\partial n$. In the integration up to the mean free surface, the terms $\partial \phi_s / \partial n \cdot \partial \phi_2 / \partial x_m$, $\partial \phi_1 / \partial n \cdot \partial \phi_1 / \partial x_m$ and $\partial \phi_2 / \partial n \cdot \partial \phi_s / \partial x_m$ have contributions. In the integral from the mean free surface to the instantaneous free surface η , the terms which have contributions are $\partial \phi_s / \partial n \cdot \partial \phi_1 / \partial x_m$ and $\partial \phi_s / \partial x_m \cdot \partial \phi_1 / \partial n$.

By using the body boundary conditions and Stokes theorem (Ogilvie & Tuck [5]) it can be shown that the following terms

$$\iint_{S_{C0}} (-\rho \nabla \phi_s \cdot \nabla \phi_2 n_m + \rho \frac{\partial \phi_s}{\partial n} \frac{\partial \phi_2}{\partial x_m} + \rho \frac{\partial \phi_2}{\partial n} \frac{\partial \phi_s}{\partial x_m}) ds \quad (24)$$

$$+ \oint_{C_C} \frac{\partial \phi_s}{\partial x_m} \frac{\partial \phi_1}{\partial n} \left(-\frac{1}{g} \frac{\partial \phi_1}{\partial t} \right) dl$$

will partly cancel. S_{C0} means the control surface up to the mean free surface and C_C is the water line between the mean free surface and the control surface (see Fig. 5). For $m = 1, 2$ expression (24) is zero. For $m = 3$ it is equal to $\rho \partial \phi_s / \partial n \oint_{C_C} \phi_2 dl$. However, this will

be cancelled by a similar term in the last integral in equation (23). When we integrate over S_B in equation (23) we follow a similar procedure as outlined by Ogilvie [6] for zero current velocity. The final expressions for mean wave drift forces are

$$\bar{F}_m = -\frac{\rho}{2g} \oint_{C_C} \left(\frac{\partial \phi_1}{\partial t} + \nabla \phi_s \cdot \nabla \phi_1 \right)^2 n_m dl$$

$$+ \frac{\rho}{2} \iint_{S_{C0}} |\nabla \phi_1|^2 n_m ds$$

$$- \rho \iint_{S_{C0}} \frac{\partial \phi_1}{\partial x_m} \frac{\partial \phi_1}{\partial n} ds - \rho \oint_{C_C} \frac{\partial \phi_1}{\partial x_m} \eta \frac{\partial \phi_s}{\partial n} dl \quad (25)$$

$$+ \begin{cases} 0, & m=1,2 \\ - \iint_{S_B} \rho g z n_m ds + \end{cases}$$

$$+ \rho \iint_{S_{F0}} \left[\eta \frac{\partial}{\partial z} \left(\frac{\partial \phi_1}{\partial t} + \nabla \phi_s \cdot \nabla \phi_1 \right) + \frac{\partial}{\partial z} (\nabla \phi_1) \eta + \frac{1}{2} |\nabla \phi_1|^2 \right] n_m ds$$

$$- \rho \oint_{C_B} \left(\frac{\partial \phi_1}{\partial t} + \nabla \phi_s \cdot \nabla \phi_1 \right) (\vec{\eta} + \vec{\alpha} \times \vec{r}) \cdot \vec{n} dl, \quad m=3$$

where S_{F0} is the mean free surface. C_B is defined in Fig. 5. In the integral over C_B , \vec{n} is the normal vector to C_B in the horizontal plane with positive direction out of the body volume. Further $\vec{\eta} = (\eta_1, \eta_2, \eta_3)$ and $\vec{\alpha} = (\alpha_1, \alpha_2, \alpha_3)$. The derivations is based on the body surface is wallsided at the intersection between the mean free surface and the body sur-

face. We note that the second order potential does not contribute in equation (25).

The mean wave forces can also be obtained by using direct pressure integration. By following a similar analysis as outlined by Ogilvie [6] for zero current velocity we find that

$$\begin{aligned} \bar{F}_m = & - \rho \int \int_{S_{B_0}} \{ \frac{1}{2} |\nabla \phi_1|^2 + \\ & \frac{(\vec{n} + \vec{\alpha} \times \vec{r}) \cdot \nabla (\frac{\partial \phi_1}{\partial t} + \nabla \phi_s \cdot \nabla \phi_1) + \nabla \phi_s \cdot \nabla \phi_2 \}}{n_m} \\ & + \frac{(\vec{\alpha} \times \vec{n})_m (\frac{\partial \phi_1}{\partial t} + \nabla \phi_s \cdot \nabla \phi_1)}{ds} \\ & - \frac{1}{2} \rho g \oint_{C_B} [\eta^2 - 2\eta(\eta_3 + y\eta_4 - x\eta_5)] n_m dl \\ & - \iint_{S_B} \rho g z n_m ds, \quad m = 1, 2, 3 \end{aligned} \quad (26)$$

where S_{B_0} is the mean wetted body surface. When the body is fixed it is possible to show that the second order potential does not contribute.

One possible source of large inaccuracies in the procedure outlined above as well in other procedures is the presence of the m_j -terms in the body boundary conditions (see equation (14)). This will be further discussed in the following section.

Discussion of the m_j -terms

We will illustrate the difficulties with the m_j -terms by giving some simple examples with two-dimensional bodies in infinite fluid. We will start with studying the detail of the behaviour of the first and second order derivatives of the velocity potential at the body boundary. This will be done by a similar panel method as we used in the three-dimensional flow case. We write the velocity potential as

$$\begin{aligned} 2\pi\phi_s(x_1, y_1) = \\ \int_{S_B} \left(\frac{\partial \phi}{\partial n} \log r - \phi_s \frac{\partial}{\partial n} \log r \right) ds(x, y) \end{aligned} \quad (27)$$

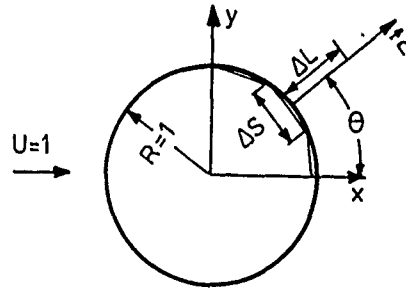


Fig. 6a Fixed circular cylinder in infinite fluid and in steady incident flow.

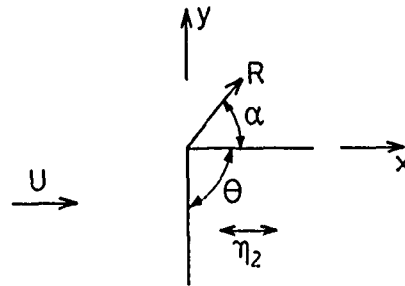


Fig. 6b Definition of parameters in the analysis of local two-dimensional flow around a sharp corner with an interior angle θ .

where $r = \sqrt{(x-x_1)^2 + (y-y_1)^2}$ and S_B is the body surface. We use plane panels with constant singularity density over each panel.

We will choose a simple case with uniform current past a two-dimensional circular cylinder ($\phi_s = Ux + \phi_{SB}$ with radius 1 and $U = 1$ in an infinite fluid domain (see Fig. 6a). The potential due to the body ϕ_{SB} is $\cos\theta/r$ and the normal derivative $\partial\phi_{SB}/\partial n$ is $-\cos\theta/r^2$ at the body boundary. We can then divide the boundary into line elements and for each element assume ϕ_{SB} and $\partial\phi_{SB}/\partial n$ are constant with values which are equal to the correct values at the mid-point of the element. The potential and its derivatives outside the body boundary can be obtained by eq. (27) and derivatives of eq. (27). Fig. 7 shows the result of ϕ_{SB} , $\partial\phi_{SB}/\partial n$, $r^{-1}\partial\phi_{SB}/\partial\theta$, $\partial^2\phi_{SB}/\partial n^2$ as a function of the distance along the normal vector to the body boundary at the mid-point of the element. The results are for $\theta = 45^\circ$ (see Fig. 5). The effect of different number of elements N_B is investigated. The horizontal axis is the ratio between the distance Δl from the boundary and the length Δs of the elements. The results show that we get convergence and correct results of ϕ_{SB} and $\partial\phi_{SB}/\partial r$ at the boundary. However, for $r^{-1}\partial\phi_{SB}/\partial\theta$ and $\partial^2\phi_{SB}/\partial r^2$ we cannot obtain correct results at the boundary. The reason is that we are not integrating

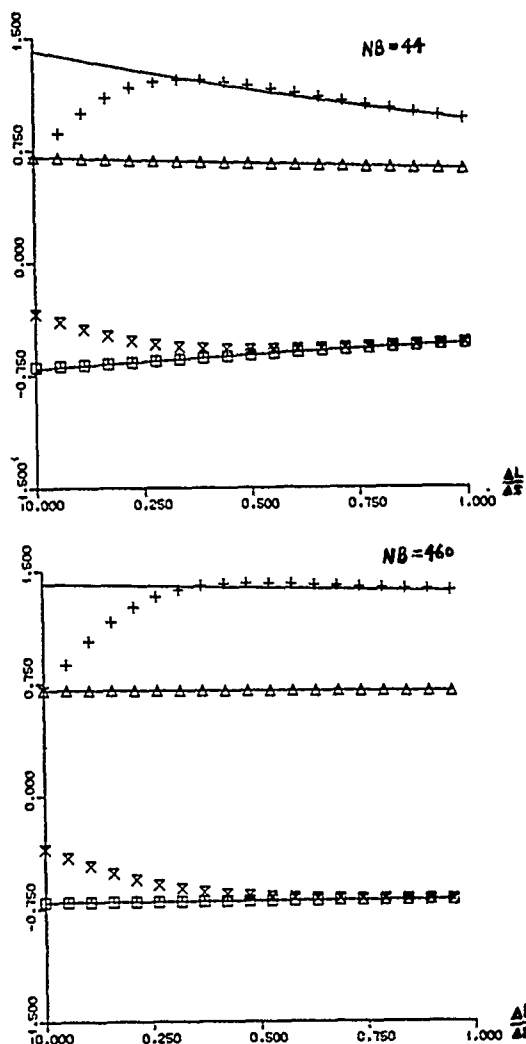


Fig. 7 Calculated values of velocity potential and its derivatives for the case presented in Fig. 6. (The steady incident flow is excluded). — Analytical solution. Numerical values: ϕ_{SB} : Δ , $\partial\phi_{SB}/\partial r$: \square , $r^{-1}\partial\phi_{SB}/\partial r$: \times , $\partial^2\phi_{SB}/\partial r^2$: \circ . (δL and δs are defined in Fig. 6) NB = number of panels.

with correct curvature and with correct variation of ϕ_{SB} and $\partial\phi_{SB}/\partial r$ over the elements. From Fig. 7 we can see that $r^{-1}\partial\phi_{SB}/\partial\theta$, $\partial^2\phi_{SB}/\partial r^2$ are satisfactorily estimated at a distance of $O(\delta s)$ along the normal vector of the element. That means we may use an extrapolation method to calculate the velocity along the body and the second order derivatives of the velocity potential. After some tests with a circular cylinder and a sphere and an ellipsoid in the three-dimensional case we found that the velocity along the body, the second order derivatives and the m_j -terms are in good agreement with the analytical solutions. The other way to integrate the term $m_j \log r$ (or $1/R$) over the body boundary is to apply the formula given by Ogilvie & Tuck (1969).

$$\iint_{S_B} m_j \log r \text{ (or } 1/R) ds = \quad (28)$$

$$- \iint_{S_B} \nabla \phi_S \nabla \log r \text{ (or } 1/R) n_j ds$$

This formula is valid for a body without sharp corners, wall-sided at the free surface and when ϕ_S satisfies the rigid free surface condition. From a numerical point of view this formula is more simple to calculate because it only includes first order derivatives of the steady potential. It is expected to give more accurate numerical results than by direct integration of the m_j -term.

For a body with sharp corners the m_j -terms are singular. The consequence is that eqs. (27) and (28) are not integrable. For example in the case of uniform current past a two dimensional section with a sharp corner the complex potential $W(z)$ in the vicinity of the edge can be approximated as (see Fig. 6b).

$$W(z) = C_1 z^{1/\lambda} + C \quad (29)$$

where $\lambda = 2 - \theta/\pi$ and C_1 and C are constants. For a rectangular section the first order and second order derivatives of the potential are $O(|z|^{-1/3})$ and $O(|z|^{-4/3})$. In the vicinity of the corner it is possible to show $m_2 = C_2 R^{-4/3}$ for $x = 0$ and $m_2 = 0$ for $y = 0$, where C_2 is a real constant (see Fig. 6b). This means eqs. (27) and (28) are not integrable. Actually, this is true for all corners with internal angles less than π . However, if we solve the wave-current-body interaction problem in the time domain by using for instance Green's second identity and satisfy the body boundary condition on the exact body boundary, the expressions are integrable. The reasons why the integrals are not integrable when the body boundary condition is satisfied on the mean position of the body boundary is that the formulation of the body boundary condition is wrong. The m_j -terms have been derived by a Taylor expression. This is not valid at a corner. We will show how we can avoid the difficulty with the m_j -terms. We divide then the velocity potential ϕ_k into two parts

$$\phi_k = \phi_k^a + \phi_k^b \quad (30)$$

where

$$\frac{\partial \phi_k^a}{\partial n} = m_k, \quad \frac{\partial \phi_k^b}{\partial n} = i\omega n_k \quad (31)$$

The following solutions of ϕ_k^a satisfy the body boundary conditions and Laplace equation

$$\phi_1^a = -\frac{\partial \phi_S}{\partial x}, \quad \phi_2^a = -\frac{\partial \phi_S}{\partial y}, \quad \phi_3^a = -\frac{\partial \phi_S}{\partial z}$$

$$\phi_4^a = -y \frac{\partial \phi_s}{\partial z} + z \frac{\partial \phi_s}{\partial y} \quad (32)$$

$$\phi_5^a = x \frac{\partial \phi_s}{\partial z} - z \frac{\partial \phi_s}{\partial x}$$

$$\phi_6^a = -x \frac{\partial \phi_s}{\partial y} + y \frac{\partial \phi_s}{\partial x}$$

By using Green's second identity we obtain the following expression for $\phi_k = \phi_k - \phi_k^a$ and ϕ_k (see Fig. 8).

$$4\pi(\phi_k - \phi_k^a) \Big|_{x=x_1} = \iint_{S_1} (\phi_k - \phi_k^a) \frac{\partial}{\partial n} \left(\frac{1}{R} \right) - \frac{\partial(\phi_k - \phi_k^a)}{\partial n} \left(\frac{1}{R} \right) ds(x,y,z) \quad (33)$$

$$4\pi \phi_k^a \Big|_{x=x_1}^C = \iint_{S_2} \left[\phi_k^a \frac{\partial}{\partial n} \left(\frac{1}{R} \right) - \frac{\partial \phi_k^a}{\partial n} \left(\frac{1}{R} \right) \right] ds(x,y,z) \quad (34)$$

where $x_1 = (x_1, y_1, z_1)$ is inside $S_1 = S_B \cup S_F \cup S_C \cup S_0$, $C=1$ when x_1 is inside $S_2 = (S_F - S_F^I) \cup S_C \cup S_0 \cup S_{INF}^I$ and $C = 0$ when x_1 is outside S_2 .

The integration surface is closed. S_F^I is part of the free surface and does not need to coincide with S_F . By subtracting equation (34) from equations (33) we find that

$$\begin{aligned} 4\pi(\phi_k - C\phi_k^a) \Big|_{x=x_1} = & \iint_{S_B} [(\phi_k - \phi_k^a) \frac{\partial}{\partial n} \left(\frac{1}{R} \right) + \frac{\partial}{\partial n} (\phi_k - \phi_k^a) \left(\frac{1}{R} \right)] ds \\ & + \iint_{S_F + S_C + S_0} (\phi_k \frac{\partial}{\partial n} \left(\frac{1}{R} \right) - \frac{\partial \phi_k}{\partial n} \left(\frac{1}{R} \right)) ds \\ & - \iint_{S_F^I + S_{INF}^I} (\phi_k^a \frac{\partial}{\partial n} \left(\frac{1}{R} \right) - \frac{\partial \phi_k^a}{\partial n} \left(\frac{1}{R} \right)) ds \end{aligned} \quad (35)$$

where $C=1$ when x_1 is outside S_2 and $C = 0$ x_1 is inside S_2 .

The last integral is a known quantity. The unknowns are $\phi_k - \phi_k^a$ on the body and ϕ_k on S_F , S_C and S_0 . By writing the integral over S_B like it is shown in equation (35) the integrand of the integral over S_B is integrable. The solution procedure to find

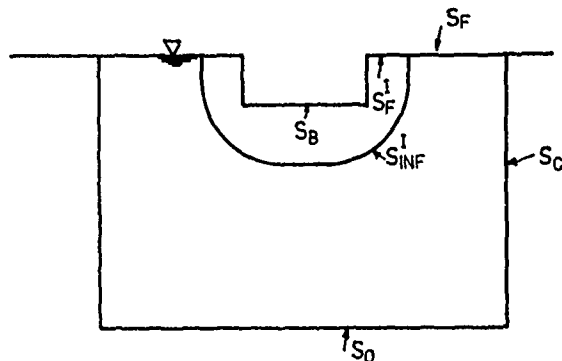


Fig. 8 Definition of surfaces used in the integration of equation (33) and (34).

the unknowns can be done similarly as in the previous section. What we have done now is to analytically isolate the difficulties with the m_j -terms. This procedure is also valid when ship motions at forward speed is evaluated. The same procedure can also be used to solve the second order potential problem where a similar difficulty occur.

We also have to be careful when we find the added mass and damping coefficient. We will illustrate this by a simple example. Fig. 9 presents results which shows the effect of bilge radius r on sway added mass for a two-dimensional body in infinite fluid. The parameters of the body is given in the figure. From Fig. 9 we can see how the added mass is dependent on the bilge radius in the cases with and without current. The added mass with current is going to infinity when the bilge radius $r \rightarrow 0$. This is an unphysical result. The reason to this behaviour can be found by studying the dynamic pressure part used in finding added mass and damping. Correct to $O(\zeta_a)$ and $O(U^2)$ we can write

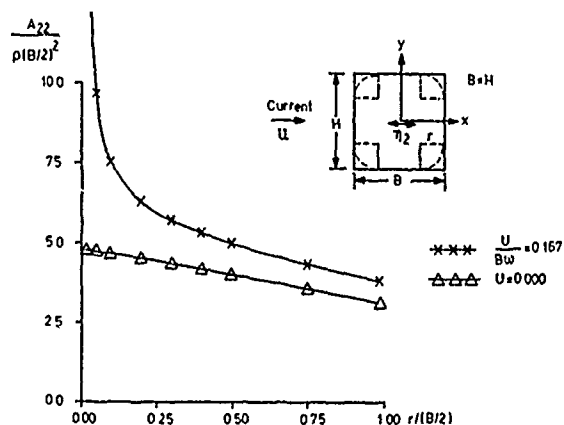


Fig. 9 Illustration of calculation of two-dimensional added mass coefficients for a body in a current can lead to unphysical results. The calculations are done for infinite fluid. (A_{22} = two-dimensional added mass in sway).

$$p = -\rho \left[\frac{\partial \phi_k}{\partial t} \eta_k + \nabla \phi_s \cdot \nabla \phi_k \eta_k + \frac{1}{2} (\vec{a} \cdot \nabla (\nabla \phi_s)^2)_k \right] \quad (36)$$

where

$$\vec{a} = (\eta_1 + z\eta_5 - y\eta_6)\vec{i} + (\eta_2 - z\eta_4 + x\eta_6)\vec{j} + (\eta_3 + y\eta_4 - x\eta_5)\vec{k} \quad (37)$$

The index k in the last term in equation (36) means that we only consider displacement in mode k .

What we have done in the calculations presented in Fig. 9 is to use the two first terms in equation (36). In this way we have included singular terms of $O(U^2)$, which are cancelled by the last term in equation (36). Actually we can write equation (36) as

$$p = -\rho \left(\frac{\partial \phi_k}{\partial t} \eta_k + \nabla \phi_s \cdot \nabla \phi_k^b \eta_k \right) \quad (38)$$

This means that $\nabla \phi_s \cdot \nabla \phi_k^b \eta_k$ cancels the last term in equation (36). If we use equation (38) we will find that the results for added mass at $U \neq 0$ is the same as for $U = 0$. However, this is not generally true when a free surface is present. What is true then is that the singular corner behaviour when the radius of curvature goes to zero is cancelled. Since our theory is correct to $O(U)$ we can also write

$$p = -\rho \left(\frac{\partial \phi_k}{\partial t} \eta_k + \nabla \phi_s \cdot (\nabla \phi_k^b) \right)_{U=0} \eta_k \quad (39)$$

This discussion illustrates that false effects can be created due to the singular corner behaviour if we are not careful in analysing the results.

Numerical results for mean wave loads

Calculations of mean wave loads require in general higher accuracy than computations of linear wave loads. We will therefore concentrate our numerical studies on mean wave loads. Both a direct pressure integration method and the equations for conservation of momentum have been used. When the current effect is incorporated, the procedure is correct to $O(U)$. Calculations have been performed both for horizontal and vertical mean wave loads.

The first case we will discuss is incident regular waves on a fixed vertical cylinder that is penetrating the free surface. The draught of the cylinder is $0.25 R$ where R is

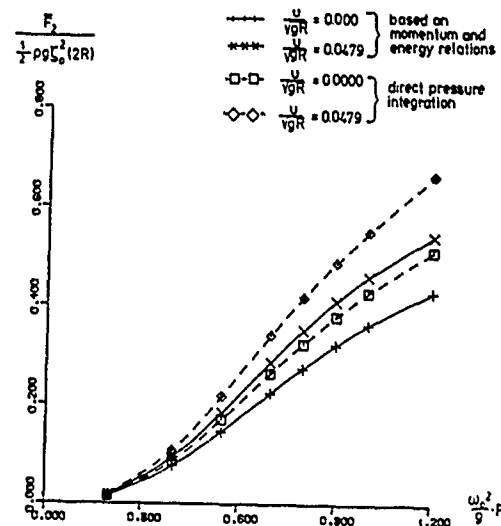


Fig. 10 Numerical results of horizontal drift force F_2 for $U/\sqrt{gR} = 0.000$, $U/\sqrt{gR} = 0.0479$ with direct pressure integration method and a method based on conservation of momentum and energy. The body is a fixed vertical cylinder with draught-radius ratio 0.25. Element distribution: $NN1 = 16$, $NN2 = 12$, $NN3 = 14$, $NN4 = 4$, $NN5 = 8$, $R = 1.0$, $R1 = 3.0$, $H = 1.2\lambda$ (see Fig. 11). Element lengths on the body are nearly constant.

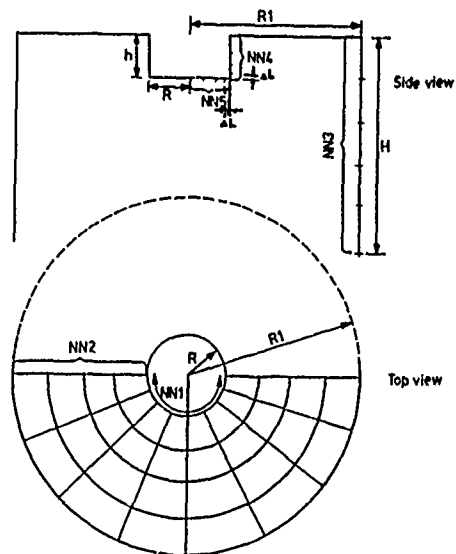


Fig. 11 Definition of number of elements and dimensions of control surfaces used in the numerical solution of flow around a vertical cylinder of finite length.

the cylinder radius. The cylinder bottom is impermeable. The current direction coincides with the wave propagation direction.

An example on results for horizontal mean wave loads are presented in Fig. 10 as a function of $\omega_0^2 R/g$ where ω_0 is the circular frequency of oscillation of the waves without current present. Both for zero and non-zero current speed we note an important difference in the calculations based on direct pressure integration and the results based on the equations for conservations of momentum in

the fluid. The panel distribution used in the calculations can be illustrated by means of Fig. 11. By referring to the nomenclature in the figure, NN1 = 16, NN2 = 12, NN3 = 14, NN4 = 4, NN5 = 8, R = 1.0, R1 = 3.0 and H = 1.2 λ (λ = incident wave-length). The panel dimensions on the body were of nearly constant equal length. The reason to the differences in the results is that the direct pressure integration method is sensitive to the distribution of the element in the vicinity of the corner at the bottom of the cylinder. This can be illustrated by Fig. 12 where the calculations are presented as a function of R/ ΔL when $\omega_0^2 R/g = 0.8$. ΔL means the length of the element nearest to the corner on the vertical side (see Fig. 11). NN1, NN2 and NN3 were the same as used in the calculations presented in Fig. 10 while NN4 varied from 4 to 12 and NN5 from 8-12. This means that the total number of elements were quite similar in the calculations presented in Fig. 10. It is the size of the elements that differs significantly. The height of the elements on the vertical side were selected so that L_{n+1}/L_n is a constant, there n = 1 means the element closest to the corner, n = 2 the element next closest and so forth. The constant ratio was always below 1.5. On the horizontal bottom the length of the element in the radial direction was selected in a similar manner, starting with an element closest to the corner. The length of the element on the bottom closest to the corner was the same order of magnitude as the height of an element on the vertical side closest to the corner. However, the most important parameter in the calculations by the direct pressure integration method was the distribution of the elements on the vertical side close to the corner. The reason was associated with the contribution from the velocity square

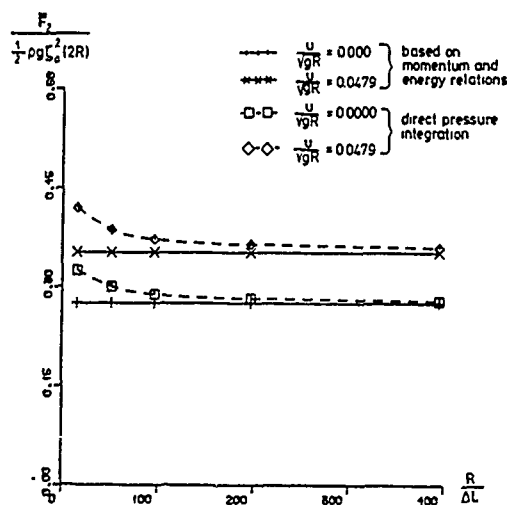


Fig. 12 Numerical results of horizontal drift forces F_2 with direct pressure integration method and a method based on conservation of momentum and energy. Data presented as a function of $R/\Delta L$ (ΔL defined in the figure 11) NN1 = 16, NN2 = 12, NN3 = 14, NN4 = 4-12, NN5 = 8-12, R = 1.0, R1 = 3.0, H = 1.2 λ (see Fig. 11). High density of elements close to the cylinder corner. The body is the same as used in Fig. 11.

term in Bernoulli's equation, which is singular, but integrable at the corner.

In Fig. 13 are shown numerical results for vertical drift forces on a vertical cylinder that is free to oscillate in surge and heave and restrained from oscillating in pitch. The incident wave propagation direction is in the positive x-direction. The draught h of the cylinder is equal to the cylinder radius. The

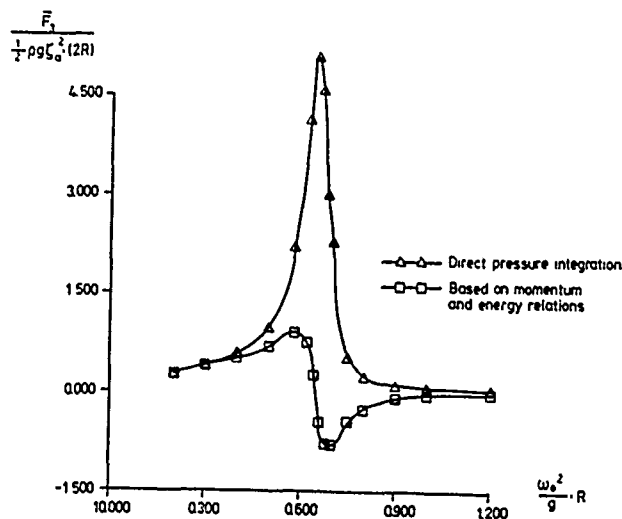


Fig. 13 Numerical results of vertical mean wave force F_3 with direct pressure integration method and a method based on conservation of momentum and energy. The body is a vertical cylinder that is free to oscillate in surge and heave and restrained from oscillating in roll. The draught-radius ratio is 1.0. Element distribution: NN1 = 16, NN2 = 10, NN3 = 14, NN4 = 8, NN5 = 8, R = 1.0, R1 = 2.5, H = 1.2 λ (see Fig. 11). Element length on the body is nearly constant. Zero current velocity.

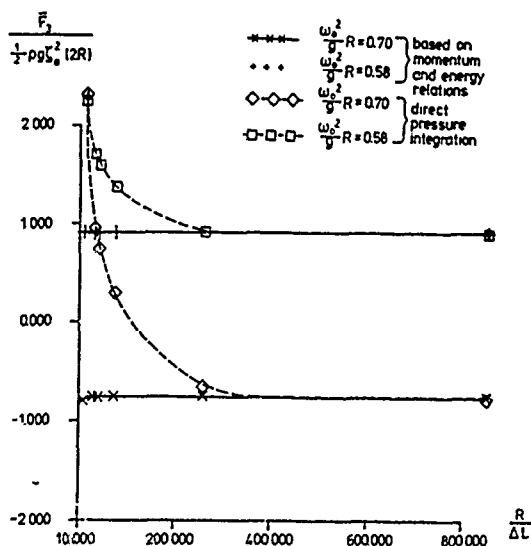


Fig. 14 Numerical results of vertical mean wave forces F_3 with direct pressure integration method and a method based on conservation of momentum and energy. Data presented as a function of $R/\Delta L$ (ΔL defined in the figure 11). NN1 = 16, NN2 = 10, NN3 = 14, NN4 = 8-12, NN5 = 8-12, R = 1.0, R1 = 2.5, H = 1.2 λ (see Fig. 13). High density of elements close to the cylinder corner. The body is the same as used in Fig. 13. Zero current velocity.

current velocity is zero. The panel dimensions of the body were of nearly equal length. By referring to the nomenclature in Fig. 11, $NN1 = 16$, $NN2 = 10$, $NN3 = 14$, $NN4 = 8$, $NN5 = 8$, $R = 1.0$, $R1 = 2.5$, $H = 1.2 \lambda$. The large differences between the two different methods occur in the vicinity of heave resonance. The reason to the differences is again that the direct pressure integration method is sensitive to distribution of the elements in the vicinity of the corner between the bottom and the vertical side of the cylinder. This can be illustrated by Fig. 14 where the calculations are presented as a function of $R/\Delta L$ when $\omega_0^2 R/g = 0.58$ and 0.7 . ΔL means in this case the length in radial direction of the element closest to the corner on the horizontal side (see Fig. 11). The distribution of elements were selected similarly as in the previous example. Total number of elements are nearly the same for all calculations presented. When the direct pressure integration method is used to calculate the vertical mean wave force, around heave resonance, the contribution from the velocity square term in equation (26) is large and of opposite sign to the other contributions in the integral over S_{g0} . The absolute values of these terms are nearly equal to the velocity square term. This means a high accuracy is needed in the integration over S_{g0} .

In Figs. 15 and 16 are presented numerical results for horizontal drift forces on a vertical cylinder with draught-radius ratio 3.0.

The method based on conservation of momentum was used. The effect of using higher density of elements close to corner between the bottom and the vertical side of the cylinder was investigated. There was a maximum of 1% difference in drift forces. The influence of number of singular points inside the body (see equation (17)) was investigated. Also the effect of number of multipoles was studied (see equation (17)). In the calculations presented in Figs. 14 and 15 number of singular points is two and number of multipoles for each singular point is 10. If only one singular point was used there was a maximum of 1% difference in drift forces. If number of multipoles was increased to 16 there was a maximum of 0.2% differences in drift forces. The effect of increasing $R1$ (see Fig. 11) from 3.0 to 5.0 was studied. The difference in results were less than 2%.

CONCLUSIONS

A theoretical method to analyse current-wave-body interactions is presented. It is demonstrated that the m_j -terms arising in the body boundary conditions can cause large errors in the numerical result. A theoretical way to provide stable numerical solutions is presented.

A method to calculate mean wave forces based on conservation of fluid momentum is presented. It is demonstrated that a direct

pressure integration method can lead to large errors in prediction of mean wave forces when the body has sharp corners.

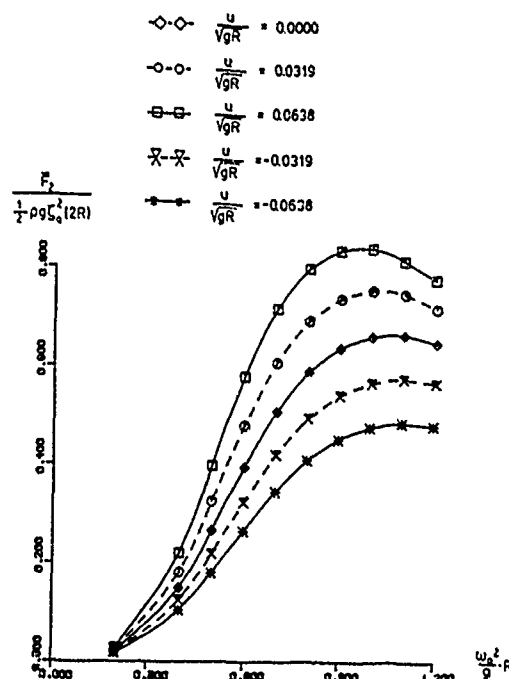


Fig. 15 Numerical results for horizontal wave drift forces on a fixed vertical cylinder with draught-radius ratio 3.0. Current velocity U is in the same direction as the wave propagation direction. Element distribution: $NN1 = 16$, $NN2 = 16$, $NN3 = 14$, $NN4 = 12$, $NN5 = 8$, $R1 = 1.0$, $R1 = 4.0$, $H = 1.2 \lambda$ (see Fig. 11). Element length on the body is nearly constant.

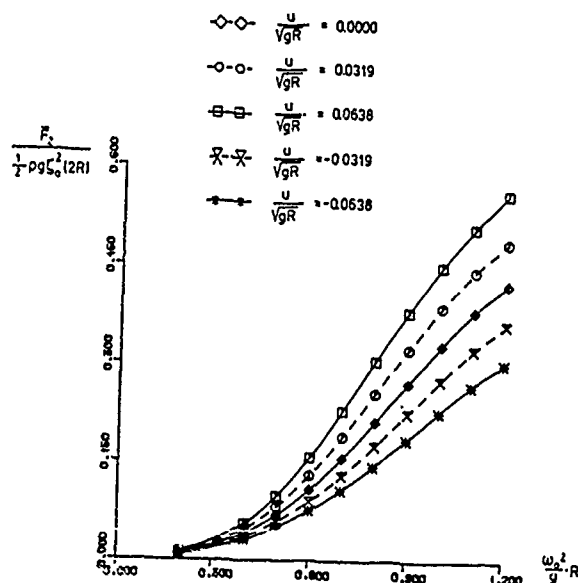


Fig. 16 Numerical for horizontal wave drift forces on a vertical cylinder with draught-radius ratio 3.0. The cylinder is free to oscillate in surge only. Element distribution is the same as used in Fig. 15.

References

1. Grekas, A. 1981, Contribution a l'etude Theorique et Experimentale des Efforts du Second Ordre et du Comportement Dynamique d'une Structure Marine Sollicitee par une Houl Reguliere et un Courant, These de Docteur Ingenieur (Ecole Nationale Superieure de Mechanique).
2. Hess, J.L., Smith, A.M.O. 1962, Calculation of Non-lifting Potential Flow about Arbitrary Three-dimensional Bodies, Report No. E.S. 40622, Douglas Aircraft Division, Long Beach, California.
3. Mavrakos, S.A. 1988, The Vertical Drift Force and Pitch Moment on Axisymmetric Bodies in Regular Waves, Applied Ocean Research, Vol. 10, No. 4.
4. Molin, B., 1983, On Second-Order Motion and Vertical Drift Forces for Three-dimensional Bodies in Regular Waves, Proc. Int. Workshop on Ship and Platform Motion, Berkeley, pp. 344-357.
5. Ogilvie, T.F., Tuck, E.O., 1969, A Rational Strip Theory of Ship Motion: Part I, Report No. 013. The Department of Naval Architecture and Marine Engineering, The University of Michigan, College of Engineering.
6. Ogilvie, T., 1983, Second-Order Hydrodynamic Effects on Ocean Platforms, Proc. Int. Workshop on Ship and Platform Motions. Berkeley, pp. 205-265.
7. Newman, J.N., 1967, The Drift Force and Moment on Ships in Waves, Journal of Ship Research, Vol. 11.
8. Newman, J.N., 1978, The Theory of Ship Motions, Advances in Applied Mechanics, Vol. 18.
9. Zhao, R., Faltinsen, O.M., 1988, Interaction Between Waves and Current on a Two-dimensional Body in the Free Surface, Applied Ocean Research. Vol. 10, No. 2.
10. Zhao, R., Faltinsen, O.M., Krokstad, J.R., Aanesland, V., Wave-Current Interaction Effects on Large-Volume Structures", BOSS '88, Trondheim.

DISCUSSION

by R. Huijsmans

I first like to congratulate the authors on their very concise treatment of the low forward speed problem. I have a few questions.

1) Can the authors elaborate on how to obtain the low frequency drift forces from their "far field" expansion of the drift force?

2) The authors identify the well known problem in using double derivatives of the stationary potential on the body. They used a kind of extrapolation procedure to avoid the problem. Have they now used the potential Φ_S on B, described by a C^2 function by using some linear variation? (results of Fig.7 of their paper for $\Delta L/\Delta S \rightarrow 0$)

3) The authors experienced some problems even for the zero speed case in determining the wave drift forces based on the pressure integration, because of the presence of sharp corners. Have they some experience on how "sharp" these corners must be in order to get into troubles.

4) The authors did not mention how they actually solved the systems of equations (directly?) and what the computational burden of their method is with respect to the number of panels. How much more expensive is the treatment of the non-zero speed case with respect to the zero speed case?

5) And the final question is regarding the use of their method without the low forward speed restriction. Can the authors give some idea how to their method can be applied for high speeds.

Author's Reply

We thank Huijsmans for his comments. The replies are as follows:

1) Our "far" field expression is based on conservation of momentum and energy which can not be applied to calculate low frequency drift forces. When we study low frequency drift forces one should also include second order potential. A discussion about this problem is given by Faltinsen and Zhao[A1].

2) We have not applied high order panel method to predict the second order derivatives of stationary potential on the body. We think for a body with sharp corners one will also get numerical problems even we use high order

panel method. In our another formulation (see eq.(35)) we can avoid to calculate the second order derivatives on the body.

3) When one calculates wave drift force based on pressure integration, it is difficult to predict the contribution from u^2 -term, because the velocity will be infinite at sharp corners. We did not investigate how "sharp" these corners must be to get into serious problem. But from our experience we think the most important thing is due to cancellation effect of the contributions from different terms. This will depend on the whole body configuration the incident wave system as well as the local sharpness of the corner. In some cases only a few percent error in predicting the contribution from u^2 -term will give 100% error in wave drift forces.

4) The usual direct equation solver was used to solve the systems of equation. The CPU time is almost the same for the case with or without current velocity.

5) Our method may apply to high speed problems. In that case one should obviously use another free surface condition and Greens function.

[A1] Faltinsen, O. and Zhao, R.: Slow-Drift Motion of a Moored Two-Dimensional Body in Irregular Waves, J. of Ship Research, Vol.33, No.2, June 1989, pp.93-106.

DISCUSSION

by A. Hermans

I only shall make some remarks about Figs.2 and 3 and the text just before those figures. It looks like the authors are not aware of a large amount of literatures about the typical nonuniform behavior of that show up in "both" figures. The way they think that (13) has been applied leads to nonuniformities at the distance of order τR , while the application of (11) leads to a nonuniform behavior at the distance of order $\tau^2 R$. Already in 1882 Lindstedt noticed and remedied this kind of nonuniform behavior in the computation of the trajectories of planets. In 1892 Poincare in his book on "Mecanique Celeste" proved that the remedy that was given is correct. In 1949 Lighthill extended their theory to problems in fluid dynamics. The approach suggested in (13) is uniformised quite easily because the exact phase relation can be used, while the approach according to (11) always will have a phase error in the far

field. The uniform version of (13) and application of (11) both lead to a correct approximation of the amplitude.

Author's Reply

We would like to thank professor Hermans for his comments. We think one has to have in mind what one should calculate when we compare the two different approaches. If one should calculate the wave drift damping coefficient that is proportional to the slow drift velocity, the two approaches should be equal. However if one want to study wave current interaction and in particular the wave elevations around the structure, the two different approaches are different. The approach that we are using, is then a better approximation.

DISCUSSION

by H.J. Choi

On this occasion, I would like to ask a

question which I have had for a long time. It is a well-known fact that incident waves deform significantly in amplitude and propagation angle, depending on the magnitude and incidence angle of current. As a result, a considerable amount of radiation stresses is to be built up in water, which might contribute to the second-order forces on marine structures, too. My question is if we could discard the effect. If it is not the case, how can you incorporate it into your method?

Author's Reply

The effect of radiation stresses is included when we calculate mean wave forces. A discussion of this is given by Longuet-Higgins[Al].

[Al] Longuet-Higgins, M.S.: The Mean Force Exerted by Waves on Floating or Submerged Bodies with Applications to Sand Bars and Power Machines, Proc. R. Soc. Lond. A.352, pp.463-480.

The Numerical Solution of the Motions of a Ship Advancing in Waves

G. X. Wu and R. Eatock Taylor
University College London
London, UK

Abstract

The hydrodynamic problem of a surface ship advancing in regular waves at constant forward speed is analysed using a three dimensional theory based on the linearized velocity potential. The potential is represented by a distribution of sources over the surface of the ship and its waterline. Various numerical schemes are introduced to overcome some of the major difficulties in this problem. Calculation is made for a submerged sphere. Results are compared with the analytical solution and very good agreement is found. Some preliminary calculations have also been made for a series 60 ship with block coefficient 0.7.

1. Introduction

The wave induced motions of a ship have several implications for ship performance, increased resistance, deck wetting, slamming, vertical acceleration and propeller emergence, etc. While all of these aspects are important subjects in ship hydrodynamics, the fundamental problem remains that of estimating the overall motion of the ship in waves.

In order to predict ship motions in waves, the ship is usually regarded as a rigid floating body having six degrees of freedom, and the fluid loading is estimated from linearized potential flow theory. This theory assumes that the fluid is inviscid and incompressible, the flow is irrotational, and both incoming wave elevation and body oscillation are small. The velocity potential therefore satisfies the Laplace equation, and the corresponding boundary condition is imposed on the mean position of the fluid boundary.

Even after such drastic assumptions have been introduced, the solution of the resulting equation is still not easy to obtain. One of the major difficulties

arises from the complicated free surface condition. Further difficulty is associated with the fact that for a

practical ship its shape is usually described by coordinates of discrete points rather than by a simple mathematical function. As a result, the solution can be only obtained numerically.

Attempts to predict ship motions in waves can be traced much earlier, but a significant breakthrough was the work by Korvin-Kroukovsky and Jacobs (1957). Based on physical intuition rather than rigorous mathematics, they provided the early version of strip theory. Even though their theory was later found to be mathematically inconsistent, (in particular it does not satisfy the Timman-Newman relation (1962)), experimental data have shown that it nevertheless provides very good results in many cases. A number of modified versions of this strip theory have since been developed, of which, that proposed by Salvesen, Tuck and Faltinsen (1970) is widely used in ship design. Another very significant step was the work of Newman (1978). He overcame the limitation of the conventional theory to the region of high frequency, and proposed a "unified strip theory" which is valid throughout the whole frequency region. In particular this theory takes some account of wave interactions between different cross sections of the ship. Numerical results for heave and pitch (Sclavounos 1985) in infinite water depth have shown that the unified theory is superior to the conventional strip theory in such a case.

Even though the strip theory can provide satisfactory results in many cases, and has had a very important role in ship design, it has its inherent limitations. It requires the ship to be slender, and the magnitudes of forward speed and encounter frequency to be in appropriate ranges. Furthermore, while it

may provide good results for the total force on the ship, it usually gives a very poor prediction for the detailed hydrodynamic pressure distribution around the hull. Thus attempts to remove some of the limitations of strip theory, by using a three dimensional approach have been initiated by Chang (1977) and others (Inglis & Price 1981, Kobayashi 1981, Guevel & Bouglis 1982). These investigations have all adopted the constant panel method (Hess & Smith 1964): the ship hull is represented by small panels on which the sources or dipoles are assumed to be constant. It has been found that these frequency domain three dimensional theories in general improve the results and provide better agreement with experimental data. However, it has been observed that the numerical solution is sensitive to the size of the panels, and high accuracy is not easy to obtain. This was also noticed in recent work by King, Beck & Magee (1988) using a three dimensional method in the time domain.

The present work is part of an investigation which aims to obtain a stable and accurate solution of the linearized three dimensional problem, using the source distribution approach. Attention is focused here on certain numerical aspects. Firstly, we use quadratic isoparametric boundary elements instead of plane constant panels. As the associated wave resistance is known to be sensitive to the shape of the ship, it seems likely that isoparametric elements should enable us to model the ship hull with a higher degree of accuracy. They also provide a more convenient means of calculating the velocity of the fluid on the ship surface. Secondly, we impose the body surface condition by averaging over the body surface using the Galerkin method, rather than at discrete nodes. Experience has shown that this method usually gives more accurate results. In this particular problem, as the body surface condition on the waterline is averaged over the body surface, we can avoid the difficulty of both the source and field points being on the free surface when solving the integral equation. The use of the Galerkin method also avoids another serious numerical difficulty: the second order derivatives of the steady potential due to forward speed (which appear in the body surface condition on the unsteady potential due to the ship oscillation) can be reduced to first order derivatives, as in the coupled finite element method (Wu & Eatock Taylor 1987a)

In the integral equation, we express the Green function in terms of the exponential integral (Wu & Eatock Taylor

1987b). Extensive tests have been carried out to try to achieve accurate evaluation of the Green function, and a technique has been introduced to remove the singularity in its integrand. We use a similar technique to that of Noblesse (1983) to reduce the order of the dipole singularity $1/r$ (where r is the distance between the source and the field points). We do not however need to evaluate the constant by integrating the Green function over the waterplane of the ship. Finally, to remove the singularity due to the source $1/r$, we adopt triangular polar coordinates when calculating the contribution of an element to itself (Li, Han & Mang 1985). An alternative method for achieving this, by subdivision of the element, has also been investigated.

These numerical procedures are found to be very effective for a submerged sphere. Compared with the analytical solution (Wu & Eatock Taylor 1988), the numerical method provides very accurate results when 12 elements for half of the sphere are used. Calculations are also made for a series 60 hull of block coefficient 0.7 at Froude number $Fn=0.2$.

2. Mathematical Formulation

We define the right-handed coordinate system $O-xyz$ so that x points in the direction of steady forward speed U of the ship and z upwards; the origin of the system is located on the undisturbed free surface and the middle section of the ship. The whole system is moving with the ship at the same forward speed. For a time-periodic incoming wave at a frequency ω_0 , the total potential can be written as

$$\Phi = -Ux + U\phi(x, y, z) + \text{Re} \left\{ \sum_{j=0}^7 \eta_j \phi_j(x, y, z) e^{i\omega t} \right\} \quad (1)$$

where ϕ is the steady potential due to unit forward speed, ϕ_j ($j=1, \dots, 6$) are radiation potentials corresponding to the six degree of freedom oscillations of the body and η_j ($j=1, \dots, 6$) are corresponding motion amplitudes; ϕ_0 and ϕ_7 are the potentials of the incident and diffracted waves respectively; and $\eta_0 = \eta_7$ is the incoming wave amplitude. The encounter frequency ω is given by

$$\omega = \omega_0 - (\omega_0^2/g)U \cos \beta \quad (2)$$

where g is the gravitational acceleration and β is the incident angle of the incoming wave and $\beta=0$ indicates a following sea.

Based on the assumptions of the linearized theory, we have for the steady potential

$$\nabla^2 \phi = 0 \quad (3)$$

in the whole fluid domain R;

$$\mu\phi_{,z} + \phi_{,xx} = 0 \quad (4)$$

on the undisturbed free surface S_F , where $\mu = g/U^2$;

$$\partial\phi/\partial n = -n_x \quad (5)$$

on the body surface S_0 , where n is the inward normal of the body surface and n_x is its component in the x direction; and

$$\partial\phi/\partial n = 0 \quad (6)$$

on the bottom S_B of the fluid or $z \rightarrow -\infty$ in the present case of infinite water depth. To complete the boundary-value problem, we also need to include the radiation condition at infinity: it is usually assumed that there is no wave due to ϕ far in front of the ship but there are waves far behind the ship.

The components of the radiation and diffraction potentials are assumed to satisfy the following equations (Newman 1978)

$$\nabla^2 \phi_j = 0 \quad \text{in } R; \quad (7)$$

$$\phi_{jz} + (\tau^2/\nu)\phi_{jxx} - 2i\tau\phi_{jx} - \nu\phi_j = 0 \quad \text{on } S_F \quad (8)$$

where $\tau = \omega U/g$ and $\nu = \omega^2/g$; and

$$\partial\phi_j/\partial n = -i\omega n_j + U m_j \quad (j=1, \dots, 6) \quad (9a)$$

$$\partial\phi_j/\partial n = -\partial\phi_0/\partial n \quad j=7 \quad (9b)$$

$$\text{on } S_0, \text{ where} \\ (n_1, n_2, n_3) = (n_x, n_y, n_z) \quad (10a)$$

$$(n_4, n_5, n_6) = X n \quad (10b)$$

$$U(m_1, m_2, m_3) = -(n \cdot \nabla) W \quad (10c)$$

$$U(m_4, m_5, m_6) = -(n \cdot \nabla)(X W) \quad (10d)$$

$$W = U\nabla(\phi - x) \quad (10e)$$

X is the position vector of a point on S_0 relative to the origin of the coordinates. The potentials ϕ_j also satisfy the same condition on the bottom of the fluid as ϕ . The radiation condition on ϕ_j states that the outgoing wave with its group velocity larger than forward speed travels far in front of the body; otherwise the waves propagate behind.

Following the derivation of Brard (1972), the unknown potential can be represented by a source distribution σ over the body surface S_0 and water line L . We have

$$\phi(P) = \frac{1}{4\pi} \left[\int_{S_0} G(P, Q) \sigma(Q) dS - \frac{U^2}{g} \int_L G(P, Q) \sigma(Q) n_x(Q) dy \right] \quad (11)$$

where G is the Green function for a pulsating translating source, which is taken in the form derived by Wu & Eatock Taylor (1987b). From the above equation, we obtain

$$\frac{\partial\phi(P)}{\partial n(P)} = \frac{-\alpha(P)}{4\pi} \sigma(P) + \frac{1}{4\pi} \left[\int_{S_0} \frac{\partial G(P, Q)}{\partial n(P)} \sigma(Q) dS - \frac{U^2}{g} \int_L \frac{\partial G(P, Q)}{\partial n(P)} \sigma(Q) n_x(Q) dy \right] \quad (12)$$

on S_0 , where $\alpha(P)$ is the inner subtended angle of the ship surface at point P and the integration excludes the point $Q=P$. Substituting equation (9) into the above equation, we can obtain the corresponding boundary-integral equation for the source distribution.

One difficulty in dealing with equation (12) is caused by the normal derivative of the Green function. It contains a second order singularity of the dipole when $Q \rightarrow P$. To avoid that we define

$$F(P, Q) = \frac{1}{r} + \frac{1}{r_1} \quad (13)$$

where r is the distance between P and Q , and r_1 is that between P and the mirror image 1 of Q about the undisturbed free surface. Applying Green's second identity in the domain enclosed by the ship and its water plane where $\partial F/\partial n = 0$, we have

$$\alpha(P) = - \int_{S_0} \frac{\partial F(P, Q)}{\partial n(Q)} dS \quad (14)$$

By substitution of equation (14) into (12), the latter becomes

$$\frac{\partial\phi(P)}{\partial n(P)} = \frac{1}{4\pi} \int_{S_0} \left[\frac{\partial G(P, Q)}{\partial n(P)} \sigma(Q) + \frac{\partial F(P, Q)}{\partial n(Q)} \sigma(P) \right] dS - \frac{1}{4\pi} \frac{U^2}{g} \int_L \frac{\partial G(P, Q)}{\partial n(P)} \sigma(Q) n_x(Q) dy \quad (15)$$

It is easy to confirm that the order of the singularity in this equation has been reduced.

3. Numerical Discretisation

We now discretise equation (15) using the shape function N_j . We write

$$\sigma = \sum_{j=1}^n \sigma_j N_j \quad (16)$$

where n is the number of nodes. By use of the Galerkin method, equation (15) can be written as

$$[A][\sigma] = [B] \quad (17)$$

where $[A]$ is the square matrix with the coefficients

$$a_{ij} = \frac{1}{4\pi} \left(\int_{S_0} \int_{S_0} \left[\frac{\partial G(P, Q)}{\partial n(P)} N_j(Q) + \frac{\partial F(P, Q)}{\partial n(Q)} N_j(P) \right] N_i(P) dS_Q dS_P - \frac{U^2}{g} \int_{S_0} \int_L \frac{G(P, Q)}{\partial n(P)} N_j(Q) n_x(Q) dy N_i(P) dS_P \right); \quad (18a)$$

and [B] contains the body surface boundary condition and has the coefficients

$$b_{ij} = \int_{S_0} \frac{\partial \phi_j(P)}{\partial n(P)} N_i(P) dS_P \quad (18b)$$

To obtain an accurate solution of the above equation, careful consideration must be given to several factors which have most significant effects. Firstly, the Green function is expressed in an integral form with a complicated and highly oscillatory integrand. The numerical evaluation of such an integral requires a very small step and takes most of the computer time. In our analysis, we have performed certain transformations of variable to reduce the oscillation. To deal with the following singularity in the Green function (Wu & Eatock Taylor 1987b)

$$I = \int_0^\gamma \frac{F(\theta)}{\sqrt{(4r \cos \theta - 1)}} d\theta$$

at $\theta = \gamma - \arccos(1/4r)$ when $r > 0.25$, we introduce the following scheme

$$I = \frac{1}{\sin \gamma} \int_0^\gamma \frac{\sin \gamma F(\theta) - \sin \theta F(\gamma)}{\sqrt{(4r \cos \theta - 1)}} d\theta + \frac{F(\gamma)}{\sin \gamma} \frac{1}{2r} \sqrt{(4r - 1)} \quad (19)$$

A similar scheme is adopted in the range $(\gamma, \pi/2)$ and is found to be effective.

The second important factor which significantly affects the accuracy is the method of discretisation of the ship. Initially, a coarse mesh can be refined by using more of the coordinates of the ship hull provided by the offsets; but this process is limited by the number of coordinates available. When a still finer mesh is needed, the commonly adopted procedure is to interpolate using the shape functions. Consequently this may refine the representation of the source distribution but it does not improve the representation of the ship hull. This leads to the problem that different shape functions will give different hulls. It may not be important when these ship hulls are close to each other; but a problem can arise when even then the results do not converge. Ultimately, different shape functions may lead to different converged solutions when the above subdivision procedure is adopted. When this happens, subdivision of elements must be based on measuring the nodal coordinates on the lines drawing of the ship.

The third factor is the integration over the body surface in equation (18). After numerous tests and careful consideration of accuracy and efficiency, we have chosen the four point Gaussian scheme. To avoid the singularity when

$Q \rightarrow P$, we have investigated two methods: that proposed by Li, Han & Mang (1985) using a triangular polar local coordinate system; and a method based on subdividing the element when the integration is performed. We have found that both schemes give very similar results and the latter has been chosen in the main computer program. To improve efficiency, we have also used the fact that components of $G(P, Q)$ are either symmetric

or antisymmetric. This reduces the computer time by almost a half.

Finally, to avoid the difficulty of calculating the second order derivatives in equations (10c) and (10d), we can perform the integration in equation (18b) by parts. This reduces the derivatives to first order (Wu & Eatock Taylor 1987a).

After the solution has been found, the added masses μ_{ij} and damping coefficients λ_{ij} can be obtained from (Newman 1978)

$$\begin{aligned} & \omega^2 \mu_{ij} - i\omega \lambda_{ij} \\ & - \rho \int_{S_0} (i\omega \phi_j + W \cdot \nabla \phi_j) n_i dS \\ & - \rho \int_{S_0} (i\omega n_i - U m_i) \phi_j dS + \rho U \int_L \phi_j \phi_z n_i dL \end{aligned} \quad (20)$$

where the second term has been transformed using the relation derived by Ogilvie and Tuck (1969). In general, the second form of this equation has no apparent advantage over the first. In fact the second order derivative in m_i makes the calculation even more difficult. However, when the steady potential ϕ can be neglected, such as for sufficiently slender ships, the latter form has the advantage of not requiring calculation of the derivatives of the unsteady potential. Thus for a slender ship we have

$$\begin{aligned} & \tau_{ij} \omega^2 \mu_{ij} - i\omega \lambda_{ij} \\ & - \rho \int_{S_0} (i\omega n_i - U m_i) \frac{1}{4\pi} \left[\int_{S_0} G(P, Q) \sigma(Q) dS \right. \\ & \quad \left. - \frac{U^2}{g} \int_L G(P, Q) \sigma(Q) n_x(Q) dy \right] dS \\ & - \rho \frac{1}{4\pi} \sum_{k=1}^N \sigma_k c_k \end{aligned} \quad (21)$$

where σ corresponds to ϕ_j and

$$\begin{aligned} c_k &= \int_{S_0} (i\omega n_i - U m_i) \left[\int_{S_0} G(P, Q) N_k(Q) dS \right. \\ & \quad \left. - \frac{U^2}{g} \int_L G(P, Q) N_k(Q) n_x(Q) dy \right] dS \end{aligned} \quad (22)$$

c_k can of course be calculated when matrix [A] is assembled rather than after the solution has been found; otherwise the computer time would almost be doubled.

4. Numerical Results

In the following calculated examples, we have taken $\phi=0$. This is in fact consistent with the linearized free surface condition given in equation (8). The presence of the steady disturbance potential in the body surface condition alone does not appear to provide a consistent improvement to the accuracy of the boundary-value problem for a surface piercing body. In general, when ϕ can not be regarded as a small quantity, its contribution should be included in the free surface condition (Newman 1978) as well as in the body surface condition. If the incoming wave is of large amplitude, a fully nonlinear mathematical model should be used.

Tables 1a and 1b give the added mass and damping coefficients for a sphere of radius a undergoing forced oscillations. Table 2 gives the exciting force on the sphere in an incoming wave with incident angle $\beta=0.75\pi$. The sphere is submerged at $h=2a$ (h being distance between the centre of the sphere and the mean free surface) and translates at a Froude number $Fn=U/(ga)=0.4$. The hydrodynamic coefficients are nondimensionalized as $r_{ij}/\rho\pi a^3\omega^2$ and the exciting force as

$F_1/\rho g\pi a^3\nu\eta_0$. In the tables, ν and ν_{0c} correspond to the values of ω and ω_0 at the critical point $r=0.25$. We have omitted r_{31} from table 1, since it is observed that the Timman-Newman (1962) relation is very well satisfied at this forward speed. The results from the numerical method (designated N in the tables) are based on an idealisation using only 12 elements (45 nodes) on one half of the surface of the sphere. These are seen to agree reasonably with results from the analytical solution (Wu & Eatock Taylor 1988), designated A in the tables. It should be noted, however, that these results are not the same as those in Wu & Eatock Taylor (1988), since the latter included the effect of the steady disturbance potential on the body surface boundary condition. We have observed that excluding this term has one marked effect: namely it leads to a non-zero rotational moment about the centre of the sphere. This should not occur, and it highlights the importance of including ϕ in this case. Nevertheless, the comparisons shown in the table provide evidence of the reliability of the numerical procedures adopted to solve the boundary value problem by equations (7) and (9).

νa	μ_{11}		μ_{22}		μ_{33}		μ_{13}	
	A	N	A	N	A	N	A	N
0.1	0.7009	0.6948	0.6939	0.6996	0.7291	0.7251	-0.0028	-0.0029
0.2	0.7200	0.7141	0.7055	0.7116	0.7607	0.7577	-0.0259	-0.0264
0.3	0.7128	0.7064	0.7075	0.7137	0.7529	0.7501	-0.0758	-0.0773
0.4	0.6077	0.5987	0.6936	0.6996	0.6259	0.6153	-0.0799	-0.0828
0.5	0.6290	0.6224	0.6722	0.6779	0.6315	0.6244	-0.0198	-0.0211
0.6	0.6374	0.6311	0.6579	0.6629	0.6271	0.6201	-0.0007	-0.0011
0.7	0.6420	0.6356	0.6482	0.6532	0.6226	0.6156	0.0102	0.0103
0.8	0.6443	0.6379	0.6416	0.6465	0.6186	0.6115	0.0170	0.0174
0.9	0.6452	0.6387	0.6371	0.6423	0.6153	0.6081	0.0212	0.0215
1.0	0.6452	0.6388	0.6341	0.6388	0.6125	0.6051	0.0236	0.0240

Table 1a. Comparison of added mass coefficients for a submerged sphere ($h=2a$, $Fn=U/(ga)=0.4$, $\nu_c a=0.3906$)

νa	λ_{11}		λ_{22}		λ_{33}		λ_{13}	
	A	N	A	N	A	N	A	N
0.1	0.0035	0.0035	0.0025	0.0023	0.0062	0.0063	0.0181	0.0184
0.2	0.0275	0.0279	0.0155	0.0153	0.0450	0.0460	0.0360	0.0367
0.3	0.0722	0.0781	0.0376	0.0380	0.1205	0.1237	0.0249	0.0253
0.4	0.0871	0.0884	0.0595	0.0605	0.1454	0.1513	-0.0891	-0.0937
0.5	0.0371	0.0380	0.0631	0.0644	0.0975	0.1013	-0.0695	-0.0712
0.6	0.0275	0.0280	0.0599	0.0609	0.0850	0.0879	-0.0592	-0.0604
0.7	0.0242	0.0245	0.0548	0.0557	0.0769	0.0793	-0.0502	-0.0511
0.8	0.0230	0.0233	0.0492	0.5000	0.0703	0.0725	-0.0420	-0.0428
0.9	0.0225	0.0228	0.0438	0.0444	0.0645	0.0665	-0.0348	-0.0355
1.0	0.0222	0.0225	0.0388	0.0393	0.0593	0.0612	-0.0285	-0.0291

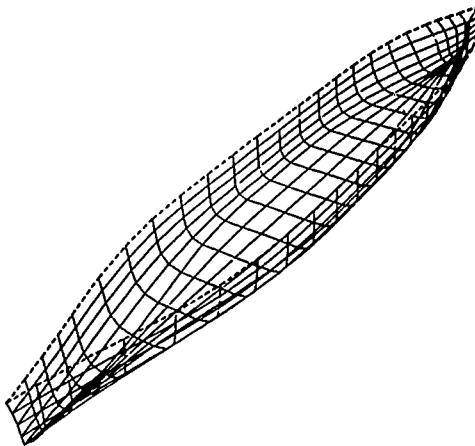
Table 1b. Comparison of damping coefficients for a submerged sphere ($h=2a$, $Fn=U/(ga)=0.4$, $\nu_c a=0.3906$)

$\nu_0 a$	$ F_1 $		$ F_2 $		$ F_3 $	
	A	N	A	N	A	N
0.1	1.0669	1.0633	1.0789	1.0859	1.5441	1.5411
0.2	0.8434	0.8402	0.8601	0.8626	1.2345	1.2342
0.3	0.6957	0.6950	0.6828	0.6846	0.9640	0.9610
0.4	0.5560	0.5548	0.5395	0.5407	0.7678	0.7661
0.5	0.4449	0.4437	0.4299	0.4306	0.6119	0.6107
0.6	0.3559	0.3548	0.3444	0.3449	0.4889	0.4881
0.7	0.2851	0.2840	0.2768	0.2772	0.3916	0.3911
0.8	0.2286	0.2278	0.2232	0.2233	0.3145	0.3143
0.9	0.1837	0.1828	0.1801	0.1802	0.2530	0.2530
1.0	0.1478	0.1470	0.1457	0.1456	0.2039	0.2042

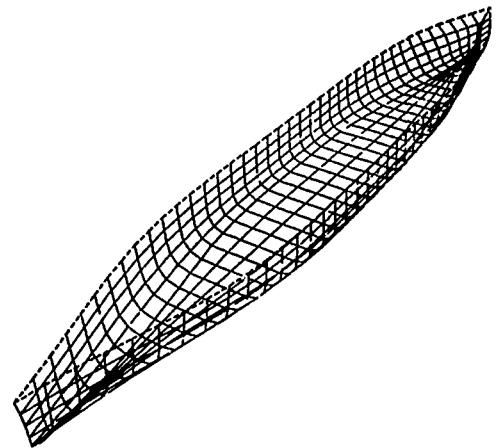
Table 2. Comparison of exciting forces on a submerged sphere
 $(h=2a, Fn=U/(ga)=0.4, \nu_0 a=0.2937, \beta=0.75\pi)$

As an application of this analysis to a surface ship, we have calculated results for a series 60 hull with block coefficient 0.7. We first investigated convergence by assuming a rigid free surface condition, and using two meshes on one half of the ship hull: with 168 elements and 567 nodes and with 280 elements and 935 nodes, as shown in figure 1. The second of these meshes is substantially finer than those used by others in earlier published work. We found that the former provides results within 3.1% and 5.3% of the finer mesh results for added mass in heave and pitch

respectively, while these two meshes give virtually identical area and volume for the ship. Next we calculated the hydrodynamic coefficients by using the translating pulsating source Green's function in equation (22), with the source strength in equation (21) based on the rigid free surface calculation. This has the advantage of providing a much more rapid calculation of source strength, and is related to the approximate method used by Newman (1961) for a submerged ellipsoid. The results from the coarse mesh are shown in figures 2 and 3.



(a) Coarse mesh (567 nodes)



(b) Fine mesh (935 nodes)

Figure 1. Mesh for Series 60 hull

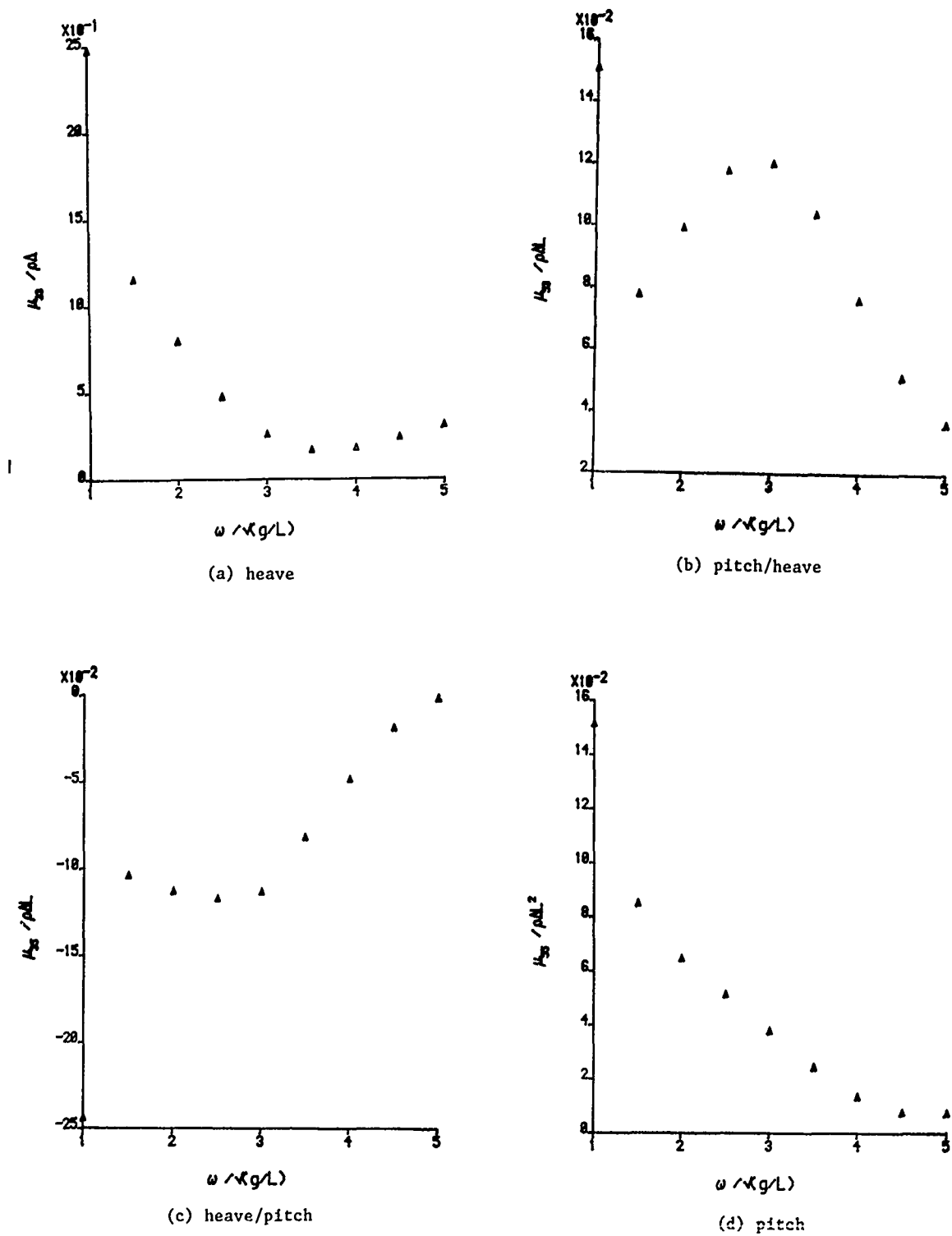


Figure 2. The added masses of the series 60 ($C_b=0.7$) at $Fn=0.2$

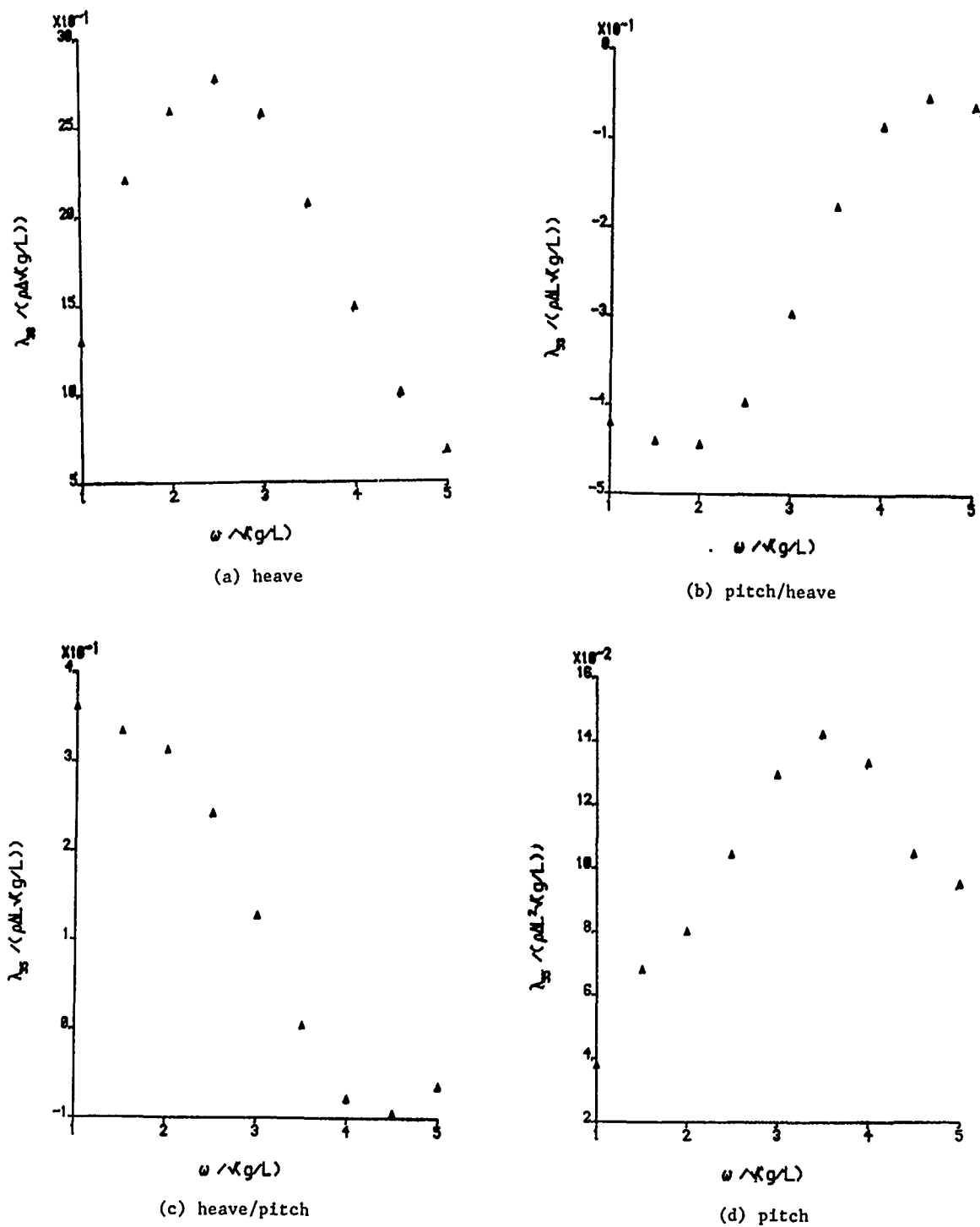


Figure 3. The damping coefficients of the series 60 ($C_b=0.7$) at $Fn=0.2$

5. Conclusions

The hydrodynamic problem of a surface ship advancing in regular waves at constant forward speed is analysed based on the linearized velocity potential theory and using the boundary integral technique. The numerical techniques introduced have been found to be effective in overcoming some difficulties encountered previously. A major remaining difficulty is the evaluation of the Green function when both source and field points are near the free surface, which appears to be the direction towards which further work in this area should be directed.

References

- Brard, R. "The representation of a given ship form by singularity distributions when the boundary condition on the free surface is linearized", J. Ship Res., Vol. 16, pp.79-92, (1972)
- Chang, M.S. "Computation of three-dimensional ship-motions with forward speed", 2nd Int. Conf. on Num. Ship Hydrodyn., pp.124-135, University of California, Berkeley, (1977)
- Guevel, P. and Bougis, J. "Ship-motions with forward speed in infinite depth", Int. Shipbuilding Prog., Vol. 29, pp.1-3-117, (1982)
- Inglis, E.B. and Price, W.G. "A three dimensional ship motion theory-comparison between theoretical predictions and experimental data of the hydrodynamic coefficients with forward speed", Trans. R.I.N.A., Vol. 124, pp.141-157, (1981)
- King, B.K., Beck, R.F. and Magee, A.R. "Seakeeping calculations with forward speed using time-domain analysis", 17th Symp. on Naval Hydrodyn., The Hague, The Netherlands, (1988)
- Kobayashi, M. "On the hydrodynamic forces and moments acting on an arbitrary body with a constant forward speed", J.S.N.A. Japan, Vol. 150, pp.61-72, (1981)
- Korvin-Kroukovsky, B.V., and Jacobs, W.R. "Pitching and heaving motions of a ship in regular waves", Trans. SNAME, Vol. 65, pp. 590-632, (1952)
- Li, H.B., Han, G.M. and Mang, H.A. "A new method for evaluating singular integral in stress analysis of solids by the direct boundary element method", Int. J. Num. Meth. Eng., Vol. 21, pp.2071-2098, (1985)
- Newman, J.N. "The damping of an oscillating ellipsoid near a free surface", J. Ship Res. Vol. 5, pp.44-58 (1961)
- Newman, J.N. "The theory of ship motions", Adv. Appl. Mech., Vol. 18, pp. 221-283, (1978)
- Noblesse, F. "Integral identities of potential theory of radiation and diffraction of regular waterwaves by a body", J Eng. Math., Vol.17, pp.1-13, (1983)
- Ogilvie, T.F. and Tuck, E. O. "A rational strip theory for ship motions" Rep. no. 013, Dept. of Naval Architecture and Marine Eng., University of Michigan, (1969)
- Salvesen, N., Tuck, E.O. and Faltinsen, O.M. "Ship motions and sea loads", Trans. SNAME, Vol. 78, pp.250-287, (1970)
- Sclavounos, P.D "The unified slender-body theory: ship motions in waves", 15th Symp. Naval Hydrodyn., O.N.R., Washington, (1985)
- Timman, R. and Newman, J.N. "The coupled damping coefficients of a symmetric ship", J. Ship Res., Vol.5, pp.1-7, (1962)
- Wu, G.X. and Eatock Taylor, R. "Hydrodynamic forces on submerged oscillating cylinders at forward speed", Proc. Roy. Soc. London, Vol. A414, pp.149-170, (1987a)
- Wu, G.X. and Eatock Taylor, R. "A Green's function form for ship motions at forward speed", Int. Shipbuilding Prog. Vol. 34, pp. 189-196, (1987b)
- Wu, G.X. and Eatock Taylor, R. "Radiation and diffraction of water waves by a submerged sphere at forward speed", Proc. Roy. Soc. London, Vol. A417, pp.433-461, (1988)

DISCUSSION

by R. Huijsmans

The authors are to be congratulated on their treatment of the full forward speed diffraction problem. We at MARIN have the experience that using the exact Green's function for the translating oscillating source as was studied by eg Bougis, Inglis needs a very careful treatment of the panel sizes. In the above mentioned studies only very coarse grids were used. In recent calculations at our Institute, we calculated added mass and damping of a series 60 ship with the number of panels increasing up to 856. Apart from the very large computational burden the results for the added mass and damping did not seem to converge really with increasing panel sizes. This was especially the case when the pressure distribution was examined. Our opinion is that there is conflicting requirement regarding the stationary and the oscillating part of the Green's function with respect to the panel sizes, especially when the forward speed is not very large.

1) Does the authors have the some experience regarding the statement made above?

2) Can the authors give some indication of the type of computer they used and computer time they have used for the non-zero speed case? Especially when comparing with the zero speed case.

3) Does the authors have some idea/indication how the local hydrodynamic quantities, like pressure and velocities behave when increasing the number of panels?

Author's Reply

We thank Dr. Huijsmans for his interesting comments. From our experience using quadratic boundary elements for the problem, we are certainly not surprised that using 850 or so constant elements to represent the series 60 hull did not always provide satisfactory results. Our own coarse mesh used 1085 nodes for the submerged hull (the numbers in Fig.1 referring to one half of the hull), and the finer mesh 1789 nodes. Like Dr. Huijsmans we have been looking at various ways of overcoming the conflicting requirements at small forward speed, and some of our thoughts on this are to be published elsewhere[A1].

We do not yet have an efficient algorithm for the Green function, and the computing time therefore still quite long. For the series 60

results given in Figs.2 and 3, they range from about 2000 to 7000 seconds per frequency on a CRX 1, with the longer runs corresponding to results at higher frequencies. We also run these programs on a Microvax II, and have to wait a few days for results at one frequency!

We have not evaluated pressures and local kinematics for the case of the body with forward speed. But we would expect to draw similar conclusions to those given in Eatock Taylor and Sincok[A2].

[A1] Wu, G.X. and Eatock Taylor, R.: The Hydrodynamic Force on an Oscillatory ship with Low Forward Speed, J. of Fluid Mech. to appear 1990).

[A2] Eatock Taylor, R. and Sincok, P.: Wave Upwelling Effects in TLP and Semi-submersible Structures, Ocean Engineering 16, pp.281-306 (1989).

DISCUSSION

by G. Jensen

Isoparametric elements are associated with numerical integration. Could you please give some more details about the computation of the velocities and may be higher derivatives on the body?

Author's Reply

The first order derivatives of the velocity potential on the body surface (and hence the fluid velocities at any point on the surface) can be obtained from the nodal solutions, using the shape functions, together with the known normal derivatives. Thus uses

$$\frac{\partial \Phi}{\partial \xi} = \frac{\partial \Phi}{\partial x} \frac{\partial x}{\partial \xi} + \frac{\partial \Phi}{\partial y} \frac{\partial y}{\partial \xi} + \frac{\partial \Phi}{\partial z} \frac{\partial z}{\partial \xi}$$

$$\frac{\partial \Phi}{\partial \eta} = \frac{\partial \Phi}{\partial x} \frac{\partial x}{\partial \eta} + \frac{\partial \Phi}{\partial y} \frac{\partial y}{\partial \eta} + \frac{\partial \Phi}{\partial z} \frac{\partial z}{\partial \eta}$$

$$\frac{\partial \Phi}{\partial n} = \frac{\partial \Phi}{\partial x} n_x + \frac{\partial \Phi}{\partial y} n_y + \frac{\partial \Phi}{\partial z} n_z$$

to solve for the derivatives of Φ in the x, y and z directions.

This approach can not be used directly to obtain the higher order derivatives. As discussed in the paper, however, it may only be the integrated effect of such derivatives that is required on the body surface, and in some circumstances this can be obtained by alternative means.

On the Numerical Solution of the Turbulent Flow-Field past Double Ship Hulls at Low and High Reynolds Numbers

G. D. Tzabiras and T. A. Loukakis
National Technical University of Athens
Athens, Greece

ABSTRACT

Turbulent flow calculations have been carried out for SSPA 720 double model at a low (5×10^6) and a high (5×10^8) Reynolds number. The partially parabolic algorithm was adopted to solve the complete momentum equations and k- ϵ model was used for the Reynolds stress modelling. At the low Reynolds number, results for a whole field solution are compared to those obtained by experimental input amidships. Comparisons are also made between low and high Reynolds calculations and conclusions concerning scaling laws are derived.

1. Introduction

Advanced numerical methods, developed during the last few years [1] have been applied with encouraging results for the calculation of the turbulent flow-field past the stern of double ship models. Most of them are based on the simultaneous solution of the velocity and the pressure field (the latter being essential at the thick boundary layer region) and use zero, one or two-equation turbulence models. Although the next step seems to be the development of methods which take into account the free surface effect and the presence of a propeller, there is still a lot of useful numerical investigation to be made on double hulls. Two of the most important problems in this investigation are the simultaneous solution of the whole flow-field past a ship hull as well as the behaviour of the numerical solution at high Reynolds numbers, which is the case with real practical interest.

In the present work both of the above problems have been worked out for the case of the SSPA 720 model, for which extended experimental information is available [2], [3]. The model has been numerically tested at a low Reynolds number of 5×10^6 , which corresponds to the test conditions and at a high Reynolds number of 5×10^8 , which corresponds to a full size ship. At the low Re No numerical results at the stern region, obtained by either using input conditions amidships from experimental data or solving the complete flow field around the ship hull, have been compared to experimental results. Moreover, the pressure coefficients at the bow region predicted by the viscous solver have been compared to measurements and to predictions from a potential

flow solution. The purpose of these exercises is to provide some insight with regard to the applicability of the method to the actual problem of ship design, for which no experimental input data is available.

The high Re No numerical experiment is obviously the more important from the practical point of view. Although experiments at such high Re Nos. do not exist, comparisons of the velocity profiles, skin friction and pressure coefficients to those predicted at the low Reynolds number can illustrate the trends of the differences between the two solutions. In this respect it is important to see if some flow phenomena (such as the strong cross flow reversal or the rapid changes in the velocity profiles around a stern frame) which occur at low Reynolds numbers are substantially less intense at a high Reynolds number. Moreover comparisons can be made between the resistance components (viscous pressure and skin friction) in order to test various assumptions concerning the scale effect, when extrapolating model test data.

The method applied in the present work is basically the fully elliptic algorithm reported in [4], which solves the complete Reynolds equations on the physical 3-D space using a sequence of locally orthogonal curvilinear coordinate systems. The Reynolds stresses are modelled in this code by the standard two-equation k- ϵ turbulence model.

2. The Numerical Method

2.1 Governing Equations

For the numerical solution of the transport equations around the ship hull the computational domain is covered by a sequence of 2D orthogonal curvilinear grids as described in [5]. The latter are generated on transverse sections by the conformal mapping method [6] taking into account the local non-orthogonality at the intersection of the section contour and the waterplane [7]. Interpolated sections, needed for grid refinement along the ship, can be easily generated by cubic interpolation between the transformation coefficients of adjacent sections. Representative 2D grids used in the present calculations are shown in Fig.1 for some sections along the model. In this figure the origin $X=0$ of the longitudinal axis coincides with the midship section.

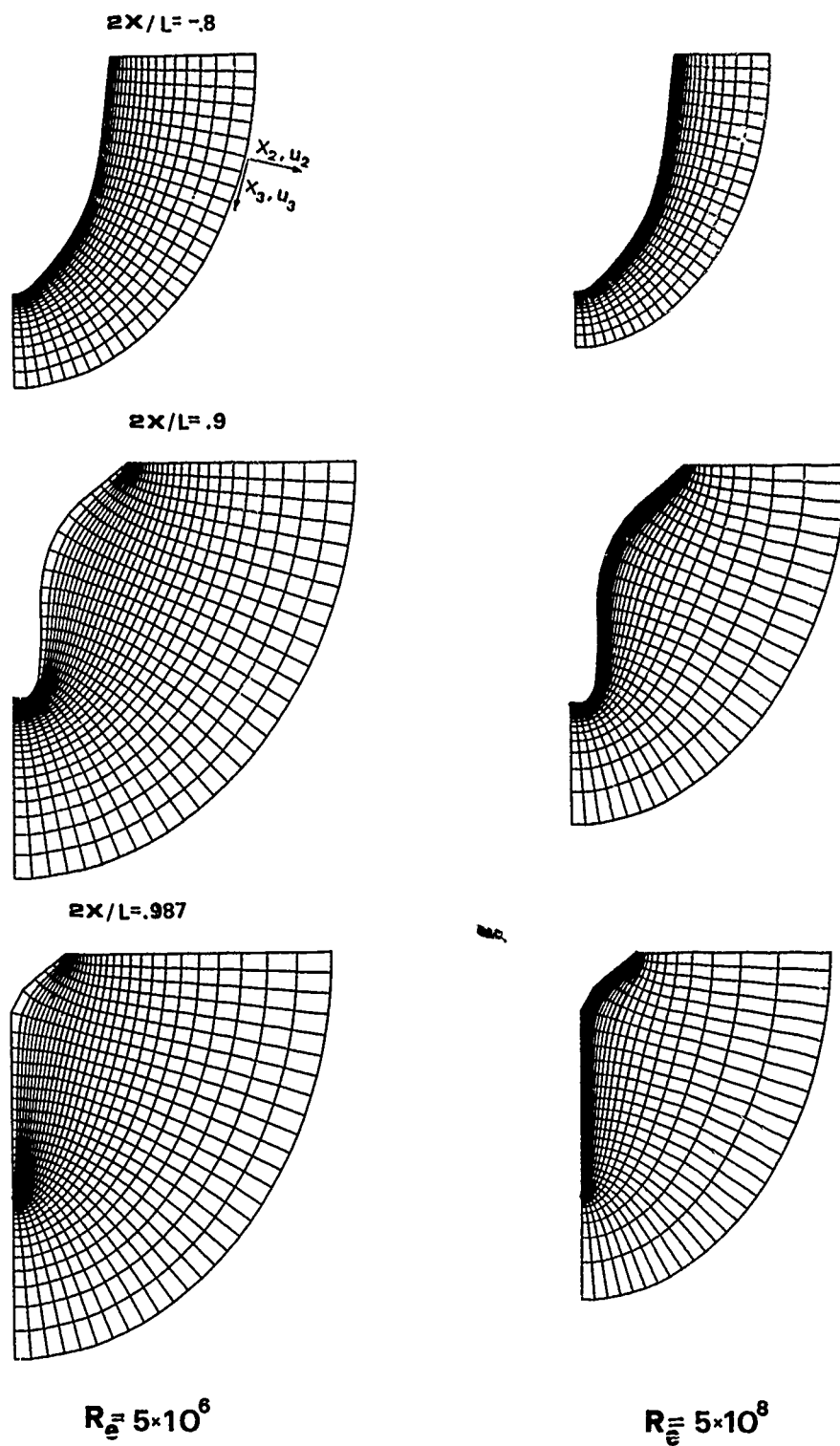


Fig. 1 Orthogonal curvilinear grids at various sections

A local 3D orthogonal curvilinear co-ordinate system corresponds to each 2D grid generated as above, whose two co-ordinate lines coincide with the grid lines and the third one is normal to the section plane. In a general orthogonal curvilinear system (x_1, x_2, x_3) with metrics (h_1, h_2, h_3) , where the indices i, j, l are in cyclic permutation, the complete u_i momentum (Reynolds) equation is written as

$$\begin{aligned} C(u_i) = & -\frac{1}{\rho} \frac{1}{h_1} \frac{\partial P}{\partial x_1} + u_j^2 K_{jj} + u_l^2 K_{ll} - u_j u_l K_{jl} \\ & - u_j u_l K_{lj} + (\sigma_{jj} - \sigma_{ll}) K_{jj} + (\sigma_{ll} - \sigma_{jj}) K_{ll} \\ & + \sigma_{jj} (2K_{jj} + K_{ll}) + \sigma_{ll} (2K_{ll} + K_{jj}) + \frac{1}{h_1} \frac{\partial \sigma_{jj}}{\partial x_1} \\ & + \frac{1}{h_j} \frac{\partial \sigma_{jj}}{\partial x_j} + \frac{1}{h_l} \frac{\partial \sigma_{ll}}{\partial x_l} \end{aligned} \quad (1)$$

where $C(u_i)$ shows the convection terms of the u_i velocity component, that is

$$C(u_i) = \frac{1}{h_1 h_j h_l} \left[\frac{\partial (h_j h_l u_i^2)}{\partial x_1} + \frac{\partial (h_j h_l u_i u_j)}{\partial x_j} + \frac{\partial (h_j h_l u_i u_l)}{\partial x_l} \right]$$

The stress tensor components appearing on the right hand side of equation (1) are defined as

$$\begin{aligned} \sigma_{jj} &= \mu_e \cdot 2e_{jj} = \mu_e \cdot 2 \cdot \left[\frac{1}{h_1} \frac{\partial u_j}{\partial x_1} + \frac{u_j}{h_1 h_j} \frac{\partial h_1}{\partial x_j} + \frac{u_l}{h_1 h_l} \frac{\partial h_1}{\partial x_l} \right] \\ \sigma_{jj} &= \mu_e \cdot e_{jj} = \mu_e \cdot \left[\frac{h_j}{h_1} \frac{\partial}{\partial x_1} \left(\frac{u_j}{h_j} \right) + \frac{h_l}{h_j} \frac{\partial}{\partial x_j} \left(\frac{u_l}{h_l} \right) \right] \end{aligned} \quad (2)$$

where the effective viscosity μ_e is modelled according to the isotropic eddy viscosity concept, i.e.

$$\mu_e = \mu + \mu_t \quad (3)$$

where μ is the fluid viscosity and μ_t the eddy (or turbulent) viscosity.

The curvature terms K_{ij} are expressed as

$$K_{ij} = \frac{1}{h_1 h_j} \frac{\partial h_1}{\partial x_j}$$

If the x_1 axis of the adopted co-ordinate system is parallel to the ship symmetry axis (i.e. normal to the ship sections) the following simplifications are valid:

$$h_1 = 1, \quad K_{12} = K_{21} = K_{31} = K_{13} = 0 \quad (4)$$

As already mentioned, in the present investigation the standard k - ϵ turbulence model [8] is employed for the modelling of the Reynolds stresses, that is the turbulent viscosity μ_t is calculated as

$$\mu_t = \rho C_D \cdot \frac{k^2}{\epsilon} \quad (5)$$

where k is the turbulence kinetic energy, ϵ its dissipation rate and C_D a constant equal to 0.09. Two more differential equations have to be solved in order to determine k and ϵ . These equations can be cast in the following common form:

$$\text{div} \left[\rho \Phi \vec{c} - \frac{\mu_t}{\sigma_\Phi} \text{grad} \Phi \right] = S_\Phi \quad (6)$$

where $\Phi = k$ or ϵ , $\sigma_k = 1$, $\sigma_\epsilon = 1.3$, $S_k = G - \rho \epsilon$,

$$S_\epsilon = 1.44 G \frac{\epsilon}{k} - 1.92 \rho \frac{\epsilon^2}{k}$$

and the generation term G is expressed as

$$G = 2\mu_t \left[e_{jj}^2 + e_{ll}^2 + e_{ll}^2 + 1/2 (e_{jj}^2 + e_{ll}^2 + e_{ll}^2) \right]$$

The complete equations (1) and (6) are solved numerically for all transverse sections following the finite volume approximation. A staggered grid is employed and the differential transport equations are integrated in the corresponding control volume of each variable Φ_P , resulting in an algebraic equation of the general form

$$\begin{aligned} A_P \Phi_P = & A_N \Phi_N + A_S \Phi_S + A_E \Phi_E + A_W \Phi_W + \\ & + A_D \Phi_D + A_U \Phi_U + S_\Phi \end{aligned} \quad (8)$$

where the notation P, N, S, E, W, D, U corresponds to grid points shown in Fig.2. Coefficients A_P, A_N, \dots take into account the combined effect of convection and diffusion terms modelled according to the hybrid scheme of Spalding [9]. Equations (8) form a system of algebraic equations which is solved by successive applications of the tridiagonal matrix algorithm.

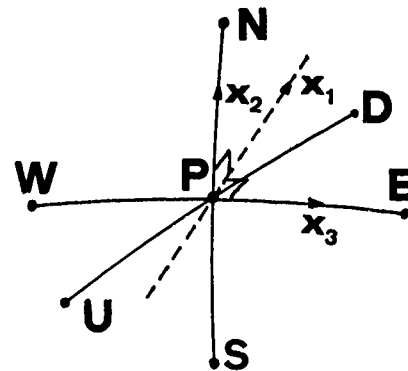


Fig.2 Specification of grid points

2.2 Boundary Conditions

The calculation domain around the ship can be divided in two sub-domains surrounding, respectively, the front and the rear part as shown in Fig. 3. In the front part domain (I), corresponding to the thin boundary layer region, relatively coarse grids can be used to model the viscous flow. Besides, high convergence rates of the numerical solution can be achieved due to the strong upstream convective influence and the existence of favorable pressure gradients over the major part of the body surface. The aft part calculation domain (II) covers the thick boundary layer region around the stern of the ship and extends in the near wake. The flow there is characterized by complex phenomena such as vortex formation, interaction between the boundary layer and the wake or adverse pressure gradients and finer grids must be applied in order to obtain reliable numerical results.

The solution of the elliptic-type algebraic equations (8) requires specification of boundary conditions at each boundary of the two sub-domains, that is at the inlet planes U, the external boundaries N, the exit planes D, the solid surface S and the symmetry planes of the ship (Fig. 3).

The input boundary values for the velocity components at the inlet plane U_I of the front part domain, located upstream the ship's bow, are calculated from the potential flow solution. The latter is obtained by the application of the classical Hess and Smith method [10] around the actual shape of the ship. The values of k and ϵ at the same boundary are assumed to be equal to zero. The corresponding input boundary conditions for the velocity components and turbulence quantities at the inlet plane U_{II} of the second calculation domain are determined from the front part flow solution by linear interpolation. At the same plane, input conditions can also be calculated by empirical formulae, whenever experimental data are available.

At the exit planes D of the domains the flow is assumed to be fully developed, corresponding to the application of Neumann conditions for each variable, except the pressure. The latter is calculated by linear extrapolation from the computed values at the previous sections.

The velocity components and the pressure at the external boundaries N are calculated from the potential flow solution, whereas for k and ϵ the normal to the boundary derivatives vanish (Neumann condition).

The turbulent flow near the solid boundary is modelled according to the standard wall function method [11] assuming that the velocity in the adjacent to the wall cells follows the logarithmic law

$$u^+ = 1/\kappa \ln(Ey^+) \quad (9)$$

where $\kappa=0.42$, $E=9.79$, y^+ the non-dimensional distance from the wall and u^+ the non-dimensional velocity parallel to it. Relation (9) is implicitly introduced in the momentum and k - ϵ equations leading to a simplified set of boundary conditions for the corresponding variables.

Finally at the two flow symmetry planes the

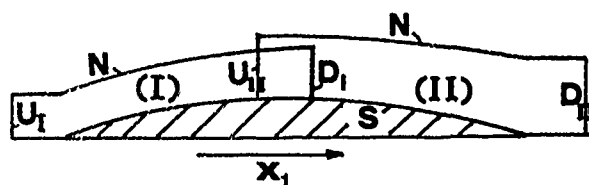


Fig.3 Definition of sub-domains

following conditions are valid:

waterplane :

$$u_3 = 0, \quad \frac{\partial \Phi}{\partial x_3} = 0, \quad \Phi = v_1, u_2, p, k, \epsilon$$

ship symmetry plane:

$$u_2 = 0, \quad \frac{\partial \Phi}{\partial x_2} = 0, \quad \Phi = u_1, u_3, p, k, \epsilon$$

2.3 The Solution Algorithm

The existence of a dominant flow direction along the co-ordinate axis x_1 , which is parallel to the symmetry axis of the ship allows for a marching solution of the governing transport equations, known as the partially parabolic algorithm [12]. The method has been originally developed to solve the parabolized Navier-Stokes equations [13] but it can also be applied to the solution of the complete form of equations (1) and (6).

According to the partially parabolic algorithm, a local numerical solution is performed in each transverse section of the calculation domain. Firstly the u_3 , u_2 and u_1 momentum equations are solved and then the pressure field and the velocity components are corrected to satisfy the continuity equation. Then the k - ϵ equations are solved and the eddy viscosities are updated using relation (5). In this local solution two-dimensional in-core storage is essentially needed for various geometrical and flow parameters, permitting the use of fine grids even with conventional computers. After solution for every section of the domain is performed, a sweep is completed and calculations start again. Several sweeps are needed until both the velocity and pressure fields converge.

The most crucial point in the application of the partially parabolic method is the treatment of the pressure field. In the present work the SIMPLE [14] algorithm has been adopted for the local correction of the pressure and the velocities. The application of this algorithm requires underrelaxation of variables during the iterative solution procedure, that is the updated value Φ of a variable is calculated as linear combination of its previous value Φ_0 and the solution Φ_n of system (8), through relation

$$\Phi = r \Phi_n + (1-r) \cdot \Phi_0$$

where r is the underrelaxation factor which is constant for every grid node of a transverse section.

Although SIMPLE and partially parabolic algorithms form the basis of the convergence procedure, it has been found that at the front part calculation domain (Fig.3) they can be combined in a different way than at the rear part domain. While at the stern region several iteration SIMPLE steps are needed to achieve local convergence, the existence of a thin boundary layer over the bow and the middle body of the ship allow a single step local solution at the front part domain. The latter results in a decrease of the computational cost by a factor of 30.

A new approach has also been applied for the numerical solution at high Reynolds numbers. The high grid densities, required to model the turbulent flow near the wall at the above numbers, lead to the generation of computational cells having their normal to the wall dimension substantially lower than the other two dimensions. This geometrical property is quite unfavorable for the pressure correction methods applied in this case, especially at the stern region where steep longitudinal and transverse pressure gradients occur. Moreover, at the same region, it is difficult to obtain the necessary grid clustering near the wall by global grid generation methods.

To overcome the aforementioned problems a special near wall treatment has been developed, as shown in Fig.4. The near wall computational cells, corresponding to the initial mesh generation, can be automatically subdivided to any desired number of sub-cells and a second computational domain is created. Two different solutions are applied in the resulting internal and external domains. For the internal solution the pressure values within the normal to the wall generated cells is assumed to be equal to the "external" value at node N. This assumption, valid near the solid boundary, is quite beneficial for the solution procedure followed: the u_3 and u_1 momentum and k - ϵ equations are solved in the sub-domain as in the external domain, while the u_2 component (normal to the wall) is calculated explicitly from the integrated continuity equation. For the external solution the SIMPLE procedure is followed. At the common boundary (B) of the two domains the boundary conditions for various variables are updated according to the adopted finite difference formulation for the convection and diffusion terms. Convergence in a transverse section is achieved after several successive internal and external solutions.

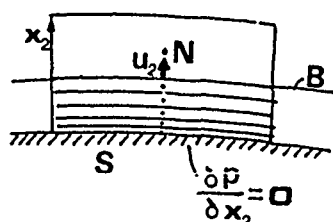


Fig.4 Near wall treatment

3. The Numerical Tests

As already mentioned in the introduction, calculations with the described methods were carried out for SSPA-720 double model.

3.1 Low Reynolds Number Computations

For the front part calculations, a $32 \times 20 \times 61$ grid was used where 32 is the number of grid nodes along the girth, 20 the number of nodes along the normal direction to the section contour and 61 the number of transverse sections. The inlet plane of the calculation domain was placed at $2X/L=1.2$ and the exit plane at $2X/L=0.30$. Convergence of the numerical solution was achieved in 80 single-step sweeps of the domain and constant underrelaxation factors equal to 0.4 were used for each variable. The values of y^+ in the adjacent to the wall cells ranged between 30 and 50, that is within the suggested region for the application of wall functions (30-150). In Fig. 6 results for the predicted C_p coefficient are compared to experiments as well as to potential flow calculations. The latter were obtained using 673 quadrilateral elements on the model surface.

For the rear part calculation domain a $32 \times 30 \times 44$ grid was used starting at $2X/L=0.1$ and extending up to $2X/L=1.4$. Both types of input boundary conditions were tested, the first one corresponding to a whole field solution and the second to an experimental input. In the second case the velocities within the boundary layer were calculated according to the $1/\eta$ power law using the experimental data of Larsson [2], while the initial values for k and ϵ were estimated by empirical formulae [5]. A total number of 35 sweeps was needed to obtain convergence in either case. An initial number of 15 iterative steps was required for local convergence in a transverse section, which reduced to one up to 5 steps during the last sweeps. The values of the underrelaxation factors at the rear part were constant and equal to 0.5 for every variable. The values of y^+ ranged between 30 and 170.

In Fig.7 computational results for the streamwise (U/U_∞) and crosswise (W/U_∞) velocity components are compared to experiments for points 11 to 17 of station $2X/L=0.9$ shown in Fig.5. In this Figure the vertical axis refers to the non-dimensionalized normal distance from the body surface with respect to the experimental [2] boundary thickness δ_e and the horizontal axis to the non-dimensionalized velocities with respect to the velocity at the edge of the boundary layer. A special output program has been developed to compute the necessary variables along normals to the body surface by linear interpolation among the stored values. It should be noted here that the experimental results were subject to blockage effects while no such effect has been accounted for in the calculations.

In Fig. 8 the calculated, non-dimensionalized by the free stream velocity, C_F coefficient is compared to the experimental data around the girth of the previous section. Results for the pressure distribution are also presented.

3.2 High Reynolds Number Calculations

The same transverse sections and girthwise points as in the case of the low Reynolds number

calculations, have been used for the high Reynolds number tests. The grid density was different only along the normal direction, as shown in Fig. 1. A $32 \times 30 \times 61$ grid was employed for the front part calculations and convergence of both the velocity and pressure fields was obtained in 150 sweeps. Constant underrelaxation factors equal to 0.3 were used for each variable. The values of y^+ ranged between 100 and 300.

A $32 \times 30 \times 44$ grid was used for the stern part calculations. The underrelaxation factors were equal to 0.5 for all variables and convergence was achieved after 25 sweeps. Two grid types have been tested, that is a coarse near the wall grid with y^+ varying from 100 to 1400 and a fine grid according to the method previously described. The latter was created by dividing the initial near wall cells in 10 sub-cells, that is a total of 40 grid nodes along the normal direction was used. Starting with the coarse grid solution, 15 more sweeps were needed to obtain convergence with the fine grid. The corresponding values of y^+ ranged between 15 and 150. Comparisons between the calculated results by the two grids as well as with the results for the low Reynolds number are presented in Figs. 9 to 12.

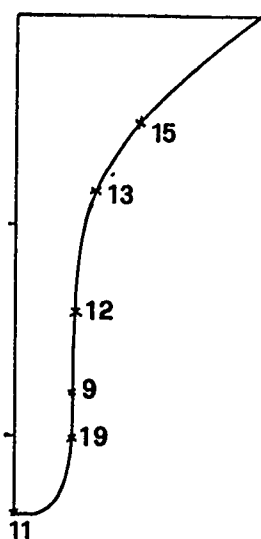


Fig.5 Distribution of calculation points at $2X/L=0.9$

4. Discussion of the Results

4.1 Low Reynolds Number

The calculated pressures along the girth of various sections of the front part of the ship compare well with the experiment values, Figs. 6 a to 6 d, when corrected for blockage effects as proposed by Larsson [15]. The agreement is good both for the viscous and the potential flow pressure calculations, with the exception of the lower part of the stern section with $2X/L=-0.93$. In this case it is believed that the discrepancy is due to the insufficient accuracy of classical Hess and Smith method near the extremities of the body.

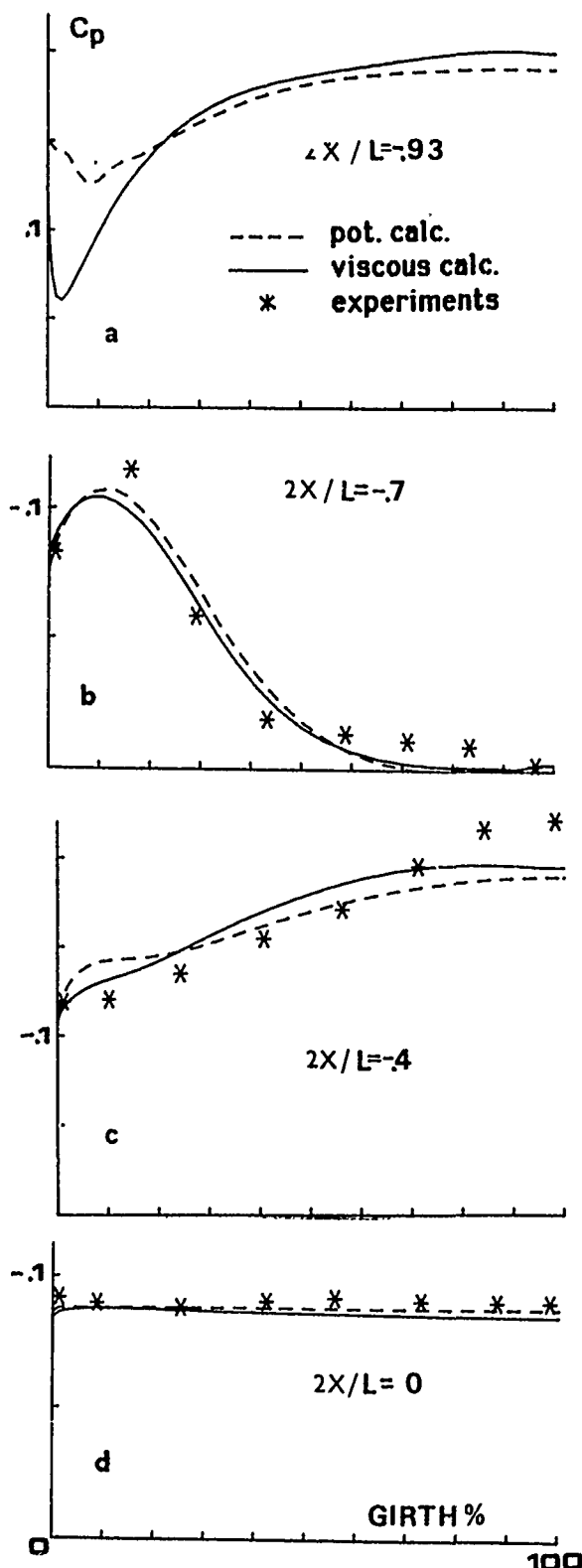


Fig.6 Comparisons of pressure coefficients at the front part for $Re=5 \times 10^6$

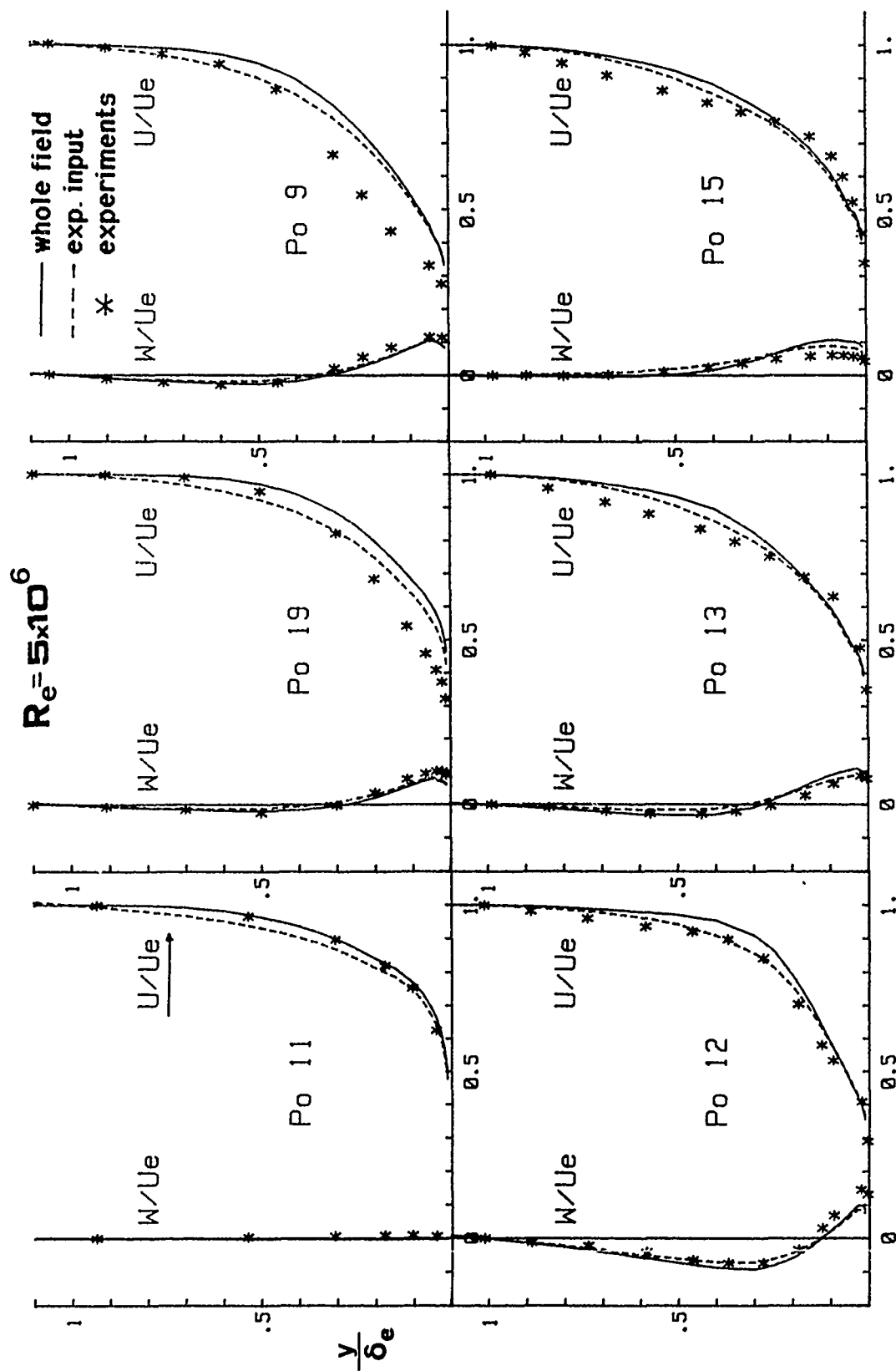


Fig. 7 Comparisons of velocity profiles. $2X/L=0.9$

Therefore it may be concluded that the proposed viscous flow calculations for the front part of the ship can be conveniently used in conjunction with the same calculation method, which is widely used for the aft end of the ship. The advantages of such calculations are that they do not require any assumptions with regard to the upstream input boundary conditions, while they automatically generate input conditions for the aft part solution. Needless to say that the method is more expensive to run than simpler approaches.

The calculated velocity profiles, using both the whole field solution and the aft part solution based on experimental input, are compared to measured values along the girth of section with $2X/L=0.9$, Fig.7.

The calculated results agree in general well with the measurement for both velocity components. The results based on experimental input are somewhat better but, as it will be pointed out later, the overall difference in the total resistance prediction between the two methods is very small. The overprediction of the streamwise velocities near the surface at points 19 and 9 can be explained by observing from fig.7 that in this region the geometry of the hull surface is rapidly changing, a situation for which the $k-\epsilon$ turbulence model is known to overpredict [1], [16], [17]. It should be noted here that the comparison between measured and calculated velocity profiles is somewhat indirect because the measured results are affected by blockage effects. However numerical calculations for the same hull [4], taking into account blockage effects, have shown that the non-dimensional velocity profiles remain practically the same.

The predicted by both aforementioned methods values for C_f along the girth of the same as above section are compared to experimental values in fig.8. The agreement is particularly good for both methods. The corresponding values for C_p , predicted by both methods shown in the same Figure, are in close agreement. No experimental pressure values exist for this section.

Finally, although there exist no measured values for the total resistance of the ship to be used for comparison purposes, it is interesting to note that the predicted by the whole field solution total resistance is 2.5% higher than the one predicted using experimental input for the stern part solution.

4.2 High Reynolds Number

The results for the velocity profiles at station $2X/L=0.9$ shown in fig. 9, allow us to conclude that the local grid refinement produces no noticeable effect, although it requires approximately 30% more computer time. The same conclusion is reached by observing Fig.10, where the girthwise results for C_p and C_f at the same station are shown. This is a remarkable result showing that at high Reynolds numbers the wall function method is valid for a wide range of y^+ . However more numerical experiments should be made for various hull forms to establish this behaviour.

The overall difference in the prediction of the total ship resistance using both methods is of the order of 1%.

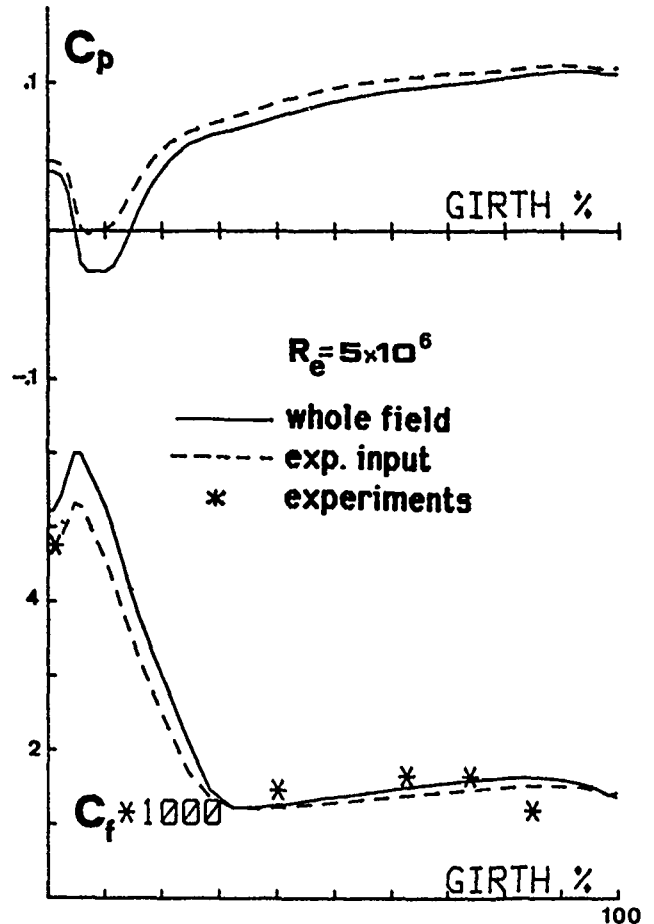


Fig.8 Comparisons of pressure and friction coefficients at $2X/L=0.9$

4.3 Comparison of the Low and High Reynolds Number Cases

The profiles of the streamwise and crosswise velocity components are shown in Fig. 11 for the station with $2X/L=0.9$. All calculations were performed using the whole field solution. The streamwise component is higher for the high Re. No., as expected, with larger differences near the keel. A more interesting conclusion is reached by observing the crosswise velocity profiles. At the high Re.No. the S shape of this profile, which exist at the low Re. No., is lost or is reduced. Consequently, the hull form is less prone to vortex formation at the high Re. No., a fact which has also been experimentally verified.

Finally the girthwise distribution of the C_p and C_f distribution for the same station are shown in Fig. 12 for both Re. Nos. In the same Figure the calculated values for pressure using potential flow are plotted. As expected the potential flow solution yields larger values than the viscous flow solutions, with the differences diminishing with increasing Re.No.

The girthwise values of C_f are more constant for the high Re.No., whereas C_f has very high values near the keel for the low Re.No.

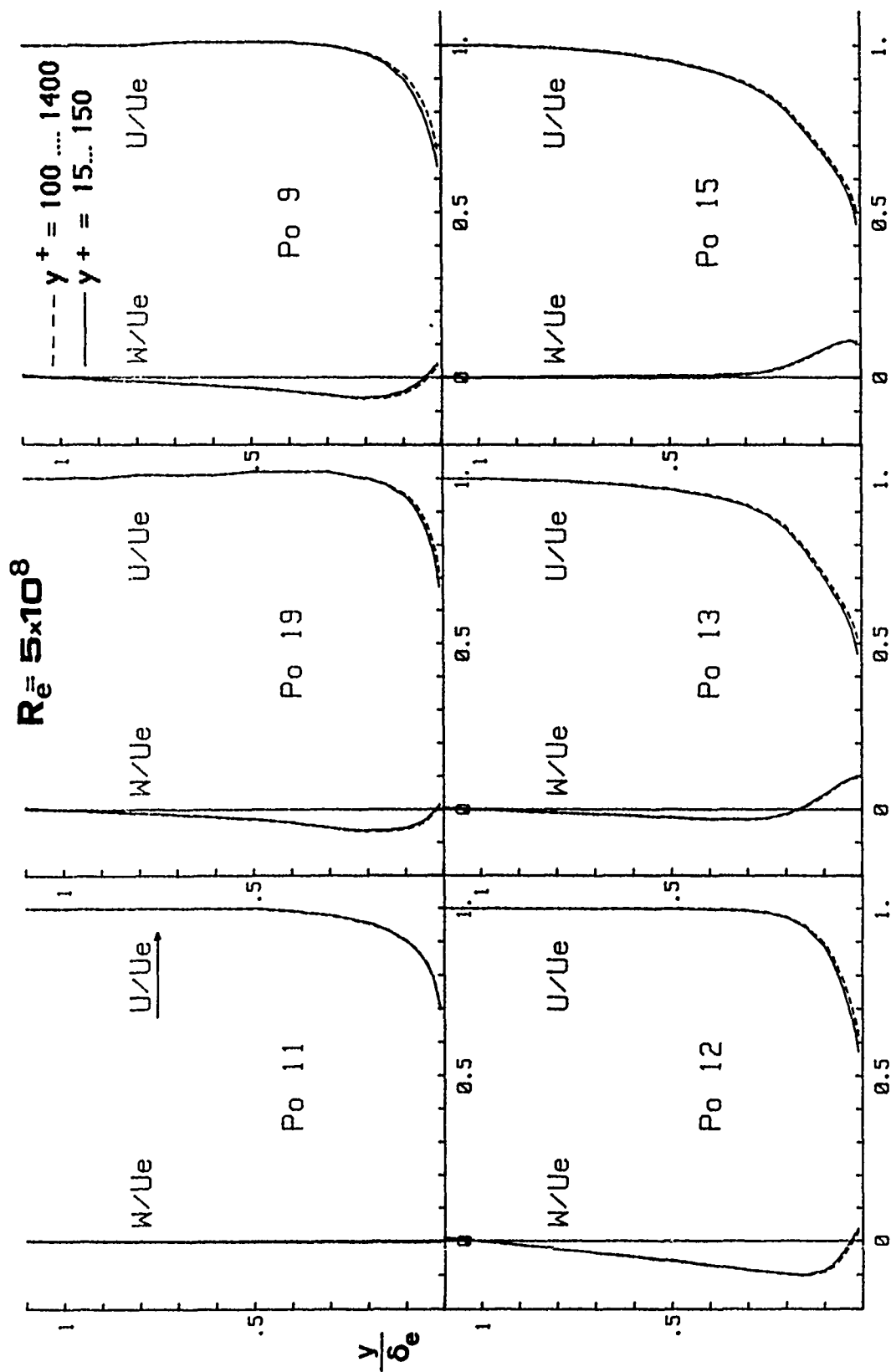


Fig.9 Comparisons of velocity profiles. $2X/L=0.9$

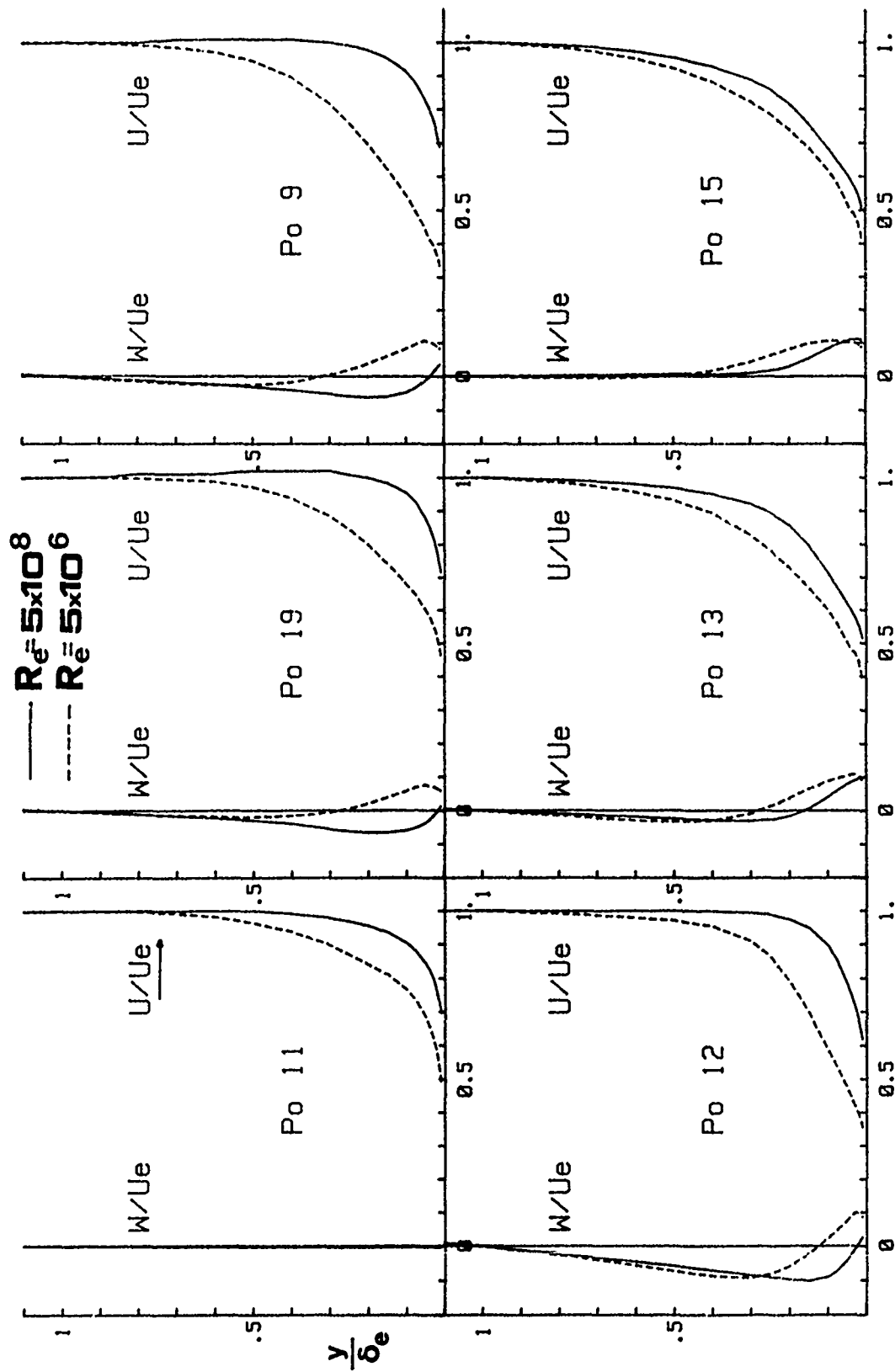


Fig.11 Comparisons of velocity profiles. $2X/L=0.9$

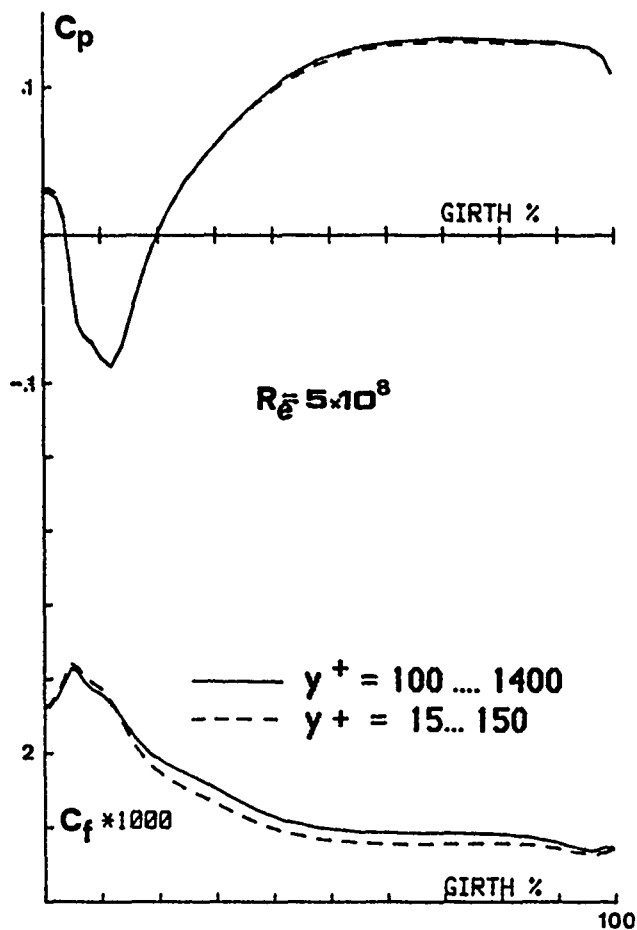


Fig.10 Comparisons of pressure and friction coefficients at $2X/L=0.9$

4.4 Scaling Laws for Ship Resistance Prediction

With regard to the independency of the numerical results to the transverse grid parameters, previous calculations with a coarser grid [4] have yielded quite similar results for the low Re No case. Similarly for the high Re No. case, a more dense grid near the body surface has produced effectively the same velocity profiles. Therefore we can assume that the numerical results are reliable in this respect. However, no such examination was performed with respect to other grid parameters, which might affect the numerical solution, e.g. the number of the hull cross sections used for the calculations especially for the low Re.No. case. Nevertheless, the numerical results seem to be good enough to allow for an attempt to demonstrate their impact on practical procedures for the prediction of the resistance of the ship. In this endeavour we are encouraged from similar trends for the case of a body of revolution

[18], for which grid independancy of the numerical solution was achieved.

As it is well known, ship resistance predictions are based on model experiments, on a flat plate friction line and on appropriate scaling laws. We now consider that the examined low Re.No case represents model tests with results shown in Table 1, which also contains the results of a corresponding full scale experiment. Since the free surface effect has been neglected, this pair of experiments is thought to be conducted at a Froude No equal to, say, 0.15.

If we now use both the form factor (κ) method and Froude's method, each in combination with both the I.T.T.C. and the A.T.T.C. friction lines, we can derive Table 2.

Then, it can be concluded that none of the above combinations predicts the ship resistance adequately and that the form factor method underpredicts, but it is closer to the calculated ship resistance than the Froude method, which overpredicts.

Needless to say that the numerical methods presented herein can be easily used for the direct prediction of the ship resistance, a fact which necessitates full scale experiments to validate their accuracy.

Finally, it should be mentioned that a complete set of calculations for a hull form require approximately 60 hours of computer time on a MicroVAX II machine, ammount which can be reduced to about 2 hours on a modern RISC technology workstation.

REFERENCES

1. Patel, V.C., "Ship stern and wake flows: Status of experiment and theory", 17th ONR Symposium, The Hague (1988).
2. Larrson, L., "Boundary layers of ships (Three-dimensional effects)", Ph.D.Thesis, Chalmers University of Technology, Göteborg (1975).
3. Lofdahl, L., "Measurement of the Reynolds stress tensor in the thick three-dimensional boundary layer near the stern of a ship model", Ph.D.Thesis, Chalmers University of Technology, Göteborg (1982).
4. Tzabiras, G., "On the calculation of the 3-D Reynolds stress tensor by two algorithms", Second International Symposium on Ship Viscous Resistance, Göteborg (1985).
5. Tzabiras, G. and Loukakis, T., "A method for predicting the flow around the stern of double ship hulls", International Shipbuilding Progress, No 345, pp 94-105 (1983).
6. von Kerczek, C. and Tuck, E.O., "The representation of ship hulls by conformal mapping functions", J.S.R., Vol.13, No.4, pp.284-298 (1969).
7. von Kerczek, C. and Stern, F., "The representation of ship hulls by conformal mapping functions: Fractional maps", J.S.R., vol.27, No.3, pp. 158-159 (1983).

8. Launder, B.E. and Spalding, D.B., "The numerical computation of turbulent flows", *Comput. Methods in Appl. Mech. and Eng.*, vol.3, pp.269-289 (1974).

9. Spalding, D.B., "A novel finite-difference formulation for different expressions involving both first and second derivatives", *Int.J. Numer. Methods in Eng.*, vol.4, pp. 551-559 (1972).

10. Hess, J.L. and Smith, A.M.O., "Calculation of potential flow about arbitrary bodies", *Prog.Aeronaut.Sci.*, vol.8, pp.1-138 (1966).

11. Rastogi, A.K. and Rodi, W., "Calculation of general three-dimensional boundary layers", *AIAA J.*, vol.16, pp.151-159 (1978).

12. Prats, V.S. and Spalding, D.B., "Numerical computation of the flow in curved ducts", *Aeronaut. Q.*, Vol.26, pp.219-232 (1975).

13. Abdelmeguid, A.M., Markatos, N.C.G. and Spalding, D.B., "A method of predicting three-dimensional turbulent flows around ship hulls", 1st Int.Symposium on Ship Viscous Resistance, Göteborg (1978).

14. Patankar, S.V. and Spalding, D.B., "A calculation procedure for heat, mass and momentum transfer in three-dimensional parabolic flows", *Int.J. Heat and Mass Transfer*, vol.15, pp.1787-1806 (1972).

15. Larsson, L. (editor), "SSPA-ITTC workshop on ship boundary layers", Göteborg, 1980.

16. Tzabiras, G., "Numerical and experimental investigation of the flow field at the stern of double ship hulls", Ph.D. Thesis, N.T.U.A. (1984).

17. Tzabiras, G., "A numerical investigation of the turbulent flow-field at the stern of a body of revolution", *J.Appl.Math.Modelling*, vol.1, pp.45-61, (1987).

18. Tzabiras, G. and Garofallidis, D., "Prediction of the resistance characteristics of an axisymmetric body with a propeller model", to be presented in PRADS-89 Conference, Varna.

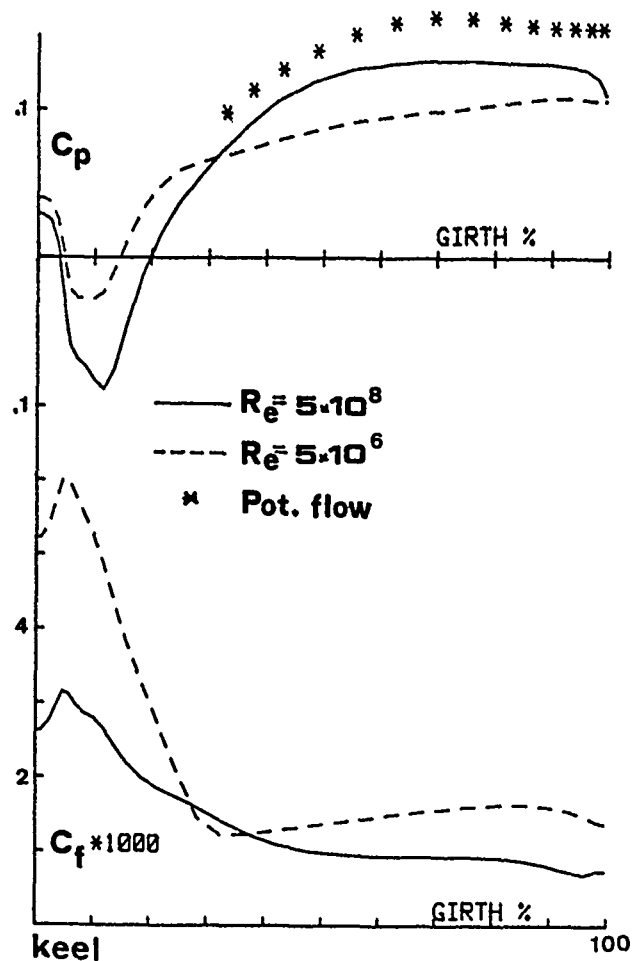


Fig. 12 Comparisons of pressure and friction coefficients at $2X/L=0.9$

Table 1: Calculated resistance coefficients

	Re = 5×10^6	Re = 5×10^8
C_T	4.754×10^{-3}	2.560×10^{-3}
C_p	1.024×10^{-3}	0.77×10^{-3}
C_F	3.73×10^{-3}	1.79×10^{-3}

Table 2: Calculation of ship total resistance coefficient by the form factor and Froude method

	$C_{TM} \times 10^3$	$C_{FM} \times 10^3$	K	$C_R \times 10^3$	$C_{FS} \times 10^3$	$C_{TS} \times 10^3$	$C_{TS} \times 10^3$ computed	% Diff.
form factor plus ITTC friction line	4.754	3.397	0.399	—	1.671	2.21	2.56	-13.6
form factor plus ATTC friction line	4.754	3.294	0.443	—	1.671	2.32	2.56	- 9.4
Froude's method plus ITTC f.l.	4.754	3.397	—	1.357	1.671	3.028	2.56	+ 17
Froude's method plus ATTC f.l	4.754	3.294	—	1.460	1.671	3.13	2.56	+ 22

Computation of Viscous Flow around a Propeller-Shaft Configuration with Infinite-Pitch Rectangular Blades

F. Stern and H. T. Kim
The University of Iowa
Iowa, USA

Abstract

A viscous-solution method is set forth for calculating marine-propeller flow fields. An overview of the computational method is given, and some example results for both laminar and turbulent flow are presented and discussed with regard to the flow physics, for the idealized geometry of a propeller-shaft configuration with infinite-pitch rectangular blades. It is shown that the flow exhibits many of the distinctive features of interest, including the development and evolution of the shaft and blade boundary layers and wakes, and tip, passage, and hub vortices. Comparisons are made with results from a lifting-surface propeller-performance program, to aid in evaluating the present method, which show that the present method accurately predicts the blade loading, including viscous effects, and clearly displays the ability to resolve the viscous regions in distinction from the inviscid-flow approach.

Introduction

Propeller-type flow fields are encountered in a wide variety of engineering problems, e.g., in the propulsion of marine vehicles, airplanes, and helicopters, in turbomachinery, and in inert and reacting swirl-flow systems. The present study concerns the development of a viscous-solution method for the analysis of incompressible propeller flows. Of particular interest are marine propellers which are unique because they operate in the thick stern boundary layer and wake such that the flow field is interactive, i.e., the propeller-induced flow is dependent on the hull flow which is itself altered by the presence of the propeller. More specifically, here we are primarily concerned with the propeller-induced flow; however, the present study is an outgrowth of a larger project concerning propeller-hull interaction and, upon extension, is expected ultimately to handle entire configurations.

Presently, only potential-flow methods are available for calculating practical marine-propeller flow fields (for a recent review see Kerwin [1]). Lifting-surface methods are available for both steady and unsteady flows (e.g., Kerwin and Lee [2]). Also, surface-panel methods have been developed for steady flow (e.g., Hess and Valarezo [3]). These methods suffer from two major problems: first, they rely on the incorrect assumption that the propeller operates in an infinite ideal fluid, but with a specified spatially varying inflow which represents the hull boundary layer and wake; and second, the results, including the propeller thrust and torque, are very sensitive to the specification of the geometry of the trailing-vortex wake sheet which requires a viscous-flow analysis for its prediction. Consistent with the first problem, the agreement with experimental thrust and torque data for nonuniform inflow has not been satisfactory. Also, the predicted pressure distributions, even for uniform inflow, do not show overall good agreement with experimental data (ITTC [4]). A complete evaluation of the theory has been hampered by the lack of knowledge of the effective inflow which is usually assumed to be the nominal wake of the bare hull.

Relatively little work has been done concerning viscous effects for rotating propeller blades. Most of the studies pertain to boundary-layer development and are restricted to laminar flow and idealized geometries (Morris [5]). Only one study has considered practical geometries and flow conditions (Groves and Chang [6]). In general, these methods suffer due to the inaccuracy of the pressure distributions predicted by inviscid-flow methods and are not easily extendable into the wake. Similar difficulties with this approach have been encountered in turbomachinery applications. Viscous effects have also been studied with regard to the tip-vortex generation process utilizing the parabolized Navier-Stokes equations (most recently, de Jong et al. [7]).

Most work on propeller-hull interaction assumes that the interaction is inviscid in nature and has focused separately on either propeller influence on hull resistance (thrust deduction) or on hull boundary layer and wake (effective wake). Recently, Stern et al. [8,9] have developed a comprehensive viscous-flow approach to propeller-hull interaction in which a viscous-flow method for calculating ship stern flow (Chen and Patel [10]) is coupled with a propeller-performance program in an interactive and iterative manner to predict the combined flow field; hereafter referred to as the interactive approach. A body-force distribution is used to represent the propeller in the viscous-flow method. The steady-flow results show good agreement with experimental data and indicate that such an approach can accurately simulate the steady part of the combined propeller-hull flow field. Although the unsteady-flow results generally follow the trends of available data, these indicate the limitations of this approach for simulating the complex blade-to-blade flow. The work of Stern et al. [8,9] is precursory to the present work.

Most of the relevant work from related applications is for high-speed flow in which shock waves have a dominating influence; therefore, the focus of these studies is, in general, quite different from that of the marine-propeller application. The most closely related work is that done to develop energy efficient turboprops and for turbomachinery applications (see Kim [11] for a more complete discussion, including references). Although advanced inviscid- and viscous-flow methods are under development, in most cases, incompressible-flow calculations are either not possible without major modifications or require the use of the pseudo-compressibility concept. In its usual form, the latter precludes time-accurate unsteady-flow calculations, although some recent studies have shown promising results for such extensions through the use of subiterations. Lastly, concerning related applications, the helicopter and swirl-flow calculations are helpful with regard to tip vortices and swirling jets and wakes, respectively; but, here again, involve large differences in both flow conditions and geometry.

It is apparent from the foregoing that present methods for calculating marine-propeller flow fields are inadequate for analyzing the detailed flow structures such as the development and evolution of the unsteady blade boundary layers and wakes, blade-to-blade flow, hub and tip vortices, and overall propeller wake. Furthermore, even the most advanced computational fluid dynamics methods from related applications are either inapplicable or require major modifications to handle marine propellers. This overall situation motivated the present study.

In the following, propeller-flow phenomena are described to aid in understanding the nature of the flow as well as the differences between the present and interactive approaches. Also, the rationale for selecting the present geometry, i.e., a propeller-shaft configuration with infinite-pitch rectangular blades (figure 1) is discussed, including its advantages and shortcomings. Next, an overview of the computational method is provided. Then, some example results are presented and discussed with regard to the flow physics, including the computational grid and conditions and calculations for both laminar and turbulent flow. Subsequently, comparisons are made with results from a lifting-surface propeller-performance program, to aid in evaluating the present method. Finally, some concluding remarks are made. The details of the computational method and the complete results, including additional calculations to study the influences of a thick-inlet boundary layer, the propeller angular velocity, and the blade number, as well as comparisons with some additional relevant experimental and computational studies are provided by Kim [11].

Propeller-Flow Phenomena

Figure 2 displays sketches of both the circumferential-average and blade-to-blade flow for the relatively simple case of a propeller-shaft configuration. The circumferential-average flow (figure 2a) clearly displays the expected features based on physical considerations, i.e., axial-velocity U increase (overshoot) and negative radial-velocity V (contraction) associated with the propeller thrust, and propeller-induced swirl W , including hub vortex, associated with the propeller torque. Also, there is a jump in pressure p across the propeller plane and a large decrease in pressure along the wake centerline due to the propeller thrust and -induced swirl, respectively, and a large increase in turbulent kinetic energy k , including two peaks, one near the wake centerline and one corresponding to the tip of the propeller blades. As discussed above, the interactive approach is able to predict accurately many details of the circumferential-average (steady) flow; however, in order to predict the complex blade-to-blade flow a more detailed representation of the propeller than the body force is required.

In comparison with the situation for the circumferential-average flow, relatively little is known concerning the complex blade-to-blade flow due, no doubt, to difficulties in performing such experiments and calculations for this type of geometry. Figure 2b displays some of the expected flow structures, including the leading-edge horseshoe, passage, tip, and hub vortices and the blade boundary layers and wakes. It should be emphasized that figure 2b is speculative. It is based on the results from the present

study to be discussed later as well as on information from other studies both for marine propellers and turboprops and for relevant geometries such as turbomachinery and simple tip and juncture flows. Here it is sufficient to point out that there are numerous fundamental issues associated with these flow structures which have yet to be explicated (see Kim [11] for a partial list). Although some of these issues are in common with other flows and applications, some are unique, and, therefore, must be addressed within the context of the marine-propeller problem.

As mentioned earlier, the goal of the present work is to develop a viscous-flow method for marine propellers, which can analyze the detailed flow structures described above. It is appropriate to initiate such an effort with as simplified a geometry as possible without sacrificing the essential physics of the flow under consideration. The geometry chosen for this purpose is a propeller-shaft configuration with infinite-pitch rectangular blades (figure 1). This geometry has the following important advantages: the grid generation is relatively simple so that the focus of attention can be given to the more basic aspects of the numerics, which is important for the initial development; fine-grid solutions are possible with the available supercomputer resources; the laminar- and turbulent-flow solutions exhibit similar flow patterns such that meaningful comparisons can be made between the two flows; and its simplicity facilitates the diagnosis of the important features of the blade-to-blade flow. Also, as will be shown below, the flow field exhibits most of the distinctive features of interest. However, it should be recognized that this geometry also has shortcomings, such as the lack of blade section geometry and, most importantly, thrust. Issues related to these aspects will be addressed in future extensions for practical geometries.

Overview of the Computational Method

Consider the viscous flow around a propeller-shaft configuration rotating at constant angular velocity ω in an infinite uniform stream with velocity U_0 (figure 1). It is assumed that the Mach and cavitation numbers are, respectively, sufficiently small and large such that the fluid is incompressible and noncavitating. Under these conditions, the flow is cyclic in both space and time. Moreover, the flow is steady and spatially cyclic at blade-to-blade intervals in noninertial coordinates, which rotate with the propeller. The situation is similar for propeller-driven axisymmetric bodies; however, for the more general circumstance of propeller-driven three-dimensional bodies the flow is unsteady, even in noninertial coordinates. For straight-ahead performance it is cyclic with angular velocity ω , whereas for maneuvering, it is noncyclic.

As mentioned earlier, the present overall computational method is based on that used previously for calculating propeller-hull interaction (Stern et al. [8,9]) in which a viscous-flow method for calculating ship-stern flow (Chen and Patel [10]) is coupled with a propeller-performance program in an interactive and iterative manner to predict the combined flow field. This is expected to facilitate future extensions for entire configurations.

In order to extend this approach for the present purpose, a number of major modifications were required, including the following: use of a noninertial coordinate system, which rotates with the propeller, and solution of the corresponding equations; implementation of boundary conditions, including periodic boundary conditions for the blade-to-blade region; adoption of an ADI scheme at each crossplane; and a complete restructuring of the program for propeller geometries, including calculations for both laminar and turbulent flow. Also, during the time period that the present work was in progress, the basic viscous-flow method of Chen and Patel [10] was upgraded for fully-elliptic calculations of the complete Reynolds-averaged Navier-Stokes equations (Patel et al. [12]). Similar modifications were made for the present work. Lastly, modifications were required to execute the program efficiently on a supercomputer.

Below, an overview of the computational method is given. A complete description is provided by Kim [11]. Also, further details of the basic viscous-flow method are provided by Chen and Patel [10] and Patel et al. [12].

Equations and Coordinate System

The Reynolds-averaged Navier-Stokes equations are written in the physical domain (figure 3a) using noninertial cylindrical coordinates (x, r, θ) rotating with constant angular velocity $\Omega = (\omega, 0, 0)$ as follows:

$$\frac{\partial U}{\partial x} + \frac{1}{r} \frac{\partial}{\partial r} (rV) + \frac{1}{r} \frac{\partial W}{\partial \theta} = 0 \quad (1)$$

$$\begin{aligned} \frac{DU}{Dt} = & -\frac{\partial}{\partial x} (p + \overline{uu}) + f_x - \frac{\partial}{\partial r} (\overline{uv}) \\ & - \frac{1}{r} \frac{\partial}{\partial \theta} (\overline{uw}) - \frac{\overline{uv}}{r} + \frac{1}{Re} \nabla^2 U \end{aligned} \quad (2)$$

$$\begin{aligned} \frac{DV}{Dt} = & \frac{W^2}{r} - 2\omega W - \omega^2 r = -\frac{\partial}{\partial x} (\overline{uv}) \\ & - \frac{\partial}{\partial r} (p + \overline{vv}) + f_r - \frac{1}{r} \frac{\partial}{\partial \theta} (\overline{vw}) - \frac{1}{r} (\overline{vw} \\ & - \overline{ww}) + \frac{1}{Re} (\nabla^2 V - \frac{2}{r} \frac{\partial W}{\partial \theta} - \frac{V}{r^2}) \end{aligned} \quad (3)$$

$$\begin{aligned} \frac{DW}{Dt} + \frac{VW}{r} + 2\omega V = & -\frac{\partial}{\partial x} (\overline{uw}) - \frac{\partial}{\partial r} (\overline{vw}) \\ & - \frac{1}{r} \frac{\partial}{\partial \theta} (p + \overline{ww}) + f_\theta - \frac{2}{r} (\overline{vw}) \end{aligned}$$

$$+ \frac{1}{Re} \left(\nabla^2 W + \frac{2}{r} \frac{\partial V}{\partial \theta} - \frac{W}{r^2} \right) \quad (4)$$

with

$$\frac{D}{Dt} = \frac{\partial}{\partial t} + U \frac{\partial}{\partial x} + V \frac{\partial}{\partial r} + \frac{W}{r} \frac{\partial}{\partial \theta}$$

$$\text{and } \nabla^2 = \frac{\partial^2}{\partial x^2} + \frac{\partial^2}{\partial r^2} + \frac{1}{r} \frac{\partial}{\partial r} + \frac{1}{r^2} \frac{\partial^2}{\partial \theta^2}$$

t is the time; U, V, W are, respectively, the longitudinal, radial, and circumferential components of mean velocity; p is the pressure; u, v, w are the Reynolds stresses; f_x, f_r, f_θ are, respectively, the longitudinal, radial, and circumferential components of the body force; and $Re = UL/\nu$ is the Reynolds number defined in terms of a characteristic velocity U and length L , which are used along with the density ρ to nondimensionalize all variables, and molecular kinematic viscosity ν . For laminar flow, equations (1) through (4) reduce to the Navier-Stokes equations by simply deleting the Reynolds-stress terms and interpreting (U, V, W) and p as instantaneous values.

Closure of the Reynolds equations is attained through the use of the standard $k-\epsilon$ turbulence model. Each Reynolds stress is related to the corresponding mean rate of strain by the isotropic eddy viscosity ν_t as follows:

$$\begin{aligned} -\overline{uv} &= \nu_t \left(\frac{\partial U}{\partial r} + \frac{\partial V}{\partial x} \right) \\ -\overline{uw} &= \nu_t \left(\frac{1}{r} \frac{\partial U}{\partial \theta} + \frac{\partial W}{\partial x} \right) \\ -\overline{vw} &= \nu_t \left(\frac{1}{r} \frac{\partial V}{\partial \theta} + \frac{\partial W}{\partial r} - \frac{W}{r} \right) \\ -\overline{uu} &= \nu_t \left(2 \frac{\partial U}{\partial x} \right) - \frac{2}{3} k \\ -\overline{vv} &= \nu_t \left(2 \frac{\partial V}{\partial r} \right) - \frac{2}{3} k \\ -\overline{ww} &= \nu_t \left(\frac{2}{r} \frac{\partial W}{\partial \theta} + 2 \frac{V}{r} \right) - \frac{2}{3} k \end{aligned} \quad (5)$$

ν_t is defined in terms of the turbulent kinetic energy k and its rate of dissipation ϵ by

$$\nu_t = C_\mu \frac{k^2}{\epsilon} \quad (6)$$

where C_μ is a model constant and k and ϵ are governed by the modeled transport equations

$$\begin{aligned} \frac{Dk}{Dt} &= \frac{\partial}{\partial x} \left(\frac{1}{R_k} \frac{\partial k}{\partial x} \right) + \frac{1}{r} \frac{\partial}{\partial r} \left(\frac{1}{R_k} r \frac{\partial k}{\partial r} \right) \\ &+ \frac{1}{r^2} \frac{\partial}{\partial \theta} \left(\frac{1}{R_k} \frac{\partial k}{\partial \theta} \right) + G - \epsilon \end{aligned} \quad (7)$$

$$\begin{aligned} \frac{D\epsilon}{Dt} &= \frac{\partial}{\partial x} \left(\frac{1}{R_\epsilon} \frac{\partial \epsilon}{\partial x} \right) + \frac{1}{r} \frac{\partial}{\partial r} \left(\frac{1}{R_\epsilon} r \frac{\partial \epsilon}{\partial r} \right) \\ &+ \frac{1}{r^2} \frac{\partial}{\partial \theta} \left(\frac{1}{R_\epsilon} \frac{\partial \epsilon}{\partial \theta} \right) + C_{\epsilon 1} \frac{\epsilon}{k} G - C_{\epsilon 2} \frac{\epsilon^2}{k} \end{aligned} \quad (8)$$

G is the turbulence generation term

$$G = \nu_t \left(2 \left(\frac{\partial U}{\partial x} \right)^2 + \left(\frac{\partial V}{\partial r} \right)^2 + \left(\frac{1}{r} \frac{\partial W}{\partial \theta} + \frac{V}{r} \right)^2 \right)$$

$$\begin{aligned} &+ \left(\frac{\partial U}{\partial r} + \frac{\partial V}{\partial x} \right)^2 + \left(\frac{1}{r} \frac{\partial U}{\partial \theta} + \frac{\partial W}{\partial x} \right)^2 \\ &+ \left(\frac{1}{r} \frac{\partial V}{\partial \theta} + \frac{\partial W}{\partial r} - \frac{W}{r} \right)^2 \end{aligned} \quad (9)$$

The effective Reynolds number R_ϕ is defined as

$$\frac{1}{R_\phi} = \frac{1}{Re} + \frac{\nu_t}{\sigma_\phi} \quad (10)$$

in which $\phi = k$ for the k -equation (7) and $\phi = \epsilon$ for the ϵ -equation (8). The model constants are:

$$C_\mu = .09, C_{\epsilon 1} = 1.44, C_{\epsilon 2} = 1.92,$$

$$\sigma_k = \sigma_\epsilon = \sigma_\nu = \sigma_\phi = 1, \sigma_\epsilon = 1.3$$

The governing equations (1) through (10) are transformed into nonorthogonal curvilinear coordinates such that the computational domain (figure 3b) forms a simple rectangular parallelepiped with equal grid spacing. The transformation is a partial one since it involves the coordinates only and not the velocity components (U, V, W) . The transformation is accomplished through the use of the expression for the divergence and "chain-rule" definitions of the gradient and Laplacian operators, which relate the orthogonal curvilinear coordinates $x^i = (x, r, \theta)$ to the nonorthogonal curvilinear coordinates $\xi^i = (\xi, \eta, \zeta)$. In this manner, the governing equations (1) through (10) can be rewritten in the following form of the continuity and convective-transport equations

$$\begin{aligned} \frac{\partial}{\partial \xi} (b_1^1 U + b_2^1 V + b_3^1 W) + \frac{\partial}{\partial \eta} (b_1^2 U + b_2^2 V + b_3^2 W) \\ + \frac{\partial}{\partial \zeta} (b_1^3 U + b_2^3 V + b_3^3 W) = 0 \end{aligned} \quad (11)$$

$$\begin{aligned} g^{11} \frac{\partial^2 \phi}{\partial \xi^2} + g^{22} \frac{\partial^2 \phi}{\partial \eta^2} + g^{33} \frac{\partial^2 \phi}{\partial \zeta^2} \\ = 2A_\phi \frac{\partial \phi}{\partial \xi} + 2B_\phi \frac{\partial \phi}{\partial \eta} + 2C_\phi \frac{\partial \phi}{\partial \xi} + R_\phi \frac{\partial \phi}{\partial t} + S_\phi \end{aligned} \quad (12)$$

where $\phi = (U, V, W, k, \epsilon)$.

Discretization and Velocity-Pressure Coupling

The convective transport equations (12) are reduced to algebraic form through the use of a revised and simplified version of the finite-analytic method (Patel et al. [12]). In this method, equations (12) are linearized in each local rectangular numerical element $\Delta \xi = \Delta \eta = \Delta \zeta = 1$, by evaluating the coefficients and source functions at the interior node P and transformed again into a normalized form by a simple coordinate stretching. An analytic solution is derived by decomposing the normalized equation into one- and two-dimensional partial-differential equations. The solution to the former is readily obtained. The solution to the latter is obtained by the method of separation of variables with specified boundary functions. As a result, a twelve-point finite-analytic formula for unsteady, three-dimensional, elliptic equations is obtained in the form

$$\phi_p = \frac{1}{1 + C_p[C_U + C_D + \frac{R}{\tau}]} \left\{ \sum_{nb} C_{nb} \phi_{nb} + C_p(C_U \phi_U + C_D \phi_D + \frac{R}{\tau} \phi_p^{n-1} - S) \right\} \quad (13)$$

where the subscript nb denotes neighboring nodes (NE:northeast, NW:northwest, etc.). It is seen that ϕ_p depends on all eight neighboring nodal values in the crossplane as well as the values at the upstream and downstream nodes ϕ_U and ϕ_D , and the values at the previous time step ϕ_p^{n-1} . For large values of the cell Reynolds number, equation (13) reduces to the partially-parabolic formulation used previously (Stern et al. [8,9]). Since equations (13) are implicit, both in space and time, at the current crossplane of calculation, their assembly for all elements results in a set of simultaneous algebraic equations. If the pressure field is known, these equations can be solved by the method of lines. However, since the pressure field is unknown, it must be determined such that the continuity equation is also satisfied.

The coupling of the velocity and pressure fields is accomplished through the use of a two-step iterative procedure involving the continuity equation based on the SIMPLER algorithm. In the first step, the solution to the momentum equations for a guessed pressure field is corrected at each crossplane such that continuity is satisfied. However, in general, the corrected velocities are no longer a consistent solution to the momentum equations for the guessed p . Thus, the pressure field must also be corrected. In the second step, the pressure field is updated again through the use of the continuity equation. This is done after a complete solution to the velocity field has been obtained for all crossplanes. Repeated global iterations are thus required in order to obtain a converged solution. The procedure is facilitated through the use of a staggered grid. Both the pressure-correction and pressure equations are derived in a similar manner by substituting equation (13) for (U,V,W) into the discretized form of the continuity equation (11) and representing the pressure-gradient terms by finite differences.

Solution Domain and Boundary Conditions

The physical and computational solution domains are shown in figure 3. It is seen that the solution domain is bounded by the inlet plane S_i ; the shaft surface S_s ; the suction and pressure sides of the blade surface S_{bs} and S_{bp} , respectively; the exit plane S_e ; the periodic symmetry planes S_{ps} and S_{pp} ; the symmetry axis L_s ; and the outer boundary S_o .

The boundary conditions on each of the aforementioned boundaries are as follows: on the inlet plane S_i , the initial conditions

for ϕ are specified from simple flat-plate solutions, initial conditions for p and p' are not required; on the shaft S_s and blade surfaces S_{bs} and S_{bp} , for laminar flow, the solution is carried out up to the actual surface where the no-slip condition is applied, for turbulent flow, a two-point wall-function approach is used; on the exit plane S_e , axial diffusion is negligible so that the exit conditions used are $\partial \phi / \partial \xi = 0$, a zero-gradient condition is used for p ; on the periodic symmetry planes S_{ps} and S_{pp} , an explicit periodicity condition is imposed, i.e., $\phi(\xi, \eta, \zeta) = \phi(\xi, \eta, \zeta + \zeta_p)$, $p(\xi, \eta, \zeta) = p(\xi, \eta, \zeta + \zeta_p)$, where ζ_p corresponds to the blade-to-blade interval; on the symmetry axis L_s , the conditions imposed are $V = W = 0$, $\partial(U, k, \epsilon, p) / \partial \eta = 0$; on the outer boundary S_o , the uniform-flow condition is applied, i.e., $U = 1$, $W = \omega r|_{S_o}$, $p = \partial(k, \epsilon) / \partial \eta = 0$.

Grid Generation

The computational grid is obtained using the technique of generating body-fitted coordinates through the solution of elliptic partial differential equations, i.e., the nonorthogonal coordinates ξ^i are related to the orthogonal coordinates x^i by the set of equations

$$\nabla^2 x^i = \frac{1}{h_1 h_2 h_3} \frac{\partial}{\partial x^i} \left(\frac{h_1 h_2 h_3}{h_i^2} \right) \quad (14)$$

where

$$\nabla^2 = g^{ij} \frac{\partial^2}{\partial \xi^i \partial \xi^j} + f^i \frac{\partial}{\partial \xi^i}$$

$$\text{and } f^i = \frac{1}{J} \frac{\partial}{\partial \xi^j} (J g^{ij}) \quad i = 1, 2, 3 \quad (15)$$

In the present context, f^i are called control functions since their specification controls the concentration of coordinate surfaces. For specified boundary conditions and control functions, equations (14) can be solved numerically to obtain the coordinates of each grid point in the physical domain.

Because of the simplicity of the present propeller geometry (figure 1), it is possible to specify the transverse and longitudinal sections of the computational domain as surfaces of constant ξ and ζ , respectively, and moreover, the three-dimensional grid is obtained by simply rotating the two-dimensional grid for the longitudinal plane. Under these conditions, equations (14) reduce substantially and can be readily solved once the control functions are specified. The control functions f^i are determined by the specified grid distributions of axial stations, radial distributions at the inlet and exit, and girthwise distributions at the inlet and on the outer boundary, respectively. These control functions were derived under the conditions $f^1 = f^1(\xi)$, $f^2 = f^2(\xi, \eta)$, and $f^3 = f^3(\zeta)$ only, which are of sufficient generality for the present application.

Results

In the following, first, the computational grid and conditions are described. Then, some example results for laminar flow are discussed to point out the essential features of the solutions. These are followed by a brief presentation of the results for turbulent flow to highlight the differences. This order and emphasis of discussion is selected since the former represent solutions to the exact governing equations, whereas the latter are dependent on the choice of turbulence model.

Computational Grids and Conditions

The geometry of the propeller-shaft configuration (figure 1; see Tables 1 and 2 of Kim [11]) was specified based on a configuration for which calculations had been previously performed, i.e., P4660 (Stern et al. [9]).

Partial views of the grid used in the calculations are shown in figures 4a,b for a longitudinal plane and a typical body cross-plane, respectively. The shaft and blade surface grid is shown in figure 1. Similar grids are used for both the laminar and turbulent calculations, but, in the latter case, the near-wall grid lines ($y^+ < 30$) are deleted in order to implement the two-point wall-function approach.

The inlet, exit, and outer boundaries are located at $x = (.54, 6)$ and $r = .9$, respectively; for laminar flow, the first grid points off the body and blade surfaces are located at $.4 < y^+ < 8$ and $1 < x^+, y^+, \text{ or } z^+ < 14$, respectively; for turbulent flow, the first grid points off the body and blade surfaces are located at $30 < y^+ < 230$ and $40 < x^+, y^+, \text{ or } z^+ < 190$, respectively; 62 axial grid points were used, with 18 over the upstream portion of the shaft up to the blade leading edge, 11 over the blade, 14 over the remainder of the shaft from the blade trailing edge to the hub apex, and 19 over the wake; for laminar flow, 40 radial grid points were used with 22 over the blade span and 18 from the tip to the outer boundary; for turbulent flow, 36 radial grid points were used with 19 over the blade span and 17 from the tip to the outer boundary; 30 and 26 angular grid points were used for laminar and turbulent flow, respectively. In summary, the total number of grid points for the laminar and turbulent calculations are 74,400 and 58,032, respectively.

The conditions for the calculations are as follows: characteristic (shaft) length $L = 1$; characteristic (uniform-stream) velocity $U = 1$; for laminar flow, $Re_L = 2.02 \times 10^6$ and $Re_c = 1 \times 10^5$, where Re_L and Re_c are the shaft- $(= UL/\nu)$ and chord-length $(= U_c/\nu)$ Reynolds numbers, respectively; for turbulent flow, $Re_L = 6.08 \times 10^6$ and $Re_c = 3 \times 10^5$; the pro-

PELLER angular velocity $\omega = .3\pi (= 9 \text{ rpm})$ (the blade section angle of attack varies from 1.2 deg at the root to 4 deg at the tip); for laminar flow, on the inlet plane, $\delta/R_h = .111$ (where δ is the boundary layer thickness and R_h the hub radius) and there is no inviscid-flow overshoot; and for turbulent flow, on the inlet plane, $\delta/R_h = .489$, $U = .04$, and the inviscid-flow overshoot T is 1.01. The δ values are based on simple flat-plate solutions and the selected Re . For laminar flow, the Re value was selected based on the fact that many investigators have performed two-dimensional flat-plate boundary-layer and wake calculations for this same value. For turbulent flow, a reasonable value of Re was selected for which fully turbulent flow over the shaft and blades is probable. The propeller angular velocity was taken to be sufficiently low such that no separation occurs over the blades.

For the nonrotating condition, the calculations were begun with a zero-pressure initial condition for the pressure field. For the rotating condition, the complete nonrotating solution was used as the initial condition. The values of the time α and pressure α underrelaxation factors and total number of global iterations used in obtaining the solutions are .02-.1, .03-.1, and 70-100, respectively. The calculations were performed on a CRAY X-MP/48 supercomputer. The central processor unit (CPU) and storage (words) that were required for each of the solutions are about 30min. and 1-1.7M words, respectively. Note that the computer codes were 23% vectorized and optimized to achieve a 65% reduction in CPU, and that the maximum normal system storage limit is 2M words.

Laminar Flow

The laminar-flow results for both the nonrotating and rotating conditions are shown in figures 5 through 13. Figures 5, 6, and 7 show the variation of some properties in the longitudinal direction, i.e., the shaft and blade surfaces and wake pressure, the wall-shear (magnitude and angle for inertial coordinates), and the wake centerline and maximum swirl velocities, respectively. Figures 8 through 11 show the detailed results for some representative axial stations in the form of velocity and pressure profiles (i.e., ϕ vs. $Y = r/R_p$, where R_p is the propeller radius), axial-velocity contours, crossplane-velocity vectors, and axial-vorticity ω_x contours, respectively. Lastly, figures 12 and 13 show close-up views of the tip vortex and the tip-vortex trajectory, respectively. Note that, in figure 8, the ordinate is Y such that the distance from the plate is larger near the tip than near the root. Also, the labeling of each of the curves corresponds to the angular grid lines shown in figure 4b.

First, consideration is given to the results for the nonrotating condition. The

shaft and blade surfaces and wake pressure variations (figure 5) for the mid-blade plane indicate a minimal influence of the blades and are typical of trailing-edge flow in the presence of a thin boundary layer; however, at this relatively low Re (laminar flow), the adverse axial-pressure gradient associated with the closing of the body is sufficient to cause a small separation region in the vicinity of the hub apex, $.96 < x < 1.01$. Note the rapid rate of recovery of pressure in the radial direction. The pressure variations for the blade plane are similar, but clearly show the effects of the blade leading and trailing edges as well as a small displacement effect of the blade boundary layer.

The wall-shear velocity magnitude U variations (figure 6a) are consistent with those just described for the pressure. For the blade plane, there is a large reduction of U in the juncture region due to the flow retardation and also in conjunction with the relatively large boundary-layer thickness there, and a downstream shift of the region of low U associated with the flow separation as compared to the mid-blade plane. The latter is consistent with the differences in separation patterns for the blade and mid-blade planes. On the blade, initially U is larger at the mid-span than at the tip in response to the larger leading-edge pressure peak at mid-span (i.e., more favorable pressure gradient), then the trend reverses. The wall-shear velocity vector (figure 6c) is generally aligned with the axial direction except near the blade leading edge where the blade displacement effects are evident and in the separation region where the complex topological nature of three-dimensional separation is displayed.

The wake centerline velocity U_c (figure 7a) displays the extent of the separation region and the recovery of the wake. The maximum swirl velocity W_{max} is, of course, nearly zero for the nonrotating condition and not shown in figure 7b. The asymptotic forms (figure not shown) display the details of the recovery of the wake. Although the exit plane is 34 diameters downstream of the propeller plane (equivalently 5 shaft lengths downstream of the hub apex), the slope of the velocity defect of the shaft wake has not yet reached its asymptotic value. This is consistent with our previous turbulent-flow calculations. In contrast, the slope of the blade wake velocity defect is close to the asymptotic value. The exit plane is 103 chord lengths downstream from the blade trailing edge.

Lastly, for the nonrotating condition, the detailed results are discussed. The discussion to follow is based on the complete results, which include the solution profiles at all the stations designated in figure 4a; however, for brevity of presentation, only the near blade wake station is shown in figure

8. At the near-inlet station, the solution displays the characteristics of the inlet conditions, i.e., an axisymmetric, thin, laminar boundary layer. At the leading-edge and mid-chord stations, the solution shows the initiation of the blade boundary layer, including leading-edge (stagnation-point) and displacement effects. Also, the juncture flow indicates a weak leading-edge horseshoe vortex. At the trailing-edge station, the trailing-edge effects of both the blade and the shaft are predominate, including a reversal of the juncture flow. At the near blade wake station and hub apex, the solution shows the initial development of the blade wake. Here again, the effects of the shaft trailing edge are quite large. Two corner vortices are apparent near the shaft axis which are an indication of the nature of the flow within the separation region. At the near, intermediate, and far shaft-blade wake stations, the solution shows the recovery of shaft and blade wakes. The crossplane flow and pressure recover more rapidly than the axial velocity component.

Next, consideration is given to the results for the rotating condition. Referring to figure 5, in the vicinity of the hub apex and in the near wake there is a decrease in pressure due to the propeller-induced swirl. The lifting effects due to the angle of attack of the blade section are clearly evident. Note that the pressure peak is at the blade leading edge such that just upstream of the leading edge very large adverse and favorable pressure gradients occur for the pressure and suction sides of the blade, respectively, whereas just downstream of the leading edge the reverse holds true.

The wall-shear velocity magnitude U (figure 6b) shows slightly increased values over the spinning portion of the shaft and greater uniformity between the blade and mid-blade planes in the separation region as compared to the nonrotating condition. For the present conditions, the rotation parameter $R = \omega R_h / U_0$ is quite small, i.e., $R = .02$, which explains the only slight increase in U as compared to the previous calculations of Stern et al. [9]. On the blades, U is smaller on the suction than on the pressure side, in conjunction with the relatively thicker boundary layer on the suction as compared to the pressure side. Consistent with the results for the nonrotating condition, U is larger at the tip than at mid-span except near the leading edge. On the rotating section, the wall-shear velocity vector (figure 6d) shows large effects due to rotation, i.e., the flow is turned towards the direction of rotation. In the blade region, the passage vortex is evident, including its helical nature. In the separation region, the flow is completely turned in the direction of rotation which results in the aforementioned greater uniformity in the separation patterns between the blade and

mid-blade planes. Over the blade, the wall-shear velocity vector is in the axial direction, except near the tip, where the flow is outward, especially on the pressure side.

Figure 7a shows that the recovery of the wake centerline velocity U_c is slower for the rotating than the nonrotating condition. This is due to the adverse axial-pressure gradient induced by the hub vortex. Also shown is the decay of the maximum swirl velocity W_{max} in the wake (figure 7b), which is associated with the intensity and decay rate of the hub vortex. Finally, the asymptotic forms (figure not shown) indicate that the shaft wake is unaffected, the blade-wake slope is increased, and the swirl decay is relatively faster than that of the axial-velocity defect.

The detailed results vividly display the complexity of the flow for the rotating condition. Here again, the discussion to follow is based on the complete results, although only representative stations are displayed in figures 8 through 11. At the near-inlet station, the solution is similar to that for the nonrotating condition, except for the W velocity component which shows a linear increase due to the use of noninertial coordinates. At the leading edge, the solution shows the initiation of the blade boundary layer, in this case, with significant differences between the suction and pressure sides of the blade due to the influences of the aforementioned abrupt changes in the pressure gradients. Interestingly, the boundary layers on both sides of the blade are thicker for the rotating than the nonrotating condition. The tip-vortex formation initiates with flow around the tip from the pressure to the suction side. The vortical flow is asymmetric such that the tangential velocity component is larger on the suction than the pressure side, whereas the situation is reversed for the radial velocity component. The passage-vortex formation also initiates and dominates the juncture flow. At the mid-chord station and trailing edge, the effects of the pressure gradient changes are clearly displayed, i.e., on the suction and pressure sides, the flow is decelerated and accelerated, respectively. On the suction side, the boundary-layer thickness varies considerably across the span. The tip vortex has lifted off the suction-side surface such that the radial velocity component is positive on both sides. Braiding of the fluid from both the suction and pressure sides is apparent, but particle trajectories were not traced to display this phenomenon. The pressure is surprisingly uniform in view of the cross-plane flow, however, very low values are observed in the tip-vortex core. The passage vortex increases in size and its core moves towards the suction side. The axial-velocity and -vorticity contours are hook shaped near the tip due to the influences of the tip vortex. At the near blade wake station and hub

apex, the solution shows the development of the blade wakes, which indicate the characteristics of the complex mixing of the suction and pressure side three-dimensional boundary layers, including significant effects of the tip, passage, and hub vortices and the hub-induced pressure gradients. The minimum velocity in the wake migrates towards the suction side. There is a rapid recovery of the pressure-side wake such that the velocity-defect region is mainly behind the shaft and off the suction side of the blade. The blade wake becomes quite thick as it merges with the wake of the shaft and the tip vortex. There is a region of backward flow near the wake axis associated with the flow separation. The tip vortex reduces in intensity and the passage vortex merges into a large asymmetric hub vortex. Finally, at the near, intermediate, and far shaft-blade wake stations, the nature of the recovery of the wake is displayed. It is clear that the circumferential mixing is faster for the rotating than the nonrotating condition which is also the case for swirling jets.

The close-up views of the tip vortex shown in figure 12 clearly display its initiation at the blade leading edge, subsequent migration off the surface along the blade chord, and decay as it is convected and diffuses into the wake. Also, they reveal the mechanism of the tip-vortex formation. At the leading edge, nearly all of the fluid forming the tip vortex originates from the pressure side, whereas further downstream the suction side fluid is "pumped" into the tip vortex. This indicates a "braiding" process, which is often referred to as the tip-vortex roll-up. The tip-vortex trajectory is shown in figure 13.

Turbulent Flow

Some limited turbulent-flow results are shown in figures 14 and 15. The turbulent-flow results are consistent with and very similar to those for laminar flow. In general, the differences are as expected based on physical reasoning, i.e., viscous effects are confined to narrower regions and the three-dimensionality of the flow is considerably reduced for turbulent as compared to laminar flow. Also, quite apparent for turbulent flow is the reduced resolution near solid surfaces and the wake centerplane due to the present wall-function approach.

The overall trends described above with regard to the shaft and blade surfaces and wake pressure, wall-shear velocity, and wake centerline and maximum swirl velocities are quite similar; however, the pressure peak at the hub apex is considerably larger and there are some differences in the wall-shear velocity behavior due to the absence of separation. The detailed results are also quite similar. However, for the nonrotating condition the juncture effects are minimal and the

crossplane flow and pressure variations are reduced, whereas, for the rotating condition, the tip and passage vortices are larger and persist longer, the latter merges into a larger hub vortex, lower pressures are observed in the tip-vortex core, and the recovery of the wake is considerably faster. The turbulent kinetic-energy profiles show two peaks, one near the wake centerline and one corresponding to the tips of the blades.

Comparison With Results from a Lifting-Surface Propeller-Performance Program

Unfortunately, no experimental information is available for the present geometry. Therefore, to aid in evaluating the present work, comparisons have been made with some relevant experimental and computational studies, including the following topics: juncture flow which is related to the present flow in the blade-hub juncture region for the nonrotating condition; tip flow which is related to the present flow in the tip region for the rotating condition; turbomachinery flow which is related to the present blade boundary-layer and wake development and blade-to-blade flow; and propeller flow which is, of course, the topic and goal of the present study. Although in most cases, the comparisons are only qualitative due to the large differences between the topic and present geometries, they support the present results in that the predicted flow structures are similar and consistent with the results from these studies. The complete comparisons are lengthy and beyond the scope of the present paper (see Kim [11]). Herein, only the direct comparisons between the present turbulent-flow results and those from a lifting-surface propeller-performance program, i.e., PUF-2 (Kerwin and Lee [2]) will be presented.

Special modifications of PUF-2 for the present idealized geometry were not deemed necessary, and, therefore, not done. A constant pitch ratio $P/D_p = 10^5$ was used to represent the infinite pitch of the present geometry. All other geometry input data was given the same values as those for the present turbulent-flow calculations. Also, the open-water condition value was used for the advance coefficient $J = 44.44$, i.e., the effective wake due to the interaction between the propeller and the shaft boundary layer was neglected. For the wake-model parameters, the standard values for the wake pitch and zero contraction were used. A value of .005 was used for the section-drag coefficient which is based on the present calculations.

Figures 16a,b show a comparison of the chordwise and spanwise distributions of the blade loading in terms of the pressure jump (figure 16a) and section-lift coefficient (figure 16b), respectively. A large difference in the pressure jump is observed near

the leading edge. Differences are also seen in the section-lift coefficient. The viscous results show considerably larger values near the root and the tip, but smaller values for the mid-span region. The higher root loading for the viscous flow is, no doubt, a result of the increased effective angle of attack due to the oncoming shaft boundary layer. However, a part of the difference may be due to the lack of hub effects in PUF-2. The lower mid-span loading is consistent with the aforementioned differences in chordwise loading near the leading edge. The higher tip loading may be due to the reduced pressure on the suction side due to the tip vortex. Interestingly, in spite of these differences in the loading distributions, the total forces and moments show remarkably close agreement.

Figures 16c,d show a comparison of the propeller-induced velocities just upstream and downstream of the propeller at the mid-span radius. For the viscous-flow solution, the propeller-induced velocity (u,v,w) is defined as the total velocity, (U,V,W) minus the freestream ($U_0,0,0$) value. Results are shown using the blade angle coordinate $\theta = \omega t$ as the abscissa for the entire blade-to-blade region from the suction ($\theta = 0$ deg) to the pressure side ($\theta = 90$ deg).

The velocity components just upstream of the propeller (figure 16c) clearly show the effects of the leading-edge stagnation point. The u velocity components show similar trends, i.e., the point of the minimum velocity shifts to the pressure side which suggests that the stagnation point also shifts to the pressure side. The increased magnitude for the viscous solution may be due to the prescribed overshoot for the oncoming shaft boundary layer. The v velocity component is nearly zero for both results. The w velocity components also show similar trends; however, the inviscid solution indicates a stronger local effect of the leading-edge stagnation point than the viscous solution such that the circumferential-average is zero for the inviscid but not the viscous solution, i.e., the viscous solution indicates small negative preswirl.

The velocity components just downstream of the propeller (figure 16d) highlight the differences between the viscous and inviscid solutions. The inviscid u velocity component shows very small positive values from the suction to the pressure side, whereas the viscous u velocity component shows a large change from the suction to the pressure side, i.e., the viscous blade wake appears as a sharp drop on both the suction and pressure sides and the effects of the retarded suction- and accelerated pressure-side boundary layers are clearly evident. The v velocity components show similar trends, but with somewhat larger variations for the viscous solution. The w velocity components also

show similar trends, but with larger swirl for the viscous solution in spite of the smaller loading.

Concluding Remarks

The present work was motivated by the limitations of the interactive approach for simulating the complex blade-to-blade flow. This has certainly been accomplished by the present viscous-solution method, albeit for an idealized geometry. In fact, the present work provides, for the first time, a very detailed documentation of the viscous flow around a propeller for both laminar and turbulent flow. It is concluded that the present approach is capable of simulating marine-propeller flow fields, including both the propeller loading and the complex blade-to-blade flow, and should be extended for practical geometries. It is also concluded, based on the comparison of the laminar and turbulent results, that, although most aspects of the flow are governed by pressure-gradient effects, improvements in turbulence-modeling procedures, especially near-wall treatment, are important to resolve certain flow features, including transition, separation, and small-scale vortical structures such as leading-edge horseshoe and secondary vortices.

Of course, much more work needs to be done to extend the method to realistic propeller and body geometries. Some of the issues that need to be addressed are as follows. Optimum coordinates, including investigations of inertial and helical systems. Optimum grid-generation techniques for complex, three-dimensional, propeller-driven bodies, including investigations of moving, adaptive, and multi-block grids. As already mentioned, improved turbulence-modeling procedures are essential and possibly a pacesetter issue. Also, further development of solution algorithms is a necessity in order to perform the required large-scale computations even on the most advanced available supercomputers. It should be recognized, that none of these issues are trivial, on the contrary, all require substantial effort so that it is expected that the present problem will remain a challenge for many years to come.

Acknowledgements

This research was sponsored by the Office of Naval Research, Accelerated Research Initiative Program in Propulsor-Body Hydrodynamic Interactions, under Contract N00014-85-K-0347. The Graduate College of The University of Iowa and the National Center for Supercomputing Applications Academic Affiliates Program provided a large share of the computer funds.

References

1. Kerwin, J.E., (1986), "Marine Propellers," Ann. Rev. Fluid Mechanics, Vol. 18, pp. 367-403.

2. Kerwin, J.E. and Lee, C.S., (1978), "Prediction of Steady and Unsteady Marine Propeller Performance by Numerical Lifting-Surface Theory," Trans. SNAME, Vol. 86, pp. 218-253.
3. Hess, J.L. and Valarezo, W.O., (1985), "Calculation of Steady Flow about Propellers using Surface Panel Method," J. Propulsion, Vol. 1, pp. 470-476.
4. ITTC, (1984), "Report of the Propeller Committee," Proc. 17th Int. Towing Tank Conf., pp. 139-194.
5. Morris, P.J., (1981), "The Three-Dimensional Boundary Layer on a Rotating Helical Blade," J. of Fluid Mech., Vol. 112, pp. 283-296.
6. Groves, N.C. and Chang, M., (1984), "A Differential Prediction Method for Three-Dimensional Laminar and Turbulent Boundary Layers of Rotating Propeller Blades," Proc. 15th ONR Symp. on Naval Hydro., pp. 429-444.
7. deJong, F.J., Govindan, T.R., Levy, R. and Shamroth, S.J., (1988), "Validation of a Forward Marching Procedure to Compute the Tip Vortex Generation Process for Ship Propeller Blades," Proc. 17th ONR Symp. on Naval Hydro., Hague, The Netherlands.
8. Stern, F., Kim, H.T., Patel, V.C. and Chen, H.C., (1988), "A Viscous-Flow Approach to the Computation of Propeller-Hull Interaction," J. Ship Research, Vol. 32, No. 4, pp.246-262.
9. Stern, F., Kim, H.T., Patel, V.C. and Chen, H.C., (1988), "Computation of Viscous Flow around Propeller-Shaft Configurations," J. Ship Research, Vol. 32, No. 4, pp. 263-284.
10. Chen, H.C. and Patel, V.C., (1985), "Calculation of Trailing-Edge, Stern and Wake Flows by a Time-Marching Solution of the Partially-Parabolic Equations," Iowa Institute of Hydraulic Research, The University of Iowa, IIHR Report No. 285.
11. Kim, H.T., (1989), Computation of Viscous Flow Around a Propeller-Shaft Configuration with Infinite-Pitch Rectangular Blades," Ph.D. Thesis, The University of Iowa, Iowa City, IA.
12. Patel, V.C., Chen, H.C. and Ju, S., (1988), "Ship Stern and Wake Flows: Solutions of the Fully-Elliptic Reynolds-Averaged Navier-Stokes Equations and Comparisons with Experiments," Iowa Institute of Hydraulic Research, The University of Iowa, IIHR Report No. 323.

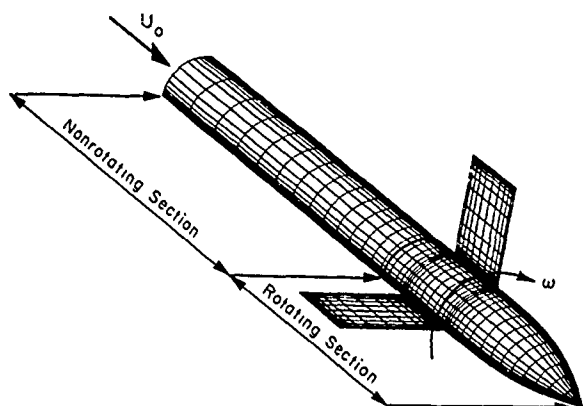
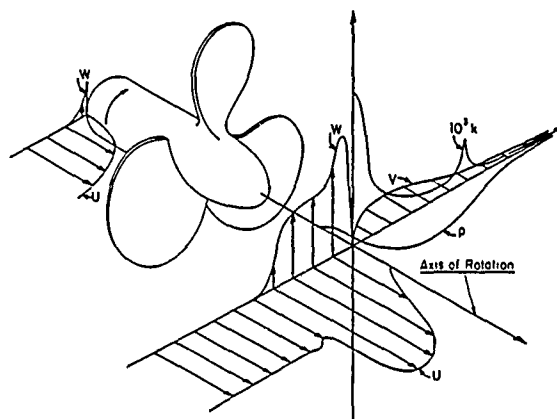
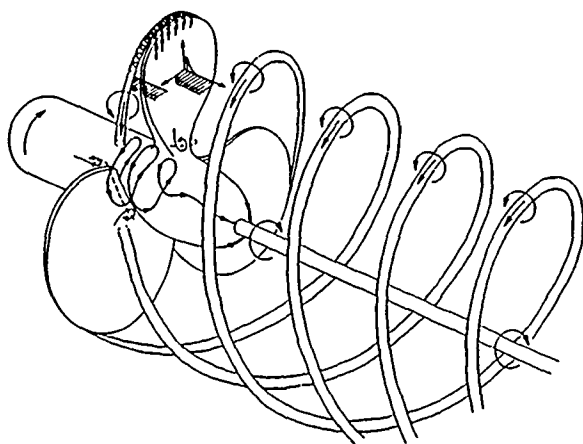


Figure 1. Propeller-shaft configuration with infinite-pitch rectangular blades.

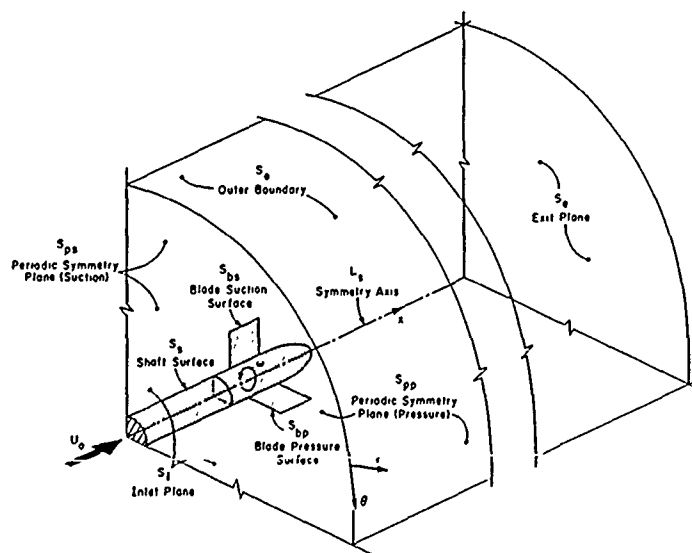


(a) circumferential-average flow

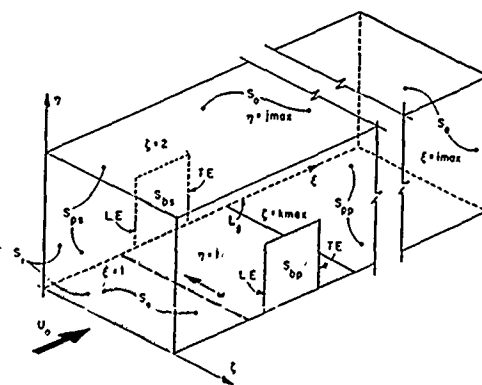


(b) blade-to-blade flow

Figure 2. Propeller-flow phenomena.



(a) physical domain



(b) computational domain

Figure 3. Solution domain.

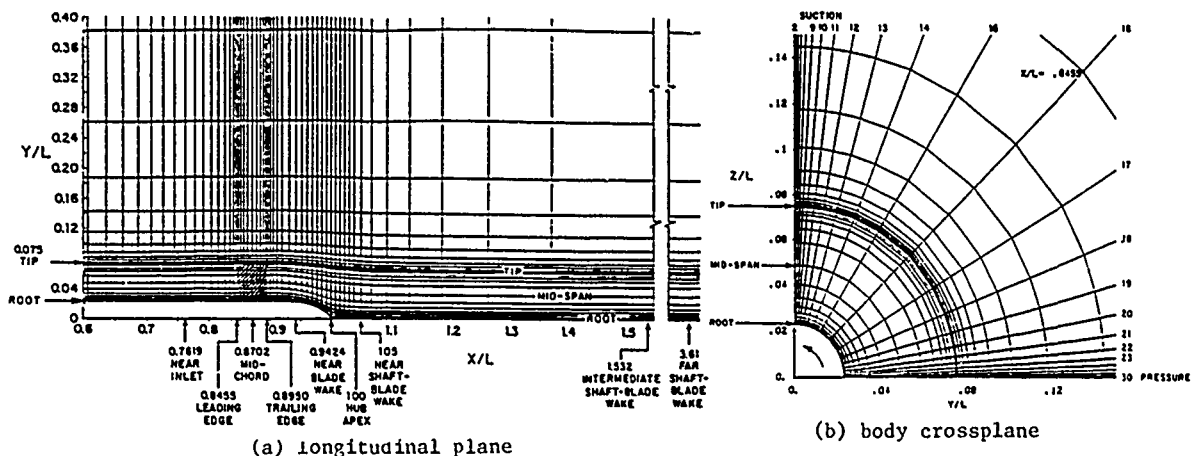


Figure 4. Computational grid,

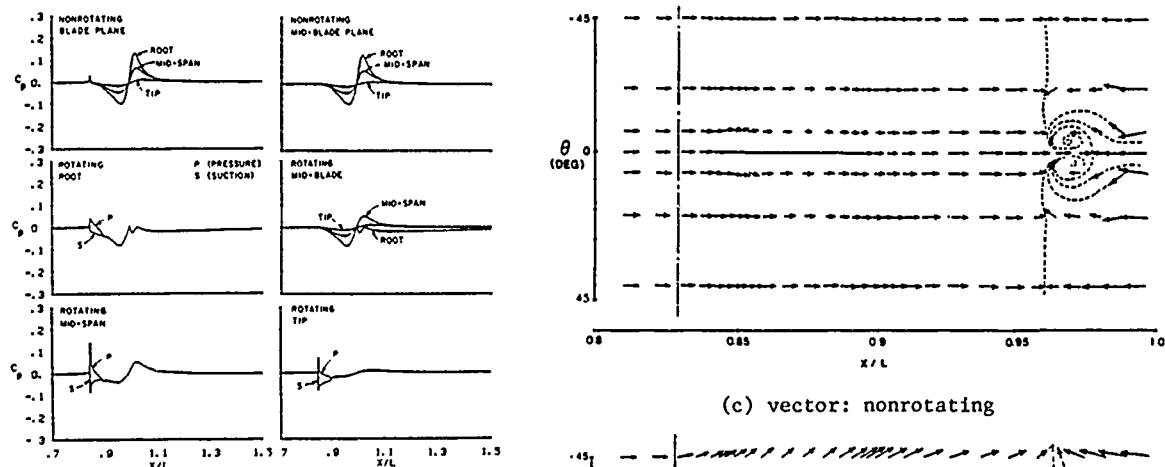


Figure 5. Shaft and blade surfaces and wake pressure: laminar flow.

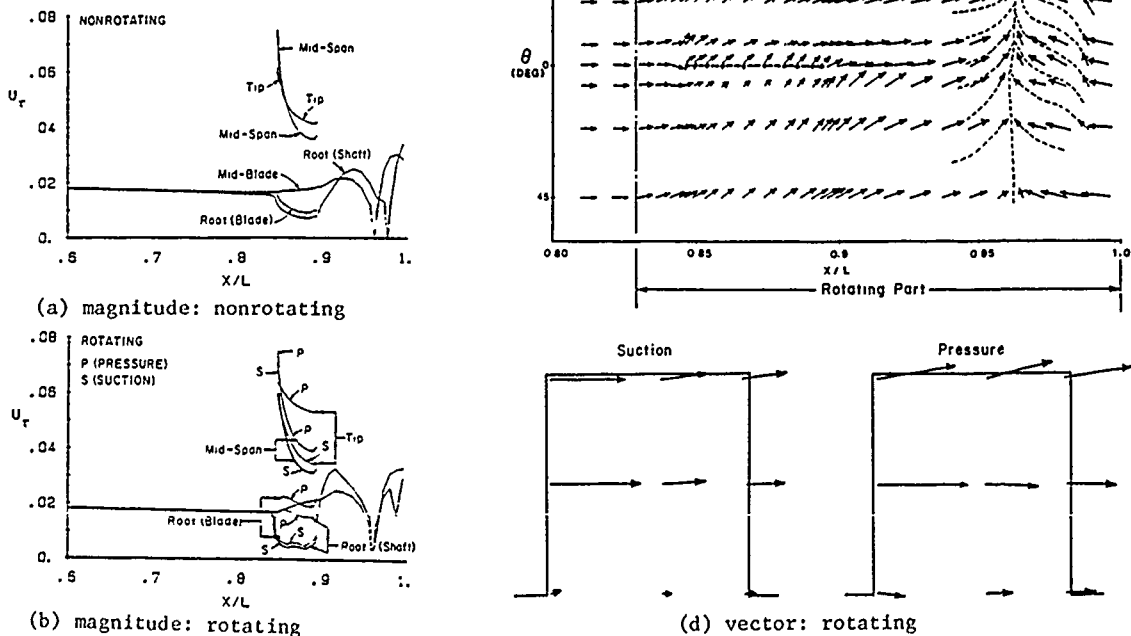
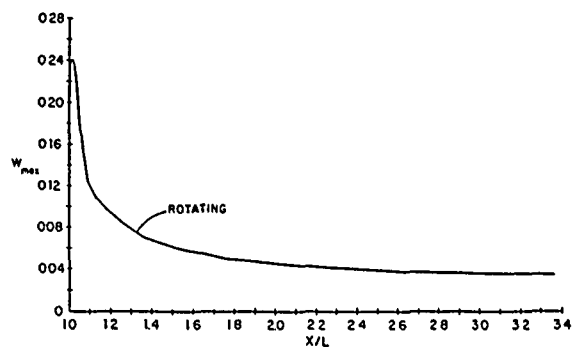
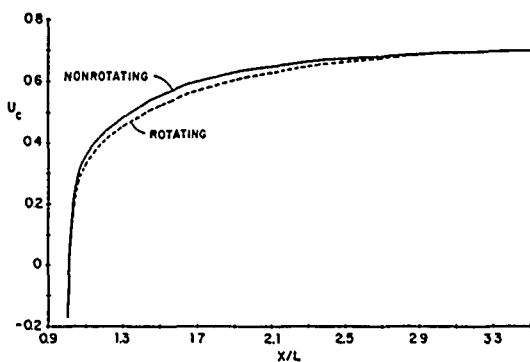


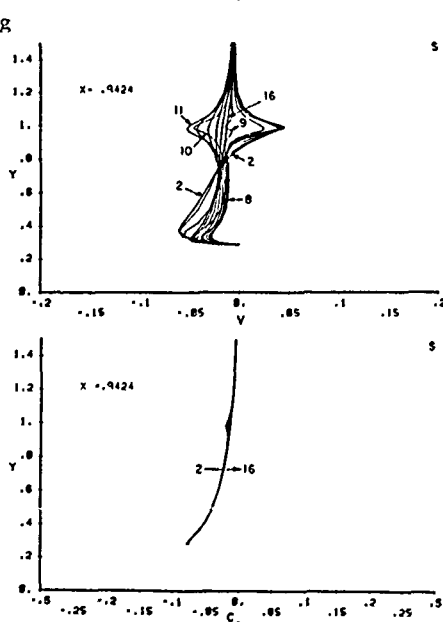
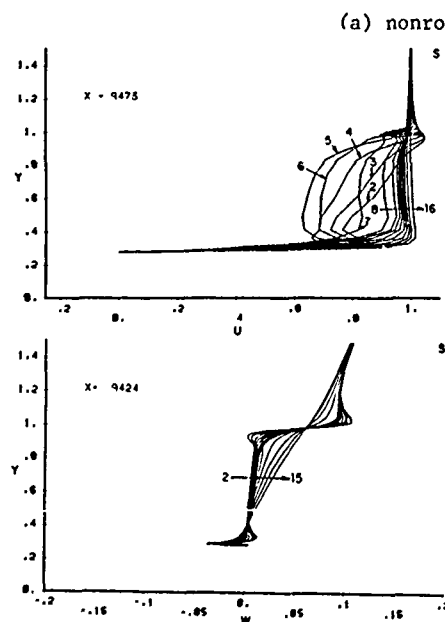
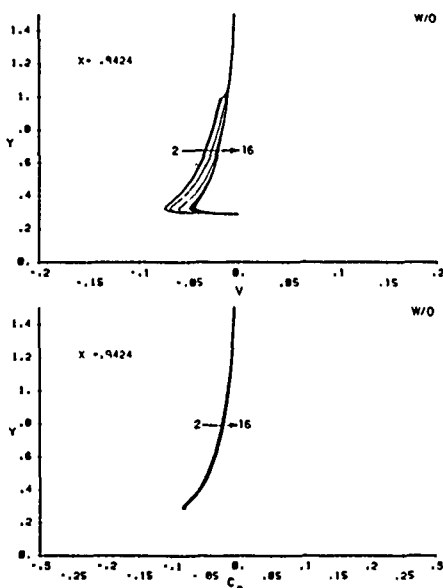
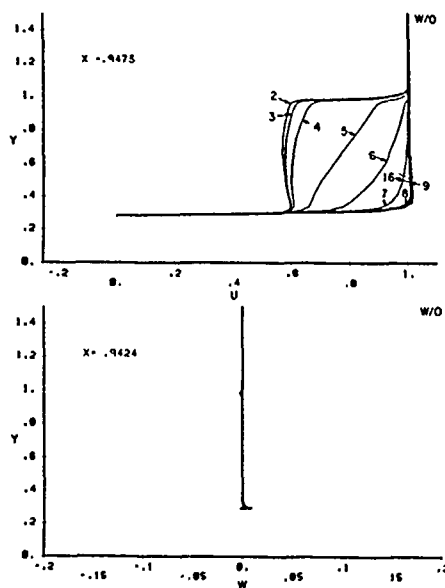
Figure 6. Wall-shear velocity: laminar flow.



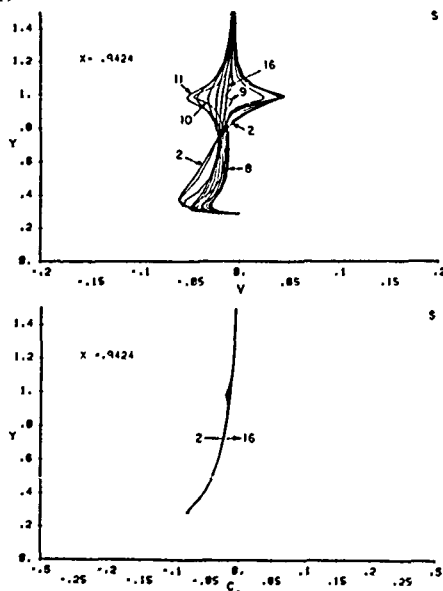
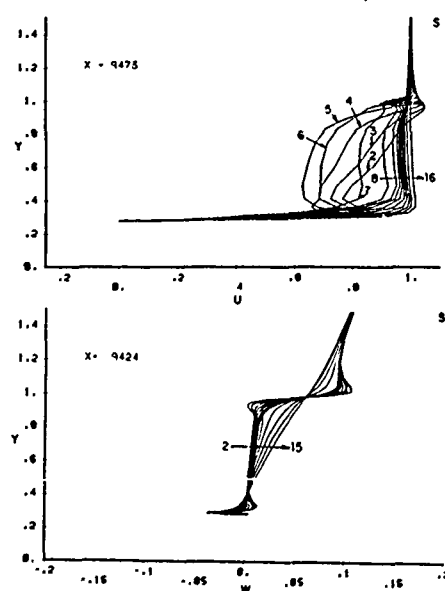
(a) centerline

(b) maximum swirl

Figure 7. Wake velocities: laminar flow.

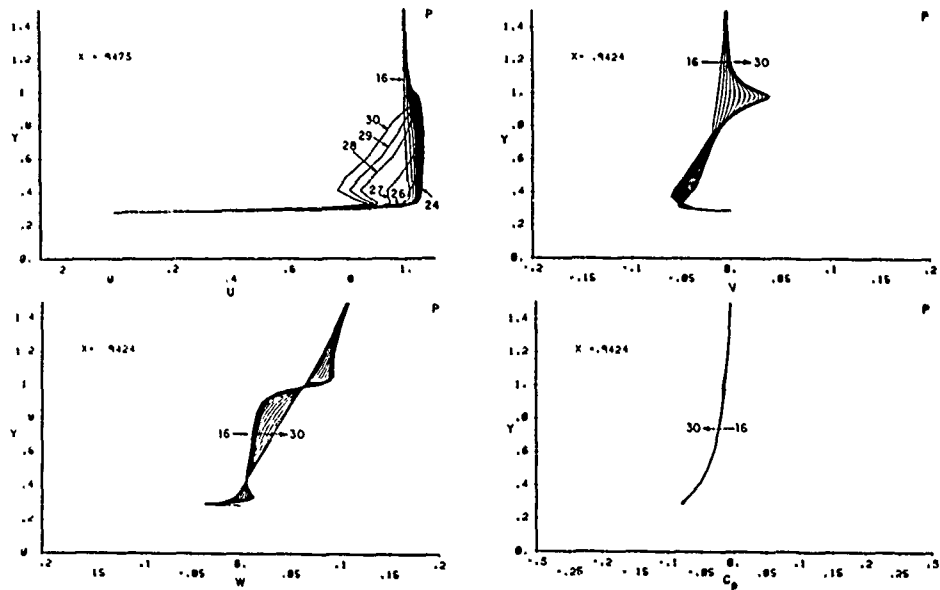


(a) nonrotating



(b) rotating: suction side

Figure 8. Velocity and pressure profiles: laminar flow.



(c) rotating: pressure side

Figure 8. (continued).

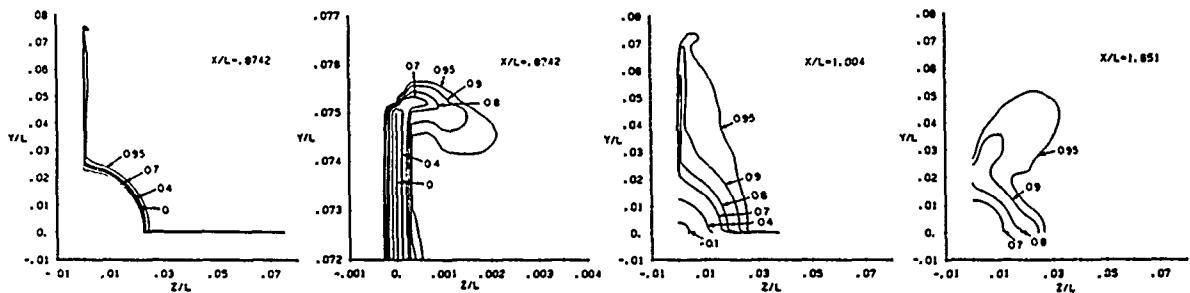


Figure 9. Axial-velocity contours: laminar flow, rotating.

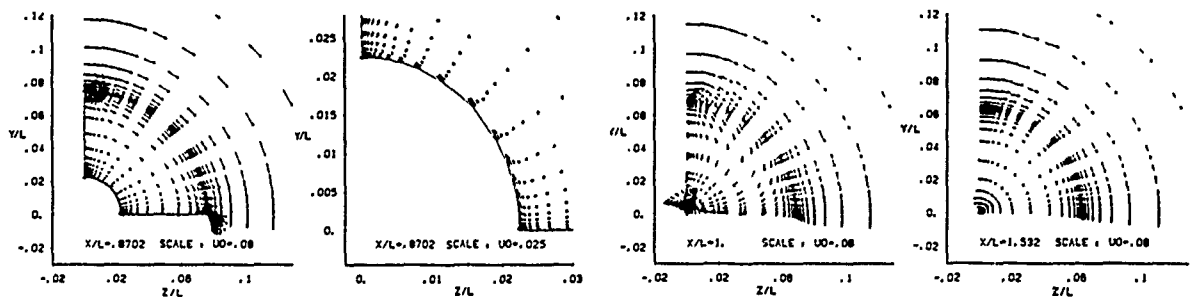


Figure 10. Crossplane-velocity vectors: laminar flow, rotating.

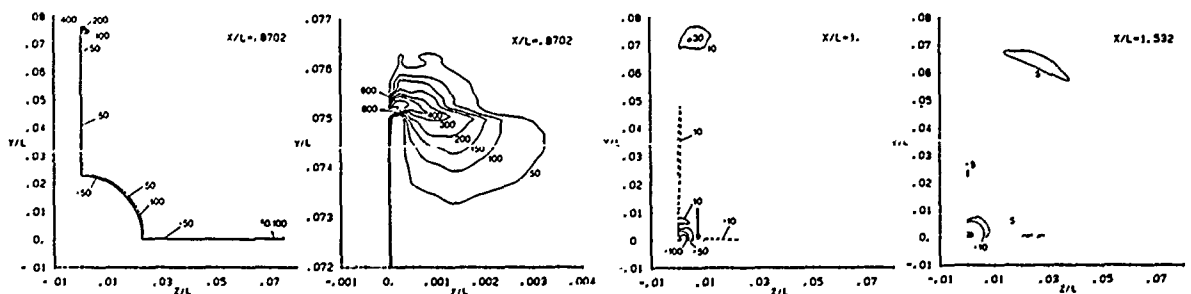


Figure 11. Axial-vorticity contours: laminar flow, rotating.

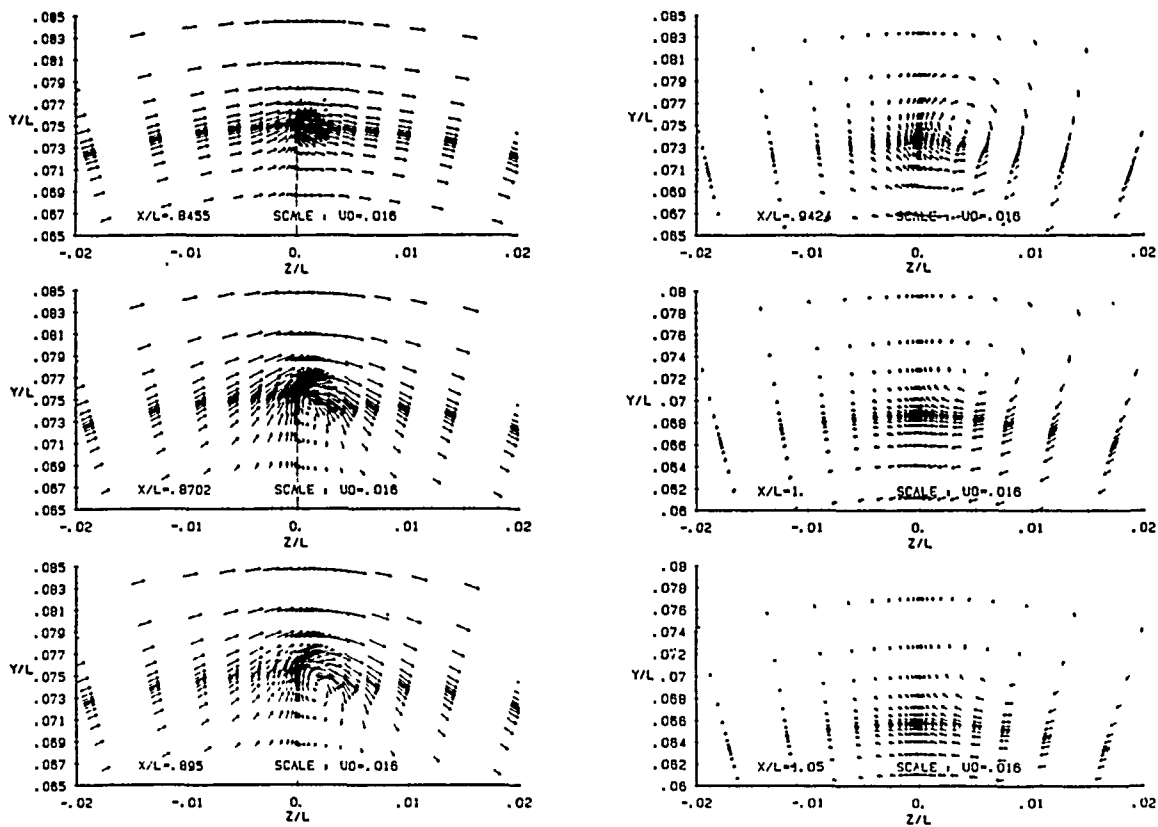


Figure 12. Close-up view of the tip vortex: laminar flow.

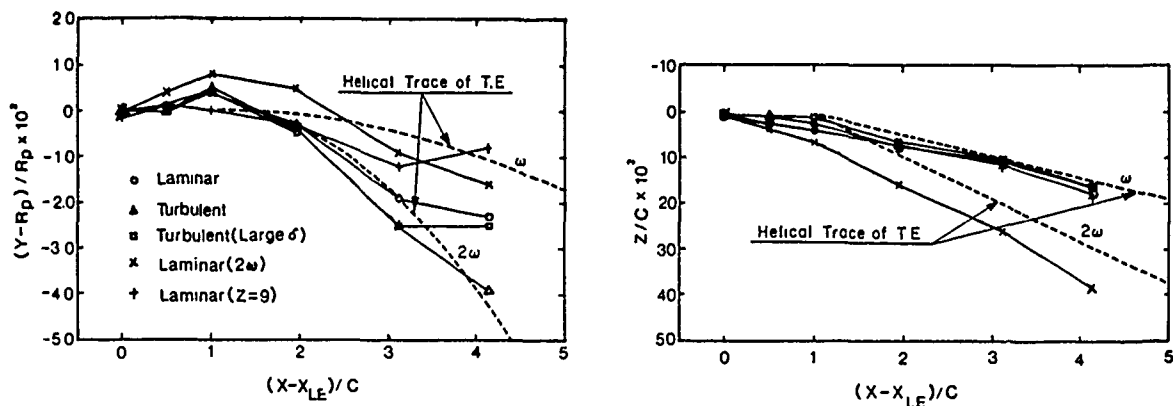


Figure 13. Tip-vortex trajectory.

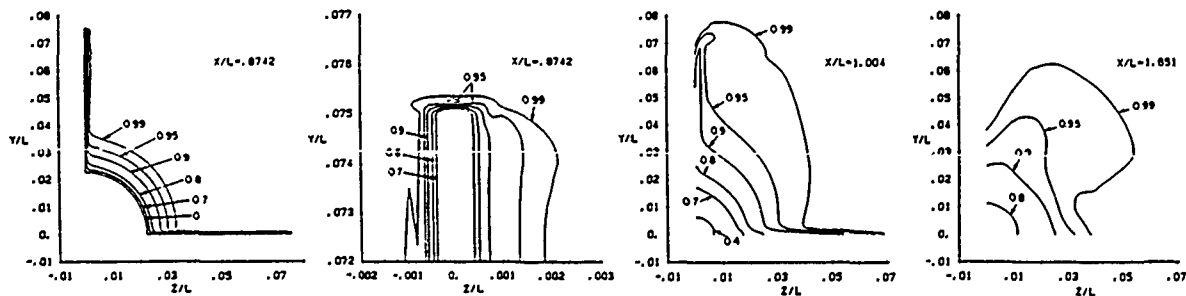


Figure 14. Axial-velocity contours: turbulent flow, rotating.

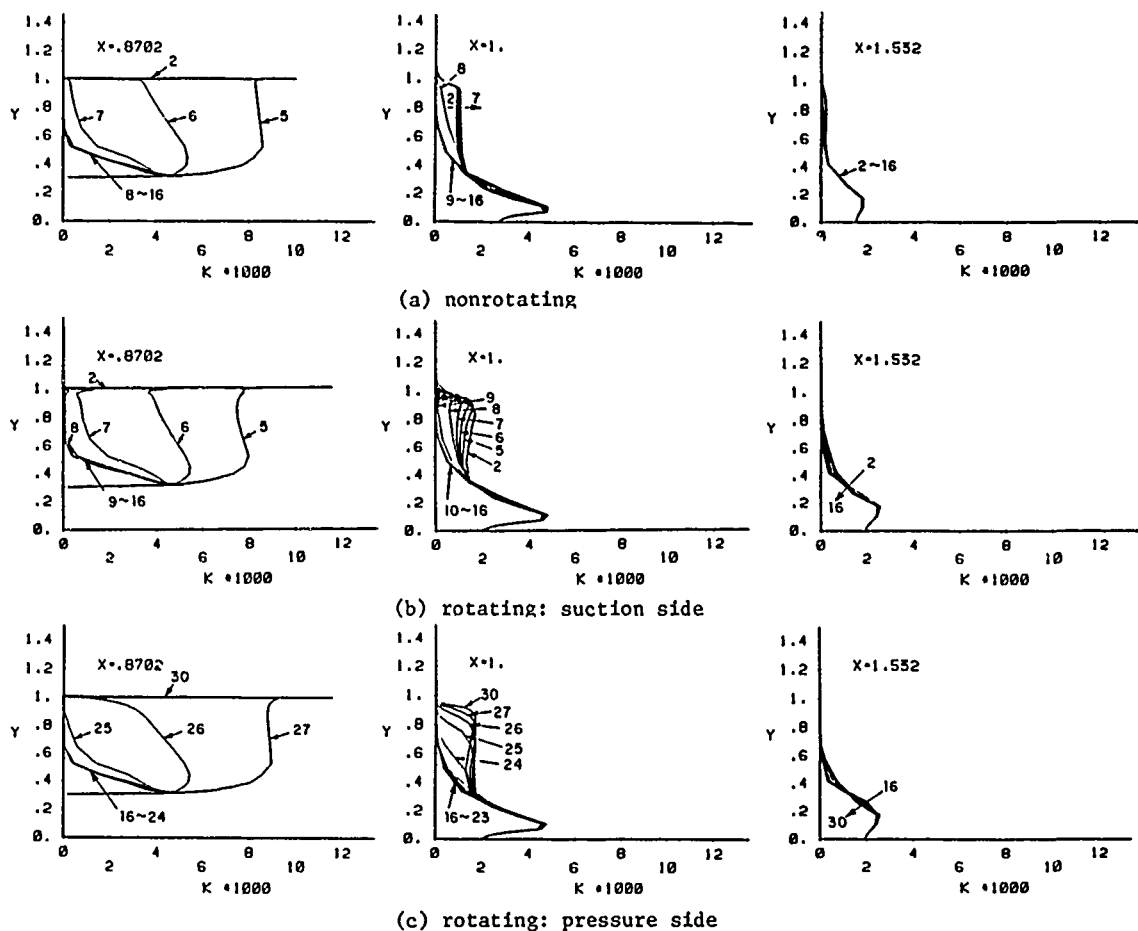


Figure 15. Turbulent kinetic energy profiles.

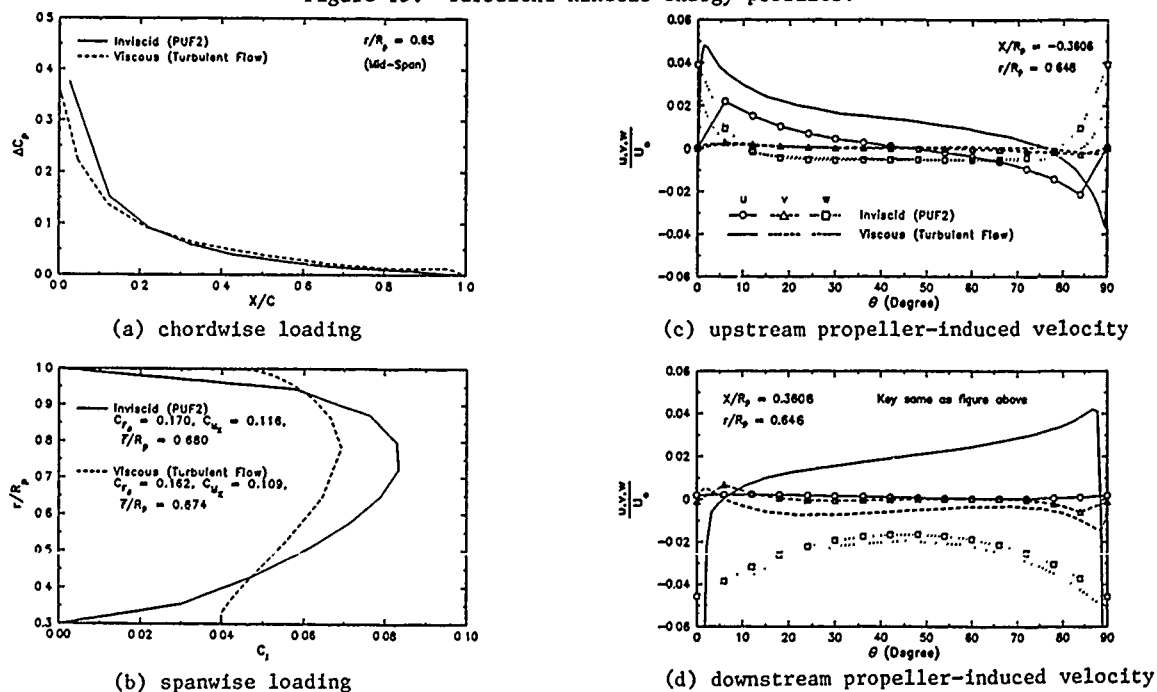


Figure 16. Comparison of turbulent-flow and lifting-surface propeller-performance program results.

DISCUSSION

by K. Mori

Although an explicit description about a systematic accuracy analysis is requested by the paper committee, no descriptions are found in the paper. Because the accuracy analysis is primarily important for the computational fluid dynamics, it should have been mentioned, although the procedures are not definite yet.

DISCUSSION

by S. Kinnas

I would like to congratulate the authors for their interesting paper. I have however two questions to raise.

1) Concerning the circulation distribution that they show in Fig.16(b) as predicted by the presented method: is it a convergent result with respect to the chordwise and spanwise grid discretization on the propeller blade?

2) In the case of a realistic propeller, with blade thickness included, what would they expect to be a reasonable grid on the propeller in order to capture the detailed flow at the propeller leading edge and tip?

Author's Reply

We thank both the oral and written discussers of our paper for their pertinent remarks.

With regard to Prof. Mori's comments, we apologize for not including an explicit statement of accuracy in the paper, and, at this time, offer the following. As stated in the paper, the present overall computational method is based on that used previously for calculating propeller-hull interaction [8,9] in which a viscous-flow method for calculating ship-stern flow [10,12] is coupled with a propeller-performance program in an interactive and iterative manner to predict the combined flow field. References [8,9] and [10,12] provide numerous applications for propeller-hull interaction and bare bodies,

respectively, including validation studies through grid-dependency and convergence check as well as comparisons with experimental data and other analytic and numerical solutions. Some limited grid dependency and convergence check were also done for the present application to test the extensions and modifications for calculating marine-propeller flow fields. That is, some preliminary turbulent-flow calculations were performed using a coarse grid, i.e. $36 \times 22 \times 16$ (16,672). The coarse-grid solutions converged more rapidly (i.e. in about 40 global iterations) than the fine-grid solutions. Qualitatively the coarse-grid solutions were very similar to the fine-grid solutions, but with considerably reduced resolution. Also, as stated in the paper, unfortunately, no experimental information is available for the present geometry; therefore, to aid in evaluating the present work, comparisons were made with some relevant experimental and computational studies, including the direct comparisons between the present turbulent-flow results and those from a lifting-surface propeller-performance program which are provided in Fig.16 (see [11] for the complete comparisons).

With regard to Dr. Kinnas's comments, the solutions presented are fully converged for the present grid. As discussed in the Concluding Remarks, grid-generation for complex geometries is an important issue which must be considered in extending the present method to realistic propeller and body geometries. Presently, calculations are in progress for the SR-7 turboprop using a single-block, H-grid of somewhat higher density than the present one (i.e. $64 \times 46 \times 36 = 105,984$), but with $x^1 = x^1(\xi, \eta, \zeta)$ in order to have the grid conform to the three-dimensional curved boundaries of the skewed and twisted blades and the nacelle. The results are very encouraging; however, it is anticipated that in order to completely resolve all the details of the flow field, especially for marine propellers, multi-block grids will be necessary, including H-, C, and O-types.

Computation of a Nonlinear Rotational Inviscid Flow through a Heavily-Loaded Actuator Disk with a Large Hub

B. Yim

David Taylor Research Center
Bethesda, USA

Abstract

A heavily-loaded actuator disk with a large hub in an open rotational inviscid flow is considered. With an assumption of axisymmetry for the flow, the governing equation is the well known Helmholtz equation for the stream function. Similar problems have been dealt with by many authors, but with no hub or for an annulus with constant hub and tip radii. The additional freedom in the boundary geometry makes the problem much more difficult but is required to allow extensive applications to ship propulsor hydrodynamics.

For the general solution, a nonlinear integral equation for the stream function is formulated by use of the Green function. The boundary conditions require both the stream function and its normal derivative on the boundary. However, although the former is known, the latter has to be derived at each iteration. The solution is obtained by successive iterative approximations substituting the first approximation into the nonlinear integral equation at each mesh point of the flow field. Convergence of the solution has been shown but the computation is quite slow. Therefore the computational method can only be applied using high speed computer of large memory.

For the solution at distances far down stream of the propulsor, the Helmholtz equation can be approximated by an ordinary differential equation, and the numerical solution can be obtained without too much difficulty. The velocity components and the pressure are obtained far downstream of an actuator disk with a given set of circulation and shear swirl distributions.

The flow near the disk is computed by an iteration method. Any physical quantities can be obtained from the stream functions. As an example of the applications of this program, the effects of shear swirl flow behind a heavily-loaded actuator disk, where the external forces act on the flow, are computed.

Introduction

Both design and performance prediction procedures for propellers [1] have made continuous progress. Lifting line theory is now only used in preliminary design, and lifting surface theory is used for the final design and

performance prediction of propellers. The theory of hull-propeller interaction has also made progress as in the consideration of effective wake in predicting propeller performance. However, present practice still employs rather crude approximations in some areas of propeller theory. In particular, the hub effect on propeller blade design in a shear flow has not been fully considered. The load distribution of a propeller blade produces bound and trailing vortices. Trailing vorticity in a shear flow is different from that in uniform flow, producing additional trailing vorticity which can be called the secondary vorticity. The effect of the secondary vorticity field on blade design and propeller performance is not well understood. In particular the effect of onset shear and swirl flow on the hub vortex has not been fully investigated. For some designs, when the propeller shaft is of small diameter and the inflow is fairly uniform, there is less necessity to handle such things. But in the case of a controllable pitch propeller where the shaft is of relatively large diameter, or a submarine propeller where the hub is part of the stern, hub effects can be very important.

Since the boundary layer thickness of a ship at the station where a propeller is located is sometimes the same order of magnitude as the propeller radius, several types of interactions have received serious attention by previous investigators [2,3]. In the design of wake adapted propellers, the effective wake is used for estimating the thrust and torque of propellers. To estimate the effective wake from the nominal wake velocities measured in the propeller plane in absence of the propeller, several methods have been used. It was either estimated empirically by multiplying the measured circumferential mean nominal wake by a constant factor or determined theoretically. One of the theoretical effective wake computations for a propeller in an axisymmetric flow field was provided by Huang and Groves [2]. Here, the computed propeller-induced velocities had to be used in solving the vorticity equations. The propeller-induced velocities were computed from potential flow theory using conventional loading and thickness singularities. Also a combination of this program with the conventional lifting surface theory was considered. Experiments showed that the total velocity profiles calculated by Huang & Groves theory immediately upstream of the propeller were in good agreement with measured values. However, Huang and

Groves only considered the region upstream of the propeller assuming that the energy was not influenced in that region by the propeller. They do not consider the flow downstream of the leading edge of the propeller, where external forces act on the fluid. Several axisymmetric approximations [4,5] draw attention to the importance of the shear flow effect on the propeller when treated as an actuator disk. Full investigation of the shear swirl flow interaction with the blade-induced velocity field and the secondary flow has not been undertaken so far in propeller theory. In the present paper, the shear swirl flow coming into the heavily-loaded propeller with a large hub is treated as a single problem rather than as the combination of separate problems. To make this manageable, we consider it as axisymmetric and the propeller as an actuator disk. In addition the behavior of swirl in the wake of a propeller in shear flow as a function of hub shape is investigated here in an axisymmetric flow analysis. For turbomachine design, similar problems have been considered extensively [6]. Thus the governing equation is well known and even exact solutions for special cases have been found. However, the equation with a general boundary condition has only been dealt with numerically for the purpose of turbomachinery design. For an open propeller without duct, the boundary conditions are different than for turbo-machines. Wu [7] considered a similar formulation of the problem for an actuator disk but no one seems to have considered the wake flow field.

A simpler method of computation of the swirl flow is first studied here and computations are performed for an example of a useful general boundary condition which can be used in propeller design, especially for the hub vortex cavity analysis.

Then a full axisymmetric nonlinear numerical problem is tackled using an iteration method. Even though this problem is for an axisymmetric actuator disk, this is in the shear swirl flow with a large hub of an arbitrary shape and heavy loading. With an application of the Green theorem and the Green function a full treatment of the boundary conditions is attempted. Both the boundary condition on the hub and the discontinuity of the velocity in the slipstream behind the propeller are properly treated. This analysis is a continuation of a previous investigation [8] with considerable improvements in accuracy and completeness.

Shear Swirl Flow Analysis

Although there have been many investigations of propeller performance and propeller design, very little is known of the flow in the propeller wake. The swirl that is closely related to hub vortex cavitation should be considered in the wake of a propeller whose hub length is finite.

The image vortices inside an infinite hub are well known. These image vortices cannot be placed on the outside surface of the hub, or in the flow. This is because the trailing vortices and the secondary vortices formed near the propeller blades would not disappear behind the propeller unless viscosity were considered, and no other vortex can be considered in addition to them.

The problem is how these vortex lines will be rearranged or roll up amongst each other while they are transported downstream where the propeller hub tapers to a point and disappears.

In experiments, the vortices around the hub roll up and vortex cavities are often formed in the hub wake. To understand this phenomenon, a simple model of axisymmetric swirl flow may be useful. In general, the common dynamic equation of incompressible inviscid steady vortex flow can be [6] represented by

$$\bar{q} \times \bar{\xi} = \nabla H \quad (1)$$

where

$$H = \frac{1}{2} q^2 + \frac{p}{\rho} \quad (2)$$

is the total head in the assumed axisymmetric flow with cylindrical polar coordinates (x, r, θ) and the corresponding velocity components $\bar{q} (u, v, w)$, and vorticity components $\bar{\xi} (\xi_x, \xi_r, \xi_\theta)$.

Considering the stream function $\Psi (x, r)$, the governing equation for Ψ is

$$\frac{\partial^2 \Psi}{\partial x^2} + \frac{\partial^2 \Psi}{\partial r^2} - \frac{1}{r} \frac{\partial \Psi}{\partial r} = r^2 \frac{dH}{d\Psi} - C \frac{dC}{d\Psi} \quad (3)$$

where

$$C(\Psi) = r\omega \quad (4)$$

is the circulation distribution in the wake. H is constant along a streamline with Ψ constant and $H = H(\Psi)$. The nominal wake is assumed to be known, i.e. the flow field without propeller is known. Accordingly, H without the propeller is known and designated by H_0 . Using an axisymmetric approximation, H can be written as [7]

$$H = H_0 + \Omega C_1 \quad (5)$$

where Ω is the angular speed of the propeller located at $x=0$ and the circulation C_1 is proportional to the blade number times the blade load distribution except for secondary vorticity. If there is no preswirl upstream of the propeller, the total circulation C will be equal to C_1 . Now both H and C immediately behind the propeller are both known functions of r and Ψ . Thus,

$$\frac{dH}{d\Psi} = \frac{dH}{dr} \bigg/ \frac{d\Psi}{dr} \quad (6)$$

$$\frac{dC}{d\Psi} = \frac{dC}{dr} \bigg/ \frac{d\Psi}{dr} \quad (7)$$

The boundary conditions at downstream infinity may be written as follows

$$u = \frac{1}{r} \frac{\partial \Psi}{\partial r} \rightarrow u_\infty, \quad \frac{\partial \Psi}{\partial x} \rightarrow 0 \text{ as } r \rightarrow \infty \quad (8)$$

$$v = -\frac{1}{r} \frac{\partial \Psi}{\partial x} \rightarrow 0 \quad \text{as } x \rightarrow \infty \quad (9)$$

On the hub,

$$r = h(x), \Psi = 0 \quad (10)$$

On the outer edge of the propeller and on the slip stream

$$\Psi(r, x) = \Psi(1, 0) \quad (11)$$

Many problems with similar governing equations have been solved for special cases, mostly for turbomachinery. For a propeller, there are some investigations for a simple case [6]. No investigation seems to exist for a propeller wake with shear swirl in the presence of a finite hub. We use non-dimensional quantities

$$r' = r/R, x' = x/R, \bar{q}' = \bar{q}/U, C' = C/(UR)$$

$$\Psi' = \Psi/(UR^2), H' = H/U^2 \text{ and } \lambda = U/(\Omega R)$$

where U is the speed at upstream infinity, R is the propeller radius. After this substitution the prime will be omitted as understood. Then we obtain the nondimensional governing Equation (3).

Although the problem could be solved numerically, it would be very complicated in the present form to obtain an accurate solution. At first, for the purpose of investigating hub vortex cavitation, the solution far downstream of the hub may be very useful. Since

$$\frac{\partial \Psi}{\partial x} \rightarrow 0, \frac{\partial^2 \Psi}{\partial x^2} \rightarrow 0 \quad \text{as } x \rightarrow \infty$$

Ψ may be considered as a function of r only in Equation (3), and the governing equation becomes an ordinary differential equation. For special functional forms of H and C , a closed form solution is possible. With the general functional form of H and C , if $\Psi(a)$ and $\partial \Psi / \partial r(a)$ are known the solution can be obtained as an initial value problem by a method such as the Runge Kutta Technique. When Ψ is obtained, u and C will be known and the pressure can be obtained by

$$\frac{p}{\rho} = H(\Psi) - \frac{1}{2} \left\{ u^2 + \frac{C^2}{r^2} (\Psi) \right\} \quad (12)$$

or by

$$\frac{1}{\rho} \frac{dp}{dr} = \frac{C^2}{r^3}$$

Here we consider $C(r)=0$ outside the slipstream. Since outside the slipstream at $x \rightarrow \infty$ the flow is uniform and the pressure should be continuous, the location of the slipstream and the pressure distribution can be uniquely determined. The solution of the differential Equation (3) with conditions (8) through (12) is obtained by solving two simultaneous ordinary differential equations

$$\begin{aligned} \frac{dF_1}{dr} &= \frac{1}{r} F_1 + f(\Psi, r) \\ \frac{d\Psi}{dr} &= F_1 \end{aligned} \quad (13)$$

where,

$$f(\Psi, r) = r^2 \frac{dH}{d\Psi} - C \frac{dC}{d\Psi}$$

with a given boundary condition at the slip stream edge $r = r_s(x)$

$$\Psi(r_s) = \Psi(r_u) \quad (14)$$

$$p = 0 \text{ where } r_s(0) \equiv r_u$$

From Equations (5) and (12)

$$\frac{d\Psi(r_s)}{dr} = r_s u = r_s [2\{H_0(r_u) + \frac{1}{\lambda} C(r_u) - C^2(r_u)/r_s^2\}]^{1/2} \quad (15)$$

Because we assumed $C(r_u) = 0$,

$$\frac{d\Psi(r_s)}{dr} = r_s \sqrt{2H_0(r_u)}$$

However, since r_s is not known, these equations may be solved for a range of r_s values and the final value selected such that

$$\Psi(r=0) = 0 \quad (16)$$

either graphically or by an iteration method. Note here that $dH/d\Psi$, $dC/d\Psi$, Ψ , $d\Psi/dr$ at $x=0$ are all known as functions of $r(x=0)$. Thus, at each step of the solution of the above simultaneous equations, from the known value of Ψ at $r(x \rightarrow \infty)$, $r(x=0)$ can be calculated to determine both $dH/d\Psi$ and $dC/d\Psi$ at $r(x=0)$ and therefore, at $r(x \rightarrow \infty)$.

Such solutions are exact at $x \rightarrow \infty$, under the assumed conditions. However, the solution with $\Psi(r=h)=0$ can also be considered to be an approximate solution at any appropriate strip of a slender hub, i.e., the hub slope is small with respect to x .

In the present study, a sample calculation of Ψ and pressure are made with the following form of the boundary conditions. At $x=0$, for H_0

$$u = (r-h)^{1/n}/D \quad \text{at } r < r_0$$

$$D \equiv (r_0-h)^{1/n}$$

$$u = 1 \quad \text{at } r \geq r_0$$

$$v = 0 \quad \text{in } r_H < r < 1 \quad (17)$$

and

$$C = a_0 + a_1 r + a_2 r^2$$

with constant coefficients a_0 , a_1 , a_2 and n . Using the above representations, the incoming velocity profile is similar to the flow in a turbulent boundary layer, and the circulation distribution has a radially parabolic shape which can take on zero values at the blade hub and tip. Then, at $x=0$

$$\psi(r) = \int_{r_H}^r u(r) r dr = \frac{1}{D} \left[\frac{(r-h)^{1/n+2}}{1/n+2} + \frac{h(r-h)^{1/n+1}}{1/n+1} \right]_{r=r_H}^r$$

at $r_H < r \leq r_0$

$$\psi(r) = \psi(r_0) + \frac{r^2}{2} - \frac{r_0^2}{2} \quad \text{at } r \geq r_0$$

$$\frac{d\psi}{dr} = \frac{1}{D} \{ (r-h)^{1/n+1} + h(r-h)^{1/n} \} \quad \text{at } r_H < r \leq r_0$$

$$\frac{d\psi}{dr} = \frac{1}{D} \{ (r_0-h)^{1/n} \} \quad \text{at } r > r_0 \quad (18)$$

Also assumed at $x=0$, from Equation (12)

$$\frac{dH}{dr} = \frac{1}{2} \frac{d}{dr} \left\{ u^2 + \frac{1}{r^2} C^2(\psi) \right\} + \frac{1}{r^3} C^2$$

or

$$\frac{dH}{dr} = \frac{1}{D^2} \{ (r-h)^{1/n} \frac{1}{n} (r-h)^{1/n-1} \}$$

$$+ \frac{a_0 + a_1 r + a_2 r^2}{r^2} (a_1 + 2a_2 r)$$

at $r_H < r < r_0$ (19)

$$= \frac{a_0 + a_1 r + a_2 r^2}{r^2} (a_1 + 2a_2 r) \quad \text{at } r \geq r_0$$

The pressure distribution induced by the particular shear swirl flow considered here through Equation (17) is given in Figure 1. Even if the circulation near the hub is zero, the pressure rapidly decreases near the axis at $x \rightarrow \infty$. If the pressure is lower than the vapor pressure p_v , a cavity may be formed and will behave like a solid boundary. If a streamline has $\psi=0$ and $p=p_v$, this will be a cavity boundary. In Figure 1, the axial and the tangential velocity components, u , w and the pressure p/q are given at each radial position for three assumed slip stream radii at $x \rightarrow \infty$, $r_s = 0.98$, $r_s = 0.95$ and $r_s = 0.915$. $\psi=0$ at $r=0$ is achieved only in one case $r_s = 0.915$. In the other two cases, $\psi=0$ for $r>0$ when the hub is infinitely long. Even when the radius of an infinitely long hub decreases, the quantities u , w and $-p/q$ increase near the hub. These quantities downstream of the actuator disk near $r=0$ increase very rapidly to ∞ . The boundary values of u and w at $x=0$ are shown as broken lines.

Full Axisymmetric Solution

Now we try to solve Equation (3) in its full axisymmetric form. We consider

$$\psi = \frac{1}{2} r^2 + r\psi \quad (20)$$

in Equation (3). Then it changes to

$$\nabla^2 \psi - \frac{\psi}{r^2} = -g \quad (21)$$

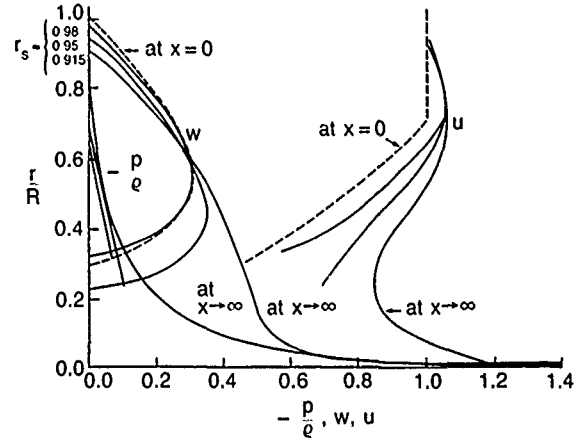


Fig. 1. Shear swirl flow field at $U/(QR) = 0.44$.

where

$$-g = r \frac{dH}{d\psi} - \frac{C}{r} \frac{dC}{d\psi}, \quad \nabla^2 \psi = \frac{\partial^2 \psi}{\partial x^2} + \frac{1}{r} \frac{\partial \psi}{\partial r} + \frac{\partial^2 \psi}{\partial r^2}$$

On the hub ψ is constant, say 0. Then

$$\psi = -\frac{r}{2} \quad \text{on the hub.}$$

At the upstream station $x=x_L$, ψ is assumed to be known. At $x=x_N$ at far downstream ψ will be obtained as a solution but ψ_N will be safely considered to be zero. At $r \rightarrow \infty$, ψ is considered to be the stream function for uniform flow and ψ and ψ_n are known. At $r=0$ behind the hub ψ and ψ_n are both zero. Then this is mixed boundary value problem for a nonlinear elliptic equation.

$$\nabla^2 \psi = f(x, r, \psi) \quad (22)$$

The existence and the uniqueness of the Dirichlet problem for this equation has been considered by Courant [9]. However, he contends that the uniqueness is guaranteed only in a sufficiently small domain or if $\partial f / \partial \psi \geq 0$. In the present boundary value problem ψ is known on $x=x_L$ and at $x \rightarrow \infty$, ψ_N is known. Thus the application of Green's theorem may be most appropriate. Therefore, at $x=x_L$ ψ and ψ_n cannot be given arbitrarily. Besides,

$$f = \frac{\psi}{r^2} - g = \frac{\psi}{r^2} + r \frac{dH}{d\psi} - \frac{C}{r} \frac{dC}{d\psi},$$

where H and C are both given functions at the boundary and

$$\frac{df}{d\psi} = \frac{1}{r^2} + r^2 \frac{d^2 H}{d\psi^2} - \frac{d}{d\psi} \left(C \frac{dC}{d\psi} \right) \geq 0 \quad (23)$$

may be another condition to guarantee a unique solution.

Application of the Green Function

We consider the Green Function $G(r, x; \rho, \xi)$ that is related to two points $P(r, x)$ and $Q(\rho, \xi)$ and that has the following properties:

$$\nabla^2 G - G/r^2 = -\delta(r - \rho) \delta(x - \xi)/r \quad (24)$$

where δ is the delta function

$$G(r, x; \varrho, \xi) = G(\varrho, \xi; r, x)$$

and

$$G(r, x; \varrho, \xi) \rightarrow 0 \text{ as } \overline{PQ} \rightarrow \infty$$

$$G_\varrho(r, x; \varrho, \xi) \rightarrow 0 \text{ as } \overline{PQ} \rightarrow \infty$$

Such a function has been obtained by Wu [7] and is represented by the 2nd order Legendre function which has a logarithmic singularity at $\overline{PQ} \rightarrow 0$. From Equations (21) and (24)

$$G\nabla^2\psi - \psi\nabla^2G = -Gg + \psi\delta(r - \varrho)(x - \xi)/r$$

Integrating this equation in the space bounded by the hub boundary and planes at $x = x_L$ and x_N we obtain

$$\iint_V (G\nabla^2\psi - \psi\nabla^2G) \varrho d\varrho d\xi = - \iint_D Gg\varrho d\varrho d\xi + \psi(r, x)$$

Using the Green theorem

$$\begin{aligned} \psi(r, x) = & - \int_{\ell} \left(G \frac{\partial \psi}{\partial n} - \frac{\partial G}{\partial n} \psi \right) \varrho d\varrho + \iint_D Gg(\varrho, \xi) \varrho d\varrho d\xi \\ & - \int_{\ell_s} G\nabla \frac{\partial \psi}{\partial n} \varrho d\varrho \end{aligned} \quad (25)$$

where ℓ is along the contour at $x = x_L$ and x_N and the hub boundary, n is the inward normal to the fluid, ℓ_s is along the slip stream where $\partial\psi/\partial n$ is discontinuous as much as $\Delta \partial\psi/\partial n$ while ψ and $\partial G/\partial n$ are continuous. Along the contour ℓ , the boundary conditions are given as

$$\psi = 0 \text{ on the hub } r = r_H$$

or

$$\psi = -\frac{r_H}{2}$$

The normal velocity on the hub is zero, or

$$\frac{\partial \psi}{\partial t} = 0$$

where \bar{t} is the unit vector along the tangent to the hub. That is,

$$\frac{\partial \psi}{\partial t} - \frac{\partial \psi}{\partial r} \frac{\partial r}{\partial t} + \frac{\partial \psi}{\partial x} \frac{\partial x}{\partial t} = 0 \quad (26)$$

However,

$$\frac{\partial \psi}{\partial n} = \frac{\partial \psi}{\partial r} \frac{\partial r}{\partial n} + \frac{\partial \psi}{\partial x} \frac{\partial x}{\partial n}$$

From Equation (21)

$$\frac{\partial \psi}{\partial n} = \frac{1}{r} \frac{\partial \psi}{\partial n} - \frac{1}{2} \frac{\partial r}{\partial n} \text{ on } r = r_H \quad (27)$$

From Equations (26) and (27)

$$\frac{\partial \psi}{\partial n} = \frac{1}{r} \frac{\partial \psi}{\partial r} \left(\frac{\partial r}{\partial n} - \frac{\partial x}{\partial n} \frac{\partial r}{\partial t} / \frac{\partial x}{\partial t} \right) - \frac{1}{2} \frac{\partial r}{\partial n} \quad (28)$$

where $\frac{\partial r}{\partial t} / \frac{\partial x}{\partial t}$ is the slope of the hub with respect to x and

$$\frac{\partial r}{\partial n} d\ell = dx, \quad \frac{\partial x}{\partial n} d\ell = -dr \quad (29)$$

Besides, at $\xi = x_L$

$$\psi = \left(\frac{1}{\varrho} \psi - \frac{\varrho}{2} \right)_{\xi = x_L} \quad (30)$$

where

$$\psi_n = \left(\frac{1}{\varrho} \psi_{\xi} \right)_{\xi = x_L}$$

When we insert Equations (28)-(30) into Equation (25) we obtain

$$\begin{aligned} \psi = & \iint_D Gg(\varrho, \xi) \varrho d\varrho d\xi - \int_{\ell} G \frac{\partial \psi}{\partial \varrho} \left\{ 1 + \left(\frac{d\varrho}{d\xi} \right)^2 \right\} d\xi \\ & - \int_{\ell_s} G\Delta \frac{\partial \psi}{\partial \varrho} \left\{ 1 + \left(\frac{d\varrho}{d\xi} \right)^2 \right\} d\xi - \int_{x_N} G_{\xi} \psi \varrho d\varrho + f(r, x) \end{aligned} \quad (31)$$

where

$$\begin{aligned} f(r, x) = & \int_{\varrho=r_H} \left(\frac{G}{2} - \frac{\partial G}{\partial \varrho} \frac{\varrho}{2} \right) \varrho d\xi + \int_{\varrho=r_H} \frac{\partial G}{\partial \xi} \frac{\varrho^2}{2} \frac{d\varrho}{d\xi} d\xi \\ & + \int_{\xi=x_L} \frac{\partial G}{\partial \xi} \left(\psi - \frac{\varrho^2}{2} \right) d\varrho - \int_{\xi=x_L} G \frac{\partial \psi}{\partial \xi} d\varrho \end{aligned} \quad (32)$$

Since $\psi_{\xi} \rightarrow 0$ as $\xi \rightarrow \infty$, the line integral at $\xi \rightarrow \infty$ disappears. Note the effect of slipstream is first included here among solutions solved by the similar technique. Although ψ is continuous throughout the flow including the slipstream, we know that the velocity or the derivatives of ψ may not be continuous across the slipstream especially when the circulation distribution is not continuous. This may cause the line integral along the slipstream to be non-negligible. Numerically this gives a considerable complexity because neither the shape of the slipstream nor the velocity discontinuity is known a priori. However, in each iteration this could be known approximately. Equation (31) is a complicated nonlinear integro-differential equation for ψ because g is a complicated nonlinear function of ψ , and ψ_{ϱ} is not known on the boundary. Wu formulated the problem for

a simple case of no shear and no hub without slipstream, only with the heavily-loaded actuator disk. He obtained the Green function and suggested solving the nonlinear integral equation by an iteration technique, showing as an example the case with a given load distribution on the propeller disk but did not obtain numerical results. Later Greenberg [10] performed the numerical computations for the same problem in a somewhat different manner with a uniform loading and a nonuniform loading, and demonstrated the convergence of the iteration with the same Green function obtained by Wu [7].

The present problem includes a large hub and incoming shear flow with pre-swirl in addition to the heavily-loaded propeller disk. Because of this complexity, there exists a line integral term, in addition to the area integral that was handled by Wu and Greenberg et al. The line integral includes the normal derivative of the unknown which changes the integral equation to an integro-differential equation.

When an approximate solution ψ is assumed everywhere, $\partial\psi/\partial n$ on the boundary will be known accordingly, and H , C and their derivatives along the streamlines can also be determined. Therefore when these quantities are inserted in Equations (31) and (32) the iterated solution can be obtained. If the continuation of this process converges to a solution, it will be the desired one if the solution exists.

Computation of Ψ

The first order solution may be considered with a straight slipstream through the blade tip ($r=1$). As a first approximation the streamlines are assumed to be constant along

$$r = \frac{m}{m_0} \{r_T - r_H(x)\} \quad m = 1, 2, \dots, m_0 \quad (33)$$

The stream functions at $x=x_L$ is given as $\Psi(r)$ from which we obtain the shear distribution

$$\frac{1}{r} \frac{\partial \Psi}{\partial r}, \text{ or vice versa.}$$

At $x=x_L$, g can be calculated from the given Ψ , H and C at $x=x_L$. Then along each streamline Ψ , H , C , $dH/d\Psi$ and $dC/d\Psi$ are constant. Therefore when Ψ is known at any field point H , C , $dH/d\Psi$, and $dC/d\Psi$ will be known automatically. Thus g will be known and we can evaluate the area integral of Equation (31). The mesh is created with lines (33) and the vertical lines

$$x = \pm n\Delta x \quad (34)$$

with Δx intervals.

At each mesh point, the value of G is precalculated by a good approximation [10]. Then

$$\int_{r_H}^{r_u} G g q dq \quad (35)$$

is first calculated at each vertical line by Simpson's rule. The logarithmic singularity of G in the numerical integration of Equation (35) and in the slipstream line integral is treated as follows:

when $x=\xi$, and $q \rightarrow r(\neq 0)$

$$G \sim -\frac{1}{4\pi} \frac{1}{r} \log \frac{(r-q)^2}{r^2}$$

Though the integration of the log function does not produce any singular behavior, the numerical treatment requires care.

$$\begin{aligned} \int_{r_H}^{r_u} G g q dq &= \int_{r_H}^{r_u} \left\{ G g q + \frac{g_0}{2\pi} \log |r-q| \right\} dq \\ &+ \frac{g_0}{2\pi r} [(r_H-r)\{\log|r_H-r|-1\} - (r_u-r)\{\log|r_u-r|-1\}] \end{aligned}$$

where g_0 is the value of gq at $q=r$, the singular point. Then the values of Equation (35) at $\xi = \pm n\Delta x$ are integrated by Simpson's rule to produce the area integral.

Since Ψ on the boundary is given from the boundary condition, the function $f(r,x)$ in Equation (32) is determined and it does not change by iteration. However $\partial\Psi/\partial q$ on the hub $r=r_H$, $\partial\Psi/\partial\xi$ on $x=x_L$ and ψ at $x=x_N$ are not known a priori. The line integral terms have to be iterated by calculating $\partial\Psi/\partial q$ and $\partial\Psi/\partial\xi$ from the first approximated Ψ distribution.

When the mesh (33) is set from the beginning, the iterated solution Ψ will change at the given mesh points at each iteration and will converge to a solution if the solution exists. There, H , C and the derivatives which are only functions of Ψ have to be interpolated numerically at each point from the given values of $H(\Psi)$, $C(\Psi)$, etc. at $x=x_L$. Since the values of Ψ on the boundary are already known from the boundary conditions, they do not have to be calculated on the boundary. This fact is very convenient because the boundary integral/the line integral is more singular than the area integral. However the values of the line integral at the points other than at the boundary have to be calculated and need special care.

Iteration and Convergence

Iteration techniques for nonlinear equations are familiar to those who use high speed computers. However, since the present problem may be considered to involve simultaneous equations with an extremely large number of variables, it is rather impractical to use the conventional Newton Raphson method. Because it might be rather simpler and more economic to consider a naive first order iteration without modification of values, this approach was tested first. However in this case sometimes the solution seemed to oscillate after a certain course of convergence, so that a simple modified quasi Newton Raphson method was considered [8].

The convergence using the simple modified quasi Newton Raphson method was found to be very sensitive

to the computational error. Whenever any error exists in the computation the solution does not converge. This has been studied in detail in a previous paper [8]. However, even though it just converges it is not necessarily the right solution. Besides the question of uniqueness, the solution has to satisfy all of the boundary conditions. In fact it converged without line integrals along the lines $x = x_L$ and the slipstream, giving a wrong solution. It also converged to an unreasonable solution when unreasonable values were given as the boundary condition. Therefore not only the convergence but also satisfaction of boundary conditions must be checked.

Propeller Characteristics

Now the axisymmetric stream function is obtained everywhere, all the physical quantities can be computed. These are used for the characteristics of an infinite bladed propeller.

Well known formulae for propeller characteristics are given as follows: The thrust coefficient

$$C_T = \frac{T}{\rho \Omega^2 R^4} = 4\lambda^2 \int_{r_H}^1 w_1(r, 0^+) \left\{ \frac{r}{\lambda} - w_2(r, 0^+) \right\} r dr$$

where $2w_1r$ equals the circulation distribution Γ_∞ corresponding to the propeller blade circulation Γ with a Z bladed propeller such that

$$\lim_{Z \rightarrow \infty} Z\Gamma = \Gamma_\infty / K = 2w_1r$$

where K is the Goldstein factor and w_2 is the θ component of the velocity at the actuator disk. The torque coefficient

$$C_Q = \frac{Q}{\rho \Omega^2 R^5} = 4\lambda^2 \int_{r_H}^1 u(r, 0) w_1(r, 0) r^2 dr$$

The efficiency

$$\eta = \lambda C_T / C_Q$$

The pitch angle

$$\phi = \cot^{-1} (r\eta_c(r)/\lambda)$$

where $\eta_c(r)$ is the radial distribution of the propeller efficiency

$$\eta_c(r) = \left\{ 1 - \frac{\lambda}{r} w_2(r, 0^+) \right\} / u(r, 0)$$

The other conventional thrust coefficients $C_{T5} = T / (\rho/2 U^2 \pi R^2)$ has the relation with C_T , $C_T = 0.5\lambda^2 C_{T5}$.

Numerical Examples and Discussions

For checking the numerical accuracy and solution behavior for parameter changes, two examples were numerically tested. One example uses the boundary conditions given in Equation (17) and the other uses a

set of data obtained in a water tunnel experiment. The first example has already been used for an approximate analysis as shown in Figure 1. The full axisymmetric analysis with the boundary conditions given in Equation (17) are now tested for the hub geometry shown in Figure 2. The efficiency changes corresponding to the inflow velocity distributions shown in Figure 3 are shown in Figure 4. These changes are compared with the results calculated by simple momentum theory without considering the thrust deduction. It is obvious from the C_Q equation that C_Q will decrease when u decreases, thus increasing the efficiency. However, the reduction in u may be as the result of increment in the friction and/or form drag of the ship. The second example corresponds to one of the sets of test data of Huang and Groves as shown in Table 1 with the hub geometry shown in Figure 5. The velocity distribution is taken from the measured longitudinal velocity component at the station $x = x_L = -0.482$ as shown in Figure 6.

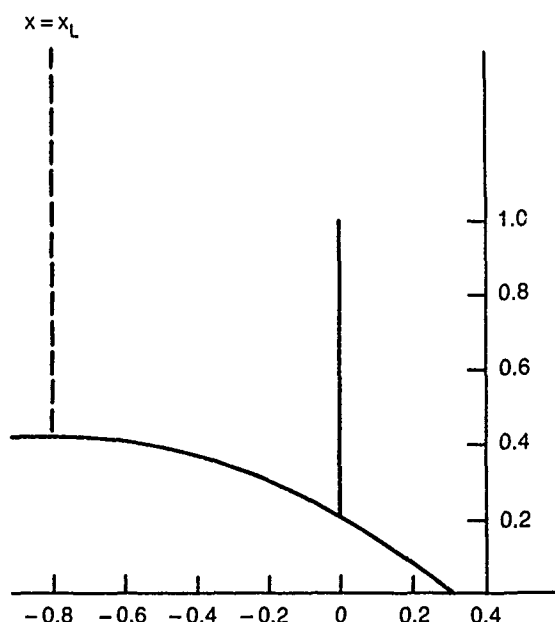


Fig. 2. Hub geometry I.

The head distribution from Equations (2) and (5) is approximated from the nominal wake values because not enough information is available for the head. The blade circulation given in the Table is converted by the relation

$$Z\Gamma \sim \Gamma_\infty = 2w_1r$$

taking the Goldstein factor $K = 1$ because for the 7-bladed propeller k is very close to 1. With this approximation, the thrust coefficient C_{T5} , using the Γ values of Table 1, is very close to the measured value and the value from the lifting surface computation.

The velocity components at the propeller plane ($x = 0$) and a little downstream of the plane ($x = 0.192$) are shown in Figure 6. These values are taken at the iteration where the average relative error is less than 0.005% with 20 iterations. A simple approximation assuming that $u = \text{nominal wake} + \Gamma_\infty / (2r \tan \phi)$ from actuator disk theory is also plotted in Figure 6. The three calculated

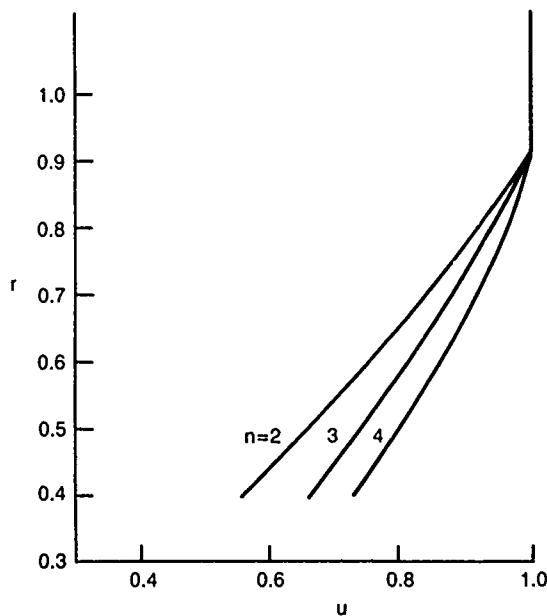


Fig. 3. Shear distribution at $x = -0.8$.

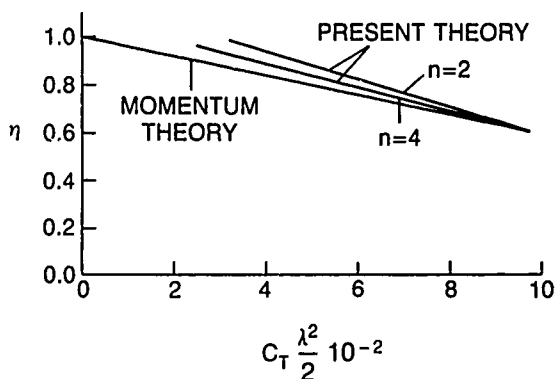


Fig. 4. Efficiency-thrust coefficient relation.

Table 1. Tested propeller data.
 $C_{Ts} = 0.356$, $\pi\lambda = 1.268$

r/R	Nominal Wake	Γ
0.211	0.387	0.0000
0.250	0.417	0.0023
0.300	0.454	0.0051
0.400	0.520	0.0107
0.500	0.579	0.0150
0.600	0.631	0.0172
0.700	0.677	0.0169
0.800	0.720	0.0140
0.900	0.763	0.0089
0.950	0.785	0.0055
1.000	0.806	0.0000
1.050	0.826	0.0000
1.100	0.845	0.0000
1.200	0.880	0.0000

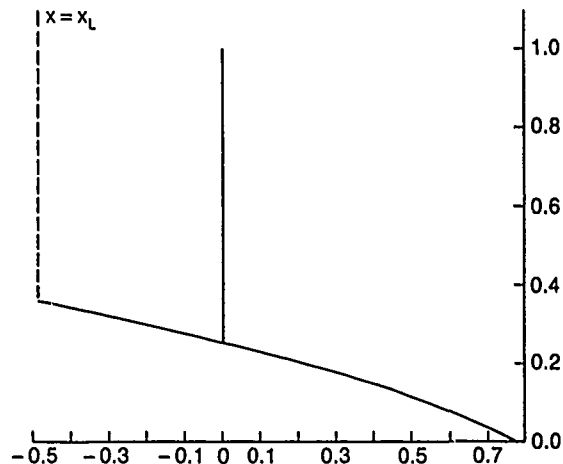


Fig. 5. Hub geometry II.

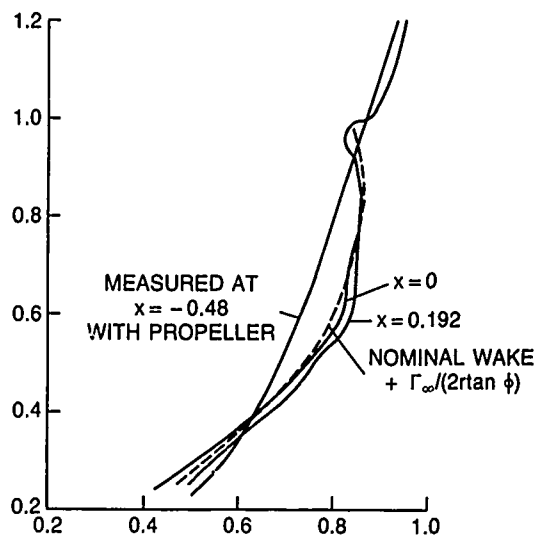


Fig. 6. Axial velocity components near the propeller disk.

curves are very close to each other. The efficiency computed with the boundary condition given by the measured longitudinal velocity at $x = -0.480$ is 1.15 which is close to the value 1.17 from actuator disk theory.

If uniform inflow is assumed, the propeller efficiency with the same value of Γ_∞ in open water is 0.82 this means the approximate corresponding wake fraction w_f is 0.287 from $1.15(1 - w_f) = 0.82$. It is well known that the overall propulsive efficiency also depends upon the thrust deduction which reduces the efficiency. The numerical results show that when $\Gamma_\infty = 0$ at the blade tip, the effect of the slipstream line integral is negligible. This is reasonable because it has been analytically proven [11] that both u and w are proportional to Γ_∞ on the propeller plane when hub is absent.

Since the governing equation (31) holds in a shear swirl flow and no explicit vortex distribution is used for the solution, it is not clear here how the conventional bound and trailing vortices plus secondary vortices [12] are involved. However, this could be interpreted using the vortex ring method [13].

The numerical program with iterations adopted in the present paper is mainly for the purpose of checking the feasibility of the application of the iteration method to a nonlinear problem with the reasonable convergent results. The convergence is quite stable with the change of mesh size and the degree of interpolation (when a Lagrangian interpolation is used).

Because the present problem neglects viscosity, the effect of viscosity on the shear flow cannot be computed. The effect of shear on the propeller can be computed from the measured velocities or the computed velocities by the method of reference [2]. Therefore the present program could be most effectively used to find the propeller shear interference at or behind the propeller plane with the measured upstream velocities or the effective wake computed by the Huang and Groves method. Since experiments show that the propeller does not affect the flow beyond about two propeller diameters upstream [2] of the propeller the nominal wake at a station two propeller diameters upstream of the propeller plane may be effectively used to compute total flow using Equations (2), (5) and (3). If there is no shear or swirl upstream of the propeller, the problem becomes much simpler because the area integral outside the domain bounded by the slipstream, the propeller plane, and the hub disappears. However, the line integrals along the hub and the slipstream (when Γ_∞ (tip) $\neq 0$) are needed in addition to the area integral.

The present program may be further extended to evaluate ducted propellers and multistage propellers such as contra-rotating propellers in the shear swirl flow. In fact for the problem of contra-rotating propellers in shear swirl flow, the present computer program can be applied without too much change.

Acknowledgments

The investigation reported herein was supported by the David Taylor Research Center's Independent Research Program. The author would like to thank Dr. T.T. Huang, Mr. Justin McCarthy, Dr. William B. Morgan, and Dr. Milton Martin for their continuous encouragement.

References

1. Kerwin, J.E. and C.S. Lee, "Prediction of Steady and Unsteady Marine Propeller Performance by

Numerical Lifting Surface Theory," Trans. SNAME, Vol. 86, 1978.

2. Huang, T.T. and N.C. Groves, "Effective Wake Theory and Experiment," Proceedings of 13th Symposium of Naval Hydrodynamics, ONR, 1980.
3. Nagamatsu, T. and T. Sasajima, "Effect of Propeller Suction on Wake," Jour. of SNJE, Vol. 137, pp. 58-63.
4. Dyne, Gilbert, "A Note on the Design of Wake-Adapted Propellers," J.S.R., Vol. 24, No. 4, Dec. 1980, pp. 227-231.
5. Goodman, Theodore R., "Momentum Theory of a Propeller in a Shear Flow," J.S.R., Vol. 23, No. 4, Dec. 1979, pp. 242-252.
6. Horlock, J.H., "Actuator Disk Theory, Discontinuities in Thermo-Fluid Dynamics," McGraw-Hill, Inc., 1978.
7. Wu, T.Y., "Flow Through a Heavily Loaded Actuator Disk," Schiffstechnik, Bd. 9, Heft 47, 1962, pp. 134-138.
8. Yim, B., "An Iteration Method for a Nonlinear Shear Flow Through a Heavily-Loaded Actuator Disk With a Large Hub," Proceedings of the International Conference on Numerical Methods in Engineering; Theory and Application, Edited by G.N. Pande & J. Middleton, Martinus Nijhoff Publishers, 1987.
9. Courant, R., "Method of Mathematical Physics," Vol. II, Interscience Pub. New York, 1862.
10. Greenberg, M.D., "Nonlinear Actuator Disk Theory," Zeitschr. Flugwissensch, Bd. 20, Heft 3, 1972.
11. Morgan, W.B. and Wrench, J.W. Jr., "Some Computational Aspects of Propeller Design," Method in Mathematical Physics, Vol. 4, Academic Press Inc., New York, pp. 301-331, 1965.
12. Yim, B., "A Note With Secondary Vortex Caused by a Thin Foil in a Nonuniform Flow," J.S.R., Vol. 32, Nov. 1988.
13. Cox, B.D. "Vortex Ring Solutions of Axisymmetric Propeller Flow Problems," MIT, Dept. of Naval Arch. & Marine Eng., Rept 68-13, June 1968.

Computations of 3D Transom Stern Flows

Bill H. Cheng
David Taylor Research Center
Bethesda, USA

Abstract

A practical computational method for 3D transom stern flows is presented. The theory and numerics of computing transom stern flows are described in detail. The special treatment of the linearized free surface boundary condition is included. In particular, the boundary condition for a dry transom is derived within the framework of a free surface potential flow. The transom is treated as an inflow boundary and the transom boundary condition is then used to specify the starting values of a linearized free surface calculation. This computational method has been incorporated into a Rankine source panel method, the XYZ Free Surface (XYZFS) program version 2.0. The XYZFS program has been used to predict the wave resistance for a large number of transom stern ships. The computed wave resistance has compared favorably with measured wave pattern resistance, correctly predicting the relative merit of competing hulls. The agreement with experimental measurements is remarkably good for Froude numbers between 0.35 and 0.50, corresponding to the normal speed range of high-speed transom stern ships.

1. Introduction

A practical computational method for transom stern flows is of special interest to ship hydrodynamicists. Such interest is intensified by the peculiar property of the flow pattern. If the ship speed is high enough, the transom clears the surrounding water and the entire transom area is exposed to the air. The transom flow detaches smoothly from the underside of the transom, and a depression is created on the free surface behind the transom. Saunders [1] described this flow pattern in his book on hydrodynamics and his description of a dry transom is reproduced in Fig. 1. This flow pattern has been credited with the reduced wave resistance for high-speed transom stern ships, as compared to their cruiser stern equivalents.

Early numerical studies encountered problems in modeling transom stern flows. Rankine source and Havelock source methods were hampered by the difficulty of treating the intersection curve between the transom and the free surface. Many investigators replaced the fluid domain behind the transom with solid surfaces. For example, Gadd [2] and Chang [3] simulated the surface depression by adding a tapering extension to close the body behind the stern. Realistic flow patterns cannot be obtained in this way and more accurate computations of transom stern flows are needed.

This paper describes an improved method for computing transom stern flows. The theory and numerical method for computing 3D transom stern flows are presented step by step. The special treatment of the linearized free surface boundary condition is given in detail. The boundary condition for a dry transom is derived within the framework of a free surface potential flow. The physical constraints imposed by this transom boundary condition require that the static pressure be atmospheric and that the flow leave tangentially at the transom. This computational technique has been successfully incorporated into a Rankine source panel method originally developed by Dawson [4,5] and further developed as the XYZ Free Surface (XYZFS) program Version 2.0.

The XYZFS program has been used to analyze the wave resistance and local flowfield for a large number of transom stern ships. Comparisons of wave resistance prediction and experimental measurements have been made and have shown general agreement. Cheng et al. [6] described the hydrodynamic analyses of DTRC Model 5403 and Model 5404, which represent typical transom stern ships with bow domes. A parametric study on stern wedges, as an example, of transom stern variations, was described by Cheng et al. [7]. An FFG-7 hull with a 15-degree stern wedge was

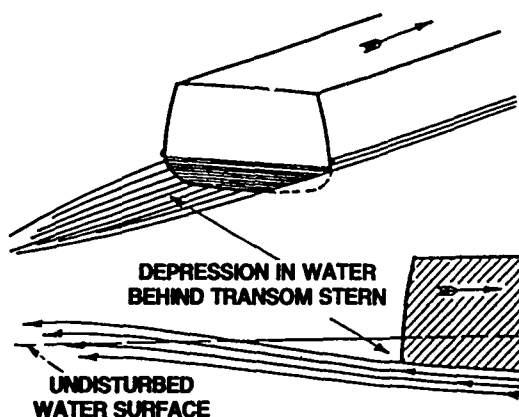


Fig. 1. Flow pattern behind a transom stern (sketch from Saunders [1]).

analyzed by Hoyle et al. [8]. Cheng et al. [9] presented a comparison of the computed propeller inflow with the corresponding data from wake survey experiments for a variant of the research vessel, R/V Athena hull.

Transom stern studies prior to 1983 were summarized by Cheng et al. [6]. Subsequently, Wilson and Thomason [10] published a parametric study on transom sterns. The effects of transom depth and transom width variations were identified using a combined numerical and experimental approach. More recent studies on transom sterns included residual resistance computations for Series 64 by Tulin and Hsu [11]. These computations used a strip theory which is applicable in the limit of an infinite Froude number.

In this paper, the computed flow pattern behind the transom is presented and compared with experimental measurements by Jenkins [12] for the R/V Athena hull. In addition, a comparison of wave resistance prediction and experimental measurements is presented for DTRC Model 5416.

2. Physical problem

Consider a steady flow directed from bow to stern of a ship. Attention is focused on the region just forward and aft of the stern as shown in Fig. 1. Figure 2 is a schematic diagram representing a sideview of a transom stern flow in a centerplane. The keel line typically slopes upward relative to the mean water level, which is designated by a horizontal dashed line in Fig. 2. The wavy solid line represents a streamline which passes under the transom, detaches from the stern, and forms part of the free surface. Immediately downstream of the transom, the water rises rapidly toward the mean water level, overshoots, and then reaches a maximum elevation before descending under the

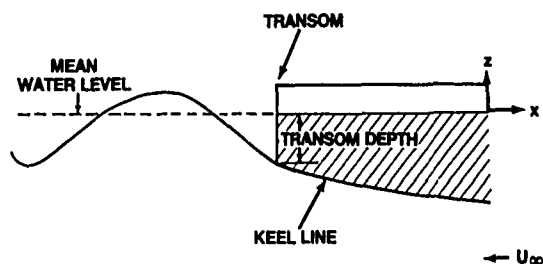


Fig. 2. Schematic of transom stern flow for the centerplane shown in a sideview.

influence of gravity. Such ascending and descending motion is repeated further downstream. The wave motion described here can be seen in the wave pattern computed by Coleman [13] using a finite difference method.

3. Numerical method

3.1 Panel method for cruiser stern flows

Before the computational method for 3D transom stern flows is introduced, a panel method for cruiser stern flows is described. The usual treatment of cruiser sterns is presented since the special treatment for transom sterns is similar and is an extension of the cruiser stern method.

In the Rankine source panel method, a hull surface is mathematically subdivided into hundreds of small source panels. Each panel is characterized by its centroid, normal unit vector, and area. The velocity at the control point (i.e., centroid) of a given panel i induced by another panel j is a function of the geometry of panel j and of the distance between panel i and panel j . For example, the x -component of the velocity induced by panel j on panel i is equal to the induced velocity (per unit source strength), denoted as the influence coefficient CX_{ij} , multiplied by the source strength S_j , which is a constant for each panel. The sum of the free stream velocity U_∞ and the velocity induced by all other panels j gives the velocity at panel i :

$$u_i = U_\infty + \sum_{j=1}^N CX_{ij} S_j \quad (1)$$

In Eq. 1, the summation is carried out for all the panels on the hull surface, and the quantity N denotes the total number of panels. The unknowns on each panel are the source strength to be determined from a solution of the boundary value problem subject to the Neumann boundary condition on the hull surface. This panel method scheme was developed by Hess and Smith [14] for the flow of an infinite fluid past a ship-like body.

Another way of modeling a ship is to combine the submerged ship hull with its mirror image above a plane of symmetry at the mean water level. This combination is referred to as the double model in the literature. The flow past a double model is obtained by a numerical solution of the boundary value problem subject to the Neumann boundary condition on the double model hull. This double model solution is the approximate solution to the free surface problem in the limiting case of zero Froude number when the free surface is approximated by a rigid wall.

After the double model solution is obtained, the double model streamlines are traced on the mean water level. These streamlines will not penetrate the hull surface and are used to set up a free surface grid. Constant source panels are placed on this free surface grid. Then, the free surface boundary condition is linearized using the double model solution as the basic solution in the sense that the deviation from the double model flow is considered small:

$$\phi = \Phi + \phi', \quad (2)$$

where ϕ denotes the velocity potential for the free surface flow, Φ the velocity potential for the double model, and ϕ' the perturbation velocity potential. Dawson [4] gave the resulting free surface boundary condition with the double model linearization as

$$(\Phi_t^2 \phi_t)_t + g \phi_z = 2 \Phi_t^2 \phi_{tt} \quad (3)$$

at the mean water level $z = 0$. The free surface boundary condition involves the gradient of the velocity potential along a streamwise direction designated by l , and differentiation is carried out along the corresponding double model streamlines. For example, the streamwise velocity on the free surface is computed by

$$\phi_t = \frac{\Phi_x}{\sqrt{\Phi_x^2 + \Phi_y^2}} \phi_x + \frac{\Phi_y}{\sqrt{\Phi_x^2 + \Phi_y^2}} \phi_y. \quad (4)$$

Note that this differentiation scheme approximates the free surface flow direction by the double model flow direction. This approximation is a crucial step to be used later in the derivation of the transom boundary condition.

In the numerical calculation of the convective term, finite differencing is used to calculate derivatives between adjacent panels along a double model streamline. A four-point upstream

finite differencing scheme is used to eliminate upstream propagating disturbances as recommended by Dawson [4]. For the foremost upstream point, a two-point upstream finite difference operator is used. The starting values are specified by a uniform flow and a corresponding wave elevation of zero.

In the panel method for free surface flows, the source strength distribution must satisfy simultaneously the linearized free surface boundary condition and the Neumann boundary condition on the hull. For a case with N panels representing the total number of the hull panels and free surface panels combined, the resulting system of N by N equations is full, nonsymmetrical, and not diagonally dominant. A Gaussian elimination scheme is used to solve this system of equations.

For the case of a transom stern, the main section of the free surface (as shown in Fig. 3) can be handled in the same way as for cruiser sterns. The double model linearization and the upstream finite difference operator are also used. However, the flow domain behind the transom presents a new problem and needs special treatment. In particular, a new section of free surface panels is introduced, the transom is treated as an inflow boundary, and the starting values of a free surface calculation must be specified at the transom. This problem is addressed in the remainder of this paper.

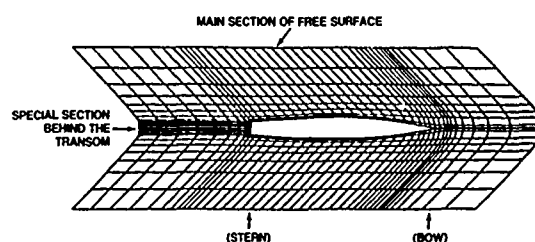


Fig. 3. An aerial view of the free surface paneling for a transom stern hull.

3.2 Theory of the transom boundary condition

As for a cruiser stern case, a transom stern solution begins with a double model computation. The geometric model for a transom stern hull is shown in Fig. 4. Note that the transom is intentionally left open and there are no panels on the transom. The hull surface for the double model serves as a stream surface separating the external flow about the hull from a fictitious internal flow. The double model flow computed in this way is appropriate for a dry transom with the exit flow detaching at the transom tangential to the hull surface.

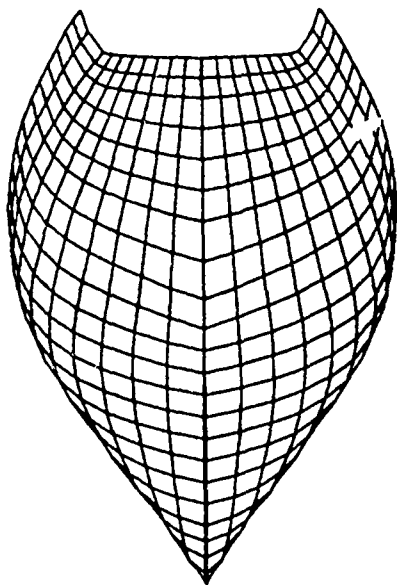


Fig. 4. Perspective view for the numerical model of a transom stern hull. Note the open transom.

For the free surface solution, the free surface boundary conditions must be adapted to the transom stern geometry. To simplify the analysis of transom flows in practical applications, several assumptions are made in the theory for transom stern flows. It is assumed that the transom is left open as in the double model flow computations and that the potential flow detaches from the transom at well defined locations. These locations are identified as the points on a curve which has the same shape as the transom bottom. The shape of the transom bottom may be described by specifying the transom depth z_T as a function of the transverse coordinate y :

$$z_T = f(y) \quad \text{at } x = x_T, \quad (5)$$

where the subscript T denotes the transom and x_T the longitudinal coordinate of the transom. Along the intersection curve between the transom and the free surface, the static pressure is equated to the atmospheric pressure p_∞ since the transom clears the surrounding water and is exposed to the air:

$$p_T = p_\infty \quad \text{at } x = x_T \text{ and } z = z_T \text{ for a given } y \quad (6)$$

In Eq. 6, the effect of an air wake behind the transom is neglected and the atmospheric pressure is considered a global constant. With the dependence on pressure removed, Bernoulli's equation describes a steady-state balance of kinetic

energy and potential energy :

$$\frac{1}{2} [\phi_x^2 + \phi_y^2 + \phi_z^2] + gz_T = \frac{1}{2} U_\infty^2, \quad (7)$$

where (ϕ_x, ϕ_y, ϕ_z) denotes the gradient of the velocity potential in (x, y, z) directions. Eq. 7 may be rearranged as

$$\frac{\phi_x^2 + \phi_y^2 + \phi_z^2}{U_\infty^2} = 1 - \frac{2g}{U_\infty^2} z_T. \quad (8)$$

Thus, the kinetic energy for the water at the transom can be determined by the right hand side of Eq. 8, where z_T lies below the mean water level and takes on a negative value. This equation is the first constraint for transom stern flows.

Since a flow cannot penetrate an impermeable surface, another constraint to be satisfied at the transom is that the exit flow must be tangential to the hull surface. The magnitude of the velocity at this point is given by the square root of the right hand side in Eq. 8. The flow direction is part of the free surface solution and is determined by the transom geometry, which can be specified by a (local) tangential unit vector:

$$t_x = \frac{\phi_x}{\sqrt{\phi_x^2 + \phi_y^2 + \phi_z^2}} \quad (9)$$

$$t_y = \frac{\phi_y}{\sqrt{\phi_x^2 + \phi_y^2 + \phi_z^2}} \quad (10)$$

$$t_z = \frac{\phi_z}{\sqrt{\phi_x^2 + \phi_y^2 + \phi_z^2}} \quad (11)$$

A first approximation of the tangential unit vector is obtained by replacing the potential in Eqs. 9 through 11 by the double model potential to give the tangential unit vector in the direction of the double model flow :

$$T_x = \frac{\Phi_x}{\sqrt{\Phi_x^2 + \Phi_y^2 + \Phi_z^2}} \quad (12)$$

$$T_y = \frac{\Phi_y}{\sqrt{\Phi_x^2 + \Phi_y^2 + \Phi_z^2}} \quad (13)$$

$$T_z = \frac{\Phi_z}{\sqrt{\Phi_x^2 + \Phi_y^2 + \Phi_z^2}}, \quad (14)$$

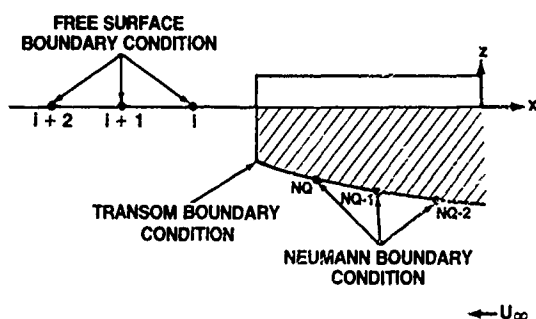


Fig. 5. Description of boundary conditions for transom, free surface, and hull.

where the vector (ϕ_x, ϕ_y, ϕ_z) represents the velocity of the double model flow for a hull panel whose centroid lies just forward of the sharp corner at the transom. This hull panel has the same y -value as the transom and is denoted by the index NQ as shown in Fig. 5. The approximation of the free surface flow direction by the double model flow direction is consistent with applying the free surface boundary condition along double model streamlines on the main section of the free surface, as specified by Eq. 4. The validity of this approximation has been verified by comparing computed and measured wave profiles behind the transom.

When the velocity magnitude from Eq. 8 is combined with the flow direction from Eqs. 12 through 14, the three velocity components at the transom are approximated by:

$$u_T = \sqrt{1 - \frac{2z_T}{U_\infty^2}} T_x \quad (15)$$

$$v_T = \sqrt{1 - \frac{2z_T}{U_\infty^2}} T_y \quad (16)$$

$$w_T = \sqrt{1 - \frac{2z_T}{U_\infty^2}} T_z, \quad (17)$$

where the vector (u_T, v_T, w_T) has been nondimensionalized by $|U_\infty|$ and denotes the velocity at the transom in the (x, y, z) directions, respectively. The sign of the vector (u_T, v_T, w_T) is determined by the tangential unit vector. The quantity $\frac{U_\infty^2}{gz_T}$ represents the square of the Froude number based on the transom depth. In usual numerical calculations, it is more common to use the Froude number based on the waterline length L . This convention is achieved by scaling

(x, y, z) by $1/2 L$. Equations 15 through 17 can then be rewritten as follows:

$$u_T = \sqrt{1 - \frac{2z_T}{Fn^2}} T_x \quad (18)$$

$$v_T = \sqrt{1 - \frac{2z_T}{Fn^2}} T_y \quad (19)$$

$$w_T = \sqrt{1 - \frac{2z_T}{Fn^2}} T_z, \quad (20)$$

where $Fn^2 = U_\infty^2 / gL$ and $Z_T = 2z_T / L$. Equations 18, 19, and 20 are applied as the transom boundary conditions for the free surface calculations in the case of a dry transom. In so doing, the static pressure is forced to be atmospheric and the free surface flow is forced to leave the transom tangentially in a direction specified by the double model flow. The transom boundary conditions show that the velocity at the transom is directly related to transom depth and the Froude number and is indirectly related to other transom characteristics (i.e., the buttock angle, the deadrise angle, and the run angle) through the direction of the double model flow.

3.3 Implementation of the free surface boundary condition

In this section, the special treatment for the free surface boundary condition behind a transom stern is described. The free surface boundary condition in this region uses the conventional linearization about a uniform flow:

$$2Fn^2 u_x + w = 0, \quad (21)$$

where the length is nondimensionalized by $1/2 L$ and the vector (u, v, w) represents the perturbation velocity in a dimensionless form. The free surface boundary condition is applied at the mean water level, on which flat panels are placed. Computations are performed for the centroid of a panel, as indicated by "bullets" in Fig. 5. In the discretization of the convective term in Eq. 21, an upstream finite difference operator is used to eliminate upstream propagating waves. In particular, a two-point upstream finite difference operator must be used to start the computations for transom stern flows:

$$u_{x,i} = CA_i u_i + CB_i u_1, \quad (22)$$

$$\text{where } CB_i = \frac{1}{x_i - x_1} = -CA_i. \quad (23)$$

In Eqs. 22 and 23, the index i denotes the foremost point behind the transom and the index t the upstream point at the transom. The quantity u_i is an unknown to be determined and u_t , the velocity at the upstream point, must be specified. The value u_t is taken from the transom boundary condition Eq. 18. However, a minor modification is required here since u_T represents the total velocity and u_i represents the perturbation velocity superimposed on the uniform flow. Thus

$$u_i = 1 + u_T. \quad (24)$$

Substituting Eqs. 22 and 24 into Eq. 21 and rearranging gives,

$$2Fn^2 CA_i u_i + w_i = -2Fn^2 CB_i [1 + u_T]. \quad (25)$$

This equation is the discretized form of the free surface boundary condition at a particular y -value for the foremost free surface panel with index i next to the transom. The unknowns reside on the left hand side and the knowns on the right hand side. For the the downstream panel at the same y -value with index $i+1$, the following equation is used:

$$2Fn^2 [CA_{i+1} u_{i+1} + CB_{i+1} u_i] + w_{i+1} = 0, \quad (26)$$

$$\text{where } CB_{i+1} = \frac{1}{x_i - x_{i+1}} = -CA_{i+1}. \quad (27)$$

Equations 26 and 27 are applied to succeeding panels with indices $i+2$, $i+3$, etc. until the downstream boundary is reached. Equations 22 through 27 are applied for other y -values to cover the special section of free surface (Fig. 3) downstream from the transom.

The resulting system of difference equations is then solved using the Rankine source panel method. Substituting Eq. 1 into Eqs. 25 and 26 gives

$$2Fn^2 \sum_{j=1}^N CA_i CX_{i,j} S_j - 2\pi S_i = -2Fn^2 CB_i [1 + u_T] \quad (28)$$

and

$$2Fn^2 \sum_{j=1}^N [CA_{i+1} CX_{i+1,j} + CB_{i+1} CX_{i,j}] S_j - 2\pi S_{i+1} = 0. \quad (29)$$

The index N denotes the total number of panels for the hull surface, the main section of free surface, and the special section behind the transom. The influence coefficient $CX_{i,j}$ denotes the x -component of velocity induced on panel i by panel j per unit source strength. In the computations of influence coefficient for each hull panel, the contribution from its mirror image must be added. The source strengths S_i are the unknowns to be determined through the solution of a boundary value problem, and a Gaussian elimination scheme is used in the numerical solution. The distribution of source strength must satisfy simultaneously the free surface boundary condition and the Neumann boundary condition on the hull, as represented in Fig. 5.

A two-point upstream finite difference operator has been used in the special section behind the transom for wave resistance computations. These calculations are applied to a short computational domain covering one half of a ship length downstream from the transom. The four-point operator will be introduced for future calculations, which extend farther downstream, to improve the numerical accuracy of transom stern computations.

4. Comparison with experiments

This section presents a comparison of numerical predictions with the corresponding experimental measurements for high-speed transom stern ships. Such a comparison shows the extent to which the numerical model of transom stern flows can predict the hydrodynamics of the physical model. Another objective is to identify opportunities for future research in transom stern flows. Two examples are presented here: the local flow field around a ship and the force on a ship. The local flow field is represented by the wave pattern behind the transom for R/V Athena. The force on a ship is represented by the wave resistance for DTRC Model 5416.

4.1 Wave profiles

Figure 6 gives a sideview of the computed wave profile behind the transom for R/V Athena. The vertical and horizontal axes are nondimensionalized by $1/2 L$ and are plotted to the same scale. The numerical model of the transom stern is shown on the right. The dashed line represents the mean water level and the solid wavy line represents the free surface computed on panels closest to the centerplane. The computations were performed for a Froude number of 0.48. The free surface has a small slope, which is appropriate for this Froude number, and the flow

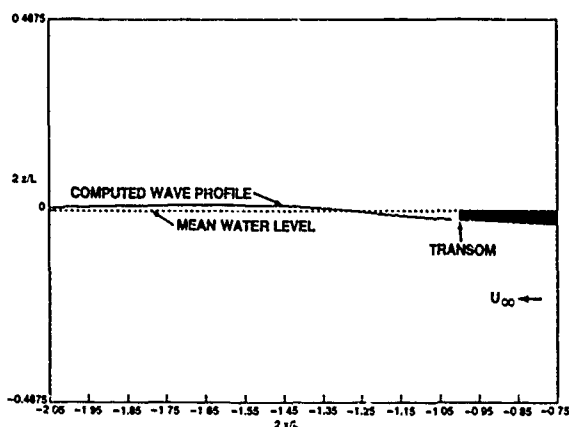


Fig. 6. Computed wave profile in the centerplane behind the transom for R/V Athena at a Froude number of 0.48.

angle can be measured graphically. Notice the ascending motion followed by the descending motion as expected. A gap is left between the transom and the computed free surface to indicate the centroid location of the foremost panel, where the free surface calculations are started. An upstream extrapolation of the free surface shows that the free surface intersects the transom at the transom depth Z_T .

Figure 7 gives a close-up view of Fig. 6 near the transom. Again the dashed line and solid wave line represent the mean water line and the computed free surface closest to the centerplane, respectively. The corresponding wave profile measured by Jenkins [12] is represented by isolated points and the rearmost point indicates the extent of experimental data. Thus, the experiment indicates that the transom clears the water and the assumption of a dry transom is valid for a Froude number of 0.48. The numerical prediction and experimental measurements of wave profiles behind the transom show close agreement, especially just downstream of the transom. The double model approximation of the flow direction seems justified in this case.

4.2 Wave resistance.

DTRC Model 5416 represents a typical high-speed transom stern ship without a bulbous bow. Dr. Michael Wilson of DTRC designed this hull form as a candidate for a low resistance ship. The computations for Model 5416 were performed at least one year prior to model construction and tank testing at DTRC. The model tests involved a longitudinal wave cut experiment using capacitance wave probes to measure wave profiles. A wave spectrum analysis of the measured wave profiles gave the measured wave pattern resistance. The

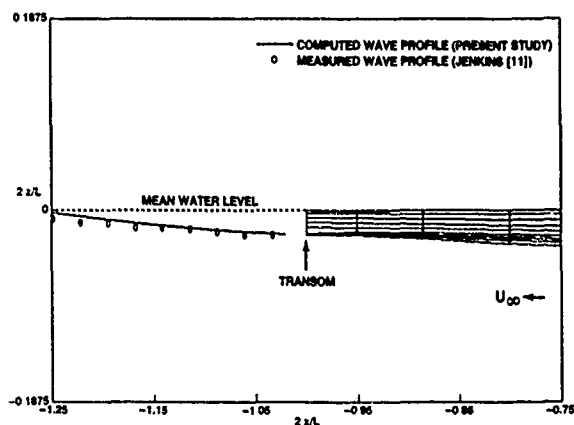


Fig. 7. Comparison of the computed and measured wave profiles for R/V Athena at a Froude number of 0.48.

measured wave pattern resistance was then compared to the wave resistance predicted by integrating the pressure on the hull using the XYZFS program version 2.0.

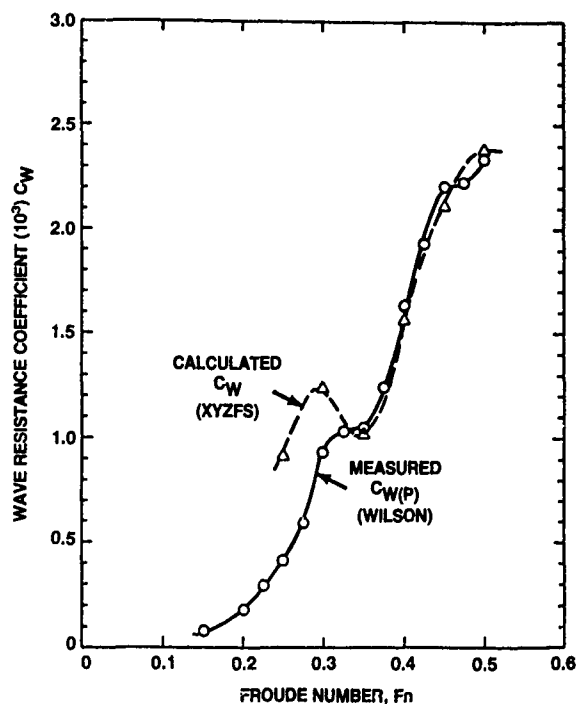


Fig. 8. Comparison between calculated wave resistance and measured wave pattern resistance versus Froude number for Model 5416.

This comparison of computed wave resistance and measured wave pattern resistance is presented in Fig. 8. The computations were performed for Froude numbers from 0.25 to 0.50 at increments of 0.05. The hull form was held fixed

at the even keel position for these computations and for the experiments. The calculated wave resistance and measured wave pattern resistance show general agreement. The agreement is remarkably good for Froude numbers from 0.35 to 0.50, corresponding to the operating speeds of high-speed transom stern ships and corresponding to the case of a dry transom. For Froude numbers below 0.35, the slope of the wave resistance curves is in agreement. However, computations predict a hump around a Froude number of 0.3, which is absent from the measured wave pattern resistance. This discrepancy is partially attributed to the breakdown of the dry transom assumption at lower Froude numbers. Transom stern flow at lower Froude numbers is the subject of a future study, and further numerical and experimental research is needed.

5. Conclusion

A practical computational method for 3D transom stern flows has been developed. A dry transom boundary condition has been derived for linearized free surface potential flows. The physical constraints imposed by the transom boundary condition require that the static pressure be atmospheric and that the flow leave tangentially at the transom. The pressure constraint has been applied to Bernoulli's equation to determine the magnitude of the velocity at the transom as a function of transom depth and Froude number. The velocity tangency constraint has been enforced by requiring the free surface flow to leave the transom tangentially in a direction specified by the double model flow. The numerical implementation of the free surface boundary condition involves the use of an upstream finite difference operator to eliminate upstream waves. The transom boundary condition has been used to specify the starting values for the free surface calculations in a special sector behind the transom. This computational method has been incorporated into a Rankine source panel method, the XYZFS program version 2.0.

The computed flow pattern behind the transom has been presented and compared with experimental measurements for the R/V Athena hull. Comparison of wave resistance prediction and experimental measurements have been presented for DTRC Model 5416. The results show that the wave resistance predictions are remarkably good for Froude numbers between 0.35 and 0.50, corresponding to the normal speed range of high-speed transom stern ships.

Acknowledgments

This study was supported by the Surface Ship Technology Exploratory Development Program and managed by the Ship Hydromechanics Department (SHD) of the David Taylor Research Center (DTRC). The author is indebted to Mrs. Joanna W. Schot of DTRC for her encouragement and support during the course of this study. The author wishes to thank Dr. Henry Haussling of DTRC for his advice and his constructive comments on the manuscript. Dr. Michael Wilson of SHD kindly furnished the experimental results for Model 5416. Mrs. Janet Dean of DTRC has contributed helpful suggestions and discussions.

References

1. Saunders, H.E., "Hydrodynamics in Ship Design," SNAME, Vol. 1, pp.326-327 (1957).
2. Gadd, G.E., "A Method of Computing the Flow and Surface Wave Pattern Around Full Forms," *Trans. RINA*, Vol. 118, p. 207 (1976).
3. Chang, M.S., "Wave Resistance Predictions by Using a Singularity Method," *Proc. of the Workshop on Ship Wave-Resistance Computations*, DTNSRDC, Bethesda, MD (Nov 1979).
4. Dawson, C.W., "A Practical Computer Method for Solving Ship Wave Problems," in *Proc. Second International Conference on Numerical Ship Hydrodynamics*, University of California, Berkeley (Sep 1977).
5. Dawson, C.W., "Calculations with the XYZ Free Surface Program for Five Ship Models," *Proc. of the Workshop on Ship Wave-Resistance Computations*, DTNSRDC, Bethesda, Maryland, (Nov 1979).
6. Cheng, B.H., J.S. Dean and J.L. Jayne, "The XYZ Free Surface Program and Its Application to Transom Stern Ships with Bow Domes," in *Proc. Second Workshop on Ship Wave-Resistance Computations*, DTNSRDC, Bethesda, MD (Nov 1983).
7. Cheng, B.H., G.G. Borda, J.S. Dean and S.C. Fisher, "A Numerical/ Experimental Approach to Wave Resistance Predictions," in *Computer Aided Design, Manufacture and Operation in the Marine and Offshore Industries*, Washington, D.C. (Sep 1986).
8. Hoyle, J.W., B.H. Cheng, B. Hays, B. Johnson, and B. Nehrling, "A Bow Bulb Design Methodology for High Speed Ships," *Transactions SNAME*, Vol. 94 (Nov 1986).

9. Cheng, B.H., J.S. Dean, R.W. Miller, and W. L. Cave III, "Hydrodynamic Evaluation of Hull Forms with Podded Propulsors," *Naval Engineers Journal*, Vol. 101, (May 1989).
10. Wilson, M.B. and T.P. Thomason, "Study of Transom Stern Ship Hull Form and Resistance," DTNSRDC report 85/072, DTNSRDC, Bethesda, MD (Apr 1986).
11. Tulin, M.P. and C.C. Hsu, "Theory of High-Speed Displacement Ships with Transom Sterns," *Journal of Ship Research*, Vol. 30, No. 3 (Sep 1986).
12. Jenkins, D.S., "Resistance Characteristics of the High Speed Transom Stern Ship R/V ATHENA in the Bare Hull Condition, Represented by DTNSRDC Model 5365," DTNSRDC report 84/024, DTNSRDC, Bethesda, MD (June 1984).
13. Coleman, R.M., "Nonlinear Flow about a 3-D Transom Stern," *Fourth International Conference on Numerical Ship Hydrodynamics*, Washington, D.C. (Sep 1985).
14. Hess J.L. and A.M.O. Smith, "Calculation of Potential Flow About Arbitrary Bodies," Pergamon Press Series, *Progress in Aeronautical Science*, Vol. 8 (1966).

DISCUSSION

by K. Nakatake

I appreciate your paper treating the transom stern flow. Fig.8 shows a good agreement of calculated and measured C_w . But, in this high Fn range, the effects of trim and sinkage become important. Did your calculation include such effect? If possible, please show the wave height contour around the model.

Author's Reply

Dr.Nakatake asked about the effects of sinkage and trim in the computations. The results presented in Fig.8 of my paper correspond to the fixed case for both the computations and experiments. To include sinkage and trim effect, we can reposition the hull according to sinkage and trim predictions from fixed case calculations. We did not analyze and plot wave height contours for a sunk and trimmed case and is presented in Fig.A1. The corresponding wave pattern resistance curve, as measured by Dr. Michael Wilson of DTRC, is presented for comparison. The computed results could be further improved by using the experimentally measured sinkage and trim to reposition the hull.

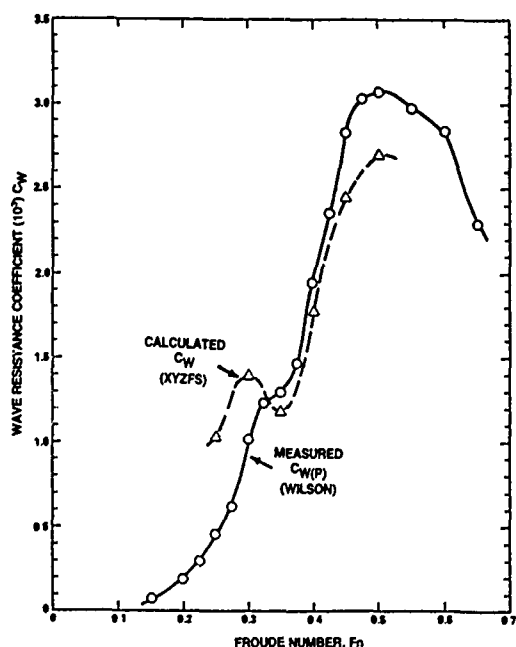


Fig.A1 Comparison between calculated wave resistance and measured wave pattern resistance versus Froude number for Model 5416 (sunk and trimmed case)

DISCUSSION

by J. Ando

I'd like to congratulate for your good results for 3D transom stern flow, and I'd like to discuss on the radiation condition. When we try to satisfy the radiation condition, if we use finite difference operator, we have some troubles. In my experience, point-to-point oscillation of the source strength occurred near the downstream boundary. Sometimes, the source strength oscillates so large that the wave pattern is affected. And the results change due to the kind of finite difference operator which uses number of points. Did you have such experience?

So I'd like to present a method which does not use any finite difference operator in order to satisfy the radiation condition. In this method, the radiation condition is satisfied automatically by shifting the source panel in the downstream direction by one panel length. We call it Kyushu University method which is abbreviated as KU method.

Next, I show some results for Wigley hull. Fig.A2 shows panel arrangement on the still water surface. By KU method, we don't use any finite difference operator along the stream line of the double model flow. Fig.A3 shows comparison of wave patterns. This pattern by KU method looks like the experimental result. Dawson's method gives wider propagation of free waves.

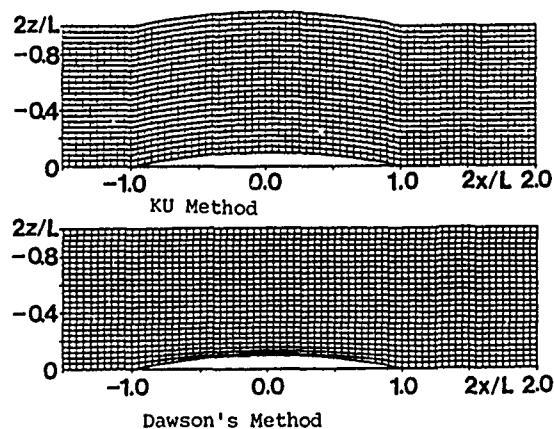


Fig.A2 Comparison of panel arrangement

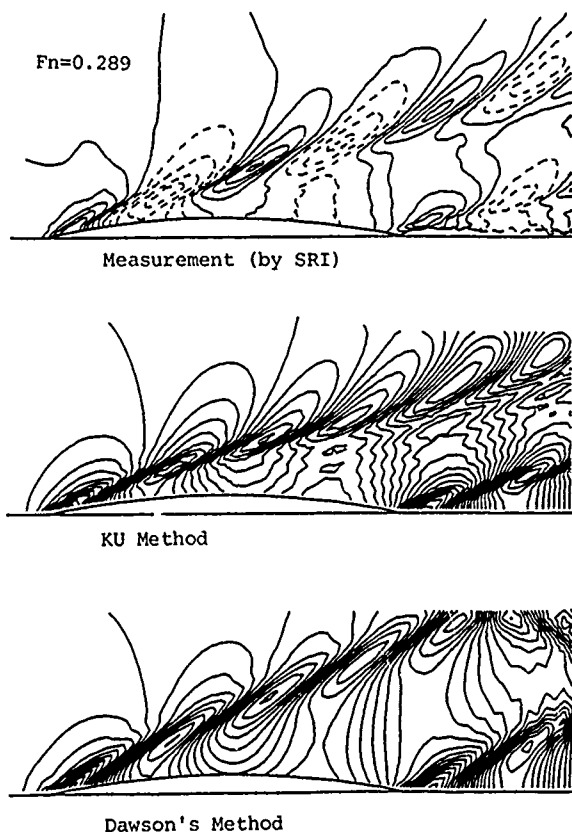


Fig.A3 Comparison of wave pattern

Author's Reply

I would like to thank Mr. Ando for his interest in my paper. It is true that the XYZ Free Surface problem uses upstream finite difference operators to eliminate upstream propagating waves, thus satisfying the radiation condition numerically. However, we have not experienced the point-to-point oscillations of the source strength near the down stream boundary as referred to by Mr. Ando. The reason is that we handle the downstream boundary in the following manner. As the downstream boundary is approached, a four-point operator is switched to a three-point operator and then to a two-point operator for the rearmost panel. The two-point operator gives considerable numerical damping when the rearmost panel is relatively large. Mr.Ando's "Dawson method" calculation seems to include a reflection from the side boundary. Such a reflection can be avoided by extending the side boundary of the computational domain to one ship length, measured from the ship's centerline.

The Kyushu University (KU) method for satisfying the radiation condition sounds interesting and seems to be similar to the method by Jensen[A1]. It would be helpful for the research community to know more about the KU method than has been presented in Mr. Ando's discussion. The results of the Wigley hull look promising and I encourage Mr. Ando to continue his studies on the radiation condition.

[A1] Jensen, P.S.: On the Numerical Radiation Condition in the Steady State Ship Wave Problem, J. of Ship Research, 1988.

Ship Wave-Resistance Computations

G. Jensen
Ingenieurkontor Lübeck, Germany
V. Bertram and H. Söding
Institut für Schiffbau Hamburg, Germany

Abstract

A method for the numerical determination of the potential flow around a ship moving steadily at the free surface of an ideal fluid solves iteratively for the non-linear boundary condition at the free surface, the body boundary conditions and the equilibrium floating position. The method can also be applied to shallow water and hulls with transom stern. The radiation condition and the open boundary condition are enforced by a special arrangement of the collocation points at the discretisation boundaries. This paper also describes a new simple and flexible panel method for satisfying the body boundary condition; the method could be used for other potential flow problems as well.

1. Symbols

B breadth of the hull
 D draught
 D_0 draught at rest
 c_F frictional resistance coefficient
 c_w wave resistance coefficient
 \vec{e}_z unit vector pointing in the direction of the towing force
 \vec{F} pressure force on the body
 f panel area
 \vec{F}_A additional force on the body
 F_n $= U^2 / \sqrt{gL_{PP}}$, Froude number
 g acceleration of gravity
 G weight
 \vec{G} $= (0, 0, G)$
 $G(\vec{p}, \vec{q})$ potential at point \vec{q} due to unit source at \vec{p}

H water depth
 \vec{k} point on tangential sphere
 L_{PP} ship length between perpendiculars
 M source strength
 \vec{n} unit normal pointing into body
 \vec{p} point
 P projection of a point on the body surface onto the tangential sphere
 p pressure
 \vec{q} point
 r ratio between the area of the projection and that of the original surface element
 R radius of tangential sphere
 R_w wave resistance
 S wetted or panelized body surface
 S_0 wetted surface at rest
 \vec{s}, \vec{t} vectors tangential to the body surface
 \vec{T} moment due to pressure on body
 \vec{T}_A additional moment on body
 U free stream velocity
 v_n velocity component normal to body surface
 v_s, v_t components of velocity tangential to body surface
 \vec{x} point on free surface
 x, y, z right-handed coordinate system; the x and y axes are on the undisturbed free surface, x points upstream, z vertically downward
 \vec{x}_Z point of action of towing force
 \vec{x}_G center of gravity of ship's mass
 \vec{Z} towing force
 δ submergence of dipole
 μ moment of dipole
 θ trim angle (bow down trim is positive)
 θ_0 trim angle at rest
 ϕ velocity potential
 Φ approximation of ϕ
 φ $= \phi - Ux$
 $\bar{\varphi}$ correction of Φ
 ρ density of water
 σ nondimensional sinkage at midship section; see (26)

τ	nondimensional trim; see (26)
ζ	z-coordinate of free surface
Z	approximation of ζ

suffices:

1,2,3	vector component in direction of the x-, y- or z-axis resp.
F	refers to point or source at the free surface
k	refers to point \bar{k}
K	refers to point or source on the body surface
n	component in direction of the normal \bar{n}
p	refers to point \bar{p}
q	refers to point \bar{q}
x, y, z	partial derivatives

2. Introduction

For the design of a ship hull and its power requirement it is of great practical interest to know the flow and the resulting forces due to the steady motion at the surface of a calm ocean. Experimental techniques try to separate viscous from potential-flow forces to scale measured force coefficients from a model to the full-scale ship. Due to the difficulty of computing viscous flow forces for high Reynolds numbers, the same separation is used in numerical predictions as well. Serious efforts to compute the potential flow and the accompanied wave resistance of a ship started with the pioneering work of Michell [1] in 1898. In spite of the great emphasis placed on this problem, numerical solutions are only now at the threshold of practical applicability. They neglect breaking waves, spray, bow vortices and other details of the flow, which may then be described by a potential satisfying Laplace's equation and boundary conditions at all fluid boundaries.

The major difficulty in this problem is the nonlinear boundary condition at the unknown location of the free surface. To circumvent this difficulty, most known methods use, apart from the *physical* simplifications stated above, additional *mathematical* simplifications: Almost exclusively a linearized free-surface boundary condition is implied at the location of the undisturbed free surface, and in most cases the solution is described by a superposition of complicated singularities that meet this linearized free-surface condition identically. All linear methods show good agreement with measurements only for special hull forms or high Froude numbers $F_n = U^2/\sqrt{gL_{PP}}$, where U is ship speed, g acceleration of gravity, and L_{PP} the ship length between perpendiculars.

In 1978 Dawson [2] published a method using a distribution of Rankine sources (potential = 1/distance) on the body surface and on a local part of the free surface around the body. The flow is imagined to be superimposed from the double-body flow, i.e. the flow which would result in case of a rigid free surface, and a correction $\bar{\varphi}$. The source strength distribution is determined from the body boundary condition and a so-called double-body linearization of the free-surface condition. This linearization neglects nonlinear terms in $\bar{\varphi}$ and is applied at the plane, undisturbed water surface. The radiation condition which states that waves may occur only behind the ship is enforced by a one-sided finite-difference operator for the second derivative of the potential in the direction of the double-body streamlines appearing in Dawson's free-surface boundary condition. This numerical method of satisfying the radiation condition has the disadvantage that the surface waves are damped a little and are slightly shorter than they should be.

Several authors have tried to extend Dawson's method to an iterative solution of the exact, nonlinear problem, but it was only quite recently that Ni [3] and Jensen [4] succeeded. Both methods show good agreement with resistance force measurements for the few cases compared so far.

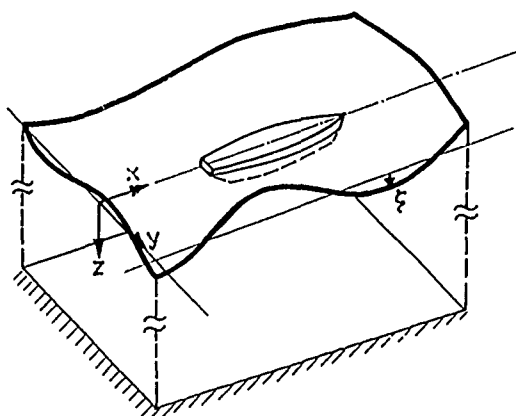
Ni's method uses source-panels on the wetted part of the body surface and on a local part of the free surface as computed in the previous iteration step. In each step the body boundary condition and linearized dynamic and kinematic free-surface conditions are used to derive a system of linear equations for the unknown source strengths and surface elevations at control points. After solving this system the body is repanelized automatically up to the computed waterline. The radiation condition is enforced by means of a one-sided finite-difference operator as in Dawson's method.

Our method, on the other hand, employs Rankine point sources in a layer above the water surface, and in each iteration step it uses the same panelization of the body and a mirror image of it above the water surface. A linearized free-surface boundary condition for the flow potential is used in each step of the iteration together with the body boundary condition. After solving the resulting system of linear equations for the source strengths, the shape of the free surface is determined from the dynamic free-surface condition. The radiation condition and the open boundary condition are enforced by adding an extra row of control points at the upstream end of the free surface mesh, and an extra row of source points at the downstream end. The effectiveness of this simple method was shown already in [4,5]. For the body boundary condition a new, flexi-

ble panel method with simple numerical integration of the influence function is used.

3. Problem

We want to compute the stationary flow of an incompressible, irrotational fluid around a laterally symmetric body at or near the free surface of an otherwise unbounded fluid. Far upstream the fluid has the uniform velocity U opposite to the direction of the x -axis of our Cartesian x, y, z coordinate system with z pointing downward.



The velocity potential ϕ meets Laplace's equation:

$$\Delta\phi = 0 \quad (1)$$

at points below the free-surface height ζ and outside of the body and, in case of limited water depth, above the bottom.

The velocity potential is subject to the following boundary conditions:

No flow across the body surface with normal direction \vec{n} :

$$\vec{n} \nabla \phi = 0 \quad \text{on the wetted body surface.} \quad (2)$$

In case of a ship with transom stern we assume that the transom is dry. We require: At the edge of the transom stern the pressure in the flow is equal to the pressure at the free surface.

The pressure on the free surface is constant. If p is the pressure difference with respect to the free-surface pressure, we obtain from Bernoulli's equation

$$p = \rho \left(-\frac{(\nabla\phi)^2}{2} + gz + \frac{U^2}{2} \right) \quad (3)$$

the dynamic free-surface condition; for $z = \zeta$ outside the body:

$$\frac{1}{2} (\nabla\phi)^2 - g\zeta = \frac{1}{2} U^2 \quad (4)$$

No flow across the free surface; for $z = \zeta$ outside the body:

$$\nabla\phi \nabla\zeta = \phi_z \quad (5)$$

(For simplification we write $\zeta(x, y, z)$ with $\zeta_z = 0$.)

Far from the body the flow field tends to a uniform flow:

$$\lim_{x^2+y^2+z^2 \rightarrow \infty} \nabla\phi = (-U, 0, 0). \quad (6)$$

In some distance from the body waves appear only within a sector downstream (radiation condition).

In case of shallow water there is no flow across the (plane) bottom; for $z = H$:

$$\phi_z = 0 \quad (7)$$

The pressure force \vec{F} acting on the body is determined by integrating the pressure difference p over the wetted part S of the hull:

$$\vec{F} = \int_S p \vec{n} dS. \quad (8)$$

The moment due to the fluid pressure is

$$\vec{T} = \int_S p \vec{x} \times \vec{n} dS. \quad (9)$$

The equilibrium floating position of the body is determined from the condition that the forces and moments on the body add up to zero. To compare computed results with resistance experiments for towed ship models, besides \vec{F} and \vec{T} the weight \vec{G} , the towing force \vec{Z} acting at \vec{x}_Z , and the force \vec{F}_A due to the viscous part of the model resistance together with the corresponding moments have to be accounted for. Therefore the equilibrium conditions are

$$\vec{F} + \vec{G} + \vec{Z} + \vec{F}_A = 0 \quad (10)$$

and

$$\vec{T} + \vec{x}_G \times \vec{G} + \vec{x}_Z \times \vec{Z} + \vec{T}_A = 0. \quad (11)$$

The wave resistance coefficient c_w is defined as

$$c_w = -\frac{F_1}{\frac{\rho}{2} U^2 S_0}. \quad (12)$$

S_0 is the wetted surface at rest, F_1 the x -component of \vec{F} .

4. Free surface boundary condition

The unknown surface height ζ can be eliminated from (4) and (5); at $z = \zeta$:

$$\frac{1}{2} \nabla \phi \nabla (\nabla \phi)^2 - g \phi_z = 0. \quad (13)$$

This free-surface condition is nonlinear; it is valid at the unknown location of the water surface. Therefore we iterate solutions with a linearized condition which assures that - if convergence is reached - the solution fulfills (13).

To derive this condition, let Φ and Z be approximations for ϕ and ζ . We substitute $\phi = \Phi + \bar{\varphi}$ in (13), neglect terms nonlinear in derivatives of $\bar{\varphi}$, and obtain at $z = \zeta$:

$$\begin{aligned} & \nabla \Phi \nabla \left(\frac{1}{2} (\nabla \Phi)^2 + \nabla \Phi \nabla \bar{\varphi} \right) \\ & + \nabla \bar{\varphi} \nabla \left(\frac{1}{2} (\nabla \Phi)^2 \right) - g(\Phi_z + \bar{\varphi}_z) = 0 \end{aligned} \quad (14)$$

Φ and $\bar{\varphi}$ are developed into a Taylor series about Z . The series is truncated after the linear term. If products of $\zeta - Z$ with derivatives of $\bar{\varphi}$ are neglected, (14) becomes

$$\begin{aligned} & \nabla \Phi \nabla \left(\frac{1}{2} (\nabla \Phi)^2 + \nabla \Phi \nabla \bar{\varphi} \right) + \nabla \bar{\varphi} \nabla \left(\frac{1}{2} (\nabla \Phi)^2 \right) \\ & - g(\Phi_z + \bar{\varphi}_z) + \left[\frac{1}{2} \nabla \Phi \nabla (\nabla \Phi)^2 - g \Phi_z \right]_x (\zeta - Z) = 0 \end{aligned} \quad (15)$$

at $z = Z$. The index z designates partial derivatives. To decrease the number of unknowns, ζ is substituted by expressions involving Z , $\Phi(Z)$ and $\bar{\varphi}(Z)$ only. To this end (4) is developed into a Taylor series as well and linearized:

$$\begin{aligned} \zeta &= \frac{1}{2g} [(\nabla \phi)^2 - U^2]_{z=\zeta} \\ &= \frac{1}{2g} [(\nabla \Phi)^2 + 2\nabla \Phi \nabla \bar{\varphi} - U^2]_{z=\zeta} \\ &= \frac{1}{2g} [(\nabla \Phi)^2 + 2\nabla \Phi \nabla \bar{\varphi} \\ & \quad + 2\nabla \Phi \nabla \bar{\varphi}_z (\zeta - Z) - U^2]_{z=Z}. \end{aligned} \quad (16)$$

This gives

$$\zeta - Z = \frac{\frac{1}{2} [(\nabla \Phi)^2 + 2\nabla \Phi \nabla \bar{\varphi} - U^2] - gZ}{g - \nabla \Phi \nabla \bar{\varphi}_z}, \quad (17)$$

with Φ and $\bar{\varphi}$ being evaluated at $z = Z$.

Inserting (17) into (15) and substituting $\bar{\varphi}$ by $\phi - \Phi$, we obtain the linearized free surface condition

$$\begin{aligned} & \nabla \Phi \nabla \left[-(\nabla \Phi)^2 + \nabla \Phi \nabla \phi \right] + \frac{1}{2} \nabla \phi \nabla (\nabla \Phi)^2 - g \phi_z \\ & + \left[\frac{1}{2} \nabla \Phi \nabla (\nabla \Phi)^2 - g \Phi_z \right]_x \\ & \frac{\frac{1}{2} [-(\nabla \Phi)^2 + 2\nabla \Phi \nabla \phi - U^2] - gZ}{g - \nabla \Phi \nabla \bar{\varphi}_z} = 0 \end{aligned} \quad (18)$$

at $z = Z$ outside of the body. The denominator in the last term is zero if the vertical component of the particle acceleration $\nabla \Phi \nabla \bar{\varphi}_z$ is equal to the acceleration of gravity g ; this is the stability limit of the approximate flow Φ .

5. Radiation and open boundary condition

ϕ is approximated as the sum of the potentials of the uniform stream, a regular mesh of point sources in a layer above the free surface and the potential of singularities on the body surface. The point sources are generally located vertically above the collocation points. Only at the upstream end of the grid there is an additional row of collocation points, and at the downstream end there is an additional row of point sources.

To validate this simple scheme to enforce the radiation condition and the open boundary condition, the flow around a submerged dipole with Kelvin condition at the free surface was computed and compared to analytical solutions given by Nakatake [6]. Figs. 1 and 2 show the resulting free surface deformation from the analytical and the numerical solution for different submergence speed parameters $F = g\delta/U^2$. δ is the submergence of the dipole. The numbers at the contour lines indicate values of $\zeta g \delta^3 / (4\pi U \mu)$, where μ is the moment of the dipole. The agreement is excellent.

6. Body boundary condition

The Neumann condition (2) at the body surface is fulfilled using a new panel method [4]. The commonly used method of Hess and Smith [7] uses plane quadrilateral panels with constant source strength and control points in the (suitably defined) centre of each panel. The integral over the derivatives of the source potential can be evaluated analytically for each panel. This results in complicated expressions containing transcendental functions. Such expressions are expensive to evaluate numerically.

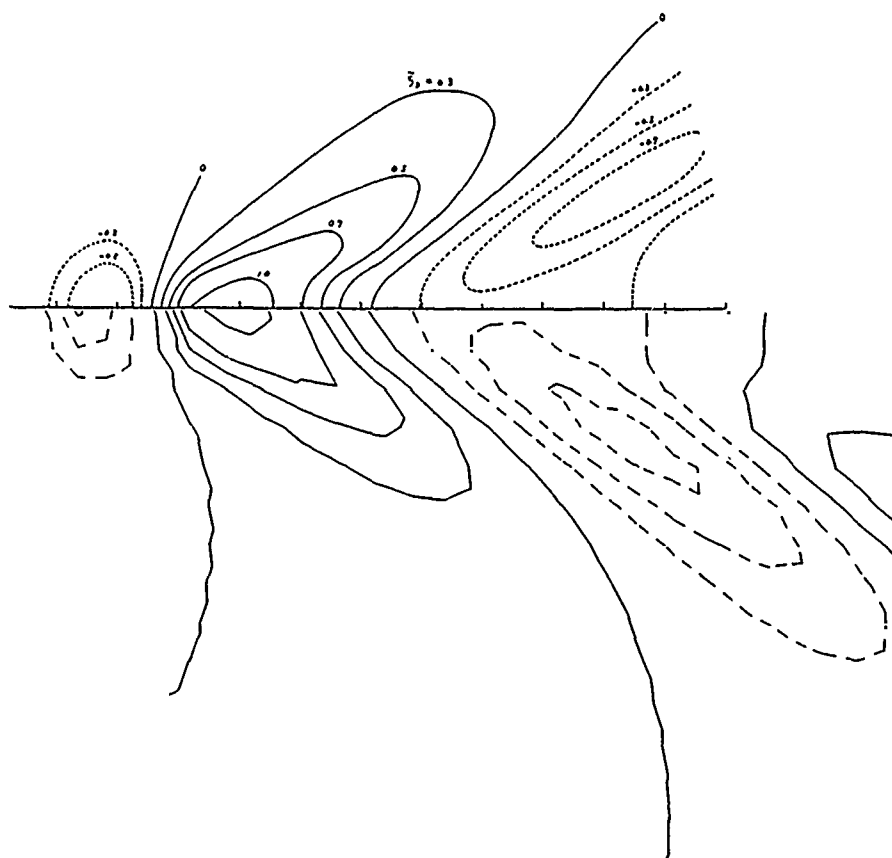


Fig.1. Contour lines of surface elevation due to a submerged dipole for $F = 0.5$
The upper half shows the analytical solution due to Nakatake [6],
the lower half shows the numerical solution

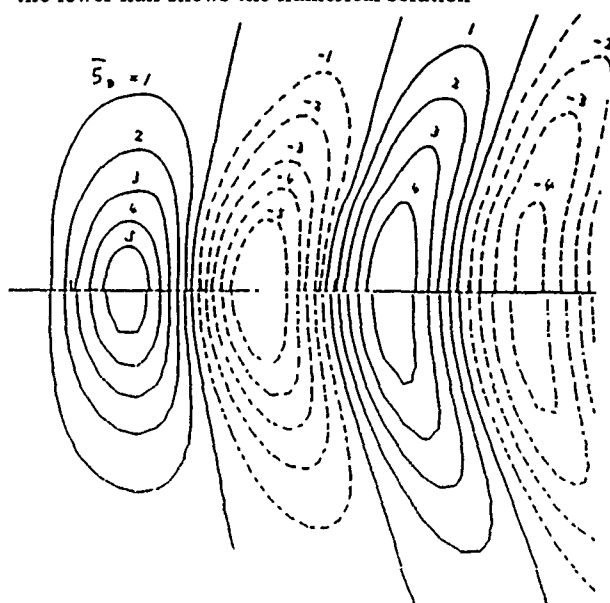


Fig.2. Contour lines of surface elevation due to a submerged dipole for $F = 3.0$
The upper half shows the analytical solution due to Nakatake [6],
the lower half shows the numerical solution

Here we show a possibility to evaluate these integrals with simple numerical integration by eliminating the singularity of the integrand at the control point on the panel:

$$\phi(\vec{q}) = \int_S M(\vec{p}) G(\vec{p}, \vec{q}) dS_p, \quad (19)$$

$\phi(\vec{q})$ is the potential at a point \vec{q} induced by a source distribution M on the body surface S ; $G(\vec{p}, \vec{q})$ is the potential of the unit source at \vec{p} : $G = -(4\pi|\vec{p} - \vec{q}|)^{-1}$. The normal velocity on the body surface S is

$$v_n(\vec{q}) = \vec{n}(\vec{q}) \nabla_{\vec{q}} \phi(\vec{q}) = \quad (20)$$

$$\int_S M(\vec{p}) \vec{n}(\vec{q}) \nabla_{\vec{q}} G(\vec{p}, \vec{q}) dS_p - \frac{1}{2} M(\vec{q}).$$

If the normal velocity is prescribed by the boundary condition, the velocity on S in two different tangential directions \vec{t} is to be determined only:

$$v_t = \vec{t}(\vec{q}) \nabla_{\vec{q}} \phi(\vec{q}) = \oint_S M(\vec{p}) \vec{t}(\vec{q}) \nabla_{\vec{q}} G(\vec{p}, \vec{q}) dS_p. \quad (21)$$

For a 3-dimensional flow the integrand in (20) is singular for $\vec{p} \rightarrow \vec{q}$ for a curved surface; inside a plane panel it is zero. But the integrand in (21) is unbounded even within a plane panel with constant source strength. So there is no difficulty to evaluate (20) numerically, but (21) must be transformed to allow numerical integration. This is possible using the following idea:

A source distribution of constant strength on the surface S of a sphere does not induce any tangential velocity on S :

$$\int_S \vec{t}(\vec{q}) \nabla_{\vec{q}} G(\vec{k}, \vec{q}) dS_k = 0 \quad \text{for } \vec{q} \text{ and } \vec{k} \text{ on } S. \quad (22)$$

The sphere is placed touching the body tangentially at the point \vec{q} . If the centre of the sphere is within the body, there exists a projection $\vec{k} = P(\vec{p})$ of every point \vec{p} on the body surface to a unique point \vec{k} on the sphere surface, the projection being defined by a straight line passing through \vec{k} , \vec{p} and the sphere's centre. The projection of all body points will cover the whole sphere surface at least once. Surface elements dS_k on the sphere are projected onto surface elements dS_p on the body. Let r be the area ratio of the surface elements: $dS_k = r dS_p$. The sign of r is defined by the sign of the scalar product of the corresponding normal vectors pointing into the body or sphere, respectively. With these definitions, (22) can be transformed into an integral over the body surface:

$$\oint_S \vec{t}(\vec{q}) \nabla_{\vec{q}} G(P(\vec{p}), \vec{q}) r dS_p = 0. \quad (23)$$

This expression is multiplied by $M(\vec{q})$ and subtracted from (21):

$$v_t = \vec{t}(\vec{q}) \nabla_{\vec{q}} \phi(\vec{q}) = \oint_S [M(\vec{p}) \vec{t}(\vec{q}) \nabla_{\vec{q}} G(\vec{p}, \vec{q}) - M(\vec{q}) \vec{t}(\vec{q}) \nabla_{\vec{q}} G(P(\vec{p}), \vec{q}) r] dS_p. \quad (24)$$

If \vec{p} approaches \vec{q} the integrand is still singular in general, but within a panel of constant source strength it approaches zero. Details can be found in [4].

To evaluate (24) numerically the closed surface of the body is discretized into N panels. For each of them area f_i , midpoint \vec{x}_i , unit normal \vec{n}_i and two approximately orthogonal tangent vectors \vec{s}_i and \vec{t}_i are determined, and the radius of the tangential sphere is chosen. The radius turned out to have negligible influence on the results within wide limits. At each collocation point on S the normal velocity v_n is prescribed (e.g. $v_n = U n_1$).

The panel midpoints \vec{x}_i are used both as control (collocation) points where the boundary condition is fulfilled, and as integration points for the numerical integration over the body surface, which is performed simply by adding the products of integrand times panel area. This gives a system of linear equations for the unknown source strengths.

Computing time and accuracy of this method were found to be similar to those of the Hess&Smith method [4]. But this new method is more flexible in the discretisation since panels with arbitrary numbers of corners are handled without difficulty. Furthermore, the programming is simplified, especially if higher derivatives of the potential have to be determined also.

The potential at a point \vec{q} outside of the body is computed as

$$\phi(\vec{q}) = \int_S M(\vec{p}) G(\vec{p}, \vec{q}) dS_p. \quad (25)$$

The integrand is regular, but the numerical evaluation of the integral by this formula is not very accurate if the distance between \vec{q} and S is small compared to the panel size. Derivatives of the potential are computed by using the corresponding derivatives of G in (25).

As an example the flow around a sphere in uniform flow in an unbounded domain was computed using triangular panels. In this case we know the analytical solution. The following table shows the maximum error of the velocity vector at the collocation points in percent of the free stream velocity.

Table 1: Error depending on discretization
 N number of elements

N	1	4	16	64	256	1024
error	13.5	5.62	3.19	1.58	0.78	0.39

This shows that the method (like that of Hess&Smith) is of first order; the error decreases proportional to the mesh spacing.

As in most panel methods a smooth body surface is required. Ships often have sharp stems or sterns. The body boundary condition will always be violated near such a corner. The panel method may still be applicable for practical purposes if the overall solution is not disturbed. Figure 3 validates this property by showing the computed deviation from the parallel flow for a Wigley double model with different panelizations.

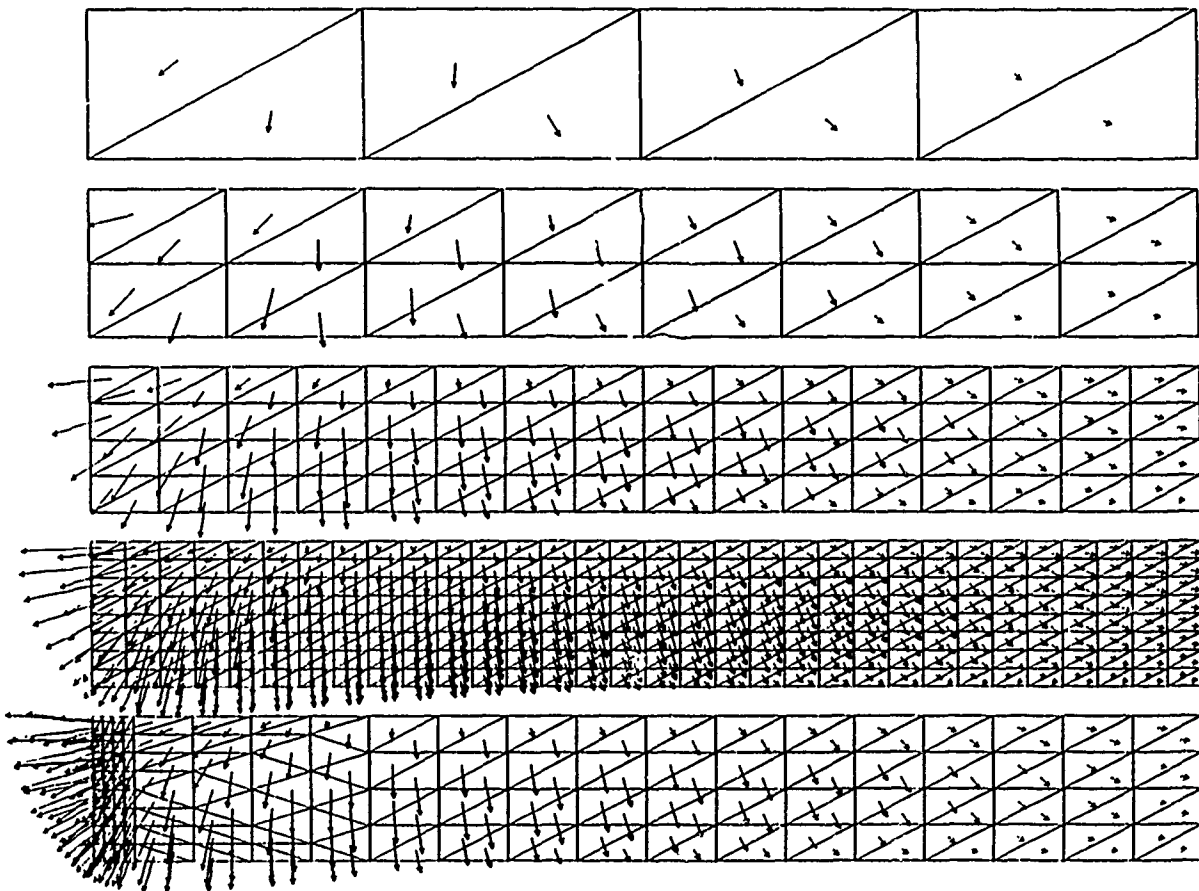


Fig.3. View of the forward lower half of a Wigley double model in direction of the y -axis. The arrows show the deviation from the parallel flow for 8, 32, 128 und 512 panels on one eighths of the hull surface and for a grid with 208 panels, which is the 128 panel grid with local refinement near the stem.

7. Body at the free surface

For determining the stationary potential flow about a body sailing steadily at a free surface of an ocean of finite depth, the methods described in the preceding sections are combined as follows. Source panels are used

- on the wetted starboard hull surface, and
- on a part of the above-water surface up to a plane above the uppermost point of the assumed waterline at the hull.
- Further source panels of equal source strength as those below this plane are arranged on a mirror image of the hull surface above this plane. The reason for this is that, on one hand, our special panel method requires the source panels to constitute a closed surface, and, on the other hand, this mirror image reduces the necessary width of
- the grid of further sources arranged along the free water surface. Here it is sufficient to use point sources above the free water surface instead of source panels on the free surface. We use point sources located one grid spacing above the free surface.
- Further, all these sources are mirrored both at the symmetry plane of the ship and – in case of shallow water – at the bottom to satisfy the respective boundary conditions.

The source strengths are determined from the following conditions:

- On the ship surface up to the plane somewhat above the water surface, the condition of vanishing flow velocity normal to the surface is satisfied. For the part of the hull surface above the water, this condition is applied for two reasons: On one hand, we do not know in advance where the actual water surface is, and, on the other hand, the continuous source strength along the continuous ship surface and its mirror image above the horizontal plane helps to obtain a smooth potential at the intersection between body and waterline. The same argument could and has been proposed for a continuation of the free-surface source panels into the body. However, because we use sources not at, but above the water surface, at the free surface the potential due to these sources is smooth anyway.

- The transom stern is also covered by source panels. However, if the water flow is assumed to separate smoothly at the transom such that the transom face is not wetted, the usual condition of vanishing normal velocity is not applied on the transom. Instead, at the collocation points on the transom we assume a normal velocity through the transom of a size which satisfies the dynamic (pressure) condition at the boundary between the transom and the rest of the ship surface, assuming the normal velocity to be constant over the whole area of the panel. This results in a normal velocity greater than the ship's speed U if the edge of the transom is below the undisturbed water surface, and a normal velocity smaller than U if the transom edge is above the undisturbed water surface. Only if the edge of the transom is at or above the stagnation height level, the condition of vanishing normal velocity is applied. Whether the transom is wetted or not, has to be guessed in advance.
- At the free water surface the linearized free surface condition (18) is imposed.

These boundary conditions are satisfied at, typically, 1000 collocation points on the body and on the free surface. When the source strengths have been determined, the free surface elevation is computed from the dynamic boundary condition. The collocation points on the free surface are moved to this height. Then the process is repeated to get an iterative solution of the nonlinear free surface conditions.

On the water surface, the collocation points form a regular grid outside of the body up to a distance which was determined by test calculations and which depends on the Froude number. Usually, point sources are located about one grid length above each collocation point. However, if the distance between source and collocation point is smaller than about 3 grid lengths, instead of one collocation point a pattern of 4 points is used, and the average error of the boundary condition at those 4 points is considered.

It may be questioned whether our numerical methods applied to solve the potential-flow problem are correct for derivatives up to 3rd order. Without theoretically investigating this matter, we simply found that the method usually converges to a solution in which the errors of the nonlinear free-surface conditions are indeed extremely small at all collocation points, usually below 1/1000th of the ship speed if they are expressed in form of a velocity. Due to the smoothness of the potential, errors are relatively small also between collocation points. To obtain such an accuracy, it was necessary to apply a normalization of the equations

which led to approximately equal values on the main diagonal of the coefficient matrix.

To decrease the cases of divergence, we found it helpful to determine the maximum error of the free-surface condition at the newly determined positions of the free surface both with the previous and with the current source strength, and to use intermediate source strengths if the maximum error was larger with the new than with the old source strengths.

In the iteration to solve the nonlinear free-surface condition the pressure distribution is integrated on the actually wetted part of the hull to obtain the resulting forces and moments. Together with corrections for the pitch moment of the viscous resistance and the towing or propeller force, a correction of the equilibrium floating position is determined, and the panel grid of the body is shifted and rotated correspondingly before the next iteration step is performed.

The linear system of equations obtained during each iteration step is solved by a combination of elimination steps with a Gauß-Seidel iteration: At first, only those elements below the main diagonal the absolute value of which exceeds a certain limit are eliminated to improve the condition number of the matrix. If the following Gauß-Seidel iteration indicates no convergence, further incomplete eliminations using a smaller limit are performed. This method constitutes a completely safe and quick solution scheme.

8. Applications

8.1 Series 60 with $C_B = 0.6$ in deep water

The Series-60 hull shape with a block coefficient $C_B = 0.6$ was chosen because extensive and careful experiments and resistance evaluations have been performed for this form by Ogiwara [8]. The principle relations of his model are:

$$\text{breadth } B = \frac{L_{PP}}{7.5}; \quad \text{draught at rest } D_0 = \frac{L_{PP}}{18.75},$$

$$\text{wetted hull area at rest } S_0 = \frac{L_{PP}^2}{5.8685}.$$

The hull surface was panelized up to a height $0.3125D_0$ above the floatation line at rest. There were 453 panels used on one half of the body. As in Ogiwara's experiments the horizontal towing force was applied at $0.485L_{PP}$ from the aft perpendicular and $0.461D_0$ under the floatation line at rest. The viscous resistance coefficient $c_F = R_f/(0.5\rho U^2 S_0)$ was estimated to be $3.5 \cdot 10^{-3}$ for all speeds. For the speed

range investigated here it had only a small influence on the results. The height of the centre of gravity which is not given by Ogiwara was assumed in the floatation line at rest.

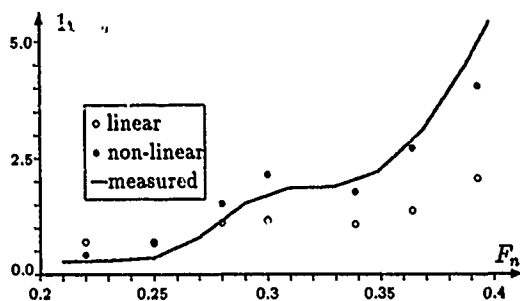


Fig.4. Computed wave resistance coefficients for Series-60 with $C_B = 0.60$ and values measured by Ogiwara [8]

In Fig. 4 our computed wave resistance coefficients are compared to Ogiwara's measurement evaluations. For comparison also the results of the Neumann-Kelvin problem are included. The results were obtained with the same program (1. iteration step) and the same grids; trim and sinkage were suppressed and the still-water line used as an integration limit for the pressure integration. Especially for higher Froude numbers non-linear results agree much better with experiments.

Figures 5 and 6 show the nondimensional sinkage and trim defined by

$$\sigma = \frac{2}{F_n^2} \frac{D_0 - D}{L}; \quad \tau = \frac{2}{F_n^2} (\theta_0 - \theta) \quad (26)$$

as functions of the Froude number. For sinkage the agreement is good. The curve for the computed trim is similar to the corresponding measurements, but appears to be shifted somewhat to aft trim.

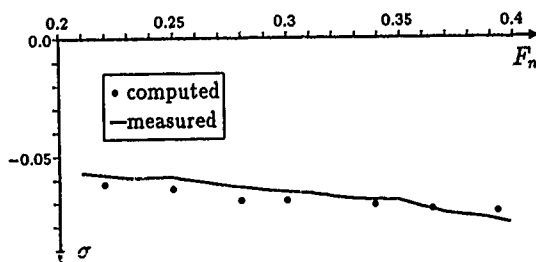


Fig.5. Computed and measured [8] nondimensional sinkage σ at midship section of a Series-60 model with $C_B = 0.60$

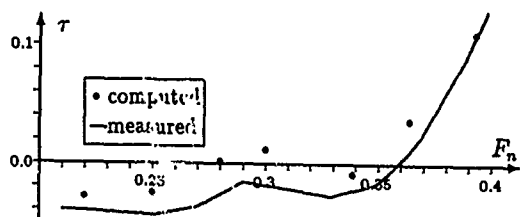


Fig. 6. Computed and measured [9] nondimensional trim τ for a Series-60 model with $C_B = 0.60$

Fig. 7 shows the computed elevation of the free surface for the solution obtained with the linearized free-surface condition (Kelvin condition)

$$U^2 \phi_{xx} - g \phi_z = 0 \text{ at } z = 0 \quad (27)$$

and the solution with the exact nonlinear condition (13) for $F_n = 0.25$.

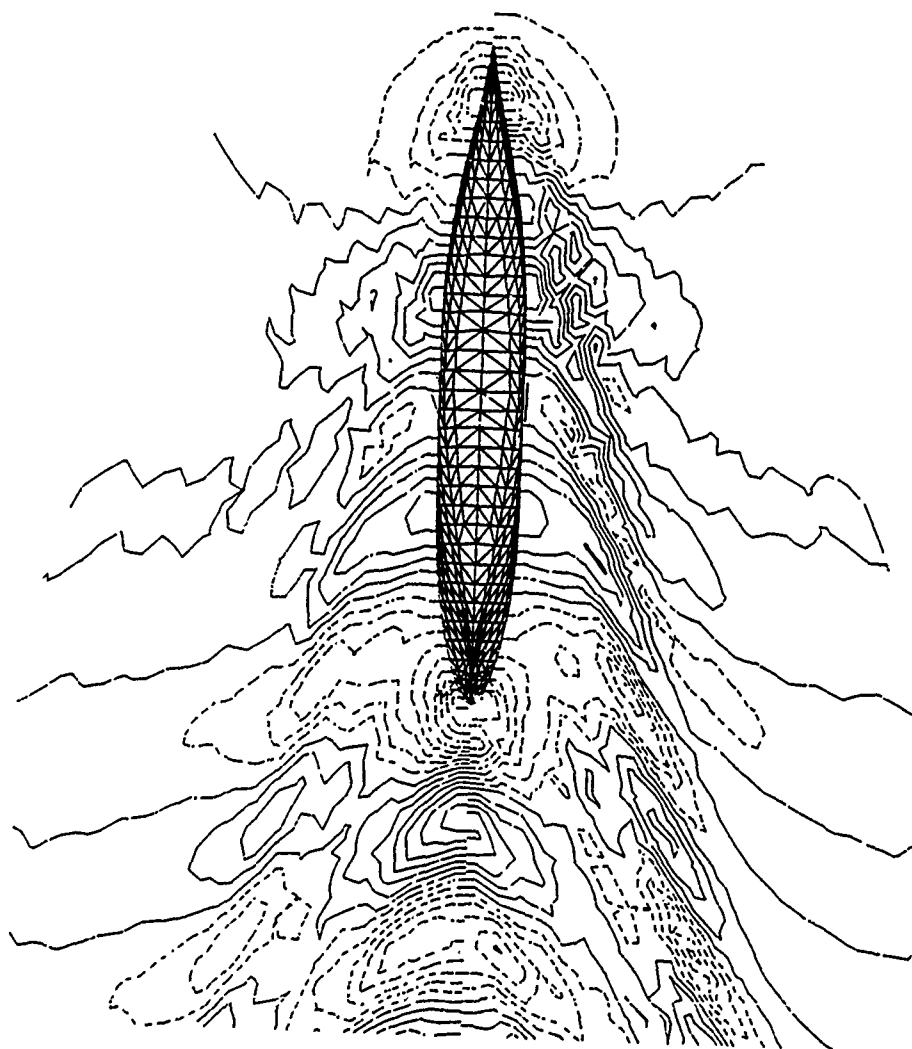


Fig. 7. Contour lines of deformed water surface for a Series-60 model, $C_B = 0.60$, at $F_n = 0.25$.
Left side: linear solution; right side: nonlinear solution.
The vertical distance between contour lines is $10^{-3} L_{PP}$.

8.2 Containership in shallow water

The following results apply to a containership the principal data of which are shown in the following table.

Table 2: Principal data of investigated containership

length between perpendiculars	161.44	m
breadth	28.40	m
draught at $U=0$	10.00	m
trim at $U=0$	0	m
block coefficient	0.68	
designed load waterline coefficient	0.82	

Dynamic sinkage and trim of ships on shallow water are of interest not only because of possible grounding. Forward trim usually encountered on shallow water can reduce yaw stability so severely that ships may lose their ability to keep course.

Figure 8 shows results for the draught at the forward perpendicular divided by the stagnation height $U^2/2g$ depending on depth Froude number F_{nh} and length Froude number F_n . The theoretically most interesting region around depth Froude numbers of 1 can be investigated only in case of relatively large length Froude numbers because otherwise the ship touches the ground. Limits of ground-touching are indicated in Figure 9. This is the reason for investigating also high length Froude numbers which are unrealistic for a containership. As can be seen, near to a depth Froude number of 1 large changes of the squat are experienced. This is known also from model experiments and small boats.

To determine the accuracy of these results, model experiments are being performed but not yet finished. Instead, Figure 10 shows results of approximation formulae according to Barras [9] which were established on the basis of model experiments and measurements aboard ships, and results of the slender-body theory of Tuck [10] applied to our ship. The nearly exact coincidence with Tuck's formula is striking; however, near to the critical depth Froude number 1 this formula is not applicable.

Possible errors of our method were investigated also on the basis of numerical experiments with different grids on the body and on the free surface. In the following tables ϵ denotes the difference in sinkage to the most accurate computation in % of sinkage at forward perpendicular FP.

The results indicate that for the small length Froude number of 0.15 (6 m/s) our results are doubtful.

Table 3: Influence of grid spacing at water surface

U (m/s)	H (m)	grid spacing	ϵ	
			at AP	at FP
6	14	4.5m \times 4.5m	—	—
6	14	5m \times 5m	-20%	5 %
6	14	6m \times 6m	6%	16%
10	14	6m \times 6m	—	—
10	14	8m \times 8m	2%	-3%

Table 4: Influence of grid size behind aft perpendicular AP and sideways

U (m/s)	H (m)	grid size		ϵ	
		aft	side	at AP	at FP
6	14	-135m	93m	—	—
6	14	-70m	70m	-1%	18%
10	14	-191m	101m	—	—
10	14	-135m	85m	2%	-1%

Table 5: Influence of height of source points over still water plane

U (m/s)	H (m)	height	ϵ	
			at AP	at FP
6	14	4m	—	—
6	14	6m	25%	-14%
12	18	8m	—	—
12	18	10m	-2%	0%
12	18	12m	-3%	2%

Table 6: Influence of distance limit for taking 4 collocation points instead of 1

U (m/s)	H (m)	distance limit	ϵ	
			at AP	at FP
6	14	2.0 \times grid spacing	—	—
6	14	3.3 \times grid spacing	-1%	0%
6	14	5.5 \times grid spacing	-1%	0%

The reason for this is held to be the fact that, due to limitations of the maximum number of grid points, the grid length is not small compared to the 23 m length of the transverse surface waves and the even shorter diagonal waves generated at this small Froude number. Fortunately, in practice the squat is hardly relevant at such small speeds. On the other hand, for Froude numbers of 0.25 and more, the table seems to indicate that errors due to the discretization are small.

Computing times are about 10 minutes for each iteration step on a VAX 8550 in case of about 1000 collocation points. The necessary number of iteration steps to obtain an accuracy of 1 cm for the squat ranges typically from 2 to 5, depending mainly on depth Froude number.

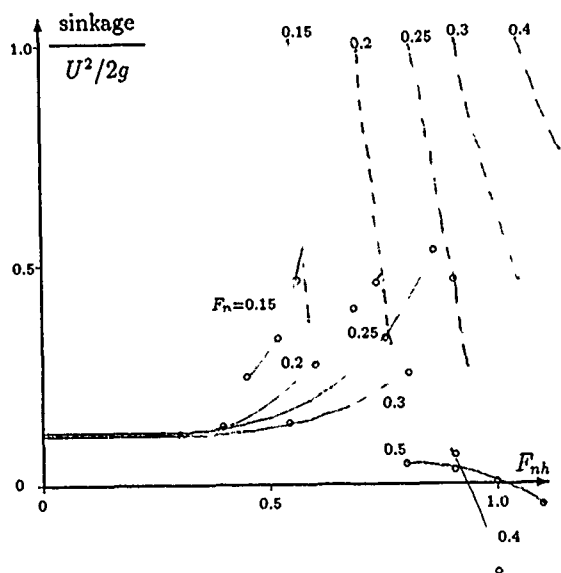


Fig. 8. Nondimensional sinkage at FP
Dotted lines are limits of ground-touching

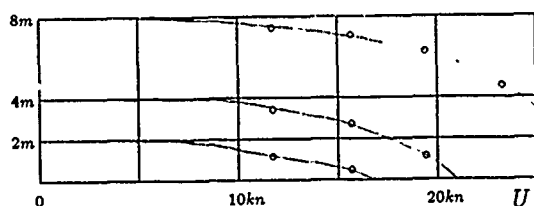


Fig. 9. Distance between ship bottom and sea bottom
at FP depending on speed for 3 water depths

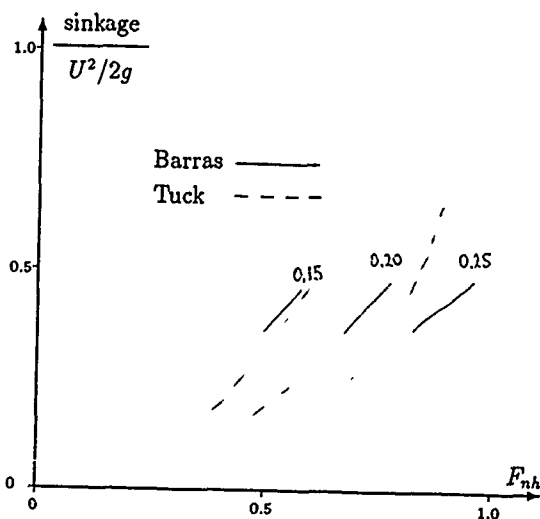


Fig. 10. Nondimensional sinkage at FP
according to Barras [9] and Tuck [10]

8.3 SWATH ship

For an research SWATH ship of the German navy we used our method for wave resistance prediction. We estimated frictional and viscous pressure resistance as in Salvesen et. al. [11]. The rather unusual shape of the cross section caused some difficulties in the non-linear computation. Therefore, in each iteration step the free-surface collocation points were not only shifted in height but also in horizontal direction according to the current waterline. For a demihull this modification ensured rapid convergence. The error in the free surface was reduced by a factor of 10 in each iteration step. Each demihull induces a slightly oblique flow at the other demihull. Due to limitations in time, we did not incorporate a Kutta condition at the rear of each strut which would be necessary to take this effect properly into account. We felt justified in this decision by the results of Bai et al. [12] who found for another SWATH ship that including a Kutta condition had no significant effect on the wave resistance. Bai et al. reported only some differences in the local velocity field near the trailing edges of the struts. Figure 11 shows a comparison of computational results with experiments of the Hamburg Towing Tank HSVA. Unlike the computational model the experimental model was equipped with rudders, fins and a propeller guard.

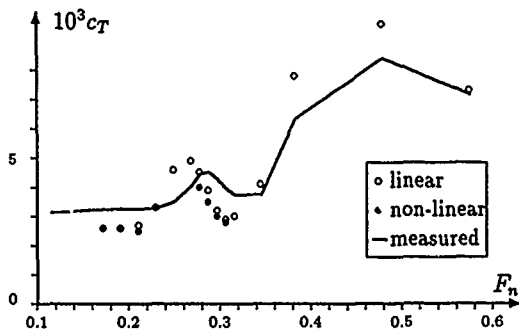


Fig. 11. Computed total resistance coefficients for
SWATH ship and values measured by HSVA

Only in a few cases a nonlinear solution succeeded. The agreement with experiments is worse than for conventional ships. For the medium Froude-number range we noticed a considerable phase shift between the waves on the inside and the outside of each demihull before the computation breaks down. The point with the highest error in the free-surface condition and also the highest vertical acceleration was at the end of the strut. This seems to indicate that cross-flow effects after all might be important for nonlinear solutions despite Bai's et al. findings. For high Froude numbers the computation breaks down at a point behind the SWATH ship at the plane of symmetry. Two wave crests starting from the trailing edges of the struts superimpose resulting in a splash. This phenomenon

can also be observed in reality. This violates one of the fundamental assumptions of our method. More research will be necessary before breaking waves can be included. Similar agreement with experiments was found for sinkage, [13]. Trim was suppressed both in computations and model tests.

9. Final remarks

For many practical hull forms the present method can be used to compute the potential flow with nonlinear free-surface conditions. The wave resistance is predicted quite well, although we do not yet achieve the accuracy of experiments. More comparisons to measurements are required to gain experience.

The squat of the container ship seems to have been determined accurately by our panel method for Froude numbers above 0.20 in case of depth Froude numbers below 0.9 and perhaps also for critical and over-critical depth Froude numbers. However, the extremely simple slender-body formula of Tuck gives the same results for sub-critical depth Froude number, including small length Froude numbers.

10. References

- [1] MICHELL, J. H.: "The Wave Resistance of a Ship", *Phil.Mag.* Vol 45, 1898.
- [2] DAWSON, C. W.: "A Practical Computer Method for Solving Ship-Wave Problems", Second International Conference on Numerical Ship Hydrodynamics, University of California, Berkeley 1977.
- [3] NI, S.-Y.: "Higher Order Panel Methods for Potential Flows with Linear or Nonlinear Free Surface Boundary Conditions", Chalmers University of Technology, Göteborg, 1987.
- [4] JENSEN, G.: "Berechnung der stationären Potentialströmung um ein Schiff unter Berücksichtigung der nichtlinearen Randbedingung an der freien Wasseroberfläche", Institut für Schiffbau Hamburg, Report No. 484, Juli 1983.
- [5] JENSEN, G., MI, Z.-X., SÖDING, H.: "Rankine Source Methods for Numerical Solutions of the Steady Wave Resistance Problem", Sixteenth Symposium on Naval Hydrodynamics, University of California, Berkeley, 1986.
- [6] NAKATAKE, K.: "On the Wave Pattern Created by Singular Points", *Journal of Seibu Zosen Kai West Japan*, No. 31, 1966
- [7] HESS, J. L., SMITH, A. M. O.: "Calculation of Non-Lifting Potential Flow about Arbitrary Three-Dimensional Bodies", Douglas Aircraft Division Report No. E.S.40622, 1962.
- [8] OGIWARA, S.: "Tank Experiments and Numerical Works on Series 60 Model in IHI Ship Model Basin", Report to the Cooperative Experiment Program of 18th ITTC, Kobe, Japan, October 1987.
- [9] BARRAS, C.B.: "A Unified Approach to Squat Calculations for Ships", *Bulletin of the PIANC* 1, No. 32, 1979
- [10] TUCK, E.O.: "Shallow-water Flow past Slender Bodies", *J. Fluid Mech.* 26, Part 1, 1966
- [11] SALVESEN, N., von KERCZEK, C.H., SCRAGG, C.A., CRESSY, C.P., MEINHOLD, M.J.: "Hydro-Numeric Design of SWATH-Ships", *SNAME Trans.*, Vol. 93, 1985
- [12] BAI, K.J., KIM, J.W., KIM, J.W.: "The Cross Flow Effect on the Force and Moment acting on a SWATH Ship" Seventeenth Symposium on Naval Hydrodynamics, The Hague, 1988
- [13] BERTRAM, V.: "Numerische Widerstandsprognose für SWATH-Schiffe", *Schiffstechnik* Vol. 35, No. 3, 1988

DISCUSSION

by A. Musker

Have you tried the non-linear calculation of Fig.4 with the ship fixed and compared with the data compiled by ITTC on the experiment of Kim and Jenkins?

The novel treatment of the radiation condition deserves further study to see how it behaves with high resolution surface grids.

Author's Reply

We did not try the non-linear calculation with fixed trim and sinkage for the Series 60. Fig.4 shows the result for the first and the final step of the interaction for the same computation.

We believe that our treatment of the radiation condition will also work in the limit of very small grid spacing. The derivative are taken analytically and the free surface boundary condition is symmetric.

What is needed to get the desired solution is a numerical stimulation for an asymmetric solution.

If the source distribution is in a layer above the free surface, as in our method, the vertical distance has to be decreased with the mesh size.

We performed trial computations with 50 points per wave length for the 2-d case and did not have any problems.

Numerical Solution of Viscous Flows about Submerged and Partly Submerged Bodies

P. G. Esposito

Istituto Nazionale di Studi ed Esperienze di Architettura Navale

Roma, Italy

G. Graziani and P. Orlandi

Università di "La Sapienza"

Rome, Italy

Abstract

In this paper a finite difference method based on the Navier-Stokes equations in generalized curvilinear coordinates is applied to the simulation of unsteady viscous flows with free surface. An accurate analysis of the method is performed by comparing numerical and experimental results for several physical cases related to ship hydrodynamics.

1 Introduction

The flow of a viscous fluid past a body shows a very complex behaviour when a free surface is involved. In fact the free surface strongly affects the flow field. The detailed analysis of the interactions between body and fluid is very important in the field of naval hydrodynamics in order to quantify the viscous and wave resistance. Experimental investigation can provide global information at reasonable cost, while velocity and pressure measurement are difficult or even impossible and very expensive, instead numerical simulation gives the complete flow field quantities provided particular care is devoted to implement the numerical scheme. The validation of the numerical solution by a comparison with the experimental findings is necessary to verify the accuracy of scheme. The best results, however, are obtained when the two fields of analysis complement each other.

In this paper a numerical method for the solution of the Navier-Stokes equations in general curvilinear coordinates based on an implicit finite difference scheme is presented. The physical domain bounded by the moving free surface is mapped onto a fixed computational domain. The time dependent coordinate transformation introduces extra terms that account for the grid velocity. For a complete test of the numerical method, the scheme has been applied to different physical problems with increasing complexity. As a first case the 2-D flow field past a wall-mounted

square obstacle in a channel has been considered [1]. When the geometry is mapped onto a computational domain, the coordinate lines turn out to be highly distorted. The comparison with experimental results suggests that very fine meshes are required for an accurate resolution of flow reversal.

To verify the treatment of the time dependent geometry, the flow field inside a rectangular enclosure with a moving indentation has been studied and the temporal evolution has been compared with the experimental findings.

The 2-D free surface flow over a semicircular bump on a straight wall has been considered because it is closely related to ship design. This case is relevant for the presence of large recirculating regions and of the free surface. Experimental results are also available [2].

2 Governing Equations

The simulation of a two dimensional incompressible viscous flow has been considered as a first step to build a numerical scheme for 3-D flows. The governing equations are:

$$\frac{\partial v^i}{\partial x_i} = 0 \quad (1)$$

$$\frac{\partial v^i}{\partial t} + \frac{\partial v^i v^j}{\partial x_j} = -\frac{\partial p}{\partial x_i} + \frac{1}{Re} \frac{\partial^2}{\partial x_j \partial x_j} v^i + f^i \quad (2)$$

where v^1, v^2 are the Cartesian velocity components and $f^i = (0, -1/Fr^2)$ is the gravitational force. The equations are nondimensionalized by the maximum inlet velocity U and a length L characteristic of each case examined. The Reynolds and the Froude numbers are $Re = UL/\nu$ and $Fr = U/\sqrt{gL}$, where ν is the kinematic viscosity and g the acceleration of gravity.

When the free surface is present and is advected by the unknown velocity field, the physical domain varies in time. The numerical solution of the gov-

erning equations describing such complex phenomena requires an accurate computational scheme. Among the several possibilities to represent the behaviour of the free surface, such as the Marker and Cell method [3], in this paper it has been chosen to map the physical domain (x_i) into a Cartesian computational domain (ξ_j) at each time step. Interpolations to enforce boundary conditions are thus avoided.

The choice of Cartesian velocity components as dependent variables allows a simple form of the equations in the ξ_j coordinate system. The adoption of other velocity components as unknowns require the introduction of higher order metric coefficients, as shown in Ref. [4].

Introducing the time dependent coordinate transformation $x_i = x_i(\xi_j, t)$ into equations (1) and (2), it follows

$$\frac{1}{J} \frac{\partial(\gamma_j^i v^j)}{\partial \xi_i} = \frac{1}{J} \frac{\partial q^i}{\partial \xi_i} = 0 \quad (3)$$

$$\begin{aligned} \frac{1}{J} \frac{\partial(J v^i)}{\partial t} + \frac{1}{J} \frac{\partial}{\partial \xi_j} (\tilde{q}^j v^i) = \\ - \frac{1}{J} \gamma_j^i \frac{\partial p}{\partial \xi_j} + \frac{1}{Re} \frac{1}{J} \frac{\partial}{\partial \xi_k} \alpha^{kl} \frac{\partial}{\partial \xi_i} v^l + f^i \end{aligned} \quad (4)$$

where $q^i = \gamma_j^i v^j$ are the fluxes and $\tilde{q}^i = q^i - \gamma_j^i (\frac{\partial x_i}{\partial t})_{\xi}$ accounts for the time dependence of the mapping. The notation is given in Appendix A.

Eq. (3) is a very important constraint for incompressible flows, which is fulfilled in a simple way by locating the fluxes q^i at the cell sides.

The equations for fluxes q^i are obtained by a linear combination of (4). The momentum equations become

$$\begin{aligned} \frac{\partial q^i}{\partial t} + \frac{q^i}{J} \frac{\partial J}{\partial t} - \beta_j^i q^j \frac{\partial \gamma_j^i}{\partial t} + \frac{1}{J} \gamma_j^i \frac{\partial}{\partial \xi_i} (\tilde{q}^j q^k \beta_k^j) = \\ - \alpha^{ij} \frac{\partial p}{\partial \xi_j} + \frac{1}{Re} \frac{1}{J} \frac{\partial}{\partial \xi_k} \alpha^{kl} \frac{\partial}{\partial \xi_i} q^k \beta_k^j + \gamma_j^i f^j \end{aligned} \quad (5)$$

Eq. (5) can be rewritten as

$$\frac{\partial q^i}{\partial t} - \frac{1}{Re} \Delta^2(q^i) = -P^i - R^i \quad (6)$$

where

$$R^i = H^i - F^i + G^i - \frac{1}{2Re} (D_1^i + D_2^i) \quad (7)$$

the convective term is

$$H^i = \frac{1}{J} \gamma_j^i \frac{\partial}{\partial \xi_i} (\tilde{q}^j q^k \beta_k^j) \quad (8)$$

the pressure gradient is

$$P^i = \alpha^{ij} \frac{\partial p}{\partial \xi_j} \quad (9)$$

the body force term is

$$F^i = \gamma_j^i f^j \quad (10)$$

and the quantity

$$G^i = \frac{q^i}{J} \frac{\partial J}{\partial t} - \beta_j^i q^j \frac{\partial \gamma_j^i}{\partial t} \quad (11)$$

accounts for the time dependence of the grid. The following definitions have been used:

$$\Delta^2(q^i) = \sum_{j,k} \frac{\gamma_j^i}{J} \frac{\partial}{\partial \xi_k} \alpha^{kl} \frac{\partial}{\partial \xi_k} q^k \beta_k^j \text{ no sum over } i \quad (12)$$

$$D_1^i = \sum_{j,k} \frac{\gamma_j^i}{J} \frac{\partial}{\partial \xi_k} \alpha^{kl} \frac{\partial}{\partial \xi_k} q^k \beta_k^j \quad s \neq i \quad (13)$$

and

$$D_2^i = \sum_{j,k,l} \frac{\gamma_j^i}{J} \frac{\partial}{\partial \xi_k} \alpha^{kl} \frac{\partial}{\partial \xi_l} q^k \beta_k^j \quad (14)$$

where Δ^2 contains only second derivatives of q^i along ξ_k , while the remaining part of the diffusive term is accounted for in D_1^i and D_2^i

3 Numerical Model

Eq. (6) are discretized on a staggered grid where the pressure p is defined at the node (i, j) , q^1 at $(i+1/2, j)$ and q^2 at $(i, j+1/2)$. The discretized equations need the metric coefficients at (i, j) , $(i+1/2, j)$, $(i, j+1/2)$ and $(i+1/2, j+1/2)$. These metric quantities are evaluated by second order centered finite differences. Interpolation of the metric coefficients introduces truncation errors [5]. To avoid such problem, in the present work, the metric quantities are evaluated on a grid twice finer than the computational grid. The governing equations are solved by a fractional step method [6,7,8], where a first step yields the non-solenoidal field \tilde{q}^i .

$$\begin{aligned} \frac{\tilde{q}^i - (q^i)^n}{\Delta t} - \frac{1}{2Re} \Delta^2(\tilde{q}^i - (q^i)^n) = \\ - (P^i)^n - \frac{1}{2} [3(R^i)^n - (R^i)^{n-1}] \\ + \frac{1}{Re} \Delta^2(q^i)^n \end{aligned} \quad (15)$$

To have a second order time accurate method the R^i have been discretized by the Adams-Bashforth scheme requiring a restriction on the time step (Courant number < 1). The direct inversion of Eq. (15) requires a large amount of memory and CPU time. The approximate factorization scheme [9,10] reduces the number of operations. It consists on the approximation of the LHS by the product of two three-diagonal matrices.

Eq. (15) becomes:

$$\begin{aligned} (1 - A_1)(1 - A_2)(\tilde{q}^i - (q^i)^n) = \\ - \Delta t (P^i)^n - \frac{\Delta t}{2} [3(R^i)^n - (R^i)^{n-1}] + \\ + 2(A_1 + A_2)(q^i)^n \end{aligned} \quad (16)$$

Where A_k accounts for the discrete differential oper-

ators of the laplacian along ξ_k .

The velocity field $(q^i)^{n+1}$ is obtained by introducing a scalar Φ at the second step,

$$(q^i)^{n+1} = \bar{q}^i - \frac{\Delta t}{2} \alpha^{ij} \frac{\delta \Phi}{\delta \xi_j} \quad (17)$$

By applying the discrete divergence operator at the grid point (i, j) , the equation for Φ follows

$$\frac{1}{J} \frac{\delta}{\delta \xi_i} \alpha^{ij} \frac{\delta \Phi}{\delta \xi_j} = \frac{2}{J \Delta t} \frac{\delta \bar{q}^i}{\delta \xi_i} \quad (18)$$

A significant amount of the CPU time of the entire computation is devoted to the solution of Eq. (18). Direct methods, like LU decomposition, yield a solution within round-off error, but their application to very fine grids ($N = N_1 \times N_2$) is impossible both for memory requirements and for number of operations $O(N^2)$. Generally iterative methods do not efficiently reduce low wave number errors. For such reason a linear Correction Storage multigrid method [11,12] has been applied with a reduction of CPU time.

The pressure field p appearing in Eq. (6) is evaluated from Φ

$$p^{n+1} = p^n + \frac{1}{2} \left(\Phi - \frac{\Delta t}{2Re} \frac{1}{J} \sum_{k=1}^2 \frac{\delta}{\delta \xi_k} \alpha^{kk} \frac{\delta \Phi}{\delta \xi_k} \right) \quad (19)$$

After the second step the overall accuracy remains of $O(\Delta t^2)$.

4 Boundary Conditions

No-slip boundary conditions have been assumed on solid walls. An assigned profile of the Cartesian component v^1 together with $v^2 = 0$ has been imposed at the inlet, and the fluxes are derived by Eq. (A.6).

At the outflow a developed flow condition

$$\frac{\partial v^i}{\partial \xi_1} = \frac{\partial q^i \beta_j^i}{\partial \xi_1} = 0 \quad (20)$$

has been assumed when free surface problems are treated. The assumption of radiative conditions, that is done for the other cases, gives rise to instabilities in presence of free surface. Work is in progress to avoid this numerical instability.

The Navier-Stokes equations require one kinematic and two dynamic conditions at the free boundary. The balance of the forces between the inner and the outer fluid gives the dynamic conditions. With zero external pressure and stresses, the normal and shear stresses must vanish. These conditions cannot be easily implemented by an implicit scheme. Therefore the simpler conditions of ref. [15] have been used:

$$\frac{\partial v^i}{\partial \xi_2} = \frac{\partial q^i \beta_j^i}{\partial \xi_2} = 0 \quad (21)$$

For slightly deformed grids the previous conditions are approximately equivalent to require the vanishing of normal and tangential stresses.

The kinematic condition enforces the fluid particles to remain on the free surface. If the free surface configuration is described by the function

$$x_2 = \eta(x_1, t) \quad (22)$$

the kinematic condition

$$\frac{D(x_2 - \eta)}{Dt} = 0 \quad (23)$$

yields

$$\frac{\partial \eta}{\partial t} = v^2 - v^1 \frac{\partial \eta}{\partial x_1} = v^2 - v^1 \frac{c_1^2}{c_1} \quad (24)$$

At every time step the free surface is moved using the previous equation. To eliminate the possible occurrence of instabilities, the new configuration is smoothed with the same filter used by [13,14,15].

5 Results

To test the complexities associated with the described numerical scheme, several cases have been chosen, each one enlightening a particular complexity. The flow in a steady domain and the flow in a domain where a boundary moves with a prescribed law have been considered as test cases before solving the free surface flow past a semicylinder.

5.1 Flows in steady complex domains

The use of a general curvilinear coordinate system is the main characteristic of the present method. Therefore to analyze the influence of the grid on the numerical solution the flow past an obstacle inside a channel has been considered. The sketch of the domain and the mesh obtained by an analytical function based on a conformal transformation is given in Fig.1. Fig. 2 shows, by a stream function plot, that the numerical method reproduces the main features revealed in the experiment of Ref. [1]. To capture the relevant details at least a 64×32 grid with refinements in the regions of flow reversal is necessary. The reattachment length X_r of the main separation bubble, is the significative parameter of this flow. The numerical values of X_r , together with the experimental data, are given in table 5.1 for two Reynolds numbers ($Re = 144$ and $Re = 288$). The numerical simulations have been

Re	X_r Num.	X_r Exp.
144	5.5	6.7
288	9.5	12.1

Table 1: Values of X_r by present work and by Ref. [1]

done respectively by a 64×32 and a 96×32 grid. The coarseness of the grid is the main reason to explain the disagreement between the numerical and the experimental results. A second reason, to a lesser extent, is ascribed to the fact that the calculation was interrupted before a real stationary solution was reached. As it occurs for the backward facing step, numerical solutions usually present a very steep growth of X_r within a short time. Later on X_r grows in time very slowly and the steady state is reached using a large amount of CPU time. However the obtained results can be acceptable as a presentation of the method. A more accurate computation to obtain a physically interesting solution will be presented in the future.

5.2 Flows in complex domains moving with a prescribed law

In order to verify the accuracy of the numerical scheme to describe flows driven by an unsteady boundary, the flow inside a channel with a moving indentation has been considered. For such a case experimental [16] and numerical [17] results allow to test the treatment of the grid time dependence. The numerical results of ref. [17] have been obtained by a vorticity-stream function method on a very fine grid (1440×48). The same time dependent law of the indentation considered in Ref. [16,17] has been used. Although this flow is not relevant to ship hydrodynamics, it has been considered as a test case. A sequence of counter rotating eddies close to the upper and lower walls and separated by a wavy core flow is generated downstream the indentation. The eddies move downstream with a defined group velocity. This physical problem has been solved for $Re = 760$ and $St = 0.025$ and the same flow time history reported by [17] has been obtained. The time sequence of instantaneous streamlines is reported in Fig. 3 for a sequence of time steps within one period and it shows the same position, shape and temporal development of the eddies of Ref. [17]. The values of the positions of the crests and troughs corresponding to eddies B, C and D are shown in Fig. 4 in comparison with numerical [17] and experimental [16] values. In this case the better agreement derives from the much finer grid (384×32) used in this case with respect to that used in the previous case.

These preliminary numerical results assess that the numerical model provides good flow simulation in presence of steady and unsteady irregular domains.

5.3 Free surface flows

Free surface flows involve the difficulty of irregular and time dependent domain, where boundary moves according to the velocity field. The correct enforce-

ment of free-slip conditions gives the deformation of the free surface which strongly affects the inner velocity field. To our knowledge few experimental results concerning free surface flows are available. One experiment [2] deals with the flow over a semicylindrical obstacle. We have chosen to verify the validity of the approximated form of the free surface boundary condition specified by Eq. (21). A proper treatment of the free surface conditions is very difficult particularly when implicit schemes are used. In this case the exact free-slip conditions require an iterative procedure which increases the CPU time.

Preliminary results were obtained at lower Re and higher Fr than those used in Ref. [2] because a coarse grid was employed. However also in this case the free surface is largely deformed. The velocity vector plot, shown in Fig. 5 for $Re = 400$ and $Fr = 0.5$, qualitatively resembles the expected flow field. Also the dynamic pressure reported in Fig. 6 and the development of the recirculating regions qualitatively agree. However, it is to be noted that the flow field simulation is not possible up to the steady state because the free surface conditions are not correctly enforced when the deformation of the interface becomes relevant. A better treatment of such boundary conditions is required to achieve a complete and accurate flow simulation.

6 Conclusions

The purpose of this paper is restricted only to the description of the numerical method, which has been tested by using coarse grids, certainly larger than those required by the physics of the flow. This is the main reason for the discrepancies between the numerical and experimental results in the two cases firstly considered. More work should be done to define the best grid transformation for the wall mounted obstacle case. On the contrary, the case of the flow generated by a moving indentation shows that the grid time dependence is very accurately handled by our scheme. In fact our results computed on a relatively coarse mesh are in very good agreement with the numerical results obtained with a larger number of grid points in Ref. [17].

At the moment the lack of the method to accurately describe free surface flows is mainly related to two intimately connected aspects: the choice of the grid transformation and the approximations on the boundary conditions at the free surface. The present results show that the generation of a grid with coordinate lines orthogonal to the boundaries reduces the truncation errors. If such effect is large for solid boundaries, the effect is amplified at the free surface. The generation of coordinate lines nearly orthogonal

to the free surface is more difficult and requires a high CPU time but avoids the approximations in at the free surface boundary conditions. In the future our work will be focused on these aspects and only afterwards real ship related flows will be successfully simulated.

Appendix

A Metric Notation

In this section a brief review of the tensorial notations used throughout our paper is given.

Let us consider the coordinate transformation between a Cartesian reference system x_i and a curvilinear system ξ_j , being the base vectors respectively e_i and g_j . If we introduce the coefficients c_j^i defined as

$$c_j^i = \frac{\partial x_i}{\partial \xi_j} \quad (\text{A.1})$$

the cartesian components v^i of a vector v are related to the contravariant components u^j

$$v = v^i e_i = u^j g_j \quad (\text{A.2})$$

by the transformation

$$v^i = c_j^i u^j \quad (\text{A.3})$$

If we consider the inverse transformation c^{-1} then

$$u^j = (c^{-1})_i^j v^i \quad (\text{A.4})$$

If the vector v introduced above represents a velocity field the fluxes q^j are defined as

$$q^j = J u^j = J (c^{-1})_i^j v^i = \gamma_i^j v^i \quad (\text{A.5})$$

and

$$v^i = J^{-1} c_j^i q^j = \beta_j^i q^j \quad (\text{A.6})$$

where $J = \det(c_j^i)$ is the Jacobian of the transformation, $\gamma_i^j = J (c^{-1})_i^j$ and $\beta_j^i = J^{-1} c_j^i$.

Using the matrix c we can write the metric tensors as

$$g_{ij} = g_i \cdot g_j = c_i^l c_j^l \quad (\text{A.7})$$

$$g^{ij} = g^i \cdot g^j = (c^{-1})_i^l (c^{-1})_j^l \quad (\text{A.8})$$

$$g = \det(g_{ij}) = J^2 \quad (\text{A.9})$$

The gradient and the Laplacian operators in curvilinear coordinate are

$$(\nabla \phi)^i = g^{ij} \frac{\partial \phi}{\partial \xi_j} \quad (\text{A.10})$$

$$\nabla^2 \phi = \frac{1}{J} \frac{\partial}{\partial \xi_i} \left(J g^{ij} \frac{\partial \phi}{\partial \xi_j} \right) \quad (\text{A.11})$$

the metric quantities α^{ij} which appear in the equations for fluxes are simply given by

$$\alpha^{ij} = J g^{ij} \quad (\text{A.12})$$

References

- [1] Tropea C.D., Gackstatter R. "The Flow Over Two-Dimensional Surface-Mounted Obstacles at Low Reynolds Numbers" *J. Fluids Eng.* 107 (1985), 109
- [2] Miyata H., Matsukawa C., Kajitani H. "Shallow Water Flow with Separation and Breaking Wave" read at The Autumn Meeting of The Society of Naval Architects of Japan Nov. 1985
- [3] Welch J.E., Harlow F.H., Shannon J.P., Daly B.J. "The MAC method: A computing technique for solving viscous, incompressible, transient fluid-flow problems involving free surfaces", LA 3425, Los Alamos Scientific Labs. (1966)
- [4] Levi Civita T., "The absolute differential calculus" Dover, 1977
- [5] Thompson J.F., Warsi Z.U.A., Mastin C.W. "Numerical Grid Generation" North-Holland, 1985
- [6] Chorin A.J., "A Numerical Method for Solving Incompressible Viscous Flow Problems" *J. Comp. Phys.* 2 (1967), 12
- [7] Kim J., Moin P. "Application of a Fractional-Step Method to incompressible Navier-Stokes Equations" *J. Comput. Phys.* 59 (1985), 309
- [8] Orlandi P., Kim J., Moin P. "Numerical Solution of 3-D Flows Periodic in One Direction and with Complex Geometries in 2-D" unpublished
- [9] Beam R.M., Warming R.F., "An Implicit Finite-Difference Algorithm for Hyperbolic Systems in Conservation-Law Form" *J. Comp. Phys.* 22 (1976), 87
- [10] Briley W.R., McDonald H., "Solution of the Multidimensional Compressible Navier-Stokes Equations by a Generalized Implicit Method" *J. Comp. Phys.* 24 (1977), 372

- [11] Brandt A. "Multi-level Adaptive Grid Solutions to Boundary Value Problems" *Math. Comp* 31 (1977), 330
- [12] P.G. Esposito, P. Orlandi "A Multigrid Solver for the Pressure Equation for Incompressible Navier-Stokes Computations in Curvilinear Coordinates" unpublished
- [13] Longuet-Higgins M.S., Cokelet E.D. "The Deformation of Steep Surface Waves. I. A Numerical Method of Computation" *Proc. Roy. Soc. A* 350 (1976), 1
- [14] Haussling H.J., Coleman R.M. "Finite Difference Computations Using Boundary-fitted Coordinates for Free-surface Potential Flows Generated by Submerged Bodies" in *Proceedings of the 2nd Intern. Conf. on Numerical Ship Hydrodynamics, Berkeley, 1977*, 221
- [15] Miyata H., Sato T., Baba N. "Difference Solution of a Viscous Flow with Free Surface Wave about an Advancing Ship" *J. Comput. Phys.* 72 (1987), 393
- [16] Pedley T.J., Stephanoff K.D. "Flow along a Channel with a Time-Dependent Indentation in One Wall: the Generation of Vorticity Waves" *J. Fluid Mech.* 160 (1985), 337
- [17] Ralph M.E., Pedley T.J. "Flow in a Channel with a Moving Indentation" *J. Fluid Mech.* 190 (1988), 337

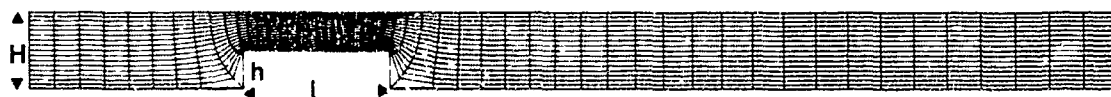


Fig. 1 A sample 32×16 grid for the solution of the flow past a surface-mounted obstacle in a channel ($h/H = 0.5$, $l/h = 4$)

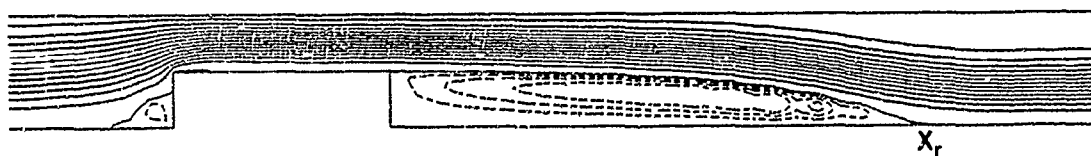


Fig. 2 Stream function plot for $Re = 288$; dashed lines correspond to negative values. The interval between contour lines is 0.02 for negative values and 0.1 for positive ones.

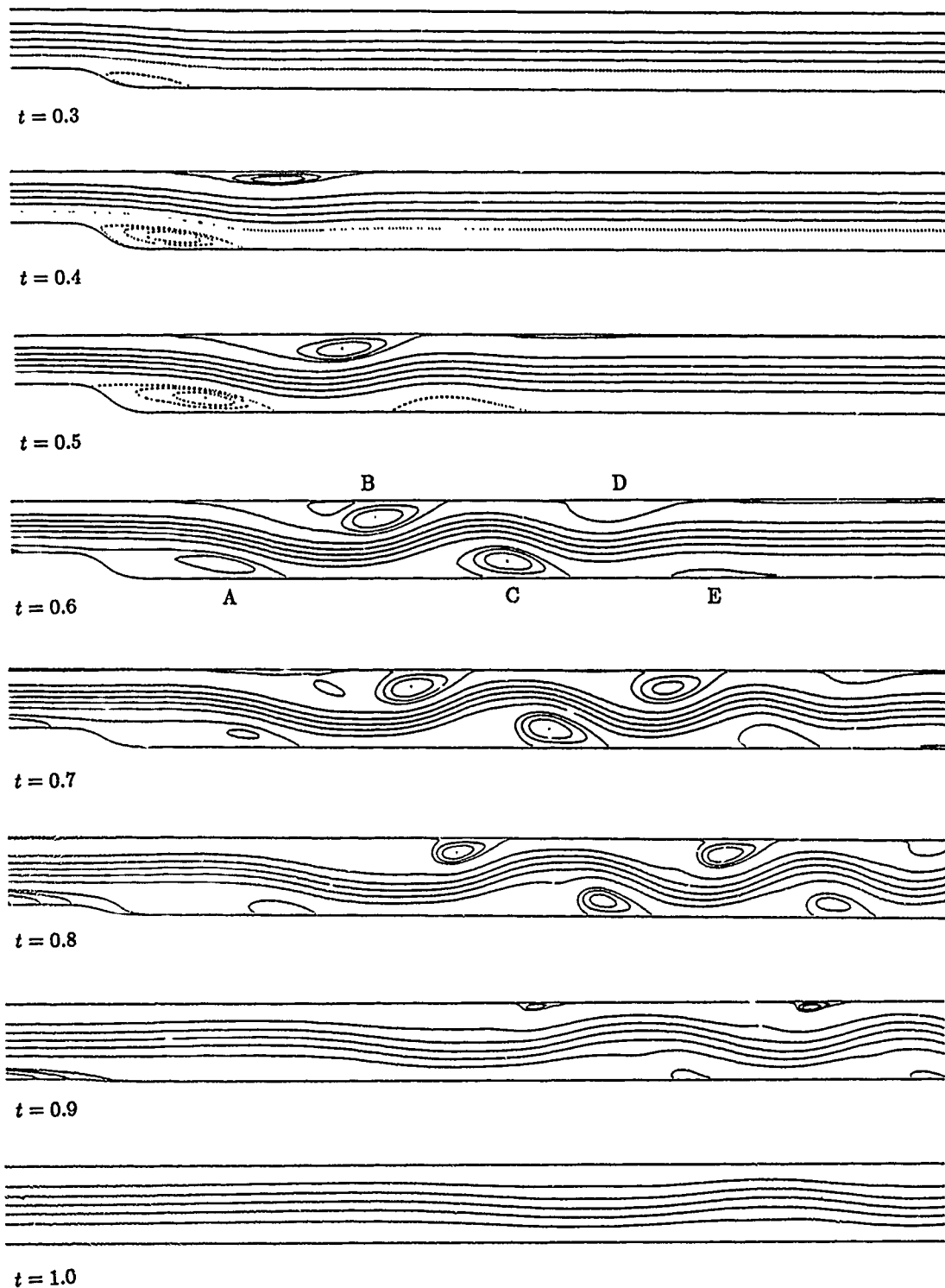
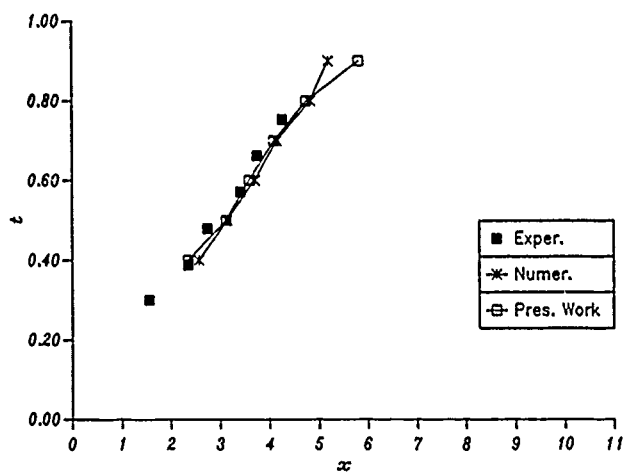
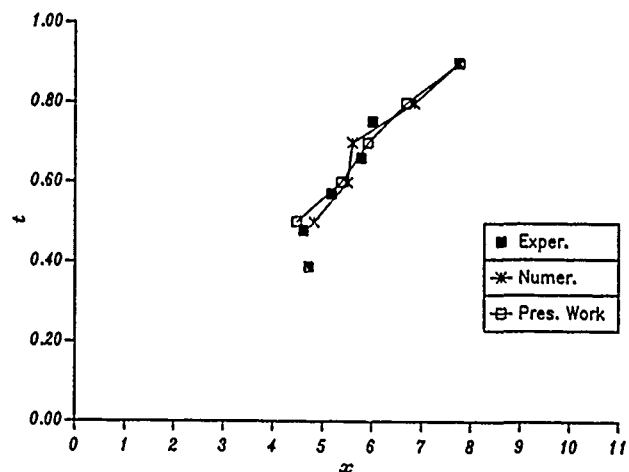


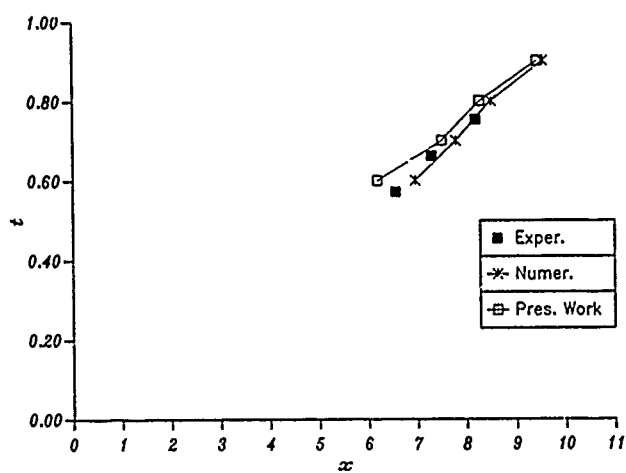
Fig. 3 Instantaneous streamline plots within one period for the flow in channel with a moving indentation



(a) Eddy B



(b) Eddy C



(c) Eddy D

Fig. 4 Time histories of the eddies B, C and D for the flow in a channel with a moving indentation

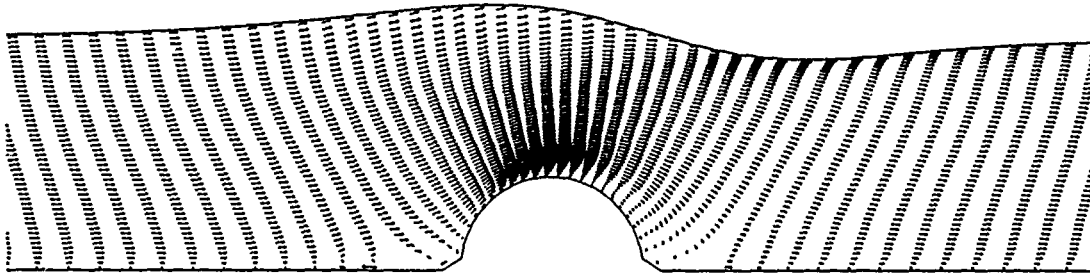


Fig. 5 Velocity vector plot at $t=0.8$, $Re = 400$, $Fr = 0.5$ for the flow over a semicylindrical bump

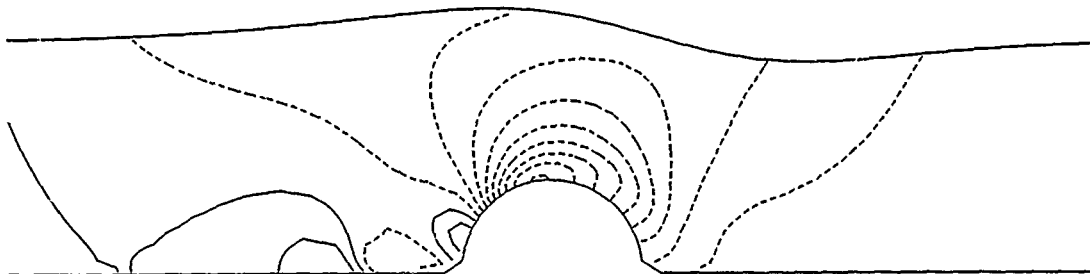


Fig. 6 Pressure contour map at $t=0.8$, $Re = 400$, $Fr = 0.5$ for the flow over a semicylindrical bump. The increment between two isolines is 0.05

Simulation of the Hydrodynamic Loading and Structural Response of a Marine Riser

A. Dercksen and F. van Walree
Maritime Research Institute Netherlands
Wageningen, The Netherlands

Abstract

The flow around circular cylinders at moderate to high Reynolds numbers is characterized by vortex shedding. Hydroelastic oscillations are caused by the oscillatory in-line and transverse forces, induced by this periodic shedding of vortices. The hydrodynamic loading and structural response of a marine riser is simulated using the results of several flow simulations with the vortex blob method. A three-dimensional vortex blob method is discussed. Operator splitting is used to obtain a formulation in which the viscous effects are incorporated using a stochastic process, while the inviscid flow is described by the evolution of a flow map. The numerical algorithm consists of an accurate and efficient spectral model combined with a variational formulation. A comparison with experimental results and semi-empirical models is used for validation. A description of the computational aspects related to the coupling of the results obtained from the vortex blob method to an existing structural analysis code is given. Finally some computed results of the dynamic response of a flexible riser, a pipe and a cable subjected to environmental forces due to current will be compared with experimental and full scale results.

1. Introduction

Hydroelastic oscillations are caused by the periodic shedding of vortices from the boundary layer of a flexible cylindrical blunt body, inducing transverse and in-line forces. The vortex shedding frequency may lock on to the natural frequency of the system, provided the internal structural damping is sufficiently low. The structure extracts energy from the flow resulting in a motion amplitude increase to values of once to twice the characteristic length. An important issue is the increased drag force and risk of

fatigue due to the high frequency oscillations of the structure.

Several semi-empirical formulae exist for the prediction of drag and lift forces. These models all have in common that details of the flow field are not taken into account, i.e. they are chiefly based on mechanical and electrical analogons. More advanced models contain tuning parameters to fit the model to experimental observations. Again, these parameters have no physical interpretation other than their analogons in other fields. On the contrary, very advanced numerical schemes exist for solving the instationary viscous Navier Stokes equations. These methods certainly take into account the flow field, but even with present day computing power such complex simulations will impose an economical limit on their use for practical problems.

The authors stress that these models are invaluable for research purposes such as understanding more about the details of such complex flows. Attempts have been made to couple the direct flow simulation to a structural code by e.g. Hansen et al. [1]. The limitations on computer power require many simplifications and heuristic arguments in the model. The predictive abilities of this approach are therefore rather doubtful. For practical situations such as hydroelastic oscillations, simplified models must be developed, drawing on the results and insights obtained from large scale, systematic computations and experiments. As a first step in this direction, a wake-oscillator model (e.g. Griffin [2],[3],[4]) is tuned to the results obtained by performing a number of simulations using a vortex blob method for solving the Navier-Stokes equations. The calculations were conducted for a two-dimensional flow around a spring mounted circular cylinder. The tuned model is subsequently used in a structural analysis code to simulate the hydrodynamic loading and structural response of a marine riser, a pipe and a cable in current.

2. Theory Vortex Blob Method

The equations governing the evolution of a vorticity field ω , defined as the curl of the velocity field \hat{u} , in a viscous incompressible fluid in a Eulerian reference frame are commonly known as the viscous vorticity transport equations. They can be summarized as:

$$\frac{D\omega}{Dt} = \omega \cdot \nabla \hat{u} + \nu \nabla^2 \omega \quad (1)$$

with the incompressibility constraint $\nabla \cdot \hat{u} = 0$ for the velocity field. In addition the velocity field must satisfy the no-slip boundary condition at a smooth body surface S and approach a uniform velocity field U far ahead of the body. It is therefore advantageous to define the total velocity field \hat{u} as the sum of two components, viz. $\hat{u} = \underline{u} + \underline{u}^\infty$ with \underline{u} the disturbance velocity field which approaches a zero value far away from the body, and \underline{u}^∞ the velocity field of the irrotational flow around the body. The set of equations is completed with an initial vorticity field ω_0 which is assumed to be tangential to the body surface. The left-hand side of the vorticity transport equation is the material derivative of the vorticity field, whereas the right-hand side is responsible for vortex stretching and diffusion of vorticity. Note that in two-dimensional flows, the stretching term is absent.

The vortex blob method is based on operator splitting, where all relevant physical processes are modelled subsequently in time. The solution of the viscous vorticity transport equations is approximated by successively solving the inviscid vorticity transport equations for a small time step, followed by the diffusion of vorticity and the creation of vorticity at the body surface, in order to maintain the no-slip condition. Several authors have investigated this fractional step algorithm as was proposed by Chorin, e.g. Chorin [5], Beale [6],[7],[8]. Recently, Van der Vegt [9] has given a convergence proof of a product algorithm for the approximation of the solution of the viscous vorticity transport equations.

In order to state the algorithm, it is necessary to introduce some definitions. The inviscid flow map \hat{R} is defined as an invertible continuously differentiable mapping from the initial fluid volume Ω_0 to the fluid volume Ω at time t :

$$\hat{R}(\mathbf{r}', t, t_0) : \Omega_0 \rightarrow \Omega \quad \forall t \in [t_0, t_1] \quad (2)$$

with \mathbf{r}' the position of a fluid particle at initial time t_0 . The position \mathbf{r} of a fluid particle at time t then is given by the relation:

$$\mathbf{r} = \hat{R}(\mathbf{r}', t, t_0) \quad (3)$$

If \mathbf{r}' is kept fixed, while t varies, equation (3) represents the path of a fluid particle initially at \mathbf{r}' . The flow map \hat{R} must have a Jacobian determinant unity due to the incompressibility constraint, [10]. Analogous to the velocity field \hat{u} it is advantageous to separate the total flow map \hat{R} in a part R^∞ , related to the velocity field of the potential flow around the body and a disturbance flow map R by means of the relations:

$$\hat{R}(\mathbf{r}', t, t_0) = R^\infty \circ R(\mathbf{r}', t, t_0) \quad (4)$$

with:

$$R^\infty(\mathbf{r}', t, t_0) = \mathbf{r}' + \underline{u}^\infty(t - t_0) \quad (5)$$

where \underline{u}^∞ is the velocity field for the irrotational flow, i.e. the potential flow.

The vector stream function \hat{A} can be defined by relating the curl of the vector stream function to the total velocity field \hat{u} . The use of the vector stream function has the advantage that this representation immediately satisfies the incompressibility constraint for the flow field. The relation between the fluid particle velocity $\dot{\hat{R}}$ and the Eulerian field velocity \hat{u} now can be expressed as:

$$\begin{aligned} \dot{\hat{R}}(\mathbf{r}', t, t_0) &= \nabla_{\mathbf{r}'} \times \hat{A}(\mathbf{r}, t) \\ &= \nabla_{\hat{R}} \times \hat{A}(\hat{R}(\mathbf{r}', t, t_0), t) \end{aligned} \quad (6)$$

The relation between the vorticity field in both coordinate systems can be constructed likewise, [10], yielding:

$$\omega(\mathbf{r}, t) = \omega_0(\mathbf{r}') \cdot \nabla_{\mathbf{r}'} \hat{R}(\mathbf{r}', t, t_0) \quad (7)$$

The introduction of the flow map has transformed the problem of determining the vorticity field by solving the inviscid vorticity transport equation into the calculation of the flow map \hat{R} and the vector stream function \hat{A} . The system of equations (6) and (7) must be completed by deriving equations for the vector stream function. This can most conveniently be done by first separating the vector stream function \hat{A} into several components:

$$\hat{A} = A + A^\infty + \nabla \psi \quad (8)$$

where the vector stream function A^∞ has a curl equal to \underline{u}^∞ . The function ψ which must be twice differentiable can always be chosen such that the disturbance vector stream function A is divergence free. It is, however, not necessary to calculate the function ψ

because in the vortex model only the curl of the total vector stream function is required, hence the gradient in equation (8) will give no contribution to the velocity field.

The relation between the vorticity field ω_0 and the disturbance vector stream function A now is obtained by using the definition of the vorticity field and the divergence freedom of A :

$$\nabla^2 A(\mathbf{r}, t) = -\omega(\mathbf{r}, t) \quad (9)$$

The boundary conditions for the vector stream function A can be directly obtained from the no-flux condition for the velocity field at the surface S in an inviscid fluid and equation (8), yielding:

$$\mathbf{n} \cdot \nabla \times A = -\mathbf{n} \cdot \nabla \times A^\infty = 0 \quad \text{at } S \quad (10)$$

since A^∞ is the stream function for the potential flow around the cylinder. At great distance from the body the disturbance vector stream function A must satisfy:

$$A \rightarrow 0 \quad (11)$$

The whole system of equations for the disturbance flow map, vector stream function and vorticity field (6), (7) and (9) was put by Van der Vegt [9] in a Lagrangian variational formulation for bodies with an arbitrary geometry by means of the following Action Principle:

$$J[\mathbf{r}, A, t_0, t_1] = \int_{t_0}^{t_1} dt L[\mathbf{R}, A, t] \quad (12)$$

with Lagrangian functional:

$$L[\mathbf{R}, A, t] = \int_{\Omega_0} d^3r (\omega_0(\mathbf{r}') \cdot \nabla_{\mathbf{r}'} \mathbf{R}(\mathbf{r}', t, t_0) \cdot \left(\frac{1}{4} \mathbf{R}(\mathbf{r}', t, t_0) \times \dot{\mathbf{R}}(\mathbf{r}', t, t_0) - A(\mathbf{R}, t) \right) + \frac{1}{2} \int_{\Omega} d^3r |\nabla \times A(\mathbf{r}, t)|^2 \quad (13)$$

together with the initial condition $\mathbf{n} \cdot \omega_0$ at S for the vorticity field and boundary condition $\mathbf{n} \cdot \nabla \times A = 0$ at S for the vector stream function yields the set of equations for the flow map and vector stream function after variations $\delta \mathbf{R}$ and δA , with $\mathbf{t} \cdot \delta A = 0$ at the body surface S with tangential vector \mathbf{t} . Here the integration in the Lagrangian functional is conducted over both the initial fluid volume Ω_0 as well as the fluid volume Ω at time t .

The Eulerian-Lagrangian formulation requires at first sight the determination of both a disturbance flow map and a vector stream function after which

the vorticity field can be determined. The disturbance flow map can, however, be obtained from the Taylor series expansion of the flow map. This is accomplished by deriving from the Lagrangian formulation a Hamiltonian formulation using a Dirac bracket. An extensive discussion of this reduction process can be found in [9]. The result, which can be verified by using (7), reads:

$$\begin{aligned} \mathbf{R}(\mathbf{r}', t + \Delta t, t) = & \mathbf{R}(\mathbf{r}', t, t) + \\ & \Delta t (\nabla_{\hat{\mathbf{R}}} \times A(\hat{\mathbf{R}}, t)) + \\ & \frac{1}{2} \Delta t^2 (\nabla_{\hat{\mathbf{R}}} \times A(\hat{\mathbf{R}}, t)) \cdot \nabla_{\hat{\mathbf{R}}} (\nabla_{\hat{\mathbf{R}}} \times A(\hat{\mathbf{R}}, t)) \\ & + \mathcal{O}(\Delta t^3) \end{aligned} \quad (14)$$

The determination of the flow map $\hat{\mathbf{R}}$ is the first step in the product formula. The next step is the modelling of the effects of viscosity, i.e. diffusion and creation of vorticity. The model is based on the random walk interpretation of the incompressible Navier-Stokes equations given by Peskin [11]. The effect of viscosity is to generate a random disturbance on the particle paths generated by the flow map $\hat{\mathbf{R}}$. The stochastic flow map is defined as the sum of the inviscid flow map and a disturbance flow map which is a random vector from a sphere of radius $(12\nu\tau)^{\frac{1}{2}}$, τ being a small time step. The viscous vorticity evolution operator is represented by the following sequence of maps:

$$\omega \rightarrow \Phi \circ E_\tau \circ D_\tau \omega \quad (15)$$

where Φ is an operator which reflects particles, which diffuse into the body, across the boundary. The inviscid evolution operator E_τ is defined by equation (7). The diffusion operator D_τ causes a random translation of each point of the vorticity field.

The main result of Van der Vegt [9] states that, provided the inviscid flow map exists and is unique, the expectation of the viscous evolution operator converges to the evolution operator of the viscous vorticity transport equations. Analogously, the expectation of the particle paths, converge to the real particle paths. More details and a proof of convergence can be found in Van der Vegt [9].

In the next section, the numerical implementation of the vortex blob model is discussed.

3. Numerical Implementation

The numerical implementation of the vortex model described in the previous section requires the discretization of the vorticity field and an algorithm to

evaluate the flow map. For two-dimensional flows several schemes have been suggested. In the point vortex method the vorticity field is represented by a set of point vortices as follows:

$$\omega(\mathbf{r}, t) = \sum_{i=1}^N \Gamma_i \delta(\mathbf{r} - \mathbf{r}_i(t)) \quad (16)$$

where N is the number of vortices, \mathbf{r}_i represents the trajectory of the vortex with index i .

The flow map is then calculated by means of the Biot-Savart law of interaction, resulting in the following set of ordinary differential equations for the particle trajectories:

$$\dot{\mathbf{r}}_j = -\frac{1}{2\pi} \sum_{i \neq j} \frac{(\mathbf{r}_j - \mathbf{r}_i) \times \mathbf{e}_z \Gamma_i}{|\mathbf{r}_j - \mathbf{r}_i|^2} + \mathbf{u}_B(\mathbf{r}_j, t) \quad (17)$$

Here \mathbf{u}_B is an additional velocity due to an onset flow and the disturbance velocity caused by the body. The advantage of this procedure is that it is gridless, so that numerical problems related to grid generation and stability criteria for high Reynolds numbers are avoided. However, the algorithm has an operation count proportional to N^2 , and suffers from singular behaviour in the induced velocities when two vortices approach each other. The singularities lead to chaotic motions after some time steps. A variation to the point vortex method is the vortex in cell method in which the flow map is calculated on a fixed grid, reducing the singular behaviour and gaining numerical efficiency at the cost of accuracy.

The discretization used in this paper is the vortex blob approximation:

$$\omega(\mathbf{r}, t) = \sum_{i=1}^N \Gamma_i \gamma(|\mathbf{r} - \mathbf{r}_i(t)|) \quad (18)$$

where γ is a function of compact support e.g. a Gaussian distribution. This method is more suitable for flows with a smooth vorticity field, and eliminates the singular behaviour in the induced velocities.

The vorticity field obtained by this discretization, however, does not satisfy the inviscid transport equations. Convergence criteria for the two-dimensional vortex blob methods are given by Hald et al. [12], [13]. In order to calculate the trajectories of the blobs, the stream function is needed. As was mentioned earlier, the use of Biot-Savart's law is numerically inefficient. Improvements are made by solving the Poisson equation for the stream function on a grid fixed in space. This results in an operation count proportional to the number of vortex blobs N , plus some overhead for a fast Poisson solver.

The procedure discussed in this paper is based on the results from Section 2. For two-dimensional flows, the stream function has only one non-zero component. The stream function is separated into three parts:

$$\hat{A} = A^h + A^p + A^\infty \quad (19)$$

where A^p is the solution of the Poisson equation in an unbounded domain, A^h is the solution of the Laplace equation with boundary conditions at the body surface S , and A^∞ has a curl equal to the uniform onset velocity \mathbf{U}^∞ :

$$\nabla^2 A^p = -\omega \quad (20)$$

$$\nabla^2 A^h = 0 \quad (21)$$

$$\begin{aligned} \mathbf{n} \cdot (\nabla \times A^h \mathbf{e}_z) = \\ - \mathbf{n} \cdot ((\nabla \times A^p \mathbf{e}_z) - \mathbf{u}_w + \mathbf{U}^\infty) \end{aligned} \quad (22)$$

The velocity of the surface S is given by \mathbf{u}_w . Both stream functions A^p and A^h must have a curl equal to zero at infinity. Substituting A^p and ω in the action principle, results in:

$$\begin{aligned} J[\mathbf{r}_j, A^p] = \frac{1}{2} \int_{t_0}^{t_1} dt \int d\mathbf{r}' |\nabla A^p(\mathbf{r}')|^2 \\ - \sum_{i=1}^N \Gamma_i \int_{t_0}^{t_1} dt \left\{ \int d\mathbf{r}' \gamma(|\mathbf{r}' - \mathbf{r}_i(t)|) A^p(\mathbf{r}') \right. \\ \left. + \frac{1}{2} \left(X_j \frac{dY_j}{dt} - Y_j \frac{dX_j}{dt} \right) \right\} \end{aligned} \quad (23)$$

in which $\mathbf{r}_j = (X_j, Y_j)$ is the trajectory of a vortex blob with index j in an unbounded fluid. The stream function A^p is expanded in Fourier harmonics with period L_x and L_y in x and y -direction:

$$A^p(\mathbf{r}') = \sum_{\mathbf{k}} A_{\mathbf{k}}^p \exp(i\mathbf{k} \cdot \mathbf{r}') \quad (24)$$

Substituting this relation in (23) and taking variations with respect to $A_{\mathbf{k}}^p$, X_j and Y_j leads to the following set of equations:

$$L_x L_y |\mathbf{k}|^2 = P(|\mathbf{k}|) \sum_j \Gamma_j \exp(-i\mathbf{k} \cdot \mathbf{r}) \quad (25)$$

$$\frac{dX_j}{dt} = \frac{\partial}{\partial Y_j} P(|\mathbf{k}|) \sum_{\mathbf{k}} A_{\mathbf{k}}^p \exp(i\mathbf{k} \cdot \mathbf{r}) \quad (26)$$

$$\frac{dY_j}{dt} = \frac{\partial}{\partial X_j} P(|\mathbf{k}|) \sum_{\mathbf{k}} A_{\mathbf{k}}^p \exp(i\mathbf{k} \cdot \mathbf{r}) \quad (27)$$

where the filter function P is defined as:

$$P(|\mathbf{k}|) = \int d\mathbf{r}' \gamma(|\mathbf{r}' - \mathbf{r}_i(t)|) \exp(i\mathbf{k} \cdot \mathbf{r}') \quad (28)$$

For each vortex, the number of trigonometric functions to be evaluated equals the number of vortices N . This can be avoided by employing cubic spline approximations to the exponentials, which has the extra advantage of being able to use Fast Fourier Transforms. Several of the spline approximations were tested, and are discussed in Van der Vegt et al. [14]. After calculating the stream function A^p , the boundary conditions for A^h are immediately known, and A^h can be determined. The paths of the vortices depend, however, only on the curl of stream function so that it is more efficient to formulate the problem in terms of $\underline{u}^h = \nabla \times A^h \underline{e}_z$. Bearing in mind the product formula for the solution of the Navier-Stokes equations, and the fact that the only way to introduce vorticity in a flow is through the no-slip condition at a solid boundary, the following integral formulation was derived:

$$\pi \gamma_p^* + \int_S \gamma_q^* (\underline{t}_p \cdot \underline{K}_2(p, q)) dS_q - \int_S (\underline{u}_q \cdot (\underline{u}_{wq} - \underline{U} - \nabla \times A_q^p \underline{e}_z)) (\underline{t}_p \cdot \underline{K}_1(p, q)) dS_q \quad (29)$$

in which γ^* is the strength of a vortex layer over the body surface S , \underline{t} is the tangential vector on the surface, and $\underline{K}_1, \underline{K}_2$ are given by:

$$\underline{K}_1(p, q) = \nabla_p \ln |\underline{r}_p - \underline{r}_q| \quad (30)$$

$$\underline{K}_2(p, q) = \underline{e}_z \times \underline{K}_1(p, q) \quad (31)$$

More details on the derivation of the boundary integral representation can be found in e.g. Hunt [15]. The integral equation for γ^* does not have a unique solution (Hunt, [15]). When the body surface is discretized by panels with a constant source strength and vortex strength, this leads to a matrix which is nearly singular. Since vorticity can only be introduced through the no-slip condition, the integral of γ^* over the surface must be equal to zero:

$$\int_S \gamma_q^* dS_q = 0 \quad (32)$$

Adding this condition to the boundary integral equation poses a problem with a unique solution. The inviscid vorticity transport can now be summarized as follows:

$$\dot{\underline{R}} = \underline{u}^p + \underline{u}^h + \underline{U} \quad (33)$$

which is solved using a second order Runge-Kutta method. The resulting tangential velocity jump (vorticity layer) at the surface, is represented by a set of blobs, which are diffused into the fluid through application of the random walk.

The two-dimensional model as presented here is discussed in more detail in Van der Vegt et al. [9], [16], [14]. More information about two-dimensional methods for solving the viscous transport equations can be found in e.g. Sarpkaya [17], Tiemroth [18] and Leonard [19]. For simulation of high Reynolds number flows, many blobs and small time steps are required, resulting in a large computational effort. The extension of the vortex blob model to three dimensions is not straightforward. Due to the large number of vortices required to obtain a realistic description the flow field, the tracking of individual vortices is not feasible. Furthermore the stretching term in the viscous vorticity evolution equation introduces extra difficulties. For the three-dimensional flows, a more advanced computational scheme is required. Van der Vegt [9] developed a special purpose spectral model to calculate the flow map. The discretization of the vorticity field also requires special attention. A new representation of the vorticity, employing blobs which are modified to account for the presence of a body, is presently under development. Results and theoretical details will be published in the near future.

4. Vortex Induced Cylinder Oscillations

The wake of a bluff body is comprised of an alternating vortex street. The shedding frequency f_v of the vortices is a function of the ambient flow velocity U , cylinder diameter D and Reynolds number. This relation was first discovered by Strouhal. The non-dimensional Strouhal number S is defined as:

$$S = \frac{f_v D}{U} \quad (34)$$

and is more or less constant over a wide range of Reynolds numbers ($100 < Re < 10000$): $S = 0.2$, for smooth cylinders. If the cylinder is flexibly mounted, there are non-linear interactions between the shedding frequency and the cylinder motion. Provided the damping is sufficiently low, the cylinder can extract energy from the flow, exciting sustained oscillations at a frequency close to, or coincident with, its natural frequency. In water both cross-flow and in-line excitation occurs. The in-line oscillations are excited at much lower velocities than required for cross-flow excitation.

Two dimensionless numbers which are often used in analyzing experimental data are the reduced velocity:

$$V_r = U / f_n D \quad (35)$$

and the stability parameter:

$$K_S = 2m\delta / \rho D^2 l \quad (36)$$

where f_n is the natural frequency of the spring mounted cylinder, m is the virtual mass, δ is the logarithmic decrement of damping, ρ the fluid density and l the cylinder length. Experiments have shown that the cross-flow excitation range extends over $4.5 < V_r < 10$ with a maximum amplitude of 1.5 diameters. For in-line oscillations there are two instability regions within $1.25 < V_r < 3.8$ with a maximum amplitude of 0.20 diameters. More details on experimental results can be found in the review of Sarpkaya [20].

During a test program conducted at MARIN, measurements were performed on the spring mounted cylinder. A general arrangement including the co-ordinate system is presented in Fig. 1.

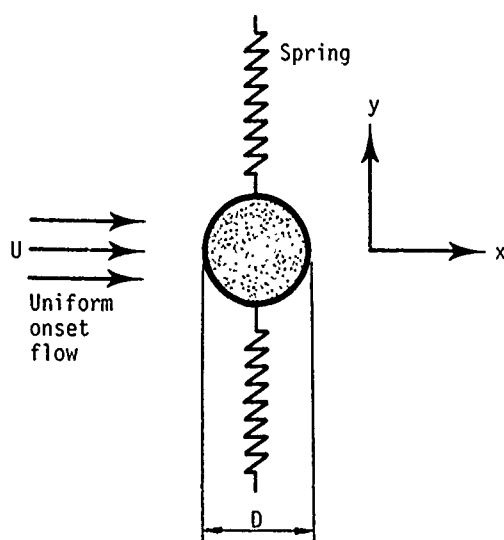


Fig. 1. Spring mounted cylinder arrangement

Cross-flow and in-line oscillation experiments were performed. A comparison with the semi-empirical wake-oscillator as proposed by Griffin is discussed in [22]. The results appeared very promising, and are rendered valuable for validating the vortex blob method. The two-dimensional vortex blob code has been tested on a number of cases of practical interest. Calculations on a fixed cylinder and on a cylinder forced to oscillate were presented in [16] and [21]. For the spring mounted cylinder, the method was supplemented with a module for solving the equation of motion of a spring mounted cylinder. At each time step, the exciting force originating from the flow field is used as the forcing term for the equation of motion of the cylinder, which is then displaced, causing a modification of the flow field. The region which is of practical importance is the lock-in region, where

the vortex shedding frequency is near the natural frequency of the mass-spring system. The added mass and damping are incorporated in the calculation of the forces from the vorticity field. The equation of motion is calculated using a second order Runge-Kutta method in time, as is the case for the update of the blob positions.

5. Structural Analysis Code

The structural analysis code available at MARIN is a general purpose time domain simulation program to compute the three-dimensional behaviour of submerged cylindrical bodies excited by end motions, waves and current. Although the program was developed for flexible risers, it may also be applied to other submerged flexible slender structures, such as flowline bundles, hoses, umbilicals and mooring lines.

The mathematical model is based on a discrete element technique known as the lumped mass method. This technique involves the lumping of mass, excitation forces and reaction forces at a finite number of nodes along the structure. All forces are formulated in terms of element properties, i.e. position and orientation. By formulating the laws of dynamic equilibrium and the stress-strain relations for each node, a set of equations of motion results. Additional equations are derived for the element twist motions due to torsion. These equations are solved in the time domain using finite difference and iterative procedures. It is assumed that the structural elements have axisymmetrical properties with respect to dimension, fluid force coefficients and stiffness.

A detailed description of the computer program can be found in Van den Boom et al. [23]. In this paper the discussion is limited to the incorporation of vortex induced fluid forces and motions in the model. At each time step the velocity and acceleration vectors of the structural elements are known. From these vectors, the cross-flow velocity and acceleration components are determined. Using these quantities, equation (37) is solved using a second order Runge-Kutta method. The cross-flow hydrodynamic lift force is then known. The drag force is derived from equation (40) and the time history of the structural response. The lift and drag forces are then evenly distributed along each element. From the excitation forces and reaction forces, the program computes the kinematics for the next time step. This process is repeated for each time step. A circular cross-section is assumed in this approach, i.e. element rotation is assumed to be perpendicular to the flow. The flow along each element is further assumed

to be fully correlated, i.e. two-dimensional. This assumption is valid as the amplitude of motion increases [20]. Although the fluid loading is thus essentially two-dimensional on each element, the structural response computational scheme allows for three-dimensional responses.

6. Wake-Oscillator Models

As an attempt to collect all observed phenomena in a compact model, several semi-empirical approaches exist [20]. One of the models is the wake-oscillator model, in which a non-linear oscillator for the lift force is coupled to the equation of motion of the cylinder. The response parameter $S_G = 2\pi S^2 K_S$ is the main parameter of importance. The governing equations of the so-called Griffin Model are:

$$\begin{aligned} \ddot{C}_L + \omega_s^2 C_L - [C_{L0}^2 - C_L^2 - (\dot{C}_L/\omega_s)^2] \\ [\omega_s G \dot{C}_L - \omega_s^2 H C_L] = \omega_s F \dot{Y}/D \end{aligned} \quad (37)$$

for the lift coefficient, and:

$$\ddot{Y} + 2\zeta\omega_n\dot{Y} + \omega_n^2 Y = (\rho U^2 D/2m) C_L \quad (38)$$

for the equation of motion in the direction normal to the onset flow. The shedding frequency ω_s follows from the Strouhal relation and the natural frequency from $\omega_n = \sqrt{k/m}$, where k is the spring stiffness. The dimensionless coefficients F, G and H are to be determined from experimental results.

The major drawbacks of the model are the facts that it is based on fluid damping in still water and that there is a continuous phase angle variation between the exciting force and the response of the cylinder. Additional damping has therefore been added to the Griffin model. This damping is a function of the cross-flow displacement and is given for $\sigma_Y > 0.25$ by:

$$\zeta = \frac{\pi \rho L D^2}{4m} \left[\frac{4.5}{\sqrt{Re_\omega}} + 0.25(\sigma_Y - 0.25) \right] \quad (39)$$

This is a slightly modified form of the empirical equation as proposed by Skop et al., see e.g. Sarpkaya [20].

For the drag coefficient of the oscillating cylinder, the following empirical formulation is used:

$$C_D = \bar{C}_D + J \sin(2\omega t) \quad (40)$$

where:

$$\bar{C}_D = \bar{C}_{D0} (1 + I(\sigma_Y/D)^{0.65}) \quad (41)$$

where ω is the frequency of cross-flow motion, σ_Y is the standard deviation of the cross-flow motion and I and J are constants to be determined from numerical

results obtained with the vortex blob method. C_{D0} is the mean drag coefficient for a stationary cylinder, $Re_\omega = \omega_n D^2/\nu$ is the Reynolds number based on the oscillation.

7. Discussion of Vortex Blob Calculations

Calculations using the vortex blob method, were performed for values of the reduced velocity ranging from 5.0 to 7.0. The Reynolds number ranged from 0.9×10^5 to 1.2×10^6 . Table 1 shows a comparison between experimental and computational results for the cross-flow motion of a spring mounted rigid cylinder, with $V_r = 5.25$, and $D=0.1$ m:

Table 1

Cross-flow results: measured and calculated

Quantity	Measured	Computed	
		$\Delta t^* = 0.05$	$\Delta t^* = 0.005$
\bar{C}_D	2.26	3.49	4.50
σ_{C_D}	1.10	0.59	0.52
ω_{C_D}	18.33	19.60	19.60
C_{Lmax}	6.77	4.40	8.33
σ_{C_L}	3.83	1.70	2.50
ω_{C_L}	9.25	9.75	9.75
y_{max}	1.27	0.20	0.22
σ_Y	0.79	0.13	0.10
ω_Y	9.25	9.80	9.80

The most striking result is the difference between the maximum amplitudes of the motion. The calculated value seems to be closer to normal values reported in literature, while the measured value belongs to the largest values reported. As was mentioned before, the calculations were not performed to get conclusive numerical results, but to capture the relevant phenomena involved. The calculated quantities show a reasonable resemblance with the measured data. Of course the comparison above does not take into account the details of the flow field. The vortex blob algorithm contains parameters, some of which must be determined through numerical tests. Interesting items in the calculations were:

- start-up time, i.e. dimensionless time passed before the cylinder was allowed to oscillate,
- time step,
- panel size,
- grid spacing,
- vorticity reduction scheme

In the present simulations, the flow field is largely determined by the motion of the cylinder. For this reason, some precautions must be made with respect to the coupling of the flow field calculation and the motion of the cylinder. In order to prevent the system from decoupling, the time integration and the start-up time must be chosen correctly. In simulations without a start-up time, the system became unstable in the lock-in region for a dimensionless time step $\Delta t^* = U\Delta t/D$ larger than 0.05, i.e. the cylinder disappeared out of the computation domain which was 8 cylinder diameters in both directions. A grid of 64×64 was used in all calculations, with 64 panels on the cylinder surface. A start-up time of $t^* = 20$ was chosen, see e.g. Sarpkaya [20]. In order to keep the number of blobs within reasonable limits, i.e. less than 40000, no experiments could be performed with a smaller time step, unless very crude vorticity reduction was applied.

Earlier calculations pointed out that the vorticity reduction should not be applied in the close vicinity of the cylinder, to prevent loss of accuracy. The reduction or clustering process must be applied with great care, since it distorts the flow field, and there-

fore the shedding process. A bi-cubic interpolation to a fixed grid sufficiently far away from the cylinder did not cause dramatic disturbances in the motion of the cylinder, although it was noticeable in the force registration.

Sensitivity to changes in grid and panel size were not investigated in this study. Numerical results concerning these parameters can be found in e.g. Van der Vegt [9].

The calculations discussed above were performed on an ETA-10P232, and a typical simulation required 20 to 30 hours of computing time.

8. Practical Results

In this section some practical results obtained from calculations with the structural code will be presented. A first case concerns a vertical marine riser subjected to a uniform incoming flow. For this application, results obtained from another computer program are also available, see Hansen et al. [1]. The main parameters are shown in Table 2, while Fig. 2 shows a general arrangement. Some statistical results of the vibration properties of the riser are shown in Table 3.

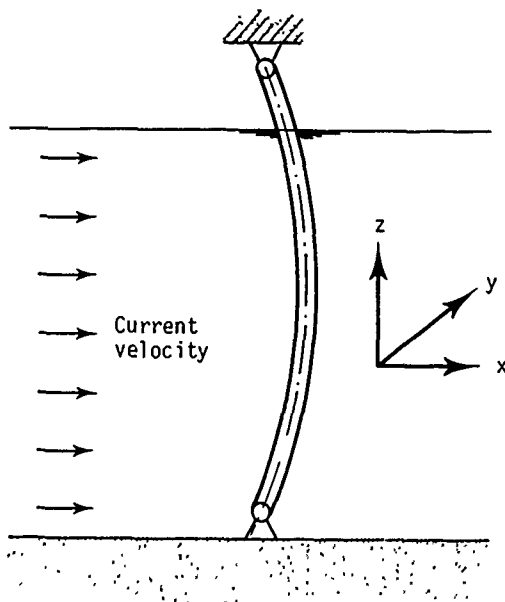


Fig. 2. Vertical riser arrangement

Table 2
Vertical riser properties

Quantity	Unit	Value
Length	m	100
Diameter	m	2
Mass	kg/m	3220
Natural frequency	rad/sec	0.71
Flow velocity	m/s	1.0
Tension	N	1.6×10^6
Response parameter	—	0.15

Table 3
Comparison between calculated results
for vertical riser

Quantity	Unit	Calculated	Hansen
x_{min}	m	1.05	1.35
x_{max}	m	2.60	2.80
y_{min}	m	-3.05	-3.40
y_{max}	m	3.05	3.40
\bar{C}_D	—	1.75	1.60
ΔT_{max}	N	8.5×10^4	8.0×10^4

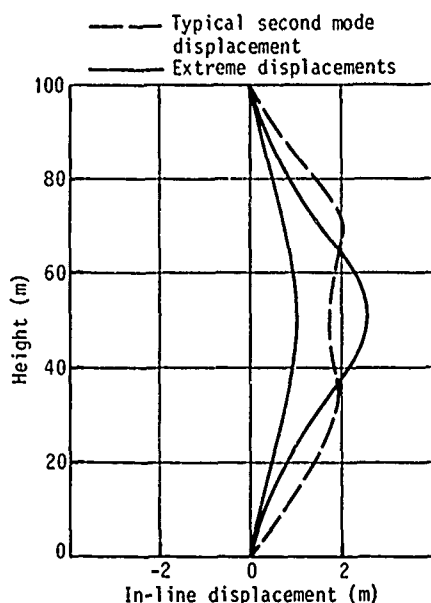


Fig. 3. In-line displacements of vertical riser

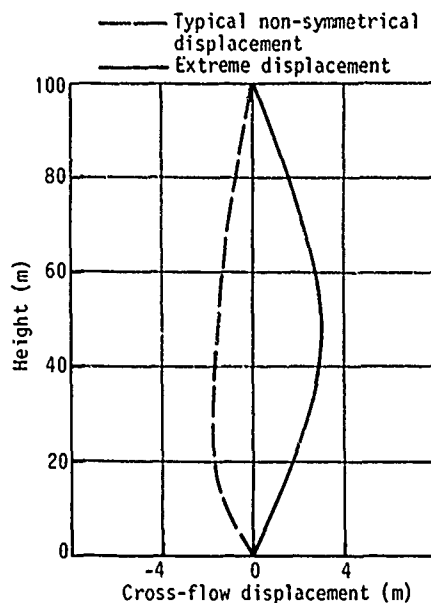


Fig. 4. Cross-flow displacements of vertical riser

Relatively large displacements are shown which are not unusual for lightly damped structures. The resemblance with results obtained from Hansen et al. [1] is good, although their maximum cross-flow and in-line displacements are larger. This may be caused by the fact that they use no structural damping at all. Using the present structural code this is not possible due to numerical instabilities for very lightly damped structures.

Figs. 3 and 4 show the extreme in-line and cross-flow displacements. The in-line displacement is dominated by a static part due to the mean drag force. The dynamic in-line displacement is dominated by a second mode vibration. This is due to the frequency of the drag force which is twice the cross-flow force frequency. The cross-flow frequency is pronounced and vibrates in the first excitation mode at a frequency close to the natural frequency.

The second case concerns a horizontal pipe and cable in a uniform tidal current. Full scale measurement data are provided by Vandiver [24]. Fig. 5 shows the experimental arrangement and Table 4 shows the pipe and cable particulars.

The agreement between calculated and measured vibration data is good, as shown in Table 5.

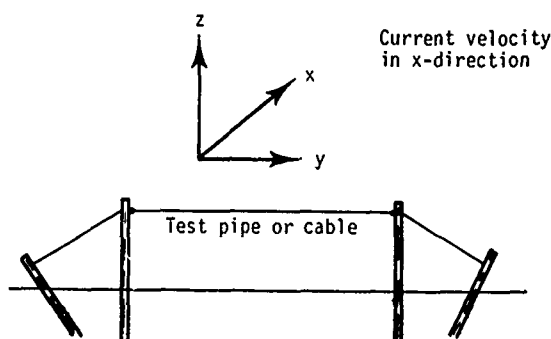


Fig. 5. Horizontal pipe and cable arrangement

Table 4
Horizontal pipe/cable properties

Quantity	Unit	Value	
		pipe	cable
Length	m	23	23
Diameter	m	0.0414	0.0318
Mass	kg/m	3.327	1.952
Natural frequency	rad/sec	4.53	5.78
Flow velocity	m/s	0.5	0.5
Tension	N	3500	3500
Response parameter	—	0.24	0.27
Reynolds number	—	18800	14500

Table 5

Comparison between computed results and experimental (full scale) results for horizontal pipe and cable

PIPE			
Quantity	Unit	Calculated	Experiment
$\sigma_{z/D}$	—	0.121	0.125
$\sigma_{x/D}$	—	0.362	0.411
\bar{C}_D	—	1.625	1.67

CABLE			
Quantity	Unit	Calculated	Experiment
$\sigma_{z/D}$	—	0.015	0.063
$\sigma_{x/D}$	—	0.440	0.383
\bar{C}_D	—	2.30	2.07

The standard deviation of the in-line cable motion is, however, overpredicted by the structural code. The calculated data show a lock-in behaviour of the pipe and cable which involved the second and third mode of vibration. This behaviour corresponds to the observed vibrations of the experimental results. Fig. 6 shows a plot of a typical pipe response under non-lock-in conditions. It is in reasonably good agreement with the observed response.

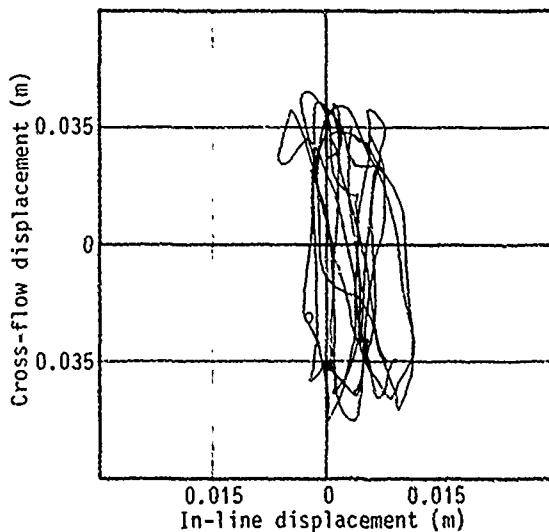


Fig. 6. Pipe response under non-lock-in conditions

The results shown here are in a general good correlation with experience and experimental data.

9. Conclusions

The results presented in this paper support the authors' view that complex flow simulations based on the Navier Stokes equations are invaluable for understanding flow phenomena. The Navier Stokes solvers should not be used as black box modules. Especially in flow problems which are not fully understood at present, the predictive abilities of computational procedures must not be taken for granted. The insight obtained from the numerical methods should be used, together with experimental data and experience, to obtain simpler models for engineering applications.

The wake-oscillator model which was used to describe hydrodynamical loading contains a minimum of information of the flow field. The results, however, are rendered to be sufficient for use in practice.

References

- [1] Hansen, H.T., Skomedal, N.G. and Vada, T., "Computation of vortex induced fluid loading and response interaction of marine risers", *Proceedings of Eight International Conference on Offshore Mechanics and Arctic Engineering*, The Hague (1989).
- [2] Griffin, O.M., Skop, R.A. and Ramberg, E.R., "The resonant, vortex-excited vibration of structures and cable systems", *Proceedings of Offshore Technology Conference*, Houston, Paper 2319 (1975).
- [3] Skop, R.A. and Griffin, O.M., "An heuristic model for determining flow-induced vibrations of offshore constructions", *Proceedings of Offshore Technology Conference*, Houston, Paper 1843 (1975).
- [4] Griffin, O.M., Skop, R.A. and Koopmann, G.H., "Measurements of the response of bluff cylinders to flow induced vortex shedding", *Preprints of Proceedings of Offshore Technology Conference*, Houston (1973).
- [5] Chorin, A.J., "Numerical study of slightly viscous flow", *Journal of Computational Physics*, Vol. 57, pp. 785-796 (1973).
- [6] Beale, J.T. and Majda, A., "Vortex methods 1, convergence in three dimensions", *Mathematics of Computation*, Vol. 39, pp. 1-27 (1982).
- [7] Beale, J.T. and Majda, A., "Vortex methods 2, higher order accuracy in two and three dimensions", *Mathematics of Computation*, Vol. 39, pp. 29-52 (1982).

- [8] Beale, J.T. and Majda, A., "A convergent 3-D vortex method with grid free stretching", *Mathematics of Computation*, Vol. 46, pp. 401-424 (1986).
- [9] Vegt, J.J.W. van der, *A variationally optimized vortex tracing algorithm for three dimensional flows around solid bodies*, PhD thesis, Technical University Delft, The Netherlands (1988).
- [10] Serrin, J., *Mathematical principles of classical fluid mechanics*, Volume 8/1 of *Encyclopedia of Physics*, Springer Verlag (1959).
- [11] Peskin, C.E., "A random walk interpretation of the incompressible Navier-Stokes equations", *Communications on Pure and Applied Mathematics*, Vol. 38, pp. 845-852 (1985).
- [12] Hald O.H. and Del Prete, M., "Convergence of vortex methods for Euler's equations", *Mathematics of Computation*, Vol. 32, pp. 791-809 (1978).
- [13] Hald, O.H., "Convergence of vortex methods for Euler's equations 2", *SIAM Journal of Numerical Analysis*, Vol. 16, pp. 726-755 (1979).
- [14] Vegt, J.J.W. van der and Huijsmans, R.H.M., "Numerical simulation of flow around bluff bodies at high Reynolds numbers", *Proceedings of 15th Symposium on Naval Hydrodynamics* (1984).
- [15] Hunt, B. *Numerical Methods in Applied Fluid Dynamics*, Academic Press (1980).
- [16] Vegt, J.J.W. van der and Boom, W.C. de, "Numerical simulation of flow around circular cylinders at high Reynolds numbers", *Proceedings of the 4th International Conference on Behaviour of Offshore Structures (BOSS '85)*, Delft (1985).
- [17] Sarpkaya, T., "Computational methods with vortices - the 1988 Freeman Scholar Lecture", *Journal of Fluids Engineering*, Vol. 111, pp. 5-52 (1989).
- [18] Tiemroth, E.C., *The simulation of the viscous flow around a cylinder by the random vortex method*, PhD thesis, Department of Naval Architecture and Offshore Engineering, University of California, Berkeley (1986).
- [19] Leonard, A., "Vortex methods for flow simulation", *Journal of Computational Physics*, Vol. 37, pp. 289-335 (1980).
- [20] Sarpkaya, T., "Vortex-induced oscillations , a selective review", *Journal of Applied Mechanics*, Vol. 46, pp. 241-258 (1979).
- [21] Oortmerssen, G. van, Vegt, J.J.W. van der and Walree, F. van, "Forces on cylinders in oscillatory flow: a comparison of the results of numerical and physical models", *PRADS 1987*, Trondheim (1987).
- [22] Vegt, J.J.W. van der and Walree, F. van, "Progress in the prediction of forces on cylinders", *Proceedings of a Workshop on Floating Structures and Offshore Operations*, Wageningen (1987).
- [23] Boom, H.J.J. van den, Dekker, J.N. and Elsäcker, A.W. van, "Dynamic aspects of offshore riser and mooring concepts", *Proceedings of the 19th Offshore Technology Conference*, Houston, Paper 5531 (1987).
- [24] Vandiver, J. Kim, "Drag coefficients of long flexible cylinders", *Proceedings of the 15th Offshore Technology Conference*, Houston, Paper 4490 (1983).

Stability and Accuracy of a Non-Linear Model for the Wave Resistance Problem

A. J. Musker
Admiralty Research Establishment
Haslar, England

Abstract

A non-linear Rankine-source method for predicting the wave resistance of a surface ship in calm water has recently been published by the author. In the present paper, an investigation into the stability and accuracy of the method is presented. The method is shown to be quite insensitive to changes in the various parameters which are necessarily associated with the numerical procedure but which do not feature in the mathematical formulation of the problem. A stable parameter regime is identified which has been found to give excellent agreement with towing tank data for the Series 60 hull.

1. Introduction

During the last decade there has been a great deal of activity in the field of numerical ship hydrodynamics. New methods for simulating a wide range of phenomena have been proposed; such methods invariably involve the generation of a grid covering either the boundaries of the domain (as in a panel method) or the complete interior of the domain (as in an Euler or a Navier-Stokes code).

Although it is usual to compare any numerical predictions with available experiment data (or, where appropriate, analytic data) it is somewhat rare to find examples of the effect of systematic variations in grid geometry on the accuracy of the solution. Equally, there may be factors other than the grid geometry which affect the outcome of a simulation and these too are often overlooked. In addition to the accuracy of a method, its stability also needs to be assessed. This may be achieved with the aid of theoretical treatment but ultimately the degree of stability of a method can usually only be gauged by its actual behaviour in trial calculations.

This paper addresses both the accuracy and stability aspects of a panel method due to

Musker [1] designed to calculate the potential flow past a ship hull in steady translation in calm water. The method employs non-linear forms of the free-surface boundary conditions and on the basis of some initial tentative calculations it has been found to give good agreement with experiment data for both the Wigley hull and the Series 60 hull (see Musker [2]).

Although the above problem can be formulated in terms of an integral of a source density distributed on the hull and the free surface, in practice the domain boundaries are made discrete by representing them using a finite number of panels. In addition, the free surface is not known a priori because it is part of the solution. Consequently panels must be associated either with the calm free-surface (with the actual free-surface represented by means of a Maclaurin expansion of the prevailing boundary conditions) or with the approximate free-surface relating to the most recent iterate in a convergent sequence of surfaces. The present method employs the first of these two options and clearly falls into the category of so-called Rankine source methods.

Rankine source methods have been the subject of intense development in recent years in connection with a particular formulation of the Neumann-Kelvin problem (see, for example, Raven [3]). The Neumann-Kelvin (NK) problem models the wave-making of a hull by a solution of Laplace's equation subject to a linearised form of the free-surface condition and an exact form of the kinematic condition on the hull surface. Despite the much disputed problems of uniqueness of solution for the NK problem a large number of computer codes have been prepared based on this theory. The beauty of the Rankine source method lies in its inherent ability to provide engineering solutions to the NK problem (usually in a modified form using double-body linearisation) whilst at the same time providing the potential for addressing the

non-linear problem. On the other hand, the more conventional approach to solving the NK problem, using a Havelock or Kelvin wave-making source distribution, has the important advantage of requiring fewer panels which automatically satisfy the important radiation condition that waves should travel downstream.

Staying with the linear problem for the moment, it is interesting to note the great diversity of solutions quoted in the literature. Figure 1 shows a collection of computer predictions of wave resistance for the Series 60 hull ($C_B = 0.6$, model fixed) drawn from the two Workshops on Ship Wave-Resistance Computations held at the David Taylor Research Center (see references [4] and [5]). All these predictions use linearised theory for treating the free surface but differ in their method of solution (NK using Rankine source technique, NK using Havelock source technique, thin ship theory - in which the hull boundary condition is applied at the centre-plane etc). It is interesting to note that a mean curve drawn through the data would be significantly above the tank results. More recently, Chen and Noblesse [6] have remarked on the considerable scatter evident in published predictions of wave resistance based on similar theory. As noted by Bai [4] if no algebraic or computer truncation errors are incurred then results of numerical computations based on the same mathematical formulation should be the same. Clearly this is not the case.

If the possibility of algebraic or coding error is dismissed (itself a dangerous assumption) then the explanation for the disparity in the predictions most likely lies in the mechanism whereby truncation errors appear. The obvious source of such errors is the manner in which the hull is divided into facets or panels. The distribution of such panels around the hull, particularly near the bow, stern and waterline is bound to have an effect on the solution. In the case of a Havelock source the numerical evaluation of the Green function poses its own problems.

If a Rankine source rather than a Havelock source is used then perhaps an even greater problem presents itself: how large an expanse of the free surface in the vicinity of the hull needs to be modelled using additional panels and how should the resolution of this region be chosen? The manner in which the source density is distributed algebraically on each panel will also affect the solution. Recent work by Ni [7] has shown that the use of higher order curved panels with linearly varying source density is computationally more efficient compared with constant density panels. Finally, Rankine source methods invariably employ Dawson's approach [8] to satisfy the radiation condition that waves

should not travel upstream of the hull. This approach involves the use of an upwind finite difference advection scheme for the wave disturbance and can take many forms.

Clearly the operator of any Rankine source code has a great deal of freedom in the manner in which a particular problem is posed. The purpose of the present paper is to investigate the effect of making certain decisions about the geometry of the mesh and the type of advection scheme used for the particular case of the method described in Reference [1]. This method is first outlined for completeness and the 'degrees of freedom' at the operator's disposal are identified and minimised to manageable proportions. These are then systematically adjusted and the effect on the accuracy of prediction and the stability of solution is recorded. All the calculations were performed for the Series 60 hull ($C_B = 0.6$).

2. Methodology

A Cartesian coordinate system is used in which the xy plane is in the calm free surface with the x axis positive upstream and the z axis positive downwards. The fluid is assumed to be inviscid, incompressible, irrotational and infinitely deep.

A scalar velocity potential is defined such that $-\text{grad}\phi$ is the local fluid velocity vector. This potential satisfies Laplace's equation everywhere within the fluid subject to the following boundary conditions.

$$(\text{grad } \phi) \cdot \hat{n}' = 0 \quad (1)$$

on the hull surface,

$$\left[\frac{\partial \phi}{\partial z} \right]_0 + \zeta \left[\frac{\partial^2 \phi}{\partial x \partial z} \right]_0 = \frac{\partial \zeta}{\partial l} \left[\frac{\partial \phi}{\partial l} \right]_0 + \zeta \frac{\partial \zeta}{\partial l} \left[\frac{\partial^2 \phi}{\partial x \partial z} \right]_0 \frac{dx}{dl} + \left[\frac{\partial^2 \phi}{\partial y \partial z} \right]_0 \frac{dy}{dl} \quad (2)$$

and

$$\begin{aligned} & \zeta \left[-g + \left[\frac{\partial \phi}{\partial x} \right]_0 \left[\frac{\partial^2 \phi}{\partial x \partial z} \right]_0 \right. \\ & \left. + \left[\frac{\partial \phi}{\partial y} \right]_0 \left[\frac{\partial^2 \phi}{\partial y \partial z} \right]_0 + \left[\frac{\partial \phi}{\partial z} \right]_0 \left[\frac{\partial^2 \phi}{\partial z^2} \right]_0 \right] \\ & = \frac{1}{2} \left[U_\infty^2 - \left[\frac{\partial \phi}{\partial x} \right]_0^2 - \left[\frac{\partial \phi}{\partial y} \right]_0^2 - \left[\frac{\partial \phi}{\partial z} \right]_0^2 \right] \quad (3) \end{aligned}$$

on the calm free-surface. In the above equations, \hat{n}' (n'_x, n'_y, n'_z) represents the outward normal vector on the hull surface, l represents a distance measured along a double-body streamline measured positive in the locally upstream direction, U_∞ is the ship speed, g is the acceleration due to gravity and ζ represents the wave elevation. The last two boundary conditions are non-linear and result from Maclaurin expansions of the exact boundary conditions prevailing on the free surface [1]. For the purpose of comparison, the above set of boundary conditions reduces to the Neumann-Kelvin problem if the spatial velocity gradients are set to zero. The ship speed is defined such that

$$\text{grad } \phi = (-U_\infty, 0, 0) \quad (4)$$

at ∞ except where waves are present. Dawson's approach [8] is used to ensure that waves are advected downstream.

The velocity potential is prescribed by means of a source density distribution associated with the hull (and its optical image in the $z = 0$ plane) and the free surface. Constant, planar, source density panels are used throughout the analysis and in the case of the free surface panels these are raised very slightly above the calm water-plane to improve the modelling of the spatial velocity gradients [9], [10]. The latter are calculated analytically and great care has been taken to avoid singular regions (in the numerical sense) by employing suitable asymptotic expressions within the program. To avoid leakage, an additional system of vertical panels (referred to loosely as 'deck panels') joins the water-line on the hull to the neighbouring system of free-surface panels; a Neumann condition is imposed at the centroids of these panels.

Successive application of the boundary conditions at a large number of control points on the hull and calm water-plane leads to a system of non-linear simultaneous algebraic equations for the unknown source densities and wave elevations. The associated Jacobian matrix is calculated analytically and the equations are solved iteratively using Newton's method without relaxation; each associated linear system is solved directly using a Crout factorisation. The criterion adopted for complete convergence is that the root mean square of the sum of the residuals (comprising the most recent corrections to the source densities and wave elevations) is less than 0.002. Although strictly dimensionally inconsistent, in practice this criterion relates to a correction in wave elevation

of 1 mm for a hull of length 100 m. Further details of the non-linear algorithm used can be found in Reference [1].

Having solved the equations, the pressure at a particular control point on the hull is found from:

$$p = \rho g z + \frac{1}{2} (U_\infty^2 - |\text{grad } \phi|^2) \quad (5)$$

The wave resistance is found by integrating the pressure around the hull taking due account of the hydrostatic correction associated with the predicted water-line (note that for consistency with the applied boundary conditions this correction is not performed for the linear case):

$$R_W = - \iint_S p n'_x \, ds \quad (6)$$

where S is the wetted area. As is often found in panel methods, a residual resistance is observed at zero speed because of the manner in which the hull is made discrete. Accordingly, the result for the double body calculation (where no waves are present) is first subtracted to yield the final wave resistance.

The free surface grid uses double-body streamlines generated by Runge-Kutta integration to within a lateral error of 10^{-4} of the ship length. These streamlines are separated laterally by equal intervals at the upstream edge of the calm free-surface and for each streamline the control points are positioned at equal intervals in arc-length; this process is facilitated using cubic splines. The free surface panels are constructed automatically such that their stream-wise edge projections onto the $z = 0$ plane follow the streamlines and have edges along the water-line which are equal in length. An additional constraint is imposed in that the panel aspect ratio away from the hull is typically unity.

A four-point upwind finite difference scheme is used to advect disturbances in the downstream direction. The boundary condition imposed on the first three control points at the upstream end of a given free-surface streamline is different from equations 2 and 3. Instead, the vertical fluid velocity in this region is forced to be zero. In addition, the last three control points at the downstream end are treated differently. Here, the coefficients in the advection scheme are reduced gradually to 25 per cent of their normal value to dampen the waves at the edge of the domain.

It should be noted that the method does not employ any clustering of panels in the vicinity of the bow and stern - in the author's opinion such clustering provides too many extra degrees of freedom to allow a sensible study to be undertaken. In addition, the highly variable step-length for the finite difference advection operator in such a scheme will almost certainly affect the stability of the solution algorithm.

The hull panels are arranged to mesh exactly with the free surface nodes along the water-line. Below the water-line, panels are constructed automatically in one of two ways. Firstly, they can be constructed such that an equal number of quadrilateral panels is used at each longitudinal station ('single-patch method' - see [1]). Secondly, a mixture of quadrilateral and triangular panels is used to allow the number of panels at a particular section to be reduced in the ratio of local section depth to keel depth. This is done in such a way as to maintain a reasonably constant panel area and aspect ratio (which are thought intuitively to be important from the point of view of numerical stability) whilst at the same time lifting the restriction imposed by the single-patch method that the hull panels below the water-line must be generated on the basis of strictly vertical stations. This is known as the 'multi-patch' method and was developed to extend the capability of the panel code to hulls with more complicated geometry - particularly in the bow and stern regions. The BLINES computer-aided design system [11] is used for interpolation purposes.

3. Stability and Accuracy Study

The following list defines the most important factors which need to be addressed before a calculation can be performed for a particular hull geometry:

- a. Length of domain.
- b. Half-width of domain (ie excluding image in xz plane).
- c. Distance between the bow and the leading edge of the domain.
- d. Free-surface grid resolution.
- e. Hull grid resolution.
- f. Free-surface panel elevation (above $z = 0$ plane).
- g. Type of advection scheme.

Experience with the code suggests that there are significant differences in predicted resistance between large and small domains. Not surprisingly, however, at any particular Froude number and for a fixed grid

resolution, the resistance approaches an asymptote as the size of the domain increases. Accordingly, in order to decrease the number of degrees of freedom for the present study, a large domain was used throughout the investigation. This was set to 3 ship lengths in the longitudinal direction and extended to 1.5 ship lengths transversely measured from the centre-plane. The distance between the bow and the leading edge of the domain was set to one half of the ship-length; this was based on previous experience with the method.

The hull and free-surface grids are related in the sense that the water-line nodes are forced to coincide prior to the construction of the vertical deck panels. In addition, an optional facility exists to position extra hull panels between water-line stations defined by the free-surface nodes so that the hull panel density (defined as the number of stream-wise hull panels per free-surface panel) can assume any integer value. If this option is invoked then the grid generator positions these extra panels such that their stream-wise edges form equal divisions along the water-line. In this way the grid generating code can automatically calculate the mesh on the hull once the hull panel density and free-surface resolution have been set since only an integer number of panels is allowed along the water-line (in practice the latter condition is met within the computer program by a very minor adjustment to the absolute length of the domain).

It can be seen, therefore, that there are now only four degrees of freedom which need to be considered: the grid resolution, the hull panel density, the free-surface panel elevation and the type of advection scheme. It should be noted that no other operator intervention is called for once these factors have been set.

4. Numerical Experiment

The Series 60 ($C_B = 0.6$) hull was used for all the computer runs described in this investigation. The hull was fixed and no allowance was made for sinkage or trim (in the author's opinion this in no way detracts from the usefulness of the study). Unless otherwise stated, the following default conditions were used for all the runs:

hull panel density = 1

and

panel elevation = 15 per cent of
average panel
diagonal

The latter figure was based on previous experience with the code and careful analysis of the ability of constant source density panels to model spatial gradients of fluid velocity [10].

Four numerical experiments were performed with the aim of determining the effect of varying any one of the above-mentioned degrees of freedom. The runs were performed at the following Froude numbers:

0.239, 0.271, 0.287, 0.303, 0.319, 0.335 and 0.351

based on ship-length at the water-line. All arithmetic was performed using 64 bit precision. The experiments are labelled A, B, C and D and are described below.

Experiment A (effect of free-surface grid resolution)

This was performed in two stages. Firstly (experiment A1), three free surface grids were generated each of which was fixed, in relation to the ship-length, for all Froude numbers (henceforth such grids will be termed 'mode 1' grids). They are referred to as coarse (1166 free-surface panels), medium (1904 free-surface panels) and fine (2673 free-surface panels). The number of free-surface panels distributed along the water-line of the hull was 17, 23 and 27 respectively. Single-patch hull meshes were used for this experiment.

Secondly (experiment A2), grids were generated such that their resolution related not to the ship-length but rather to the wave-length of the transverse waves expected to be shed by the hull. In this instance the grid resolution was described by a parameter, n , where n is the number of panels per transverse wave-length. The total number of panels positioned along the length of the free-surface domain is thus:

$$\frac{n \times \text{domain-length}}{2\pi F_r^2 \times \text{ship-length}}$$

This meant that for each Froude number a new grid (henceforth termed a 'mode 2' grid) had to be calculated to conform to the chosen value of n . This exercise was carried out for values of n ranging from 4 to 12 in intervals of 2 (it was not anticipated that a value of n as low as 4 would perform very well but for the sake of completeness it was included in the experiment). Multi-patch hull meshes were used for this experiment.

Experiment B (effect of hull panel density)

This experiment compared the performance of the method using two different values of the hull panel density; the values used were

1 and 3. Mode 2, multi-patch grids were employed throughout, with n set to 10.

Experiment C (effect of panel elevation)

This experiment was designed to investigate the effect of elevating the free-surface panels above the calm water-plane. As for Experiment B, mode 2, multi-patch grids were employed throughout, with n set to 10. Three different elevations were tested: zero, 15 and 30 per cent of the average panel diagonal.

Experiment D (effect of choice of advection scheme)

The above three experiments were performed with two different upwind advection schemes for the stream-wise wave-slope:

$$\text{Taylor Scheme: } \text{Slope}_i = -\frac{1}{\Delta l} x$$

$$\left[1.667\zeta_i - 2.5\zeta_{i-1} + \zeta_{i-2} - 0.167\zeta_{i-3} \right]$$

$$\text{Spline Scheme: } \text{Slope}_i = -\frac{1}{\Delta l} x$$

$$\left[1.555\zeta_i - 2.177\zeta_{i-1} + 0.689\zeta_{i-2} - 0.0667\zeta_{i-3} \right]$$

where Δl = the increment in l . The first (Taylor Scheme) is identical to Dawson's scheme [8] except that Dawson allowed the increments between free-surface nodes to be variable. The spline scheme uses knots at each interior node with a quadratic correction term for the rate of change of slope at the first node. This experiment concentrated on monitoring the effect of changing the advection scheme from the default four-point Taylor scheme to the four-point spline scheme.

5. Discussion of Results

In the following section, all results for Experiments A, B and C are associated with the use of the Taylor advection scheme. Absence of a data point in any of the accompanying graphs indicates that the algorithm failed to converge within the specified tolerance (often, but not always, this meant that the algorithm diverged; occasionally the root mean square of the residuals wandered about a mean value above the selected tolerance - such runs were deemed to have failed even though the associated wave resistance had apparently converged to within a finer tolerance). Convergence was usually attained after about 5 iterations. All results are compared with the Series 60 tank data of Kim and Jenkins [12] for the case of a fixed model.

Experiment A

A comparison of the coarse and fine grids is shown in Figure 2 and a summary of the results is presented in Figure 3. The method converged for all speeds using the coarse grid. For the medium grid the method failed at a Froude number of 0.335 whilst for the fine grid the method failed for the three highest Froude numbers within the Range used.

It should be recalled here that Experiment A1 was designed around the original method described in Reference [1] employing mode 1 free-surface grids and single-patch hull grids. It is perhaps surprising that the coarse grid should have led to such good agreement with experiment data particularly at the lower Froude numbers where shorter wave-lengths are prevalent. It is similarly curious to observe the closer agreement between the coarse and fine meshes at the lower Froude numbers compared with the medium mesh results.

The results for experiment A2 (mode 2, multi-patch hulls) are summarised in Figure 4. It can be seen that all the runs converged successfully for values of n from 4 to 10. For $n = 12$, however, the method diverged for Froude numbers of 0.319 and 0.335 (note that the lowest Froude number case was not processed because it exceeded the capacity of the computer - this was the only run in the whole investigation which could not be processed because of size limitations). Not surprisingly, values of $n = 4$ or 6 appear to be quite inadequate to resolve the flow-field and hence the wave resistance. The data for $n = 8$ define the shape of the curve well but slightly under-estimate the resistance for the higher Froude numbers. Excellent agreement is obtained for $n = 10$ and no improvement in accuracy is achieved for the stable runs when $n = 12$.

Experiment B

In this experiment mode 2 free-surface grids and multi-patch hull grids were used with a hull panel density of 3 (see Section 3). Figure 5 shows a perspective view of one of the meshes from a point below the water-line looking towards the hull. The effect of the increased resolution of the hull can be seen in Figure 6 to be quite weak. At the higher Froude numbers the increased hull panel density consistently lowers the resistance by a very small amount whilst little or no effect is observed at the lower Froude numbers. All the runs performed were completely stable.

Experiment C

Figure 7 illustrates the effect of elevating the free-surface panels above the

calm water-plane. The absence of data points for the case of zero panel elevation indicates the instability inherent in introducing spatial derivatives of fluid velocity calculated using panels of constant source density if the control point lies in the plane of the panel [10]. With the possible exception of the two runs at a Froude number of 0.271 it can be seen that there is little difference between the results for 15 per cent and 30 per cent panel elevations. All the runs performed with elevated free-surface panels were stable.

Experiment D

Attention here will be focussed on three results of significance. In the first two cases the data refer to mode 2, multi-patch grids with $n = 10$. Figure 8 shows the very small effect the spline advection scheme has on the accuracy of the predicted wave resistance compared with the Taylor scheme; the results are very nearly identical. Figure 9 shows the data for Experiment C with zero panel elevation replotted using the results for the spline advection scheme. The results are compared with the single Taylor result from Figure 7. Two important conclusions emerge from these data. Firstly, the effect on the accuracy of using a spline scheme is minimal. Secondly, the results for zero panel elevation are not only inherently unstable using the Taylor scheme, as observed above, but also inherently inaccurate when they can be made stable by employing a spline scheme. This again reinforces the findings of Reference [10].

Further evidence of the more stable nature of the spline scheme is offered in Figure 10, which shows the spline results for Experiment A2 with $n = 12$, compared with the Taylor results with $n = 10$. The results for Froude numbers 0.319 and 0.335 when $n = 12$ are now stable - thus allowing a comparison in accuracy between $n = 10$ and $n = 12$ to be made throughout the whole speed range. It can be seen that there is little advantage to be gained by increasing n above 10.

The stability of panel methods for the linear problem has been analysed recently using Fourier techniques by Sclavounos and Nakos [13]. They found that the numerical damping associated with upwind finite difference schemes decreases as the grid becomes finer or as the number of upstream nodes included in the scheme at a particular control point increases. Although the present technique is non-linear this nevertheless probably explains why the method has a tendency to diverge for the finest grid tested ($n = 12$) using the Taylor scheme. Their work may also explain the stability problems experienced by the only other non-linear methods which, to the best of the author's knowledge, have appeared in the

literature since 1985 (Maruo and Ogiwara [14], Xia [15], Ni [7] and Rong et al [16]).

Maruo and Ogiwara used a two-point formula but still experienced quite severe convergence problems, whilst Xia and Ni both used three-point formulas. Xia found that this method diverged for all cases tested if a 4-point scheme was adopted but much better convergence characteristics were observed when this was abandoned in favour of a (less accurate) 3-point scheme. Ni employed a sophisticated higher order panel scheme very successfully using a three-point scheme but again found stability a problem using an extra upstream node. In the present method, using mode 2 free-surface grids and multi-patch hull grids, stability only became a problem at the highest resolution (for the highest Froude number only) and this was completely alleviated by utilising a four-point spline rather than a four-point Taylor scheme. In the method of Rong et al a two-point scheme was used near the stern region to provide sufficient damping to ensure convergence.

Mention should be made of the practice of elevating the free-surface panels above the calm water-plane. It might be argued that the ensuing system of equations will be less well conditioned in the sense that a control point on the $z = 0$ plane would not be so strongly associated with its corresponding panel if the panel were raised above it. On the other hand, the author has shown that the modelling of the spatial gradients of fluid velocity which are required in the non-linear formulation is inadequate if the control points are contained in the plane of the panels. Indeed, it is so inadequate as to cause the method to diverge.

It should be noted that the amount by which the panels need to be raised is very small - typically between 0.8 per cent and 1.5 per cent of the ship length, depending on the Froude number, when $n = 10$. In addition, Figure 7 demonstrates that the predicted resistance appears not to be particularly sensitive to the panel elevation. Xia [15] also tried raising his free-surface panels and found improved convergence at some expense in accuracy. Panel elevations used by Xia, however, were much larger - typically between 2.5 per cent and 10 per cent of the ship-length - and in the author's opinion these values are too large. Ni [7] has circumvented the problem altogether by adopting higher order panels with linearly varying source density which follow the calculated free surface as it progresses towards its final converged solution. The present work suggests that such sophistication may not be necessary.

Finally, a synopsis of the published data for the above non-linear methods is presented

in Figure 11. The Series 60 data for the method of Maruo and Ogiwara is taken from Reference [17]. The present results using the default conditions of 15 per cent panel elevation (based on average panel diagonal, not ship-length), four-point Taylor advection scheme, mode 2, multi-patch grids with $n = 10$ are included for comparison.

6. Conclusions

A panel method based on a boundary integral approach to solving the non-linear free-surface wave-making problem has been thoroughly tested against tank data for the Series 60 hull. The number of degrees of freedom at the disposal of the operator of the computer code has been minimised with the aim of investigating systematic changes to the input parameters which may affect the numerical solution but which do not feature in the mathematical formulation.

Two types of grids were tested. The first type, labelled mode 1, single-patch, uses panel geometries on the calm free surface which are independent of Froude number but which are kept constant with respect to the ship-length. The hull panels are organised so that the same number of panels is used at each station. The second type, labelled mode 2, multi-patch, uses panel geometries which depend on the Froude number in the sense that a fixed number, n , of free-surface panels per transverse wave is selected. In addition, the hull panels are organised into quadrilateral or triangular panels automatically such that the size and shape of panels do not change significantly from station to station.

The following conclusions can be drawn:

a. As expected, the method was unstable for zero free-surface panel elevation. The method was invariably stable, however, for non-dimensional panel elevations (based on average panel diagonal) of 15 per cent and 30 per cent. Furthermore, the solution was observed to be reasonably insensitive to the choice of non-zero panel elevation.

b. Accurate results were obtained using a coarse, mode 1, single-patch grid for all Froude numbers. This approach became unstable as the grid became finer.

c. The mode 2, multi-patch grids exhibited greater stability and were used for the remainder of the investigation. The results approached the tank data asymptotically as n increased from 4 to 12, with very little difference in the accuracy between 10 and 12. The $n = 12$ results diverged at

two of the higher Froude numbers using the four-point Taylor advection scheme.

d. No case of instability or significant change in accuracy of prediction was recorded for any value of n using the four-point spline scheme.

e. A threefold increase in hull panel density in relation to the free-surface grid resulted in no significant effect on the stability or accuracy of the method.

f. Comparison with other non-linear methods described in the recent literature shows the method to be very stable and accurate using mode 2, multi-patch grids with n set to 10.

Having identified a stable and accurate parameter regime, it is hoped to perform a similar investigation in the near future to determine the effect of decreasing the extent of the free surface surrounding the hull. Tests with different hull geometries are also planned.

7. Acknowledgements

This project would never have been completed without the skill and dedicated support of Mrs P R Loader of the Admiralty Research Establishment, Haslar. The author would like to thank her for her sustained effort and enthusiasm. Dr G Michel of Aerobel Defence Technology (formerly Principia Mechanica) provided the interface software for BLINES and Mrs C Patis attended to many of the computer runs. Their help is gratefully acknowledged.

8. References

1. Musker, A J, "A Panel Method for Predicting Ship Wave Resistance", Proceedings of the 17th Symposium on Naval Hydrodynamics, The Hague, August 1988.
2. Musker, A J, "A Solution of the Non-Linear Wave Resistance Problem", Proceedings of the International Symposium on Ship Resistance and Powering Performance, Shanghai, April 1989.
3. Raven, H C, "Variations on a Theme by Dawson", Proceedings of the 17th Symposium on Naval Hydrodynamics, The Hague, August 1989.
4. Bai, K J and McCarthy, J H, "Proceedings of the Workshop on Ship Wave-Resistance Computations", DTNSRDC, November 1979.
5. Noblesse, F and McCarthy J H, "Proceedings of the Second DTNSRDC Workshop on Ship Wave-Resistance Computations", DTNSRDC, November 1983.
6. Chen, C Y and Noblesse, F, "Comparison between Theoretical Predictions of Wave Resistance and Experimental Data for the Wigley Hull", Journal of Ship Research, Vol 27, No 4, December 1983.
7. Ni, S Y, "Higher Order Panel Methods for Potential Flows with Linear or Non-Linear Free Surface Boundary Conditions", Chalmers University of Technology, 1987.
8. Dawson, C W, "A Practical Computer Method for Solving Ship-Wave Problems", Proceedings of the Second International Conference on Numerical Ship Hydrodynamics, Berkeley, 1977.
9. Musker, A J, "A Note on Free-Surface Flow Prediction", ARE Technical Memorandum TM(UHR)86306, March 1986.
10. Musker, A J and Loader, P R, "A Modified Boundary Element Method for Predicting Ship Wave Resistance", Proceedings of the 7th International Conference on Finite Element Methods in Fluid Flow Problems, The University of Alabama, April 1989.
11. Catley, D, Okan, M B and Whittle C, "Unique Mathematical Definition of a Hull Surface, its Manipulation and Interrogation", WEMT, Paris, July 1984.
12. Kim, Y H and Jenkins, D, "Trim and Sinkage Effects on Wave Resistance with Series 60, $C_B = 0.6$ ", DTNSRDC Report SPD-1013-01, September 1981.
13. Sclavounos, P D and Nakos, D E, "Stability Analysis of Panel Methods for Free-Surface Flows with Forward Speed", Proceedings of the 17th Symposium on Naval Hydrodynamics, The Hague, August 1989.
14. Maruo, H and Ogiwara, S, "A Method of Computation for Steady Ship-Waves with Non-Linear Free Surface Conditions", Proceedings of the 4th International Conference on Numerical Ship Hydrodynamics, Washington DC, 1985.
15. Xia, F. "Numerical Calculations of Ship Flows with Special Emphasis on the Free Surface Potential Flow, Chalmers University of Technology, 1986.

16. Rong, H, Liang, X and Wang, H, "A Numerical Method for Solving Non-Linear Ship-Wave Problem", Proceedings of the 18th International Towing Tank Conference, Kobe, October 1987.
17. Ogiwara, S, "Numerical Prediction of Steady Ship Waves of Series 60 Model and Comparison with Experimental Measurements", Proceedings of the 18th International Towing Tank Conference, Kobe, October 1987.

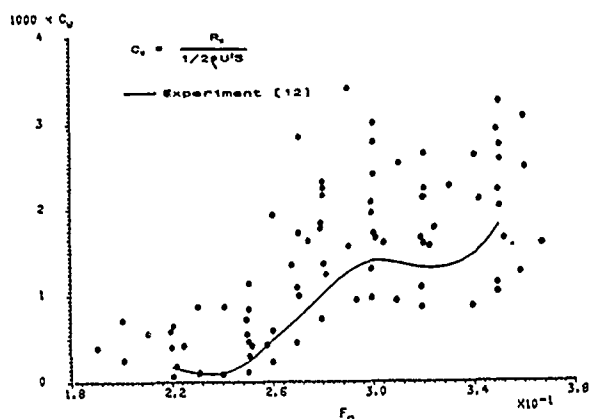


Fig 1 Predictions using Linear Theory

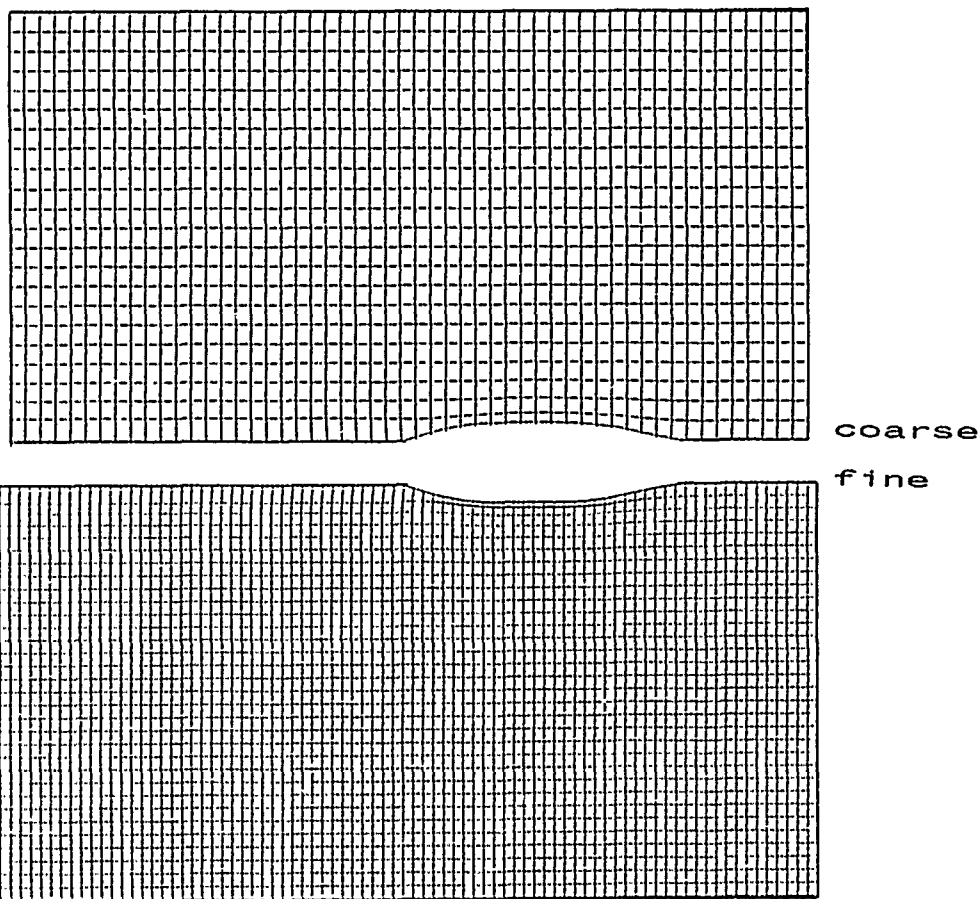


Fig 2 Coarse and Fine Grids
(experiment A1)

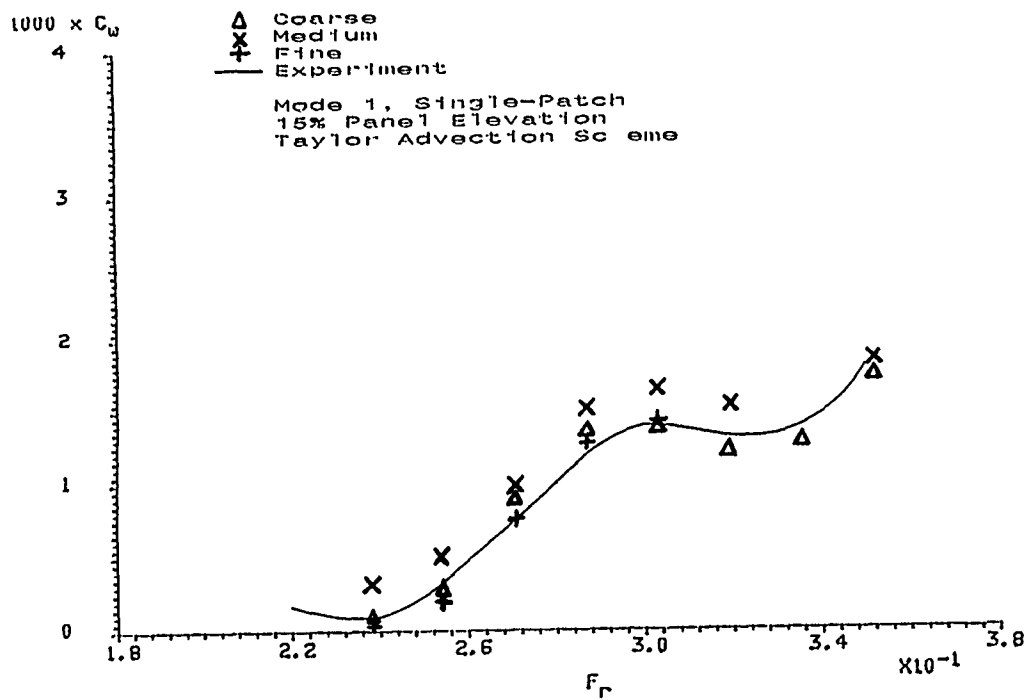


Fig 3 Effect of Grid Resolution

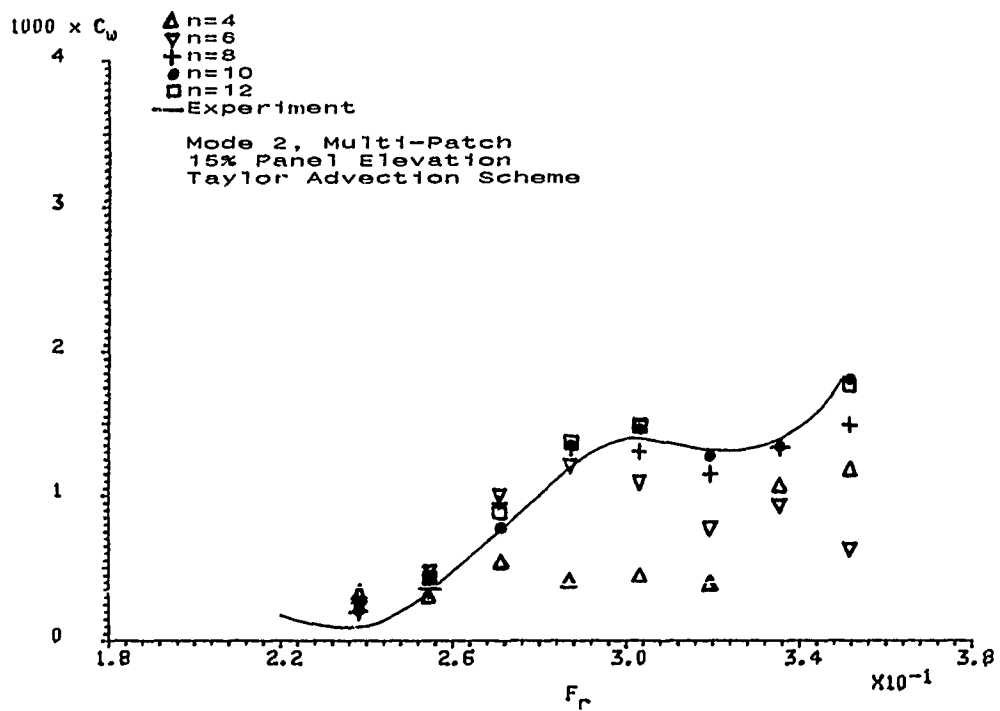


Fig 4 Effect of Grid Resolution

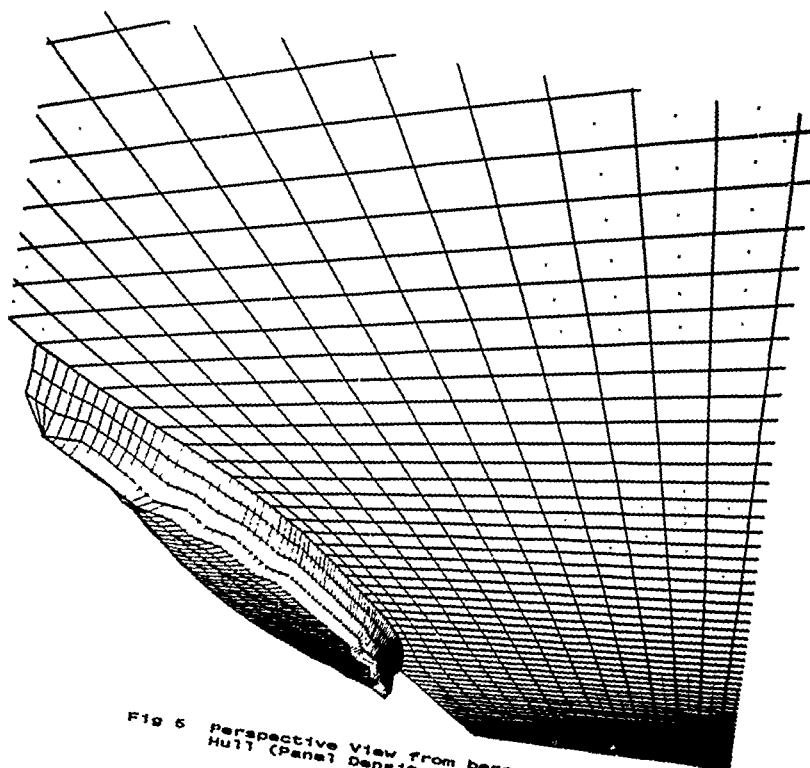


Fig 5 Perspective View from beneath
Hull (Panel Density = 3)

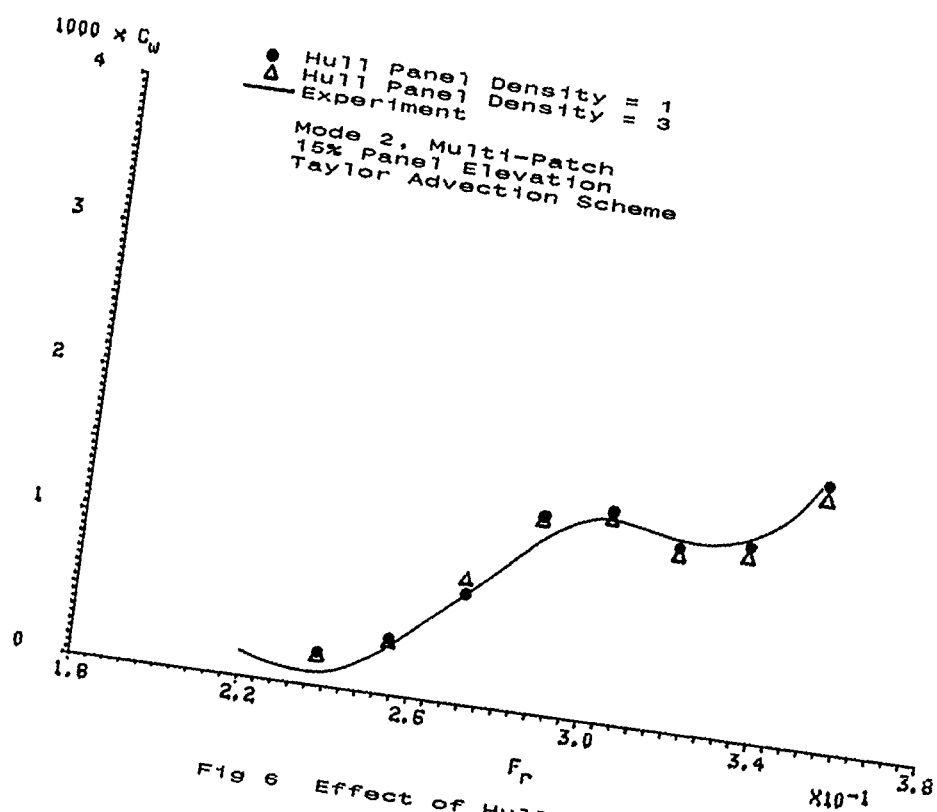


Fig 6 Effect of Hull Panel Density

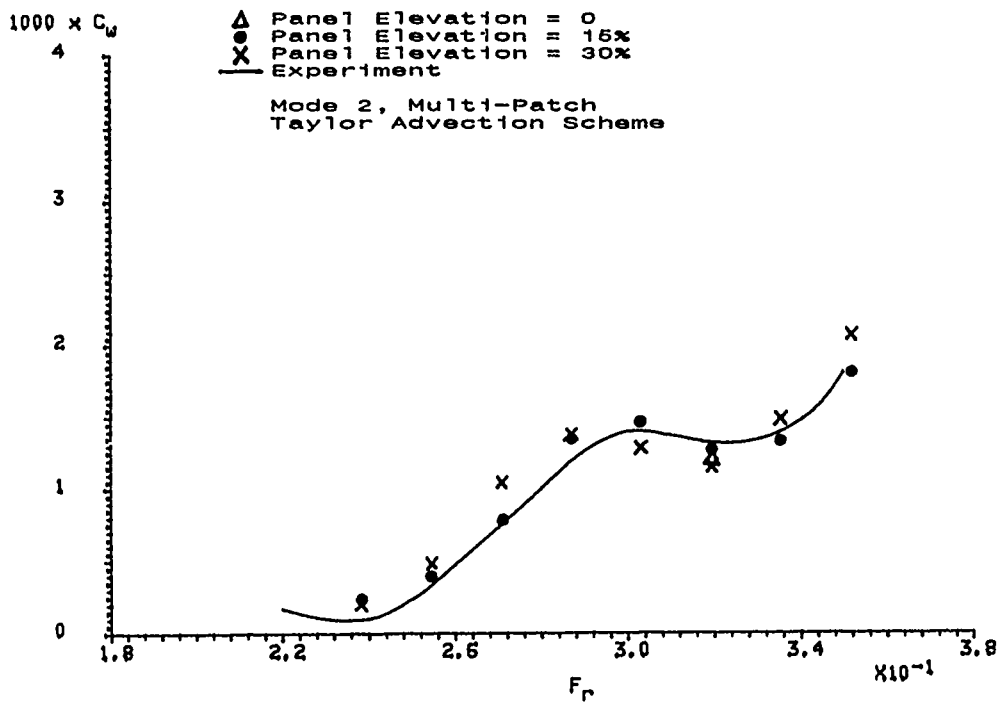


Fig 7 Effect of Free-Surface Panel Elevation

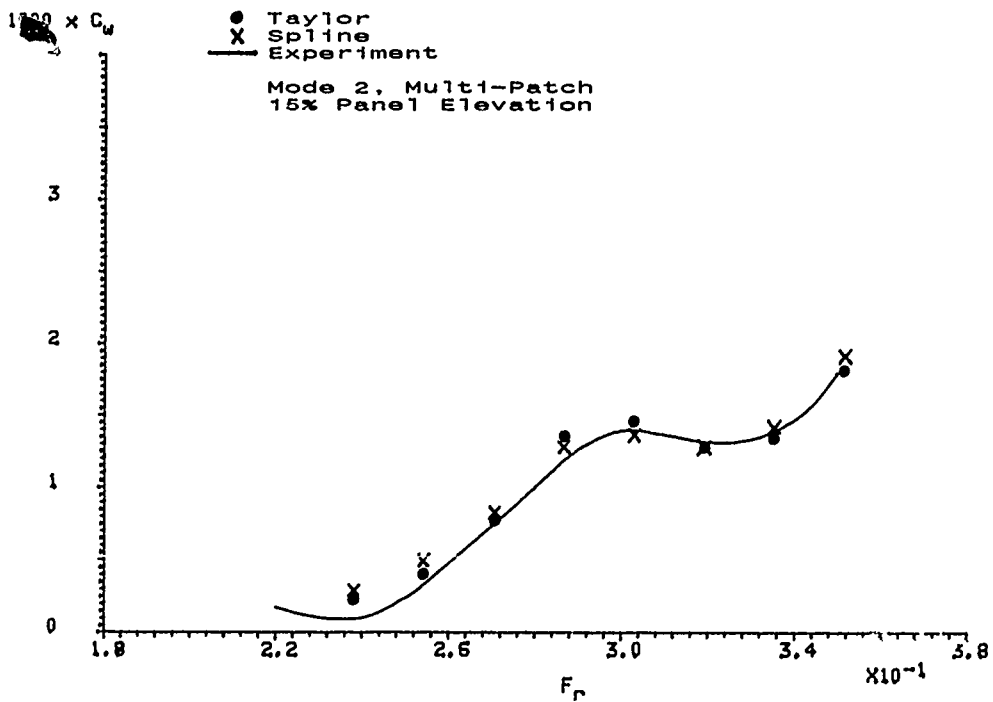


Fig 8 Effect of Advection Scheme

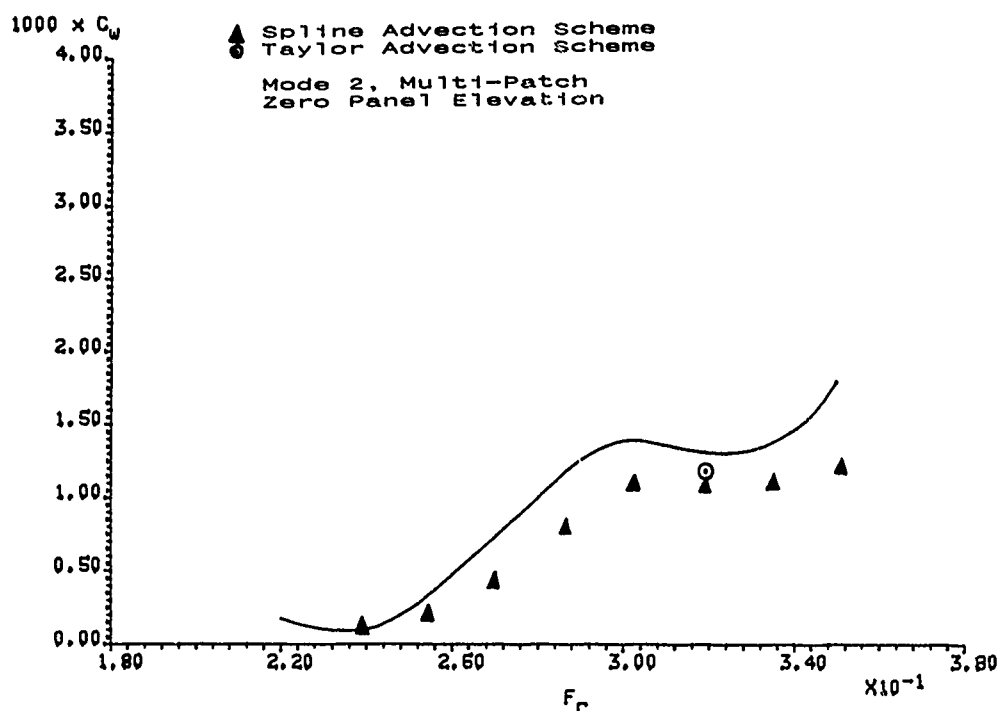


Fig 9 Spline Calculation for Zero Panel Elevation

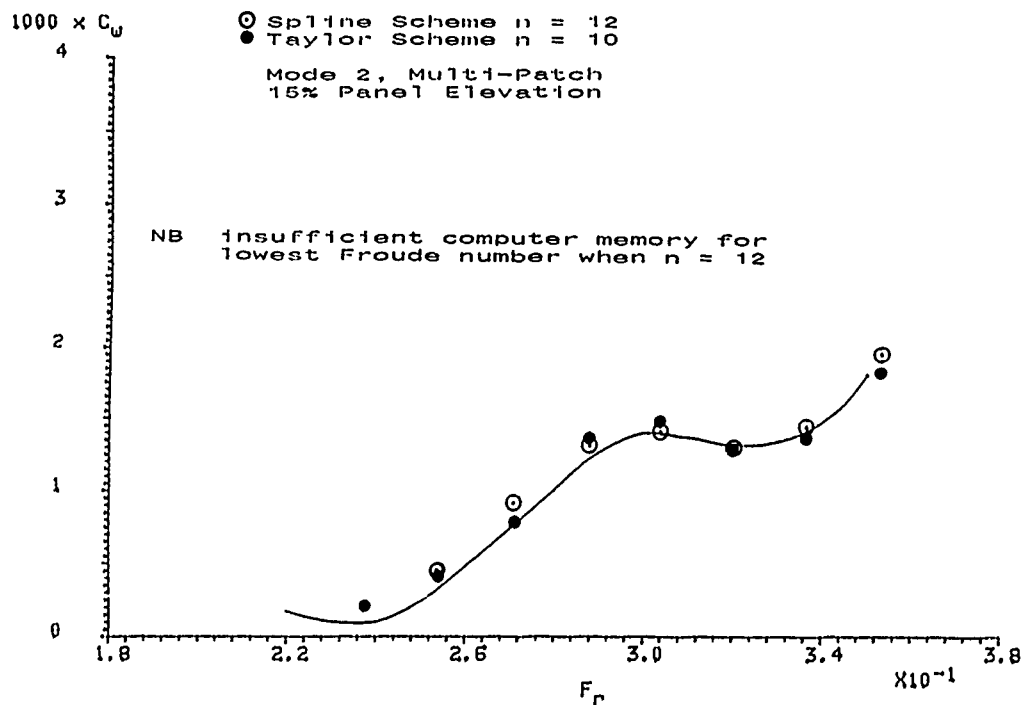


Fig 10 Effect of Spline Scheme for $n = 12$

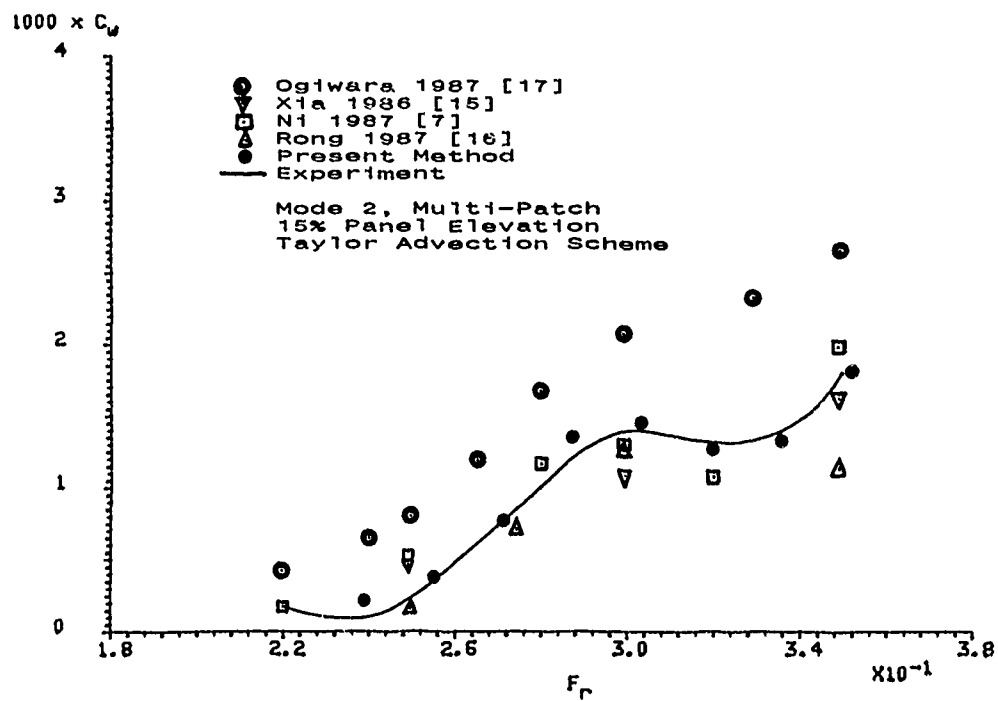


Fig 11 Comparison with Other Non-Linear Methods

Calculation of Free-Surface Flow around a Ship in Shallow Water by Rankine Source Method

H. Yasukawa
Mitsubishi Heavy Industries
Nagasaki, Japan

Abstract

Rankine Source Method was applied to the shallow water and channel problems, and calculations were made of free-surface flow around a ship moving in calm water and her wave-making resistance. The calculated results were compared with experiments and calculations by conventional linearized analytical method. It was shown that the Rankine Source Method promises an improvement in predicting free-surface flow around a ship in shallow water than the conventional linearized analytical method.

1. Introduction

Flow around a ship traveling in shallow and restricted water is much different from that in deep and unrestricted water due to the influence of sea bottom and bank walls. Therefore many studies have been carried out for investigation of performance and safe navigation of the ship in the shallow and restricted water such as river, coast, harbor, channel and so on.

The theory on ship waves and wave-making resistance in shallow water was presented by Havelock in 1922 [1]. Kinoshita and Inui corrected the Havelock's theory so as to satisfy the boundary condition of sea bottom exactly [2]. Further Inui extended its theory to the channel problems [3]. By these studies the hydrodynamic characteristics of waves and wave-making resistances near the critical speed ($F_{nh} = 1.0$, where F_{nh} means Froude number based on water depth h) were made clear. Kirsch carried out calculations of wave-making resistance in various water depth and channel width for mathematical ship hull form and discussed the shallow and channel effect [4]. Bai calculated wave-making resistances in shallow channel by localized Finite Element Method [5]. Mueller compared experiments with calculations by conventional linear theory in shallow water, and indicated that the conventional linear theory could not predict free-surface elevation and pressure distributions with sufficient accuracy [6]. Recently Mei and Choi presented the higher order theory on

a slender ship moving in channel [7].

The other hand, there is Rankine Source Method developed by Gadd [8] and Dawson [9], a kind of numerical method for solving steady free-surface potential flow in deep water. In this method the free-surface condition based on double body flow is employed, and the accuracy of predicting wave-making resistance is generally better than the conventional linear calculations. Further detailed informations for wave elevations, pressure distributions and velocity fields around ships can be obtained easily.

In this paper the Rankine Source Method was applied to the shallow water and channel problems. Calculations of free-surface flows and wave-making resistance were made for Inuid S-201 ship hull form [10], and the calculated results were compared with experiments and calculations by conventional linearized analytical method. It was shown that the Rankine Source Method promises an improvement in predicting free-surface flow around a ship in shallow water than the conventional linearized analytical method.

2. Formulation of Shallow Water and Channel Problems by Rankine Source Method

Let us consider a ship moving in center of channel in calm water. We assume that sectional shape of the channel is uniform in lengthwise direction. The coordinate system is defined as shown in Fig.1. x-axis coincides with the direction of steady uniform stream whose velocity U is identical with the ship speed. The origin of the axis is at the point of intersection of still water surface, midship section and center plane of the ship. y-axis is horizontal and normal to x-axis, and z-axis directing vertically upwards.

Supposing a ship is in an inviscid, irrotational, incompressible fluid, the velocity potential ϕ , which represents flow around the ship and satisfies Laplace's equation $\nabla^2 \phi = 0$, is introduced. ϕ has to satisfy the following boundary conditions :

$$\phi_x \zeta_x + \phi_y \zeta_y - \phi_z = 0 \text{ on } z = \zeta, \quad (1)$$

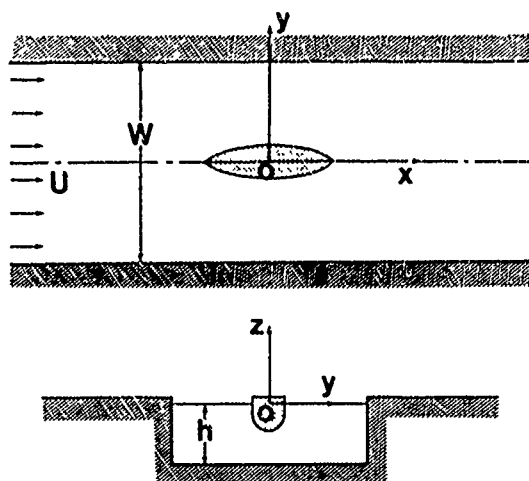


Fig.1 Coordinate system

$$\frac{1}{2}(\phi_x^2 + \phi_y^2 + \phi_z^2 - U^2) + g\zeta = 0 \text{ on } z = \zeta, \quad (2)$$

$$\phi_{n_H} = 0 \text{ on ship hull surface}, \quad (3)$$

$$\phi_{n_C} = 0 \text{ on channel surface}, \quad (4)$$

where ζ is elevation of free-surface, g the acceleration of gravity. n_H and n_C mean the outward normal directions on ship hull and channel surface respectively. Eqs.(1) and (2) represent the exact free-surface conditions. Eqs.(3) and (4) represent the boundary conditions of ship hull and channel surface. Here in order to simplify the calculation, the exact free-surface conditions (1) and (2) are linearized as :

ϕ is expressed by following form :

$$\phi = \phi_0 + \phi_1, \quad (5)$$

where

ϕ_0 : velocity potential for double body flow,
 ϕ_1 : velocity potential for steady wavy flow.
 It is assumed that the double body flow is dominant in the flow field, and we neglect higher order terms with respect to ϕ_1 for eqs.(1) and (2). Then the linearized free-surface condition based on double body flow is derived [9] as :

$$\phi_{0S}^2 \phi_{1SS} + 2\phi_{0S} \phi_{0SS} \phi_{1S} + g\phi_{1z} = -\phi_{0S}^2 \phi_{0SS} \quad \text{on } z = 0, \quad (6)$$

where the subscript S means partial derivative along the streamline of double body flow on still water surface. In this paper eq.(6) is employed for the free-surface condition. Double body potential ϕ_0 can be obtained by Hess and Smith's method [11]. Therefore our concern becomes to solve the ϕ_1 so as to satisfy the boundary conditions.

Now ϕ_1 is expressed as :

$$\phi_1 = \phi_F + \phi_H + \phi_C, \quad (7)$$

where

ϕ_F : velocity potential representing free-surface,

ϕ_H : added velocity potential representing ship hull due to the presence of free-surface,

ϕ_C : added velocity potential representing channel due to the presence of free-surface.

ϕ_F , ϕ_H and ϕ_C are represented by Rankine sources which are distributed on undisturbed free-surface S_F , ship hull S_H and channel surface S_C as follows :

$$\phi_F(P) = \iint_{S_F} \sigma_F(Q) G_F(P, Q) dx' dy', \quad (8)$$

$$\phi_H(P) = \iint_{S_H} \sigma_H(Q') G_H(P, Q') dS_H, \quad (9)$$

$$\phi_C(P) = \iint_{S_C} \sigma_C(Q'') G_C(P, Q'') dS_C, \quad (10)$$

respectively. Here σ_F , σ_H and σ_C are strength of source distributions for free-surface, ship hull and channel respectively. P is field point (x, y, z) . Q , Q' and Q'' are source points for free-surface, ship hull and channel respectively, and are defined as follows :

$$Q = (x', y', 0),$$

$$Q' = (x_H, y_H, z_H),$$

$$Q'' = (x_C, y_C, z_C).$$

G_F is represented as :

$$G_F(P, Q) = 1/R_F, \quad (11)$$

where

$$R_F = \sqrt{(x-x')^2 + (y-y')^2 + z^2}.$$

G_H and G_C are representing the double body flows for ship hull and channel as :

$$G_H(P, Q') = 1/R_H + 1/R_H', \quad (12)$$

$$G_C(P, Q'') = 1/R_C + 1/R_C', \quad (13)$$

where

$$R_H = \sqrt{(x-x_H)^2 + (y-y_H)^2 + (z-z_H)^2},$$

$$R_H' = \sqrt{(x-x_H)^2 + (y-y_H)^2 + (z+z_H)^2},$$

$$R_C = \sqrt{(x-x_C)^2 + (y-y_C)^2 + (z-z_C)^2},$$

$$R_C' = \sqrt{(x-x_C)^2 + (y-y_C)^2 + (z+z_C)^2}.$$

3. Numerical Procedure

Eqs.(3), (4) and (6) can be discretized by following procedures :

- A finite area of the still water is divided into M_F rectangular panels Σ_{Fj} ($j = 1 \sim M_F$), the hull surface into M_H panels $\Sigma_{H\ell}$ ($\ell = 1 \sim M_H$) and the channel surface into M_C panels Σ_{Cn} ($n = 1 \sim M_C$).
- It is assumed that variable on each panel is represented by value on the panel, and the source strength is constant in each panel.

The system of simultaneous equations with respect to the source strength σ_{Fj} ($j = 1 \sim M_F$), $\sigma_{H\ell}$ ($\ell = 1 \sim M_H$) and σ_{Cn} ($n = 1 \sim M_C$) are composed as follows :

$$\left. \begin{aligned} [A_{1j}]\{\sigma_{Fj}\} + [B_{1\ell}]\{\sigma_{H\ell}\} + [C_{1n}]\{\sigma_{Cn}\} &= \{C_{01}\} \\ [D_{kj}]\{\sigma_{Fj}\} + [E_{k\ell}]\{\sigma_{H\ell}\} + [F_{kn}]\{\sigma_{Cn}\} &= \{0\} \\ [G_{mj}]\{\sigma_{Fj}\} + [H_{m\ell}]\{\sigma_{H\ell}\} + [I_{mn}]\{\sigma_{Cn}\} &= \{0\} \end{aligned} \right\} \quad (14)$$

where

$$A_{1j} = \left[\iint_{\Sigma_{Fj}} (A_{01} \frac{\partial^2 G_F}{\partial S^2} + B_{01} \frac{\partial G_F}{\partial S}) dx' dy' \right]_{P=P_1} - 2\pi\delta_{1j}, \quad (15)$$

$$B_{1\ell} = \left[\iint_{\Sigma_{H\ell}} (A_{01} \frac{\partial^2 G_H}{\partial S^2} + B_{01} \frac{\partial G_H}{\partial S}) dS_H \right]_{P=P_1}, \quad (16)$$

$$C_{1n} = \left[\iint_{\Sigma_{Cn}} (A_{01} \frac{\partial^2 G_C}{\partial S^2} + B_{01} \frac{\partial G_C}{\partial S}) dS_C \right]_{P=P_1}, \quad (17)$$

$$D_{kj} = \left[\iint_{\Sigma_{Fj}} \frac{\partial G_F}{\partial n_H} dx' dy' \right]_{P=P_k}, \quad (18)$$

$$E_{k\ell} = \left[\iint_{\Sigma_{H\ell}} \frac{\partial G_H}{\partial n_H} dS_H \right]_{P=P_k}, \quad (19)$$

$$F_{kn} = \left[\iint_{\Sigma_{Cn}} \frac{\partial G_C}{\partial n_H} dS_C \right]_{P=P_k}, \quad (20)$$

$$G_{mj} = \left[\iint_{\Sigma_{Fj}} \frac{\partial G_F}{\partial n_C} dx' dy' \right]_{P=P_m}, \quad (21)$$

$$H_{m\ell} = \left[\iint_{\Sigma_{H\ell}} \frac{\partial G_H}{\partial n_C} dS_H \right]_{P=P_m}, \quad (22)$$

$$I_{mn} = \left[\iint_{\Sigma_{Cn}} \frac{\partial G_C}{\partial n_C} dS_C \right]_{P=P_m}, \quad (23)$$

$$\left. \begin{aligned} A_{01} &= \phi_{0s1}^2 / \varepsilon \\ B_{01} &= 2\phi_{0s1}\phi_{0ssi} / \varepsilon \\ C_{01} &= -\phi_{0s1}^2\phi_{0ssi} / \varepsilon \end{aligned} \right\} \quad (24)$$

δ_{ij} is the Kroenecker delta function.

For the calculations of $\partial^2/\partial S^2$ terms in eqs.(15) - (17), the 4 points upstream differencing was used so as to satisfy the radiation condition of free-surface numerically [9]. The σ_{Fj} ($j = 1 \sim M_F$), $\sigma_{H\ell}$ ($\ell = 1 \sim M_H$) and σ_{Cn} ($n = 1 \sim M_C$) are obtained by solving the matrix of eq.(14).

4. Wave Height and Wave-Making Resistance

Wave height ζ is represented by a linearized form of eq.(2) with respect to ϕ_1 as :

$$\zeta = \frac{1}{2g}(U^2 - \phi_{0x}^2 - \phi_{0y}^2 - 2\phi_{0x}\phi_{1x} - 2\phi_{0y}\phi_{1y})|_{z=0}, \quad (25)$$

Pressure p is represented by a linearized form of Bernoulli's equation as :

$$p = \frac{1}{2}\rho(U^2 - \phi_{0x}^2 - \phi_{0y}^2 - \phi_{0z}^2 - 2\phi_{0x}\phi_{1x} - 2\phi_{0y}\phi_{1y} - 2\phi_{0z}\phi_{1z}), \quad (26)$$

where ρ is water density.

Wave-making resistance R_w is evaluated by integration of pressure on ship hull as :

$$R_w = -\iint_{S_H} p n_{Hx} dS_H, \quad (27)$$

where n_{Hx} is x-component of directional cosines of the ship hull surface.

In this paper, p and R_w are represented by the following non-dimensional expressions :

$$C_p = p / \frac{1}{2}\rho U^2, \quad (28)$$

$$C_w = R_w / \frac{1}{2}\rho S_0 U^2, \quad (29)$$

where S_0 is wetted surface area of ship hull in still water.

5. Results and Discussions

For evaluation of the present method, calculations in deep and shallow water were carried out for Inuid S-201 ship hull form [10] and compared with experimental data [6][10]. Further, calculations were made of wave-making resistance of the ship in channel.

5.1 Results in deep water

First, calculations in deep and unrestricted water were carried out. Fig.2 shows panel arrangements for ship hull surface. We used 2 types of panels for validation. Panel H-1 has 220 panels and panel H-2 has 440 panels. Fig.3 shows panel arrangements for free-surface. Panel F-1 has swept back [9], and panel F-2 has not. When we calculated the flow by using the free-surface panels with rapid change of panel width in lengthwise, oscillations occurred in the calculated results for free-surface source strength. So the free-surface panels with smooth change of the panel width were used to prevent the oscillations. Fig.4 shows variation of calculated wave-making resistance with respect to the size of free-surface panel region. Wave-making resistance coefficient C_w converges around $B_{pp}/L = 0.4$, where B_{pp} is lateral width of free-surface panel region and L the ship length.

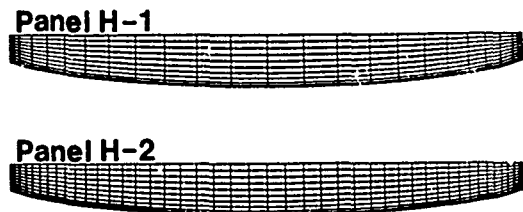


Fig.2 Arrangements of hull surface panels

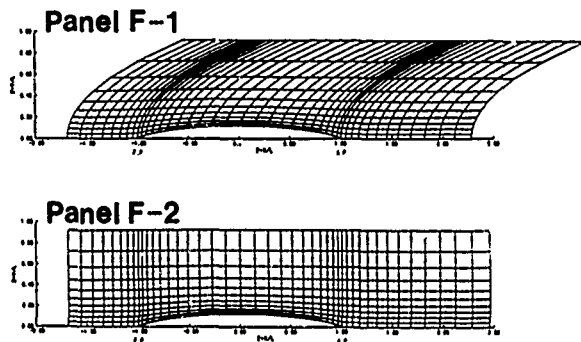


Fig.3 Arrangements of free-surface panels

Fig.5 shows comparison of wave-making resistance curves in deep water. In this figure, 'fixed cond.' means to take no account of sinkage and trim into the computations. The calculated results by using panel H-1 and F-1 show good agreement with the results by panel H-2 and F-1, so the panel H-1 seems to be sufficient for the number of hull surface panels. For the hump and hollow in C_w curve the results for panel H-1 and F-1 show better agreement with Inui's experiments [10] than the results for panel H-1 and F-2. There is a discrepancy between the present calculation and the Dawson's one [12]. The reason for the discrepancy may be due to the difference of number of the panels. (Dawson used total 512 panels [12].)

5.2 Results in shallow water

Next, calculations in shallow and unrestricted water with horizontal sea bottom were carried out. We calculated in $h/d = 2.389$ and 3.413 , where h/d means the ratio of water depth and ship draft. For this case Mueller has made detailed experiments [6]. Panel H-2, F-1 and the sea bottom panels as shown in Fig.6 were used for the computations. Fig.7 shows variation of calculated wave-making resistance for the free-surface and sea bottom panel regions in shallow water. The sea bottom panel region is larger than the free-surface region by 10% of ship length. It seems that the convergence does not achieve yet at $B_{FP}/L = 0.65$. Thus we need larger

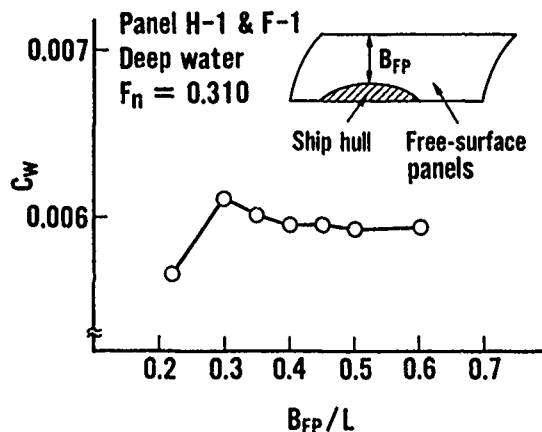


Fig.4 Variation of calculated wave-making resistance for free-surface panel region in deep water

panel region than that in deep water. In the present calculations, however, the free-surface panels with $B_{FP}/L = 0.55$ ($B_{FP}/L = 0.65$, where B_{FP} is lateral width of bottom surface panel region) were employed for saving computation time.

Figs.8 and 9 show comparison of wave-making resistance curves in shallow water. The present calculations (in 'fixed cond.') are a little larger than Mueller's experiments [6] in low speed range, and the tendency of hump and hollow in C_w curve shows good agreement with the experiments. However, Froude number at the calculated maximum C_w is different from the experiment. The tendency of hump and hollow in calculated C_w curve by conventional linear theory (Havelock's integral) [6] is a little different from the experiments. However the C_w values show good agreement with the experiments as well as the present calculations.

Now, let us compare C_w curves in Figs.5, 8 and 9. In the present calculations, with decrease of water depth C_w near the critical speed increase and Froude number at the maximum C_w becomes smaller. These tendencies agree with the experimental results. However, the Froude number at the maximum C_w is larger than the experiment and the difference of this Froude number becomes larger with decrease of water depth. The present method of calculation does not take into account the effect of sinkage and trim. For reference, therefore, attempts were made of calculations of wave-making resistance by use of sinkage and trim estimated from Mueller's experiments [6]. In this computation hull surface panels were rearranged. In Figs.8 and 9 'free cond.' means the calculation made by this way. Froude number at maximum C_w in 'free cond.' becomes smaller than that in 'fixed cond.' and comes closer to the experiment. Thus, it is suggested that for the improvement of the present method the effect of sinkage and trim should be included.

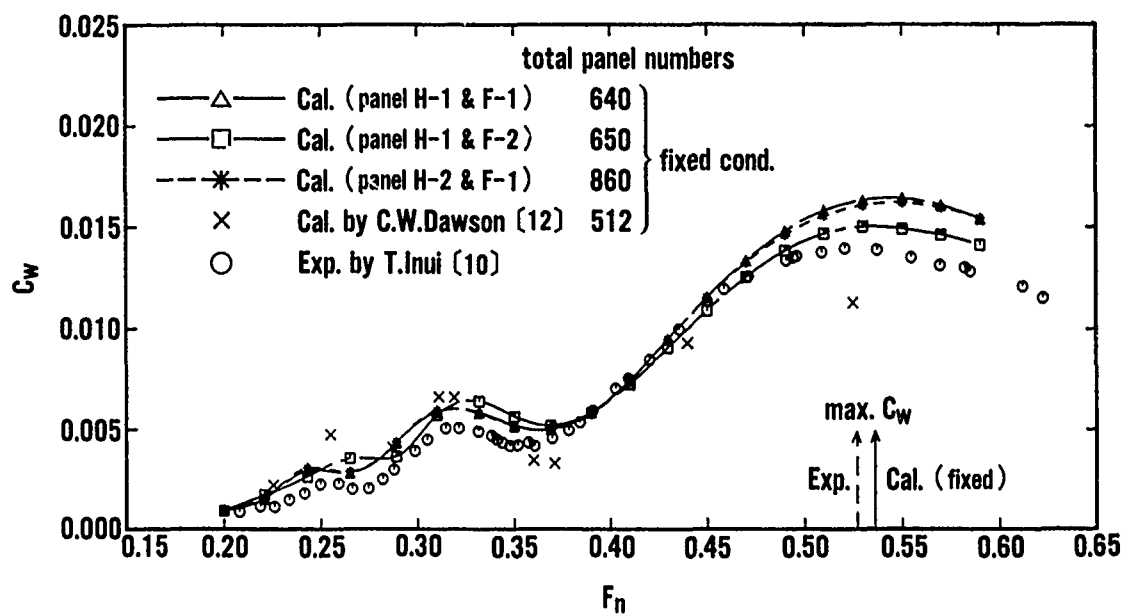


Fig.5 Comparison of wave-making resistance curves in deep water

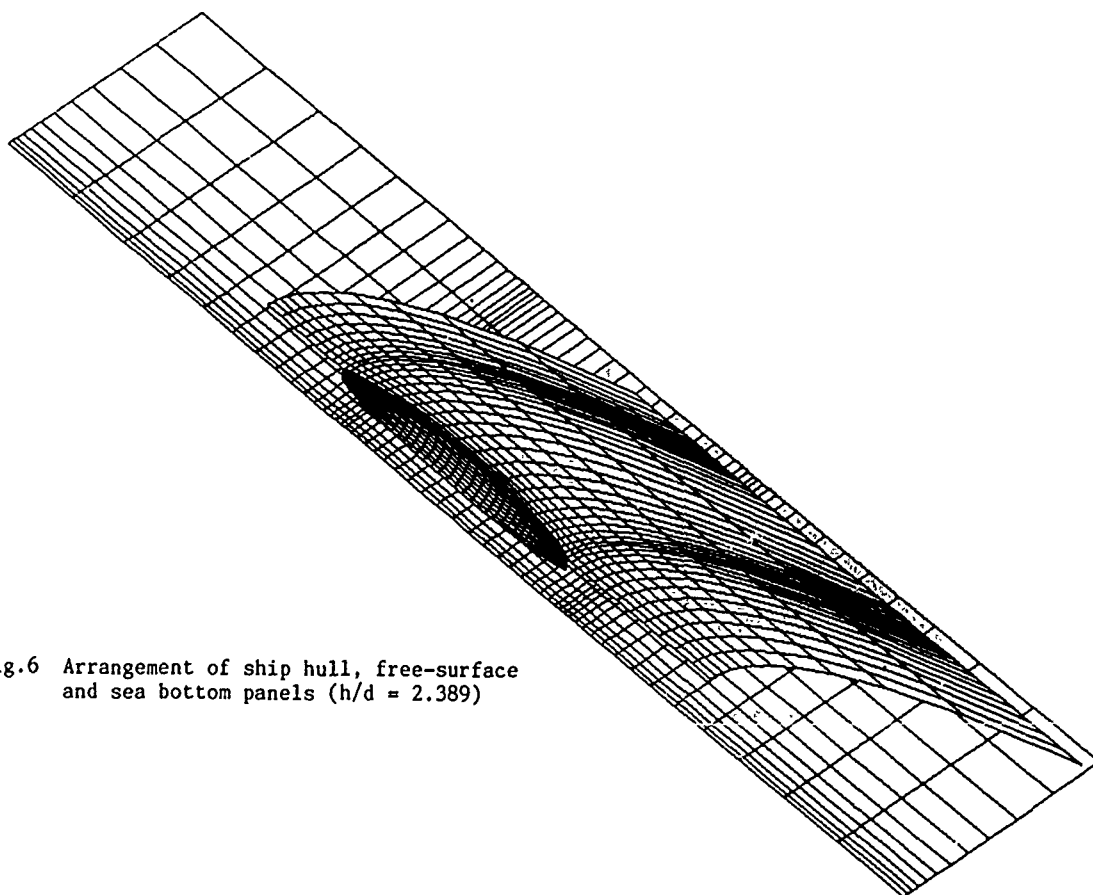


Fig.6 Arrangement of ship hull, free-surface and sea bottom panels ($h/d = 2.389$)

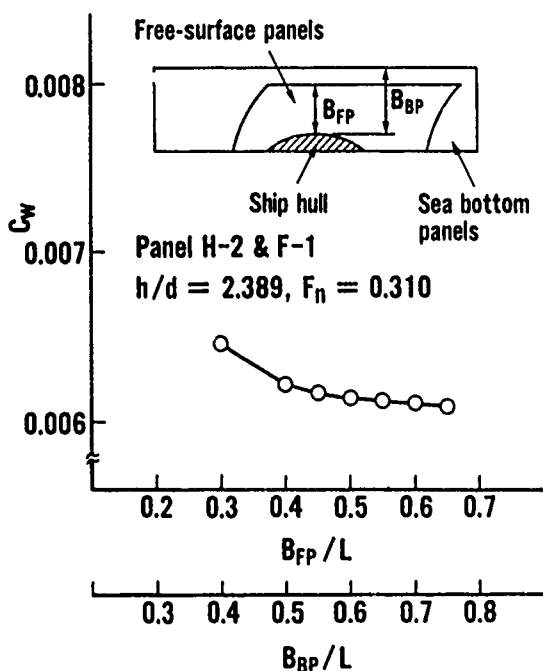


Fig.7 Variation of calculated wave-making resistance for free-surface and sea bottom panel regions in shallow water

Fig.10 shows comparisons of wave profiles in shallow water ($h/d=2.389$). Agreement between the present calculations and Mueller's experiments is good as a whole. However, it can be pointed out that calculated wave height at the fore part is lower and tendency of wave profiles at the aft part is a little different from the experiments. The reason for this difference seems to be the nonlinear effect of free-surface condition and the viscous effect which are neglected in the present formulations. The conventional linear calculations are less satisfactory than the present calculations. The difference of the calculated results in between 'fixed cond.' and 'free cond.' is small.

Fig.11 shows comparisons of pressure distributions on sea (tank) bottom in shallow water ($h/d=2.389$). The present calculations show fairly good agreement with Mueller's experiments at the tank bottom below the hull surface $y_0/L = 0.0$ where y_0 is lateral distance from center line of ship. The conventional linear calculations show good agreement with the experiments also. The pressure coefficient at $y_0/L = 0.1667$ is smaller than the experimental one near the negative peak value. The conventional linear calculations are also smaller than the experiments near the negative peak value. The difference of the calculated results in between 'fixed cond.' and 'free cond.' is small.

Figs.12 and 13 show comparisons of prospect view of wave-pattern and wave contour around a

ship for different water depth. Froude number in the computations is $F_n = 0.410$ ($F_{nh} = 0.849$ for shallow water case) and at its Froude number the wave-making resistance increases remarkably in shallow water. From the figure it is found that the waves go down near the midship and much swell behind the ship hull in shallow water. Thus the effect of shallow water on the ship waves appears more remarkably near the stern part than at the fore part of the ship.

It was shown that the present Rankine Source Method made an improvement of predicting the wave-pattern around a ship (wave profile), and we can predict the change of wave-pattern for various water depth as shown in Fig.12. However, the accuracy of predicting the wave-making resistance by the present method was same order as that by the conventional linear calculations. Thus, improvement of the present method may be required for better prediction.

5.3 Results in channel

Finally, calculations in shallow channel with rectangular section were carried out. We calculated in $h/d = 2.048$ and $W/L = 2.0$, where W/L means the ratio of channel width and ship length. For this case Inui has made the calculations by conventional linear theory [10]. Panel H-2, F-1 and the channel panels as shown in Fig.14 were used for the computations.

Fig.15 shows comparison of wave-making resistance curves in the channel. The conventional linear calculations by Inui [10] are larger than the present calculations as a whole, and particularly increase of the wave-making resistance due to channel effect is much larger near the critical speed. Further the shift of hump and hollow in C_w curve can be seen between both calculations. The discontinuity of C_w curve at $F_{nh} = 1.0$ occurs in the conventional linear calculation, but it does not in the present calculation. Thus, it was showed that the present calculation of wave-making resistance was different from the conventional linear calculation.

6. Concluding Remarks

The Rankine Source Method was applied to the shallow water and channel problems. Calculations were made of wave-making resistance, wave-pattern around a ship (wave profile) and pressure distributions on sea bottom. The calculated results were compared with experiments and calculations by conventional linear analytical method. It was shown that the Rankine Source Method made an improvement of predicting the wave-pattern around a ship in shallow water. However, the accuracy of predicting the wave-making resistance by the present method was same order as that by the conventional linear theory. Improvement of the present method may be required for better prediction. For example, the effect of sinkage and trim should be considered exactly.

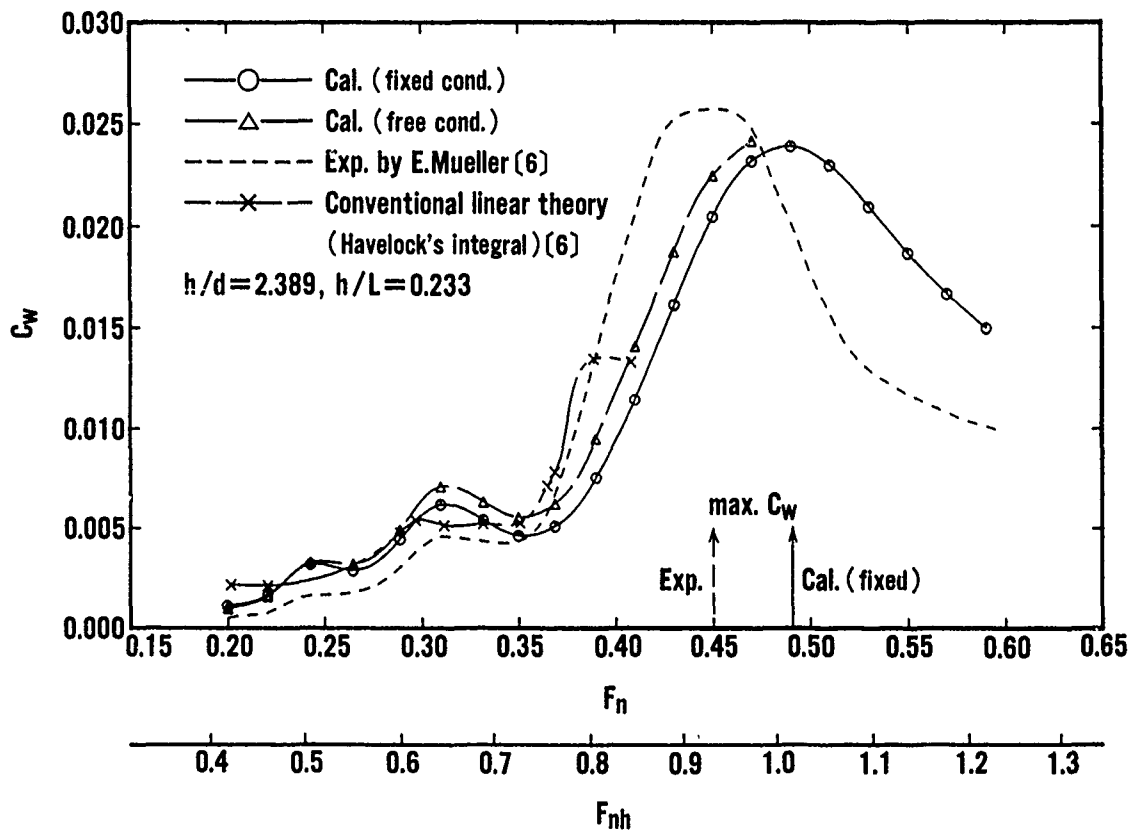


Fig.8 Comparison of wave-making resistance curves in shallow water ($h/d = 2.389$)

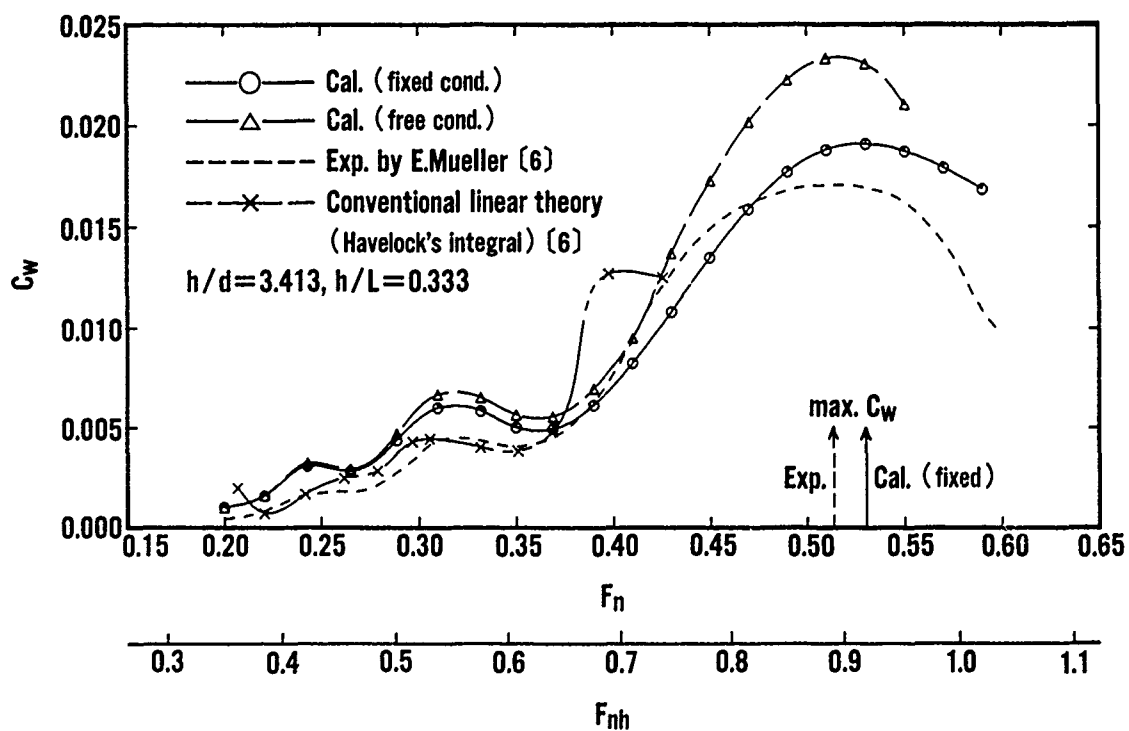


Fig.9 Comparison of wave-making resistance curves in shallow water ($h/d = 3.413$)

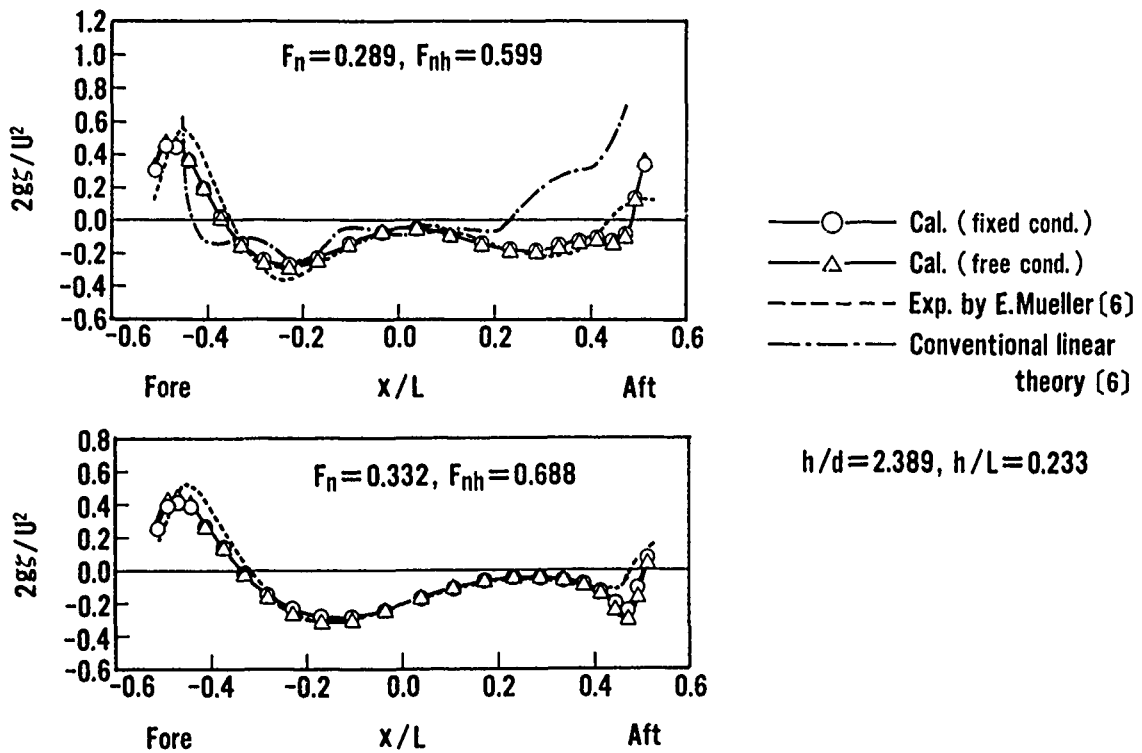


Fig.10 Comparison of wave-profiles in shallow water ($h/d = 2.389$)

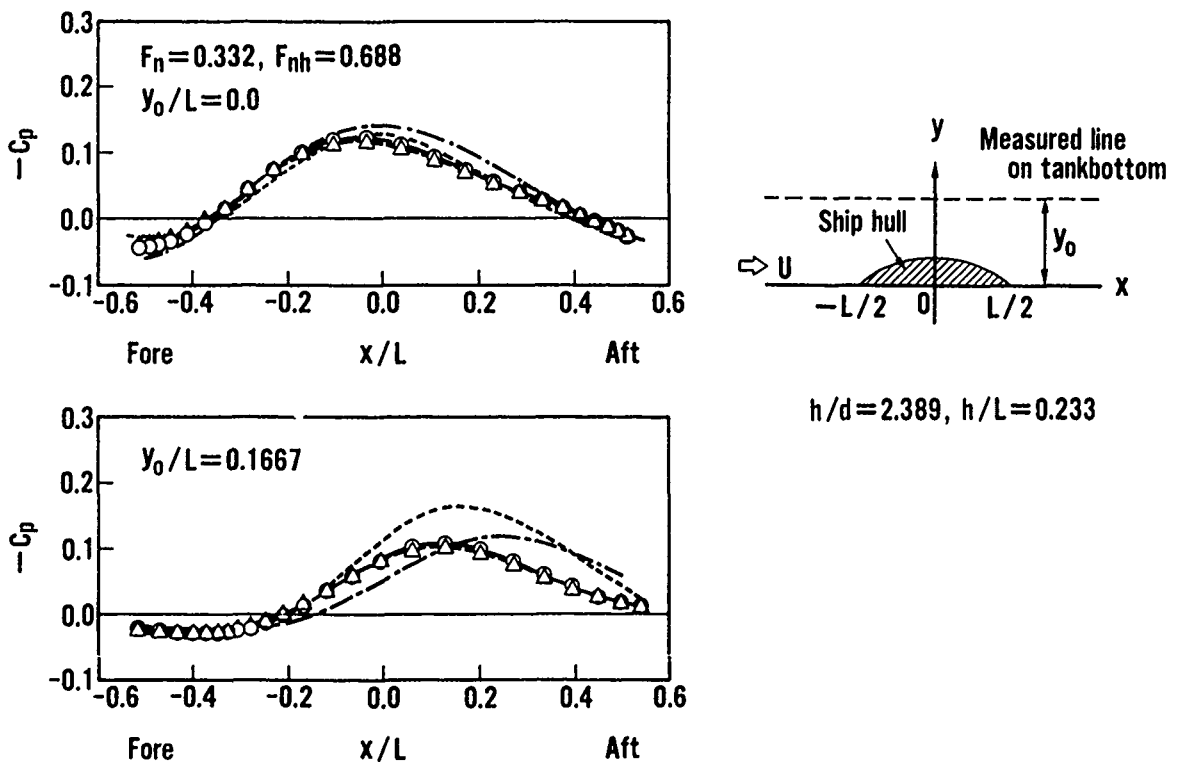


Fig.11 Comparison of pressure distributions on sea bottom in shallow water ($h/d = 2.389$)

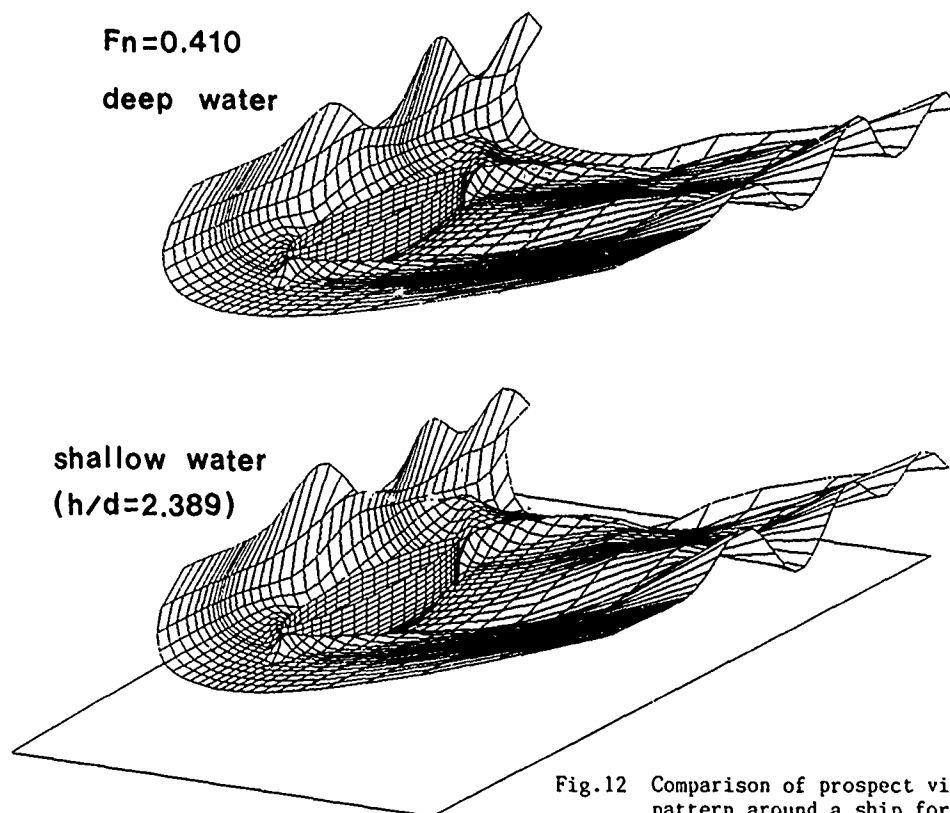


Fig.12 Comparison of prospect view of wave-pattern around a ship for different water depth
(factor of wave height is 1.5)

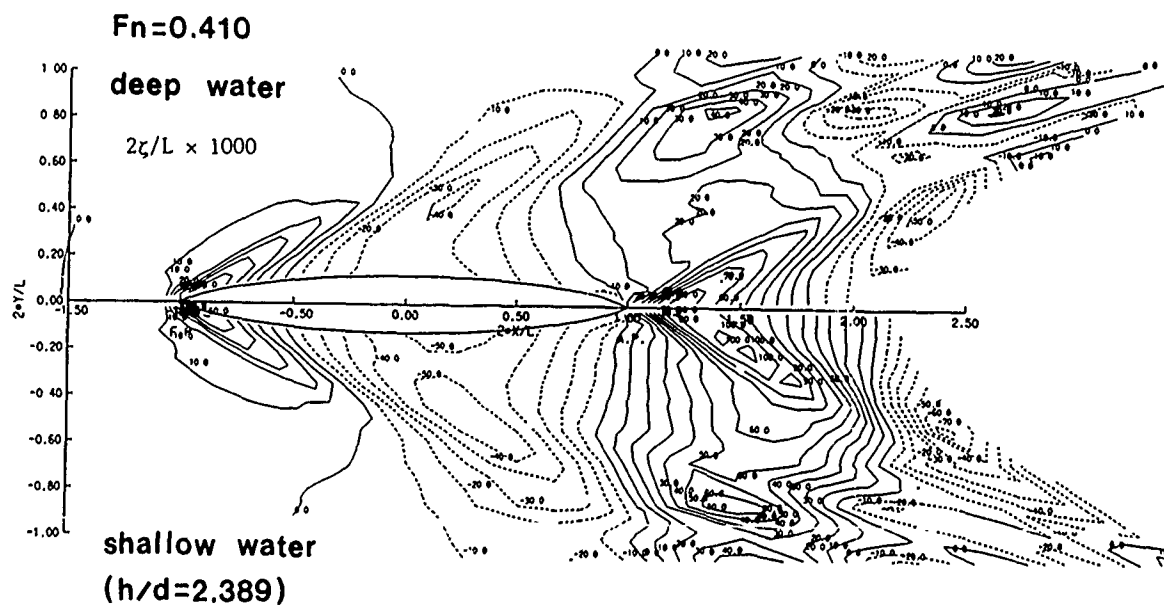


Fig.13 Comparison of wave contour around a ship for different water depth
(contour interval $\Delta\zeta$ is 10.0)

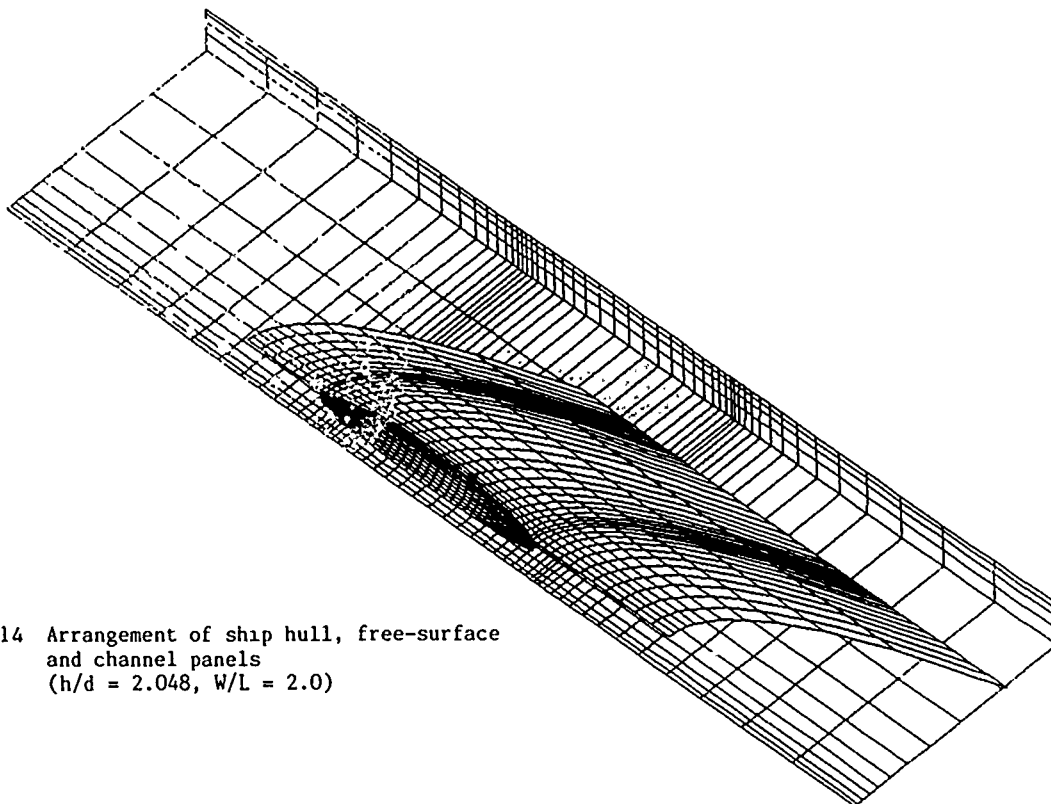


Fig.14 Arrangement of ship hull, free-surface and channel panels
($h/d = 2.048$, $W/L = 2.0$)

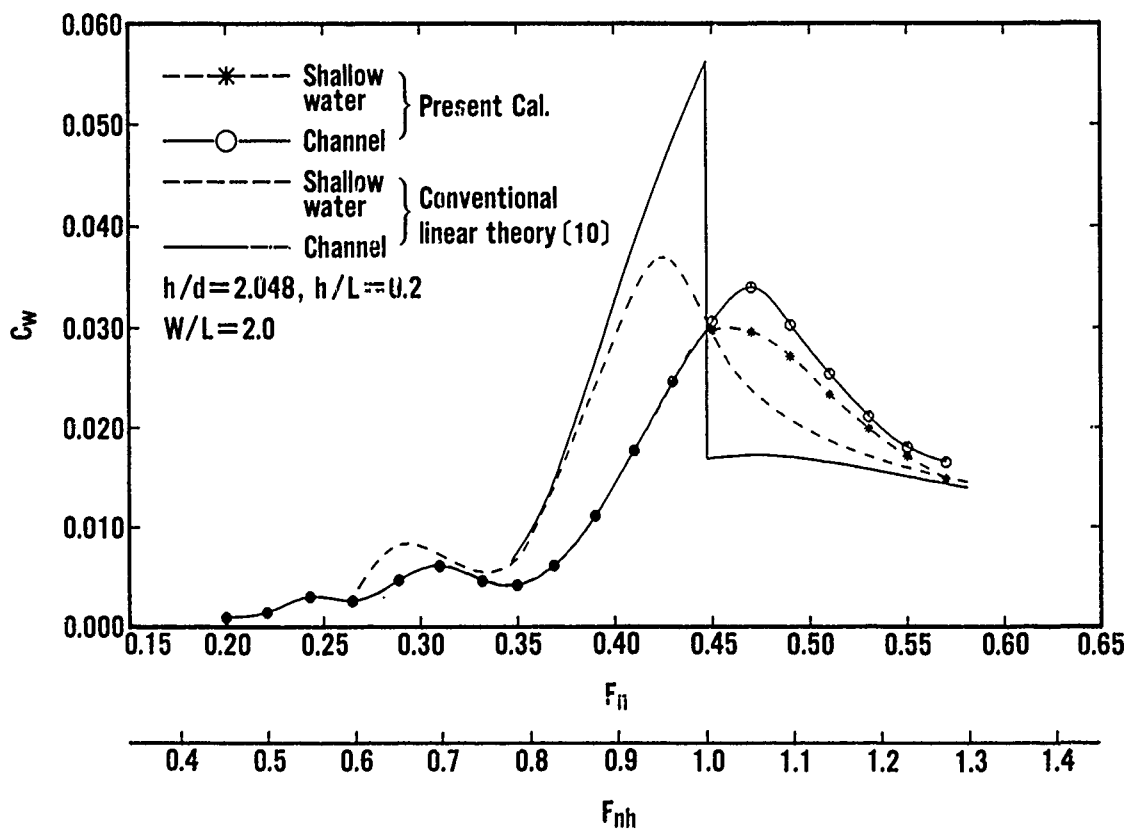


Fig.15 Comparison of wave-making resistance curves in channel

Computation including the sinkage and trim can be made by improvement of the present method as the following iteration procedures:

- (a) First, computation of the flow around the ship fixed is made, and the vertical forces (sinkage force and trim moment) are calculated.
 - (b) From the vertical forces, we determine the amounts of sinkage and trim needed to hydrostatic balance.
 - (c) The panels for the ship hull surface are rearranged to take the sinkage and trim into account, and the flow is recomputed.
- Furthermore, the nonlinear effect of free-surface condition should be considered.

Acknowledgments

The author would like to express his sincere gratitude to Dr. E. Baba, Manager of Ship Hydrodynamics Laboratory of Nagasaki Research and Development Center, MHI, and Dr. T. Nagamatsu, Research Manager of the same laboratory, for their guidance and valuable discussions.

References

1. Havelock, T.H., "The Effect of Shallow Water on Wave Resistance", Proceedings of the Royal Society, A. Vol.100, pp.499-505 (1922).
2. Kinoshita, M. and Inui, T., "Wave-Making Resistance of a Submerged Spheroid, Ellipsoid and a Ship in a Shallow Sea", Journal of the Society of Naval Architects of Japan, Vol.75, pp.119-135 (1953), (presented in 1944).
3. Inui, T., "Wave-Making Resistance in Shallow Sea and in Restricted Water, with Special Reference to its Discontinuities", Journal of the Society of Naval Architects of Japan, Vol.76, pp.1-10 (1954), (presented in 1946).
4. Kirsch, M., "Shallow Water and Channel Effects on Wave Resistance", Journal of Ship Research, Vol.10, No.4, pp.164-181 (1966).
5. Bai, K.J., "A Localized Finite-Element Method for Steady Three-Dimensional Free-Surface Flow Problems", 2nd International Conference on Numerical Ship Hydrodynamics, Berkeley, pp.78-87 (1977).
6. Mueller, E., "Analysis of the Potential Flow Field and of Ship Resistance in Water of Finite Depth", International Shipbuilding Progress, Vol.32, No.376, pp.266-277 (1985).
7. Mei, C.C. and Choi, H.S., "Forces on a Slender Ship Advancing Near Critical Speed in a Shallow Channel", 4th International Conference on Numerical Ship Hydrodynamics, Washington D.C. (1985).
8. Gadd, G.E., "A Method of Computing the Flow and Surface Wave Pattern Around Full Forms", The Royal Institution of Naval Architects, Vol.18, pp.207-219 (1976).
9. Dawson, C.W., "A Practical Computer Method for Solving Ship-Wave Problems", 2nd International Conference on Numerical Ship Hydrodynamics, Berkeley, pp.30-38 (1977).

10. Inui, T., "Study on Wave-Making Resistance of Ships", 60th Anniversary Series, The Society of Naval Architects of Japan, Vol.2, pp.173-355 (1957).
11. Hess, J.L. and Smith, A.M.O., "Calculation of Non-Lifting Potential Flow About Arbitrary Three-Dimensional Bodies", Report No.E.S.40622, Douglas Aircraft Co. Ltd. (1962).
12. Dawson, C.W., "Calculations with the XYZ Free Surface Program for Five Ship Models", Proceedings of the Workshop on Ship Wave-Resistance Computations, Vol.2, Bethesda, Maryland, pp.232-255 (1979).

Appendix Determination of wave-making resistance from Mueller's experiments

Mueller provides total resistance and residual resistance curves for Inuid S-201 in shallow water [6]. In this paper, the wave-making resistance was determined from Mueller's measured total resistance by following formula :

$$C_w = C_t - C_{fo}(1+K), \quad (30)$$

where

C_t : total resistance coefficient,
 C_{fo} : frictional resistance coefficient corresponding to the flat plat,
 K : form factor.

C_{fo} was calculated by Hughes' formula. Form factor K was determined as :

$$\begin{aligned} K &= 0.265 & \text{for } h/d &= 2.389, \\ K &= 0.230 & \text{for } h/d &= 3.413. \end{aligned}$$

DISCUSSION

by R.C. Ertekin

I wish to make some comments on your paper. First of all, it is very surprising that you do not mention the existence of upstream waves in shallow water. There are 3 papers presented in this conference on the subject, where you can find all the related references. Your parameters in shallow water falls in the range we used in our experiments (Ertekin, Webster, Wehausen, 1984, 15th ONR Symp., Hamburg). I am not familiar with Mueller's paper but if he hadn't observed these waves the something is wrong with his observations. In any case, I will seriously question the results and data for F_{nh} larger than, say 0.6 or 0.7 in shallow water because linear theory is no longer valid, also steadiness, in general, is not possible.

Even though we have not paid any attention to Thews and Landweber's (1935) work in the last 50 years, we now know that in very shallow water linear and steady results do not have much meaning.

In shallow water, the angle that divergent waves make with the waterline of the ship must be much wider than the deep water case. Even the linear theory can predict this. Therefore, I do not think that your Fig.13 is accurate. It doesn't look right so it must be wrong.

By the way, considering that you are using linear theory, could you explain why you need to distribute source on the sea floor (which is flat) and on the free surface? Thank you.

Author's Reply

Thank you for your comments. The present paper deals with steady wave-making problem, so we did not refer to the papers of unsteady wave-making problem in detail. The detailed review on the unsteady wave-making problem in restricted water is shown in ref.[7].

As expressed in Dr. Ogiwara's reply, we think that the influence of the solution is small for unrestricted shallow water.

The present method is a kind of the panel method where Rankine sources are distributed on boundary surface, so we need to distribute the source on the free-surface and sea bottom surface. In case of flat sea bottom, there is the method which takes into account infinite image of the sources distributed on the free-surface and ship hull surface. However this method can not apply to non-horizontal sea

bottom generally and has much time for calculation of the infinite image. For the above reasons we employed not the infinite image method but the source distribution method on the sea bottom.

DISCUSSION

by S. Ogiwara

As referred by your paper, T.H. Havelock (1922) studied shallow water effect on ship wave resistance, in which he predicted significant feature of wave pattern that the angle of diverging wave increases as the water depth decreases. Could you simulate the same feature by the proposed Rankine source method?

Moreover, considering the case of extremely shallow water, we can find the soliton which generates periodically forward upstream from the bow, as pointed out by T.Y. Wu and others.

The method, you proposed here, is not able to treat such phenomena, because this method is involved in the framework of steady state. How do you think about the limitation of water depth (or $F_{nh} = U/\sqrt{gh}$), to which this method is able to apply?

Finally, Resistance and Flow Committee of the 19th ITTC is carrying out the evaluation of shallow water effect on ship resistance and flow around a hull through the Cooperative Experimental Program. You are encouraged to conduct new experiments in order to verify the effectiveness of your numerical method, and to contribute to ITTC.

Author's Reply

Thank you for your discussions and comment. So far as we observed the comparison of calculated wave-height distributions for different water depth (see Fig.13), it does not seem that the remarkable change of diverging waves appears in the present calculation. The reason why the change does not appear may be due to adoption of linear free-surface condition based on double-body flow in the present method.

The linear free-surface condition is employed in the present method, so predicting accuracy becomes poorer in high speed range. Actually we can not see that the tendency of wave-making resistance curve in the present calculations agrees with that in the experiments for water depth Froude number larger than 0.8 (see Figs.8 and 9). However,

from the view point of practical use, the present method has sufficient accuracy for the Froude number smaller than 0.8. Needless to say, for better prediction non-linear effect of free-surface condition should be considered.

It is well known that when a ship moves in shallow channel near the critical speed, solution generates periodically forward upstream from the bow and the flow around the ship becomes unsteady[A1][A2]. The generation of the solution is related with blockage coefficient of the channel (or towing tank) and the amplitude of the solution decreases as the blockage coefficient decreases[A3]. All calculations in the present paper except Fig.15 are for unrestricted shallow water

taking no account of the channel walls.

- [A1] Huang, D.B., Sibul, O.J. and Wehausen, J.V.: Ships in Very Shallow Water, Festkolloquium zur Emeritierung von Karl Wieghardt, Institut für Schiffbau der Universität Hamburg, Bericht Nr.427, pp.29-49, 1982.
- [A2] Wu, D.M. and Wu, T.Y.: Three-dimensional Nonlinear Long Waves due to Moving Surface Pressure, Proc. of 14th Symp. on Naval Hydrodynamics, Ann Arbor, pp.103-129, 1982.
- [A3] Ertekin, R.C., Webster, W.C. and Wehausen, J.V.: Ship-Generated Solitons, Proc. of 15th Symp. on Naval Hydrodynamics, Hamburg, pp.347-364, 1984.

A Hybrid Model for Calculating Wave-Making Resistance

V. Aanesland
Norwegian Marine Technology Research Institute
Trondheim, Norway

Abstract

A hybrid method for calculating the wave-making resistance of ships has been developed. The method is based on three-dimensional potential theory, and the flow is assumed to be steady. The fluid is divided into an inner and outer domain by two vertical control surfaces. These surfaces are parallel to the free stream, extending to infinity and one at each side of the body. The internal flow is matched to the external flow on the control surfaces in order to satisfy the radiation condition.

A three-dimensional source-sink method is adopted in the numerical treatment of the problem, using a source function for an infinite fluid. A distribution of source density on the wetted part of the body, on a local part of the free surface and on the control surfaces has to satisfy the boundary conditions in the inner domain.

The wave resistance can be calculated by two different methods. One is to calculate the pressure distribution on the wetted hull surface and to integrate for the force in longitudinal direction. The other is to use the inner solution combined with a control surface integration. The fluid velocity and wave elevation along the control surface are needed.

Introduction

For a ship in service it is important to have as low total resistance as possible in realistic sea conditions. Both model tests and calculations have been used extensively in order to be able to estimate the resistance at the design stage. Methods of varying sophistication have been developed, and many restrictions and assumptions are made in each case.

A large number of contributions on the wave-making problem have been published. Concentrating on theoretical and numerical solution methods which are independent of model tests, an important contribution was given by J. H. Michell, [1], who introduced thin-ship

theory where the resistance is given by the geometry of the hull. T. H. Havelock, [2], used a Green's function method instead of the Fourier-integral method used by Michell and confirmed the results of Michell. The reason for referring to these two authors is not only because they were among the first to attempt to solve the problem theoretically, but also because their results will be used in the present solution method. For a comprehensive review on the wave resistance problem, see for example Wehausen, [3]. Two other contributions will be of importance when relating the present work to already existing theories. G. E. Gadd, [4], and C. W. Dawson, [5], introduced the idea of distributing discrete source panels on both the ship hull and the mean free surface. The wave-making part of the velocity potential is calculated as a perturbation to the double-body flow. Gadd used a nonlinear free-surface boundary condition, while Dawson linearized with respect to the double-body flow. In the former case an iterative procedure was adopted because the position of the free surface is unknown.

It can be argued that the methods of Gadd and Dawson need a considerable amount of computer power and time. If preliminary results are needed quickly, a number of thin ship and slender ship methods are available. On the other hand, the restrictions set by these methods can be troublesome. For the present author, the flexibility of the method is of greater importance than a fast running program on a medium-size computer. The capacity of new computers is increasing rapidly, and the corresponding cost is decreasing. Indeed, the use of supercomputers minimize this problem. The present program has been run on both VAX785 and CRAY X-MP. On the latter computer a speed up factor of about 100 is typical. In other words a computation of about 1 hour on the VAX machine is finished in half a minute on the CRAY.

The present method incorporates some ideas from Gadd and Dawson, the thin ship theory and some new ideas. Results are presented for a single point source, the Wigley parabolic model and the Series 60 block 0.60 ship.

The boundary value problem

The steady-state wave-making problem is formulated in a Cartesian coordinate-system x, y, z moving with the ship velocity. The $x-y$ plane describes the undisturbed free surface with the x -coordinate positive towards the stern, see figure 1. Another coordinate-system x_1, y_1, z_1 is fixed in the ship and coincides with x, y, z when the ship is in its equilibrium position and with no forward velocity. The fluid is assumed ideal, (i.e. inviscid, incompressible and homogeneous), and its motion is irrotational. Surface tension is neglected.

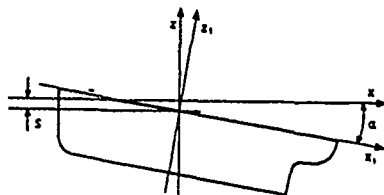


Figure 1: Coordinate systems

The problem is formulated as a potential flow problem where the total fluid motion is described by the velocity potential $\Phi(x, y, z)$. The following conditions have to be satisfied:

(i) Laplace's equation in the fluid

$$\nabla^2 \Phi = 0. \quad (1)$$

(ii) the dynamic boundary condition on the free surface

$$g\zeta + \frac{1}{2}(\Phi_x^2 + \Phi_y^2 + \Phi_z^2 - U^2) = 0 \quad \text{on } y = \zeta(x, y). \quad (2)$$

where subscripts denotes partial differentiation.

(iii) the kinematic boundary condition on the free surface

$$\Phi_x \zeta_x + \Phi_y \zeta_y - \Phi_z = 0 \quad \text{on } y = \zeta(x, y). \quad (3)$$

(iv) the kinematic boundary condition on the hull

$$\Phi_x h_x \pm \Phi_y h_y + \Phi_z h_z = 0 \quad \text{on } S_B \quad (4)$$

where $y \pm h(x_1, z_1) = 0$ defines the hull surface

(v) the kinematic boundary condition on the sea bottom

$$\Phi_{zz} = 0 \quad \text{on } z = -d, \quad (5)$$

which in the infinite depth case is replaced by

$$\lim_{z \rightarrow -\infty} \nabla \Phi = U. \quad (6)$$

(vi) radiation conditions.

The hull surface is defined in the body-fixed coordinate system.

$$y_1 = \pm h(x_1, z_1) \quad (7)$$

The transformation from one coordinate system is easily performed by using the relations

$$x_1 = x \cos \alpha - (z - s) \sin \alpha \quad (8)$$

$$y_1 = y \quad (9)$$

$$z_1 = x \sin \alpha + (z - s) \cos \alpha \quad (10)$$

$$(11)$$

where s is the sinkage and α is the trim angle.

The hydrodynamic forces in x and z direction and the trim moment are calculated by integration of the pressure over the wetted part of the hull.

$$F_x = - \int_{S_B} p(x, y, z) n_x dS \quad (12)$$

$$F_z = - \int_{S_B} p(x, y, z) n_z dS \quad (13)$$

$$M_G = \int_{S_B} p(x, y, z) [n_x(z - z_G) - n_z(x - x_G)] dS \quad (14)$$

The Bernoulli equation is used to evaluate the pressure,

$$p = -\frac{\rho}{2}[(\nabla \Phi)^2 - U^2] - \rho g z \quad (15)$$

and the normal unit vector n is positive into the fluid.

Solution method

The fluid is divided into an inner and outer domain as shown in figure 2. The inner domain is bounded by the body surface, S_B , the free surface, S_F , two vertical control surfaces, S_1 , and a surface at infinity, S_∞ . The outer domain consists of the rest of the fluid domain, which is two segments of a sphere, marked by the dotted lines in the figure. The outer domain is mainly used in order to find a boundary condition on the matching surfaces, while the main task is to find a solution in the inner domain. The use of Green's second identity in the outer domain gives the boundary condition. The derivation is described in appendix A.

The reason for introducing the vertical control surfaces is partly to restrict the computational domain and partly to obtain well defined radiation conditions. The numerical scheme will show that a disadvantage is that panels have to be distributed on a restricted part of the

control surfaces in addition to the hull surface and the free surface. On the other hand many elements can be excluded from the free surface compared to the method of Dawson and Gadd. It is assumed that the wave effect will decrease rapidly with depth and a large part of the control surface can be truncated.

In addition to the two above-mentioned reasons for using two domains, the scheme also suggests to linearize the free-surface condition differently in the outer and inner domain. A low-speed linearisation is adopted in the inner domain (similar to the one used by Dawson) and a free-stream linearisation in the outer domain (similar to Kelvin's thin ship formulation). Assuming that the free stream linearisation is satisfactory in the outer domain, other linear or nonlinear boundary conditions on the free surface in the inner domain may be used. Another possibility is to use a totally different numerical solution method in the inner domain. A finite difference scheme may be of interest when a local flow phenomenon is studied, and the fluid can be described by more complex equations.

In the present case the appropriate boundary condition on the free surface is found by linearizing the equations (2) to (3). On the free surface in the inner domain, the double-body flow is used as the main flow upon which the wavy perturbation flow is superimposed. The total potential is divided into three parts.

$$\begin{aligned}\Phi &= Ux + \phi \\ &= \phi_d + \phi_1 \\ &= Ux + \phi_0 + \phi_1\end{aligned}\quad (16)$$

where

- Ux = free-stream potential
- ϕ_d = double-body potential
- ϕ_0 = disturbance potential in double-body theory
- ϕ_1 = disturbance potential in low-speed theory
- ϕ = disturbance potential in thin-ship theory.

The free surface condition is simplified as described by Dawson even though Raven, [11], has reported that the formulation is inconsistent. (Anyhow, the difference in calculated wave resistance is within a few percent.) The subscript s denotes differentiation with respect to the streamlines of the double-body solution. Neglecting quadratic and higher-order products of ϕ_1 and its derivative, the following equation is obtained.

$$\Phi_z = -\frac{1}{g}[(\phi_{ds}^2 \Phi_s), -2\phi_{ds}^2 \phi_{ds}] \quad \text{on } z = 0. \quad (17)$$

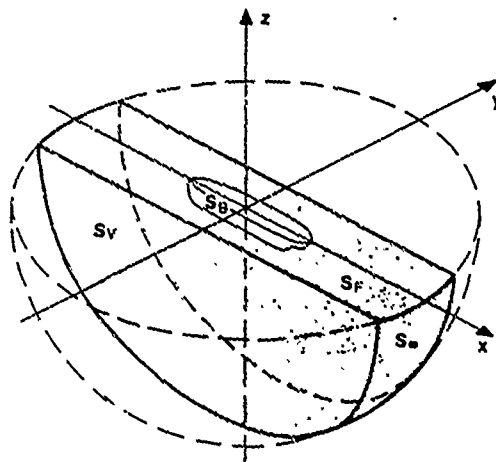


Figure 2: Inner and outer domains

This is the same result as Dawson obtained in his equation (14), [5].

When matching is performed on the vertical control surfaces, ϕ from the outer solution has to equal $\phi_0 + \phi_1$. Equation (17) can be written in the form

$$\begin{aligned}\phi_z &+ \frac{1}{g}[\phi_{ds}^2 \phi_{ss} - 2\phi_s \phi_{ds} \phi_{ds}] \\ &= \frac{1}{g}[2\phi_{ds}^2 \phi_{ds}, -(\phi_{ds}^2 (Ux)_s)] \quad \text{on } z = 0. \quad (18)\end{aligned}$$

The problem is solved with respect to source strength which automatically gives the velocity components i.e. the first derivatives of the velocity potential. A numerical operator identical to the one obtained by Dawson, [5], is adopted in order to estimate the second derivative with respect to s .

The vertical control surfaces are assumed to be so far from the body that the waves will satisfy the linear free-surface condition. It is then appropriate to use the Kelvin source function, G_K , to describe the outer flow. It is shown in appendix A that the boundary condition on the vertical control surfaces is

$$\phi = \frac{1}{2\pi} \iint_{S_v} G_K \phi_n dS \quad \text{on } y = \pm b \quad (19)$$

and the corresponding boundary condition on the hull is

$$\phi_n = -Un_r \quad \text{on } z = 0. \quad (20)$$

The radiation condition in the inner domain is satisfied by using an upstream differential operator when satisfying the free-surface condition. The operator insures that waves are only present behind the ship. On the downstream boundary, an artificial damping is applied to the free surface condition. The inner solution is only affected a short distance upstream of the damping

F_n	0.10	0.20	0.30	0.40	0.50
H_{11}/L	0.03	0.13	0.29	0.51	0.79

Table 1. Minimum depth of the vertical control surfaces as function of Froude number.

area. The calculation of the wave resistance by control surface integration is obtained from the undisturbed part of the inner domain. A far-field solution may be applied instead as a matching condition on a downstream transverse boundary.

The necessary depth of the vertical control surfaces can be estimated by use of the fundamental wave length, λ_f , defined by the Froude number, F_n , and the length of the ship at waterline, L .

$$\lambda_f = 2\pi F_n^2 L. \quad (21)$$

As seen from the formula, the wave length increases as the square of the Froude number. Using the assumption that an elementary wave disturbs to a depth of half the wave length, the minimum depth of the control surfaces, H_{11} , is given by

$$\frac{H_{11}}{L} = \frac{\lambda_f}{2L} = \pi F_n^2 \quad (22)$$

Table .1 indicates the necessary depth of the vertical control surfaces. At the higher Froude numbers, however, the results obtained using depths much smaller than indicated by the table are good. On the other hand, it is necessary to have a depth about twice the draft of the hull, which indicates that the near-field flow about the hull is dominating the wave making. While running the program, the contribution to the wave resistance from the first vertical row, the last vertical row and the bottom horizontal row of panels on the vertical control surface is checked in order to control the extension of the surface. The depth of the surface can then be within the limits of confidence without actually satisfying the numbers in table .1.

The evaluation of the Kelvin Green's function, G_K , is only needed on the vertical control surfaces. Until recently the calculation of this function has been rather time consuming. In the present work, nondimensional values have been tabulated and linear interpolation has been used. New, fast algorithms are now available, for example Newman [6], and can easily be included in the program.

Numerical tests of a single point source

Verification of a computer program is very important, [10]. The present code has been tested using single point sources and single point dipoles situated below the free surface. The results have been compared with results obtained by Nakatake [9] in the case where the double-body linearisation in the inner domain is replaced by the common free stream linearisation. Figure 3 shows the panel distribution in the case of 8 longitudinal rows of elements on the free surface.

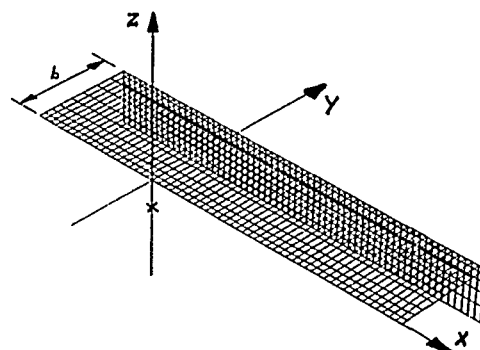


Figure 3: Panel distribution on one fourth of the surfaces in the case of a single point source situated at $F = 1$. b is the distance between the center plane and the vertical control surfaces.

Different aspects were important to investigate in these single point tests. The first was to check the radiation condition on the vertical control surfaces. The closer to the center plane it was possible to position the surfaces, the better. Then a very limited part of the free surface was needed to be panelized. The effect of moving the control surfaces was checked by investigating the wave elevation along the innermost row of panels compared to the wave elevation obtained by using the Greens function definition, equation 25, in appendix A. The plots presented in figures 4 and 5 show the case when the nondimensional vertical position of the point source is $F = \kappa(-z) = g/U^2(-z) = 1.0$. Figure 4 includes the results as presented by Nakatake.

Secondly, the number of elements needed to discretize the inner domain was checked. It was found that a number of about 20 elements pr wave length was needed to obtain a stable solution. By increasing the number of elements beyond that limit, nearly no difference was observed in the case of 8 longitudinal rows of elements on the free surface. In the case of 3 rows of elements on the free surface however, even a higher number of elements would increase the accuracy of the wave elevation as seen in figure 5 where three different grid sizes in longitudinal direction is presented. Also included are the curve when the control surfaces are removed. It is obvious that this solution is totally wrong both with

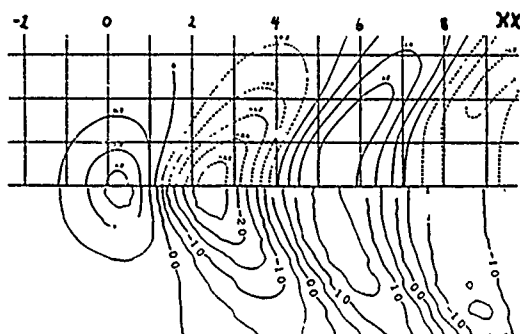


Figure 4: Contour plot of the wave elevation due to a single point source situated at $F = 1$. The upper part of the figure is from Nakatake.

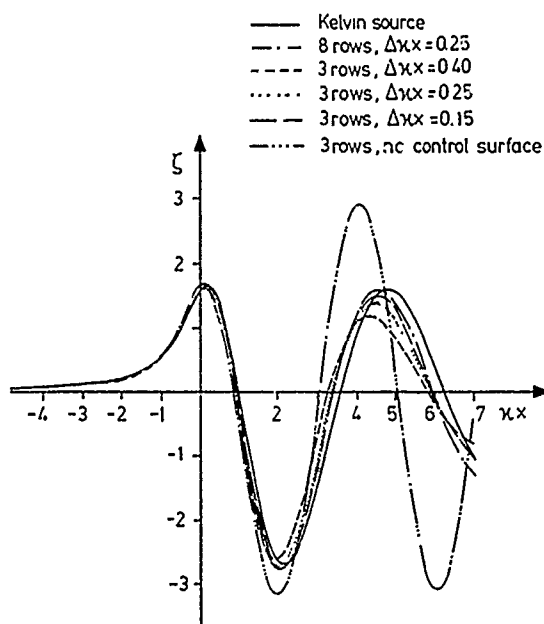


Figure 5: Wave elevation along the innermost row of panels. The results for different positions of the vertical control surfaces are compared with results using the centre plane source function.

	Wigley	Series 60
B/L_{pp}	0.1000	0.1333
H/L_{pp}	0.0625	0.0625
L/L_{pp}	1.0000	1.0167
C_B	0.444	0.600
C_s	0.661	0.710

Table .2: Main parameters of the hulls

respect to the wave length and wave amplitude. In addition the result for the Kelvin Green's function evaluated at the center plane is given in figure 5.

A third aspect of importance is the behaviour of the numerical differential operator. Two-, three- and four-point upwind operators were tested and the last one was selected. As can be seen from the curves in figure 5, a reduction of the first wave length of about 5 percent is observed. But additional computations have shown that the wave length is very good further downstream. This might be caused by the boundary condition applied on the control surfaces.

Finally, it is important to check to influence of combining a double-body linearisation in the inner domain and a free-stream linearisation in the outer domain. New tests were carried out for the single point source using these conditions. The wave elevation changed, as expected, somewhat compared to the tests with only free-stream linearisation in the inner domain, but the effect of using the vertical control surfaces where similar. Tests have also been carried out for single point dipoles which confirm the results.

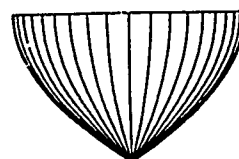
The Wigley hull

The hull surface of the Wigley parabolic hull is defined by the equation

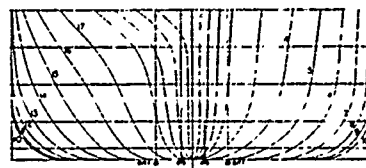
$$y_1 = \frac{B}{2} \left[1 - \left(\frac{2x_1}{L} \right)^2 \right] \left[1 - \left(\frac{z_1}{L} \right)^2 \right] \quad (23)$$

where $-L/2 \leq x_1 \leq L/2$ and $-H \leq z_1 \leq 0$.

The main parameters are given in table .2, and the body plan in figure 6, which has smooth lines and fore-aft symmetry. A lot of numerical and experimental data



The Wigley hull



The Series 60 hull

Figure 6: Body plans of the different ship hulls.

exists which makes the hull well suited for comparisons. Data was taken from the 1.st and 2.nd Workshops on Wave Resistance Computations, [12] and [13], and plotted in figure 7 as the envelope of residual resistance coefficients. In addition, the mean values of the experiments of the two workshops are plotted separately in the case of a restrained ship and a ship free to sink and trim.

In [7], the results of a great number of test cases are listed, varying the number of elements on the hull, free surface and control surfaces. Also the position and extent of the vertical control surfaces were changed. Two configurations will be presented. The first is a reference case, where the control surfaces are positioned at a sufficient distance from the hull surface so that reflections as described by Dawson are avoided. The solution is essentially the same as Dawson's solution.

Computer programs, essentially based on the same

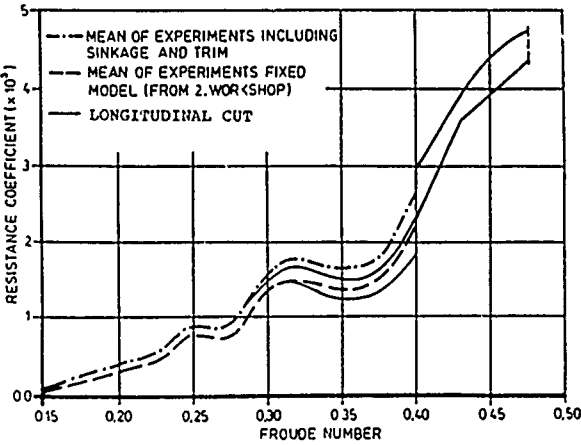


Figure 7: Wave-resistance coefficients calculated from experiments using the longitudinal cut method.

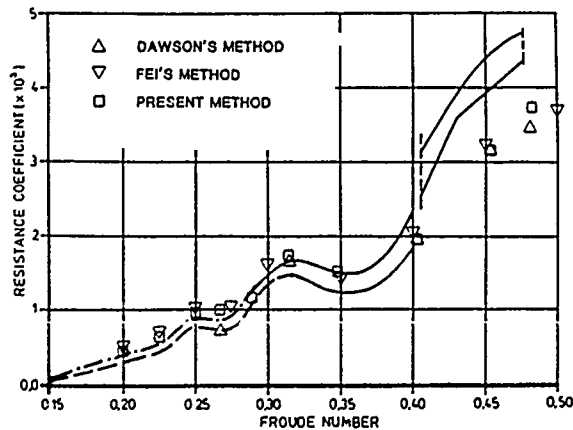


Figure 8: Wave-resistance coefficients calculated by computer programs.

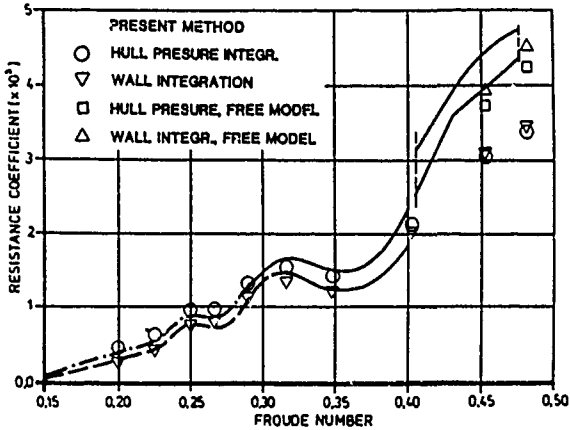


Figure 9: Wave-resistance coefficients calculated by the present method using both hull-pressure integration and control-surface integration.

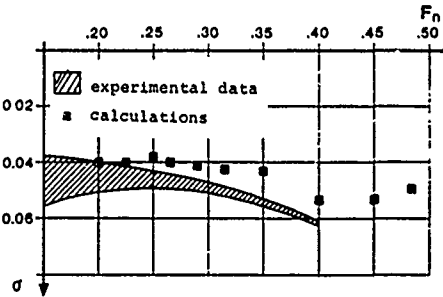


Figure 10: Nondimensional sinkage of the Wigley hull.

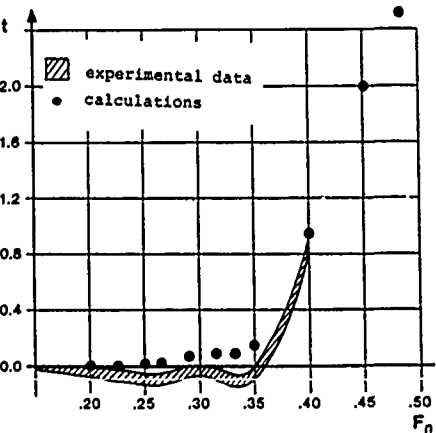


Figure 11: Nondimensional trim of the Wigley hull.

theory, have often produced results with a large spreading. In figure 8 the numerical results of both Dawson, [5], and Xia Fei, [14], have been plotted as reference to the present data. Sinkage and trim have been neglected. The discrepancy is small compared to the known limits of experimental data. Note that the plotted curves are the experimental values of the wave-resistance coefficients estimated using the longitudinal-cut method.

The wave-resistance coefficients plotted in figure 9 are results of the second test case where the vertical control surfaces are inserted at $y/L = \pm 0.07$. Remembering that the half-breadth of the hull is $0.05L$ it is obvious that the control surfaces are very close to the hull surface. This configuration is presented because it gives satisfactory results even though the matching surface is closer than what would be a reasonable distance were linear waves assumed. The wave resistance coefficients are in good agreement with the results obtained in the first test case. The effect of including sinkage and trim is obvious at the higher Froude numbers. The resistance obtained from both pressure integration over the hull surface and over the control surface is plotted. Some differences are observed between the two methods which can be explained by errors when truncating control surfaces or local effects close to the body which are eliminated in the far field.

The sinkage, nondimensionalized with respect to $U^2/2g$ and trim, nondimensionalized with respect to the length are plotted in figure 10 and 11.

The Series 60 hull ($C_B = 0.60$)

The Serie 60 is a collection of ship forms with block coefficients varying from 0.60 to 0.80. The $C_B = 0.60$

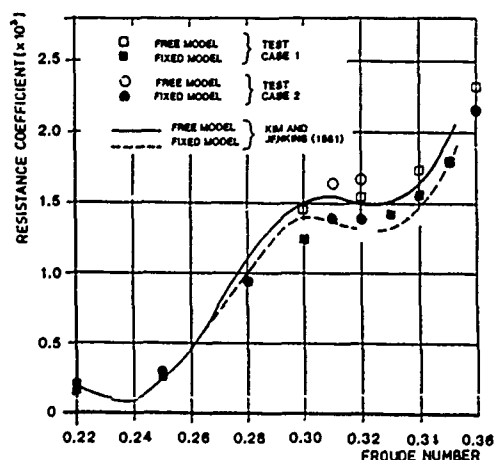


Figure 12: Wave-resistance coefficients calculated by the present method and experimental results from Kim and Jenkins, [16].

case is tested in the present paper and the main parameters are given in table .2. Experimental data, from Kim and Jenkins (1981), [16], are plotted together with numerical results in figure 12. Mewis and Heinke (1984), [17], have published almost the same results, which confirm the difference between the ship fixed and free to undergo sink and trim. The experimental wave-resistance coefficients are obtained by using the longitudinal-cut method.

Two numerical test cases are considered where the difference is basically the number of panels used. The position of the vertical control surfaces and the upstream and downstream truncation boundaries are kept constant. The computer time for solving the equation sys-

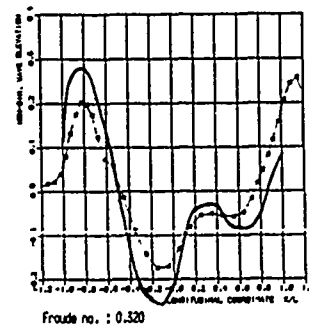
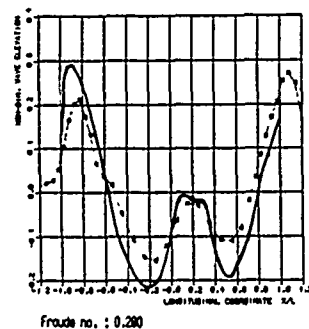
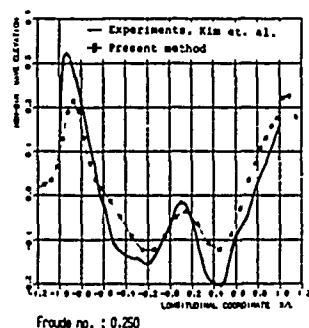


Figure 13: Wave elevation along the hull for Serie 60 ship.

tem in test case number 2 is about four times the time in case 1. The values plotted by filled markers in figure 12 include the effects of sinkage and trim. The numerical results are in good agreement with experimental data, and the convergence of the method is reasonable. Figure 13 shows the wave elevation along the hull plotted for three different Froude numbers. The main observation is that the calculations underpredict the wave crests and troughs, while the wave length is well predicted.

Conclusions

The present method has proved to be successful in solving the linear wave-making problem. Results for the single point source show that the combination of an inner and outer domain is working well and that the prediction of the wave elevation is good.

Numerical tests have been carried out in order to verify the computer code. In specific the Kelvin Green's function, the numerical differential operators and the panel sizes have been tested.

Results such as wave-making resistance, wave elevation, sinkage and trim are generally in good agreement with experimental data.

Only limited number of ship forms have been tested in the present work. Further development of the method should include a number of additional test cases. The high Froude number range ($F_n > 0.5$) is especially important. The knowledge thereby obtained, will be useful in refinements of the numerical method.

The theory has many possibilities for further development. By means of moderate changes in the program, both the velocity field in the fluid and the streamlines and equipotential lines on the body can be calculated. Further, the method should be well suited for ships in channels or when wall effects is investigated.

The present method can be extended to include non-linear free-surface conditions in the inner domain. The matching boundaries have to be situated at a sufficient distance from the hull so that the waves in the outer domain can be treated by linear theory.

Acknowledgements

The work has been carried out as a dr. ing. study at the Norwegian Institute of Technology, and I wish to express my sincere thanks to my advisor Prof. Odd M. Faltinsen. The study was financed by a scholarship from the Norwegian Institute of Technology and the computer costs paid for by the Norwegian Council for Scientific and Industrial Research (NTNF).

References

- [1] MICHELL, J. H. 1898. The Wave Resistance of a Ship. *Phil. Mag. The Collected Mathematical Works of J. H. and A. G. M. Michell*, Noordhoff, Groningen, 1964, pp. 124-141.
- [2] HAVELOCK, T. H. 1923. Studies in Wave Resistance *The Collected Papers of Sir Thomas Havelock on Hydrodynamics, published by the Office of Naval Research*, Washington D.C. 1966, pp. 30-38.
- [3] WEHAUSEN, J. V. 1973. The Wave Resistance of Ships *Advances in Applied Mechanics* No. 13, pp 93-245.
- [4] GADD, G. E. 1975. A Method of Computing the Flow and Surface Wave Pattern Around Full Forms. *RINA*, pp. 377-392.
- [5] DAWSON, C. W. 1977. A Practical Computer Method for Solving Ship-Wave Problems. *Second International Conference on Numerical Ship Hydrodynamics*, pp. 30-38.
- [6] NEWMAN, J. N. 1987. Evaluation of the Wave-Resistance Green Function: Part 1 - The Double Integral. *Journal of Ship Research*. Vol. 31, No. 2, June, pp 79-90.
- [7] AANESLAND, V. 1986. A Theoretical and Numerical Study of Ship Wave Resistance. *Dr. ing. thesis, Report UR-86-48. Norwegian University of Technology, Division of Marine Hydrodynamics*.
- [8] AANESLAND, V. 1988. Hydrodynamic Properties of Floating Bodies Calculated by Supercomputer. *CADMO 88*. Southampton, 20-22 September.
- [9] NAKATAKE, K. 1966. On the Wave Pattern Created by Singular Points of Ship Wave Resistance. *Journal of the Society of Naval Architects of West Japan*. No. 31 pp 1-19.
- [10] SCLAVOUNOS, P. D., NAKOS, D. E. 1988. Stability Analysis of Panel Methods for Free-Surface Flows with Forward Speed. *17.th Symposium on Naval Hydrodynamics* The Hague, pp.29-48
- [11] RAVEN, H. C., 1988. Variations on Theme by Dawson. *17.th Symposium on Naval Hydrodynamics* The Hague, pp.9-28.
- [12] PROCEEDINGS of The Workshop on Ship Wave-Resistance Computations. *David Taylor Naval Ship Research and Development Center*, 13.-14. November 1979.
- [13] PROCEEDINGS of The Second Workshop on Ship Wave-Resistance Computations. *David Taylor Naval Ship Research and Development Center*, 16.-17. November 1983.

- [14] FEI, X. 1984. Calculation of Potential Flow with a Free Surface. Report no. 65 ISSN 009-112X, Chalmers University of Technology, Department of Ship Hydrodynamics, Sweden.
- [15] NEWMAN, J. N. 1976. Linearized Wave Resistance Theory *International Seminar on Wave Resistance*. pp 33-43.
- [16] KIM, Y. H. and JENKINS, D. 1981. Trim and Sinkage Effects on Wave Resistance with Series 60, $C_B=0.60$. David Taylor Naval Ship Research and Development Center. Report DTNSRDC/SPD-1013-01.
- [17] MEWIS, F. and HEINKE, H. J. 1984. Untersuchungen der Umströmung eines Modells der "Serie 60" mit $C_B=0.60$. *Schiffbau Forschung*, 23 3/1984, pp. 148-154.
- [18] FRY, X. and KIM, Y. H. 1984. Bow Flow Field of Surface Ships. *Fifteenth Symposium on Naval Hydrodynamics*.

Boundary condition on the vertical control surface

Consider the volume bounded by S_1 , S_F and S_∞ , in figure 14. An arbitrary point is located on the surface S_1 at the position where the boundary condition is wanted. The point is enclosed by a hemisphere S_c with a small radius. It is assumed that the two functions ϕ and ψ together with their first and second derivatives, are finite and single valued in the closed volume. It is then possible to use Green's second identity

$$\iint_S \left(\phi \frac{\partial \psi}{\partial n} - \psi \frac{\partial \phi}{\partial n} \right) dS = \iiint_V (\phi \nabla^2 \psi - \psi \nabla^2 \phi) dV \quad (24)$$

where $S = S_1 + S_F + S_\infty$.

The surface S_1 is located at $y = b$, S_∞ on a segment of a sphere at infinity and S_F is the free surface. Replacing ψ with the Kelvin Green's function, G_K , and using ϕ as the perturbation potential

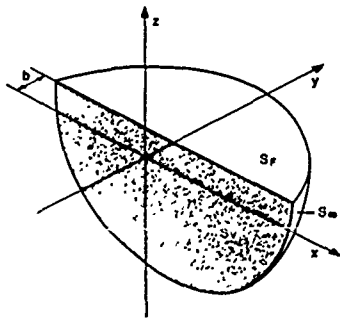


Figure 14: Outer solution

$$G_K(x, y, z; \xi, \eta, \zeta) = -\frac{1}{r} + \frac{1}{r'} + N_0(r') + W(r') \quad (25)$$

where

$$\frac{1}{r} = [(x - \xi)^2 + (y - \eta)^2 + (z - \zeta)^2]^{-\frac{1}{2}} \quad (26)$$

$$\frac{1}{r'} = [(x - \xi)^2 + (y - \eta)^2 + (z + \zeta)^2]^{-\frac{1}{2}} \quad (27)$$

$$N_0(r') = \frac{4\kappa}{\pi} \int_0^{\frac{\pi}{2}} d\theta p v \int_0^\infty dke^{\kappa(z-\zeta)} \frac{\cos[k(x-\xi)\cos\theta]\cos[k(y-\eta)\sin\theta]}{\kappa - k\cos^2\theta} \quad (28)$$

$$W(r') = 4\kappa \int_0^{\frac{\pi}{2}} d\theta \sec^2\theta e^{\kappa(z+\zeta)\sec^2\theta} \sin[\kappa(x-\xi)\sec\theta]\cos[\kappa(y-\eta)\sec^2\theta\sin\theta] \quad (29)$$

and $\kappa = g/U^2$ and $\sec\theta = 1/\cos\theta$.

Both ϕ and G_K satisfy the Laplace equation, $\nabla^2\phi = 0$ and $\nabla^2 G_K = 0$, and equation (24) becomes

$$\iint_S \left(\phi \frac{\partial G_K}{\partial n} - G_K \frac{\partial \phi}{\partial n} \right) dS = 0. \quad (30)$$

Separating the integral into three parts, the contribution from each surface can be investigated. Remembering that it is a limited part of S_1 that is needed as a control surface, S_{11} , the following integrals are considered.

The surface at infinity

$$I_\infty = \iint_{S_\infty} \left(\phi \frac{\partial G_K}{\partial n} - G_K \frac{\partial \phi}{\partial n} \right) dS \quad (31)$$

When $(x - \xi) \geq 0$ the potential ϕ and its derivative $\partial\phi/\partial n$ are of $O(1/r)$ and $O(1/r^2)$ respectively. Similarly, when $(x - \xi) < 0$, G_K and $\partial G_K/\partial n$ are of $O(1/r)$ and $O(1/r^2)$. Consequently the contribution will vanish when $r \rightarrow \infty$.

The free surface

The boundary condition on the free surface is applied to both the potential and the Green's function. By linearizing equation (2) and (3) and combining them, the condition becomes

$$\frac{U^2}{g} \phi_z + \phi_{,xx} = 0 \quad \text{on } z = 0. \quad (32)$$

$$\begin{aligned} I_F &= \iint_{S_F} \left(\phi \frac{\partial G_K}{\partial n} - G_K \frac{\partial \phi}{\partial n} \right) dS \\ &= \frac{U^2}{g} \iint_{S_F} \left(\phi \frac{\partial^2 G_K}{\partial x^2} - G_K \frac{\partial^2 \phi}{\partial x^2} \right) dS \\ &= \frac{U^2}{g} \iint_{S_F} \frac{\partial}{\partial x} \left(\phi \frac{\partial G_K}{\partial x} - G_K \frac{\partial \phi}{\partial x} \right) dS \\ &= \frac{U^2}{g} \int_C \left(\phi \frac{\partial G_K}{\partial x} - G_K \frac{\partial \phi}{\partial x} \right) dy \end{aligned} \quad (33)$$

The surface integral is now reduced to a line integral along the intersection of the free surface and both the vertical control surface and the surface at infinity. The integration along C_∞ will vanish when $r \rightarrow \infty$ by a similar argument as for the surface at infinity. The y -position of the vertical control surface is constant, which gives no contribution, and the total integral from the free surface vanishes.

The vertical control surface

By differentiating equations (26), (27), (29) and (30), $\partial G_K / \partial n$ on the vertical control surface is zero when $x \neq \xi$ or $z \neq \zeta$. The interpretation is that only the source point creates a normal velocity to the surface. For all other points on the control surface, only a component in the plane itself exists. The contribution from the source itself is found by enclosing the source point by a small hemisphere with radius ϵ .

When $z < 0$ and $r \rightarrow 0$, $\partial G_K / \partial y \rightarrow (y - b) / r^3$

$$\begin{aligned} I_1 &= \iint_{S_V} \phi \frac{\partial G_K}{\partial n} dS - G_K \frac{\partial \phi}{\partial n} dS \\ &= \iint_{S_V} \phi \frac{\partial G_K}{\partial n} dS - \iint_{S_V} G_K \frac{\partial \phi}{\partial n} dS \\ &= \lim_{\epsilon \rightarrow 0} \iint_{S_V} \phi \frac{\partial G_K}{\partial n} dS - \iint_{S_1} G_K \frac{\partial \phi}{\partial n} dS \\ &= 2\pi\phi - \iint_{S_V} G_K \frac{\partial \phi}{\partial n} dS \end{aligned} \quad (34)$$

Finally $I_\infty + I_T + I_1 = 0$ which gives

$$\phi = \frac{1}{2\pi} \iint_{S_V} G_K \phi_n dS \quad \text{on } y = \pm b \quad (35)$$

Wave resistance calculated from control-surface integration

Wave resistance can be calculated by pressure integration over the hull. An alternative procedure is to calculate the change of momentum in a closed volume. Newman [15] derived an alternative expression based on the fluid velocity and wave elevation at an arbitrary control surface. Using the perturbation potential ϕ , the formula is:

$$\begin{aligned} R_{W'} &= -\rho \iint_{S_C} \left[\frac{1}{2} (\phi_x^2 + \phi_y^2 + \phi_z^2) n_x - \phi_x \phi_n \right] dS \\ &\quad - \frac{1}{2} \rho g \oint_{\Sigma_C} \zeta^2 dy \end{aligned} \quad (36)$$

The concept of an inner and outer domain is especially attractive since it makes use of the matching surfaces as a part of the control surface, $S_C = S_1 + S_\infty$, as described in figure 2. Σ_C is the intersection between the free surface and the S_C . In the case where the vertical control surfaces are extended to infinity, only S_1 will give a contribution to the integral because $\nabla\phi$ and ζ vanish at infinity. Equation (36) then simplifies to

$$R_{W'} = 2\rho \iint_{S_C} \phi_x \phi_n dS \quad (37)$$

Here continuity has been used, ($\iint_{S_C} \phi_n dS = 0$).

In the computer program only a restricted part, S_{11} , of the vertical control surfaces S_1 is used. Consequently two transverse control surfaces, S_{11}^- and S_{11}^+ , have to be inserted in order to enclose the control volume. The corresponding part of Σ_C is Σ^- and Σ^+ . Figure 15 describes the configuration.

Finally the equation becomes

$$\begin{aligned} R_{W'} &= 2\rho \iint_{S_{11}} \phi_x \phi_n dS \\ &\quad - \rho \iint_{S_{11}^- + S_{11}^+} \left[\frac{1}{2} (\phi_x^2 + \phi_y^2 + \phi_z^2) n_x - \phi_x \phi_n \right] dS \\ &\quad - \frac{1}{2} \rho g \oint_{\Sigma^- + \Sigma^+} \zeta^2 dy \end{aligned} \quad (38)$$

The normal vector n_x of the elements on S_{11}^- and S_{11}^+ is ± 1 , and the disturbance potential and the wave elevation vanish rapidly upstream. Consequently the computational domain will have contributions only from the vertical control surfaces and the transverse control surface behind the ship.

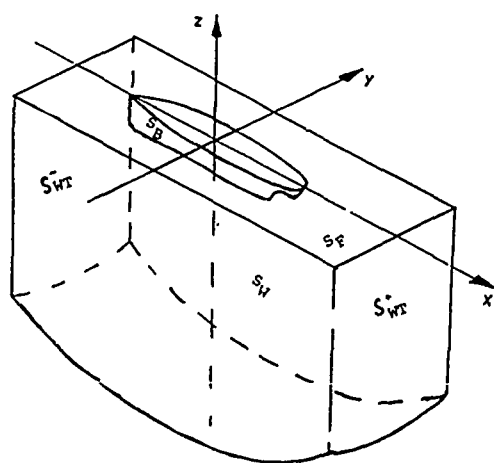


Figure 15: Control surfaces for calculating wave resistance.

Finite Difference Analysis of Unsteady Cavitation on a Two-Dimensional Hydrofoil

A. Kubota, H. Kato and H. Yamaguchi
University of Tokyo
Tokyo, Japan

Abstract

The authors present a new cavity model, which is named a Bubble Two-phase Flow (BTF) model, to explain the interaction between viscous fluid and bubble dynamics. This BTF cavity model treats the inside and outside of a cavity as one continuum by regarding the cavity as a compressible viscous fluid whose density varies widely. Navier-Stokes equations including cavitation bubble clusters are solved in finite difference form by a time-marching scheme. The growth and collapse of a bubble cluster is given by a modified Rayleigh's equation. Computation was made on a two-dimensional flow field around a hydrofoil NACA0015 at an angle of attack of 8.0 deg. The Reynolds number was 3×10^5 . The computational results showed the occurrence of the attached cavity at the foil leading edge. Furthermore, the present results predicted the generation of cavitation clouds with large-scale vortices. The newly proposed BTF cavity model is very flexible and promising.

1. Introduction

When the pressure of a liquid is reduced at constant temperature by either static or dynamic means, a state is reached at which vapor or vapor-filled bubbles exist. This phenomenon is called cavitation [1]. Cavitation results in performance deterioration of hydraulic machinery, generation of noise, vibration and erosion. This is because cavitation is a dynamic phenomenon, as it concerns itself with the growth and collapse of cavities. In spite of many excellent studies, the actual structure of cavitation is not

yet fully understood. In order to accurately predict the generation of noise or onset of erosion, it is particularly important to illuminate the unsteady structure of cavitation.

Vortex cavitation is often observed in the flow downstream of attached cavitation. It is caused by vorticity shed into the flow field just downstream of the cavity. Such vortex cavitation generates a large cavitation cloud under certain conditions. The vortex cavitation impinges on the body and its subsequent collapse results in erosion [2]. In previous work, the authors performed an experimental investigation of the unsteady structure (velocity distribution) of cloud cavitation on a stationary two-dimensional hydrofoil using a conditional sampling technique [3]. It was found that the cloud cavitation observed in the experiment was a large-scale vortex with many small cavitation bubbles. Consequently, the importance of the interaction between large-scale coherent vortices in the flow field and cavitation bubbles was recognized.

Much theoretical work also has been done in order to obtain a better understanding of the physics of cavitation phenomenon. Researchers have continually developed new models of cavitating flow based mainly on the assumption that the flow is irrotational (inviscid). For example, Tulin [4][5] proposed small-perturbation (linearized) theory for the case of a supercavitating hydrofoil. He has treated the cavity as a single vapor film and assumed that the pressure inside the cavity is constant. This is a sort of macroscopic analysis of cavitation. Using this model, many researchers have gradually improved the

calculation methods [6][7][8][9][10][11]. The single vapor film model is now well established. It can also predict macroscopic cavity characteristics fairly well. However, they all dealt with only steady cavitation. Furness and Hutton [12] treated the case of an unsteady attached cavity on a stationary two-dimensional body by the singularity method. This calculation result showed unsteadiness of the cavity surface and a reentrant jet [1]. Their methods, however, could not predict the behavior of a detached cavity after the attached cavitation splits into two parts. Tulin and Hsu [13] and van Houten [14] have solved the unsteady cavity problem on a periodically oscillating hydrofoil. Their method also could not predict the generation of detached cavitation clouds. This is because of a limitation of the cavity model, which treats the cavity as a single vapor film where pressure is constant. Therefore, a new model of cavitation is required to theoretically study the breakoffs of attached cavitation and cavitation clouds.

How to model the cavity trailing edge, where the cavity collapses, is the most difficult problem for the above-mentioned single film, constant pressure cavity model. When one observes actual cavitation, it is found that the sheet cavity splits into minute bubbles with vortices in the end region. Then the bubbles collapse. One can often observe many vortex cavities in this region even if the sheet cavity is stable. Van Wijngaarden [15][16], Mørch [17], Chahine and Lie [18], d'Agostino and Brennen [19] and others have studied the dynamics of bubble clusters. The bubble cluster is a kind of microscopic modeling of cavitation. However, these studies treated only a cluster of collapsing bubbles under given conditions. Hence, they could not answer how the unsteady attached cavity sheds cavitation clouds.

Highly vortical fluid motion such as a cavitation cloud is often observed downstream of a cavity. Experimental observation shows a close relationship between large-scale coherent vortex and cavitation [3]. Therefore, it is necessary to develop a theoretical elucidation of the mechanism that generates the large-scale vortex structure. There is a strong interaction between the large-scale vortex and

cavitation. The occurrence of attached cavitation yields boundary layer separation. The separated shear layer rolls up, thus turning into a large-scale vortex [20]. On the contrary, the large-scale vortex yields a low pressure region at its center. In the low pressure region, bubbles grow and remain. Existing cavity models are powerless to explain the nonlinear vortex dynamics of the above problem since they assume inviscid flow.

In this paper, the authors will propose a new cavity model that can explain the interactions between vortices and bubbles. The authors call this new model a Bubble Two-phase Flow (BTF) cavity model. In a macroscopic (coarse-grained) view, this model treats the cavity flow field phenomenologically as a compressible viscous fluid whose density varies greatly. It can treat the inside and outside of the cavitation as a single continuum and hence it can express the detached cavitation clouds. In a microscopic view, this model treats cavitation structurally as bubble clusters. By coupling these two views, the BTF cavity model can clarify the nonlinear interaction between macroscopic vortex motion and microscopic bubble dynamics. The authors have developed a program code SACT-III (Solution Algorithm for Cavitation and Turbulence, version III) to solve the BTF model equations using the finite difference method. They will apply this program to cavity flow around a stationary two-dimensional hydrofoil in order to verify its ability.

2. Formulation

An attached cavity, which is formed at the leading edge of a cavitating hydrofoil, collapses at the mid-portion of the hydrofoil. It is also well known that the attached cavity oscillates cyclically within a certain range of cavitation number. This unsteady cavity sheds a cavitation cloud in each cycle [3]. The front part of the attached cavity is a film of vapor where pressure is constant. At its rear part, the vapor film splits up into tiny bubbles. A large-scale vortex caused by the cavity rolls up the bubbles, thus generating a cavitation cloud. There are two cavity types in a microscopic view. As shown in Figure 1, these are the vapor film and the bubble cluster (with vortices).

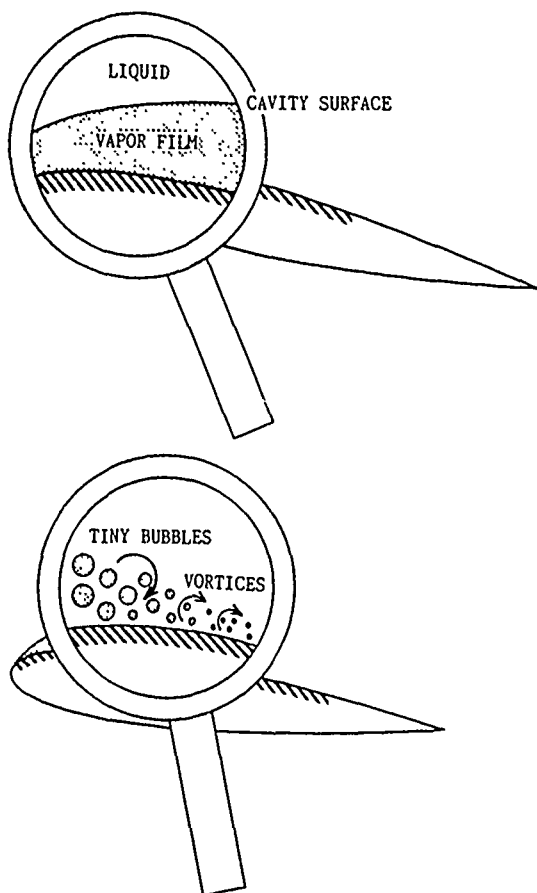


Figure 1 Two microscopic views of cavitation, vapor film types (above) and bubble cluster types (below).

There is, however, a third type of cavitation. This is traveling cavitation or bubble cavitation [1]. This phenomenon is not treated in this paper.

2.1 Macroscopic Modeling

In the macroscopic view, the Bubble Two-phase Flow (BTF) model treats the inside and outside of the cavitation as one continuum. This is because it regards the cavity flow field as a compressible viscous fluid whose density varies greatly. According to this phenomenological modeling, contour lines of void fraction (volume fraction of cavities) express the shape of the cavity as shown in Figure 2. Governing equations of the macroscopic flow field are as shown below.

The equation of continuity is

$$\frac{\partial \rho}{\partial t} + \nabla(\rho \mathbf{v}) = 0, \quad (1)$$

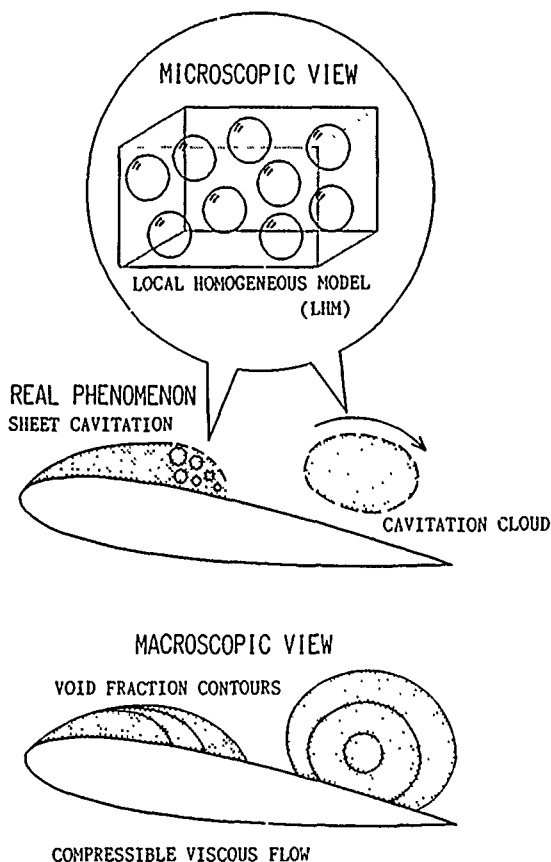


Figure 2 Modelling concept of Bubble Two-phase Flow (BTF) cavity model.

where t , $\rho \mathbf{v}$, \mathbf{v} and ρ are time, mass flux vector ($\rho u, \rho v, \rho w$), velocity vector (u, v, w) and density of the mixture, respectively.

The conservation equation for momentum: Navier-Stokes equation is

$$\frac{\partial(\rho \mathbf{v})}{\partial t} + \nabla(\rho \mathbf{v} \mathbf{v}) = -\nabla P + \frac{1}{Re} \mu \{ \nabla^2 \mathbf{v} + \frac{1}{3} \nabla(\nabla \cdot \mathbf{v}) \}, \quad (2)$$

where P is the pressure in the mixture, μ is the viscosity of the mixture, and Re is the Reynolds number. This equation is in conservation form [21]. The nondimensionalized quantities based on the uniform flow velocity and a reference length have been employed in the above two equations.

The BTF cavity model assumes that a fluid of variable density replaces the water-vapor mixture. The density of the water containing bubbles (mixture) is defined as follows:

$$\rho = (1 - \Gamma_g) \rho_L, \quad (3)$$

where ρ_L is the water density and f_g is the local void fraction. The mass and momentum of the vapor are ignored, since they are small compared with those of the liquid. The actual ratio comparing the density of vapor to that of liquid is of the order 10^{-4} . The change of liquid mass due to the phase change is also ignored.

The viscosity of the mixture is assumed to be as follows:

$$\mu = (1 - f_g)\mu_L + f_g\mu_G, \quad (4)$$

where μ_L is the water viscosity and μ_G is the vapor viscosity.

2.2 Microscopic Modeling

- Local Homogeneous Model -

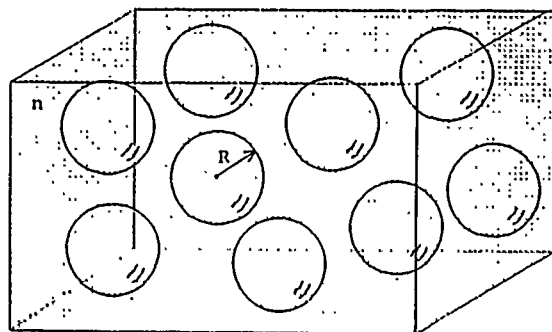
To calculate the macroscopic flow field, it is necessary to know the local void fraction function $f_g(t, x, y, z)$. The greatest problem is to develop a model that gives the relationship between the flow field condition and the void fraction. The present BTF model treats cavitation microscopically as bubble clusters. This is because bubbles play important roles in the cavity inception [22]. Furthermore, one of the main purposes of the BTF model is to study the mechanism of the cavity collapse. The sheet-type cavity splits up into tiny bubbles there. This structural microscopic model cannot be basically applied to the vapor film type cavitation. However, the type of the microscopic model has less effect on the macroscopic model when the void fraction is high. The present BTF model introduces a Local Homogeneous Model (LHM), which is a sort of Mean Field Approximation (MFA), for simplicity. It treats the cavity as a local homogeneous cluster of spherical bubbles as shown in Figure 2. Bubble number density and a typical radius are assumed locally. This typical bubble radius is obtained from the growth-collapse equation of the bubble cluster. This equation is derived from the growth-collapse equation of one spherical bubble (Rayleigh's equation).

The LHM gives the local void fraction f_g by coupling the bubble density and the typical bubble radius as follows:

$$f_g = n \cdot \frac{4}{3}\pi R^3, \quad (5)$$

where n is the bubble number density and R is the typical bubble radius (see Figure 3). In this paper, the bubble

density is assumed to be constant all over the computational domain though real cavity flows have a distributed bubble density. This is because it is too difficult to formulate coalescence and fragmentation of the bubbles.



$$f_g = n \cdot \frac{4}{3}\pi R^3$$

$$\rho = (1 - f_g)\rho_L$$

Figure 3 Local homogeneous microscopic cavity model (LHM).

The LHM assumes that cavities form in the shape of spherical bubbles. The bubbles remain separate and distant enough from each other so that their shapes remain spherical. Interaction between bubbles occurs through the local pressure that develops in the liquid as bubbles grow.

Lord Rayleigh originally derived the equation of radial motion (growth and collapse) of an isolated spherical bubble in a homogeneous infinite medium [23]. This equation is widely known as Rayleigh's equation. It takes the following form, neglecting the effect of surface tension and viscous damping,

$$R \frac{d^2 R}{dt^2} + \frac{3}{2} \left(\frac{dR}{dt} \right)^2 = \frac{P_v - P}{\rho_L}, \quad (6)$$

where P_v is the vapor pressure. In this study, the vapor pressure is assumed constant. This is because the behavior of the bubble is nearly isothermal and gas inside the bubble is also ignored.

The finite-difference method was employed in SACT-III. In this method, a continuous domain is discretized into finite grid points. Hence, an interaction between individual bubbles within the grid spacing must be considered to eliminate the effect of the computational grid. This effect is a sub-grid-scale (SGS) bubble interaction.

Next, let us consider the SGS bubble interaction of the LHM, deriving analytically the equation of motion of the bubble cluster.

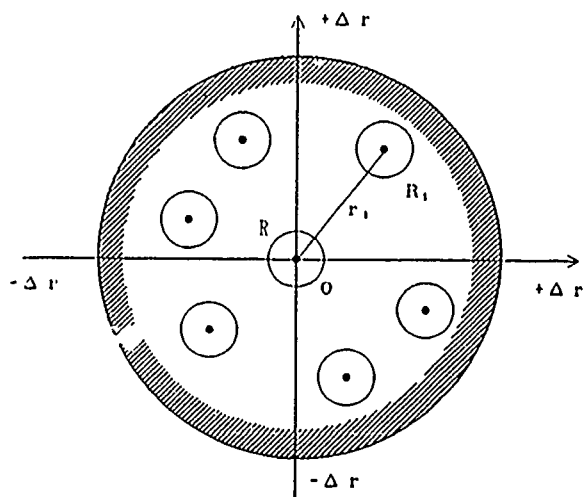


Figure 4 Sub-grid-scale (SGS) bubble interaction model.

As shown in Figure 4, we consider the influence of the other bubbles which exist inside of the distance Δr (=grid spacing). The total velocity potential due to the other bubbles at the origin 0 is

$$\sum \frac{1}{r_i} \frac{dr_i}{dt} R_i^2, \quad (7)$$

when $R_i < r_i$. From the local homogeneous assumption,

$$\nabla \left(\sum \frac{1}{r_i} \frac{dr_i}{dt} R_i^2 \right) = 0, \quad (8)$$

and

$$R_i = R. \quad (9)$$

The following equation is therefore obtained by adding the time derivative of Equation(7) to the original Equation(6):

$$\frac{\partial}{\partial t} \left(\sum \frac{1}{r_i} \frac{dR}{dt} R^2 \right) + R \frac{d^2 R}{dt^2} + \frac{3}{2} \left(\frac{dR}{dt} \right)^2 = \frac{P_v - P}{\rho_L}. \quad (10)$$

The number of bubbles which exist inside the sphere of radius Δr is

$$n \cdot \frac{4}{3} \pi \Delta r^3. \quad (11)$$

Then the first term of the left-hand side in Equation(10) becomes

$$\begin{aligned} \frac{\partial}{\partial t} \left(\sum \frac{1}{r_i} \frac{dR}{dt} R^2 \right) &= \frac{\partial}{\partial t} \left(\frac{dR}{dt} R^2 \sum \frac{1}{r_i} \right) \\ &\approx \frac{\partial}{\partial t} \left(\frac{dR}{dt} R^2 n \int_0^{\Delta r} \frac{1}{r} 4\pi r^2 dr \right) \end{aligned}$$

$$= \frac{\partial}{\partial t} \left(\frac{dR}{dt} R^2 n \cdot 2\pi \Delta r^2 \right)$$

$$= 2\pi \Delta r^2 \left(n R^2 \frac{d^2 R}{dt^2} + \frac{dn}{dt} R^2 \frac{dR}{dt} + 2n R \frac{dR}{dt} \right). \quad (12)$$

Combining Equations(10) and (12) and replacing the time derivative with

$$\frac{D}{Dt} \left(= \frac{\partial}{\partial t} + (\mathbf{v} \cdot \nabla) \right),$$

we obtain the LHM's equation of motion as follows:

$$\begin{aligned} (1 + 2\pi \Delta r^2 n R) R \frac{D^2 R}{Dt^2} + \left(\frac{3}{2} + 4\pi \Delta r^2 n R \right) \left(\frac{dR}{dt} \right)^2 \\ + 2\pi \Delta r^2 \frac{Dn}{Dt} R^2 \frac{dR}{dt} = \frac{P_v - P}{\rho_L}. \quad (13) \end{aligned}$$

Referring to Equation(13), it is found that the effect of the other bubbles decreases with a decrease in Δr . This is a preferable characteristic in solving the present problem. This is because the other bubbles do not affect the referred bubble if the grid interval was zero.

Quantities in the above equations have been nondimensionalized based on the uniform flow velocity U_∞^* and a reference length d^* . Hence:

$$\begin{aligned} P^* &= \rho_L^* U_\infty^{*2} P, \quad t^* = \frac{td}{U_\infty^*}, \quad \mathbf{v}^* = U_\infty^* \mathbf{v}, \\ \rho^* &= \rho_L^* \rho, \quad \mu^* = \mu_L^* \mu, \\ n^* &= \frac{n}{d^{*3}}, \quad R^* = d^* R, \\ x^* &= d^* x, \quad y^* = d^* y, \quad z^* = d^* z, \end{aligned} \quad (14)$$

where $*$ denotes dimensional values. In the following computation, the chord length of a hydrofoil has been chosen as d^* . The Reynolds number Re , pressure coefficient C_p and cavitation number σ are defined as follows:

$$\begin{aligned} Re &= \frac{U_\infty^* d^*}{\nu_L^*} = \frac{U_\infty^* d^* \rho_L^*}{\mu_L^*}, \\ C_p &= \frac{P^* - P_\infty^*}{\frac{1}{2} \rho_L^* U_\infty^{*2}}, \\ \sigma &= \frac{P_\infty^* - P_v^*}{\frac{1}{2} \rho_L^* U_\infty^{*2}}. \end{aligned} \quad (15)$$

3. SACT-III Program

The program SACT-III is the third version of the SACT series. The purpose of the SACT series is to study theoretically the unsteady structure of cavitation using the BTF model. Over several years, we developed a program SACT-II (SACT, version II; two-

dimensional rectangular cell version). The results computed by SACT-II explained cavity formation caused by large-scale coherent vortices behind a rectangular obstacle on a wall [24]. The present SACT-III employs the finite difference method in the body fitted coordinates to solve the governing partial differential equations given in the preceding section. This section explains the computational procedure and the finite difference scheme of SACT-III. The computational procedure is basically the same as the Marker-and-Cell(MAC) method [25] except for the use of a regular mesh system, instead of the staggered mesh system.

3.1 Quasi-Poisson Equation for Pressure

By taking the divergence of the Navier-Stokes equation(2), the following Poisson equation for pressure is given:

$$\nabla^2 P = -\nabla \left(\frac{\partial(\rho \mathbf{v})}{\partial t} \right) + \nabla(\rho \mathbf{v}, \mathbf{v}) \quad (16)$$

$$= -\frac{\partial}{\partial t} (\nabla(\rho \mathbf{v})) + \nabla(\rho \mathbf{v}, \mathbf{v}) ,$$

where

$$\nabla(\rho \mathbf{v}, \mathbf{v}) = -\nabla \left[\nabla(\rho \mathbf{v} \mathbf{v}) + \frac{1}{Re} \mu \left\{ \nabla^2 \mathbf{v} + \frac{1}{3} \nabla(\nabla \cdot \mathbf{v}) \right\} \right] \quad (17)$$

Substituting the continuity equation(1) into Equation(17),

$$\nabla^2 P = \frac{\partial^2}{\partial t^2} \rho + \nabla(\rho \mathbf{v}, \mathbf{v}) \quad (18)$$

From Equations(3) and (5), which represent the basic assumptions of the LHM,

$$\rho = (1-n) \frac{4}{3} \pi R^3 \rho_L \quad (19)$$

To simplify the LHM, $n=\text{constant}$ is assumed in this study as mentioned in section 2.2. By differentiating Equation(19) twice with respect to t , we have the following equation:

$$\frac{\partial^2 \rho}{\partial t^2} = -\rho_L 4n\pi \left\{ R^2 \frac{\partial^2 R}{\partial t^2} + 2R \left(\frac{\partial R}{\partial t} \right)^2 \right\} \quad (20)$$

From the LHM's equation of motion(13),

$$\frac{\partial^2 R}{\partial t^2} = \mathfrak{H}(\rho \mathbf{v}, \mathbf{v}, \frac{\partial R}{\partial t}, R) + \mathfrak{P}(P) \quad (21)$$

where

$$\begin{aligned} \mathfrak{H}(\rho \mathbf{v}, \mathbf{v}, \frac{\partial R}{\partial t}, R) &= -\left\{ 2(\mathbf{v} \cdot \nabla) \frac{\partial R}{\partial t} + (\mathbf{v} \cdot \nabla)(\mathbf{v} \cdot \nabla) R \right\} \\ &\quad - \frac{\frac{3}{2} + 4\pi \Delta r^2 n R}{(1+2\pi \Delta r^2 n R) R} \left(\frac{\partial R}{\partial t} + (\mathbf{v} \cdot \nabla) R \right)^2 \\ &\quad - \frac{2\pi \Delta r^2 R^2}{(1+2\pi \Delta r^2 n R) R} \left\{ \frac{\partial n}{\partial t} + (\mathbf{v} \cdot \nabla) n \right\} \left\{ \frac{\partial n}{\partial t} + (\mathbf{v} \cdot \nabla) R \right\} \end{aligned} \quad (22)$$

and

$$\mathfrak{P}(P) = \frac{P_v - P}{(1+2\pi \Delta r^2 n R) R \rho_L} \quad (23)$$

If $n=\text{constant}$, the last term of the right-hand side becomes zero in Equation(22).

Substituting Equations(20) and (21) into (18), we obtain the quasi-Poisson equation for pressure including the motion of the bubble cluster as follows:

$$\nabla^2 P + \mathfrak{P}(P) = \mathfrak{H}(\rho \mathbf{v}, \mathbf{v}, \frac{\partial R}{\partial t}, R) + \nabla(\rho \mathbf{v}, \mathbf{v}) \quad (24)$$

where

$$\mathfrak{P}(P) = -\rho_L 4n\pi R^2 \cdot \mathfrak{P}(P) \quad (25)$$

$$\begin{aligned} \mathfrak{H}(\rho \mathbf{v}, \mathbf{v}, \frac{\partial R}{\partial t}, R) &= -\rho_L 4n\pi R \left\{ \mathfrak{H}(\rho \mathbf{v}, \mathbf{v}, \frac{\partial R}{\partial t}, R) + 2 \left(\frac{\partial R}{\partial t} \right)^2 \right\} \end{aligned} \quad (26)$$

The left-hand side in Equation(24) is approximated by the second-order finite differencing scheme. As a consequence, simultaneous equations of pressure P are obtained if the right-hand side is given in Equation(24). SACT-III solves the simultaneous equations derived from Equation(24) with a point successive relaxation method. Equation(24) is equivalent to the normal MAC method's Poisson equation of incompressible flow [25] when

$$\mathfrak{P} = \mathfrak{H} = 0$$

They are always set to zero for non-cavitating conditions. If the mixture is filled with liquid, Equation(13) cannot be solved since the bubble radius R becomes zero. If the mixture is filled with vapor, Equation(2) cannot be solved since density of the mixture becomes zero. Hence, when the void fraction f_g is less than $f_{gmin}(>0.0)$ or more than $f_{gmax}(<1.0)$, the bubble radius becomes fixed. Then, \mathfrak{P} and \mathfrak{H} are also set to zero. In the following computations, f_{gmin} and f_{gmax} are set as follows:

$$f_{gmin} = n \cdot \frac{4}{3} \pi R_0^3$$

$$f_{gmax} = 0.95$$

where R_0 is the initial bubble radius.

3.2 Numerical Methods

Equations(2) and (13) are time-integrated with and Euler explicit scheme using the value of pressure P obtained by solving Equation(24). To solve a high-Reynolds-number flow, each nonlinear term in Equation(2), for example $\frac{\partial}{\partial x}(\rho u v)$, was approximated with

the fourth-order centered finite-differencing scheme with the fourth-derivative term:

$$\frac{1}{2}|u| \cdot \frac{\partial^4}{\partial x^4} (\rho v) \Delta x^3. \quad (27)$$

The fourth-derivative term plays an important role in stabilizing the calculation. Physically, fourth-derivative term means shorter-range diffusion compared with the second-derivative viscous term [26]. The fourth-derivative term consequently stabilizes the computation without decreasing the Reynolds number and introducing any turbulent models. The universal availability of this fourth-derivative term has not been ascertained yet for the turbulent flow calculation. However, SACT-III introduces no turbulent model since there exists no established one for the two-phase (cavity) flow at present.

All the other space differential terms in Equations(2) and (13) are approximated with the second-order centered differencing scheme. Equation(13), however, has no spatial diffusive term for bubble radius R and its time-derivative. The second-derivative term is accordingly added in equation (13) to eliminate the instability of the nonlinear terms. For example,

$$|u| \cdot \frac{\partial^2 R}{\partial x^2} \Delta x \quad (28)$$

is added to $u \frac{\partial R}{\partial x}$. This term means diffusion.

To compute the high-Reynolds-number flow around a body of arbitrary shape, it is convenient to use body-fitted coordinates through coordinate transformation. Figure 5 shows the grid system for the present problem of flow around a two-dimensional hydrofoil. This system is called a C-type grid [27]. The connected physical (x,y,z) domain around the hydrofoil is mapped onto the rectangular computational (ξ,η,ζ) domain. Here the pair of planes forming the branch cut are both on the same plane of the transformed region. The surface of the body is also mapped on the same plane with the branch cut.

A regular mesh system is employed. Velocities, pressure and bubble radius are given on the grid points. As shown in Figure 5, the uniform flow boundary

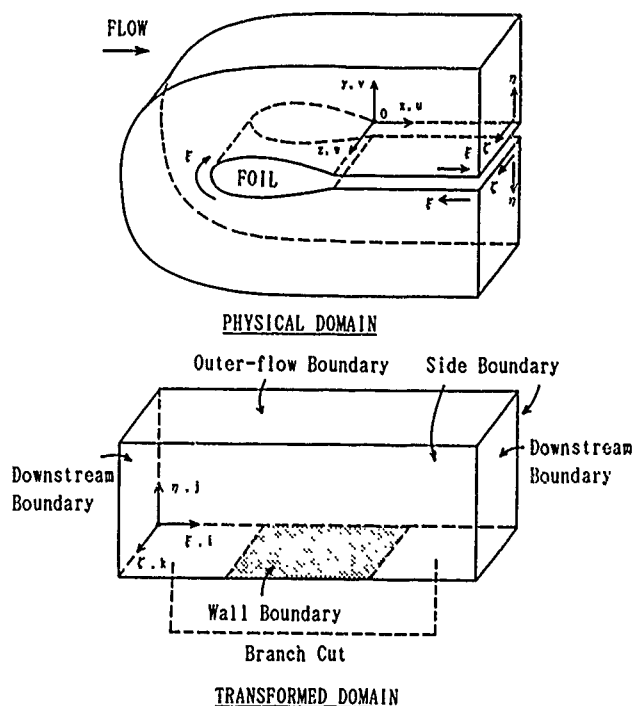


Figure 5 C-grid system around a two-dimensional hydrofoil.

conditions are imposed at the outer-flow boundary. These are:

$$\begin{aligned} u=1, v=w=0, \\ \frac{\partial u}{\partial \eta} = \frac{\partial v}{\partial \eta} = \frac{\partial w}{\partial \eta} = 0, \\ R=R_0, \frac{\partial R}{\partial t} = 0, P=0. \end{aligned} \quad (29)$$

At the downstream and side boundaries, the boundary conditions of the zero-th order (zero-gradient) extrapolation are imposed. At the branch cut boundaries, the periodic boundary conditions are imposed. At the wall boundary, the following boundary conditions are imposed.

$$\begin{aligned} u=v=w=0, \\ \frac{\partial P}{\partial \eta} = \frac{\partial R}{\partial \eta} = 0. \end{aligned} \quad (30)$$

First order (linear) extrapolation in (ξ,η,ζ) domain is used for the velocities to calculate the nonlinear terms of Equation(2). The terms are approximated by the fourth-order centered differencing scheme with the fourth-derivative term.

4. Computational Results and Discussion

4.1 Condition of Computation

A hydrofoil section with a simple mathematical configuration, NACA0015 [28], was chosen for the computation.

The computation was performed at angles of attack α of 0.0, 8.0 and 20.0 degrees [29]. However, this paper discusses only the results at $\alpha = 0.0$ and 8.0 degrees. The Reynolds number Re was 3×10^5 in all the computations. It is based on the uniform flow velocity and chord length of the hydrofoil. The viscosity ratio μ_G/μ_L was 9.12×10^{-3} . The computation at $\alpha = 0.0$ deg. was performed only for non-cavitating conditions to evaluate numerical accuracy. Experimental observation at $\alpha = 8.0$ deg. shows laminar separation without bursting near the leading edge. For cavitating conditions, an attached type cavity accordingly occurs near the foil leading edge.

The hydrofoil was accelerated from $u=0$ to the steady speed of 1 for $T=0-1$. The cavitation number was also decreased gradually for $T=2-3$ so as to compute stably for cavitating conditions. The time increment τ was determined in each computational step to keep the Courant number less than 0.25. The relaxation factor was set to be 0.8 when

Equation(24) was solved with the successive relaxation method. However, it was reduced to 0.3 for cavitating conditions. The convergence condition of the pressure computation is as follows:

$$\max(|\Delta P|) < 0.001$$

(for non-cavitating conditions)

$$\max(|\Delta P|) < 0.01$$

(for cavitating conditions),

where ΔP is the residue of pressure in an iterative calculation.

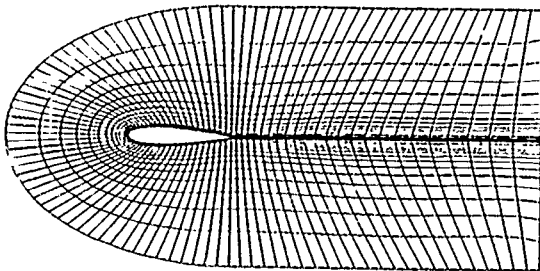


Figure 6 C-grid system around NACA0015 hydrofoil at $\alpha = 0.0$ deg, $101(\xi) \times 31(\eta) \times 3(\zeta)$.

Preceding the computations for cavitating conditions, it is necessary to evaluate numerical accuracy of SACT-III for non-cavitating conditions. The angle of attack was 0.0 degrees. Figure 6 shows the c-grid system. The grid was uniform in the spanwise section. The number of grid points was $101(\xi) \times 31(\eta) \times 3(\zeta)$. The distance between the trailing edge and the upper or lower boundaries was 1.2. The distance between

the trailing edge and the downstream boundary was 3.0. The shape of the front part of the outer-flow boundary was oval as shown in Figure 6. A direct numerical method [30] was used for the grid generation. The minimum grid spacings at the leading and trailing edges were 0.70×10^{-4} and 1.54×10^{-4} , respectively. The minimum spacing was about one twelfth of $Re^{-0.5}$ at the trailing edge.

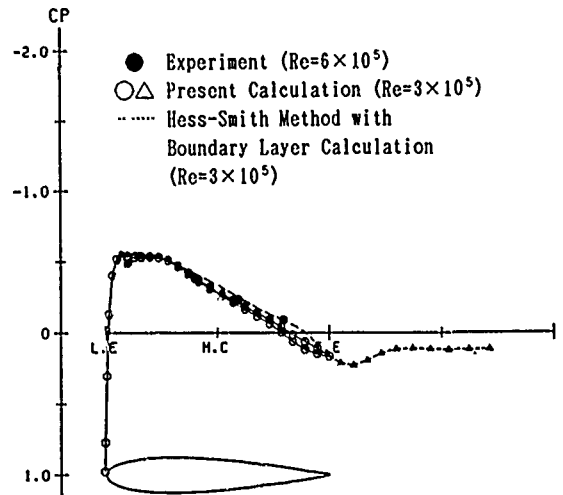
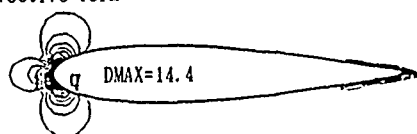


Figure 7 Foil surface and wake pressure, NACA0015; $\alpha = 0.0$ deg.; $T = 2.0$.

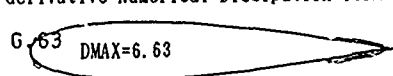
Figure 7 shows the pressure distributions on the foil surface at $T=2$. The circles show the distribution of C_p on the foil surface. The triangles show the distribution of C_p in the wake, i.e., on the branch cut shown in Figure 6. The computational results are compared with the computation using the Hess-Smith method [31] and the measurement at $Re=6 \times 10^5$ by Izumida [32]. The Hess-Smith method is a sort of numerical solution method of potential flow based on the boundary element method. The foil shape was modified by adding the computed displacement thickness of the foil surface boundary layer [33]. The laminar boundary layer was computed using Thwait's method, with the empirical constants derived by Curle and Skan [34]. The length of the separation bubble was 150 times as long as the momentum thickness at the laminar separation point. The Head's entrainment method modified by Cebeci [35] predicted the turbulent boundary layer development. The turbulent separation was predicted to occur when the form factor H_{12} exceeds 2.1. The computed pressure distribution agrees very well

with the others as shown in Figure 7. Furthermore, the pressure coefficient is .982, which is almost equal to 1.0, at the front stagnation point. As a consequence, the present numerical method has good accuracy when the grid system is fine enough. The computed pressure distributions disagree with the experimental result when the coarser grid systems are used [29].

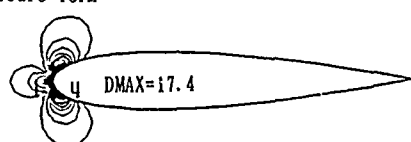
Convective Term



Fourth-derivative Numerical Dissipation Term



Pressure Term



Truncation Error of Pressure Term

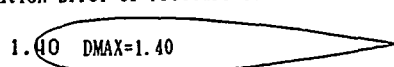


Figure 8 Distribution of convective, fourth-derivative, pressure and its truncation error terms in x-momentum equation, NACA0015; $\alpha = 0.0^\circ$; $Re = 3.0 \times 10^5$; $T = 2.0$.

Figure 8 shows the distributions of the convective term, the fourth-derivative term, the pressure terms and its truncation error in the x-momentum equation. The contour interval is 1.0. DMAX shows the maximum. The maximum of the fourth-derivative term is not negligible compared with the convective and pressure terms. However, it is distributed only near the foil surface around the leading and trailing edges. This result shows that the effect of the fourth-derivative term is local but important to stabilize the computation. The truncation error of the pressure term is sufficiently small compared with the main differenced terms.

4.2 Unsteady Attached Cavity

Figure 9 shows a close-up of the grid system around the NACA0015 hydrofoil. The angle of attack was 8.0° . The number of grid points was $101(\xi) \times 31(\eta) \times 3(\zeta)$. It was the same as that at $\alpha = 0.0^\circ$. The minimum spacing was 0.70×10^{-4} at the

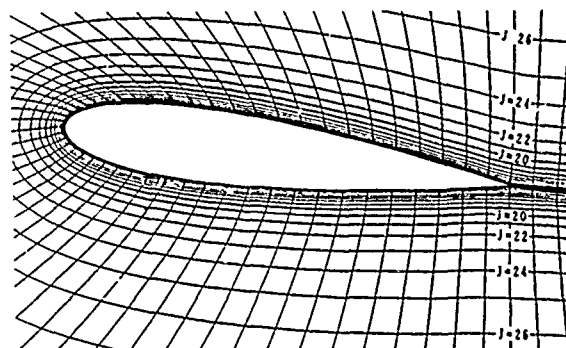


Figure 9 Close-up of the grid system around NACA0015 hydrofoil, $\alpha = 8.0^\circ$, $101(\xi) \times 31(\eta) \times 3(\zeta)$.

trailing edge. It was almost the same as that of the grid system at $\alpha = 0.0^\circ$. Figure 10 shows the time-averaged velocity vectors from $T=2$ to 4 for non-cavitating conditions. The computation was performed stably. The boundary layer separates at $X=0.74$ on the back side. Instantaneous velocity vectors, however, show unsteady vortex shedding from the foil trailing edge region. In the other region, the flow is almost steady. No separation occurs near the leading edge.

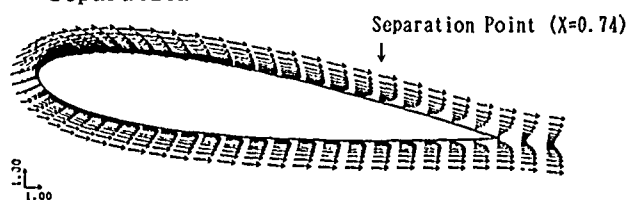


Figure 10 Time-averaged ($T=2 \sim 4$) velocity vectors around NACA0015 hydrofoil, $\alpha = 8.0^\circ$; $Re = 3.0 \times 10^5$.

Figure 11 shows the chordwise distribution of boundary layer displacement thickness on the foil surface. The present result agrees well with the boundary layer calculation at the front part of the back side. However, it cannot predict a laminar separation bubble because of the insufficiency of the grid points in the ξ -coordinate. The separation point is further upstream than in the boundary layer calculation. On the contrary, the agreement of the separation point is good on the face side. However, the boundary layer is thicker near the leading edge.

Figure 12 shows an example of the velocity profiles using wall variables. The present profile closely follows the law of the wall. The present method can consequently express the turbulent boundary layer without any turbulent models.

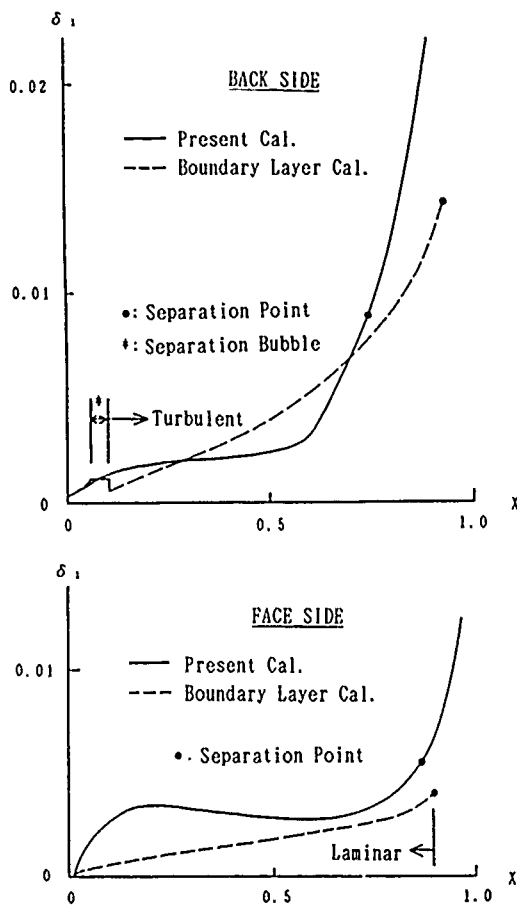


Figure 11 Boundary layer displacement thickness distribution on NACA0015 hydrofoil, $\alpha = 8.0 \text{ deg.}$; $Re = 3.0 \times 10^5$.

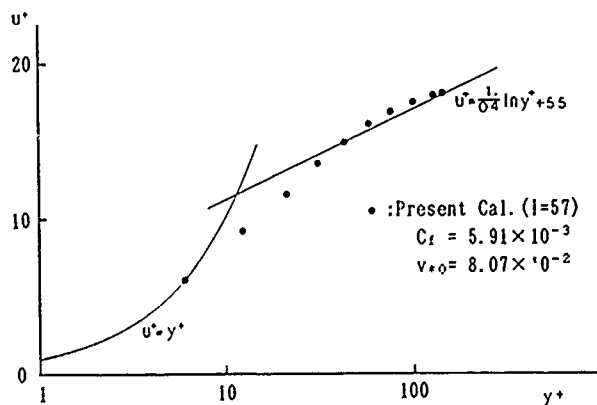
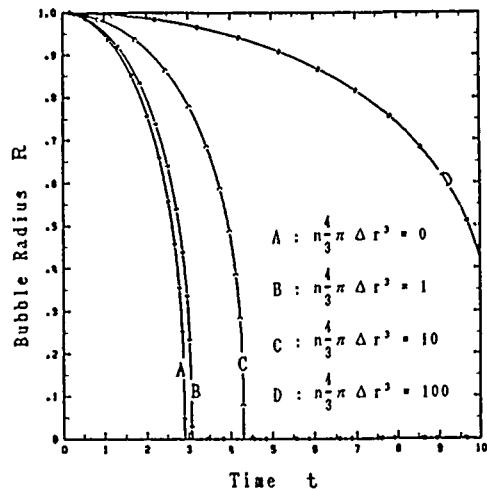


Figure 12 Velocity profile in boundary layer on NACA0015 hydrofoil using wall variables, $\alpha = 8.0 \text{ deg.}$; $Re = 3.0 \times 10^5$; $I = 57$ ($X = 0.0827$).

While the velocity profiles are predicted well, the pressure is not predicted quite so well. The present lift coefficient C_L is only about 58% of that obtained by the experiment.

However, the shape of the pressure distribution agrees well with the experiments. Hence, the disagreement of pressure hardly affects the nature of the unsteady cavitation.

$$\frac{P_v - P}{\rho} = -0.1$$



$$\frac{P_v - P}{\rho} = +0.1$$

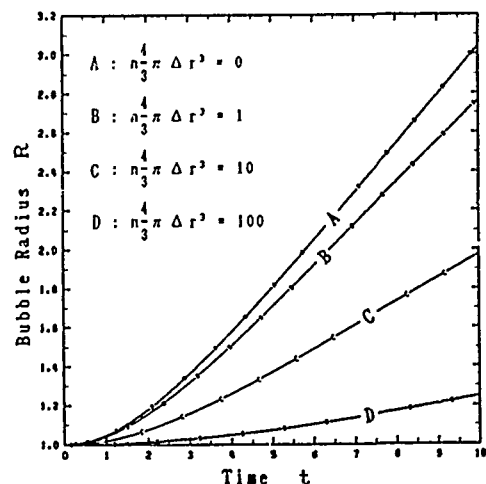


Figure 13 Influence of the SGS bubble interaction model on bubble collapse (above) and growth (below).

Before analyzing the cavitating flow field, we should check the effect of the SGS bubble interaction model. Figure 13 shows the effect of the SGS bubble interaction when the ambient pressure P has changed stepwise with the amplitude of $\pm(P_v - P)/\rho = 0.1$. $n(4/3)\pi\Delta r^3$ is the number of bubbles within the grid scale Δr . The convective terms were neglected in Equation(13). The Runge-Kutta-Gill method was used to solve the differential Equation(13). The bubble radius is nondimensionalized using its

initial value. The case A is the calculation of isolated bubbles, i.e., with no-bubble interaction effects. As shown in this figure, presence of other bubbles delays growth and collapse of the bubbles. Fujikawa et al. [36] carried out a theoretical analysis on the interaction between two bubbles. Their result shows that the collapse is delayed when the two bubbles have the same radius. The present result shows the same tendency.

In the following computation, the grid scale of the SGS bubble interaction model is assumed as follows:

$$r = \left(\frac{g'}{\pi} \right)^{\frac{1}{2}}, \quad (31)$$

where

$$g' = x_{\xi} y_{\eta} - x_{\eta} y_{\xi}$$

(two-dimensional Jacobian).

This is because the flow structure is two-dimensional. Accordingly, the SGS bubble interaction effect is independent of the grid spacing in the spanwise direction.

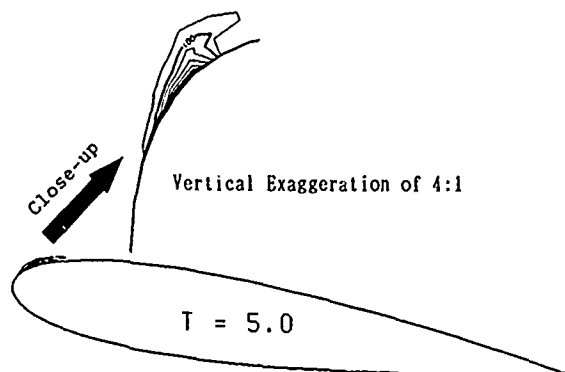


Figure 14 Void fraction contours around NACA0015 hydrofoil, $\sigma = 1.5$; $\alpha = 8.0^\circ$; $Re = 3.0 \times 10^5$; the contour interval is 0.1 except for the outermost line.

Figure 14 shows contour lines of void fraction at $\sigma = 1.5$. The initial bubble radius R_0 and the bubble number density n are 4×10^{-4} and 1×10^6 , respectively. In this paper, we define a cavity as a region where void fraction is more than 0.1. The bold contour lines are those of $f_g = 0.1$ in this figure. Contour lines are drawn at intervals of 0.1 except for the most outer line of $f_g = 0.01$. As seen in this figure, thin steady attached cavity incepts smoothly.

Figure 15 shows the time series contour lines of void fraction at

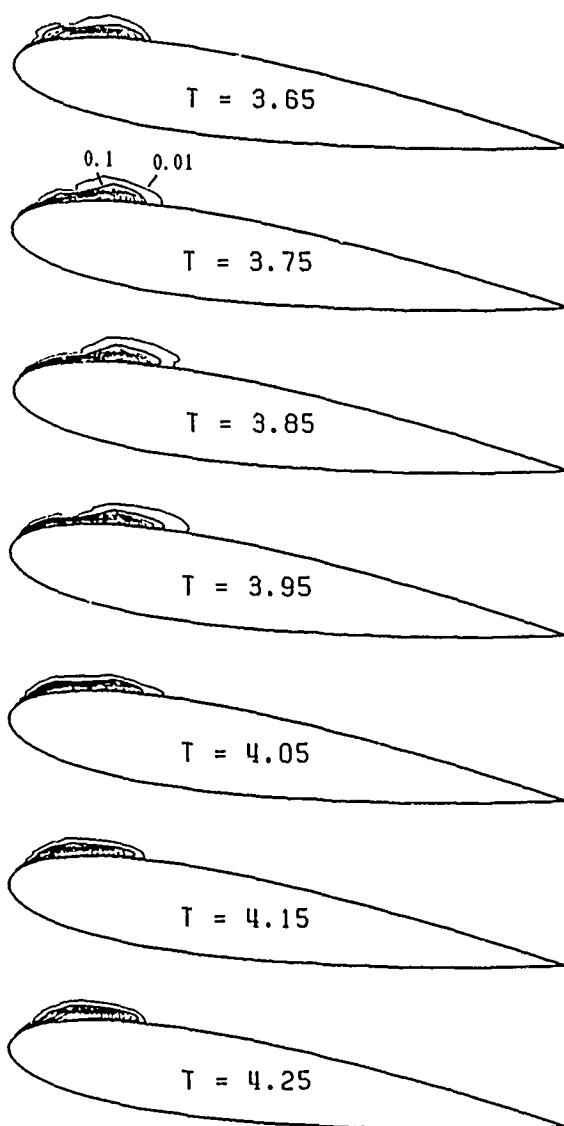


Figure 15 Void fraction contours around NACA0015 hydrofoil, $\sigma = 1.2$; $\alpha = 8.0^\circ$; $Re = 3.0 \times 10^5$; the contour interval is 0.1 except for the outermost line.

$\sigma = 1.2$. The void fraction is more than 0.9 at the center of the cavity. The rear portion of the cavity oscillates cyclically. Not only does the cavity length change but the cavity itself rises up at its rear part. The unsteady characteristics computed here agree with the experimental observations of sheet-type cavitation [32]. It is therefore concluded that the BTF cavity model can express the features of sheet-type cavitation beyond its microscopic model, which is essentially suitable to the bubble cluster flow.

Figure 16 shows the time-averaged pressure distribution on the foil

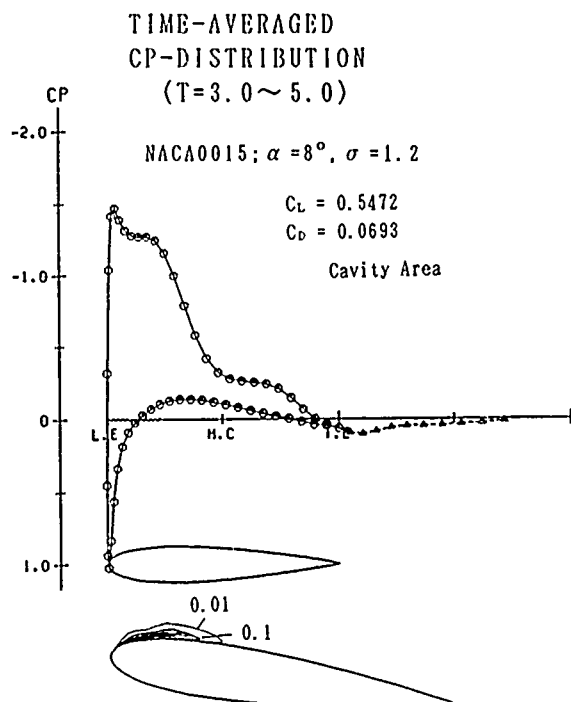


Figure 16 Time-averaged pressure distribution and void fraction contours around NACA0015 hydrofoil, $\sigma=1.2$; $\alpha=8.0^\circ$; $Re=3.0 \times 10^5$, the contour interval is 0.1 except for the outermost line.

surface and void fraction contour lines. The foil surface pressure where cavity exists is almost constant and equal to the vapor pressure ($C_p=-1.2$). However, a small pressure peak exists at the front part of the cavity. The pressure distribution is similar to the calculated result by a nonlinear free-stream line theory [10]. Furthermore, the time-averaged cavity shape is similar to the experimental observation of sheet-type cavity. These facts also suggest that the present BTF model can be applied to sheet type cavitation beyond its micro structure limitation.

Figure 17 shows the time-averaged pressure contours and flow velocity vectors. The contour line of $f_g=0.1$ (the bold broken line) agrees approximately with that of $C_p=-1.2$. This is the reason why the cavity is defined as a region where void fraction is more than 0.1. The reverse flow is observed clearly in the neighborhood of the end of the cavity.

Bold lines in Figure 18 show time-averaged velocity profiles in the cavity wake boundary layer along the η -coordinate. Fine ones are profiles

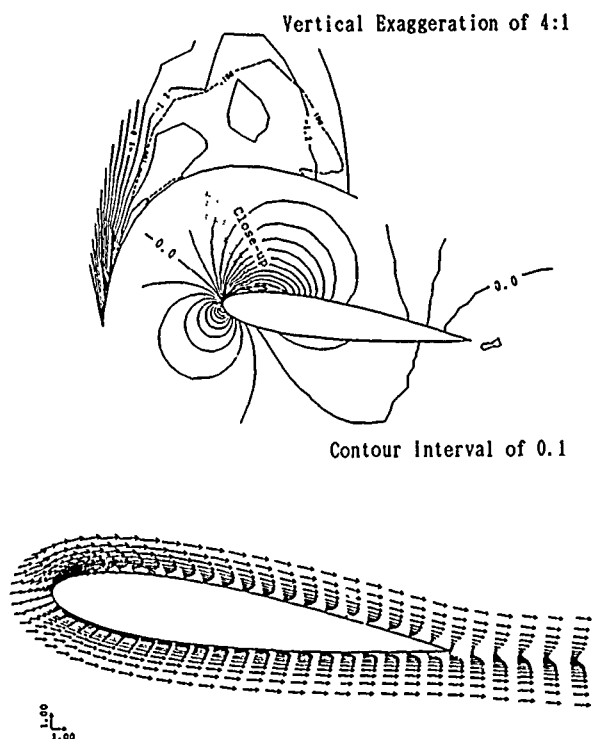


Figure 17 Time-averaged pressure coefficient contours and velocity vectors around NACA0015 hydrofoil, $\sigma=1.2$; $\alpha=8.0^\circ$; $Re=3.0 \times 10^5$, the contour interval is 0.1, the bold broken lines are void fraction contours of 0.1.

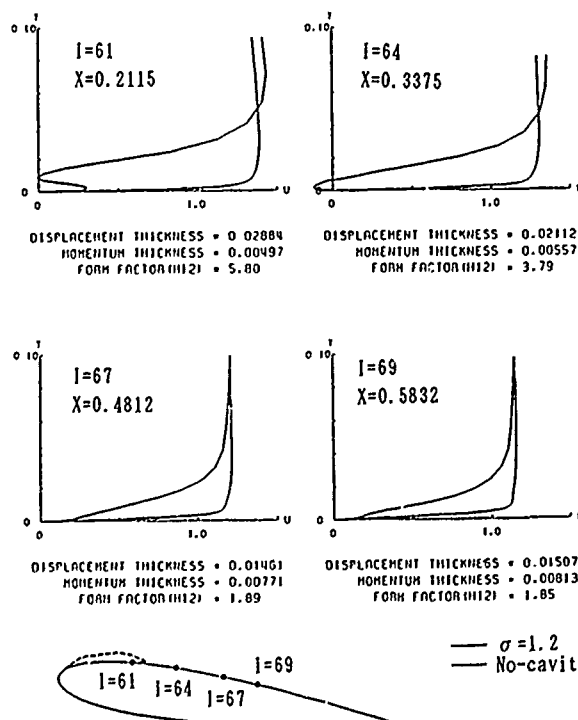


Figure 18 Time-averaged velocity profiles in cavity wake region, $\sigma=1.2$; $\alpha=8.0^\circ$; $Re=3.0 \times 10^5$, fine lines show the boundary layer velocity profiles for non-cavitating conditions.

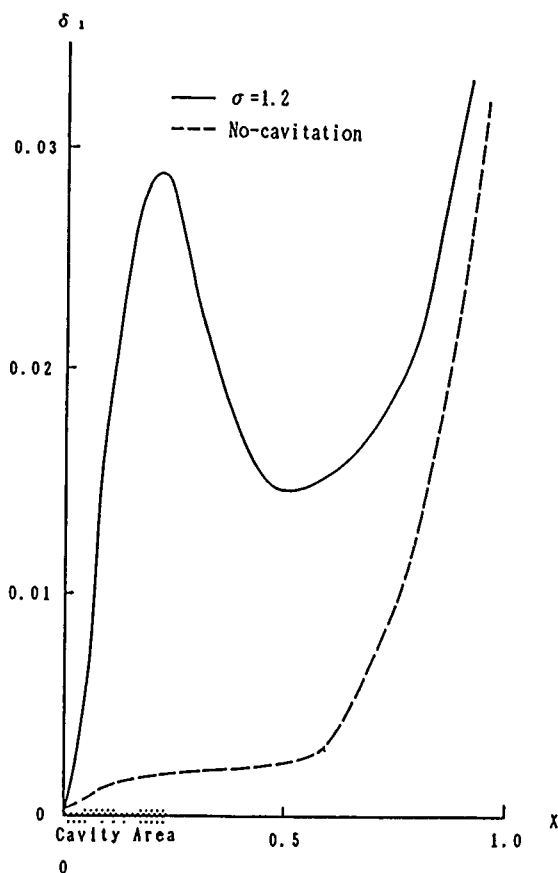


Figure 19 Comparison of boundary layer displacement thickness distribution on the back side of NACA0015 hydrofoil, $\alpha=8.0^\circ$; $Re=3.0 \times 10^5$. for non-cavitating conditions. As shown in the section of $I=61$ ($X=0.2115$), the flow inside the cavity is quite slow except near the foil surface. At the section of $I=64$ ($X=0.3375$), strong reverse flow occurs. At $I=67$ and 69 ($X=0.4812$ and 0.5832), the flow reattaches and inflection points exist in the velocity profiles. The measurement result downstream of a stable sheet cavity shows similar inflection points in the velocity profile [37][38]. As shown in this figure, the generation of cavity causes an increase in the boundary layer thickness behind it. Figure 19 shows the comparison of the chordwise distributions of the boundary layer displacement thickness for cavitating and non-cavitating conditions. For cavitating conditions, the displacement thickness decreases at the cavity collapsing region. It becomes minimum near the mid-chord, then it begins to increase again. This is also the same tendency that the experimental results show [33].

4.3 Cloud Cavitation

Figure 20 shows void fraction contour lines at $\sigma=1.0$ with a time increment of 0.2. The initial bubble radius R_0 and the bubble number density n are 1×10^{-3} and 1×10^6 , respectively. For this condition, unsteady cavities continuously grow and collapse. The highly distorted attached cavity sheds cavitation clouds cyclically ($T=5.9$ and 7.1), which soon collapse. This phenomenon agrees well with many experimental observations [32][39][40][41][42][43]. Figure 21 shows an example of the photographs of cloud cavitation [29]. The position of the cavity break off point agrees well with the computational result.

Figure 22 shows velocity vectors around the foil. Overlaid bold broken lines are void fraction contours of 0.1. As mentioned before, they show instantaneous cavity shapes. As shown in this figure, the unsteady attached cavity sheds not only cavitation clouds but also vortices (see marks A, B and C). The experimental result has confirmed such vortex shedding phenomena [3]. The position of cavitation clouds, however, does not agree very well with that of shedding vortices. There are two possible explanations for this discrepancy. One is the phase delay of the cavity growth. The other is that the present cavity model does not consider nuclei convection towards the center of vortices.

Figure 23 shows a close-up of the velocity vectors around the cavity. This figure elucidates the mechanism of cavitation cloud shedding. At $T=5.5$, a new separation vortex occurs at the cavity leading edge. Then it induces the flow toward the foil surface ($T=5.7$). Fluid density and pressure on the foil surface increase due to the impinging flow. It causes the cavity to break and tear off ($T=5.9$, separation of the cavitation cloud). The impinging flow turns into a jet along the foil surface. The jet sweeps away the cavitation cloud ($T=6.1$). This is the scenario of the generation of a cavitation cloud.

5. Concluding Remarks

In this study, the authors presented a new modeling concept of cavitation called BTF (Bubble Two-phase Flow). In a

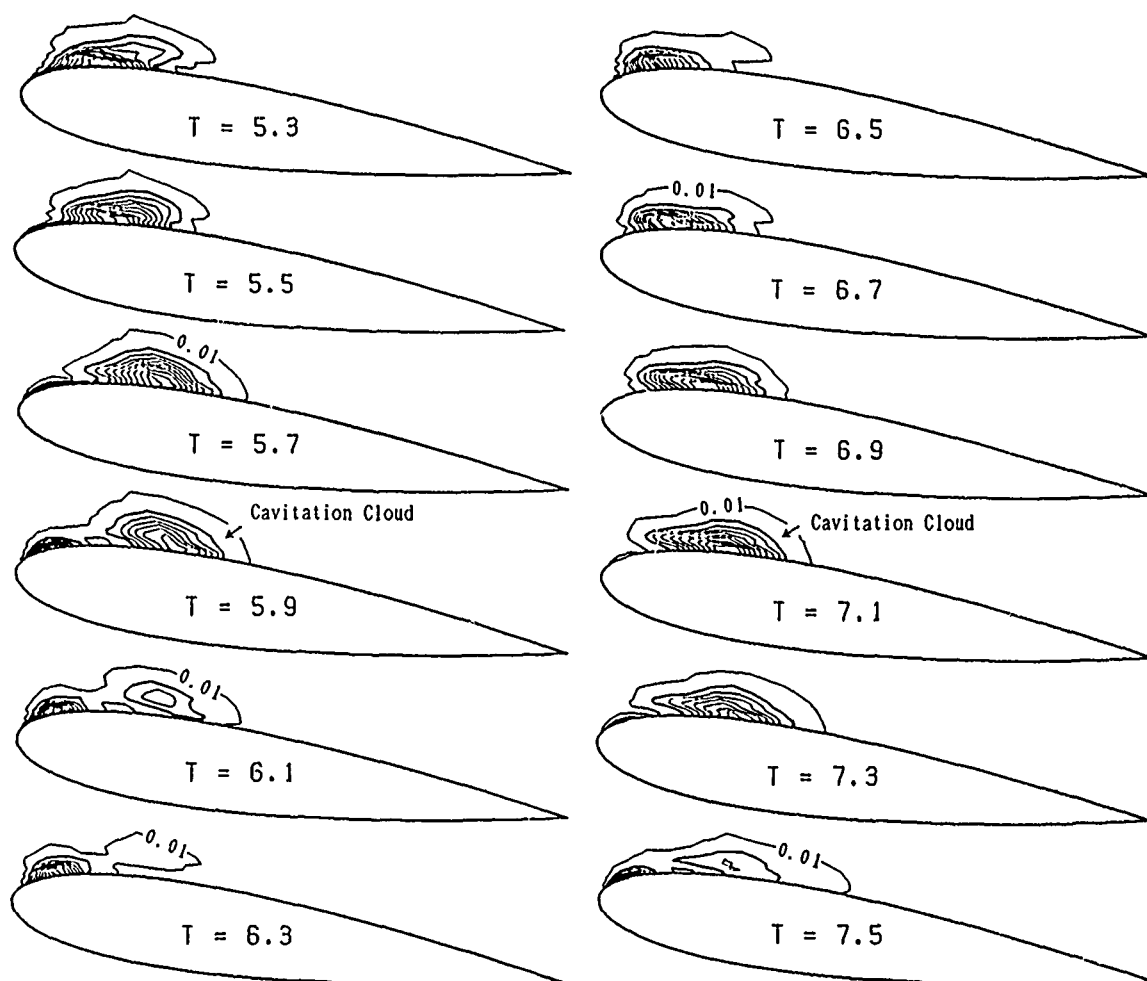


Figure 20 Void fraction contours around NACA0015 hydrofoil, $\sigma=1.0$; $\alpha=8.0\text{deg.}$; $Re=3.0 \times 10^5$, the contour interval is 0.1 except for the outermost line.

macroscopic view, this new cavity model treats the inside and outside of a cavity as one continuum. That is, it regards the cavitating flow field phenomenologically as a compressible viscous fluid whose density varies greatly. Contour lines of void fraction can express the cavity shape. In a microscopic view, a simple LHM (Local Homogeneous Model) is introduced. This is a kind of Mean Field Approximation. This structural microscopic model treats a cavity as a locally homogeneous bubble cluster. Assuming bubble density and a typical bubble radius, a local void fraction function is given. The BTF cavity model is significant in the following points: (1) The BTF cavity model can investigate the nonlinear interaction between large-scale vortices and cavitation bubbles, (2) The BTF cavity model can consider the effects of bubble nuclei on cavitation inception,

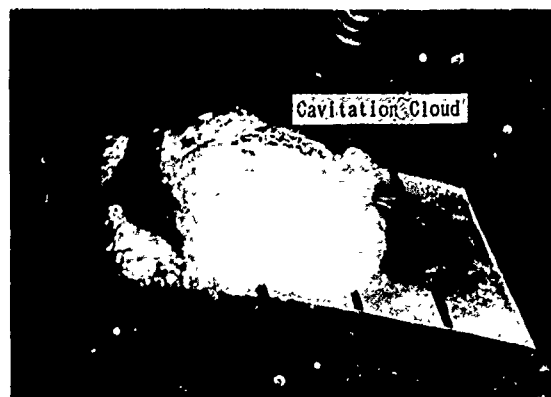


Figure 21 Cavity appearance on NACA0015 hydrofoil, $\sigma=1.30$; $\alpha=8.0\text{deg.}$; $Re=3.0 \times 10^5$.

(3) The BTF cavity model can express unsteady characteristics of cavitation. The BTF cavity model, therefore, includes three essential factors for cavitation. Those factors are pressure, nuclei and time. By examining the

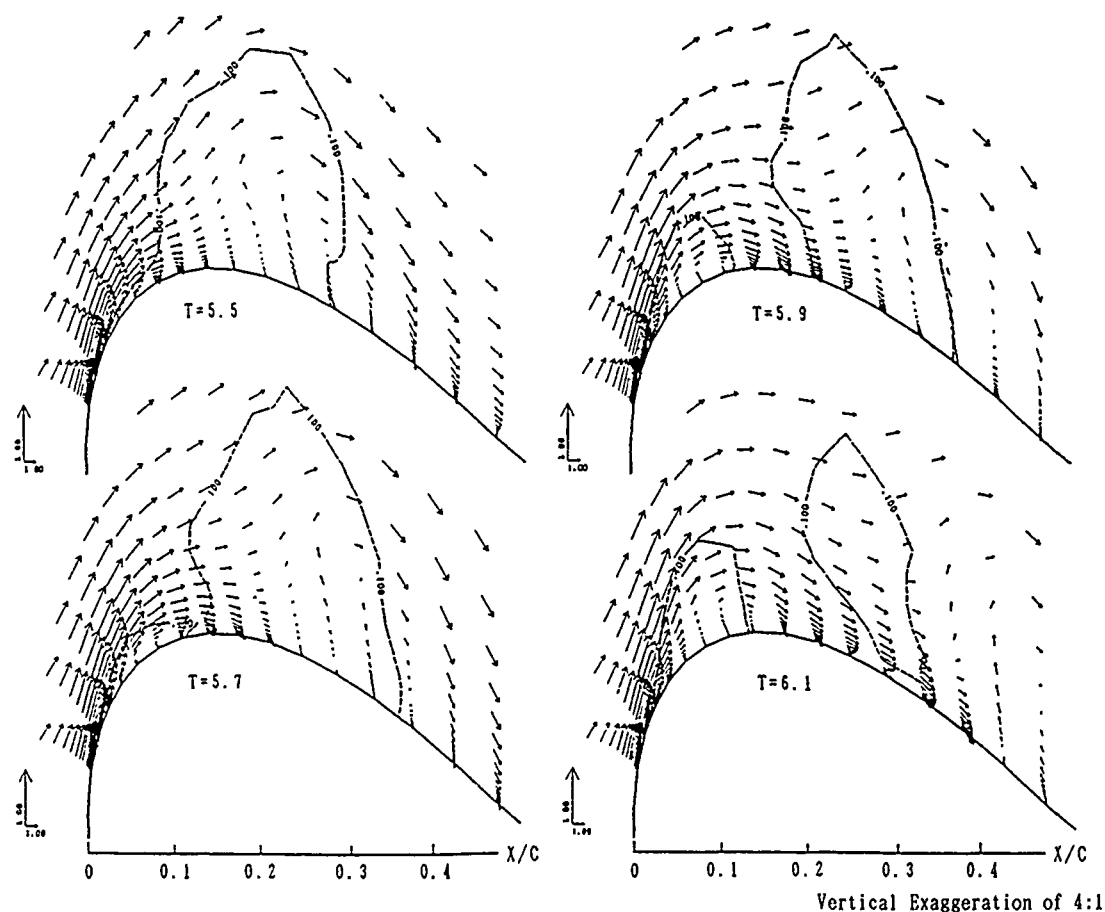


Figure 23 Close-ups of velocity vectors around NACA0015 hydrofoil, $\sigma=1.0$; $\alpha=8.0\text{deg.}$; $Re=3.0 \times 10^5$, the bold broken lines are void fraction contours of 0.1.

20. Kiya, M. et al., J.Fluid Mech., Vol.154, pp.463-491 (1985).
21. Roache, P.J., "Computational Fluid Dynamics", Hermosa Publishers (1976).
22. Kodama, Y. et al., J. Fluids Eng., Trans. of ASME, Vol.103(4), pp.557 (1981).
23. Lamb, H., Dover Pub., "Hydrodynamics", pp.112 (1932).
24. Kubota, A. et al., Theoretical and Applied Mechanics, Vol.36, University of Tokyo Press, pp.93-100 (1988).
25. Harlow, F.H. et al., Phys. Fluids, Vol.8, No.12, pp.2182 (1965).
26. Kawamura, T. et al., AIAA paper 84-0341 (1984).
27. Thompson, J.F. et al., "Numerical Grid Generation", Elsevier Science Pub. (1985).
28. Abbott, I.H. et al., "Theory of Wing Sections", Dover Publications (1958).
29. Kubota, A., Doctoral Dissertation, Department of Naval Architecture, University of Tokyo (1988).
30. Kodama, Y., J. Soc. Naval Architects of Japan, Vol.164, pp.1-8 (1988).
31. Hess, J.L. et al., Progress in Aero. Science, Pergamon Press, Vol.8 (1967).
32. Izumida, Y. et al., Proc. 10th IAHR Symp, Tokyo, pp.169-181 (1980).
33. Yamaguchi, H. et al., J. Soc. Naval Architects of Japan, Vol.164, pp.28-42 (1988).
34. Curle, N. et al., Aero. Quart., Vol.8, pp.257 (1957).
35. Cebeci, T. et al., "Momentum Transfer in Boundary Layer", Hemisphere Co (1977).
36. Fujikawa, S. et al., Proc. Int. Symp. on Cavitation, Vol.1, Sendai, Japan, pp.55-60 (1986).
37. Yamaguchi, H. et al., LDV and Hot Wire/Film Anemometry, pp.29-38 (1985).
38. Kato, H. et al., Proc. Vol.2 18th ITTC, Kobe, pp.433-437 (1987).
39. Kermeen, R.W., Hydrodynamic Lab., CALTEC, Pasadena, California, Report No. 47-5 (1956).
40. Wade, R.B. et al., J.Fluid Eng. Trans. ASME, Vol.88, No.1, pp.273-283 (1966).
41. Alexander, A.J., Conf. on Cavitation, Edinburgh, IME, pp.27-35 (1974).
42. Shen, Y.T. et al., 12th Symp. on Naval Hydro., Washington, pp.470-493 (1978).
43. Franc, J.P. et al., J. Fluid Mech., Vol.154, pp.63-90 (1985).

DISCUSSION

by F. Stern

I would like to congratulate the authors on a very interesting paper which appears to present a new approach for unsteady cavitation. The authors discuss the fact that cloud cavitation is often periodic. In my own work on unsteady cavitation (Stern, F., "Comparison of Computational and Experimental Unsteady Cavitation on a Pitching Foil", J. of Fluids Engineering, Vol.111, No.3, September 1989, pp.290-299), close correlation was shown between the experimental cloud-cavitation shedding frequency and the predicted cavity natural frequency. Do the authors' results provide an estimate for the cloud-cavitation shedding frequency and how does it compare with the experimental value?

Author's Reply

The authors would like to thank Prof. F. Stern for his valuable discussion.

The computed time period of cavitation cloud shedding, which is nondimensionalized based on the uniform flow velocity and the chord length of the hydrofoil, is about 1.4 at a cavitation number of 1.0. The

dimensionalized shedding period is $1.4 \times (\text{chord length}) / (\text{uniform flow velocity})$. It becomes 0.0117 sec (85.7 Hz) when the chord length and the uniform flow velocity are 50 mm and 6.0 m/s, respectively (the experimental condition). The authors did not measure the time period of the cavitation cloud in their experiments. However, the authors' similar experiment [A1] showed that the nondimensionalized time period of cloud cavitation shedding was 2.1. This value is very close to the present computed result.

The main purpose of this study was to clarify the generation mechanism of cloud cavitation. The computed result showed a close relationship between the behavior of the separated shear layer and the cavitation cloud. This is because the cavitation cloud shedding frequency also depends on the Reynolds number. Further theoretical investigation is needed to predict the cavitation cloud shedding frequency for arbitrary flow conditions.

[A1] Kubota, A. et al.: Unsteady Structure Measurement of Cloud Cavitation on a Foil Section Using Conditional Sampling Technique, ASME J. Fluid Eng., Vol.111, No.2, 1989, pp.204-210

Theoretical Prediction of Midchord and Face Unsteady Propeller Sheet Cavitation

S. A. Kinnas and N. E. Fine
Massachusetts Institute of Technology
Cambridge, USA

Abstract

In this work, first the linearized hydrofoil problem with arbitrary cavity detachment points is formulated in terms of unknown source and vorticity distributions. The corresponding integral equations are inverted analytically and the results are expressed in terms of integrals of quantities which depend only on the hydrofoil shape.

Then, the cavitating hydrofoil problem is solved numerically by discretizing the problem into point source and vortex distributions and by applying the boundary conditions at appropriately selected collocation points.

Finally, the discrete vortex and source method is extended to predict unsteady propeller sheet cavitation with arbitrary midchord and/or face detachment.

1 Introduction

Cavitation has always been a great concern in the design of marine propellers. A successful propeller design is one which precludes cavitation at design conditions. In recent times, however, with an increasing demand for higher propeller loadings and higher efficiencies, the propeller cavitation is very often unavoidable. The task of the hydrodynamicist is, therefore, to predict and control the propeller cavitation and its undesirable side effects. An analysis method for the prediction of unsteady propeller cavitation is, therefore, an indispensable design tool. Furthermore, this propeller cavitation analysis method should be able to treat cavities which start on the suction side behind the leading edge towards the blade midchord and/or on the pressure side, "face", of the propeller in front of the blade trailing edge, since these types of cavitation are very likely to occur at the design conditions.

Cavitating or free-streamline flows have been studied extensively in the last century. First, the flow around flat plates or polygonal bodies at zero cavitation number was analyzed. The analysis of these problems was achieved by applying the hodograph technique as introduced by

Helmholtz and Kirchhoff [3] more than a century ago.

The analysis of cavitating flows at non-zero cavitation numbers created a lot of diversity on the cavity termination models, i.e. the Riabouchinsky model [28], the reentrant jet model [7], [21], the spiral vortex models [32], etc. A complete description of the different cavity termination models can be found in [32] and [38]. The difficulty of the hodograph technique to treat general shaped boundaries necessitates the introduction of the linearized cavity theory.

Linear theory was first applied by Tulin [30] to the problem of a supercavitating symmetric section at zero incidence and zero cavitation number. It was then applied to general camber meanlines at zero cavitation number [33], and to a supercavitating flat plate at incidence and arbitrary cavitation numbers [31].

Linear theory was subsequently extended to supercavitating hydrofoils of general shape at non-zero cavitation numbers [39], [11], [27], [8], [29].

The partially cavitating hydrofoil problem has also been addressed in linear theory and analytical results have been produced for some special hydrofoil geometries [1], [13], [12], [14], [37].

The problem of a supercavitating hydrofoil with arbitrary cavity detachment was first formulated by Fabula [8], who also gave results for a flat plate with different detachment points.

Hanaoka [15] formulated the linearized partial and supercavitating hydrofoil problem with arbitrary cavity detachment. He also gave series representations for the cavitation number and the hydrodynamic coefficients when the hydrofoil shape could be expressed in terms of polynomials in the chordwise coordinate. Nishiyama and Ota [29] also gave integral expressions in terms of known quantities, for the cavitation number and the hydrodynamic coefficients for general shape hydrofoils with arbitrary detachment.

An alternative way of formulating the linearized partial and supercavitating problem has been given in [21] and [20]. The linearized boundary conditions have been

expressed in terms of singular integral equations of unknown source and vorticity distributions. Those integral equations are inverted analytically and expressions for the cavitation number, the source and vorticity distributions are given in terms of integrals of functions which depend only on the geometry of the hydrofoil. Those integrals are then computed numerically and the cavity shapes are finally computed [21], [20]. The same technique has also been extended for partial cavities with arbitrary detachment [23]. The leading edge correction has also been implemented in the formulation of the cavitating hydrofoil problem to account for the non-linear foil thickness effects [23].

In the present work, the technique used in [21] for supercavitating hydrofoils is extended to treat supercavities with arbitrary detachment on either the suction side and/or the pressure side of the hydrofoil. The effect of the detachment point on the cavity shapes and foil pressure distributions is investigated. In the case where the supercavity detaches on the pressure side in front of the trailing edge, an equation for the chordwise location of the cavity detachment point is given.

The cavitating hydrofoil problem with arbitrary suction and/or pressure cavity detachment is then solved by employing a discrete vortex and source method.

A numerical vortex and source lattice method has been developed at MIT for the prediction of the unsteady propeller sheet cavitation in spatially non-uniform wakes [25], [4], [18]. The computer program which implements this method is called PUF-3.

Finally, PUF-3 is modified to predict unsteady propeller sheet cavitation with arbitrary detachment on either the pressure or the suction side of the propeller. The effect of the location of the cavity detachment on the time history of the cavity volume and the cavity shapes is investigated.

2 The Cavitating Hydrofoil - The Analytical Method

In this section, the linearized cavitating hydrofoil problem is formulated in terms of unknown vorticity and source distributions. For given cavity length and specified cavity detachment points, the involved singular integral equations are inverted analytically. Expressions are then found for the corresponding cavitation number, vorticity and source distributions in terms of integrals of quantities which depend only on the foil geometry.

First, the supercavitating hydrofoil problem for three different cavity detachment situations is considered.

2.1 Leading Edge Detachment

Consider a hydrofoil of chord length one, subject to a uniform flow U_∞ and supercavitating at a length $x = l$, as shown in Figure 1. The cavity starts at the leading edge $x = 0$ on the suction side and at the trailing edge $x = 1$ on the pressure side.

The corresponding cavitation number σ is defined as.

$$\sigma = \frac{p_\infty - p_v}{\frac{\rho}{2} U_\infty^2} \quad (1)$$

where p_∞ is the ambient pressure and p_v the vapor pressure inside the cavity.

In the context of the linearized cavity theory the corresponding Hilbert problem can be formulated [21] in terms of vorticity and source distributions $\gamma(x)$ and $q(x)$ respectively, located on the x axis as shown in Figure 1.

With the use of the definitions:

$$\bar{\gamma}(x) = \frac{\gamma(x)}{\sigma U_\infty} \quad (2)$$

and

$$\bar{q}(x) = \frac{q(x)}{\sigma U_\infty}, \quad (3)$$

the complete boundary value problem becomes [21]:

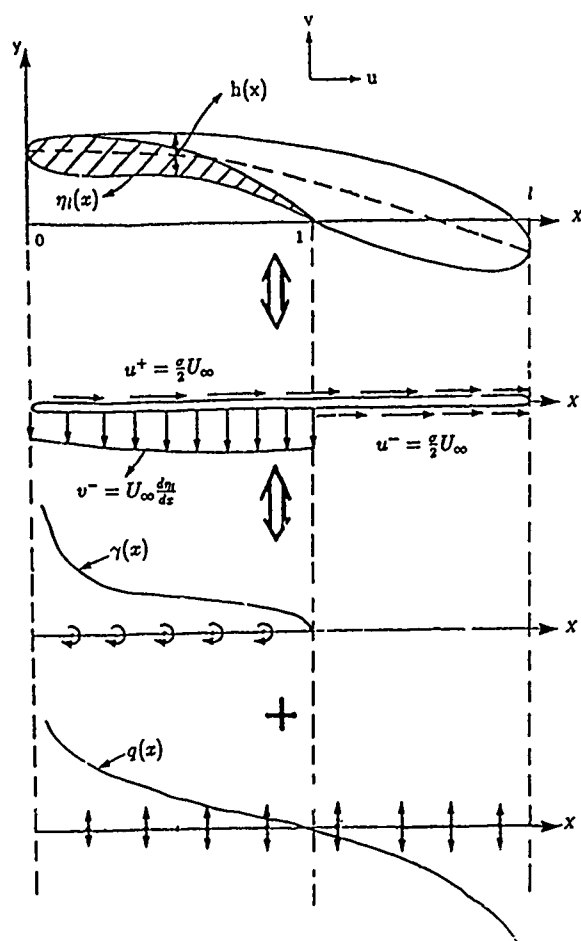


Figure 1: Supercavitating hydrofoil

1. Kinematic Boundary Condition

$$-\frac{\bar{q}}{2} + \frac{1}{2\pi} \int_0^l \frac{\bar{\gamma}(\xi) d\xi}{\xi - x} = \Theta_l^*(x) \quad 0 < x < l; \quad y = 0^- \quad (4)$$

2. Dynamic Boundary Condition

$$\frac{\bar{q}}{2} - \frac{1}{2\pi} \int_0^l \frac{\bar{\gamma}(\xi) d\xi}{\xi - x} = \frac{1}{2} \quad 0 < x < l \quad y = 0^+ \quad (5)$$

3. Kutta condition

$$\bar{\gamma}(l) = 0 \quad (6)$$

4. Cavity Closure Condition

$$\int_0^l \bar{q}(x) dx = 0 \quad (7)$$

where

$$\Theta_l^* = \frac{1}{\sigma} \frac{d\eta_l}{dx} \quad (8)$$

and, $\eta_l(x)$ is the ordinate of the lower hydrofoil surface, as shown in Figure 1.

The singular integral equations of Cauchy type, 4 and 5, can be inverted to produce expressions for the unknown σ , $\gamma(x)$ and $q(x)$ in terms of the cavity length l and $\eta_l(x)$, as follows [21]:

$$\sigma = \frac{4\sqrt{2}r^4}{\pi(r^2 + 1)} \int_0^l \sqrt{\frac{\eta}{t - \eta}} \cdot \frac{\sqrt{r^2 + 1} + \eta\sqrt{r^2 - 1}}{(1 + \eta^2)^2} \left[-\frac{\partial \eta_l}{\partial x} \right] d\eta \quad (9)$$

$$\bar{\gamma}(z) = -\frac{(1 + z^2)}{\pi} \sqrt{\frac{t - z}{z}} \int_0^l \sqrt{\frac{\eta}{t - \eta}} \frac{\frac{z}{2} - \Theta_l^*(\eta)}{(1 + \eta^2)(z - \eta)} d\eta \quad (10)$$

$$\bar{q}(z) = -\Theta_l^*(z) + \sqrt{\frac{t + z}{z}} \cdot \frac{(\sqrt{r^2 - 1} - z\sqrt{r^2 + 1})}{2\sqrt{2}r^2} - \frac{1 + z^2}{\pi} \sqrt{\frac{t + z}{z}} \int_0^l \sqrt{\frac{\omega}{t - \omega}} \frac{\Theta_l^*(\omega) d\omega}{(1 + \omega^2)(z + \omega)} \quad (11)$$

for $z < t$, and:

$$\begin{aligned} \bar{q}(z) = & \sqrt{\frac{t + z}{z}} \cdot \frac{(\sqrt{r^2 - 1} - z\sqrt{r^2 + 1})}{2\sqrt{2}r^2} - \\ & \frac{1 + z^2}{\pi} \sqrt{\frac{t + z}{z}} \int_0^l \sqrt{\frac{\omega}{t - \omega}} \frac{\Theta_l^*(\omega) d\omega}{(1 + \omega^2)(z + \omega)} - \\ & \sqrt{\frac{z - t}{z}} \cdot \frac{(z\sqrt{r^2 + 1} + \sqrt{r^2 - 1})}{2\sqrt{2}r^2} - \\ & \frac{1 + z^2}{\pi} \sqrt{\frac{z - t}{z}} \int_0^l \sqrt{\frac{\omega}{t - \omega}} \frac{\Theta_l^*(\omega) d\omega}{(1 + \omega^2)(z - \omega)} \quad (12) \end{aligned}$$

for $z > t$, where:

$$z = \sqrt{\frac{x}{l - x}}, \quad t = \sqrt{\frac{1}{l - 1}}, \quad r^4 = 1 + t^2 \quad (13)$$

The integrals in equations 9, 10, 11 and 12 are computed numerically with special care taken at the singularities of the integrands [21].

The cavity thickness $h(x)$, which also includes the foil thickness as shown in Figure 1, is determined by integrating the equation:

$$U_\infty \frac{dh}{dx} = q(x) \quad (14)$$

2.2 Face Detachment

For thick symmetric foils at small angles of attack and for many foils at negative angles of attack, it is found that the supercavity detaches forward of the trailing edge on the pressure side of the foil, as shown in Figure 2.

The point of separation, s , may be found by considering the following two conditions:

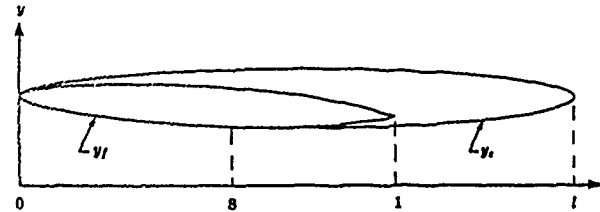


Figure 2: Face detachment on a supercavitating hydrofoil

1. the pressure on the wetted foil surface must be greater than the cavity pressure
2. the cavity and foil surface must not intersect aft of the separation point.

In linear theory, condition 1 is equivalent to

$$\gamma(x) > 0 \quad \text{for } 0 < x < s \quad (15)$$

The corresponding boundary value problem may be solved by using the analysis in the previous section and by considering as foil the part of the original foil between $x = 0$ and $x = s$, cavitating at a cavity length l/s .

The vorticity distribution between $x = 0$ and $x = s$ is given by equation 10, with the cavity length, however, being scaled to l/s . The behavior of the vorticity distribution at $x = s$ can be found, by using equation 10, to be as follows:

$$\gamma(x) \sim A(s, l) \sqrt{s - x} \quad (16)$$

where A , for a given foil geometry, depends only on the point of separation and the length of the cavity:

$$A(s, l) = -\frac{\pi}{2\sqrt{2}r^2} \cdot \frac{1}{1 + z_s^2} \left[\sqrt{r^2 - 1} + z_s \sqrt{r^2 + 1} \right]$$

$$\begin{aligned}
& + \int_0^t \sqrt{\frac{\eta}{t-\eta}} \cdot \frac{\Theta_t^*(z_s) - \Theta_t^*(\eta)}{(z_s - \eta)(1 + \eta^2)} d\eta \\
& + \Theta_t^*(z_s) \frac{\pi}{\sqrt{2}r^2} \cdot \frac{[\sqrt{r^2 + 1} - z_s \sqrt{r^2 - 1}]}{1 + z_s^2} \quad (17)
\end{aligned}$$

where

$$z_s = \sqrt{\frac{s}{l-s}}; \quad t = \sqrt{\frac{1}{l-1}}; \quad r^2 = \sqrt{1+t^2} \quad (18)$$

By observing the behavior of the vorticity distribution by varying s , we conclude that the correct detachment point is the one for which the vorticity distribution goes to zero at s with zero slope. This can be seen in Figures 3 to 5, where the cavity shapes and the vorticity distributions as predicted by the presented analytical method, are shown for different detachment points. In Figure 3, the circulation distribution is negative at the trailing edge ($A(s, l) < 0$), thus violating the condition 15. In Figure 4 the vorticity distribution is positive everywhere on the foil ($A(s, l) > 0$), but the cavity intersects the foil. The correct detachment point is somewhere between these two, and the one which satisfies both conditions is the one for which the vorticity has a zero slope at s , which is shown in Figure 5. At this point, we should have:

$$A(s, l) = 0 \quad (19)$$

A different approach of deriving equation 19, is given in Appendix A.

The detachment point is determined by solving equation 19 with respect to s numerically, utilizing a Newton Raphson (secant) method [9]. A typical case requires about five iterations, depending on the accuracy of the initial guesses.

The effect of the location of the detachment point on the cavitation number and the lift and drag coefficients is shown in Table 1. The importance of the correct face

S	CL	CD	SIGMA
.200	.0136	.0010	.1224
.542	.0247	.0018	.1329
.700	.0138	.0017	.1248

Table 1: Lift and drag coefficient and cavitation number for the foils shown in Figures 3, 4 and 5.

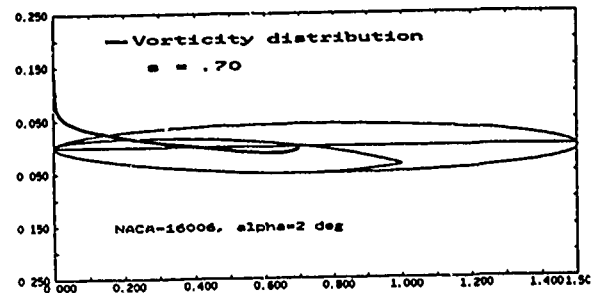


Figure 3: Cavity shape and vorticity distribution - $A(s, l) < 0$

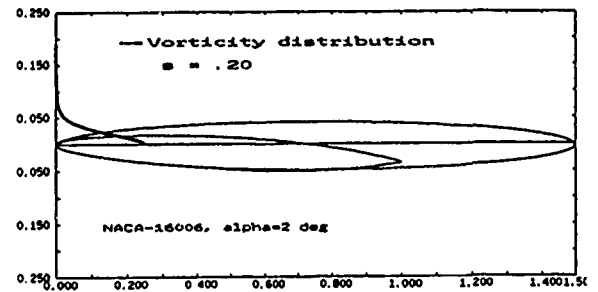


Figure 4: Cavity shape and vorticity distribution - $A(s, l) > 0$

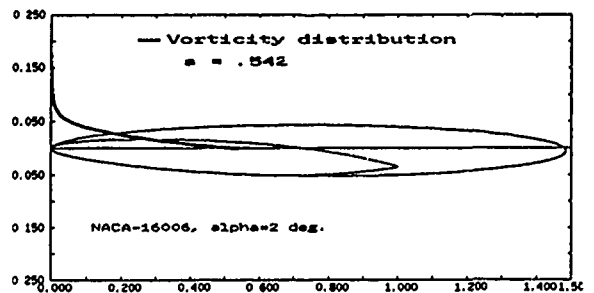


Figure 5: Cavity shape and vorticity distribution - $A(s, l) = 0$

detachment point in the prediction of the cavity extent and the forces on the foil is apparent.

Some further discussion on the determination of the correct cavity detachment point is given in the Section 6.

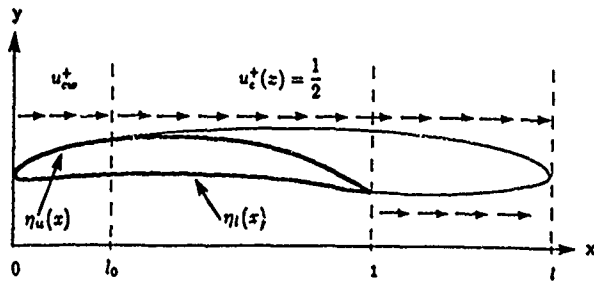


Figure 6: Midchord detachment on a supercavitating foil.

2.3 Midchord Detachment

For the case where the supercavity detaches aft of the leading edge on the suction side of the foil, as shown in Figure 6, the linearized boundary value problem can be formulated as follows:

The dynamic boundary condition on the cavity:

$$\frac{\bar{\gamma}(x)}{2} - \frac{1}{2\pi} \int_0^l \frac{\bar{\gamma}(\xi)d\xi}{\xi - x} = u_c^+(x) = \frac{1}{2} \quad l_0 < x < l, \quad y = 0^- \quad (20)$$

The kinematic boundary condition on the pressure side:

$$-\frac{\bar{q}}{2} + \frac{1}{2\pi} \int_0^l \frac{\bar{\gamma}(\xi)d\xi}{\xi - x} = \Theta_l^* \quad 0 < x < l, \quad y = 0^- \quad (21)$$

The kinematic boundary condition on the suction side:

$$\frac{\bar{q}}{2} + \frac{1}{2\pi} \int_0^l \frac{\bar{\gamma}(\xi)d\xi}{\xi - x} = \Theta_u^* \quad 0 < x < l_0, \quad y = 0^+ \quad (22)$$

where:

$$\Theta_u^* = \frac{1}{\sigma} \frac{d\eta_u}{dx} \quad (23)$$

with η_u being the ordinate of the upper hydrofoil surface as shown in Figure 6.

Equations 20 and 21 can be reduced to the following form:

$$\frac{\bar{\gamma}^*}{2} - \frac{1}{2\pi} \int_0^l \frac{\bar{\gamma}(\xi)d\xi}{\xi - x} = \frac{1}{2} \quad 0 < x < l \quad (24)$$

$$-\frac{\bar{q}}{2} + \frac{1}{2\pi} \int_0^l \frac{\bar{\gamma}^*d\xi}{\xi - x} = \Theta_2^*(x) \quad 0 < x < 1 \quad (25)$$

with the use of the definitions:

$$\begin{aligned} \bar{\gamma}^* &= \bar{\gamma} - 2(u_{cw}^+ - \frac{1}{2}) ; \quad 0 < x < l_0 \\ \bar{\gamma}^* &= \bar{\gamma} ; \quad l_0 < x < 1 \end{aligned} \quad (26)$$

and,

$$\Theta_2^* \stackrel{\text{def}}{=} \Theta_l^* + F \quad (27)$$

with:

$$F(x) \stackrel{\text{def}}{=} -\frac{1}{\pi} \int_0^{l_0} \frac{u_{cw}^+ - \frac{1}{2}}{\xi - x} d\xi \quad (28)$$

where u_{cw}^+ is the horizontal perturbation velocity on the wetted part on the suction side of the foil.

Equations 25 and 24 are in the same form as equations 4 and 5. Therefore, to invert these equations the same methodology can be followed as described in section 2.1. The perturbation velocity u_{cw}^+ , however, is still an unknown.

To determine u_{cw}^+ for $0 < x < l_0$ the kinematic boundary condition, equation 22, is applied. The solution for u_{cw}^+ is described in Appendix B.

The analysis described in this section has been applied for a VLR section [16] and the results are shown in Figure 7. The top of Figure 7 shows the predicted cavity shape for a midchord detachment at $l_0 = 0.2$. At the lower part of Figure 7, the corresponding total source distribution is shown together with the thickness source distribution. Notice that the two source distributions are identical for $0 < x < l_0$, as required by equation 56.

The described theory is applied for a VLR foil [16] for a fixed cavity length $l = 1.5$ and for different values of the detachment point l_0 . The predicted cavity shapes and pressure distributions on the suction side are shown in Figures 8 to 11. The cavities in Figures 8 and 9 are unacceptable, because they intersect the foil surface. The cavity in Figure 11 is also unacceptable because it produces pressures in front of the detachment point which are smaller than the cavity pressure. The correct detachment point seems to be the one corresponding to Figure 10. It appears to be the point for which the pressure distribution in front of the detachment point has a zero slope. No attempt has been made by the authors, however, to generalize this condition, since the detachment point on the suction side should be determined by the viscous flow in front of the cavity [10], rather than by any other potential flow criterion. Some more discussion on cavity detachment is given in section 6.

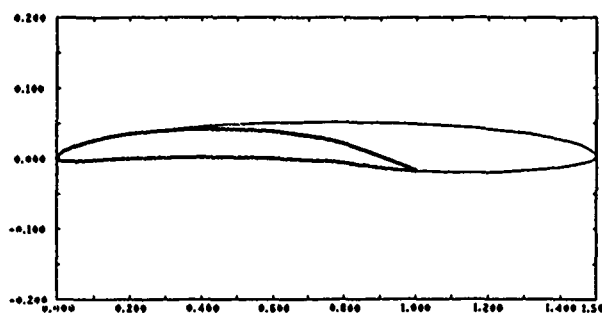


Figure 7: Cavity shape, total and thickness source distributions for a VLR thickness profile with NACA $a=.8$ meanline supercavitating with midchord detachment $l_0 = .20$.

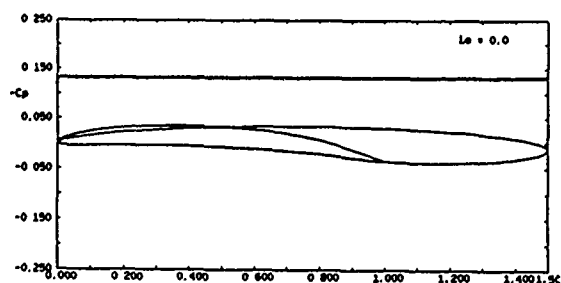


Figure 8: Cavity shape and pressure distribution on the suction side of a supercavitating foil with cavity detachment at $l_0 = 0$. VLR thickness form and NACA $a=0.8$ meanline, maximum thickness/chord=0.04, maximum camber/chord=0.03, $\rho_L = 0.001613$, $\alpha = 2^\circ$, $l = 1.5$

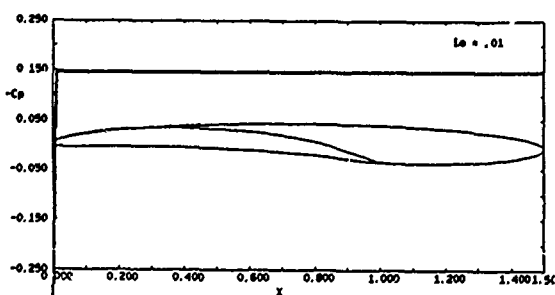


Figure 9: Cavity shape and pressure distribution on the suction side of a supercavitating foil with cavity detachment at $l_0 = 0.01$. Same foil as in Figure 8

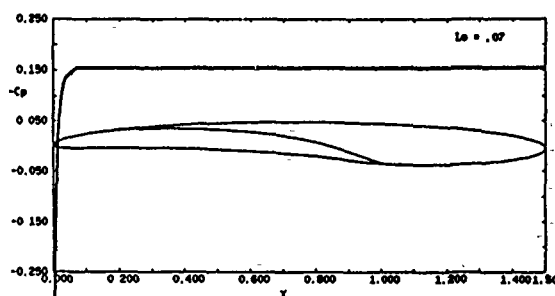


Figure 10: Cavity shape and pressure distribution on the suction side of a supercavitating foil with cavity detachment at $l_0 = 0.07$. Same foil as in Figure 8

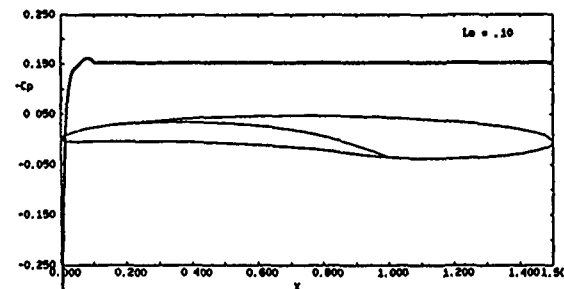


Figure 11: Cavity shape and pressure distribution on the suction side of a supercavitating foil with cavity detachment at $l_0 = 0.10$. Same foil as in Figure 8

2.4 Partial Cavities

In the case where the cavity is smaller than the chord of the foil, as shown in Figure 12, the linearized cavity problem can be formulated in a similar way as in the case of the supercavitating foil, in terms of vorticity and cavity source distributions [20], [18], [22].

For given cavity end, l , and cavity detachment, l_0 , the corresponding cavitation number, the vorticity and cavity source distributions can be given in terms of integrals of u_w^+ , the horizontal perturbation velocity of the fully wetted foil, between l_0 and l [23].

2.5 The Leading Edge Correction

The linearized partial cavity theory is known to predict that, for given flow conditions, increasing the foil thickness results in an increase in the cavity extent and volume. This is contrary to experimental evidence, the non-linear theory [35], and the short cavity theory [34].

An alternative way of including the non-linear thickness effects in the linear cavity theory can be achieved via the *leading edge correction* [23], [22]. It essentially consists of including Lighthill's correction [26] in the formulation of the linearized cavity problem. It can be proven [23] that this can be achieved by modifying the linearized dynamic boundary condition on the cavity from

$$u_c = \frac{\sigma}{2} U_\infty ; \text{ on the cavity} \quad (29)$$

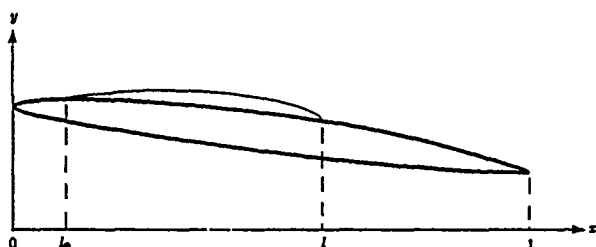


Figure 12: Partially cavitating hydrofoil

to

$$u_c = (\sqrt{1 + \sigma \sqrt{\frac{x + \rho_L/2}{x}}} - 1)U_\infty; \text{ on the cavity (30)}$$

where x is the distance from the foil leading edge and ρ_L is the leading edge radius.

The modified boundary value problem with the introduction of equation 30 has been solved and the solution has been expressed in terms of integrals of known quantities [23].

A direct comparison of the linear cavity theory, with or without the leading edge correction, and the non-linear theory is shown in Figures 13 and 14. The cavity shapes as predicted by the linear theory, with or without the leading edge correction, are added normal to the foil and the produced foil geometry is analyzed with a potential based panel method [17], where the exact kinematic boundary condition is applied on the exact foil or cavity surface. The pressure distributions produced from the panel method are shown in Figures 13 and 14, together with the linearized pressure distributions from linear theory with or without the leading edge correction. In these Figures the pressure distribution from the linear theory with or without the leading edge correction is constant on the cavity, since this has been required via the dynamic boundary condition. The pressure distribution from the panel method, however, is not exactly constant on the cavity and this is a measure of the accuracy of the linear cavity theory. Comparing Figures 13 and 14, the substantial improvement of the linear theory, when the leading edge correction is included, becomes apparent.

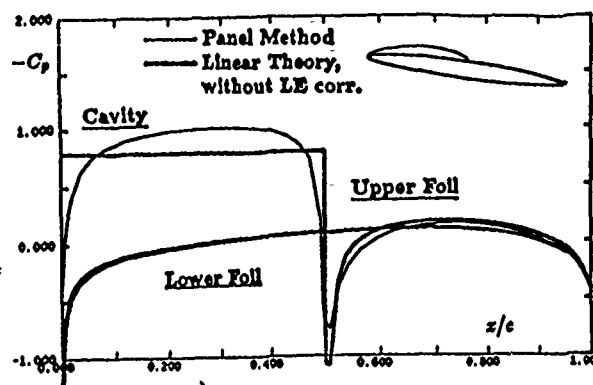


Figure 13: Pressure distributions on an NACA 16-009 section with a 30% cavity at $\alpha = 3^\circ$ from panel method and linear theory *without* leading edge corrections. $C_p = p - p_\infty / \rho U_\infty^2 / 2$

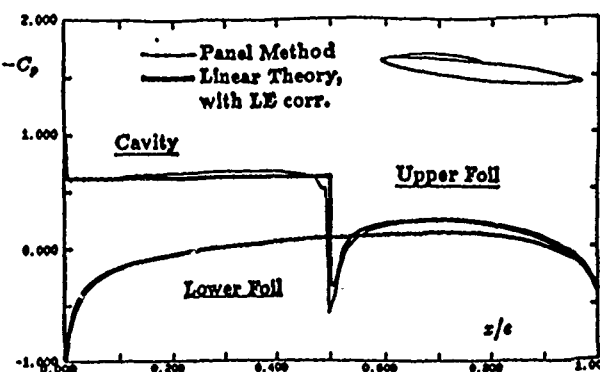


Figure 14: Pressure distributions on an NACA 16-009 section with a 50% cavity at $\alpha = 3^\circ$ from panel method and linear theory *with* leading edge corrections. $C_p = p - p_\infty / \rho U_\infty^2 / 2$

3 The Cavitating Hydrofoil- The Numerical Method

The numerical method consists of discretizing the chord and the cavity into a finite number of segments on which the vorticity and source distributions are approximated with point vortices and sources respectively.

The spacing of the panels is half cosine on the foil and constant in the wake. The arrangement of the vortex and source panels is shown in Figure 15. The following notation is used:

- $X_{p_i}^s$ = boundaries of source panels
- X_{s_i} = position of point sources
- $X_{p_i}^v$ = boundaries of vortex panels
- X_{v_i} = position of point vortices
- X_{k_i} = position of kinematic boundary condition collocation points
- X_{d_i} = position of dynamic boundary condition collocation points

(31)

The arrangement of the vortex and source panels is such that the expected source and vorticity singularities at the leading edge of the foil, as well as the square root singularity of the source distribution at the trailing edge of the cavity, are modeled accurately. The collocation points for the application of the kinematic and dynamic boundary conditions are chosen such that the Cauchy principal value of the involved singular integrals is computed accurately. The detailed analysis for the selection of the panels and control points is given in [18], [6] and [9].

The presented numerical method was developed originally for partially and supercavitating hydrofoils with the cavities starting at the leading edge on the suction side and at the trailing edge on the pressure side of the foil [6], [18], [9].

To extend the numerical method to also predict face and/or midchord supercavities, we assume that the detachment points are X_s on the suction side and X_p on the pressure side. The points X_s and X_p coincide with any of the source panel boundaries $X_{p_i}^s$ on the foil.

By separating the total source q into the thickness source q_c and the cavity source q_w , the corresponding boundary integral equations become:

The kinematic boundary conditions

$$\frac{q_c}{2} + \frac{1}{2\pi} \int_0^1 \frac{\gamma(\xi) d\xi}{\xi - x} = U_\infty \frac{d\eta}{dx} \quad y = 0^+ \quad 0 < x < X_s \quad (32)$$

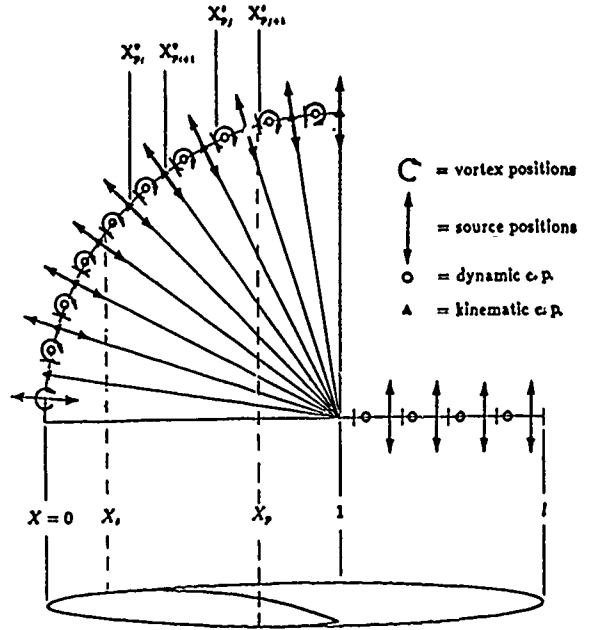


Figure 15: Discrete singularities method for supercavitating foil with arbitrary detachment points

$$-\frac{q_c}{2} + \frac{1}{2\pi} \int_0^1 \frac{\gamma(\xi) d\xi}{\xi - x} = U_\infty \frac{d\eta}{dx} \quad y = 0^- \quad 0 < x < X_p \quad (33)$$

where $\eta(x)$ is the foil mean camber surface.

The dynamic boundary conditions

$$-U_\infty \frac{\sigma}{2} + \frac{\gamma}{2} - \frac{1}{2\pi} \int_0^1 \frac{q_c(\xi) d\xi}{\xi - x} = u_{th} \quad y = 0^+ \quad X_s < x < 1 \quad (34)$$

$$-U_\infty \frac{\sigma}{2} - \frac{\gamma}{2} - \frac{1}{2\pi} \int_0^1 \frac{q_c(\xi) d\xi}{\xi - x} = u_{th} \quad y = 0^- \quad X_p < x < 1 \quad (35)$$

where u_{th} is the horizontal perturbation velocity due to foil thickness, given as:

$$u_{th} = \frac{1}{2\pi} \int_0^1 \frac{q_w(\xi) d\xi}{\xi - x} \quad (36)$$

To discretize the above integral equations, we make the following definitions:

- N = number of discrete vortices Γ_i
- M = number of discrete cavity sources Q_i
- NS = number of fully wetted panels upstream of X_s
- NP = number of fully wetted panels upstream of X_p

The strengths of the discrete vortices and cavity sources are related to the corresponding vorticity and source distributions as follows:

$$\Gamma_i = \gamma(X_{v_i}) \cdot (X_{p_{i+1}}^v - X_{p_i}^v) \quad (37)$$

$$Q_i = \bar{q}_c^i \cdot (X_{p_{i+1}}^s - X_{p_i}^s) \quad (38)$$

where \bar{q}_c^i is the mean value of the cavity source at the corresponding source panel.

At this point, we will assume, without loss of generality, that $U_\infty = 1$.

The discretized boundary conditions become:

The kinematic boundary conditions

a) On the suction side:

$$\frac{Q_i}{2(X_{p_{i+1}}^s - X_{p_i}^s)c_i^f} - \frac{1}{2\pi} \sum_{j=1}^N \frac{\Gamma_j}{X_{k_i} - X_{v_j}} = \left(\frac{d\eta}{dx} \right)_i \quad i = 1, \dots, NS \quad (39)$$

b) On the pressure side:

$$-\frac{Q_i}{2(X_{p_{i+1}}^s - X_{p_i}^s)c_i^f} - \frac{1}{2\pi} \sum_{j=1}^N \frac{\Gamma_j}{X_{k_i} - X_{v_j}} = \left(\frac{d\eta}{dx} \right)_i \quad i = 1, \dots, NP \quad (40)$$

where c_i^f is defined as: $c_i^f = \bar{q}_c^i / q_c(X_{s_i})$ and is approximated with its value for a flat plate cavitating at the same cavity length [6] and [9].

The dynamic boundary conditions

a) On the suction side:

$$-\frac{\sigma}{2} + \frac{\Gamma_i}{2(X_{p_{i+1}}^v - X_{p_i}^v)} + \frac{1}{2\pi} \sum_{j=1}^M \frac{Q_j}{X_{d_i} - X_{s_j}} = u_{th}^i \quad i = NS + 1, \dots, M \quad (41)$$

b) On the pressure side:

$$-\frac{\sigma}{2} - \frac{\Gamma_i}{2(X_{p_{i+1}}^v - X_{p_i}^v)} + \frac{1}{2\pi} \sum_{j=1}^M \frac{Q_j}{X_{d_i} - X_{s_j}} = u_{th}^i \quad i = NP + 1, \dots, N \quad (42)$$

The cavity closure condition:

$$\sum_{i=1}^M Q_i = 0 \quad (43)$$

There are N+M+1 unknowns:

- N discrete vortices Γ_i

- M discrete cavity sources Q_i

- 1 cavitation number σ

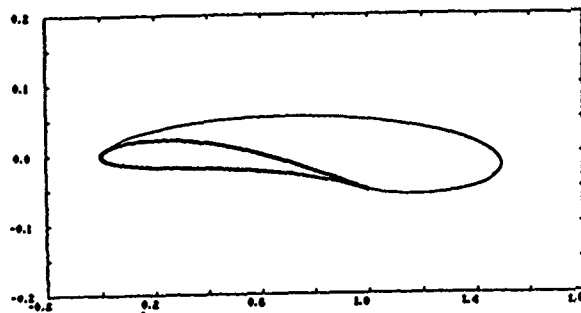
There are also N+M+1 equations:

- NP + NS kinematic boundary conditions
- M - NP + N - NS - 1 dynamic boundary conditions
- 1 cavity closure condition
- 1 equation relating Γ_1 to Q_1

The last equation, which relates the discrete singularities Q_1 and Γ_1 , replaces the first dynamic boundary condition [18]. However, in the case of midchord detachment, there is no dynamic boundary condition to be satisfied on the first source panel and this relation is not applied.

The convergence of the described numerical method is shown in Table 2 for different numbers of elements on the foil. The analytical results shown in Table 1 have been found by using the analysis described in Section 2.

Finally, the predicted cavity shapes from the analytical and the numerical method are shown in Figure 16.



# of Elements	Numerical Sigma	Analytical Sigma	Numerical Volume	Analytical Volume
5	.3057	.2357	.0988	.0771
10	.2082	.2070	.0883	.0872
20	.2111	.2110	.0852	.0853
40	.2131	.2131	.0843	.0844
80	.2095	.2100	.0858	.0858
100	.2095	.2099	.0859	.0858

Table 2: Convergence of the numerical method. Supercavitating Joukowski thickness form with parabolic meanline, maximum thickness/chord=0.04, maximum camber/chord=0.02, $\alpha = 3^\circ$, $l = 1.5$

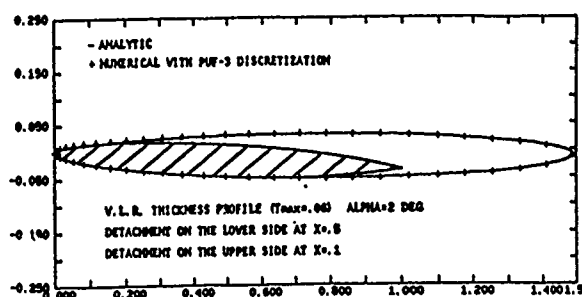


Figure 16: Cavity shapes from numerical and analytical method

4 The Unsteady Cavitating Propeller Numerical Method.

A numerical method has been developed for the unsteady sheet cavitation of marine propellers in spatially non-uniform wakes [25], [4], [18]. The corresponding computer code is called PUF-3. The complete three dimensional linearized unsteady cavity problem is solved for given propeller geometry, inflow wake and cavitation number. The propeller cavitation number is defined as:

$$\sigma_n = \frac{p_{shaft} - p_v}{\frac{\rho}{2} n^2 D^2} \quad (44)$$

where:

- p_{shaft} = pressure at the axis of the propeller shaft
- p_v = vapor pressure
- n = propeller revolutions
- D = propeller diameter

The flow around the blades and the cavities is modeled by a lattice of vortices and line sources located on the mean camber surface of the blades and their trailing vortex wakes, as shown for one blade in Figure 17. The chordwise arrangement of the vortices and sources is the same as in the hydrofoil case, described in Section 3. The spanwise spacing is constant with quarter inset at the tip. Details of the numerical grid can be found in [25] and [18].

The time history of the cavity shapes is determined for each blade strip by applying the three-dimensional linearized unsteady cavity boundary conditions [25]. The extent of the cavity on each strip is determined iteratively until the pressure on the cavity becomes equal to the vapor pressure p_v . The effect of the other strips on the same blade as well as on the other blades is accounted for in an iterative sense.

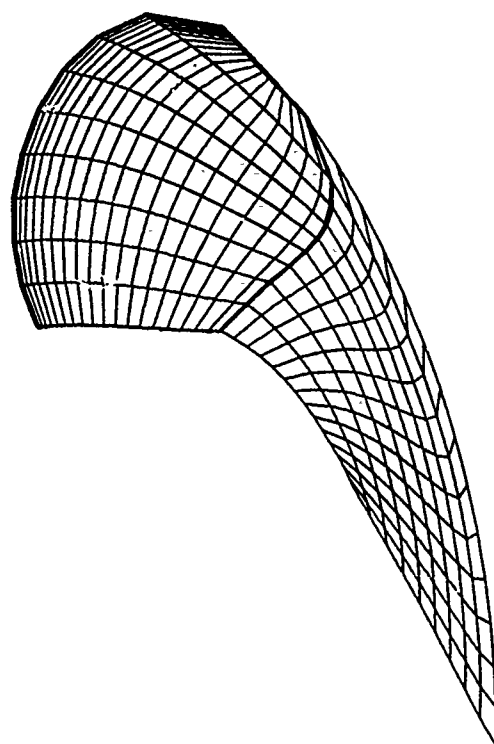


Figure 17: Numerical grid on one propeller blade and its wake.

The leading edge correction, described in section 2.5, has also been implemented in the numerical method for the propeller, in order to account for the non-linear blade thickness effects [18].

In the present work, the numerical method for the unsteady propeller cavitation is extended to predict cavities with prescribed midchord and/or face detachment. This has been accomplished by a direct application in the propeller problem of the numerical method for mid-chord and face hydrofoil cavitation, which was described in Section 3.

The modified PUF-3 has been applied for the DTRC N4497 propeller [19]. The advance coefficient is $J = VSHIP/n/D = .8$ and the cavitation number $\sigma_n = 1.5$. The time history of the cavity volume is shown in Figure 18 for different detachment points on the suction side of the blades. The three-dimensional perspective plots for some blade sections and their cavities are also shown in Figures 19 to 21 for different detachment points. Those figures show the effect of the detachment point on the cavity extent and shape to be substantial.

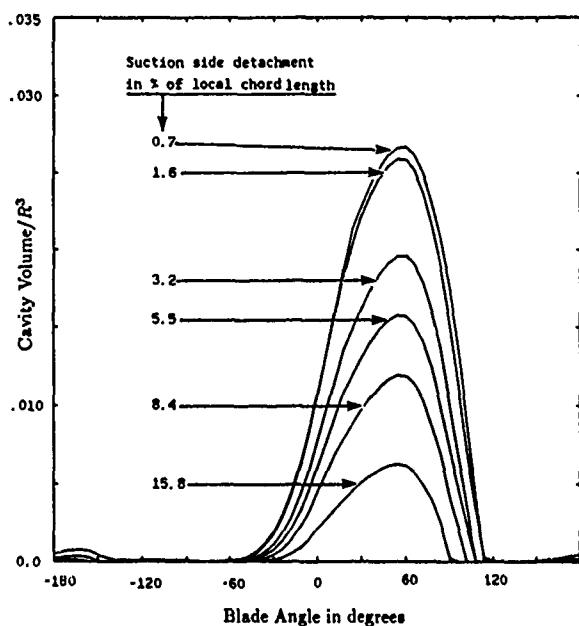


Figure 18: Cavity volume per blade for different detachment points on the suction side of the N4497 propeller as predicted by the modified PUF-3, $\sigma_n = 1.5$, $J = V_{SHIP}/n/D = 0.8$.

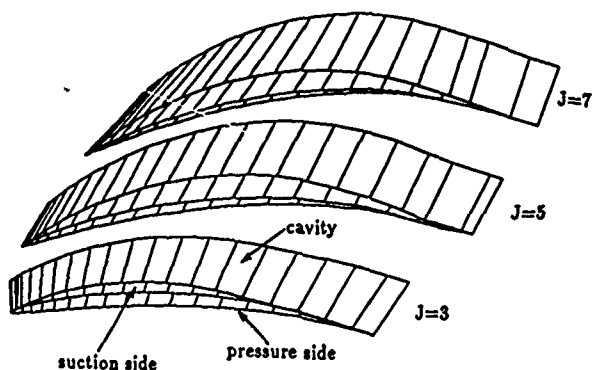


Figure 19: Cavity shapes for propeller N4497 at blade sections No. 3, 5 and 7 as predicted by the modified PUF-3. Detachment on the suction side, at 0.7% of the local chord; Blade angle = 12° from the top, $\sigma_n = 1.5$, $J = V_{SHIP}/n/D = 0.8$

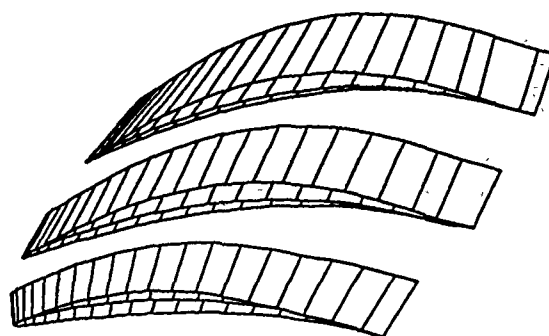


Figure 20: Cavity shapes for propeller N4497 at blade sections No. 3, 5 and 7 as predicted by the modified PUF-3. Detachment on the suction side, at 3.2% of the local chord; Blade angle = 12° from the top, $\sigma_n = 1.5$, $J = V_{SHIP}/n/D = 0.8$

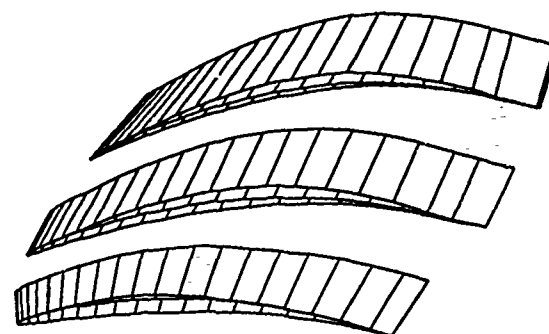


Figure 21: Cavity shapes for propeller N4497 at blade sections No. 3, 5 and 7 as predicted by the modified PUF-3. Detachment on the suction side, at 8.4% of the local chord; Blade angle = 12° from the top, $\sigma_n = 1.5$, $J = V_{SHIP}/n/D = 0.8$

5 Conclusions

The following has been accomplished in the presented work:

- The cavitating general shape hydrofoil problem, with arbitrary detachments, has been formulated in terms of singular integral equations of unknown source and vorticity distributions. Those equations are inverted analytically and the cavitation number, cavity shapes and pressure distributions, are expressed in terms of integrals of known quantities.
- The effect of the detachment point on the cavity solution has been investigated. In the case where a supercavity detaches forward of the trailing on the pressure side of a hydrofoil, an equation for the location of the cavity detachment point has been found.
- A numerical discrete vortex and source method has been developed to predict the cavitation on hydrofoils with arbitrary cavity detachment points.
- The numerical method has been extended to predict unsteady propeller sheet cavitation with arbitrary midchord and/or face cavity detachment. The effect of the location of the cavity detachment on the cavity volume and the cavity shapes has been investigated.

6 Future Research

The following items need to be addressed in order to improve on the presented work:

- Perform experiments on cavitating hydrofoils with cavities showing midchord and/or face detachment, in order to validate the presented theoretical results.
- Improve on the prediction of the cavity detachment points by coupling the presented method with a boundary layer calculation on the wetted part of the foil in front of the cavity. It is known from experiments [2], [10] that the cavity detachment point has to be determined in relation with the boundary layer separation point, rather than from any potential flow criterion. The potential flow cavity detachment criterion, however, should still be valid if no boundary layer separation occurs in front of the predicted detachment point.

- Perform experiments on cavitating propellers which show midchord and/or face cavity detachment. Determine the detachment lines from the experiment and run the modified PUF-3 with those detachment lines as input. Compare the predicted cavity shapes and propeller forces from PUF-3 with the experiment.
- Employ the cavity detachment criteria in PUF-3.

7 Acknowledgements

Support of this research was provided by the AB Volvo-Penta Corporation. At this point the authors wish to thank Professor Justin E. Kerwin of MIT, Mr. Lennart Brandt and Mr. Ted Rosendal of Volvo-Penta for their valuable comments and discussions during the course of this work.

References

- [1] A.J. Acosta. *A Note on Partial Cavitation of Flat Plate Hydrofoils*. Technical Report No. E-19.9, California Institute of Technology, Hydrodynamics Laboratory, October 1955.
- [2] H. Arakeri. Viscous effects on the position of cavitation separation from smooth bodies. *Journal of Fluid Mechanics*, vol 68(No. 4):pp 779-799, 1975.
- [3] G. Birkhoff and E.H. Zarantonello. *Jets, Wakes and Cavities*. Academic Press Inc., New York, 1957.
- [4] J.P. Breslin, R.J. Van Houten, J.E. Kerwin, and C-A Johnsson. Theoretical and experimental propeller-induced hull pressures arising from intermittent blade cavitation, loading, and thickness. *Trans. SNAME*, 90, 1982.
- [5] M. Brillouin. Les surfaces de glissement de helmholtz et la resistance des fluides. *Ann. Chim. Phys.*, vol. 23:pp. 145-230, 1911.
- [6] C.N. Corrado. *Investigations of Numerical Schemes for the Evaluation of the Cavitating Flow Around Hydrofoils*. Master's thesis, MIT, June 1986.
- [7] A.G. Efros. Hydrodynamic theory of two-dimensional flow with cavitation. *Dokl. Akad. Nauk. SSSR*, vol 51:pp 267-270, 1946.
- [8] A.G. Fabula. Thin-airfoil theory applied to hydrofoils with a single finite cavity and arbitrary free streamline detachment. *Journal of Fluid Mechanics*, vol 12:pp 227-240, 1962.
- [9] N.E. Fine. *Computational and Experimental Investigations of the Flow Around Cavitating Hydrofoils*. Technical Report No. 88-6, MIT, Department of Ocean Engineering, September 1988.

- [10] J.P. Franc and J.M. Michel. Attached cavitation and the boundary layer: experimental investigation and numerical treatment. *Journal of Fluid Mechanics*, vol. 154:pp 63-90, 1985.
- [11] J.A. Geurst. Linearized theory for fully cavitating hydrofoils. *International Shipbuilding Progress*, vol 7(No. 65), January 1960.
- [12] J.A. Geurst. Linearized theory for partially cavitating hydrofoils. *International Shipbuilding Progress*, vol 6(No. 60):pp 369-384, August 1959.
- [13] J.A. Geurst and R. Timman. Linearized theory of two-dimensional cavitation flow around a wing section. *IX International Congress of Applied Mechanics*, 1956.
- [14] J.A. Geurst and P. J. Verbrugh. A note on camber effects of a partially cavitating hydrofoil. *International Shipbuilding Progress*, vol 6(No. 61):pp 409-414, September 1959.
- [15] T. Hanaoka. Linearized theory of cavity flow past a hydrofoil of arbitrary shape. *Journal of the Society of Naval Architects, Japan*, vol. 115:pp. 56-74, June 1964.
- [16] J.E. Kerwin. Private communication.
- [17] J.E. Kerwin, S.A. Kinnas, J-T Lee, and W-Z Shih. A surface panel method for the hydrodynamic analysis of ducted propellers. *Trans. SNAME*, 95, 1987.
- [18] J.E. Kerwin, S.A. Kinnas, M.B. Wilson, and McHugh J. Experimental and analytical techniques for the study of unsteady propeller sheet cavitation. In *Proceedings of the Sixteenth Symposium on Naval Hydrodynamics*, Berkeley, California, July 1986.
- [19] Kerwin, J.E. and C-S Lee. Prediction of steady and unsteady marine propeller performance by numerical lifting-surface theory. *Trans. SNAME*, vol 86, 1978.
- [20] S.A. Kinnas. *Cavity Shape Characteristics for Partially Cavitating Hydrofoils*. Technical Report 85-1, MIT, Department of Ocean Engineering, February 1985.
- [21] S.A. Kinnas. *Cavity Shape Characteristics for Supercavitating Hydrofoils*. Technical Report 84-13, MIT, Department of Ocean Engineering, October 1984.
- [22] S.A. Kinnas. Leading edge corrections to the linear theory of partially cavitating hydrofoils. *Submitted for publication*, March 1989.
- [23] S.A. Kinnas. *Non-linear Corrections to the Linear Theory for the Prediction of the Cavitating Flow Around Hydrofoils*. Technical Report 85-10, MIT, Department of Ocean Engineering, June 1985.
- [24] G. Kreisel. *Cavitation with Finite Cavitation Numbers*. Technical Report No. R1/H/36, Admiralty Res. Lab., 1946.
- [25] Chung-Sup Lee. *Prediction of Steady and Unsteady Performance of Marine Propellers with or without Cavitation by Numerical Lifting Surface Theory*. PhD thesis, M.I.T., Department of Ocean Engineering, May 1979.
- [26] M.J. Lighthill. A new approach to thin aerofoil theory. *The Aeronautical Quarterly*, vol 3(no 2):pp. 193-210, November 1951.
- [27] B.R. Parkin. *Munk Integrals for Fully Cavitating Hydrofoils*. Technical Report P-2350-1, RAND, November 1961.
- [28] D. Riabouchinsky. On steady fluid motions with free surfaces. *Proceedings of London Math. Soc.*, Vol. 19:pp 206-215, 1921.
- [29] Nishiyama T. and Ota T. Linearized potential flow models for hydrofoils in supercavitating flows. *Transactions of the ASME*, December 1971.
- [30] M.P. Tulin. *Steady Two-Dimensional Cavity Flows About Slender Bodies*. Technical Report 834, DTMB, May 1953.
- [31] M.P. Tulin. Supercavitating flow past foils and struts. In *Symposium on Cavitation in Hydrodynamics*, NPL, Teddington, England, September 1955.
- [32] M.P. Tulin. Supercavitating flows - small perturbation theory. *Journal of Ship Research*, vol 7(No. 3):pp. 16-37, 1964.
- [33] M.P. Tulin and M.P. Burkart. *Linearized Theory for Flows About Lifting Foils at Zero Cavitation Number*. Technical Report C-638, DTMB, February 1955.
- [34] M.P. Tulin and C.C. Hsu. New applications of cavity flow theory. In *19th Symposium on Naval Hydrodynamics*, Tokyo, Japan, 1980.
- [35] J.S. Uhlman. The surface singularity method, applied to partially cavitating hydrofoils. *Journal of Ship Research*, vol 31(No. 2):pp. 107-124, June 1987.
- [36] H. Villat. Sur la validite des solutions de certain problem d'hydrodynamique. *J. de Math.*, vol 6(No. 10):pp 231-290, 1914.
- [37] R. B. Wade. Linearized theory of a partially cavitating plano-convex hydrofoil including the effects of camber and thickness. *Journal of Ship Research*, vol 11(No. 1):pp 20-27, 1967.
- [38] T.Y. Wu. Cavity flows and numerical methods. In *First International Conference on Numerical Ship Hydrodynamics*, 1975.

- [39] T.Y. Wu. *A Note on the Linear and Nonlinear Theories for Fully Cavitated Hydrofoils*. Technical Report No. 21-22, California Institute of Technology, Hydrodynamics Laboratory, August 1956.

Appendix A

Details of Face Detachment

The Villat-Brillouin condition [36], [5] at the cavity detachment point requires the cavity to have the same slope and curvature with the foil. This condition satisfies, locally, the requirements that the cavity does not intersect the foil and that the pressures on the foil are larger than the cavity pressure. If y_c and y_f are the ordinates of the cavity and the foil at the vicinity of the separation point s , as shown in Figure 2, then we should have:

$$\left[\frac{dy}{dx} \right] = \frac{dy_c}{dx}(s^+) - \frac{dy_f}{dx}(s^-) = 0 \quad (45)$$

$$\left[\frac{d^2y}{dx^2} \right] = \frac{d^2y_c}{dx^2}(s^+) - \frac{d^2y_f}{dx^2}(s^-) = 0 \quad (46)$$

Equations 45 and 46, via the kinematic boundary condition on either the cavity or the foil, become:

$$[v] = v(s^+) - v(s^-) = 0 \quad (47)$$

$$\left[\frac{dv}{dx} \right] = \frac{dv}{dx}(s^+) - \frac{dv}{dx}(s^-) = 0 \quad (48)$$

$$(49)$$

where $v(x)$ is the vertical perturbation velocity on the cavity or foil.

In the context of linearized theory:

$$v(x) = -\frac{q(x)}{2} + I(x) \quad (50)$$

where:

$$I(x) = \frac{1}{2\pi} \int_0^s \frac{\gamma(\xi)d\xi}{\xi - x} \quad (51)$$

The total source distribution $q(x)$ is continuous at s and so is $I(x)$ because $\gamma(s) = 0$. This makes the first condition, equation 47, always valid.

By using equations 10, 11 and 12 it can be shown that:

$$\frac{dq}{dx}(s^+) - \frac{dq}{dx}(s^-) \sim -\frac{A(s,l)}{2} \cdot \frac{1}{\sqrt{\epsilon}} \quad (52)$$

$$\frac{dI}{dx}(s^+) - \frac{dI}{dx}(s^-) \sim \frac{A(s,l)}{4} \cdot \frac{1}{\sqrt{\epsilon}} \quad (53)$$

where $s^+ - s = s - s^- = \epsilon$, and $A(s,l)$ is defined in equation 16.

Finally, by using equations 50, 52 and 53, we get:

$$\left[\frac{dv}{dx} \right] \sim \frac{A(s,l)}{2} \cdot \frac{1}{\sqrt{\epsilon}} \quad (54)$$

Thus, in order for the condition 48 to be valid we should have:

$$A(s,l) = 0 \quad (55)$$

Appendix B

Details of Midchord Detachment

The solution $\bar{\gamma}$ and \bar{q} to the system of equations 24 and 25, is given by the expressions 10, 11 and 12 where Θ_1^* has to be replaced by Θ_2^* , as defined in equation 27.

To determine the unknown u_{cw}^+ for $0 < x < l_0$, the kinematic boundary condition 22 must be applied on the upper wetted part of the hydrofoil.

Combining equations 22 with 21 it can be proven that the condition 22 is equivalent to:

$$\bar{q}(x) = \frac{q_w(x)}{\sigma U_\infty} \quad \text{for } 0 < x < l_0 \quad (56)$$

where $q_w(x)$ is the foil thickness source defined as follows:

$$q_w(x) = U_\infty \frac{d(\eta_u - \eta_l)}{dx} \quad (57)$$

By using the coordinate transformation defined in equation 13 and by introducing t_0 :

$$t_0 = \sqrt{\frac{l_0}{l - l_0}}, \quad (58)$$

it can be proven [9] that equation 56 is equivalent to:

$$\frac{q_w(z)}{\sigma U_\infty} - H(z) = \frac{1+z^2}{\pi} \int_0^{t_0} \sqrt{\frac{\eta}{\eta+t}} \cdot \frac{(u_{cw}^+ - \frac{1}{2})d\eta}{(1+\eta^2)(\eta-z)} \quad (59)$$

where $H(z)$ is defined as:

$$H(z) = \frac{\sigma_0}{\sigma} \bar{q}_0(z) + (1 - \frac{\sigma_0}{\sigma}) R(z) \quad (60)$$

with $R(z)$ defined as:

$$R(z) = \sqrt{\frac{t+z}{z}} \cdot \frac{1}{2\sqrt{2}r^2} \cdot (\sqrt{r^2-1} - z\sqrt{r^2+1}) \quad (61)$$

and with σ_0 and \bar{q}_0 being the cavitation number and the cavity source solution, respectively, corresponding to a supercavity with the same extent $x = l$ but starting at the leading edge, i.e. for $l_0 = 0$. The values for σ_0 and \bar{q}_0 are given from the equations 9 and 11.

Equation 59 can finally be inverted to obtain [9]:

$$u_{cw}^+ - \frac{1}{2} = \frac{1+\eta^2}{\pi} \cdot \frac{\sqrt{(\eta+t)(t_0-\eta)}}{\eta} \cdot \left[\frac{1}{\sigma} M(\eta) - \left(1 - \frac{\sigma_0}{\sigma}\right) N(\eta) \right] \quad (62)$$

where

$$M(z) \stackrel{\text{def}}{=} \int_0^{t_0} \sqrt{\frac{\eta}{t_0 - \eta}} \sqrt{\frac{\eta}{t + \eta}} \cdot \frac{(q_w - \sigma_0 U_\infty \bar{q}_0) d\eta}{(1 + \eta^2)(\eta - z)} \quad (63)$$

and

$$N(z) \stackrel{\text{def}}{=} \int_0^{t_0} \sqrt{\frac{\eta}{t_0 - \eta}} \sqrt{\frac{\eta}{t + \eta}} \cdot \frac{R(\eta) d\eta}{(1 + \eta^2)(\eta - z)} \quad (64)$$

Equation 62 is the solution of the integral equation 59 which satisfies the condition that $u_{cw}^+ - \frac{1}{2} = 0$ at t_0 .

The cavitation number, σ , is obtained by applying the cavity closure condition 7. It can be shown that [9]:

$$\sigma = \sigma_0 - \frac{M_\sigma}{1 - N_\sigma} \quad (65)$$

with the following definitions:

$$M_\sigma \stackrel{\text{def}}{=} \frac{8\sqrt{2}r^4}{\pi^3(r^2 + 1)} \int_0^t \sqrt{\frac{\eta}{t - \eta}} \cdot \frac{\sqrt{r^2 + 1} + \eta\sqrt{r^2 - 1}}{1 + \eta^2} \cdot M_F(\eta) d\eta \quad (66)$$

and

$$N_\sigma \stackrel{\text{def}}{=} \frac{8\sqrt{2}r^4}{\pi^3(r^2 + 1)} \int_0^t \sqrt{\frac{\eta}{t - \eta}} \cdot \frac{\sqrt{r^2 + 1} + \eta\sqrt{r^2 - 1}}{1 + \eta^2} \cdot N_F(\eta) d\eta. \quad (67)$$

where:

$$M_F(z) \stackrel{\text{def}}{=} \int_0^{t_0} \frac{\sqrt{(\omega + t)(t_0 - \omega)}}{\omega^2 - z^2} \cdot M(\omega) d\omega \quad (68)$$

and

$$N_F(z) \stackrel{\text{def}}{=} \int_0^{t_0} \frac{\sqrt{(\omega + t)(t_0 - \omega)}}{\omega^2 - z^2} \cdot N(\omega) d\omega \quad (69)$$

The integrations in equations 66, 67, 68 and 69, are performed numerically with special care taken at the singularities of the involved integrands [9].

DISCUSSION

by H. Kato

I appreciate the authors' effort in calculating sheet type cavitation. The authors did not compare their results with experiments. Therefore I am afraid that some of the assumptions and conditions are different from experimental observations. Firstly the sheet cavitation is closely related with boundary layer separation. The leading edge of sheet cavitation coincides with the separation point of boundary layer according to the observation by Franc and Michel[10] and Yamaguchi and Kato [A1,A2]. We can not choose the location of the cavity leading edge arbitrarily as the authors did in the paper.

The authors also mention that the pressure distribution shown as Fig.11 is not realistic. However, we usually observe a negative pressure peak in the front of the cavity where the pressure is lower than the cavity pressure.

The third point I would like to point out is the cavity closure condition; Eq.(7). A sheet cavitation is followed by wake flow which can not be neglected in many cases. The calculation under the assumption of Eq.(7) does not agree with the experiment especially when the sheet cavity length approaches to the foil length.

- [A1] H. Yamaguchi and H. Kato: A Study on a Supercavitating Hydrofoil with Rounded Nose, Naval Architecture and Ocean Engineering, Soc. Naval Arch. Japan, Vol.20 (1982).
- [A2] H. Yamaguchi and H. Kato: On Application of Nonlinear Cavity Flow Theory to Thick Foil Sections, 2nd Int. Conf. Cavitation, I Mech E, Edinburgh, (1983) pp.167-174.

Author's Reply

First, we want to thank Prof. Kato taking the time to read our paper and for making comments on it.

It is correct that we did not compare the results of our method with experimental results, and we are actually planning, as stated in Section 6 of our paper, a systematic series of experiments in the future. The objective of this paper was to produce a consistent and convergent numerical method for the midchord and fate unsteady propeller cavitation.

Concerning Prof. Kato's comment on the pressure distribution of Fig.11, we do not state that the pressure distribution "is not realistic". We rather say that it is "unacceptable" according to the conditions imposed in the beginning of Section 2.2. In addition, at the end of Section 2.3 as well in Section 6, we also state, as does he, that the midchord detachment point in front of the cavity[10].

Finally, in eq.(7), we assumed cavity closure at the trailing edge of the cavity. this assumption is in accordance with a linearized Riaboushinsky or reentrant jet an cavity model. We agree, however, that more physical model, is an open cavity model with the "openness" supplied from further knowledge of the cavity viscous wake. This "openness" does not affect much the predicted cavity shape and the cavitation number, in the case of supercavitating flows. Thus, in the presented analysis of the supercavitating hydrofoils, we decided for simplicity, to take the cavity " openness" equal to zero. For partially cavitating hydrofoils, however, the cavity wake is important and should be included. An experimental analysis of the cavity wake in the case of partially cavitating hydrofoils is included in [9].

Propeller Inflow Correction for Improved Unsteady Force and Cavitation Calculations

T. S. Mautner
Naval Ocean Systems Center
San Diego, USA

Abstract

An existing propeller design method was modified and used to calculate the spatial variation of propeller performance, velocity components and blade pressures for use in determining unsteady forces and cavitation. The calculations showed only small changes in the magnitude of the velocity components and blade pressures when compared to typical counterrotating propeller design results. Approximate agreement was found between the absolute magnitude of both the harmonic coefficients and the total unsteady forces obtained using the calculated axial velocity and the measured wake. However, the unsteady force distributions associated with the calculated axial velocity, which includes propeller effects, resulted in small reductions in the magnitude of the total unsteady forces on the propulsor. The calculated blade pressures and cavitation index also showed only small variations in magnitude with circumferential position.

Nomenclature

a_n, b_n	Fourier coefficients
A_F	Vehicle frontal area
c^*	Complex Fourier coefficient = $a_n - ib_n$
C	Propeller blade chord
C_D	Vehicle drag coefficient = $\text{Drag} / \frac{1}{2} \rho V_\infty^2 A_F$
C_L	Blade section lift coefficient
C_p	Pressure coefficient
C_P	Power coefficient = $Q\Omega / \frac{1}{2} \rho V_\infty^3 \pi R^2$
C_Q	Torque coefficient = $Q / \frac{1}{2} \rho V_\infty^2 \pi R^3$
C_T	Thrust coefficient = $T / \frac{1}{2} \rho V_\infty^2 \pi R^2$
D	Propeller diameter
D_B	Vehicle diameter
F_x, F_y	Unsteady side forces
$F_z^{(n)}$	Unsteady thrust for the n-th harmonic
Δh_{BL}	Change in energy from freestream to local
Δh_p	Change in pressure through propeller disk
j	Index taking on values = 1, ..., P
J	Advance ratio = $\pi V_\infty / \Omega R$
k	The reduced frequency = $\frac{1}{2} C\omega / V_\infty$
$K(k)$	Sears' function
L	Lift force on an airfoil or blade section
L_B	Vehicle length
m	Index taking on values = nN_b
M	Moment/Torque on a blade element
n	Order of the propeller force harmonic
N_b	Number of propeller blades
p	Pressure

P	Number of blade elements having width Δr
PC	Propulsive coefficient = $(\text{Thrust} (1-\tau) V_\infty) / (\text{Torque } \Omega)$
Q	Propeller torque
r	Radial coordinate
Δr_j	Width of the j-th blade element
R	Propeller radius
R_B	Vehicle radius
SL	Propeller stacking line location
t	Time
t/C	Blade thickness-to-chord distribution
T	Propeller thrust
T_x, T_y	Unsteady moments
$T_z^{(n)}$	Unsteady torque for the n-th harmonic
$\hat{T}(k)$	Horlock's function
u	Measured inflow velocity
v	Axial velocity with propellers present
v_a	Axial component of the interference velocity
v_i	Axial inflow velocity with propellers not present
v_t	Tangential component of interference velocity
Δv	Change in axial velocity due to propellers
V	Resultant velocity of blade section and fluid
V_∞	Free stream velocity or vehicle speed
ΔV	Overvelocity due to thickness and lift
w_a	Axial component of self-induced velocity
w_t	Tangential component of self-induced velocity
x, y, z	Rectangular coordinates
\bar{x}	Radial position = $(r - r_B) / (R - r_B)$
\bar{y}	Non-dimensional chordwise coordinate
α	Angle of attack of a blade element
β	Blade section pitch angle (radians)
η	Propeller efficiency = $J C_T / \pi C_Q$
ω	Frequency
Ω	Angular velocity of the propeller
ϕ	Potential function
ψ	Mid-chord skew angle
ρ	Fluid density
σ	Cavitation number
τ	Thrust deduction factor = $\Delta \text{Drag} / \text{Thrust}$
θ	Angular coordinate in the direction of propeller rotation
Γ	Bound circulation

Subscripts

F	Forward propeller
A	After propeller

Introduction

One current and important issue in the design of marine propellers is the reduction of propulsor generated noise due to both the transmission of unsteady propeller forces through shafting into the vehicle and propeller noise radiated into the near and far fields. The unsteady blade forces/pressures and cavitation calculations to be discussed in this paper result from the passage of a propeller blade through the spatially varying wake generated by upstream appendages. It is known that when a propeller blade passes behind an appendage, unsteady blade pressures and loadings occur and, with an appropriate velocity and pressure field surrounding the propeller blade, periodic propeller blade cavitation will occur.

While there are a wide range of techniques available to calculate unsteady forces and blade pressures, these methods require accurate knowledge of the wake incident upon the propeller. One method of determining the incident flow field required in propeller design is to make wake measurements at the proposed propeller stacking line locations. Typically, these measurements are made without a propulsor present, and only simple corrections, if any, are made to determine an effective wake. For single propellers, one could reasonably assume that the appendage generated wake is incident upon the propeller without further distortion or modification by the propeller induced velocity field. However, for compound propulsors, the wake incident upon the aft blade row now passes through the forward propeller (or stator) and is modified by propeller induced velocities and interactions.

In recent years measurements have been made detailing propeller velocity fields. For example, Thompson's [24] fig. 6 shows the change in harmonic content of the axial velocity distribution for a body with and without a propeller. In general, the results show a reduction in the magnitude of the harmonic components when a propeller is operating. Another example is the work of Blaurock and Lammurs [1] which, for three values of thrust coefficient, illustrates the significant changes in axial, radial and tangential velocity components before and after an operating propeller. Additional examples of propeller flow studies can be found in refs. 7, 10, 11, and 22.

The above mentioned experimental results and uncertainties in the velocity field used in calculation of unsteady forces, blade pressures and cavitation performance provide the motivation to explore, analytically, the effect of a spatially varying wake on propeller forces and cavitation. The continued success of the propeller design method of Nelson [17-20] suggests that if the lifting-line portion of the design method can accurately predict propeller performance using circumferential mean data, the possibility exists of using the same calculation techniques, with some modification, to explore the effect of spatial variations in the wake. The selection of Nelson's lifting-line method was also based upon its availability and ease of modification. Certainly, there are many lifting-surface methods, panel methods and blade pressure calculation techniques [2, 5, 8, 9, 23] which might be used for this purpose.

The discussion to follow will present a description of the propeller design method and the geometry, velocity fields, harmonic content, unsteady forces (blade-rate) and blade pressures associated with a counterrotating propeller set.

Measured Velocity Field

In the design of wake-adapted propellers, it is important that the inflow velocity distribution at the propeller stacking lines be properly specified. Even though circumferentially averaged velocity profiles are sufficient for propeller design calculations, the calculation of unsteady forces and pressures requires that both the radial and circumferential distributions of the wake be considered.

The velocity data used in this study was obtained from wind tunnel tests [21] where boundary layer measurements were made on a 0.6 scale model. Pitot tubes, oriented approximately parallel to the afterbody surface, were used to obtain both the static pressure and the total head over a Reynolds number range of $1.3-2.4 \times 10^6$. To avoid strut interference effects and to utilize body symmetry, measurements were made over the top 90° of the body where the zero degree point coincides with the centerline of the fin trailing edge. The measured wake at the forward and after propeller stacking line locations is shown in fig. 1.

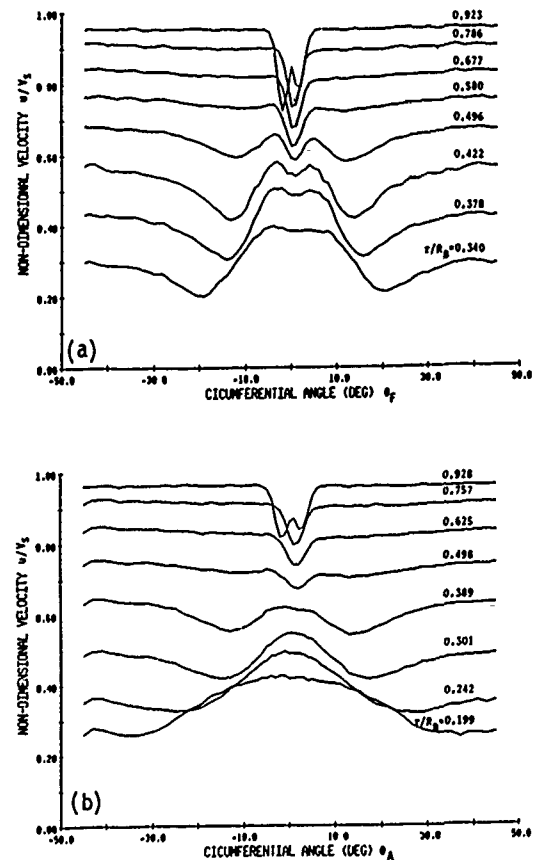


Fig. 1. Circumferential variation of the measured inflow velocity u/V_∞ at the a) forward and b) after measurement locations.

Propeller Geometry

The propeller geometry used in this study is that for a counterrotating propeller set designed using the method developed by Nelson [17-20]. The design utilized the parameters given in table 1, and the circumferential mean inflow velocity, u/V_∞ , and static pressure, C_p , formed from the measured data [21]. Thrust deduction calculations were made using the circumferentially averaged, three-dimensional potential flow velocity profiles calculated using a 3-D body coordinate generator [13] and a 3-D panel method [3, 4]. The details of the input velocity and pressure profiles, the circulation distribution and thickness distributions are given in refs. 15-16.

Using the inputs described above, a counterrotating propeller design was performed. The calculated performance parameters are given in table 1, the radial distribution of chord-to-diameter, local pitch angle and resultant blade section velocity are listed in table 2 and the geometry is sketched in fig. 2. In addition to calculating the aft propeller circulation distribution required for tangential velocity cancellation, the design method determines the minimum value of C/D required to meet cavitation ($\sigma=0.75$), blade stress (40 ksi maximum) and lift coefficient ($C_{L,MAX}=0.5$) requirements. A distribution, which also satisfies the given hub and tip values of C/D , is fit about this value of C/D and has the shape shown in fig. 2.

Vehicle Velocity - V_∞ (knots)	40
Drag Coefficient - C_D	0.1165
Vehicle L_B/D_B	11.77
Propulsive Coefficient - PC	0.929
Propulsive Efficiency - η	1.08
Thrust Deduction - $1-\tau$	0.860
Advance Ratio - J	2.12
Thrust Coefficient - C_T	0.212
Torque Coefficient - C_Q	0.133
Power Coefficient - C_P	0.196
Torque Ratio - Q_A/Q_F	1.00
Thrust Ratio - T_A/T_F	1.02
Blade Surface Cavitation - σ	0.75
Maximum Stress (ksi)	40

Parameter	Forward Propeller	After Propeller
Blade Number	6	4
SL/D _B	11.46	11.67
R/R _B	0.781	0.705
r _{hub} /R _B	0.3280	0.1823
RPM	1400	1400
C _{TIP} /C _{MAX}	0.4	0.4
C _{HUB} /C _{MAX}	0.6	0.6
(C/D) _{MAX}	0.255	0.380
(t/C) _{HUB}	0.18	0.16
(t/C) _{TIP}	0.09	0.08
(C _L) _{MAX}	0.346	0.435
V _{TIP} /V _∞	1.733	1.606

Table 1. Summary of Counterrotating Propeller Design Inputs and Calculated Results Using Circumferential Mean Inflow Data

R _F /R _B	C/D) _F	β_F	V/V _{∞F}
0.3393	0.1586	0.5567	0.7199
0.3619	0.1698	0.5924	0.7922
0.4072	0.1906	0.6411	0.9300
0.4525	0.2094	0.6797	1.0503
0.4978	0.2259	0.7102	1.1566
0.5431	0.2397	0.7101	1.2567
0.5884	0.2501	0.6894	1.3526
0.6337	0.2548	0.6622	1.4457
0.6790	0.2448	0.6190	1.5378
0.7243	0.2064	0.5657	1.6273
0.7696	0.1286	0.5217	1.7133

R _A /R _B	C/D) _A	β_A	V/V _{∞A}
0.1953	0.2367	0.7779	0.6411
0.2215	0.2540	0.7593	0.6924
0.2738	0.2864	0.7562	0.8236
0.3261	0.3154	0.7708	0.9701
0.3783	0.3405	0.8100	1.1155
0.4306	0.3611	0.8260	1.2384
0.4829	0.3757	0.8074	1.3372
0.5352	0.3783	0.7724	1.4177
0.5875	0.3575	0.7117	1.4818
0.6398	0.2981	0.6218	1.5334
0.6920	0.1883	0.5503	1.5919

Table 2. Propeller Geometry and Operating Characteristics Determined Using Circumferential Mean Inflow Data

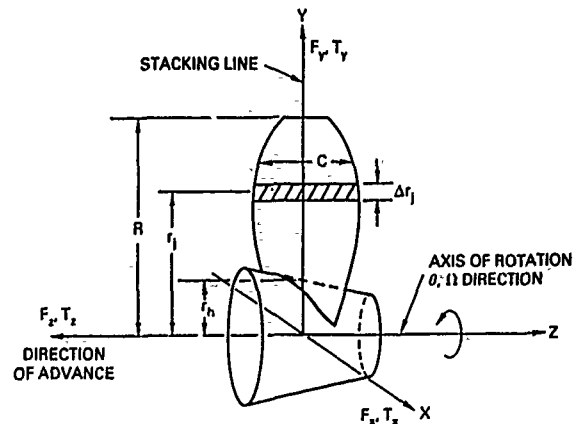


Fig. 2. Description of a typical propeller and its geometry.

Unsteady Force Calculation Method

The method used in this paper to calculate unsteady blade forces was developed by Thompson [24] and extended by Mautner [14]. The method divides the propeller blade into strips which are considered two-dimensional airfoils, and two-dimensional unsteady airfoil theory is used to consider sinusoidal velocity fluctuations normal and parallel to the inflow velocity. Corrections to the blade lift force due to the presence of adjacent propeller blades, the inclusion of camber and the calculation of the total force and moment on the propeller have been included. The expressions used to calculate the unsteady thrust and torque are

$$F_z^{(n)} = N_b \sum_{j=1}^P L_{j(nN_b)} e^{-inN_b \psi_j} \quad (1)$$

$$T_z^{(n)} = N_b \sum_{j=1}^P M_{j(nN_b)} e^{-inN_b \psi_j} \quad (2)$$

where the lift and moment are determined using

$$L_{jm} = - \left[\frac{\partial C_L}{\partial \alpha} \right]_j \rho^{1/2} C_j V_{\infty} c_{m_j}^* \cdot \left\{ \hat{K}(k_{mj}) \cos \beta_j - \alpha_j \hat{T}(k_{mj}) \sin \beta_j \right\} \Delta r_j \cos \beta_j \quad (3)$$

and

$$M_{jm} = L_{jm} \tan \beta_j r_j \quad (4)$$

Examination of the unsteady force equations (1)-(4) and a Fourier analysis of the current four cycle wake where the velocity is represented by

$$\frac{v(r, \theta)}{V_{\infty}} = \frac{a_0(r)}{2} + \sum_{n=1}^{\infty} \left[a_n(r) \cos(n\theta) + b_n(r) \sin(n\theta) \right] \quad (5)$$

show that the harmonic numbers of interest, for a 6x4 propeller set, are $nN_b = 12, 24, 36, \dots$ for the forward propeller and $nN_b = 4, 8, 12, 16, \dots$ for the after propeller. Thus, only the unsteady thrust and torque require calculation.

Blade Pressure and Cavitation Calculation Method

The starting point in calculating blade pressures is the unsteady Bernoulli equation

$$p = -\rho \frac{\partial \phi}{\partial t} - \frac{1}{2} \rho V^2 + c(t) \quad (6)$$

applied in a constant total head stream annulus located in an inertial frame of reference. After evaluating the potential function, ϕ , and determining the constant $c(t)$, one obtains the following expression for the pressure coefficient along the blade's suction surface

$$\frac{p_{\infty} - p}{\frac{1}{2} \rho V_{\infty}^2} = H_1 + H_2 \quad (7)$$

where

$$H_1 = -1 - \frac{\Delta h_{BL}}{\frac{1}{2} \rho V_{\infty}^2} - \frac{\Delta h_p}{\frac{1}{2} \rho V_{\infty}^2} + \left(\frac{v}{V_{\infty}} + \frac{v_a}{V_{\infty}} + \frac{w_a}{V_{\infty}} \right)^2 - 2 \frac{w_t(\bar{y})}{V_{\infty}} \left(\frac{\Omega r}{V_{\infty}} + \frac{v_t}{V_{\infty}} \right) + \frac{w_t(\bar{y})}{V_{\infty}} + \left(\frac{v_t}{V_{\infty}} \right)^2 \quad (8)$$

$$\frac{\Delta h_{BL}}{\frac{1}{2} \rho V_{\infty}^2} = \left(\frac{v}{V_{\infty}} \right) + C_p - 1 \quad (9)$$

$$\frac{\Delta h_p}{\frac{1}{2} \rho V_{\infty}^2} = 2 \left(\frac{v_t}{V_{\infty}} \right) \left(\frac{\Omega r}{V_{\infty}} \right) \quad (10)$$

and

$$H_2 = 2 \left(\frac{V(\bar{y})}{V_{\infty}} \right)^2 \left(\frac{\Delta V(\bar{y})}{V(\bar{y})} \right) + \left(\frac{V(\bar{y})}{V_{\infty}} \right)^2 \left(\frac{\Delta V(\bar{y})}{V(\bar{y})} \right)^2 \quad (11)$$

In the above expression for the blade pressure, Δh_{BL} represents the change in energy per unit volume from far upstream to where the boundary layer is measured, Δh_p represents the change in pressure through the propeller disk and ΔV accounts for the increase in velocity along an airfoil section due to thickness and lift. In the calculation w_t varies along the airfoil while the other induced velocities are considered to be constant. Both $w_t(\bar{y})$ and $\Delta V(\bar{y})$ are functions of the radial distribution of circulation and the chordwise loading. The overvelocity ΔV due to thickness is determined from the experimental data for NACA 0010-64 airfoil adjusted for local blade section thickness. If the pressure p on the suction surface is defined as the vapor pressure, a cavitation number, based upon free stream conditions, can be defined as $\sigma = (p_{\infty} - p_{\text{vapor}}) / \frac{1}{2} \rho V_{\infty}^2$. It should be noted that, although not shown here, the pressure equation has been extended to include the axial, radial and tangential components of the inflow velocity field.

Velocity Field Components

During the design of wake-adapted propellers, one must account for velocities arising from several sources, and these velocities are shown in the velocity diagram given in fig. 3. The resultant relative velocity (V) between the blade section and the fluid is determined from the tangential velocity due to propeller rotation (Ωr), the axial inflow velocity with propellers not present (v_i), the axial and tangential components of the self-induced (w_a, w_t) and interference (v_a, v_t) velocities and the change in the axial inflow velocity (Δv) due to the presence of the propellers.

Development of expressions for the velocity components are given by Nelson [17-20] and have been summarized by Mautner [16]. Briefly, in determining the radial variation of Δv , one considers an axisymmetric flow having a radial variation of total head as it passes through a single propeller. As

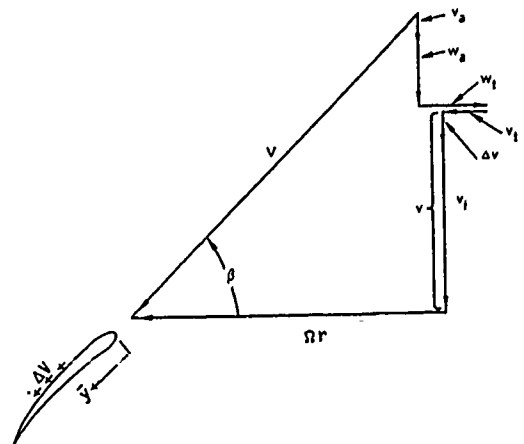


Fig. 3. Relative flow velocity diagram at the lifting-line.

the boundary layer flow moves through the propeller, the induced velocity field of the propeller rearranges the vorticity in the boundary layer and consequently alters the boundary layer profile. Using a potential flow model, an approximate calculation is made to determine Δv .

The interference velocities are calculated using an extension of the work of Hough and Ordway [6]. Using classical vortex system representation, Hough and Ordway developed expressions, in terms of Fourier coefficients, for the induced velocities of a finite bladed propeller with arbitrary circulation distribution. The zeroth harmonic, or steady component, of their expressions have been extended by Nelson to the case of a moderately loaded, wake-adapted propeller with non-zero circulation at the hub.

The self-induced velocities are calculated using an extended version of Lerbs' [12] induction factor method. Lerbs' original method was restricted to circulation distributions which go to zero at the hub. For wake-adapted, counterrotating propellers this restriction is not desirable because circulation distributions having non-zero circulation at the hub are more efficient (more work done on slower moving fluid near the hub) and the after propeller may be used to remove the tangential velocity from the forward propeller so that the hub vortex can be avoided. Thus, Lerbs' method was extended by Nelson to include non-zero circulation at the hub.

The blade pitch and the relative flow angle are related by $r \tan \beta = V_\infty / \Omega$ and this expression has been extended to the moderately loaded, wake-adapted propeller case by replacing V_∞ / Ω with its equivalent $r \tan \beta$. The result is

$$\beta = \tan^{-1} \frac{v + v_a + w_a}{\Omega r + v_i + w_i} \quad (12)$$

From this expression it can be seen that the calculated velocities and propeller geometry are not independent but must be determined in an iterative fashion to account for the effects of both the forward and after propellers.

Propeller Calculations

As stated before, one problem inherent in the calculation of unsteady forces involves the use of wake data obtained without a propeller present. While the propeller design method of Nelson calculates changes in the circumferential mean inflow velocity field due to the presence of a propulsor, the uncorrected, spatially varying inflow has been used to determine the unsteady forces acting on the propeller blades. It is known that the presence of a propulsor will cause changes in streamlines due to acceleration of the flow, that there may be additional unsteadiness due to the relative motion of the blade rows and that the propeller will change the amplitude and phase of the incident flow distortions. From these few facts it is apparent that the measured wake should be "corrected" to reflect propulsor induced velocity field and then be used in unsteady force, pressure and cavitation calculations.

Calculation Procedure

Before velocity or unsteady force calculations could begin, complete specification of the input velocity and static pressure profiles was required. Due to the fact that the design method requires the velocity and static pressure at the hub surface (numerical requirements specify a slip condition

at the wall), the measured radial distributions of u/V_∞ and C_p were extrapolated to the wall for $-45^\circ \leq \theta \leq +45^\circ$. Since the 3-D potential flow distributions, for the body with appendages, show only minor deviations from the circumferential mean, (max $\approx 0.3\%$ of V_∞), the circumferential mean profiles will be used for all cases. The measured wake data was specified in "look up" table format.

In an attempt to account for, at least first order, propeller effects in the calculation of unsteady forces and pressures, the lifting-line portion of Nelson's design method was modified to provide the calculation of the circumferential variation in velocity components required to form the resultant velocity V/V_∞ (fig. 3) at each blade section. The technique used fixed the velocity profile, u/V_∞ , at a particular forward propeller angle, θ_F , and then calculations were performed as the after propeller angle θ_A was varied from -45° to $+45^\circ$. In the region of large inflow velocity changes, $-10^\circ \leq \theta \leq +10^\circ$, single degree increments were used, and outside this region calculations were made at increments of 4-6 degrees.

Velocity Components and Performance Parameters

For comparison purposes, the counterrotating propeller design results obtained using circumferential mean inflow data are presented in fig. 4 and tables 1 and 2. Referring to fig. 4, it is seen that, for the forward propeller, the constant magnitude of v_a is small compared to w_a over the central portion of the blade, while at the after propeller these velocities are similar in magnitude. Furthermore, it is found that the maximum value of Δv (change in v_i) is of comparable magnitude to the maximum value of w_a . This infers that Δv plays an equal role with w_a in determining the radial distribution of blade pitch. The data also shows a small, constant value of v_i on the forward propeller while the after propeller v_i and both the forward and after propeller values of w_i have comparable magnitudes. The radial variation of σ indicates that the region on the blade most prone to blade surface cavitation occurs at $\bar{x} \approx 0.75$, and the C_L profile (not shown) reflects the change from large loading at the blade root to the unloading of the blade tip region. It should be noted that while these results are for a specific design, they are typical of counterrotating propeller designs obtained using Nelson's design method.

Next, the results obtained by variation of the forward and after propeller inflow will be presented. During the calculation procedure, 49 values of \bar{x} were used to determine the radial variation of parameters. An example of the calculated variation of propeller parameters with both θ_F and θ_A is the variation in the change in the axial inflow velocity (Δv). The results, given in fig. 5, show that the most significant variation in Δv occurs in the region of $\theta_F = 0$, $\theta_A = 0$ and near the hub surface ($\bar{x} = 0$). As one moves away from the hub surface the region of large parameter change narrows from $\pm 20^\circ$ at $\bar{x} = 0$ to only a few degrees at $\bar{x} = 1.0$. Although not shown here, similar variations are found for v and β while the spatial distribution of the induced and interference velocities, lift and drag coefficients have a nearly constant magnitude except for very small changes in a narrow region centered about $\theta_F = 0$ and $\theta_A = 0$.

The spatial distribution of propeller performance parameters (ref. 16) indicates that, with the design constraint of constant C_N , the performance parameters PC , $1-\tau$, η and C_Q show only small variations in the region of $\theta_F = 0$ and $\theta_A = 0$. It should be remembered that the circumferential variation of potential flow was not included. Thus, due to the fact that

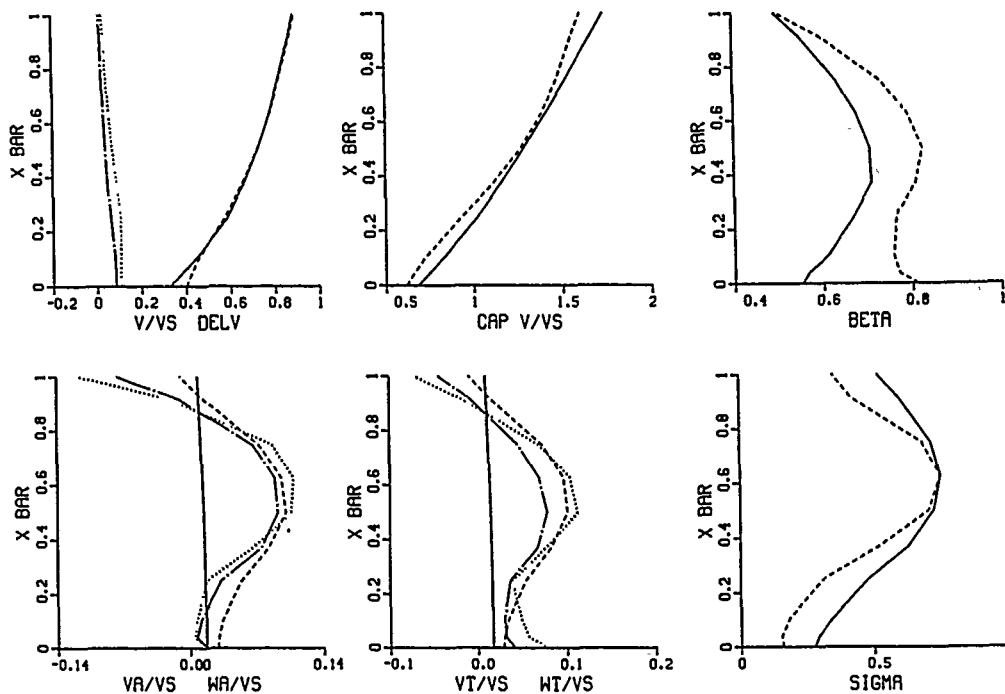
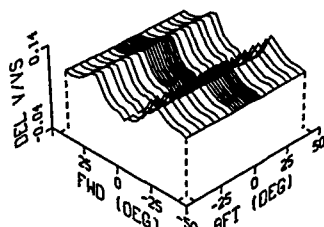
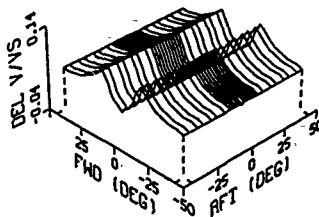


Fig. 4. Velocity components and geometric parameters for the forward and after propellers calculated using circumferential mean inflow data.

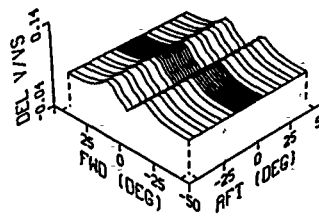
v/V_s : —, forward; —, after. $\Delta v/V_s$: —•—, forward;, after.
 V/V_s : —, forward; —, after. v_a/V_s : —, forward; —, after.
 w_a/V_s : —•—, forward;, after. v/V_s : —, forward; —, after.
 w/V_s : —•—, forward;, after. β : —, forward; —, after.
 σ : —, forward; —, after.



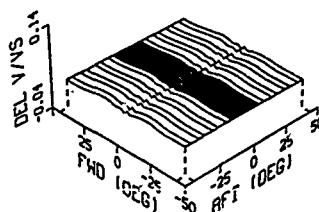
X BAR = 0.0000



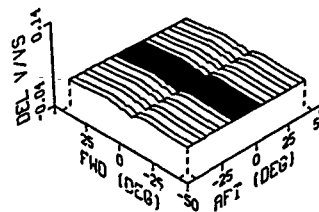
X BAR = 0.2500



X BAR = 0.5000



X BAR = 0.7500



X BAR = 1.0000

Fig. 5. Circumferential variation of the calculated change in axial inflow velocity, $\Delta v/V_s$, for the forward propeller at various \bar{x} . θ_F - FWD (DEG). θ_A - AFT (DEG).

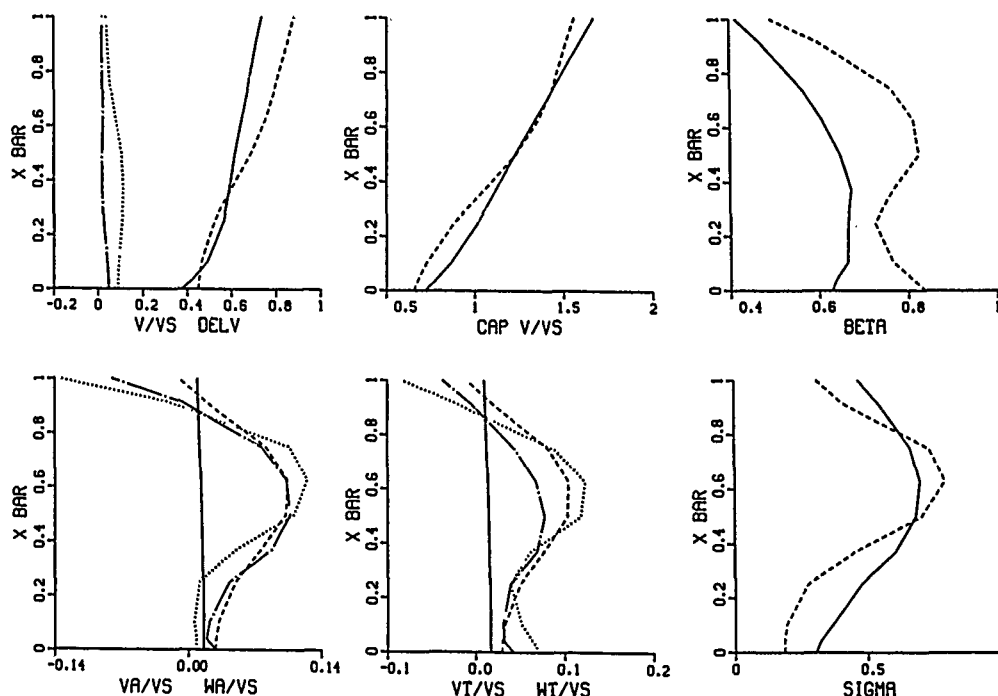


Fig. 6. Velocity components and geometric parameters for the forward and after propellers. $\theta_F=0$ and $\theta_A=14^\circ$.

v/V_s : —, forward; ----, after. $\Delta v/V_s$: —•—, forward; ·····, after.
 V/V_s : —, forward; ----, after. v_n/V_s : —, forward; ----, after.
 w_n/V_s : —•—, forward; ·····, after. v_t/V_s : —, forward; ----, after.
 w_t/V_s : —•—, forward; ·····, after. β : —, forward; ----, after.
 σ : —, forward; ----, after.

PC is a function of the thrust deduction factor, one can conclude that there would be additional small changes in PC with $\theta_{F,A}$ if the circumferential variation of the potential flow were included; however, calculations made for the forward propeller indicate that changes in PC would be on the order of 0.5%.

To further illustrate the results obtained by varying θ_F and θ_A , the radial distribution of parameters for the case when $\theta_F=0^\circ$ and $\theta_A=14^\circ$ is given in fig. 6. Comparison of this data set with the circumferential mean data presented in fig. 4 indicate that the magnitude and radial distribution of the profiles are very similar. However, the complete set of calculated data shows the sensitivity of the results to the relative angular position of the propellers and to the lack of total symmetry in the measured wake.

Unsteady Forces

The axial velocity component of the measured wake and the calculated axial inflow velocity were used in both Fourier analysis and unsteady forces calculations. The data was supplemented with the geometric parameters found in tables 1 and 2. First, Fourier analysis and unsteady force calculations were made using u/V_s , which due to the measurement procedure, contains both axial and radial components. Figure 7 presents the radial distribution of Fourier coefficient magnitude and unsteady thrust and torque for the forward and after propellers. For the forward propeller, the results show the dominance of the 12th harmonic (a_n), espe-

cially in the region of $r/R_F < 0.6$, and the rapid approach toward zero of the 24th and higher harmonics. The harmonic content distribution for the after propeller shows the dominance of the 4th harmonic and, when compared to the forward propeller, a slower decrease in magnitude of the 8th, 12th and higher harmonics. As in the forward propeller case, the large magnitude of a_n is located in the region of $r/R_F < 0.6$. For both propellers, the magnitude of b_n is nearly zero for all harmonic numbers, and the magnitude of a_n becomes nearly constant for $r/R_F > \approx 0.6$. Results for higher harmonics can be found in ref. 14, and, in general, harmonic component magnitude changes are in agreement with previous work [24].

The calculated radial distributions of F_z and T_z associated with the forward propeller's 12th harmonic (fig. 7) show that regions of large forces occur in both the inner and outer portions of the propeller blade. Also, there is a distinct minimum force region, located at $r/R_F \approx 0.7$, which coincides with the minimum velocity defect/excess region of $r/R_B \approx 0.45$ shown in fig. 1a. For the after propeller, the unsteady forces for the 4th harmonic show a minimum point at $r/R_F \approx 0.38$ which coincides with the region of greatest velocity excess at $r/R_B \approx 0.3$ (fig. 1b). Even though the 4th harmonic has a small and nearly constant magnitude over the outer region of blade, the force and moment distributions have large magnitudes in both the inner and outer regions of the blade. With increasing harmonic number, $nN_B=8$ and 12, the minimum force point moves outward along the after pro-

propeller blade's span to $r/R_F \approx 0.52$ and coincides with the region of minimum velocity excess/defect, $r/R_B \approx 0.48$ (fig. 1b). Finally, for $N_b=8$ and 12, the shape and magnitude of the force and moment distributions become more like that found for the forward propeller.

Next, data will be presented to illustrate the unsteady forces obtained by varying the propulsor inflow. Figures 8 and 9 present the radial distribution of harmonic coefficient magnitude and unsteady forces for the calculated axial velocity fields obtained by specifying (a) $\theta_A=0^\circ$ and (b) $\theta_F=0^\circ$ while the other propeller ((a) forward, (b) after) used wake data over the range $-45^\circ \leq \theta_A \leq +45^\circ$. Fourier coefficients and unsteady forces were calculated using the measured axial velocity v_1 and the calculated axial velocity, $v=v_1+\Delta v$. For $\theta_A=0^\circ$ (fig. 8), the harmonic coefficient distributions show total removal of the small magnitude of b_n previously obtained in the Fourier analysis of u/V_A . Also, the sign of a_n has been reversed while its (absolute) magnitude remains nearly the same. The radial distribution of F_x and T_x obtained using v_1 are nearly equal to that calculated using u/V_A . For the calculated axial velocity distribution, v/V_A , the magnitude of a_n for the 12th harmonic has been reduced in the region of $r/R_F < 0.5$ where the peak magnitude has been reduced by $\approx 25\%$. The unsteady forces associated with v show a reduction in magnitude over the inner radii, an increase in magnitude over the outer radii and movement of the minimum force point to a smaller radii, $r/R_F \approx 0.65$.

When $\theta_F=0$ and θ_A is varied, the measured axial velocity field results in a sign change for the 4th and 12th harmonics while the magnitude of a_n remains approximately the same. As in the previous case, the small magnitude of b_n has been removed. The characteristics of the unsteady force distributions are nearly the same as those obtained for u/V_A ; however, they show a lower magnitude of F_x and T_x at the other radii. The harmonic content obtained from the Fourier analysis of v/V_A reveals a reduction in a_n for all harmonic numbers, over the after propeller blade's inner radii. Also, the minimum force point has been shifted to a smaller radii, $r/R_F \approx 0.35$ for the 4th harmonic and to $r/R_F \approx 0.57$ for 8th and 12th harmonics. Only small deviations from the results given above were found for other combinations of θ_F and θ_A .

In addition to the radial distribution of unsteady forces given above, the total forces on the forward and after propellers were calculated. The results for the measured and calculated wakes are given in table 3. It can be seen that removal of the radial component from the measured inflow, u/V_A , results in the introduction of unsteady forces associated with the 6th and 18th harmonic components, on the forward propeller, which were zero for the measured inflow case. The magnitudes of these forces are substantially lower (3.4-4.9 times) than those obtained for the 12th and 24th harmonics and are probably an artifact of the computation procedure. The data in table 3 also shows a general reduction in unsteady force magnitude for v_1/V_A data on both the forward and after propellers when compared to the u/V_A results. While the unsteady forces obtained using v/V_A show a reduction in magnitude for most harmonic numbers, small increases in magnitude, over the u and v_1 data, are found for T_{12F} at the 12th harmonic and T_{8A} at the 8th harmonic.

Cavitation and Blade Pressures

An integral part of Nelson's propeller design method is the ability to determine the blade geometry (C/D) required to satisfy a given blade surface cavitation requirement. The counterrotating propeller geometry detailed in tables 1 and 2 reflect the chord-to-diameter ratio required to meet the cavitation requirement of $\sigma=0.75$. In all subsequent cavitation and blade pressure calculations, the blade geometry was held constant, and, since cavitation is the parameter of interest, only suction surface pressures will be calculated. The variation of σ with both forward, θ_F , and after, θ_A , propeller angles is presented in figs. 10 and 11. The results show that σ has the same type of variation from the circumferential mean data as did the various velocity components, blade pitch and performance factors (see fig. 5 and ref. 16). The variation of σ is greatest in the region of $-20^\circ < \theta_{FA} < 20^\circ$. As shown by equations (6)-(11), σ and the blade section C_p distribution depend on all the velocity components comprising the local blade section velocity diagram (fig. 3). However, as mentioned before, both w_b and Δv are functions of the chordwise trapezoidal loading distribution and the radial distribution of circulation. Thus even with corrections for thickness, lift and circumferential variation of velocity com-

For θ_A	Use Vel	F_x for $N_b =$				T_x for $N_b =$			
		6	12	18	24	6	12	18	24
----	u/V_{A_F}	0	32.3	0	12.4	0	10.8	0	4.9
0-45	v_1/V_{A_F}	3.9	25.5	3.7	12.1	2.0	8.0	1.5	4.9
0-45	v/V_{A_F}	4.8	23.3	3.2	10.8	2.2	9.8	1.3	4.4
For θ_F	Use Vel	F_x for $N_b =$				T_x for $N_b =$			
		4	8	12	16	4	8	12	16
----	u/V_{A_A}	79.1	24.4	20.7	8.1	32.9	7.3	7.5	3.0
0-45	v_1/V_{A_A}	60.4	24.7	17.5	7.4	26.7	7.4	6.0	2.8
0-45	v/V_{A_A}	63.3	20.8	14.8	7.2	26.6	7.7	5.6	2.9
For θ_F or $\theta_A = 0-40$, the values of F_x (lb) and T_x (ft-lb) are representative θ_F or θ_A was fixed while the other propeller angle was varied									

Table 3. Calculated Total Unsteady Forces for the Forward and After Propellers

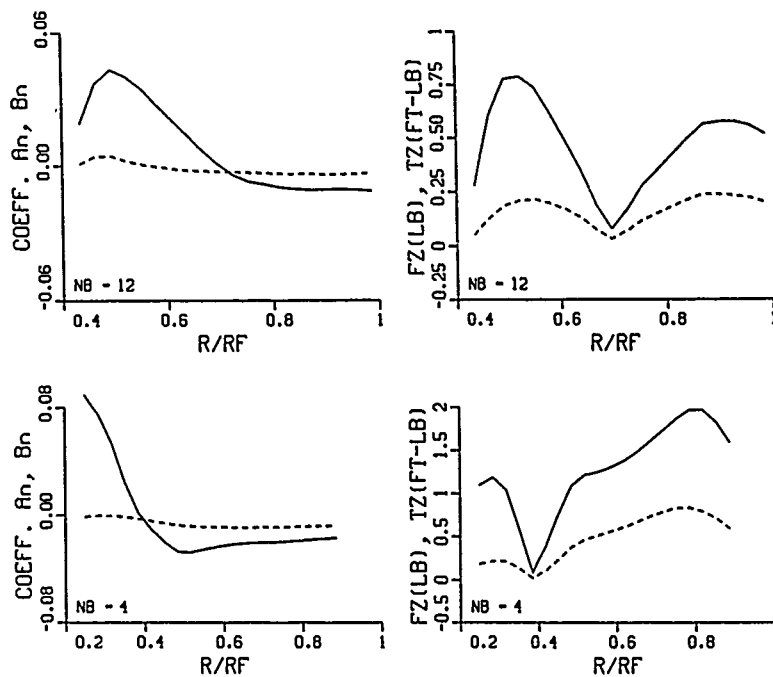


Fig. 7. Variation of Fourier coefficient magnitude (a_n, b_n) and unsteady thrust (F_z) and torque (T_z) with radial position (r/R_F) for the forward and after propellers using the measured inflow u/V_s . a) forward propeller, $nN_b=12$. b) after propeller, $nN_b=4$.
—, F_z ; ----, T_z .

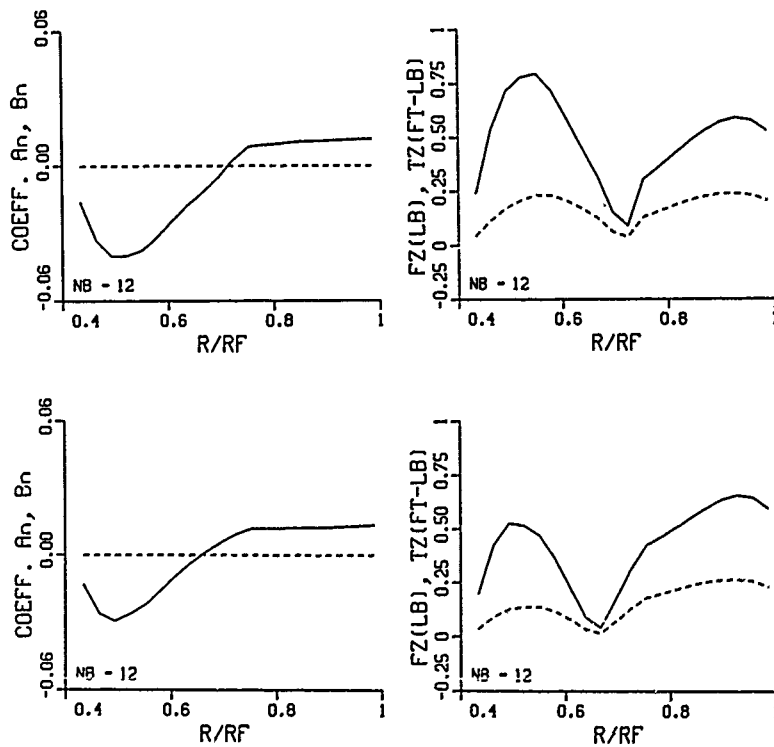


Fig. 8. Variation of Fourier coefficient magnitude (a_n, b_n) and unsteady thrust (F_z) and torque (T_z) with radial position (r/R_F) for the forward propeller.
 $\theta_A=0$, $nN_b=12$. a) v_i/V_s ; b) v/V_s . —, F_z ; ----, T_z .

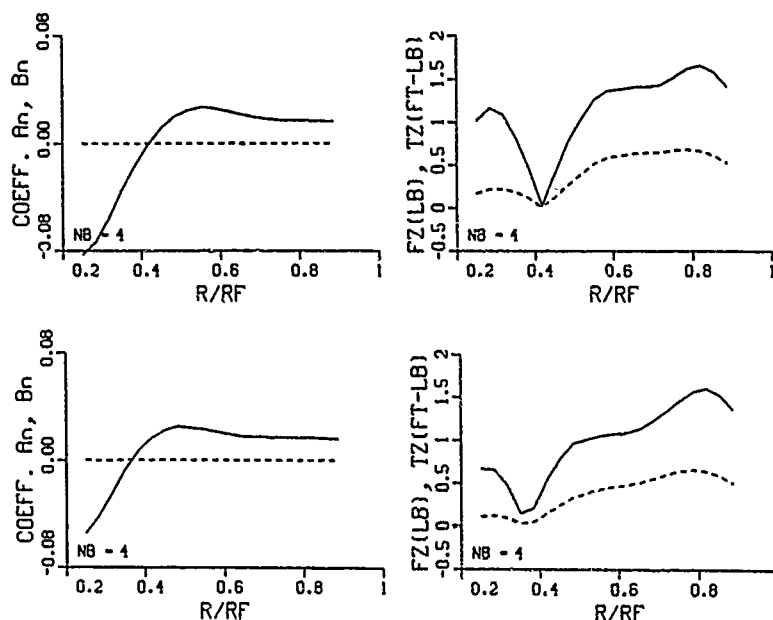


Fig. 9. Variation of Fourier coefficient magnitude (a_n, b_n) and unsteady thrust (F_z) and torque (T_z) with radial position (r/R_F) for the after propeller. $\theta_F = 0^\circ$, $n_{NB} = 4$. a) v_1/V_∞ ; b) v/V_∞ . —, F_z ; - - - - , T_z .

ponents, only small changes in σ are noted. The variation of σ in figs. 10 and 11 also represent the maximum (negative) pressure on the blade's suction surface, and, if the blade geometry were allowed to vary as required by the calculation at each θ , one might obtain larger changes in σ .

Figures 12 and 13 are representative of the variation in pressure along the suction surface of the blade at various radial locations. First, fig. 12 gives the values obtained for the counterrotating propeller set using circumferential mean inflow data. The data shows that the shape and magnitude of suction surface pressure coefficient are typical of that found on various airfoils and are in general agreement with the results of other researchers (for example refs. 2, 5 and 9). It can also be noted that the magnitude of C_p is nearly the same for both the forward and after propellers. Figure 13 gives the results for the case when $\theta_F = 0^\circ$ and $\theta_A = 14^\circ$ where the C_p calculation uses the data presented in fig. 6. Comparison of figs. 12 and 13 indicate very small differences in C_p . This result is consistent with the σ data presented in figs. 10 and 11 and is typical for the range of θ used in the study. When the equation for the suction surface pressure is derived from the Euler equations (see for ref. 9) in a rotating frame of reference, an additional term equal to Δh_p (eqn. 10) is obtained. The blade pressure results for this formulation reflect small changes in magnitude due the additional Δh_p , however, the magnitude and shape of the suction surface pressure remain in general agreement with previous work [2,5,9].

Conclusion

An existing propeller design method was modified and used to calculate the spatial variation of propeller performance, blade pressures and velocity components for use in determining changes in blade-rate forces and cavitation per-

formance. The calculations showed only small changes in the magnitude of the various velocity components, forces and blade pressures when compared to the counterrotating propeller design results. In general, there was approximate agreement between the (absolute) magnitude of both the harmonic coefficients and unsteady forces obtained using the axial component of the inflow velocity and the measured wake data. However, the unsteady force distributions associated with the calculated axial velocity, which includes propeller effects, showed an increase in magnitude at the inner radii with minimal change in its general shape. Overall, there was a small reduction in the magnitude of the total unsteady forces on the propulsor. The circumferential variation of both the cavitation index and suction surface pressure distributions showed only small variations with blade position. Also, the difference between the forward and after propeller blade pressure distributions were small.

While the simple approach used in this paper did not reveal large changes in the inflow velocity field, cavitation or unsteady forces, it did show that the design method has the tendency to modify the measured inflow velocity field in such a way that both the forward and after propeller "see" nearly identical velocity fields. This result indicates a "smoothing" of the incident velocity field. From a design standpoint this is desirable since one would not want propeller performance to be highly sensitive to small perturbations in the inflow. However, these results can only be considered first order and require extension of the calculation procedure to account for additional effects due to the unsteady flow field such as blade interaction terms and flow acceleration due to the moving blade rows.

Acknowledgments

This work was supported by the Naval Ocean Systems Center's Independent Research and Independent Exploratory Development Programs.

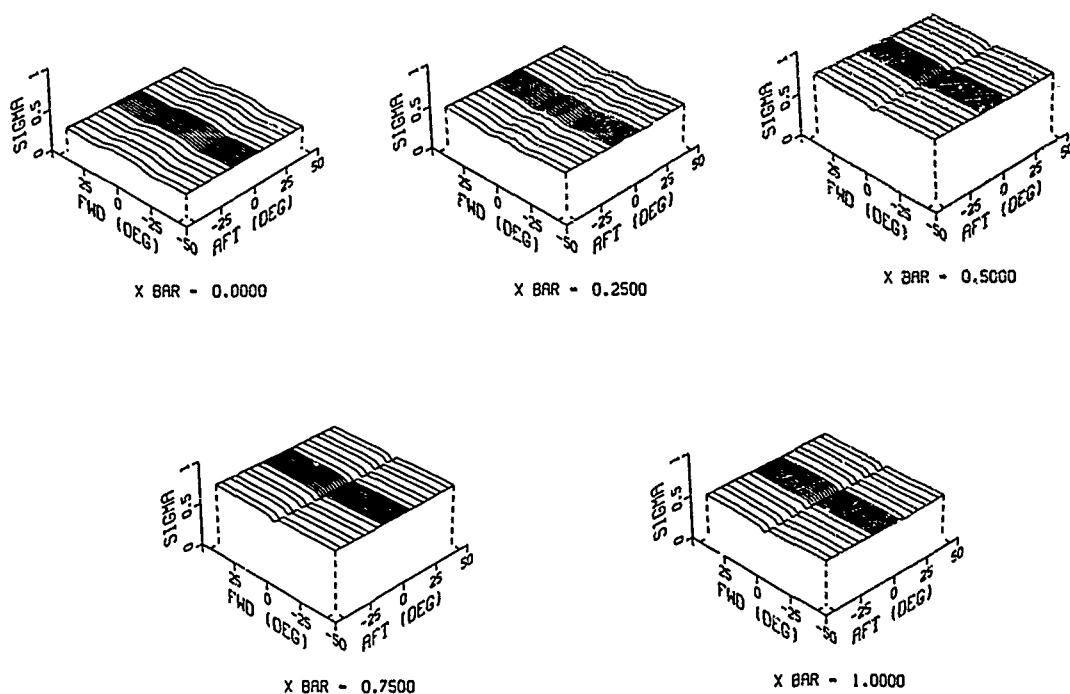


Fig. 10. Circumferential variation of the cavitation index σ , for the forward propeller at various \bar{x} locations.
 θ_F - FWD (DEG). θ_A - AFT (DEG).

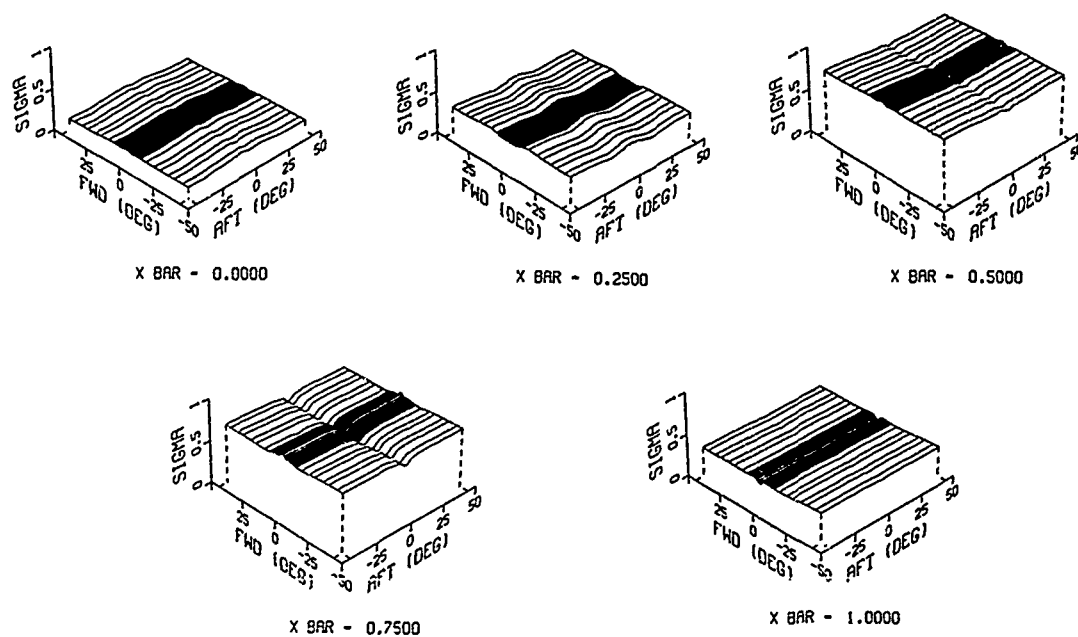


Fig. 11. Circumferential variation of the cavitation index σ , for the after propeller at various \bar{x} locations.
 θ_F - FWD (DEG). θ_A - AFT (DEG).

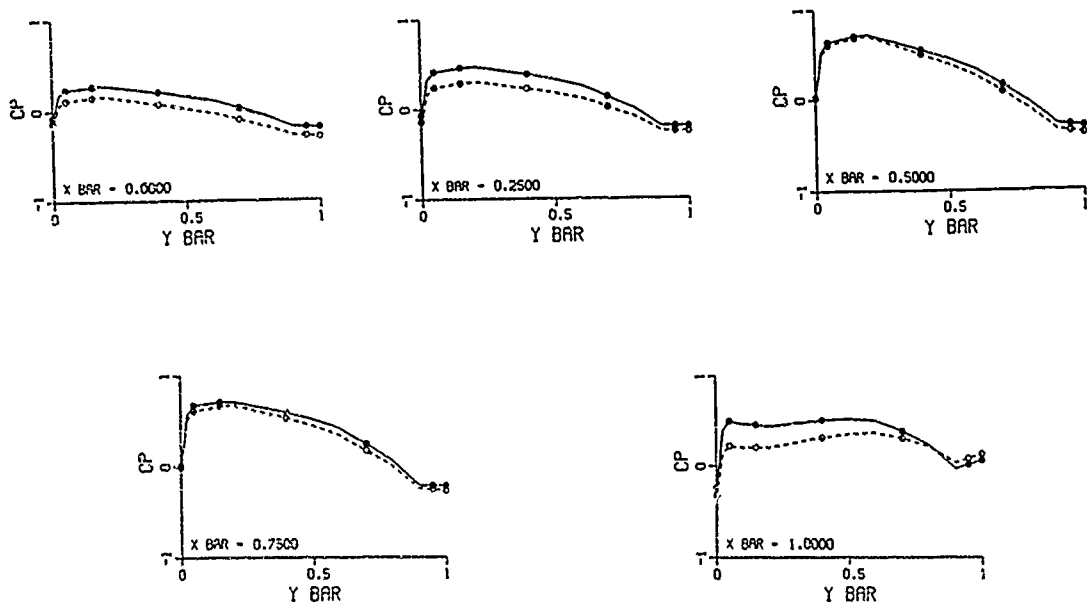


Fig. 12. Variation of suction surface pressure coefficient, $C_p = (p_\infty - p) / \frac{1}{2} \rho V_\infty^2$, calculated using circumferential mean data for the forward and after propellers at various \bar{x} locations. —●—, forward propeller; —○—, after propeller.

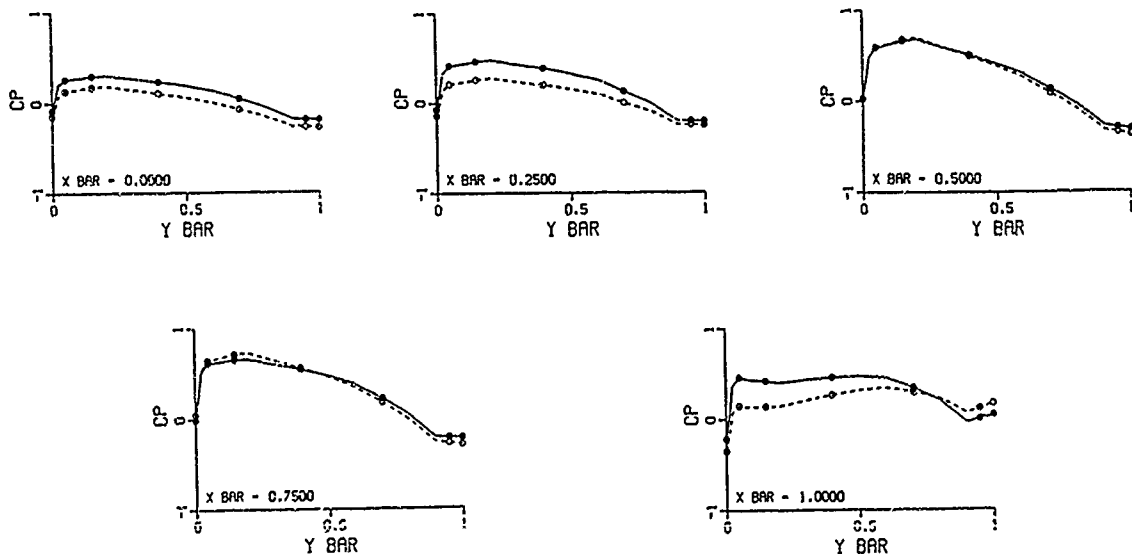


Fig. 13. Variation of suction surface pressure coefficient $C_p = (p_\infty - p) / \frac{1}{2} \rho V_\infty^2$, calculated for the forward and after propellers at various \bar{x} locations with $\theta_F = 0^\circ$ and $\theta_A = 14^\circ$. —●—, forward propeller; —○—, after propeller.

References

1. Blaurock, J. and G. Lammers, "Measurements of the Time Dependent Velocity Field Surrounding a Model Propeller in Uniform Water Flow," AGARD Symp. Aero. and Hydro. Studies Using Water Facilities, Paper No. 30, Monterey, CA, Oct., 1986.
2. Brockett, T.E., "Lifting-Surface Hydrodynamics for Design of Rotating Blades," SNAME Proceedings Propellers' 81, Paper No. 20, 1981.
3. Hess, J.L. and A. M. O. Smith, "Calculation of Nonlifting Potential Flow about Arbitrary Three-Dimensional Bodies," Douglas Aircraft Company Report ES40622, 1962.
4. Hess, J.L. and A. M. O. Smith, "Calculation of Potential Flow About Arbitrary Bodies," Progress in Aeronautical Sciences Series, Vol. 8, Pergamon Press, 1966.
5. Hess, J.L. and W.O. Valarezo, "Calculation of Steady Flow About Propellers by Means of a Surface Panel Method," AIAA Paper No. 85-0283, 23rd Aerospace Sciences Meeting, Reno, NV, 1985.
6. Hough, G.R. and D.E. Ordway, "The Generalized Actuator Disk," Term Advanced Research, Report No. TAR-TR 6401, 1964.
7. Jessup, S.D., C. Schott, M. Jeffers and S. Kobayashi, "Local Propeller Blade Flows in Uniform and Sheared Onset Flows Using LDV Techniques," Proceedings 15th Symp. Naval Hydrodynamics, Washington, D.C., 1985.
8. Kerwin, J.E. and C. Lee, "Prediction of Steady and Unsteady Marine Propeller Performance by Numerical Lifting-Surface Theory," SNAME Transactions, Vol. 86, 1978, pp. 218-253.
9. Kim, K. and S. Kobayashi, "Pressure Distribution on Propeller Blade Surface Using Numerical Lifting Surface Theory," SNAME Proceedings Propellers' 84, Paper No. 1, 1984.
10. Kotb, M.A. and J.A. Schetz, "Detailed Turbulent Flow field Measurements Immediately Behind a Propeller," SNAME Proceedings Propellers' 84, Paper No. 3, 1984.
11. Laudan, J., "The Influence of the Propeller on the Wake Distribution as Established in a Model Test," SNAME Proceedings Propellers' 81, Paper No. 13, 1981.
12. Lerbs, H.W., "Moderately Loaded Propellers With a Finite Number of Blades and an Arbitrary Distribution of Circulation," Society of Naval Arch. and Marine Engineers, Transactions, Vol. 60, 1952.
13. Mautner, T.S., "A Computer Program Package for Providing Input to the Douglas Three-Dimensional Potential Flow Program: A User's Manual," NOSC, TR 352, 1978.
14. Mautner, T.S., "An Optimization Method for the Reduction of Propeller Unsteady Forces," AIAA Paper 88-0265, 26th Aerospace Sciences Meeting, Reno, NV, Jan., 1988.
15. Mautner, T.S., "Comparison of the Counterrotating and Pre-Swirl Propeller Concepts for Marine Propulsion," Paper AIAA-88-3088, AIAA/ASME/SAE/ASEE 24th Joint Propulsion Conference, Boston, MA, July, 1988.
16. Mautner, T.S., "Preliminary Results in the Development of a Method to Correct Propeller Inflow for Improved Unsteady Force Calculations," AIAA Paper No. 89-0436, 27th Aerospace Sciences Meeting, Reno, NV, 1989.
17. Nelson, D.M., "A Lifting-Surface Propeller Design Method for High Speed Computers," NOTS TP 3399, 1964.
18. Nelson, D.M., "Numerical Results from the NOTS Lifting-Surface Propeller Design Method," NOTS TP 3856, 1965.
19. Nelson, D.M., "Development and Application of a Lifting Surface Design Method for Counterrotating Propellers," NUC TP 326, 1972.
20. Nelson, D.M., "A Computer Program Package for Designing Wake-Adapted Counterrotating Propellers: A User's Manual," NUC TP 494, 1975.
21. Nelson, D.M. and J.J. Fogarty, Private communication, 1977.
22. Schetz, J.A., "The Flow field Near the Propeller of a Self-Propelled Slender Body with Appendages," SNAME Proceedings Propellers' 81, Paper No. 1, 1981.
23. Tsakonas, S., J.P. Breslin and W.R. Jacobs, "Blade Pressure Distribution for a Moderately Loaded Propeller," J. Ship Research, Vol. 27, No. 1, 1983, pp. 39-55.
24. Thompson, D.E., "Propeller Time-Dependent Forces Due to Nonuniform Flow," Applied Research Laboratory, Pennsylvania State Univ., Tech. Mem. TM No. 76-48, 1976.

CONCLUDING REMARKS

Francis Noblesse
David Taylor Research Center

As chairman of the last session, I have the task of officially closing the Fifth International Conference on Numerical Ship Hydrodynamics, although Professor Mori asked me to urge you to participate in the Group Discussions following the Conference. I also have the privilege of briefly reflecting upon the Conference.

On behalf of all the participants, I wish first and foremost to thank the organizers for an absolutely flawless and superb organization. We are well aware that the organization of the Conference has required an enormous amount of work by Professor Mori and many other persons around him. We do want him and everyone else who helped in the organization of the Conference to know that we deeply appreciate their efforts on our behalf.

I feel confident in expressing that there exists a clear consensus among the participants that the Conference was highly successful. I believe that at least three reasons for the success of the Conference can be cited. A first reason resides in the well-chosen, highly informative four keynote lectures. Another reason is the large number of excellent papers presented at the Conference. A third reason is that the importance of validating numerical methods was emphasized at this Conference to much greater extent than previously. I believe we all leave this Conference with an increased awareness of the need for establishing the robustness and the reliability of the numerical methods which we develop or apply. This greater awareness represents a healthy and important development, and attests to the progress that has been made in the field of numerical ship hydrodynamics. In this respect, I think the Conference may come to be remembered as something of a turning point in the history of the development of numerical methods in ship hydrodynamics, and the organizers have done a great service to our community by employing the need for validation.

There also exists a clear consensus among the participants that the Conference was not only successful from a technical point of view but also highly pleasant and enjoyable. Several factors have contributed to making the Conference a particularly enjoyable experience. A first factor is that Hiroshima, surrounded by a beautiful skyline of mountains and divided by several graceful rivers, is a lovely city, especially under the splendid weather we enjoyed. The charm and kindness of the people of Hiroshima also contributed to creating an enjoyable experience. The kindness and hospitality of the people of Hiroshima is quite well demonstrated by the following personal story which I would like to tell. I happened to get lost while walking through the city yesterday afternoon. So I asked a middle-aged Japanese man for directions. He not only pointed me in the right direction but insisted that I follow him to a nearby parking lot so that he could take his car and drive me to my hotel! The reception Sunday evening, the buffet party Tuesday evening, and the boat cruise to Miyajima yesterday evening were also very enjoyable. I believe the evening cruise to Miyajima provided a specially pleasant setting for enjoying the company of old friends as well as making new ones, and will be remembered. The Conference was a particularly enjoyable experience not only because of several events arranged by the organizers but also because of the warmth and kindness of the Japanese participants, who invited many of us who traveled from outside Japan in the evening and made us feel at home.

On behalf of all the participants from outside Japan, I simply wish to say "domo arrigato go say mashita". May I finally invite the participants from outside Japan to join me in expressing our deep appreciation to our Japanese hosts by applauding them.

Group Discussions

Summary of the Group Discussion on Rankine Source Methods

Chairman: A. J. Musker
Admiralty Research Establishment
Haslar, England
Co-chairman: S. Ogiwara
Ishikawajima-Harima Heavy Industries Co.
Yokohama, Japan

The Group Discussion on Rankine Source Methods was attended by approximately 50 leading researchers from 12 nations. Attention was focussed on the following items, although there was necessarily a high degree of overlap between the topics:

- (i) Radiation condition
and its application
- (ii) Resolution of divergent waves
-higher order panels
- (iii) Water-line problem
-effect on stability
- (iv) Calculation of wave resistance
- (v) Existence and uniqueness

Three different approaches to satisfying the radiation condition were discussed: Dawson's approach, involving a one-sided finite difference operator (eg Larsson, Musker), staggered collocation points (Jensen, Ando, Nakatake) and a hybrid approach, first suggested by Gadd, involving a Kelvin source density distributed on the hull and a Rankine source density distributed on the free-surface but confined to the nearfield (Yim).

The errors associated with various formulations of a four-point Taylor series operator were discussed (Van). A recent study had drawn the same conclusions as Dawson, namely that the 2nd and 4th derivatives should be eliminated in its formulation.

The method of staggered or shifted collocation points was discussed at some length. Jensen described the change in wave pattern resulting from different ways of staggering the free-surface grid. Waves were found to propagate upstream and downstream depending on the chosen configuration. The question remained as to whether a regime could be identified for which the results were realistic as well as being insensitive to small changes in mesh geometry.

The lack of rigour in treating the radiation condition used in the more popular methods described in recent years was criticised by Bai. Suggestions that the approaches were nearer to art than science were quickly refuted by the more pragmatic users of the methods since the experience has been that the methods do provide good engineering predictions provided the algorithms remain stable.

There was general agreement about the desire to use higher order panels to resolve the divergent wave system and to better model the larger gradients in the bow region (Yim, Larsson, Mori, Baubeau). Larsson referred to the 1977 paper by Hess which addressed the two dimensional problem of the flow over a submerged vortex. His conclusion was that a higher order line source method was required. For ship-flows, the case for higher order panels is not as strong if the panels are not positioned in the calm-water plane (Baubeau, Musker), although the stability

of the solution algorithms does seem to improve. Larsson made a strong case that the higher order method is more economical in terms of computing requirements and that an additional benefit arose in that the pressure integration around the body, required in the calculation of resistance, was more accurate.

It was the general feeling that the resistance should be calculated by pressure integration and not by momentum considerations. This recommendation was largely the result of experience in comparing both methods with experiment rather than a rigorous appraisal of the numerical issues involved. Numerical damping in the far-field probably accounts for the disparity.

Difficulties remain in the vicinity of the water-line. Whilst the available methods behave reasonably well with the Wigley and Series 60 hulls, great difficulties have been experienced with the HSVA tanker (Jensen, Larsson). In Jensen's case, the collocation points near to the water-line were suppressed to achieve convergence. The existence of solutions to the potential flow formulation of the wave resistance problem was discussed at some

length in the context of instabilities near the water-line.

In the real world, we know that spray and wave-breaking occur -especially near the bow; both viscous and surface tension effect are present (Jensen). Thus the potential flow model cannot be expected to cope with these complexities and it is then necessary to consider whether, when these (non-linear) regimes are being approached in a Rankine-Source calculation, a solution exists at all. Divergence of a scheme may then be truly reflecting the mathematics - not the numerical techniques invoked (Musker, Larsson), in which case it might be possible to identify an upper limit in terms of the utility of such methods. A consensus on this issue could not be reached.

Notwithstanding the above difficulties, however, it was agreed that Rankine-Source methods had a very definite role to play in ship design to predict wave resistance and that they should also be used, in conjunction with Navier-Stokes methods, to investigate the wave-viscous interaction problem (Yim).

Summary of the Group Discussion on Navier-Stokes Solvers

Chairman: J. Piquet

ENSM

Nantes, France

Co-chairman: Y. Kodama

Ship Research Institute

Tokyo, Japan

First, questions, fields and issues on which this Group Discussion should be focused are given (Kodama). Then a general table, given hereafter, of the methods presented during the meeting is briefly discussed (Piquet). It appears that, among the fourteen papers presenting numerical solutions of Navier-Stokes equations, only three methodologies are used; an unsegregated approach (Hoekstra) in which the solenoidality of the flow is enforced at each iteration; other contributions satisfy the incompressibility condition at convergence either by means of the so-called artificial compressibility method (Yang, Kodama) or by means of a pressure correction technique-projection type method (Zhu, Hino, Doi) or simple-like methods (Tzabiras, Larsson, Oh, Masuko, Piquet, Stern).

It should be therefore necessary to compare in a more detailed way the methods, in order to isolate their differences and the resulting effects (Stern). As a first important difference, the choice of independent variables is felt significant (Tzabiras) although no clear evidence of optimal choice has been provided.

Several specific aspects are then addressed in the discussion: geometric singularities created by the curvilinear structured grid, averaging procedures (Kodama); orthogonality constraints on the grid, needed regularity of the control functions in the elliptic grid generation procedure (Ju), convergence problems on fine grids (Piquet). The question of accuracy measures is posed, from a 2D example, for an inner problem where momentum conservation implies strongly different results on the drag forces coefficients C_{DP} and C_{DM} when computed from the integration of forces and from the global momentum balance (Kubota). The problem of conservation of mass, close to the boundaries - e.g. the free surface (Hino) - as well as that of momentum is discussed.

Problems connected to the turbulence model are then addressed. Corrections for the free-surface problems (Hino) and existence of a model adequate for lifting problems (Tzabiras) are questioned. The need to avoid the "highly convenient" wall function approach is

emphasized (Hoekstra). In any case, it appears difficult to check the influence of the turbulence model on the numerical results in an unbiased way.

The discussion is then displaced towards what should be done now (Tzabiras), given the existence of several Navier-Stokes codes able in principle to deal with complex problems. A few possibilities are put forward and, among the noticed fields of applications, the impact of Navier-Stokes codes on the propeller research is not considered "too optimistically" (Hoekstra).

Endly, the boundary conditions are discussed mainly in relation with the numerical scheme considered (Tzabiras, Kodama) although the natural mathematical character of the Neumann pressure condition is pointed out (Hoekstra).

To try a tentative evaluation, the chairmen of the discussion feel that the brief survey of technical problems that has been attempted gives a good picture of collective weaknesses, given the rather small size of the community working on Navier-Stokes solvers for hydrodynamic problems.

The discussion was felt either too specific - and so could be considered as a disappointing specialist discussion (Himeno) - or not detailed enough to allow an appreciation of the pros. and cons. of the presented works and methodologies. May be, this can be attributed to the fact that not only our mutual work is not known in enough details, but also that the concerned aspects are so numerous that a complete assessment of each detail of the used methods is difficult.

The weaknesses of the discussions appeared also on a conceptual level, for instance in the treatment of boundary conditions and on the views over accuracy. Recognized inadequacies in the treatment of the geometry - e.g. the HSWA tanker - did not raise the question of the use of partially unstructured grids. Recognized difficulties in enforcing conservativity (geometrical, mass, momentum) did not raise the question of the use of Galerkin-type methods. May be, these problems should call for a better consideration of the literature

issued from applied mathematics.

Because a lot of time has been spent on the technical aspects of the work, and probably also because of the way the discussion has been conducted, the practical importance of the whole set of aforementioned prob-

lems was not evaluated. A fortiori, the ability to use Navier-Stokes solvers to understand flow situations was not considered, although these solvers offer a unique opportunity to get information on the flow at a level of details not possible with experiments.

Table of the 14 papers related to Navier-Stokes solvers presented during INC-5 (Part 1).

AUTHORS	VARIABLES & LAYOUT	GRID GENERATION	INCOMPRESS. CONSTRAINT	PRESSURE SOLVER	MOMENTUM SOLVER
HOEKSTRA	covariant VW contravariant U collocated	Schwarz Christoffel transv. ortho.	Unsegregated	multiple relax. sweep	CSIP
YANG et Al.	UVWP collocated	Algebraic	artif. comp.	relaxation + IAF	relaxation + IAF
KODAMA	UVWP collocated	Geometrical [interp.btw.] surface grids	artif. comp.	IAF(Implicit Approximate Factorization)	IAF
ZHU et Al.	contravariant	Elliptic	MAC	relaxation	explicit
HINO	UVWP collocated node-centered	Algebraic	MAC	relaxation	explicit
KINOSHITA et Al.	UVWP collocated	Algebraic	MAC	relaxation	explicit
KUBOTA et Al.	UVWP collocated	Geometrical	compressible (cavitation)	relaxation	explicit
DOI		No (channel flow)	Projection		
TZABIRAS LOUKAKIS	UVWP staggered	Elliptic	SIMPLE	relaxation	relaxation
LARSSON et Al.	contravariant staggered	Elliptic	SIMPLER	relaxation	relaxation
OH et Al.	phys. polar staggered	Elliptic	SIMPLE	relaxation	relaxation
MASUKO OGIWARA	UVWP staggered	Elliptic	SIMPLE	relaxation	relaxation
PIQUET VISONNEAU	UVWP collocated	Transfinite + Elliptic	PISO	ILU-PBCG	relaxation
STERN KIM	UVWP staggered	Elliptic	SIMPLER	plane ADI	plane ADI

Table of the 14 papers related to Navier-Stokes solvers presented during INC-5 (Part 2).

AUTHORS	TURBULENCE	WALL	SPACE	TIME	FREE SURFACE
HOEKSTRA	Mixing length (CS)	damping factor	pressure downstream 2nd-order V upstream	implicit	no
YANG et Al.	Baldwin-Lomax	damping factor	TVD(Roe)	implicit (Δ form)	no
KODAMA	Baldwin-Lomax	damping factor	centered 2nd-order artif.dissipation	implicit (Δ form)	no
ZHU et Al.	SGS	damping factor	centered 4th-order artif.dissipation	explicit	no
HINO	Baldwin-Lomax	wall function	2nd-order P 3rd-order conv.	explicit	yes $F_n=0.25$
KINOSHITA et Al.	none	no slip	2nd-order P 3rd-order conv.	explicit	no
KUBOTA et Al.	none	no slip	2nd-order P 3rd-order conv.	explicit	cavitation
DOI	SGS	damping factor	3rd-order conv. artif.dissipation	Adams-Bashforth (explicit)	no
TZABIRAS LOUKAKIS	k- ϵ	wall ftn.	Hybrid	implicit	no
LARSSON et Al.	k- ϵ	wall ftn.	Finite-Analytic	implicit	no
OH et Al.	k- ϵ	wall ftn.	Finite-Analytic	implicit	no
MASUKO OGIWARA	k- ϵ	wall ftn.	Hybrid	implicit	no
PIQUET VISONNEAU	k- ϵ	wall ftn.	Finite-Analytic	implicit	no
STERN KIM	laminar k- ϵ	wall ftn.	Finite-Analytic	implicit	no

Table of the 14 papers related to Navier-Stokes solvers presented during INC-5 (Part 3).

AUTHORS	START	INLET	FAR FIELD	GRID ξ, η, ζ	NO. of ITER.	CPU TIME	TEST CASES
HOEKSTRA	potential $P_\eta = 0$	thin B.L. midship	potential	45x49x29 10^{-3} resid	24	.5-1h Cray2	HSVA tanker
YANG et Al. KODAMA		far upstream	uniform	91x25x29	220 5000	17' Cray YMP 40"/iter. Stellar GS1000	Afterbodies 1,2,5 Bodies at incidence Flat plate, Wigley, Series 60 (Cb=0.6,0.7,0.8)
ZHU et Al.	rest	far upstream	uniform	170x30x50 (255000 to 340000 pts)		20h Hitac S820/80	Wigley hull
HINO	rest	far upstream	uniform	100x20x38	11000	2h/1000steps ACOS 910	Wigley hull Series 60 (Cb=0.6)
KINOSHITA et Al.	rest	rest	rest	140x60	5000	70' VP-100	Oscillating circular cylinder
KUBOTA et Al.	uniform	far upstream	uniform	101x31x3		Hitac M-680H	NACA0015 wing section
DOI	rest	periodic	no				Channel flow LES
TZABIRAS LOUKAKIS	rest	thin B.L. midship	potential	44x32x30	35 (20% resi.red. / iter)	60hrs. μ Vax	SSPA ship liner
LARSSON et Al.	rest	thin B.L. midship		60x21x15			SSPA ship liner
OH et Al.	rest	1/7 + eq. midship	uniform	54x32x25	190	1600" VP-100	SSPA ship liner
MASUKO OGIWARA	rest	far upstream	uniform	94x25x21			Series 60 (Cb=0.6) IHI-BO tanker
PIQUET VISONNEAU	rest	thin B.L. midship	uniform	80x40x31		2hrs Cray 2	HSVA tanker
STERN KIM	rest +rot. case	thin B.L.	uniform (relative frame)	80000		Cray XMP	Propeller shaft

Summary of the Group Discussion on Boundary Integral Method for Radiation/Diffraction Problems

Chairman: O. M. Faltinsen
Norwegian Institute of Technology
Trondheim, Norway
Co-chairman: M. Takaki
Hiroshima University
Hiroshima, Japan

More than 40 participants took part in this group discussions and actively discussed about the following topics.

1. Singularities due to the body

Zhao showed the behaviour of the potential near the corner of a rectangular cylinder by using a lower order panel method based on Green's second identity. The method assumes the velocity potential and its normal derivative are constant over each element. By comparing with analytical solutions it was demonstrated that the velocity potential at the element closest to the corner will always be wrong.

2. Free-surface intersection, line integral

Zhao showed the behaviour of the wave elevation near the intersection between the free-surface and the body surface in the case of a plate suddenly starts to move with a constant velocity. The solution is based on linear free-surface condition. The analytical solution by Roberts shows the wave amplitude is finite everywhere. However, the wave elevation near the intersection point between the free-surface and the body has infinite number of oscillations. That means we cannot numerically solve the problem by using a finite number of elements and assuming the velocity potential to be constant over each element.

Regarding the latter problem, Cointe, Pawloski, and Takagi commented that the linear theory is inconsistent, we should treat it as a nonlinear problem.

Kyouzuka presented 2-D second order forces

by the perturbation theory. Singularities occurred in the 2nd order theory at the intersection between the free-surface and the body. In order to overcome this problem, it is useful to integrate analytically the potential on a few free-surface elements which are close to the body.

Higo showed that the line integral did not effect significantly hydrodynamic forces on a vertical circular cylinder. Ohkusu commented that the line integral effects the wave field near the body much more than the forces on a body, therefore the effect of the line integral should be checked by the values of wave field.

Kashiwagi investigated the validity of a linear solution for an oscillating and moving surface piercing body. The solution is based on the classical free-surface condition. A singular solution occurs at the intersection between the free-surface and the body surface. The multiple expansion method is useful for overcoming that problem. It was found that additional contribution to the rate of energy flux arise from the solution around an intersection point.

3. Radiation condition

Takagi and Naito investigated the linear- and a nonlinear radiation condition due to 2-D BEM (Boundary Elemental Method). They explained that the idea of the active wave absorber could be used for the radiation condition for BEM. Cointe pointed out that we should not use the word wave radiation condition. It is better to call it wave absorption condition.

4. Calculation of velocity on the body and the m_k -terms

Kinnas told about calculation of velocity near the body by using a lower order panel method. There will always be numerical problems in calculating the velocity at the body boundary. He recommended that we should use a higher order scheme. Zhao mentioned that a similar problem occurred in the calculation of the m_k -terms.

5. Verification procedures

The following items were addressed by the chairman.

- a. Convergence by increasing panel numbers.
This does not always occur, for instance near sharp corners.
- b. Importance of analytical results.
- c. How to qualify errors.

Ohkusu talked about a 3-D panel method with forward speed. He carried out numerical calculations on a submerged spheroid to exclude the problem of the line integral. A convergence by 3-D panel method becomes better by increasing number of panels. 1200 panels on a submerged spheroid are good enough. So we have already reached to the confident result

from a practical point of view. However, as the body is close to a free-surface, the accuracy of results becomes worse. This means the calculations for surface piercing bodies create problems.

Validations of numerical results about 3-D panel method have still the following problems:

- a. How many panels do we have to use?
- b. How should we treat the wave component with a shorter wavelength?
- c. Are there any singularities at the intersection between the free-surface and the body surface?

Lee commented that using established relations is better than checking the convergence by increasing the number of panels. This means we should check the mass conservation and the body boundary condition etc.

6. Iterative solution of large equation system

Hermans told that there are a lot of references in the literature about iterative solvers. For different problems we should use different iterative solvers. It is difficult to know which one is the best for a given numerical problem.

List of Participants

Aanesland, Vidar	MARINTEK	Norway
Ando, Jun	Kyushu University	Japan
Baba, Eiichi	Mitsubishi Heavy Industries Ltd.	Japan
Bai, Kwang-June	Seoul National University	Korea
Baubeau, Robert	Bassin d'Essais des Carènes	France
Bessho, Masatoshi	Defense Academy	Japan
Bulgarelli, Ulderico	INSEAN	Italy
Casciola, Carlo Massi	INSEAN	Italy
Cheng, Bill Hsi.	David Taylor Research Center	USA
Cho, Il-Hyoung.	Seoul National University	Korea
Choi, Hang S.	Seoul National University	Korea
Cointe, Raymond	Institut Français du Pétrole	France
Davies, Melvyn E.	BMT Fluid Mechanics Ltd.	UK
Della Loggia, Bruno	CETENA	Italy
Dercksen, Albertus	Maritime Research Institute of the Netherlands	Netherlands
Doi, Yasuaki	Hiroshima University	Japan
Dong, Shi-Tang	China Ship Scientific Research Center	China
Eatock Taylor, Rodney	University of Oxford	UK
Ebira, Kazuyuki	Hiroshima University	Japan
Eguchi, Tatsuya	Mitsui Engineering and Shipbuilding Co., Ltd.	Japan
Ertekin, R. Cengiz	University of Hawaii	USA
Esposito, Piergiorgio	INSEAN	Italy
Falch, Sigurd	MARINTEK	Norway
Faltinsen, Odd M.	Norwegian Institute of Technology	Norway
Fujii, Akihiko	Mitsui Engineering & Shipbuilding Co., Ltd.	Japan
Fujii, Kozo	The Institute of Space and Astronautical Science	Japan
Fujino, Masataka	University of Tokyo	Japan
Fujisawa, Yasuo	Ohbayashi Corporation	Japan
Fujiwara, Akihiro	University of Osaka Prefecture	Japan
Fukasawa, Toichi	University of Tokyo	Japan
Funeno, Isao	Kawasaki Heavy Industries Ltd.	Japan
Ha, Mun Keun	Hiroshima University	Japan
Haimov, Anri	Bulgarian Ship Hydrodynamics Center	Bulgaria
Hamasaki, Junichi	Tsuneishi Ship-Building Co., Ltd.	Japan
Hatano, Shuji	Hiroshima University	Japan
Hermans, Aad	Delft University of Technische	Netherlands
Higo, Yasushi	Hiroshima University	Japan
Himeno, Yoji	University of Osaka Prefecture	Japan
Hino, Takanori	Ship Research Institute	Japan
Hirao, Saburo	Hiroshima University	Japan
Hirayama, Tsugukiyo	Yokohama National University	Japan
Hoekstra, Martin	Maritime Research Institute of the Netherlands	Netherlands
Hong, Seok Won	Korea Institute of Machinery & Metals	Korea
Horinokita, Katsuro	Shipbuilding Research Association of Japan	Japan
Hotta, Takio	Hiroshima University	Japan
Huang, De-Bo	Harbin Shipbuilding Engineering Institute	China
Huijsmans, R. H. M.	Maritime Research Institute of the Netherlands	Netherlands
Hwang, Jong-Heul	Seoul National University	Korea
Ikehata, Mitsuhsa	Yokohama National University	Japan
Inoue, Yoshiyuki	Yokohama National University	Japan
Inui, Takao	University of Tokyo	Japan
Ishikawa, Satoru	Mitsubishi Heavy Industries	Japan
Ito, Masamitsu	Toba National College of Maritime Technology	Japan
Iwashita, Hidetsugu	Kyushu University	Japan
Jankowski, Jan	Polish Register of Shipping	Poland
Jensen, Gerhard	Ingenieur Kontor Lübeck	Germany
Jensen, Peter S.	Danish Maritime Institute	Denmark
Ju, Sangseon	Daewoo Shipbuilding & Heavy Machinery Ltd.	Korea
Kagemoto, Hiroshi	University of Tokyo	Japan
Kajitani, Hisashi	University of Tokyo	Japan
Kamioka, Takashi	Hiroshima University	Japan
Kan, Makoto	Ship Research Institute	Japan
Kanai, Takeshi	Shipbuilding Research Center of Japan	Japan

Kang, Chang-Gu	Korea Institute of Machinery & Metals	Korea
Kang, Shin-Hyoung	Seoul National University	Korea
Kasahara, Yoshikazu	NKK Corporation	Japan
Kashiwagi, Masashi	Kyushu University	Japan
Kashiyama, Kazuo	Hiroshima Institute of Technology	Japan
Kataoka, Katsumi	Kyushu University	Japan
Kato, Hiroharu	University of Tokyo	Japan
Katz, Joseph	The Johns Hopkins University	USA
Kawaguchi, Noboru	Mitsubishi Heavy Industries Ltd.	Japan
Kawahara, Mutsuto	Chuo University	Japan
Kawano, Takeshi	Japan Marine Science and Technology Center	Japan
Kawashima, Toshihiko	Research Institute of Fisheries Engineering	Japan
Kijima, Katsuro	Kyushu University	Japan
Kim, Dong Jin	Hyundai Heavy Industries Co., Ltd.	Korea
Kim, Jang-Whan	Seoul National University	Korea
Kim, Keun Jae	Chalmers University of Technology	Sweden
Kim, Younghwan	Daewoo Shipbuilding & Heavy Machinery Ltd.	Korea
King, Bradley	Bassin d'Essais des Carènes	France
Kinnas, Spyros	Massachusetts Institute of Technology	USA
Kinoshita, Takeshi	University of Tokyo	Japan
Kobayashi, Toshio	University of Tokyo	Japan
Kodama, Yoshiaki	Ship Research Institute	Japan
Kohara, Shigeaki	Hiroshima National College of Maritime Technology	Japan
Kose, Kuniji	Hiroshima University	Japan
Krokstad, Jorgen R.	University of Trondheim	Norway
Kubo, Hironao	Nakashima Propeller Co., Ltd.	Japan
Kubota, Akihiro	University of Tokyo	Japan
Kudo, Tatsuro	Ship Research Institute	Japan
Kwaq, Seung-Hyun	Hiroshima University	Japan
Kyozuka, Yusaku	Kyushu University	Japan
Lalli, Francesco	INSEAN	Italy
Larsson, Lars	SSPA Maritime Consulting	Sweden
Lee, Choung Mook	Pohang Institute of Science and Technology	Korea
Lee, Young-Gill	University of Tokyo	Japan
Liapis, Stergios	University of New Orleans	USA
Lin, Wen-Chin	David Taylor Research Center	USA
Liu, Hao	Yokohama National University	Japan
Marubayashi, Eisaku	Hiroshima University	Japan
Masuda, Kouichi	Nihon University	Japan
Masuko, Akira	Ishikawajima-Harima Heavy Industries Co., Ltd.	Japan
Masure, Bernard	Bassin d'Essais des Carènes	France
Matsumura, Kiyoshige	Osaka University	Japan
Matsushima, Isao	Hiroshima National College of Maritime Technology	Japan
Matusiak, Jerzy	VTT Ship Laboratory	Finland
Mautner, Thomas	Naval Ocean Systems Center	USA
McCarthy, Justin	David Taylor Research Center	USA
Miyajima, Shogo	University of Tokyo	Japan
Miyata, Hideaki	University of Tokyo	Japan
Mizuno, Toshiaki	Defense Academy	Japan
Montagne, Jean-Louis	Bassin d'Essais des Carènes	France
Mori, Kazu-hiro	Hiroshima University	Japan
Murakami, Kyoji	Hiroshima University	Japan
Murashige, Sunao	University of Tokyo	Japan
Musker, Anthony J.	Admiralty Research Establishment	UK
Nagamatsu, Tetsuo	Mitsubishi Heavy Industries Ltd.	Japan
Naito, Shigeru	Osaka University	Japan
Nekatake, Kuniharu	Kyushu University	Japan
Nakato, Michio	Hiroshima University	Japan
Ninomiya, Shinji	Hiroshima University	Japan
Nishimoto, Hitoshi	West Japan Fluid Engineering Laboratory Co., Ltd.	Japan
Nishio, Shigeru	University of Osaka Prefecture	Japan
Noblesse, Francis	David Taylor Research Center	USA
Nozawa, Kazuo	Kawasaki Heavy Industries Ltd.	Japan
Ogawa, Futoshi	Shin Kurushima Dockyard Co., Ltd.	Japan
Ogino, Shigeyuki	Sanoyasu Dockyard Co., Ltd.	Japan
Ogiwara, Seiko	Ishikawajima-Harima Heavy Industries Co., Ltd.	Japan
Ohde, Akira	Onomichi Dockyard Co., Ltd.	Japan
Ohkusu, Makoto	Kyushu University	Japan
Okamoto, Yukihiro	NKK Corporation	Japan
Okuno, Taketoshi	University of Osaka Prefecture	Japan

Orszag, Steven A.	Princeton University	USA
Park, In Kyu	Hyundai Heavy Industries Co., Ltd.	Korea
Pawlowski, Jacek S.	National Research Council	Canada
Piquet, Jean	Ecole Nationale Supérieure de Mécanique	France
Pot, Germain	Electricité de France	France
Pukhnachov, Vladislav	Lavrentyev Institute of Hydrodynamics	USSR
Reed, Hellen	Arizona State University	USA
Rood, Edwin	Office of Naval Research	USA
Saito, Fumitoshi	Imabari Shipbuilding Co., Ltd.	Japan
Saito, Kimio	Osaka University	Japan
Saric, William S.	Arizona State University	USA
Sasaki, Seniti	Nippon Kaiji Kyokai	Japan
Sasaki, Noriyuki	Sumitomo Heavy Industries Ltd.	Japan
Sawada, Shinichi	Ishikawajima-Harima Heavy Industries Co., Ltd.	Japan
Schot, Joanna W.	David Taylor Research Center	USA
Seto, Hideyuki	Mitsubishi Heavy Industries Ltd.	Japan
Shin, Mei-Shu	KRISO	Korea
Shirai, Mikito	Ishikawajima-Harima Heavy Industries Co., Ltd.	Japan
Soejima, Shunji	Mitsui Engineering & Shipbuilding Co., Ltd.	Japan
Stern, Fred	The University of Iowa	USA
Sturova, Izol'da V.	Lavrentyev Institute of Hydrodynamics	USSR
Suzuki, Kazuo	Yokohama National University	Japan
Suzuki, Toshio	Osaka University	Japan
Suzuki, Katsuo	Defense Academy	Japan
Takagi, Ken	Osaka University	Japan
Takagi, Matao	Hitachi Zosen Technical Research Laboratory	Japan
Takaki, Mikio	Hiroshima University	Japan
Tamashima, Masahiro	West Japan Fluid Engineering Laboratory Co., Ltd.	Japan
Tamura, Kinya	Mitsubishi Heavy Industries Ltd.	Japan
Tanaka, Ichiro	Osaka University	Japan
Tanaka, Hisao	Hitachi Zosen Technical Research Laboratory	Japan
Terao, Yutaka	Tohoku University	Japan
Tokuda, Kouji	Hiroshima University	Japan
Toyama, Satoshi	Ishikawajima-Harima Heavy Industries Co., Ltd.	Japan
Tsumura, Shinichi	Hiroshima University	Japan
Tzabiras, George	National Technical University of Athens	Greece
Ukon, Yoshitaka	Ship Research Institute	Japan
Uto, Shotaro	Ship Research Institute	Japan
Van Oortmerssen, G.	Maritime Research Institute of the Netherlands	Netherlands
Van, Suak-Ho	Korea Institute of Machinery & Metals	Korea
Vieillard-Baron, B.	Institut de Recherches de la Construction Navale	France
Wang, Henry T.	Naval Research Laboratory	USA
Xu, Ping	Hiroshima University	Japan
Xu, Qi	Hiroshima University	Japan
Yabushita, Kazuki	Osaka University	Japan
Yamaguchi, Kenji	NKK Corporation	Japan
Yamasaki, Shosaburo	Kobe Steel Ltd.	Japan
Yamazaki, Ryusuke	Kyushu University	Japan
Yang, Chen-Jun	West Japan Fluid Engineering Laboratory Co., Ltd.	Japan
Yang, Cheng-I	David Taylor Research Center	USA
Yang, Chi	Shanghai Jiao Tong University	China
Yasukawa, Hironori	Mitsubishi Heavy Industries Ltd.	Japan
Yim, Bohyun	David Taylor Research Center	USA
Yoshida, Yasushi	Development Institute Japan Defense Agency	Japan
Yoshihara, Hideo	Office of Naval Research	Japan
Zhao, Rong	Norwegian Institute of Technology	Norway
Zheng, Yan	Hiroshima University	Japan
Zhu, Ming	University of Tokyo	Japan

Commission on Physical Sciences, Mathematics, and Applications

Norman Hackerman (Chair), Robert A. Welch Foundation
George F. Carrier, Harvard University
Herbert D. Doan, The Dow Chemical Company (retired)
Dean E. Eastman, IBM, T. J. Watson Research Center
Marye Anne Fox, University of Texas
Gerhart Friedlander, Brookhaven National Laboratory
Phillip A. Griffiths, Duke University
Neal F. Lane, Rice University
Christopher F. McKee, University of California at Berkeley
Richard S. Nicholson, American Association for the Advancement of Science
Jeremiah P. Ostriker, Princeton University Observatory
Roy F. Schwitters, Superconducting Super Collider Laboratory
Larry L. Smarr, University of Illinois

Norman Metzger, Executive Director

Naval Studies Board

Robert J. Hermann (Chair), United Technologies Corporation
George F. Carrier, Harvard University
Seymour J. Deitchman, Institute for Defense Analyses
John F. Egan, Lockheed Electronic Systems Group
Ivan A. Getting, Los Angeles, California
Ralph R. Goodman, University of Mississippi
Willis M. Hawkins, Lockheed Corporation
David W. Hyde, Science Applications International Corporation
Sherra E. Kerns, Vanderbilt University
Ray L. Leadabrand, Science Applications International Corporation
John D. Lindl, Lawrence Livermore National Laboratory
Chester M. McKinney, Jr., Applied Research Laboratory
William J. Moran, Los Altos, California
George A. Paulikas, The Aerospace Corporation
Alan Powell, University of Houston
Robert C. Spindel, Applied Physics Laboratory
Donald L. Stivender, General Motors Corporation
J. Pace VanDevender, Sandia National Laboratories
Vincent Vitto, Lincoln Laboratory, Massachusetts Institute of Technology
George M. Whitesides, Harvard University

Navy Liaison Representatives

Frank E. Shoup III, Office of the Chief of Naval Operations
Ronald N. Kostoff, Office of Naval Research

Staff

Lee M. Hunt, Staff Director